

ECIO 2003

European Conference on Integrated Optics

Collected Manuscripts

(c) Copyright 2003 The ECIO Board. All rights reserved.

Contents

ID	Author	Title
WeP1	M. Erman	Optoelectronics industry and telecommunications market: past, present, future (plenary talk)
WeA1	Nick Borelli	Femtosecond Laser Interaction with Glasses and Crystals (invited paper)
WeA1.1	R. Osellame, G. Cerullo, S. Tacc	Fabrication of Telecom Grade Active Waveguides by Femtosecond Laser Pulses
WeA1.2	Maria Cristina Didavide, Livio C	UV Written Buried Waveguide on P-B Codoped Silica on Silicon Layer
WeA1.3	A.K.Sheridan, C.B.E Gawith, G. D	UV-Written Channel Waveguides in Ion-Exchanged Pyrex
WeA1.4	G. D. Emmerson, C. B. E. Gawith,	Direct UV Writing of Bragg Grating Channel Waveguides in a Single Step Process
WeB1	Kiyoshi Asakawa	Fabrication and Characterization of Photonic Crystal Waveguide Components and Application to Ultra-Fast Optical Signal Processing Devices (invited paper)
WeB1.1	Pierre Pottier, Iraklis Ntakis,	Photonic Crystal Continuous Taper for Efficient Coupling into 2D Photonic Crystal Channel Waveguides
WeB1.2	Ségolène Olivier1, H. Benisty1,	All-Photonic-Crystal Add-Drop Filter Exploiting Low Group-Velocity Modes
WeB1.3	YewJun Chai1, Chris Morgan1, Ric	Compression of picosecond pulses using photonic crystals
WeB1.4	V.M.N. Passaro, F. De Leonardis,	Novel Group Delay Lines Formed by Multi Quantum Well Defective Photonic Crystals
WeA2.1	J.-S. Koo, C. B. E. Gawith, V. A	Integrated Optical Structures Written in a Polymer Film By UV-Induced Refractive Index Modification
WeA2.2	K.N. Andersen, W.E. Svendsen, R.	Silicon Rich Nitride Micro-resonators
WeA2.3	O. Bertoldi1 J.-E. Broquin2, G.	Realisation of Adiabatic Transition Between Surface and Buried Ion-Exchanged Channel Waveguides Made on Glass
WeA2.4	C.Y. Tai, Bayram Unal, James S.	Self-assembled microsphere gratings on rib waveguides
WeB2.1	D.L. Boiko, G. Guerrero, E. Kapo	Homostructure and Heterostructure Photonic Crystals Based on VCSEL Arrays
WeB2.2	Mulot, M. Swillo, M. Qiu, M. Str	Investigation of Fabry-Pérot Cavities Based on 2D Photonic Crystals Fabricated in InP Membranes
WeB2.3	A. Talneau1 , M. Mulot2, S. Anan	Modal Behaviour of Single-line Photonic-Crystal Bends and Combiners on InP Substrate
WeB2.4	M. Augustin, H.-J. Fuchs, E.-B.	Efficient Waveguiding in Low Index Photonic Crystal Films
WeA3	Jesper Mørk	Optical signal processing using electro-absorption modulators (invited paper)
WeA3.1	R. Noé1, Zhan Gao2	Mach-Zehnder Lattice Based Tunable Chromatic Dispersion Compensator Design with Simplified Control and Dispersion Slope Mitigation
WeA3.2	Arkady Kaplan, Kobi Achiam	LiNbO3 Integrated Optical QPSK Modulator and Coherent Receiver
WeA3.3	G. Gilardi , L.Gobbi, A.Beretta,	A Versatile 40 GBit/s Optical Transmitter Platform for NRZ, RZ and CarrierSuppressed (CS) RZ Transmission Formats
WeA3.4	Reinhold Noé, David Sandel	Reduced Number of Control Variables for Fast Control and Zero-Mean Voltages For DC Drift Suppression in Distributed LiNbO3-based PMD Compensators
WeA3.5	S. Bhandare and R. Noé	Pushing distributed PMD compene sator performance toward highest bit rates by Lithium Niobate-Tantalate or Lithium Tantalate crystals
WeB3	Olivier Leclerc	Optical vs. electronic in-line signal processing in optical communication

		systems: an exciting challenge for optical devices (invited paper)
WeB3.1	Andrea Melloni1, Francesco Moric	Slow-wave wavelength converter
WeB3.2	Jie Hyun Lee, Yoo Hong Min, Wern	All Optical Wavelength Selective Switching Exploiting the Nonlinear Phase Shift Induced by Cascaded Sum and Difference Frequency Generation (cSFG/DFG) in a Ti:PPLN Channel Waveguide
WeB3.3	R. Hanfoug, J. J. G. M. van der	Wavelength Conversion With Polarisation Labelling for Rejection and Isolation of Signals (POLARIS)
WeB3.4	J. Slovak, C. Bornholdt, B. Sart	All-Optical 3R Regenerator Applying Compact Semiconductors for Clock Recovery and Decision
WeB3.5	Jyh-Tsung Hsieh, Jingshown Wu, S	Novel 3R Regeneration by Light-Holding SOA’s at Transparency in a Mach-Zehnder Configuration
ThP1	Jörg Schmiedmayer	Integrating light and matter wave optics on Atom Chips (plenary talk)
ThP2	Toshiaki Suhara	Quantum photonic devices: waveguide NLO devices and semiconductor lasers for generation of squeezed light and correlated twin photons (plenary talk)
ThP3	Yuzo Yoshikuni	Recent Progress of Semiconductor Integrated Optics for WDM Photonic Networks (plenary talk)
ThA1.1	Volkmar Dierolf and Christian Sa	Confocal Luminescence Microscopy: Application to Periodically Poled LiNbO3 Devices
ThA1.2	Sébastien Aubert1, Aurélien Bruy	Characterization of ion exchanged integrated lightwave devices with an apertureless scanning near-field optical microscope
ThA1.3	Nadège Courjal1 and Henri Porte2	Method for measuring frequency chirping in external Mach-Zehnder modulators
ThA1.4	Gunnar Arvidsson, Magnus Olson,	A Novel Technique For High Precision Measurement of Alignment Accuracy of Single-Mode Optoelectronic Components
ThB1	Richard V. Penty	Integrated SOA Devices for Metro System Applications (invited paper)
ThB1.1	U. Khalique1, Y.C. Zhu1, J.J.G.M	Polarization-based Integration Scheme (POLIS) for Active and Passive Components
ThB1.2	F.H. Groen1 and Y.C. Zhu2, J.J.G	Compact Polarisation Converter on InP/InGaAsP Using an Asymmetrical Waveguide
ThB1.3	D. Caprioli, J. H. den Besten, E	A 10 Gb/s Traveling Wave MZ-Modulator for Integration with a Laser
ThB1.4	S. Palmgren1,2, H. Weman1,2, A.	Single-Quantum-Wire Waveguide Modulator with High on/off Ratio and Low Voltage Swing
ThA2	Hélène Debrégeas-Sillard	Tunable semiconductor lasers for telecommuncations applications (invited paper)
ThA2.1	E.A.J.M. Bente1, Y. Barbarin1, J	Characterisation and Modelling of a Compact Multiwavelength Ringlaser
ThA2.2	Lionel Bastard1, Jean-Emanuel Br	DWDM DFB Laser Matrix Realized by Ion Exchange on Glass Substrate
ThA2.3	G. Sorbello1, S. Taccheo1, G. de	Single-Frequency Er:Yb Phosphate Glass Waveguide Laser Array
ThA2.4	S. Reza, H. Herrmann, V. Quiring	Frequency Shifted Feedback Ti:Er:LiNbO3 Waveguide Laser of Wide Tunability
ThA2.5	S.J.Hettrick, J.Wang, C.Li, J.S.	An Experimental Comparison of Linear and Parabolic Tapered Waveguide Lasers
ThA2.6	Guang-Hua Duan, Christophe Gosse	40 GHz All-Optical Clock Recovery Using Polarisation-Insensitive Distributed Bragg Reflector Laser
ThB2	R. Baets, INTEC, Ghent Universit	Photonic Crystal Integrated Optics (PCIC EU project review)
ThB2.1	Kazuya Terabe1, Shinji Higuchi1,	Nanoscale-domain Engineering

ThB3	Heinz-Gunter Bach	InP-based High-Speed Photoreceivers for Optical Fibre Communications (invited paper)
ThB3.1	Xueliang Song, Daisuke Miyashita	InGaAsP/InP Compact Monolithic SOA-Integrated Mach-Zehnder Interferometer All-Optical Switches by Single-Step Selective-Area MOVPE and their Switching Performance
ThB3.2	S. Matsuo, Y. Yoshikuni, T. Sega	A Widely Tunable Optical Filter Using Ladder-Type Structure
ThP01	A. Cucinotta1, S. Selleri1	Finite Element Analysis of Optical Notch Filters Based on Photonic Crystals
ThP02	M. Belmonte, V. Pruneri and M. O	Domain Inversion in Phase-Velocity Matched LiNbO3 Electro-Optic Modulators For Large Bandwidth and Low Driving Voltage
ThP03	M. Domenech, E. Cantelar, G. Lif	Laser Oscillation in Proton Implanted Nd:YAG Waveguides
ThP04	E. Cantelar, G. A. Torchia, J.A.	CW, Broadly Tunable, Red, Green and Blue Light Generation in Aperiodically Poled Zn-Diffused LiNbO3:Er3+/Yb3+ Channel Waveguides
ThP05	Vittorio M. N. Passaro, Daniele	Modeling of Holographic Gratings in Photorefractive Graded-index Planar Waveguides
ThP06	S.M. Kostritskii1, Yu.N. Korkish	Characterization of Static and Photorefractive Scattering in Channel LiNbO3 Waveguides Fabricated by Novel High Temperature Proton Exchange Technique
ThP07	S.M. Kostritskii1, Yu.N. Korkish	Broadband DBR Recorded Holographically into Cu-Doped Ti-Indiffused Channel Waveguide on Z-Cut LiNbO3
ThP08	Eric Cassan, Laurent Vivien, and	90°-Turns with Polarization-Independent Single-Mode Waveguide on Silicon-on-Insulator for Telecommunication Wavelengths
ThP09	Marco Wiedenhaus, Andreas Ahland	Nonlinear Algorithms for the Quantum Mechanical Simulation of Electroabsorption
ThP10	H.S. Djie, S.L. Ng, O. Gunawan,	Experimental and Theoretical Analysis of Polarization Insensitive Integrated-Waveguides Fabricated Using Ion Implantation-Induced Disordering
ThP11	M. Marangoni1, R. Osellame1, R.	Radiation to Guided Modes Power Transfer for the Characterization of Reverse-Proton-Exchanged Waveguides
ThP12	Rosa Maria Montereali, Angelo Pa	Amplified Spontaneous Emission in Broad-band Confining Embedded Strips Produced By Electron-Beam Lithography in LiF Crystals and Films
ThP13	Yuri Korkishko, Vyacheslav Fedor	Optical and Structural Properties of Proton Exchanged MgO:LiNbO3 waveguides
ThP14	Rita Asquini1, Antonio d’A	Electro-Optic Guided-Wave Router Using Nematic Liquid Crystals
ThP15	Dong Lu, Oleg V. Mishechkin, Mah	Hybrid Sol-gel Integrated Optics on High Index Substrate for Heterogeneous Integration
ThP16	H. C. Tsoi, W. H. Wong, and E. Y	Long-Period Waveguide Gratings
ThP17	Takanori Suzuki, Yutaka Shibata,	Design and Fabrication of the Small V-Bend Optical Waveguide Using an Elliptic Mirror
ThP18	P. Nagtegaele, E. Brasselet and	Anisotropy and dispersion of quadratic nonlinear properties of electrooptic azopolymer thin films
ThP19	Luca Razzari, Carlo Liberale, Il	Numerical Study of a Wavelength Converter Based on Cascaded Interactions in a PPLN Waveguide
ThP20	A. Petraru, J. Schubert, M. Schm	Epitaxial and Polycrystalline Ferroelectric BaTiO3 Thin Films Used for Optical Switching
ThP21	Joris van Lith, Paul V. Lambeck,	The Segmented Waveguide Sensor: Principle and Experiments
ThP22	Haiyan Ou	Reactive Ion Etching in Silicaon-Silicon Planar Waveguide Technology

ThP23	Andrei Tsarev, Eugeny Kolosovsky	The Multiple Channel Acoustooptic Tunable Filter With Super Narrow Optical Linewidth Based on the Set of Multi-Reflector Beam Expanders
ThP24	Pavel Capek1, Josef Schröfel1, A	Erbium Incorporation and Optical Properties of Er3+ Ions in APE Er:LiNbO3 Waveguides
ThP25	P.J. Moreira1, P.V.S. Marques1,2	Hybrid Sol-Gel Silica Channel Waveguide Bragg Grating Fabrication Using Single-Step UV Patterning
ThP26	Vladymir Shandarov, Pavel Karpus	Features of Photorefractive Gratings Recorded with Two-Color Scheme in Doubly Doped Surface Layer of a Lithium Niobate Crystal
ThP27	Carl J. Marckmann1 Rune Shim, Yi	Interpretation of High Poling Effects with Short Lifetimes
ThP28	Charles K.F. Ho, Dexter C.L. Gwe	Planar Optical Waveguides Fabricated by Sol-Gel Derived Inorganic Silicate Glass
ThP29	Andrea Melloni1,	Analysis of the Resonant Wavelength Router
ThP30	K.Brzd¸kiewicz, M. Karpierz, War	Discrete Solitons in Liquid Crystals Waveguide Arrays
FrA1	Philippe Lalanne	Bloch wave engineering for high Q’s small V’s optical microcavities (invited paper)
FrA1.1	M. Gioannini, I. Montrosset	Time Domain Numerical Model for Linear and Nonlinear Grating Assisted Codirectional Coupler
FrA1.2	Elena A.Romanova, Leonid A.Melni	Detailed Analysis of Spatiotemporal Stability of the Ultra-Short Optical Pulses Propagating in Non-Linear Step-Index Optical Waveguide
FrA1.3	Jim Katsifolis1, Laurie Cahill1,	Transition Loss in Bent Waveguides and Fibres
FrA1.4	A Al-Jarro, P Sewell, TM Benson,	Effective and Flexible Analysis for Propagation in Time Varying Waveguides
FrA1.5	Mitsuru Takenaka and Yoshiaki Na	Proposal of an All-Optical Flip-Flop Using a Cross-Coupled MMI Bistable Laser Diode
FrA1.6	Hugo J.W.M. Hoekstra, Joris van	The Spectral Decomposition Method: a Transparent Theory for Losses in Segmented Waveguides
FrB1	Wolfgang Sohler	Nonlinear Integrated Optics with Periodically Poled Waveguides in LiNbO3 (tutorial)
FrA2.1	Rumen Iliew, Christoph Etrich, U	Efficient Waveguide Bend Design in Photonic Crystals
FrA2.2	Wim Bogaerts, Peter Bienstman, R	Sidewall Roughness in Photonic Crystal Slabs: A Comparison of High-Contrast Membranes and Low-Contrast III-V Epitaxial Structures
FrA2.3	D. Michaelis1, U. Peschel2, C. W	Photonic Crystal Waveguides in Highly Dispersive Materials
FrA2.4	Manfred Hammer, Didit Yudistira	Grating Assisted Rectangular Integrated Optical Microresonators
FrB2	Koichi Takiguchi	Photonic Functional Devices Based on a Silica Planar Lightwave Circuit (invited paper)
FrB2.1	F.S. Tan, D.H. Geuzebroek, A. Dr	Design of Compact Spectral Slicers Based on Vertically Coupled Microring Resonators
FrB2.2	S. Musa, A. Borreman, A. A. M. K	Multimode Arrayed Waveguide Grating-Based Demultiplexers for Short-Distance Communication
FrB2.3	Rudolf Wessel, André Heid, Fred	Planar Lightwave Circuits for Polarisation Mode Dispersion and Residual Chromatic Dispersion Compensation at 40 Gbit/s
FrB2.4	Andrea Melloni1 and Raffaella Co	Experimental Investigation on Ring Resonator Based Filters in Sion Technology
FrA3	Falk Lederer	Ultrafast All-Optical Signal Processing in Engineered Quadratic Nonlinear Waveguides (invited paper)
FrA3.1	A. Boudrioua1, B. Vincent1, R. K	Second Harmonic Generation in He+-Implanted Oxoborates and PPLN

		Waveguides
FrA3.2	Vyacheslav Fedorov1, Yuri Korkis	Recovery of Second Order Optical Nonlinearity in H:LiNbO3 Waveguides by Reverse Proton Exchange
FrB3.1	Payam Rabiei, William H. Steier	Tunable Double Micro-Ring (DMR) Filters for Widely Tunable Lasers
FrB3.2	D.H. Geuzebroek, E.J. Klein, H.	Wavelength Tuning and Switching of a Thermo-Optic Microring Resonator
FrB3.3	Milan Hubálek, Jirí Ctyroký, Lad	Optimizing Geometry of Ring Microresonators with Respect to Bending Losses
FrPD1	M.G. Thompson1, C. Marinelli1, D	Hybrid and passive mode-locking of Quantum dot lasers at ~10 GHz
FrPD2	Dirk Taillaert and Roel Baets	A Compact Two-dimensional Grating Coupler used as a Polarization Splitter
FrPD3	H. Chong and R.M. De La Rue	Planar Photonic Crystal Microcavities for Add/Drop Filter Functionality

Femtosecond Laser Interaction with Glasses and Crystals

N. F. Borrelli and A. M. Streltsov

ABSTRACT

A brief description of the phenomenon involved in the interaction of short fs-pulses with glass is given. Multi-photon (or tunneling) electron excitation occurring in a time much shorter that the electron-hole recombination time leads to a very high electron concentration or plasma. The permanent refractive change that is produced by fs-laser exposure is related to the specific effect of this plasma decay mechanism. A number of different possible mechanisms will be compared and discussed. One can use this fs-laser derived optical phenomenon to create a number of photonic structures in 3-D which will be shown and discussed. Among those mentioned will be waveguides, directional couplers, amplifiers, and 3-D gratings. The interaction with certain single crystals will also be briefly mentioned.

Introduction

In the last few years as the result of the rapid development of mid-infrared ultra-short laser pulses (in particular Ti-sapphire laser operating at 800-nm) there has been produced an entirely new way of fabricating three-dimensional photonic structures [1-3]. These ultra-short pulses (<100fs) offer a way to obtain very high peak intensities of the order of 10^{15}W/cm^2. For example, a laser pulse with a pulse width of 100fs and pulse energy of 10μJ focused to a spot size of 5μm produces a peak intensity of that order. A unique aspect of using <100fs pulses is the way in which the interaction with transparent and absorbing materials occurs as a consequence of the pulse duration. The reason for this originates from a distinctive mechanism of the interaction with solid materials. We will discuss this point briefly in the next section

The practical use of the ultra-short laser pulse technique in material fabrication technology falls into two broad categories. The first is in the high pulse energy regime where the laser is used to physically remove material through ablation as the mode of making precise patterns. This often referred to as laser micro-machining[4]. Although laser ablation is not new, it will be shown how the use of short pulses avoids many of the problems heretofore associated with laser ablation. .

The second category is the low exposure intensity regime where the refractive index (or any other physical modification) of transparent media such as silica and other glasses can be modified by fs-laser exposure without physical or mechanical damage [1-3] One distinct advantage of this technique is that because of the highly nonlinear nature of the laser/material interaction, one can produce patterns inside a body on a three-dimensional way.

We will be interested here in the lower fluence interaction with transparent media such as silica where the refractive index can be altered up to values of 0.01.[1] We will present the results of applications and devices based on this phenomenon.

Induced Refractive Index

The unique as aspect of the interaction of fs-laser pulses with glass is the ability to produce permanent refractive index changes without physical damage. In other words, up till now we have been describing phenomena which cause significant physical

changes, like ablation or the formation of micro-voids. An example of an over exposed track, where physical damage is clearly observed is shown in FIGURE 1. For the most part these phenomena are ultimately driven by a thermal mechanism. What we are to discuss below is not likely thermally induced, although this point has been argued. Nonetheless, there appears to be in addition some sort of structural change that is discernible only through a change in the refractive index. This ability has led to a number of very interesting suggestions and demonstrations for optical devices. The idea of a 3-D structure of coupled light guides is one of the more fascinating suggestions.

Experimental

A Spectra Physics Spitfire amplifier seeded by the oscillator is typically the source of 800-nm, 40-100fs pulses having a repetition rate of 20 kHz and energies up to 30 μJ. Mitutoyo objectives, typically 0.26 NA are used and they give a good compromise between a reasonably tight focusing and about 3-cm long working distance enabling to fabricate waveguides in thick samples. There are essentially two writing methods, the first is the "longitudinal" writing technique when the sample is traversed parallel to the optical axis of the beam, while the other is the "top writing " method. These are depicted in FIGURE -2a and 2b. In either case the positioning of the beam is accomplished by a three-dimensional translation stage usually with speeds ranging from 1 μm/s to 1 mm/s. The longitudinal writing method has the advantage of producing a cylindrical profile compared to an elliptical one in case of top-writing scheme.

Results

Waveguide-like patterns have been written in silica and other glasses by both methods shown in FIGURE -2.[1-3,5] The index profile of a waveguide written by the longitudinal method is shown in FIGURE -3.[3]. The dependencies of the Δn magnitude on the laser-pulse energy have been measured and the typical curve is presented in FIGURES.-4a for SiO2 irradiated by 800-nm pulses. The functional dependence of the induced index change on translational velocity is shown in FIGURE 4b.[3] For the fixed velocity of 10 μm/s the refractive-index increase in fused silica is saturated at pulse energies around 0.75 μJ and then decreases slightly. Visual inspection of light-coupling into the waveguide written either with pulse energies in excess of 1 μJ or at translation velocities below 5-10 μm/s showed the presence of scattering centers along the written track that lead to losses. This appears to be the result of physical damage

Discussion of Physical Mechanism for Index Change

The physical origin of the refractive index change that can be produced in glass by fs-laser exposure is not really well understood. The exposures that are being used are well below the estimated physical damage thresholds, yet some sort of permanent alteration of the refractive index is occurring. Below we are examining the effects that may cause the increase of the refractive index in glasses as a result of irradiation by femtosecond laser pulses.

Thermal Model

Although the explicit thermal mechanism is not known, it is thought to involve the local rapid heating of a small volume of the glass at the focal spot. Heating the glass and freezing in the high temperature state could produce a lowering of an index, instead of an increase. However, one might imagine a shock wave generated by the rapid expansion leading to compression and an increase of refractive index. [2].

Streltsov et al [3] measured the absorbed energy from fs- laser pulses that were focused inside the bulk of the sample, which was constantly translated so not to maintain the focus in the same spot of the sample. The energy after exiting the sample was monitored relative to the input. They then modeled the thermal situation corresponding to the experimental exposure conditions using a finite-element heat diffusion equation with a heat source term due to the absorption added appropriate to the pulse energy, pulse duration, repetition rate, and translational speeds. In the case studied with a 20kHz repetition rate, the time between pulses was sufficiently long relative to the thermal diffusion time (around 1 μs) so that only one pulse does the heating. Since the translation speed is slow in comparison to the repetition rate, the spot is relatively fixed.

The temperature rise was calculated using the absorbed energy that was obtained from the measured value of the absorption coefficient. On the basis of the absorbed energy data and the thermal model, they were able to make an estimate of the temperature rise associated with experimental exposure. This is shown as the dashed line in Figs. 4b for silica. Although, the predicted temperature rise is significant and seems to track the

index change initially, it is nonetheless difficult to conclude on the basis of these data that the temperature is the dominant parameter.

Color Center Model

It has been suggested that the possible source of the induced refractive index change is that where the effect of the radiation is to produce color centers in sufficient number and strength as to alter the index through a Kramers-Kronig mechanism. This has been a proposed mechanism for the index change produced by deep-UV excitation of the Ge-doped silica fibers resulting to fiber Bragg gratings [6]. Streltsov et al[3] measured the dominant color center produced by the fs-laser exposure is shown (i.e. in the case of silica it was the Si E' center). The measured results indicate that color centers of the order $3x10^{19}cm^{-3}$ are being produced. This is to be compared to the Ge-doped silica case where the order of $10^{17}/cm^3$ centers are produced corresponding to refractive index changes of 10^{-3}.

They used the comparison of annealing behavior to learn if the color centers and the induced refractive index might have a common origin. In Fig.-5 is plotted the normalized induced refractive index change as a function of temperature for silica and compared it to the normalized E' concentration. The color center signal is seen to diminish at a faster rate with annealing temperature compared to the induced refractive index change. On the other hand, different thermal stability notwithstanding, the positive argument for the color center origin for the induced refractive index is that because of the high electron density produced by the fs-laser exposure there are sufficient trapped species (color centers) created to produce the index change via Kramers-Kronig.

Structural Change Model

There is the possibility that induced refractive index changes derive from some sort of structural change which in turn produces an index change. An example of this would be deep-UV induced density changes that have been observed in silica and other binary systems [7]. In the 800-nm laser exposure case we would appeal to a multi-photon excitation of the same phenomenon as observed with deep-UV exposure. A representative set of stress birefringence patterns is shown in Fig. 6a for writing speeds of 10-100 μm/s at pulse energy of 1μJ. The scan of the measured retardance for a 0.5-mm sample thickness is shown in FIGURE. 6b. the resulting refractive index change calculated from the measured birefringence as a function of the writing speed for two exposure energy is an order of magnitude smaller indicating that densification alone can not account for the entire effect.

There is another study alluding to fs-laser-induced structural changes evident from change in the Raman spectrum [8] (see discussion and references therein). Raman spectrum peaks at 490 cm^{-1} and 605 cm^{-1} have been correlated to structural features that are changing with exposure. On the other hand, Streltsov[3] using a micro-Raman measurement directly examined four tracks each corresponding to different exposure energy ranging from 1-4 μJ. They found, only at the highest energy of 4μJ was there any evidence of a change in the Raman spectrum. On the other hand, measurable refractive index changes of $>10^{-3}$ was obtained for all the tracks although the track written at 4 μJ had a visible mechanical damage

fs-laser Interaction with Single Crystals

Although one can easily damage single crystals with fs-laser exposure, it is not generically true that one can induce refractive index change as one can with glass. A simple explanation for this is that crystals have fewer structural degrees of structural freedom. Whereas a glass structure can rearrange slightly to accommodate some perturbing structural change produced by the exposure, a crystal cannot do so without some catastrophic consequence. Nonetheless, Streltsov[9] has been able to produce an index change without any evidence of physical damage in single crystal CaF_2, quartz, and $LiNbO_3$. In the case of the former two, one sees a decrease in the refractive index with exposure. Electron microscopy shows the absence of a distinct diffraction pattern in the exposed region indicating a high degree of disorder. This disorder could arise from a high density of laser-induced point defects, for example. In the case of $LiNbO_3$ the situation seems more complicated in that the point defects have not been observed.

Applications

Photonic Structures

The induced index change that can be produced by controlled fs-laser exposure has been used to produce a number of novel structures that could have photonic device implications. The general view is that it extends one's ability to create index patterns in real 3-D dimensions, like a 1cm cube. . The optimum lens used has an NA of the order of 0.25 and a working distance of around 20mm. In the following sections we will review the structures that have been made and their performance.

The first optical structure that was made utilizing the fs-laser exposure-induced refractive index change was an optical waveguide embedded in a piece of silica, or glass. Hirao et. al[1] were the first to report writing such structures. They used an amplified 810-nm Ti-sapphire laser with 120fs operating at 200kHz with an average power of 1W. A 5-mm beam was focused using a 5-20X microscope objective to a moving XYZ stage. They were able to write measurable tracks in a wide variety of glasses such as silica, fluoride glasses, lead-silicate and even a sulfide glass using this technique.

Homoelle et al [5] reported on a study of the induced refractive index of silica and boron-doped silica as a function of writing fluence and speed. The method used to estimate the refractive index of the waveguide was to measure the NA from the far-field pattern. Hirao et al [1] reported losses as low as 0.1db/cm, but without any description of the method by which it was obtained.

If one were to implement a true 3-D structure using the fs-laser technique one would need to make directional couplers and gratings to direct the light from one part of the 3-D structure to another. Hoemelle et al[5] were the first to demonstrate a Y-coupler. .The structure was made using a 60fs pulse at 1 μJ with a writing speed of 30 μm/s. An Ar-laser was used to show the relative coupling efficiency. More recently Streltsov et al [11] wrote a directional waveguide structure and measured the splitting ratio to be near 3db. Their results are indicated in FIGURE 7.

A more ambitious 3-D structure is shown in FIGURE 8[11]. Here a central straight waveguide is coupled to two adjacent guides as shown. When light is input into the central guide one can see equal amount of light in the two adjacent guides as shown in (a).When light is entered through one of the adjacent guides, one can see light coupled to the central guide and only a very weak amount to the other adjacent guide as expected. This result is shown in (b).

Optical Storage

There have been a few attempts to utilize the ability to produce highly spatially localized optically altered regions as a basis for a 3-D memory. Glezer et al [12] showed the results of patterned damage in a cube of fused silica using a 0.5μJ, 100fs pulse focused through a 0.65 NA microscope objective. The bit is read by use of transmitted light in a microscope with a 0.95 NA objective. The spacing between bits was 2m. The spacing between recorder layers was 15μm.

The other attempts have proposed to use a photo-thermal material as the recording medium. By photo-thermal is meant that the initial exposure initiates the effect in the material, but the index change is not manifest until a subsequent thermal treatment is performed. Streltsov and Borrelli[13] used a Ag-Ce photosensitive glass using exposure at 800nm pulses of 30fs and 1nJ pulse energy. They used a shutter so to make distinct exposure spots as would be the case for a memory application. The exposure pattern in a given plane is shown in FIGURE -9a. The dots correspond to the subsequently thermally formed NaF phase. FIGURE -9b shows the developed pattern looking in from the side.

The length of the NaF-containing region comes from the Rayleigh range of the focusing objective. In FIGURE 9c is shown the diffraction pattern

References

1) K. Miura, J. Qui, H. Inouye, T. Mitsuyu, and K. Hirao, Photowritten optical waveguides in various glasses with ultrashort pulse laser, Appl. Phys. Lett. **71**(23), 3329-3331,(1997) and K. Hirao and K. Miura, "Writing waveguides and gratings in silica and related materials by a femtosecond laser" J. Non-Crystalline Sol., **239**, 91-95, (1998), and
2) C.B. Schaffer, A. Brodeur, and E. Mazur, "Laser-induced breakdown and damage in bulk transparent materials induced by tightly focused femtosecond laser pulses", Measurement Science and Technology, **12**, 1784-1794, (2001)
3) A. M. Streltsov and N. F. Borrelli, "Study of fs-laser-written waveguides in glasses,"JOSA, **19**(10), 2496-2504, (2002)
4) X. Liu, G. Mourou, "Ultrashort laser pulses tackle precision machining," Laser Focus World, 101-118, August 1997
5) D. Homoelle, S. Wielandy, A. L. Gaeta, N. F. Borrelli,and C. Smith, Infrared photosensitivity in silica glasses exposed to femtosecond laser pulses," Opt. Lett., **24**(18),1311-1313,.(1999)
6) K.O. Hill and G. Meltz, J. Lightwave Techn., "Fiber Bragg grating technology fundamentals and overview", **15**(8), 1263-1267, (1997)
7) N. F. Borrelli, C. M. Smith, and D. C. Allan, "Excimer-laser-induced densification in binary silicate glasses," Opt. Lett. **24**(20), 1401-1403, (1999)
8) J. Chan, T. Huser, S. Risbud, and D. Krol, "Structural changes in fused silica after exposure to focused femtosecond laser pulses", Opt. Lett., **26**(21), 1726 (2001)
9) A. M. Streltsov, private data

10) A. M. Streltsov and N. Borrelli, "Fabrication and analysis of a directional coupler written in glass by nanojoule femtosecond laser pulses", Optics Letters, **26**(1), 42-43, (2001)

11) A. M. Streltsov, and N. F. Borrelli, Characterization of laser-written waveguides in glasses. OSA Anuual meeting, 2001, ThAA4.

12) E. N. Glazer, M. Milosavljevic, L. Huang, R. J. Finlay, T-H Her, I. P. Callan, and E Mazur, Opt. Lett. **23,** 2023, (1996)

13) A. M Streltsov and N. F. Borrelli, private data.

FIGURE CAPTIONS

Figure 1 Photomicrograph of light propagating through a damaged fs-laser written waveguide where an excessive dose was used.

Figure 2 Schematic of the waveguide writing methods; (a) longitudinal or axial writing technique, (b) top-writing set-up.

Figure 3 Typical refractive index profile for a fs-laser-written wavguide.

Figure 4 Dependence of induced refractive index change in silica (HPFS^{tm}) on a) translation velocity with fixed pulse energy 1 μJ and b) on laser pulse energy with fixed velocity 10 μm/s (the dotted line is the estimated temperature rise, see text)

Figure 5 Annealing temperature dependence of normalized SiE' color center defect concentration, circles compared to measured induced refractive index, triangles.

Figure 6 (a) stress birefringence profiles of exposed tracks. The photograph shows the intensity pattern under crossed polarizers, and (b) measure of the birefringence along the dotted line as shown..

Figure 7 (a) Directional coupler pattern written with 30fs 2.5nJ pulses at a speed of 10μm/s, (b) near field output, (c) far field output.

Figure 8 Writing pattern for 3-D coupler. Output as indicated by the arrows.

Figure 9 Writing a 3-D pattern in a photosensitive glass, (a) microscope picture of developed pattern, (b) side view of developed pattern, (c) diffraction pattern from structure.

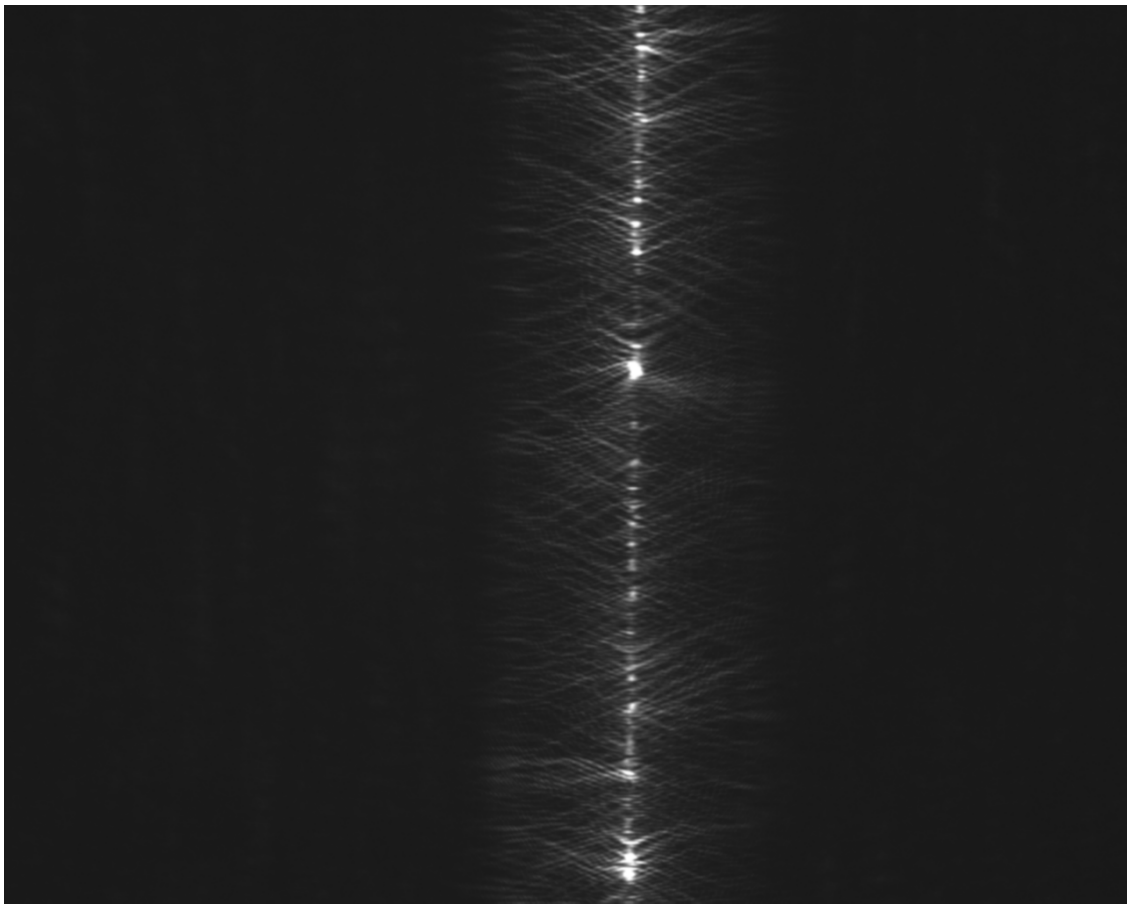


Fig. 1

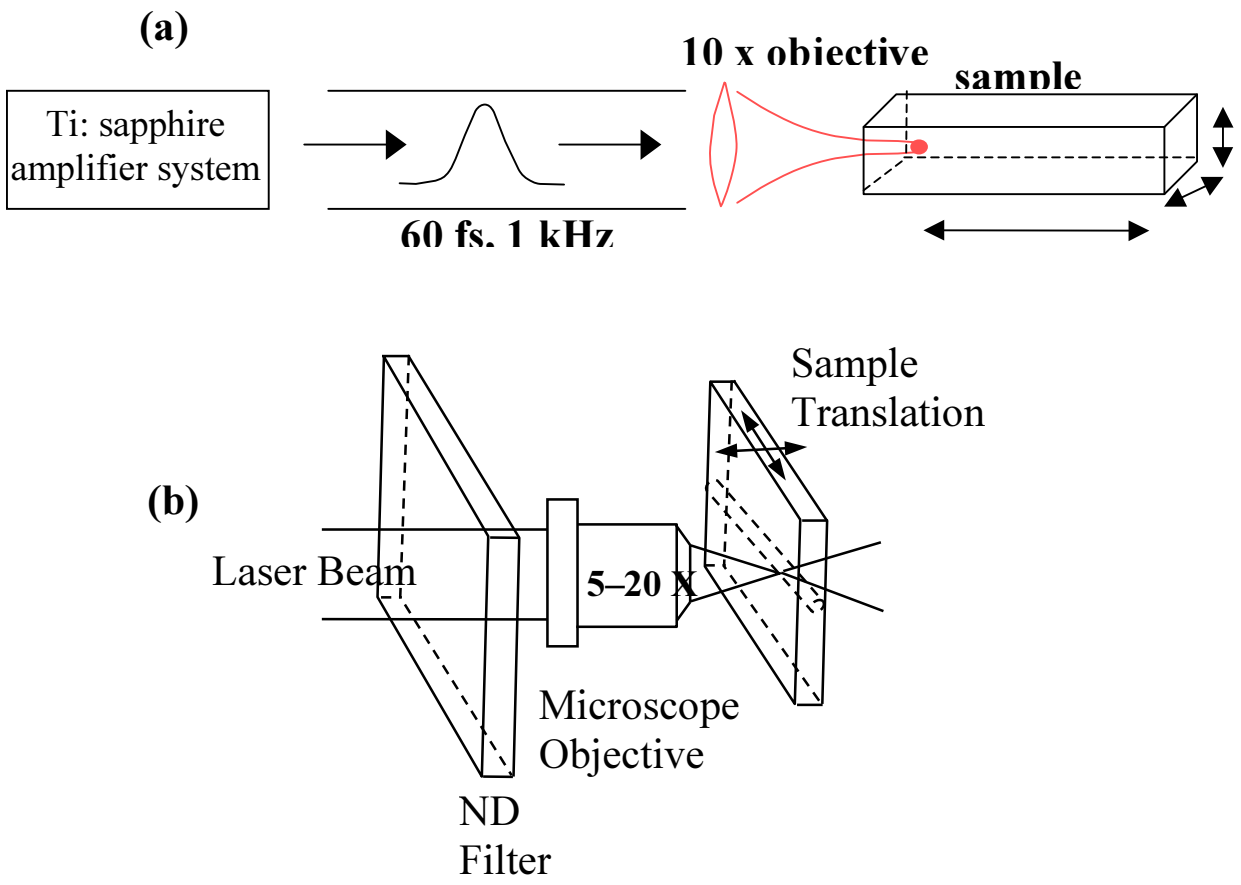

(a)
Ti: sapphire
amplifier system
10 x objective
sample
60 fs, 1 kHz
(b)
Laser Beam
5–20 X
Sample
Translation
Microscope
Objective
ND
Filter

Fig. 2

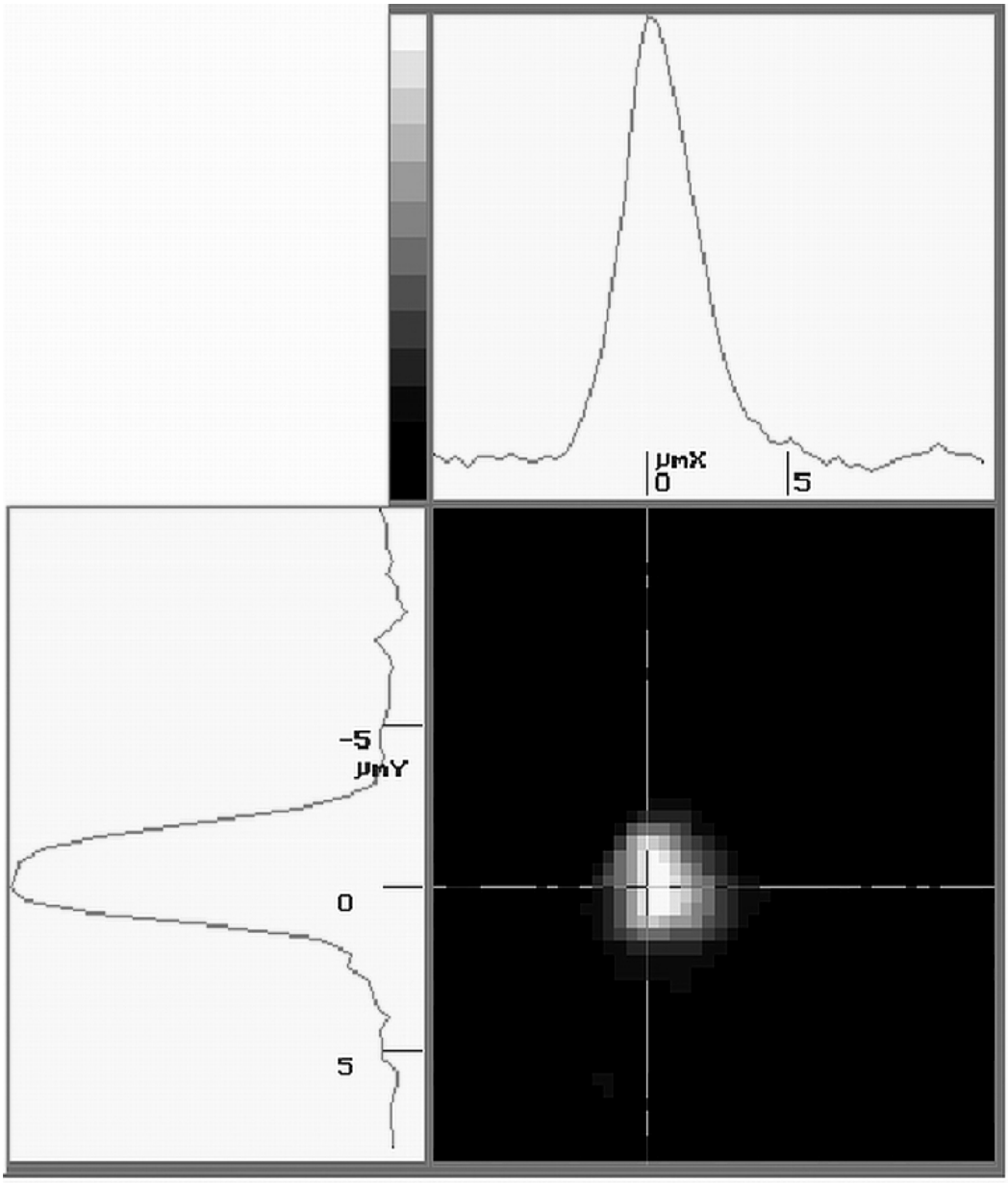
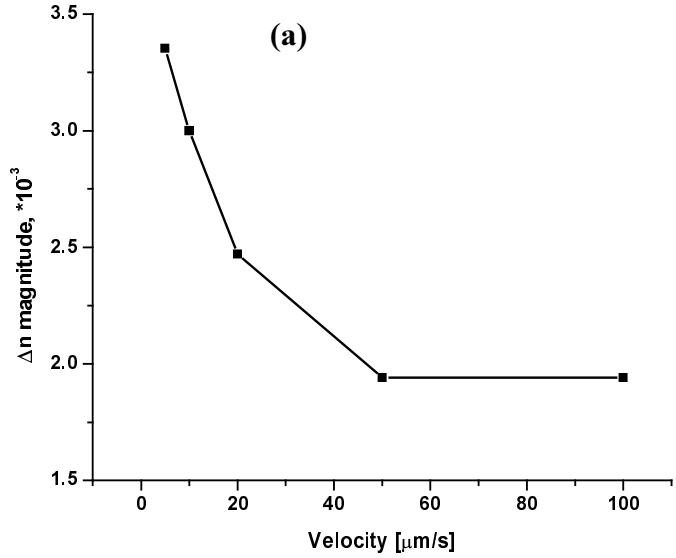


Fig. 3


(a)
3.5
3.0
2.5
2.0
1.5
Δn magnitude, *10^-3
0
20
40
60
80
100
Velocity [μm/s]

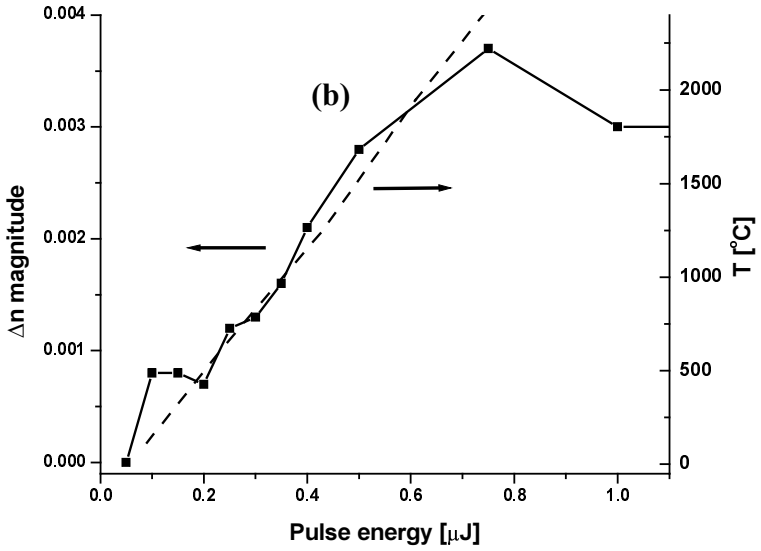

(b)
0.004
0.003
0.002
0.001
0.000
Δn magnitude
2000
1500
1000
500
0
T [°C]
0.0
0.2
0.4
0.6
0.8
1.0
Pulse energy [μJ]

Fig. 4

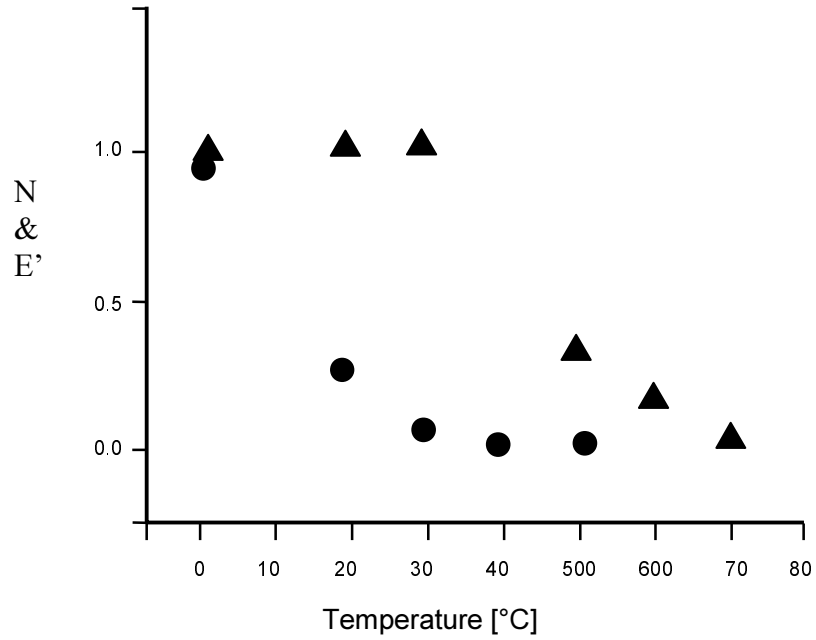
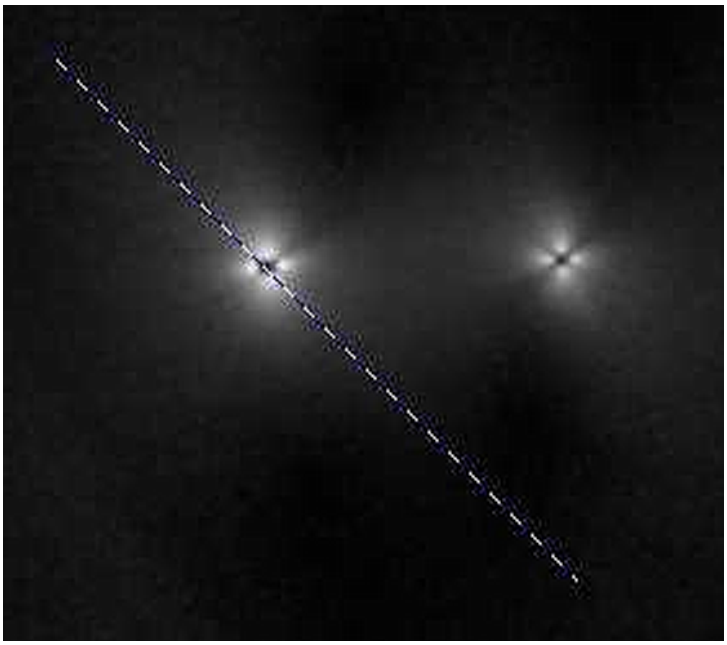
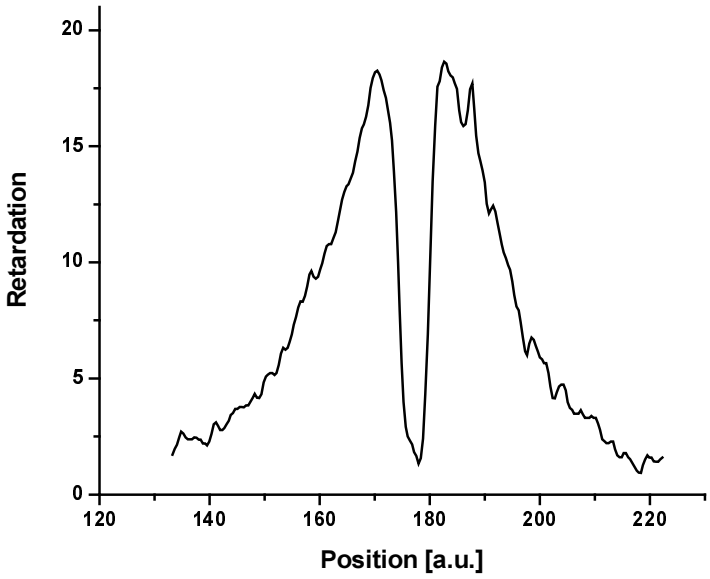


Figure 5



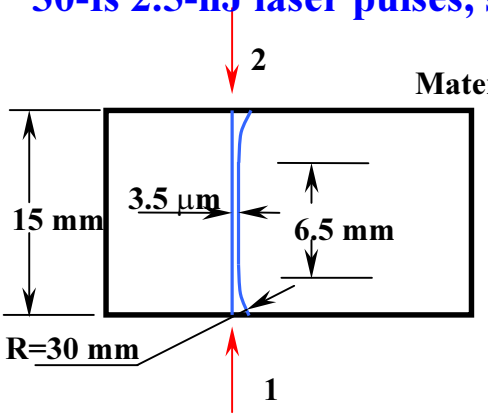
(a)

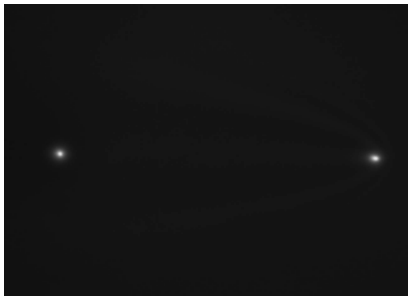


(b)

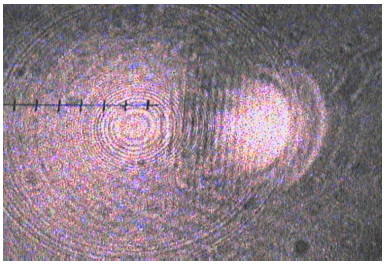
Fig. 6

Directional coupler written by 400-nm 30-fs 2.5-nJ laser pulses, speed - 10 μm/s

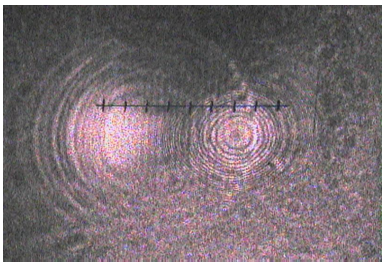




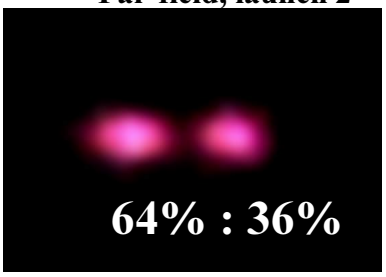
Micrograph, 50x objective
Spot dia. - 3 μm
(Looking in direction "1", while illuminated by the beam "2")



Far-field, launch 1



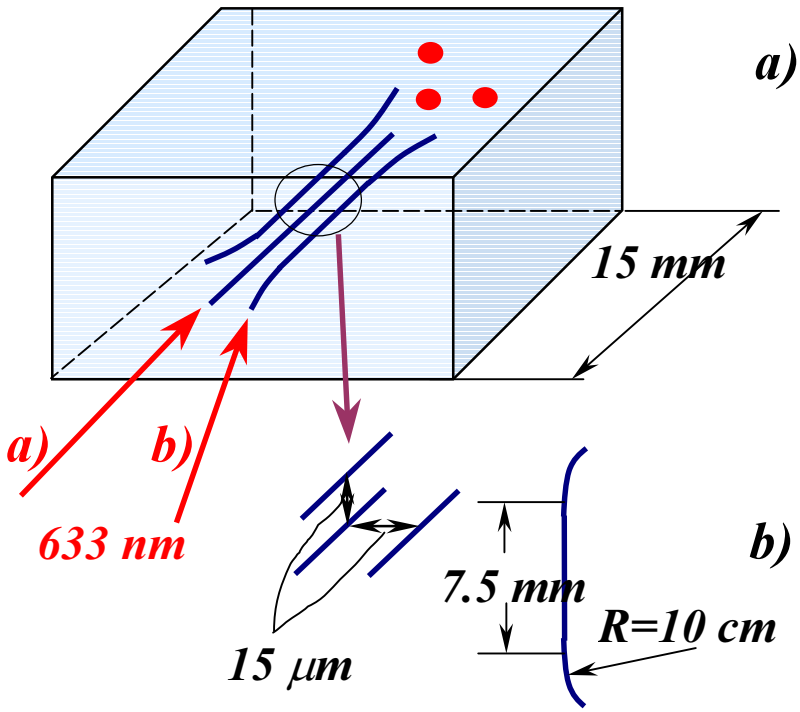
Far-field, launch 2

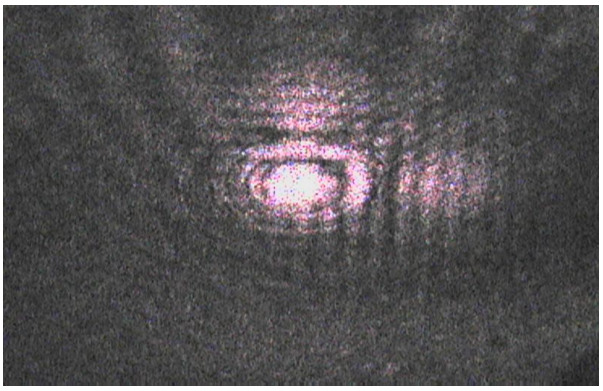


Far-field, closer dist., launch 2

Fig. 7

Fig. 8 *"3-D coupler" in SiO_2*







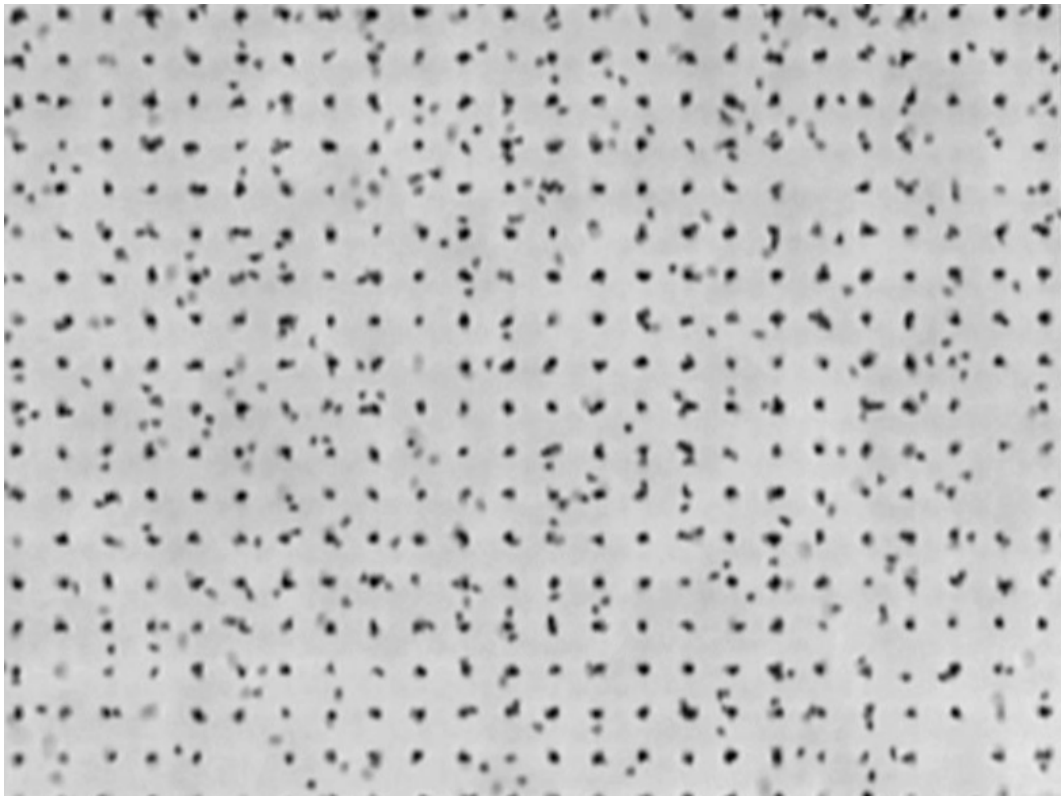


Fig. 9a

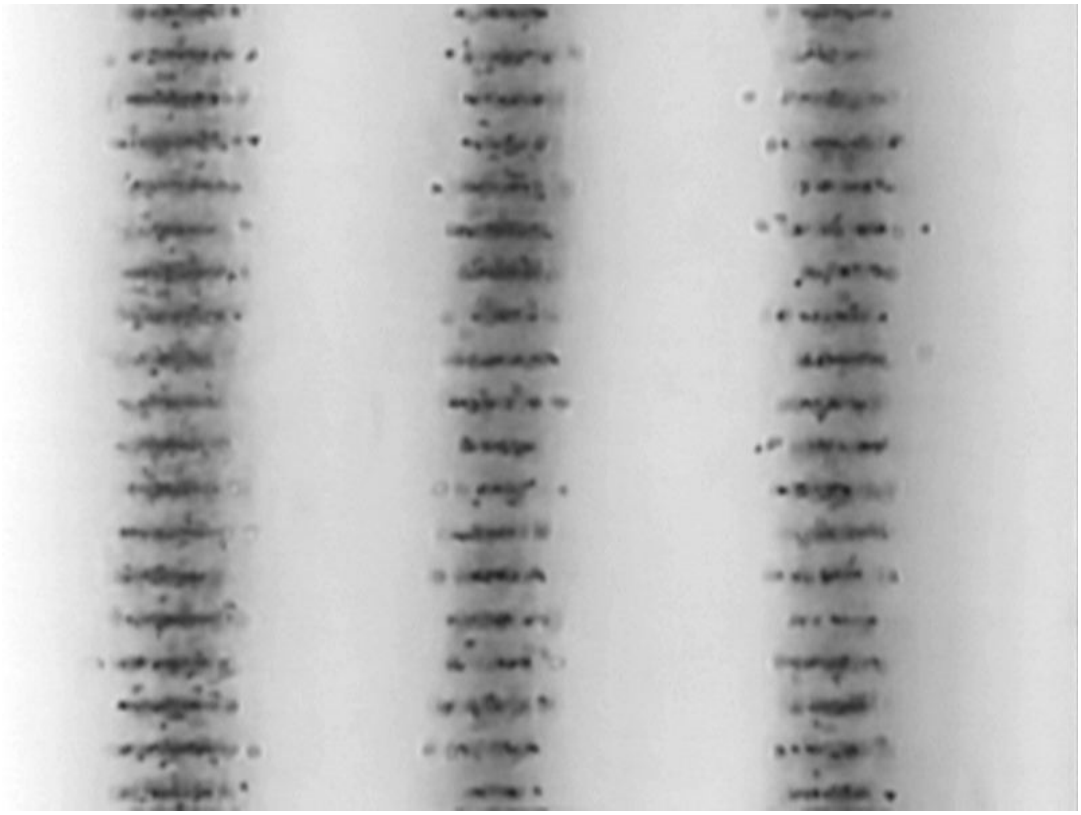


Fig. 9b



Fig. 9c

Fabrication of Telecom Grade Active Waveguides by Femtosecond Laser Pulses

R. Osellame, G. Cerullo, S. Taccheo, M. Marangoni, D. Polli, P. Laporta, S. De Silvestri, R. Ramponi

INFM, Dipartimento di Fisica-Politecnico and IFN-CNR
P.zza L. da Vinci, 32, 20133 Milano, Italy
e-mail: roberto.osellame@polimi.it

High quality waveguides are fabricated in Er:Yb-doped glasses by means of femtosecond laser pulses. Shape control of the transverse profile and optical gain in the whole C-band are demonstrated in single-mode active waveguides.

Keywords: Integrated optics, active waveguides, laser micromachining

Introduction

Permanent modifications of the refractive index in transparent materials can be obtained by tightly focusing femtosecond laser pulses [1, 2]. A hot electron plasma is generated by a combination of multiphoton absorption and avalanche ionization; transfer of the plasma energy to the lattice allows to increase the refractive index in a small volume of the material surrounding the focus [3]. Exploiting this index gradient, a wide variety of waveguide devices, both active and passive, can be produced [4, 5]. Advantages of the femtosecond technique with respect to other standard techniques, such as ion exchange or glass on silicon, are the capability of direct device writing without any photolithographic process and the possibility of fabricating three-dimensional waveguide structures.

Two laser systems can be used for waveguide fabrication: low repetition rate (1-100 kHz) amplified Ti:sapphire systems, with pulse energy of a few μJs, and high repetition rate (5-20 MHz) long cavity Ti:sapphire oscillators [6, 7], with pulse energy of a few tens of nJs. In the latter case very high processing speeds are possible, but the short working distances required by tight focusing limit the flexibility and the three-dimensional capabilities. For the low-frequency systems, two different writing geometries are possible: longitudinal, in which the sample is translated along the beam propagation direction, and transverse, in which the sample is translated perpendicularly to the beam propagation direction. The longitudinal geometry produces intrinsically symmetric waveguides, but their length is limited by the focal length of the focusing objective and their quality is degraded by spherical aberrations, which vary with the depth of the focus inside the glass. The transverse geometry provides more flexibility to the system and allows to write waveguides of arbitrary length, but gives rise to an intrinsic asymmetry in the waveguide cross section. This asymmetry becomes particularly severe when the waveguide dimensions are increased, as required to achieve waveguiding at 1.5 μm, thus greatly reducing the efficiency of fiber butt coupling in conventional telecom setups.

The novel approach that we are proposing is based on astigmatic shaping of the femtosecond writing beam, which allows both the elimination of the waveguide asymmetry in the transverse geometry and the control of its size. We apply this method to the fabrication of waveguides in erbium-ytterbium doped glasses and demonstrate single-mode waveguiding and amplification in the telecom window at 1.5 μm.

Nonlinear absorption modeling

In low repetition rate systems, as the one we are using, the local index gradient is produced essentially by the single pulse and cumulative effects can be neglected. To determine the size and shape of the material volume modified by the femtosecond pulse, one can, to a first approximation, calculate the density profile of free electrons *n(t)* generated by the ultrashort pulse inside the medium and assume that the refractive index profile follows the electron density profile. The evolution of *n(t)* in a medium exposed to an intense laser pulse can be described by the following rate equation [8]:

$$\frac{dn}{dt} = \alpha I(t) n(t) + \sigma_k I^k(t) \qquad (1)$$

where a is the avalanche coefficient, s_k is the k-photon absorption coefficient, and $I(t)$ is the pulse temporal profile. k is chosen as the smallest integer such that k times the photon energy exceeds the bandgap of the material. By solving (1) in different points of the focal volume and plotting the asymptotic value $n(\infty)$ as a function of x,y,z, one can obtain a map of the free electron density generated inside the material. The simulations presented in this work have been calculated by using the parameters of a barium aluminum borosilicate glass (k = 3, a = 1.2 cm^2/J, $s_3 = 7\times10^{17}$ cm^{-3} ps^{-1} $(cm^2/TW)^3$) [8].

Set-up and experimental results

We have experimentally demonstrated the above described technique by fabricating active waveguides in erbium-ytterbium doped glass substrates. We have used a standard amplified Ti:sapphire laser (model CPA-1 from Clark Instrumentation), generating 150-fs pulses at 1 kHz repetition rate at the wavelength of 790 nm. The beam had a nearly TEM_{00} symmetric transverse profile and energies ranging between 0.5 and 5 μJ were used for the micromachining. The experimental setup is shown in Fig. 1.

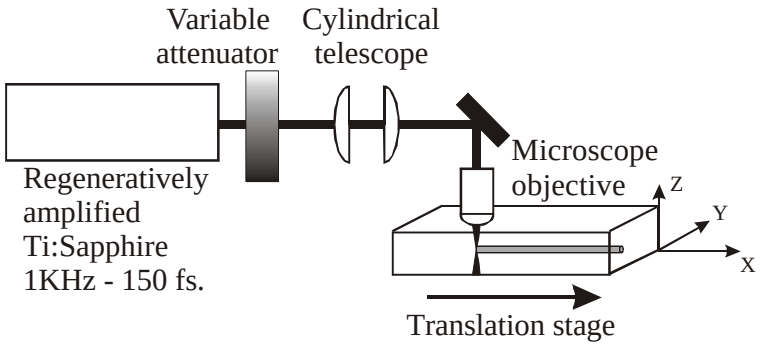


Figure 1. Setup for waveguide writing.

The laser beam was focused by a long working distance 20× microscope objective, with 0.3 numerical aperture. Waveguides were written in a 25-mm long phosphate glass base, doped with both Er and Yb with a total absorption of ≈5.5 dB at 1534 nm and ≈37 dB at 976 nm.

The first waveguides have been realized without the cylindrical telescope (see Fig.1). Figure 2a shows a microscope image of the exit face of a waveguide manufactured by 0.5 μJ pulses focused to a waist of w_0 = 3 μm, together with the simulation obtained from the previously described model.

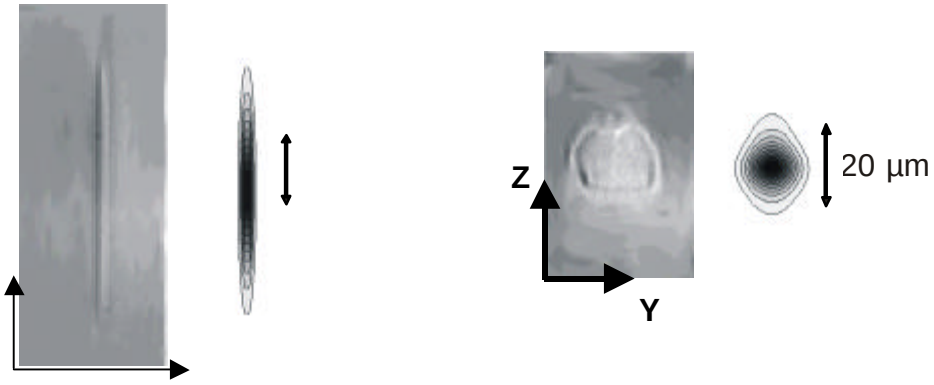


Figure 3. Comparison between microscope images of the end face of the waveguides and simulated electron density distributions for a standard (a) and an astigmatic (b) laser beam; see text for focusing conditions.

Two features are important: (i) the profile is strongly asymmetric, extending over less than 3 μm in the *y* direction and over 60 μm in the *z* direction, causing highly inefficient coupling to standard telecom fibers; (ii) the *y* extent of the profile is too small to support a mode at 1.5 μm. The reason for this asymmetry is essentially due to the fact that the waveguide dimension in the *y* direction is related to $2w_0$, while the *z* extension scales as twice the Rayleigh range of the Gaussian beam, $z_R = \frac{\pi w_0^2}{\lambda}$. To increase the waveguide symmetry without further decreasing the *y* dimension, one needs to decrease z_R independently from w_0. Here we propose to use an astigmatic beam to independently control the *z* and *y* size of the waveguide transverse profile.

In the transverse writing geometry the size of the beam along the *x* direction does not influence the waveguide size, because it is the direction along which the sample is translated (see Fig. 1), so that a lower writing velocity can compensate for a tighter focusing. We can exploit this fact to focus very tightly in the *x* direction so as to reduce the *z* waveguide extension by decreasing z_{Rx}, while simultaneously choosing the focal spot size in the *y* direction to optimize the waveguide *y* dimension. To achieve perfect circularity, one needs to increase the ratio w_{0y}/w_{0x} to about 10. A simpler approach consists in slightly offsetting the two waist positions along *z*, in this case the waveguide cross section becomes nearly perfectly symmetrical with w_{0y}/w_{0x} of about 3 and a z_0 offset of about 200μm (Fig.2b) [9]. To produce the astigmatic focus, the beam size along the y direction was reduced by a cylindrical telescope, providing a magnification by a factor 2.5 in the focus of the objective. The relative position of the waists along the *z* direction was finely controlled by translating one of the cylindrical lenses.

We have tested the performance of the waveguides at the wavelengths of 0.633 μm and 1.5 μm. The waveguide in Fig. 2b is single-mode at 1.5 μm. By a comparison between the mode profiles of the waveguide and of the standard telecom coupling fiber we estimated coupling losses of 2.4 dB; a measurement of the transmitted power allowed to evaluate propagation losses of 0.6 dB, corresponding to 0.24 dB/cm. Symmetric waveguides obtained with this technique exhibited enhancement and internal gain when used in a standard optical amplifier setup [10], but due to the very high Yb doping

only short waveguide can be pumped in their entire length. Optical gain results for a 9mm sample are reported in Fig. 4.

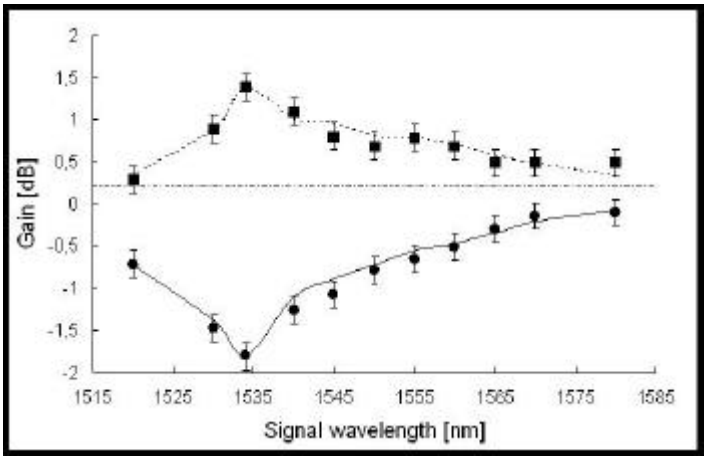


Figure 4. Absorption and optical gain for a 9mm long waveguide in the telecommunication C-Band.

It is worth noting that for the first time optical gain has been demonstrated in the whole C-band for a waveguide fabricated by means of femtosecond laser pulses. Despite further optimization of the Er:Yb doping is needed, this result is very promising in view of the realization of waveguide amplifiers and lasers with this technique.

Conclusions

A novel approach to waveguide writing with femtosecond pulses based on astigmatic beam focusing has been introduced and experimentally demonstrated. By controlling both the spot size asymmetry and the relative position of the beam waists, we can achieve symmetric waveguides which are single mode at the optical communication wavelength of 1.5 μm. For the first time optical gain has been observed on the whole C-band, with 1.4 dB peak value, in a 9mm waveguide written with femtosecond laser pulses.

[1] K.M. Davies, K. Miura, N. Sugimoto, and K. Hirao, *Opt. Lett.* **21**, 1729 (1996).
[2] D. Homoelle, S. Wielandy, A.L. Gaeta, N.F. Borrelli, and C. Smith, *Opt. Lett.* **24**, 1311 (1999).
[3] J.W. Chan, T. Huser, S. Risbud, and D.M. Krol, *Opt. Lett*. **26**, 1726 (2001).
[4] Y. Sikorski, A.A. Said, P. Bado, R. Maynard, C. Florea, and K.A. Winick, *Electron. Lett*. **36**, 226 (2000).
[5] A.M. Streltsov and N.F. Borrelli, *Opt. Lett*. **26**, 42 (2001).
[6] C.B. Schaffer, A. Brodeur, J.F. Garcia, and E. Mazur, *Opt. Lett*. **26**, 93 (2001).
[7] K. Minoshima, A.M. Kowalevicz, I. Hartl, E.P. Ippen, and J.G. Fujimoto, *Opt. Lett.* **26**, 1516 (2001).
[8] M. Lenzner, J. Krueger, S. Sartania, Z. Cheng, Ch. Spielmann, G. Mourou, W. Kautek, and F. Krausz, *Phys. Rev. Lett.* **80**, 4076 (1998).
[9] G. Cerullo, R.Osellame, S. Taccheo, M. Marangoni, D. Polli, R. Ramponi, P. Laporta, S. De Silvestri, *Opt. Lett.* **27**, 1938 (2002).
[10] R. Osellame, S. Taccheo, G. Cerullo, M. Marangoni, D. Polli, R. Ramponi, P. Laporta, S. De Silvestri, *Electron. Lett.* **38**, 964 (2002).

UV Written Buried Waveguide on P-B Codoped Silica on Silicon Layer

Maria Cristina Didavide, Livio Cognolato, Oriana Rossotto
Agilent Technologies Turin Technology Centre, Via Reiss Romoli 274, 10148 Turin, Italy
mariacristina_didavide@agilent.com, oriana_rossotto@agilent.com

Keywords: UV written waveguides

Introduction

Several years ago much attention has been devoted to processing of the UV induced refractive index change in silicate glasses [1] and its application, especially for Fiber Bragg Gratings (FBGs) fabrication. UV writing can strongly simplify the fabrication process of thin film photonics devices, because several complicated processing steps like photolithography and reactive ion etching may be bypassed. In recent years directly UV written planar waveguides were demonstrated in photosensitive germanium doped silica thin films [2], followed by UV written waveguide devices such power splitters and directional couplers. In this paper we demonstrate the UV photoinduction of singlemode buried waveguides through the metallic mask and UV excimer laser beam on Boron-Phosphorous codoped silica on silicon. Refractive index profiles of the written waveguides have been deduced from the measure of the near-field intensity field distribution of guided modes.
Low insertion loss (<0.5 dB/cm, including the propagation loss and the coupling loss) waveguides have been obtained.

Experiment

The samples used for UV writing consist of three layers buffer/core/uppercladding grown by Low Pressure Chemical Vapour Deposition (LPCVD) for the buffer and core layers, Plasma Enhanced Chemical Vapour Deposition (PECVD) for the uppercladding, on silicon 6 inches wafers. The buffer layer is a 15 μm of undoped silica, the core layer is a 6.5 μm of a codoped Boron-Phosphorous silica, Boron has been added to have an index matched layer with the buffer and the uppercladding that is a 10 μm of undoped silica. Prism coupling technique has been chosen to measure @ 1.55 μm the refractive index of three layers that are respectively 1.4444, 1.4434, 1.4396.
Straight waveguides have been written into the photosensitive core layer covering the sample with a mask fabricated by an aluminum deposition (~500 nm) on a UV transparent silica bulk and wet etching to discover the desired geometry. The width of the stripes on the aluminum layer is around 5.5 μm. The UV beam (dim=15×30 mm^2) of a pulsed excimer laser @ 193 nm (fluence=20 mJ/cm^2/pulse, rate=50 Hz) has been used to irradiate the sample through the mask (Fig.1). Before the UV exposure the samples were hydrogen loaded at room temperature, 100 atm, 20 days to enhance the photosensitivity. After UV writing, the samples were annealed at 80 °C for around 20 hours to increase the hydrogen outdiffusion.

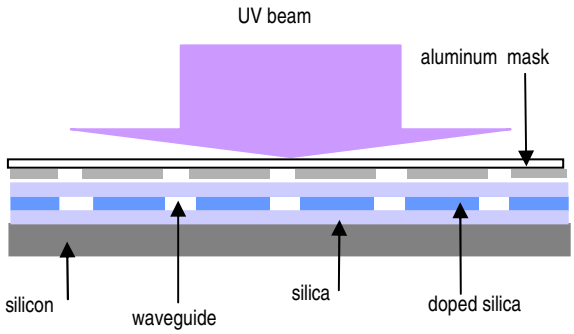


Fig.1: Scheme of waveguide fabrication technique

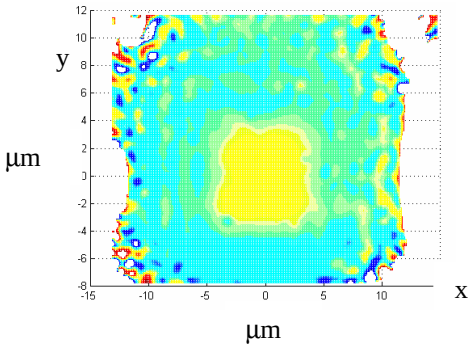
To measure the refractive index profile of the UV induced waveguide an optical bench, using the near field pattern (NFP) method has been set up. This is a well-known technique [3][4], which calculates the bidimensional refractive index profile from simplified Helmoltz equation if the transverse waveguide power distribution is known.

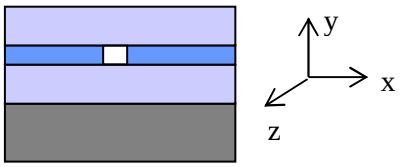
$$\Delta n(x,y) - \frac{n_{eff}^2 - n_s^2}{2n_s} = -\frac{1}{2n_s k_0^2}\frac{\nabla_t^2\sqrt{I(x,y)}}{\sqrt{I(x,y)}} \qquad (1)$$

n_{eff} is the waveguide effective index, k_0 the wavenumber, $n(x,y)=\Delta n(x,y)+n_s$ the local refractive index , n_s the substrate index and $I(x,y)$ the intensity distribution (NFP). Device (CCD) array infrared camera has been used to have high linearity, uniformity and low levels of dark current and noise. The refractive index measurement has been done @ 1.55 um.
Insertion loss measurements have been performed coupling light from a 1.55 um diode laser to the polished waveguide facet using a cleaved standard singlemode silica fibre (SMF). On the output waveguide polished facet, light has been coupled on a second cleaved silica fibre.

Results and discussion

The results of the NFP measurement on UV written planar waveguides are described below. Figure 2 shows the reconstructed index maps of a buried waveguide; it is easy to see the waveguide square shape around 8×8 μm^2. A strong and symmetrical index variation (around 6×10^{-3}) is shown in the horizontal cut (x) (see fig. 3). On the vertical cut (y) is shown the depth of the UV photoinduction and the different index value of the uppercladding and buffer intrinsic to the growth process.





Three layers structure silica on silicon

Fig. 2: Refractive index mapview of a buried waveguide

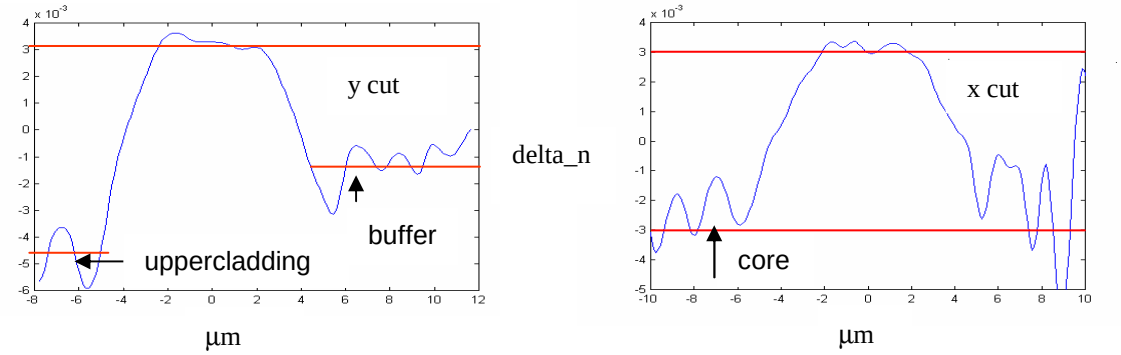
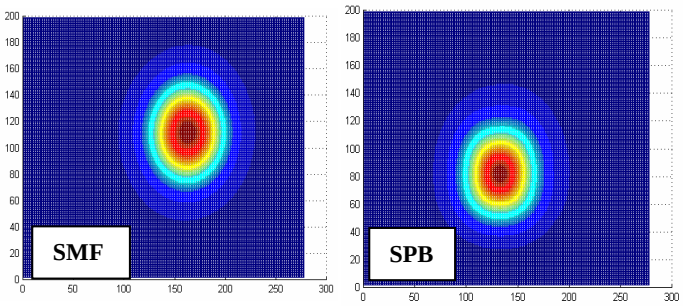


Fig. 3: Two main cuts of the refractive index profile

In figure 4, the effect of the index matching on waveguide intensity mode profiles is shown. The profile of a single mode standard fibre (SMF) is shown for reference (a).



(a) (b)

Fig. 4: Guided mode intensity distribution: mapview (a) single mode fiber (SMF), (b) waveguide silica P-B doped (SPB)

By using the measured mode profiles (Tab.1) of the fiber and of the waveguide the overlap integrals have been calculated to estimate the fiber-waveguide coupling loss due to the mis-match. The calculated value is 0.05 dB for each coupling.

	W_x	W_y
SMF	10 µm	10 µm
SPB	9.0 µm	9.8 µm

w = mode profile width @$1/e^2$

Table 1

So the total coupling losses could be estimated around 0.1 dB and the propagation losses around 0.4 dB/cm.

Conclusion

UV photoinduction of singlemode buried waveguides through the metallic mask and UV excimer laser beam on Boron-Phosphorous codoped silica on silicon have been demonstrated. Refractive index profiles of the written waveguides have been deduced from the measure of the near-field intensity field distribution of guided modes. The reconstructed index of the buried waveguide shows a square shape around 8x8 μm^2 and a strong index variation (around 6×10^{-3}). Low insertion loss (<0.5 dB/cm, including the propagation loss and the coupling loss) waveguides have been obtained. By using the measured mode profiles of the fiber and of the waveguide the overlap integrals have been calculated. The value is 0.05 dB for each coupling, so the total coupling losses could be estimated around 0.1 dB and the propagation losses around 0.4 dB/cm.

Acknowledgments: The authors are grateful to Domenico Di Mola, Simone Visona' and Pietro Della Casa, of Agilent Technologies, for supplying silica doped glass wafers, on which photoinduction experiments have been carried out and Fabio Pozzi and Lucas Beda Soldano for their suggestions on optical benches and their helpful comments.

References

[1] M. Douay et al., "Densification involved in the UV-based photosensitivity of silica glasses and optical fibers", *Journal of Lightwave Techn.*, vol. 15, no. 8, pp. 1329-1342, 1997.

[2] M. Svalgaard, C.V. Poulsen, A.Bjarklev, O. Poulsen, "Direct UV writing of buried singlemode channel waveguides in Ge-doped silica films", *Electronics Letters*, vol. 30, no.17, pp. 1401-1403, 1994.

[3] L. McCaughan, E. E. Bergmann, "Index distribution of optical waveguides from their mode profile", *J. Lightwave Techn.*, vol. LT 1, no. 1, pp. 241-243, 1993.

[4] D. Brooks, S. Ruschin, "Improved near field method for refractive index measurement of optical waveguides", *Photonics Technology Letters*, vol. 8, no. 2, pp. 254-256, 1996.

UV-Written Channel Waveguides in Ion-Exchanged Pyrex

A.K.Sheridan, C.B.E Gawith, G.D.Emmerson, P.G.R. Smith, J.S.Wilkinson
Optoelectronics Research Centre, University of Southampton, Southampton
SO17 1BJ, UK
aks@orc.soton.ac.uk

In this paper we demonstrate that a positive change in refractive index can be induced by UV radiation in bulk Pyrex, an inexpensive, commercially available glass that is not specifically designed to be photosensitive. We describe the fabrication of channel waveguides in Pyrex by direct UV writing and show that a potassium-ion exchanged layer can be used to host single mode waveguides. The change in refractive index due to the UV writing is found to be 2 x 10^{-3}.

Keywords: UV writing, ion-exchange, bulk glass, Pyrex, channel waveguides, planar waveguides

Introduction

Direct UV writing has recently attracted a great deal of attention as a potential route to low cost integrated optical glass components [1,2]. Waveguides can be written due to the localized change in refractive index caused by short wave radiation. UV writing has the advantage that it is a single step process for waveguide fabrication, unlike the traditional techniques of ion exchange or chemical vapour deposition, both of which require multiple processing steps. This typically involves either reactive ion etching or patterning through a photolithographic mask that can be both time-consuming and expensive. In direct UV writing this is avoided by writing the chosen structure in one step into the glass, offering the additional benefit of the flexibility to quickly define new structures at will, without the need to first produce a photolithographic mask.

Much of the UV writing work to date has been performed with deposited layer glasses that rely on germanium for their photosensitivity [3-5]. Other work has shown that photosensitivity can be increased by hydrogen or deuterium loading the glass [6]. There have also been reports of UV induced refractive index change in ion-exchanged channel waveguides in bulk glasses, such as silver ion-exchanged BGG31 [2,7], where the silver ions are reported to be responsible for making the glass photosensitive. There has also been a report of photowriting into a potassium ion-exchanged boroscilicate glass, but in this case it was first necessary to sensitise the waveguide with gamma rays [8].

In this paper we describe the fabrication of UV written channel waveguides in bulk Pyrex without the need for the addition of a photosensitive layer by ion exchange or doping. There are many advantages of using a bulk glass; Pyrex is cheap and commercially available, the composition is customizable, and there is the possibility of introducing a large number of components and active ions to increase the photosensitivity or other useful properties. We show that Pyrex is photosensitive and that a positive refractive index is achieved after irradiation with a frequency doubled argon ion laser at 244 nm. We also demonstrate that single mode channel waveguides

can be written into a potassium ion-exchanged layer in Pyrex. Here the ion-exchanged layer acts as a host for the channel waveguide structures, improving the confinement of the modes. This demonstration of photosensitivity provides the possibility, with further optimization, of making more complex structures such as gratings, Y-splitters, directional couplers, and ultimately complete planar lightwave circuits.

Experimental

Two Pyrex samples were prepared for UV writing. Both were cleaned thoroughly, diced to form an area of 25 mm^2 and end-face polished. The first sample was used foe direct UV writing experiments without any additional procedures. The second was placed in a KNO_3 melt at 385 ºC for 13 hours and 20 minutes to form an ion-exchanged layer with a depth of approximately 6 μm.

Direct UV writing was performed using a frequency doubled argon ion laser at 244 nm and a high precision three-dimensional translation stage [4]. Focussing the UV beam with a 35 mm lens formed a 3 μm spot and this was adjusted so that maximum intensity was achieved at the surface of the sample. The sample was then translated under the UV beam to induce a refractive index change as shown in Figure 1. To optimise the writing conditions, translation speeds between 1 and 10 mm/min and input powers between 20 and 70 mW were used.

The channel waveguides were observed using an unpolarized HeNe laser and imaged with a microscope objective. Mode profiling of the waveguide output was performed using a silicon camera and computer based evaluation software.

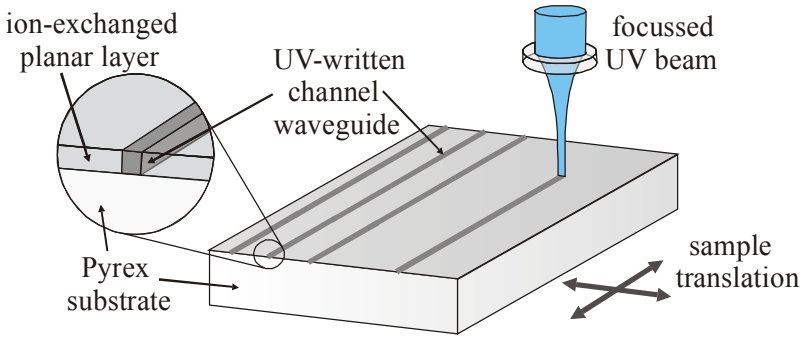


Figure 1. Direct UV writing of channel waveguides using a UV beam focussed to a 3μm spot.

Results

Refractive index structures were first written in the plain Pyrex sample. We observed that the waveguides written into the Pyrex extended approximately 1 mm into the sample so that a stripe rather than a spot was observed. This is due to the weak absorption of Pyrex at 244 nm. Due to the shape of the mode and the poor contrast between the UV induced refractive index change and that of the background; it was not possible to take an image of the mode profile. However, the positive index change observed, even at depths of up to 1 mm, where the incident power was much lower than that at the surface, indicates that Pyrex is itself a photosensitive glass. Closer examination of the surface of the samples using an alpha-step profileometer showed that there was no measurable expansion or compaction of the surface due to the UV writing. This indicates that the induced index change is not due to localized

compaction of the glass or to ablation but may be defect driven as in other silica glasses [4].

In order to achieve better confinement of the mode, an ion-exchanged sample was used as previously described. An example of a typical mode profile obtained is shown in figures 2a and 2b. It was observed that the output was in the fundamental spatial mode, with Gaussian like mode profiles in both guided directions. The spot size ($1/e^2$ intensity diameter) was found to be 6 μm x 14 μm in the vertical and horizontal (UV written) planes respectively. The mode is confined in the vertical plane by the higher index of the ion-exchange layer compared to that of the substrate (1.474 and 1.471 respectively). The ion-exchanged layer may also increase the photosensitivity of the glass although this has yet to be investigated. It has been shown that the addition of silver ions through silver-ion exchange increases the photosensitivity of BGG31 [8] and this may be evidence that potassium ions have a similar effect. The width of the mode is dependent on the UV writing conditions: the spot size, writing speed and incident power. Through optimisation of these parameters it should be possible to produce more confined modes. Improved mode shape and confinement could also be achieved by burying the waveguide through field assisted ion-exchange or by adding a secondary ion-exchanged layer to reduce the refractive index near the surface.

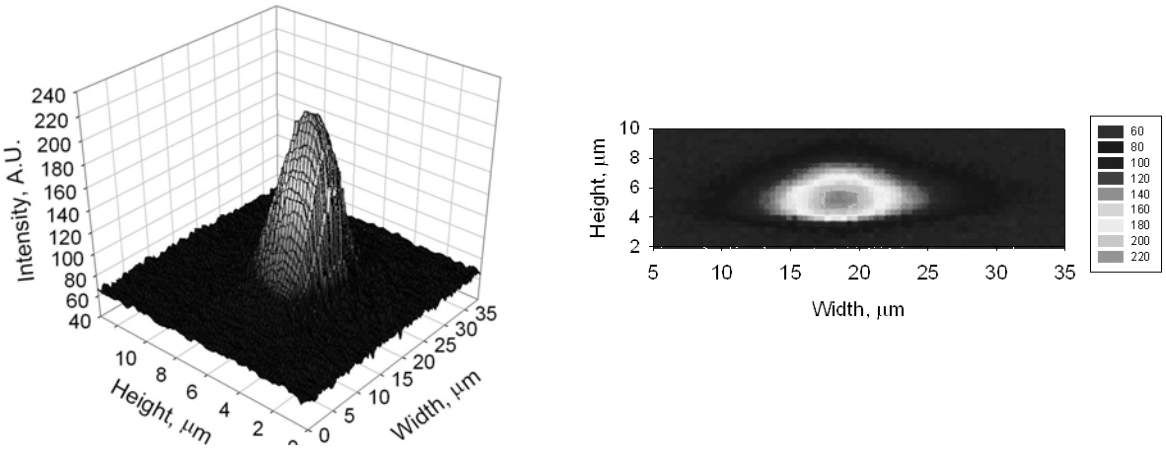


Figure 2. Typical mode profiles obtained from UV written channels in ion-exchanged pyrex; a) 3d mode profile b) 2d intensity plot.

The effective index (n_{eff}) of the guided mode in the UV written channel waveguide was measured using prism coupling giving an n_{eff} of 1.475. A BPM (beam propagation method) computer simulation package was used to calculate the refractive index of the channel, which would give an effective index of 1.475. For this calculation the thickness of the layer was assumed to be 5μm, refractive index of the ion exchanged Pyrex was taken to be 1.474 and the refractive index of Pyrex was 1.471. A value of 1.476 was found for the refractive index of the UV written channels. This gives a change in refractive index of the ion-exchanged layer, due to

UV writing, of 2 x10^{-3}. In order to confirm this measurement, a separate calculation was performed using the BPM software. In this case the width and refractive index of the waveguide were varied until the mode profile calculated was similar to the mode profile measured from the channel. Using this method, a channel width of 4 μm and a refractive index of 1.476 was obtained. This is in good agreement with the value measured by prism coupling.

Conclusions

In conclusion we have demonstrated that Pyrex is a photosensitive glass and that a positive refractive index change can be induced by irradiation at 244 nm. We have shown that by introducing an ion-exchange layer, channel waveguides with mode dimensions of 6 μm x 14 μm can be written. Further work is in progress to measure the losses and to optimise the writing conditions. It is expected that these results will lead to better mode confinement and more complex waveguide structures in ion-exchanged Pyrex glass. The ability to incorporate rare-earth ions, such as Erbium and Ytterbium, into the bulk glass also provides a route towards efficient low-cost integrated channel waveguide laser devices [9].

References

[1] M. Svalgaard, C.V. Poulson, A. Bjarklev, O. Poulsen, Electron. Lett. **30** 1401 1994

[2] D.F. Geraghty, D. Provenzano, W.K. Marshall, S. Honkanen, A. Yariv, N. Peyghambarian, Elec. Letts. **35** 585 1999

[3] M. Svalgaard, European Conference on Integrated Optics (ECIO) 1999

[4] C.B.E.Gawith, A. Fu, T. Bhutta, P.Hua, D.P. Sheperd, E.R. Taylor, P.G.R. Smith, Appl. Phys. Letts, **81** 3522 2002

[5] D. Milanese, A. Fu, C. Contardi, E.R.M. Taylor, M. Ferraris, Opt. Mats. **18** 295 2001

[6] P.J. Lemaire, R,M. Atkins, V. Mizrahi, W.A. Reed, Electron. Lett. **29** 1191 1993

[7] C. Monero, C. Gomez-Reino, J.L. Brebner, Opt. Letts. **24** 1487 1999

[8] J.E. Roman, K.A. Winick, Opt. Lett. **18** 808 1993

[9] T. Feuchter, E.K. Mwarania, J. Wang, L. Reekie, J.S. Wilkinson, IEEE Photon Tech. Lett. **4** 542 1992

Direct UV writing of Bragg grating channel waveguides in a single step process

G. D. Emmerson, C. B. E. Gawith, S. P. Watts, V. Albanis, R. B. Williams and P. G. R. Smith
Optoelectronics Research Centre, University of Southampton, SO17 1BJ, United Kingdom
gde@orc.soton.ac.uk

S. G. McMeekin, J. R. Bonar and R. I. Laming
Alcatel Optronics UK, Starlow Park, Livingston, EH54 8SF, United Kingdom

We present a development of Direct UV writing that allows simultaneous definition of channel waveguides with or without Bragg gratings in a single process in photosensitivity locked planar silica-on-silicon samples.

Keywords: direct UV writing, photosensitivity locking, Bragg grating, channel waveguides

Introduction

Direct UV-writing is a Planar Lightwave Circuit fabrication process based on the refractive index increase occurring in specific materials in response to irradiation in the UV. This increase in index has conventionally been used to fabricate periodic index modulations in the core of photosensitive fibres to form Bragg gratings [1]. Previously this index change has been implemented in planar technology to allow direct definition of channel waveguides and hence complex devices in photosensitive planar channels [2]. This process results in low loss channel waveguides manufactured without the need for photolithography or etching processes. In previous work on directly written structures, planar Bragg grating have been fabricated using a secondary exposure through a phase mask [2] onto existing channel waveguides.

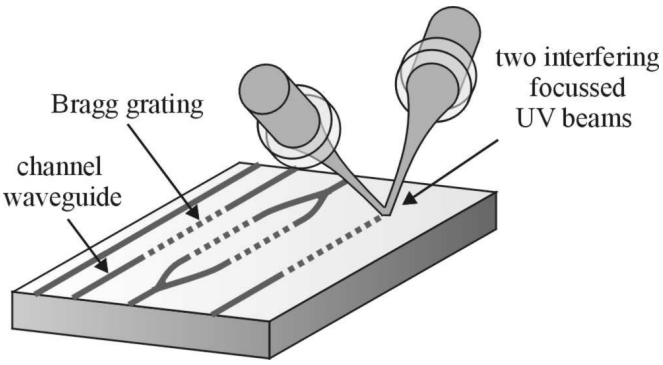


Figure 1: Simultaneous Direct UV writing of channel waveguides and Bragg gratings using focused beam interference in the photosensitive core of a 3-layer silica-on-silicon sample

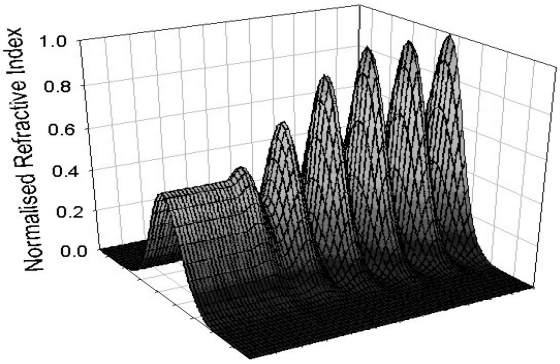


Figure 2: Illustration of the refractive index profile of a channel waveguide connecting to a Bragg grating structure when using the simultaneous writing technique showing the build up of the grating strength along the channel

Recently, we have reported the first implementation of a variant of Direct UV writing allowing the simultaneous definition of channel waveguides with integral Bragg gratings in a single step [3]. Our single-step process is based on a writing spot with a periodic modulation and was developed to allow both the grating and channel to utilise the full photosensitivity of the material with no need for a phase mask. This is achieved using two writing beams, each individually focused and aligned to create a single writing spot with an intrinsic interference pattern defined by the wavelength and intersection angle of the two beams (Figure 1).

As the sample is translated relative to the spot, the intensity of the laser is modulated with a period such that the maxima of the intensity pattern in the writing spot overlaps the maxima of the

previous exposure, inducing a channel waveguide with an inherent Bragg grating index modulation. To define standard channel waveguide structures the sample is translated with the writing power held constant, and so the effect of the intra-spot intensity pattern is averaged out resulting in a uniform channel. Since all structures are defined in the software, entire devices comprising of multiple waveguide structures containing gratings can be written in a single process.

Bragg gratings and channel waveguides that are defined at the same time provide improved control of the grating and channel contrast than over the two-step techniques. Rather than the grating index modulation adding to that previously defined for the channel structure, the grating modulation contrast can be the maximum Δn available from the photosensitive material. This can result in high contrast gratings that are average-index-matched to reduce unwanted Fabry-Perot reflections (Figure 2).

Deuterium loading has long been used to enhance the photosensitivity of germanosilicates [4], reducing the need for excessive dopant levels. However, the conventional approach of deuterium loading used in fibres is problematic for planar samples, as the thin over-clad layer typical in silica-on-silicon samples (~20μm) results in the deuterium diffusing rapidly out of the core. To this end our group has developed a 'Photosensitivity locking' technique, a process of thermally cycling freshly deuterium loaded silica-on-silicon samples to produce a non-volatile photosensitivity enhancement. It is likely that the locking mechanism is due to thermally induced bonding of deuterium to the oxygen atoms present at the germanium sites, increasing the percentage of germanium oxygen deficient centres in the silica matrix. This development is important because our interferometric beam setup has an increased sensitivity to phase errors that can arise from the sample cooling process used by other workers to reduce deuterium out-diffusion [2].

Experimental

The samples used during these experiments were 3-layer silica-on-silicon wafers, some manufactured in-house using flame hydrolysis deposition (FHD), and some commercially produced wafers supplied by Alcatel Optronics UK. The core layers of each wafer were germanium doped to produce an initial intrinsic photosensitivity. Samples that were enhanced through deuterium loading were loaded at ~150 bar for >5 days. Photosensitivity locked samples were subjected to heat treatment of 1400˚C for 5 seconds after removal from the deuterium cell to initiate the locking process.

Direct UV writing into the samples was performed using a CW frequency doubled Ar-ion laser (λ at 244nm) and the beam power controlled via an acoustic optical modulator. To produce the intra-spot interference pattern the beam path was split to form two separate branches that were recombined at an angle of 29° in the plane of the sample. Each beam was individually aligned and focused to a controllable spot size (3 to 6μm) at the point of intersection (Figure 1). The samples were mounted on a computer controlled 2D translation stage providing translation relative to the writing spot.

The gratings were analyzed using an EDFA based ASE source coupled to a polarization controller. An OSA was used to monitor both the reflected and transmitted spectra from the Bragg gratings.

Results

In our deuterium-locked samples a Bragg grating reflection of greater than 80% with FWHM of 0.1nm was achieved, an example spectral profile of which is given in Figure 3. After the initial result, we retested one of the very first wafers that was subjected to photosensitivity locking 18 months ago and used this new writing process to compare the photosensitivity to a newly locked sample. The resultant channels waveguides and Bragg gratings were virtually identical for the same UV writing conditions. Figure 4 is a mode profile of a full length channel and grating, confirming the behaviour of the channel as expected.

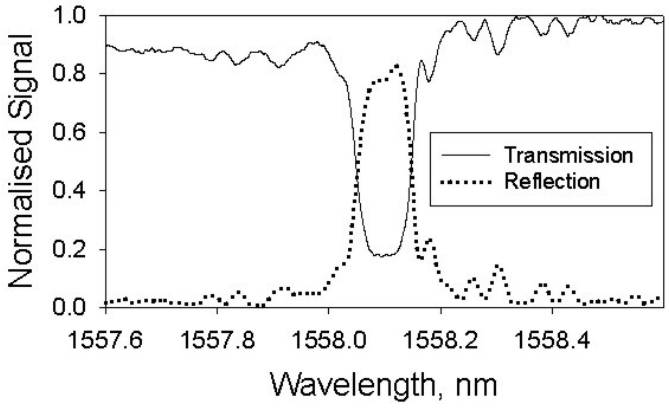


Figure 3: Spectral response from simultaneously written channel and Bragg grating demonstrating >80% reflection with a FWHM = 0.1nm

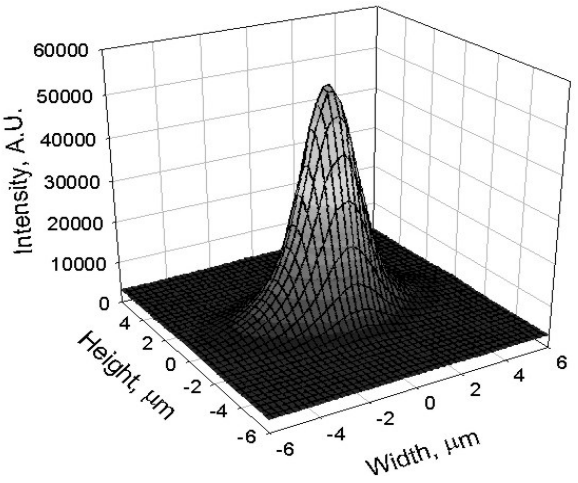


Figure 4: Mode profile of channel waveguide with Bragg grating, $1/e^2$ full width= 5µm x 4µm

One of the significant advantages of this grating writing process is centre-wavelength detuning [3]. This process was used to produce a wide range of Bragg gratings of various pitches from the same fixed interference pattern. Figure 5 demonstrates such a range of gratings, all written with the same fluence. As shown by the graph, it is possible to write gratings covering the entire C-band with no change to our setup, the defined period of the grating controlled solely through software. It should be noted that the limiting factor to the range of wavelengths measured in Figure 5 is the output range of the broadband source used during our analysis, not the writing process.

As the peak reflected wavelength of a given grating is dependent on the effective refractive index of the channel waveguide (as defined by the Bragg relation $\lambda_b = 2\Lambda n_{eff}$), writing gratings with the same period but different translation speeds allowed us to assess the variation in strength of the UV induced channel waveguides with the writing power, or *fluence* [5]:

$$F = \frac{I_{UV} \times a}{v_{scan}}. \qquad (1)$$

Where F is the fluence ($KJcm^{-2}$), I_{UV} is the average laser intensity ($KJcm^{-2}s^{-1}$), a is the writing spot diameter (cm) and v_{scan} is the translation velocity (cms^{-1}). Fluence is an integrated representation of the energy incident on the material, but is not alone sufficient to characterise the writing process. This is because the resultant channels and gratings also depend on the absolute spot size and translation speed for a given beam power. Our technique of simultaneous writing of channels and Bragg gratings provides an accurate and robust measurement of the response of the material. Figure 6 shows the relationship between n_{eff} and fluence for different peak powers (and

hence translation speeds). This data helps provide an insight into the different processes occurring within the glasses.

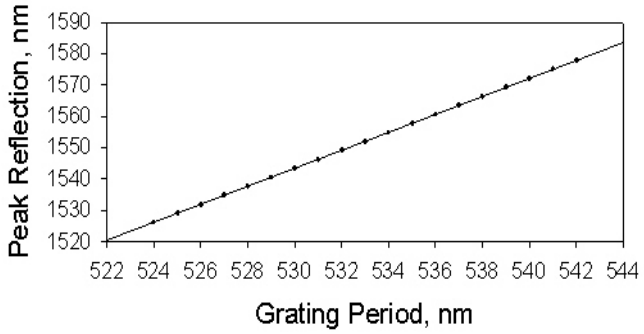


Figure 5: Range of grating periods achievable through centre wavelength detuning, demonstrated across the C-band

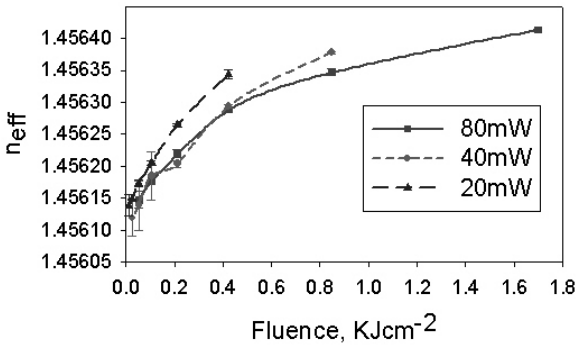


Figure 6: n_{eff} vs. fluence, demonstrating the effect of different writing spot powers

Conclusion

In conclusion, we present a development of the process of direct UV writing that allows us to define both a channel waveguide and Bragg grating structure in a single step, with initial results providing a reflectivity >80% and FWHM of 0.1nm. This process requires no phase mask and is entirely computer controlled. Computer based operation allows full control over the grating parameters including the ability to centre-wavelength detune the grating period from the period of the interference pattern in the writing spot. Using this detuning process, we have demonstrated the writing of Bragg gratings with peak reflections over the entire C-band. In parallel we have developed a 'photosensitivity locking' technique that results in a persistent photosensitive enhancement that has a lifetime of well over a year at room temperature.

[1] K.O.Hill, G.Meltz, *J. Lightwave. Technol*. **15**, 1263-1276, 1997.
[2] M.Svalgaard, *ECIO, Turin, Italy.* 333-338, 1999.
[3] G.D.Emmerson, S.P.Watts, C.B.E.Gawith, V.Albanis, M.Ibsen, R.B.Williams, P.G.R.Smith, *Electron. Lett.* **38**, (24), 1531-1532, 2002.
[4] P.J.Lemaire, R.M.Atkins, V.Mizrahi, W.A.Reed, *Electron. Lett.* **29**, (13), 1191-1193, 1993.
[5] M.Svalgaard, M.Kristensen, *Electron. Lett.* **33**, (10), 861-863, 1997

Fabrication and Characterization of Photonic Crystal Waveguide Components and Application to Ultra-Fast Optical Signal Processing Devices

Kiyoshi Asakawa

The Femtosecond Technology Research Association, 5-5, Tokodai, Tsukuba, 300-2635 Japan
asakawa@festa.or.jp

Current status of two-dimensional photonic crystal (2DPC) waveguide technologies and application to a photonic integrated circuit (PIC) has been reviewed. The emphasis is placed on our recent advancement on theoretical design, fabrication and characterization of the 2DPC-based defect-waveguides such as straight, 60°-bend and directional coupler necessary for the PIC application. A scenario and key issues for application to an ultra-fast all-optical switch are also described.

Keywords: photonic crystal, slab waveguide, band structure, transmission spectrum, bend waveguide, directional coupler, nonlinear waveguide, all-optical switch

Introduction

Recently, a two-dimensional (2D) photonic-crystal (PC) slab has attracted much attention as a novel opto-electronic material/structure capable of providing an ultra-small photonic integrated circuit (PIC) with miniaturized light sources, optical switches and waveguide components (1-4). In particular, combination of the 2DPC and an optical nonlinear (ONL) material such as quantum dot (QD) has a potential ability to achieve an ultra-small and ultra-fast all-optical switching device (5). This is because the QD has a large ONL property in itself and the 2DPC waveguide has a large dispersion property including a low group velocity Vg (6). These two features are capable of enlarging the phase shift induced by the ONL refractive-index change, thus reducing the optical switching energy (OSE). So far, our group has developed nano-technologies for achieving such 2DPC- and QD-structures (7-12). This paper reviews fabrication and characterization of 2DPCs for realizing such a PC- and QD-based all-optical switching device.

Concept and Key Issues of PC-SMZ

Proposal of PC-SMZ

In 1993, Tajima has proposed a symmetrical Mach-Zehnder (SMZ)-type all-optical switch with compound semiconductor ONL materials, the speed of which is not restricted to the carrier lifetime of the ONL material (13). Using this device, his group has so far demonstrated sub-ps-level ultra-fast all-optical switching operations and also carried out optical DEMUX experiments. Further developments are going on for reducing an OSE and improving the stable operation. We have recently proposed a 2DPC-based SMZ-type all-optical switch with embedded QDs for the ONL materials (hereafter, referred to simply as a PC-SMZ). This device has a potential ability to further reduce the OSE, thus providing an ultra-small and ultra-fast photonic switch. Figure 1 shows a schematic picture of the PC-SMZ. Owing to the ONL refractive-index-change (Δndot) of the QD, selectively embedded in the two ONL waveguides, the phase shift $\Delta\phi$ is caused by two control pulses whose time slots differ by a delay time generated by the integrated PC-based delay element. At a switch-on time, two ONL waveguides are designed so that $\Delta\phi = \pi$ between two signal pulses due to the Δndot , quite similarly to the principle of the conventional SMZ switch.

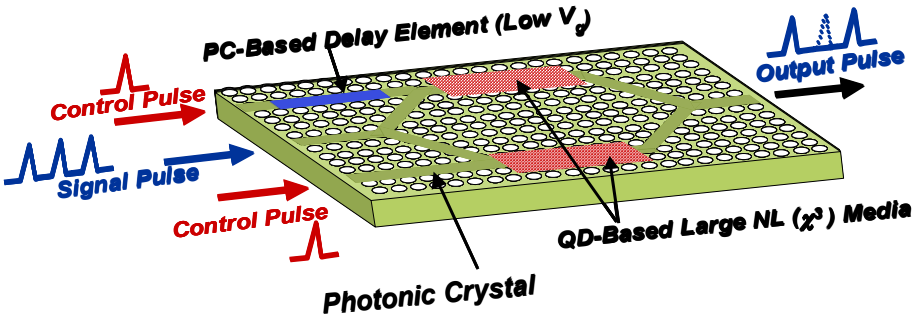


Fig.1 Concept of the PC-SMZ including the 2DPC and QD.

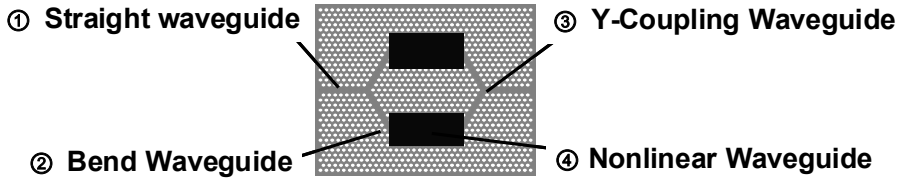


Fig.2 Key issues of the PC-SMZ.

Key issues of PC-SMZ

Due to the structural difference between the conventional SMZ and PC-SMZ devices, the PC-SMZ has several technical key issues, as shown in Fig. 2. Here, we take notes of the straight, bend, Y-coupling and ONL defect-waveguides (DWGs). For reduction of the OSE in the PC-SMZ, in particular, usage of the low V_g in the ONL DWG[6] is effective for enhancing the phase shift $\Delta\phi$, as mentioned above [12]. In addition, an optimized design of the ONL DWG for satisfying the low V_g is important. Another important key issue is a design of the output Y-junction DWG. At the junction, an optical beam in one ONL DWG should not propagate into another ONL DWG for preventing unnecessary ring modes. We have proposed the idea of introducing a novel directional coupler for the Y-junction to solve this problem, as shown later. This paper emphasizes the properties of the 2DPC, and fabrication and characterization of the QDs are described elsewhere [14-16].

Two-Dimensional Photonic-Crystal Waveguide Technologies

Slab waveguide structure

In general, an application of the 2DPC to the miniaturized low-loss PIC requires a slab structure with core/clad refractive-index contrast for strong optical beam confinement in the vertical direction. One candidate is an air-bridge (AB)-type structure and another is an oxide-cladding (OC)-type one. Figures 3 (a) and (b) show schematic cross-sectional views of the AB- and OC-types, respectively, where SEM photographs of the fabricated structures are also shown[7]. The AB-type structure was fabricated by using electron-beam (EB) lithography, dry etching (chlorine-based reactive ion beam etching) and selective wet etching, while the OC-type structure was fabricated by thermally oxidizing the lower sacrificing clad layer instead of the wet-etching method. The sample wafer was a 250-nm-thick $Al_{0.1}Ga_{0.9}As$ core layer grown by MBE on top of a 2-μm-thick $Al_xGa_{1-x}As$ lower sacrificing clad layer (x=0.7~0.9) on a GaAs substrate. As shown later, simulated and measured transmission spectra were obtained mainly for the AB type, while the OC-type is currently under development for the future practical application.

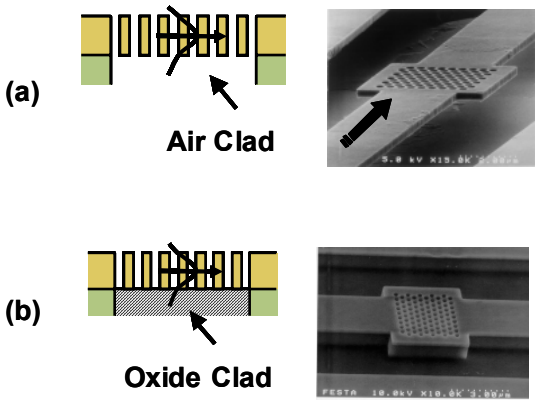


Fig.3 Two types of 2DPC slab waveguide; (a) AB-type. (b) OC-type. Left: schematic cross-sectional views. Right: SEM photographs of the experimented structures.

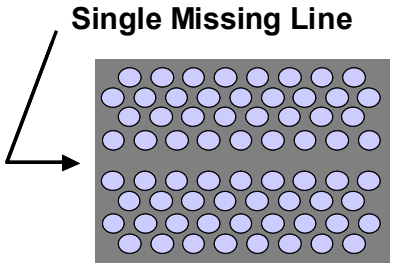


Fig.4 Triangular-lattice DWG pattern with single missing line.

Figure 4 shows a schematic plan-view diagram of the triangular-lattice straight DWG pattern on the 2DPC slab with a missing single-line air-hole array. For designing a single mode at a wavelength of ~1.3μm, a lattice constant (*a*) of 360~420nm, air-hole diameter of ~200nm and slab thickness of 200~250nm are needed.

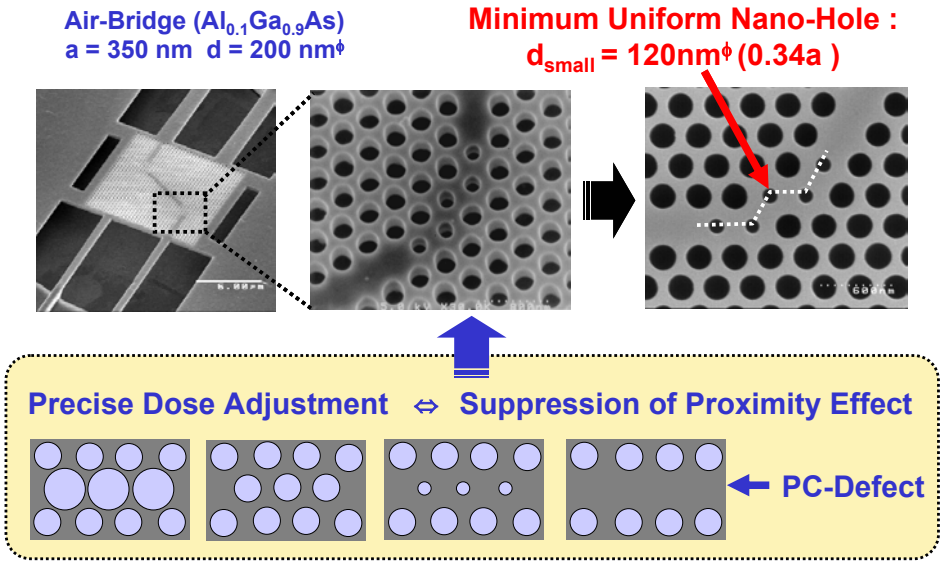


Fig.5 Demonstrated nano-fabrication of ultra-small air- holes resulted from the precise EB dose adjustment.

Fabrication of triangular-lattice defect waveguide

A key technology for precise fabrication of the 2DPC array is an establishment of high-precision EB lithography. One of the main reasons for the site/size fluctuation in the EB

patterning is a proximity effect specific to the EB irradiation on the substrate. This effect is prominent if patterns with different sizes coexist in the same area. In many cases for 2DPC patterning, introduction of the DWG in the homogeneous 2DPC array leads to coexistence of air holes with different diameters. In such a case, precise EB dose adjustment is inevitable for complete suppression of the proximity effect mentioned above. For this reason, EB doses were carefully adjusted depending on the 2DPC patters. Typical uniform nano-holes in the bend DWG in the AB-type 2DPC are shown in Fig. 5. It should be noted that the minimum diameter of the air-hole array is 120nm.

Characteristics of 2DPC Defect Waveguides

Band structure of the straight defect waveguide

A photonic band diagram is calculated by using a three-dimensional finite-difference time-domain (3D FDTD) method. Figure 6 shows the resultant band diagram of the DWG, as shown in Fig. 4, for the TE-like guided modes. There are two bands between the lower and upper slab bands, that is, the even and odd guided modes in the photonic bandgap (PBG). However, since the odd mode is not easily excited in the practical experiment, later calculations are performed only for the even mode. This even mode is single and non-leaky in the normalized frequency range $0.258 \leq a/\lambda \leq 0.276$, where c is a velocity of the light in the vacuum.

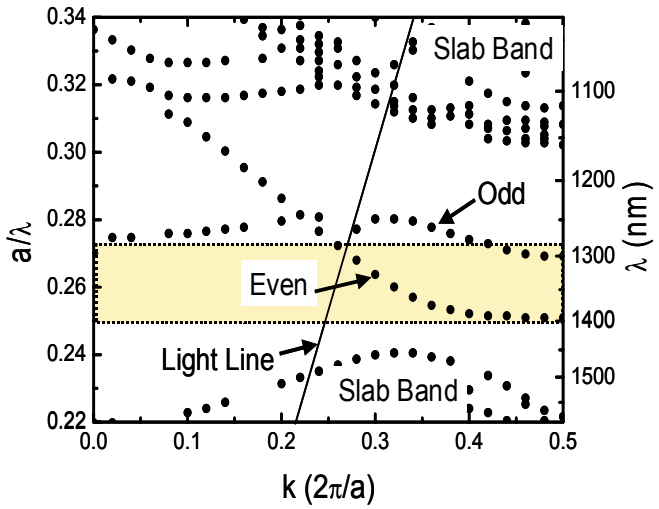


Fig.6 Band structure of the GaAs-based straight defect-waveguide with a triangular-lattice air-holes.

Straight and 60°-bend defect waveguide

Transmittance spectra of these DWGs were theoretically calculated by using the 3D FDTD method. They were also measured by using a wide wavelength-range optical transmission measurement system developed recently[17]. Figures 7 and 8 show measured and calculated transmittance spectra for the GaAs-base straight and 60°-bend DWGs in the 2DPC slabs, respectively [17]. It should be emphasized that they are in good agreement between the measured and calculated spectra both for the straight and bend DWGs. This suggests that the air-hole array used in the experiment has been fabricated with excellent accuracy.

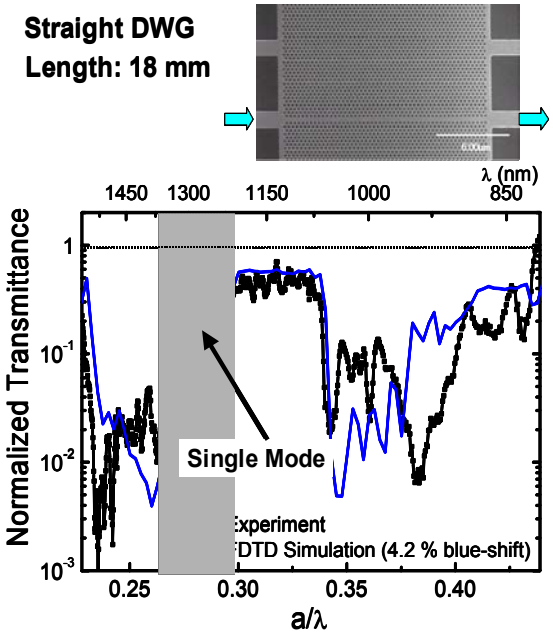


Fig.7 Measured and calculated transmission spectra of the GaAs-based straight DWG with a triangular-lattice air-hole array. The hatched frequency area gives the single mode[17].

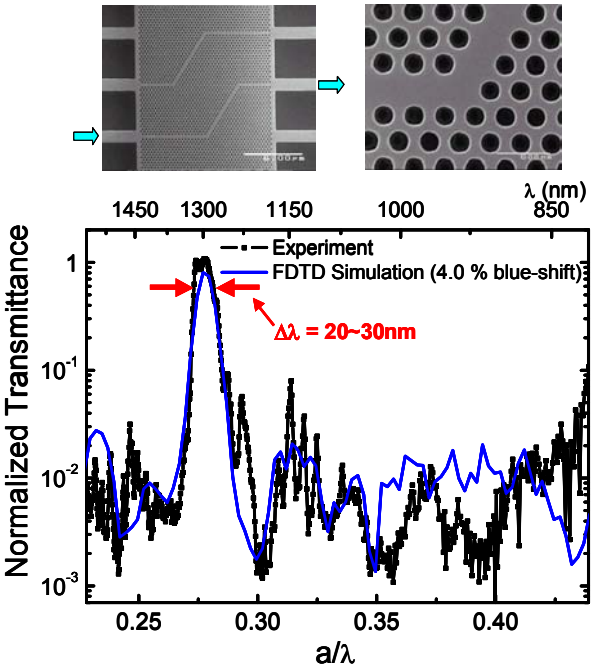


Fig.8 Measured and calculated transmittance spectra of the GaAs-based 60°-bend DWG with a triangular-lattice air-hole array [17].

Characteristics of Y-Coupling Waveguide

As mentioned above, an optical beam propagating through one ONL DWG and impinging into the Y-junction in the PC-SMZ, as shown in Fig. 9 (a), should not propagate into another ONL DWG for preventing an unnecessary ring mode which disturbs a successful SMZ interference. However, as long as the three-fold symmetry Y-junction DWG is used, the incident beam splits into both the ONL DWG and the output port. Usage of a directional coupler (DC) instead of the three-fold symmetry Y-junction DWG is a simple solution for this problem. Figure 9 (b) shows the DC based on the 2DPC slab with a parallel-coupled single-

defect waveguide (PSW) separated by a triple-line air-hole array. Some missing air holes named the coupling-strength-control defect (CCD) are inserted in the middle of the separation. Hereafter, the DC with the CCD is referred to as the coupling-strength-controlled DC (CC-DC) [18]. The CCD length is defined in the figure. The DC is connected with 60°-bend waveguides. In the figure, calculated beam intensities at each port for the design of the 3-dB beam splitter are also shown. Calculation was carried out by using a 2D FDTD method with an effective refractive-index of 2.81, other parameters being the same as those used for the band and transmittance calculation in Fig. 6 to Fig. 8. It is noted that, since the output at the port **b** is zero, this structure is available for the output Y-coupling region in the PC-SMZ, as mentioned above. Another note is that the CCD length of only 7.2μm for a wavelength of ~1.3μm is short enough for realizing a very compact PC-SMZ.

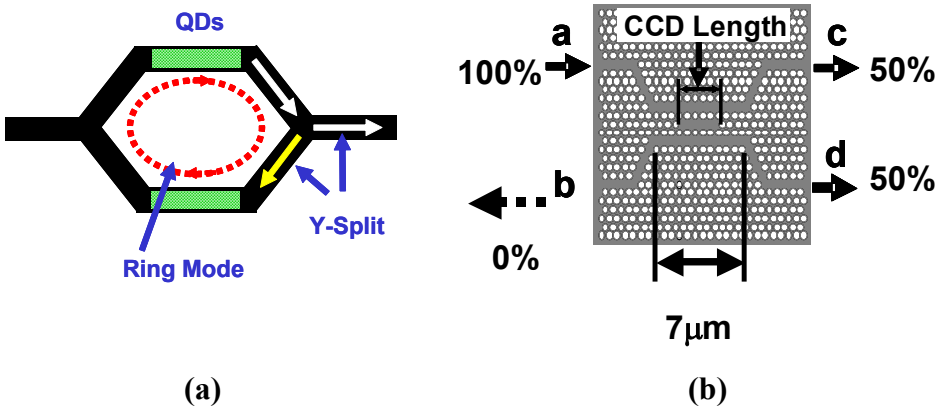


Fig.9 (a) Schematic picture of the DWG configuration in the PC-SMZ, showing the beam-propagation direction for the three-fold symmetry Y-junction DWG. (b) Schematic picture of the CC-DC and the CCD length. Beam intensities at each port for the design of the 3-dB beam splitter are also shown.

Characteristics of Nonlinear Waveguide

As mentioned in the introductory section, prediction of the refractive-index-change (Δn)-induced phase shift $\Delta\phi$ in an AB-type AlGaAs 2DPC slab DWG is important for designing the ONL DWG in the PC-SMZ. First of all, if the ONL-induced Δn will change the propagation band so seriously that the transmittance will be changed significantly, the principle of the SMZ does not operate well. For checking this point, we calculated the Δn effect on the transmission spectrum by using the 3D-FDTD method. We sent an input pulse into the input waveguide and measured the flux in the output waveguide, as shown in Fig. 10 (a) [19]. Calculated transmission spectra, as shown in Fig. 10 (b), resulted in the shift to higher frequency with Δn changing from 0 to -0.01 and -0.1. Since the predicted Δn for the present ONL material, that is, the QD is ~ -0.001, the QD-induced transmittance change is negligibly small in this case. Next, we calculated the Δn-induced phase shift by using the 3D-FDTD method. At the input In-1 and In-2 in Fig. 10 (a), the structure was excited by using dipole sources of the fixed frequency $f = 0.270\ c/a$. Figure 10 (c) shows two output waveforms of the optical beams detected at Out-1 (Δn =0) and Out-2 (Δn =0.07) and their composite waveform. The resultant extinction ratio between amplitudes of the input and composite waveforms is -20dB, an enough value for an optical switch.

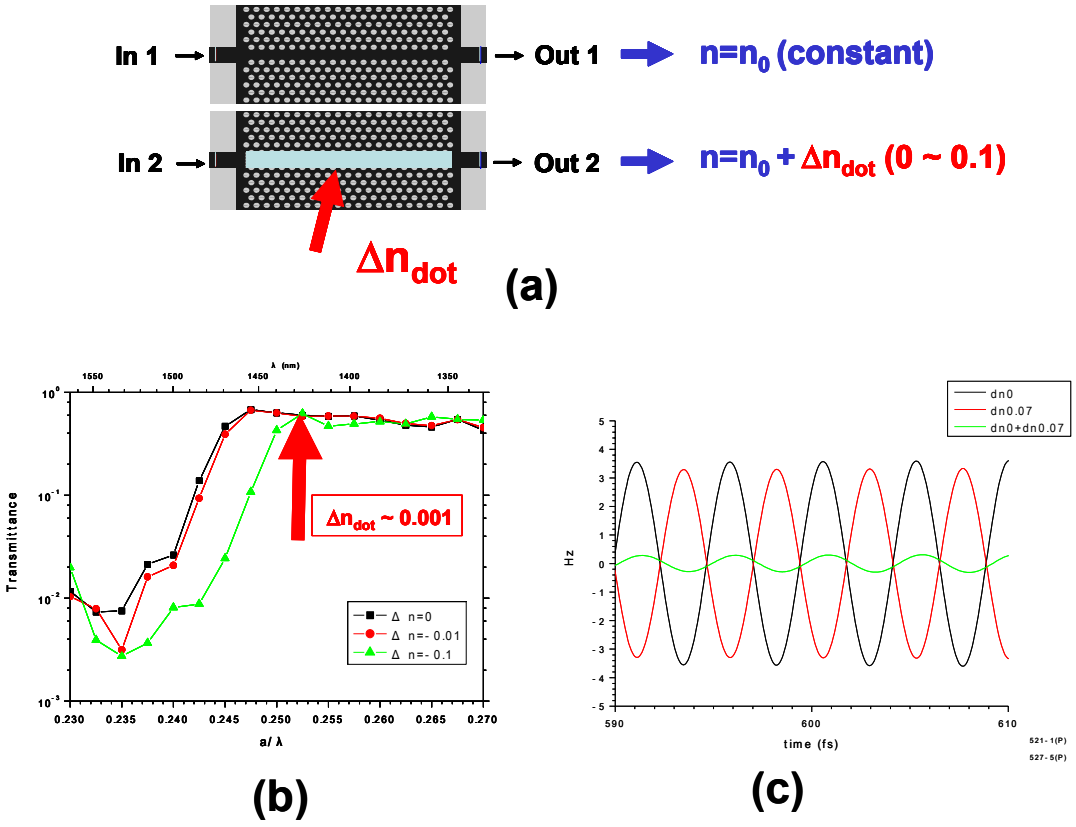


Fig. 10 (a) Waveguide structure for calculating the phase shift in the ONL DWG. (b) Calculated transmission spectra as a function of the Δn (0, -0.01 and -0.1). (c) Calculated waveforms for Δn =0 and -0.07, and composite waveform subject to the extinction ratio of -20dB.

Grand Design of the PC-SMZ

Taking into account Δn of ~ -0.001 for a predicted actual material for evaluating the ONL DWG in the PC-SMZ, a waveguide length necessary for the π-phase-shift in the PC-SMZ was found to be ~100μm owing to the reduced group velocity for a lattice constant of 0.36μm and a wavelength of ~1.3μm. The resultant grand design for the PC-SMZ is shown by the schematic picture in Fig. 11. The result suggests the possibility of achieving a 500μm x 500μm compact ultra-fast all-optical switch.

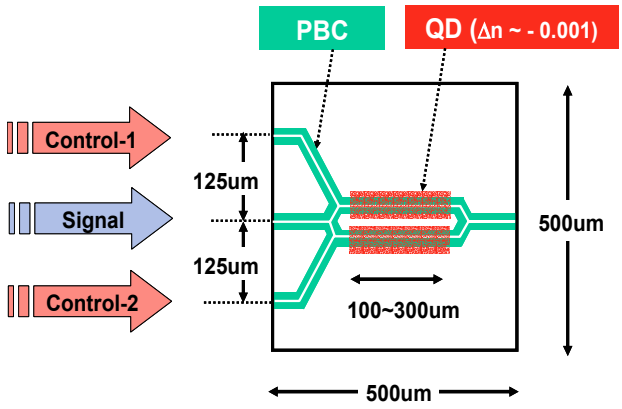


Fig.11 Grand design of the PC-SMZ

Conclusion

Simulation, fabrication and characterization of several 2DPC DWGs suggested that the PC-SMZ is promising for integrated ultra-small and ultra-fast all-optical switches with a low optical switching energy.

Acknowledgments

This work was supported by the New Energy and Industrial Technology Development Organization (NEDO) within the framework of the Femtosecond Technology Project.

The author would like to express his thanks to H. Nakamura, Y. Sugimoto, N. Ikeda, T. Yang, Y. Tanaka, Y. Nakamura, S. Ohkouchi, S. Lan, K. Kanamoto and H. Ishikawa of The Femtosecond Technology Research Association (FESTA), Y. Watanabe, N. Yamamoto and K. Komori of National Institute of Advanced Industrial Science and Technology (AIST), K. Inoue and K. Ishida of Chitose Institute of Science and Technology (CIST) for continuous cooperation on this work.

References

1. T. F. Krauss, R. M. De La Rue, and S. Brand: Nature, **383** (1996) 669.
2. T. Baba, et al., Jpn. J. Appl. Phys., **35** (1996) 1346.
3. S. G. Johnson, S. Fan, P. R. Villeneuve, and J. D. Joannopoulos, Phys. Rev. B, **60** (1999) 5751.
4. S. Noda, A. Chutinan, and M. Imada, Nature, **407** (2000) 608.
5. Y. Sugimoto, N. Ikeda, N. Carlsson, K. Asakawa, N. Kawai and K. Inoue, J. Appl. Phys., **91** (2002) 922.
6. K. Inoue, N. Kawai, Y. Sugimoto, N. Carlsson, N. Ikeda, and K. Asakawa, Phys. Rev. B, **65** (2002) 121308.
7. Y. Sugimoto, N. Carlsson, N. Ikeda and K. Asakawa, K. Inoue and N. Kawai, *MRS Symp. Proc.,* **637,** E5.10.1, 2001.
8. Y. Sugimoto, N. Ikeda, N. Carlsson, K. Asakawa, N. Kawai and K. Inoue, Appl. Phys. Lett., **79** (2001) 4286.
9. Y. Sugimoto, N. Ikeda, N. Carlsson, K. Asakawa, N. Kawai and K. Inoue, J. Appl. Phys., **91** (2002) 3477.
10. Y. Sugimoto, N. Ikeda N. Carlsson, K. Asakawa, N. Kawai and K. Inoue, Optics Lett., **27** (2002) 388.
11. Y. Sugimimoto, N. Ikeda, N. Carlsson, K. Asakawa, N. Kawai and K. Inoue, IEEE J. Quantum Electronics, **38** (2002) 760.
12. H. Nakamura, et al., Proceedings of LEOS2001, San Diego (2001) Wu2.
13. K. Tajima, Jpn. J. Appl. Phys., **32** (1993) L1746.
14. S. Kohmoto, H. Nakamura, T. Ishikawa and K. Asakawa, Appl. Phys. Lett., **75** (1999) 3488.
15. H. Nakamura, S. Kohmoto, T. Ishikawa and K. Asakawa, Physica E, **7** (2000) 331.
16. S. Kohmoto, et al., J. Vac. Sci. Technol. B, **20** (2002) 762.
17. K. Inoue, T. Maruyama, K. Miyashita, K. Ishida, Y. Sugimoto, N. Ikeda, Y. Tanaka and K. Asakawa, unpublished.
18. K. Asakawa, T. Yang, H. Nakamura, Y. Sugimoto, N. Ikeda and Y. Tanaka, unpublished.
19. Y. Watanabe, H. Nakamura, Y. Sugimoto, S. Lan, K. Asakawa, N. Yamamoto, K. Komori and K. Inoue, unpublished.

Photonic Crystal Continuous Taper for Efficient Coupling into 2D Photonic Crystal Channel Waveguides

Pierre Pottier, Iraklis Ntakis, and Richard M. De La Rue
Optoelectronics Research Group, Department of Electronics & Electrical Engineering, University of Glasgow, Oakfield Avenue, Glasgow G12 8LT, Scotland, UK
pottier@elec.gla.ac.uk

A new kind of photonic crystal (PhC) taper is presented. A transmission factor of 90 % into a one row (W1) PhC channel waveguide is shown experimentally, over a length of only 5 µm with a width reduction factor of 5.

Keywords: photonic crystals, tapers, waveguides, insertion losses, integrated optics

Introduction

Photonic crystal (PhC) devices could play a key role in photonic integrated circuits, but several problems remain to be solved satisfactorily, such as the achievement of low insertion loss between narrow PhC channel waveguides and the exterior. In-plane techniques can be used to couple light from and to ridge waveguides via tapers [1] while an alternative way is to use out-of-plane coupling [2]. Realising a taper within the PhC environment can produce a large reduction in length compared to the situation for low index contrast waveguides - and lateral losses, which can arise from the sidewall roughness of deep ridge waveguides, are avoided. Several configurations have been presented, e.g. removing holes from parts of the PhC lattice [3, 4] and grading the hole size [5]. Here, we describe a new kind of full PhC taper that shrinks the beam continuously using a distorted PhC lattice.

Structure design

A realisation of the proposed device is shown in Fig. 1a. It consists of a PhC channel waveguide formed by removing one row of holes (W1), preceded by a taper structure where the width of the PhC waveguide varies progressively through the use of two lateral tilted-PhC lattices. Connecting the access ridge waveguide firstly to a wider PhC channel waveguide (~W5) is much less critical than coupling directly to a W1 channel. Given sufficient precision in positioning, access ridge waveguides could also potentially be eliminated completely by placing PhC tapers directly at the facets of the sample, leading directly into a full PhC environment and avoiding an additional source of losses by mismatch. The continuous shape of this taper is expected to provide a better mode-matching approach.

We have used a two-dimensional finite difference time domain (2D FDTD) computational method to simulate the devices. The lattice is triangular, has six-fold rotational symmetry and, with air holes in a semiconductor of effective refractive index $n = 3.4$ (corresponding to the fabricated structure), the period is 215 nm (for operation at $\lambda = 850$ nm). The air filling-factor is 0.35, corresponding to a hole diameter of 134 nm, and the selected polarisation is TE (i.e. with the $\vec{E}$-field in plane). We have analysed the impact of varying several parameters and in particular the taper angle. Areas of high transmission can be found, while pronounced drops in transmission also appear, corresponding to regularly spaced, wavelength-specific, reflections of the taper that are dependent on the taper angle. The simulation curve in Fig. 2 illustrates the situation and is obtained for a combined taper-down to taper-up structure with each PhC taper being 22 periods long and having a half angle of 6°.

A maximum transmission of 96 % is possible with such a double taper, which is 4.6 µm long and shrinks the beam-width by a factor of 5, from 1.21 µm to 0.24 µm.

Fabrication and measurements

The PhC tapers were realised in an AlGaAs/GaAs epitaxial waveguide structure composed of a 150 nm $Al_{0.6}Ga_{0.4}As$ top cladding layer, 320 nm $Al_{0.19}Ga_{0.81}As$ guiding core and 1.8 µm $Al_{0.6}Ga_{0.4}As$ lower cladding layer on a GaAs substrate. The photonic crystal patterns were written directly via electron beam lithography at 50 kV using proximity effect correction on a 200 nm thick polymethyl-methacrylate resist layer. They were then transferred by reactive ion etching into an intermediate SiO_2 mask layer (200 nm) and finally into the AlGaAs/AlGaAs material to a depth of 0.6 µm (Fig. 1) (using $SiCl_4/O_2$ at a flow rate of 15 sccm/0.5 sccm, pressure of 7 mTorr and an r.f. power level of 250 W).

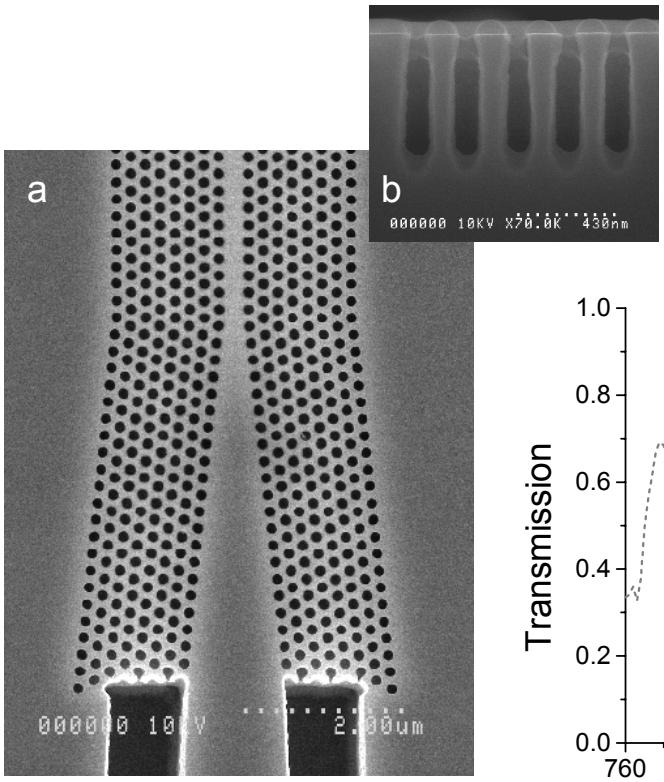


Fig. 1: Top view of a PhC continuous taper accessed by a ridge waveguide (a) and etch profile of the holes (b).

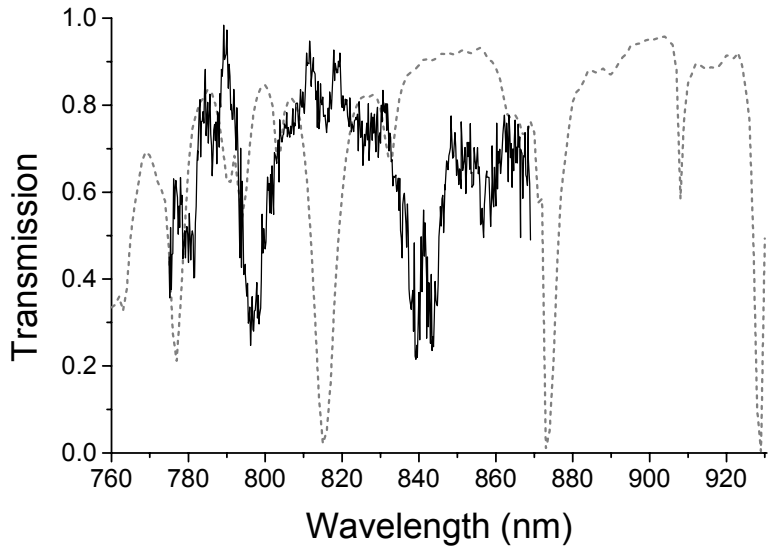


Fig. 2: Simulated (- - - -) and experimental (———) results of transmission of PhC taper to PhC taper.

We have realised the device simulated above (PhC taper to PhC taper), with deeply etched ridge access waveguides of width 2 µm, tapered down to 1.21 µm at the entry of the PhC taper. We have characterised the structures with a tunable Ti-sapphire laser coupled to the ridge waveguides with objective lenses. The experimental results are also shown in Fig. 2 over a range limited by the laser tuning capability. The estimated transmission is obtained by normalising with respect to a 2 µm ridge waveguide having the same overall length. Clear drops in the transmission are observed

experimentally at particular points in the wavelength spectrum, as expected, but a full identification between simulation and experiment is not possible. However a shift of the experimental trace somewhat to the right gives a close alignment of the major features. Errors in fabrication are the most likely origin of the shift in the drop features. Our simulations show that a difference of only 10 nm in the hole diameter corresponds to a shift of 18 nm in wavelength for the major drop features. Nevertheless, a transmission as high as 90 % is obtained for some wavelengths, which is in good agreement with the simulation. Furthermore, the experimental losses (10 %) include the possible losses in the ridge tapers and the coupling losses between the ridge guide sections and the PhC tapers. Concerning bandwidth, more than 65 % transmission is demonstrated over 3.6 % of the spectrum, which would be sufficient to cover the C- or L-bands used in wavelength division multiplexing, for an appropriately re-scaled device. Experimental errors that occur when re-aligning and re-measuring a particular device, or between identical devices realised at different locations on the sample, can also be on the order of 5 to 10 %.

Conclusions

We have designed a novel and efficient kind of PhC taper for coupling guided light into planar (2D) PhC channel waveguides. High transmission factors have been validated experimentally and fuller results will be given in the conference presentation. The tapers also show potentially useful spectral selection properties and structures of this type could be important in augmenting the implementation possibilities for PhC-based integrated circuits.

Acknowledgements

This work was supported by the EPSRC (UK) as part of the Ultrafast Photonics Collaboration. I. Ntakis also acknowledges the support of Bookham Technology (formerly Nortel Networks).

References

[1] K. De Mesel, I. Moerman, R. Baets, B. Dhoedt, P. Van Daele, and J. Stulemeijer, "Spot size converters for low cost PICs", *Proceedings of the 9th European Conference on Integrated Optics (ECIO 99)*, Torino, Italy, pp. 253-258, 1999.

[2] D. Taillaert, W. Bogaerts, P. Bienstman, T.F. Krauss, P. Van Daele, I. Moerman, S. Verstuyft, K. De Mesel, and R. Baets, "An out-of-plane grating coupler for efficient butt-coupling between compact planar waveguides and single-mode fibers", *IEEE Journal Of Quantum Electronics*, vol. 38, no. 7, pp. 949-955, 2002.

[3] T.D. Happ, M. Kamp, and A. Forchel, "Photonic crystal tapers for ultracompact mode conversion", *Optics Letters*, vol. 26, no. 14, pp. 1102-1104, 2001.

[4] P. Sanchis, J. Marti, A. Garcia, A. Martinez, and J. Blasco, "High efficiency coupling technique for planar photonic crystal waveguides", *Electronics Letters*, vol. 38, no. 17, pp. 961-962, 2002.

[5] A. Talneau, Ph. Lalanne, M. Agio, and C.M. Soukoulis, "Low-reflection photonic-crystal taper for efficient coupling between guide sections of arbitrary widths", *Optics Letters*, vol. 27, no. 17, pp. 1522-1524, 2002.

All-Photonic-Crystal Add-Drop Filter Exploiting Low Group-Velocity Modes

S. Olivier, H. Benisty(*), C. Weisbuch
Laboratoire PMC, Ecole Polytechnique, 91128 Palaiseau cedex, France
(*) also at LCFIO, Institut d'Optique, 91403 Orsay, France
hb@pmc.polytechnique.fr

C.JM. Smith, T.F. Krauss(**),
Optoelectronics Research Group, University of Glasgow, Glasgow G12 8LT, Scotland
(**) now at School of Physics and Astronomy, University of St Andrews, Fife, KY16 9SS, Scotland

R. Houdré, U. Oesterle
IPEQ, Ecole Polytechnique Fédérale de Lausanne, CH-1015

We propose and give a preliminary measurement of a compact, fault-tolerant add-drop filter based on coupling the fundamental mode to "slow" modes in a pair of adjacent photonic crystal channel waveguides.

Keywords: photonic crystals, coupled-mode theory, add-drop filter, losses.

Introduction

The hope that photonic crystals (PhC's) help implementing miniature integrated optics functions concerns particularly the add-drop filter (ADF) for WDM networks. While the 50%-drop function has been realised in the lab [1], the reproducibility of tiny high-Q cavities seems too delicate in real environments[2]. Furthermore, substrate-type PhC, require loss-compliant designs: the losses of photonic-crystal channel waveguides (PCCW) is expected to lie around 10-20 cm^{-1}.

We show here that using distributed action, inherent to the periodicity of PCCW's, together with low-group velocity modes, one can retain compactness but largely alleviate the difficulties encountered towards real-life devices. We did not fully explore all the potential and variants of the present proposal but have convincing theoretical and experimental data, illustrated by a specific examples as well as a first successful measurement at around 1000 nm on a GaAs substrate PhC.

The generally accepted scheme for a compact ADF between two adjacent waveguides comprises typically either two cavities [3] or a ring, supporting two quasi-degenerate resonant modes that ensure both selectivity (related to the cavity/ring Q) and directionality by interference of the two modes in the second guide. In a ring, the two counterpropagating whispering-gallery modes are used, but in PhCs, the splitting in ring-like systems is too large and only cavities are presently used.

Photonic crystal Add-Drop Scheme using Low-Group Velocity Modes : principle

Our compact design is based on adjacent coupled *multimode* photonic-crystal waveguides whose fundamental modes are used for propagation and well-defined higher modes for selective and directional coupling. In straight PCCWs themselves (carved in a triangular array of holes etched through a GaAs or InP heterostructure [4-6]), corrugation of the boundaries induces an inter-modal coupling [7], appearing as a mini-stop-band (MSB) or mode gap, (see also [8]). This coupling (Fig.1a) generalises the counterpropagating DBR. The advantage of PCCWs is to have specific coupling of the fundamental mode to very low group velocity modes fully confined in the guide and not leaking as they would in ordinary rib or stripe loaded waveguides. A signal launched in the input guide at the MSB normalised frequency u_o in the fundamental mode feeds a higher-order, low group velocity mode, which easily traverses the inter-guide "wall" (Fig.1b). Because it retains, through this process, a well-defined wavevector k, it undergoes the reciprocal coupling to the

fundamental mode in the proper direction. A four-wave coupled-mode theory was devised to model the filter. The following formulation between the amplitudes A_1, A_2, B_1, B_2 of fundamental (A's, subscript a) and higher-order (B's, subscript b) modes in the upper (1) and lower (2) waveguides describes the core of the ADF :

$$\frac{d}{dz}\begin{pmatrix} A_1 \\ B_1 \\ A_2 \\ B_2 \end{pmatrix} = \begin{pmatrix} -i\delta_a & -i\kappa_{ab} & 0 & 0 \\ i\kappa_{ab} & i\delta_b & 0 & i\kappa_{bb} \\ 0 & 0 & -i\delta_a & -i\kappa_{ab} \\ 0 & i\kappa_{bb} & i\kappa_{ab} & i\delta_b \end{pmatrix} \begin{pmatrix} A_1 \\ B_1 \\ A_2 \\ B_2 \end{pmatrix}, \quad (1)$$

In this equation, κ_{ab} describes the mechanism of Fig.1a, whereas κ_{bb} describes the coupling between higher order "b" modes, "aa" coupling being neglected. δ_a and δ_b are the detuning with respect to the Bragg condition. Extreme asymptotic regimes are $\kappa_{ab} >> \kappa_{bb}$ (coupling of "b" modes is a perturbation to single MSB's)) and $\kappa_{ab} << \kappa_{bb}$ (there are two split modes $b_1 \pm b_2$ built from the "b" modes, and separate MSB effects occur with the two degenerate "a" modes). Note that we have separately validated the two-modes case (Fig.1a) for an isolated three-missing-rows PCCW ("W3") with the same losses as in [9], as will be presented elsewhere.

Using eqns. (1) and standard calculations, we find the optimal design *analytically* in the lossless case, when only mode "a" is launched in channel 1 and unity amplitude is imposed in the cross port ($A_2(L_{opt})=1$) and zero in the bar port ($A_1(L_{opt})=0$). Simply speaking, power flows through the barrier just at the same rate as it is created by the exciting wave. One finds :

$$\sqrt{\frac{\kappa_{bb}^2}{4} - \kappa_{ab}^2} = \frac{\kappa_{bb}}{3} \iff \kappa_{ab} = \frac{\sqrt{5}}{6}\kappa_{bb} \qquad \text{and} \qquad L_{opt} = \pi \left(\frac{\kappa_{bb}^2}{4} - \kappa_{ab}^2 \right)^{-1/2} = \frac{3\pi}{\kappa_{bb}} \qquad (2)$$

Also, the quality factor Q at optimal condition is, fortunately, far smaller than the MSB width.

Design example with a pair of "W4" PCCWs

We consider an example based on 4-missing-rows ("W4"[CJMS]) PCCW's with a spacing formed by 4 rows of holes, shifted by $a/2$ to get PCCWs with symmetric boundaries (air-filling factor f=0.37 and background dielectric constant ε=10.4). Fig. 2a shows the mode dispersion relations for an isolated W4 waveguide computed by the plane wave method [7]. A minigap of width $\delta u_{ab} = 1.14\ 10^{-3}$ between modes a(#1) and b(#7) occurs at the normalised frequency $u_o=a/\lambda=0.282$ ($n_{ga}=3.28$, $n_{gb}=71$) leading to a dimensionless coupling constant $a\kappa_{ab} = \pi\delta u_{ab}(n_{ga}+n_{gb})/2 = 0.133$. Then eq.(2), dictates $a\kappa_{bb}= 0.357$ for optimal operation.

A close value, $a\kappa_{bb} = 0.361$ is obtained for the 4-rows separation (we do not even change f to stress how easy first-order design is), related to a bb splitting $\delta u_{bb} = 1.62\ 10^{-3}$determined far from the MSB regions. Fig.2b shows the dispersion relation of the two coupled waveguides. The optimal length L_{opt} (cross operation) is then $L_{opt}=26a$, hence 11 μm in a λ=1.5 μm application (a~0.44 μm). Fig. 3 shows the bar and cross signal vs. frequency around the frequency u_o calculated in the lossless case by the coupled-mode theory. The peak at the u_o has a 98.7% transmission and a quality factor Q=1500. At the stage of the present proposal, there is a larger window (Q~100) related to the basic W4 MSB where partial transfer occur, especially at MSB edges. In the 100 or 50 GHz WDM scheme, with tens of close channels, this would restrain the use of the present filter to the specific case of interleaved set of signals, where sub-combs with e.g. 800 GHz spacings are used in local loops. However, clever extensions of the present scheme should alleviate this penalty. One simple way to limit the unwanted leakage at ~ constant κ_{bb} would be to insert an extra 24a-long

cavity between the two parallel waveguides ([10]), as sketched in Fig.1c . One property of foremost importance in the WDM networks is the very neat zero at u_o to allow direct re-use of the dropped channel. We checked that this signal remains below 5% (-13 dB) for fluctuation of the air-filling factor $\delta f \sim \pm 0.01$ (in fact $\delta(a\kappa_{bb}) \sim \pm 0{,}01$), for losses α_b up to about 1200 cm^{-1} (note that n_{gb}=71.0, however) and losses α_a up to ~100 cm^{-1} (far more than published in the more lossy W3 case [6,9]). Losses even tend to make the bar-spectrum "flat-bottomed". Drop efficiency in this first proposal spans the range –1.5 dB to -4 dB with the same values. Finally, dropped power in the wrong direction takes the form of only a small amount of higher mode B_2 ($A_2(0)$=0) that will not sizably propagate back, i.e. crosstalk is by construction negligible. Detailed investigation of fault-tolerance among holes is the next step allowed specifically by, e.g. FDTD modeling [11].

Experimental realization based on "W3" and "W5" PCCW's

In our GaAs-based prototype, the air filling factor f~37%. The 60*a*-long guides have five-missing rows ("W5") along ΓK [5,7], and are separated by 5 rows. They are fed by three-missing-rows "W3" guides on all ports. For the a=260 nm period of the PhC, the ADF is 15 μm long. We excited at the focus of a laser diode the PL of InAs dots in the GaAs guide core and collected spectra at a nearby cleaved edge the guided PL light crossing the structures [5] as follows : Fig.4a, W5 guide alone, 100a-long, shows the 7-nm-wide MSB-dip at 920 nm [7-9]. Fig.4b shows that this dip is modified by the presence of the adjacent W5 guide, shifting to 930-935 nm. Fig.4c shows the energy dropped with Q~>100 at 935 nm in the adjacent waveguide, when detection is shifted to the adjacent channel. To avoid parasitic light from the through channel, its end is fitted with a "photon dumper" PC pattern that does not impact on the coupler. Grey lines are coupled-mode curves using the MSB fit of Fig. 4a. The Q degradation has here two extrinsic causes : out-of-plane losses of our basic PC structure [9,11] and losses induced by the embedded InAs dots [4]. It is obvious that in our prototype, the coupling length L and strength $a\kappa_{bb}$ were not adjusted to the optimum. However, the dropping effect is well present and this was checked for other separations and lengths.

Conclusion

We believe that photonic crystals have a good chance to go to real-life devices if the options exemplified here, namely distributed action and confined low-group velocity modes, are further pursued. Already at the present stage, we are able to envision acceptable performances penalties for modal propagation losses which are in the state-of-the-art range and a Q value of 1500 compatible with WDM. Enhancing the design to cover multiple channel ADF and making it adequate to close-spaced WDM channels seems at hand in the space of parameters yet unexplored. The future of this class of PhC-based concept is therefore extremely promising

The present work was supported by the EU IST project 11239 "PCIC".

[1] S. Noda, A. Chutinan, M. Imada, *Nature,* **407**, 608-610, 2000.
[2] Yoshie et al., Appl. Phys. Lett. **79**, 4289-4291, 2001.
[3] S. Fan, et al. *Phys. Rev. Lett.*, **80**, 960-963 (1996).
[4] D. Labilloy, et al., *Phys. Rev.*, **B59** 1649-1652, 1999.
[5] C. J. M. Smith et al. *Appl. Phys. Lett.*,**77**, 2813-2815, 2000.
[6] A. Talneau, L. Le Gouezigou, and N. Bouadma, *Opt. Lett.* **26**, 1259-1261, 2001.
[7] S. Olivier,et al., *Phys. Rev.* **B63**, 113311, 4 pages, 2001.
[8] C. J. M. Smith et al. *Appl. Phys. Lett.*, **78**, 1487-1489 (2001).
[9] E. Schwoob et al. *J. Opt. Soc. Am. B,* **VV**, ppp-ppp 2002.
[10] H. Benisty, S. Olivier, C. Weisbuch, French patent pending n°0207957
[11] H. Benisty, et al. *IEEE J. Quantum Electron.* **QE-38**, 770-785, 2002.
[12] M. Notomi et al. *Phys. Rev. Lett.* **87**, p.253902, 2001.

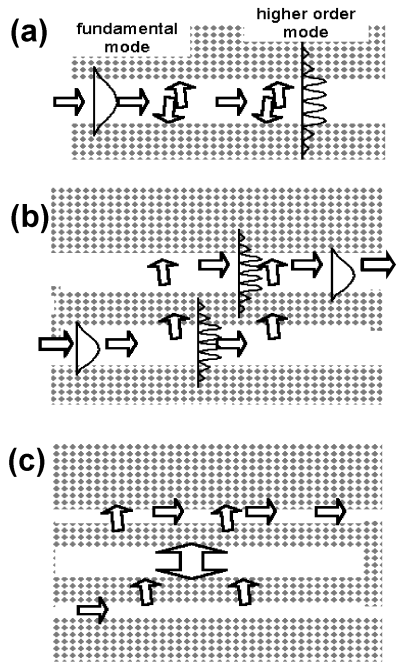


Fig.1 : (a) Principle of MSB in a multimode photonic-crystal waveguide, $\Delta k_{//} = 2\pi/a$ between the two modes; (b) the MSB-based Add-Drop Filter proposal ; (c) Insertion of an elongated cavity to raise the ADF selectivity.

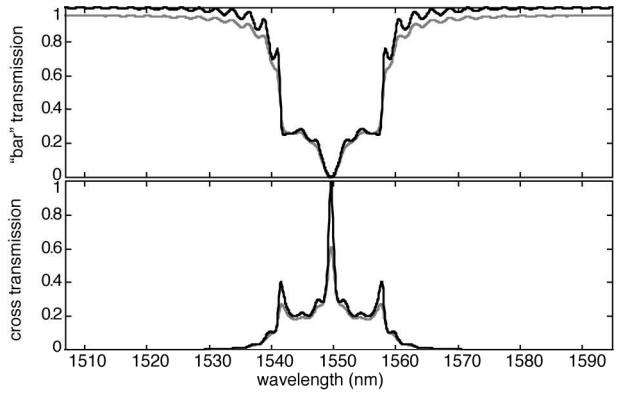


Fig.3 : black line : "bar" and "cross" transmission spectra as indicated, on a linear scale in the lossless case; Q=1600 at the peak ; grey line, same quantities with propagation losses α_a = 20 cm^{-1} (fundamental mode) and α_b = 400 cm^{-1} (higher-order mode)

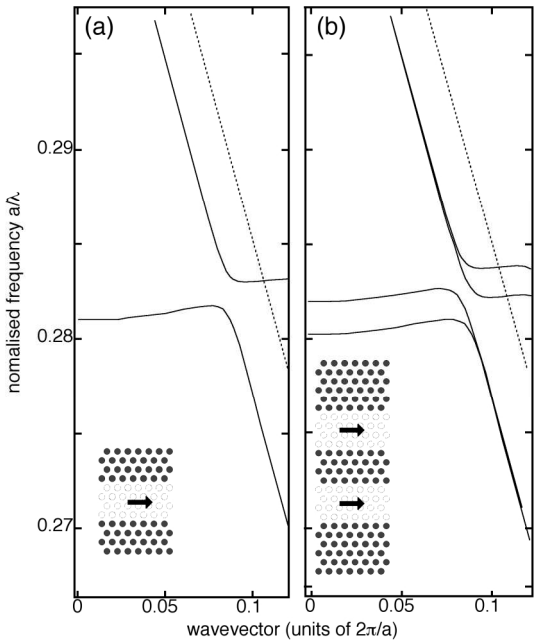


Fig.2 : (a) dispersion relation of an isolated "W4" waveguide; (b) dispersion of the two coupled waveguides at optimum of eq.(2).

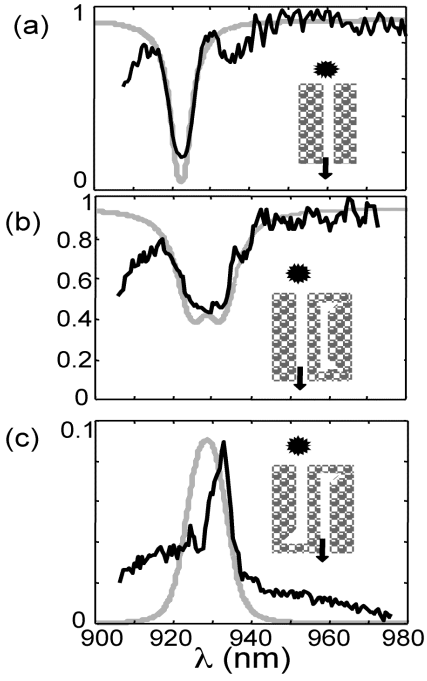


Fig.4 : (a) transmission spectrum through the W5 guide, with the MSB dip at 920 nm; (b) Same but now through the ADF, with 5 rows separation from the other W5; (c) Cross signal, Q~100. Note the triangular cavity, reflection-free, "photon dumpers" at guide ends to avoid collection of spurious signal.

Compression of picosecond pulses using photonic crystals

YewJun Chai, Chris Morgan, Richard Penty and Ian White
Ultrafast Photonics Collaboration, Centre for Photonic Communication Systems Research,
Cambridge University Engineering Department,
Trumpington Street, Cambridge, CB2 1PZ, United Kingdom
cnm20@cam.ac.uk

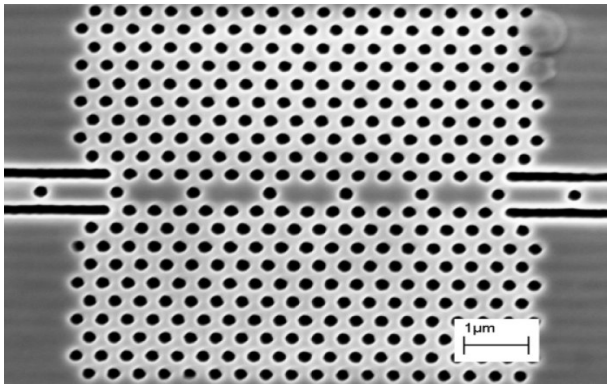
Tim Karle and Thomas Krauss
Ultrafast Photonics Collaboration,
School of Physics & Astronomy, University of St Andrews,
North Haugh, St Andrews, Fife, KY16 9SS, United Kingdom

We demonstrate picosecond pulse compression of up to 40% by transmission through a 6µm long planar photonic crystal waveguide. The corresponding dispersion value is $>10^6$ larger than that of standard single mode fibre.

Keywords: guided-wave optics, photonic crystals, periodic structures, pulse compression

Introduction

The recent development of integrated photonic crystals placed within planar waveguides offers the potential of high density integrated optics with significant functionality [1]. Here the high refractive index contrast structure achieved within the photonic crystals leads to strong spatial and temporal effects, which in turn enable ultracompact components to be formed. Of particular interest to optical communications are devices that are designed to operate in the 1.3µm and 1.55µm wavelength regimes, where photonic crystal based wavelength filters and dispersion compensators could have impact in future high speed systems. However although wavelength filtering has been readily observed in photonic crystals [1], to date pulse compression has not been achieved to the authors knowledge. In this work therefore we report preliminary studies of photonic crystal transmission guides which show significant pulse compression.

a) 

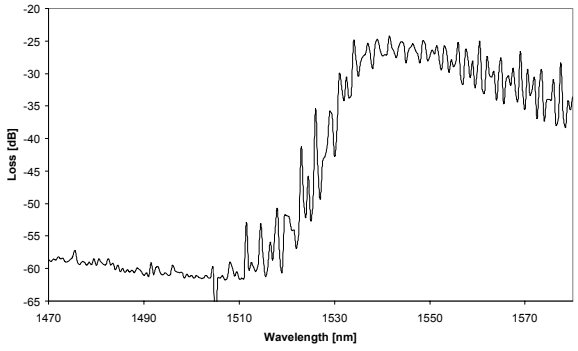
b) 

Figure 1 : a) SEM image of photonic crystal in deep etched waveguide, b) Transmission passband characteristic of lattice constant a=460nm.

The photonic crystal structures employed in this paper are L2in1 coupled cavity waveguides [1,2], as shown in figure 1a). The photonic crystal and waveguide are fabricated in a GaAs heterostructure slab waveguide by a two step reactive ion etch process. The etch depth is typically 1µm for the 200-300nm diameter holes in the photonic crystal. By changing the lattice constant, the effect of the photonic crystal can be tuned over a wide spectral range. Figure 1b) shows the measured transmission characteristic for a lattice constant of 460nm, where a strong rising edge for

the passband can be observed between 1520nm and 1540nm. The authors have reported initial investigations of the transmission of picosecond pulses through these structures [3], where for the first time the effect of the photonic crystal on high repetition rate pulses in the C-band EDFA region (1535-1560nm) was observed. This paper demonstrates the ability of the photonic crystal to compress sub-picosecond pulses by factors of up to 40%.

Experimental arrangement

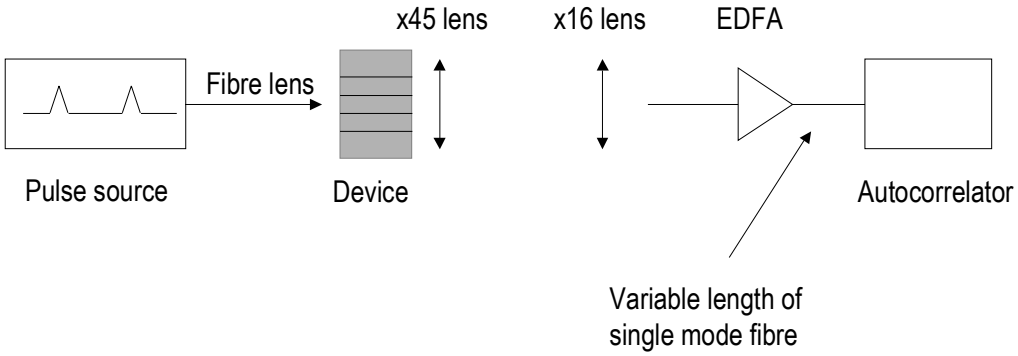
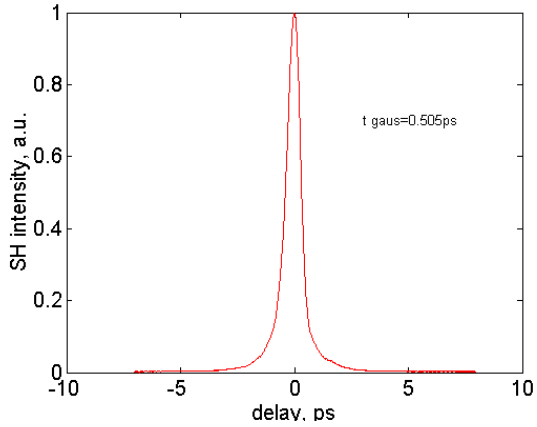


Figure 2 : Experimental setup for pulse compression measurements.

Figure 2 shows the experimental arrangement. The pulse source uses a gain switched DFB laser operating at 1536.1nm with a repetition rate of 1GHz. The pulses are then passed, in turn, through a length of dispersion compensated fibre (DCF) to provide linear pulse compression of the chirped pulse, a length of dispersion shifted fibre (DSF) followed by standard single mode fibre (SMF) to provide nonlinear compression and finally a dispersion-imbalanced loop mirror which acts to suppress the pulse pedestal and broaden the pulse spectrum [4]. After compression, the pulse is transform limited to a minimum width of 500fs, and has a spectral width of 7nm. Due to this short minimum duration, the pulse can be reliably broadened by increasing or decreasing the overall length of standard single mode fibre (SMF) in the system after the DILM. This technique is used to allow pulse compression measurements to be carried out at a range of different input pulse widths. In order to assess the absolute pulse compression performance of the dispersive photonic crystal, measurements of the pulse transmission through the photonic crystal are carried out and compared with transmission measurements through an identical waveguide without a photonic crystal.

Results



a)

Figure 3: Observed autocorrelation trace of transform limited 500fs width pulse.

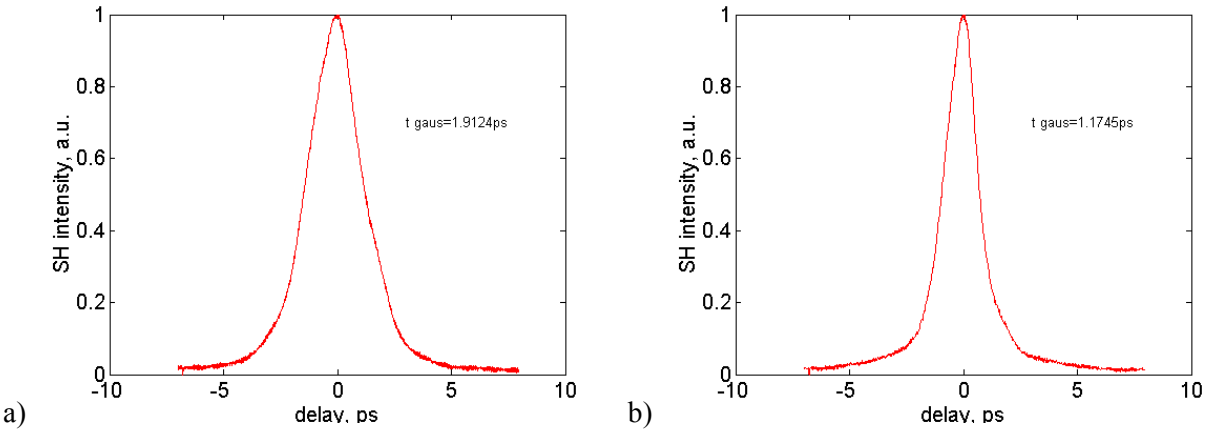


Figure 4: Observed autocorrelation traces of pulse for same fibre length after transmission a) through blank waveguide, b) through waveguide with L2in1 photonic crystal.

Experiments have been carried out to determine the dispersive properties of the photonic crystal by examining the autocorrelation traces of the transmitted pulses. Examples of these are shown in figures 3 and 4. Figure 3 shows the autocorrelation trace of the transform limited input pulse with a duration of 500fs; adding extra fibre to the system increases the pulse width and figure 4 shows the resulting pulses transmitted (a) through the control waveguide without the photonic crystal and (b) that with the photonic crystal. It is clearly observed that the pulse transmitted through the photonic crystal is output with a significantly shorter pulse width (1.17ps) compared with that from the conventional waveguide with a pulse width of 1.91ps. The photonic crystal has therefore caused a pulse compression of 40% in this case.

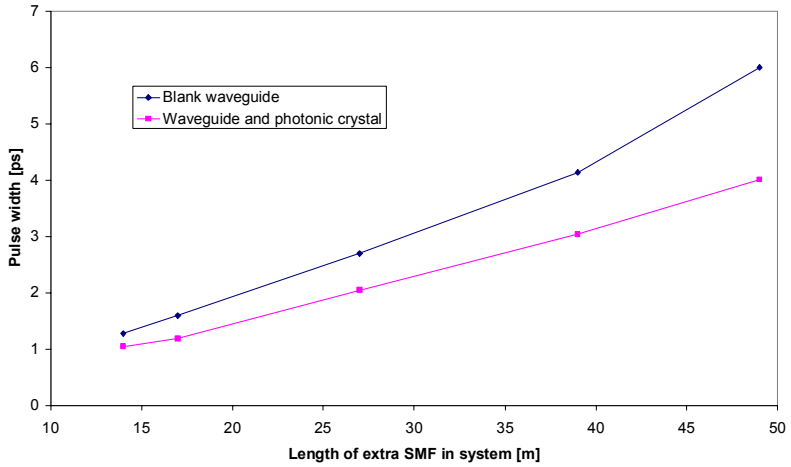


Figure 5: Variation of pulse width with increase of length of SMF in system.

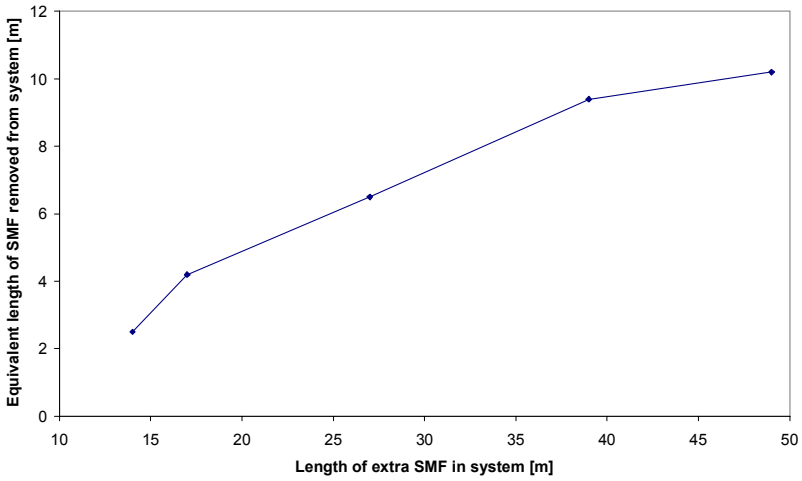


Figure 6: Equivalent length of SMF required to produce compression observed due to photonic crystal.

Furthermore, a series of measurements have been carried out to investigate the compression effect of the photonic crystal as the length of SMF within the system is greatly increased. Figure 5 shows the measured pulse widths for both the blank waveguide and the photonic crystal waveguide, indicating pulse width reductions of up to 2ps across the range of SMF lengths measured.

Comparisons of the length of fibre in the system required to produce a given pulse width through the blank waveguide with the pulse widths observed for the photonic crystal waveguide can be made. These values demonstrate the length of fibre that needs to be removed to produce a compression equivalent to that achieved by the photonic crystal. Figure 6 illustrates these values, showing that the 6μm long photonic crystal can achieve compressions equivalent to SMF lengths of up to 10m. Thus the dispersion induced by the photonic crystal is $>10^6$ larger than that of standard single mode fibre at these wavelengths.

Conclusions

We have shown picosecond pulse compression using an integrated photonic crystal. Compression values of up to 40% were achieved, with the dispersion value being $>10^6$ larger than standard SMF. We believe that this is the first demonstration of pulse compression observed in a planar photonic crystal waveguide using the dispersive properties of the photonic crystal. Such high dispersion is very attractive as it will allow photonic crystals to be used in applications such dispersion compensation and integrated nonlinear components where dispersion is used as part of the switching mechanism. It is believed that higher compression ratios can be achieved by careful design of the photonic crystal dispersion characteristics and the use of a shorter pulse with a broader spectrum.

References

[1] T.J. Karle, D.H. Brown, R Wilson, M. Steer, T.F. Krauss, *IEEE J. Sel. Topics in Quantum Electronics,* **8**, 909-918, 2002.

[2] M. Bayindir, E. Ozbay, *Physical Review B*, **62**, 2247-2250, 2000.

[3] T.J. Karle, Y.J. Chai, C.N. Morgan, I.H. White, T.F. Krauss, *Proceedings of LEOS 2002*, 881-883, 2002.

[4] I.Y. Khrushchev, I.H. White, R.V. Penty, *Electron. Lett.*, **34**, 1009-1010, 1998.

Novel Group Delay Lines Formed by Multi Quantum Well Defective Photonic Crystals

Vittorio M. N. Passaro, Francesco De Leonardis, Caterina Ciminelli and Mario N. Armenise
Optoelectronics Laboratory, Dipartimento di Elettrotecnica ed Elettronica, Politecnico di Bari
Via Edoardo Orabona 4 - 70125 Bari, Italy, Fax N. +39-0805963315, passaro@poliba.it

In this paper, highly efficient novel group delay lines in guided-wave multi-quantum-well one-dimensional photonic bandgap structures are designed for very high rate data streams in all-optical signal processors and telecommunications systems by using the Floquet-Bloch formalism.

Keywords: guided-wave optics, photonic bandgap structures, multi quantum wells

Introduction

Optical delay lines can be used in a large number of optical signal processing applications including data storage, parallel-serial converters, optically-controlled phased array antennas and optical communications. Compact delay devices to be used with ultrashort pulses are also required by demultiplexing and optical computing systems. Photonic bandgap (PBG) crystals are one of the most suitable materials for fabricating very compact and fully integrable optical delay lines. Wideband (> 5 GHz) transmit/receive phased array antennas require low-cost and low-loss delay lines. At the best, tens of millimiters long lines can be fabricated by electronic technology to obtain hundreds of picosecond delays [1]. GaAs-based PBG structures can be used to produce low-cost, low-loss either fixed or programmable delay lines. 1D PBG delay lines (4.5 μm long, 200 fs at λ = 1.038 μm) have been experimentally studied in GaAs/AlAs multistack architectures [2] for use in optical beam steering for phased array antennas. In Ref. [3] photonic crystal waveguide in Si has been used to obtain optical delay lines, 20 μm long, with delay of the order of 600 fs with pulses 110 fs wide, for optical signal processing applications.

In the optical communication systems delay lines are fundamental elements in tunable optical add/drop multiplexing (OADM), compensation of polarization mode dispersion (PMD), suppression of cross-phase modulation (XPM) and packet timing in optical time division multiplexing (OTDM). A tunable OADM using fiber optic tapped delay line (OTDL) transversal filter has been proposed [4] with a round-trip delay of 2 ps. The effects of the PMD are the signal degradation and data loss which results in a power penalty and outage probability. Following criteria proposed by ITU (International Telecommunication Union), the maximum tolerable differential group delay (PGD) is 10% of the bit duration to maintain acceptable receiver error rates. For 10 Gb/s and 40 Gb/s systems, a PMD of 10 ps and 2.5 ps, respectively, is recommended. Typical PMD compensators consist of a polarization controller followed by a fixed or variable DGD section.

XPM is another strong critical effect in long-distance WDM transmissions, which limits the maximum power that can be injected in the transmission line. Optical delay lines are the basic elements of the XPM suppressors. A total delay of 80 ps has been proved useful to strongly reduce the penalties in a 10x10 Gb/s transmission over five spans of 100 km [5]. Fast wavelength switching has been demonstrated [6] using an OTDM channel selector based on both parallel and serial optical delay line. Wavelength switching was achieved with an average latency of 100 ps for a parallel delay structure on 16 channels at 40 Gb/s and an aggregate bit rate of 160 Gb/s.

In this paper the design of novel guided-wave MQW 1D defective PBG delay lines is described. The new configuration can be used to produce delay elements for applications both in optical signal processing and telecommunication systems. Tunability is also allowed by varying the refractive index of the materials with the use of an external electric field.

Delay line architecture

The schematic diagram of the delay line including periodicity defects is shown in Fig. 1.

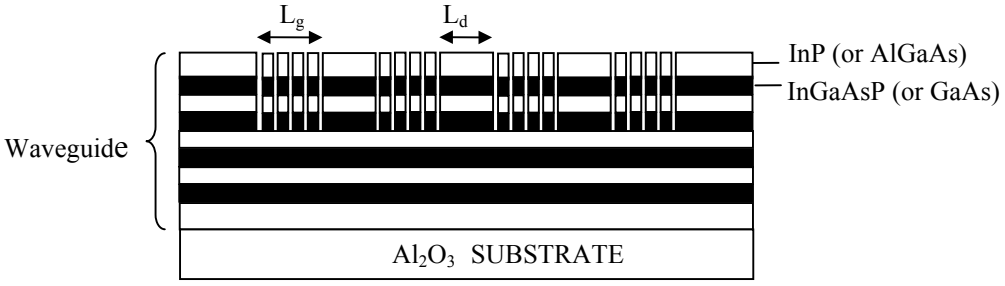


Fig. 1. Scheme of guided-wave planar MQW single grating.

The periodic perturbation, having rectangular profile with tooth width w, period Λ and length L_g, is partially etched inside a MQW with four wells and five barriers, each layer being isotropic and homogeneous. The configuration in Fig. 1 has been demonstrated to be highly efficient with respect to the photonic bandgap effect [7]. A number of N+1 gratings, each one having M periods, are separated by N unperturbed waveguide sections (defects), each one L_d long. Two types of MQW structures have been investigated: one based on GaAs technology to design delay lines at wavelengths around 850 nm; the other, based on InP, is focused for applications at 1550 nm. An Al_2O_3 substrate has been considered. In both cases, the grating depth is 80 nm (50% etched) and the duty cycle 70%. The grating period is 157 nm for GaAs and 357 nm for InP. Index contrast is 2.49 for the GaAs structure and 2.31 for the InP one.

According to the Floquet-Bloch formalism [7-8], the electromagnetic field inside the grating region has been described as a combination of two rigorous solutions (forward and backward leaky modes) of the lossy infinite structure without any approximation for guided-wave high contrast gratings, both partially or fully etched. Then, these solutions have been used in a closed-form multiple reflection cavity model, to take into account the presence of an arbitrary numbers of defects. The group delay time δ, suffered by the optical wave traveling along the MQW structure, has been calculated with respect to vacuum as:

$$\delta = \frac{L}{v_g} - \frac{L}{c} = \frac{d\varphi}{d\omega} + L\left(\frac{d\beta_u}{d\omega} - \frac{1}{c}\right) \tag{1}$$

where v_g and c are the group velocities inside the grating and in vacuum, respectively, φ is the transmission phase, β_u is the unperturbed waveguide propagation constant and L is the delay line length. To characterize the behaviour of any delay line and compare the performance, an appropriate dimensionless figure-of-merit has been used, i.e. the group index $n_g = \delta c / L + 1$.

Numerical results

TE optical polarization has been considered. A number of calculations have been carried out by varying the device parameters, i.e. N, M, L_d, L_g. The aim was to maximize the value of n_g, i.e. to obtain the maximum delay with minimum total length. Another parameter has been simultaneously considered, the time duration of the incident signal pulse, which is very important when very fast ultrashort data streams are considered in telecommunications systems. In Fig. 2 the spectral behaviour of transmittivity and group delay in case of M = 4 periods for both GaAs- and InP-based MQW structures are sketched.

A number of cases have been considered by changing N. All the gratings and defects of the structures are equal. As we can see from the curves, the transmittivity and delay bandwidth become more and more flat as large as the number of defects, so giving the possibility to transmit narrower delayed pulses. However, the delay line length increases with N and, then, the best trade-off between conflicting requirements must be found.

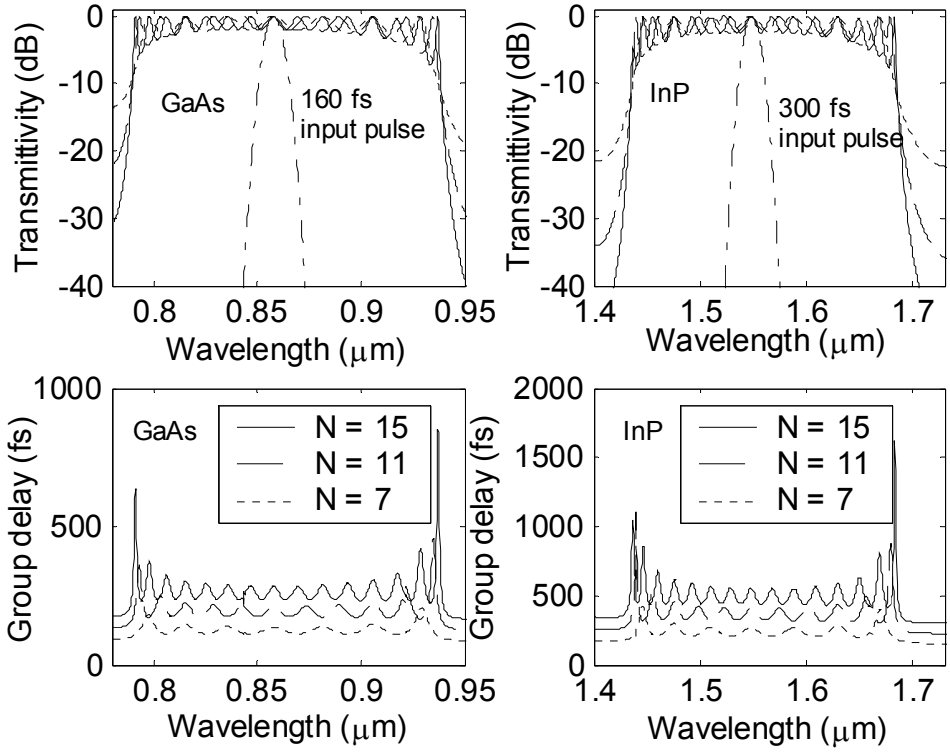


Fig. 2. Transmittivity and delay for GaAs- and InP-based defective PBG delay lines.

Therefore, the different cases have been compared in terms of figure-of-merit $n_g = \delta c / L + 1$, showing that the optimal number of defects is N = 15 in both technologies. Table I summarizes the performance parameters of the best delay lines investigated.

Table I. Delay line performance.

Parameters	*GaAs structure*	*InP structure*
Grating length, L_g (nm)	628 (M = 4)	1428 (M =4)
Defect length, L_d (nm)	538	1224
Number of defects, N	15 (optimal)	15 (optimal)
Delay line length (nm)	18126	41215
Group index, n_g	5.3	4.62
Wavelength, λ (nm)	858	1548
Delay, δ (fs)	260	498
Pulse time duration (fs)	160	300
Data stream rate (Tb/s)	2.5	1.33

Other calculations made with N = 150 for InP structure (L ~ 400 μm) have given delays as large as 4.9 ps with a bit rate of 40 Gb/s. It is important, in the choice of the structure parameters, to find the resonance condition inside the passive cavities formed by two neighbour gratings, in order to

form an allowed band inside the bandgap spectral region of the single grating. It critically depends on the ratio between the defect length and the grating tooth width. This condition has been found in our structures as $L_d / w =$ 4.9. The bandwidth enlargment and its relevant ripple, which we can note from Fig. 2, is due to the presence of defects and is also related to the small length of the gratings, having only four periods in these cases. In fact, with increasing M, the device spectral behaviour tends to approach that of a single, very long grating, the influence of the defects tends to disappear, the bandwidth dramatically decreases and the delay increases. Then, this behaviour could be followed by delay lines with large delays and very narrow bandwidths, in applications where a single monochromatic CW signal (not pulsed) must be transmitted [9].

The high performance of these delay lines is demonstrated by the value of group index, larger than 4.5 in both cases. This means that the MQW PBG structure delayes the input pulse more than in a homogeneous material characterized by the maximum refractive index of the structure, i.e. 3.6 for the first and 3.45 for the second structure. Moreover, it is clear from Table I that ultrafast data streams (>1 Tb/s) can be delayed and transmitted by these devices.

We have compared the n_g values with those typical, ~ 4 (i.e. 250 ps after 25 mm) of the GaAs-based OTDLs for beam forming, and proved another advantage of our architecture. Moreover, the total loss in our configurations is 2 dB, well lower than the OTDL typical values, > 10 dB.

In conclusion, we have presented the design of a new configuration of optical delay lines. The novel delay elements are formed by a guided-wave MQW structure including periodicity defects. This new configuration is fully versatile since it can be adopted to produce optical delay lines for both optical signal processing and telecommunications systems. In fact, it is possible to vary the geometrical and physical parameters to obtain the desired value of the group delay. Tunability can also be accomplished in these devices by decreasing the semiconductor layer indices by the injection of electrons, or by using nonlinear effects induced by high input powers, or by applying electric fields [10]. This performance, together with the full monolithic integration allowed by waveguiding MQW PBG structures, well demonstrate the theoretical superiority of these MQW PBG architectures as group delay lines.

[1] Santec Corp. 2002 Products, http:\\www.santec.com.

[2] M. Scalora, R. J. Flinn, S. B. Reinhardt, R.L. Fork, M.J. Bloemer, M.D. Tocci, C.M. Bowden, H. S. Ledbetter, J.M. Bendickson, J.P. Dowling and R.P. Leavitt, *Phys. Review E* **54**, R1078-R1081, 1996.

[3] Y. Sugimoto, S. Lan, S. Nishikawa, N. Ikeda, H. Ishikawa and K. Asakawa, *Appl. Phys. Lett*. **81**, 1946-1948, 2002.

[4] C.-H. Yoon, H. Kim and J.-D. Shin, *IEEE CLEO Conf. Proc*., pp. 785-786, 1999.

[5] G. Bellotti, S. Bigo, P.-Y. Cortes, S. Gauchard and S. La Rochelle, *IEEE Photon. Tech. Lett*. **12**, 1403-1405, 2000.

[6] B. C. Wang, I. Glesk, R. J. Runser and P. R. Prucnal, *Optics Express* **8**, 599-604, 2001.

[7] V. M. N. Passaro, F. De Leonardis, C. Ciminelli and M. N. Armenise, submitted to *J. Opt. A: Pure and Appl. Opt*.

[8] A. Giorgio, A. G. Perri and M. N. Armenise, *J. Lightwave Technol*. **19**, 1598-1613, 2001.

[9] L.J. Gamble, W. M. Diffey, S. T. Cole, R. L. Fork, D. K. Jones, T. R. Nelson, Jr., J. P. Loehr and J. E. Ehret, *Optics Express* **5**, 267-272, 1999.

[10] T. R. Nelson, Jr., J. P. Loehr, Q. Xie, J. E. Ehret, J. E. Van Nostrand, L. Gamble, D. K. Jones, S. T. Cole, R. A. Trimm, W. M. Diffey, R. L. Fork and A. S. Keys, *Proc. SPIE* **3714**, 12-23, 1999.

Integrated optical structures written in a polymer film by UV-induced refractive index modification

J. –S. Koo, C. B. E. Gawith, V. Albanis, S. P. Watts, G. D. Emmerson,
R. B. Williams, and P. G. R. Smith
Optoelectronics Research Centre, University of Southampton, Southampton, SO17 1BJ, UK
jk@orc.soton.ac.uk

M. C. Grossel
Chemistry Department, University of Southampton, Southampton, SO17 1BJ, UK

Integrated optical devices are demonstrated in poly(methylmethacrylate/2-methacryloylethylmethacrylate) copolymers by direct UV writing. This new technique uses a UV-induced refractive index change without etching. Y-splitter junction losses of 0.4dB and splitting ratios of 50:50 ±1% were obtained.

Keywords: polymer waveguide, integrated optical devices, direct UV writing

Introduction

The expansion of high capacity optical transmission techniques into price-sensitive areas such as datacomms and access networks requires a major reduction in the cost of optical components. Polymer waveguides are promising for low cost devices, especially at shorter wavelengths, because of their easy processing, flexibility in design, and cost effectiveness [1]. In this paper we present UV-written integrated optical devices using a PMMA-based crosslinkable copolymer family [2].

Direct UV writing is based on a localised change in refractive index caused by short wavelength radiation and has been demonstrated in silica for writing devices such as channel waveguides, Y-splitters, and directional couplers [3]. While polymer-based waveguide devices such as Y-splitters and directional couplers have also been reported, these have previously been based on chemical wet etching processes to create buried channel waveguides [4]. Our novel approach has the significant advantage that it does not require photolithography, wet chemical developing or gas phase etching.

During our UV-writing process, waveguides are photowritten in a single step using a focused spot of UV laser light that increases the refractive index of a polymer film. Each UV-written waveguide is based on a thermally crosslinked polymer layer, which can be translated under the focused spot on computer controlled air-bearing stages to allow complex refractive index structures to be literally drawn into the photosensitive material. The translation system is capable of sub-micron positional control, making this a rapid and inexpensive mask-less process.

The copolymers used during these experiments were prepared from hydroxyethylmethacrylate (HEMA) and methylmethacrylate (MMA), to which we have introduced crosslinkable sites onto the hydroxyethyl side chains to create poly(methylmethacrylate/2-methacryloylethylmethacrylate) (P(MMA/MAOEMA)) [2]. These P(MMA/MAOEMA) copolymers have several distinct advantages for our process as they can be either thermally or UV crosslinked without the need for photochromic additives [5]. Even after thermal crosslinking these polymers remain photosensitive to allow further refractive index changes via UV-illumination, a characteristic which makes them highly suitable for direct UV writing.

To this end, these results describe our initial investigation towards the fabrication of integrated optical structures in P(MMA/MAOEMA) copolymers by direct UV writing. Initial structures based on channel waveguides, S-bend structures, and Y-splitters are described and characterized in terms of propagation, bend, and junction loss and UV-induced refractive index change. We also present our first results on a new minimal pre-bake technique designed to give enhanced photosensitivity and higher NA waveguides.

Polymer film preparation and waveguide fabrication

Fabrication of the polymer film was performed by spincoating a ~4μm-thick P(MMA/MAOEMA) [poly(methylmethacrylate/2-methacryloylethylmethacrylate)] layer onto a polished silica substrate, which was then thermally crosslinked at a temperature of 140°C for 2 hours [2]. Refractive indices for the polymer core and silica substrate layers were 1.498 and 1.457 respectively.

Direct UV writing into the polymer layer was performed using a frequency-doubled argon-ion laser operating at 244nm with a focused spot size of approximately 6μm diameter (Figure 1). UV writing powers of 1 – 10mW and scan speeds of 16 – 480 mm/min were investigated for the definition of channel waveguides in the polymer layer, resulting in a fluence range of between 0.4 and 4.6 J/mm^2. Straight channel waveguides were written by translating the sample in a straight line under the focused beam, while S-bends and Y-splitters were designed with cosine circular arcs in the curved waveguide region. This simple combination of structures provides the basis of many integrated optical devices, while allowing early evaluation of waveguide parameters such as propagation loss, bend loss, and mode profile, etc. From initial inspection it was found that a UV writing fluence of 1.6 J/mm^2 gave the best results in this material. The devices were completed by spincoating a polymer overcladding layer to form an ~8μm-thick layer of the same P(MMA/MAOEMA) material, which was again thermally crosslinked after deposition.

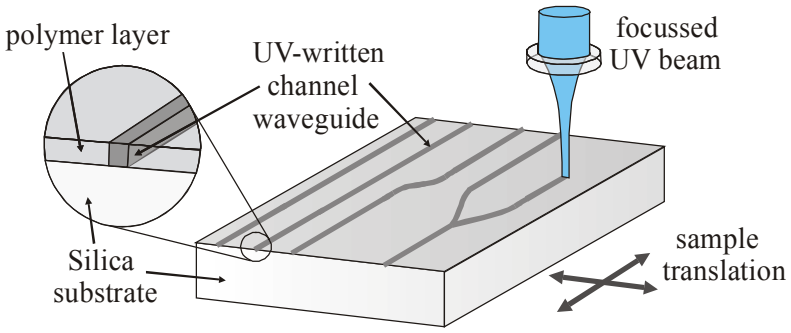


Figure 1. Direct UV writing of channel waveguide structures in a polymer layer.

Device characterization

For characterization, light from HeNe (633nm) and fibre laser (1310nm) sources were individually coupled into the waveguide with single-mode fibres for each respective wavelength. Transmission measurements were taken with an optical power meter and mode profiles were obtained using a silicon camera and computer-based evaluation software. From cut-back measurements the propagation loss in straight channel waveguides written with a fluence of 1.6J/mm^2 was found to be ~1dB/cm at 633nm, with a coupling loss of around 2 dB and loss difference between T_E and T_M modes of <0.1dB/cm. Mode profiles were largely independent of polarization with a single circular spot at both 633nm and 1310nm indicating single-mode operation at these wavelengths. The measured NA (at 633nm) of 0.05 (±0.01) corresponds to a UV-induced refractive index change of 1×10^{-3} in the core polymer layer.

The relationship between bend loss and radius of curvature was investigated by fabricating an array of S-bend channel waveguides with different bend radii in the range of 2 – 200mm (a process performed by changing the length of consecutive S-bends between 1 and 10mm while maintaining a consistent bend displacement of 125μm). Transmission results obtained from this array demonstrate that bend losses were minimized for radii of curvature greater than 50mm (Figure 2). Based on these results, Y-splitter structures designed for minimized bend loss in this material were fabricated

with output arm separations of 250μm and 50μm and curved Y-junctions of 10mm-long, corresponding to radii curvatures of 200mm and 1000mm respectively. Direct UV conditions of 1mW power at a translation speed of 16mm/min were used to define each Y-splitting structure (corresponding to the same 1.6J/mm^2 fluence), and several straight waveguides were also written to allow direct comparison with the split channel waveguides in each sample. The two Y-splitter types were characterized at 633nm and 1310nm in terms of splitting ratio, branch loss and the shape of the mode profile. In each case the power-splitting ratio was measured to be 50:50 ±1% with symmetrical mode profiles typical of those given in Figure 3. It should be noted that the observed splitting ratios were near ideal, with no need for modification of the writing parameters between the two arms [6]. When compared with the S-bend insertion loss, it was found that Y-splitters featured an additional junction loss of less than 0.4dB at 633nm.

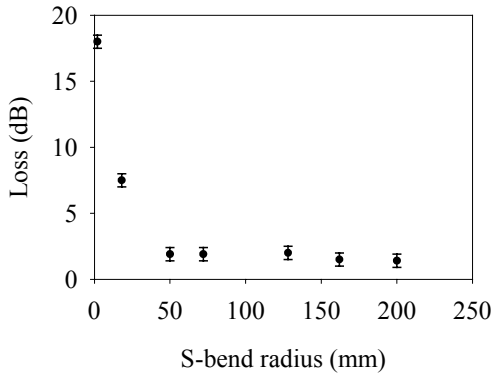


Figure 2. S-bend loss as a function of bend radius (λ = 633nm).

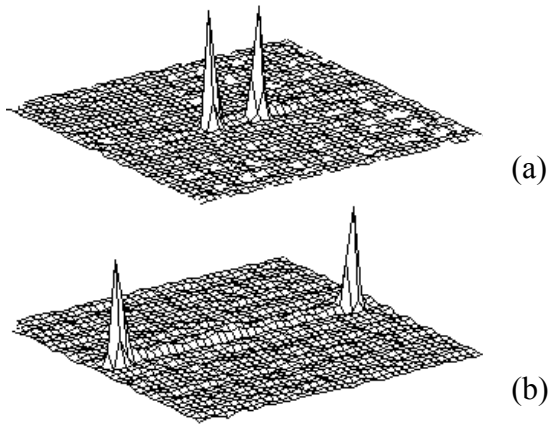


Figure 3. Mode profiles of 50:50 Y-splitters with an arm spacing of (a) 50μm and (b) 250μm (λ = 633nm).

Non-crosslinked pre-bake process for enhanced photosensitivity

Having achieved encouraging figures for Y-splitter junction loss we have continued to investigate new approaches towards obtaining a higher refractive index contrast in the channel waveguide structures. A new technique was developed which resulted in much higher NA waveguides, in which the polymer layers are pre-baked at a much lower temperature and shorter time (90°C for 10 min). Under these processing conditions, most of the solvent is removed but the polymer does not appreciably crosslink. Channel waveguides can then be written in the same way as before, but with optimised exposure conditions of 5mW power and scan speeds of 32 – 1024mm/min, corresponding to a fluence range 0.1 – 4.0J/mm^2. The sample is then crosslinked under normal conditions (140°C for 2hrs) and an overcladding layer applied.

Straight channel waveguides fabricated using this technique were characterized in terms of mode profiles and NA. It was discovered that channel waveguides written with a fluence between 0.3 and 1.1J/mm^2 supported multi-mode operation at 633nm but were single-mode at 1310nm (Figure 4). The NA of these waveguides was measured to be 0.10 (±0.01) at 633nm, corresponding to a much larger UV-induced refractive index change of ~3×10^{-3} in the core polymer layer.

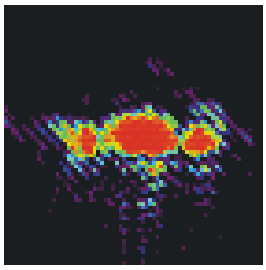
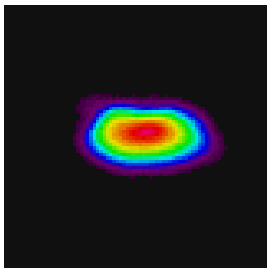

(a)

(b)

Figure 4. Mode profiles for channel waveguide structures UV-written into a non-crosslinked pre-bake P(MMA/MAOEMA) polymer film, as measured at (a) λ = 633nm and (b) λ = 1310nm.

Conclusions

In conclusion, we present a new technique for the definition of direct-UV-written integrated optical devices based on a UV-induced refractive index modification of PMMA-based crosslinkable copolymers, a process that eliminates the need for wet chemical developing and gas phase etching. Straight waveguides fabricated with this technique demonstrate propagation losses of ~1dB/cm, and a polarization dependent loss of <0.1dB/cm. Single-mode operation was obtained in channel waveguides with a NA of 0.05, and S-bend fabrication provided information on minimized bend loss for designing Y-splitters. Y-splitters with 200 and 1000mm radii provided symmetrical power distribution (splitting ratio 50:50%) and junction losses of less than 0.4dB. A new minimal pre-bake technique for preparation of the polymer films resulted in an enhanced photosensitivity and a larger channel waveguide NA of 0.1. These results demonstrate that direct UV writing provides a simple and versatile new solution for the fabrication of polymer integrated optical devices.

[1] B. L. Booth, *J. Lightwave Technol.* **7** (10), 1445-1453, 1989.

[2] J. –S. Koo, P. G. R. Smith, R. B. Williams, M. C. Grossel, and M. J. Whitcombe, *Chem. Mater.* **14** (12), 5030-5036, 2002.

[3] M. Svalgaard, *Elect. Lett.* **33** (20), 1694-1695, 1997.

[4] L. Xu, C. C. Eldada, K. M. T. Stengel, L. W. Shacklette, and J. T. Yardley, *J. Lightwave Technol.*, **14** (7), 1704-1712, 1996.

[5] A. G. Hallam, I. Bennion, and W. J. Stewart, *ECIO*, **201**, 26-28, 1981.

[6] K. Faerch and M. Svalgaard, *IEEE Photon. Technol. Lett.*, **14** (2), 173-175, 2002.

Silicon Rich Nitride Micro-resonators

K. N. Andersen, W. E. Svendsen, R. K. Sandberg, H. T. Philipp and J. Hübner
COM, Ørsteds Plads, DTU build. 345V, DK-2800 Kgs. Lyngby, Danmark
ka@com.dtu.dk

Abstract: We report optical resonance in planar waveguide silicon rich nitride (SRN) ring resonators with radii down to 29 μm. Due to their high finesse and large free spectral range, these resonators are shown to be well suited as building blocks for highly integrated optical components.

Keywords: Ring resonator, integrated optics, high index contrast materials

Introduction

Digital optical filters are a major field of interest, because of the fact that nearly arbitrary filter functions can be built out of a few rather simple building blocks using digital signal processing theory [1]. One of the main disadvantages in realizing these filters has been the limitation in bending radii, leading to large and thereby expensive components and at the same time limiting the free spectral range of the resonators. Using silicon rich nitrite (SRN) as waveguide material, we have demonstrated resonators having a factor of hundred smaller bend radii than normally used in silica based components. This means that the required area for one resonator loop is nearly four orders of magnitude smaller allowing in principle a 10000 times higher integration density of integrated optical components.

In this article we will discuss the material properties of SRN with a step index of $\Delta n = 0.615$, with respect to properties of microring resonators and coupling to straight SRN waveguides. We show examples of measured resonances, which are in very good agreement with the theoretical predictions.

Silicon rich nitride (SRN)

Thermal oxide (~10 μm) serving as buffer layer was grown on a 4” silicon wafer, upon which the SRN core layer was deposited by low-pressure chemical vapor deposition (LPCVD). Standard photolithography and subsequent reactive ion etching was used to make the structures. The cladding consists of~12 μm boron phosphorous-doped glass (BPSG) deposited by plasma enhanced chemical vapor deposition (PECVD) [2]. The propagation loss of straight SRN waveguides situated on the same wafer as the ring resonators, was measured by the cut back method to be 3.2± 0.4 dB/cm. Polarization dependent loss was measured to around 3 dB. The elevated propagation loss compared to earlier reported values (as low as 0.73 dB/cm [2]) is attributed to particle contamination due to a minor leakage in the deposition equipment.

Ring resonators

In order to couple light in and out of the straight SRN waveguide, a high NA fiber with a mode field diameter of around 4 μm was spliced to a standard fiber. To obtain the required spectral resolution of 1 pm a tuneable laser in connection with an optical spectrum analyser was used to record the narrow transmission resonance. The polarization was adjusted using a polarization controller.

A structure consisting of one or three SRN rings adjacent to a straight SRN waveguide has been studied. All the resonators are in a racetrack configuration as shown in fig. 1.

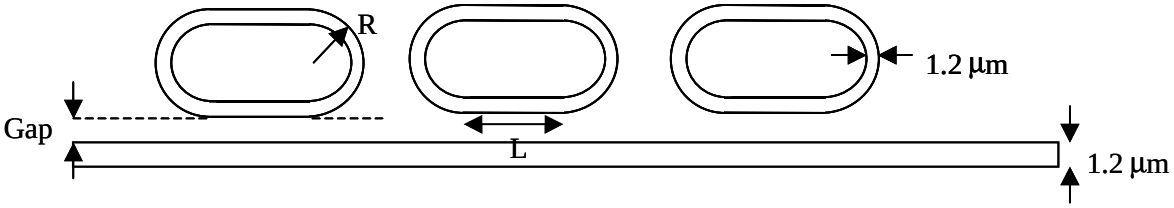


Figure 1. Ring resonator. R is the radius of curvature, and L is the coupling length.

The waveguide width in the resonators as well as the straight waveguide is 1.2 µm and the height is 0.61 µm. The dimension for single mode square waveguides in SRN with a refractive index of 2.06 at 1550 nm is approximately 0.6 µm x 0.6 µm. Although the measured waveguides are able to support higher order modes we do not observe any resonance that can be attributed to other than the fundamental mode. This is due to the elevated bend loss in the resonator loop for higher order modes.

A transmission spectrum of a ring resonator is show in fig. 2. It can be seen that the coupling intensity increases with wavelength. The inserted graph in fig. 2 is a transmission spectrum two single peaks. Different racetrack-structured resonators, with varying radius, ring and coupling length have been analysed.

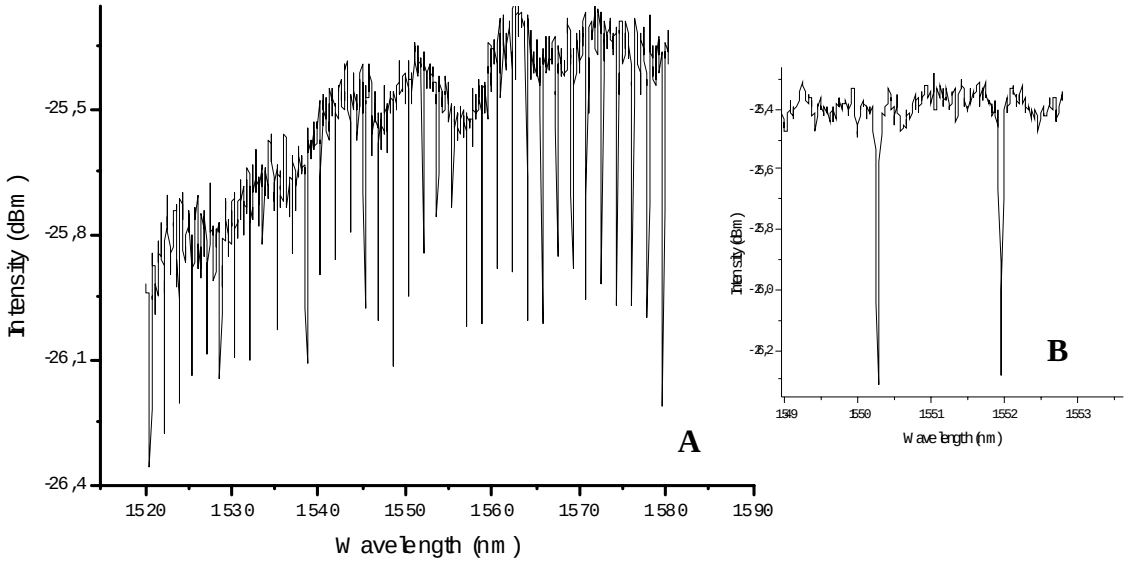


Figure 2. A) Transmission spectrum of a resonator with a radius of 100 µm, separation between resonator and waveguide is 1.0 µm. B) A close up of two peaks, FSR = 1.7 nm at 1550 nm.

When measuring on structures with three resonators, three different resonances are observed for each resonator as illustrated in fig. 3. The spectrum is shown for a resonator with a radius of 31 μm. The free spectral range (FSR) is 2.14 nm.

Racetrack-shaped resonators with radii varying from 29 to 100 μm were investigated. The transmission spectra were analysed using a Lorentzian fit to each absorption peak, determining the free spectral range (FSR) and the full width half maximum (FWHM). In fig. 4 the measured free spectral range (FSR) of the resonators is compared to the theoretical values, showing good agreement. The finesse of these resonators is around 65.

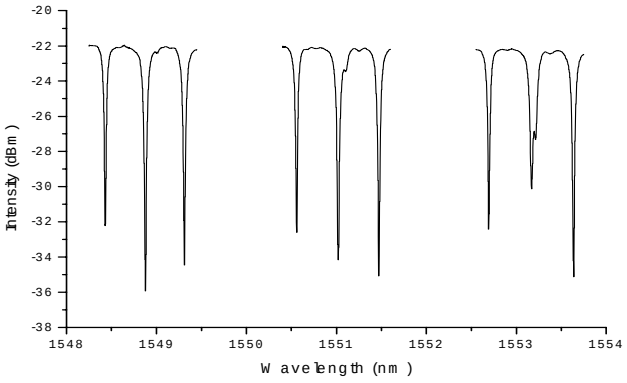


Figure 3. Transmission spectra of resonators with radii of 31 μm, separation between resonator and waveguide is 1.0 μm.

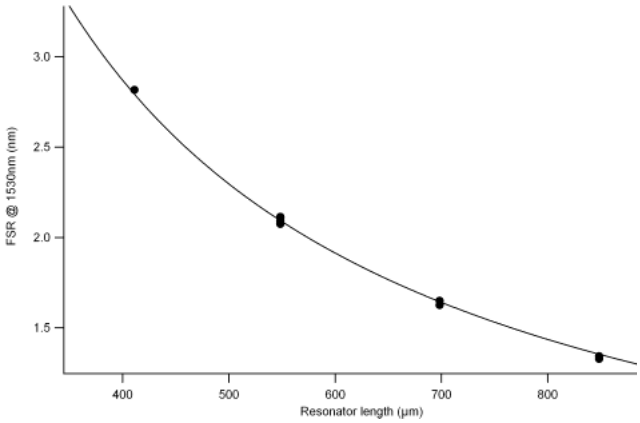


Fig 4. Free spectral range (FSR) as a function of ring resonator length. The round symbols are the measured values; the curve is a theoretical fit.

The curvature loss of the ring resonators is critical. In order to determine the curvature loss, several waveguides with different radius of curvature, and with a varying number of bends from two to ten were measured. We could not measure a difference in insertion loss as a function of the number of bends in a waveguide even for the smallest radius of 20 μm. From these measurements we conclude that the bend loss for one 90-degree bend with 20 μm is below 0.1 dB. This means that in these particular samples the propagation loss in the waveguide is the dominating loss mechanism within the resonator.

To investigate the coupling we use a schematic as illustrated in fig. 5. A fraction (κ) of the intensity of the propagating field in the straight waveguide mode (E_{11}) is coupled evanescently with the resonator mode yielding a field (E_{22}) propagating in the resonator. While this field propagates in the resonator the modal amplitude decreases due to the propagation and bend loss of one round trip in the resonator (γ) yielding a field (E_{12}) coupling out of the resonator with a coupling coefficient (κ). This field interferes with the field in the straight waveguide yielding a field (E_{21}) now propagating in the straight waveguide.

Writing the electric field equations for this scenario:

$$E_{21} = E_{11}\sqrt{1-\kappa} - jE_{12}\sqrt{\kappa}$$
$$E_{22} = E_{12}\sqrt{1-\kappa} - jE_{11}\sqrt{\kappa}$$
$$E_{12} = E_{22}\sqrt{1-\gamma}\cdot\exp(j\cdot 2\pi\tfrac{L_{ring}\cdot n_{eff}}{\lambda})$$

where L_{ring} is the physical length of the resonator and n_{eff} is the effective group index. Solving we get the output intensity of the resonance spectra.

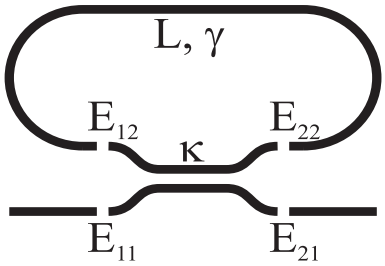


Figure 5. Coupling scheme used for the resonators

$$I_{out} = E_{21}\cdot E_{21}^{*} = |E_{11}| = \frac{2-\kappa-\gamma-2\sqrt{1-}\kappa\sqrt{1-\gamma}\cos(j\cdot 2\pi\tfrac{L_{ring}\cdot n_{eff}}{\lambda})}{2-\kappa-\gamma+\kappa\gamma-2\sqrt{1-}\kappa\sqrt{1-\gamma}\cos(j\cdot 2\pi\tfrac{L_{ring}\cdot n_{eff}}{\lambda})}$$

Using this expression and inserting the values of the FSR and the total loss in ring, the coupling coefficient for each resonator configuration can be found. The fractional coupling (κ) was calculated for two resonators with different round trip and coupling lengths. The measured and calculated data is displayed in table 1. The loss has been estimated as a propagation loss corresponding to the resonator length and the resulting fractional coupling (κ) is in good agreement with the theory of directional couplers, from which we have $\kappa = \mathrm{Sin}^2(C*L_{Coup})$. Taking the coupling coefficient C to be $1.77\cdot10^{-3}$ yields an almost perfect fit with the experimental values of κ.

Resonator length(μm)	548.38	548.38	698.26	698.26
FSR @1530nm (nm)	2.079	2.093	1.628	1.640
Round trip loss in dB	0.1863	0.1863	0.2374	0.2374
Fractional loss, γ	0.0420	0.0420	0.0532	0.0532
Coupling length (μm)	175.9	175.9	34.97	34.97
Fractional coupling, κ	0.0984	0.0896	0.00347	0.00422

Table 1. Measured and calculated data for two resonators.

Conclusion

We have demonstrated microresonators consisting of a waveguide loop made of silicon rich nitrite coupling to a straight waveguide of the same material. Strong resonance with suitable high finesse was observed with a free spectral range of several nanometers. Bend loss is smaller than 0.1 dB per 90 degree bend, down to a radius of 20 um. These resonator loops are an important building block for add-drop multiplexers and digital optical filters, which proves that silicon rich nitrite is a suitable platform for optical large scale integration.

References

[1] Christi K. Madsen, Jian H. Zhao, Optical Filter Design and Analysis: A Signal Processing Approach, 1999, Wiley.

[2] K. N. Andersen, P.C. Nielsen and W. Svendsen. Proceedings of Integrated Photonics Research conferences (IPR) 2002.

Realisation of adiabatic transition between surface and buried ion-exchanged channel waveguides made on glass

O. Bertoldi[1], J.-E. Broquin[2], G. Vitrant[2]
1) GeeO, 16 chemin du Vieux Chêne, 38240 Meylan, France
2) IMEP, 23 avenue des Martyrs, 38016 Grenoble Cedex 01, France

A new method for the realisation of selectively buried waveguides made by ion-exchange in glass substrates is presented. Simulations and measurements of the waveguides burying depth are reported. It is demonstrated that this easy to implement method permits to obtain an adiabatic transition between buried waveguides and surface waveguides and is easy to implement.

Keywords: ion-exchange process, selectively buried waveguide, adiabatic transition.

Introduction

Among all the technologies developed to realise integrated optic devices, ion-exchange in glass substrates has proved to be an efficient low cost and high performance solution [1], [2].

The first kind of ion-exchanged realised devices were surface channel waveguides made by a single-step ion-exchange process [3]. One of the drawback of this process is that the coupling with optical fibres is difficult because of the semi-elliptical shape of the waveguides. Another one is that the guided waves are very sensitive to the glass surface defects (roughness, impurities, …) and to the superstrate modification, if any. These problems are solved by the use of buried channel waveguides which are made by a two-step ion-exchange process [3], [4]. The shape of these waveguides are almost circular so that fibre coupling is strongly improved. In addition, the optical isolation to any phenomena occurring on the surface is ensured.

However, a localised interaction with a superstrate may be necessary for some applications (optical sensor [5], lasers or filters [6]). This implies the realisation of surface waveguides on a defined area of the device, the remaining parts of the integrated optical circuit being made with buried waveguides. For this purpose, it is necessary to realize adiabatic transitions between buried and surface waveguides. A first solution that has been already proposed was based on a mask put on the surface of the glass substrate [7]. This mask prevents the migration of the ions inside the substrate. However, this process requires an accurate control of the tilt angle between the axes of the mask and the waveguides to be lossless. In this paper, another solution is presented. It consists in the use of a mask deposited on the back side of the optical wafer. This solution presents several advantages, such as a low dependency on the mask alignment and a smooth variation of the applied electric field implying a adiabatic transition between the surface and buried waveguides.

Principle of realisation

A two steps ion-exchange process is required for the fabrication of buried waveguides. During the first step, a surface waveguide is obtained by an exchange of Ag^+-Na^+ ions through a mask deposited on the glass substrate (Figure 1(a)).

During the second step, two methods can be used to move Ag^+ ions inside the glass substrate. The first one is achieved by isotropic thermal diffusion in a molten $NaNO_3$ salt (Figure 1(b1)). In order to obtain a sufficient burying depth, the diffusion time has to be high. However, this lead to the spreading of the Ag^+ ions and finally to the destruction of the waveguide. To prevent this effect, the thermal diffusion is usually assisted by an external electric field applied to the wafer (Figure 1(b2)) so that the ion migration inside the wafer due to their electrical mobility is much faster than their diffusion spreading.

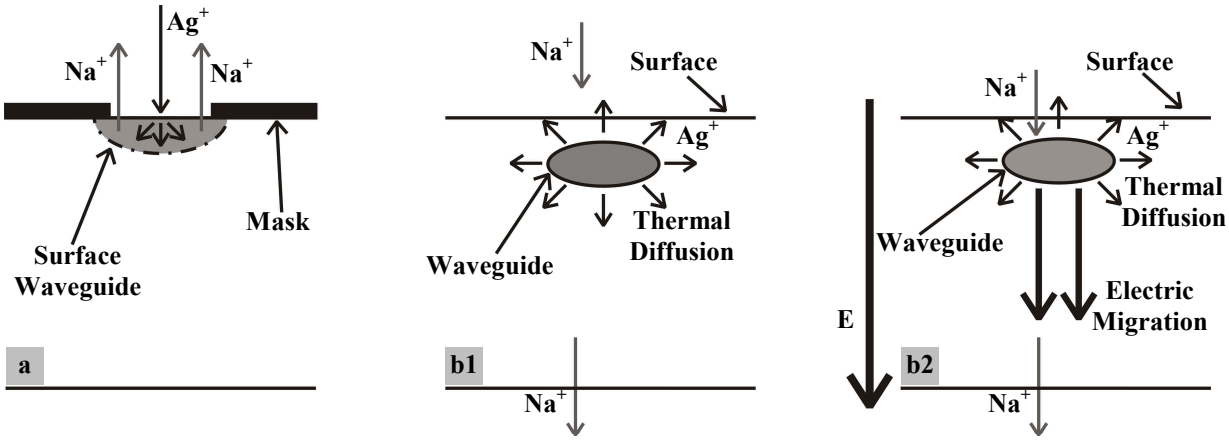


Figure 1: (a) First step of the ion-exchange process; (b) Second step of the ion exchange process made by (1) Isotropic thermal diffusion, (2) Thermal diffusion assisted by an electric field

By this way, the burying depth depends on both the applied electric field and the migration time. Usually, time is used to set the waveguide depth and the applied electric field remains constant. However, in order to bury selectively a waveguide, it is easier to adjust the burying depth by the amplitude of the applied electric field. Numerical simulations based on models of ionic diffusion [8], [9] have been performed to evaluate the value of burying depth when the voltage varies. The results are presented in Figure 2(b). The burying depth is defined as the distance between the surface and the maximum of the electric field as shown on Figure 2(a). Figure 2(b) shows that the waveguides can be buried at a depth from 3 µm, when no voltage is applied, to 15 µm when a voltage of 600V is applied. The minimum depth corresponds to the purely thermal diffusion.

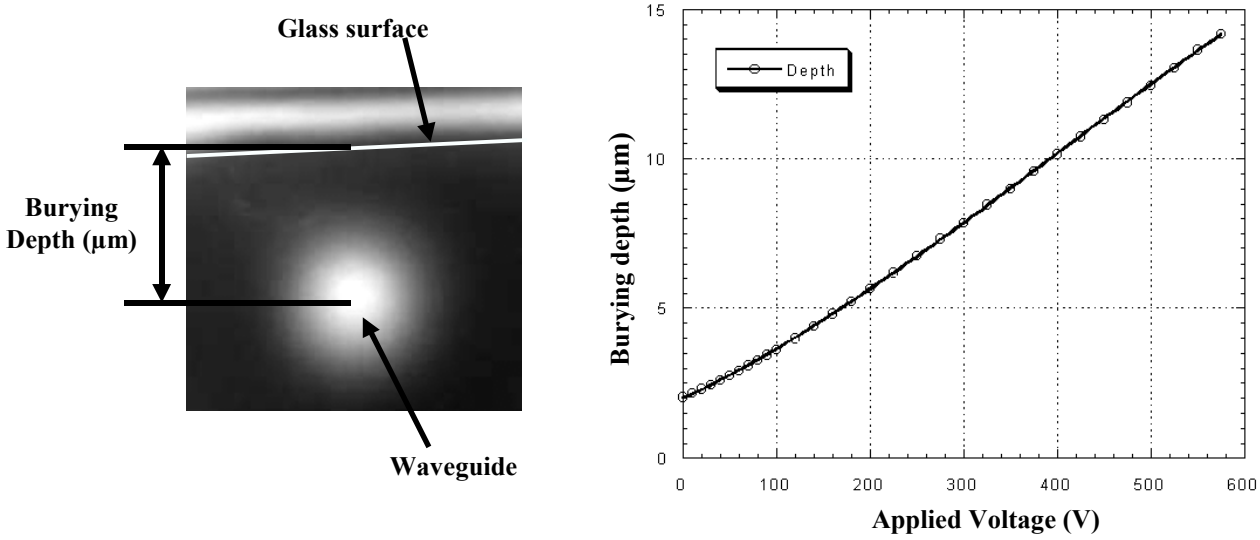


Figure 2: (a) Definition of the burying depth on a waveguide near field picture, (b) Evolution of the burying depth of a waveguide in regards with the applied voltage

In order to control the applied electric field value, the solution developed here consists in depositing a mask on the back side of the glass substrate. Consequently, when an electric field is applied, the Ag^+ and Na^+ ions both migrate along the direction of this field. In the unmasked region, the migration of these ions is free whereas above the mask, it is impossible for the Na^+ ions to escape from the glass substrate. Therefore, a space-charge zone appears and an induced electrostatic electric-field compensates the applied electric field. As a result, the electric charge distribution is

not uniform leading to a potential distribution. To determine this distribution, Poisson's equation with hybrid Dirichlet and Newman conditions has to be solved. An example of the obtained potential distribution is presented in Figure 3. From this potential distribution, the value of the electric field applied along the surface waveguide can be determined. The results of these calculations are shown in Figure 4(a). Thanks to these results, the burying depth of the waveguide is computed. The variation of the burying depth of the waveguide obtained by the simulations for a 10 mm wide mask is presented in Figure 4(b). As explained previously, in the middle of the mask where the electric field applied is minimum, the waveguide is only buried at a depth of 3 µm.

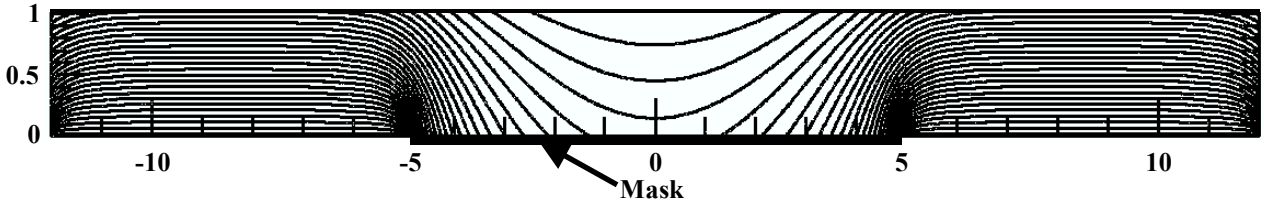


Figure 3: Distribution of the potential in the substrate for a mask of 10 mm wide (the origin of the horizontal axis is taken in the middle of the mask)

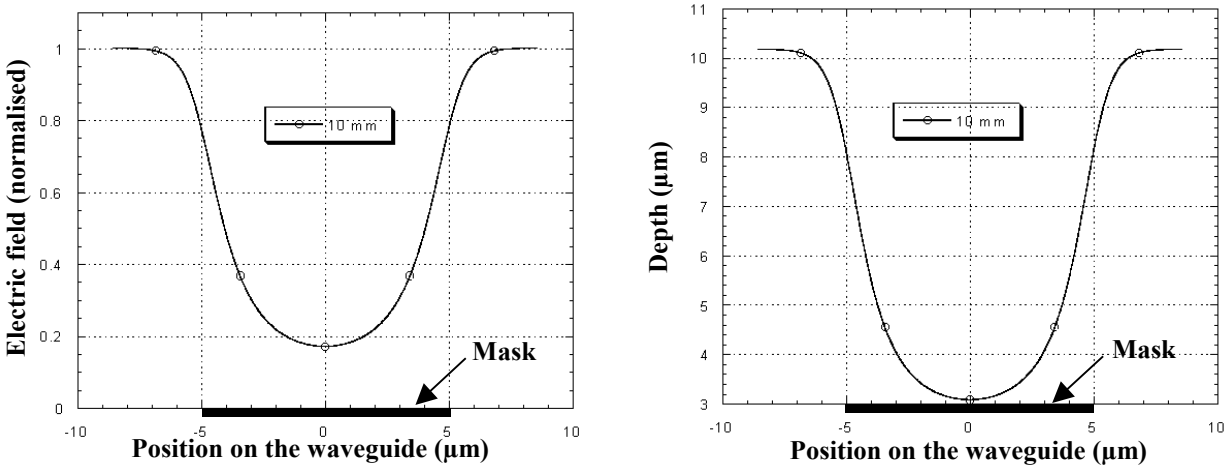


Figure 4: Evolution of (a) the value of the electric field applied to the surface waveguide and (b) the burying depth along a longitudinal section of the waveguide for a mask of 10 mm wide (the origin of the axes is taken in the middle of the mask).

Experimental results

The validation of these simulations are performed on the following sample. On one side of the substrate 48 straight identical waveguides have been processed. On the opposite side, a mask of 10 mm width has been deposited, tilted by 30° with respect to the axis of the waveguides. Therefore, the waveguides end at different positions with respect to the centre of the mask. Then, the burying depth of the 48 waveguides is measured along one cut perpendicularly to the axis of the waveguides, by the near field imaging technique at 1.3 µm.

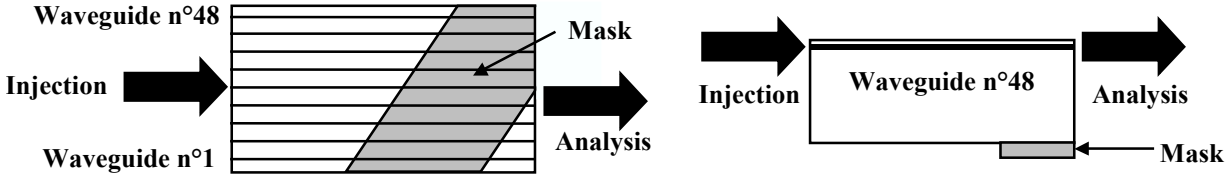


Figure 5: (a) Top view of the structure and (b) Longitudinal section of the 48th waveguide before the second step

The results of the waveguide burying depth measurements are presented on Figure 6(a) and picture of near field measurement for waveguide in the masked region (Figure 6(b1)) and in the unmasked region (Figure 6(b2)) are shown.

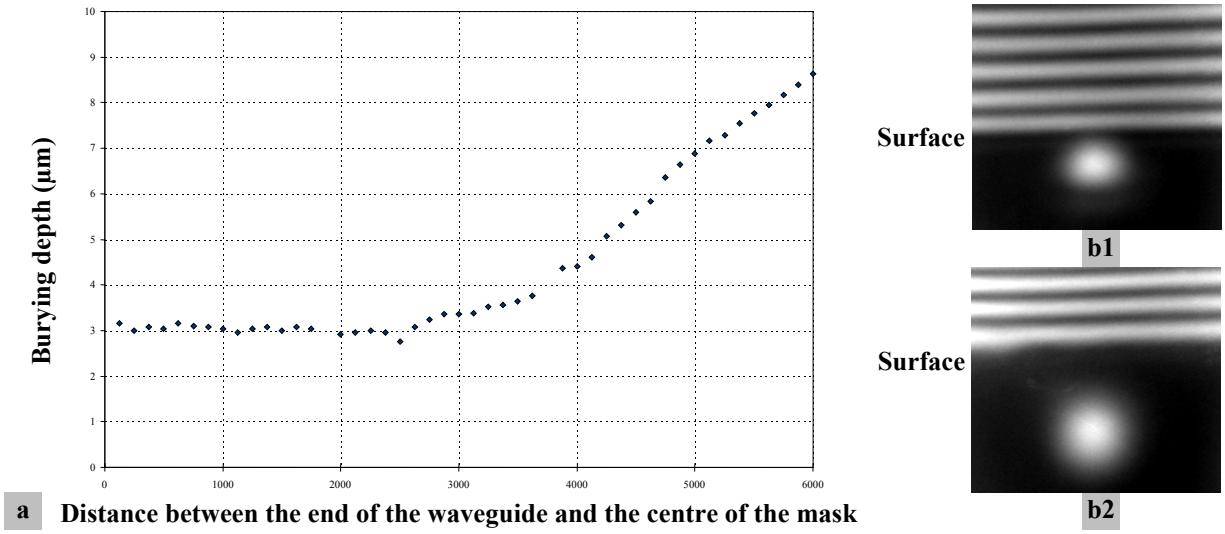


Figure 6: (a)Experimental burying depth of the 48 waveguides along one cut; (b) Near field waveguide pictures in (1) The masked region, (2) The unmasked region

In the unmasked region, the maximum field is located 10 µm under the surface. The isolation between the waveguide and the surface is thus ensured. The transition is 3mm long. Thus, the curvature radius is important enough to prevent any excess losses and the transition is adiabatic. In the masked region, the value of the burying depth of the maximum field is 3 µm. In order to confirm that no electric field has buried this waveguide, a purely thermal diffusion process has been applied to another sample. The burying depths of the waveguides of this sample have been measured and compared to the one of the previous waveguide n°48. The obtained values are identical within the measurement accuracy.

Conclusion

In this paper, we have demonstrated that the use of a mask on the back side permits a control of the burying depth. This technique is found to be very powerful. It allows to fabricate smooth transitions between almost surface waveguides to buried ones. Such 3D waveguide structures will be very helpful in integrated optic telecommunication or sensor applications.

[1] J.E. Broquin, *Proceedings of the SPIE*, vol. **4277**, 105-117, 2001.
[2] J. Linares, C. Montero, V. Moreno, M.C. Nistal, X. Prieto, J.R. Salgueiro, D. Sotelo, *Proceedings of the SPIE*, vol. **3936**, 227-238, 2000.
[3] T. Findakly, *Optical Engineering*, vol. **24**, p244-250, 1985.
[4] T. Izawa, H. Nakagome, *Applied Physics Letters*, vol. **21**, 584-586, 1972.
[5] C.R. Lavers, K. Itoh; S.C. Wu, M. Murabayashi, I. Mauchline, G. Stewart, T. Stout, *Sensors and Actuators B*, **B69**, 85-95, 2000.
[6] S. Blaize, L. Bastard, C. Cassagnetes, G. Vitrant, J.E. Broquin, *Proceedings of the SPIE*, vol. **4640**, 218-225, 2002
[7] F. Rehouma, D. Persegol, A. Kervorkian, *Sensors and Actuators B*, **B29**, 406-409, 1995.
[8] J. Hazart, V. Minier, *IEEE Journal of Quantum Electronics*, vol. **37**, 606-612, 2001.
[9] A. Lupascu, A. Kervorkian, T. Boudet, F. Saint-Andre, D. Persegol, M.Levy, *Optical Engineering*, vol. **35**, 1603-1601, 1996.

Self-Assembled Microsphere Gratings on Rib Waveguides

Chao-Yi Tai, Bayram Unal, James S. Wilkinson
Optoelectronics Research Centre, University of Southampton, Highfield, Southampton, SO17 1BJ, United Kingdom
cyt@orc.soton.ac.uk

Mohamed A. Ghanem and Philip N. Bartlett
Chemistry Department, University of Southampton, Highfield, Southampton, SO17 1BJ, United Kingdom

We report the spectral transmission of a rib waveguide side-coupled to a self-assembled polystyrene microsphere array. A transmission stopband was observed at $\lambda \approx 1590$nm, showing the potential for realising wavelength-selective devices.

Keywords: self-assembly, distributed feedback, planar lightwave circuits

Introduction

There is ongoing interest in integrating more functionality in planar lightwave circuits (PLCs). Wavelength selective devices are in particularly high demand due to their ability to provide filtering, routing and feedback, which are fundamental requirements for signal processing. Bragg gratings realised in planar waveguides date back to the early 1970's [1] and intensive research on distributed feedback structures has been pursued since then. Photosensitive [2,3] and etched relief gratings [4,5] are presently the most widely used structures. Relief gratings provide greater material flexibility because there is no requirement for special photosensitivity. However, sub-micron scaled patterning and stringent etching tolerances are unavoidable for transferring patterns onto waveguides, resulting in high fabrication costs.

In this paper, we present a promising new technique based upon the combination of self-assembly [6] and conventional photolithography. Sub-micron polystyrene spheres were self-assembled to one side of a photolithographically-defined rib waveguide, forming a linear array. As the spheres are placed against the waveguide, the optical field is drawn out resulting in a strengthened interaction with the spheres. The resultant periodic perturbation of the refractive index experienced by the modal evanescent field leads to coupling to the backward-travelling mode at the Bragg wavelength. The waveguide was designed to be single mode at the wavelength of operation, sufficiently narrow to ensure that a significant proportion of the modal power travelled in the lateral evanescent region, and with a sufficient height to physically trap the microspheres. Polystyrene has a refractive index of approximately 1.59, so that a higher index waveguide material was chosen (Ta_2O_5; $n \approx 2$) from which to form the rib waveguides. The great advantage of this configuration is that all the fabrication techniques employed are relatively simple, inexpensive and compatible with existing planar devices which makes this an attractive candidate for scaling up to more sophisticated PLCs. Furthermore, this technique provides a simple route to hybrid circuits combining microspheres in novel functional materials with waveguides in conventional materials.

Fabrication Process

A layer of 500nm thick tantalum pentoxide (Ta_2O_5) was first sputtered from a Ta_2O_5 target in a Ar/O_2 atmosphere onto a Si wafer with 2μm SiO_2 buffer layer, with the substrate held at 250°C. The film was then photolithographically patterned with stripes of photoresist of nominal width 1 μm, and argon ion beam milled to transfer the pattern into the Ta_2O_5 resulting in a rib waveguide with an etch depth of 400 nm, and a width of approximately 1.3 μm.

In preliminary work, microspheres were assembled on both sides of the waveguide, but this led to degradation in the effective strength of the grating due to misalignment between the two sides. To avoid such a phase error, we intentionally assembled polystyrene spheres along only one side of the rib waveguide. To achieve this, photoresist was coated over one side of the waveguide surface. A fluidic cell was then assembled by sandwiching a thin frame of Para film (0.5 mm) between the waveguide substrate and a cover glass. A suspension of mono-dispersed polystyrene spheres (1wt%, 499±5 nm in diameter, obtained from Brookhaven) was then injected into the cell with a syringe. The sample was then placed vertically in a temperature-controlled (25°C) incubator, enabling the liquid slug which pushes the polystyrene spheres to sweep across the sample at a speed of 1.5 mm/h during the dewetting process. Once the spheres were physically trapped by the rib waveguide, the capillary immersion force forced the beads to adjust themselves into a well-packed array lined up along the waveguide. When the cell had dried, the sample was heated to 90°C for 1 minute in order to stick the polystyrene spheres to the surface of the waveguide. The remaining photoresist was then removed using 2-propanol, lifting off the microspheres on one side of the rib. A microsphere array of approximately 5mm length was formed along the waveguide. A schematic diagram of the fabrication process sequence is shown in Fig. 1, and a scanning electron micrograph of part of the resultant device is shown in Fig. 2.

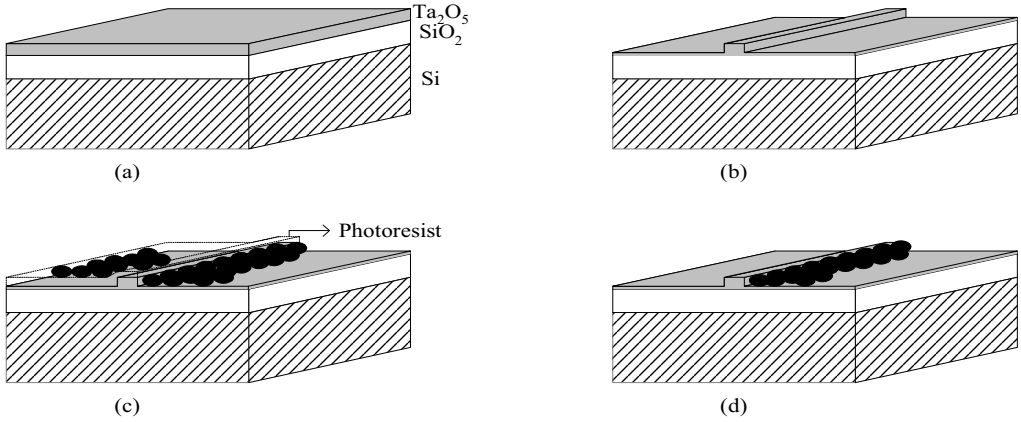


Fig. 1. The fabrication process. (a) Deposit Ta_2O_5 thin film by sputtering. (b) Etch the rib waveguide. (c) Cover one side of the waveguide surface with photoresist and self-assemble the spheres on the surface. (d) Remove the photoresist and fix the spheres in place by thermal an nealing.

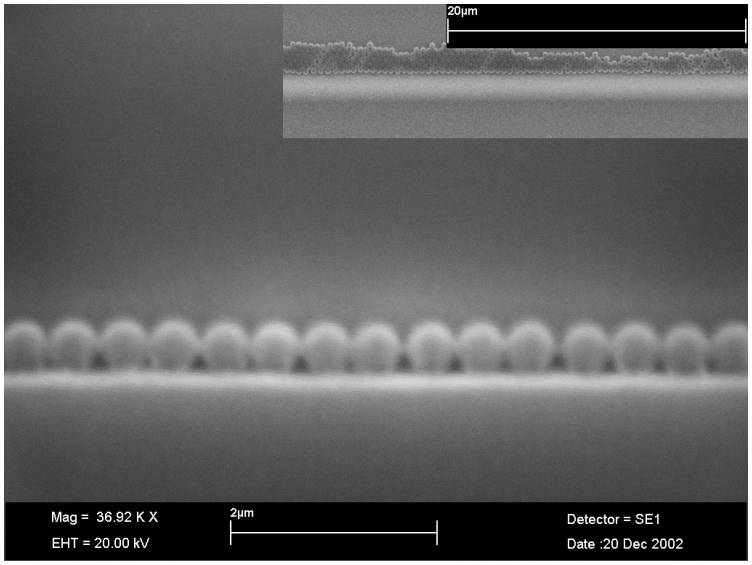


Fig. 2. SEM image of the fabricated sample. The inset details a larger area.

Characterisation and discussion

The transmission spectrum of the sphere-waveguide coupled system was measured using the apparatus shown in Fig. 3. White light from a 150W tungsten lamp was chopped and end-fire launched into a single mode fibre using a 10× microscope objective lens. The fibre was then butt-coupled to the rib waveguide under investigation. The light emerging from the waveguide was collected using a 40× objective lens, passed through a monochromator onto an InGaAs detector, and the signal was fed into a lock-in amplifier and recorded on a computer.

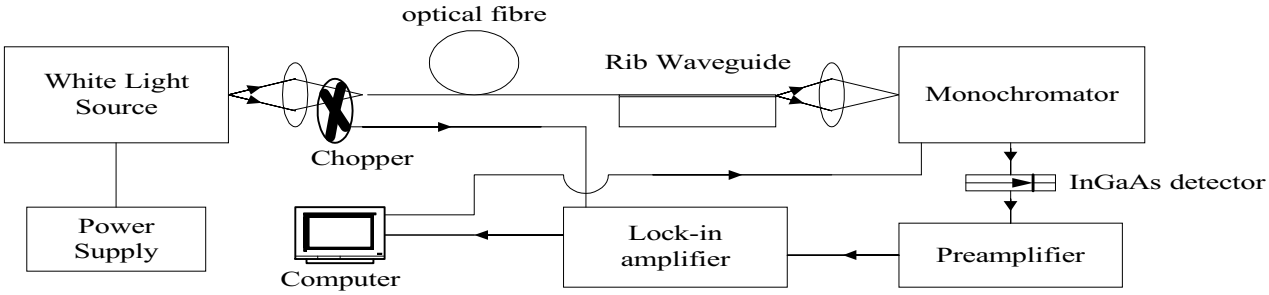


Fig. 3. Experimental arrangement for transmittance measurement.

The transmission spectrum was measured for the same waveguide before assembly of the microspheres and with cladding media of air, water (n≈1.33) and oil (n≈1.71) after assembly of the microspheres. Fig. 4 shows the transmission spectra for the three cladding media, normalised to that obtained in the absence of spheres. When the device was surrounded by air, the transmission spectrum shows a notch centred at λ=1583 nm with a depth of approximately 0.9 dB (18.7%) and a bandwidth at full width at half maximum power ($\delta\lambda_{FWHM}$) of 16 nm. As the refractive index of the overlay increases to n=1.33 (water), the centre of the stopband shifts to a longer wavelength of λ=1589 nm and exhibits a greater depth of 1.55 dB (30%) and a bandwith $\delta\lambda_{FWHM}$ of 12nm. Further increase in the refractive index of the cladding medium by using index matching oil (n=1.712) shifts the centre of the stopband to λ=1596 nm with a 0.73 dB (15.5%) transmission drop and a bandwidth $\delta\lambda_{FWHM}$of 14nm.

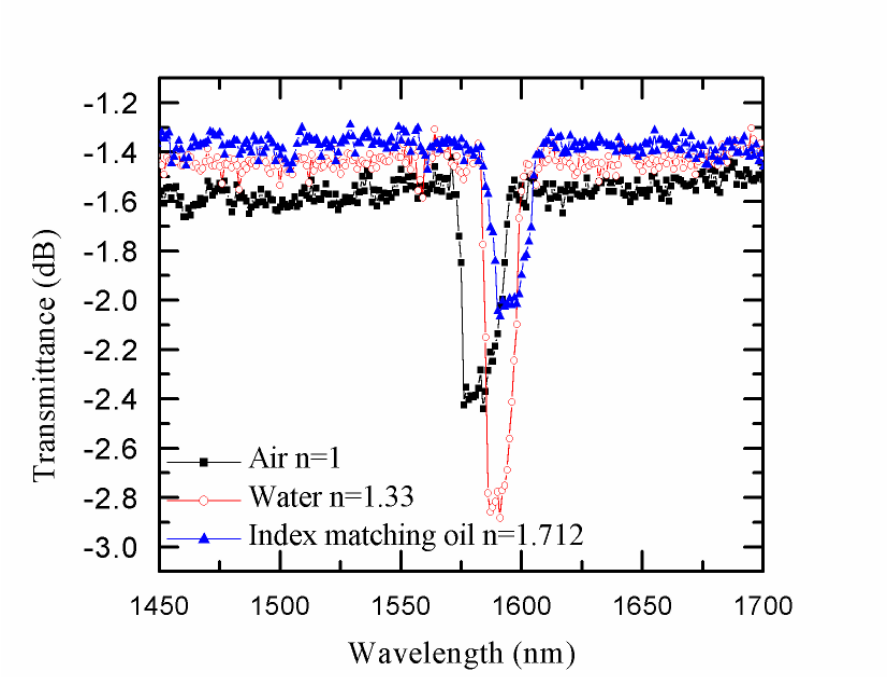


Fig. 4. Transmission spectra for different cladding media.

The reflection wavelength is given by $\lambda_{Bragg} = 2N_{eff}\Lambda$, where N_{eff} is the effective refractive index of the waveguide and Λ is the grating period. The value of N_{eff} for the present Ta_2O_5 (n~2±0.05) rib waveguide on a silica substrate (n~1.46) is determined by the finite-difference beam propagation method (FD-BPM) to be 1.61 for the case of an air cladding. If it is assumed that the microspheres are well packed, the grating period Λ, is given by the diameter of the polystyrene spheres (499±5 nm). Taking into account the deviation of the particle size and the uncertainty in N_{eff}, Bragg reflection is expected to take place between λ=1581 nm to λ=1613 nm, which is in close agreement with our experimental results. The shift of the resonant wavelength towards longer wavelengths as the cladding index increases agrees with the expected increase in N_{eff}. The grating strength is dependent upon the index contrast of the periodic perturbation and the overlap of the modal power with the periodic structure. As the index increases from 1.0 to 1.33, the notch in the transmission spectrum deepens, indicating a stronger interaction. This is attributed to the evanescent field extending further into the cladding medium whilst the index contrast between spheres and cladding remains high. A further increase in the cladding index results in reduced grating strength, believed to be due to further field extension being counteracted by the reduced sphere/cladding contrast. The bandwidths of the spectral notches are much greater than would be expected from a weak uniform grating of 5mm length. However, the deviation in the diameters of the spheres, imperfections in the periodicity of the packing and imperfections in the rib waveguide will contribute to this broadening and will also cause a reduction in the depth of the transmission notch. Further investigations of improved sphere diameter control and more uniform assembly are underway.

Conclusions

In conclusion, we have demonstrated a side-coupled rib waveguide microsphere grating using a simple low-cost self-assembly process. The optical coupling between the lateral evanescent field and the self-assembled array results in a stopband in the transmission spectrum, at a wavelength of ≈ 1590nm, in good agreement with theory. Grating strength adjustment has been examined by varying the refractive index of the overlaid cladding medium, and an extinction of 30% has been obtained. This study demonstrates the potential for self-assembly of microspheres with waveguides for wavelength-dependent devices, and it is expected that this may be extended to microspheres and microsphere resonators of other materials or as part of more sophisticated planar lightwave circuit configurations.

References

[1] D. C. Flanders, H. Kogelnik, R. V. Schmidt, and C. V. Shank, *Appl. Phys. Lett*. **24**, 194, 1974.

[2] M. Ibsen, J. Hubner, J. E. Pedersen, R. Kromann, L. –U. A. Andersen, and M. Kristensen, *Electron. Lett*. **35**, 585, 1996.

[3] D. F. Geragthy, D. Provenzano, W. K. Marshall, S. Honkanen, A. Yariv, and N. Peyghambarian, *Electron. Lett*. **35**, 585, 1999.

[4] J. E. Román and K. A. Winick, *Appl. Phys. Lett*. **61**, 2744, 1992.

[5] R. Adar, C. H. Henry, R. C. Kistler, and R. F. Kazarinov, *Appl. Phys. Lett*. **60**, 1779, 1992.

[6] Yadong Yin, Yu Lu, and Younan Xia, *J. Mater. Chem*.,**11**, 987, 2001.

Homostructure and Heterostructure Photonic Crystals based on VCSEL Arrays

D.L. Boiko, G. Guerrero, E. Kapon
Laboratory of Physics of Nanostructures
Institute of Quantum Electronics and Photonics, Swiss Federal Institute of Technology Lausanne
EPFL, IPEQ, 1015, Lausanne, Switzerland.
dmitri.boiko@epfl.ch

Active homostructure and heterostructure photonic crystals were realized using phased coupled arrays of vertical cavity surface emitting lasers (VCSELs), and their photonic modes were studied theoretically and experimentally.

Keywords: photonic crystals, VCSEL arrays, heterostructures

Introduction

Phase-locked arrays of vertical cavity surface emitting lasers (VCSELs) represent a two-dimensional (2D) photonic crystal loaded with optical gain and loss. Both periodic [1] and quasi-periodic [2] VCSEL photonic crystals have been studied experimentally and theoretically. However, little progress has been made in understanding the polarization characteristics of [3] and the impact of a photonic heterostructure configuration on [4] the photonic modes in these structures.

In this paper, we introduce a model of equivalent 3D photonic crystal suitable for a standard method of analysis based on orthogonal plane waves (OPW) expansion [5]. The band structure and the supermode field pattern of rectangular-lattice photonic crystals are analyzed using this approach. The homostructure and heterostructure VCSEL photonic crystals are realized using electrically pumped InGaAs/AlGaAs devices emitting at 970 nm wavelength. The band structure and supermode patterns of these structures are measured and compared with our model.

Model of Photonic States and Energy Bands

The 2D lateral periodicity of phase-locked VCSEL arrays is effectively introduced by patterning the reflectivity of the top distributed Bragg reflector (DBR) using higher-reflectivity metallic pixels separated by a lower-reflectivity grid [1]. The VCSEL cavity formed by the top and bottom DBRs results in an effective periodicity in the third direction, along the cavity axis (z- axis). Since the periodicity in reflectivity patterning enters through the boundary conditions, an equivalent, unfolded 3D photonic crystal is formed and can be analysed using an OPW expansion method.

The photonic modes are given by an electromagnetic Bloch wave propagating in the crystal with a periodically varying noninertiality given by

$$\mathbf{D}=\varepsilon\mathbf{E}+[\mathbf{H}\times\mathbf{g}] \quad \mathbf{B}=\mu\mathbf{H}+[\mathbf{g}\times\mathbf{E}] \quad \mathbf{g}=-\hat{\mathbf{z}}\frac{ic}{\omega}\ln r(x,y)\sum_{N}\delta(z-2NL) \tag{1}$$

where r(x, y) is the spatially modulated reflectivity with period Λ , and L is the cavity length. In a typical VCSELs array, the photonic mode propagates nearly parallel to the z-axis ($|\mathbf{K}_{\perp}| << K_z$). In this case, the electric and magnetic field wave function $|\mathbf{v}_{m\mathbf{K}}\rangle$ obeys the 2D Schrödinger equation

$$\left[m_0\left(\frac{c}{n}\right)^2+\frac{\hat{\mathbf{p}}_{\perp}^2}{2m_0}+i\frac{c\hbar}{n}\frac{\ln(r(\mathbf{r}_{\perp}))}{2L}\right]|\mathbf{v}_{m\mathbf{K}}\rangle=\hbar\omega_{m\mathbf{K}}|\mathbf{v}_{m\mathbf{K}}\rangle, \qquad m_0=\frac{\hbar|K_z|n}{c} \tag{2}$$

where n is the refraction index in the cavity and $\omega_{m\mathbf{K}}$ assume complex values. The analytic solution at the high symmetry points Δ, Z and T of the Brillouin zone (BZ) was obtained in the case of square symmetry of the reflectivity patterning [Fig. 1]. The intensity patterns of the main polarization components defined by the wave functions $|\mathbf{v}_{m\mathbf{K}}\rangle$ are given in Fig. 2 [all states are

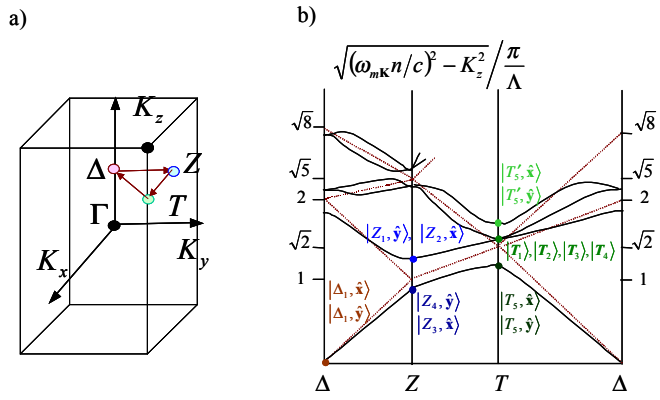


Fig.1. Brillouin zone of the photonic crystal (a); empty lattice test (dashed lines) and a simplified diagram of the energy bands (solid lines) (b).

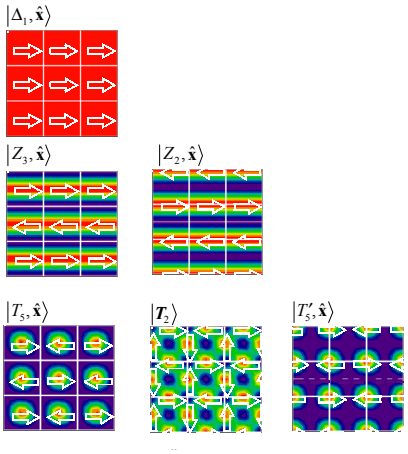


Fig 2: Calculated intensity patterns of the main polarization components at *Δ*, *Z*, and *T* points of BZ , arrows shows polarization.

doubly degenerate by polarization].

The *T* point [$\mathbf{K} = \left(\frac{\pi}{\Lambda}, \frac{\pi}{\Lambda}, K_z\right)$] is of significant, practical interest [Fig.1.b], since the photonic state T_5 has the lowest loss [Fig.3.a] and is the main lasing mode of the VCSEL array. This state is doubly degenerate by polarization and the electric field for $|T_5,\hat{\mathbf{x}}\rangle$ and $|T_5,\hat{\mathbf{y}}\rangle$ is given by

$$\begin{aligned}\hat{\mathbf{E}}|T_5,\hat{\mathbf{x}}\rangle &\propto \hat{\mathbf{x}}\cos\tfrac{\pi}{\Lambda}x\cos\tfrac{\pi}{\Lambda}y - \hat{\mathbf{z}}\tfrac{i\pi}{\Lambda K_z}\sin\tfrac{\pi}{\Lambda}x\cos\tfrac{\pi}{\Lambda}y + \hat{\mathbf{y}}\tfrac{\pi^2}{2\Lambda^2K_z^2}\sin\tfrac{\pi}{\Lambda}x\sin\tfrac{\pi}{\Lambda}y \\ \hat{\mathbf{E}}|T_5,\hat{\mathbf{y}}\rangle &\propto \hat{\mathbf{y}}\cos\tfrac{\pi}{\Lambda}x\cos\tfrac{\pi}{\Lambda}y - \hat{\mathbf{z}}\tfrac{i\pi}{\Lambda K_z}\cos\tfrac{\pi}{\Lambda}x\sin\tfrac{\pi}{\Lambda}y + \hat{\mathbf{x}}\tfrac{\pi^2}{2\Lambda^2K_z^2}\sin\tfrac{\pi}{\Lambda}x\sin\tfrac{\pi}{\Lambda}y\end{aligned} \qquad (3)$$

It exhibits the anti-phase modulation at adjacent lattice sites and has intensity maxima (z-component of the Poynting vector) located at the high-reflectivity pixels. The intensity pattern is defined by the main polarization component since the z component of the field does not contribute to the energy flow along the z- axis, and $\pi/\Lambda K_z << 1$. This state is a hybrid mode ($E_z, H_z \neq 0$) and has an orthogonal polarization component with intensity maxima located at the cross points of the array grid.

The full 2D transversal photonic band gap is opened if the photon energy in the $|Z_2,\hat{\mathbf{x}}\rangle$ states is higher than for $|T_5,\hat{\mathbf{x}}\rangle$. The calculated photon energies are plotted in Fig.3. b [the phase difference $\Delta\varphi$ between the complex reflection coefficients at the pixel and at the grid is 0.1 rad]. The analysis

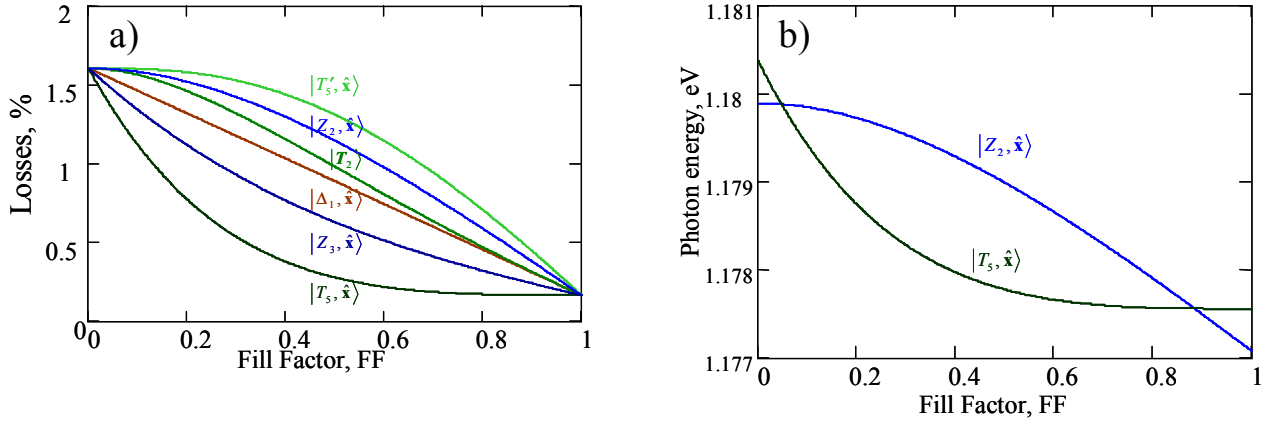


Fig.3. Losses of different modes (a) and photon energies in states $|Z_2,\hat{\mathbf{x}}\rangle$ and $|T_5,\hat{\mathbf{x}}\rangle$ (b) as a function of fill factor FF (ratio of the areas of the high-reflectivity pixel and of the unit cell)

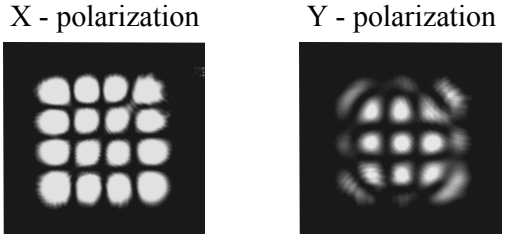


Fig.4 Measured polarization-resolved NF intensity pattern in $|T_5, \hat{\mathbf{x}}\rangle$ state of a CW lasing 4x4 VCSEL array.

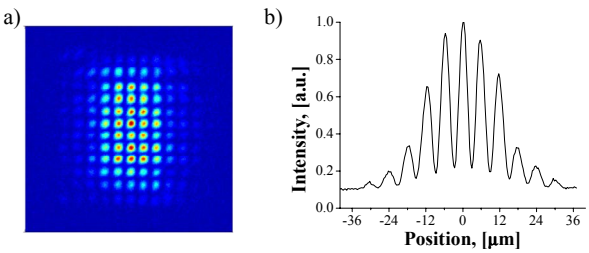


Fig.5. Measured near filed intensity pattern (a) and near field cross section (b) of 16x16 VCSEL photonic heterostructure: Λ=6 μm, $FF_{core} = 0.69, FF_{clad} = 0.34$, core region contains 5x10 pixels.

reveals an optimal fill factor FF at which a minimal phase contrast $\Delta\varphi$ is required to open this gap:

$$\frac{\Lambda^2 n}{\lambda L} > \frac{2.5}{\Delta\varphi} \quad at \quad FF_{opt} = 0.34 \tag{4}$$

Measured Polarization-Resolved Mode Patterns

The measured polarization-resolved near field (NF) pattern of a 4x4 VCSELs array [Fig. 4] confirms the field distribution predicted by (3). It corresponds to the state $|T_5, \hat{\mathbf{x}}\rangle$, with the main polarization component directed along the x- axis and with intensity maxima located at the VCSEL pixels ("pixel mode"). The weak y- polarized component of the field arises from the last term in (3). This component has intensity maxima located at the cross points of the array grid, which coincides with the intensity pattern of $|T_5', \hat{\mathbf{y}}\rangle$ (and $|T_5', \hat{\mathbf{x}}\rangle$) states ("grid cross mode"). Note that the detected polarization-resolved pattern in Fig.4 can be significantly influenced by the mixing of pixel mode states and of grid cross mode states due to the finite size of the array.

In fact, in arrays incorporating N×N pixels, the state at the boundary of BZ cannot be realized because of the quantization of the transverse component of the wave vector **K**. A simple analysis based on coupled mode theory shows that the mode closest to the T point of BZ is detuned by $\mathbf{k}_\perp = \frac{\pi}{\Lambda}\left(\frac{-1}{N+1}, \frac{-1}{N+1}\right)$ from the T point. A $\mathbf{k}_\perp \cdot \hat{\mathbf{p}}_\perp$ perturbation analysis of (2) demonstrates that for small energy gap $\hbar\omega_{T_5'} - \hbar\omega_{T_5}$ values, the band mixing can enhance the amplitude of the complementary grid-type pattern.

Realization and Analysis of Photonic Crystal Heterostructures

Photonic crystal heterostructures represent a hybridization of two (or more) periodic photonic crystals of different lattice and/or unit cell configurations [4]. The 2D photonic heterostructures studied here consist of a "core" region of larger pixel size VCSELs embedded in a "cladding" region of smaller size pixels. These heterostructures serve to confine the envelope function of the supermode to the vicinity of the large-pixel region. The envelope function exhibits a standing wave pattern in the core and decays exponentially in the cladding (see Fig. 5) [4].

The two regions of the heterostructure differ by the fill factor. This difference in the FF gives rise to a different dispersion, which induces the envelope function optical confinement. In the particular case of VCSELs photonic heterostructures, this confinement is related to the imaginary part of the dispersion curve $\mathrm{Im}(\omega_{m,\mathbf{k}_\perp})$, which determines the VCSEL cavity loss. A $\mathbf{k}_\perp \cdot \hat{\mathbf{p}}_\perp$ perturbation analysis of (2) yields the photon energy dispersion in the parabolic approximation:

$$\hbar\omega_{T_5+\mathbf{k}_\perp} = \hbar\omega_{T_5} + \frac{\hbar^2 k_\perp^2}{2m^*}, \qquad \frac{1}{m^*} = \frac{1}{m_0} - \frac{4}{m_0^2}\frac{P^2}{\hbar\left(\omega_{T_1} - \omega_{T_5}\right)} \tag{5}$$

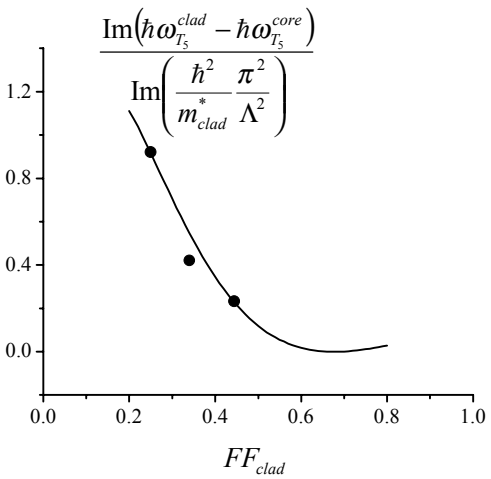


Fig. 6 Calculated (curve) and measured (points) relative band gap offset as a function of FF in the cladding, $FF_{core} = 0.69$

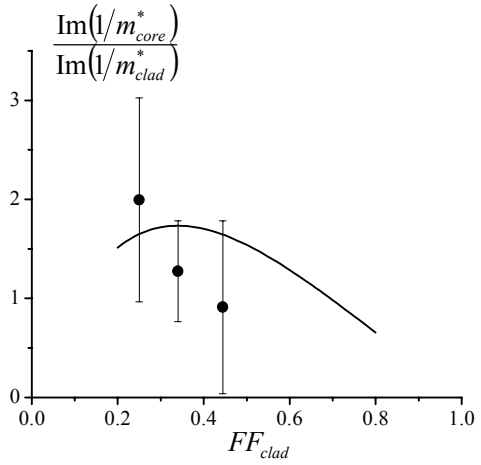


Fig.7 Calculated (curve) and measured (points) effective mass ratio as a function of FF of the cladding, $FF_{core} = 0.69$.

where *P* is the matrix element of the momentum operator. In the single band approximation, the parameters defining the confinement are the relative band offset at the band edge (see solid line in Fig 6) and the ratio of the effective masses (solid line in Fig.7).

In the experiment, these parameters were measured using a series of photonic heterostructure VCSELs with different array size and FF values. The FF of the core region was fixed at 0.69 while the one at the cladding was varied between 0.25 and 0.44. The fit of the measured near field envelope function has allowed to deduce the propagation constants in the core and cladding regions. To evaluate the relative band edge offset and effective mass, two points on the dispersion curve are required (in the parabolic approximation). To access different values of the transverse wave vector near the band edge, the intensity patterns of arrays with different number of pixels along the *x*-axis (with fixed values of the FF in the core and the cladding) were evaluated. Reasonable agreement with the calculated values was obtained (see symbols in Figs. 6 and 7). The discrepancy of measured and calculated ratio of effective mass can be partly explained by the finite size (up to 16X16 pixels) of the measured arrays.

Conclusion

Coherent VCSELs arrays provide an efficient configuration for manipulating the polarization state and the intensity patterns of lasing photonic modes. In particular, the realization of photonic crystal heterostructures yields a new approach for achieving confinement of the envelope functions of photonic modes. We have developed a model for analyzing the polarization modes in 2D photonic crystal consisting of coupled VCSELs. The similarity of the method to the formalism of solid-state physics of electronic crystals allows the $\mathbf{k}\cdot\hat{\mathbf{p}}$ perturbation method to be applied for the analysis of the dispersion, and the effective mass Hamiltonian is applicable for the analysis of the photon confinement in photonic heterostructures. The results of the analysis are in good agreement with our experimental observation.

[1] M. Orenstein, E. Kapon, N.G. Stoffel et al., *Appl. Phys. Lett.* **58**, 804-806,1991.
[2] H. Pier, E. Kapon and M. Moser, *Nature* **407**, 880-883, 2000.
[3] P. Debernardi, G.P. Bava, F. Monti di Sopra and M.B. Willemsen, *IEEE J. Quantum Electron.* **39**, 1-12, 2003.
[4] C.-A. Berseth, G. Guerrero, E. Kapon et al., *Proc. CLEO 2000*, pp 171-172, CtuA48, 2000.
[5] K.M. Leung, Y.F. Liu, *Phys. Rev.B* **41** , 10 188- 10 190, 1990

Investigation of Fabry-Pérot cavities based on 2D Photonic crystals fabricated in InP membranes

M. Mulot, M. Swillo, M. Qiu, M. Strassner, S. Anand
Royal Institute of Technology, Department of Microelectronics and Information Technology, Kista, Sweden
mulot@imit.kth.se

The properties of Fabry-Pérot cavities based on photonic crystals etched in suspended InP membranes are presented. For a cavity with 2-hole mirrors and a resonance wavelength around 1.55 μm, a quality factor of 3200 is achieved.

Keywords: photonic crystals, wavelength division multiplexing, optical filters

Introduction

Two-dimensional photonic crystal (2D PhC) structures with a photonic bandgap opening in the near-infrared wavelength range are widely studied for applications in integrated optics. In particular, PhC based high finesse resonant cavities are attractive for DWDM applications [1].

In order to confine the light in the third dimension, 2D PhCs are usually realized in a step-index planar waveguide. Such a structure is called quasi-2D PhC. Quasi-2D PhCs suffer from out-of-plane losses since drilling holes through the planar waveguide induces out-of-plane coupling of guided modes into radiative modes into the claddings. However, step index waveguides with high index contrast between the core and the cladding layers feature theoretically lossless propagation compared to the low index contrast alternative [2]. The main disadvantage of high index contrast quasi-2D PhCs is their high sensitivity to any breaking of the crystal periodicity: engineered irregularities or defects within the PhC lattice, such as resonant cavities, may result in drastically increased out-of-plane radiation [2]. This is why careful design is required to achieve better quality factors in PhC cavities etched in semiconductor membranes [3].

In this work, we investigate Fabry-Pérot (FP) cavities based on 2D PhCs etched in InP suspended membranes. The transmission spectra of the FP cavities are measured using the end-fire method. Out-of-plane radiation sources are identified by imaging the sample with a Vidicon infrared camera.

Design

The fabricated structures are entirely designed from a perfectly periodic 2D PhC. The PhC is a triangular array of air holes with a 450 nm period and a hole size of 270 nm, resulting in an air-filling factor of 35%. The FP cavity is integrated within a waveguide that is obtained by removing the central row of the PhC. This type of waveguide is often referred as W1 waveguide. The cavity is formed by putting back air holes as mirrors (see Fig. 1). The length of the FP cavity is 30 PhC periods, which corresponds to about 13.5 μm. Cavities with mirrors formed of one and two holes have been realized.

Fabrication

The InP/InGaAs heterostructure consists of a 400 nm thick InGaAs layer and of a 400 nm thick InP layer grown by metal-organic vapor-phase epitaxy on an n-doped InP substrate [4]. The 2D PhCs were patterned into the InP-based heterostructure using electron beam lithography and subsequent chemical assisted ion beam etching (Ar/Cl_2). The sample is then cleaved a few microns before both ends of the 340 μm long PhCs to obtain direct access to the W1 waveguides. The sacrificial InGaAs layer is selectively removed using a $FeCl_3/H_2O$ etch solution. The etch solution

reaches the InGaAs layer by diffusing through the holes of the PhCs. As a result, a high refractive index contrast slab waveguide is created.

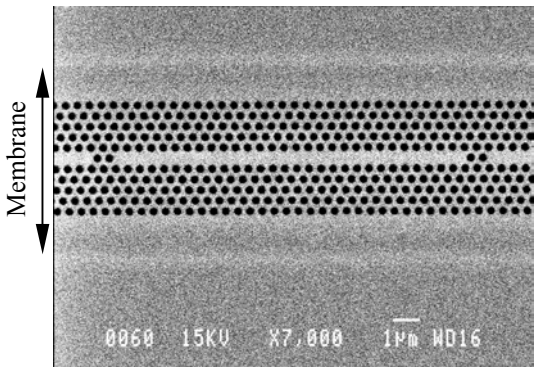


Fig. 1: top view of a photonic crystal based Fabry-Pérot cavity with 2-hole mirrors.

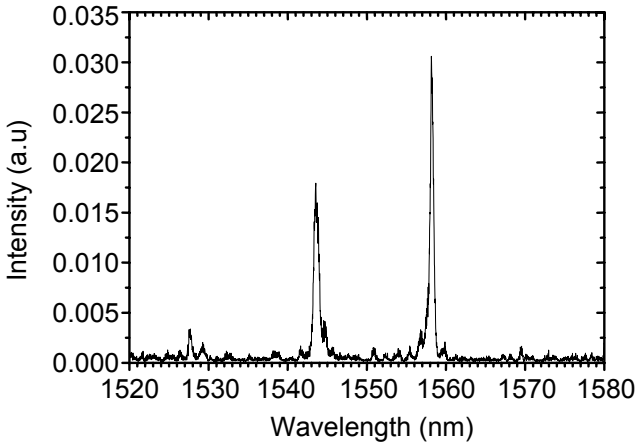


Fig. 2: transmission spectrum for the Fabry-Pérot cavity with 2-hole mirrors.

Transmission measurements

The transmission spectra of the FP cavities are measured using the end-fire method. Light from a tuneable laser passes through an optical polarizer. With the help of a GRIN lens, the linearly polarized light is launched into the input W1 waveguide and excites TE-like polarized fundamental modes. On the output side, the guided light passes through an optical analyzer, which filters out any residual TM polarization component in the transmitted light. A microscope objective focuses the output light on a multimode fiber (core diameter 64 μm) that is connected to an InGaAs photodiode.

The transmission spectrum of the FP cavity with 2-hole mirrors shows two resonance peaks (Fig. 2). The maximum intensity of the resonance peaks follows the transmission profile for the W1 waveguide. The bandwidth of the largest resonance peaks (λ=1558.3 nm) is 60 GHz, which corresponds to a quality factor $Q=f/\Delta f$ of 3200. In comparison, we measured a quality factor of 2800 for a FP cavity with 1-hole mirror (λ=1553.4 nm).

At resonance, the transmission through the FP cavity does not exceed a few percent of that for a simple W1 waveguide for the same wavelength. This suggests that out-of-plane radiation losses are important in the structure. Top views of the cavity recorded with a Vidicon infrared camera show that the cavity mirrors are major scattering sources in the structure. Consequently, a better design of the mirrors would improve the transmission at resonance as well as the quality factor of the FP cavities.

Conclusion

PhC based Fabry-Pérot cavities fabricated into 400 nm thick InP membranes were characterized. A quality factor as high as 3200 was obtained for resonant cavities with 2-hole mirrors. The quality factor as well as the transmission at resonance is limited by out-of-plane scattering from the cavity mirrors.

[1] “Photonic Crystals and Light Localization in the 21st Century”, ed. C. M. Soukoulis, Kluwer Academic Publishers, Dordrecht (2001).
[2] W. Bogaerts, P. Bienstman, D. Taillaert, R. Baets, D. De Zutter, “Out-of-plane scattering in photonic crystal slabs”, *IEEE Photonics Technol. Lett.* **13**, 565, 2001.
[3] J. Vučković, M. Lončar, H. Mabuchi, A. Scherer, “Design of photonic crystal microcavities for cavity QED”, Physical Review E **65**, 016608, 2001
[4] M. Strassner, N. Chitica, A. Tarraf, “Investigations of growth conditions for InP suited for Micro Opto Electro Mechanical Systems for data communication”, in Proceedings of the 14th Indium Phosphide and Related Materials Conference, Stockholm, 2002, p. 351.

Modal behaviour of single-line Photonic-Crystal bends and combiners on InP substrate

A.Talneau
CNRS/ Laboratoire de Photonique et de Nanostructures, Route de Nozay, F-91460 Marcoussis
anne.talneau@lpn.cnrs.fr

M.Mulot and S.Anand
Royal Institute of Technology, Department of Microelectronics and Information Technology, S-164 40 Kista, Sweden

S.Olivier
Laboratoire de Physique de la Matière Condensée, Ecole Polytechnique, UMR 7643 CNRS 91128 Palaiseau, France

M. Agio [1,2] M. Kafesaki,[3] C. M. Soukoulis [2,3]
[1]INFM-Dipartimento di Fisica ``A. Volta'', Universita di Pavia, via Bassi, 6 I-27100, Pavia, Italy
[2] Ames Laboratory and Department of Physics and Astronomy,Iowa State University, Ames, IA 50011
[3] Research Center of Crete, IESL-FORTH, Heraklion, Crete, Greece

Keywords : photonic crystals, guiding structures, photonic integrated circuits

Abstract : We have investigated both theoretically and experimentally the modal behaviour and polarization dependence of transmission through single-missing-row Photonic Crystal bends and combiners.

Introduction: Strongly confined single-missing-row Photonic Crystal Waveguides (PCW) will be credible candidate for Photonic Integrated Circuits provided they demonstrate high transmission through complex guiding structures such as bends and combiners. A single-missing-row PCW, named W1, is obtained by removing an entire row of holes in a uniform Photonic Crystal (PhC) in the ΓK direction; no hole size variation within the guide or on the first inner row are investigated here. This W1 PCW is an attractive candidate as it may support a single even mode for our investigated wavelength domain. Polarization conversion is a severe drawback of index-guided sharp bends [1], and will always limit the size reduction of Photonic Integrated Circuits (PIC) based on the classical index-contrast guiding mechanism. We exhibit here measurements on different PCW W1-based sharp bends which demonstrate that no polarization conversion occurs. Also, we demonstrate on a 2>1 combiner the advantage of additional small holes in the combining region, which prevent excitation of higher order modes. These measurements are in agreement with the FDTD simulations. We remind that being on InP substrate we always propagate above the light cone.

General description of sample structure
PCW are fabricated on a two-dimensional PhC consisting of a triangular array (period a=450nm) of holes drilled on a 500nm thick GaInAsP confining layer. These holes are etched by Chemically Assisted Ion Beam Etching (CAIBE) using Ar/Cl2 chemistry [2]. A micrograph of the etched holes shows in Fig. 1(a) holes deeper than 3µm for an air-filling factor f=40% . For a reproducible coupling of the light in and out the PhC section, the W1 PCW is inserted in-between two ridge access guides also supporting a single even mode and limited by cleaved facets [3]. A tapered section based on a gradual variation of holes size and

depth [3] is inserted at every ridge/W1 transition. Such a taper is visible for example on the two entrances and on the exit of a combiner, on the micrograph of fig.1(b). This taper adds a spectral contribution in the u=0.3 wavelength domain which will be described elsewhere. Measurements are performed in TE polarization, on a 1500-1590nm wavelength span covered by a polarization-maintaining-output tunable-laser source.

Modal and polarization behaviour of double-bends

The band diagram of the W1 straight PCW is plotted in fig 1(c) in the case f=36%. A single even mode exits in the u=0.283-0.3 domain. Previous results obtained on a double bend with 1-hole-moved were encouraging [4], so we investigate here again such a design fig.2(a) in the case of our presently optimised etching . An adiabatic bend following the design proposed by Arentoft et al. [5] has also been fabricated and measured. With the objective of easing the fabrication, only one 60° bend has the adiabatic geometry, the second one is a 1-hole-moved see fig.2 (b). Both PhC bends have an air filling factor f=36%, measured on micrographs. The good absolute transmission observed for the adiabatic bend parallels the results published in [5]. The reason of the reduced absolute level in the 1-hole-moved case could be explained following [6]. As already pointed out in [7], in these bend/combiner geometries the discrete translational symmetry of the lattice is ruined and one cannot classify anymore the modes following the same classification as for the straight guide. An attempt has been proposed in [6] to consider the modes in the bend region as if it were an infinite PCW in the ΓM direction. Following this approach, we calculate the band diagram for a W1 PCW in the ΓM direction and find additional modes in the u=0.283-0.3 wavelength domain (fig.2(a) left). As the bend breaks the symmetry , it allows coupling between modes which do not have the same symmetry; part of the power is coupled to these modes and lost in the bend. This modal conversion would not occur in the adiabatic bend where one could always consider the local ΓM direction, resulting in a higher transmission .

Considering now the polarization behaviour, both bends transmit all the optical power on the TE mode, the TM level being at least –17dB below the TE one, which is the polarization selectivity of the external tunable source (fig.2 bottom). Clearly no polarization conversion has occured . We recall here that we previously measured some polarization conversion in a three-missing-rows W3 PCW [8]. We tentatively conclude that in a W3 bend, both gap-guiding and index-guiding are present, and the index-guiding mechanism contributes to polarization conversion as it occurs in purely index-guided sharp bends [1]. In the case of the W1 PCW, gap-guiding is strongly dominant and no polarization conversion occurs in a sharp bend.

Combiner without and with additional holes

Integrated circuits will require combiners (splitters) to implement interferometric functions (Mach Zehnder...). Going on with a monomode guide, we fabricated Y-geometry based combiners as presented in fig.1(b). In order to be broadband, we do not consider the alternative resonant combining geometries. The “enlarged” combining sections are visible on the micrographs of fig.3 top. In case (a), the combining section, locally larger than W1, allows higher order modes to be excited, whereas in case (b) small holes have been added to prevent such an excitation. Measurements of transmission through both combiners are presented in fig.3 (middle), for both cases, again with the straight guide as a reference. One has to consider that the absolute level through the whole combiner includes the combining region itself and one 60° bend (report to general overview of fig.1(b)). As the bend is the same in both cases, this allows us to conclude that including these two small holes increases the combiner

transmisson by 5dB. Some internal reflections are still visible through large oscillations, and could be limited by means of additional holes along the straight guide as proposed by Boscolo and al. in [9]. In case (b), a discrepancy is visible between the 2 entrances. This could be due to the fact that the two additional small holes do not have the same size. Our measurements are in agreement with FDTD simulations plotted in fig.3 (bottom) for both cases which also demonstrate the advantage of these additional holes in the wavelength domain around u=0.29. The ε_{im} parameter is a phenomenological parameter describing the losses [10].

Conclusion

The propagation through strongly confined Photonic Crystal bends and combiners has been investigated, and the experimental results have been related to the modal structure. No polarization conversion occurs in W1-based PhC bends, which demonstrate the potential for this guiding geometry for high compactness Photonic Integrated Circuits. Also small additional holes are evidenced to play an important role in combining geometries. The remaining challenging step is the fabrication of very small holes with an accurate size.

References

[1] C.van Dam, L.H.Spiekman, F.P.G.M.van Ham, F.H.Groen, J.J.G.M.van der Tol, I.Moerman, W.W.Pascher, M.Hamamcher, H.Heidrich, C.M.Weinert and M.K.Smit, IEEE Photn. Tech. Lett., **8**, (10), p.1346-1348, (1996)

[2] M.Mulot, S. Anand, C.F.Carlstrom, M.Swillo, A.Talneau, Physica Scripta (in press)

[3]A.Talneau, Ph.Lalanne, M.Agio and C.M.Soukoulis, Optics Letters, **27**, (17), p.1522-1524,(2002)

[4] A.Talneau, L.Legouezigou, N.Bouadma, M.Agio, Appl. Phys. Lett., **80**, (4), p.547-549, (2002)

[5] J.Arentoft, T.Sondergaard, M.Kristensen, A.Boltasseva, M.Thorhauge and L.Frandsen, Elec. Lett., **38**, (6), p.274-276,(2002)

[6] A.Chutinan, M.Okano and S.Noda, Appl. Phys. Lett., **80**, (10), p.1698-1700, (2002)

[7] J.D.Joannopoulos,R.D.Meade and J.N.Winn "Photonic Crystals" (Princeton University Press, Princeton, NJ,1995)

[8] H.Benisty, S.Olivier, C.Weisbuch, M.Agio, M.Kafesaki, C.M.Soukoulis, M.Qiu, M.Swillo, A.Karlsson, B.Jaskorzynska, A.Talneau, J.Moosburger, M.Kamp, A.Forchel, R.Ferrini, R.Houdré, U.Oesterle, IEEE, J. of Quantum Elec., **38**,(7), p.770-785, (2002)

[9] S.Boscolo and M.Midrio, T.F.Krauss, Optics Lett., **27**, (12), p.1001-1003, (2002)

[10] H.Benisty, D.Labilloy, C.Weisbuch, C.J.M.Smith, T.F.Krauss, D.Cassagne, A.Beraud and C.Jouanin, Appl. Phys. Lett., **76**, (5), p.532-534, (2000)

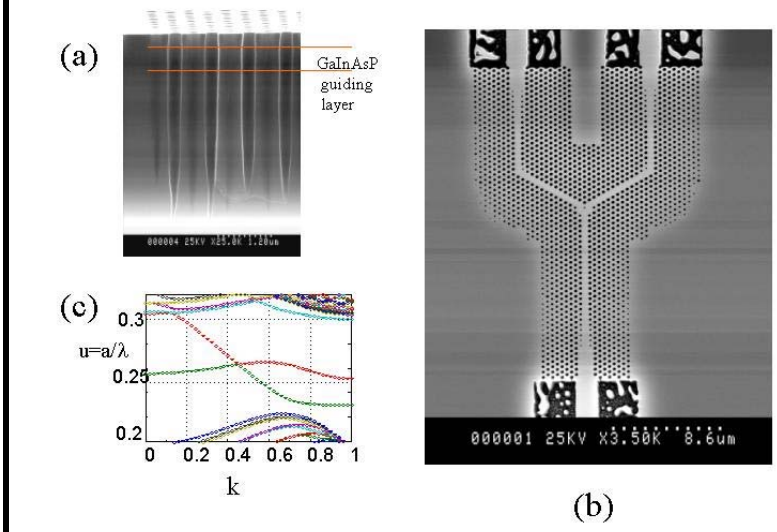


Figure 1:
(a) Micrograph of CAIBE etched holes deeper than 3µm
(b) General view of a w1 based combiner, with taper access on all arms
(c) band diagram of a W1 PCW ΓK direction, f=36%

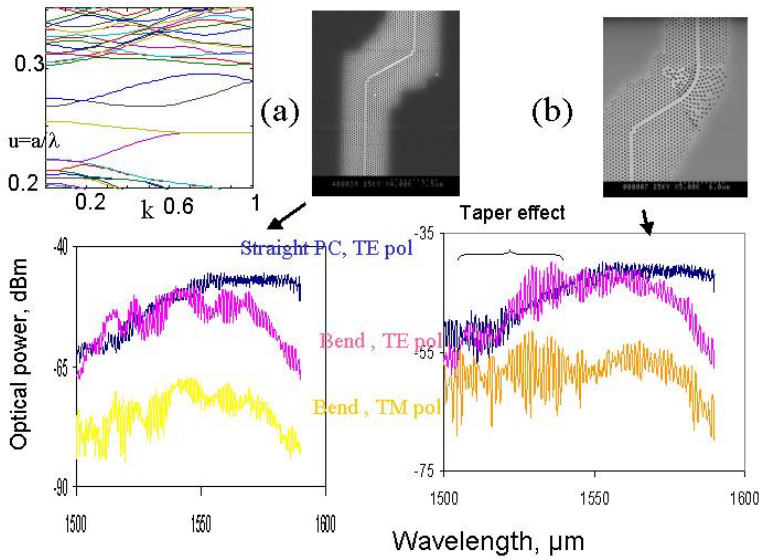


Figure 2 : top view of W1-based double bends:
(a) 1 hole moved
(b) adaibatic bend
In case (a) band diagram of the W1 PCW in the ΓM direction
bottom: Transmission spectra versus polarization, the straight PC is plotted as a reference

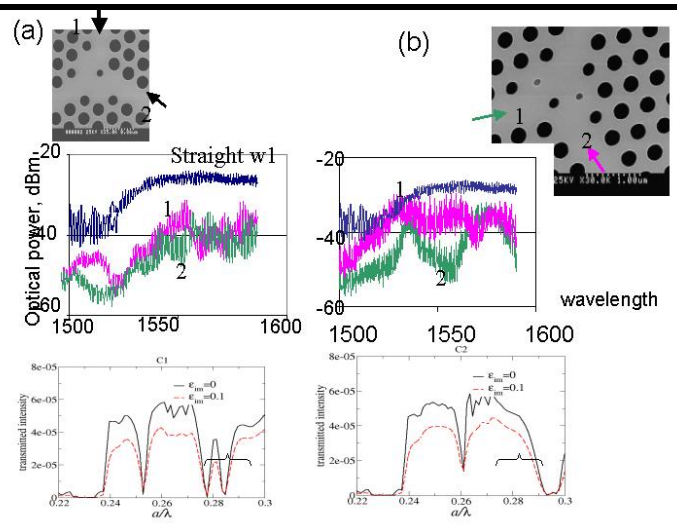


Figure 3 : Micrographs and transmission through w1 combiners
(a)with no hole in the enlarged section
(b) adding holes in the enlarged section
bottom: FDTD simulation of combiners' transmission

Efficient Waveguiding in Low Index Photonic Crystal Films

M. Augustin, H.-J. Fuchs, E.-B. Kley, S. Nolte, and A. Tünnermann
Institut für Angewandte Physik, Friedrich-Schiller-Universität Jena,
Max-Wien-Platz 1, 07743 Jena, Germany
augustin@iap.uni-jena.de

R. Iliew, C. Etrich, U. Peschel, and F. Lederer
Institut für Festkörpertheorie und Theoretische Optik, Friedrich-Schiller-Universität Jena,
Max-Wien-Platz 1, 07743 Jena, Germany

We experimentally investigate a sandwich photonic crystal film made from glass-like amorphous materials. For the first time polarization sensitive waveguiding in such low-index contrast photonic crystal waveguides and waveguide bends has been observed.

Keywords: photonic crystals, periodic structures, characterization methods, low index materials

Introduction

To control light on a micrometer scale many experimental efforts have focused on the investigation of photonic crystals (PCs). In particular waveguides embedded into PCs are predicted to have completely new and exciting properties. Although most of the recent experimental studies have concentrated on 2D-PCs with a high in-plane index contrast [1] the use of amorphous low index materials, like Nb_2O_5 and SiO_2, has also potential advantages. Losses are usually smaller, mature fabrication technologies exist and they fit much better to the well established fiber technology. In this contribution we will report on the realization of sandwich photonic crystal films including defect waveguides and bends in glass-like oxides with a relatively low refractive index of 2.17. We will discuss the advantages and disadvantages of these components regarding propagation and coupling losses, relative size of the band gap and dimensions for single mode waveguiding and bend efficiencies.

Design

Due to the low index contrast a proper design of the in-plane PC structure and of a proper film thickness for single mode guidance is crucial for obtaining a band gap guided defect mode at the desired wavelength of operation of 1.55 µm. The sandwich system (see Fig.1) was designed to be symmetric to minimize mixing between TE and TM modes.

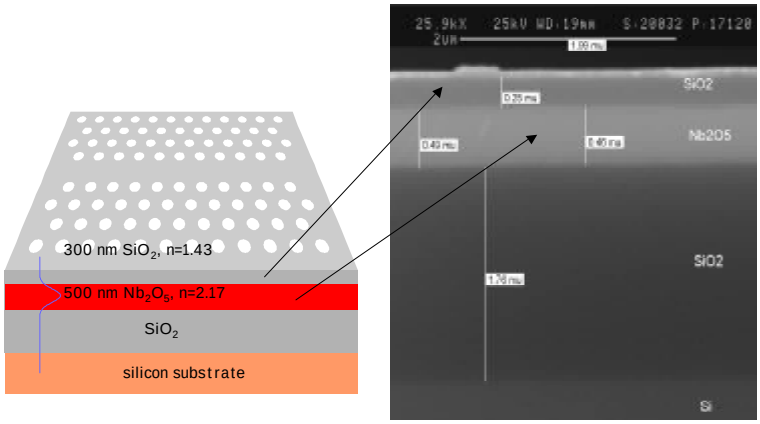


Fig.1: The $SiO_2/Nb_2O_5/SiO_2$ sandwich system

The final structures were designed by means of 3D band structure calculations and show a band gap for TE polarized light. Hexagonal lattices of air holes of diameters ranging from 415nm to 465nm and of 620nm separation with an etching depth of 800nm were analyzed with the help of 3D band structure and finite-difference time-domain (FDTD) calculations and show a maximum band gap around an operation wavelength of 1530-1600nm. W1 defect channels inside these PCs were formed by leaving a row of holes along the ΓK direction of the crystal unstructured. These defect channels can guide light because of the photonic band gap, but since the effective index of the PC is lower than that of the defect channel, waveguiding also occurs by total internal reflection.

Sandwich system

The samples under investigation were made from a layered composite with a waveguiding film consisting of 500nm of Nb_2O_5. A 300nm-cladding layer and a 2000nm buffer layer made from SiO_2 (n=1.43) were used to isolate the guiding region from air and from the silicon substrate, respectively (see Fig.1).

Fabrication

The structures are exposed by e-beam lithography. After exposure the PC pattern is transferred into the sandwich system by means of a three-layers-resist. For etching a combination of reactive ion etching (RIE) and inductive coupled plasma (ICP) etching is used. After the etching process the sample is cleaved to obtain facets for the optical characterization. To couple light into the photonic crystal waveguides ridge waveguides of the same width are used. (see Fig. 2).

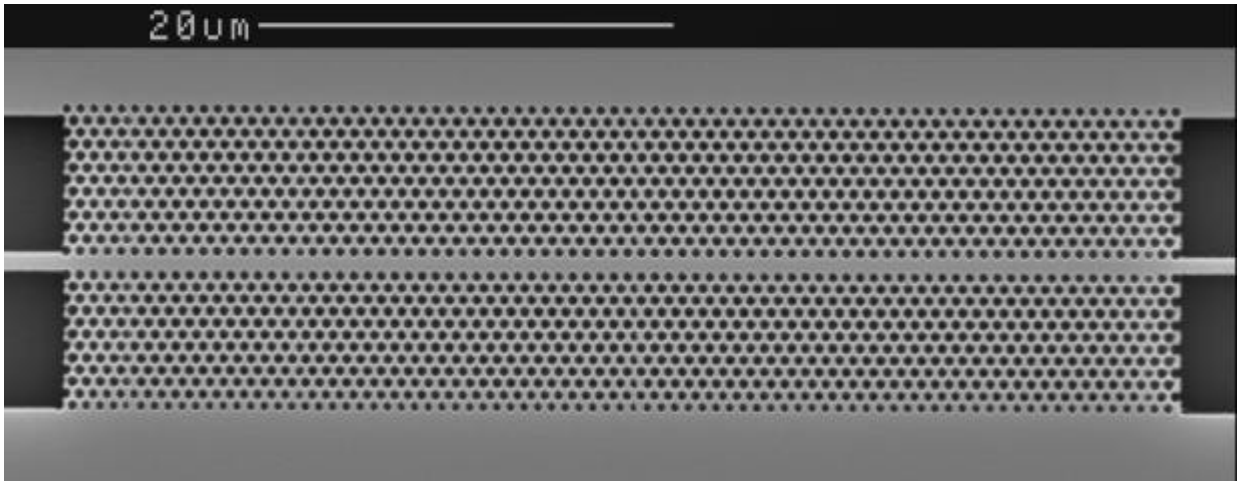


Fig.2: W1-photonic crystal waveguide

Characterization

The optical response of the waveguides was analyzed to determine what kind of waveguiding mechanism dominates. For TE polarization in the spectral range of the photonic band gap a 2 to 4 times higher transmission could be detected (see Fig.3).

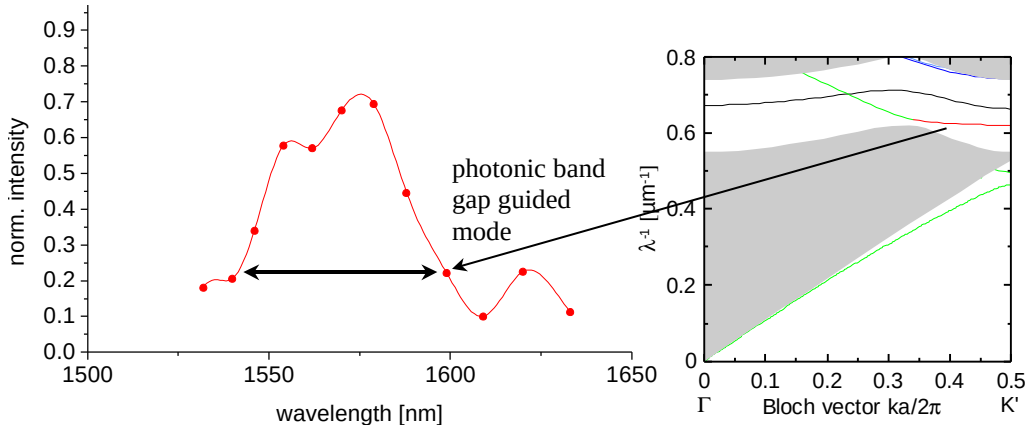


Fig.3: Optical response of W1-PC-waveguide with a period of 620nm and different diameters.

After having experimentally established that the photonic band gap enforces the waveguiding mechanism we realized a W5-PC waveguide double bend (2x 60°) by omitting five rows of holes (diameter ~260 nm, period 595 nm; see Fig.4). This structure shows very efficient single mode waveguiding with a transmission of app. 50% per bend for TE polarization) at 1677 nm (see Fig.5).

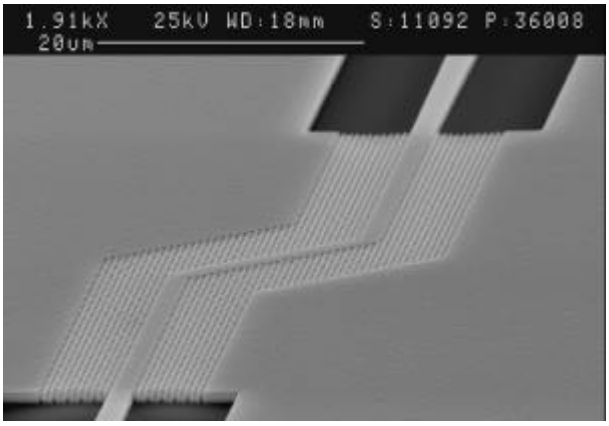


Fig.4: SEM image of the fabricated PC-structure with a W5 double bend.

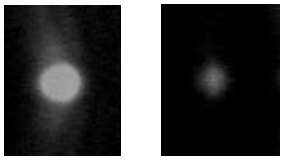


Fig.5: Near-field distribution of 1677 nm radiation (TE polarized (left) and TM polarized) for a W5-pc-waveguide bend.

Conclusion

We observed good agreement between 3D finite-difference time-domain propagation calculations of PC waveguides and bends with the experimentally obtained results.

The research has been partly funded by the Deutsche Forschungsgemeinschaft und the Bundesministerium für Bildung und Forschung.

[1] E. Chow, S. Y. Lin, J. R. Wendt, S. G. Johnson and J. D. Joannopoulos, "Quantitative analysis of bending efficiency in photonic-crystal waveguide bends at λ=1.55 µm wavelengths," *Opt. Lett.* **26**, 286-288 (2001).

Optical signal processing using electro-absorption modulators

J. Mørk, F. Romstad, S. Højfeldt, L. Oxenløwe,
K. Yvind, L. Xu, F. Öhman, L. J. Christiansen, A. Tersigni
Research Center COM, Technical University of Denmark
Build. 345v, DK-2800 Kgs. Lyngby, Denmark. E-mail: jm@com.dtu.dk

K. Hoppe, M. Løbel and J. Hanberg
GiGA Aps – an Intel Company, Mileparken 22, DK-2740, Skovlunde, Denmark

Reverse-biased semiconductor waveguides are efficient saturable absorbers and have a number of promising all-optical signal processing applications. Results on ultrafast modulator dynamics as well as demonstrations and investigations of wavelength conversion and regeneration are presented.

Keywords: Electro-absorption, modulator, optical processing, ultrafast dynamics

Introduction

Primary incentives for the use of all-optical signal processing in optical communication system are the larger data rates and increased flexibility that all-optical devices offer, as well as the cost-reduction that may be achieved by avoiding conversion back and forth between the optical and the electronic domain. To be practical and competitive, all-optical switching devices should fulfill criteria similar to those of electronic devices: They should be small and allow for integration of different functionalities, and have the potential for cheap mass-production.

Presently, various kinds of devices comprising a semiconductor optical amplifier (SOA) as the main active element are among the primary contenders for integrated all-optical devices [1]. The large values of gain and differential gain that may be achieved in SOAs allow switching with power levels in the range of milliwatts, and various functionalities have been demonstrated using a number of different schemes at speeds in excess of 100 Gb/s [2]. Electro-absorption modulators (EAMs), i.e., p-i-n waveguide structures quite similar to SOAs, but reverse biased, have been developed with the main purpose of electrically modulating an injected CW optical signal at high data rates and with low chirp. Presently, high-quality EAMs are available at bitrates up to 40 Gb/s. However, it has been demonstrated that the EAM has a number of other interesting applications, both when modulated electrically but also under optical control [3,4]. The optical control of an EAM, which is the main focus of this paper, relies on cross-absorption modulation between two optical beams in the device, quite similar to the effect of cross-gain modulation at play in SOAs. A major difference from an SOA is the fact that in an EAM the recovery time is governed mainly by carrier sweep-out from the active region under an applied external (reverse) field, which may lead to recovery times in the picosecond region. On the other hand, being an absorptive device, an optically controlled EA needs to be pumped by a strong optical beam in order to exhibit a strong modulation contrast.

Applications of electro-absorption modulators

Figs. 1 and 2 show examples of various EA applications, where the device is modulated either electrically (Fig. 1) or optically (Fig. 2). When a reverse bias is applied to a quantum-well (QW) EAM, the absorption of the device changes due to the quantum-confined Stark effect. This effect forms the basis of the so far most common application of EAMs; the imprinting of data onto a CW signal generated by a laser (external to the EAM or monolithically integrated with it). A main advantage of this configuration is the lower chirp compared to a directly modulated laser. This

application is illustrated in Fig. 1a, along with an example of a 40 Gb/s eye diagram for a ridge waveguide quantum-well (QW) type modulator operating at 1550 nm.

Fig. 3 shows examples of measured and calculated absorption spectra at different reverse voltages. There is always a trade-off between obtaining a low insertion loss in the on-state (the transmissive state) and getting a low modulation amplitude (that is, the voltage modulation span required to obtain a certain, say 10 dB, extinction ratio of the modulated optical signal). In the electrical demultiplexing application, one utilizes the nonlinearity of the transmission versus voltage characteristic of the EAM to open a switching window in the EAM transmission that may be significantly narrower than the applied electrical signal would seem to imply. Also, the possibility of electrically generating a short switching (transmission) window in the EAM may be used for recovery of the base-rate clock signal for a high-data rate optical-time-division-multiplexed (OTDM) signal; e.g. the recovery of the 40 GHz clock signal from a 4×40 Gb/s signal. In this case, the EAM will usually be part of a phase-locked loop incorporating a voltage-controlled oscillator. As an example of the versatility of an EAM, it may be mentioned that it has been shown to work as the only active component in the transmitter and the receiver in an entire system operating at 160 Gb/s [5], or even at 320 Gb/s when using polarization multiplexing [6].

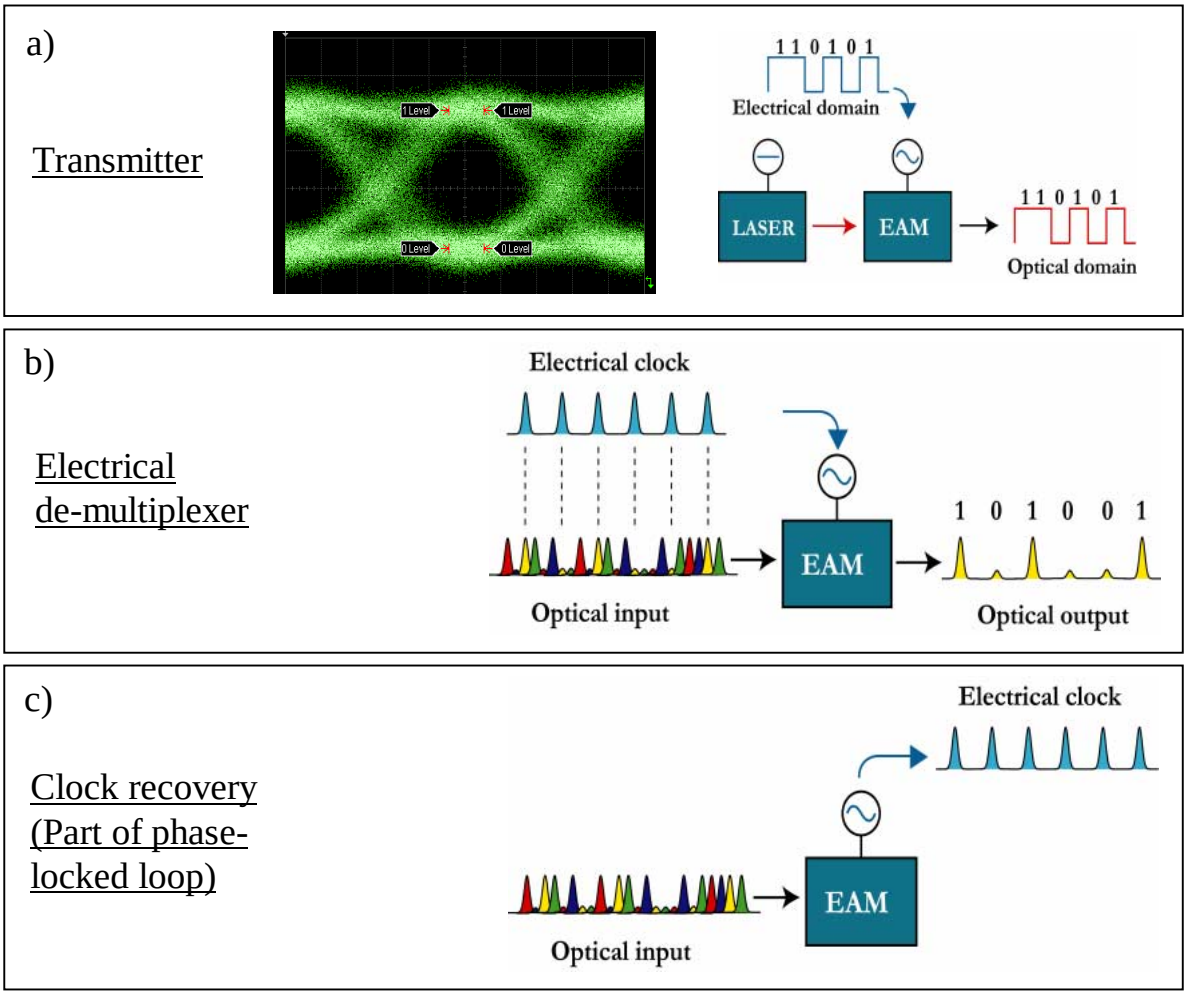


Fig. 1 Applications where the EAM is electrically controlled. a) Standard transmitter application. b) Electrical de-multiplexing may be achieved by utilizing the nonlinear transmission characteristic of the EAM. c) In (subharmonic) clock recovery one utilizes the EAM as a nonlinear mixer between an electrical clock signal and the data signal.

As mentioned, the optical control of an EAM relies on cross-absorption modulation between two optical beams in the device. A strong optical (pump) signal injected into the waveguide will thus reduce the material absorption, thereby increasing the transmission of another (probe) signal injected into the waveguide. The effects leading to absorption bleaching are bandfilling induced by the carriers excited by the pump signal, as well as the screening of the external field that these carriers induce, which in turn decreases the field-induced absorption. In contrast to the use of cross-gain modulation in an SOA, an EAM thus conserves the polarity of the signal; there is no data inversion. All-optical wavelength conversion, e.g., may be achieved in a manner much similar to the case of SOAs, cf. Fig. 2c. Presently all-optical wavelength conversion has been achieved at data rates of 40 Gb/s [3,4,7].

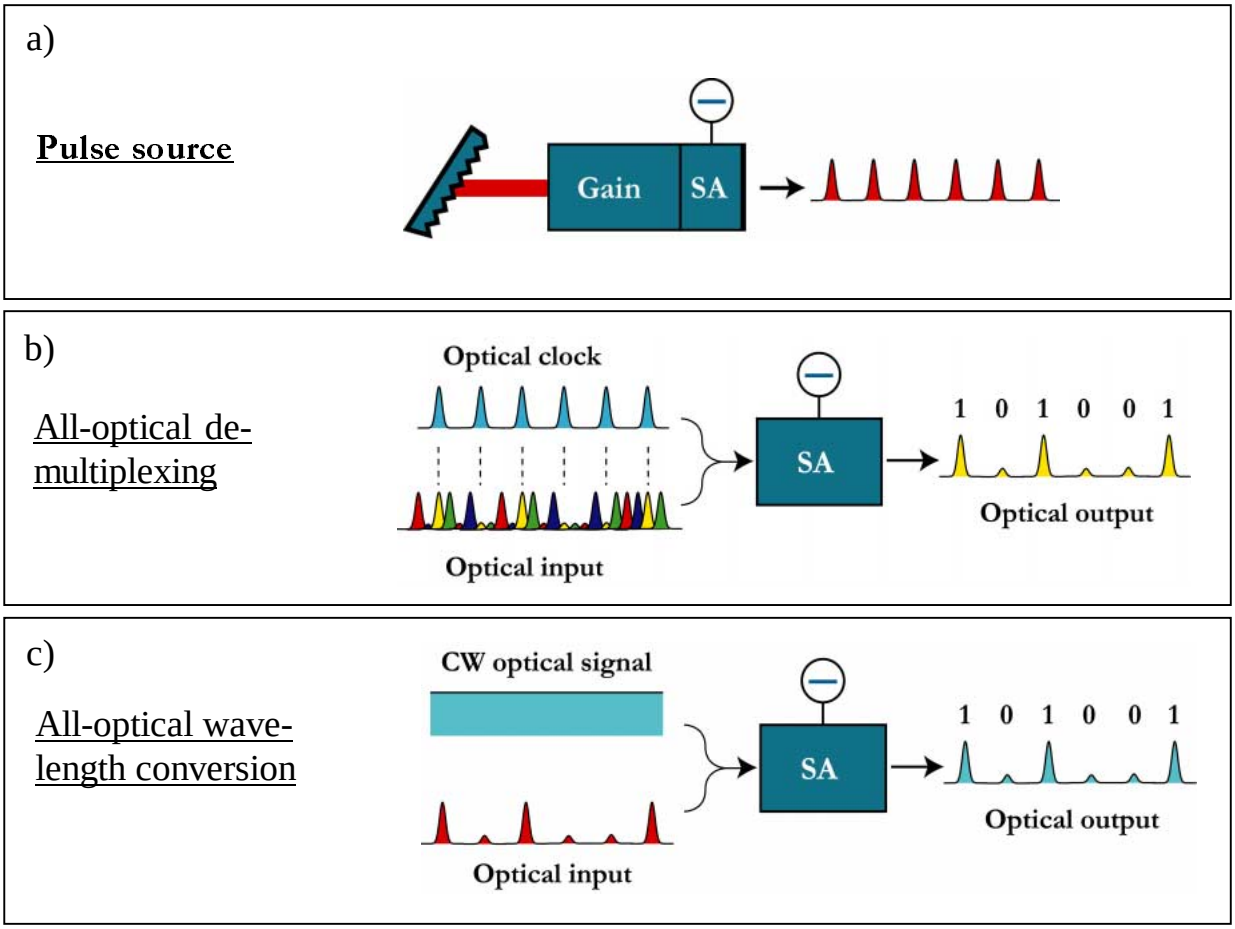


Fig. 2 Applications where the EAM is optically controlled. a) Saturable absorber (SA) element in mode-locked semiconductor laser. b) All-optical demultiplexing, where a strong optical clock signal, through band-filling and screening, opens up a narrow switching window for an optical data signal. c) All-optical wavelength conversion, where the data signal is imprinted on a (weak) CW data signal at another wavelength.

Basic properties of electro-absorption modulators

In Fig. 3 we compare measured and calculated absorption spectra (TE polarized light) for a 10 QW ridge waveguide structure. The qualitative agreement is quite good; the reason for the lower measured absorption is believed due to residual waveguide transmission, not accounted for by the model. The model for the absorption consists of a self-consistent solution of Schrödinger's equation for the wavefunctions of the quantum wells and Poisson's equation for the field and charge distribution across the heterostructure [8]. The bandstructure of the semiconductor is treated quite simplistically through parabolic subbands.

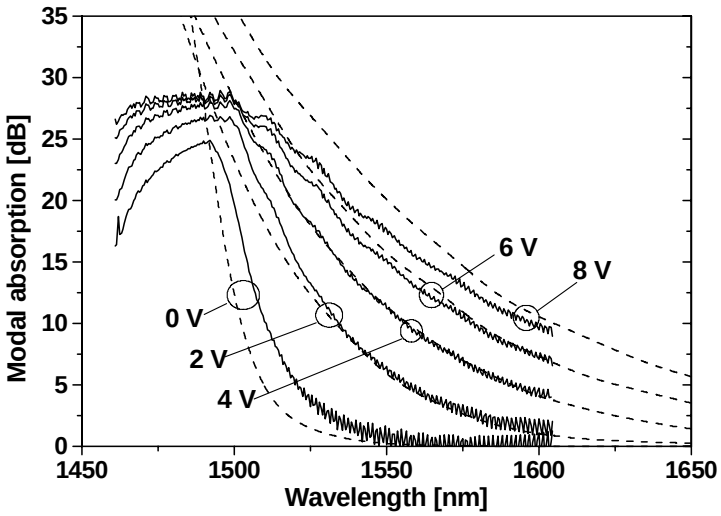


Fig. 3 Measured and calculated absorption spectra for a 250 μm long, 10 QW ridge waveguide structure for different values of reverse voltage. An insertion loss of 10 dB has been subtracted from the experimental curves.

Under electrical modulation, a most important device characteristic limiting the modulation bandwidth is the intrinsic device capacitance. Travelling wave configurations have been adopted in order to improve the bandwidth [9], and may extend the bandwidth beyond 40 Gb/s, which can be reached using standard electrode designs. In the case of optical modulation, however, a significant amount of carriers are generated in the QWs, and a number of transport processes, illustrated in Fig. 4, determine the speed of the device.

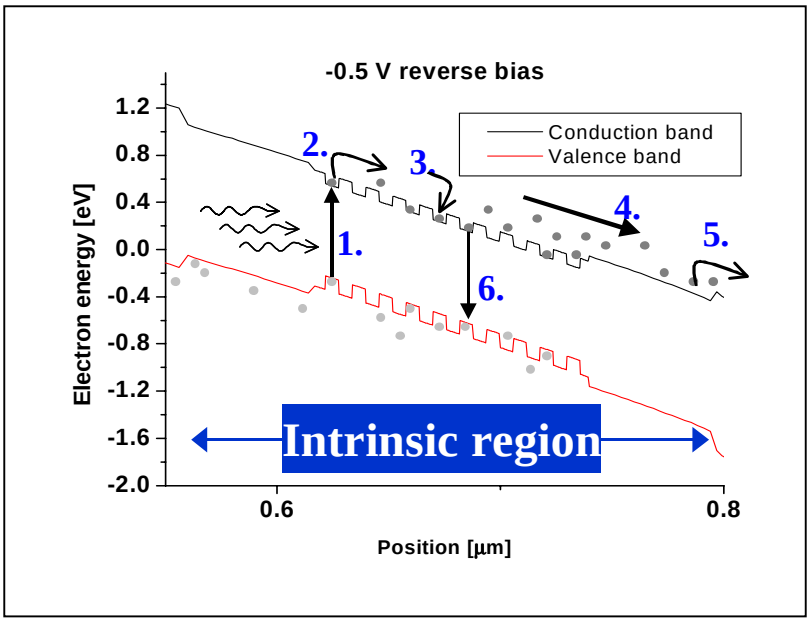


Fig. 4 Schematic illustration of transport processes in the intrinsic region of an EAM.
(1) Carrier excitation by absorption of a photon.
(2) Carrier escape from QWs.
(3) Carrier recapture.
(4) Drift-diffusion transport.
(5) Transport over hetero-junctions.
(6) Recombination.

The speed of the EAM under optical excitation can be measured using a pump-probe technique employing short optical pulses. In our case we use a heterodyne detection technique [10], which allows simultaneous measurement of the temporal change of the absorption as well as the refractive index following excitation by a short optical pulse. Fig. 5a shows the measured probe transmission for an EAM with a reverse bias of 10 V when a 200 fsec pump pulse with an energy of 3 pJ excites the EAM at time zero. The transmission is normalised to 1 prior to the excitation. The probe transmission has two main components: A fast component, with a characteristic relaxation time on the order of a couple of picoseconds, and a slow component with smaller amplitude, which relaxes on a time scale of the order of 100 ps. The measurements are seen to be well fitted by a double exponential fit, leading to values for the amplitude of the two components and their characteristic (1/e) relaxation times. Pump-probe measurements have been carried out for a number of different reverse voltages, and in Figs. 5b and c we show the corresponding variation of the time constants and the amplitudes. It is observed that at low reverse bias the two components have similar time constants, but as the voltage is increased, one of these become much faster and dominant in amplitude. Although the slow component seems relatively small at reverse voltages exceeding, say, 4V, it has to be kept in mind that for high data rate applications one may get an accumulated build up of carriers in the device. Single pulse pump-probe measurements are thus not sufficient to conclude on the actual system application of the device.

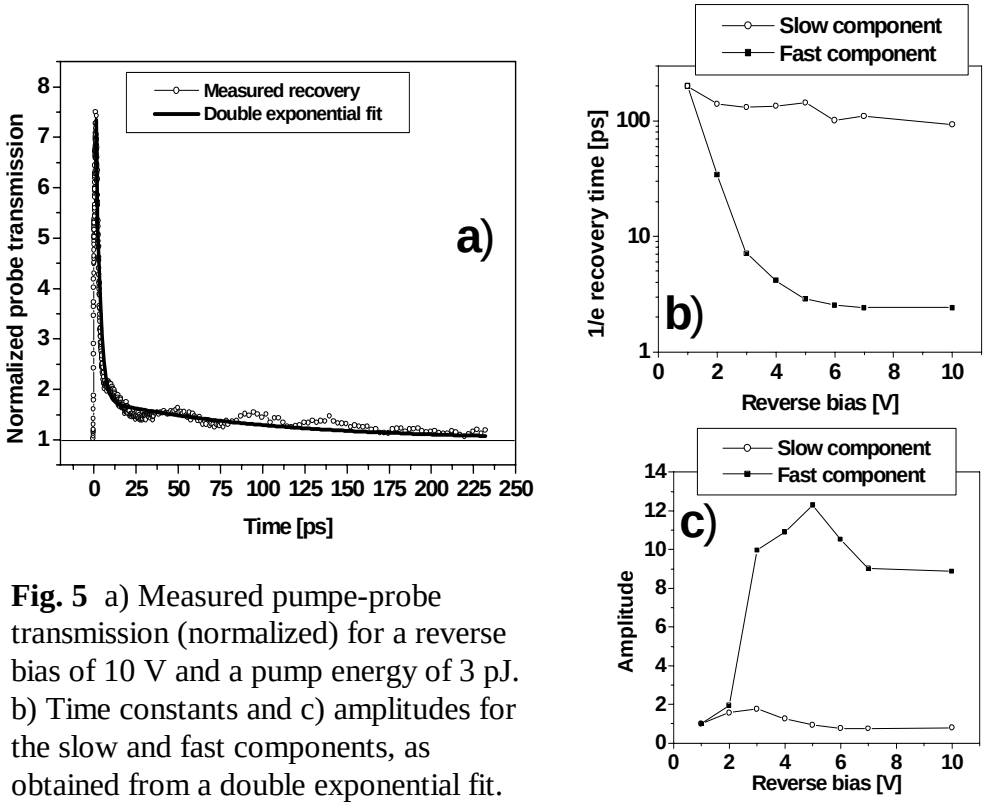


Fig. 5 a) Measured pumpe-probe transmission (normalized) for a reverse bias of 10 V and a pump energy of 3 pJ. b) Time constants and c) amplitudes for the slow and fast components, as obtained from a double exponential fit.

The association of the different time constants with the physical transport processes in the QW structure is not obvious. The fast component may well reflect carrier escape from the quantum wells due to thermionic emission or tunnelling (process (2) in Fig. 4), see e.g. [11], whereas the slower component could be due to screening of the electrical field, induced by carriers trapped at the

heterojunction interfaces (process (5) in Fig. 4), cf. [12]. Support for this interpretation is found from Fig. 6, which shows examples of calculated probe transmisson curves based on our dynamical model for the EAM, including the carrier and electric field dynamics of the device. In agreement with [12] it is found that carrier pile-up at the edges of the heterostructure may significantly slow the overall recovery through a prolonged influence of field screening. Results are shown in Fig. 6d for two different separate confinement structures, i.e., a one- and a two-step structure. In the two-step structure, the rate of thermionic emission is significantly enhanced. Also, the calculations in Fig. 6b illustrate a strong influence from the process of recapture into QWs. Thus, if the recapture time is small, the carriers are transported, rather than by uniform drift in a strong electrical field, by a "hopping" motion from well-to-well, leading to a increase of the relaxation time of the slow component in the recovery. This could explain the experimental observation of a long recovery tail.

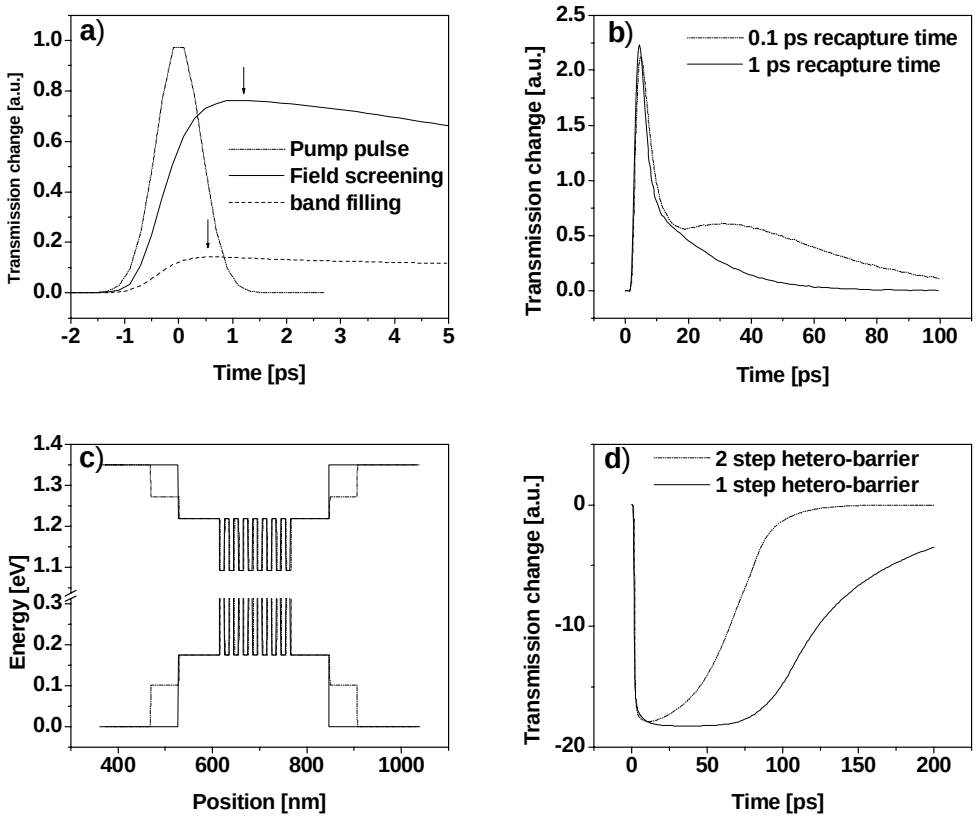


Fig. 6 Simulation results for an MQW EAM. a) Bandfilling and field screening contributions to the absorption dynamics following excitation by a 1 ps wide pulse with energy 1 pJ. b) The effect of recapture in an 8 QW structure. c) Banddiagrams for two different separate confinement structures, i.e., with one or two steps. d) Absorption changes induced by field screening for the two structures.

We have also found that for strong pump pulse energies the recovery may be significantly slowed down. The observation is well accounted for by the dynamical model, and is explained by an initial very strong field screening due to many carriers excited into the separate confinement region. Until a certain fraction of these carriers have recombined, the field cannot build up and the recovery proceeds very slowly with characteristic time similar to the carrier lifetime. However, once the field gains strength the recovery is accelerated and characterized by the sweep-out time from the separate confinement region.

Wavelength conversion

We now briefly present some examples of wavelength conversion in EAMs and the dependence on parameters such as reverse bias and pump power [7,13]. The experimental set-up is shown in Fig. 7. An erbium fibre ring laser (EFRL), working at 1552nm, generates short optical pulses at 10GHz which are data modulated by a MZ modulator and then optically multiplexed to 40Gb/s, to be used as the pump signal. The probe light, generated by a tunable laser (TL), is injected into the EAM together with the pump signal, and through the process of cross-absorption modulation the pump data signal is transferred to the probe. The converted signal is afterwards demultiplexed back to 10Gb/s by a non-linear optical loop mirror (NOLM) which consists of 500m highly non-linear dispersion-shifted fibre (HN-DSF).

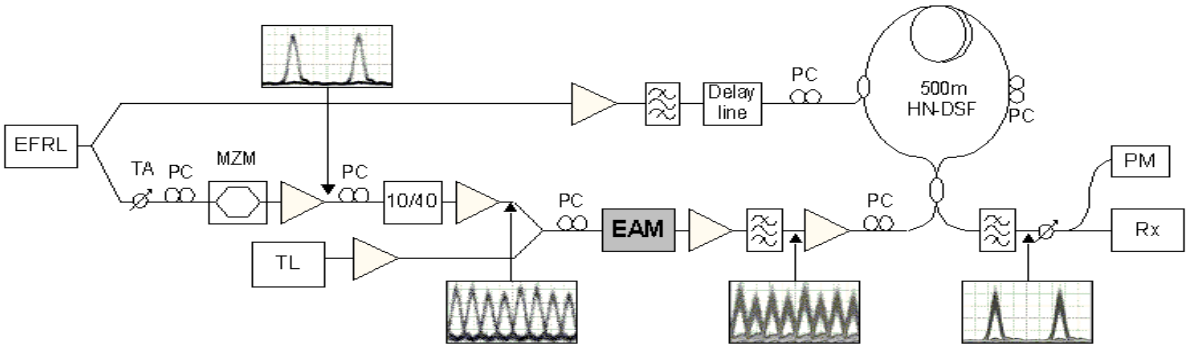


Fig 7. Experimental set-up. EFRL: Erbium fibre ring laser, TA: Tunable laser, PC: Polarization control, TL: Tunable laser

In Fig. 7 the eye diagram of the original signal at 1552nm and that of the converted signal at 1561nm are depicted, together with the signal demultiplexed by the NOLM. In this case the receiver sensitivity for a Bit-Error-Rate (BER) of 10^{-9} is about –26.6dBm, which can be further improved by optimising the receiver and the NOLM.

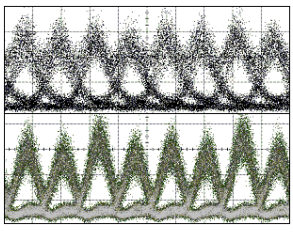


Fig 8. The converted signal for pump power levels of 16dBm (upper) and 20dBm (lower).

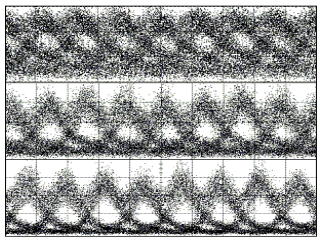


Fig 9. The converted signal for 16dBm pump power @ reverse bias of -1.5 V (upper), -2.0 V(middle) and -2.5 V(lower).

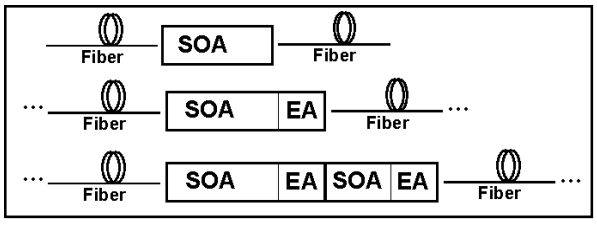
In Fig. 8 we compare two cases corresponding to pump power levels of 16 dBm and 20 dBm, showing that higher pump power leads to a better eye-opening. The BER quoted above was thus obtained for 20dBm pump power, while it wasn't possible to achieve such a low BER at a pump power level of 16dBm. The dependence of bias voltage of the EAM was also studied. As shown in Fig. 9, under a fixed pump power (16dBm), higher reverse bias is beneficial. Lower bias thus leads to a long "tail" in the eye diagram, which is attributed to a longer carrier recovery time under weak electric field.

It should be noted that although the present results indicate higher pump power to be beneficial, one should be careful in the use of excessive pump power levels. Since the number of photo-generated carriers increases with pump power, the recovery time may suddenly be drastically increased, as mentioned earlier, due to excessive field screening preventing carrier sweep-out. This may be counterbalanced by the use of a higher reverse bias, which will, however, also increase the insertion loss of the device. Beyond this, the reliability of an EAM under such extreme conditions also needs consideration.

The performance at various probe wavelengths has also been investigated and it is found that the original signal at 1552 nm can be converted to wavelengths ranging from 1537 nm to 1564 nm, resulting in clear and open eyes. This suggests that EAM-based wavelength conversion has a wide wavelength range of operation. It is, however, found that in some wavelength ranges an appreciable dc-offset exists, which limits the achievable extinction ratio. The dc component reflects the fact that a part of the probe beam passes though the device without being modulated. Measurements of the chirp properties of EAM-wavelength converted signals have shown that shorter wavelength operation lead to lower chirp (alpha-) parameter. In all cases investigated, the output chirp was lower than the input chirp, suggesting the capability of an EAM-based wavelength converter to reduce chirp and even possibly generate a negatively chirped signal.

Regeneration and integrated devices

The regenerative properties of a saturable absorber due to absorption bleaching are well documented, both as a stand-alone component [14,15] and integrated with a semiconductor optical amplifier (SOA) [16,17]. The signal improvement is achieved by suppressing low intensity noise on the zero-level while the high intensity one-level bleaches the absorption and thus experience much less absorption. We have recently proposed [18] a novel device, which contains a cascade of SOAs and electro absorbers (EA); see Fig. 10. We have in mind a monolithically integrated device, with forward and reverse biased waveguide sections. This is similar to a mode-locked laser design, and the device performs signal shaping and pedestal suppression similar to the shaping of pulses circulating in a mode-locked laser. We have theoretically analyzed the regenerative properties and noise of the proposed device.



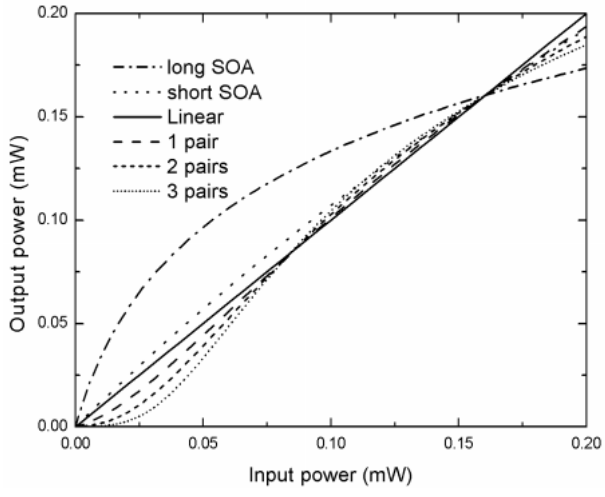


Fig. 10 Investigated devices, containing a cascade of SOA and EA sections (above). Transfer function, i.e., output power versus input power for different device combinations (to the right).

The static transfer functions for different combinations of single SOAs and SOA-EA pairs are shown in Fig. 10. The transfer functions include the fibre loss, which has been chosen to precisely compensate the device gain at the power level for the logical ”1”, i.e. at about 0.16 mW where the output power from one span is equal to the input power. The total gain of the modules at this operating point is 18.6 dB for the long SOA and 10.3 dB for the SOA-EA pairs, the short SOA and the linear amplifier. The non-linear transfer functions result from the saturation of the EA absorption and the SOA gain. The small signal absorption of the EAs is high and suppresses the low intensity noise, but the device is bleached at higher powers, if the saturation power of the SOA is high enough. At even higher powers the SOA saturates and gives a flat transfer function that redistribute the noise at the “1”-level. Since the device operates in saturation the response time needs to be fast compared to the bit rate; justifying a quasi-cw approach for evaluating the BER-penalties from amplified spontaneous emission noise [19]. The analysis also has to include the fact, that insertion of an absorptive element needs to be balanced by an increase of the SOA gain, thus increasing the amount of amplified spontaneous emission (ASE) noise. The resulting BER is plotted in Fig. 11 versus the total link loss for one, two and three SOA-EA pairs as well as for the long and short SOA and for the linear amplifier with no noise redistribution. For few regenerators the noise of the input signal dominates, but as more ASE accumulates from several regenerators, the BER increases from the added noise. For many regenerators the BER strongly increases for the case of stand-alone SOAs, while the incorporation of saturable absorbers is seen to slow down the BER accumulation. In particular it is seen that for a large number of regenerators the sharper transfer functions of the multi-section devices do indeed improve the performance of the system.

The analysis thus suggests that substantial improvements in the cascadability of fibre-amplifier links can be obtained by incorporating saturable absorber sections, i.e. the device has regenerative properties.

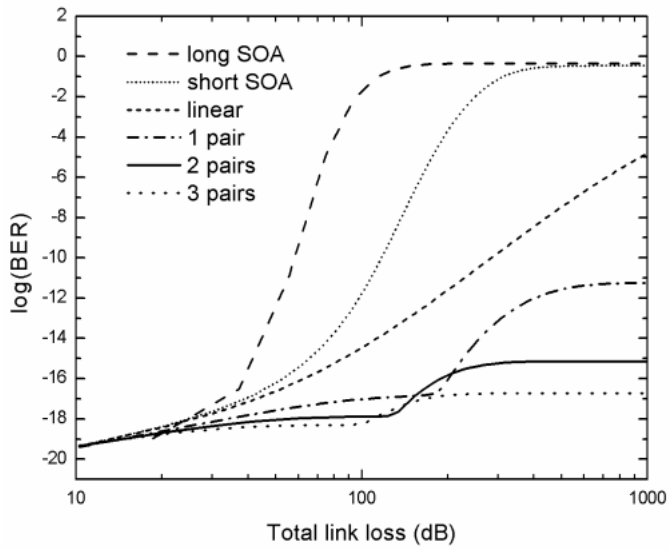


Fig. 11 Calculated BER versus total link loss for concatenated spans of fibers and regenerators. Different device configurations are compared

Summary and conclusions

Electro-absorption modulators offer a number of interesting opportunities for performing all-optical signal processing at high bitrates. Wavelength conversion, de-multiplexing, regeneration, and other more advanced functionalities, such as label swapping, have been demonstrated using relatively simple device geometries. One of the main advantages of the electro-absorption modulator in

comparison to other all-optical switching devices, e.g. interferometers employing semiconductor optical amplifiers, is the simple device geometry and its simple operation. On the other hand, electro-absorption modulators require quite high optical pump power and the device design needs to ensure that a fast sweep-out of carriers can be sustained at these high pump power levels. An example of a new type of regenerator exploiting the linear and nonlinear properties of electro-absorption modulators as well as semiconductor optical amplifiers was presented. Such integrated designs may offer new and improved functionalities in the future.

References

[1] K. Stubkjaer, IEEE J. Select. Topics Quentum Electron., vol. 6, pp. 1428-1435, Nov. 2000.

[2] S. Nakamura, Y. Ueno and K. Tajima, IEEE Photon. Technol. Lett., vol. 13, pp. 1091-1093, Oct. 2001.

[3] N. Edagawa, *IEICE trans. on electronics*, vol. E81-C, No. 8, pp. 1251-2157, 1998.

[4] T. Otani et al., *J. Lightwave Technol*., vol. 20, pp. 195-200, 2002.

[5] B. Mikkelsen et al., Proc. ECOC 2000, paper 6.1.1, Munich, Germany, Sept. 2000.

[6] B. Mikkelsen at al., IEEE Photon. Technol. Lett., vol. 12, pp. 1400-1402, 2000.

[7] L. Xu et al., Proc. IEEE/LEOS Annual Meeting, pp. 111-112, Glasgow, Nov. 2002.

[8] S. Højfeldt et al., IEEE J. Select. Topics Quantum Electron., vol. 8, pp. 1265-1276, 2002.

[9] S. Irmscher et al., Proc. ECOC 2002, Paper 10.5.5, Copenhagen, Sept. 2002.

[10] P. Borri et al., Opt. Commun., vol. 169, pp. 317-324, Sep. 1999.

[11] L. R. Brovelli et al., J. Appl. Phys., vol. 76, pp. 7713-7719, Dec. 1994.

[12] T. Yoshida et al., Opt. Quantum Electron., vol. 33, pp. 735-743, 2001.

[13] L. Xu et al., ECOC 2002, paper P1.26 (2002).

[14] H. Yokoyama et al., Tech. Dig. CLEO'98, pp. 502–503, 1998.

[15] S. Højfeldt et al., J. Lightwave technol., vol. 18, 1121, 2000.

[16] C. Knöll et al., Opt. Commun., vol. 187 (2001), 141-153.

[17] Z. Bakonyi et al. IEEE Photon. Technol. Lett., vol. 12, pp. 570-572, 2000.

[18] F. Öhman et al., 2002 IEEE/LEOS Annual Meeting Conference Proceedings, pp. 895-896, Glasgow, Scotland, Nov. 2002.

[19] P. Öhlén et al., IEEE Photon. Technol. Lett., vol. 9, pp. 1011-1013, 1997.

Mach-Zehnder lattice based tunable chromatic dispersion compensator design with simplified control and dispersion slope mitigation

Reinhold Noé
Univ. Paderborn, Optical Communication and High-Frequency Engineering, Warburger Str. 100, D-33098 Paderborn, Germany
noe@upb.de

Zhan Gao
Infineon Technologies AG, Otto-Hahn-Ring 6, 81739 München, Germany

Abstract: The number of externally controlled phase shifts is halved if the power equidistribution between the branches is monitored and controlled in each Mach-Zehnder section. Suitably chosen delays yield an increased tunability and, in multichannel compensators, a selectable dispersion slope.

Keywords: chromatic dispersion compensator, dispersion slope, differential group delay profile

Introduction

Planar lightwave circuits are attractive for the realization of tunable chromatic dispersion compensators because an integration with wavelength DEMUXs is possible. Starting with pioneering work [1] a number of practical equalizers have been reported, e.g. [2-5]. Each stage has a coupler which is adjusted according to the required chromatic dispersion. However, the differential phase shift in each of the differential group delay (DGD) sections also needs to be adjusted. It is difficult to keep track of that, at least if the substrate temperature floats. This limits the practically controllable number of Mach-Zehnder stages. Other issues of interest are a wide tunability range, and dispersion slope mitigation. Dispersion slope compensation has been shown [3, 4], but only on an intrachannel basis, not in such a way that the chromatic dispersion varies from channel to channel. Improvements in several areas of compensator design are proposed here: Local control of the differential phase shifts using monitor diode taps, nonnegligible DGDs in tunable couplers for dispersion slope mitigation in WDM multichannel devices, and apodization of DGDs vs. position for optimized tunability.

Compensator structure and power splitting control

Consider the schematically sketched planar waveguide structure of Fig. 1. There are n sections DGD_i (i=1...n) with DGDs t_i, separated by n-1 tunable couplers C_i. Each DGD section is directly followed by a differential microheater (hatched) which introduces a differential phase shift j_i. The input light is being split in a coupler C_{in} with equal powers into both branches of DGD_1. After the last DGD section DGD_n an output coupler C_{out} directs most of the light into one output waveguide. Each tunable coupler C_i consists of two cascaded 3dB couplers, separated by an auxiliary DGD section with a DGD $t_{C,i}$ and an auxiliary differential phase shift $j_{C,i}$. We assume all wt_i, $wt_{C,i}$ are odd multiples of π at the carrier frequency w of a channel in the middle of a WDM band. The various $j_{C,i}$ are controlled externally to adjust the chromatic dispersion. All j_i need to be adjusted in such a way that the powers in both waveguides after passing C_{i+1} are equal. This is possible if we place two taps at the outputs of the next coupler C_{i+1}. The difference of the detected tap signals is integrated, and the integrator output controls j_i. This local feedback greatly eases the control requirements because it halves the number of external control variables. If a true 3dB input coupler C_{in} can not be fabricated reliably it can be made variable by a differential phase shift j_{in} between two nominal 3dB couplers, the phase shift being controlled to yield equal power distribution in DGD_1. An analogous procedure can be implemented to control light focusing into the output waveguide. For this the output coupler C_{out} must have three outputs. The signal exits at the center

waveguide, and the light power difference between the two lateral monitor outputs is made to become zero by suitable adjustment of the last differential phase shift j_n.

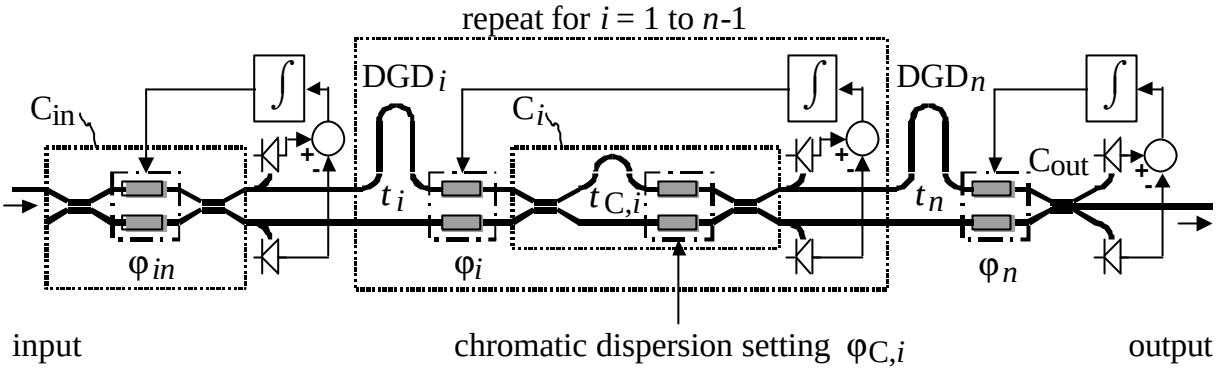


Fig. 1: Schematic of planar chromatic dispersion compensator

Compensator structure and power splitting control

Lossless coupling and differential delay of two modes can be represented in the normalized Stokes space by so-called DGD profiles, as has been explained for the case of polarization mode dispersion in [6]. The DGD or PMD vector was defined here to point in the direction of the fast mode and to have a length which equals the DGD. In the tunable dispersion compensator the modes are not two orthogonal polarization modes but two equipolarized modes in either arm of the lattice structure. The DGD profile is a sequence of concatenated DGD or PMD vectors in a common, input-referred reference system. Therefore each of them is backtransformed by the transposes of all 3x3 rotation matrices which represent in the normalized Stokes space the 2x2 complex transfer matrices of the two electric field modes. In doing so, all couplers and all DGD sections prior to the element under consideration have to be taken into account in the correct order.

To give an example, we consider n=12, $t_{1,11}$=-$t_{2,12}$=5ps, $t_{3,5,7,9}$=-$t_{4,6,8,10}$=10ps, $j_{1...12}$=0, $\tau_{C,1...11}$= -25fs, $j_{C,i}$=0. This choice allows for a fairly regular, space-saving meandering waveguide pattern. At the center frequency the DGD profile is depicted in Fig. 2. The input signal which is fed to one interferometer arm is represented by an input arrow in Ω_1 direction. The various rods in the Ω_2-Ω_3 plane represent DGD$_i$ and have lengths t_i. They must lie in the Ω_2-Ω_3 plane. This corresponds to equal power splitting between the two arms, which is achieved by the local control loops. Otherwise the dispersion compensation capability could be seriously hampered. Between the DGD$_i$ there are rods along Ω_1 with lengths $t_{C,i}$, representing the DGD sections inside coupler C$_i$. Note that the Ω_1 coordinate in Fig. 2 is stretched by a factor of 50 for better viewability. Each rod twists about its own axis as a function of w because its differential phase shift wt_i, $wt_{C,i}$ is proportional to w. The angle change between various rods represents mode coupling. The 3dB couplers C$_{in}$, C$_{out}$ as well as those inside C$_i$ are represented by concentrated 90° turns. Looking at the whole DGD profile, if θ is the angle between the output arrow and the input arrow (along Ω_1) then $\cos^2\theta$ is the power fraction transmitted to the output. According to the above DGD vector definition the group delay experienced by the signal is -1/2 times the Ω_1 coordinate of the DGD profile endpoint. The factor 1/2 applies because the DGD equals the difference of the group delays of one mode, which is exited, and the other mode, which could be exited at the other, unused input port of C$_{in}$. A *linear movement of this endpoint as a function of w* is necessary for chromatic dispersion compensation.

A simulated 43Gbit/s eye diagram is shown in Fig. 3 left. It virtually coincides with the back-to-back eye diagram. In the vicinity of the center frequency the DGD profile stays very similar to that of Fig. 2 because the frequency-dependent twists of adjacent but oppositely directed sections DGD$_i$ cancel well.

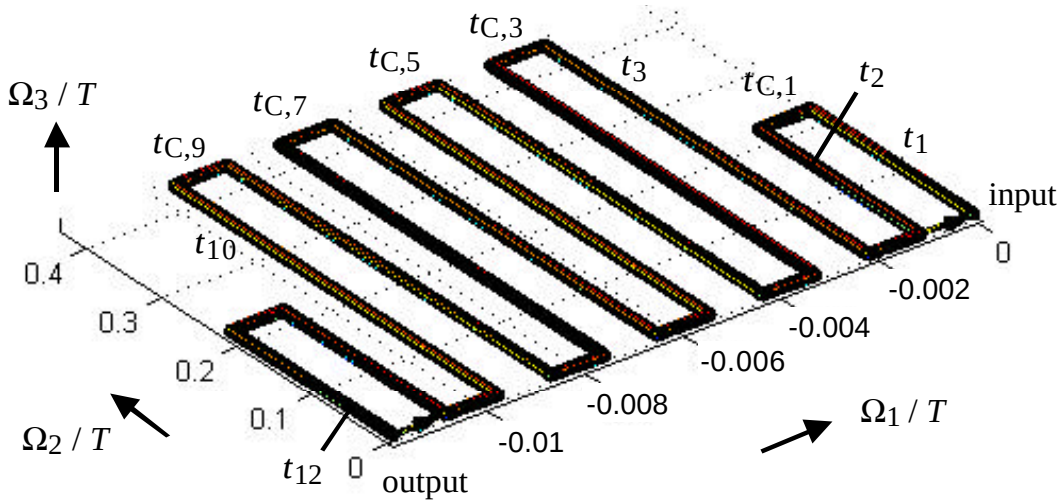


Fig. 2: DGD profile without chromatic dispersion at the center frequency. Scaling unit is the bit duration T = 23.3ps.

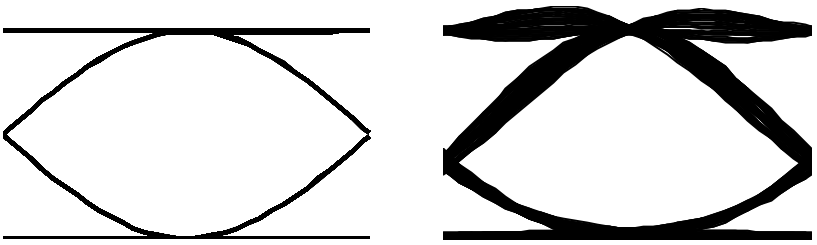


Fig. 3: Simulated 43Gbit/s eye patterns behind compensator, with 0ps/nm (left) or 160ps/nm (right) of chromatic dispersion compensated

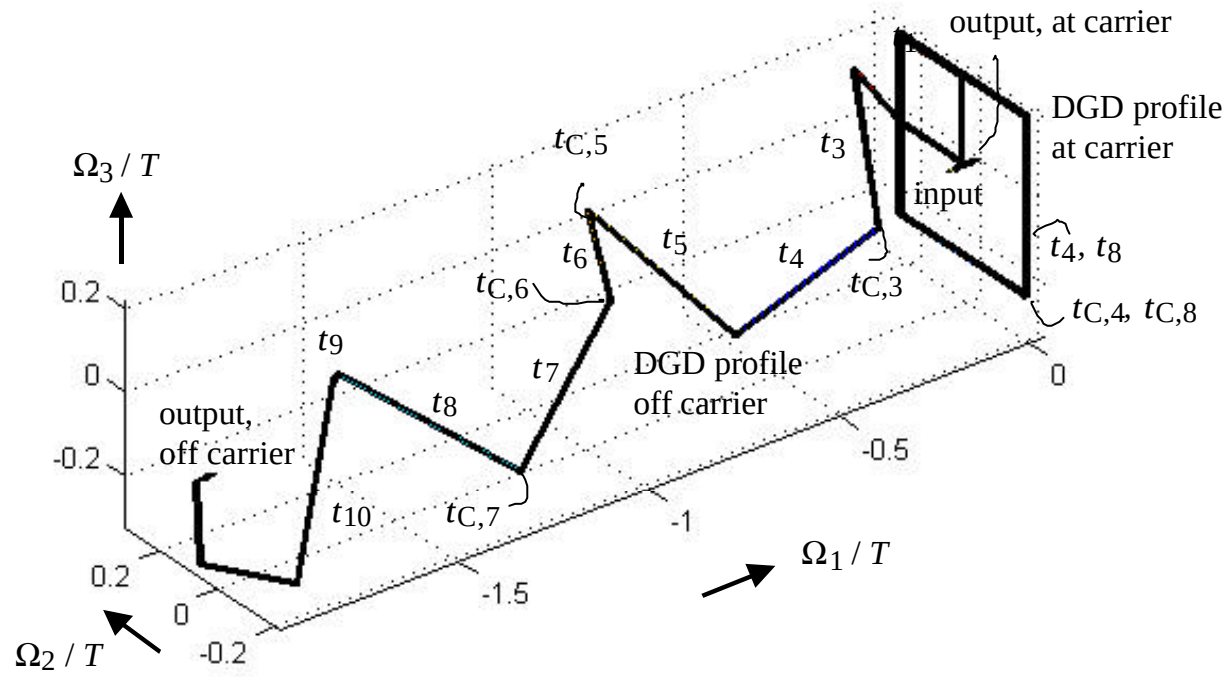


Fig. 4: DGD profile at carrier frequency and 20GHz off carrier when a 160ps/nm chromatic dispersion is compensated, using $j_{C,i}$=-π/2. – When $j_{C,i}$=0 is used, Fig. 2 applies for a centered carrier frequency, and Fig. 4 simultaneously applies for a carrier frequency having a -10THz offset with respect to the centered carrier frequency. A ~2ps/nm^2 dispersion slope compensation is thereby provided.

Next we want to compensate for the chromatic dispersion *DL* (given in ps/nm) of a transmission fiber. A fairly good coupler phase shift setting is $\kappa_{C,i}=0.0098*DL$, valid up to about $|\kappa_{C,i}|=0.6\pi$. This corresponds to a ~±190ps/nm tuning range. Individual optimization of the $\kappa_{C,i}$ yields a slightly wider tuning range. For $\kappa_{C,i}=-\pi/2$ the DGD profile at the center frequency looks like a "discrete" spiral (right part of Fig. 4). All DGD_i rods lie essentially in one plane. 20 GHz higher the DGD profile spiral is pushed far apart by the twist of the rods about their axes, thereby providing the desired wavelength dependence of the group delay (rest of Fig. 4). For negative frequency offsets the spiral extends in the other direction. Obviously, a symmetry of τ_i and $\kappa_{C,i}$ settings with respect to the center of the compensator yields a regular DGD profile and is advantageous. Fig. 3 right shows the eye diagram if a 160ps/nm fiber dispersion is now compensated.

The DGD profile repeats every 200ps, but not exactly because of the non-zero $\tau_{C,i}$. With $\kappa_{C,i}=0$ the DGD profile at the center frequency is given by Fig. 2. A large frequency offset lets the DGD sections inside C_i twist noticeably. Specifically, for a carrier frequency offset of -10THz, where they twist by 1/4 turn, and for a frequency offset of -9.98THz the DGD profiles are again given by Fig. 4, and the eye diagram while compensating 160ps/nm is given by Fig. 3 right. This shows that the device compensates a dispersion slope of ~2ps/nm^2. The slope compensation changes its sign if we set $\kappa_1=\kappa_{12}=\pi$ and replace the signs of all $\kappa_{C,1...11}$. This has the same effect as a sign change of all $\tau_{C,1...11}$. The desired dispersion slope must be chosen when compensation starts. Later it can not be changed online without temporary loss of compensation. Compensation of much larger (e.g., 10ps/nm^2) or smaller slopes can also be implemented by proportional changes of the $\tau_{C,i}$. More finely selectable or truly variable amounts of slope compensation require more complicated variable coupler structures. These can be found intuitively using DGD profiles.

Another feature of our design example is the apodization of the τ_i vs. i. Here the two first and two last DGD sections are shorter than the middle ones, more than in [1]. The apodization greatly reduces unwanted distortions, in our case at the expense of the need for two separate compensators and AWG DEMUXs for even and odd 100GHz-spaced WDM channels. The quantized τ_i yield periodic dispersion compensation windows. If periodicity is not needed then a τ_i apodization similar to a single sine halfwave (sampled from 0 to π for i = 1 to n) may be more advantageous.

Summary

Solutions to several design issues of Mach-Zehnder lattice based tunable dispersion compensators have been proposed: Local control of the differential phase shifts using monitor diode taps halves the number of degrees-of-freedom. Nonnegligible DGDs in the tunable couplers provide a dispersion slope with selectable sign for WDM multichannel operation. Apodized DGDs vs. section number optimize the tunability. Not the least, the representation by DGD profiles provides a graphical understanding of Mach-Zehnder lattices and allows an intuitive design of these and other advanced structures.

[1] M. Sharma et al., *J. Lightwave Technology*. **JLT-12**, 1759-1765, 1994
[2] K. Takiguchi et al., *J. Lightwave Technology*. **JLT-14**, 2003-2011, 1996
[3] K. Takiguchi et al., *J. Lightwave Technology*. **JLT-16**, 1647-1656, 1998
[4] G.L. Bona et al., *Proc. ECOC2002*. Kopenhagen, Denmark, Vol. II., 4.2.1, 2002
[5] M. Bohn et al., *Proc. ECOC2002*. Kopenhagen, Denmark, Vol. II., 4.2.3, 2002
[6] R. Noé, *Proc. ECOC2002*. Kopenhagen, Denmark, Vol. II., T4, 2002

$LiNbO_3$ Integrated Optical QPSK Modulator and Coherent Receiver

Arkady Kaplan, Kobi Achiam,
Art Greenblatt, Geof Harston and Pak Shing Cho,
CeLight Inc. 12200, Tech Road, Silver Spring, MD, 20904, USA
Phone: +732-829-1641, e-mail: akaplan@celight.com

Abstract:
These devices, reported for the first time, are X-Cut highly integrated $LiNbO_3$ Optical Modulator and Hybrid Receiver developed for coherent QPSK (Quadrature Phase Shift Keying) fiber optical communications, as well as other applications. Preliminary tests of the integrated LN optical hybrid were conducted.
Keywords: integrated optics, $LiNbO_3$, modulator, receiver, QPSK, coherent communication.

1. Introduction

Coherent optical communications utilizes the transmission of phase information instead of amplitude (i.e. on/off) modulation. When used in fiber links it requires considerably lower SNR/Bit and lower transmit power, while providing enhanced receiver sensitivity and longer reach [1]-[2]. In free-space it supports signal amplification for near quantum (shot noise) limited operation (fewer photons per bit). PSK is inherently frequency-selective which eliminates the requirement for optical filtering enabling lower cost/complexity. Down-conversion to baseband allows the cost-effective electrical filtering and digital signal processing. Figure 1 illustrates the QPSK Modulation principle that has been effectively exploited in CeLight original architecture.

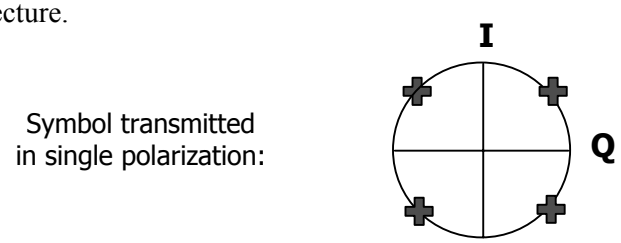


Figure 1. QPSK modulation principle (2 bits/symbol).

CeLight's coherent optical communications architecture, originally developed to deliver innovative optical networking, is based on the following *Ti*-in-diffused $LiNbO_3$ components:

- **Integrated $LiNbO_3$ optical coherent modulator.**
- **Integrated optical coherent receiver based on $LiNbO_3$ hybrid.**

The system Implementation of these components is schematically shown in Figure 2.

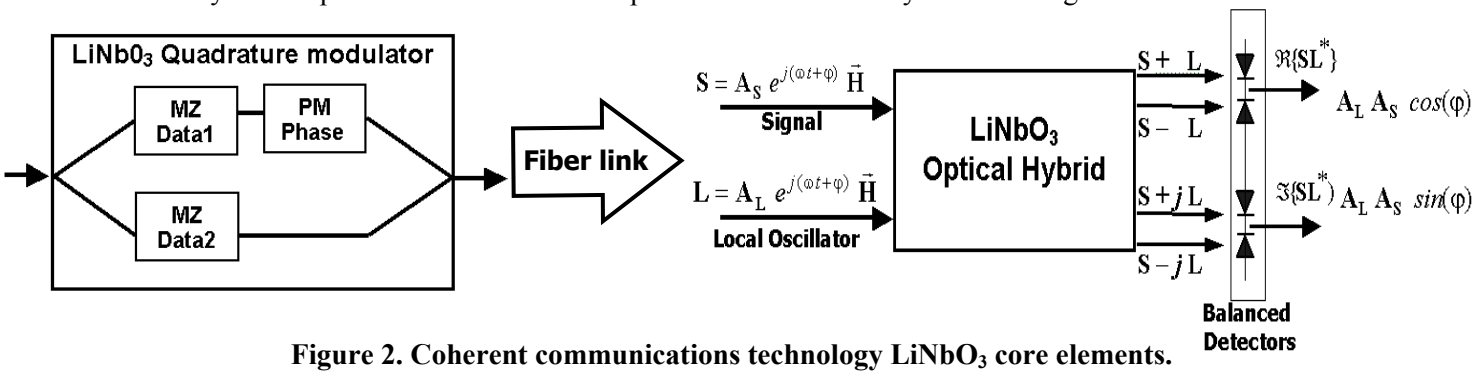


Figure 2. Coherent communications technology $LiNbO_3$ core elements.

In the modulator design, the carrier is separated into two branches, an in-phase (I) branch and a quadrature-phase (Q) branch. The two branches are kept at 90° using the phase modulator (PM). Each branch is amplitude and phase modulated using a Mach-Zehnder (MZ) interferometer. Finally, the two branches are combined.

In the receiver, the signal S is combined with the local laser L using directional couplers (DCs) to produce four optical outputs: S+L, S-L, S+jL and S-jL. The phase relations between S and L are controlled by two phase-modulators (not shown in diagram). Two pairs of balanced diodes are used to produce the real (I) and imaginary (Q) parts of the product SL^*. These signals are then used to decode the received bits.

2. Design and Fabrication

2.1 $LiNbO_3$ Quadrature modulator

The main advantage of the proposed optimized design is the high integration level of electro-optical components within a single $LiNbO_3$ crystal wafer [3]-[4]. A quadrature modulator with the structure shown in Figure 3 was designed and fabricated.

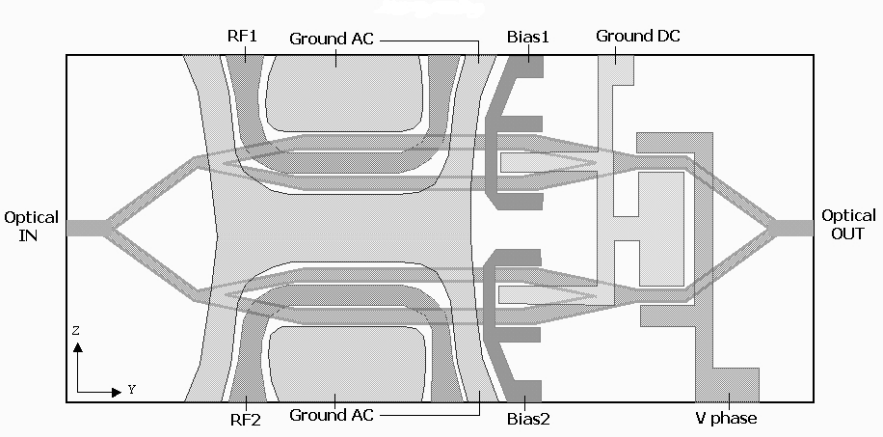


Figure 3. Schematic of the integrated $LiNbO_3$ Quadrature Modulator.

The single X-cut $LiNbO_3$ chip consists of:

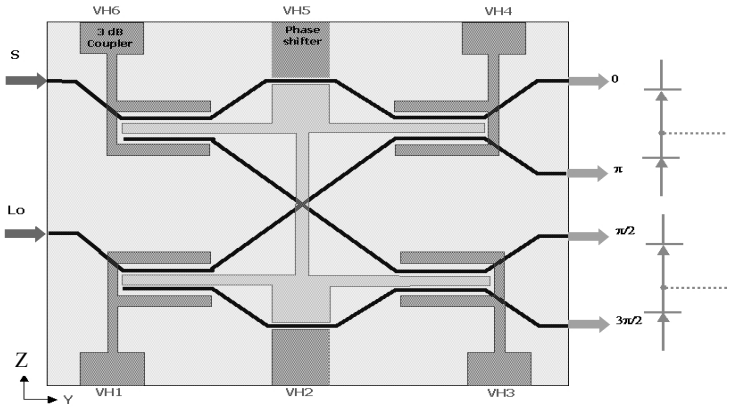
- Two passive 3dB Y-Junctions for separating and combining the optical signals.
- Two MZ electro-optical "push-pull" modulators.
- Two "push-pull" phase shifters for the MZ modulators' bias adjustments.
- One phase shifter for phase difference introduction between the two modulated signals before combining.

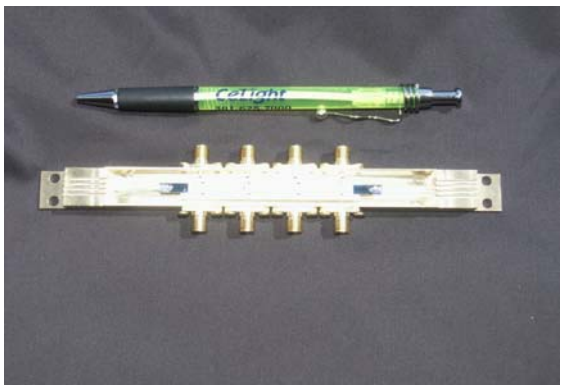
The device was designed for a 4" $LiNbO_3$ wafer, using titanium in-diffused technology. The waveguides are designed for single-mode TE operation on X-cut, Y-propagation crystal. Diffusion time and temperature were 10 hours and 1000 ^oC, respectively. The substrate is coated with a buffer layer of silicon dioxide. A thick plated gold coplanar-waveguide (CPW) traveling-wave type electrode structure is formed on the buffer layer. SiO_2 and gold thickness were optimized for velocity matching of the optical and electrical signals. Each MZ is driven by RF signals applied to the on-chip CPWs. The CPWs were designed for 50 Ohms impedance. The lengths of the RF electrodes are about 40 mm. The integrated phase modulator package was designed for at least for tens of Giga symbol/s quadrature or binary phase shift keying modulation. The actual device was optimized for 12 GHz. Two MZ type modulators are combined using two 3-dB Y-junctions at the input and output. The MZ modulator is an optical switch that splits the incoming lightwave into two optical beams and then combines them after an appropriate distance. Separate bias pads are utilized to optimize the DC bias point of each MZ modulator. An additional V-phase pad has

been added to obtain quadrature phase difference between the two Mach-Zehnder modulators. The modulator is pigtailed with polarization maintaining fibers. The half wavelength voltages were designed to be 5V at DC and 7V at 10 GHz. The optical insertion loss, including waveguide propagation loss, branch loss, and connection loss between the waveguide and fibers was optimized to be less than 8 dB.

2.2 Balanced 90° $LiNbO_3$ coherent receiver (hybrid)

The architecture of the integrated balanced phase diversity receiver [5]-[6] comprising the optical hybrid is shown in Figure 4a. X-cut $LiNbO_3$, titanium diffused integrated 3" wafer technology was used. The single hybrid chip includes four tunable 3dB couplers for mixing the optical signals and two electro-optical phase-shifters.





(a) **(b)**

Figure 4: a. Schematic of the integrated $LiNbO_3$ Coherent Receiver
b. $LiNbO_3$ Coherent Receiver package

The design is optimized for use with balanced photodetectors for coherent detection of QPSK and BPSK signals.

The design includes the following features:

- Optical "I" (in-phase) and "Q" (quadrature) outputs.
- External DC biasing capability of optical hybrid for optical amplitude and phase compensation.
- Separate optical input for Local Oscillator (LO) laser to heterodyne (or homodyne) with signal on chip.
- Package includes the option for Thermo Electric Cooler (TEC) and thermistor for temperature control and monitoring.

The input signal is fed into input S and split by tunable 3dB coupler VH6. The phase between the signals at the upper ports of VH4 and VH3 can be tuned by phase-shifter VH5. The local oscillator signal is fed into input LO and split by VH1. If the phase between the LO signals at the lower ports of VH4 and VH3 is adjusted to 90°, the signals at the device output ports will show the desired phase relation of the 90° hybrid: {180, 90, 270} with respect to the first output. Figure 4b shows the actual packaged $LiNbO_3$ Coherent Receiver.

4. Experiment

Typical measured insertion loss of the hybrid is about -10 dB including fiber-to-fiber coupling loss, waveguide absorption/scattering, and bending losses. Preliminary testing of the integrated hybrid was conducted using an optical differential binary phase-shift-keyed (DBPSK) input signal at 12.5 Gbits/s (Figure 5a). A self-homodyne detection scheme with one symbol relative delay was used to demodulate and detect the signal. The one symbol delay was achieved by fusion splicing an external 3-dB fiber coupler

with a relative length difference corresponding to the one symbol period. Bias voltages in the 10-20V range were applied to four couplers providing the 3dB operation. The output of the hybrid (R1) was directed to a photodetector to examine the eye diagram. An open eye was obtained when the differential phase shift was 0 or π for DBPSK signal at the R1 output of the hybrid (Figure 5b).

Slow drift of the eye (gradual opening and closing) was observed due to environmental perturbations on the fibers of the 3-dB coupler connected to the input of the hybrid. Stabilization of the output eye was obtained using a phase control loop (Figure 5a). A control voltage was applied to the phase shifter sections of the hybrid. It was shown that the drift of the hybrid itself was completely dominated by the drift of the fiber coupler.

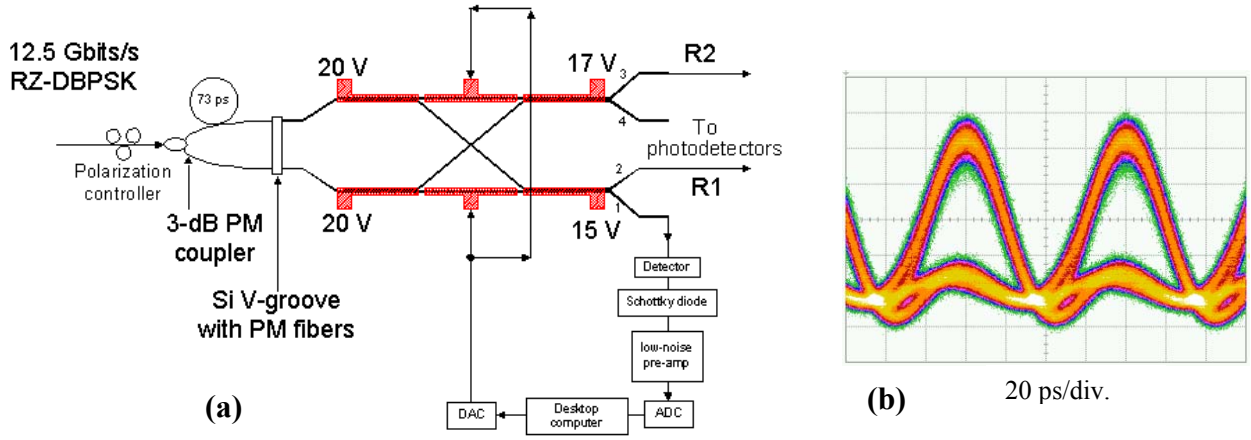


Figure 5: a) Demodulation setup; b) Eye diagram of the demodulated 12.5 Gbits/s RZ-DBPSK signal

5. Conclusions

A novel $LiNbO_3$ electro-optical device has been developed for use in coherent communication technology. These highly integrated devices will enable low manufacturing cost and high SNR in coherent optical communication systems. The integration of all components in a single $LiNbO_3$ chip dramatically reduces the cost, improves performance, and provides better stability and control to increase communication distance. Some particular parameters of the proposed devices will be discussed during the presentation.

6. References

[1] L. G. Kazovsky and O. K. Tonguz, "ASK and FSK coherent lightwave systems: A simplified approximate analysis", IEEE Journal of Lightwave Technology, Vol. 8, #3, pp. 338-353, 1990.

[2] V. Grigoryan, P. Cho, I. Shpantzer, "Nonlinear penalty reduction of RZ-DBPSK versus RZ-OOK modulation format in fiber communications,'' Conference publication of the 28th ECOC, Copenhagen, Denmark, Sept. 8-12, 2002, TuD16, pp. 353-354.

[3] S. Shimotsu at. al. "Single side-band modulation performance of a $LiNbO_3$ integrated modulator consisting of four-phase modulator waveguides", IEEE Photon. Tech. Letters, Vol.13, #4, pp. 364-366.

[4] R. A. Griffin, at. al, "10 Gb/s optical differential quadrature phase shift key (DQPSK) transmission using GaAs/AlGaAs integration", Proceedings OFC-2002, Anaheim, CA, post-deadline paper.

[5] F. Ghirardi, at. al., "InP-Based 10-GHz Bandwidth Polarization Diversity Heterodyne Photoreceiver with Electro-optical Adjustability", IEEE Photon. Tech. Letters, Vol.6, #7, pp. 814-816, 1994.

[6] D. Hoffmann at all. "Integrated Optics Eight-Port 90° hybrid on $LiNbO_3$", IEEE Journal of Lightwave Technology, Vol. 7, #5, pp. 794-798, 1989.

A Versatile 40 GBit/s Optical Transmitter Platform for NRZ, RZ and Carrier-Suppressed (CS) RZ Transmission Formats

G. Gilardi , L.Gobbi, A.Beretta, P.Milanese, S.Pensa, A.Nespola, S. Schmid, P.Andolfo, A.Vannucci
Corning OTI S.p.A , Viale Sarca 222, 20126 Milano, Italy
Vannuccia@corning.com
W. S. Lee, M. Martin
SHF Communication Technologies AG, Amalienstrasse 14, 12247 Berlin, Germany

In this paper we show optimization of both modulator and driving electronics in order to allow the commercial deployment of the first 40 G platform for NRZ, RZ and CS-RZ transmission for long haul application.

Keywords: $LiNbO_3$ modulators, 40 GBit/s, RZ and CS-RZ modulation format

Introduction

During the last two years of the photonic components "market slow down", the research has been working mainly on two issues: cost reduction and product innovation. For both aims a new race, towards 40 GBit/s transmission, is now open. All major system integrators and many small but highly technology oriented companies are developing 40 G solutions, both for SONET/SDH and WDM. The 40 GBit/s component technology has made essential progress and also at the transmitter level new and more effective coding techniques have been developed.
It is anticipated that NRZ will remain limited to short reach while advanced RZ-based modulation formats like CS-RZ, help to overcome the high sensibility of NRZ against chromatic dispersion and fiber non-linearities for long haul transmission links. The CS-RZ format adds a higher spectral efficiency to the robustness of RZ format and it is even more tolerant against SPM than standard RZ transmission.
In this paper we describe the performance of chirp free X-cut Lithium Niobate MZI modulators for long haul transmission and a versatile 40 GBit/s optical transmitter platform for NRZ, RZ and CS-RZ transmission formats. Very broad band modulators and drivers are matched to generate CS-RZ signals with exceptional low jitter enabling long haul 40 GBit/s transmission systems.

40 GBit/s Lithium Niobate modulator performance

LN X-cut based MZ modulators are designed with low loss RF coplanar electrodes grown on a silica buffer layer. Silica layer and coplanar micro strip electrodes are optimized for the velocity matching between the optical and the RF waves.
The small signal characterization of the modulator is shown in Figure 1 and 2.
State of the art 40 GBit/s X-cut LN modulators with an electro-optical bandwidth greater than 30 GHz as shown in Figure 2 together with a driving voltage lower than 6 V that is compatible with 40 GBit/s modulator drivers are currently available on the market.

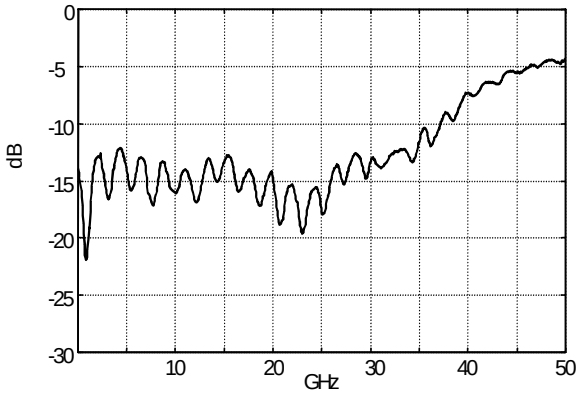


Figure 1: S11- Electrical return loss

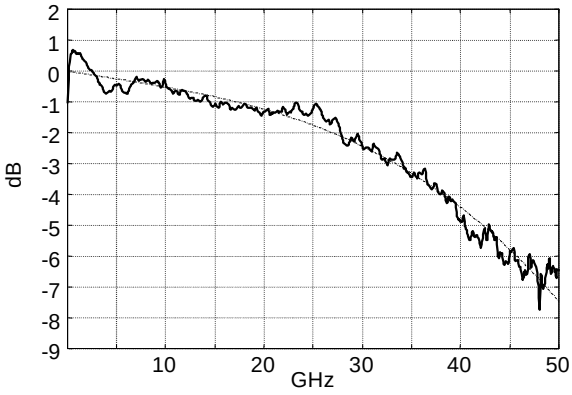


Figure 2: S21-Electro-optical response

A 20 GHz clock modulator has been developed for CS-RZ pulse generation too. The modulator has been optimized both for the required RF operating frequency and a low Vpi at the 20 GHz clock frequency. This pulse generating modulator with a Vpi of 7 V at 20 GHz and 4 dB of optical insertion loss has been added as a first stage of the transmitter. The Vpi plot vs frequency has been measured and compared with the predicted values calculated from the electro-optical S21 of the modulator. Figure 3 shows the excellent agreement obtained.

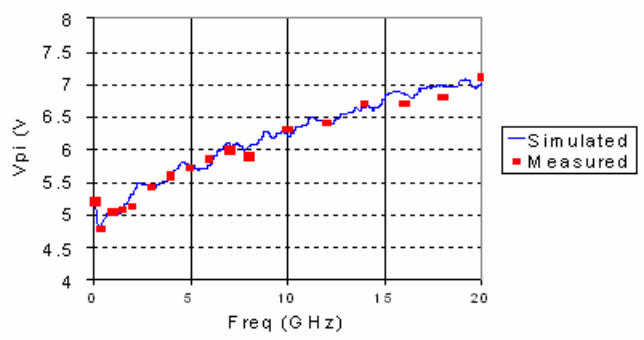


Figure 3: V_π vs Freq

Transmitter architecture

Figure 4 shows the basic transmitter architecture comprising a cascade of two chirp-free X-cut Lithium Niobate modulators. Both the pulse generation and data modulators have PM fiber at both inputs and outputs.

These modulators feature single-ended drive. The pulse generating modulator is driven by a narrow band GaAs RF amplifier with a pass band from 18 to 27 GHz. At mid-band the RF amplifier exhibits a voltage gain of 34 dB and the maximum output power was limited to 28 dBm to avoid overdriving the modulator. The output of the clock driver exhibits harmonic suppression of better than 30 dB below the clock signal, when driven with a 20 GHz signal for RZ pulse generation.

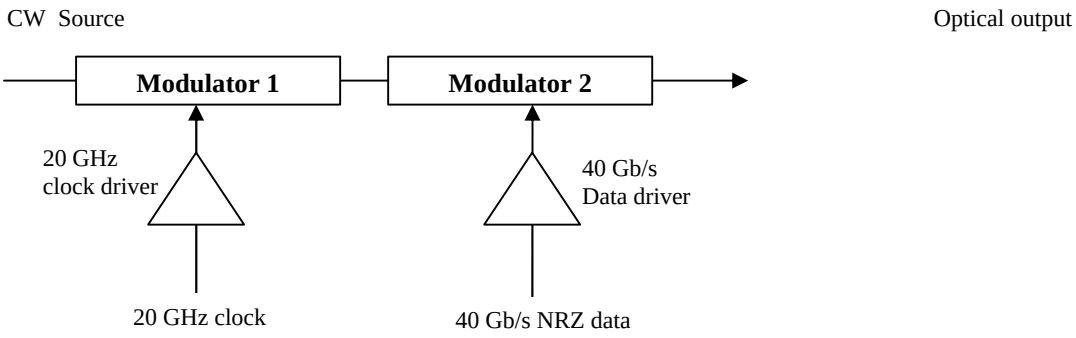


Figure 4: Basic transmitter schematic

The data modulator is driven with a broad band power amplifier [1] with 3 dB bandwidth of typically 42 GHz. Moreover 26 dB mid-band gain with a very low group delay ripple (peak-peak) has been achieved. This multi-stage amplifier is based on GaAs PHEMT MMICs.
To obtain the optimum transmitter performance, the frequency response of the modulator driver amplifier is designed to have a positive gain slope to compensate for the frequency response of the modulator. The increase in amplifier gain is typically 2 to 3 dB up to the -3 dB bandwidth of the modulator. Under this 'matching' condition, the added timing jitter of the amplifier is typically 500fs <RMS> and Figure 5 shows the optical waveforms for NRZ operation.

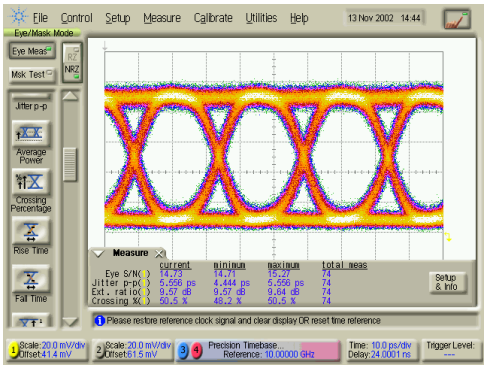


Figure 5: 40 GBit/s NRZ output signal

For RZ operation, the pulse modulator is biased to the maximum transmission point of the MZ response curve. The resultant optical pulse width (FWHM) is in the range of 10-12 ps. For CS-RZ operation, the modulator bias is set to the null of the MZ curve with a corresponding pulse width that is typically 15 ps. Figure 6 shows the measured optical pulse response and the corresponding spectral characteristics.
These optical pulse waveforms were measured using a 70 GHz bandwidth detector coupled into a 70 GHz electrical sampling head. Precision time base operation was used to show the real timing jitter performance. The significant reduction in the timing jitter of the RZ and CS-RZ optical signal was obtained with the re-timing operation of the low jitter clock signal used to generate the initial optical pulses. Special care to design for an extremely small group delay ripple even in the low frequency regime below 1 GHz was one of the key factors to this success.

RZ operation CS-RZ operation

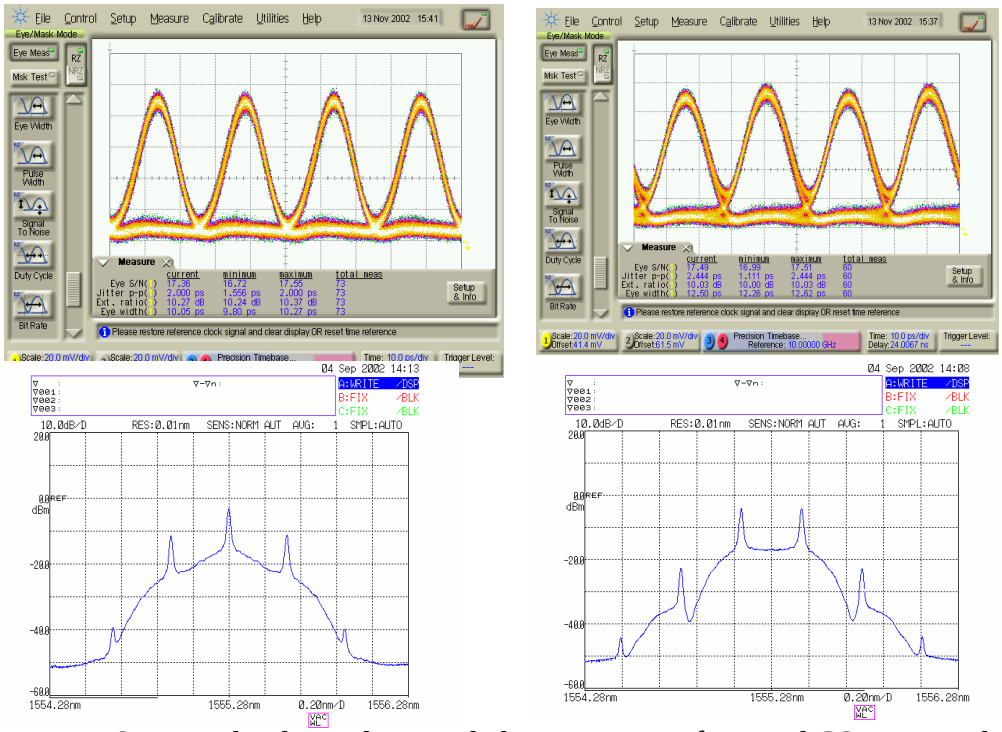


Figure 6: optical pulse and spectral characteristics of RZ and CS-RZ signal

The narrower optical spectral width achieved with the CS-RZ signal compared to RZ is also evident in the spectral plots of Figure 6. This reduced spectral width, together with the optical phase inversion between consecutive pulses, are key attributes towards the realization of a robust high capacity 40 GBit/s transmission for the next generation cost effective optical networks.
The obtained results for jitter and signal to noise ratio are of so far unseen quality. It is not longer the transmitter section putting limits to 40 G optical transmission. This is a real milestone on the way towards 40+ G optical systems.

Conclusions

In this paper the electro-optical characterization of a zero chirp $LiNbO_3$ modulator at 40 GBit/s with the RZ and the CS-RZ coding for the ultra-long haul applications are shown. The results demonstrate that by lowering the transmitter jitter, related to the development of the proper electronics, the system performance has been optimized. The state of the art double modulator and the related driver amplifiers allows the commercial deployment of the first 40 G platform for NRZ, RZ and CS-RZ transmission for long haul application. Now a chirp free 40 GBit/s transmitter solution is available to systems integrators.

References

1. W. S. Lee and M. Martin, ‘High performance broadband optical modulator driver amplifiers to power the optical network’, Technology and Services section, Business Briefing, Global Optical Communications 2002

Reduced number of control variables for fast control and zero-mean voltages for DC drift suppression in distributed $LiNbO_3$-based PMD compensators

Reinhold Noé, David Sandel
Univ. Paderborn, Optical Communication and High-Frequency Engineering, Warburger Str. 100, D-33098 Paderborn, Germany; noe@upb.de

Abstract: Cascaded mode converters on a birefringent X-cut, Y-propagation $LiNbO_3$ chip are ideal "distributed" PMD compensators. Here we show how the number of needed control variables can be significantly reduced, and how DC drift can be suppressed.

Keywords: PMD compensator, $LiNbO_3$, differential group delay profile, DC drift

Introduction

Polarization mode dispersion (PMD) [1] is a big obstacle for high-capacity, long-haul optical communication systems, but can in principle be fully removed by an optical PMD compensator (PMDC) [2]. A "distributed" PMDC with cascaded in-phase and quadrature mode converters in X-cut, Y-propagation $LiNbO_3$ is best suited for this task because of its ability to correct also higher orders of PMD [3, 4]. Waveguide nonuniformity can significantly decrease the conversion efficiency of long mode converters. Apart from improved fabrication the only way to combat it is to subdivide the mode converters into fairly short sections. However, it has been argued that a large number of electrode voltages can not be controlled sufficiently fast. Here we show that this is not true, that waveguide nonuniformity, highest mode conversion efficiency and fastest control speed do not exclude each other. Another potential problem is DC drift: Charges generated by the pyroelectric effect are separated under the influence of a static external electric field, thereby weakening this field inside and near the waveguide. Ion migration in the buffer layer and/or conductivity disturbances of the crystal cause a similar effect. DC drift limits are not specified for commercial $LiNbO_3$ polarization transformers, for good reasons. We show that distributed PMDCs can be driven by DC-free voltages, which avoids drift altogether.

Reduced number of control parameters tolerates waveguide-nonuniformity

An in-phase and quadrature mode converter may be called a Soleil-Babinet analogon $\mathrm{SBA}(\jmath,\gamma)$ [2] because of the analogy to a Soleil-Babinet compensator. It is described by a Jones matrix or a 3×3 rotation matrix

$$\begin{bmatrix} \cos\jmath/2 & je^{j\gamma}\sin\jmath/2 \\ je^{-j\gamma}\sin\jmath/2 & \cos\jmath/2 \end{bmatrix}, \quad \begin{bmatrix} \cos\jmath & -\sin\gamma\sin\jmath & \cos\gamma\sin\jmath \\ \sin\gamma\sin\jmath & \cos^2\gamma+\sin^2\gamma\cos\jmath & \cos\gamma\sin\gamma(1-\cos\jmath) \\ -\cos\gamma\sin\jmath & \cos\gamma\sin\gamma(1-\cos\jmath) & \sin^2\gamma+\cos^2\gamma\cos\jmath \end{bmatrix},$$

respectively. A DGD τ is represented by a phase shifter $\mathrm{PS}(-w\tau)$ with Jones and rotation matrices

$$\begin{bmatrix} 1 & 0 \\ 0 & e^{jw\tau} \end{bmatrix}, \quad \begin{bmatrix} 1 & 0 & 0 \\ 0 & \cos w\tau & \sin w\tau \\ 0 & -\sin w\tau & \cos w\tau \end{bmatrix},$$

respectively, where w is the optical angular frequency. The whole distributed PMDC is approximately described by the Jones or rotation matrix product

$$\mathrm{PMDC} = \prod_{i=n}^{1}\left(\mathrm{PS}(-w\tau_i)\mathrm{SBA}(\jmath_i,\gamma_i)\right). \qquad (1)$$

The product must be executed from left to right with descending index i while the light passes the SBAs and PSs in ascending order i. A longitudinally variable pattern of in-phase voltages $V_{1,i}$ and quadrature voltages $V_{2,i}$ couples TE and TM modes. Using a constant G we can write

$$j_i e^{jy_i} = G\left(V_{1,i} + jV_{2,i}\right). \tag{2}$$

A pigtailed PMDC similar to that in [3, 4] was electrooptically investigated. It had n = 69 pairs of in-phase and quadrature electrodes, each segment $i = 1...n$ being ~1.27mm long. The total PMD was ~23ps, which is good for 40Gbit/s PMD compensation. The PMDC was operated with a horizontal input polarization in the waveguide. A polarimeter was connected to the PMDC output. Consider the case when all voltages except those of segment i are zero. With PMDC expressed by its Jones or its rotation matrix the output polarization state is given by the Jones or normalized Stokes vector

$$\begin{bmatrix} \cos j_i/2 \\ je^{-j(y_i+z_i)} \sin j_i/2 \end{bmatrix} = \mathrm{PMDC}\cdot\begin{bmatrix}1\\0\end{bmatrix}, \qquad \begin{bmatrix} \cos j_i \\ \sin(y_i+z_i)\sin j_i \\ -\cos(y_i+z_i)\sin j_i \end{bmatrix} = \mathrm{PMDC}\cdot\begin{bmatrix}1\\0\\0\end{bmatrix}, \tag{3}$$

respectively. Unequal phase shifts $z_i = -w\sum_{k=i}^{n} t_k$ (modulo $2p$) represent waveguide nonuniformity. Four voltage pairs $V_{1,i} + jV_{2,i} = 20\,\mathrm{V}\cdot\{1, j, -1, -j\}$ were applied sequentially to each of the electrodes in section i, and the output polarization state was measured. Eqns. (2), (3) allowed to determine j_i and z_i. Performance was best at l = 1540nm, where j_i varied somewhat as a function of i but not too much (Fig. 1). However, z_i varied a lot. If a number of adjacent in-phase electrodes were connected in parallel, and likewise for quadrature electrodes, then a low mode conversion efficiency would result, especially for i = 25...45 where adjacent z_i differ by about p.

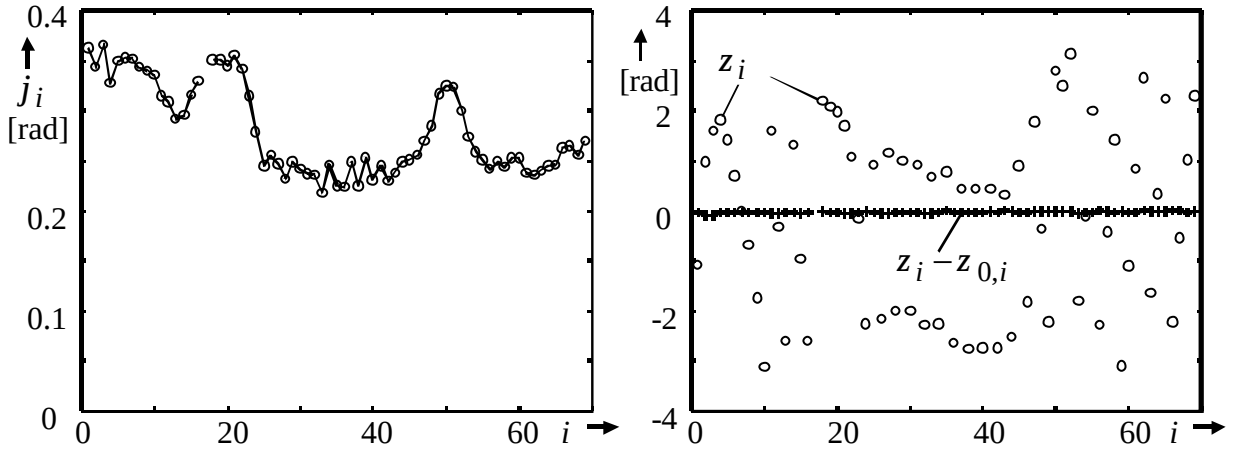


Fig. 1: Polarization change j_i (left), and its orientation z_i (o) and orientation error $z_i - z_{0,i}$ (+, solid line) for $V_{1,i} + jV_{2,i} = 20\mathrm{V}$ (right). Point i = 17 is omitted where both electrodes had internal shorts to ground.

There is a simple remedy: The voltage pairs $V_{1,i} + jV_{2,i}$ in (2) are not applied directly but are first multiplied by $e^{-jz_{0,i}}$. This replaces $y_i + z_i$ in (3) by $y_i + z_i - z_{0,i}$. The values $z_{0,i}$ should be equal to z_i and must be measured once in factory for all i. We took the measured z_i values as the calibration set $z_{0,i}$, and repeated the measurement to obtain new z_i values and test stability. Fig. 1

shows the resulting orientation error $z_i - z_{0,i}$. It ranged from –0.08 to +0.01 rad and may be partly due to multipath reflections at the straight chip endfaces. Now the effects of any set of segments can be combined because the quantity $j_i e^{j(y_i+z_i)} \approx j_i e^{j(y_i+z_{0,i})}$ has become user-accessible.

In PMD compensation algorithms it is common to dither various electrode voltages, one at a time, and to optimize them by a multidimensional gradient search using one or more control criteria. For a maximum voltage of 55V (= 10V/mm) a waveguide length of ~4...6mm will be needed for full mode conversion, and it is therefore possible to reduce the number of control variables below $2n$. A straightforward approach is to specify, say, 4 "discrete" polarization transformers at 0, $L/4$, $L/2$ and $3L/4$ where L is the chip length. This PMDC needs ≤48 voltages but just 8 control variables, and is 4 times more powerful than a PMDC featuring one commercial X-cut, Z-propagation $LiNbO_3$ device, which requires up to 16 control variables for its 8 waveplates.

An alternative approach, which may permit highest PMDC performance, employs a number of spatial Fourier coefficients $F_k = n^{-1}\sum j_i e^{j(y_i+z_{0,i})} e^{-j2\pi ik/n}$ as control variables. The required inverse Fourier transform and multiplication can be implemented in an FPGA for fast execution,

$$V_{1,i} + jV_{2,i} = G^{-1} e^{-jz_{0,i}} \sum F_k e^{j2\pi ik/n}.$$

The PMD vector Ω has a length equal to the differential group delay (DGD) and points in the direction of a principal state-of-polarization in the 3-dimensional normalized Stokes space. If n DGD sections are cascaded the overall PMD vector is given the sum $\Omega = \sum_{i=1}^{n} \Omega_i$ of individual PMD vectors $\Omega_i = \mathbf{R}_{<i}^{-1} \Omega_{local,i}$. The Ω_i are referred to the input of the whole cascade whereas $\Omega_{local,i}$ are the local individual PMD vectors. $\mathbf{R}_{<i}$ is the 3×3 rotation matrix representing all DGD sections (PSs) and SBAs which precede the DGD section i. Plotting the sequence of Ω_i in such a way that the tail of Ω_{i+1} starts from the head of Ω_i results in a DGD profile [5, 2]. Its endpoint is given by Ω. For a distributed PMD compensator the DGD profile is a straight rod as long as no voltages are applied. The Fourier coefficient F_0 causes a bend or loop, and F_k with $k \neq 0$ a spiral of the DGD profile. The coefficiencts permit a precise control of the DGD profile shape. Some 38 control variables or so (real and imaginary parts of F_k, $k = -9,-8,...,9$) may be sufficient for a 96mm long chip. To significantly improve PMD compensation speed the F_k with small $|k|$ may be optimized more often than those with large $|k|$. If the center of gravity of the coefficient spectrum, rms-averaged over extended times, is not near $k = 0$ there may be a static phase mismatch. To overcome it one may correct the chip temperature accordingly.

Zero-mean voltages for suppression of DC drift effects

Fig. 2 shows DGD profiles of two distributed PMD compensators. When bending radii are short enough these DGD profiles are equivalent. In one of the PMDCs (static case) DC drift may cause the joints to straighten out instead of staying bent, thereby distorting the DGD profile or requiring higher and higher voltages. In the other PMDC, an SBA performing a full mode conversion (U turn) under a suitable, slowly and linearly time-variable orientation angle is added at the input. It shifts the TE-TM phase difference by $y_0 = 2\pi ft$. The frequency f may be in the µHz ... Hz range. As a consequence all following SBAs must rotate their orientations by y_0 to approximately maintain the overall DGD profile shape. Mathematically speaking, the expression (1) is identical with

$$\begin{aligned}\mathrm{PMDC} = \mathrm{SBA}(p, y_0/2)\mathrm{SBA}(p, p + y_0)\cdot\prod_{i=n}^{2}(\mathrm{PS}(-wt_i)\mathrm{SBA}(j_i, y_i + y_0)) \\ \cdot \mathrm{PS}(-wt_1)\mathrm{SBA}(p - j_1, y_1 + p + y_0)\mathrm{SBA}(p, y_1 + y_0/2)\end{aligned} \quad (4)$$

The $\mathrm{SBA}(p, y_0/2)\mathrm{SBA}(p, p + y_0)$ at the end of the PMDC may be left out if, as usual, a constant output polarization is not needed. That case, where a full mode conversion SBA is added only at the PMDC input, is illustrated in Fig. 2 for three different y_0. All driving voltages are pure AC voltages. DC drift is thereby avoided, at the cost of losing direct control over 1...1.5ps of DGD in a small input portion of the PMDC. Errors which may occur due to imperfect PMDC characterization can be corrected by the control algorithm which simultaneously optimizes all j_i, y_i in (4) or all F_k, while $y_0 = 2pft$ is being incremented automatically at a sufficiently low speed.

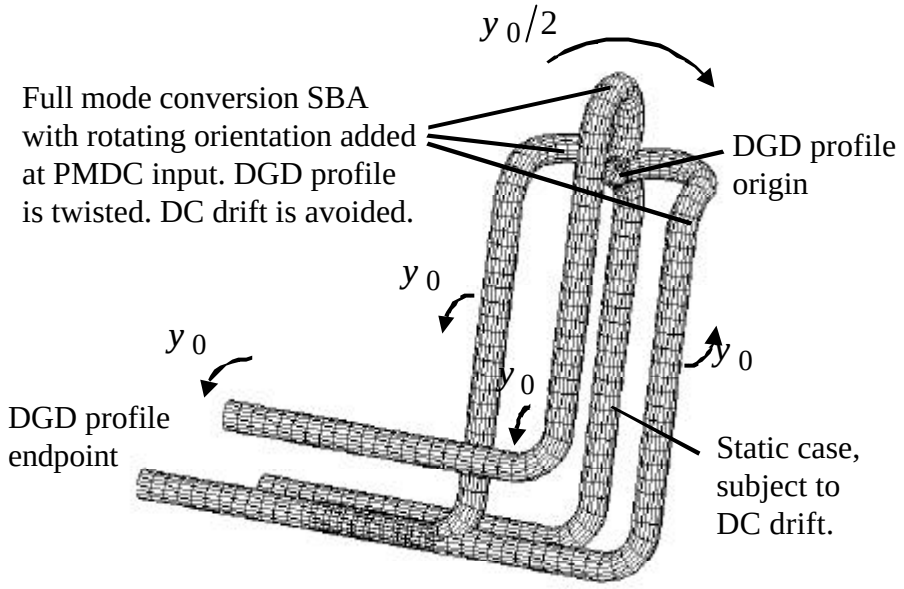


Fig. 2: Mechanical analogon with flexible but torsion-stiff rod: DGD profiles of two similar PMDCs

Summary

Solutions for the most challenging practical problems of distributed PMD compensators in X-cut, Y-propagation $LiNbO_3$ have been pointed out: Waveguide nonuniformity effects can be calibrated out, and a limited number control variables, possibly Fourier coefficients, provides an efficient control even though there may be many electrodes. DC drift, which is a severe limiting factor in X-cut, Z-propagation $LiNbO_3$ polarization transformers, can be avoided altogether in distributed PMDCs because they can be driven by pure AC voltages.

Acknowledgement

is made to R. Ricken, H. Herrmann and W. Sohler (Univ. Paderborn) for device fabrication, and to Siemens ICN for funding part of this work.

[1] C. D. Poole, R. E. Wagner, *Electron. Letters*. **22**, 1029-1030, 1986
[2] R. Noé et al., *IEEE J. Lightwave Technology*. **JLT-17**, 1602-1616, 1999
[3] D. Sandel, R. Noé, *Proc. ECIO'99*. Turin, Italy, 237-240, April 14-16, 1999
[4] D. Sandel et al., *Proc. ECIO'99*. Turin, Italy, PDP volume, 17-19, April 14-16, 1999
[5] R. Noé, *Proc. ECOC2002*, Kopenhagen, Denmark, Vol. II., T4, 2002

Pushing distributed PMD compensator performance toward highest bit rates by Lithium Niobate–Tantalate or Lithium Tantalate crystals

S.Bhandare and R. Noé
Dept. of Optical Communication and High-Frequency Engineering,
University of Paderborn, Warburger Str. 100, 33098 Paderborn, Germany
suhas@ont.upb.de, noe@upb.de

Abstract: Simulations show that cascaded integrated optical TE-TM mode converters with endlessly adjustable coupling phase permit distributed PMD compensation at 160 Gbit/s and 640 Gbit/s if they are implemented in $LiNb_{1-y}Ta_yO_3$ or $LiTaO_3$ crystals, respectively.

Keywords: Polarization mode dispersion, Lithium Niobate, Lithium Tantalate, guided-wave optics

Introduction

Polarization mode dispersion (PMD) is caused by noncircular fiber cores and limits the capacity of optical trunk lines. It can be compensated if appropriately oriented birefringence is added at the receiver side in reverse order. Particularly suited is *X*-cut, *Y*-propagation $LiNbO_3$ (LN). Its natural birefringence (0.24 ps/mm) can be oriented by electro-optical mode converters in order to cancel the differential group delay (DGD). The principle is based on the spatially weighted coupling between two waves with different propagation constants [1]. The phase difference between one mode and the coupled mode therefore depends on the position where coupling occurs and is periodic with the beat length $\Lambda = \lambda/\Delta n$ of ~22μm. Interdigital electrodes are needed for phase matching. The widths W of fingers and gaps G are ~Λ/4. The coupling factor is $\kappa \cong \hat{\Gamma}(\pi/2)n^3 r_{51}(V/G)\lambda^{-1}$, where $\hat{\Gamma}$ is a weighted field overlap integral factor and n is the average refraction index of the waveguide. r_{51} is the relevant electrooptic coefficient in pm/V and V is the inter-electrode voltage.

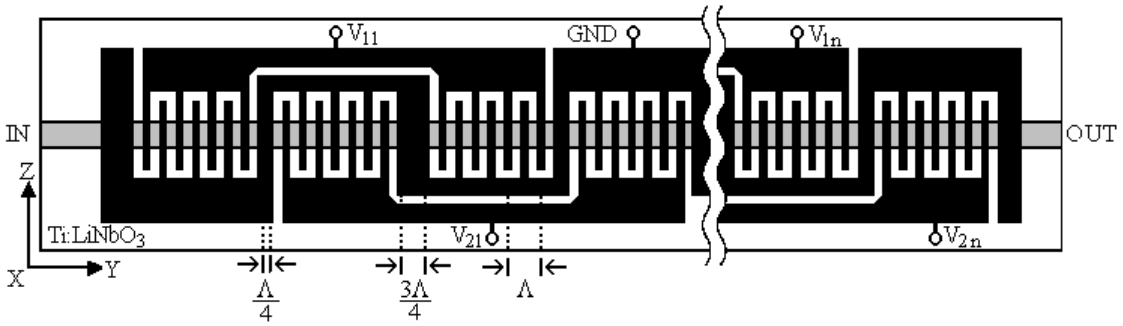


Figure 1: Structure of 2-phase mode converters on *X*-cut, *Y*-propagation $LiNbO_3$

Figure 1 shows the electrode structure of a chip used in [2, 3] where successful PMD compensation was demonstrated. Voltage $V_{1,i}$ $(i = 1...n)$ acts on one set of comb electrodes and performs mode conversion in phase. Voltage $V_{2,i}$ acts on another set of comb electrodes which are translated, with respect to the first, by $\Lambda/4$, and performs mode conversion in quadrature. The resulting local complex coupling factor is proportional to $V_{1,i} + jV_{2,i}$ [4]. This type of LN-based PMD compensator (PMDC) should work up to at least 40 Gbit/s. At 160 Gbit/s a poor performance is to be expected because the experimentally needed length for one full mode conversion is on the order of 5 mm. This means that the corresponding DGD of about 1.2 ps is only partly orientable. However, PMD compensation at 160Gbit/s or beyond seems to be mandatory to maximize dispersion-shifted fiber capacity, in particular in all Japan. We show that $LiTaO_3$ (LT) and a

mixture $LiNb_{1-y}Ta_yO_3$ (LNT), also known as lithium niobate─tantalate, are suitable for PMD compensation at highest bit rates.

LNT crystals

Mixed ferroelectrics have been the focus of intensive fundamental and applied research for many years. Interest in the study of these materials arises from the fact that the physical properties of crystalline materials are governed to a large extent by the composition of the crystals, thus can be tuned by varying the composition. One of the simplest ferroelectric mixed crystal systems is lithium niobate─tantalate (LNT), as both end members exhibit the same crystal structure (space group *R3c*) with only slight differences in the lattice and positional parameters. The physical properties can be very easily tuned by varying the parameter y in the composition of LNT crystals. To a certain degree, the mixed system yields a simple crystal modelling that may lead to well functional materials and devices, which has direct implication for PMD compensation in optical communication.

Lithium niobate is a slightly nonstoichiometric, typically Li-deficient, preferably grown at the congruently melting composition with 48.5 Mol% of Li_2O. A large variety of dopants ranging from +1 valent state H^+ to the +3 valent state such as rare earth cations can be introduced into the crystal structure frame of lithium niobate. Most are known to occupy Li-sites. In contrast to these Li-site dopants, tantalum is isomorphic to niobium and replaces niobium when introduced into the crystal structure frame of LN. Tantalum can substitute niobium up to 100%. Any changes in the crystal composition will finally affect all physical properties of the crystal such as the linear dielectric response, i.e. refractive index, electro-optic coefficients and so on. It has been shown in [4] that refractive index and electro-optic coefficients depend linearly on the Ta content y in LNT crystals. Therefore one can tailor the birefringence of this mixed crystal especially for PMD compensation at higher bit rates.

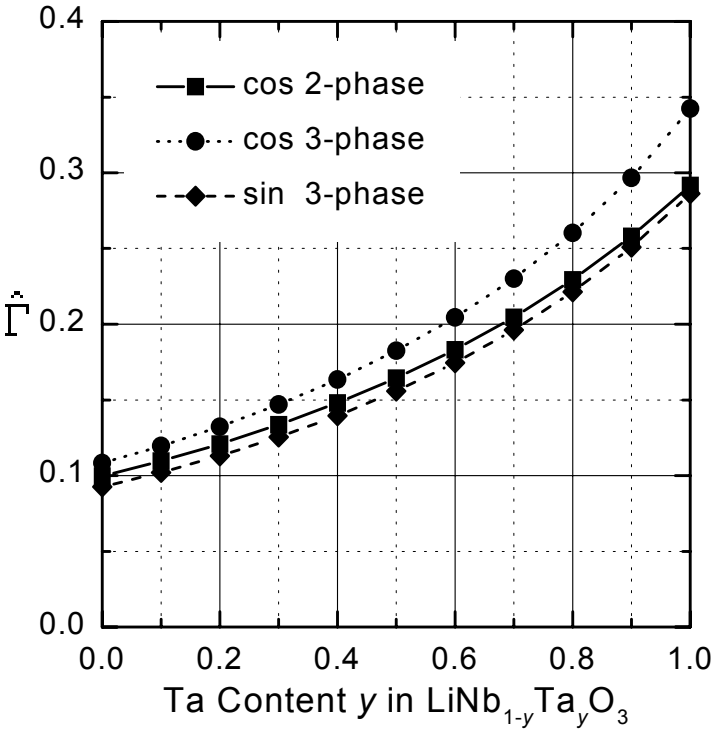


Figure 2: Weighted field overlap integral factor $\hat{\Gamma}$ as a function of Ta content y for TE-TM mode converters in lithium niobate tantalate crystals

X-cut, Y-propagation LNT

As has been mentioned in [5], the 2-phase implementation is not the only possible choice. If isolated electrodes crossings are available then 3-phase electrodes can be used with electrode widths and gaps equal to $\Lambda/6$. For further details of 3-phase electrode design the reader is referred to [6]. The ordinary refractive index n_o and the relevant electro-optic coefficient r_{51} depend linearly on the Ta content y in LNT crystals: n_o=2.2125-0.07y, and r_{51}=28-8y. Figure 2 shows the calculated optimum weighted field overlap integral factor $\hat{\Gamma}$, as defined in [7], for 2-phase as well as two representative cases of 3-phase TE-TM mode converters with interdigital electrodes. The numbers can be directly compared

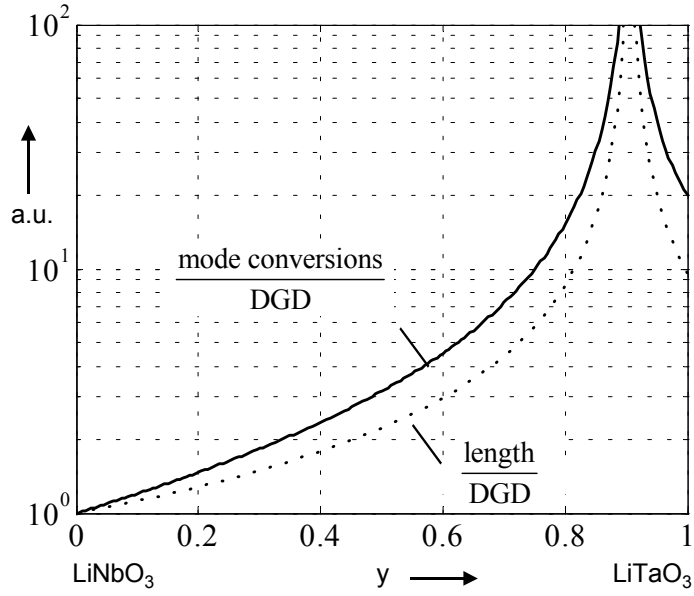


Figure 3: mode conversions/DGD and length/DGD for a TE-TM mode converter in LNT as a function of Ta content *y*.

because the 2-phase $\hat{\Gamma}$ has been halved due to the fact that the 2-phase design need at least twice the length of the 3-phase design.

Using this $\hat{\Gamma}$ and assuming 2-phase electrodes, the achievable number of full mode conversions per DGD at electric field strength near breakdown (10V/μm), and the required length per DGD have been calculated as a function of the Ta content *y* in the LNT crystals (Figure 3). Pure LN allows for ~8 full mode conversions / ps in theory if $\hat{\Gamma} = 1$, and ~0.8/ps experimentally, in agreement with theory ($\hat{\Gamma} \approx 0.1$). Pure LT allows for ~20 time more mode conversions/DGD. The length/DGD is ~4.2mm/ps in LN, and ~42mm/ps in LT. But this should not be problematic since less PMD may be expected in links for highest bit rates. LT alone should work in principle up to at least 640 Gbit/s. Appreciable advantages over pure LN with the potential of reaching 160 Gbit/s can also be expected for low *y* which may be accessible either by incorporating Ta into LN during crystal growth or later by thermal in-diffusion. An interesting situation occurs near $y = 0.9$ where the sign reversal of Δn promises Tbit/s PMD compensation. A major problem for large *y* in LNT and pure LT are the large beat lengths, which scale proportional to the length/DGD. High voltages are required to reach fields near breakdown, even for 3-phase electrodes where the gaps are smaller (~370 V in LT).

Z-cut LT

This problem is solved in *Z*-cut $LiTaO_3$. Figure 4 shows the needed electrode pattern. Several periods will form one in-phase and quadrature mode converter and several mode converters will form a distributed PMD compensator. The voltage requirements are independent of the beat length Λ because the electric field perpendicular to the waveguide, parallel to the chip surface is decisive. Small gaps of 6...10 μm gaps yield already large overlap factors but require modest voltages (110 V for 10 μm, conveniently accessibly by 300 V transistors). The gaps between neighbour electrodes may be slightly wider than those across the waveguide. This is not a problem since Λ is large. Multiphase electrodes are therefore most efficient. An advantageous example is a 4-phase design which only needs two independent voltages (Figure 4).

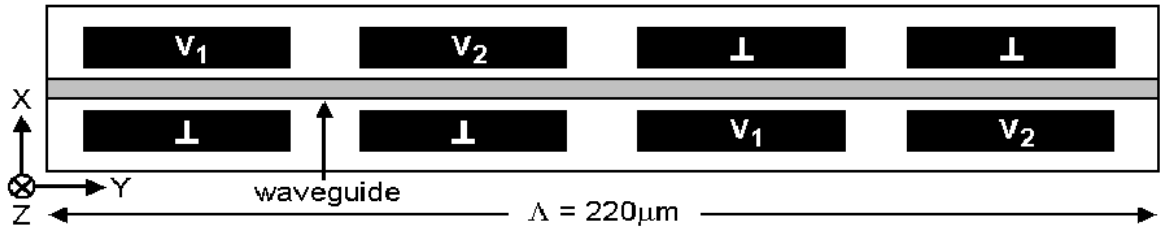


Figure 4: Electrode structure of a one period of a mode converter on Z-cut $LiTaO_3$

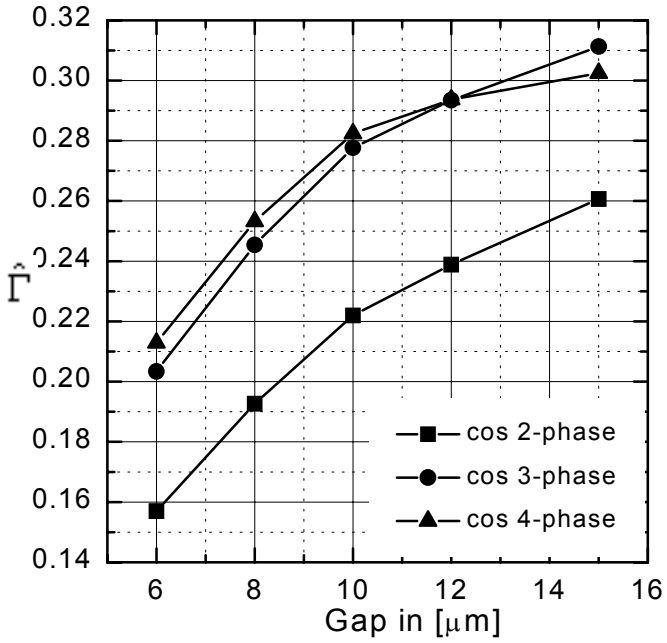


Figure 5: Weighted field overlap factor $\hat{\Gamma}$ as function of gap in μm

Figure 5 shows the weighted field overlap factor $\hat{\Gamma}$ for representative voltage patterns as function of the gap in μm. The other cases, shifted by Λ/12 for the 3-phase and by Λ/8 for the 4-phase case, behave roughly equivalent. The 4-phase outperforms the 3-phase case unless the lateral gap is so large that the compulsory longitudinal gaps consume too large a percentage of a period Λ. For a 10 μm gap, $\hat{\Gamma}$ is about the same (0.28) as for *X*-cut *Y*-propagation LT. So we may expect ~16 mode conversions/DGD, which is ~20 times more than in LN, and this should be fine for up to 640Gbit/s.

Conclusions

The birefringence Δn and the r_{51} electrooptic coefficient decrease linearly with increasing Ta content *y* in lithium niobate-tantalate crystals. A Ta content *y* of up to 0.5 is good to realize a PMD compensator for about 160 Gbit/s. *Z*-cut LT is suitable for PMD compensation up to 640 Gbit/s. In the *Z*-cut the voltage requirements are independent of the beat length, and 4-phase electrodes are attractive.

Acknowledgement

is made to Prof. W. Sohler, Prof. K. Buse, and Prof. K. Betzler for useful discussions.

References

[1] F. Heismann and R. Ulrich, *IEEE J. Quantum Electron.*, **QE-18**, 767-771, 1982.
[2] D. Sandel et al., *Proc. ECIO'99*. Turin, Italy, **PDP**, 17-19, April 14-16, 1999
[3] R. Noé et al., Electron. Lett. **35**, 652-654, 1999
[4] D. Sandel, R. Noé, *Proc. ECIO'99*. Turin, Italy, 237-240, April 14-16, 1999
[5] D. Xue, K. Betzler, H. Hesse, *Solid State Comm*., **115**, 581-585, 2000.
[6] S. Bhandare and R. Noé, *Proc. ECIO'01*, Paderborn, Germany, 172-174, 2001
[7] S. Bhandare and R. Noé, *Appl. Phys. B*, **73**, 481-483, 2001.

Optical vs. Electronic in-line Signal Processing in Optical Communication Systems : An exciting challenge for Optical Devices

Olivier Leclerc
Alcatel Research & Innovation , Route de Nozay, 91460 Marcoussis, France
Tel : +33(0)169631523 Fax: +33(0)169631865 E-mail : Olivier.Leclerc@alcatel.fr

Abstract: In this article, we recall the basic principles of Optical Regeneration in optical communication systems and review the current technology alternatives foreseen for future 40Gbit/s transmission system implementation. The alternative offered by opto-electronic regeneration is also discussed, as to identify and highlight the advantages of the all-optical approach.

Keywords: Optical Communications, Optical Regeneration, All-optical devices, Nonlinear optics, Semiconductor components, Interferometers

1. Introduction

The breakthrough of optical amplification combined with the techniques of Wavelength-Division Multiplexing (WDM) and dispersion management have made it possible to exploit a sizeable fraction of the optical fiber bandwidth (several terahertz). Systems based on 10Gbit/s per channel bit-rate and showing capacities of several terabit/s with transmission capabilities of hundreds or even thousands of kilometers have reach the commercial area.

While even greater capacities and spectral efficiencies are likely to be reached with the current technologies, there is potential economical interest in reducing the number of wavelength-channels by increasing the channel rate (e.g. 40Gbit/s). However, such fourfold increase in the channel bit rate clearly results in significant increase in propagation impairments, stemming from the combined effects of noise accumulation, fiber dispersion, fiber nonlinearities, and inter-channel interactions and contributing to two main forms of signal degradation. The first one is related to the amplitude domain; power levels of marks and spaces can suffer from random deviations arising from interaction between signal and Amplified Spontaneous Emission (ASE) noise or with signals from other channels through cross-phase modulation (XPM) from distortions induced by chromatic dispersion. The second type of signal degradations occurs in the time domain; time position of pulses can also suffer from random deviations arising from interactions between signal and ASE noise through fiber dispersion. Preservation of high power contrast between "1" and "0" and of both amplitude fluctuations and timing jitter below some acceptable levels are mandatory for high transmission quality, evaluated through Bit-Error-Rate (BER) measurements or estimated by Q-factors. Moreover, in future optical networks, it appears mandatory to ensure similar but high optical signal quality at the output of whatever nodes in the networks as to enable successful transmission of the data over arbitrary distance.

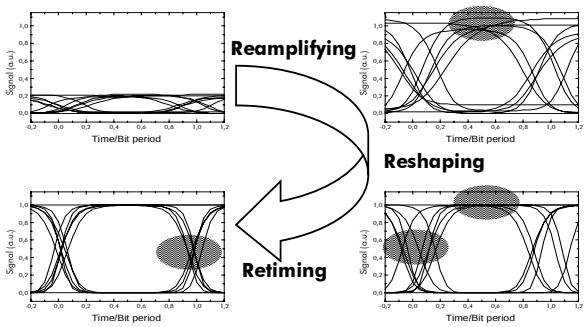


Figure 1: Principle of 3R regeneration, as applied to NRZ signals (1) Re-Amplifying (2) Re-Shaping and (3) Re-Timing. NB: Such eye diagrams can be either optical or electrical eye diagrams.

Among possible solutions to overcome such systems limitations is the implementation of Optical Signal Regeneration either in-line for long-haul transmission applications or at the output of an network nodes. Such Signal Regeneration performs or should be able to perform three basic signal-processing functions that are Re-amplifying, Re-shaping and Re-timing, hence the generic acronym "3R" (Figure 1). When Re-timing is absent, one usually refers to the regenerator as "2R" device, which has only re-amplifying and re-shaping capabilities. Full 3R regeneration with retiming capability thus requires clock extraction.

Given system impairments after some transmission distance, two solutions remain for extending the actual reach of an optical transmission system or the scalability of an optical network.. The first consists in segmenting the system into independent trunks, with full electronic repeater/transceivers at interfaces (we shall refer to this as "opto-electronic regeneration" or OEO Regeneration in the rest of this article). The second solution, ie. All-Optical Regeneration or OOO Regeneration, is not the optical version of the first which would have higher bandwidth capability but still performs the same signal-restoring functions with far reduced complexity. At this point, it should be noted that Optical 3R techniques are not necessarily void of any electronic functions (eg. when using electronic clock recovery and O/E modulation), but the main feature is that these electronic functions are narrowband (as opposed to broadband in the case of electronic regeneration).

Some key issues have to be considered when comparing such Signal Regeneration approaches. The first is the fact that today's and future optical transmission systems or /and networks are WDM networks. Under this condition, the WDM compatibility – or the fact that any Regeneration solution can simultaneously process several WDM channels- represents a key advantage. The maturity of the technology –either purely optical, hybrid optical and electronic or purely electronic- also plays an important role in the potential (pre-)development of such solutions. But the main parameter that will decide for the actual technology (and also technique) relies on the tradeoff between actual performance of the regeneration solutions and their costs (device and implementation) depending on the targeted applications (long-haul system, medium haul transport, wide area optical network, …).

In this article, we review the current alternatives for both OEO and OOO techniques for Optical Signal Regeneration, considering both theoretical and experimental performance and practical implementation issues. Key advantages and possible drawbacks of each solutions will be discussed, as to sketch the picture in this field. However, prior to doing so, we first focus on some generalities about Signal Regeneration and the way to define (and qualify) such regenerator performance. In a second part, OEO solutions will be considered and described. The third section of this paper will detail the currently-investigated optical solutions for Signal Regeneration with a specific highlight for semiconductor-based solutions using either Semiconductor Optical Amplifiers (SOA) technology or newly-developed Saturable Absorbers. Optical Regeneration techniques based on Synchronous Modulation will also be discussed in this section. The conclusion will summarize the different key features of each and every described solutions as to underline the very demanding challenge optical components are facing for this application.

2. Generalities on Signal Regeneration

2.1 Generic principle of Signal Generation

In the general case, Signal Regeneration is performed using a decision element exhibiting a nonlinear transfer function. Provided with a threshold level and when associated with an amplifier, such an element then performs the actual Re-shaping of the incoming data (either in the electrical or optical domain) and completes a 2R Signal Regenerator. Figure 2 shows the generic structure of such a Signal Regenerator in the general case as applied to NRZ data. Clock recovery block can be added (dotted lines) as to provide the decision element with time reference and hence perform the third R (Re-timing) of full Signal 3R Regeneration. At this point, it should be mentioned that the decision element can operate either on electrical signals (standard electrical DFF) provided that optical-> electrical and electrical->optical signal conversion stages are added or directly on optical signals using the different techniques described below. The clock signal can be of electrical nature as for electrical DFF in OEO regenerator or either an electrical or a purely optical signal in OOO regenerators.

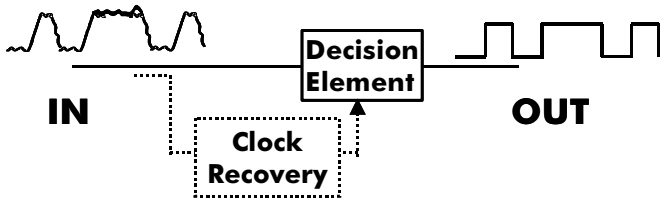


Figure 2: Generic structure of Signal 2R/3R Regenerator based on Decision Element (2R) and Decision Element and Clock Recovery (3R)

Prior to reviewing and describing the different current technology alternatives for such Optical Signal Regeneration, the issue about the actual characterization of regenerator performance need to be explained and clarified. As was previously mentioned, the core element of any Signal regenerator is the decision element showing a nonlinear transfer function that can be of different steepness. As will be seen below, the actual regenerative performance of the regenerator will indeed depend upon the degree of nonlinearity of the decision element transfer function.

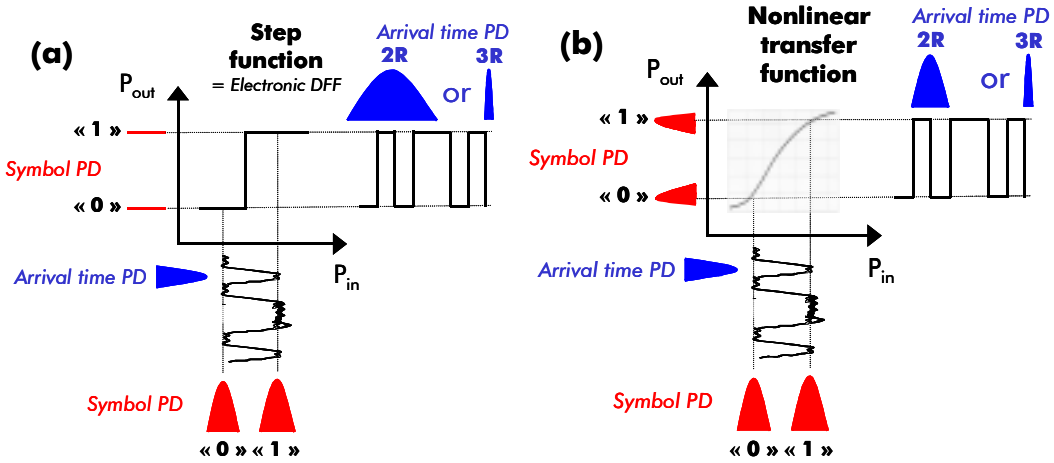


Figure 3: Signal Regeneration process using Nonlinear Gates with (a) Step transfer function (=Electronic DFF) and (b) "moderately" nonlinear transfer function. As an illustration of the Regenerator operation "1" and "0" symbols amplitude probability density (PD) and arrival time probability density (PD) are shown in red and blue, respectively.

Figure 3 shows the principle of operation of a regenerator incorporating a decision element with two different steepness of the nonlinear transfer function. In any case, the "1" and "0" symbols amplitude probability densities (PD) are squeezed after passing through the decision element. However, depending upon the addition or not of a clock reference for triggering the decision element, the symbol arrival time PD will be also squeezed (clocked decision= 3R regeneration) or enlarged (no clock reference = 2R regeneration) as a result in that case from conversion of amplitude fluctuations to time position fluctuations. As for system performance - expressed through BER- regenerative capabilities of any regenerator simultaneously depend upon both output amplitude and arrival time PD of the "1" and "0" symbols. In the peculiar case of 2R regeneration (no clocked decision), a tradeoff has then to be derived considering both the reduction of amplitude PD and the enlarged arrival time PD induced by the regenerator, as to ensure sufficient signal improvement. In Fig.3(a), we consider a step function for the transfer function of the decision element. In this case, amplitude PD are squeezed to Dirac PD after the decision element and depending upon addition or not of a clock reference, arrival time PD is reduced (3R) or dramatically enlarged (2R). In Fig.3(b), the decision element exhibit a moderately nonlinear transfer function. This results in an asymmetric and less-pronounced squeezing of the amplitude PD compared to the previous case but in turn in a significantly less enlarged arrival time PD when no clock reference is added (2R regeneration). Comparison of these two decision element of different nonlinear transfer function indicates that for 3R regeneration applications, the more nonlinear the transfer function of the decision element the better performance, the ideal case being the step function. In the case of 2R regeneration applications, a tradeoff between the actual reduction of the amplitude PD and enlargement of timing PD is to be derived and clearly depends upon the actual shape of the nonlinear transfer function of the decision element.

2.2 Qualification of Signal Regenerator performance

As to further illustrate the impact of the actual shape of the nonlinear transfer function of the decision element in 3R application, the theoretical evolution of BER with number of concatenated regenerators have been plotted for regenerators having different nonlinear responses [1]. Figure 4 shows the numerically calculated evolution of the BER of a 10Gbit/s NRZ signal with 24dB/0.1nm OSNR at the input of the first 3R regenerator as a function of the cascaded regenerator incorporating nonlinear gates with nonlinear transfer function of different depths. From Figure 4, one observes different behaviors depending on the

nonlinear function shape. As previously stated, the best regeneration performance is obtained with an ideal step function (case a), which is actually the case for OEO regenerator using electronic DFF. In that case, BER linearly increase (i.e. more errors) in the cascade. Conversely, when nonlinearity is reduced (cases (b) and (c)), both BER and noise accumulate until the concatenation of nonlinear functions is reaching some steady-state pattern, from which BER linearly increases. Concatenation of nonlinear devices thus magnifies shape differences in their nonlinear response, and hence their regenerative capabilities.

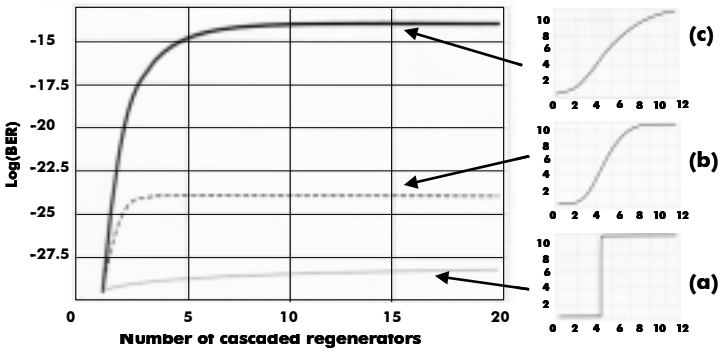


Figure 4: Evolution of the BER with concatenated regenerators for nonlinear gates with nonlinear transfer function of increasing depths from case (a) to (c) (step function).

Moreover, as can be seen in Figure 4, all curves standing for different regeneration efficiencies pass through a common point defined after the first device. This clearly indicates that it is not possible to qualify the regenerative capability of any regenerator when considering the output signal after only one regenerator. Indeed, the BER is the same for either a 3R regenerator or a mere amplifier if only measured after a single element. The origin of this comes from the initial overlap between noise distributions associated to marks and spaces, that can not be suppressed but only minimized by a single decision element through threshold adjustment.

As a general result, the actual characterization of the regenerative performance of any regenerator should *in fine* be conducted considering a cascade of regenerators. In practice this can easily be done with the experimental implementation of the regenerator under study in a recirculating loop. Moreover, such an investigation tool will also enable to assess the regenerator performance with respect to the transmission capabilities of the regenerated signal, which should not be overlooked.

Let us now consider the physical implementation of such Signal Regenerators, considering first OEO solutions and then OOO techniques along with the key features offered by the different alternatives.

3 Opto-Electronic (OEO) 2R/3R Regeneration

The generic layout of OEO Optical 2R/3R Signal Regenerator are shown in Figure 5. Figure 5a corresponds the standard structure of an OEO regenerator that could easily operate up to 10Gbit/s data-rates. The incoming optical signal is converted into the electrical domain by means of an ultrafast photodiode (bandwidth scaling with input data rate), which is then amplified in a transimpedance amplifier (TIA) before entering the actual decision element (i.e Decision Flip-Flip) operating or capable of operation at the incoming data bit-rate. The regenerated electrical data signal has then to be converted back in the optical domain, which is performed using a broadband RF power amplifier associated with an electro-optical modulator. In fact, the circuitry of OEO repeater/regenerators is broadband and its integration from the input photodiode to the output laser driver though rather complex can easily be achieved up to 10Gbit/s data rates using mature semiconductor technologies. At this point, it should be emphasized that such OEO solutions stand for the ultimate solutions for the actual best 3R regeneration performance, as a result from the step transfer function of electrical DFF (whatever bit-rates). This key advantage for 3R regeneration however turns out to be a drawback when considering lower-cost 2R regeneration applications. Such opto-electronic solutions are also wavelength flexible when associated with a tunable laser at the output. In particular the restoration of the initial signal wavelength after the regenerator can easily be implemented using a DFB laser of fixed but appropriate wavelength. Such a wavelength conversion feature actually appear of key importance when considering future but ready-to-be-developed 2.5 and 10G transparent networks. From the

principle of operation, the major (and only ?) drawback of the OEO approach would then rely on the fact that it absolutely requires a parallel, channel-by-channel implementation.

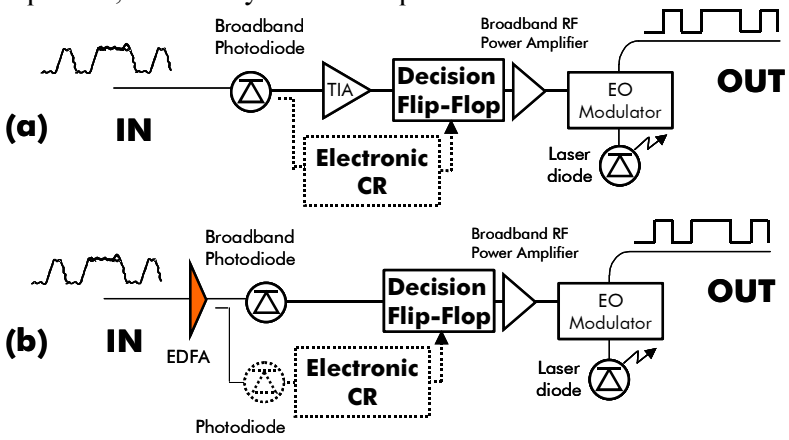


Figure 5: (a) Standard structure of OEO Signal 2R/3R Regenerator based on Decision Element (2R) and Decision Element and Clock Recovery (3R) and (b) Current (lab) implementation for 40G OEO Regenerator.

The overall picture completely changes when considering applications of such OEO structures for 40Gbit/s data rates. In this case, not only the complete integration of the OEO becomes an issue but also the actual realization of the basic key functions in the regenerator such as broadband amplifier or decision. The current (lab) version of such 40G OEO regenerator is shown in Fig.5(b). Due to the performance limitations in the entire electrical chain (poor sensitivity of DFF, inappropriate gain characteristics of TIAmplifiers) and as to circumvent these limitations, the optical signal needs to be optically pre-amplified to high power levels (typ. 10dBm) by means of a costly EDFA prior to entering the OEO regenerator. For the time being, such a technical solution enables the actual lab demonstration of such OEO 40G regenerator but clearly severely impacts on its possible implementation costs. Major technical improvements (then leading to cost improvements) are hence still required in high-speed electronics (SiGe , InP, GaAs technologies) and in opto-electronic devices ($LiNbO_3$, InP, GaAs technologies), considering first the actual performance and then the mandatory integration of the different key functions, to actually develop such an OEO approach in future 40G transmission systems.

4 All-Optical (OOO) 2R/3R Regeneration

Prior to describing the different solutions for OOO in-line Optical Signal Regeneration, it should be mentioned that since the polarization states of the optical data signals can not be preserved during propagation, it is requires that the regenerator (exhibits an extremely low polarization-sensitivity. This clearly translates in a careful optimization of all the different optical components composing the 2R/3R regenerator. It should be noted that such a remark also applies to the OEO solutions but is of limited impact since only the photodiode has to be polarization-insensitive.

4.1 Optical Regeneration using optical nonlinear gates

Figure 6 illustrates the generic principle of operation of an OOO Optical 3R Regenerator using optical nonlinear gates. Contrary to what occurs in OEO regenerator where the extracted clock signal drives electrical decision element, the incoming and distorted optical data signal triggers the nonlinear gate, hence generating a switching window which is applied to a newly-generated optical clock signal as to reproduce the initial data stream on the new optical carrier.

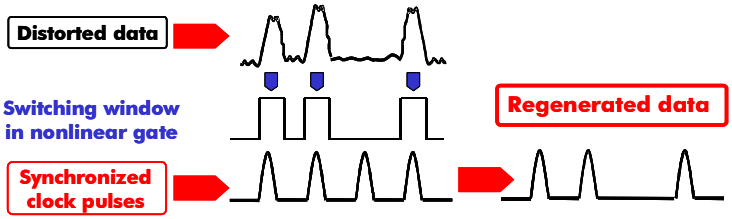


Figure 6 : Principle of operation of an OOO Optical Signal 3R Regenerator using nonlinear gates

In the case of 2R Optical Signal Regeneration, a CW signal is substituted to the synchronized optical clock pulses. As previously mentioned, the actual regeneration performance of the 2R/3R devices will mainly depend upon the nonlinearity of the transfer function of the decision element but in 3R applications the quality of the optical clock pulses has to be also considered. In the following, we describe current solutions to realize the two main building blocks of OOO Optical Signal Regenerators: the decision element (i.e nonlinear gate) and the clock recovery (CR) elements.

4.1.1 Optical Decision element

In the physical domain, optical decision elements with ideal step response –as for electrical DFF- do not exist. Different nonlinear optical transfer functions approaching more or less the ideal case can be realized in various media such as fiber, SOA, electro-absorption modulator (EAM), and laser. In the general case and as will be described below, the actual response (hence the regenerative properties of the device) of such optical gates directly depend upon the incoming signal instantaneous power. Under this condition, it appears mandatory to add an adaptation stage as to reduce intensity fluctuations (as caused by propagation or crossing routing /switching nodes and provide the decision element with fixed power conditions. In practice, this results in the addition of a control circuitry (either optical or electrical) in the Re-amplification block whose complexity directly depends on actual system environment (ultra-fast power equalization for packet-switching applications and compensation of slow power fluctuations in transmission applications).

As previously described the decision gate performs Re-shaping (and Re-timing when clock pulses are added) of the incoming distorted optical signal, and represent the regenerator's core element. Ideally, it should also act as a transmitter with characteristics ensuring the actual propagation of the regenerated data stream. In that respect, the chirp possibly induced by the optical decision gate onto the regenerated signal - and the initial quality of the optical clock pulses in 3R applications - should be carefully considered (ideally by means of loop transmission) as to adequately match line transmission requirements.

Different solutions have been proposed and extensively investigated for the actual realization of the optical decision element using for example cross gain modulation in SOA devices [2] but the most promising and flexible devices probably are interferometers, for which the generic principle of operation is the following. Consider a CW signal (probe) at λ_2 wavelength injected in an optical interferometer in which one arm incorporates a nonlinear medium in which an input signal carried by λ_1 wavelength (command) is injected. Such a signal at λ_1 wavelength induces a phase shift through cross phase modulation (XPM) in this arm of the interferometer, the amount of which depends upon power level $P_{in,\lambda 1}$. In turn, such phase modulation (PM) induces amplitude modulation (AM) on the signal at λ_2 wavelength when recombined at the output of the interferometer and translates the information carried by wavelength λ_1 onto λ_2. Under this condition, such optical gates clearly act as wavelength converter (it should be mentioned that WConversion is however not necessarily equivalent to Regeneration ; i.e a linear transfer function performs suitable WConversion but by no means Signal Regeneration)

Opical interferometers can be classified according to the nature of the nonlinearity exploited to achieve a π phase shift. In the case of fibre-based devices such as the nonlinear optical loop mirror (NOLM), the phase shift is induced through Kerr effect in an optical fibre. The key advantage of fiber-based devices such as NOLM lies in the near-instantaneous (fs) response of the Kerr nonlinearity, making them very attractive for ultra-high bit-rate operation (≥160Gbit/s). Polarization-insensitive NOLMs have been realized, although with the same drawbacks concerning integrability. A comprehensive overview of NOLM potentialities for all-optical signal processing and 3R regeneration is given in [3]. With recent development in Highly NonLinear (HNL) fibers, however, the required NOLM fiber length could be significantly reduced, hence dramatically reducing environmental instability.

A second type of device to consider is the integrated SOA-based Mach-Zehnder interferometers (MZI). In MZIs, the phase shift is due to the effect of photo-induced carrier depletion in the gain saturation regime of one of the SOAs [4]. Control and probe can be launched in counter- or co-directional ways. In the first case, no optical filter is required at the output of the device for rejecting the signal at λ_1 wavelength but operation of the MZI is limited in speed. At this point, one should mention that the photo-induced modulation effects in SOAs are intrinsically limited in speed by the gain recovery time, which is a function of the carrier

lifetime and the injection current. An approach referred to as differential operation mode (DOM), which takes advantage of the MZI's interferometric properties, makes it possible to artificially increase the operation speed of such "slow" devices up to 40Gbit/s [5-6]. Such a complex mode of operation for addressing 40G bit-rates will probably be discarded when we consider the recent demonstration of standard-mode wavelength conversion at 40Gbit/s, which uses a newly-designed active-passive SOA-MZI incorporating evanescent-coupling SOAs [7]. The device architecture is moreover flexible in the number of SOAs, thus enabling easier operation optimization and reduced power consumption, leading to simplified architectures and operation for 40Gbit/s optical 3R regeneration.

As discussed earlier, the nonlinear response is a key parameter for regeneration efficiency. Combining two interferometers is a straightforward means to improve the nonlinearity of the decision element transfer function, and hence regeneration efficiency. This approach was first validated at 20Gbit/s using a cascade of two SOA-MZI [8], see Figure 8 left. Such a scheme offers the advantage of restoring data polarity and wavelength, hence making the regenerator inherently transparent. Finally, the second conversion stage can be used as an adaptation interface to the transmission link achieved through chirp tuning in this second device [9].

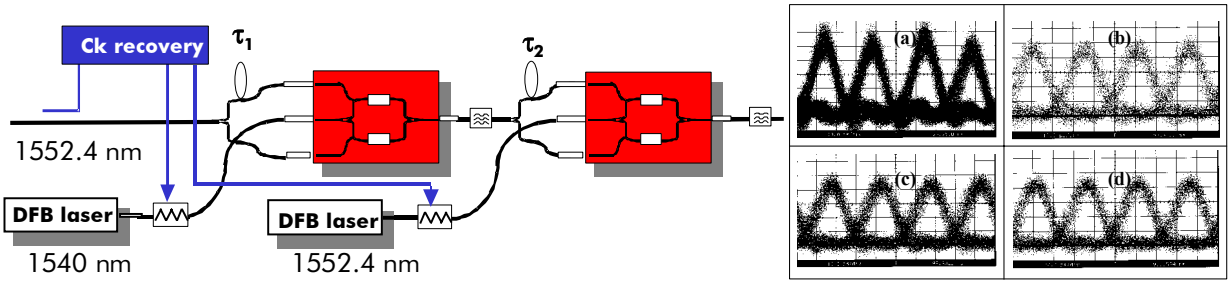


Figure 8 : (left) Optimized structure of a 40Gbit/s SOA-based 3R regenerator & (right) 40Gbit/s eye diagram evolution: (a) B-to-B, (b) 1 lap, (c) 10 laps, (d) 100 laps.

Such an Optical 3R Regenerator was upgraded to 40Gbit/s using DOM in both SOA-MZIs with validation in a 40Gbit/s loop RZ transmission [10]. The 40Gbit/s eye diagram monitored at the regenerator output after 1, 10 and 100 circulations are shown in Figure 8 (right) and are seen to remain unaltered by distance. With this OOO regenerator structure, the minimum OSNR tolerated by the regenerator (1dB sensitivity penalty at 10^{-10} BER) was found to be as low as 25dB/0.1nm. Such results clearly illustrate the high performance of this SOA-based regenerator structure for 40Gbit/s optical data signals.

Based on the same concept of wavelength conversion for Optical 3R Regeneration, it should be noted many devices have been proposed [11] and experimentally validated as wavelength converters at rates up to 84Gbit/s [12], but with cascadability issue still to be demonstrated to assess their actual regenerative properties.

4.1.2 Clock-recovery block

Next to the decision, the CR is a second key function in 3R regenerators. One possible approach for CR uses electronics while another only uses optics. The first goes with OE conversion by means of a photodiode and subsequent EO conversion through a modulator. This conversion becomes more complex and power–hungry as the data-rate increases. It is clear that the maturity of electronics gives a current advantage to this approach. But considering the pros and cons of electronic CR for cost-effective implementation, the all-optical approach seems more promising, since full regenerator integration is potentially possible with reduced power consumption. In this view, we shall focus here on the optical approach and more specifically on the self-pulsating effect in three-sections DFB lasers [13] or more recently in DBR lasers [14]. Results from [15-16] illustrate potentials of such devices for high bit rates, broad dynamic range, broad frequency tuning, polarization insensitivity, and relatively short locking times (1ns). This last feature makes these devices good candidates for operation in asynchronous-packet regime. A 40Gbit/s loop experiment made possible to assess the recovered optical clock quality and its robustness to long series of consecutive "0" in a transmission system [14]. Another loop demonstration concerned all-optical 10Gbit/s 3R regeneration, illustrating the technical feasibility of truly all-optical approaches [17].

4.2 Optical Regeneration by Saturable Absorbers

We consider next saturable absorbers (SA) as nonlinear elements for optical regeneration. Figure 9 (left) shows a typical SA transfer function and illustrates the principle of operation. When illuminated with an optical signal with peak power below some threshold (P_{sat}), the photonic absorption of the SA is high and the device is opaque to the signal (low transmittance). Above P_{sat}, the SA transmittance rapidly increases and asymptotically saturates to transparency (passive loss being overlooked). Such a nonlinear transfer function only applies to 2R optical regeneration.

Different technologies for implementing SAs are available, but the most promising approach uses semiconductors. In this case, SA relies upon the control of carrier dynamics through the material's recombination centers. Parameters such as on-off contrast (ratio of transmittance at high and low incident powers), recovery time (1/e) and saturation energy are key to device optimization. Solutions such as low-temperature-grown (LTG) strained multi-quantum wells (MQW) [18] and ion irradiation of MQW structures [19] were investigated. In the following, we consider a newly-developed ion-irradiated MQW-based device incorporated in a micro-cavity and shown on Figure 9 (right) [20]. The device operates as a reflection-mode vertical cavity, providing both a high on/off extinction ratio by canceling reflection at low intensity and a low saturation energy of 2pJ. It is also intrinsically polarization-insensitive. Heavy ion-irradiation of the SA ensures recovery times (at 1/e) shorter than 5ps (hence compatible with bit-rate above 40Gbit/s), while maintaining a dynamic contrast in excess of 2.5dB at 40GHz repetition rate.

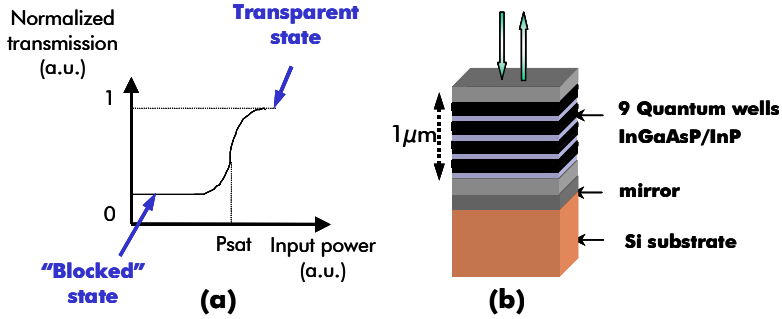


Figure 9: (a) Saturable Absorber (SA) ideal transfer function and (b) Structure of Multi-Quantum Well SA

The regenerative properties of SA make possible to reduce cumulated amplified spontaneous emission (ASE) in the "0" bits, resulting in higher contrast between mark and space, hence increasing system performance. Yet, SAs do not suppress intensity noise in the marks, which makes the regenerator incomplete. A solution for this noise suppression is optical filtering with nonlinear (soliton) pulses. The principle is as follows. In absence of chirp, the soliton temporal width scales like the reciprocal of its spectral width (Fourier-transform limit) times its intensity (fundamental soliton relation). Thus, an increase in pulse intensity corresponds to both time narrowing and spectral broadening. Conversely, a decrease in pulse intensity corresponds to time broadening and spectral narrowing. Thus, the filter causes higher loss when intensity increases, and lower loss when intensity decreases. The filter thus acts as an automatic power control (APC) in feed-forward mode, which causes power stabilization. The resulting 2R regenerator (composed by the SA and the optical filter) is fully passive, which is of high interest for submarine systems where the power consumption must be minimal, but it does not include any control in the time domain (no Re-timing).

System demonstrations of such passive SA-based Optical Regeneration have been reported in [21] with a 20Gbit/s single-channel loop experiments. Implementation of the SA-based 2R Regenerator with 160km loop periodicity made it possible to double the error-free distance (Q=15.6dB or 10^{-9} BER) of a 20Gbit/s RZ signal. As to extend the capability of passive 2R regeneration to 40Gbit/s systems, an improved configuration was derived from numerical optimization [22] and experimentally demonstrated in a 40Gbit/s WDM-like, dispersion-managed loop transmission [23], showing more than a fourfold increase in the WDM transmission distance at 10^{-4} BER (1650km without the SA-based regenerator and 7600km when implementing the 2R regenerator with 240km periodicity).

Such a result illustrates the potential high interest of such passive optical 2R regeneration in long-haul

transmission (typically in noise-limited systems) since the implementation of SA increases the system's robustness to OSNR degradation without any extra power consumption. Reducing both saturation energy and insertion loss along with increasing dynamic contrast represent key future device improvements. Regeneration of WDM signals from the same device such as one SA chip with multiple fibers [24] implemented between Mux/DMux stages should also be thoroughly investigated. In this respect, SA wavelength selectivity in quantum dots [25] could possibly be advantageously exploited.

4.3 Synchronous Modulation technique

All-optical 3R regeneration can be also achieved through in-line Synchronous Modulation (SM) associated with narrowband filtering (NF) [26]. Figure 11 shows the basic layout of such an Optical 3R Regenerator. It is composed of an optical filter followed by a Intensity and Phase Modulator (IM/PM) driven by a recovered clock. Periodic insertion of SM-based modulators along the transmission link provides efficient jitter reduction and asymptotically controls ASE noise level, resulting in virtually unlimited transmission distances [26]. Re-shaping and Re-timing provided by IM/PM intrinsically requires nonlinear (soliton) propagation in the trunk fiber following the SM block. Therefore, one can refer to the approach as distributed optical regeneration. This contrasts with lumped regeneration, where 3R is completed within the regenerator (see above with Optical Regeneration using nonlinear gates), and is independent of line transmission characteristics.

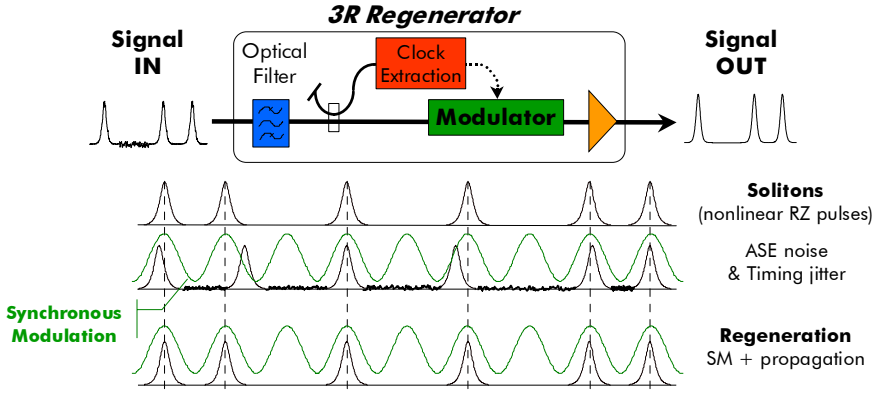


Figure 11: Basic layout of the All-Optical Regenerator by Synchronous Modulation and Narrowband Filtering and illustration of the principle of operation.

However, when using a new approach referred to "black box" optical regeneration (BBOR) [27], it is possible to make the SM regeneration function and transmission work independently in such a way that any type of RZ signals (soliton or non-soliton) can be transmitted through the system. The BBOR technique consists to include an adaptation stage for incoming RZ pulses in the SM-based regenerator, which ensures high regeneration efficiency regardless of RZ signal format (linear RZ, DM-soliton, C-RZ, etc). This is achieved using a local and periodic soliton conversion of RZ pulses by means of launching an adequate power into some length of fiber with anomalous dispersion. The actual experimental demonstration of the BBOR approach and its superiority over the "classical" SM-based scheme for DM transmission was experimentally investigated in 40Gbit/s DM loop transmission [28]. Under this condition, one can then independently exploit dispersion management (DM) techniques for increasing spectral efficiency in long-haul transmission, while ensuring high transmission quality through BBOR.

One of the key properties of the SM-based OOO Regeneration technique relies on its WDM compatibility. The first (fig.12, left) and straightforward solution to apply Signal Regeneration to WDM channels amounts to allocating a regenerator to each WDM channel after. The second consists in sharing a single modulator, thus processing the WDM channels at once in serial fashion [29]. This approach requires WDM synchronicity, meaning that all bits be synchronous with the modulation, that can be achieved either by use of appropriate time-delay lines located within a DMux/Mux apparatus (fig.12, up right), or by making the WDM channels inherently time-coincident at specific regenerator locations (fig.12, bottom right). Clearly, serial regeneration scheme is far simpler and cost-effective than the parallel version; however, optimized re-synchronization schemes still remain to be developed for realistic applications. Experimental demonstration

of this concept was assessed by means of a 4x40Gbit/s dispersion-managed transmission over 10,000km in which a single modulator was used for the simultaneous regeneration of the 4 WDM channels [30]. In this experiment asymptotic Q-factors for all 4 channels were measured greater than 14.5dB (BER<5.10^{-8}) at 10,000km distance for 2^{31}-1 coding length.

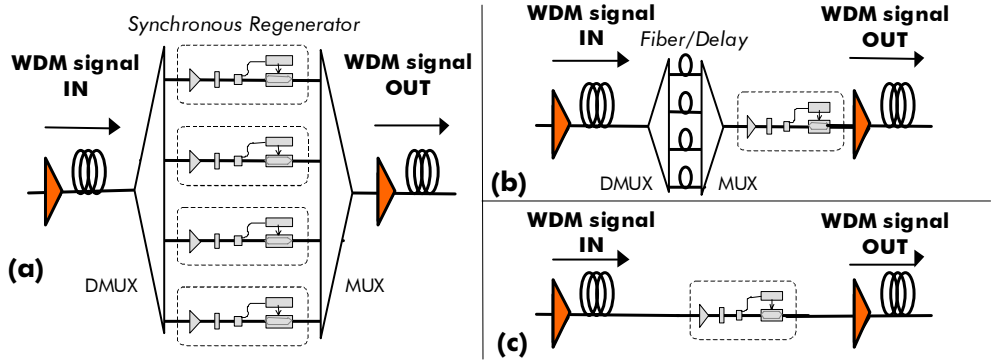


Figure 12: Basic implementation schemes for WDM all-Optical Regeneration : (a) parallel asynchronous, (b) serial re-synchronized and (c) serial self-synchronized.

Considering next OOO regeneration schemes with ultra-high speed potential, a compact and loss-free 40Gbit/s Synchronous Modulator based on optically-controlled SOA-MZI was proposed and loop–demonstrated at 40Gbit/s with an error-free transmission distance in excess of 10,000km [31]. Moreover, potential ultra-high operation of this improved BBOR scheme was recently experimentally demonstrated by means of a 80GHz clock conversion with appropriate characteristics through the SOA-MZI [32]. One should finally mention all fiber-based devices such as NOLM [3] and NALM for addressing ultra-high speed SM-based Optical Regeneration, though no successful experimental demonstrations have been reported yet in this field.

In summary, optical solutions for Signal Regeneration present many key advantages. These are the only to date to possibly ensure WDM compatibility of the regeneration function (mostly 2R related). Such optical devices clearly exhibits the best 2R regeneration performance (wrt to OEO solutions) as a result of the moderately nonlinear transfer function (which in turn can be considered as a drawback in 3R applications) but the optimum configuration is still to be clearly derived and identified depending upon the system application. Optics also allow to foresee and possibly target ultrafast applications above 40G for signal regeneration if needed. Among the current drawbacks, one should mention the relative lack of wavelength/formats flexibility of these solutions (compared to OEO solutions). It is actually complex or difficult to restore the input wavelength or address any C-band wavelength at the output of the device or to successfully regenerate modulation formats other than RZ. In that respect, investigations should be conducted as to derive new optical solutions capable of processing more advanced modulation formats at 40G. Finally, the fact that the nonlinear transfer function of the optical is in general triggered by the input signal instantaneous power also turns out to be a drawback since it requires control circuitry. The issue of cost (footprint, power consumption, …) of these solutions compared to OEO ones is still open. In that respect, purely optical solutions incorporating all-optical clock recovery, the performance of which is still to be technically assessed are of high interest for reducing costs. Complete integration of an OOO 2R/3R regenerator or parallel such regenerators onto a single semiconductor chip should also contribute to make OOO cost-attractive even though acceptable performance of such fully integrated devices is still to be demonstrated.

5 Conclusion

We have reviewed the current status of Optical Signal Regeneration technologies. A variety of solutions was described, including opto-electronic solutions and all-optical alternatives based on saturable absorbers, nonlinear interferometer/gates and synchronous modulators. Operating at 40Gbit/s or above, these solutions correspond to a vast array of possibilities, all having potential for dense/compact integration and hence reduced operational cost. While in-line Optical Regeneration clearly represents a key alternative for future progress in long-haul transmission, several technical and economical issues remain to be addressed for

practical/industrial implementation.

From the technical side, a workable solution for optical regeneration should include all aspects of system engineering, from power consumption issues to packaging issues. A 3R regenerator is in itself a subsystem, which implies a high level of reliability, with enhanced supervision and monitoring requirements. Conceptually, regenerators should accept any number of WDM channels. As mentioned in this article, OOO solutions for Optical Signal Regeneration offers a unique possibility for simultaneous regeneration of WDM channels, as opposed to the classical opto-electronic approach. However, this requires WDM channel re-synchronization and that all channels have identical transmitter clocks. These issues being eventually solved, there will remain a problem of power-handling limit for the regenerator. Considering 10G line-rates, OEO solutions for Signal Regeneration clearly have the lead over OOO solutions from either the technical performance (ultimate performance of signal regeneration) and from the cost viewpoint for 3R applications but 2R applications may offer some opportunity for OOO solutions when extremely simple solutions such as XGM-SOA are considered. When moving to 40G operation rates, no clear performance or cost advantage can be derived for either approaches, since major technological progress in either high-speed electronics or in optical components and their integration are still awaited.

From the economical side, the challenges of Optical Regeneration are not specifically different from those concerning new telecom technologies : performance enhancements are measured in $-per-wavelength and time-to-market figures. Albeit the added value of Optical Regeneration is tangible for point-point links, its merits in optical networking have still to be considered and remain to be put in perspective.

From today's status concerning the two alternative approaches for in-line regeneration (OEO or OOO), it is safe to say that the choice between either solution will be primarily dictated by both engineering and economical considerations. It will result from a tradeoff between overall system performance, system complexity and reliability, availability, time-to-market and rapid returns from the technology investment.

[1] P.Öhlén, E.Berglind, IEEE Photon. Technol. Lett., vol.9, n°7 (1997).
[2] A.D.Ellis et al., Electron. Let., vol.34, n°20 (1998)
[3] S.Bigo et al., IEEE J. Selected Topics on Quantum Electronics, Vol.3, n°5, pp.-1208-1223 (1997)
[4] T.Durhuus et al., J. of Ligthwave Technol., vol.14, n°6 (1996)
[5] S.Fischer et al., Electron. Lett., vol.35, n°23 (1999)
[6] J.Leuthold et al, Elec. Letters, Vol.38, n°16, pp.890-892 (2002)
[7] B.Dagens et al., paper PD 3.1, ECOC'02, Copenhague, Denmark, 2002
[8] B.Lavigne et al., OFC'2000, paper ThF7, Vol.4, pp.93, Baltimore, 2000
[9] P.Guerber et al., ECOC'2000, Paper 8.4.3. Vol.3, pp121, Munich, Germany, 2000.
[10] B.Lavigne et al., paper We.F.2.6, Vol.3, pp290, ECOC'2001, Amsterdam, Netherlands, 2001.
[11] T.Otani et al., We.F.2.1, ECOC'2001, Amsterdam.
[12] Y.Ueno et al. Th.F.2.1, ECOC'2001, Amsterdam.
[13] B.Sartorius etal., IEEE J. Quantum Electronics, vol. 33, n°2 (1997).
[14] Duan et al. this conference
[15] S.Bauer et al., ThM5, OFC'2002, pp478, (Anaheim), 2002
[16] C.Bornholdt et al., ECOC'99, PD 3-5, pp54, Nice France, 1999
[17] B.Lavigne et al., ECOC'99, Paper ThA2-3, Vol.2, pp262, Nice, France, 1999.
[18] R.Takahashi et al.,, Applied Physics lett., Vol.65, n°14, p1790-1792 (1994).
[19] E.Lugagne-Delpon et al., Applied Physics Lett., Vol.72, n°7, pp759-761 (1998).
[20] J.Mangeney et al., Electron. Lett., Vol.36, n°17, p1486 (2000).
[21] O.Leclerc et al., Electron. Lett., Vol.36, n°23, pp.1944 (2000).
[22] M.Matsumoto and O.Leclerc, Electron. Lett., Vol.38, n°12 p.576 (2002)
[23] D.Rouvillain et al., OFC'2002, FD11, Anaheim, 2002.
[24] A.Shen et al., ECOC'02, paper 5.4.5, Vol.2, Copenhagen, Denmark, 2002.
[25] T.Akiyama et al., ECOC'2000, Paper 9.3.6, p. 291, Munich, Germany, 2000.
[26] M.Nakazawa et al., Electron. Lett., Vol.27, n°14, pp.1270 (1991).
[27] P.Brindel et al., Electron. Lett., Vol.35, n°6, pp.480-481 (1999).
[28] B.Dany et al., Optics Lett., Vol.25, n°11, pp.793-795 (2000).
[29] E.Desurvire et al., Optics Lett., Vol.21, n°14, pp.1026-1028 (1996).
[30] O.Leclerc et al., Electronics Letters, Vol.36, n°18, pp.1574-1575 (2000).
[31] O.Leclerc et al., Paper WF6, OFC'2001, Anaheim 18-23 March (2001).
[32] O.Leclerc et al., "Optical Fiber Technologies IVA", Chapter 15, Kaminow and Li Editors, Academic Press, San Diego, 2002

Slow-wave wavelength converter

*Dipartimento di elettronica e Informazione
Politecnico di Milano, via Ponzio 34/5 , 20133 Milano, ITALY.
melloni@elet.polimi.it

Francesco Morichetti, Silvia Pietralunga, Mario Martinelli*
CORECOM, via G. Colombo 81, 20133 Milano, ITALY.
morichetti,pietralunga,martinelli@corecom.it

A novel four-wave-mixing based wavelength converter is presented. The device is based on the slow-wave propagation in a direct-coupled resonator structure, which enhances the conversion efficiency without introducing bandwidth impairments.

Keywords: guided-wave optics, periodic structures, resonators, nonlinear optics.

Introduction

Optical Wavelength Division Multiplexing (WDM) networks require devices able to efficiently shift a modulated signal from an optical carrier to another to prevent wavelength blocking and easing cross connecting. Wavelength converters based on four-wave-mixing (FWM) process offer several advantages [1], such as modulation format transparency and wide spectral response. However, as the efficiency of all-optical interactions in typical nonlinear materials is extremely low, long devices and high pump powers are required to obtain a significant converted power.

It is also well-known that the conversion efficiency may be increased by means of optical resonant structures, such as Fabry-Perot cavities or optical micro-rings, in which nonlinearities are strongly enhanced [2, 3]. However, a high-finesse cavity is required to obtain a strong nonlinear enhancement and hence an efficient wavelength conversion is feasible only on narrow-band optical signals.

On the contrary, when a series of directly coupled resonators are suitably cascaded to realize an optical Slow-Wave Structure (SWS), the enhancement given by the resonant propagation can be exploited without introducing impairments on the spectral response, which can be designed to efficiently fit wide-band channels requirements.

Properties of optical Slow-Wave Structures

An optical SWS consists of a sequence of direct-coupled resonators inserted into or coupled to an optical waveguide. It can be realized, for instance, by cascading partially reflecting elements, such as Bragg gratings, inside an optical waveguide, or by directly coupling a chain of micro-rings (Fig. 1). Even photonic crystals [4, 5] and bulk multilayers could be deployed to build up a SWS. The main property of a SWS is that wave propagation, which is allowed only within a comb of periodic passing bands, is substantially slowed down with respect to propagation in a straight waveguide. To avoid detrimental ripples in the spectral response, the high impedance of the SWS needs to be matched to that of the input-output waveguides by means of few resonators with a suitably lower finesse [6].

If a sufficiently high number of equal resonators are cascaded, an optical wave propagates through the SWS as in a periodic media. By imposing the Bloch condition on the propagating field, the dispersion relationship for a SWS results

$$cos(\beta d) = \frac{sin(kd)}{t}, \tag{1}$$

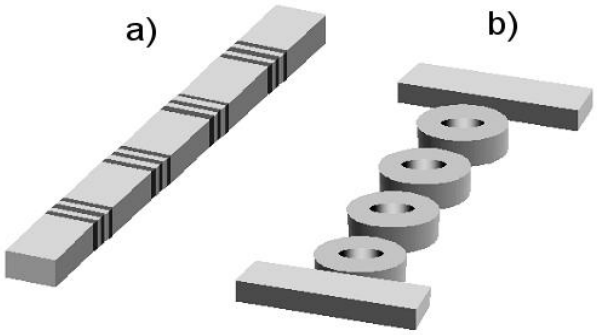


Fig. 1. Two examples of optical direct-coupled resonator SWS: the direct coupled Fabry-Perot SWS (a) and the direct coupled microring SWS (b)

where β is the propagation constant of the SWS, k is the propagation constant of the waveguide and $2d$ is the round trip of each resonator. The field coupling ratio t between two consecutive resonators is assumed wavelength independent for simplicity. From eq.(1) the bandwidth of each SWS pass-band is straightforwardly derived as

$$B = \frac{2FSR}{\pi} sin^{-1}(t), \tag{2}$$

where the Free Spectral Range, $FSR = c/2n_0d$, is the distance between two consecutive resonant frequencies, and n_0 is the waveguide effective index.

The SWS introduces a chromatic dispersion that is typically several orders of magnitude higher than material and waveguide dispersion. To the first order, the SWS-induced dispersion leads to the reduction of the optical group velocity v_g with respect to the wave velocity $v = c/n_0$ in an equivalent straight waveguide. The velocity reduction is expressed by the *slowing ratio* $S = v/v_g$, which may be directly derived from eq.(1),

$$S = \frac{cos(kd)}{\sqrt{t^2 - sin^2(kd)}}. \tag{3}$$

As shown in Fig. 2 the group velocity v_g of an infinitely long SWS assumes its maximum value $v_g(f_0) = c/n_0t$ at each resonance, then v_g drops to zero moving towards the band edges. Note as v_g may be arbitrarily reduced just by reducing the coupling ratio t, even though the bandwidth B narrows as well. At resonance the second order dispersion β_2 vanishes, so an optical pulse can propagate undistorted for several resonators.

As a consequence of the group velocity reduction, the effective length covered by the propagating field inside the SWS is enhanced by a factor proportional to S with respect to the waveguide physical length. In particular an enhancement equal to $(S+1)/2$ is found for the progressive wave, whereas $(S-1)/2$ is obtained for the regressive wave. Also the intra-cavity power is increased with respect to the input power P_{in}, as it happens inside a single optical cavity. The ratio between the power of the regressive wave P_- and the progressive wave P_+ is given by $P_-^2/P_+^2 = (S-1)/(S+1)$ and, by imposing the power conservation condition $P_+ - P_- = P_{in}$, the expressions of $P_+ = (S+1)P_{in}/2$ and $P_- = (S-1)P_{in}/2$ are straightforwardly obtained.

Thanks to these properties, SWSs can be efficiently deployed in several nonlinear applications, as shown in the following section, where the performance of a slow-wave wavelength converter are evaluated.

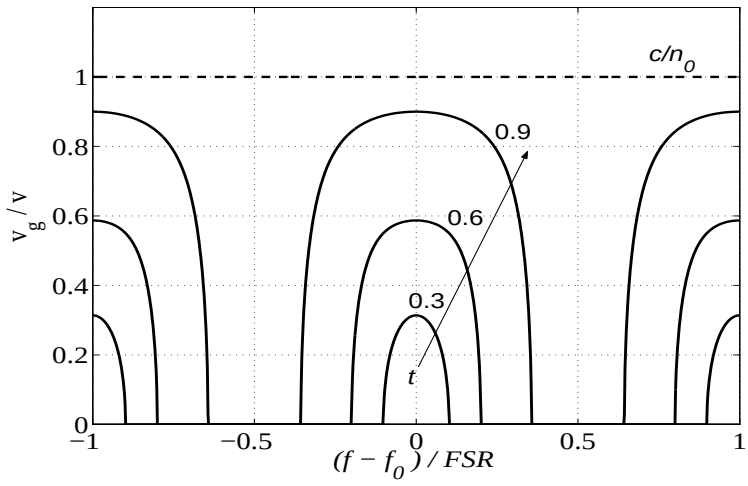


Fig. 2. The group velocity reduction of an infinitely long SWS for three different values of t.

The slow-wave wavelength converter

Let us consider an intense pump and a weak signal tuned at two different SWS resonances, respectively named f_{0p} and f_{0s}. An idler wave is generated by FWM at a third SWS resonance $f_{0c} = 2f_{0p} - f_{0s}$. The slow-wave propagation affects the conversion process by means of the two above discussed effects, that are the intra-cavity power enhancement of all the propagating fields (pump, signal and idler) and the enhancement of the effective interaction length. By introducing these enhancement terms into the expression for FWM wavelength conversion [1], the converted power P_c at the end of a SWS of length L is obtained

$$P_c(L) = \gamma^2 P_p^2 P_s L^2 \left(\frac{S^2+1}{2}\right)^2 \mathrm{sinc}^2\left(\frac{\Delta\beta L}{2}\right), \tag{4}$$

where P_p is the pump power, P_s is the signal power and γ is the well-know nonlinear constant. Eq.(4) shows that the slow-wave propagation increases the FWM based frequency generation by the fourth power of S, so that an extremely high conversion enhancement can be achieved by using SWS made of weakly coupled resonators. Since the SWS bandwidth decreases versus S, an accurate design of the device must be carried out in order to obtain a wide-band high efficiency wavelength converter.

The maximum power that can be converted by a single SWS is limited by the intra-cavity phase mismatch $\Delta\beta = \Delta k\, S$, being $\Delta k = k_s + k_c - 2k_p$ the phase mismatch in the absence of resonators. Since highly nonlinear materials are often highly dispersive, the phase mismatch Δk is mainly due to material dispersion and the second order approximation $\Delta k = \hat{\beta}_2(2\pi\Delta f)^2$ generally holds, where $\hat{\beta}_2$ is the material dispersion coefficient at the pump frequency and Δf is the frequency detuning between f_{0p} and f_{0s}. The converted power reaches its maximum value $P_{c,max}$ after $N_{max} = \pi/dS\Delta k$ cavities,

$$P_{c,max} = P_p^2 P_s \left(\frac{2\gamma}{\Delta k}\right)^2 \left(\frac{S^2+1}{2S}\right)^2, \tag{5}$$

then the power transfer starts to reverse from the converted wave to the pump wave. In eq.(5) the term in the first bracket only depends on the material parameters, whereas the term in the second bracket is related to the SWS.

The converted power can be further increased by cascading several SWS interleaved by suitable linear rephasing devices, so as to realize a *quasi-phase-matched* SWS. Fig. 3 shows the performance of a quasi-phase-matched SWS having B=20GHz, FSR=200GHz and operating a wavelength conversion over 4THz. The SWS provides an enhancement of more than 26dB with respect to an straight waveguide of the same physical length.

In conclusion, we have shown that nonlinear interactions, and specifically frequency mixing phenomena, can be highly enhanced by using waveguiding structures including one or more SWSs. The conversion enhancement is found to be proportional to the fourth power of the slowing ratio, does not implies significant bandwidth impairments and does not depend on the waveguiding material.

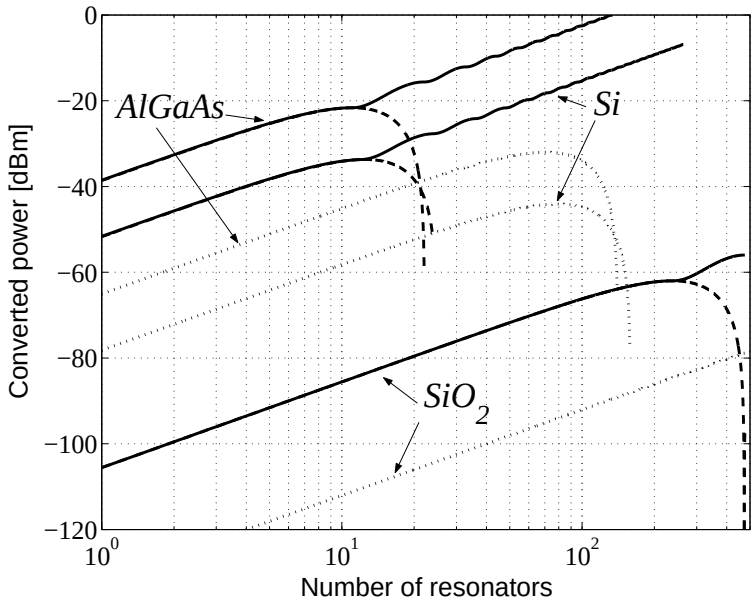


Fig. 3. Solid lines show the performance of a FWM based SWS wavelength converter (B=20 GHz, FSR=200 GHz) for three different nonlinear materials (AlGaAs, Si and SiO2). Dashed lines indicate the inversion of the power transfer from the converted wave to the pump wave in absence of rephasing at the end of the first stage. Rephasing elements are required every 11 resonators for AlGaAs, 12 for Si and 237 resonators for SiO2. Dotted lines represent the converted power in absence of resonators, 26 dB below the SWS converted power. A 100mW pump power and 10mW signal power are used.

References

[1] G. P. Agrawal, *Nonlinear Fiber Optics*, Academic Press, New York, 1999.

[2] P. P. Absil, J. V. Hrynicwicz, B. E. Little, P. S. Cho, R. A. Wilson, L. G. Joneckis, P.-T. Ho, *Opt. Lett.* **25**, 554–556, 2000.

[3] S. Jiang, M. Dagenais, *Appl. Phys. Lett.* **62**, 2757-2759, 1993.

[4] S. Mookherjea, A. Yariv, *IEEE Journal of selected topics in quantum electronics* **8**, 448–456, 2002.

[5] M. Soljacic, S. G. Johnson, S. Fan, M. Ibanescu, E. Ippen, J. D. Joannopoulos, *J. Opt. Soc. Am. B* **19**, 2052-2059, 2002 .

[6] A. Melloni, M. Martinelli, *J. Lightwave Technol* **20**, 296–303, 2002.

All-Optical Wavelength Selective Switching Exploiting the Nonlinear Phase Shift Induced by Cascaded Sum and Difference Frequency Generation (cSFG/DFG) in a Ti:PPLN Channel Waveguide

Jie Hyun Lee*, Yoo Hong Min, Werner Grundkötter, Victor Quiring, and Wolfgang Sohler
** on leave from Department of Electric Engineering, KAIST, Taejon, 305-701 KOREA*
Department of Applied Physics, University of Paderborn, D-33098 Paderborn, Germany.
sol_ym@physik.uni-paderborn.de

All-optical wavelength selective switching is demonstrated in a polarisation interferometer with a Ti:PPLN waveguide as cSFG/DFG section for nonlinear phase shift. The extinction of the signal was measured to be –19.8 dB and 76.7% was routed to the different output channel at a pump power of 1120 mW.

Keywords: all-optical switch, cascaded sum and difference frequency generation, nonlinear phase shift, Ti indiffused periodically poled lithium niobate

Introduction

The predicted growth of broadband services, has led to extensive research for high capacity systems and networks. Current efforts are concentrated on the investigation of optical time-division multiplexing (OTDM) techniques combined with wavelength-division multiplexing (WDM) in order to fully utilize the potential of the installed fibers.

All-optical switches, which can route a signal spatially, are one of the fundamental building blocks for the realization of broadband WDM/OTDM systems. Cascaded sum and difference frequency generation (cSFG/DFG) provides a challenging possibility to realize ultrafast all-optical switching operations. A large nonlinear phase shift of π can be obtained with a moderate optical pump power of less than 1W at exact phase matching for SFG. Since there is no essential time limit for operation of all-optical devices based on nonlinear parametric interactions, even THz switching can be achieved.

Recently, an all-optical gating device of a $LiNbO_3$ waveguide Mach-Zehnder interferometer with cSFG/DFG section was demonstrated by T. Suhara et al. [1]. However it showed very poor switching efficiency. G. S. Kanter et al. investigated ultrafast all-optical switching of 5 ps pulses in a proton exchanged periodically poled $LiNbO_3$ channel waveguide [2]. Since the proton exchanged $LiNbO_3$ guide only sustains TM mode, a complicated interferometer structure was used to demonstrate a switching operation based on a cSFG/DFG induced nonlinear phase shift.

In this contribution, we report the demonstrated of all-optical switching based on π-phase shift induced by cSFG/DFG. The device configuration is a polarization interferometer with a Ti-indiffused periodically poled (Ti:PPLN) channel waveguide as the core element for cSFG/DFG. Moreover, wavelength selective switching was demonstrated for the first time. Compared with the previous works, our device is very compact and easily extended to an all-optical 2×2 spatial switch.

In the following sections, experimental and numerical results of optical switch will be presented together with linear and nonlinear optical characterizations of the Ti:PPLN channel waveguide.

Ti:PPLN channel waveguide : fabrication and characterisation

A Ti:PPLN channel waveguide with a homogeneous QPM microdomain structure of 16.6 μm periodicity was fabricated following the method reported in [3]. The input side of the sample was angle polished in order to avoid multiple reflections of the sum frequency wave inside the channel; both sides were anti-reflection coated for λ=1550 nm. The width and the length of the channel waveguide are 7 μm and 92 mm, respectively. Its optical propagation loss was measured to be 0.12

dB/cm at λ=1550 nm for TM polarisation. Second harmonic generation (SHG) was investigated first to assess the waveguide quality. The phase matching wavelength is λ_{pm}=1551 nm at an operating temperature of 163.3 ^{o}C. The normalised SHG conversion efficiency was measured to be 450 %/W with a FWHM bandwidth of the conversion characteristics of $\Delta\lambda$=0.18 nm, corresponding to an effective interaction length of 53.9 mm.

Experiments & discussion

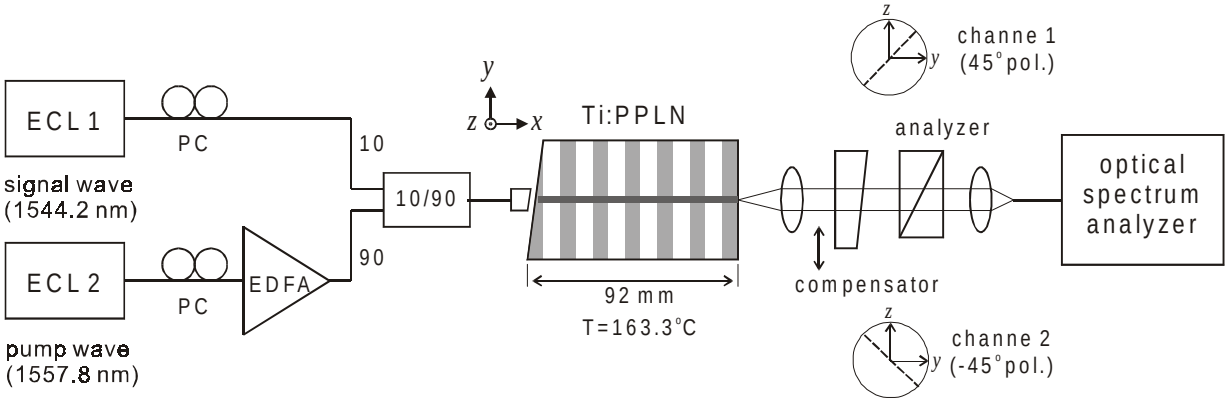


Fig. 1 : Schematic diagram of the experimental setup.

In a cSFG/DFG process in a Ti:PPLN channel waveguide three waves - signal (λ_s), pump (λ_p), and sum frequency ($1/\lambda_{sf}=1/\lambda_s+1/\lambda_p$) - interact with each other. At exact phase matching for SFG the signal is more and more depleted by SFG with increasing pump power. After complete depletion the signal is regenerated by DFG of pump and sum frequency waves accompanied by a π-phase shift. Because of the polarity of the Ti:PPLN channel waveguide, only TM polarization component experiences the nonlinear phase shift by SFG and back conversion.

Taking advantage of this polarization dependent nonlinear phase shift and adopting a configuration of a polarization interferometer an all-optical switching is demonstrated in a Ti:PPLN channel waveguide. Fig. 1 shows the schematic diagram of the experimental set up.

In order to avoid photorefractive damage effects the experiments were done at an elevated sample temperature of 163.3 ^{o}C. Two extended cavity semiconductor lasers (ECL) were used as signal and pump sources. A signal wave and an amplified pump or control wave were launched

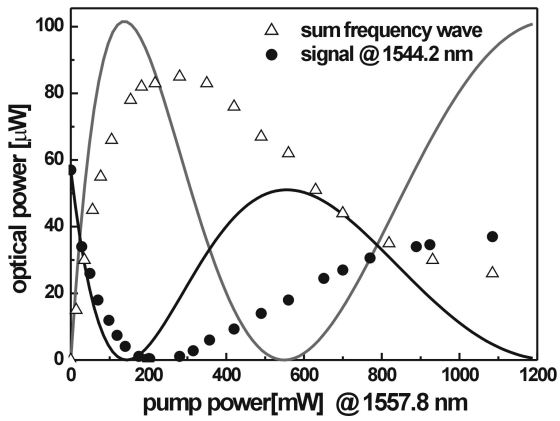


Fig. 2 : Measured and calculated signal and sum frequency output powers versus pump power.

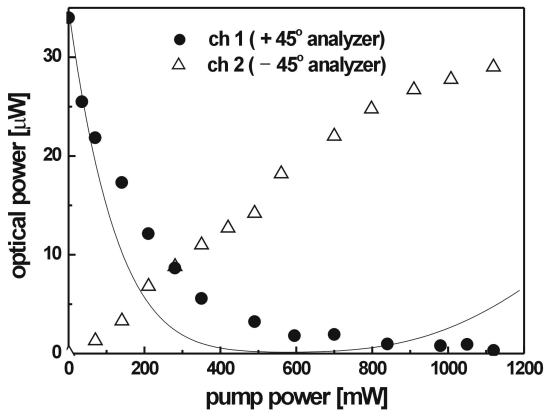


Fig. 3 : Optical output power in channel 1 and channel 2 versus pump power. Solid line gives theoretical result.

together into the Ti:PPLN channel waveguide by fiber butt coupling. The transmitted signal from the output end face was collimated by a microscope objective lens (×10) to pass through a Soleil-Babinet compensator and an analyzer (45° with respect to the waveguide surface), and finally coupled into a fiber to be monitored using an optical spectrum analyzer (OSA).

Firstly, the cSFG/DFG process was investigated when both, the signal and pump were controlled to be TM polarised. Fig. 2 shows the change of the signal and the sum frequency powers as function of a coupled pump power measured at the output facet of the channel waveguide. Full depletion (-23.1 dB extinction ratio) of the signal was achieved at a pump power of P_c=230 mW. Above P_c the signal is generated again with a π-phase shift by DFG. The discrepancy between the measured and theoretical results might be due to photorefractive damage effects, which still remained at the elevated operating temperature.

For demonstration of switching operation the pump was TM polarized; the polarization of the signal was controlled in such a way that the amplitudes of TM and TE components at the output facet became equal. The compensator controlled the relative phase shift between TM and TE components; it was adjusted in such a way to give a linear state of polarization (SOP) of the transmitted signal parallel to the direction of the analyzer. With increasing pump power, the linear polarisation of the signal gradually rotated due to the optical power change (see Fig. 2) together with the π-phase shift of the TM component. At a specific switching power of 1120 mW the signal polarisation rotated by 90° by a full restoration of the signal amplitude by DFG. Two linear polarisation states which are parallel and vertical to the transmission axis of the analyser can be considered as two different channels (channel 1, channel 2). If a polarization beam splitter is used instead of an analyser, the two ports are spatially separated.

Fig. 3 shows the operational characteristic of the all-optical switch. The signal power transmitted by the analyser in 45° and –45° directions, respectively was measured versus the pump power. With

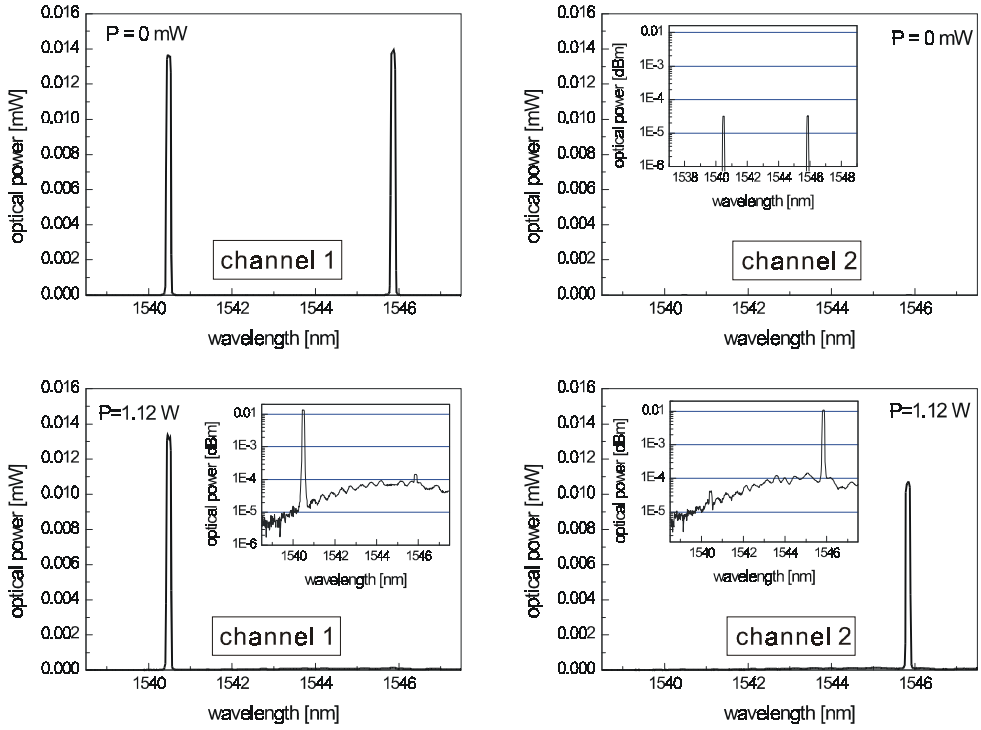


Fig. 4 : Wavelength selective switching; One signal at channel 1 is switched off and regenerated at channel 2 with a pump wavelength of λ_p=1556.2nm exactly phase matched with this signal for SFG. The spectra were measured in the resolution bandwidth of 0.2 nm.

increasing pump, the signal at channel 1 decreases while the output of channel 2 increases. The two curves intersect each other at the pump power level around 230 mW, where the TM component is completely depleted (see Fig. 2). The extinction ratio of the signal at channel 1 was –20.2 dB and 85.3 % was observed at channel 2 with a pump power of 1120 mW.

The limited acceptance bandwidth of $\Delta\lambda \leq 0.2$ nm for SFG makes it possible to realize wavelength selective switching by changing the pump wavelength. This was demonstrated experimentally. Two signals with different wavelengths of λ_{s1}=1541.64 nm and λ_{s2}=1545.88 nm and a pump were launched together into the channel waveguide (see Fig. 4). The two signals were controlled to be at channel 1 and the pump was TM-polarized. When the wavelength of the pump was tuned to meet phase matching for SFG with wavelength λ_{s2}, this signal was switched off and routed to the channel 2. At a pump power level of 1120 mW -19.8 dB depletion of the input signal was obtained and 76.7 % was observed at the channel 2. In this experiment the wavelength spacing between the two signals was set to be 4.24 nm. The lower limit of the spacing is determined by the acceptance bandwidth and the sidelobes of the SFG tuning curve. Wavelength selective optical switch with a wavelength spacing below 1 nm can be easily obtained with a Ti:PPLN channel waveguide of high quality.

Conclusions

In summary all-optical wavelength selective switching exploiting the π-phase shift induced by cSFG/DFG was demonstrated using a Ti:PPLN channel waveguide as the core element of a polarisation interferometer. One of the two input signals with different wavelengths was selectively switched off and routed by tuning the pump wavelength. At a switching pump power of 1120 mW the extinction ratio of the input signal was measured to be –19.8 dB and 76.7% of the initial signal power was routed to the different output channel. This scheme can be easily extended to an all-optical 2x2 spatial switch. Due to its ultrafast switching speed (below 1 ps) reported in Ref. 2, the all-optical switch by cSFG/DFG is very promising especially for future applications in DWDM/OTDM networks or all-optical packet switching system.

We acknowledge the support of this work within the European IST-program under the contract no.IST-2000-26005(“ROSA”).

[1] T. Suhara et al., “Integrated QPM Sum-Frequency Generation Interferometer Device for Ultrafast Optical Switching,” IEEE Photon. Technol. Lett., vol . **13**, 1203-1205 (2001).

[2] G. S. Kanter et al., “Wavelength-Selective Pulsed All-Optical Switching Based on Cascaded Second-Order Nonlinearity in a Periodically Poled Lithium-Niobate Waveguide,” IEEE Photon. Technol. Lett., vol . **13**, 341-343 (2001).

[3] G. Schreiber et al., “Efficient cascaded difference frequency conversion at 2GHz and 10GHz repetition rate in a periodically poled Ti:$LiNbO_3$ waveguide,” Appl. Phys. B, vol. **73**, 501-504 (2001)

Wavelenght conversion with Polarisation Labelling for Rejection and Isolation of Signals (POLARIS).

R. Hanfoug, J.J.G.M. van der Tol, L. M., Augustin, M. K. Smit
Opto-electronic devices group. Eindhoven University of Technology
PO-box 513, 5600 MB, Eindhoven, The Netherlands
r.hanfoug@tue.nl

VPI-simulation of a new all-optical wavelength converter is presented. It is based on interferometric effects in two Mach-Zehnder interferometers (MZI), parallel connected by polarization components (PLCs). The PLCs provide filtering between probe and control wavelengths, and polarization-insensitive operation. Different efficiency values for PLCs are taken into account. Simulation shows wide operational range (> 10 dB) for the input power. Results obtained are also suitable for cascading these devices in optical networks (extinction ration (power difference between level one and zero signal in dB) >10 dB, isolation >20 dB).

Keywords: wavelength conversion, filter free, polarization insensitive operation, VPI simulation

Introduction

For wavelength routed optical networks, a compact and monolithical integration of components for all-optical wavelength conversion is highly needed. It increases the flexibility of networks by offering a dynamic exchange of signals between different wavelengths. Interferometric wavelength converters based on cross phase modulation (XPM) by using Semiconductor Optical Amplifiers (SOA) as nonlinear elements seems to be the most promising. They are compact, stable, they give low chirp and high extinction ratio. In these configurations, SOAs are placed in the two arms of a standard Mach Zehnder interferometer (MZI).

The swapping of the wavelengths is produced by launching the new wavelength (the probe) coming from a CW laser equally in the two arms of the MZI. Simultaneously the old wavelength (the control signal) is introduced in one of the arms in such a way that a phase difference between two arms can be obtained, resulting in different interference at the output of the MZI. Co-directional coupling (the two signals propagate in the same direction) has a better performance (higher extinction ratio (ER)), larger input dynamic range) at high speed than counter-directional because the interaction time between the two signals in the SOA is longer. Also co-propagation gives higher optical signal to noise ratio compared to counter-propagation [1]. However tunable filters are needed in that case at the output of the wavelength converter to separate the control and the probe signals. These filters introduce losses and can modify the pulse form. They are difficult to integrate, they are expensive and conversion to the same wavelength is impossible. This latter option is desirable to keep full flexibility, to provide the implicit regeneration at the wavelength converter and to strip the frequency and phase noise from the signal. To circumvent external wavelength filters and have the possibility to convert to the same wavelength, a counter-propagation configuration may be used despite the limitations mentioned above.

As the signal in the network has an unknown state of polarization, polarization insensitive wavelength converters are needed. This can be achieved by using polarization insensitive SOAs. This will limit the design options for these devices [2].

In this paper we present POlarisation LAbelling for Rejection and Isolation of Signals (POLARIS). It is new co-directional polarization insensitive SOA-based wavelength converter. POLARIS allows polarization insensitivity (even when using polarization sensitive SOAs), filter-free, co-propagation wavelength conversion and conversion to the same wavelength. It uses MZIs and polarization components which can be monolithically integrated.

Concept of POLARIS

The POLARIS concept is shown in figure 1. It consists of two Mach-Zehnder interferometers (MZIs) parallel connected by polarization components. The aim of using the polarization components is to have a polarization insensitive co-propagation wavelength-converter even when using polarization sensitive SOAs, and high isolation between the two signals.

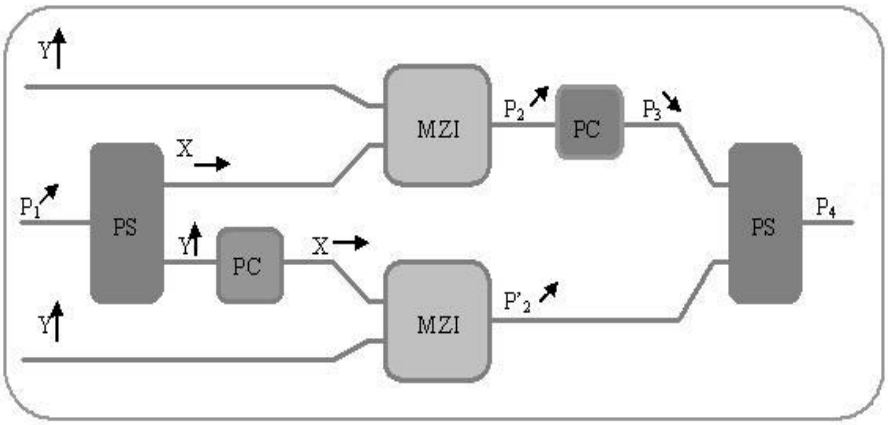


Fig. 1: POLARIS layout, MZIs provide the wavelength conversion and the polarization components ensure the polarization insensitivity and free filtering operations. PS: polarization splitter/combiner, PC: polarization converter.

In this configuration the probe coming from the CW laser is launched in two MZIs with polarization Y (e.g. TM), however the control signal coming from the network is with the other polarization X (e.g. TE). As the control signal has an arbitrary polarization a polarization splitter (PS) [3] is used to split the signal into X and Y polarizations. Then a polarization converter (PC) [4] rotates Y polarization to X polarization. In this way, the control can be dropped out by the PS at the output of POLARIS after modulating the probe in the MZIs. One of the advantage of POLARIS is that injecting the control signal in one of the MZI branches, does not require a 3 dB-coupler anymore, but can be done with a PS, thereby avoiding 3dB loss.The PS component is a 1x2 directional coupler. It is described in detail in [3]. It can be used for splitting or combining two orthogonal polarizations. For the combination function, from one of the input waveguides of the PS only X polarization is coupled to the output, from the other input waveguide only Y polarization. Hence, for combining the probe and dropping the control, a PC is introduced at the appropriate branch after the MZIs. In the case of the figure 1, a PC is introduced in the upper branch. It converts the Y polarization of the probe to the X polarization and the X polarization of the control to the Y polarization. Therefore, Y polarization of the control will be irradiated and the same thing will happen to the X polarization of the control in lower branch.

Simulation results

In the simulation study, some key parameters of the basic components are changed to find out the tolerance allowed in their fabrication. Parameters of the SOA used in the simulation are shown in table 1. The polarization components are assumed to have efficiencies of 95 % or 99 %. And excess loss of 2 dB.

In figure 2 the Bit Error Rate (BER) versus input power for different incoming polarizations is presented. It is clear from the curves that this configuration shows a wide operation range despite the change in polarization and power of the input signal. When the linewidth enhancement factor and the polarization efficiency are increased, shift of the curves to lower powers is found.

The isolation between the probe and the control signal is also studied, since the polarization components are introduced mainly to separate the two signals from each other.

Figure 3 shows the isolation versus the input power for a polarization of 45° (worst case). To reach high isolation (more than 20 dB), polarization components with 99 % efficiency and SOAs with linewidth enhancement factor of 8 are needed. The reason is that for high line width enhancement factors the control signal modulates the probe signal stronger. Furthermore, increase in the efficiency of the polarization components improves the filtering of the signals, as well as corrects the polarization for best interaction in the MZI. In the case where devices with such performance can not be obtained, devices with lower performance are studied.

Table 1 : parameters of SOA used for simulation

Injection current	250 mA
Length	500 µm
Width	2 µm
Height	80e-9 m
Confinement factor	0.25
Internal losses	40e2 m^{-1}
Differential Gain	2.78e-20 m^2
Carrier density at transparency	1.4e24 m^{-3}
Linewidth enhancement factor	**5 or 8**
Recombination constant A	1.43e8 s^{-1}
Recombination constant B	1e-16 m^3/s
Recombination constant C	3e-41 m^6/s
Initial carrier density	3e24 m^{-3}

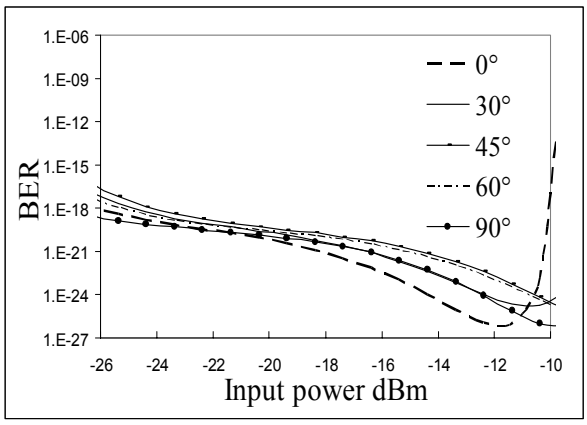


Fig. 2: BER for different polarizations of the incoming light. Results obtained for linewidth enhancement factor of 8 and polarization components efficiency of 99%

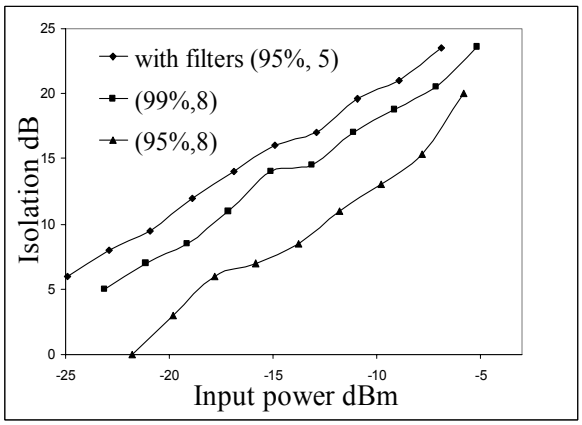


Fig. 3: Isolation between the probe and the control signal for polarization of the control signal of 45° (worst case). The data are shown for different values of the PLC efficiency and the line width enhancement factor.

In the figure 3, the upper curve is found in case of polarization components with 95 % (already achieved) and SOAs with linewidth enhancement factor of 5. For this alternative extra filters are used. These filters are nothing else than PSs. Therefore, in case of figure 1, the X polarization is filtered in the both branches before reaching the MZIs, the same thing for the Y polarization before reaching the output PS. With these filters more than 20 dB isolation is obtained for the highest input power. Of course, even higher isolation can be obtained by combing the best considered performance with extra filters.

Values more then 20 dB offer the possibility to cascade POLARIS converters in the network. Another crucial parameter for cascading these devices is the extinction ratio (ER). In figure 4, the behavior of this parameter as a function of input power, linewidth enhancement factor and polarization components efficiency is shown. The input ER was 7 dB. 2R regeneration can be obtained for input power less than -9 dBm. The upper curve in the figure 4 is obtained in case filters are added. As can be seen, better results for the ER also are achieved. therefore, well defining of the polarization seems to improve also the ER. Furthermore, ER improves also when the line width enhancement factor and the filtering increase. This is presumably because of the same reasons as mentioned before for the isolation between the wavelengths.

We also looked at the change in the output power versus the input power for different polarizations of the incoming light (Figure 5). The output power shows a weak dependence on the polarization of the incoming signal. This low variation in output power avoids the problem of the dynamic range of the functionality of these devices. The losses introduced by the polarization components contribute slightly to the variation of the output power, since the signal will see somewhat different losses according to its polarization.

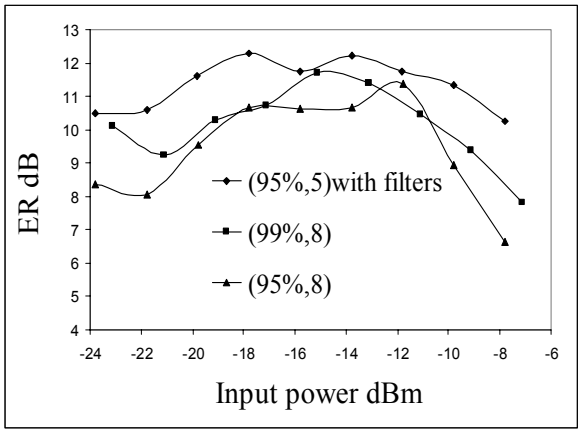


Fig. 4: Extinction ratio versus input power for polarization of the control signal of 45° (worst case).The data are shown for different values of the PLC efficiency and the line width enhancement factor .

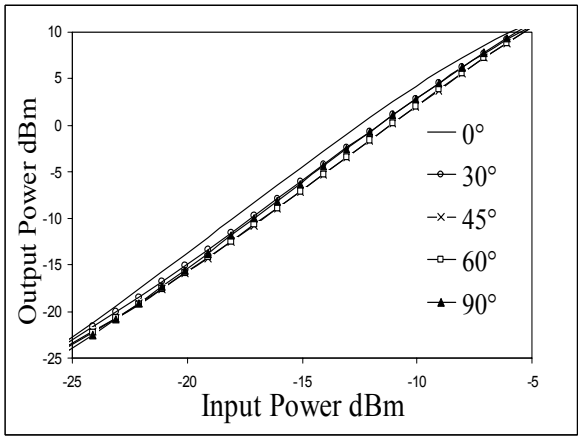


Fig. 5: Output power versus input power for different polarizations of the incoming signal (results obtained for linewidth enhancement factor of 5 and polarization efficiency of 95 % with filters)

Conclusions and discussion

As a conclusion, we studied a new configuration for a wavelength converter based on XPM in a SOA-MZI, which uses polarization components to isolate the probe and the control signals.

The configuration seems promising since it works in co-propagation and allows conversion to the same wavelength. Despite the wide range in which the BER is lower than 10^{-12}, only a narrow input power range (of around 3 dB) can be found where high ER (more than 10 dB), high isolation (more than 20 dB) and low BER can be obtained at the same time. This range is found around -11 dBm in this simulation study. And is typical for SOA-MZI wavelength converter [1,2].

The polarization components needed for an integration of this configuration on InP based materials are already fabricated in our laboratory. The structure will be developed and realized within the framework of the European project IST-STOLAS. The European commission is acknowledged for financing the project.

References

[1] C. Joergensen, S. L. Danielsen, K. E. Stubkjaer, M. Schilling, K. Daub, P. Doussiere, F. Pommerau, P. B. Hansen, H. N. Poulsen, A. Kloch, M. Vaa, B. Mikkelsen, E. Lach, G. Laube, W. Idler, and K. Wunstel, *IEEE Journal of selected Topics in Quantum Electronics*. **3**, 1168-1180, 1997.

[2] Juerg Leuthold, Pierre-Andre Besse, Emil Gamper, Marcus Dülk, Stefan Fischer, Georg Guekos and Hans Mechior, *Journal of Lightwave technology*. **17**, 1056-1065, 1999.

[3] J. J. G. M. van der Tol, J. W. Pedersen, E. G. Metaal, J. J. –W. Van Gaalen, Y. S. Oei, and F.H. Groen, *IEEE Photonics Technology Letters,* **9**, 209-211, 1997.

[4] Y. C. Zhu, F. H. Groen, X. J. M. Leijtens and J.J.G.M. van der Tol, *Proceedings Symposium IEEE/LEOS Benelux Chapter*. 209-212, 2001.

All-Optical 3R Regenerator Applying Compact Semiconductors for Clock Recovery and Decision

J. Slovak, C. Bornholdt, B. Sartorius, M. Möhrle, H. P. Nolting
Fraunhofer-Institut für Nachrichtentechnik, Heinrich-Hertz-Institut, Einsteinufer 37,
D-10587 Berlin, Germany
slovak@hhi.de

All-optical 3R regeneration is performed using a dc-operated self-pulsating DFB laser (0.8 mm) for optical clock recovery and an SOA (1.5 mm) for decision. The assembled regenerator uses the novel **A**lternating **D**ata **C**lock (**ADC)** scheme. An excellent regeneration performance is demonstrated at 10 Gbit/s.

Keywords: all-optical 3R regeneration, optical clock recovery, self-pulsating laser, semiconductor optical amplifier, cross gain modulation.

Introduction

All-optical 3R signal regeneration (Re-amplification, Re-timing, Re-shaping) is a key function for future transparent networks with optical cross-connects. Compact and cost effective solutions are needed because all WDM channels have to be regenerated individually. In this paper we apply a self-pulsating DFB laser for optical clock recovery and a semiconductor optical amplifier (SOA) for the decision stage. The assembled 3R regenerator, which use the novel ADC architecture /1/ offers a very advantageous combination of signal regeneration and λ-conversion. The ADC regenerator equipped with an all-optical clock is investigated for the first time.

This paper begins with an overview of the assembled 3R regenerator. Next the self-pulsating DFB laser for optical clock is presented and its locking and jitter characteristics are demonstrated. The operation of SOA as decision stage in ADC-scheme is described. Finally the regenerative performance of the complete ADC-3R regenerator is investigated.

Experimental set-up of the ADC-3R regenerator

The scheme of regenerator and experimental set-up is shown in Fig. 1. A 10 Gbit/s RZ PRBS 2^{31}-1 data signal at 1555 nm is generated and subsequently degraded. A split off part of the signal is injected into the self-pulsating laser for all-optical clock recovery. The clock emits a 10 GHz stable pulse stream at 1563 nm. Data and clock signal are delayed by half a bit, balanced in power and combined. The combined ADC-signal is injected into the SOA used for decision. A CW signal at 1548 nm is also launched into the SOA. The information of the ADC-signal is transformed by cross gain modulation (XGM) onto the CW wavelength. The CW wavelength is filtered out and the quality of the according (regenerated) signal is analysed using a sampling oscilloscope.

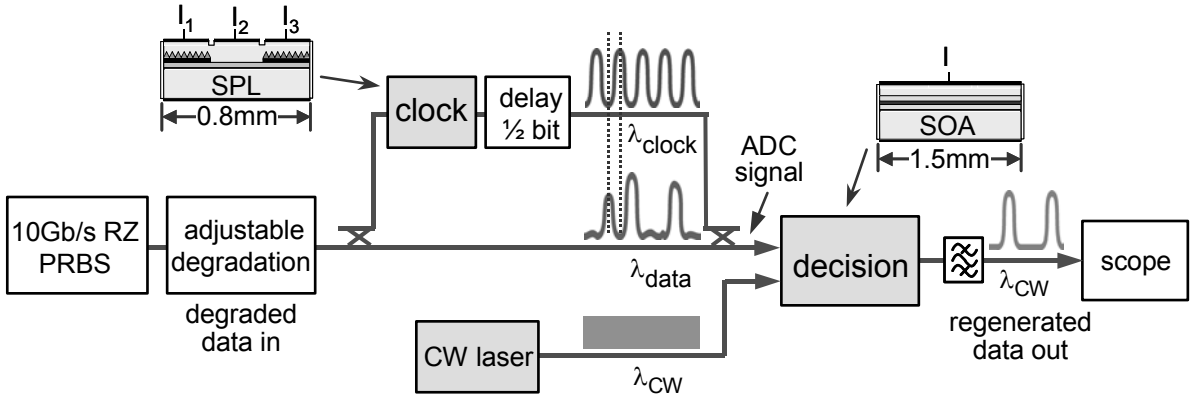


Fig. 1: Experimental set-up of the ADC-3R regenerator

Self pulsating laser for optical clock recovery

The self-pulsating laser (SPL) is a three-section InGaAsP/InP ridge waveguide device (Fig. 2a). It consists of two DFB sections (each of 250 μm length) and one integrated phase tuning section (300 μm long) /2/. The first DFB section is pumped above threshold resulting in single mode lasing operation. The second DFB section is operated close to transparency and acts as a dispersive reflector (Fig.2b). The correlation of lasing wavelength with a steep slope in the spectral reflectivity of the reflector generates self-pulsations characterised by dispersive Q-switching (DQS) /3/. Due to the chirp a rising laser pulse shifts to longer wavelengths. This leads to a decreasing feedback of the dispersive reflector. As a consequence the SPL switches itself off after emitting a short pulse and switches on again after a short time. The selection of the lasing mode and its tuning to the negative reflector slope of the stopband is done by adjusting the current in the phase section.

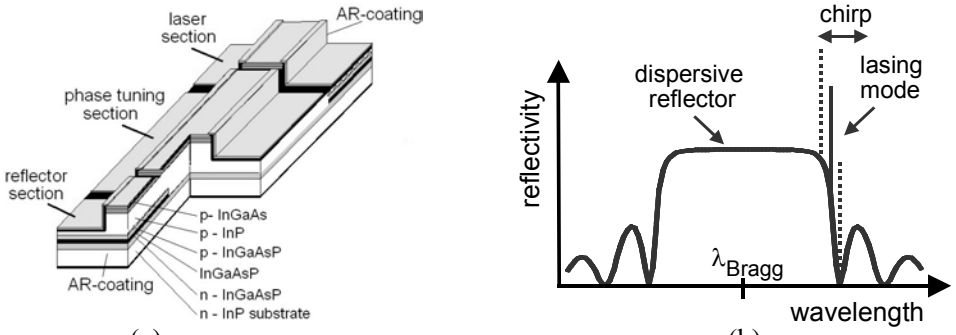


Fig. 2: Three-section self-pulsating laser (a) and the reflectivity spectrum of a DFB grating operated at transparency (b)

The repetition rate of the self-pulsations can be tuned continuously over a wide frequency range via the operating currents (2 GHz – 26 GHz). In our experiment, the frequency is adjusted close to 10 GHz (free running RF spectrum in Fig. 3b). The self-pulsation synchronises to the 10 Gbit/s RZ PRBS 2^{31}-1 data signal that is injected into the clock module (Fig 3a). Locking of the self-pulsation can be detected by a shift of the frequency to the data rate and a narrowing of the RF-line (Fig. 3b). The locking performance of the SPL is investigated using a sampling oscilloscope. Fig. 4a shows an ideal RZ data signal (upper trace, jitter: 2.8 ps), which is injected into the DQS-clock. A stable 10 GHz pulse stream (lower trace, jitter: 1.9 ps) of the extracted clock signal can be observed. Next, the data signal is strongly degraded by additional amplitude fluctuations and timing jitter (Fig. 4b upper trace, jitter: 9.1 ps). Also in this case pattern free clock pulses with significantly reduced jitter are detected on the clock output (Fig. 4b lower trace, jitter: 3.2 ps). Thus, an excellent retiming function of the DQS-clock is verified. Please note that for any regenerator the quality of the output signal is determined mainly by the quality of the clock pulses.

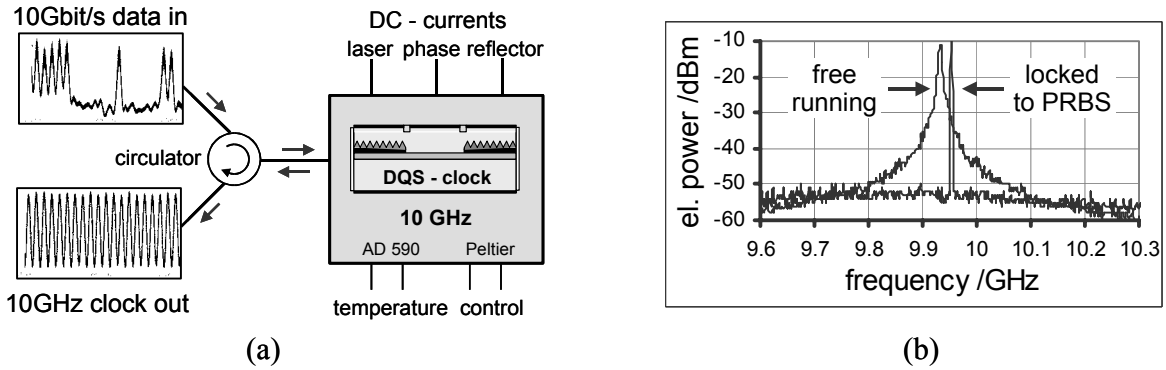


Fig. 3: Locking principle (a) and RF spectrum (b) of the self-pulsating laser

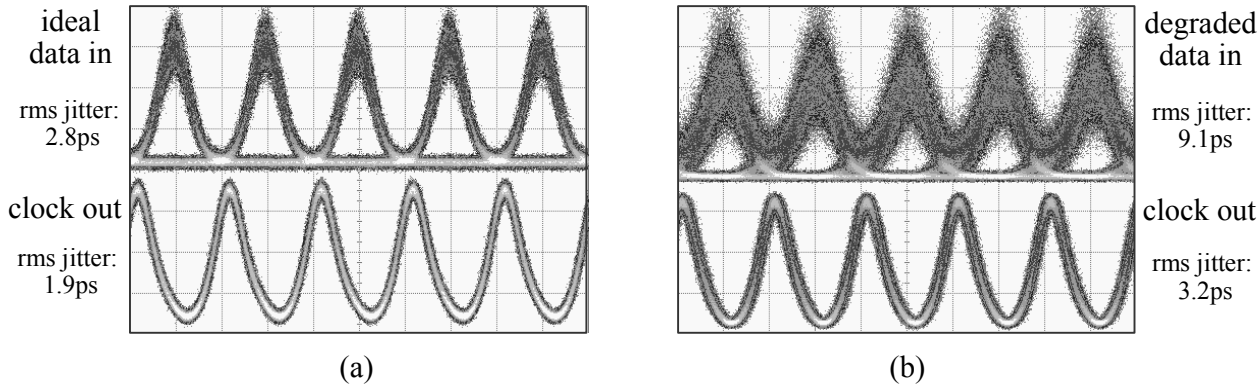


Fig. 4: 10 Gbit/s RZ PRBS ideal (a) and degraded data (b) on SPL input and the recovered clock

Wavelength converting decision using an SOA in the ADC-scheme

A 1.5 mm-long semiconductor optical amplifier (SOA) is applied for wavelength converting decision function. The SOA is polarisation insensitive with a gain peak at 1570 nm. Cross gain modulation (XGM) is used to transfer the information of the combined ADC-signal to the CW wavelength. It is well known that XGM relies on inter-band recombinations, so the modulation bandwidth is determined by the carrier dynamics /4/. Conventional XGM λ-conversion of an RZ data signal at 10 Gbit/s is thus characterised by a slow recovery time of the SOA (Fig. 5a), resulting in pattern effects and degradation of the extinction ratio.

The ADC-scheme overcomes this drawback. As mentioned above, the ADC-signal consists of a combined data and clock signal delayed by half a bit and balanced in power. The power level of the ADC signal remains constant if only "1" bits are transmitted and drops down between two adjacent clock pulses if a "0" bit is presented /1/. The resulting converted ADC signal has RZ format and is inverted in logic, the "1" bits appear as "0" and vice versa. The sharp pulses with stable amplitude demonstrate the speed improvement of the SOA by operation in the ADC scheme. The pulse shape and the timing of the new signal is determined by the clock pulses and is independent of the quality of the data signal.

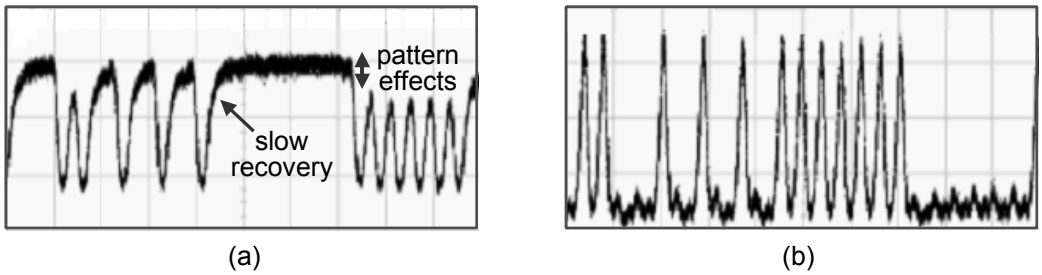


Fig. 5: Conventional XGM at 10 Gbit/s with slow recovery time (a) and XGM in ADC-scheme with enhanced speed potential (b)

Signal regeneration with ADC-3R

Finally the regenerative performance of the complete all-optical 3R regenerator is investigated by eye diagrams using a sampling oscilloscope. First an ideal 10 Gbit/s RZ signal is launched into the regenerator (Fig. 6a upper trace). The data signal on the regenerator output shows no significant difference (Fig. 6a lower trace). The timing jitter remains identical for both signals. Next a supplementary degradation unit is used to add amplitude fluctuations and timing jitter to the input data signal. The signal obtained behind this unit can be seen in Fig. 6b (upper trace). The according

output signal is shown in the lower trace of Fig. 6b. Comparing input and output in this case one can notice the significantly improved eye opening obtained by the regenerator. The amplitude and timing stability of the regenerated output pulses is only marginally affected by the strong amplitude fluctuations and the timing jitter of the degraded input signal. The excellent regenerative function, even for strongly degraded input signals, demonstrates the very good performance of our all-optical ADC-3R regenerator.

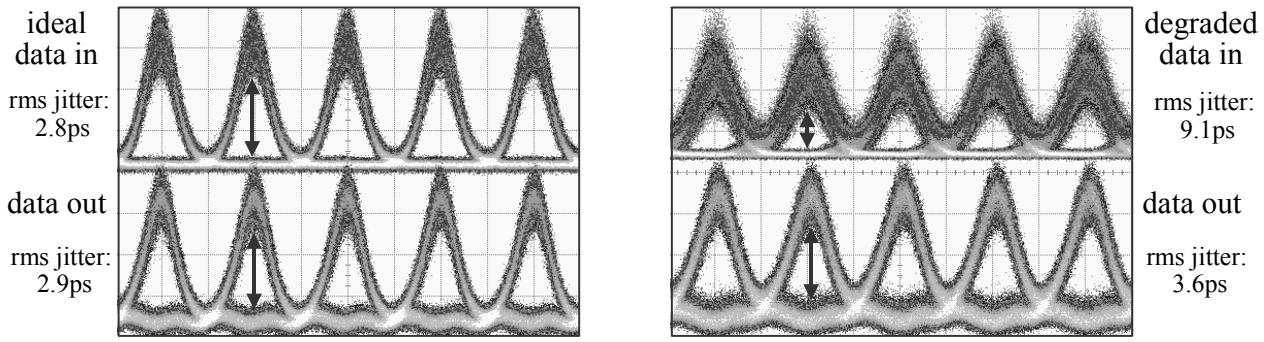


Fig. 6: 10 Gbit/s RZ PRBS ideal (a) and degraded data signal (b) on ADC-3R input and the regenerated output signal

Summary

An all-optical 3R regenerator is assembled applying compact and cost effective semiconductor devices for clock recovery and decision. The novel ADC-3R architecture equipped with an optical clock recovery is tested for the first time. The optical clock recovery is based on a self-pulsating DFB laser and delivers a low jitter pulse trace even in the case of strongly jittered input signals. The speed and performance of XGM in the SOA used for decision and wavelength conversion is significantly enhanced due to the ADC operation scheme. The performance of the complete ADC-3R regenerator is investigated at 10 Gbit/s using a sampling oscilloscope. Output pulses stable in amplitude and time and a significantly improved eye opening demonstrate the excellent function of the semiconductor based ADC-3R regenerator.

References

[1] B. Sartorius et al.: “Novel 3R Regenerator Architecture with Wavelength Flexible Output”, ECOC 2002, Copenhagen, paper No. 06.3.3, (2002).

[2] B. Sartorius et al.: “All-optical clock recovery module based on self-pulsating DFB laser”, Electronics Lett., 20th August 1998, Vol. 36, No. 17.

[3] B. Sartorius et al.: “Dispersive Self-Q-Switching in Self-Pulsating DFB Lasers”, IEEE of Quantum Electronics, Vol. 33, No. 2, February 1997.

[4] T. Durhuus et al.: “All-Optical Wavelength Conversion by Semiconductor Optical Amplifiers”, Journal of Lightwave Technology, Vol. 14, No.6, June 1996.

Novel 3R Regeneration by Light-Holding SOA's at Transparency in a Mach-Zehnder Configuration

Jyh-Tsung Hsieh and Jingshown Wu
Graduate Institute of Communication Engineering and Department of Electrical Engineering,
National Taiwan University, Taipei, Taiwan, Republic of China.
jyh_tsung@pchme.com.tw

San-Liang Lee
Department of Electronic Engineering, National Taiwan University,
Taipei, Taiwan, Republic of China.

A novel optical decision gate based on a Mach-Zehnder interferometer with light holding semiconductor optical amplifiers at transparency in each arm is proposed. Simulation results predict excellent reshaping function and adjustable decision characteristics by varying the holding light power and wavelength in both amplifiers.

Keywords: optical decision gate, reshaping, Mach-Zehnder interferometer, semiconductor optical amplifiers, decision threshold

Introduction

All-optical regeneration will be essential in future high-speed optical systems to suppress the accumulation of noise and jitter, which severely limit the network node cascadability. Several techniques for all-optical regeneration have been investigated, and some of the most promising results have been achieved with interferometric wavelength converters (IWCs). In these devices, 2R regeneration is accomplished due to the nonlinear transfer function of the converter [1]. Nevertheless, the amplitude imbalance decreases the extinction ratio of the interferometer.

Improved regeneration was proposed utilizing an interferometric structure incorporating gain-clamped SOAs (GCSOAs) as phase shifters [2,3]. However, relaxation oscillations and dark holes are present due to interaction between the internal laser light and the amplified signal via the carrier density.

A SOA configuration proposed by Dupertuis [4], called OSAT (optical speedup at transparency), uses an assist light beam injected at the transparency point of the SOA, which gives rise to very high speed operation at a current identical to that of a conventional SOA, without reducing the available gain or gain bandwidth, and without relaxation oscillations or dark holes. Here, a numerical simulation for the proposed all-optical decision gate (AODG) by incorporating two light holding SOA's at transparency into both arms of a Mach-Zehnder interferometer is conducted. We predict the excellent 2R regeneration characteristic from our novel structure.

SOA model for numerical simulation

In order that the carrier dynamics can be studied along the length of the amplifier, the SOA is segmented into a number of smaller sections. In our model, the SOA is divided into 20 longitudinal sections of equal length, and a simplified model with uniform carrier and averaged photon densities is used for each section. The ASE spectrum is divided into 32, 16-nm-wide, spectral slices. The accurate description of the spontaneous emission is essential to reveal gain saturation effects caused by ASE, that are relevant for small-signal intensity and/or high current injection.

In this work we consider the InGaAsP direct bandgap bilk-material active region, taking into account light- and heavy-hole band transitions, energy gap dependence on carrier density, and the quasi-Fermi levels are calculated according to the Nilsson approximation. The material gain g_{m_i} is given by

$$g_{m_i}(\hbar\omega) = \frac{\sqrt{2}(m_r^*)^{3/2} e^2 |M_T|^2}{3\pi n_r \varepsilon_o m_o^2 \hbar^2 c \cdot (\hbar\omega)} \cdot (\hbar\omega - E_g)^{1/2} \cdot [f_n(E_2) - f_p(E_1)]. \quad (1)$$

Electron-rate equations are then applied to each section of the cavity in stationary conditions (i.e., dN/dt =0).

$$\frac{dn_i}{dt} = \frac{I}{qwdL} - \frac{n_i}{\tau_{si}} - \sum_{k=1}^{N} \upsilon_g g_{m_{ik}} S_{av_{i,k}} - \upsilon_g g_{m_i} \cdot (S_{av_{i,sp}} + S_{av_{i-1,ASE}}) \quad (2)$$

Here, the subscript i corresponds to the different amplifier sections and k refers to the different optical input beams. n_i is the carrier density in section i; t is the time; I is the drive current; q is the electronic charge; and d, L and w are thickness, length, and width of the SOA, respectively. $\tau_{si} = (A+Bn_i+Cn_i^2)^{-1}$ is the carrier recombination lifetime in section i, $g_{m_{ik}}$ is the material gain in section i for input beam k. v_g is the group velocity, and $S_{av_{i,k}}$ presents the average photon density in segment i of the SOA cavity and for beam k. We neglect the facet reflectivity of the SOA in this paper. The ASE stimulated recombination depends on both the spatially averaged spectral density of spontaneous photons generated within the ith section and on the spatially averaged spectral density of ASE photons, generated in all sections, that enter the ith section from both sides. All parameters of the SOA are shown in Table I.

Table 1. PARAMETERS OF THE SOA

Parameters	Value
Recombination coefficient, A	2.8×10^{8} s^{-1}
Recombination coefficient, B	4.3×10^{-17} m^3s^{-1}
Recombination coefficient, C	8.0×10^{-41} m^6s^{-1}
SOA length, L	1 mm
Active layer width, w	2.5 μm
Active layer thickness, d	0.25 μm
Carrier density at transparency, n_0	1.1×10^{24} m^{-3}
Confinement factor, Γ	0.35
Internal loss, α	$(62+ \Gamma\cdot75\times10^{-24}\cdot n_i)$ cm^{-1}
Refractive index, n_{eff}	3.5
Change in refractive index with carrier density, dn/dN	-1.2×10^{-26} m^3
Carrier density at original threshold, n_{th}	3×10^{24} m^{-3}

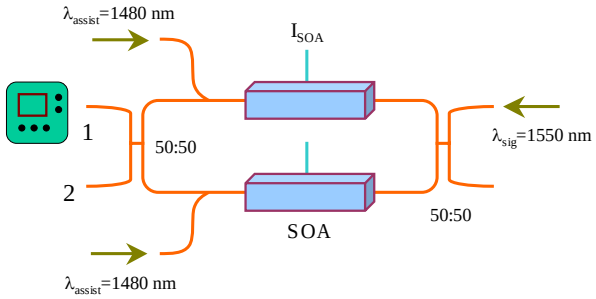


Fig. 1. Symmetrical MZI-based implementation of an optical decision gate.

The transparent condition of a SOA corresponds to the condition that the material gain of the SOA is zero for the incident wavelength. The transparent current for an assisted beam can be determined from comparing the gain-vs-current curves at a given wavelength between the presence and absence of the assisted beam. The transparency locates at the intersection of the two curves

since the gain is not changed for the presence of the assisted beam. We depict the gain curves at 1550 nm for the cases with and without a 1460-nm assisted beam. The two curves intersect at 135 mA of bias current, which corresponds to the transparent current for the 1460-nm light. The transparent current is larger for a shorter wavelength. Results also show that the assisted beam does not affect the unsaturated gain at the transparent condition and raises the saturation power by ~5dB.

Simulation results on the MZI

The regenerator has a Mach-Zehnder interferometric structure with light holding SOAs (LHSOAs) in both arms (Fig. 1). The operation of this regenerator is based on the specific property of a LHSOA that its amplification in the linear regime is independent of the holding light power. Calculated characteristics of 2 LHSOA's with different holding light powers at transparency are shown in Fig. 2. The LHSOA's are assumed to be completely identical and to have a different holding light power. They, therefore, give an identical and constant amplification and phase shift below the saturation power, but they exhibit a different saturation power. In the linear regime, both arms of the MZI give the same signal gain and a constant phase delay. If we compensate the phase delay, a completely destructive interference below the input saturation powers of both LHSOA's is obtained at the output of the MZI. As can also be seen in Fig. 3, above the saturation power of both LHSOA's, the phase difference between both arms is also constant, and the output powers from both LHSOA's are saturated, such that a constant output power is also obtained at the output of the MZI and hence a digital-like decision characteristic is achieved with the MZI regenerator. Furthermore, different decision characteristics such as output 1 levels can be obtained by varying the holding light power in both amplifiers (Fig. 3). A utilization of this function is the AGC (Automatic Gain Control) amplifier in the receiver of a fiber optic data link, whose purpose is to adjust automatically receiver gain according to received signal amplitude.

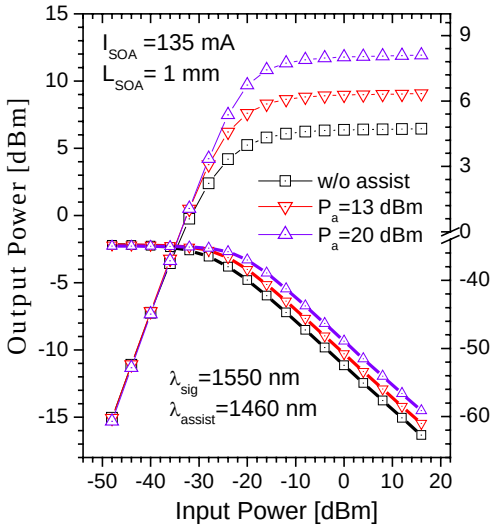


Fig. 2. Amplitude and phase characteristics of LHSOA's with different holding light powers.

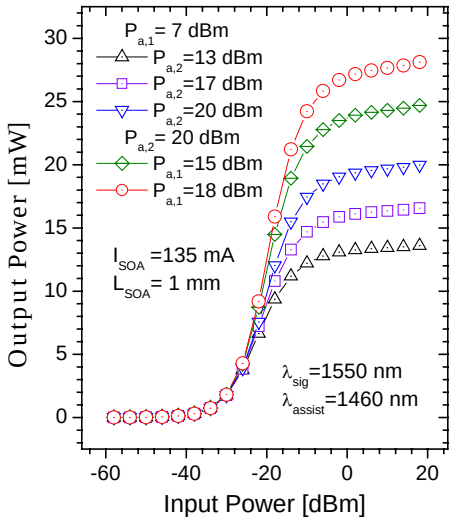


Fig. 3. Output power versus input power of a symmetric decision gate.

In general, the decision threshold is fixed and determined by the structure and, therefore, can't be modified to take into account the properties of the incoming signal. In our scheme, however, the decision threshold can alter by changing the spectrum characteristics of the assist light. Accordingly, higher injection current is set to make the waveguide transparent for the assist light shift to shorter wavelength. By doing this, the material gain will increase to cause a larger differential gain for the

signal light. A smaller input saturation power that determines the decision threshold is thus attained due to the promoted differential gain as shown in Fig. 4.

To meet the practical requirement for future all-optical 3R regeneration, a novel scheme based on the LHSOA is proposed. A clock light with constant power $P_{a,2}$ is introduced into the SOA on either arm of MZI. The data signal light is lunched into the input port of AODG. The ON/OFF of the control clock pulses stimulates the timing extraction of distorted data signal and the power determines the output 1 level of the reshaped data signal. Schematic diagram of this device and the relationship of output 1 level versus peak power of clock pulses are displayed in Fig. 5. The AODG works and 2R regeneration is evaluated for the incoming data signal only when $P_{a,2}$ is ON. Reamplification, reshaping and retiming of the distorted data signal can thus be performed via the control of clock pulses. Clearly, this novel device can represent all-optical 3R regeneration.

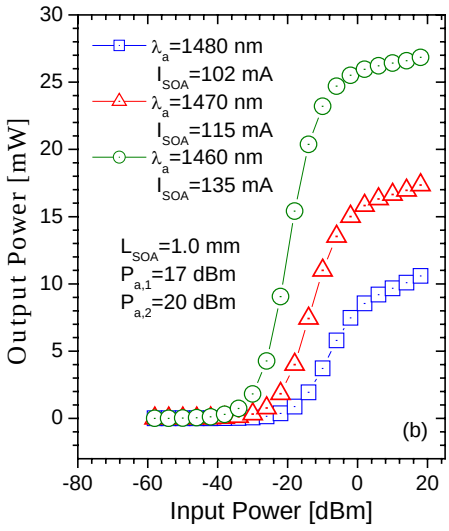


Fig. 4. Output power versus input power of a symmetric decision gate with different wavelength of assist light.

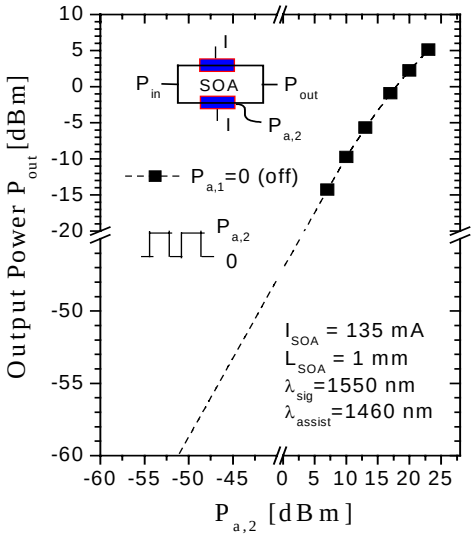


Fig. 5. Output 1 level of all-optical decision gate versus control clock light power.

Conclusions

We have reported new structures utilizing light holding SOAs at transparency to allow for all-optical 2R signal regeneration. Numerical simulations of the structures have been performed and have shown nearly ideal optical decision characteristics results. Improved gain recovery and no relaxation oscillations or dark holes could remove the speed limitation occurred in the GCSOA. Setting the waveguide transparent for the assist light in the shorter wavelength range will lead to a smaller decision threshold, which is mainly caused as a result of enhanced differential gain. Novel application is also proposed for future all-optical 3R regeneration system.

[1] D. Wolfson, B. Mikkelsen, S. L. Danielsen, H. N. Poulsen, P. B. Hansen and K. E. Stubkjaer: *Tech. Dig. OFC'98, San Jose, USA, 1998*, Paper WB3.

[2] G. Morthier, J. Sun, T. Gyselings and R. Beats, *IEEE Photon. Technol. Lett.*, 10, p.1162, 1998.

[3] G. Morthier, M. Zhao, and R. Beats, *IEEE Photon. Technol. Lett.*, 12, p.1516, 2000.

[4] M. A. Dupertuis, J. L. Pleumeekers, T. P. Hessler, P. E. Selbmann, B. Deveaud, B. Dagens, and J. Y. Emery, *IEEE Photon. Technol. Lett.*, 12, p.1453, 2000.

Integrating light and matter wave optics on Atom Chips

Jörg Schmiedmayer
Phyikalisches Institut, Universität Heidelberg, Philosophenweg 12, D-69120 Heidelberg Germany

Scientific and technological progress in the last decades has proven that miniaturization and integration are an important step towards the robust application of fundamental physics. Be it electronics and semiconductor physics in integrated circuits, or optics in micro optical devices and sensors. In this contribution i will describe our effort to achieve the same for miniaturizing and integrating matter wave optics on a chip. In our vision the Atom Chip [1] as a monolithic integrated matter wave device combining the best of two worlds: The extensive techniques of coherent quantum manipulation established in quantum optics and atomic physics with the capabilities of micro-fabrication, micro-electroncs and micro-optics to implement these processes in a very robust way. A successful implementation will allow us to establish a new experimental toolbox to study fundamental questions in mesoscopic quantum physics and may lead to wide spread applications from highly sensitive inertial sensors to quantum information technology.

Cold neutral atoms can be stored, guided and manipulated in miniaturized magnetic traps above a substrate using either microscopic patterns of permanent magnetization or micro fabricated wire structures carrying current or charge. Bose-Einstein condensates (BEC) can be loaded into such atom chip microtraps, which then serves as a coherent source of atoms. The next step is be to individually select, address, manipulate and detect single atoms and small mesoscopoic ensembles on the chip. To achieve this we work towards the integration with other quantum optics, micro optics and photonics techniques like micro lenses, waveguides, micro cavities, photonic bandgap materials.

As an example we will discuss a scheme to detect single atoms using moderate Q cavity micro cavities. Such cavity could be created for example by two wave guides on a chip or using a DBR fiber cavity with a small gap for the cold atoms. Having atoms localized to better then 100 nm ($\ll$ wavelength of light) in steep traps should allow a small gap a small waist and precise positioning of the atom for maximum coupling. Recently we could show that signal to noise ration of $> 5\sigma$ can be obtained for detection of a single atom in 10 μs using existing technology [2]. I will discuss the progress towards an experimental realization of such a detector.

This research is funded by European Union (Contract No. IST-1999-11055 ACQUIRE, Contract No. IST-2001-38863 ACQP), the DFG, and the Landesstiftung Baden-Wuerttemberg.

Keywords: matter waves, micro optics, guided wave optics, photonic crystals

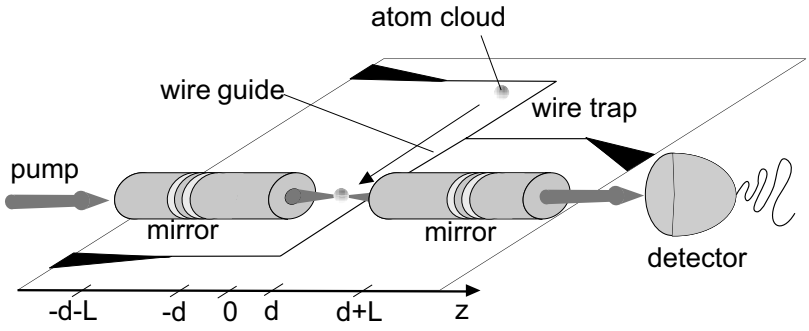


Fig. 1. Schematic presentation of the fiber cavity for atom detection on an atom chip. The atoms will be guided from the reservoir (wire trap) towards the detector along the wire guide.

[1] For a comprehensive review see: R. Folman, P. Krueger, J. Schmiedmayer, J. Denschlag, and C. Henkel, Adv. At. Mol. Opt. Phys. **48**,263 (2002).

[2] P. Horak, et. al, quant-ph/0210090, Phys. Rev. A accepted (2003).

Quantum Photonic Devices: Waveguide NLO Devices and Semiconductor Lasers for Generation of Squeezed Light and Correlated Twin Photons

Toshiaki Suhara

Department of Electronics, Graduate School of Engineering, Osaka University
2-1 Yamada-Oka, Suita, Osaka, 565-0871 Japan
suhara@ele.eng.osaka-u.ac.jp

Waveguide nonlinear-optic devices and integrated semiconductor lasers with appropriate design can perform quantum-optics functions that are potentially useful for R&D of quantum information processing. This paper reports the current status of the work of the authors group in this new subarea *"Quantum Photonic Devices"*, including theoretical background, design and fabrication of quasi-phase matched $LiNbO_3$ waveguide devices for generation of squeezed light and correlated twin photons, and high-efficiency InGaAs QW DBR lasers for generation of squeezed light.

Keywords: nonlinear optics, quantum optics, waveguide devices, semiconductor lasers, photons

1. Introduction

There has been increasing research interest in quantum information processing, including, quantum cryptography, quantum dense coding, quantum teleportation and quantum computing [1], [2]. Among various schemes, quantum optics approaches that utilize the characteristics of light as photons offer several advantages such as small decoherence problem, long range transmission of information, and availability of devices developed for conventional optical communications. Extensive theoretical and experimental studies are being made. The key quantum optic functions such as generation of photons of squeezed states, twin photons, and entangled photons can be implemented by nonlinear optic (NLO) techniques [2]. The experimental studies, however, have employed free-space optics with bulk NLO crystals and high-power gas or solid-state pump lasers.

One of the essential requirements for further development of this new area is to implement more practical and convenient devices that perform quantum optic functions. Obviously, integrated optics techniques can play an important role. The quasi-phase matched (QPM) waveguide NLO devices in combination with semiconductor lasers can offer higher engineering flexibilities to implement devices of potentially higher performances, and compact and stable structure. The possibility of integrated optic devices for squeezed light generation was addressed a decade ago [3]. Generation of pulse squeezed vacuum and squeezed light in QPM $LiNbO_3$ waveguides has been demonstrated by Serkland, et al. [4],[5]. Efficient parametric fluorescence twin photon generation in QPM $LiNbO_3$ waveguides was demonstrated by Ostrowsky et al. [6]. Kanter, et al. reported pulse squeezing in an integrated $LiNbO_3$ waveguide circuit consisting of QPM NLO (SHG and DOPA) sections, couplers, and mode filters [7].

Another important device for implementation of quantum optic functions is semiconductor laser. It has been shown by Yamamoto, et al. that squeezed (sub-Poissonic) light can be generated by driving a semiconductor laser in a constant-current driving mode with a high-impedance power source [8]-[11]. Related research work includes squeezed light generation in an external cavity semiconductor laser [12] and development of multimode semiconductor lasers specially designed for squeezed light generation [13].

Recent work of the authors group is directed to this new area of *Quantum Potonic Devices*. The work includes implementations of $LiNbO_3$ waveguide QPM NLO devices for generation of squeezed light and twin photons, and high-efficiency InGaAs QW DBR lasers for generation of squeezed light. In this paper, the author would like to summarize the basic concepts of the quantum optics, outline the theories useful for design and performance prediction of quantum photonic devices, and report the current status of the experimental work.

2. Quantum States of Optical Wave

Optical field of a mode with frequency ω is quantized by representing the amplitude by amplitude operators a and $a^\dagger$, which obey the boson commutation relation $[a,a^\dagger]=aa^\dagger-a^\dagger a=1$. The photon number operator is defined by $N=a^\dagger a$, and the Hamiltonian is given by $H=\hbar\omega(N+1/2)$.

Coherent States Although the eigenstates of N, the number states $|n\rangle$, are convenient to deal with optical transition, a single $|n\rangle$ is not appropriate to represent realistic field. A quantum state appropriate is coherent states $|\alpha\rangle$, which are eigenstates of a ($a|\alpha\rangle=\alpha|\alpha\rangle$). The time dependence of the expectation value for the field amplitude is $\langle E(t)\rangle = \mathrm{Re}\{\alpha\exp(-i\omega t)\}$, which coincides with the wave of complex amplitude α. A special case is $|\alpha\rangle$ of $\alpha=0$, which coincides with a number state $|0\rangle$, i.e., the vacuum state. Waves emitted from lasers optically pumped well above threshold are described by a coherent state. The fact that coherent states are eigenstates of a does not imply that the amplitude is certain. The field amplitude and phase do exhibit fluctuations. Fig.1 (a) and (b) illustrates the time-dependent field amplitude and fluctuation of vacuum and coherent states.

Squeezed States Squeezed states are quantum states where uncertainty of one of the conjugate quadratures is reduced by allowing increase of uncertainty of the other within the uncertainty principle. They are defined by using a generalized amplitude operator b given by

$$b=\mu a+\nu a^\dagger, \quad \mu=\cosh s, \quad \nu=\exp(+i\Psi)\sinh s \quad (s,\ \Psi: \text{real}) \tag{1}$$

where μ and ν are chosen so as to ensure the commutation relation $[b,b^\dagger]=bb^\dagger-b^\dagger b=1$. An eigenstate of b and the eigenvalue are denoted as $|\beta\rangle$ and β ($b|\beta\rangle=\beta|\beta\rangle$). The state $|\beta\rangle$ for $s=0$ coincides with a coherent state, and $|\beta\rangle$ for $s>0$ describes a squeezed state. The expectation value for the field amplitude coincides with the sinusoidal classic wave of complex amplitude $\alpha=\beta\cosh s-\beta^* e^{+i\Psi}\sinh s$. The fluctuation of the field, however, exhibits unique behavior unlike the coherent states. Fig.1 (c) and (d) illustrate the time-dependent electric field amplitude and the fluctuation of amplitude squeezed state and phase squeezed state, where amplitude and phase fluctuations, respectively, are reduced. A squeezed state of $\alpha=0$ is called squeezed vacuum.

Covariance Matrix and Squeezing Ratio To describe and analyze the quantum fluctuations, it is convenient to use a covariance matrix defined by

$$[V]=\begin{bmatrix} V_{11} & V_{12} \\ V_{21} & V_{22} \end{bmatrix}=\begin{bmatrix} \langle \Delta a \Delta a^\dagger\rangle & \langle \Delta a \Delta a\rangle \\ \langle \Delta a^\dagger \Delta a^\dagger\rangle & \langle \Delta a^\dagger \Delta a\rangle \end{bmatrix}=\left\langle \begin{bmatrix} \Delta a \\ \Delta a^\dagger \end{bmatrix}\begin{bmatrix} \Delta a \\ \Delta a^\dagger \end{bmatrix}^\dagger \right\rangle. \tag{2}$$

Then the variance of the field amplitude fluctuation can be written simply as

$$\langle \Delta E(t)^2\rangle=(1/4)S(\theta),\ \theta=-\omega t; \qquad S(\theta)=V_{11}+V_{22}+e^{+2i\theta}V_{12}+e^{-2i\theta}V_{21}. \tag{3}$$

We can symmetrize $[V]$ so that V_{11} V_{22} for simplified expressions. For coherent states $|\alpha\rangle$, from the commutation relation and the eigenvalue equation, we have symmetrized covariance matrix

$$[V]=\frac{1}{2}\begin{bmatrix} 1 & 0 \\ 0 & 1 \end{bmatrix}, \tag{4}$$

and then $S(\theta)=4\langle \Delta E(t)^2\rangle=1$. This is called standard quantum limit (SQL). The fluctuation is temporally constant as shown in Fig.1(a) and (b). For squeezed state $|\beta\rangle$ ($s>0$), $[V]$ is calculated as

$$[V]=\frac{1}{2}\begin{bmatrix} \cosh 2s & -e^{+i\psi}\sinh 2s \\ -e^{-i\psi}\sinh 2s & \cosh 2s \end{bmatrix}. \tag{5}$$

We see from (2), (3) and (5) that the magnitude of the field fluctuation is not constant but varies with time. Such fluctuations are shown in Fig.1(c) and (d).

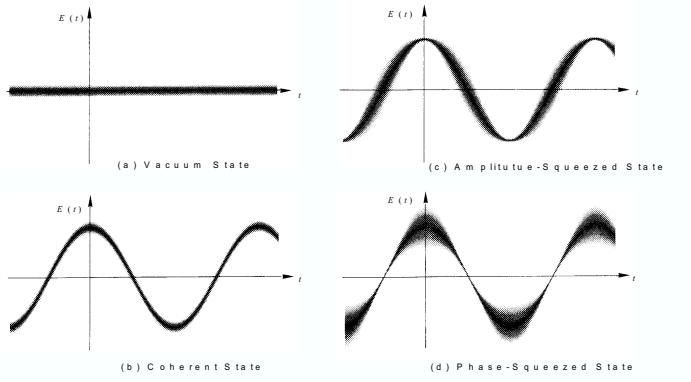


Fig.1 Illustration of field amplitude and fluctuation of optical waves in various quantum states.

Assuming $\langle\beta|a|\beta\rangle=\alpha$ is real, amplitude squeezed states and phase squeezed states are described by $\psi=0$ and $\psi=\pi$, respectively, with $s>0$.

As a simple numerical figure to describe the degree of squeezing in a form normalized by SQL, a squeezing ratio is defined by $S=\mathrm{Min}\{S(\theta)\}$. Although actually $[\boldsymbol{V}]$, $S(\theta)$ and S should be described as functions of fluctuation frequency Ω, in many cases they are nearly constant in a wide range and can be represented by the low-frequency values. Noting that $V_{12}=V_{21}^*$, from (3) we obtain

$$S=\mathrm{Min}\{S(\theta)\}=V_{11}+V_{22}-2|V_{12}|. \quad (6)$$

For squeezed states $|\beta\rangle$, from (5) and (6), S and s are correlated by $S=\exp(-2s)$.

The relative intensity noise (RIN) is represented by $\langle\Delta N^2\rangle/\langle N\rangle=S(\phi)$ ($\phi=-\arg\{\alpha\}$), which means that the intensity noise is dominated by the field fluctuation at the instant of maximum field amplitude. For coherent states the relative variance is the SQL value $\langle\Delta N^2\rangle/\langle N\rangle=1$ corresponding to the classic shot noise. For amplitude squeezed states the variance is reduced to $\langle\Delta N^2\rangle/\langle N\rangle=S$ (<1). Thus S is useful also as a measure for the intensity noise.

3. Waveguide Nonlinear-Optic Quantum Photonic Devices

Waveguide NLO devices can perform various quantum photonic functions. Fig.2 illustrates squeezed light generation by second harmonic generation (SHG) and twin photon generation by parametric fluorescence in $LiNbO_3$ quasi-phase matched (QPM) waveguides.

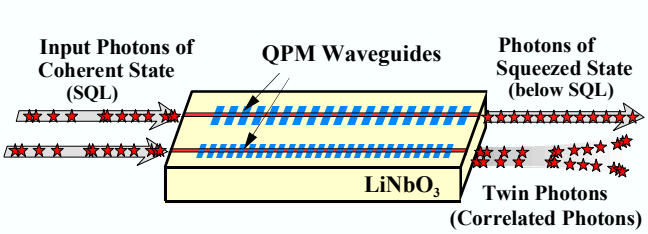


Fig.2 Illustration of quantum photonic functions of QPM waveguides.

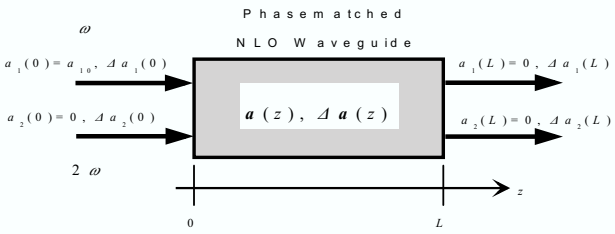


Fig.3 Schematic of traveling-wave second- harmonic generation device.

3.1 Design Theories

Squeezed Light Generation by SHG Transformation of quantum state of optical waves in second-order NLO devices can be analyzed by using a fluctuation propagation matrix [14]-[16]. Consider traveling-wave SHG ($\omega\rightarrow 2\omega$) configuration as shown in Fig.3. Assuming complete quasi-phase matching, the complex amplitudes of the pump and harmonic waves, $a_1(z)$, $a_2(z)$ normalized for quantization, satisfy the coupled-mode equations:

$$\frac{d}{dz}a_1(z)=i\kappa^* a_2(z)a_1^*(z),\quad \frac{d}{dz}a_2(z)=i(\kappa/2)\{a_1(z)\}^2. \quad (7)$$

The amplitudes are written as $a_1+\Delta a_1$, $a_2+\Delta a_2$ with operators Δa_1, Δa_2 for the fluctuations. Then we obtain linearized differential equations for Δa_1 and Δa_2

$$\frac{d}{dz}\Delta a_1(z)=i\kappa^*\{a_2(z)\Delta a_1^{\dagger}(z)+a_1^*(z)\Delta a_2(z)\},\quad \frac{d}{dz}\Delta a_2(z)=i\kappa a_1(z)\Delta a_1(z). \quad (8)$$

These equations can be written in a vector form as

$$[\Delta\boldsymbol{a}(\zeta)]=\begin{bmatrix}\Delta a_1(\zeta)\\ \Delta a_1(\zeta)^{\dagger}\\ \Delta a_2(\zeta)\\ \Delta a_2(\zeta)^{\dagger}\end{bmatrix}, \quad (9) \qquad \frac{d}{d\zeta}[\Delta\boldsymbol{a}(\zeta)]=[\boldsymbol{J}(\zeta)][\Delta\boldsymbol{a}(\zeta)]. \quad (10)$$

where $\zeta=|\kappa|a_{10}z/(2)^{1/2}$ is a normalized coordinate. The elements of $[\boldsymbol{J}]$ can be obtained by using the well-known steady state solution for SHG [17]. Since (10) is a linear differential equation, the values at the output port can be correlated with the initial values at $\zeta=0$ by a linear relation:

$$[\Delta\boldsymbol{a}(\zeta_L)]=[\boldsymbol{M}(\zeta_L)][\Delta\boldsymbol{a}(0)], \quad (11)$$

where $\zeta_L=|\kappa|a_{10}L/(2)^{1/2}$ is a normalized interaction length. The matrix $[\boldsymbol{M}]$ is a fluctuation

propagation matrix that describes the propagation of the input amplitude fluctuation through the device to the output port. The elements of [$\boldsymbol{M}$] can be calculated by using the solutions of the coupled-mode equations and the conservation of the commutation relation.

In order to analyze the fluctuations and squeezing of the pump and harmonic waves, we make an expansion of (2) to define a 4×4 covariance matrix

$$[\boldsymbol{V}] = [\boldsymbol{\Delta a}]\,[\boldsymbol{\Delta a}]^{\dagger}, \tag{12}$$

where [$\boldsymbol{\Delta a}$] is given by (9). Then squeezing ratios for the pump and harmonic waves are given by

$$S^{\omega} = V_{11} + V_{22} - 2|V_{12}|, \quad S^{2\omega} = V_{33} + V_{44} - 2|V_{34}|. \tag{13}$$

From (11) and (12), the covariance matrixes for the input and output waves are correlated by

$$[\boldsymbol{V}]_{out} = [\boldsymbol{M}][\boldsymbol{V}]_{in}[\boldsymbol{M}]^{\dagger}. \tag{14}$$

For a case where the input pump wave is a coherent state, the input fluctuation is given by

$$[\boldsymbol{V}]_{in} = \frac{1}{2}\begin{bmatrix} 1 & 0 & 0 & 0 \\ 0 & 1 & 0 & 0 \\ 0 & 0 & 1 & 0 \\ 0 & 0 & 0 & 1 \end{bmatrix}, \tag{15}$$

which describes the inevitably introduced vacuum fluctuations. A case of pumping by a squeezed light can be considered by replacing the upper left quarter of (15) by (5). The squeezing ratios for the output waves can be obtained by inserting (15) into (14) and calculating (13) for $[\boldsymbol{V}]_{out}$

Both the pump and harmonic waves are amplitude squeezed. Fig.4 shows the dependence on normalized input pump amplitude ζ_L of the squeezing ratios S^{ω}, $S^{2\omega}$. The curve indicated by η shows the SHG conversion efficiency. The curve for $S^{\omega}{}_0$ (s=0) shows the result for coherent pump input. With increasing input pump power, S^{ω} for pump wave decreases monotonously and approaches asymptotically to 0, implying that substantial squeezing takes place in the high-η region and nearly complete squeezing is obtained for ζ_L>>1. Since the SHG interaction converts the pump wave into harmonic with efficiency proportional to the pump power, the interaction acts as filtering which removes photon bunching, and therefore amplitude squeezing takes place. On the other hand, the decrease of $S^{2\omega}$ for the harmonic wave with increasing input pump power is limited down to 1/2. We also see from the curve for $S^{\omega}{}_0$<1 in Fig.4 that amplitude squeezing for the output harmonic wave is improved by using pump wave of amplitude squeezed state ($S^{\omega}{}_0$<1).

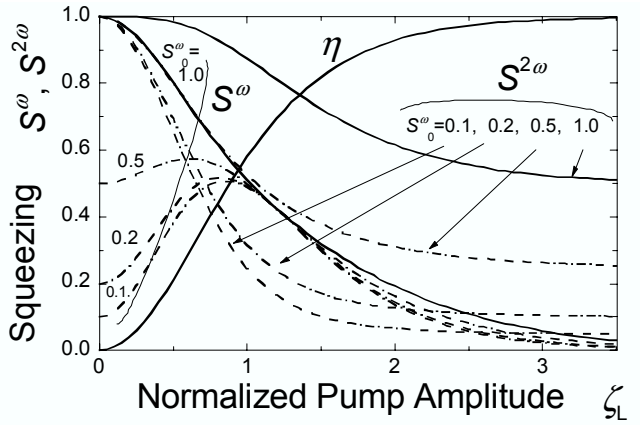


Fig.4 Fluctuation and squeezing characteristics of traveling-wave SHG device.

The above described theoretical analysis based on the fluctuation propagation matrix has been extended to degenerate optical parametric amplification (DOPA), sum frequency generation (SDG) and difference frequency generation / optical parametric amplification (DFG/OPA) [15],[16]. It has been shown that DOPA allows generation of squeezed vacuum and amplitude/phase squeezed states, and that SFG and DFG allows wavelength conversion of squeezed light.

Twin photon Generation by Parametric Fluorescence Consider a case where there is no input for signal (ω_1) and idler (ω_2) waves in (nondegenerate) OPA. Then the output amplitudes are $\langle a_1(L)\rangle$=$\langle a_2(L)\rangle$=0. However, if pumping (ω_3) is strong so that the OPA gain G=$\cosh^2\Gamma L$ (Γ: the gain factor) is large, incoherent light emission (parametric fluorescence; PF) occurs caused by the vacuum fluctuation. For phase matched OPA, the output signal/idler photon numbers are calculated as are $\langle N_1(L)\rangle$=$\langle N_2(L)\rangle$=$\sinh^2\Gamma L$; the generated photon number per mode is such that one

virtual input photon is amplified by the DFG gain $\sinh^2 \Gamma L (=G-1)$. The total PF power can be calculated by integrating the power for modes within the phase matching bandwidth to yield

$$P_1(L) = \int \frac{\hbar\omega_1}{2\pi} D(\Gamma, \Delta) d\omega_2 \cong \begin{cases} (\hbar\omega_1 c/|n_1 - n_2|L)\sinh^2 \Gamma L, & (\Gamma L << 1), \\ (\hbar\omega_1 c/|n_1 - n_2|L)\sqrt{\Gamma L/\pi}\sinh^2 \Gamma L, & (\Gamma L >> 1), \end{cases} \quad (16)$$

where $D(\Gamma,\Delta)$ is DFG gain dependent on phase mismatch Δ, and n_1, n_2 are group indexes at ω_1, ω_2. The dependence of the normalized output power $P_1/(\hbar\omega_1 c/|n_1-n_2|L)$ is plotted against normalized pump power $\Gamma^2L^2 = (\omega_1\omega_2/\omega_3^2)|K_3|^2P_3L^2$ in Fig.5. Due to the nearly exponential gain and the bandwidth broadening, the output powers increase superlinealy with increase of pump power.

PF emits equal number of ω_1 and ω_2 photons. The fluctuation of each output is above the SQL. Consider next the difference of photocurrents produced signal and idler photons, represented by $N_1(L)$-$N_2(L)$. The expectation value is $\langle N_1(L)\text{-}N_2(L)\rangle=0$, and the variance is calculated as

$$\langle [\Delta\{N_1(L) - N_2(L)\}]^2 \rangle = \langle \{N_1(L) - N_2(L)\}^2 \rangle = 0 \,. \quad (17)$$

This result implies that the differential noise is suppressed due to complete correlation between signal and idler photons. The correlated photons are called twin photons. The ω_1 and ω_2 outputs can be spatially separated by a dispersion element such as a grating. The existence of photon correlation can be interpreted in terms of the Manley-Rowe relation. The twin photons provide a unique means for detecting one-photon phenomena by using one as a signal and another as a reference, and offer many applications in in quantum information processing [2].

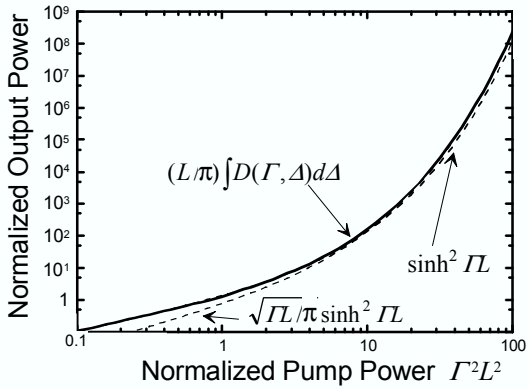


Fig.5 Dependence of parametric fluorescence output power on input pump power.

3.2 Experimental Work on $LiNbO_3$ Waveguide QPM NLO Quantum Photnic Devices

Squeezed Light Generation Device QPM SHG devices using $LiNbO_3$ waveguides with normalized conversion efficiencies over 1000%/W have been demonstrated for pumping in 800nm [18] and 1500nm bands [19]. Simple theoretical estimation using the result of Fig.4 shows that it is possible to obtain substantial squeezing of CW fundamental wave using these SHG devices and a semiconductor laser of 100mW class for pumping. Preliminary experiment has been made using the short-wave SHG device [18], an external-cavity tunable semiconductor laser of 100mW output in 830nm band for pumping, and balanced detection optics for measurement of the squeezing ratio with reference to the SQL level. The experimental setup is shown in Fig.6. The PBS and $\lambda/2$ plate are used for 1:1 beam splitting, and the + and – outputs of the RF hybrid gives the noise and SQL levels, respectively. Thus far successful result has not been obtained, because of the insufficient pump power, and excess noise and insufficient spectral purity of the pump laser.

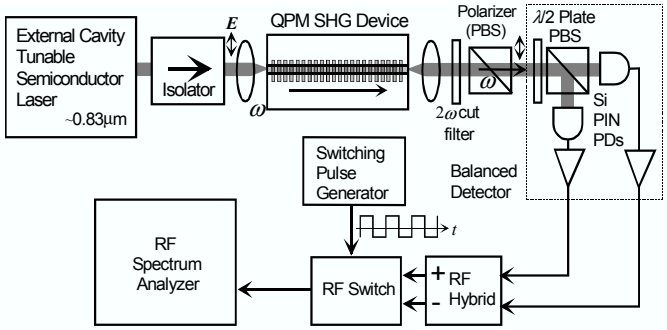


Fig.6 Experimental setup for squeezed light generation by waveguide QPM SHG. and detection.

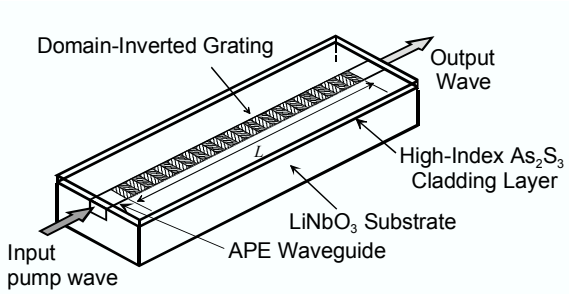


Fig.7 Waveguide QPM-SHG device using high-index As_2S_3 cladded APE $LiNbO_3$ waveguide for efficiency enhancement.

In the recent work of author's group, $LiNbO_3$ waveguides QPM-SHG devices of 30mm interaction length for pumping in 1500nm band are being fabricated, and efficiencies up to 320%/W have been obtained for the device using ordinary annealed proton exchanged (APE) waveguides. The efficiency has been improved up to 790%/W by high-index cladding on the APE waveguide as shown in Fig.7 to enhance the overlap between the pump and harmonic modes [20]. Further improvement of the efficiency is required to accomplish CW squeezed light generation with a low-power pump semiconductor laser (use of powerful Er-doped fiber amplifier involves problems related to increase of the pump noise).

Twin Photon Generation Device A $LiNbO_3$ waveguides QPM device for generation of twin photons at wavelengths in and around 1500nm band by pumping with a semiconductor laser was designed and fabricated. The period of the domain-inverted grating for QPM is 17.4μm, and the interaction length is 30mm. The QPM device was fabricated by standard domain inversion and annealed proton exchange. The measured normalized SHG (1560nm→780nm) efficiency was approximately 200%/W. As a preliminary experiment, parametric fluorescence measurement was made using a setup shown in Fig.8. Fig.9 shows signal and idler wavelengths dependent on the pump wavelength, and Fig.10 shows the fluorescence spectrum measured for pumping at 784.5nm wavelength. For pumping power of 12mW, fluorescence power of 0.9nW, in the same order of magnitude with the theoretical prediction using Fig.5, was obtained.

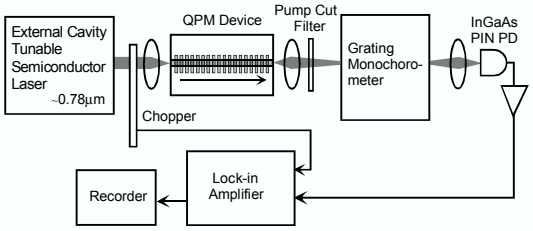


Fig.8 Experimental setup for parametric fluorescence generation and detection.

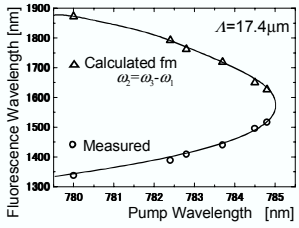


Fig.9 Measured fluorescence wavelength dependent on pump wavelength.

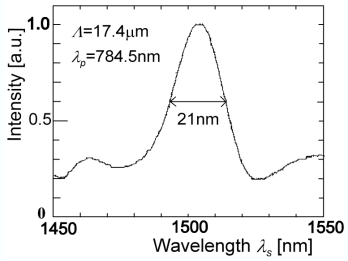


Fig.10 Measured parametric fluorescence spectrum.

Fabrication of Zn:$LiNO_3$ Waveguides and QPM Structures in MgO:$LiNbO_3$ An important requirement for implementation of stable and high output power quantum photonic devices is to use a waveguide free from photorefractive damage. In order to implement a waveguide NLO device for generation of polarization-entangled photons [2], a waveguide which supports both TE and TM modes is required. APE waveguides supports only extraordinary mode, while Ti-indiffused waveguides involve damage problem. As a candidate of damage-resistant TE/TM waveguides, we are studying fabrication of Zn-diffused $LiNbO_3$ waveguides. A new fabrication technique by Zn diffusion from sputtered ZnO film and Zn/Ni film as a Zn source in low-pressure atmosphere (1-10Torr, air) has been developed. Single-mode TE/TM guides with 1dB/cm loss have been obtained. QPM SHG devices were fabricated using the Zn:$LiNbO_3$ guides and preliminary SHG performance of 15%/W efficiency has been obtained [23]. Although a NLO device for generation of polarization-entangled photons can be implemented by using a Type-II QPM planar TE/TM waveguide, sophisticated device configuration using channel guides must be developed to accomplish a higher efficiency and facilitate for fiber coupling.

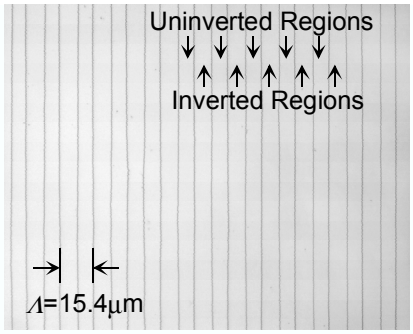


Fig.11 Ferroelectric domain inverted grating formed in MgO-doped $LiNbO_3$ crystal.

Fabrication technique of domain-inverted gratings for QPM in damage-resistant MgO-doped $LiNbO_3$

crystals has not been fully established. Most recently, we developed a new technique for fabrication of domain-inverted gratings in MgO:$LiNbO_3$, where uniform electric field is applied to the crystal under ultraviolet light irradiation with periodic spatial modulation [24]. The technique offers a simple and convenient means and requires no lithography process on each crystal. Fig.11 shows the fabricated QPM structure.

4. Squeezed Light Generation by Semiconductor Laser

4.1 Quantum-Well DBR Laser as Squeezed Light Source

The major origin of the intensity noise in the output of a semiconductor laser with a high quantum efficiency under strong excitation, in frequency range lower than the relaxation oscillation frequency, is the noise in the pump current. The conventional DC constant-current driving, when observed in radio frequency (RF) range, is substantially close to constant voltage driving, and the pump current involves the shot noise. When a laser is driven by a source of a high RF impedance, on the other hand, the RF fluctuation of the driving current is reduced (wideband constant-current driving). This means that the shot noise in the injection current can be suppressed, and squeezed light of intensity noise lower than SQL can be generated by converting the sub-shot-noise electron flow into the photon flow with a quantum efficiency close to unity [8]-[10].

Earlier experimental work was performed using Fabry-Perot (FP) multimode TJS lasers at low temperature and constant current driving with a series resistor [9], [10]. A multimode TJS laser optimized for squeezed light generation has been developed [13]. Single-mode lasers operating at room temperature are more advantageous in many applications, and quantum well (QW) lasers are advantageous to obtain low threshold and high excitation at room temperature. Lasers using nondoped QW, however, involve inhomogeneous gain broadening, and if multimode oscillation takes place, modes are not sufficiently anticorrelated and the mode partition noise disables effective squeezing. Thus an important requirement is to accomplish a high side mode suppression ratio (SMSR). Room temperature squeezed light generation in an external cavity laser using a FP QW laser by constant current driving has been demonstrated [12].

The author's group is working toward squeezed light generation in an InGaAs quantum-well DBR laser with a ridge structure and a curved DBR grating [25]. The DBR configuration allows a high side mode suppression ratio (SMSR) without external cavity. Use of an InGaAs strained QW, along with a high-reflectivity DBR grating and an optimized output facet reflectivity, allows accomplishment of low threshold and high excitation. Fig.12 illustrates squeezed light generation in the DBR laser by wideband constant-current driving with a series inductor.

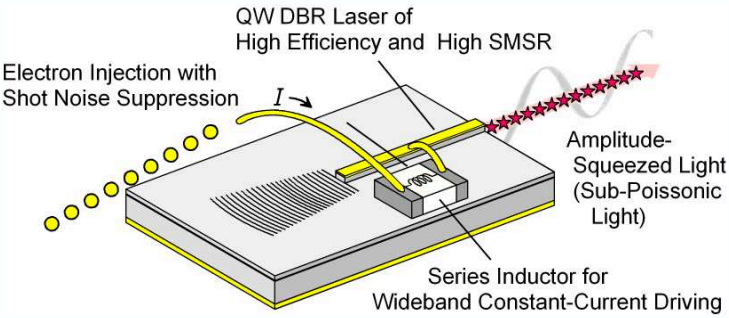


Fig.12 Schematic illustration of squeezed light generation in QW DBR laser by wideband constant-current driving.

4.2 Theoretical Analysis

The intensity noise and squeezing of semiconductor laser light can be analyzed by solving the rate equations including the Langevin noise sources [8], [9]. In the author's work, simplified analytical expressions were formulated. Assuming single-mode lasing, the rate equations for the carrier density N and the photon density S are given by

$$d/dt\ N = -\Gamma GS - N/\tau_s + J/dq + F_N, \qquad d/dt\ S = +\Gamma GS - S/\tau_{ph} + C_s N/\tau_s + F_S \tag{18}$$

where G is the gain factor, Γ the confinement factor, τ_s and τ_{ph} are carrier and photon lifetime, J is the injection current density, d the active layer thickness, q the elementary charge, C_s the

spontaneous emission factor, and F_N and F_S represent Langevin noise sources. From (18) we obtain linearized rate equations for the fluctuations δN and δS

$$d/dt\ \delta N = -\Gamma(G+G_sS)\ \delta S -(\Gamma G_N S+1/\tau_s)\ \delta N +F_N,$$
$$d/dt\ \delta S = (C_sN/\tau_sS\Gamma G_SS)\ \delta S+(\Gamma G_NS+C_s/\tau_s)\delta N+F_S, \tag{19}$$

where G_S and G_N are derivatives of G by S and N. Since each term of the right hand side represents independent event, each fluctuation term can be treated as shot noise. Assuming a case where the fluctuation in the injection current is suppressed down to γ times the shot noise level, the correlation functions of the noise sources are calculated as

$$F_NF_N\ =D_{NN}\delta(t);\ D_{NN}=2C_sNS/\tau_s+(1+\gamma)N/\tau_sV_a-(1-\gamma)S/\tau_{ph}V_a,$$
$$F_SF_S\ =D_{SS}\delta(t);\ D_{SS}=2C_sNS/\tau_s;\quad F_NF_S\ =D_{NS}\delta(t);\ D_{NS}=-2C_sNS/\tau_s+S/\tau_{ph}V_a, \tag{20}$$

where V_a is active volume. The noise spectrum of S, $S_S(\Omega)$, can be calculated by using the Wiener-Khintchen's theorem with Fourier transforms $\delta N(\Omega)$, $\delta S(\Omega)$ obtained from (19),(20), as

$$S_S(\Omega)=\frac{2\tau_{ph}^2|H(\Omega)|^2}{\Gamma^2G_N{}^2S}\left\{\frac{C_sN}{\tau_s}\left(\Omega^2+\frac{1}{\tau_s{}^2}\right)+\frac{\Gamma G_N}{\tau_{ph}\tau_sV_a}\left(1+\frac{1+\gamma}{2}G_N\tau_{pa}N\right)S+\frac{1+\gamma}{2}\frac{\Gamma^2G_N{}^2}{\tau_{ph}V_a}S^2\right\}, \tag{21}$$

$$H(\Omega)=\Omega_R{}^2/\left(\Omega_R{}^2-\Omega^2-2i\Gamma_R\Omega\right),\quad \Omega_R{}^2\cong\Gamma G_NS/\tau_{ph},\quad 2\Gamma_R=1/\tau_s+\Gamma(G_N-G_S)S+C_SN/\tau_sS,$$

where $H(\Omega)$ is the modulation transfer function, Ω_R and Γ_R are frequency and damping factor of relaxation oscillation From (21) we see that $S_S(\Omega)$ (for large S and low Ω) for γ=0 is half that for γ=1. This means that the half of the noise results from the pump noise and the other half results from photon shot noise. We next derive expressions for the noise in the output power P (in photon number per unit time), which is given by

$$P=KS,\quad K=F_{stm}V_a/\tau_{ph}, \tag{22}$$

where F_{stm} ($0<F_{stm}<1$) is the output coupling factor. Let F_p be the Langevin noise source representing the photon partition noise caused by partial outcoupling of the stored photons, and let $\delta P=K\delta S+F_p$ be the fluctuation of P. The correlation functions are given by

$$F_PF_P\ =D_{PP}\delta(t),\ D_{PP}=+P;\quad F_SF_P\ =D_{SP}\delta(t),\ D_{SP}=-P/V_a;\quad F_NF_P\ =0. \tag{23}$$

In the similar manner as (4), the noise power spectrum of P, $S_p(\Omega)$, can be calculated as

$$S_P(\Omega)=\left[2K\left(\frac{K\tau_{ph}|H(\Omega)|}{\Gamma G_NP}\right)^2\left\{\left(\frac{C_sN}{\tau_s}+\frac{\Gamma G_S}{V_a}\frac{P}{K}\right)\Omega^2+\frac{C_sN}{\tau_s{}^3}+\left(\frac{1+\gamma}{2}\frac{\Gamma^2G_N{}^2N}{\tau_sV_a}+\frac{\Gamma G_S}{\tau_s{}^2V_a}\right)\left(\frac{P}{K}\right)+\left(\frac{\Gamma^2G_NG_S}{\tau_sV_a}+\frac{\gamma-1}{2}\frac{\Gamma^2G_N{}^2}{\tau_{ph}V_a}\right)\left(\frac{P}{K}\right)^2\right\}+1\right]P. \tag{24}$$

Since the SQL noise is given by $S_P(\Omega)=P$, the noise power spectrum normalized by the SQL level is given by $S_P(\Omega)/P$. The relative intensity noise (RIN) is given by $RIN(\Omega)= S_P(\Omega)/P^2$. For low Ω where$|H(\Omega)|^2\approx1$, equation (24) can be approximated as

$$S_P(\Omega)/P\approx\left[\frac{\tau_{ph}K}{V_a}\left\{(\gamma+1)\frac{\tau_{ph}N}{\tau_sS}+(\gamma-1)\right\}+1\right]=\left[F_{stm}\left\{(\gamma+1)\frac{\tau_{ph}N}{\tau_sS}+(\gamma-1)\right\}+1\right]. \tag{25}$$

This result shows that, for a laser of high quantum efficiency and $F_{stm}\approx1$ and for strong excitation where $\tau_{ph}N/\tau_sS$ is reduced, reducing the pump noise as γ 0 gives rise to mutual cancellation of the shot noise and the partition noise of photons, and amplitude squeezed light of $S_P(\Omega)/P$ 0 is generated. Using $N\approx N_{th}=(\tau_s/dq)J_{th}$, $S\approx\tau_{ph}(J-J_{th})/dq$ with the threshold current J_{th}, the normalized noise level for $F_{stm}\approx1$ and complete suppression of pump noise ($\gamma\approx0$) is given approximately by

$$S_P(\Omega)/P\approx\frac{\tau_{ph}N}{\tau_sS}=\frac{1}{J/J_{th}-1}, \tag{26}$$

which shows $S_P(\Omega)/P$ decreases in inverse proportion to the increasing excitation ratio J/J_{th}-1.

4.3 Design and Fabrication of QW DBR Lasers for Squeezed Light Generation.

The quantum noise characteristics were calculated based on (24), by assuming lasing wavelength 962nm, internal quantum efficiency η_i=0.80, transparency carrier density N_g=2.5×10^{18}/cm^3,

differential gains ΓG_N=9.0×10^{-9}cm^3/sec, ΓG_S=-3.0×10^{-8}cm^3/sec, active region 0.006×2.6μm^2, cavity length L=0.60mm, internal loss α_i=3.0/cm, facet and DBR reflectivities R_f=0.12, R_b=0.61, carrier lifetime τ_s=4.2nsec, photon lifetime τ_{ph}=5.4psec, threshold current I_{th}=10.3mA, external differential quantum efficiency η_d=0.66, and spontaneous emission factor C_s=1.0 10^{-5}, as device parameters expected to be feasible with the DBR laser of Fig.12.

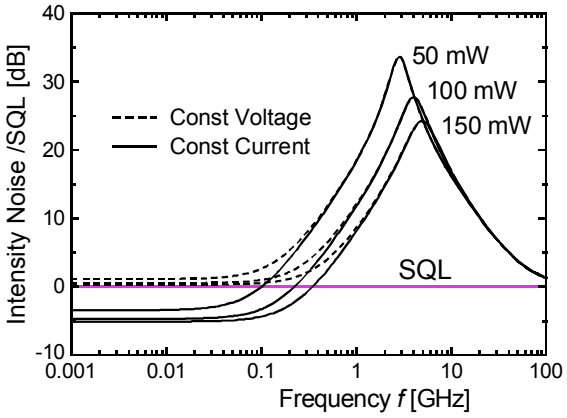


Fig.13 Calculated intensity noise spectrum for a semiconductor laser. The dashed curves are for ordinary driving, and the solid curves are for wideband constant-current driving.

Fig.13 shows the calculated normalized noise power spectrum $S_P(\Omega)/P$. The dashed curves are for ordinary driving (constant-voltage driving in RF range), which involves pump noise of shot noise level (γ=1). The optical noise level for output power larger than ~100mW and for frequency range lower than 50MHz is close to SQL (shot noise) level. The solid curves are for wideband constant-current driving with the pump noise suppression (γ=0). The result shows that amplitude squeezed light is generated; the optical noise level for output lower larger than ~100mW is reduced to ~5dB below the SQL level.

A DBR laser for squeezed light generation shown in Fig14 was fabricated using an InGaAs/AlGaAs GRIN-SCH-SQW structure. The QW in the DBR grating region was selectively disordered by bithickness SiO_2 capping and rapid thermal annealing to reduce the propagation loss in the passive waveguide [26]. Active channel was fabricated by forming a ridge of 2.6μm width and 600μm length by EB writing and RIE. The curved DBR of 200μm length was designed (96% theoretical reflectivity and 1.6nm wavelength bandwidth), and was formed by second EB writing and RIE. The output facet was LR coated with SiO_2 to reduce the reflectivity down to 5% and enhance the COD level. Fig.15 shows the measured lasing characteristics of the fabricated DBR laser. DBR reflectivity of 71%, 20mA threshold current, 180mW maximum output power, excitation ratio I/I_{th} as large as 12.5, external differential quantum efficiency of 64%, side mode suppression ratio (SMSR) as large as 52dB, have been obtained [27]. We are preparing the quantum noise measurement using the balanced detection technique. Squeezed light generation is expected, since the obtained lasing performances are approaching to those assumed in the theoretical calculation to obtain Fig.13.

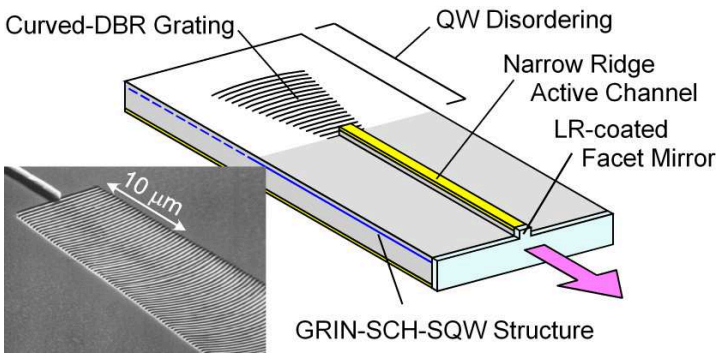


Fig.14 QW DBR laser fabricated for squeezed light generation.

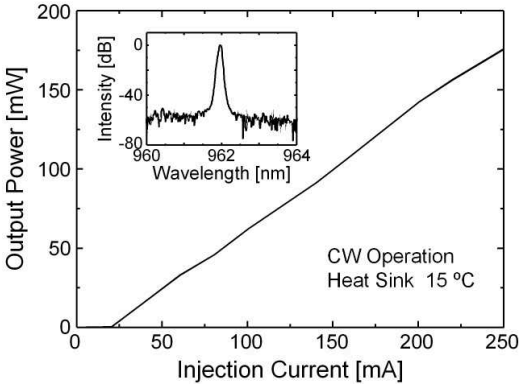


Fig.15 Lasing characteristics of the fabricated QW DBR laser.

5. Conclusion

Fundamental theoretical considerations for design of quantum photonic devices have been outlined, and the current status of the work in the author's group has been reported. Although the experimental work of the authors group is at the preliminary stage, encouraging results showing the potential feasibility are being obtained, and subjects for future work have been clarified. It is hoped that many *integrated quantum photonic devices* will be implemented to contribute substantially to research and development of quantum information processing.

Acknowledgements

The author would like to thank his coworkers, Drs. M.Fujimura and M.Uemukai and graduate students included as coauthors of his publications quoted in the references for their contributions. This work has been supported by Grant-in-Aid for Scientific Research form Ministry of Education, Culture, Sports, Science and Technology (MEXT), and by Handai Frontier Research Center (FRC).

References

[1] H.Lo, S.Popescu and T.Spiller, ed., Introduction to Quantum Computation and Information, World Scientific, Singapore, 1998.
[2] D.Bouwmeester, A.Ekert and A.Zeilinger, ed., The Physics of Quantum Information, Springer, Berlin, 2000.
[3] E.Giacobino, Squeezed states using parametric processes, D.B.Ostrowsky and R.Reinisch ed., Guided Wave Nonlinear Optics, pp.29-48, Kluwer Academic Pub., Dordrecht, 1992.
[4] D.K.Serkland, M.M.Fejer, R.L.Byer and Y.Yamamoto, Opt. Lett., **20**, pp.1649-1654, 1995.
[5] D.K.Serkland, P.Kumar, M.A.Arbore and M.M.Fejer, Opt. Lett., **22**, pp.1497-1499, 1997.
[6] D.B.Ostrowsky, P.Baldi, M.DeMicheli, S.Tanzilli, H.DeRiedmatten, W.Tittel, H.Zbinden, and N.Gisin, Proc. 10th European Conf. Integrated Optics (ECIO'01), Paderborn, pp.139-146, 2001.
[7] G.S.Kanter, P.Kumar, R.V.Roussev, J.Kurz, K.R.Parameswaran and M.M.Fejer, Opt. Exp., **10**, pp.177-182, 2002.
[8] Y.Yamamoto, S.Machida and O.Nilsson, Phys. Rev. A. **34**, pp.4025-4042, 1986.
[9] Y.Yamamoto and S.Machida, Phys. Rev. A. **35**, pp.5114-5130, 1987.
[10] S.Machida, Y.Yamamoto and Y.Itaya, Phys. Rev. Lett., **58**, pp.1000-1003, 1987.
[11] J.Kim, S.Somani, Y.Yamamoto, Nonclassical Light from Semiconductor Lasers and LEDs, Springer, Berlin, 2001.
[12] M.J.Freeman, H.Wang, D.Steel, R.Craig and D.Scifres, Opt. Lett., **18**, pp.2141-2143, 1993.
[13] S.Lathi, K.Tanaka, T.Morita, S.Inoue, H.Kan and Y.Yamamoto, IEEE J. Quantum Electron., **35**, pp.387-394, 1999.
[14] T.Suhara, M.Fujimura, K.Kintaka, H.Nishihara, P.Kurz, and T.Mukai, IEEE J. Quantum Electron., **32**, pp.690-670, 1996.
[15] T.Suhara, H.Nishihara: Trans. IEICE, **J82-C-I**, pp.326-334, 1999; Electron. Commun. Japan, Pt.2, **82**, 12, pp.48-56, 1999.
[16] T.Suhara, Quantum Theory of Nonlinear-Optic Devices, Ch.5 in T.Suhara and M.Fujimura, Waveguide Nonlinear-Optic Devices, Springer, 2003, to be published.
[17] T.Suhara, and H.Nishihara, IEEE J. Quantum Electron., **26**, , pp.1265-1276, 1990.
[18] T.Sugita, K.Mizuuchi, Y.Kitaoka and K.Yamamoto, Opt. Lett., **24**, pp.1590, 1999.
[19] R.Parameswaran, R.K.Route, J.R.Kurz, R.V.Roussev, M.M.Fejer and M.Fujimura, Opt. Lett., **27**, pp.179-181, 2002.
[20] D.Sato, T.Morita, T.Suhara and M>Fujimura, IEEE Photon. Tech. Lett., **15**, no.4, 2003, to be published.
[21] T.Suhara, T.Fujieda, M.Fujimura and H.Nishihara, Jpn. J. Appl. Phys., **39**, Pt2, pp.L864-L865, 2000.
[22] Y.Shigematsu, M.Fujimura and T.Suhara, Jpn. J. Appl. Phys., **41**, Pt.1, pp.4825-4827, 2002.
[23] M.Fujimura, H.Ishizuki, T.Suhara and H.Nishihara, CLEO/PR'01, pp.I96-96, Makuhari, 2001.
[24] M.Fujimura, T.Sohmura and T.Suhara, Annual Spring Meeting Jpn. Soc. Appl. Phys, 2003.
[25] M.Uemukai, A.Yoshimoto, N.Matsumoto, T.Suhara, H.Nishihara, N.Eriksson and A.Larsson, Electron. Lett., **33**, pp.1464-1465, 1997.
[26] N.Shimada, Y.Fukumoto, M.Uemukai, T.Suhara, H.Nishihara and A.Larsson, IEEE J. Selectred Topics Quantum Electron., **7**, pp.350-354, 2001.
[27] K.Kitano, M.Uemukai, N.Shimada and T.Suhara, Annual Spring Meeting Jpn. Soc. Appl. Phys, 2003.

Recent Progress of Semiconductor Integrated Optics for WDM Photonic Networks

Yuzo Yoshikuni

NTT Photonics Laboratories,
3-1 Morinosato-wakamiya, Atsugi
kanagawa, 243-0198 Japan
Phone:+81 46 240 2857,Fax: +81 46 240 2859
E-mail: yosikuni@aecl.ntt.co.jp

The integrated devices are indispensable to make next generation WDM networks at a reasonable cost and in a reasonable space. Semiconductor is a promising material for making integrating optical devices. This paper reviews resent progress of semiconductor optical integrated devices.

I. Introduction

The explosive growth of Internet traffic makes the development of integrated photonic devices an important issue for next-generation photonic systems. The large number of devices needed in future optical systems means that integrated devices will be indispensable if we want to make such systems at a reasonable cost and in a reasonable space. Monolithic integration on semiconductor substrates is attractive because it allows the semiconductor devices for optical systems, such as lasers, modulators, and photo-detectors, to be included on a single chip. Starting from a simple integrated device containing a DFB laser and an EA-modulator, various kinds of integrated photonic devices have been developed by using hybrid and monolithic technologies. Recent progresses in fabrication technologies and device design have made it possible to extend semiconductor monolithic technologies to passive devices. Fabrication technologies, such as crystal growth and dry etching, enable fabrication of waveguides with uniform and smooth interfaces and also enable the precise control of waveguide thickness needed to fabricate polarization insensitive waveguides. Moreover, the recent progress in development of the arrayed waveguide grating (AWG) enables us to make optical devices with significantly improved fabrication tolerance. With these technologies, we can extend the application of semiconductor materials to passive optical devices and, consequently, to complicated monolithic circuits containing both passive and active devices. This paper describes introduces some typical examples of the semiconductor monolithic devices reported so far.

II. Semiconductor Integrated Devices

Although active integrated devices have been used practically, application of semiconductor monolithic

integration to passive devices at more than just a primitive level has only recently become possible, thanks to recent progress in fabrication technologies and device design. The development of the AWG has significantly accelerated development of monolithic circuits or monolithic devices. AWGs, by providing filtering function for multiplexing and demultiplexing signals, have been instrumental in expanding the application of semiconductor devices to WDM systems.

The first generation of the integrated devices was fabricated with only one waveguide structure and waveguide material. Starting from a simple device such as AWG integrated photo-detectors, even more complicated one have been fabricated. Limitation in waveguide structure and material, however, restricts ability of the monolithic integration. The technologies for connecting waveguides with different structures and materials, then, enable us to make complicated circuits containing various devices which require their own waveguide structures and materials. Monolithic circuits is, then, possibly fabricated with important devices including the semiconductor optical amplifiers and optical modulators.

A. Monolithic Integration of semiconductor AWGs and photo-detectors

Integration with a photodiode is relatively easy but the advantage of the integration is clear, therefore multi-wavelength AWG receiver[1,2,3,4] and WDM monitoring devices[5] have been fabricated at many laboratories. A multi-wavelength AWG receiver of eight channels that is about the same size as a conventional laser diode module can be fabricated.

Figure 1 shows an example of the semiconductor AWG integrated with photo-detectors. As shown in the right bottom figure, the device contains AWG connected to 16 photodiodes. The input signal, which contains 16 different wavelengths, is demultiplexed by the AWG and then each signal is detected by corresponding photo-detectors. On the left, is a photograph of the chip. A small bending radius of 250 μm makes the chip as small as 3.4 x 4.4 mm^2. The device has 16 photo-detectors for electrical monitoring and one optical output port for easy characterization of the chips. The AWG has 114 waveguides in the grating arm. A 2.45-μm-wide and 4.0-μm-deep ridge waveguide structure is used for obtaining

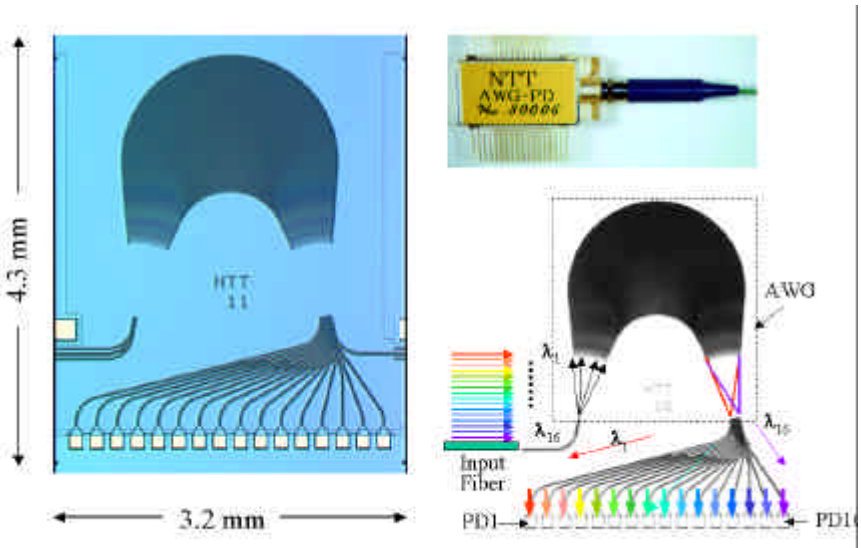


Figure 1 An AWG integrated with photodiodes.

polarization-insensitive characteristics. The path length difference ΔL is 27.25 μm, which gives a free spectral range (FSR) of 3.2 THz and the corresponding order of 56 at around 1.55 μm. Figure 2 shows wavelength dependence of the detection sensitivity of the 16-detectors in the integrated device. The sensitivity of each detector has clear peak at the channel wavelength spaced by 100 GHz. The maximum sensitivity of about 0.1 A/W is obtained with the crosstalk of less than –20 dB for the other channels.

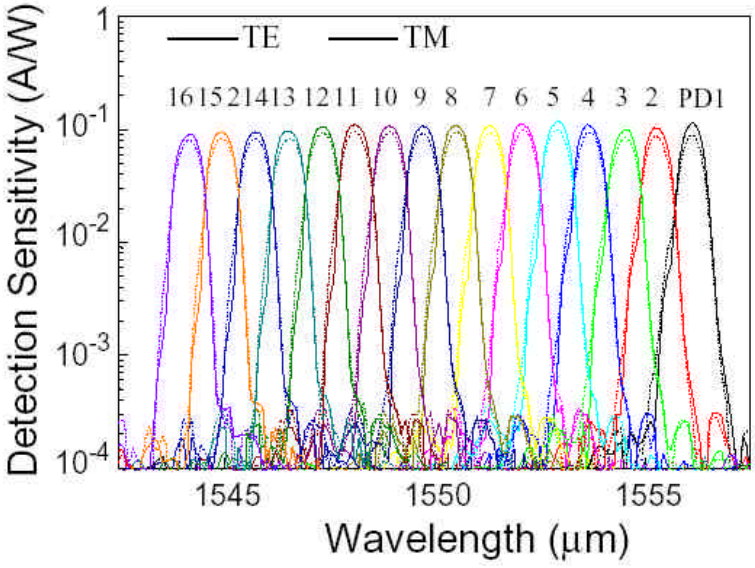


Figure 2. . Spectrum response of the efficiencies in an AWG integrated with photo-detectors.

The promising application for the photo-detector integrated devices is power and/or wavelength monitor in WDM systems[6]. The monitor application requires only low frequency signal and is free from the issue associated with multi-channel high-speed circuits. Although the implementation of multi-channel high-speed circuits is a severe issue, some prototype of the multi-wavelength receivers has been fabricated.

Figure 3(a) shows the fabricated 16-channel WDM receiver[7]. The compact integrated device enables us to install an AWG, 16-channel photo-detectors, and 16-electrical amplifiers in the industry standard of Compact PCI 6U 4-slot. The receiver consists of a WDM receiver board and a Compact PCI interface board. The WDM receiver board, which is shown in Fig 4(b), contains the AWG-PD module, trans-impedance amplifiers, and limiting amplifiers. The AWG-PD module is a

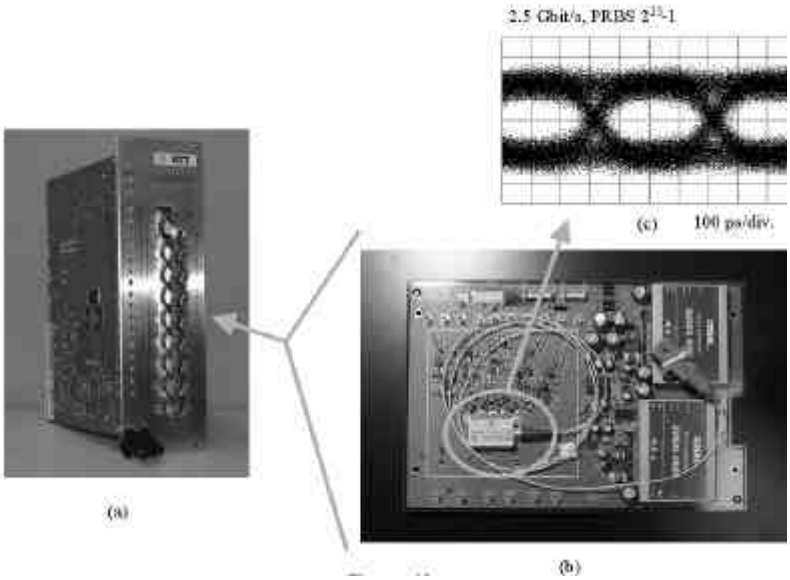


Figure 3. A 16-channel WDM receiver

polarization-insensitive multi-wavelength photo-detector with 16-channel, 100-GHz channel spacing and 3.2-THz free spectral range, which is the core element of the receiver. The AWG-PD module itself is designed for high-speed signal detection of up to 2.5 Gbit/s/ch[8]. Figure 3(c) shows an eye diagram for a 2.5 Gbit/s NRZ 2^{23}-1 pseudorandom bit stream detected by the integrated AWG-PD.

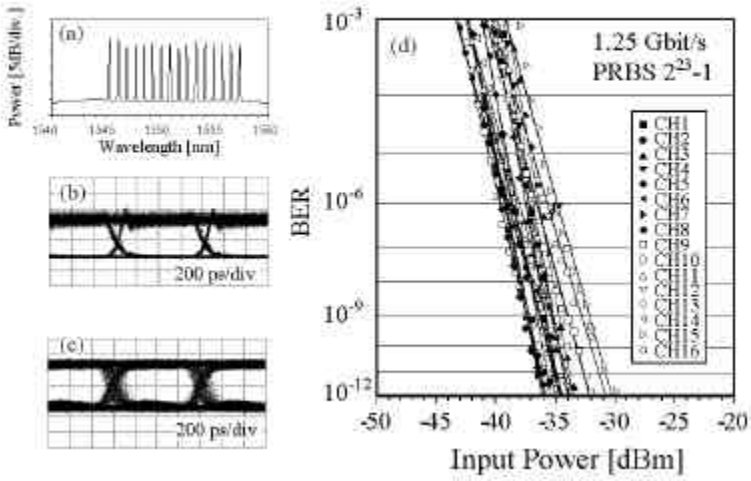


Figure 4. Detection characteristics of the 16-channel WDM receiver

The simultaneous detection of 16-signals has been tested at 1.25 Gbit/s, which corresponds to the bit rate of the Gigabit Ethernet. The optical sources with16 LDs were used to generate frequencies ranged from 192.50 THz to 194.00 THz (1545.32 nm – 1557.36 nm) with a channel spacing of 100 GHz. The 16 optical carriers were multiplexed by a silica-based AWG and modulated by an electroabsorption (EA) modulator with a 1.25 Gbit/s NRZ 2^{23}-1 pseudorandom bit stream. Transmission through an 80-km standard single-mode fiber (SMF) with dispersion of 17 ps/km/nm de-correlated the bit-stream of signals in different wavelength. The 16 signals were coupled into the WDM receiver after being pre-amplified by an erbium-doped fiber amplifier (EDFA) whose gain was 38 dB. A spectrum of the input lights before coupling into the WDM receiver is shown in Fig. 4(a). Eye diagram detected by a conventional detector is shown in Fig. 4(b) and output from the WDM receiver is shown in Fig. 4(c). It should be noted that there are no degradation in the eye diagram in Fig. 4(c) although the received signal was measured with crosstalk from all interfering channels.

Bit error rates (BERs) were measured for all 16 channels on the condition that all signals were simultaneously coupled into the WDM receiver. The BERs are shown in Fig. 4(c), where the input power is defined as the power of the measured signal before it is coupled into an optical preamplifier. The WDM receiver sensitivity was between -38 and -32 dBm for 1.25 Gbit/s NRZ 2^{23}-1 pseudorandom bit stream at a bit error rate of 1×10^{-9}..

B. Monolithic integration of AWG and semiconductor optical amplifiers

Integration with semiconductor optical amplifiers (SOAs) is also an attractive target. The optical gain provided by SOAs may compensate the relatively large insertion loss in semiconductor monolithic circuits and consequently enables us to make larger-scale optical circuits. The SOA is also attractive as an optical gate or switch because fast and low-crosstalk optical gating is possible only by on/off control

of the currents. The device shown in Figure 5, a WDM channel selector[9,10], is a good example of the integration of an SOA.

WDM channel selectors, that contain two AWGs connected by SOAs, will be key components in advanced WDM-based photonic network systems. Fast, low-crosstalk operations are expected because arbitrary demultiplexed signals can be selected by using only an on/off control of the SOA currents. WDM channel selectors are composed of numerous waveguides and components; therefore, reduction of device size is an issue in achieving low-cost mass production. The device in the figure uses a hybrid waveguide structure to make it compact and reliable;. a deep-ridge structure with a small bending radius is used for passive waveguides, and a buried waveguide structure, whose reliability has been confirmed in conventional lasers, is used in the SOA regions

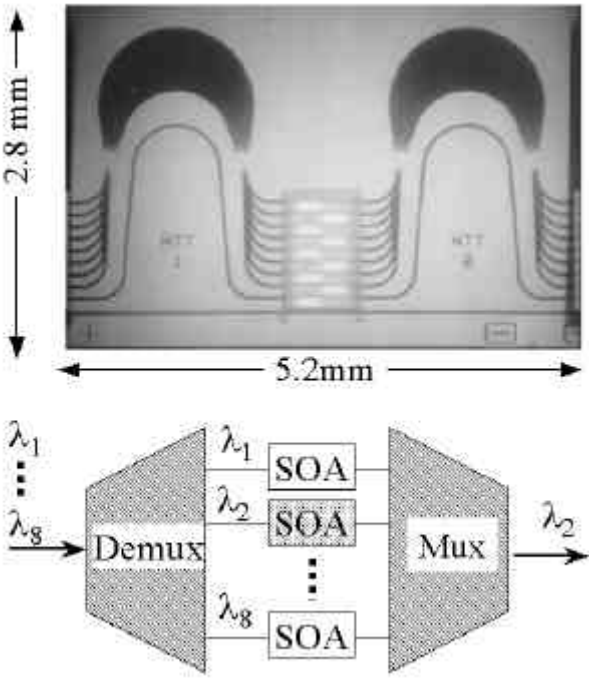


Figure 5. Photograph of the WDM channel selector consisting of an AWG andSOAs.

The device consists of two AWGs and an 8-ch. SOA array. Each AWG has 8 input and 8 output waveguides and an array of 28 waveguides. The free spectral range and the channel spacing are 1.6 THz and 200 GHz, respectively. Eight 600-μm-long SOAs are located between the two AWGs. The spacing in the SOA array is 125 μm. Total device size is 5.2 x 3.6 mm^2. WDM signals, which are fed into one of the input waveguides, are demultiplexed by the first AWG, and some of the demultiplexed signals are selected by adjusting the current of the eight SOA gates. Then, the selected signals are multiplexed into one output waveguide by the second AWG..

The deep-ridge structure is used in most of the passive waveguide regions. The waveguide layer is a 0.5-μm-thick InGaAsP(λ_g=1.05μm). A non-doped InP buffer layer is inserted above the waveguide layer to prevent absorption loss in the p-type InP. The 2.5-μm-wide, 4.5-μm-deep ridge waveguide is designed to obtain low polarization dependence[12,24,11]. Because light is strongly confined by air against the lateral direction, a small bending radius is allowed in the waveguide layout, without excess loss. A minimum bending radius of 250 μm was chosen, which makes the AWGs as small as 2.2 x 3.6 mm^2. On the other hand, the buried waveguide structure s is used in the SOA regions. The active layer of the SOA is a 0.3-μm-thick InGaAsP(λ_g=1.55μm). The buried waveguide is the same as that of conventional laser diodes. The injection current is almost completely confined to the active waveguide by the current blocking layers. This structure should provide high reliability because the active layer is buried in InP. The optical couplings between the two waveguides were calculated by the finite difference method

(FDM).[12] Even though the structures are quite different, we can make field distributions of about the same size by choosing appropriate sizes for the waveguides. Therefore, coupling loss as small as 0.2 dB can be obtained. The losses estimated from the excess loss of test waveguides with many interfaces, were below 0.3 dB .

The filtering characteristics of the WDM channel selector are shown in Figure 6. WDM signals containing eight different wavelengths from 1546.0to 1557.2nm with a spacing of 1.6 nm (200 GHz) were used for input. The power of each channel was adjusted to ~-8 dBm, as shown in .the top left of the figure. The WDM signals were passed through the device with a pair of lensed fibers, and the filtered light was measured using an optical spectrum analyzer. The top figure shows the spectra of the filtered light, when one channel was selected by the SOA gate control. The SOA current was 200 mA in the ON state. All 8 channels were well selected with a low crosstalk of less than –40 dB, where the crosstalk is defined as the ratio between a selected signal and an unselected signal. The amplified spontaneous emission (ASE) passed through the second AWG filter are observed at a ~30 dB lower level than the signal. Figure 7 shows the fiber-to-fiber transmittance for each channel as a function of the SOA current. The power of the input light is -12.4 dB with TE-polarization. Zero-insertion-loss operations are obtained for all channels. High extinction ratios of more than 50 dB are also obtained due to large absorption in the SOA.

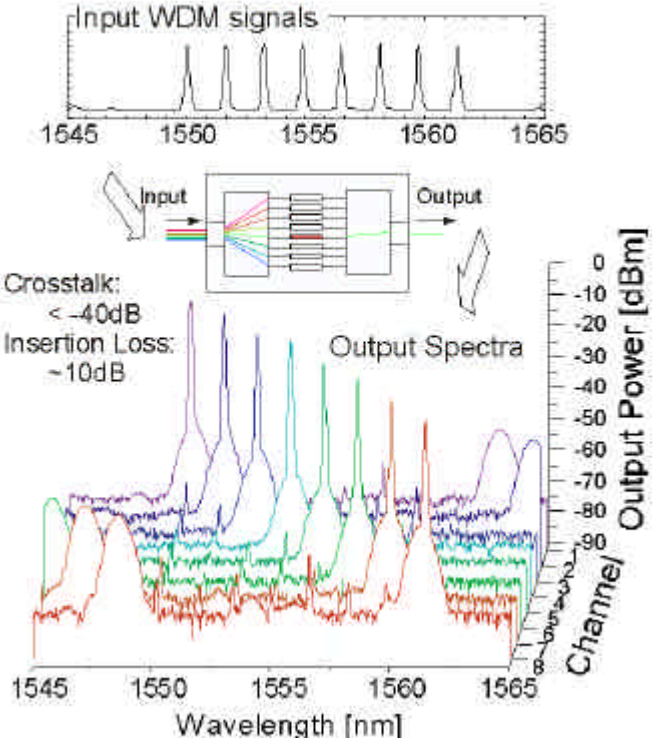


Figure 6. Channel selection of WDM signal in the AWG-SOA integrated device

Although the channel selector is an attractive device, it has an inherent issue for increasing number of WDM channels. As each WDM channel need a SOA for gating, increase in a number of channels requires as many SOAs and consequently requires large chip size. The large chip size and wiring issue associated with a large number of SOAs imply that this configuration may not be suited for WDM systems with a large number of channel. A

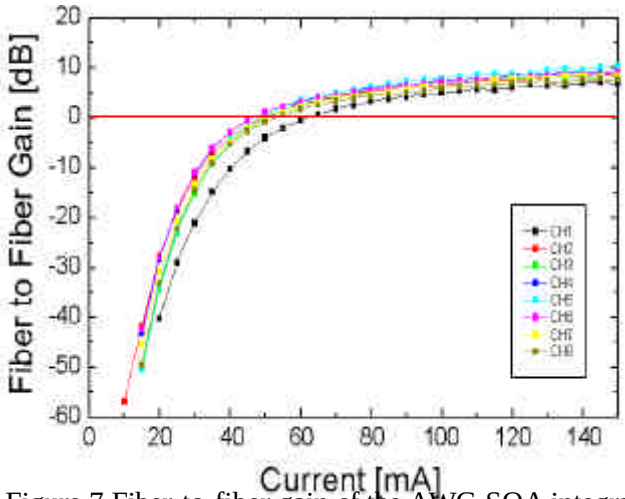


Figure 7 Fiber-to-fiber gain of the AWG-SOA integrated device as a function of the amplifier current

new configuration with cascaded AWGs and SOAs may solve this issue.

Figure 8 shows a 64-channel WDM channel selector with cascaded AWGs and SOAs where we can see a photograph (upper) and a schematic structure (lower) of the device[13]. The device consists of a 1 x 8 AWG, the first stage SOA gates, an 8 x 8 rear AWG, the second-stage SOA gates, an 8 x 1 multimode interference (MMI) coupler, and a booster SOA. The front AWG, which has a channel spacing of 50 GHz with a FSR of 400 GHz, sorts the incoming 64-signals into eight groups on it's eight output ports. The each group contains 8-signals at frequencies separated by the FSR of the first AWG. One of the first stage SOAs then select a group to pass through and lead to the second AWG. The second AWG has a cannel spacing of 400 GHz and an FSR of 3.2 THz where the allocation of the input port is carefully designed to obtain transmission peaks at every 64-channel frequencies. The second AWG sorts eight-signals by frequency and then a second stage SOA selects a signal at the required frequency. Thus the device can select any one of the 64-signals by choosing an appropriate pair of the first and second SOAs. Finally, the 8 x 1 MMI coupler combines 8-output waveguides into one and the booster SOA amplifies signal to compensate the internal loss of the device. Consequently the device can select 64-wavelengthes with only 16-SOAs, while conventional design for the wavelength selector requires 64 SOAs.

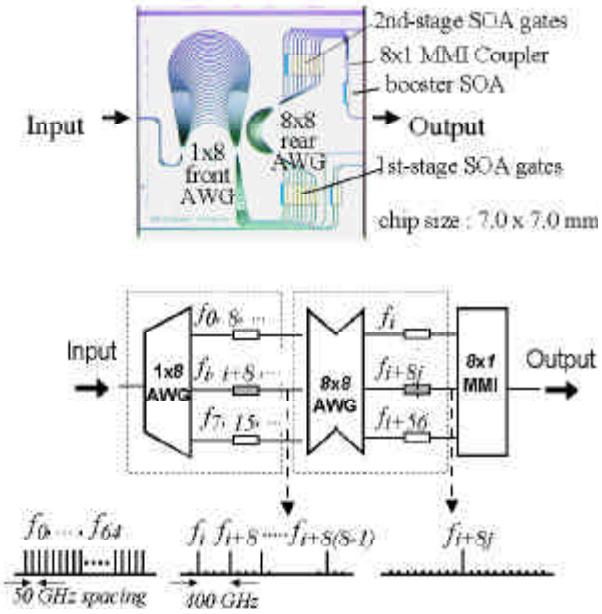


Figure 8. A 64-channel WDM channel selector with cascaded AWGs and SOA

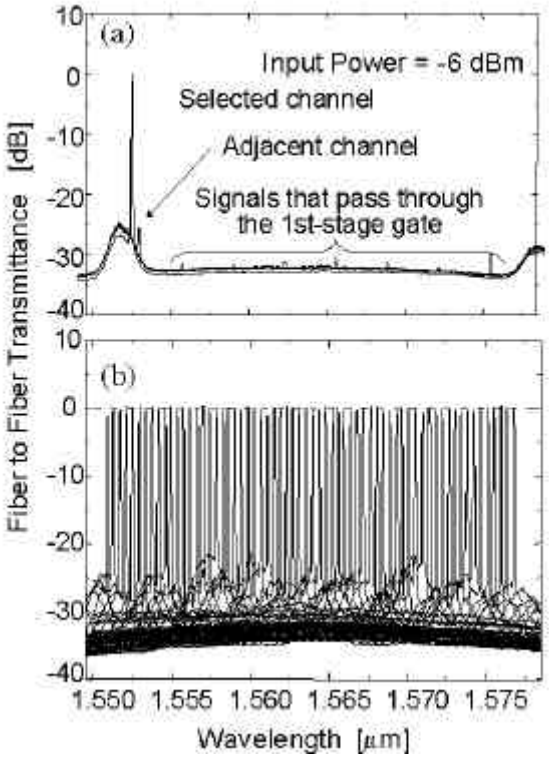


Figure 9. Output spectra of the 64-channel WDM channel selector

Figure 9 shows wavelength characteristics of a fabricated device. The device has an averaged channel spacing of 50.4GHz with standard deviation of 4.5 GHz and possibly separate 50 GHz spaced 64-signals. Figure (a) shows output spectra with a particular pair of 1st and second SOAs are active. One signal is successfully extracted with eight small peaks originated from the crosstalk in the first or second AWGs The maximum crosstalk is determined

by the adjacent peak but is less than –25 dB. Overlapped spectra in fig. (b) confirms successful channel selection for all 64-channel. The zero insertion loss operations are obtained for 62-channels with proper adjustment of SOA currents between 107 and 150 mA. The high spead operation is also reported in this device[14].

C. Integration of AWGs, SOAs and EA modulators

As shown in the previous section, the but-joint makes possible low-loss coupling between different waveguide with independent structure design of each part. Using the but-joint, we can make more complicated devices even with different material systems. Figure 10 shows a multi-wavelength modulator[15] consisting of InGaAsP SOAs and InGaAs/InAlAs electro-absorption modulators (EAMs). The operation of the device is illustrated in the upper f. Incident CW lights at 8-wavelengths are split by the AWG. Next, they travel through the SOAs to compensate for the insertion loss. The EAMs modulate them individually to generate signals in 8-WDM channels. The modulated lights are launched into the same AWG again where they are multiplexed to one output port. For using the AWG twice as multiplexer and demultiplexer, the input/output ports of the AWG are designed to locate in particular positions according to periodical wavelength response. This single-AWG configuration reduces circuit size by half compared to a conventional two-AWG configuration and also assures complete spectral matching between multi-plexer and demulti-plexer.

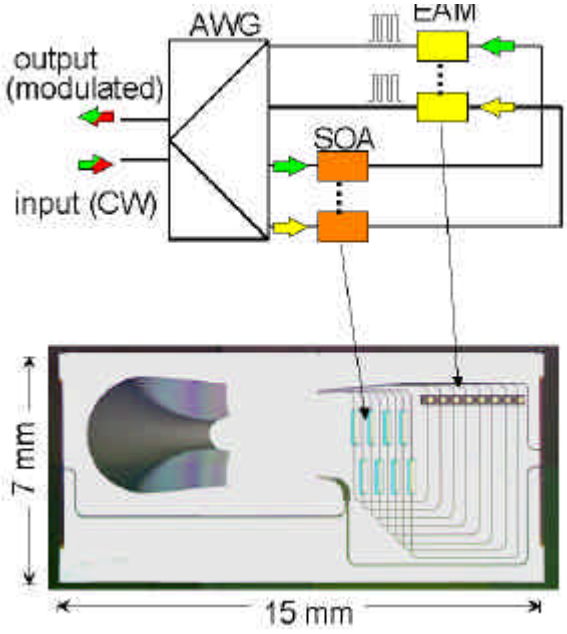


Figure 10. A multi-wavelength modulator consisting of an AWG, semiconductor optical amplifiers (SOAs) and

The butt-joints made by selective area growth technique connected the completely different structures of the AWG, SOA, and EAM. The device was formed by five steps of metal organic vapor phased epitaxy (MOVPE). First, an InGaAs/InAlAs multi-quantum-well (MQW) EAM active layer that provides polarization independent operation was grown on an n-InP substrate and partially etched off by wet etching. Then, an InGaAsP bulk SOA active layer was selectively grown using a SiO_2 mask and a p-InP cladding layer and an InGaAsP contact-cap layer were formed all over the surface. After etching off the all grown layer except for SOA and EAM region, an InGaAsP AWG waveguide layer and an undoped InP cladding layer were simultaneously butt-jointed to the EAM and SOA active layer in the second selective area growth step. The buried heterostructure (BH) was formed in the SOA region with

a semi-insulating buried layer using CH_4/H_2 dry etching and the MOVPE growth of Fe-doped InP. A deep-ridge waveguide was used for the AWG to obtain high refractive index contrast. The waveguide in the EAM region was buried with polyamide to reduce the parasitic capacitance. Thanks to the small bend radius of the deep-ridge waveguide and single-AWG configuration the whole circuit was included in a size as small as 15 x7mm^2.

Figure 11 (a) shows the output spectra of the fabricated circuit where the SOA current was 200 mA and the EAM was biased at 0V for each channel. When the input power was +5 dBm the output power of around -15 dBm was obtained, although channel 2 has no output due to a fabrication error. The measured channel spacing was 25 ± 2.5GHz for all ports. This indicates that uniform channel spacing was achieved in the AWG and the power loss due to the spectral mismatch between the MUX and the DEMUX was small enough. The single-AWG configuration is effective in eliminating the spectral mismatch as well as reducing circuit size. The estimated SOA of about 15 dB results in the fiber-to-fiber insertion loss of the circuit of about 20 dB. The gain of the SOAs is not sufficient for the purpose of complete loss compensation in this feasibility study, but could be improved up to about 25 dB by improving the fabrication process.

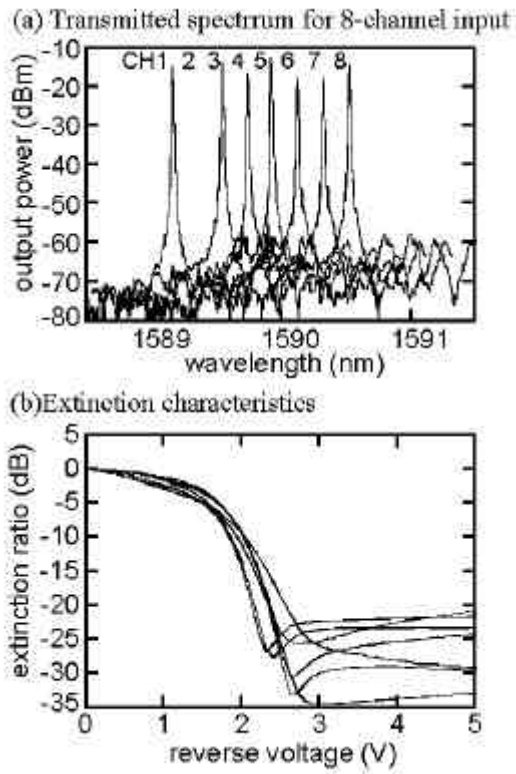


Figure 11. Characteristics of the multi-wavelength modulator.

The extinction characteristics of each port are shown in Fig. 11 (b) where the SOA current is 200 mA and the input power is +8 dBm. An extinction ratio of better than 20 dB is achieved at a reverse voltage of 3V for all ports. These high extinction characteristics come from the InGaAs/InAlAs MQW layer; that is, the fabrication process allows us to use different optimized materials for SOAs and EAMs. The fabrication process does not degrade device performance, as the value is equivalent to that of stand-alone EAMs.

.

III. Summary

The development of the arrayed waveguide grating (AWG) enables us to make optical filters good enough for WDM application on semiconductor substrates. Thanks to the progress in the fabrication technologies, now, we can fabricate integrated devices containing both passive and active devices by using the but-joint with the semiconductor AWGs. The compact devices fabricated with the monolithic integration promise next generation WDM systems possibly use a large number of optical devices with reasonable cost and with reasonable space.

[1] M. Zirngibl, C. H. Joyner, L. W. Stulz, “WDM receiver by monolithic integration of an optical preamplifier, waveguide grating router and photodiode array,” Electronics Lett vol. 31, no. 7, pp. 581 -582, 1995.

[2] C. A. M. Steenbergen, C. van Dam, A. Looijen, C. G. P. Herben, M. de Kok, M. K. Smit, J. W. Pedersen, I. Moerman, R. G. F. Baets, B. H. Verbeek, “Compact Low Loss 8 X 10 GHz Polarisation Independent WDM Receiver,” 22nd European Conference on Optical Communication, 1996. ECOC '96. proceeding on vol. 1 , pp. 129 -132

[3] M. R. Amersfoort, J. B. D. Soole, H. P. LeBlanc, N. C. Andreadakis, A. Rajhel, and C. Caneau, “8 x 2nm Polarization-Independent WDM Detector Based on Compact Arrayed Waveguide Demultiplexer,” IPR'95 PD-3.

[4] A. A. M. Staring, C. van Dam, J. J. M. Binsma, E. J. Jansen, A. J. M. Verboven, L. J. C. Vroomen, J. F. de Vries, M. K. Smit, B. H. Verbeek, “Packaged PHASAR-based wavelength demultiplexer with integrated detectors,” Integrated Optics and Optical Fibre Communications, 11th International Conference on, and 23rd European Conference on Optical Communications, pp. 75 - 78 vol.3, 1997.

[5] M. Kohtoku, S. Oku, Y. Kadota, Y. Shibata, J. Kikuchi, Y. Yoshikuni, “Unequally spaced 16 Channel Semiconductor AWG WDM Monitor Module with Low Crosstalk (<-24 dB) Characteristics,” ECIO'99 ThA2.

[6] H. Suzuki, N. Takachio, O. Ishida, and M. Koga, “Dynamic gain control by maximum signal power channel in optical linear repeaters for WDM photonic transport networks,” IEEE Photon. Technol. Lett., vol. 10, No.5, pp.734-736,1998.

[7] Ryoko Yoshimura, Yoshihisa Sakai, Hiroaki Sanjoh, Masaki Kohtoku, Hiromasa Tanobe, and Yuzo Yoshikuni, “A 16-channel simultaneous detection of gigabit signals with a compact WDM receiver containing a monolithically integrated AWG-PD,” Proc. OFC2002, Anaheim, USA, 2002.

[8] M. Kohtoku and Y. Yoshikuni, “A semiconductor arrayed waveguide grating and its application to a multiwavelength photodetector,” in IEEE Lasers and Electro-Optics Society 2000 Annual Meeting, (Institute of Electrical and Electronics Engineers, New York, 2000), Vol. 1, pp. 342-343.

[9] M. Zirngibl, C. H. Joyner and B. Grance, “Digitally tunable channel dropping filter/equalizer based on waveguide grating router and optical amplifier integration,” IEEE Photon Technol, Lett., 6, pp. 513-515, 1994.

[10] M. K. Smit and C. van Dam, “PHASAR-based WDM-deices; Principles, design and applications,” IEEE J. Select. Topics in Quantum Electron., 2, pp.236-250, 1996.

[11] M. Kohtoku, H. Sanjoh, S. Oku, Y. Kadota, and Y. Yoshikuni, “Polarization independent Semiconductor arrayed waveguide gratings using a deep ridge waveguide structure,” IEICE Trans. Electron., E81-C, pp. 1195-1204, 1998.

[12] H. Ishii, H. Sanjoh, M. Kohtoku, S. Oku, Y. Kadota, Y. Yoshikuni, Y. Kondo, and K. Kishi, “Monolithically integrated WDM channel selectors on InP substrates,” ECOC’98, vol. 1, TuD06, pp. 329-330,1998.

[13] N. Kikuchi, Y. Shibata, H. Okamoto, Y. Kawaguchi, S. Oku, H. Ishii, Y. Yoshikuni, and Y. Tohmori, “Monolithically integrated 64-channel WDM channel selector with novel configuration,” Electron. Lett., vol. 38, pp.331-332, 2002.

[14] N. Kikuchi, Y. Shibata, H. Okamoto, Y. Kawaguchi, S. Oku, H. Ishii, Y. Yoshikuni, and Y. Tohmori, “Error-free signal selection and high-speed channel switching by monolithically integrated 64-channel WDM channel selector,” Electron. Lett., vol. 38, pp.823-824, 2002.

[15] Y. Suzaki, K. Asaka, Y. Kawaguchi, S. Oku, Y. Noguch, S. Kondo, R. Iga, and H. Okamoto,”Multi-channel modulation in a DWDM monolithic photonic integratied circuit,” Proceedings 14th IPRM, pp.681-683, Stockholm, Sweden, 2002.

[16] R. Kr¨ ahenb¨ uhl, R. Kyburz, W. Vogt, M. Bachmann, T. Brenner, E.Gini, and H. Melchior, “Low-loss polarization insensitive InP/InGaAsP optical space switches for fiber optical communications,” IEEE Photon.Technol. Lett., vol. 8, pp. 632–634, May 1996.

Confocal Luminescence Microscopy: Application to Periodically Poled $LiNbO_3$ Devices

Volkmar Dierolf and Christian Sandmann
Physics Dept., Lehigh University, Bethlehem, PA 18015, USA
vod2@lehigh.edu

Using the recently developed imaging technique of confocal defect-luminescence microscopy, we investigated Er^{3+}-doped periodically-poled $LiNbO_3$ waveguide devices and found that the Er^{3+} ion can be used effectively as a local probe. Scanning over the sample, and evaluating the emission spectra, high resolution three dimensional images of the ferroelectric domain structure can be obtained non-destructively and free of topographical artifacts. The achieved contrast is based on the observation that even in well tempered samples, differences in intrinsic electric (strain) fields and defect arrangements exist for regions which have been domain inverted, are as grown, and most notably, are in the $\approx$1 μm wide region between oppositely poled domains.

Keywords: waveguide imaging, PPLN, optical spectroscopy, Er^{3+}

Introduction

Nonlinear light sources based on periodically poled $LiNbO_3$ have gained a great deal of attention due to low thresholds, ease of operation, and wide tuning range. In particular, the integrated optical versions of them, achieve, due to the confinement of light over long interaction lengths very high conversion efficiencies (see e.g.: [1, 2]). In order to optimize the latter, both the Ti-profile and the domain structure have to be engineered precisely and effects of interaction have to be under control. In order to achieve this goal we developed a novel characterization tool based on the luminescence of well characterized designer defects that we use as probes for the local environment. For our work we chose Er^{3+} ions because, through many studies [3, 4, 5, 6, 7] of this rare earth ion in $LiNbO_3$, detailed information about the optical transitions and their dependence on the local lattice environment are known. For instance, the spectral shifts, which are a signature for changes in the local electric fields in z-direction and of rearrangement of the surrounding oxygen ions, were characterized by application of electric fields and hydrostatic pressure[8]. In this paper we report how the spectral information can be used to create images of waveguides and periodically poled domain structures with sub-μm spatial resolution.

Experimental techniques and results

Samples. The periodically poled waveguide $LiNbO_3$ sample was obtained from the group of Prof. Sohler. It was produced in the "standard" way starting from commercial z-cut $LiNbO_3$ wafers. After Er^{3+} and Ti^{4+} indiffusion producing a Er^{3+}-doped planar layer and Ti:$LiNbO_3$ channel waveguides, the sample was periodically poled (period 31.42 μm) by electric field application at room temperature. To remove intrinsic stress, the sample was tempered at T>120°C, such that the domains were no longer visible in a polarization-contrast microscope. Details see Ref. [2].

Confocal defect luminescence microscopy. This technique combines the atomic-level information contained in optical spectra with the spatial resolution of a optical microscope. In our set-up the waveguide samples were mounted in a He-microscope cryostat, which allows temperatures down to 4K. The Er^{3+} ions were excited by a laser (dye-lasers or 488nm argon laser) through a home-built microscope (NA up to 0.7) operated in the confocal mode. The pinhole usually required in this mode was replaced by a single mode fiber allowing easy change of the excitation source. The resulting emission was detected in the reverse direction through the same microscope, coupled back into the fiber, and separated from the excitation light by a

dielectric mirror. Finally, the emission spectra are measured in a 0.5m-spectrometer equipped with a LN-cooled CCD array allowing the measurement of 10 spectra/s. For imaging purposes, the microscope is scanned in three dimensions over the samples in fine steps (200nm) and the first and second moments of the recorded spectra ($\approx 10^5$) are determined and displayed as a function of the probing position.

Waveguide imaging. In earlier studies [9, 10] we have shown that the optical spectrum of Er^{3+} depends strongly on the concentration of the ions Ti^{4+} or Zn^{2+} which are used to define the waveguide. Most notably, we found a strong inhomogeneous broadening of the spectral lines and a small spectral shift. Due to the nature of these changes, we obtain the highest contrast if the second moment is evaluated. An example of an image is shown in Fig. 1. For this image we excited the Er^{3+} ions at 652nm and detected their emission at around 980nm. However, other wavelength combinations work as well. The image was recorded by scanning the front surface of the waveguide focussing about 10 μm inside the sample. The best contrast is achieved when the spectra are recorded at low temperature.

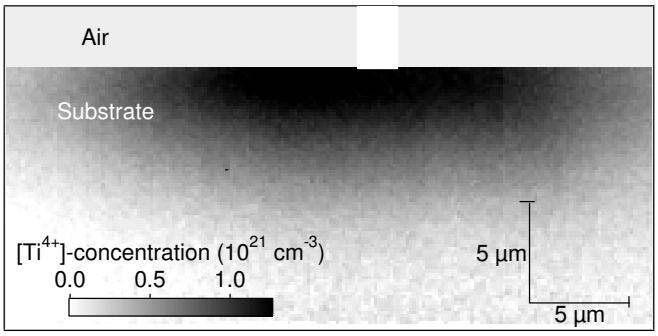


Fig.1. Image of the Ti^{4+}profile defining a single mode waveguide. The image is obtained by evaluating the emission spectra while probing over the front face of the sample

Imaging periodically poled domain structures. Figure 2 shows one out of the five measured emission bands in the green which were recorded under 488nm excitation for regions with different domain orientation (1,2) and between the domains (3). The differences are very small but notable. It has been found earlier that domain inversion changes the distribution of defect sites[11] leading to different relative emission intensities of the corresponding emission peaks. Comparing region (1) and (2), we find a small decrease on the high energy side and an increase on the low energy side which is consistent with this interpretation. More pronounced is the difference for region (3), for which a clear spectra shift is observed, which can be attributed, at least partially, to a decreased electric field in z-direction experienced by the Er^{3+} ion. The spectral changes can be quantified more precisely by evaluating the first moment for the complete spectrum. Figure 3b shows a scan along the horizontal direction covering several changes in the domain orientation. Especially for the first moment (dotted line) clearly different values are obtained for the three regions making it very suitable for imaging as shown in Fig. 3a. The image has good contrast and shows fine details of the structure. It was taken mainly in regions without waveguides. On the bottom of the image a Ti^{4+} diffused waveguide region starts, leading to a gradual change of the emission spectra and the corresponding moments.

The second moment (solid line), which characterizes the spectral width or spread of the spectra, emphasizes very strongly the change occuring in-between domains. Indeed, it is expected that changes in the intrinsic electric field, obviously occuring in theses regions, will change the Stark splitting of the 4f-levels and hence the spread of the spectrum and the second

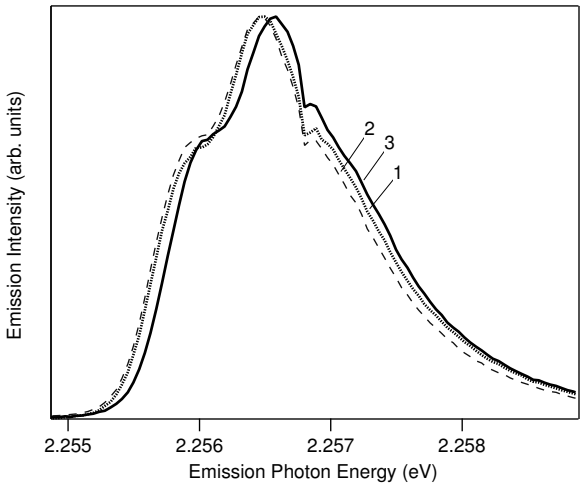


Fig. 2. Expanded view of the measured emission spectra for the regions 1,2, and 3 indicated in Fig. 3 obtained under excitation with 488nm. Only one out of the 5 measured emission bands is depicted. Changes in the other peaks are even less pronounced.

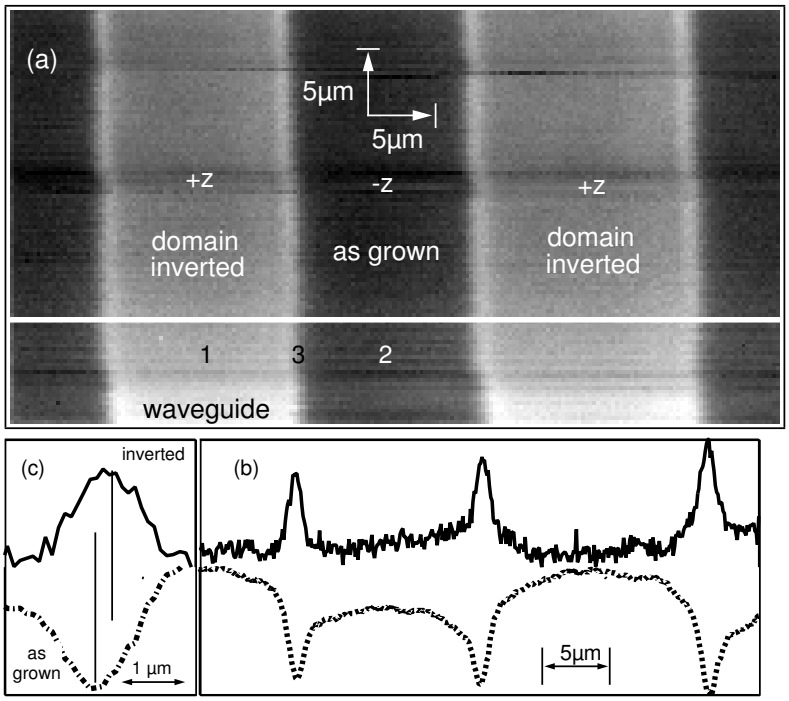


Fig. 3. (a) Image of a periodically poled $LiNbO_3$ sample obtained by evaluating the first moment of the optical spectra of Er^{3+} measured in a scanning confocal luminescence microscope. (b) Line scan of the first (dotted line) and second moment (solid line) of the spectrum. (c) same as (b), but in expanded scale in the region of the domain wall.

moment. Looking even more closely (Fig3c) at the line scans of the first and second moment in the transition regions reveals a small offset indicating that not only one cause is responsible for the change. We assume that we are dealing in the domain wall region with both a change in intrinsic electric field and a redistribution among the possible Er^{3+} defect sites. The two obviously do not (and do not have to) coincide with each other spatially.

The rate of change in the moments indicate that our spatial resolution is better than 1μm even though only an objective with numberical aperture of 0.3 was used in these measurements allowing still room for improvement. While all the measurements have been performed at low temperatures (in order to extract details), we found that optical spectra taken at room temperature are sufficient for imaging purposes.

Summary and Conclusions

We demonstrated the possibility of imaging Ti^{4+}-concentration profiles and ferroelectric domain structures in Ti:Er:$LiNbO_3$ waveguides by defect luminescence microscopy. Although, the underlying mechanism responsible for the contrast, which is an interesting topic all by itself, is not completely clarified, yet, this non-invasive technique may prove especially valuable for development of waveguide technology on $LiNbO_3$ material, which has been modified in terms of stoichiometry, co-doping and which underwent different thermal and/or chemical treatments. The concentration of e.g.: Er^{3+} probe ions can be kept very low permitting application of the method in samples for which the functionality of the ion is otherwise not required. Traces ($10^{-3} mol\%$) introduced by doping or diffusion are sufficient. Due to the fact that our imaging technique is based on evaluating the spectral information, it is insensitive to intensity fluctuations and is free of topographic artifacts.

We thank the Prof. Sohler and his group at the University of Paderborn for supplying the sample.

[1] M.H.Chou, I. Brener, M. Fejer, E. Chaban, and S. Christman, *IEEE Photon. Technol. Lett.* **11**, p. 653, 1999.

[2] G. Schreiber, H. Suche, Y. Lee, W. Grundkotter, V. Quiring, R. Ricken, and W. Sohler, *Appl. Phys. B* **B73**, p. 501, 2001.

[3] V. Dierolf and M. Koerdt, *Phys. Rev. B* **61**(12), pp. 8043–52, 2000.

[4] L. Nunez, B. Herreros, R. Duchowicz, G. Lifante, J. Tocho, and F. Cusso, *J. Lumin.* **60-61**, pp. 81–4, 1994.

[5] W. Jia, K. Lim, H. Liu, Y. Wang, J. Ju, S. Yun, F. Fernandez, and W. Yen, *J. of Lumin.* **66-67**(1-6), pp. 190–7, 1995.

[6] D. Gill, J. Wright, and L. McCaughan, *Appl. Phys. Lett.* **64**, p. 2483, 1994.

[7] G. Sole, L. Bausa, D. Jaque, E. Montoya, H. Murrieta, and F. Jaque, *Spectrochimica Acta Part A* **56**, pp. 1571–1581, 1998.

[8] V. Dierolf, A. Kutsenko, C. Sandmann, T. Tröster, and G. Corradi, *J. of Lumin.* **87-89**, pp. 989–992, 2000.

[9] V. Dierolf, A. Kutsenko, A. Ostendorf, and C. Sandmann, *App. Phys B* **73**, pp. 443–450, 2001.

[10] V. Dierolf, A. Kutsenko, A. Ostendorf, W. von der Osten, W. Sohler, and H. Suche, *Appl. Phys. B* **72**(7), pp. 803–10, 2001.

[11] V. Dierolf, C. Sandmann, S. Kim, V. Gopalan, and K. Polgar, *J. Appl. Phys.* **93**(5), in print, 2003.

Characterization of ion exchanged integrated lightwave devices with an apertureless scanning near-field optical microscope

Sébastien Aubert*, Elise Ghibaudo+, Aurélien Bruyant*, Sylvain Blaize*, Renaud Bachelot*, Gilles Lerondel*, Pascal Royer*, Jean-Emmanuel Broquin+
aubert@utt.fr

*Laboratoire de Nanotechnologie et d'Instrumentation Optique, Université de Technologie de Troyes, 12 rue Marie Curie, BP2060, 10010 Troyes cedex, France
+Institut de Microélectronique, Electromagnétisme et Photonique, LEMO-ENSERG, UMR 5530, INPG-UJF, 23 rue des Martyrs, BP257, 38013 Grenoble, France

An apertureless scanning near-field optical microscope is used to characterize ion exchange lightwave devices. Experimental images of field propagation are presented in such devices as channel and segmented waveguides. This tool permits accurate measurement of propagation constants and mode profiles.

Keywords: guided-wave optics, ion exchange technology, characterization methods, scanning near-field microscopy

Introduction

The mapping of optical field propagation in confined waveguides structures is very important for a comprehensive understanding of these structures design. Near Field Scanning Optical Microscopes (NSOM) permit non-destructive investigations of the optical evanescent field, which propagates at the surface of lightwave devices, with a subwavelenght resolution.

The technique is particularly suitable for the study of ions exchanged integrated devices because of the graded nature of the refractive index profile entailed by the ions diffusion process: the classical investigation methods as cut-back measurements are destructive, or not enough accurate to give good description of hidden characteristics such as profile and propagation constants of the guided field. In addition diffused waveguide geometry cannot be precisely known because of the lack of topography information.

There are currently two main classes of NSOM probes. First kind uses tapered optical fibers [1] used to pick up the light from the near field region of the studied structures. The light is coupled into the fiber and detected at the other fiber extremity. The alternative approach is based on the use of an apertureless sharp dielectric or metal tip, acting as a scattering center in the near field region. The radiated field emitted by the tip end is collected by an external optical detection system. This configuration is so called Apertureless-NSOM (ANSOM). This second approach presents many advantages [2] regarding the first one in term of tip design and realization facilities, tip robustness, high resolving power (related to the tip diameter) and achromatic behavior.

We propose to characterize quantitatively the signal collected with an ANSOM in the near field region of ion-exchanged waveguides realized in a silicate glass substrate. In the first part, we present the experimental apparatus. In the second part, a quantitative study of an integrated channel waveguide shows the ASNOM accuracy and preliminary results with other lightwave devices as light propagation in segmented waveguides are presented.

Experimental

The experimental configuration used for this study is depicted in Fig. 1. The ANSOM has been developed from a commercial AFM (model M5 from Park Scientific Instruments). The optical probe is a sharp silicon or metal tip with a terminal radius of above 50 nm. The waveguide sample is mounted on two nano and micro scale x-y piezoelectric scanners. Thanks to these scanners, the

tip is able to scan the sample in the surface near field zone of the guided waves. The tip to surface distance is controlled by the atomic force regulation in the intermittent-contact mode (also called “tapping mode”). This entails a tip vibration in the z direction, perpendicularly to the sample. The vibration amplitude is about 25 nm at f=180 kHz frequency. The atomic force feedback ensures constant vibration amplitude during the image recording session and leads to the topography measurement. The inset in Fig.1 shows AFM topography of the waveguide top surface recorded over a 10x10 µm2 scanned area. It reveals relics (amplitude of a couple nanometers) of the diffusion aperture mask of 1.7 µm width. This lets us localize precisely the studied waveguide. Simultaneously to this atomic force microscopy, the optical scattered flux, from the tip end in local interaction with guided waves, is far-field collected thanks to a confocal optical microscope.

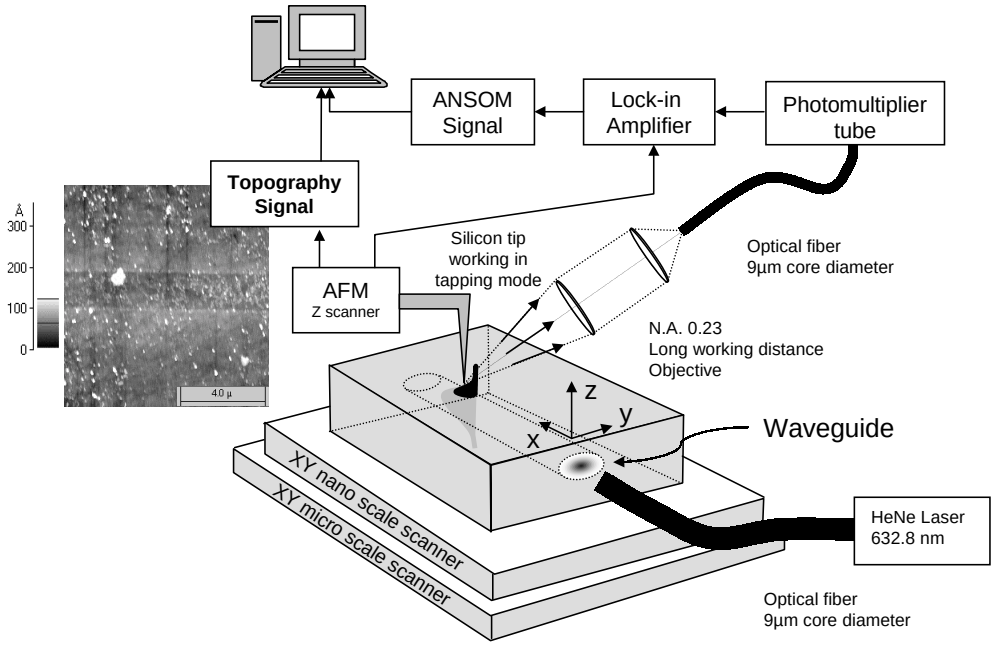


Figure 1: Experimental ANSOM configuration used for the study. An evanescent wave is generated at the air/waveguide interface by total internal reflection in the waveguide.

The optical signal part, transported in the surface evanescent field, and scattered in the detection direction is very weak, but a lock-in signal extraction technique at the tip vibration frequency f provides a reasonably high level of ANSOM signal.

Mapping the propagation of light

The optical waveguide under study has been produced using two-steps Ag+/Na+ ions exchange process in a silicate glass substrate, and buried at about 3µm beneath the glass top surface by the mean of thermal rediffusion process. A full detailed description of the fabrication steps is given elsewhere [3]. The guide was formed through a 1.7 µm diffusion aperture width. The diffusion process entails a transverse graded index profile, which is not measurable with accuracy in the case of such confined waveguide, but its mean index variation is empirically estimated to be about 10^{-2} above the substrate refractive index value of 1.515. Far field measurements of the waveguide mode field dimensions with a CCD beam profiler showed that single transverse mode at wavelength=1.55

µm was supported whereas multimode transverse operation was revealed at wavelength=0.633 µm. We set our working wavelength to 0.633 µm in order to visualize the waveguide multimode behavior with the ANSOM technique.

The ANSOM image reveals a strong intensity beat operation along the direction of propagation in the waveguide. This is characteristic of a multimode behavior. More precisely the beat occurs at least between the 3 lowest order modes. The modulus of the Fast Fourier Transform (FFT) amplitude spectrum calculated on a longitudinal profile on the direction of propagation, extracted from the raw image 1 (along the white dashed line) shows two strong maxima corresponding to periodicities of 206.9 ±0.2 nm and 207.8±0.2.These peaks reveal the presence of a periodic intensity variation in the direction of propagation due to the cavity formed between the waveguide entrance and exit facets. In fact the existence of 3 supported guided modes entails a superposition of 3 standing wave patterns with periodicities of $\lambda_0/2n_{eff(i)}$, i=0,1,2 . We showed experimentally that the deposition of an anti reflection liquid index on the output waveguide facet makes the fringes pattern to vanish. The corresponding calculated effective indexes are 1.529±0.002 and 1.522±0.002 for respectively mode TE0 and mode TE2. These values are in good agreement with the experimental measurement of the beat length. The fringes pattern related to the TE1 mode is not visible. This is due to the relatively low spectral resolution on the FFT spectrum. We need to perform a longer scan to discriminate the three modes contributions in the standing wave pattern.

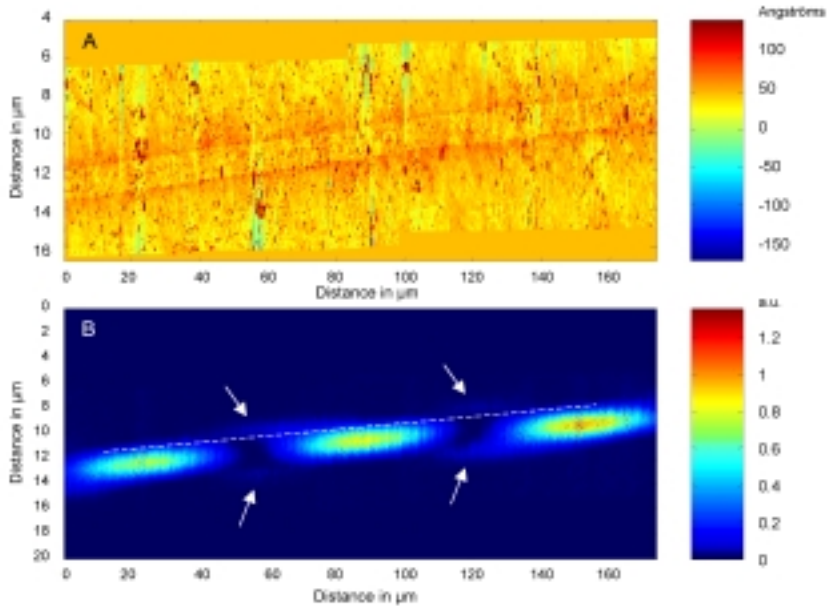


Figure 2: Waveguide characterization. A: topography image. B: Optical intensity mapping. White arrows point out the TE_2 mode contribution, the white dashed line represents the waveguide longitudinal direction. The FFT profile was performed along this line (see text for comments).

The ASNOM is a very accurate tool to determine effective index. This can be helpful in the case of segmented waveguide [4]. The segmentation can be used to obtain effective index closed to the substrate index in a controlled way by tuning the length of the segment or the period of segmentation. Fig. 3A shows the surface topography of a segmented waveguide. This optical waveguide has been produced using K+/Na+ ions exchange process in a silicate glass substrate. No burying process has been used. In this case, because of respective sizes of exchanged ions at the surface the glass inflates. Hence, one segment is visible through the topography image.

Fig 3B is the ASNOM image. The image shows a multimode behavior since the field is not centered, focusing effect is observed. These images are presently under study in our laboratory. We intend to measure effective index and study the propagation of light in such structures.

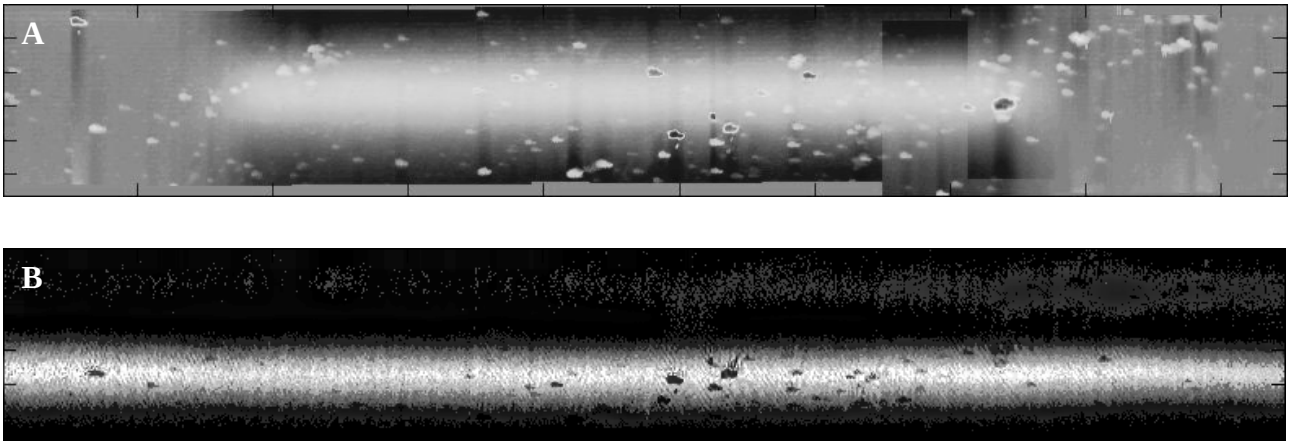


Figure 3: AFM topography image(A) and ASNOM image of a single segment on an ion exchange segmented waveguide. Both images represent a 15 μm by 110 μm scan.

Conclusion

Glass integrated ion exchanged waveguides have been successfully characterized by Apertureless Near-field Scanning Optical Microscopy (ANSOM). The experimental setup was made from the combination of a commercial AFM microscope and an optical confocal detection system. The main advantage is to record topography images and optical near-field images simultaneously, with the benefit of the high scanning probe resolution (tip radius of few tens of nanometers) along with a large scan size.

The Fourier transform analysis of the intensity profile lets us evaluate directly the effective index of eigenmodes with a precision of 2.10^{-3}. This shows that ANSOM can be an accurate tool. We intend to perform longer scans to increase precision on the refractive index measurement.

Promising investigations are made to develop a heterodyne signal detection scheme based on a Mach-Zender interferometer [5]. Besides the removal of background field contribution, the interferometric setup will allow the simultaneous mapping of both propagated field intensity and phase. We anticipate the ANSOM technique to become a key measurement tool for ion exchanged optical waveguide and more generally for integrated lightwave devices.

[1] M. L. M. Balistreri, J. P. Korterik, G. J. Veldhuis, L. Kuipers, N. F. Van Hulst, J.Appl.Phys. **89(6)**, 3307-3314, 2001
[2] R. Bachelot, P. Gleyzes, A. C. Boccara, Opt. Lett. **20**, 1924
[3] J. E. Broquin, Proc. SPIE, **4277**, 105-115, 2001
[4] Z. Weissman, A. Hardy, J. Lightwave Technol **11(11)**, 1831-1837, 1993
[5] M. L. M. Balistreri, J. P. Korterik, L. Kuipers, N. F. Van Hulst, Phys. Rev. Lett. **85(2),** 294-297, 2000

Method for measuring frequency chirping in external Mach-Zehnder modulators

Nadège COURJAL,

Laboratoire d'Optique P.M. Duffieux, UMR CNRS 6603, Université de Franche Comté,
Institut des Microtechniques (IMFC), 25030 Besançon Cedex, France
Email : nadege.bodin@univ-fcomte.fr

Henri PORTE
* Photline Technologies, 25001 Besançon CEDEX 3, BP71025
Email : henri.porte@photline.com

We propose a new simple and direct method for measuring the frequency chirping of Mach-Zehnder modulators. The interest of the method lies in the low optical and microwave powers that are required for the experiments.

Keywords: chirp measurement, Mach-Zehnder, modulation, spectral density

Introduction

Knowledge of the chirp parameter α of Mach-Zehnder modulators is essential to account for the propagation of short pulses in fibres. Several indirect [1,2,3] techniques have been suggested to determine the chirp. More direct evaluations [4] have also been proposed to extract the chirp parameter from the output density spectrum. All these experiments require several manipulations, or high optical power and driving voltage. We propose a new method to allow for the measurement of the chirp parameter at very low optical and microwave powers. This method consists in directly evaluating the sidebands amplitude in the output spectrum for two cases of bias. Part I describes the relationships that yield the determination of the chirp parameter α, and part II illustrates the method with experimental results.

Experimental setup and theory

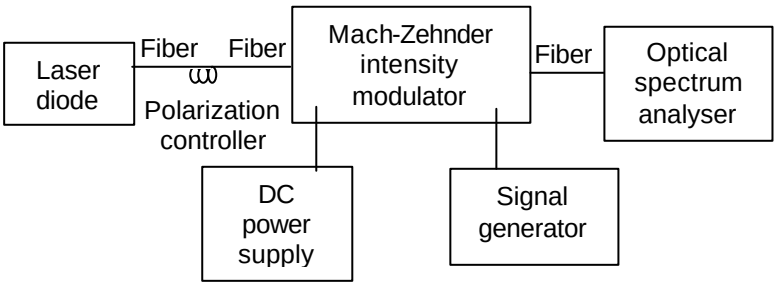


Figure 1 : Setup used to measure the chirp parameter of a Mach-Zehnder external modulator

The experimental setup for measuring α is shown in figure 1. A polarized 1.55µm light is launched at the input of a Mach Zehnder modulator. An adjustable continuous bias : $\Delta\varphi_{DC}$ is imposed between the two optical channels of the Mach-Zehnder modulator by means of a DC power supply. A high frequency sinusoï dal voltage : $V(t)=V_0 \cdot \cos(2\pi ft)$ is applied to the transmission lines of the modulator, in order to generate a sinusoï dal difference of phase $\Delta\varphi(t)$

between the two arms of the modulator. V_0 is the amplitude of the applied voltage, and f is the modulation frequency. The spectral density of the output optical field is measured by the help of a scanning Fabry Perot used as an optical spectrum analyser. This output optical field can be described as :

$$\underline{E}(t) = E_0 \cdot e^{j\omega t} \cdot e^{j\varphi(t)} \cos\left(\frac{\Delta\varphi(t)}{2} + \frac{\Delta\varphi_{DC}}{2}\right) \qquad (2)$$

where ω_0 is the pulsation of the optical wave, and E_0 is the amplitude of the optical field.

The chirp parameter of Mach-Zehnder modulators is strongly dependant on $\varphi(t)$ and $\Delta\varphi(t)$. In fact, at small signal regime and quadrature bias, the output intensity is linear with $\Delta\varphi(t)$. So the general expression of the chirp parameter [5] can be simplified to :

$$\alpha = \mp \frac{\varphi(t)}{\Delta\varphi(t)/2} \qquad (3)$$

This expression leads to $\alpha=\Phi/(\Delta\Phi/2)$ in case of a sinusoï dal modulation, where Φ and $\Delta\Phi$ are the magnitude of $\varphi(t)$ and $\Delta\varphi(t)$ respectively.
The presented method aims at determining the above parameter (3), by evaluating the output spectrum for two different bias. In case where $\Delta\varphi_{DC}=0$, the output density evaluated from (2) is :

$$I_0(f) = E_0^2 \cdot \delta(\omega_0) + \frac{E_0^2}{2} \cdot \Phi^2 \cdot \delta(\omega_0 - f) + \frac{E_0^2}{2} \cdot \Phi^2 \cdot \delta(\omega_0 + f) \quad (4)$$

Let us now consider the case where $\Delta\varphi_{DC}=\pi$. The output density spectrum becomes :

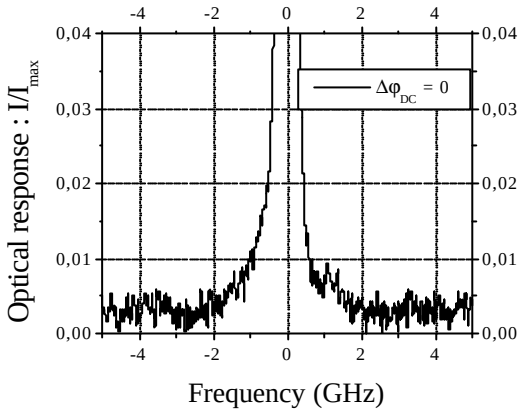
$$I_0(f) = \frac{E_0^2}{2} \cdot \left(\frac{\Delta\Phi}{2}\right)^2 \cdot \delta(\omega_0 - f) + \frac{E_0^2}{2} \cdot \left(\frac{\Delta\Phi}{2}\right)^2 \cdot \delta(\omega_0 + f) \quad (5)$$

The method for evaluating the chirp parameter $|\alpha|$ can be sumed up by two steps : at first, the 0-bias is set by monitoring the power supply so that the central intensity is maximal, which corresponds also to the minimum of the first harmonic peak. The measurement of the first sideband magnitude is then followed with the same measurement at π-bias, which is characterised by the maximum of the first order peak. The ratio of these two evaluations is the square of α.

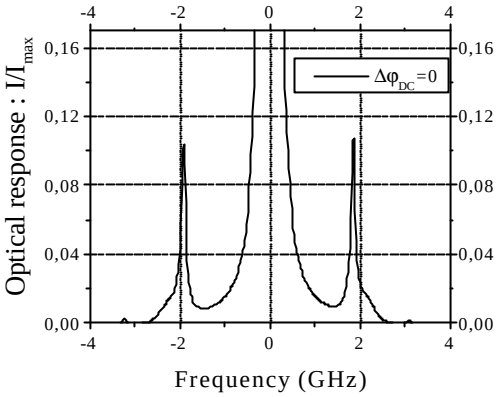
Examples of application

We performed the measurements as specified above with two kinds of $LiNbO_3$ Mach-Zehnder modulators. The microwave power was set to 15dBm, so that the magnitude of second side band was negligible. The free spectral range of the scanning Fabry Perot was 10GHz, which allowed measurements from 500MHz to 4GHz.

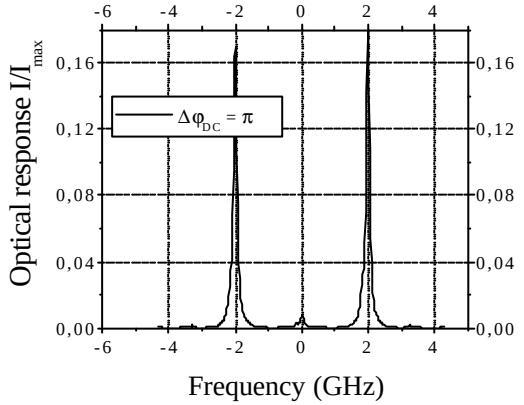
The line spectrum of the modulators are shown in fig.2, for a 2GHz modulation frequency : figure 2 a) and b) represent the normalized optical response for a 0 bias, while figure 2 b) and 2c) are relative to the optical response for a π bias. The optical power was kept the same for both spectra (P=0.2mW), so that the magnitudes inherent to each case of bias could be compared. Two kinds of modulators were successively tested. Figures 2b) and 2d) show the exprimental result corresponding to a Z-cut modulator, which chirp parameter was known to be 0.80. The line spectrum associated to a X-cut $LiNbO_3$ modulator are depicted in figures 2a) and 2c).



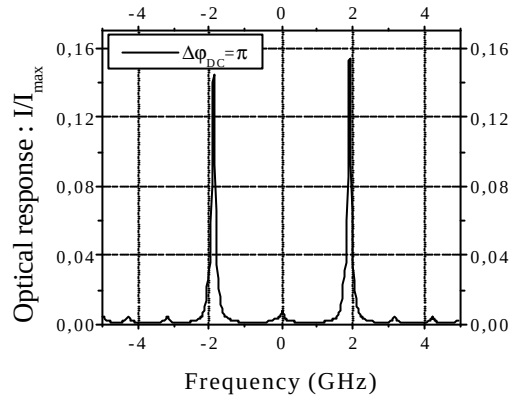
a) X-cut, $\Delta\varphi_{DC}=0$



b) Z-cut, $\Delta\varphi_{DC}=0$



c) X-cut, , $\Delta\varphi_{DC}=\pi$



d) Z-cut, $\Delta\varphi_{DC}=\pi$

Figure 2 : Optical spectrum lightwave from modulator;
Amplitude of applied RF electric signal = 2 V, Frequency of applied rf electric signal = 2GHz

The α parameter of the Z-cut modulator is evaluated from the magnitude of first sideband, as previously described, and shows out to be 0.83, which is in good agreement with the 0.80 predictions. The same method was applied for a symetric X-cut modulator, which has theoretically a zero-chirp parameter due to its symmetric structure. The very low amplitude of first sideband at 0-bias confirmed this theoretical prediction. Figure 3 shows the evolution of α with frequency for the two modulators tested. The dashed line stands for the α parameter of the Z-cut $LiNbO_3$ standard modulator, while solid line stand for the α parameter of a X-cut $LiNbO_3$ modulator. It can be seen from the figure that α is poorly dependant on f.

It should be emphasized that the above manipulation can also yield the evaluation of other main characteristics of modulation. In fact, the ratio between the central intensity at 0-bias and the central intensity at π-bias corresponds to the extinction ratio R: (R=20,6dB in case of the Z-cut modulator); Φ and $\Delta\Phi$ can be easily extracted from the relative strength of first sideband; and the knowledge of Φ, $\Delta\Phi$ and V_0 enables the determination of variation of phase per volt (η_1, η_2) for

each arm of the Mach-Zehnder modulator : $\eta_1=\frac{\frac{\Delta\Phi}{2}+\Phi}{V_0}$ for one of the optical channel, and $\eta_2=\frac{\frac{-\Delta\Phi}{2}+\Phi}{V_0}$ for the other optical channel.

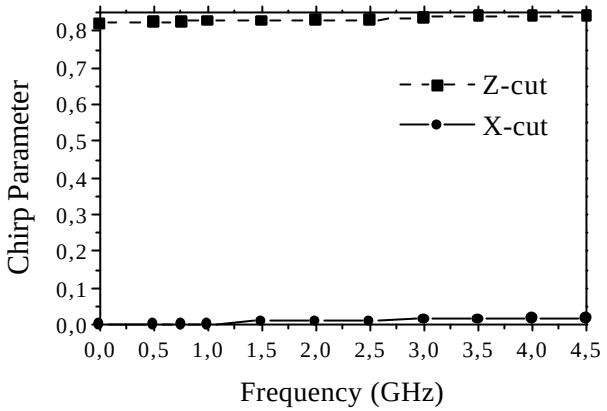


Figure 3 : Experimental evolution of α with frequency.

Conclusion

Two simple measurements with an optical spectrum analyser can yield the determination of the α parameter of Mach Zehnder modulators, with drive voltage lower than 5V, and very low optical power. In addition to the simplicity of equations and manipulation, another advantage of the experimental setup is its ability to account for the dependance of α on frequency. Finally, the proposed technique enables the evaluation of other main characteristics of the modulator, such as extinction ration, modulation depth and overlap electric/optical field coefficients.

References

[1] F. Koyoma, and Y. Suematsu," Analysis of dynamic spectra width of Dynamic-Single-Mode (DSM) lasers and related transmission bandwidth of single mode fibers", *IEEE J. Quantum Electron.*, vol QE21, pp292-297, 1985

[2] F. Devaux, Y. Sorel, and J.F. Kerdiles, "Simple measurement of fiber dispersion and of chirp parameter of intensity modulated light emitter", *J. Lightwave Technol.*, vol.11, no12, pp1937-1940, dec. 1993

[3] B. Kowalski, J. Debeau, and R. Boittin, "A simple and novel method for measuring the chirp parameter of an intensity modulated light source", *IEEE Photon. Tech. Letter*, vol.11, no6, pp700-702, june 1999

[4] T. Kawanishi, K. Kogo, S. Oikawa, M. Izutsu, ,"Direct measurement of chirp parameters of high speed Mach-Zehnder Type optical modulators", *Optics Com.*,vol.195 pp399-404, Aug. 2001

[5] F. Koyama, and K. Iga, "Frequency Chirping in External Modulators", *J. Lightwave Technol.*, vol.6, n°1, pp87-93, jan. 1988

A novel technique for high precision measurement of alignment accuracy of single-mode optoelectronic components

Gunnar Arvidsson, Magnus Olson and David Evekull
Acreo AB, Electrum 236, SE-164 40 Kista, Sweden
gunnar.arvidsson@acreo.se

We describe technologies for cost-effective assembly of single-mode optoelectronic components, and report a novel technique to verify with sub-micrometer precision the alignment accuracy by flip-chip soldering.

Keywords: self-alignment, flip-chip, low-cost, assembly, single-mode, alignment accuracy, measurement method, moiré-effects

Introduction

In the world-wide communication network the traffic is still increasing, in particular the internet traffic, and the access networks will soon become a bottle neck. An increasingly important part of the access network is the radio access network. For the next generation of high capacity mobile communication system distribution of signals into a dense mesh of radio base stations is crucial. The access networks thus need to be upgraded in the near future, and it is highly desirable to introduce optical single mode technology.

For transceivers developed for the trunk network, issues such as performance and long term reliability has been of prime interest and there has been no strong driving force to reduce the production cost. In this new scenario single mode optoelectronic components such as transceivers will be needed in very large volumes compared to the transport network and the cost for each component will not be shared by as many users as in the transport network. This will require that key optoelectronic components can be produced at substantially lower cost than previously.

Assembly of optoelectronic single mode components

Some key technologies that can contribute to lower cost for optoelectronic devices are

- hybrid integration
- passive alignment
- non-hermetic encapsulation

We will here in particular discuss passive alignment. Active alignment of, e.g., semiconductor lasers, requires that they are electrically connected. The alignment is iteratively optimised until coupling from the laser diode into a fiber is maximized. Using passive alignment electrical connections are not required. The electrooptical components are instead appropriately positioned using alignment marks or similar techniques. Several alternative methods for passive alignment have been reported, in particular:

1. Soldering using an infrared vision systems in combination with registration marks, so that alignment can be verified by IR radiation penetrating through carrier and semiconductor component [1,2]. The laser is positioned with high accuracy before it is soldered in place, and held in position during soldering
2. A soldering method similar to the previous technique, but based on very high precision mechanical system in combination with a computer controlled vision-system [3]. By observing the alignment marks before the parts are put into position, and relying on high precision mechanics, optical systems in the visible can be used.

3. Self-aligning flip-chip soldering. The laser diode is placed roughly at the correct position, e.g. using a pick and place machine. The surface tension of the solder bumps is utilized to achieve self-alignment of the laser diode to the proper position [4,5], possibly in combination with standoffs or stops [6,7].

Method 1 and 2 above are well suited for mounting one chip on each carrier, but more difficult to apply in other cases, in particular difficult to extend to wafer level assembly. The third method – on the other hand – can be used to mount several components on the same carrier and is compatible with batch soldering as well as wafer level assembly. Furthermore the moderate requirements on the initial positioning of the components makes the method compatible with conventional moderate performance pick-and-place-equipment.

We have developed a version of the self-aligning method [8,9]. The basic alignment principle is

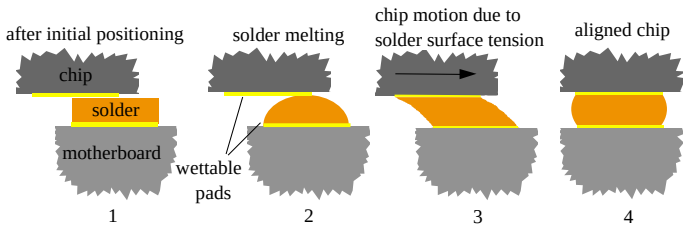


Figure 1 Schematic illustration of the self-alignment principle

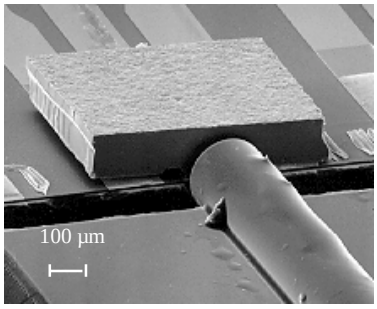


Figure 2 SEM picture of a flip-chipped diode laser self-aligned with respect to an optical fiber

schematically shown in Fig. 1. An example of a flipchip soldered laser diode is illustrated in Fig. 2 [8]. We have used this self-aligning-soldering technique to mount individual laser-diodes as well as array lasers versus fiber-grooves or polymer waveguides. Within the framework of a technology demonstrator for an array transceiver module we have furthermore mounted both an array laser and an array detector on each carrier [10]. The two components are positioned epi-side down on the appropriate solder pads on the carrier, and then both soldered in place in the same sequence and self-aligned to their proper positions

High precision measurement of alignment accuracy

When using passive alignment it would be of great interest to be able to measure with sub-micrometer accuracy the position of the chip versus the carrier. From a yield point of view, it is important to obtain this information as early as possible, before the following assembly steps. Such measurements are, however, difficult:

- The semiconductor chip is typically not diced or cleaved with enough accuracy so that the outer edges of the chip can be used as reference points for a measurement.
- Alignment marks need to be on the top face of the carrier and on the downside epi-face of the semiconductor chip. They are thus hidden between non-transparent substrates and difficult to evaluate with high accuracy.

We have developed a method based on moiré-effects, which requires only an infrared laser diode and a single photodetector together with standard electronics for evaluation. No infrared imaging optics is thus needed which strongly simplifies the implementation of the method. A periodic pattern – with a typical feature size of about five micrometers, well within standard processing limits – is formed in a metal layer on the carrier. This together with a similar pattern on the chip to

be mounted form a moiré-like pattern which can be analysed in real time during solder reflow, or, more conveniently, in a measurement phase after the soldering cycle. Various types of moiré and Vernier patterns are used to facilitate and evaluate alignment, for example with mask-aligners. Our evaluation technique, however, is novel to the best of our knowledge.

Silicon carriers and dummy chips have been fabricated. Electro-plating was used to form the solder-bumps of Au-Sn. Our first experimental tests of the method were carried out by moving a chip versus a carrier. The experimental evaluation set up is illustrated in Fig 3 and typical experimental results are shown in Fig 4. As seen in the figure a sub-micrometer resolution can be achieved.

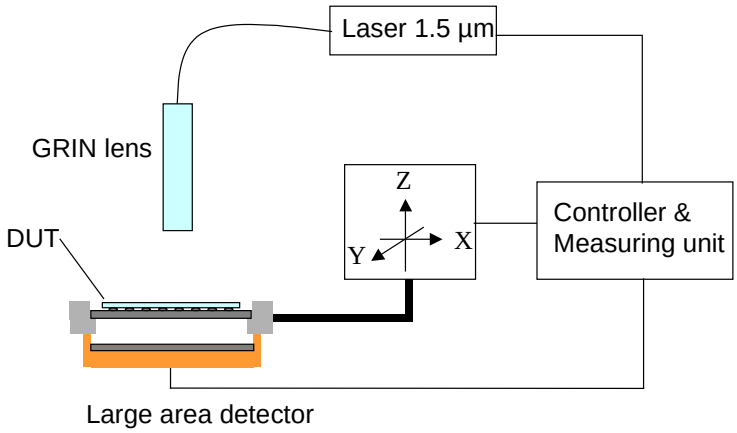


Figure 3 The set-up for verification of alignment accuracy. A fiber coupled 1.5 µm laser illuminates the moiré-pattern and a large area detector detects the transmitted light.

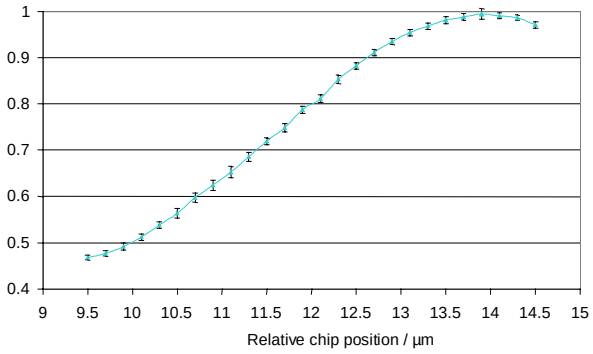


Figure 4 Output signal versus relative position for chip with respect to carrier.

In the next step we have started to do measurements after that chips have been soldered in place on carriers. In this case a somewhat more complicated pattern was used. Promising results have been obtained, illustrated in Fig 5. A number of measurements were done at different positions on the same chip. The method is designed in such a way that the minimum signal is obtained for the actual chip displacement, in this case about 0.4 µm. Further measurements are underway and analysis and more details will be reported at the conference.

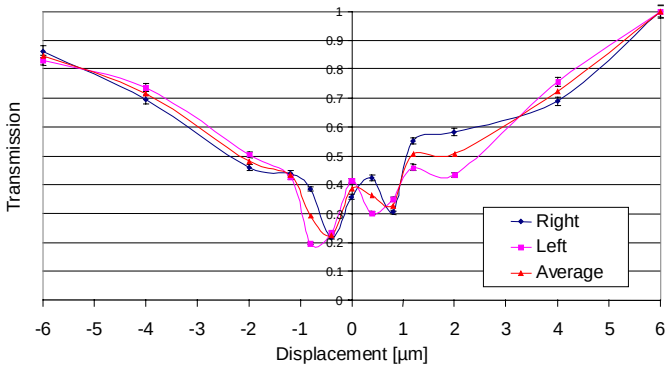


Figure 5 Measurement of alignment accuracy for chip self-aligned on silicon carrier, in this case indicating a displacement of about 0.4 µm

In conclusion: Self-aligning flip-chip soldering is a promising method for cost-effective assembly of single-mode optoelectronic modules. The method would be even more valuable if the position accuracy could be easily monitored or verified. We have developed a measurement technique, which combine sub-micrometer resolution with a comparatively simple and inexpensive evaluation equipment. The method could be used during solder reflow to monitor the process or after soldering to verify the results, as well as in future wafer level assembly.

Acknowledgements: We gratefully acknowledge the following Acreo co-workers for contributing to this work: Lennart Bäcklin (CAD design), Andy Scholes and Sara Ahlberg (process), Malin Gustavsson and Maria Is (assembly). This work was supported by Vinnova, the Swedish Agency for Innovation Systems.

[1] K. Kurata et al, "A Surface Mount Single-Mode Laser Module Using Passive Alignment", *IEEE trans. Components, Packaging, and Manufacturing Technology – Part B* **19**, pp. 524-531, 1996

[2] K. Tatsuno et al., "High-Performance and Low-Cost Plastic Optical Modules for Access Network System Applications", *J. Lightwave Techn.* **17**, pp. 1211-1216, 1999

[3] G Lecarpentier et al., "High Accuracy Machine-Automated Assembly for Opto-Electronics", *IEEE 50th Electronic Components & Technology Conference (ECTC 2000)*, Proc pp 15-20

[4] M. J. Wale and C. Edge, "Self-Aligned Flip-Chip Assembly of Photonic Devices with Electrical and Optical Connections", *IEEE Trans. Components, Hybrids and Manufact. Technol.* **13**, pp. 780-786, 1990

[5] Q. Tan and Y. C. Lee, "Soldering Technology for Optoelectronic Packaging", *46th IEEE Electronic Components & Technology Conference (ECTC 1996)*, Proc. pp. 26-36, 1996

[6] K. P. Jackson et al., "A High-Density, Four-Channel, OEIC Transceiver Module Utilizing Planar-Processed Optical Waveguides and Flip-Chip, Solder-Bump Technology", *J. Lightwave Techn.* **12**, pp. 1185-1191, 1994

[7] W. Rehm et al., "Low-Cost Laser Modules for SMT", *50th IEEE Electronic Components & Technology Conf (ECTC 2000)*, Proc. pp. 736-741

[8] S. Lindgren et al., "24-GHz Modulation Bandwidth and Passive Alignment of Flip-Chip Mounted DFB Laser Diodes", *IEEE Phot. Techn.. Lett.* **9**, pp. 306-308, 1997

[9] H. Åhlfeldt et al., "Passive Alignment of Laser Arrays to Single-Mode Fibers Using Microstructured Silicon Carriers", *IEEE/LEOS IEEJ/SAMS Intern. Conf. on Optical MEMS and their applications (MOEMS´97)*, Nara, Japan, Nov 1997, Techn. Dig. pp. 155-159

[10] G Arvidsson et al., "Hybrid integration technologies for a single mode array transceiver, including the use of polymer waveguides of benzocyclobutene", presented at SPIE's International Symposium Photonics Fabrication Europe, Brügge, Belgium, October 28 - November 1, 2002; to be published in Proc. SPIE vol 4947

Integrated SOA Devices for Metro System Applications

R.V. Penty, I.H. White, A.R. Davies, J. Sosabowski and K.A. Williams
Cambridge University Engineering Department,
Trumpington Street, Cambridge CB2 1PZ, UK
Tel: +44 1223 767029 Fax: +44 1223 767032 e-mail: rvp11@eng.cam.ac.uk

This paper will describe various applications for semiconductor optical amplifiers for metro applications. These applications include post and pre-amplification as well as more advanced functions such as gating and switching. It will show how the requirements for cascadability in future systems will necessitate the use of gain clamped SOAs and will describe a novel form of integrated gain-clamped SOA that allows variable gain. It will finally introduce a novel technique for controlling the output power of SOAs via monitoring of the SOA contact voltage without the need for any optical measurement.

Polarization based Integration Scheme (POLIS) for Active and Passive Components

U. Khalique, Y.C. Zhu, J.J.G.M. van der Tol, F.H. Groen, F. Karouta, E.J. Geluk, M.K. Smit

COBRA Inter-University Research Institute on Communication Technology,
Eindhoven University of Technology, Faculty of Electrical Engineering, Opto-Electronic Devices Group P.O.Box 513, 5600 MB Eindhoven, The Netherlands
U.Khalique@tue.nl

A.Y. Silov
Eindhoven University of Technology, Faculty of Applied Physics, Semiconductor Physics Group P.O. Box 513, 5600 MB Eindhoven, The Netherlands.

H.H. Tan
Department of Electronic Materials Engineering, Research School of Physical Sciences and Engineering, Australian National University, Canberra, ACT 0200, Australia

Polarization based integration scheme (POLIS) combines active and passive components on the same material, using polarization properties of compressively strained InGaAs/InP quantum wells. Devices have been fabricated, characterized and reasonable device performances have been observed.

Keywords: integration scheme, active, passive, polarization, indium phosphide, strained quantum well

Introduction

The evolution of information transport over optical networks is one of the drivers behind the upcoming information society. This development results in increasing demand for more complex optical functionality at ever-lower prices. The monolithic integration of these functions in an optical integrated chip (IC) opens the possibility for mass production, which will be able to fulfill this demand.

Essential to the success of mass production of optical integrated chips (IC) is a cheap, flexible and efficient integration technique. An optical IC will contain a variety of components, such as optical waveguides, light sources, detectors, optical switches etc. These functions put different requirements on the material system used, e.g. waveguides require transparent materials to keep the attenuation low, while on the other hand detectors need absorption of the light. Several solutions have been proposed and demonstrated to reconcile these conflicting requirements [1,2]. They all have however the disadvantage that additional processing steps are needed, e.g. applying extra material.

Here we report the idea of POLIS (POLarization based Integration Scheme) together with experimental results. It is based on the fact that properties of an optical IC are dependent on the polarization state of the signal. In general this is a severe problem, but here we use it to advantage. It is possible to design a layer structure on a substrate of indium phosphide (InP), which can guide light with one polarization, but absorbs light with the opposite polarization. This creates the possibility to integrate lasers and detectors together with waveguides, switches and demultiplexers on one material. The polarization is in this case a parameter that determines the material properties. Thus instead of changing the material via regrowth, the polarization state of the signal is changed to realize active and passive components. With polarization converters it is possible to obtain the required polarization, transparent or absorbing, in each component of the optical circuit.

Previously we have reported [3] that it is possible to realize efficient, short polarization converters on a wafer of indium phosphide. The TE-TM polarization conversion efficiency was more than 80% and the insertion loss was about 1.7 dB for entire structure of length 600 μm. They can be further improved to implement in POLIS technique.

Concept

As mentioned earlier, polarization for TE or TM, is the parameter that defines the active or passive part of the circuit. Therefore transparency for one polarization and absorption for the other is required at the same wavelength. This can be achieved through bandgap modification: strain in the quantum well splits the heavy hole and the light hole in the valence bandedge, and thus the two transitions give absorption at different wavelengths. At a single wavelength one polarization gives absorption while the other is transparent. Compressive strain, which moves the heavy hole (TE-transition) up in the valence band and light hole (TM-transition) down, can serve our purpose. For higher strain, the separation between the heavy-hole and light-hole valence bands increases, resulting in an increased wavelength separation between the bandgap for TE and TM polarization. Calculations [4] showed that 4 nm thick $In_{0.65}Ga_{0.35}As$ compressively strained quantum wells have both TE absorption and TM transparency at 1550 nm (800 meV) wavelength as shown in the Figure 1.

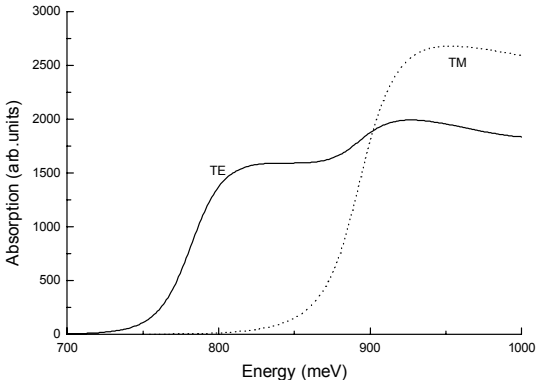


Fig. 1: Calculated absorption spectrum of a 4 nm compressively strained $In_{65}Ga_{35}As$ quantum well with InGaAsP barriers

Realization

Our material system contains InGaAs compressively strained quantum wells sandwiched between InGaAsP on an InP substrate. The designed layer structure consists of a 300 nm $In_{73}Ga_{27}As_{59}P_{0.41}$, a 3 nm compressively stained quantum well of $In_{64}Ga_{36}As$ and again 300 nm $In_{0.73}Ga_{0.27}As_{0.59}P_{0.41}$ as a waveguide layer. A layer of 505 nm InP as a cladding layer and finally a contact layer of 350 nm $In_{0.53}Ga_{0.47}As$ are needed. A layer stack according to this design was grown by MOVPE.

The layer stack was designed for 1550 nm wavelength absorption, but photoluminescence peak was found out to be at a higher wavelength i.e. at 1620 nm. A large enough separation for TE and TM absorption was observed, which is the basic requirement for the feasibility of the technique. To test the concept waveguides, detectors and light emitting diodes (LEDs) have been realized on this layer stack. The fabrication process involves standard photolithography, reactive ion etching, metal evaporation and lift off. Waveguides have widths ranging from 1 μm to 8 μm and lengths of 2 mm. On the passive waveguides the InGaAs contact layer was removed. The active structure could be used as a detector or as a light emitting diode (LED) by applying reverse or forward bias. The detectors/LEDs were 2 μm to 7 μm wide and 1.5 mm in length.

Different measurements have been performed on these devices to check their basic functionality. Both types of components passive (waveguides) and active (LEDs/detectors) are giving reasonable performance.

For waveguides transmission measurements have been done for both polarizations, TE and TM. The typical transmission curve obtained with a tunable laser is shown in the Figure 2. The curve shows transmission upto 1590 nm wavelength but transmission is measured till 1700 nm with a dye laser. For TM, transmission region is for wavelength above 1545 nm. Estimated losses for TM are about 2dB/cm at 1660 nm wavelength and above.

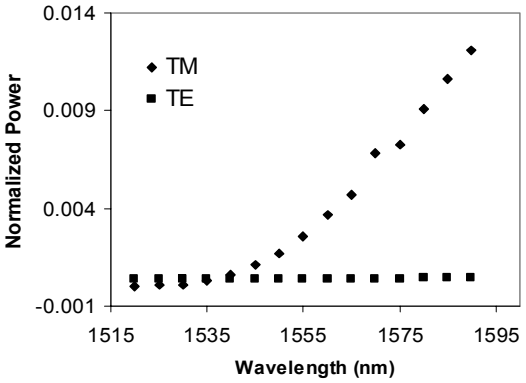


Figure 2: Transmission through waveguides as a function of wavelength for two polarizations.

For detectors and LEDs absorption and emission measurements have been performed, again for both polarizations. Detectors have shown very low dark current of 4.8 nA. The responsivity is calculated from the absorption curves and is shown in Figure 3. For TE at 1600 nm it is above 0.3 A/W and for TM polarization the peak value is around 0.2 A/W at 1480 nm wavelength including coupling losses. The two peaks are widely separated and the absorption ratio for TE and TM is above 20 at 1600 nm, which is good enough for POLIS application [5], and probably much higher at longer wavelengths.

Emission spectra measured for the two polarizations is shown in Figure 4. For TE polarization the peak value is at 1620 nm whereas for TM polarization the peaks are ranging from 1480 nm to 1500 nm for different diodes. This is also in accordance with the previous measurements. The width of the emission peak for TE is sufficient for multiwavelength applications [5]. A slight shift in the TM peak positions for different diodes may be due to the non-uniformity of the wafer.

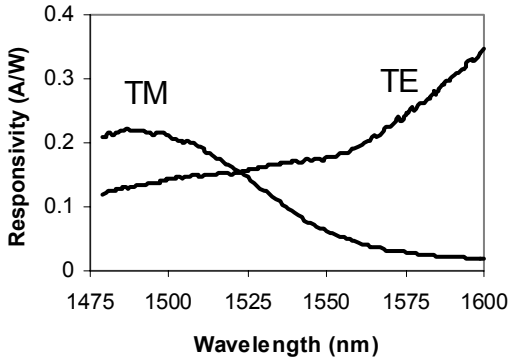


Figure 3: Responsivity of the detector for TM and TE polarizations, as a function of wavelength.

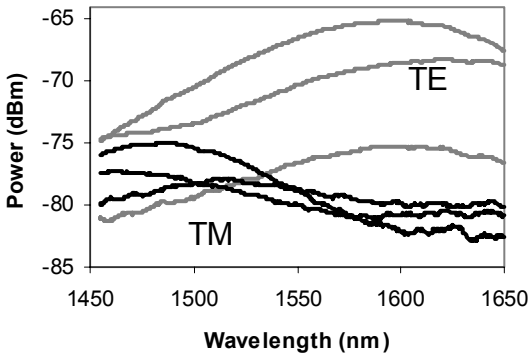


Figure 4: Emission from the LEDs at 20 mA input current for two polarizations, TE (light) and TM (dark) for three different devices.

Conclusions

The polarization based integration scheme (POLIS) can open up the possibility to integrate active and passive circuitry without regrowth. It is a simple technique to implement based on the fact that compressively strained quantum well increases the separation between the heavy-hole and light-hole valence bands, resulting in an increased wavelength separation between the bandgap for TE and TM polarization. TE polarization can be used to specify the active, TM the passive part.

Polarization can be switched from one to the other by polarization converter, which is also fully consistent with the processing of the rest of the circuit.

The idea is verified experimentally. Waveguides and LEDs/detectors fabricated on the same layer stack have given reasonable performances like low losses for waveguides, quite good responsivity for detectors and wide wavelength separation between TE and TM emission peaks for LEDs. These components can be further improved like the efficiency of the LEDs can be increased and losses of the waveguides can be reduced below 2 dB/cm by adjusting the doping profile in the layer stack.

The layer stack also needs to be adjusted for 1550 nm wavelength absorption. This can be done by choosing the right width of the quantum well, so that this technique can be used for telecommunication applications, where ultimately photonic integrated circuits have to be used.

Acknowledgement

This work is carried out under the financial support of Dutch Technology Foundation (STW).

References

[1] C.A. Verschuren, P.J. Harmsma, Y.S. Oei, M.R. Leys, H. Vonk and J.H. Wolter, J. of Crystal Growth, **188**, No. 1-4, 288-294, 1998.
[2] M. Suzuki, M. Aoki, M. Komori, H. Sato and S. Minagawa, J. of Crystal Growth, **170**, 661, 1997.
[3] Y.C. Zhu, F.H. Groen, X.J.M. Leijtens and J.J.G.M van der Tol, Benelux IEEE-LEOS symposium, Brussels, 209-211, 2001.
[4] J.J.G.M. van der Tol and J.E.M. Haverkort, Benelux IEEE-LEOS symposium, 139-142, 1999.
[5] J.J.G.M. van der Tol and J. Martinez Rey, Benelux IEEE-LEOS symposium, 37-40, 2001.

Compact Polarisation Converter on InP/InGaAsP using an asymmetrical waveguide

F. H. Groen
Optics Research Group, Dept. of Applied Sciences, Delft University of Technology
P.O. Box 5046, NL 2600 GA Delft, The Netherlands
groen@optica.tn.tudelft.nl

Y.C. Zhu, J.J.G.M. van der Tol
COBRA Inter-University Research Institute, Section Opto- Electronic Devices
P.O.Box 513, NL 5600 MB Eindhoven, The Netherlands.

An integrated Polarisation Converter, using a single waveguide with one slanted and one vertical wall has been fabricated using e-beam writing and a combination of RIE etching and wet chemical etching. The conversion efficiency of a 150 μm long converter waveguide is better than 80% and the insertion loss is 2 dB at λ = 1.55 μm. The total length of the converter is about 500 μm, including input and output tapers.

Keywords: polarisation converter, InP/InGaAsP, optical waveguides, e-beam lithography

Introduction

Integrated Polarisation Converters for photonic integration received a renewed interest in recent years, because photonic integrated circuits should be insensitive to the state of polarisation of the light emanating from fibres if they are to be used as detectors, add-drop multiplexers or cross-connects. Either all the integrated components have to be polarisation independent or only one polarisation direction should be used. For either method, a compact polarisation converter is needed. The InP/InGaAsP material system combines the highest possible refractive index contrast, which is needed for the compactness, with low loss (1-2 dB/cm) at λ = 1.55 μm.
Several types of polarisation converters in $LiNbO_3$ [1] and InP-based [2] circuits have been proposed and demonstrated. A converter, designed by van Dam [3] using hybrid bend modes in InP yielded a conversion efficiency of 85% at the optimal bend radius.
In previous work, we presented polarisation converters using concatenated waveguides with alternating slanting sidewalls, using 8-12 sections [4,5]. Here, we present a compact converter, using only one section. This type of polarisation converter is the integrated optical analogue of the half wave plate in bulk optics. A realisation of this for GaAs/AlGaAs waveguides has been presented by Huang [6]. Al these designs are highly sensitive to the parameter that influences the amplitude of the non- dominant component of the electric field. For straight converters this is the width of the asymmetric waveguides, for the curved converters this is the curve radius. To achieve the requested accuracy, the device has been produced using for the first time both e-beam lithography (‘direct write’) and e-beam aligment in all the sensitive process steps.

Polarisation converter design

The device design has been carried out with the vectorial 3D-mode solver FIMMWAVE (Photon Design). The structure of the polarisation converter is depicted schematically in Fig. 1. The device consists of a deeply etched converter section (polarisation converter waveguide: PCW), two deeply etched coupling waveguides (CW) and two standard shallow-etched waveguides (IW) used as input or output waveguide. The layer structure of the converter section on the InP substrate is a 600 nm thick InGaAsP (λ_g= 1.25 μm) waveguide layer (n=3.39 @ λ = 1,55 μm) and a 200 nm InP cladding layer (n=3.18) on top. The converter section has one almost vertical side-wall (84º with respect to the horizontal plane) and one slanting side-wall, oriented along the (111) crystal plane (54.7º). The converter section carries only two hybrid modes with effective indices of 3.23740 and 3.23258 respectively. The electrical field of each of the modes is

at an angle with respect to the horizontal plane and to a very good approximation both modes are linearly polarised, the two polarisation directions being orthogonal (Fig. 1c).

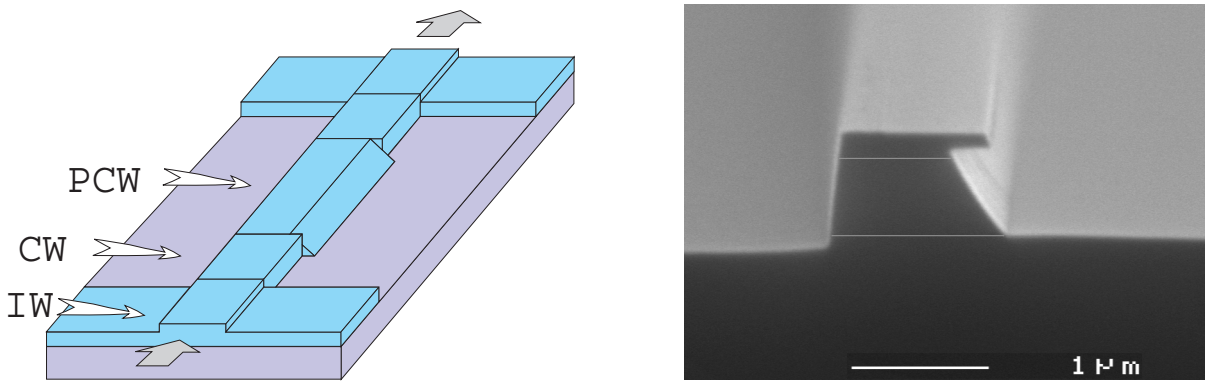
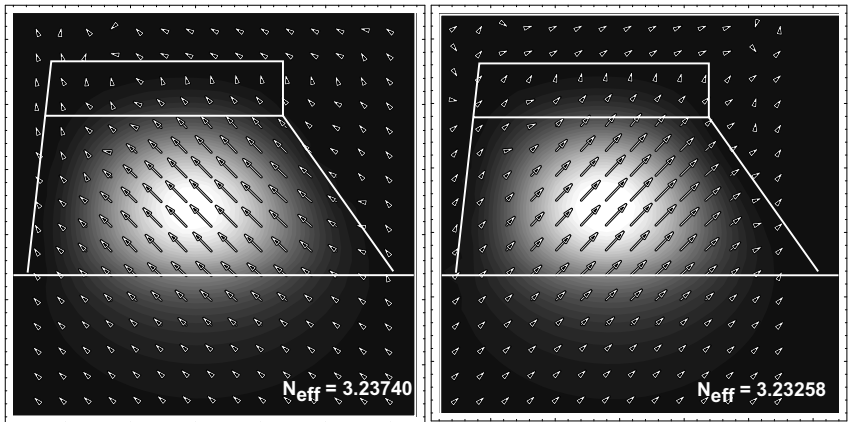


Fig 1. (Clockwise:)
a. Schematic structure of the polarisation converter. Deeply etched waveguides are etched through to the substrate.
b. SEM micrograph of a sample waveguide of the PCW type (not the correct width). The InP/InGaAsP interfaces are indicated by thin lines. The undercut in the InP cover is clearly visible at the right-hand side.



c. Plot of the power and the transversal E- field of the hybrid modes (from simulation).

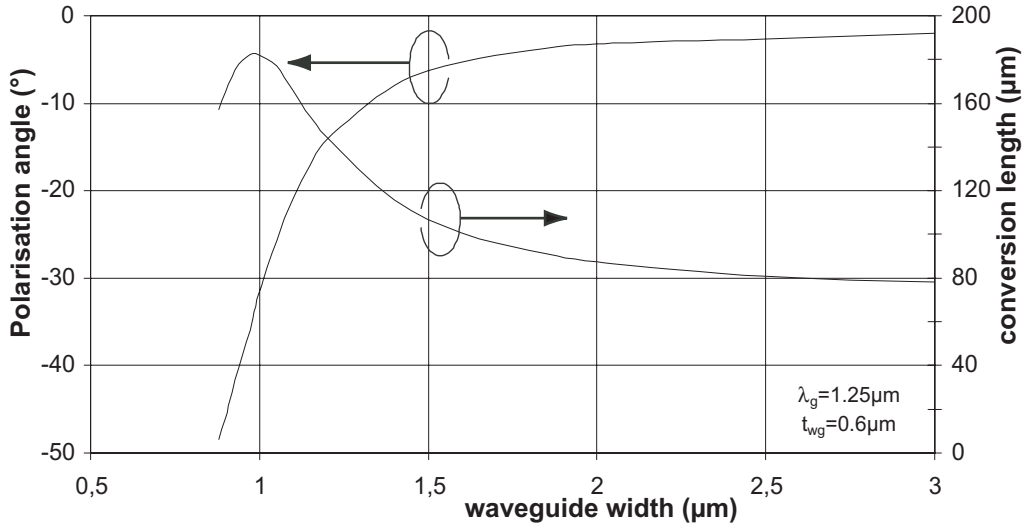


Fig. 2. Polarisation angle of one hybrid mode and conversion length vs the width of the converter waveguide.

Fig. 2 presents the calculated angle of one of the modes and half the beat length between both modes as function of the width of the converter section. From Fig. 2 it is concluded that the optimal length and width (at the top) of the polarisation converter are 160 μm and 0.9 μm, respectively. The polarisation angle of both modes is + and - 45º in that case.
Since the propagation loss of a standard shallow-etched InGaAsP waveguide on InP substrate is much lower than that of a deeply etched waveguide (<1 dB/cm vs 3-5 dB/cm) use of the former type is preferred. However, simulation reveals that the junction loss between a shallow-etched input waveguide and the converter waveguide is very high compared with the loss between a deeply etched waveguide and the converter waveguide. In the last case, the calculated loss is 0.1 dB. Therefore, a deeply etched waveguide is used between the converter section and the shallow-etched waveguide. An optimised 3 μm wide deep-shallow coupling has been used to couple the two. The loss of this junction is negligible. It is connected by adiabatic tapers to both waveguides. The optimal width of the deeply etched waveguide is 1.0 μm and the vertical side wall of this waveguide should be aligned smoothly with the corresponding side wall of the converter section.

Manufacture and experimental results

The waveguide structure was written in PMMA with e-beam lithography. The written parts were dissolved in a MIBK:IPA (=1:3 in volume) developer, followed by evaporation of Titanium and lift-off. The Ti mask was used for the subsequent RIE [7] with CH_3/O_2 to etch the shallow-etched waveguides. Prior to this, 7 x 7 μm^2 alignment markers were defined in a 100 nm thick Silicon Nitride layer, also by e-beam lithography in PMMA. They were etched 1 μm deep into the wafer to get a good contrast for alignment in subsequent e-beam steps. The critical step is the deep RIE into the substrate after the shallow etch step, since only one side of the 1 μm wide waveguide should be etched. The same Ti masking technique as in the previous step was applied using the e-beam alignment markers. Together with the Ti mask from the previous step, the new Ti mask covered top and one side of the waveguide. After the deep etch and removal of the Ti mask, the last e-beam litho was carried out, now covering the deep etched side walls with Silicon Nitride and opening a window on the other side walls for the selective wet chemical etch. Here, the InP top layer serves as a self-aligned mask for the etching of the waveguide layer.

Fig. 1b shows a SEM micrograph of the finished converter waveguide. The mask on top is the InP cover layer with a top width of 1.1 μm. The cover was partly thinned from beneath by the 0.1 μm underetching in the wet chemical etch bath. The horizontal undercut is 0.3 μm.

The converters were measured in a transmission setup using linear polarisers at the input and output sides. Discussed here are the experiments using TE input, the results for TM input are similar. Both TE and TM components were measured at the output, and compared to the (TE-) output of a neighbouring reference waveguide. The results of the measurements on a set of converters with near-optimal width and different lengths are shown in Fig. 3. The solid curves are the output of the simulation. The data fit very well to the calculations for a converter with a conversion length of 130 μm, instead of the 160 μm according to Fig. 2. This may be partly caused by the difference in shape between the model and the realised waveguide and partly by a somewhat smaller width. Even at a deviation of the mode angle of ±9° from the optimal 45°, due to a width deviation, the conversion efficiency is still above 90% of the theoretically maximal possible. This can be concluded from a simple Jones Matrix analysis, modelling the converter waveguide as a (half-wave) retarder plate with the fast axis at an angle that is given by the polarisation direction of the hybrid mode with the smallest effective index. The width deviation that can be tolerated is ± 0.1 μm, as can be read from Fig. 2. The corresponding wavelength tolerance is ± 75 nm.

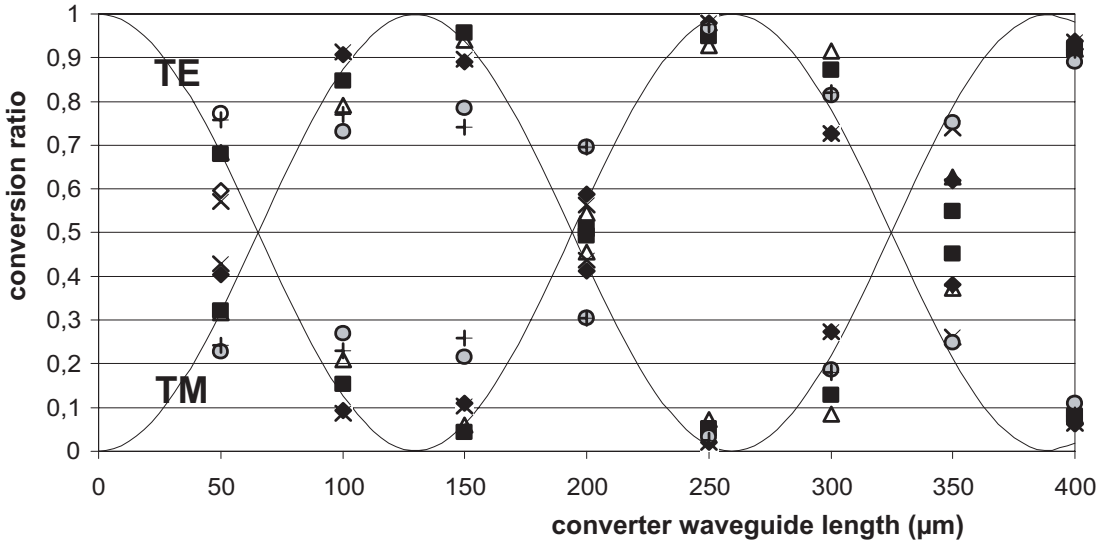


Fig 3. TE-TM conversion ratio and remaining TE polarisation as function of the length, measured on a set of 12 polarisation converters. The result of the simulation (continuous curves) is shown for comparison.

The measured insertion loss, averaged over two sets of 12 converters, is 1.7 dB. An average polarisation conversion ratio of better than 80% is measured, the maximum being 90% at a length of 150 µm. On the average, the optimal converter length is 130 µm.

Conclusion

A simple integrated polarisation converter has been theoretically modelled and was realised in InP/InGaAsP waveguide material. The TE-TM polarisation conversion efficiency is consistently better than 80%, efficiencies over 90% have repeatedly been measured. The loss was less than 2 dB. To our knowledge, this is the first time that in this material system a combination of low loss and high conversion efficiency has been obtained with such a short device.

The support of NWO- Technology Foundation STW under project no DEL.4203 is gratefully acknowledged.

References

[1] R.C. Alferness et al, "High-speed waveguide electro-optic polarization modulator" *Opt. Lett.* **7**, 500-502, 1982.

[2] M. Schlak et al, "Tunable TE/TM-mode converter on (001)-InP substrate", *IEEE Photon. Technol. Lett.* **3**, 15-16, 1991.

[3] C. van Dam et al., "Novel Compact Polarisation Converters based on Ultra Short Bends", *IEEE Photon. Technol. Lett.* **8**, 1346-1348, 1996.

[4] J.J.G.M. van der Tol et al., "A new short and low-loss passive polarization Converter on InP", *IEEE Phot. Techn. Lett.*, **7** no. 1, 32-34, jan 1995; **7**, no. 8, aug. 1995.

[5] Y. Zhu et al., "Design of short polarization converter on InP/InGaAsP using asymmetric waveguides", *Proc. Symp. IEEE/LEOS Benelux Chapter, 2000*, Delft, NL, 277-281.

[6] J.Z. Huang et al., "First realization of an ultracompact and single-mode integrated optical passive polarization Converter", *Proc ECIO'99, Turin*, 259-262, 1999.

[7] Y.S. Oei et al., "Novel RIE process for high quality InP-based Waveguide Structures", *Proc. ECIO'95*, 205-208, 1995.

A 10 Gb/s traveling wave MZ-Modulator for integration with a laser

D. Caprioli, J. H. den Besten, E. Smalbrugge, T. de Vries, X.J.M. Leijtens, M.K. Smit
Opto-Electronic Devices Group, Faculty of Electrical Engineering, Eindhoven University of Technology, NL-5600 MB Eindhoven, The Netherlands.

R. van Dijk, F.E. van Vliet
TNO Physics and Electronics Laboratory, P.O. Box 96864, 2509 JG The Hague, The Netherlands.

W. Pascher
Allg. und Theoretische Elektrotechnik, FernUniversität Hagen D-58084 Hagen, Germany.

J.J.M. Binsma
JDS Uniphase, Prof. Holstlaan 4 5656 AA Eindhoven, The Netherlands.

We report a traveling wave Mach-Zehnder modulator on InP that is compatible with our process for monolithical integration with SOA-based devices like a multi-wavelength laser. The V_π is lower than 10 V and the static extinction ratio is higher than 20 dB at 1550 nm. Microwave characteristics of the electrical lines were measured up to 40 GHz. The 3-dB bandwidth of 8 GHz allows for 10 Gb/s operation.

Keywords: rf-optical modulator, intensity modulation, electrooptic effects, integrated optics, semiconductor waveguides

Introduction

The increasing demand for high-bandwidth communications requires fast modulators. The most widely used materials for these devices are $LiNbO_3$ and III-V semiconductors, such as GaAs or InP. Lithium niobate devices have low insertion losses and high bandwidth [1], buth they have large (cm) dimensions. InP absorption modulators [2] combine small dimensions with a high switching speed and a low driving voltage. A disadvantage, as compared to LN-modulators, are the higher insertion loss and the higher chirp. InP-based Mach-Zehnder modulators can provide similar performance as LN-modulators, but with a much smaller device size. Further, they have a potential for integration with lasers and optical amplifiers [3,4]. High-speed (> 50 GHz) traveling wave MZ-modulators have been reported in GaAs [5] and InP [6], but with little detail on fabrication and performance. In this paper we report realisation and measurement results of a 10 Gb/s InP-based Mach-Zehnder modulator with a potential for 40 Gb/s operation, that is realised in a process that is compatible with our process for integration of SOA's.

Design and fabrication

The modulator is based on a Mach-Zehnder interferometer with 1-mm-long phase shifters consisting of a InGaAsP/InP ridge-type waveguide with a p-i-n doping profile. Figure 1a shows the schematic layout of the interferometer and the electrode; figure 1b shows a photograph of a realised device. The optical waveguides in the phase-shifting sections are chosen 4 µm wide to relax the fabrication tolerances; they are etched 100 nm in the quaternary waveguide layer (see fig. 2). The modulator has been optimised for low optical and RF losses, small optical-electrical velocity mismatch and a high modulation efficiency using the method of lines (MoL) [7] and Ansoft's 3D EM simulator HFSS.

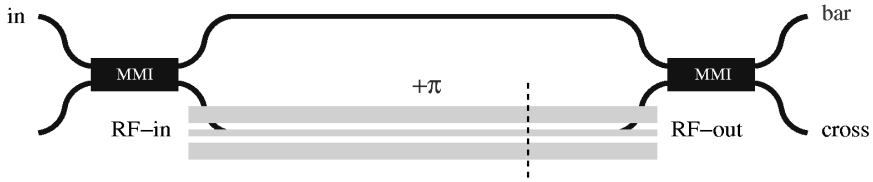


Fig. 1a. Schematic top view of modulator

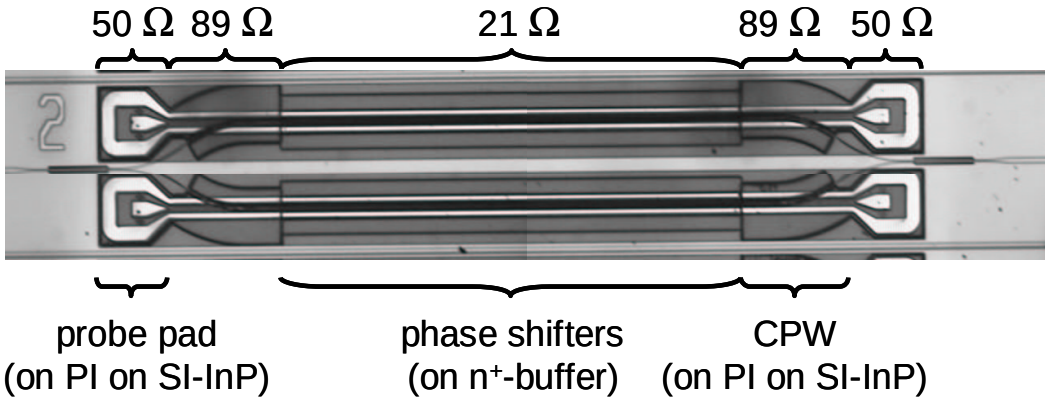
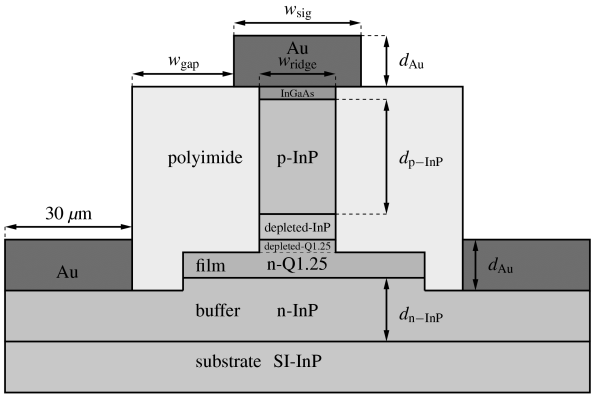


Fig. 1b. Photograph of a realized optical modulator. The impedances of the various sections are shown.

Figure 2 shows a schematic and real cross-sections of the optimised waveguide structure. The signal and ground electrode widths are chosen 12 µm and 30 µm wide, respectively, while the gap between signal and ground is 8 µm. The InP/InGaAsP film layer stack was grown using MOVPE on a semi-insulating (SI) InP substrate. The composition of the InGaAsP layer corresponds to a photoluminescence wavelength of 1250 nm and the thickness is 500 nm. This configuration is equal to the layerstack used in the multi-wavelength laser integrated with a wavelength converter published by Broeke et al. [8], indicating the high integration potential of the device published here. The optical waveguide pattern was defined with optical lithography in a 100 nm layer of SiN_x, using CHF_3 reactive ion etching. The waveguide mesas were created with an optimized CH_4/H_2 etching and O_2 descumming process [9]. SiN_x and polyimide (PI) were then used in the phase-shifters, for passivation and planarization purposes. Finally, 1.5 µm thick gold electrodes were plated. Figure 4 (upper curve) shows the computed electro-optical respons of the device. A 3-dB bandwidth of 20 GHz is predicted.



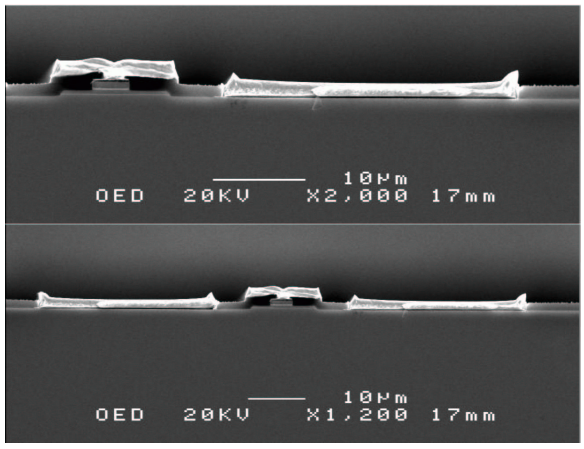


Fig. 2. Schematic cross-section (left) and SEM pictures (right) of a realized modulator at the dashed line in figure 1a.

Experiments

We performed three sets of measurements: the DC switching curves using an optical spectrum analyzer, the S-parameters of the modulator electrical lines, using an HP 8510 network analyzer, in the range 1-40 GHz, and the (electro-optical) response.

For the last measurement, the following setup has been used: the laser beam from a tunable laser source is coupled in one of the modulator arms, by means of a lensed fiber and piezo-electric positioners. The Port 1 of a Network Analyzer provides the input RF signal for the modulator, while the output is connected to a 50 Ω termination load. The modulated optical output is then amplified by a Semiconductor Optical Amplifier and detected by a high bandwidth photo-diode. Its electrical output is then connected to Port 2 of the Network Analyzer. From the electrical S-parameters, the microwave effective index and the loss coefficient were computed [10]; they are shown in figure 3b.

The switching curves of the modulator are shown in Fig. 3a: the V_π is lower than 9 V, the extinction ratio and the insertion losses are approximately 23 dB and 3 dB respectively (TE-polarized light). The computed and measured modulation efficiencies are presented in Fig. 4. The modulator 3-dB bandwidth is 8 GHz. The discrepancy between the predicted and measured bandwidth is caused by an impedance mismatch between the feed lines (89 Ω) and the phase-shifter section (21 Ω), as shown in Fig. 1b. This mismatch is due to the presence of a polyimide isolation layer, which was overlooked in the first design. After inclusion of the 89 Ω section in the simulations a good match is achieve between simulations and measurements, from which we conclude that after correction of the impedance mismatch a 20 GHz bandwidth is feasible.

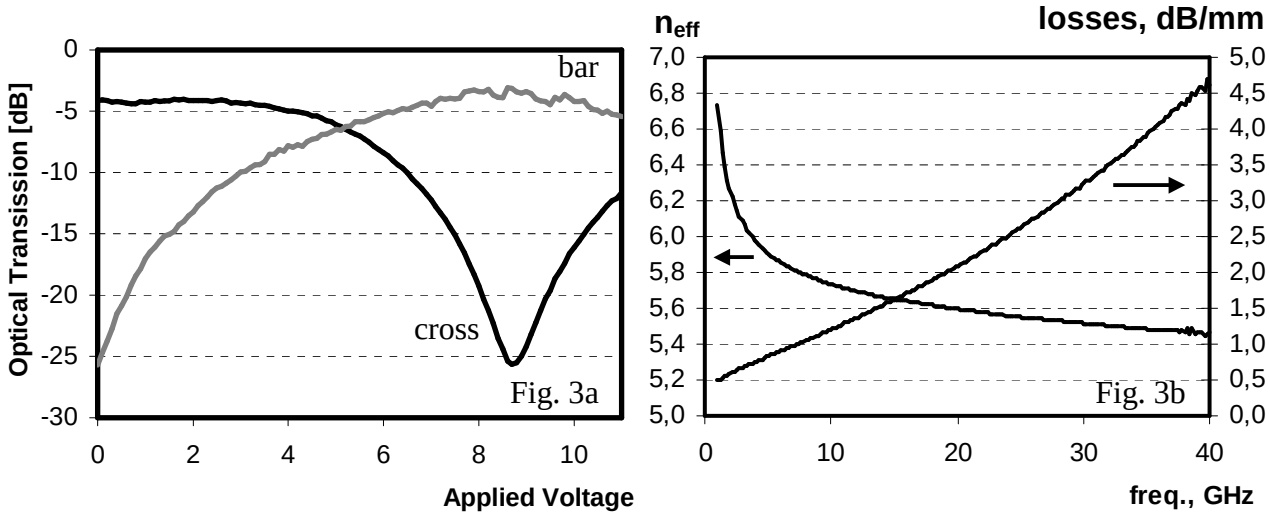


Fig. 3a. Switching curves: optical insertion losses in dB as a function of applied negative voltage.
Fig. 3b. Electrode effective microwave index and losses, extracted from measured S-parameters.

Conclusions

We realized and characterized a traveling wave MZ optical modulator in InP/InGaAsP. It shows 8 GHz bandwidth and a potential for 20 GHz bandwidth after elimination of the local impedance mismatch. It is suited for monolithic integration with semiconductor optical amplifiers, e.g. in a high-bit rate multi-wavelength transmitter.

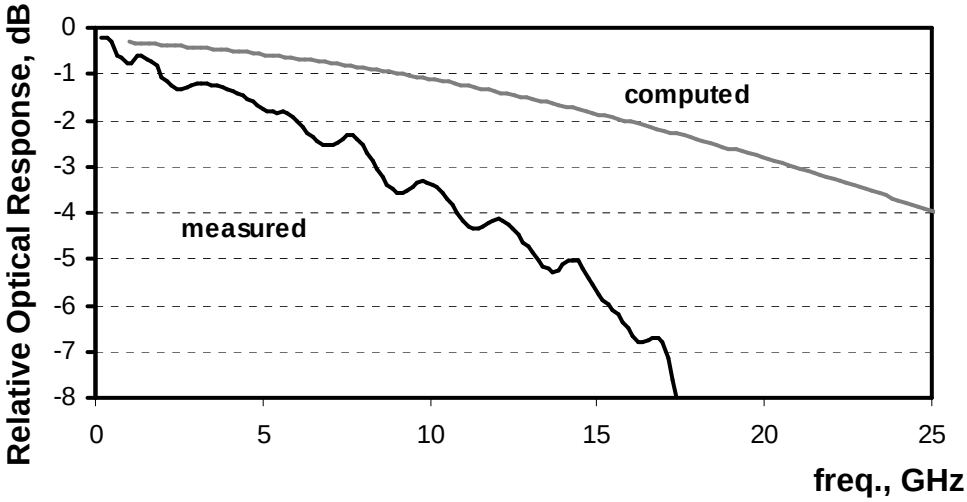


Fig. 4. Computed and measured modulation efficiency.

Acknowledgement

This work has been carried out under the framework of the OBANET IST-2000-25390 project and the Dutch NRC-Photonics programme.

[1] M. Sugiyama *et al.*, "Driver-less 40 Gb/s $LiNbO_3$ modulator with sub-1 V drive voltage", in *Techn. Digest Fiber Comm. (OFC '02), postdeadline papers*, March 19-21 2002, pp. FB6-1 – FB6-4, Anaheim, California, USA.

[2] Yi-Jen~Chiu *et al.*, "High Extinction Ratio And Saturation Power Traveling-Wave Electroabsorption Modulator", *Photon. Techn. Lett.*, vol. 14, no. 6, pp. 792-794, Jun. 2002.

[3] T.Yamanaka, "Ultrafast electroabsorption modulators with traveling-wave electrodes", in *Proc. 27th Eur. Conf. on Opt. Comm. (ECOC '01),* Sept. 30-Oct. 4 2001 pp. 328-331, Amsterdam.

[4] R.G. Walker, "High-Speed III-V semiconductor intensity modulators", *IEEE J. Quantum Electron.*, vol. 27, no.3, pp. 654-667, Mar. 1991.

[5] R.G. Walker, "GaAs/AlGaAs travelling-wave modulators for mm-wave frequencies", *IEE Colloquium Towards Terabit Transmission*, 1995, pp. 4/1-4/6.

[6] L. Mörl *et al.*, "Traveling wave electrodes for 50 GHz operation of opto-electronic devices on InP", *Proc. IPRM99 conference*, May 16-20 1999, pp. 385-388.

[7] R. Pregla and W. Pascher, "The Method of Lines", in *T. Itoh, (ed.), Numerical Techniques for Microwave and Millimeter Wave Passive Structures*, pp. 381-446, J. Wiley Publ., New York, 1989.

[8] R.G. Broeke, J.J.M Binsma, M. van Geemert, F. Heinrichsdorff, T. van Dongen, J.H.C. van Zantvoort, X.J.M. Leijtens, Y.S. Oei, and M.K. Smit, ``An all-optical wavelength converter with a monolithically integrated digitally tunable laser," in Proc. 27th Eur. Conf. on Opt. Comm. (ECOC '02). Sept. 8-Sept. 12 2002, p. PD3.2, Copenhagen.

[9] Y.S. Oei *et al.*, "Novel RIE-process for high quality InP-based waveguide structures", *Proc.7th Eur. Conf. on Integr. Opt. (ECIO '95)*, April 3-6 1995, pp. 205-208, Delft, The Netherlands.

[10] G.Gonzales, *Microwave Transition Amplifiers*, Englewood Cliffs, NJ: Prentice Hall, p. 25, 1984.

Single-Quantum-Wire Waveguide Modulator with High on/off Ratio and Low Voltage Swing

S. Palmgren,[1,2] H. Weman,[1,2] A. Rudra,[1] and E. Kapon,[1]
[1]*Laboratory of Physics of Nanostructures, Institute of Quantum Electronics and Photonics, Swiss Federal Institute of Technology (EPFL), CH-1015 Lausanne, Switzerland.*
[2]*Department of Physics, Linköping University, S-581 83 Linköping, Sweden.*
susanna.palmgren@epfl.ch

We demonstrate a waveguide modulator with an on/off ratio 50:1 at a 5 V voltage swing using a single quantum wire in a sub-micron sized waveguide. The modal absorption of the single wire is 140 cm^{-1}.

Keywords: quantum-wire, electro-absorption modulator, waveguide, semiconductor modulator

Introduction

Semiconductor quantum well (QW) waveguide intensity modulators have attracted considerable interest due to their high performance and capability of monolithic integration with laser diodes [1]. Important parameters for applications of such electro-absorption modulators are high on/off ratio, low driving voltage, high speed, low chirp and compact size. These modulators are based on either the quantum-confined Stark effect (QCSE) or quenching of exciton absorption due to phase-space-filling (PAQ). Due to the enhancement of the exciton oscillator strength in one dimensional structures, these effects are expected to be strongly modified as compared to QWs [2-3]. Here, we report on an efficient electro-absorption modulator based on a single quantum wire (QWR) embedded in a sub-micron sized V-shaped dielectric waveguide. We obtain a high on/off ratio (50:1) with a low voltage swing (5V) at 820 nm by using a 500 μm long QWR waveguide.

Experimental

The QWR waveguide samples were grown by low-pressure organometallic chemical vapor deposition (OMCVD) on n^+-doped (100) GaAs substrates patterned with 250 μm spaced V-grooves along the [1-10] direction. Each V-groove contains a dielectric AlGaAs/GaAs waveguide that incorporates a single self-organized GaAs QWR placed in the core region of a V-shaped AlGaAs optical waveguide [4]. The core region has a total thickness of 295 nm and is clad with 1 μm thick *n*- and *p*-doped $Al_{0.65}Ga_{0.35}As$ layers on the bottom and top of the core layer, respectively. The QWR was displaced upwards from the center of the core region in order to obtain an optimal mode confinement factor Γ, which was estimated to be 0.1 % for the single QWR [4]. The $Al_{0.30}Ga_{0.70}As$ waveguide core was *n*-doped to a distance of 25 nm from the QWR in order to have electron filling in the wire at flatband (FB). The V-shape of the dielectric waveguide yields a sub-μm sized, heart-shaped optical mode that is well confined in the core region of the waveguide according to our calculation of the electromagnetic field distribution of the optical modes [4]. A transmission electron microscopy (TEM) micrograph of a V-shaped optical waveguide region containing a single crescent-shaped QWR is shown in Fig. 1.

For the top ohmic *p*-contacts, a 100 μm wide Ti/Au stripe was centered on top of the V-groove, and the ohmic *n*-contact was obtained by evaporating Ni/Ge/Au on the backside followed by annealing at 420°C. The waveguide samples were then cleaved and contacted by bonding wires. The *I-V* characteristics typically showed a forward turn-on voltage of about 1.3 V with a dark current of less than 5 μA at 5 V reverse bias.

Waveguide transmission spectra were measured at room temperature (RT) as a function of the applied voltage that was varied from 1V to –5 V. For optical excitation we used a Ti-Sapphire laser

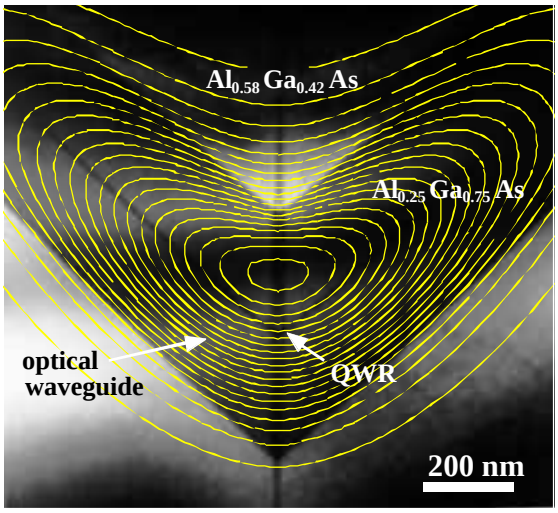


Fig.1. TEM picture of a typical V-shaped GaAs/AlGaAs dielectric waveguide with a single GaAs quantum wire. Contour lines show the mode intensity distribution of the monomode structure.

with the incoming light linearly polarized along the [110] (TE polarization) or [001] (TM polarization) directions. The mechanically chopped light was coupled into the single V-groove QWR waveguide with a microscope objective at the sample edge and guided along the QWR axis ([1-10] direction). This corresponds to the excitation of mainly the fundamental waveguide eigenmode. The out-coupled light was collected by a second microscope objective and detected with a silicon photodiode using a lock-in amplifier. To verify that the coupled light spot was centered properly on the V-shaped waveguide core, the front- and back-side facets of the device were monitored in near-field using Si CCD cameras. Absorption spectra, $\alpha(\lambda)$, are derived from the measured transmission spectra, $T(\lambda)$, by the relationship:

$$\alpha(\lambda) \quad -\ln\left[T(\lambda)\right] \tag{1}$$

Results and Discussions

Figure 2 (a) shows the RT absorption spectrum of a 500 μm long QWR waveguide device for TE polarization with a bias of 1 V applied (near flatband). A very sharp absorption edge is observed near 820 nm with several broad peaks seen in the absorbing part of the spectrum. The spectrum was measured by using a relatively low waveguide-coupled power, estimated to be near 1 μW, which was found to be well below the threshold power that causes absorption bleaching. The exact power coupled into the waveguide structure is however difficult to determine exactly, since the coupling losses depend critically on the angle and focus of the laser spot as well as on the amount of reflection loss.

For the waveguide sample discussed above, the QWR heterostructure was intentionally *n*-type doped so that about 4 electron subbands should be filled in the QWR at flatband. From previous photoluminescence (PL) and PL excitation (PLE) measurements on an *undoped* $GaAs/Al_{0.30}Ga_{0.70}As$ V-groove QWR of similar size, the estimated ground-state transition is expected to be near 1.46 eV (850 nm) at RT with a 1D lateral subband spacing of around 25 meV.

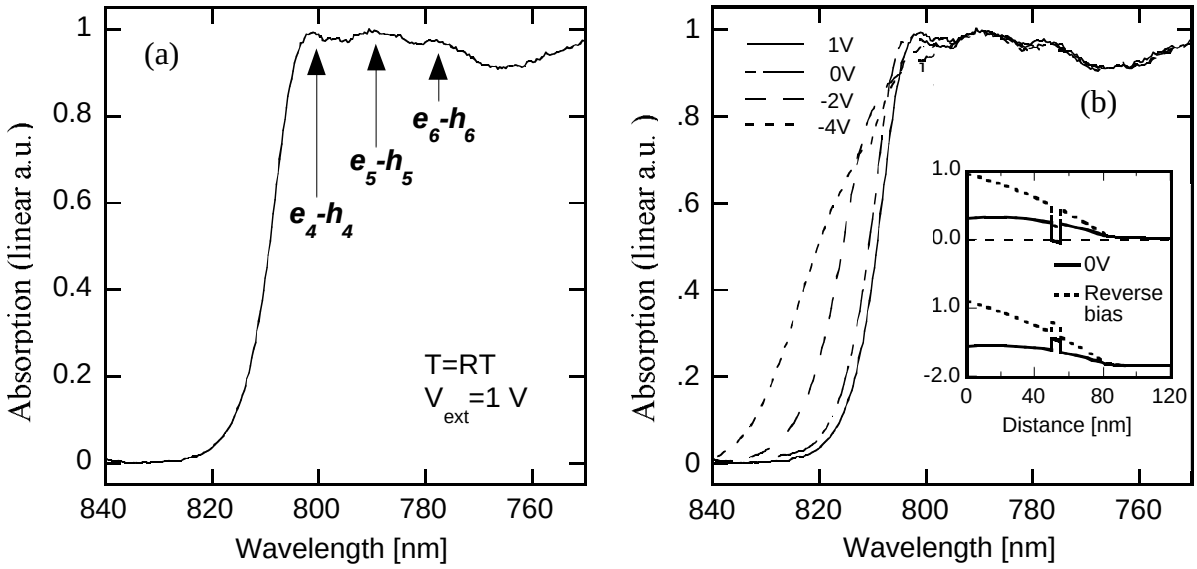


Fig. 2. (a) Linear absorption spectrum at RT of a 500 μm long QWR waveguide device for TE polarization with a bias of 1 V applied (near flatband). The modal absorption coefficient due to the single QWR at the band edge is estimated to be140 cm^{-1}. (b) Electro-absorption spectra at RT of the 500 μm long QWR waveguide device for TE polarization as a function of the applied reverse bias voltage. The inset shows the calculated band-diagram at 0V and under reverse-bias.

The sharp absorption edge near 820 nm (1.51 eV) observed in Fig. 2 (a) is therefore interpreted to be due to the transition of an electron from the valence band to the Fermi-level in the QWR somewhere between electron levels number four and five. Lower transitions are effectively absent due to the phase-space absorption quenching (PAQ) effect [5]. The three broad peaks observed in Fig. 2 (a) are interpreted as due to transitions to electron levels n = 4, 5 and 6. The measured absorption coefficient due to the single QWR at the band edge is 140 cm^{-1}. With an estimated optical confinement factor, Γ = 0.1, this yields a QWR material absorption coefficient as high as 14 000 cm^{-1}.

Fig. 2 (b) shows the electro-absorption spectra of the 500 μm long QWR waveguide device for TE polarization as a function of the applied reverse bias voltage. A clear redshift of the absorption edge is seen as the reverse bias is increased. Initially, this redshift is quite uniform over the whole absorption edge, but at higher reverse bias the absorption edge becomes less steep due to a stronger redshift at the low energy tail of the absorption edge. If measured at the absorption edge mid-point intensity the redshift is about 11 nm by increasing the reverse bias from 1V to –4V. This redshift can be interpreted as due to a decrease in the electron density in the QWR as the Fermi level is moved lower in the conduction band, as shown in the inset of Fig. 2 (b). This allows the absorption to take place at lower and lower energies (reducing the PAQ effect) as the electron density in the QWR is lowered due to the applied reverse bias. However, due to the setting of an electric field across the QWR potential under reverse bias there is also an additional QCSE effect contributing to the redshift [6]. We believe that the QCSE effect is causing the stronger absorption redshift at the low energy tail of the absorption edge.

Maximum contrast is achieved near 820 nm resulting in an on/off ratio of 50:1 (17 dB) with a voltage swing of 5V (from 1V to –4V). For the present modulator this optimum wavelength is slightly above the absorption edge. While this contrast ratio should be sufficient for device applications and in fact occurs at a lower voltage swing than is achieved with well optimized quantum well modulators [7,8], device is only a first demonstration of a QWR modulator. At present we are investigating modulators with lower filling factors and undoped QWR modulators in order to investigate the PAQ and QCSE effects separately, which will allow to further optimize the modulator performance.

Conclusions

We have measured the electro-absorption modulation in an *n*-type doped single GaAs/AlGaAs QWR, sub-micron sized waveguide modulator at room temperature. We have obtained an on/off ratio of 50:1 with a voltage swing as low as 5V. The observed absorption edge modulation is a combined effect of electron transfer out of the QWR and the quantum confined Stark effect. The measured modal absorption and estimated QWR material gain coefficient due to the single QWR is 140 cm^{-1} and 14 000 cm^{-1}, respectively.

These results make our device attractive both as a discrete, small size low-voltage intensity modulator as well as for future planar integration with V-groove QWR lasers [9].

Acknowledgements

The authors gratefully acknowledge E. Martinet, L. Sirigu, and K. F. Karlsson for assistance in the course of this work. This work was partly funded by the Swedish Foundation for Strategic Research under the “NANOPTO” Consortium.

References

[1] Semiconductor optical modulators, by K. Wakita (Kluwer academic publishers, Boston, 1998).
[2] H. Sakaki, K. Kato, and H. Yoshimura, Appl. Phys. Lett. **57**, 2800 (1990).
[3] H. Ando, H. Oohashi, and H. Kanbe, J. Appl. Phys. **70**, 7024 (1991).
[4] D. Crisinel, M.-A. Dupertuis, and E. Kapon, Optical and Quantum Electronics **31**, 797 (1999).
[5] H. Weman, E. Martinet, M.-A. Dupertuis, A. Rudra, and E. Kapon, phys. stat. sol. (a) **178**, 249 (2000).
[6] H. Weman, E. Martinet, M.-A. Dupertuis, A. Rudra, and E. Kapon, Appl. Phys. Lett. **74**, 2334, (1999).
[7] P.N. Freeman, P. Bhattacharya, M. Jaffe, J. Singh, and X. Zhang, *IEEE J.Quantum Electron.* **QE-32**, 1161, 1996.
[8] O. Blum, J.E. Zucker, T.Y. Chang, N.J. Sauer, M. Divino, K.L. Jones, and T.K. Gustafson, *IEEE Photon. Technol. Lett.* **3**, 327, 1991.
[9] E. Kapon, Optoelectronics- Devices and Technologies, **8**, 429 (1993).

Tunable semiconductor lasers for telecommunications applications

H. Debrégeas-Sillard, A. Plais, A. Vuong, Th. Fillion, D. Locatelli, J. Decobert, D. Herrati,
P. Doussière*, J. Jacquet
Alcatel CIT – OPTO+, Route de Nozay, 91460 Marcoussis, France
**Alcatel Optronics, Route de Villejust, 91625 Nozay, France*
helene.sillard@alcatel.fr

We present the various currently studied tunable lasers designs, then focus on recent optimizations and performances on 3-section DBR lasers (16nm tuning, 20mW coupled output power), electronic control, aging, and new functionalities integration (amplifier, modulator).

Keywords: tunable lasers, distributed Bragg reflector, wavelength agility, integrated semiconductor amplifier, integrated modulator

Introduction

Tunable lasers are becoming important elements in optical networks to reduce costs. They could be used particularly for systems monitoring : a reference signal is transmitted and detected on each wavelength, thus informing on transmission quality. Or inventory costs could be drastically reduced by using tunable lasers as sparing sources or even as standard sources, to avoid the obligation of owing 2 or 3 sets of fixed wavelength sources covering the whole transmission band.

Besides, with the increasing bit rate at the user level (data traffic, Fiber To The Home (FTTH)), flexibility and wavelength agility are becoming critical for routing in optical networks. Would it be to add a new wavelength in an Add and Drop, as emission lasers in 3R electro-optic regenerators, or as tunable clocks in 3R all-optical regenerators,… In such applications, tuning speed is a key characteristic : it should be a few milliseconds for circuit switching, and down to a few nanoseconds for packet switching.

Currently used sources are Distributed Feedback Lasers (DFB). To take their place, tunable lasers must not only provide maximum tunability, but also similar characteristics (20mW coupled output power, spectral linewidth below 10MHz, …), long-term reliability, and efficient control electronics, while maintaining limited overcost (below 20%).

In most applications, signal is 10Gb/s modulated, with excellent characteristics (extinction ratio over 10dB, low chirp, square eye diagram). Thus the integration of a modulator section is a promising research way.

1. Different types of tunable or selectable lasers

To face the growing demand for tunable lasers, many laboratories proposed different solutions, aiming at the various applications. Three types of tunable lasers emerged :

- **Thermally tuned distributed feedback (DFB) lasers**

The wavelength emitted by a DFB lasers varies with temperature by about 0.9 Å/°C, leading to 4nm tuning for 45°C temperature range.

To increase the achievable tuning range, cascaded DFB lasers are proposed [1] : the device is made of three DFB lasers, with different grating pitches corresponding to 5nm spaced Bragg wavelengths. Each DFB section is thermally tuned to cover 5nm tuning, leading to 15nm total tuning range, with temperature ranging between –5 and +50°C.

Another solution consists in fabricating a DFB array (up to 12 DFB lasers), with Bragg wavelength spacing around 2.5nm. The DFB waveguides are then combined by a multimode interferometer (MMI) [2], or more recently by a micro electro-mechanical (MEMs) mirror [3]. One

wavelength is selected by turning on the corresponding DFB laser, and off the others. Temperature enables fine wavelength control. 20mW fiber coupled power over 33nm (C-band) have been obtained [3].

These devices have the advantage of using very well-known and reliable DFB lasers, and wavelength control is extremely simple. But with such large temperature ranges, these solutions are very power consuming. And due to extremely long time constants of thermal effects, they can only provide slow tuning (no routing applications).

- **Mechanically tuned lasers**

To reduce tuning speed and further increase tuning range, while maintaining easy-to-control continuous tuning, solutions with mechanical modifications of the laser cavity geometry are proposed.

Firstly, external cavity lasers, where the gain medium is a high power semiconductor laser diode. The emerging beam is collimated, and diffracted on an external grating. The emitted wavelength is imposed by the incidence angle on the grating, and the Fabry-Perot modes position. Continuous tuning is obtained by synchronously varying the grating angle and the cavity length. For example 40nm tuning, with 10mW output power, with less than 15ms switching time have been obtained [4].

Secondly, vertical cavity surface emitting lasers (VCSELs), where one Bragg mirror is a MEMs. Due to the very small cavity length, only one Fabry Perot mode lases in the gain spectrum. This mode is continuously tuned by translating the MEMs mirror. With 1310nm optical pumping, 20mW over the whole C-band have been obtained [5].

- **Current injection tuned lasers**

The refractive index of a quaternary material, at a wavelength above its photoluminescence wavelength, decreases when injecting carriers, due mainly to plasma effect. Many tunable lasers are based on this phenomenon : a passive section (called Bragg section), with a Bragg grating, imposes the emission wavelength, which is modified by current injection. Gain is provided by an active section, made of active material multi quantum wells (MQW). Fine tuning is obtained by modifying the index of a phase section with current injection as well. These devices provide fast tuning, large output power, and the simplicity of integrated components. But they require sophisticated electronic control algorithms to ensure mode hop free behavior.

The basic device is a distributed Bragg reflector (DBR) laser. It will be presented in detail in this paper. The Bragg section contains a standard Bragg grating. Tuning range is limited by the acheivable achievable Bragg section refractive index : $\Delta\lambda/\lambda = \Delta n_{Bragg} / n_{Bragg}$: 16nm tuning, with 20mW coupled output power have been demonstrated [6,7].

Other structures have been proposed, based on tuning mechanisms where $\Delta\lambda/\lambda$ is no longer limited to $\Delta n_{Bragg} / n_{Bragg}$. The first structure is the grating coupler sampled reflector laser (GCSR). It relies on a tunable intracavity grating-assisted codirectional coupler filter, that tunes as $\Delta n_{passive} / (n_{g\,passive} - n_{gactive})$, where $n_{gpassive}$ and $n_{gactive}$ are the group mode indexes of the passive and active piled up waveguides respectively : 40nm tuning with more than 3mW have been demonstrated [8].

The other structure consists of a gain and phase shifter section between two sampled grating distributed reflectors (SG-DBR). A sampled grating is a conventional grating with grating elements removed in a periodic fashion, leading to reflection spectra with periodic maxima. Same types of reflection spectra can be obtained as well with superstructure gratings : grating pitches is linearly with a large periodicity (SSG-DBR). The periods of the two spectra are slightly mismatched : lasing occurs at that pair of maxima that are aligned. Phase shifter is adjusted to place a mode at this

wavelength as well. Inducing small index changes in one mirror relative to the other causes adjacent reflectivity maxima to come into alignment, shifting the lasing wavelength a large amount for a small index change : this is the "Vernier effect". The total tuning range is only imposed by the active section gain bandwidth, and by the tradeoff with side mode suppression ratio (SMSR). 40nm tuning can thus be achieved, with 4mW coupled output power [9]. Power is limited because light is transmitted through a grating, and not directly from the gain section. To overcome this, a semiconductor optical amplifier (SOA) front section is added, leading to 20mW coupled output power [10]. These devices provide excellent performances, but at the expense of a large number of sections (5), and extremely complicated control electronics. A more precise comparison is given at the end of the paper (§6).

Recently, a new device has been proposed, with a sampled grating rear section, and multiple Bragg gratings with independent current controls for the front section. Tuning current applied to one or two of the front gratings selects a wavelength band across which one line from the rear phase grating reflector is scanned to provide continuous tuning. 45nm tuning with 28mW facet output power have been demonstrated [11].

2. 3-section DBR laser

Among all these solutions, 3-section DBR laser appears as a good compromise between simplicity (only three control currents, standard technological process), tuning range (16nm tuning), power (20mW coupled without any additional semiconductor amplifier section), and fast switching (<1ms). This section presents the basic behavior of a DBR laser, then the different optimizations, and at last static and dynamic results.

2.1 DBR laser principle

The device is illustrated in figure 1.

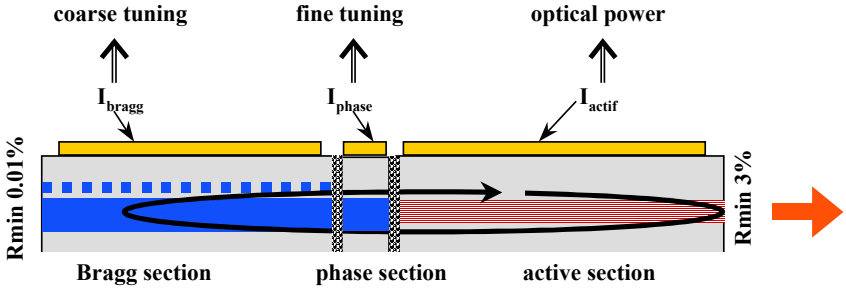


figure 1 : 3-section DBR laser scheme

Optical power is provided by injecting current (I_{active}) in the multiple quantum wells (MQW) of the active section.

The maximum reflection wavelength of a Bragg grating is given by $\lambda = 2.n_{eff}.\Lambda$, where n_{eff} is the effective index, and Λ the grating pitch. In a DFB laser, grating is etched in the active section. Above threshold, carriers density is blocked, so the emission wavelength is almost constant.

On the contrary, in a DBR laser, the emission wavelength is imposed by a grating etched in another section, in passive quaternary material, called Bragg section. The carrier density N in this section is not blocked, and increases when injecting current, through relation

$$I_{Bragg} = I_{leakage} + eV\,(AN + BN^2 + CN^3) \qquad (1)$$

where I_{Bragg} is the injected current, $I_{leakage}$ is the sum of leakage currents, e is the electron charge, V the undoped volume, and A, B and C are parameters specific to the material. Through free-carrier absorption and bandfilling, the Bragg section effective index varies as :

$$\Delta n_{eff} = \Gamma . \frac{dn_Q}{dN} . \Delta N \qquad (2)$$

where Γ is optical confinement in quaternary material, dn_Q / dN is the quaternary index variations with carrier density (negative value), and ΔN is the carrier density variation due to I_{Bragg}. This leads to a decrease of the Bragg section maximum reflection wavelength λ_{Bragg}:

$$\Delta\lambda_{Bragg} = 2.\Delta n_{eff}.\Lambda \qquad (3)$$

As shown in figure 1, light is partially reflected by the active section facet. And for wavelengths close to λ_{Bragg}, light is reflected by the Bragg grating, with a penetration length noted L_{eff}. Thus, we obtain a Fabry-Perot cavity, with optical length $n_{gactive}.L_{active} + n_{gphase}.L_{phase} + n_{gBragg}.L_{eff}$. Laser emits on the Fabry-Perot mode closest to λ_{Bragg}. When injecting current in the phase section (I_{phase}), the Fabry-Perot cavity modes are shifted, due to n_{gphase} variations (figure 2).

The SMSR is maximal when the Fabry-Perot mode wavelength coincides with the maximum Bragg reflectivity wavelength ($\lambda_{FP} = \lambda_{Bragg}$), and a mode hop occurs (with SMSR minimum) when two Fabry-Perot modes are equidistant from Bragg wavelength. Typical emission wavelength and SMSR characteristics as a function of I_{Bragg} are represented in figure 3. The wavelength levels correspond to Fabry-Perot modes, successively selected by the Bragg reflectivity spectrum, when injecting I_{Bragg}. Tuning efficiency is maximum for low Bragg currents, due to the 3^d degree polynomial variation of equation (1). For higher Bragg currents, thermal effects tend to compensate for injection-induced tuning, eventually increasing emission wavelength. The low SMSR values at first mode hops are caused by Bragg section current source noise. The effect is less frequent for large Bragg current, due to lower tuning efficiency.

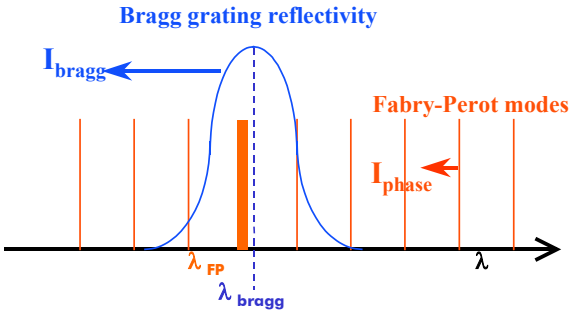


figure 2 : DBR tuning mechanism

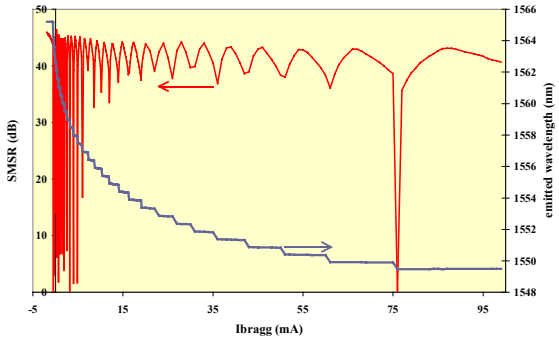


figure 3 : typical wavelength and SMSR variations with IBragg

2.2 DBR design optimizations

- Vertical structures optimization

According to equation (2), tuning range is proportional to optical confinement in quaternary material, and its index variations with injected current. Thus a very thick quaternary, with photoluminescence wavelength close to emission wavelength is preferred.

But for large power emission, the optical mode must be deconfined in the active section (to reduce losses and improve fiber coupling efficiency), overlap between active and passive sections modes must be maximized, and passive material photoluminescence wavelength should be far from emission wavelength to reduce absorption.

The adopted structures are thus a compromise between all these requirements :

- Active section is made of six 8nm thick Q1.5 compressively strained quantum wells, and five 10nm thick Q1.18 barriers, surrounded by 50nm thick undoped Q1.18 confinement layers.

- Bragg section is made of 380nm thick Q1.42 bulk material, and 70nm Q1.18 grating layer, separated by 100nm InP spacer.
- Phase section is similar to the Bragg section, except for the grating that is etched during process.

A 1.5µm wide ridge waveguide is then etched, and buried in p-doped InP. Sections are isolated by electrode and InGaAs heavily doped contact layers etching, plus deep ion implantation to suppress any interelectrodes leakage current.

- Sections lengths

Active section length has been optimized at 600µm, as it provides high output power, low threshold current, and good external efficiency, while maintaining reduced serial resistance, limiting thermally induced power saturation.

Phase section length is chosen about 50µm, that are sufficient to shift Fabry-Perot modes comb by the free spectral range (FSR) for limited injected current.

Bragg section length must be sufficient to have a high reflectivity and obtain single-mode behavior. But we observed that when increasing length, tuning range decreases due to injected carriers consumption for spontaneous amplified emission (2nm tuning range decrease for Bragg length 500µm instead of 300µm [7]).

- Grating coupling efficiency κ

The Bragg grating coupling efficiency κ has a strong impact on DBR operation. With a strong κ, Bragg section reflectivity spectrum is wide : the grating is weakly wavelength selective, with strong reflectivity. L_{eff} is thus small, enabling small Bragg lengths. But the least Fabry-Perot comb irregularity may provoke lasing on a side mode, leading to tuning curves irregularities. The device is thus extremely sensitive to any parasitic cavity (due to butt joint, Bragg facet).

On the other hand, a weak κ value releases from parasitic cavities, and generates stronger SMSR and power variations among each mode, which makes device control easier as shown further in §3. But L_{eff} is longer, imposing a long Bragg section, thereby reducing tuning range. The spectral linewidth is degraded too, due to Bragg current source noise, that creates Bragg index variations, and consequently wavelength scattering.

κ around 40cm-1 has been chosen as a standard value, leading to 300µm Bragg section length.

- Active section ridge design

To improve coupled output power, beam divergence from active section has been reduced with a lateral taper represented in figure 4. With a ridge width varying from 1.5µm to 0.8µm along the last 200µm of the active section, beam divergence has been reduced to 16° x 20° (compared to 20° x 25° for a 1.5µm straight ridge), and 75% coupling efficiency is now typical (compared to 60%).

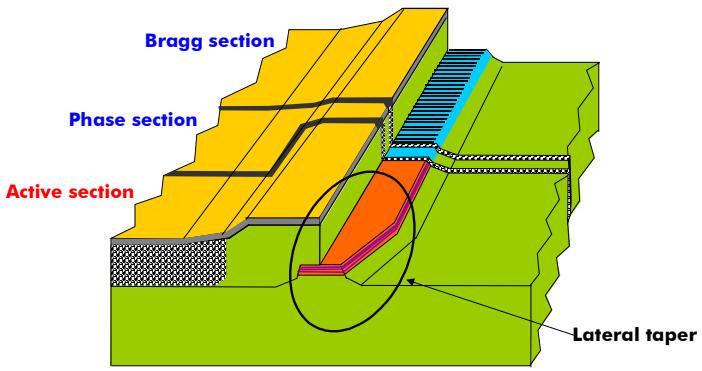


Figure 4 : schematic view of the DBR laser, with tapered active section.

2.3 Static results

With this optimized structure, we reproducibly obtain tuning over around 16nm, with SMSR above 40dB apart from mode hops (figure 3). As output power decreases with I_{Bragg}, due to free-carrier absorption in the Bragg section, the achievable output power is imposed by the least favorable operating conditions, that is maximum I_{Bragg}. As shown in figure 5, 20mW can be fiber coupled for all the modes at Iactif < 200mA, with 14.2dBm maximum power at Iactif=320mA. Half of the C-band is thus covered (40 channels 50GHz-spaced), with 20mW coupled (figure 6).

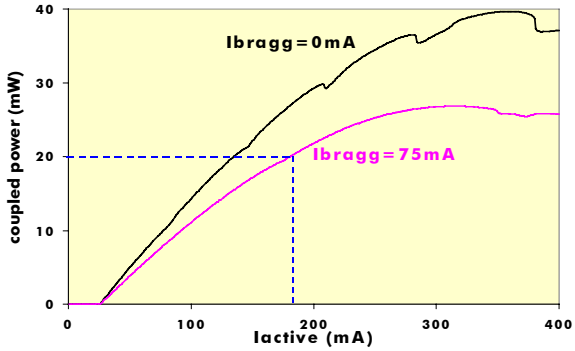


figure 5 : fibre coupled power versus Iactive, for extreme IBragg values.

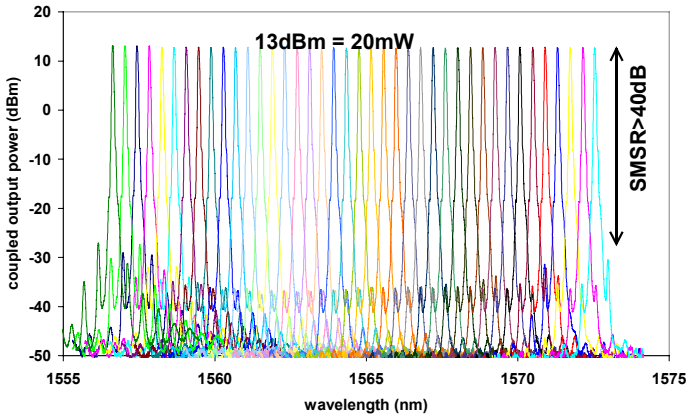


figure 6 : superimposed addressable spectra : 16nm, with 20mW fiber coupled power.

3. DBR lasers electronic control

Pigtailed DBR lasers are integrated in an electronic card, that supplies current to the three sections, and feedback control loops, with computer support.

Firstly, the laser undergoes fast characterizations (a few seconds), to define its look-up table, that is the required values of I_{active}, I_{phase} and I_{Bragg}, to obtain the required power (typically 20mW) and ITU wavelength, with maximum SMSR.

Current sources on the electronic cards, for phase and Bragg sections, must be optimized to reduce noise. Indeed, as carriers densities are not blocked in these sections, the least noise on I_{phase} and I_{Bragg} generates index variations, thereby phase variations, and drastically degrade linewidth. The effect increases with tuning efficiency, phase length and L_{eff}. We obtain, with modules integrated in electronic card, linewidth below 10MHz over the whole tuning range.

Wavelength is measured from the rear facet with a wavelength locker (2 photodiodes and a Fabry-Perot etalon), and corrected by adjusting I_{phase}.

For power control, two solutions exist. Either front facet output power is collected with a coupler. Or rear facet (transmitted through Bragg grating) is monitored, but the ratio between front and rear power depends on the position on the mode, i.e. the difference $\lambda_{Fabry\text{-}Perot} - \lambda_{Bragg}$. It is then necessary to ensure concurrently mode position stabilization. In both cases, power is maintained constant by adjusting I_{active}.

But the major difficulty is mode control, that is to avoid SMSR degradation, and especially mode hops. The problem is to find a parameter, easy to measure in module, with characteristics representative of the position on the mode. Output power has often been used as monitoring [12,13], as it varies along the mode, as shown in figure 7. But for high powers, non linear effects appear, that shift power maxima to the left edge of the modes, or even suppress these maxima [14]. To limit these effects, one can weaken modes interactions with shorter active section length, leading to larger free spectral range, or increase Bragg filter selectivity with smaller κ. I_{Bragg} is dithered, with an extremely low frequency (a few Hz) to avoid spectral linewidth degradation, and I_{Bragg} is adjusted to maintain dP/dI_{Bragg} variation constant.

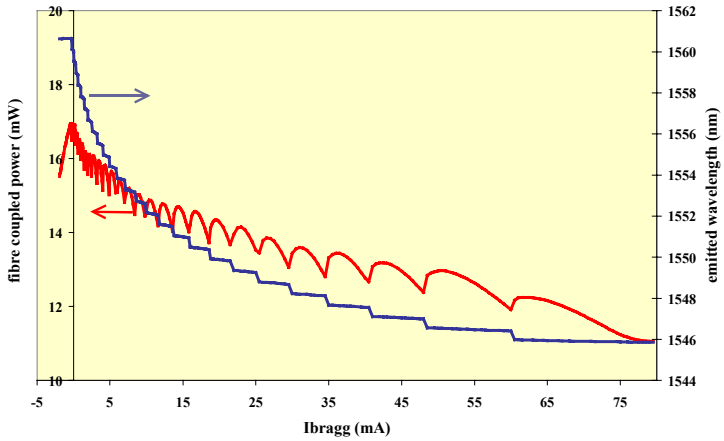


figure 7 : wavelength and power variations with I_{Bragg}, for I_{active}=150mA.

4. DBR long-term reliability

Reliability is a key factor for DBR tunable lasers. Indeed, simultaneous power, wavelength, and mode locking can ensure stable performances with aging, in particular the absence of mode hops, when the laser remains on a ITU wavelength. But when the device is tuned to another ITU wavelength, the electronic control card applies the set of currents (I_{active}, I_{phase} and I_{Bragg}) determined at the device beginning of life. Hence laser degradations must remain small enough to ensure locking algorithm convergence towards the desired ITU wavelength. In particular, if the tuning characteristic $\lambda = f(I_{Bragg})$ shifts strongly, the laser might tune to another longitudinal mode, and the wavelength locker would converge to a wrong ITU wavelength.

Bragg section aging is the main concern, as it operates with an unclamped carrier population: any aging degradation leads to a carrier density variation, hence modifying the Bragg wavelength of the mirror. Active section is expected to behave as standard Fabry-Perot lasers with the same technological process (buried ridge structure).

A study has been performed on 20 of our DBR lasers. Characteristics are first stabilized during 48 hours burning (100°C, I_{active}=300mA, I_{Bragg}=300mA), then monitored during 2000 hours accelerated aging (80°C, I_{active}=200mA, I_{Bragg}=100mA). Figure 8 shows, on a typical chip, the extremely small tuning curve shift along 2000h post-burning accelerated aging. Figure 9 demonstrates that this shift, normalized with the mode length, is below 10% on most of the 20

tested devices, and has 5% average absolute value, showing the high quality of our Q1.45 bulk material, and our current injection characteristics stability.

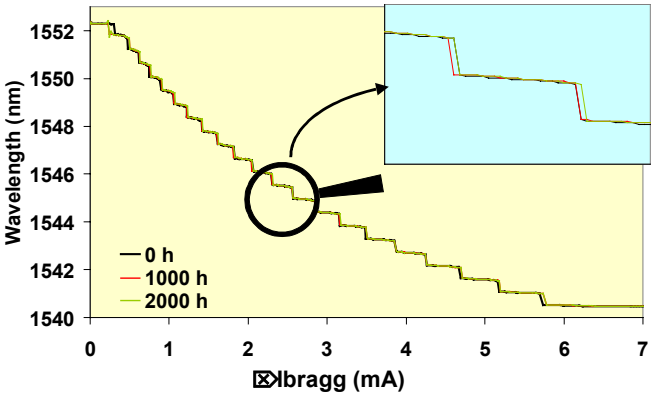


figure 8: typical tuning curve shift during 2000h post-burning accelerated aging.

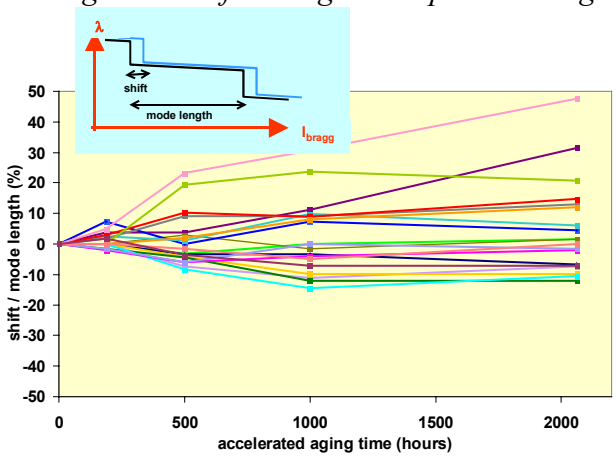


Figure 9 : 12th mode normalized shift for the 20 tested devices, during 2000h post-burning accelerated aging.

Other laboratories showed larger tuning curve shifts on their DBRs. Attributing this shift to increased non-radiative recombinations, they proposed a model that corrects the initial look-up table by extrapolating from the shift of the lasing Fabry-Perot mode [15].

5. New functionalities : amplifier and modulator sections

5.1 Semiconductor optical amplifier (SOA)

DBR lasers provide high output power, because light is emitted from the active section, and not through an absorbing and reflecting Bragg section, which enables to avoid SOA section. Still, we studied the integration of a SOA section, as it presents several advantages :

- power is provided outside cavity. Power control is totally independant from wavelength and mode control. Moreover, constraints on the active section design are loosened : active section length can be decreased, to enlarge FSR, thereby making mode control easier.
- The DBR behavior is very little affected by SOA current. In particular cavity or thermal interactions are extremely weak. The SOA section can thus be used as an optical gate, that turns off emission during I_{active} ramp, or tuning, or to allow look-up table recalibration.
- DBR lasing requires reflectivity at the active section facet. Thus if an integrated modulator is required, this modulator section cannot be added at the active section end, but compulsorily at

the Bragg section end, where emitted power is much weaker. An SOA section is then necessary to maintain power comparable with standard DFB lasers integrated with a modulator.

As the SOA section provides a high gain, and has an important reflection from the Bragg section (around λ_{Bragg}), the output facet reflectivity must be extremely low to avoid SOA lasing, leading to multicavity DBR-SOA behavior, and tuning curve irregularities. The SOA section is thus tapered (ridge width reduced from 1.5 to 0.8µm on the last 200µm), 10° tilted, and 0.01% antireflection coated.

With such a device, we obtained more than 20mW coupled output power at I_{SOA}=150mA, with unchanged tuning characteristics. And SOA as a gate seems promising, as λ_{Bragg} varies by less than 0.1nm for I_{SOA} ranging from 0 to 200mA, whereas it shifts by 0.5nm for the same I_{active} range.

5.2 Electroabsorption modulator (EAM) section

Direct modulation on a SG-DBR has been demonstrated over 40nm at 2.5Gb/s, but transmission distance is limited (75km with 4 to 6dB penalty) [16]. For most applications, a high quality modulated signal is required, which imposes the integration of an EAM section.

We use an EAM structure optimized to reduce sensitivity to $\Delta\lambda$, that demonstrated 2.5Gb/s transmission over 1000km standard fiber, over 20nm $\Delta\lambda$ variations ($\Delta\lambda$ = 45 to 65nm) [17], and transmitted at 10Gb/s over 90km standard fiber. Excellent results have been demonstrated on a DBR integrated with SOA and multi-quantum well EAM, over 9nm tuning range, with 1mW average modulated power : 2.5Gb/s transmission over 681km (RF extinction ratio>14dB with V_{EAM}=2 $V_{peak\ to\ peak}$), and 10Gb/s over 82km (RF extinction>8.5dB with V_{EAM}=1.7 $V_{peak\ to\ peak}$) [18].

6. Comparison between DBR and SG-DBR

Currently, SG-DBR lasers integrated with an SOA are very promising candidates for tunable lasers applications, because they are becoming industrially reliable, and allow high power and fast tuning over more than a whole C or L band.

As a comparison, DBR lasers have slightly inferior performances in terms of tuning range (only half C or L band), and possibly in tuning speed, due to Bragg currents up to 50mA (compared to 15mA in SG-DBR) creating more thermal effects.

Still, they could be very attractive depending on the applications, as they present several important advantages :

- DBR devices are much simpler, with only 3 sections. SG-DBR requires two bragg sections, and due to the insufficient emitted power (<20mW in fiber) an SOA output section is integrated, leading to a 5-sections device. This has an impact on industrial yield, on electronic control complexity, and imposes to monitor front facet output power for power monitoring.
- Mode control, which is the major concern for these tunable devices, only demands one current (I_{bragg}) dithering and adjustment on a DBR. Whereas for a SG-DBR, both front and rear Bragg sections currents must be dithered, at different frequencies, to monitor simultaneously parameters variations (commonly V_{active}) relatively to front and rear Bragg currents, and adjust $I_{Bragg\ rear}$ and $I_{Bragg\ front}$ consequently.
- EAM characteristics (extinction, on-state absorption, chirp, …) highly depend on the detuning $\Delta\lambda$ between lasing wavelength and modulator absorption-edge wavelength. Good characteristics can be maintained over a 16nm DBR tuning range, but not over the whole 40nm tuning range of an SG-DBR. EAM integration has been demonstrated on a widely tunable laser (SG-DBR-SOA-EAM), providing 2.5Gb/s modulation over 40nm tuning range, with more than 10dB RF extinction ratio, provided that modulator driving voltages are adjusted according to emitted wavelength. Still, the modulated signal characteristics (chirp in particular) remain insufficient,

as transmission distance is limited to 200km [19]. To our knowledge, no 10Gb/s results have been published yet. A solution is to replace EAM by a Mach-Zehnder modulator section, that is less mature, but as well less sensitive to $\Delta\lambda$ [20].

Conclusion

We presented state-of-the-art of tunable laser sources, with characteristics (tuning range, tuning speed,…) addressing various transmission or routing applications. In this context, we consider DBR laser as a good compromise between simplicity (integrated device, only 3 sections, simple and mature technological process), and improved performances (16nm tuning, 13dBm coupled output power, fast tuning, …). We took the stock on the optimizations that resulted in a device with leading performances, and on the aspects of electronic control, aging, and new functionalities integration (SOA, EAM) at the center of current studies.

[1] D.M. Adams et al., Electronics Letters, May 2001, Vol.37, No.11, pp.691-693.
[2] H. Hatakeyama et al., Optical Fiber Communication Conference 2002, WF2, pp.205-206.
[3] B. Pezeshki et al., IEEE Photonics Technology Letters, Oct 2002, Vol.14, No.10, pp.1457-1459.
[4] D. Anthon et al., Optical Fiber Communication Conference 2002, Tu07, pp.97-98.
[5] K.J. Knopp et al., LEOS 2001, TuA1.3.
[6] H. Debrégeas-Sillard et al., IEEE Photonics Technology Letters, Jan 2001, Vol.13, No.1, pp.4-6.
[7] H. Debrégeas-Sillard et al., European Conference on Optical Communications 2002, P2.29.
[8] P.J. Rigole et al., Electronics Letters, Dec 1996, Vol.32, No.25, pp.2352-2354.
[9] www.agilitycom.com
[10] T. Lilijeberg et al., Semiconductor Laser Conference 2002, TuB1, pp.45-46.
[11] D.C.F. Reid et al., Optical Fiber Conference 2002, ThV5, pp.541-543.
[12] J.E. Johnson et al., IEEE Journal of Selected Topics in Quantum Electronics, March/April 2001, Vol.7, No.2, pp168-177.
[13] H. Ishii et al., Journal of Lightwave Technology, March 1998, Vol.16, No.3, pp.433-441.
[14] A.P. Bogatov et al., IEEE Journal of Quantum Electronics, July 1975, Vol. 11, No.7, pp.510-515.
[15] D.A. Ackerman et al., IEEE Journal of Quantum Electronics, Nov. 2001, Vol.37, No.11, pp.1382-1387.
[16] M.L. Majewski et al., Optical Fiber Communication Conference 2002, ThV2, pp.537-538.
[17] H. Debrégeas-Sillard et al., IEEE Photonics Technology Letters, Nov. 1999, Vol.11, No.11, pp.1485-1487.
[18] J.E. Johnson et al., LEOS 2001, TuA2.3, pp.37-38.
[19] Y.A. Akulova et al., Optical Fiber Communication Conference 2002, ThV1, pp.536-537.
[20] E.J. Skogen et al., Semiconductor Laser Conference 2002, TuB3, pp.49-50

Characterisation and Modelling of a Compact Multiwavelength Ringlaser

E.A.J.M. Bente, Y. Barbarin, J.H. den Besten, M.K. Smit
Eindhoven University of Technology, Dept. of Electrical Engineering
Den Dolech 2, 5612 AZ Eindhoven, The Netherlands
e.a.j.m.bente@tue.nl

J.J.M. Binsma
JDS Uniphase, Prof. Holstlaan 4, 5656 AA Eindhoven, The Netherlands

Detailed spectral characteristics have been measured of an integrated compact multi-wavelength ringlaser that can produce 7 different wavelengths. The frequency selection mechanism was established and the laser was modelled using a rate equation description.

Keywords: tunable lasers, phasars, arrayed waveguide gratings

Introduction

For WDM networks, lasers that can be switched between different pre-selected wavelengths are a useful alternative for the commonly used arrays of distributed feedback (DFB) lasers or distributed Bragg reflector (DBR) lasers. Such wavelength switchable lasers can be fabricated by integrating a series of semiconductor optical amplifiers (SOA) with a PHASAR on a single chip using an active/passive integration technology. Several of such devices with different geometries and properties have been produced and demonstrated in the InP/InGaAsP material system [e.g. 1,2,3,4]. Particular issues are: a) trying to produce as many choices for wavelengths with a minimum number of SOAs and b) whether more than one wavelength needs to be delivered at the same time in one waveguide. One of the lasers that was demonstrated by den Besten et al [1], is the world's most compact wavelength switchable ring laser. It was demonstrated that driving one or two of the four SOAs could produce seven different wavelengths. In this paper we focus on the wavelength selection mechanism for the wavelengths produced when two SOAs are operated. The behaviour of the laser is simulated using a rate equation model, using parameters for the SOAs that where checked against results obtained with extended cavity FP lasers built with similar SOAs.

Laser operation

The operation of the ringlaser can be explained using the mask layout that is shown in figure 1. The laser contains four 500µm long, 2µm wide amplifiers integrated with the wavelength selective element, the PHASAR, via waveguides. Deep etching of the curved waveguides allows for the compactness of the device. A small fraction, estimated at about $5*10^{-4}$, of the laser light is coupled out of the resonator by leading the outer waveguides of the waveguide array to the edge of the chip. The PHASAR has a channel spacing of 1.6nm (200GHz) and a Free Spectral Range (FSR) of 15nm. Further details on fabrication and design can be found in [1]. When only one of the SOAs is operated at a time, four different wavelengths are produced with a spacing of 3.2 nm. This difference equals two channel spacings since the four waveguide connections to the PHASAR are equally spaced at both ends of the PHASAR. This is shown schematically in figure 2, which depicts the connections to the PHASAR. When two SOAs are operated, e.g. nrs. 1 and 2, a new wavelength λ_{AB} is generated that lies exactly in between the wavelengths

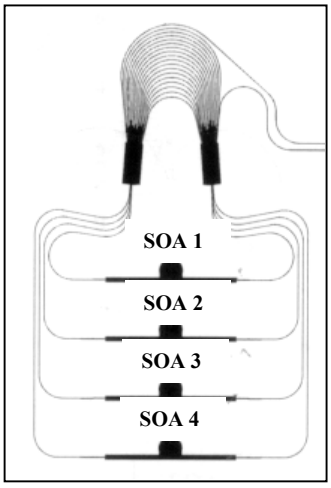


Figure 1. Mask layout of the compact ring laser.

generated using only SOA1 (λ_A) or SOA2 (λ_B). This can be understood as originating from a double roundtrip mode as indicated on the right-hand side in figure 2. Here light is coupled from port 2 on the left-hand side of the PHASAR to port 1 on the right and vice versa. The resulting wavelength λ_{AB} is thus halfway between λ_A and λ_B. To determine why this mode at λ_{AB} prevails over the modes with λ_A and λ_B, we have measured the characteristics of the laser and wrote a simple rate equation model.

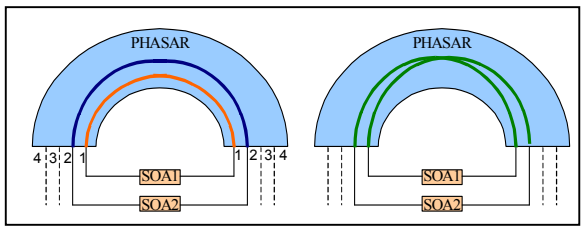


Figure 2. Diagram of the ports on the PHASAR.

Laser model

The rate equation model [5] given below was set up in a MathCAD worksheet and it describes the time derivatives of the average photon densities ϕ_A, ϕ_B and ϕ_{AB} at the three wavelengths λ_A , λ_B and λ_{AB}, and the carrier density in the two amplifiers N_A and N_B.

$$\begin{cases} \frac{d\phi_A}{dt} = \phi_A \cdot \left[(N_A - N0_A) \cdot \left(Vg \cdot \alpha \cdot \Gamma \cdot \frac{L_{SOA}}{L_{cavA}} \right) - \frac{Loss_{cavA} - \ln(1-T)}{\tau_A} \right] + B \cdot \Gamma \cdot N_A^2 \cdot \beta \\ \frac{d\phi_B}{dt} = \phi_B \cdot \left[(N_B - N0_B) \cdot \left(Vg \cdot \alpha \cdot \Gamma \cdot \frac{L_{SOA}}{L_{cavB}} \right) - \frac{Loss_{cavB} - \ln(1-T)}{\tau_B} \right] + B \cdot \Gamma \cdot N_B^2 \cdot \beta \\ \frac{d\phi_{AB}}{dt} = \phi_{AB} \cdot \left[(N_A - N0_A) \cdot \left(Vg \cdot \alpha \cdot \Gamma \cdot \frac{2L_{SOA}}{L_{cavAB}} \right) + (N_B - N0_B) \cdot \left(Vg \cdot \alpha \cdot \Gamma \cdot \frac{2L_{SOA}}{L_{cavAB}} \right) - \frac{Loss_{cavAB} - \ln(1-T)}{\tau_{AB}} \right] \\ \qquad + B \cdot \Gamma \cdot (N_A^2 + N_B^2) \cdot \beta \\ \frac{dN_A}{dt} = -Vg \cdot \alpha \cdot (\phi_A + \phi_{AB}) \cdot (N_A - N0_A) - \frac{N_A}{\tau_{car}} - B \cdot N_A^2 - C \cdot N_A^3 + W_A(t) \\ \frac{dN_B}{dt} = -Vg \cdot \alpha \cdot (\phi_B + \phi_{AB}) \cdot (N_B - N0_B) - \frac{N_B}{\tau_{car}} - B \cdot N_B^2 - C \cdot N_B^3 + W_B(t) \end{cases}$$

Here $N0_A$ and $N0_B$ are the transparency carrier densities in the amplifier; Vg is the group velocity; α is the gain per carrier; Γ is confinement factor; L_{SOA} is the length of the SOA; L_{cavA}, L_{cavB} and L_{cavAB} ($\approx Lcav_A + Lcav_B$) are the cavity lengths; $Loss_{cavA}$, $Loss_{cavB}$ and $Loss_{cavAB}$ are the intracavity losses, T is the fraction coupled out of the cavity for output; τ_A, τ_B and τ_{AB} are the cavity roundtrip times; τ_{car} is the carrier lifetime, B is the bimolecular recombination rate, C is the Auger recombination rate; and $W_A(t)$ and $W_B(t)$ are the carrier injection rates. The material parameters used have been taken from a simulation of a simple laser using the Apollo Photonics ALDS software. Using a single mode model and these parameters we have been able to fit L-I curves from a series integrated extended cavity Fabry-Perot lasers with varying amplifier length, that were fabricated on the same wafer segment as the wavelength switchable laser.

Characterisation results

When the double roundtrip loss $Loss_{cavAB}$ is taken to be: $Loss_{cavA} + Loss_{cavB}$, the model predicts that the double roundtrip mode does produce the most output power. However power at the other two wavelengths is only several dBs lower. To have the λ_{AB} mode dominate the spectrum by over 40dB this mode needs a lower intra-cavity roundtrip loss by several tenths of dBs at least. Initially we thought this lower loss could be related to the smaller mode spacing of the longitudinal modes of a double roundtrip mode. The longer cavity meant that this mode could be closer to the PHASAR transmission maximum. However, this advantage should be highly sensitive to temperature. The intensity of the three modes λ_A, λ_B and λ_{AB} should vary considerably with temperature. A series of output spectra at heatsink temperatures of 18 to 28°C, with the laser operating at the combination

wavelength of SOA 1 and SOA 2, shows that the mode is robust. A detailed comparison of the spectra reveals no significant change in the location of the cavity modes with respect to the central peak. Only a shift in wavelength of 0.12nm/°C is observed which is in line with the expected temperature dependence of the channel wavelengths of the PHASAR.

The spectra from the laser below the lasing threshold turned out to contain crucial information. The example shown in figure 3 was recorded with 58mA through both SOA1 and SOA2. It shows in total six different combs of modes related to: a single round trip cavity through SOA1 (cavity A), a single round trip cavity through SOA2 (cavity B) and the modes related to the combined wavelength cavity (cavity AB). These are visible for both TE and TM polarisation. The modes in the middle of the spectrum only appear when both amplifiers are switched on. The important observation stems from the free spectral ranges in the different combs. The comb of TE modes on the right-hand side is from cavity A with an FSR of 180pm. The comb of TE modes on the left-hand side is from cavity B with a smaller FSR of 160pm, which fits the longer optical path (see figure 1). The TE modes in the middle however show an FSR of 170pm! We would expect half of this value since the cavity length of the double roundtrip loop is approximately twice as long! This

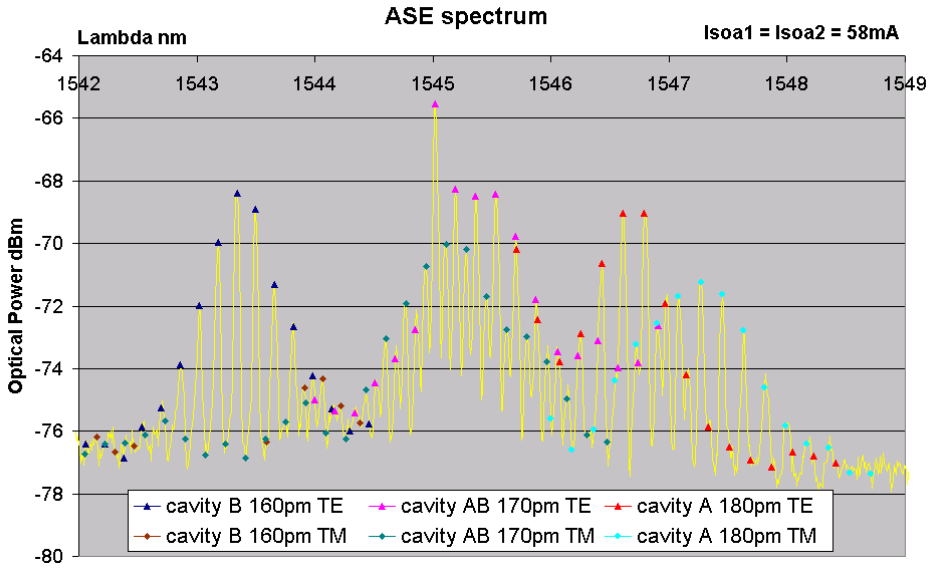


Figure 3. A sub-threshold spectrum with SOA1 and 2 pumped at 58mA.

indicates two things. Firstly, we have to conclude that there is a single roundtrip resonance condition on the combined mode. This can be caused by cross-talk between the channels in the PHASAR. The extra modes that we expected to see in between single pass modes will lead to a 180 degrees phase difference between the light fields in the two waveguides entering the PHASAR. This apparently leads to lower transmission efficiency. The cross-talk will make that the total transmission through the PHASAR of the light at λ_{AB} from two adjoining waveguides at one side, to the two adjoining waveguides at other side of the PHASAR will be highest when the phases in the waveguides are close to each other. Secondly, when the fields are in phase, part of what is otherwise lost in PHASAR transmission as cross-talk into another channel is now used. Light that gets to the other waveguide stays in the cavity. The PHASAR in this laser has a poor cross-talk specification since one would expect this not to be of importance for wavelength selection inside a laser cavity.

Using spectra as in Figure 3, we derived an effective transmission loss difference of about 1dB for the PHASAR in the single SOA modes and the combined SOA mode. Using this number we

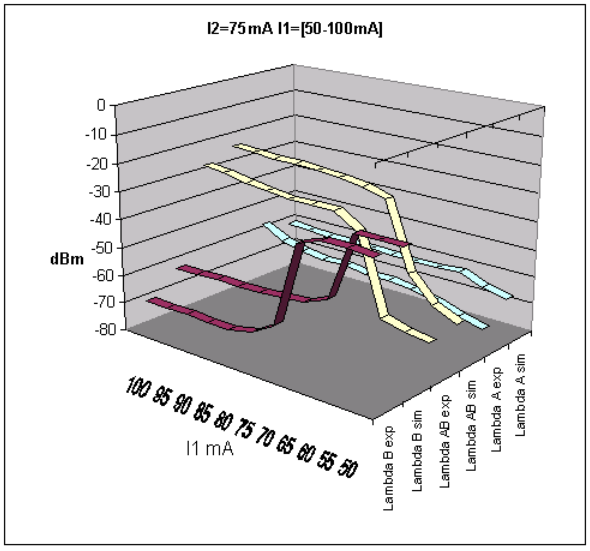


Figure 4. Measured and simulated output power levels in dBm of the multiwavelength ringlaser at the three wavelengths as a function of current (50 to 100mA) through SOA 1 with a fixed current through SOA2 (75mA).

simulated the switching of the laser between a single SOA mode and the combined SOA mode when the current in one of the SOAs was varied. An example of a comparison between measurements and modelling results is shown in figure 4. It shows the simulated and measured output power of the device at the three modes with the current in SOA 2 at 75mA and the current in SOA1 scanned from 50 to 100mA. The vertical axis is the output power in dBm. The strips connecting the points indicate, from front to back, the power in λ_B(exp.), λ_B(sim.), λ_{AB}(exp.), λ_{AB}(sim.), λ_A(exp.) and λ_A(sim.). It shows that the switching between the wavelengths can be understood correctly.

Currently work is in progress to be able to predict the roundtrip losses and detailed mode structure of the cavity for the combination wavelength from the PHASAR and cavity design parameters using the design software we have available.

Conclusion

The mechanism responsible for the wavelength selection in a PHASAR based discretely tunable ring laser turns out to be related to a property of the PHASAR when multiple inputs are used at the same time with coherent light. Using a simple three-mode rate-equation model the switching behaviour between the operating modes could be described.

This work has been carried out under the framework of the OBANET IST-2000-25390 project and the Dutch NRC-Photonics programme.

References

[1] J.H. den Besten, R.G. Broeke, M. van Geemert, J.J.M. Binsma, F. Heinrichsdorff, T. van Dongen, T.J. de Vries, E.A.J.M. Bente, X.J.M. Leijtens, M.K. Smit, “A compact digitally tunable seven-channel ring laser”. *IEEE Phot.Tech. Lett*. vol. 14, pp.753-755, 2002.

[2] J.H. den Besten, R.G. Broeke, M. van Geemert, J.J.M. Binsma, F. Heinrichsdorff, T. van Dongen, E.A.J.M. Bente, X.J.M. Leijtens, M.K. Smit, “An integrated coupled cavity 16 wavelength digitally tunable laser”, *IEEE Phot. Technol. Lett*., vol. 14, pp. 1653-1655, 2002.

[3] C. Doerr, C.H. Joyner, and L.W. Stulz, “40-wavelength rapidly digitally tunable laser.”, IEEE *Phot. Technol. Lett.*, vol. 11, no. 11, pp. 1348-1350, 1999.

[4] J.H. den Besten, R.G. Broeke, M. van Geemert, J.J.M. Binsma, F. Heinrichsdorff, T. van Dongen, E.A.J.M. Bente, X.J.M. Leijtens, M.K. Smit, "An InP-based 4x4 channel multi-wavelength laser", Accepted for publication *Phot. Technol. Lett.* March 2003.

[5] L.A. Coldren and S.W. Corzine, Diode Lasers and Photonic Integrated Circuits, Wiley series in microwave and optical engineering, John Wiley & Sons Inc., 1995, ch. 2, pp. 28-64.

DWDM DFB laser matrix realized by ion exchange on glass substrate

Lionel Bastard, Jean-Emmanuel Broquin
IMEP, 23 rue des Martyrs, 38016 Grenoble - France

Sylvain Blaize
LNIO - UTT, 12 rue Marie Curie, 10010 Troyes

Cedric Cassagnettes
Teem Photonics, 61 chemin du Vieux Chene, 38018 Grenoble CEDEX 1

This paper presents the realisation of DFB laser matrices realised on Erbium-Ytterbium codoped glass substrates. Results obtained on a multi-wavelength comb of lasers integrated on a single chip are shown. Indeed, matrices of 8 DFB lasers with a 100 GHz frequency spacing were demonstrated. The fibre output power of each laser is better than 1mW and a stable emission wavelength is achieved without any temperature regulation. Finally, packaging improvements are discussed in terms of output power and stability.

Keywords: DFB laser, glass integted optics, laser matrix, 100GHz ITU grid

Introduction

In the past decade, a huge growth of the worldwide telecommunication network occurred thanks to the development of optical information transport technology. One way to increase the bit-rate of optical telecommunication is the DWDM (Dense Wavelength Division Multiplexing), in which several signals with different wavelengths are launched in a single optical fibre. Because of the use of Erbium Doped Fibre Amplifiers (EDFA), these wavelengths are set in the third telecommunication window around 1.55μm and should be spaced by 100, 50, or even 25 GHz, as defined by ITU standards [1]. This brings important constraints on both multiplexer/demultiplexer systems and laser sources developed for this application. Considering the latter, the main issues are the output power, the laser linewidth, the wavelength stability, and finally the output power noise.

Two main families of laser sources are nowadays commonly employed around 1.55 μm : semiconductor based lasers [2] and optical fibre lasers [3]. In this paper, a third alternative is presented : glass integrated optics lasers which combines the main advantages of both semiconductor and fibres lasers. Indeed, integrated optics provides planar integration and compactness whereas the use of ion-exchanged waveguides realised on Erbium-Ytterbium doped glass entails a wide bandwidth amplifying medium with a low sensitivity to thermal variations.

This paper first deals with the realisation of the ion-exchanged DFB lasers matrices then the measurement of their performances are presented. Finally, packaging improvements are discussed.

Laser Matrix realisation

The lasers are realised on $2.5 \times 10^{26} m^{-3}$ Erbium and $2.5 \times 10^{26} m^{-3}$ Ytterbium codoped phosphate glass substrates. The phosphate glass is chosen for its excellent properties as an host for Erbium and Ytterbium ions [4]. The waveguides are realised by a silver-sodium ion exchange which enables a high index increase of 10^{-1} and the realisation of low losses buried waveguides [5]. In our case, the burying depth d has been set to 4 μm in order to preserve a good interaction of the guided mode with the surface Bragg grating in charge of the feedback. Indeed, as a single frequency emission and a planar integration are required, lasers are designed to work on a Distributed FeedBack (DFB) configuration. The realised device is depicted on

Figure 1, the chip contains 15 waveguides separated by 250 μm, and is 3 cm long. A 1.7 cm long Bragg grating has been etched by RIE on the device surface. It has been realised by a holographic exposure on a standard microelectronic photoresist [6]. Grating's path Λ has been controlled by the measurement of the angle of minimum deviation at $\lambda = 632.8\ nm$ and it is $501 \pm 1\ nm$. Grating's depth h has been measured by Atomic Force Microscopy (AFM) to be $300 \pm 50\ nm$.

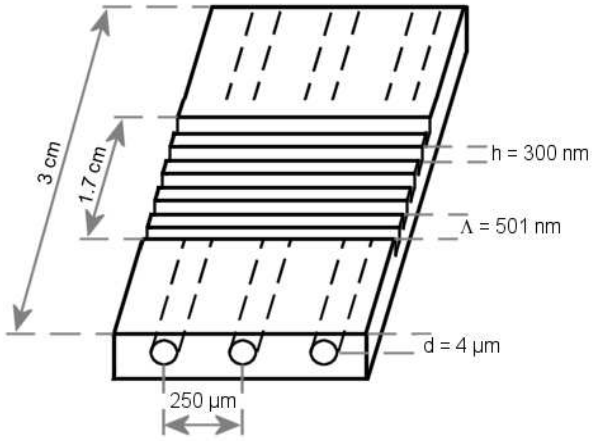


Fig. 1. Schematic representation of the realised chip

The emission wavelength λ_{em} of a DFB laser is given by the relation : $\lambda_{em} = 2\Lambda n_{eff}$, where Λ is the grating period and n_{eff} the effective index of the lasing mode. Therefore, there are two possibilities to select the emission wavelength for lasers realised on the same chip : the first one is to realise gratings with different paths, this is however really hard to achieve for 25 to $100 Ghz$ spaced lasers because it requires a control of the grating period better than the Angström; the second solution consisting in a change of the effective index has been implemented here : it is indeed possible to control the relative effective index change of ion-exchanged waveguides with an accuracy of 10^{-4} by adjusting their opto-geometrical parameters. In our case, the 15 waveguides have been realised with diffusion aperture widths ranging from 0.8 μm to 6 μm.

Characterisation

The matrix chip has been characterised in terms of emission wavelengths, output power, emission linewidth and relative intensity noise. Each laser has been individually tested with a 220 mW fibre output power laser diode emitting at $\lambda_p = 977\ nm$ as a pump . The light coming from the fibre output of the pump diode is first injected into a 980 $nm/1550\ nm$ fibre duplexer and then coupled into the laser using micro-positioning stages. The emitted light is collected on the 1.55 μm output of the duplexer and directed on either a power-meter or an Optical Spectrum Analyser (OSA). Figures 2 and 3 display respectively the comb of wavelengths obtained with that device and the fibre output power response of one of the matrix's laser (laser number 9). From Figure 2, it can be seen that two comb of respectively seven 25 GHz spaced lasers and eight 100 GHz spaced lasers have been obtained. In order to assess the stability of the emitted spectra, they have been recorded for 16 hours at maximum pump power and no drift has been measured within the accuracy of the OSA (0.07 nm). These results demonstrates the potential of the ion-exchanged integrated optics technology to realise matrix for the DWDM. The linewidth of lasers has also been measured with a Fabry-Perot analyser leading to a value of 130 MHz which is in fact the nominal resolution of the analyser. Therefore it can be said that

the linewidth of the lasers are smaller than 130 MHz and measurements based on heterodyne techniques are currently carried out to obtain their actual values. It can be noticed from Figure 3 that the fibre output power of the laser reaches 1.5 mW with a pump power of 100 mW. Laser threshold is at 35 mW of pump power for a laser efficiency of 2.5%.

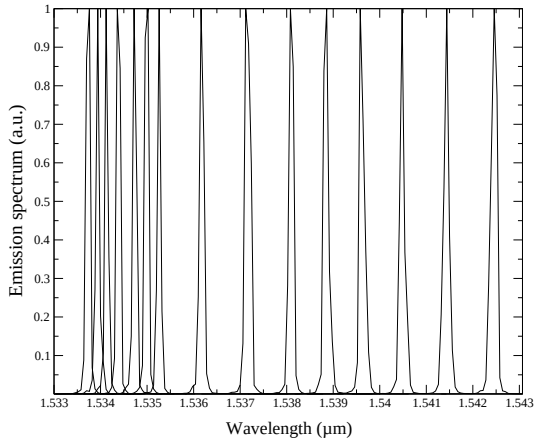


Fig. 2. Superposition of the normalized emission spectra of the 15 waveguide lasers

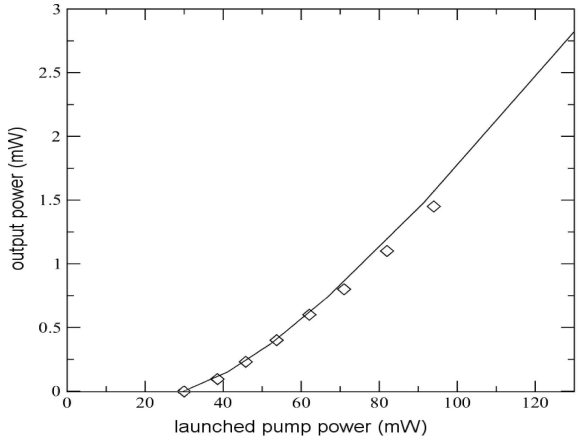


Fig. 3. Output power characteristic of laser number 9

Although the fibre output power is high enough for telecom applications, it must be noticed that the laser efficiency is actually low. This fact can be explained by the parasitical diffractive effect of the grating on the pump. Indeed, the excess losses induced the grating at λ_p have been measured to be 5.5 dB/cm. However, this problem can be overcome by adding an appropriate passivation layer on the top device. Indeed, as can be seen on figure 4, the excess losses caused to the pump decreases dramatically with an increase of the superstrate layer's refractive index whereas the coupling efficiency variation at 1.55 μm is smoother. Therefore the use of a polymer based superstrate layer with a refractive index of 1.46 has been tested and is reported on Figure 5.

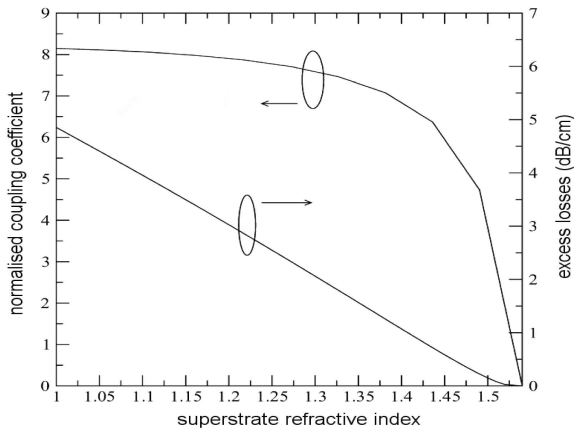


Fig. 4. Evolution of coupling coefficient and excess losses with the superstrate index

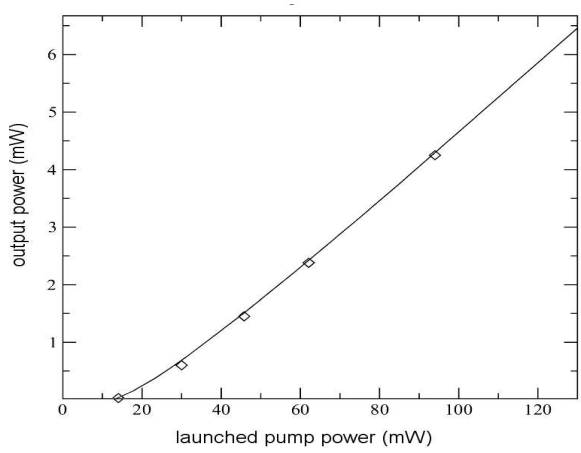


Fig. 5. Output power characteristic of laser number 9 with a superstrate layer

The threshold of the laser is now 20 mW which is the minimum amount of power required to invert the Erbium ions population, and the output power reaches 4 mW with an efficiency of 5.7%. It must also be noticed that this layer provides a mechanical and chemical protection to grating and therefore increases the device reliability.

In order to measure the RIN of the lasers, another device with a 2.4 cm long grating has been used. Its facet has been polished with an angle of 8 degrees and the extremities of the waveguides were post-diffused, creating input and output tapers and improving the coupling efficiency. Finally fibres were glued to the device, and measurement were performed. The improvements of the coupling efficiency has led to an increase of the laser efficiency from 0.07% to 2.7% without the adjunction of a passivation layer. Measurements of the RIN were performed on that device and the RIN falls below -155 dB/Hz after 200 MHz with a peak value of -84 dB/Hz at the 282 kHz relaxation frequency of the laser. These results are as good as the ones typically obtained with fibre lasers [7]. Devices combining both a passivation layer and coupling tapers are currently being realised and simulations show that the lasers efficiency would reach at least 30%.

Conclusion

In this paper, we have presented the realisation of an ion-exchanged DFB laser matrix for DWDM applications. Two comb wavelengths with spacing of respectively 25 GHz and 100 GHz were demonstrated. It was also shown that the use of an appropriate passivation layer reduces the lasers' thresholds and increases their efficiencies by a factor 2. Finally, the improvement of the waveguide coupling efficiency was demonstrated to dramatically improve the behaviour of the device, leading to a low RIN. Future improvements will be focused on the integration of both the passivation layer and coupling tapers on a same device leading to a calculated efficiency of at least 30%.

References

[1] ITU-T study group 15, *Recommendation G.694.1*, 2002.

[2] S-L. Lee, I-F. Jang, C-T. Pien, T.T. Shih, *IEEE J. Selected Topics in Quantum Electron.* **6**, 1, 197–206, 2000.

[3] T. Haber, K. Hsu, C. Miller, Y. Bao, *IEEE Photon. Technology Letters* **12**, 11, 1456–1458, 2000.

[4] B-C. Hwang, S. Jiang, T. Luo, J. Watson, G. Sorbello, N. Peyghambarian, *J. Opt. Soc. Am.B* **17**, 5, 833–839, 2000.

[5] J. Broquin, *Proceedings of SPIE* **4277**, 105–117, 2001.

[6] D.H. Norbury, J.C. Love, *Proceedings of SPIE* **1463**, 558–574, 1991.

[7] W.H. Loh, B.N. Samson, L. Dong, G.J. Cowle, K. Hsu *J. Lightwave Technology* **16**, 1, 114–118, 1998.

SINGLE-FREQUENCY Er:Yb PHOSPHATE GLASS WAVEGUIDE LASER ARRAY

G. Sorbello[+], S. Taccheo, G. della Valle, G. Jose, R. Osellame, R. Ramponi, P. Laporta
INFM, Dipartimento di Fisica del Politecnico and IFN-CNR - Piazza L. da Vinci 32, 20133 Milano
[+]*now with* Università di Catania, DIIT, 95125 Catania, Italy,
taccheo@polimi.it

E. Cianci, V. Foglietti
IESS-CNR, V. Cineto Romano, Roma 00156, Italy

We fabricated an high-power single-frequency end-pumped Er:Yb:glass waveguide laser array by ion-exchange technique. The linear cavity 1.5 µm laser emits 3.7-mW at 1534 nm and 2.9 mW at 1550 nm at 180 mW pump power.

Keywords: guided-wave laser, single-frequency laser, erbium laser, ion-exchange

Introduction

In the recent years we had an increasing demand for compact active devices at 1.5 µm for metro/local optical network applications. A promising solution is to fabricate array of waveguide devices on the same glass chip. In fact these devices are very promising in terms of cost, size and reliability. In particular active devices based on high-concentration Erbium doped glasses are very promising for making compact array of linear devices that are compatible with multifiber cable.

To obtain high gain per unit length (p.u.l.) Ytterbium codoping and phosphate glass base demonstrated to offer superior performance: Ytterbium codoping offers waveguide design flexibility and enhances pump absorption efficiency while phosphate glass base optimizes the energy transfer process between Erbium and Ytterbium ions [1]. Active fiber with gain up to 5 dB/cm [2] and amplifier with high gain p.u.l. and high output power have been reported [3-5]. Among various technique to fabricate such devices ion-exchange is a simply, reliable and rugged option and it was successfully demonstrated both using Ag-Na [4,7,8] and K-Na [9] ion-exchange. Active structures [10-12] and in particular optical amplifiers [3,4], lossless splitter [13] and single-frequency lasers [7-9] have been demonstrated. However laser devices were limited by low output power or by a cavity design requiring bi-directional pumping.

In this paper we report on a compact linear array of single-frequency waveguide lasers fabricated by a two-step ion-exchange technique. The laser emits about 3 mW at both 1534 nm and 1550 nm and shows robust single-frequency operation.

Waveguide fabrication

The laser has been fabricated by using a commercial phosphate glass base (Schott, IOG-1) with doping concentration of $2x10^{20}$ ions/cm^3 and of $6x10^{20}$ ioni/cm^3 for Erbium and Ytterbium, respectively. In the two-step ion-exchange technique we first make a superficial waveguide by Ag-Na ion-exchange and thermal diffusion. The second step is a field-assisted burial step. We therefore

performed preliminary investigation of glass parameters [14]. On the basis of this investigation we found that a first step with 0.02 surface refractive index variation and about 7 mm diffusion depth was the optimum to match the standard fiber mode profile after the burial step. The salt composition in the first step was 8% wt $AgN0_3$, 86.85% wt $KN0_3$ and 5.15% wt $NaN0_3$ and the step was performed at 330 °C for about 8 min. To reduce the waveguide loss the second burial step using Na-K fused salt was done, obtaining a mode-field profile compatible with standard SMF-28 telecom fiber. A set of sixteen 250-μm spaced buried channel array was obtained.

Single-frequency laser array

Figure 1 shows the schematic diagram of the linear laser cavity array. Two 25-GHz full-width-half maximum fiber-Bragg-gratings (FBGs) with 99.8% and 75% reflectivity, respectively, are butt-coupled by using index-matching fluid to the waveguide. By using the high-concentration glass we were able to obtain sufficient gain by using an end-pumped cavity as short as 10 mm. We thus overcame the complexity of the double pump configuration previously realized [15]. In addition the short cavity minimized mode-competition.

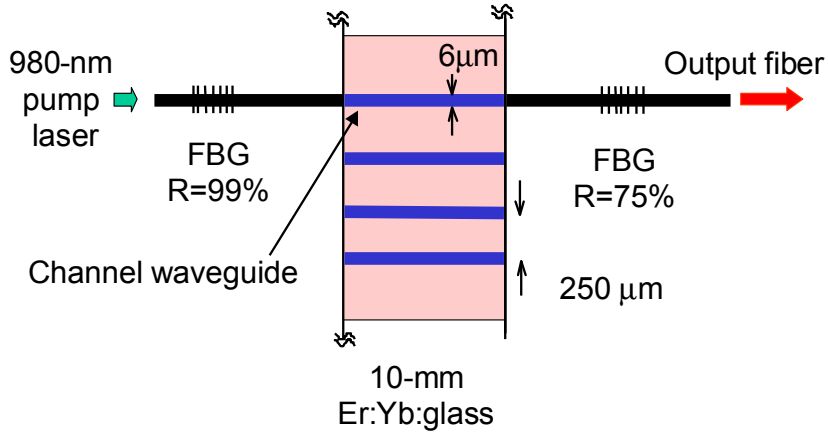


Figure 1: Schematic of the linear laser cavity

To further ensure robust single-frequency operation by inhibiting the onset of spatial hole burning, one of the two FBGs was placed ~20-cm apart, while the other was close to the active waveguide. The composed asymmetric cavity had a free-spectral-range of ~0.3GHz. The fiber-coupled 975-nm wavelength-stabilized laser pump diode was directly spliced to the 99.8% reflectivity FBG for a maximum available power of 180 mW. The single-frequency laser output was monitored by a high-finesse Fabry-Perot interferometer with resolution <100 MHz.

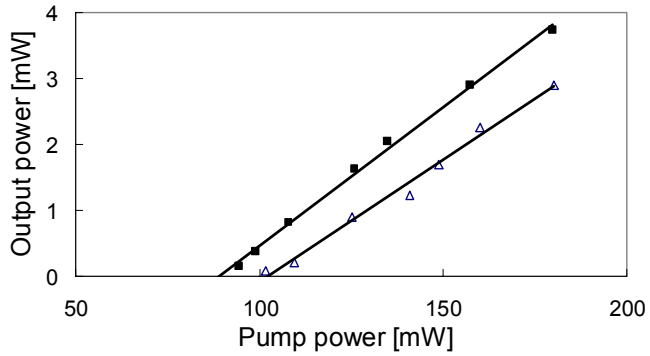


Figure 2: Output power versus pump power at 1534 nm (squares) and at 1550 nm (empty triangles).

Figure 2 shows the a typical single-frequency output power versus launched pump power curve at both 1534 nm and 1550 nm. At the peak wavelength the maximum single frequency output power was 3.7 mW at the maximum pump power with about 4.1% slope efficiency. A different channel was used as 1550 nm cavity. The laser threshold was a bit higher and the maximum output power was 2.9 mW with about 3.6% slope efficiency. By optimizing reflectivity at each wavelength we are looking for a laser array device with 3 mW output power from 1530 nm to 1565 nm. We stress that single-frequency operation was robust up to the maximum pump power however occasional mode-hopping occurred due to technical and thermal noise. To verify source suitability for external modulation we measured the relative-intensity-noise (RIN) spectra. A typical value is a RIN peak of about –80 dB/Hz at the relaxation oscillation frequency of about 180 kHz. The RIN value than decreases below –150 kHz for frequencies higher than ~3 MHz

Conclusions

In conclusion we reported on a high-power single-frequency end-pumped waveguide Er-Yb laser array operating in the C-band fabricated by the ion exchange technique using a commercial glass substrate. This device is extremely promising as compact transmission source for multi-wavelength optical network. This work was partially supported by Progetto Finalizzato MADESS II. One of the authors, G. Jose, acknowledges the support of an ICTP, Trieste Italy grant. Authors acknowledge the contribution of Daniele Costantini, EPFL-Lousanne, for measuring FBG position.

References

[1] S. Taccheo, P. Laporta, S. Longhi, C. Svelto and O. Svelto, *Appl. Phys. B*, **B63**, 425-432, 1996.
[2]Y. Hu et al., *IEEE Phot. Technol. Lett.*, **13**, 657-659, 2001.
[3]D. Barbier e al., *OFC 98*, paper TuH5
[4]C. M. McIntosh, J.-M.P. Delavaux, G.C. Wilson, C. Hullin, B. Neyret, J. Philippsen, C. Cassagnettes and D. Barbier, *OFC2001*, paper WDD5
[5] S.Taccheo, G. Jose, G. Sorbello, R. Osellame, D. Migliorati, P. Laporta, V. Foglietti, Cianci, S. Jiang, N. Peyghambarian, *ECOC2002* paper P1.37
[6]Y.C. Yan, A. J. Faber, H. de Wall, P G. Kik and A. Polman, *Appl. Phys. Lett.*, **71**, 2922-2924, 1997.
[7]S. Blaize, J. E. Broquin, D. Barbier, qnd C. Cassagnètes *CLEO/Europe2000*, paper CFG2
[8]G. Sorbello, S. Taccheo, P. Laporta, O. Svelto, E. Cienci, V. Foglietti, S. Jiang and N. Peyghambarian, *IEE Electron. Lett.*, **37**, 1014-1015, 2001.
[9]D. L. Veasey, D. S. Funk, N. A. Sanford, and J. S. Hayden, *Appl. Phys. Lett.* **74**, 789-791 1999.
[10] S. Jiang T. Luo, B.-C. Hwang, G. Nunzi-Conti, M. Myers, D. Rhonehouse, S. Honkanen and N. Peyghambarian, New Er 3+, *Opt. Eng.* **37** 3282, 1998.
[11] S. D. Conzone, J. S. Hayden, D. S. Funk, A. Roshko, D. L. Veasey, Hybrid, *Opt. Lett.* **26**, 509-511, 2001.
[12] G. C. Righini, S. Pelli, M. Brenci, M. Ferrari, C. Duverger, M. Montagna, R. Dall'Igna, *J. Non-Cryst. Solids* **284** 223, 2001.
[13] Y. Jaouen L. du Mouza, D. Barbier, J.-M. Delavaux, P. Bruno, *IEEE Photon. Technol. Lett.* **11**, 1105-1107, 1999.
[14] G. Jose, G. Sorbello, S. Taccheo, V Foglietti, E Cianci e P. Laporta, *Opt. Mat.*, submitted
[15] G. Jose, S. Taccheo, G. Sorbello. R. Osellame, D. Migliorati, P. Laporta, E. Cienci, V. Foglietti, S. Jiang and N. Peyghambarian, *IEE Electron. Lett.*, **38,** 1275-1276, 2002.

Frequency Shifted Feedback Ti:Er:$LiNbO_3$ Waveguide Laser of Wide Tunability

S. Reza, H. Herrmann, V. Quiring, R. Ricken, K. Schäfer, H. Suche, and W. Sohler
Angewandte Physik, Universität Paderborn, D-33098 Paderborn, Germany.
sol_sr@physik.uni-paderborn.de

An integrated, tunable frequency shifted feedback laser with Ti:Er:$LiNbO_3$ waveguide is demonstrated. The intracavity integrated acoustooptical filter used for tuning (from 1530 to 1577 nm) imposes a frequency shift on each round trip. The result is a broadened emission spectrum (FWHM=170 pm) without any longitudinal mode structure.

Keywords: acoustooptical filter, frequency shifted feedback laser, integrated waveguide laser, tunable laser, Ti:Er:$LiNbO_3$.

Introduction

In normal lasers, the oscillating optical field inside the cavity reproduces in amplitude and phase after each roundtrip at a discrete set of frequencies called longitudinal modes. This resonance condition is no longer required, if the intracavity field is frequency shifted during each roundtrip. By combining this frequency shifting with intracavity tunable bandpass filtering, a tunable frequency shifted feedback (FSF) laser can be realized. Using a bulk acoustooptical modulator this concept has already been demonstrated [1]. Such FSF lasers provide emission with low coherence length, which offer a variety of potential applications for instance in optical frequency domain ranging [2] and different types of measurement and sensing techniques [3-5]. We report on the first FSF Ti:Er:$LiNbO_3$ waveguide laser which utilizes a monolithically integrated acoustooptical wavelength filtering for frequency shifting and tuning simultaneously.

Laser design and operation principle

A schematic diagram of the laser is shown in Fig. 1. It has a Ti-indiffused channel waveguide structure in the Er diffusion-doped surface of a 94 mm long X-cut (Y-propagating) $LiNbO_3$ substrate. If optically pumped by an external laser diode (λ=1480 nm) intracavity optical amplification can be obtained in the wavelength range 1530 – 1577 nm.

The tuning element of the laser is an intracavity monolithically integrated acoustooptical filter. It consists of two polarization splitters and an acoustooptical mode converter with a tapered acoustical directional coupler in between [6]. Narrow-band wavelength filtering ($\Delta\lambda_{FWHM} \approx 2.3$ nm) is achieved by a wavelength selective (phase-matched) acoustooptical polarization conversion in combination with appropriate polarization filtering.

The polarization splitters are designed to route TM-polarized light to the bar-state and TE-polarized light to the cross-state. Thus wavelength filtering is achieved between the upper left channel and the lower right intracavity guide. The internal laser field follows the path marked by dots, if the laser structure is pumped via the lower left guide in TM-polarization. As a consequence the state of polarization (SOP) of the internal laser field is TE on the left and TM on the right. Alternatively, a TE-polarized pump selects the upper channel in the filter structure and therefore leads to a TE-polarized laser output with orthogonal SOPs internally in comparison with those indicated in the figure.

A frequency upshift is obtained for a collinear (contralinear) acoustooptical polarization conversion with a TE-polarized (TM-polarized) input field; this corresponds to the mode of operation as indicated in Fig. 1. During one round trip the laser field undergoes two polarization conversions with two frequency shifts in the same direction. The spectral width of the filter for net

intracavity gain determines the effective number of round-trips and, therefore, the spectral width of the laser emission. On the other hand, a frequency downshift occurs if the device is pumped in TE-polarization and the orthogonal SOPs are observed internally. Contrary to a conventional laser, the internal laser field is not reproduced in amplitude and phase after each round-trip. The frequency shifted feedback broadens the spectral width of the laser and suppresses the formation of resonant longitudinal cavity modes.

The laser cavity is formed by two dielectric multilayer mirrors deposited on the waveguide end faces. Only the end face of the lower arm of the left polarization splitter is anti-reflection coated which facilitates efficient pump power coupling from a fiber-coupled Bragg-grating stabilized laser diode.

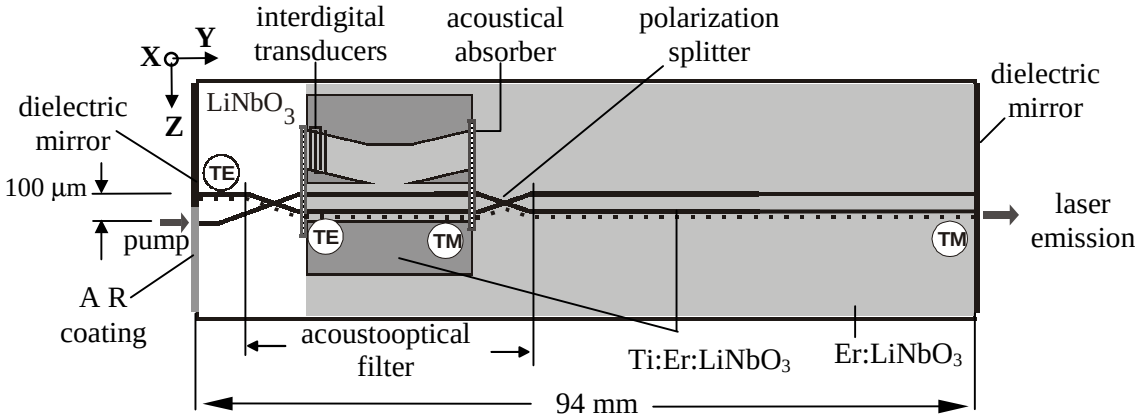


Fig. 1. Schematic diagram of the acoustooptically tunable Ti:Er:$LiNbO_3$ laser. The acoustooptical filter serves as intracavity polarization converter and frequency shifter simultaneously. The path of the intracavity laser field is indicated by dots along the waveguides optically pumped in TM-polarization.

Fabrication

At first, a planar 21.1 nm thick vacuum deposited Er-layer, covering about 80 mm of the 94 mm long sample surface, has been indiffused at 1130°C during 150 hours. In the next step, photolithographically defined 110 µm-wide acoustical waveguides have been fabricated by defining its 'cladding' via a deep indiffusion of 160 nm thick evaporated Ti-stripes at 1060°C during 24 hours. Then the optical waveguide structure together with the polarization splitters have been embedded symmetrically in the core of the acoustic waveguide: photolithographically defined 7 µm wide Ti stripes of 104 nm thickness have been indiffused at 1060°C during 7.5 hours. Typical waveguide scattering losses are ~0.05 dB/cm (TM-polarization) and 0.1 dB/cm (TE-polarization). Excess losses due to the polarization splitters are below 0.5 dB. Afterwards broadband (1.2 µm < λ < 2.0 µm) antireflection coatings have been deposited on both ends of the sample to avoid reflections during characterisation of the polarisation splitting ratios and to facilitate the pump coupling.

Interdigital transducers with 20 finger pairs have been fabricated by aluminium sputtering using the lift-off photolithography technique. An impedance matching circuit allows to excite the SAW with high efficiency. Then the acoustooptical filter characteristics has been studied to determine the phase matching frequencies and RF-power levels for best conversion efficiency. Finally, high reflection broadband dielectric mirrors of about 97.5% reflectivity (1450 nm < λ < 1700 nm) have been deposited on the end faces of both waveguides on the right and on the end face of the upper waveguide on the left (see Fig. 1.).

Laser operation

The laser is pumped using a fiber-coupled Bragg-grating stabilized laser diode of 1480 nm wavelength providing an output power up to 135 mW. The polarization of the pump radiation is adjusted either to TM or TE polarization using a fiber optical polarization controller. Fig. 2a shows the measured power characteristics at ~ 1564 nm emission wavelength as laser output power versus incident pump power. The results of both modes of operation are presented in Fig 2a for TM- (TE-) polarized pump leading to TM- (TE-) polarized output. The threshold pump power of the laser is ~ 50 mW (TM) and at ~ 70 mW (TE). The low slope efficiency of about 1.5×10^{-3}, leading to a maximum output power 120 µW (TM) and 75 µW (TE), respectively, demonstrates a large potential for further optimisation.

The emission wavelength of 1564 nm is determined by the surface acoustic wave (SAW) frequency of ~ 170 MHz; the corresponding electrical drive power for complete polarization conversion is about 80 mW. Tuning of the emission wavelength is achieved by adjusting the SAW-frequency. Continuous tuning could be demonstrated in the wavelength range 1530 nm < λ < 1577 nm with a tuning slope of about –8 nm/MHz. Due to the wavelength dependence of gain, losses, acoustooptical conversion efficiency and mode overlap the laser output power strongly varies as function of the emission wavelength (or SAW-frequency) (see Fig. 2b).

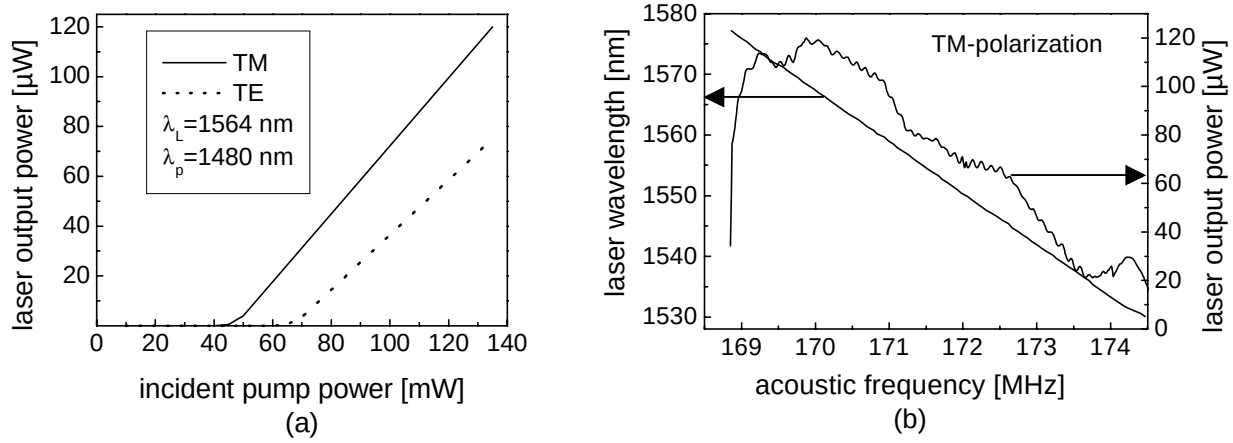


Fig. 2: (a) Laser output power versus incident pump for two modes of operation in TM- and TE-polarization, respectively. (b) laser emission wavelength (left ordinate) and output power (right ordinate) versus SAW-frequency at 135 mW of pump power in TM-mode of operation.

A frequency shifted feedback laser emission has completely different spectral characteristics compared to a normal laser. In Fig. 3a (Fig. 3b) the measured emission spectrum of the FSF laser is shown for TM (TE) pump polarisation. The chosen resolution of the spectrum analyzer of 10 pm would allow to identify a longitudinal mode spectrum of the 94 mm long cavity. The measurements however, clearly show modeless spectra of about 0.17 nm width (FWHM) with very smooth envelopes confirming FSF laser operation. The envelopes are slightly asymmetric. As a result of the frequency upshift for TM-polarization, the envelope of the spectrum is steepened at the short wavelength side (higher frequencies) (Fig. 3a), whereas downshifting in the TE-case results in a steepening on the longer wavelength side (Fig. 3b).

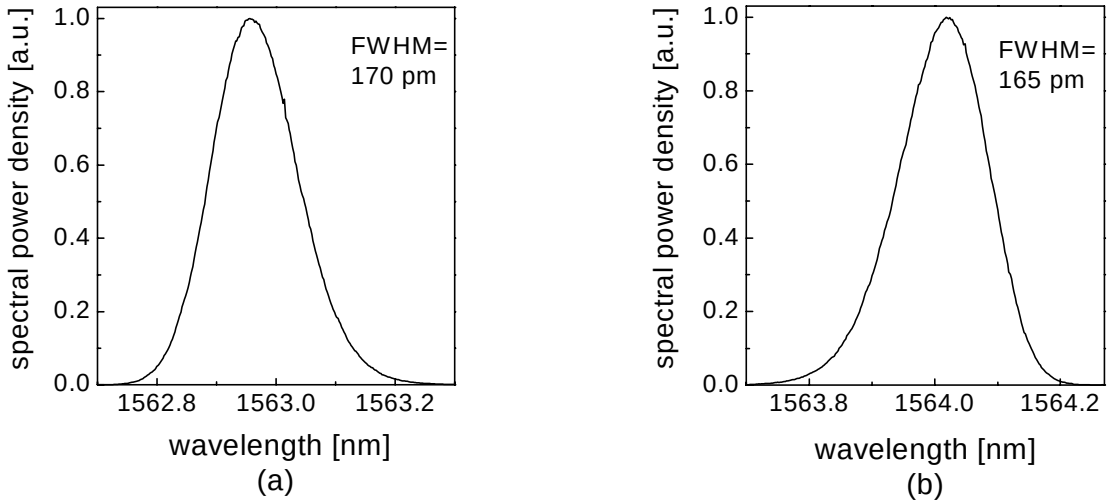


Fig. 3. Spectra of the frequency shifted feedback laser taken with a 10 pm resolution, (a) pump and emission TM-polarized and frequency upshifted (b) pump and emission TE-polarized and frequency downshifted.

Conclusions

We have demonstrated for the first time tunable frequency shifted feedback operation of a Ti:Er:$LiNbO_3$ waveguide laser. Intracavity frequency shifting and tuning over 47 nm have been achieved using the monolithically integrated acoustooptical filter. The smooth envelope of the output spectra (FWHM=0.17 nm) clearly show a modeless laser operation as expected for FSF lasers. Further detailed investigations including theoretical modeling are required to optimize laser performance.

Acknowledgement

This work has been supported by the Deutsche Forschungsgemeinschaft as one project of the research group ‘Integrated Optics in Lithium Niobate: New Devices, Integrated Circuits and Applications’.

References

[1] I. C. M. Littler et al., *J. Opt. Soc. Amer. B,* **8**, 1412-1420, 1991

[2] K. Nakamura et al., *IEEE J.Quantum Electron.* **36**, 305-316, 2000.

[3] J.R.M. Barr et al., *Optics Lettrs*, **18**, 1010-1012, 1993.

[4] M Yoshida et al., *IEEE Photon. Technol. Lett.*, **13**, 227-229, 2001

[5] K. Iiyama et al., *IEEE J. Select. Top. Quantum Electron.* **7**, 484-489, 2001.

[6] H. Herrmann et al., *J. Lightwave Technol.*, **13**, 364-374, 1995.

An Experimental Comparison of Linear and Parabolic Tapered Waveguide Lasers

S.J.Hettrick, J.Wang, C.Li, J.S.Wilkinson and D.P.Shepherd
Optoelectronics research Centre, University of Southampton, Highfield, Southampton, U.K..
dps@orc.soton.ac.uk

We compare the laser performance of linear and parabolic tapered waveguides in ion-exchanged Nd:glass, finding significant advantage for the linear guides, with demonstrated adiabatic expansion to widths of 250μm.

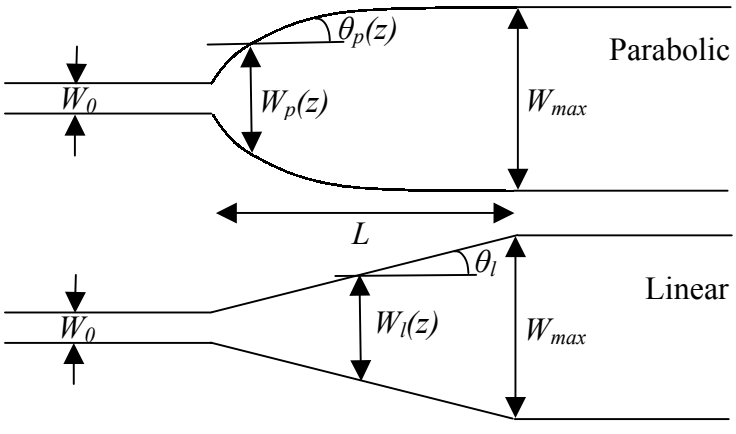
Keywords: waveguide lasers, tapers, ion-exchange

Introduction

Scaling the average power of diode-pumped integrated-optics laser sources requires the use of multimode waveguides to enable pumping by non-diffraction-limited high-power diode sources. However, a standard requirement for the integrated laser is that they give a single spatial mode, diffraction-limited output. One method of satisfying these opposing requirements is through the use of a structure that has a taper connecting a multimode, broad-stripe, planar section to a single-mode channel section of the waveguide [1-3]. The taper must be designed such that the fundamental mode propagating from the channel to the broad-stripe suffers minimal coupling to higher-order modes, as this power would be lost from the laser resonator when it returns through the taper to the channel. Several shapes for such tapers have been proposed [4] with the aim of expanding to as large an aperture in as short a length as possible. Here we experimentally compare the laser performance of linear and parabolic taper shapes opening to various widths of up to 250μm over lengths of up to 22mm.

Taper Design and Fabrication

Milton and Burns [4] proposed that considerations of diffraction and ray tracing suggest that a parabolic–shaped taper is a good design for low loss expansion, and they showed theoretically that tapers with an expansion coefficient $\alpha \leq 1$ (see figure 1) offer a reasonably adiabatic solution. Applying this design rule to a taper opening to 175μm in an ion-exchanged glass waveguide would



$$\theta_p(z) = \frac{\alpha\lambda}{2nW_p(z)} \qquad L \approx \frac{nW_{\max}^2}{2\alpha\lambda}$$

$$W_p(z) = \sqrt{\frac{2\alpha\lambda z}{n} + W_0^2}$$

$$W_l(z) = \frac{W_{\max} - W_0}{L} z + W_0$$

Figure 1 Parabolic and Linear Tapers

require a taper length of 22mm. However, our previous work on linear tapered waveguide lasers has shown that tapers produces by potassium-ion exchange through a mask opening up from 2.5μm

to 175μm over just 12.5mm give an adiabatic expansion with no noticeable increase in propagation loss compared to standard channel waveguides fabricated on the same substrate [1]. Thus, in order to experimentally investigate the limits on the aperture size of parabolic and linear-shaped tapers we fabricated the tapers detailed in table 1, alongside standard channel waveguides, on the same substrate.

Table 1 Taper Design Parameters

Shape	W_{max}/μm	L/mm	α	θ_l / deg	Channel Length / mm	Total Length / mm
Linear	175	11	-	0.449	15	46
Parabolic	175	11	2	-	15	46
Linear	200	14.3	-	0.396	11.7	46
Parabolic	200	14.3	2	-	11.7	46
Linear	250	22.3	-	0.318	3.7	46
Parabolic	250	22.3	2	-	3.7	46

$\lambda = 1.059\mu m$, $W_0 = 2.5\mu m$, n = 1.515, broad-stripe length = 2cm

A 1.5-wt.% Nd_2O_3-doped BK7 borosilicate glass slab had one large face polished in preparation for the ion exchange process. A 250nm-thick aluminium film was deposited on the polished surface and standard photolithographic techniques were used to create openings in the film corresponding to the taper designs in table 1 and to simple 2.5μm-wide channels of the same length. The waveguides were then formed by immersion in molten potassium nitrate at 395°C for 12 hours. Finally, the substrate was end-polished to yield plane end-faces at 90° to the waveguide axis.

Laser Performance Characterisation

The laser performance of the tapers and channels was investigated by pumping the channel end of the waveguide with a Ti:sapphire laser tuned to the Nd^{3+} absorption at 807nm. The laser

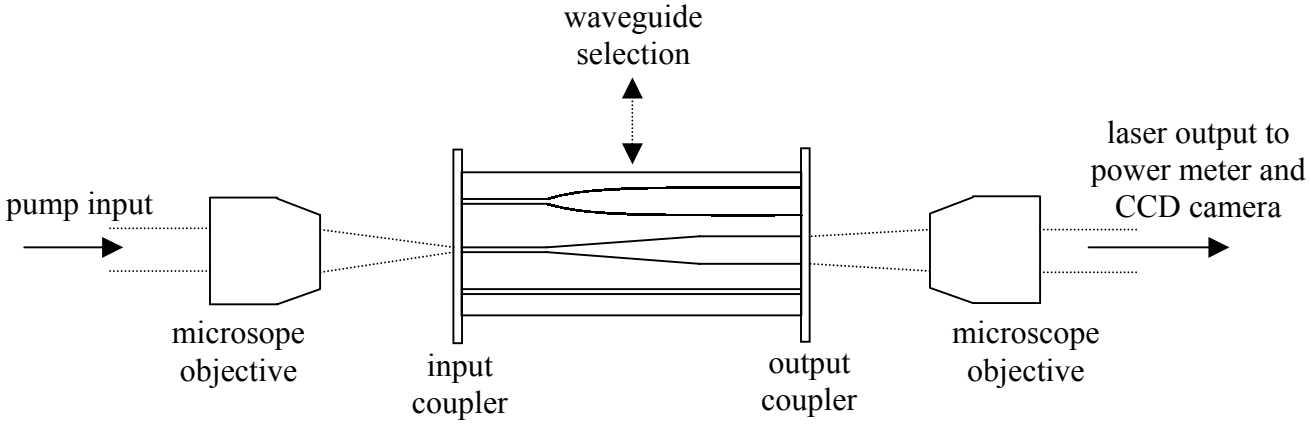


Figure 2 Experimental Set-Up

resonator was formed by butting thin mirrors to the plane end-faces of the waveguide substrate, using a thin film of fluorinated liquid to aid adhesion. The input mirror was highly reflecting at the lasing wavelength of 1.059μm and had 95% transmission at the pump wavelength. The output coupler had a reflectivity, *R*, of 80% at the lasing wavelength and was highly reflective at the pump wavelength such that the absorption of the launched pump power is effectively 100%. The experimental set-up is shown schematically in figure 2 and the thresholds and slope efficiencies obtained are tabulated in table 2.

Table 2 Laser Performance

Shape	W_{max} / μm	Threshold Power / mW	Slope Efficiency / %
linear	175	40	18
linear	200	35	21
linear	250	42	19
parabolic	175	34	23
parabolic	200	55	11
parabolic	250	115	5
channel	2.5	27	22

As an example, the spatial profiles for the output of the 200μm-wide tapers, captured by imaging the outputs onto a CCD camera, are shown in figure 3.

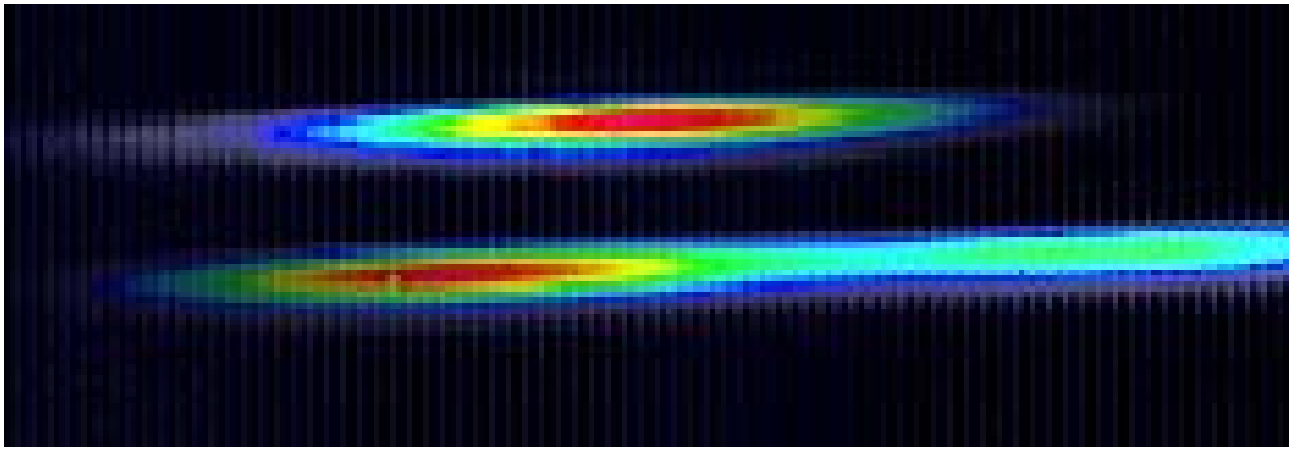


Figure 3 Imaged mode profiles for the 200μm-wide linear (upper) and parabolic (lower) tapers

Discussion

It can be seen from table 2 that, within experimental error, the slope efficiency of all the linear tapers is comparable to that of the channel guide, indicating that there is no significant increase in propagation loss due to the taper for the aperture sizes investigated here. The maximum possible slope efficiency (assuming a spatial overlap of 1) is given by [5]

$$\eta_{\max} = \frac{\lambda_p}{\lambda_s}\left(\frac{-\ln R}{-\ln R + \delta}\right),$$

where λ_p and λ_s are the pump and laser wavelengths, and δ is the round-trip loss exponent. Using this equation a maximum possible loss of 0.25dB/cm is obtained, which is a typical background propagation loss for ion-exchanged waveguide of this type. The low loss indicates an adiabatic expansion of the fundamental mode in the taper and this is confirmed by the observation of clean Gaussian output profile, as shown in figure 3.

In contrast, it can be seen that the performance of the parabolic tapers is comparable to that of the linear tapers and channel guide for the 175μm-wide aperture, but the performance gets considerably worse for the larger apertures. At 250μm the additional round-trip loss, over the 0.25dB/cm background loss, is as high as 11dB. The output spatial profiles of the larger parabolic tapers display a distinctly multimode nature, as shown in figure 3.

Summary

The performance of linear and parabolic tapers with fast expansion rates (α=2) to apertures of up to 250μm has been compared. The linear tapers show no significant additional losses over the background propagation loss of the ion-exchanged waveguide for the range of apertures investigated here, whereas parabolic tapers of the same length show a significant drop-off in performance for the larger aperture sizes. The large losses found for the parabolic tapered waveguide laser resonator were confirmed by the qualitative observation of higher-order modes in the spatial profile of the output from the broad-stripe region. These results suggest that linear tapers are compatible with high-average-power pumping by broad-stripe diode lasers and should allow integrated lasers with powers at the Watt level.

[1] S.J.Hettrick, J.I.Mackenzie, R.D.Harris, J.S.Wilkinson, D.P.Shepherd, A.C.Tropper, *Opt. Lett.* **25**, 1433-1435, 2000.

[2] T.Tamanuki, T.Sasaki, M.Kitamura, *Opt. Quantum Electron.* **28**, 513-517, 1996.

[3] J.D.Minelly, L.A.Zenteno, M.J.Dejneka, W.J.Miller, D.V.Kukzenkov, M.K.Davis, S.G.Crigler, M.E.Bardo, *Digest of Optical Fiber Communications Conference*, paper PD2-1, 2000.

[4] A.F.Milton, W.K.Burns, *IEEE J. Quantum Electron.* **QE-13**, 828-835, 1977.

[5] W.P.Risk, *J.Opt. Soc. Am.* **5**, 1412-1423, 1988.

40GHz all-optical clock recovery using polarization-insensitive distributed Bragg reflector lasers

Guang-Hua Duan, Christophe Gosset*, Bruno Lavigne, Romain Brenot, Bruno Thedrez, Joël Jacquet, and Olivier Leclerc

ALCATEL Research & Innovation, Route de Nozay, 91460 France
Tel : 33 (0) 1 69 63 46 64 Fax : 33 (0) 1 69 63 14 22
Email: Guanghua.Duan@alcatel.fr

Current address: Département Communications et Electronique
Ecole Nationale Supérieure des Télécommunications
46, rue Barrault, 75634 Paris Cedex 13, France

Abstract: All-optical clock recovery over 40Gbit/s optical signals using polarization-insensitive distributed Bragg reflector lasers is demonstrated. Low time jitter (<1ps), good extinction ratio (>7dB) and the maintain of locking even for a series of 48 zeros are obtained.

Keywords: self-pulsation, clock recovery, injection locking, semiconductor lasers

1. Introduction

All-optical clock recovery is commonly identified as a key function for all-optical signal processing. Up to now, two types of self-pulsating (SP) lasers have been studied for high bit-rate (>10Gbit/s) clock recovery: distributed feedback (DFB) lasers [1-2], and distributed Bragg reflector (DBR) lasers [3]. The DBR-based solutions offer many advantages such as simplicity of use, possible control of the number of lasing modes, high extinction ratio when associated with a saturable absorber. However, polarization-insensitive clock recovery using DBR lasers without saturable absorber has not yet been demonstrated.

In this paper, we report a polarization-insensitive DBR laser operating as a 40GHz optical clock recovery, along with its free-running SP characteristics. System performance of the device such as phase noise of the recovered clock and its ability to maintain locking for a series of consecutive zeros are also investigated.

2. Laser structure and free running SP characteristics

A schematic view of the DBR laser is shown in figure 1. The laser has 3 sections: an active, a phase and a Bragg section [4]. The active section has a length of 790µm. The guiding layer is a bulk quaternary material with a thickness of 0.4µm and a width of 0.6µm. Such a quasi-square cross-section allows to obtain a polarization-insensitive modal gain. The modal analysis shows a difference of 0.1 in the TE and TM confinement factors with a mean value of 0.58. In the phase section of a length of 130µm, the width of the waveguide expands linearly to match the 1.8µm wide Bragg section. This wider Bragg waveguide has a larger lateral confinement factor for the TE mode. It acts thus as a polarization filter to obtain only TE emission for the DBR laser. The short 200µm-long Bragg section enables to have at least two longitudinal modes inside the 3dB linewidth of the Bragg reflection spectrum. As a result, the DBR laser operates in a multimode regime. It should be noted that there is no saturable absorber inside the laser cavity.

The DBR lasers show a mean threshold current of 40mA with a maximum output power around 20mW. The output wavelength is around 1550nm.

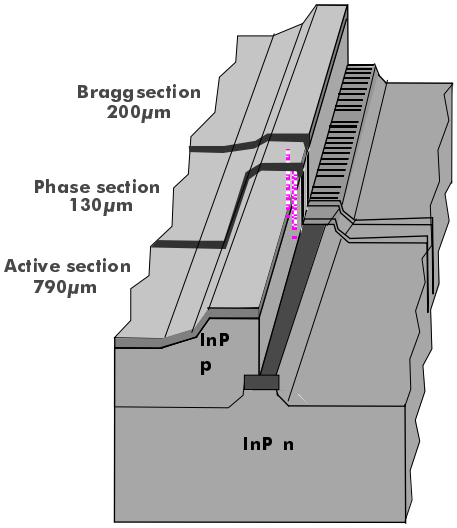
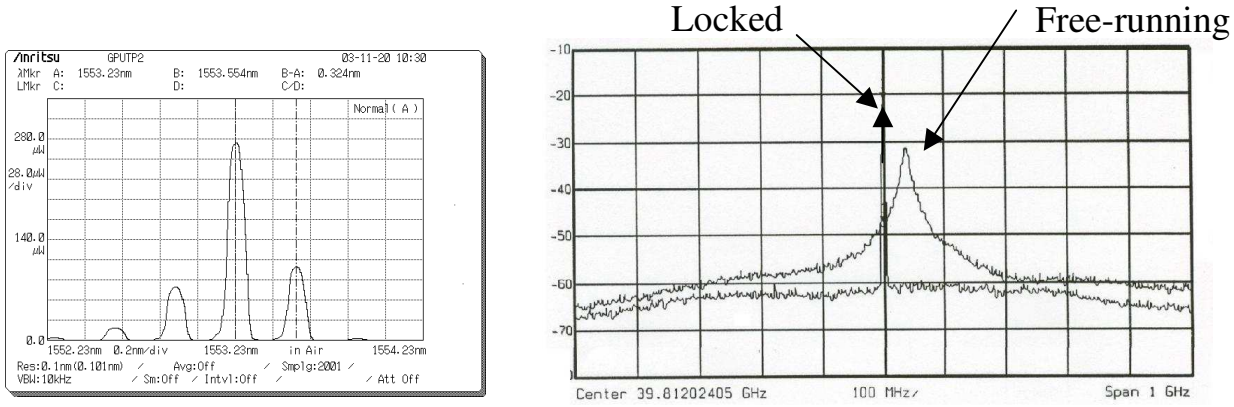


Fig. 1. Structure of the DBR laser.

Figure 2 (a) shows a typical example of the emission optical spectrum in a linear scale. One can observe the presence of 4 modes, with a frequency spacing around 40GHz. Due to the mode beating inside the active section through carrier density modulation and intraband nonlinear effects (spectral hole burning and carrier heating), the modes are partly correlated, leading to self-pulsation [5]. Figure 2 (b) shows the RF spectrum of the output power detected by a large bandwidth photodiode. A SP peak is clearly observed with a full width at half maximum of around 12MHz.



(a) (b)

Fig. 2. (a) optical spectrum, and (b) RF spectrum of the photocurrent.

The dependence of the SP frequency on the injection current to the active and Bragg sections and on the temperature has been studied. Figure 3 shows an example of the SP frequency as a function of the injection current I_B into the Bragg section. One can see a periodic variation of the SP frequency with I_B, which is due to the jumps of the dominant mode. Inside a period, the SP frequency increases with I_B, due to an increase of the Bragg wavelength through thermal effects. Consequently, the dominant mode approaches the Bragg wavelength, leading to a decrease of the effective length of the Bragg section. The tunability of the SP frequency is around 400MHz. The SP

frequency can also be tuned by the temperature change. An average value of 80MHz/K was measured for these lasers.

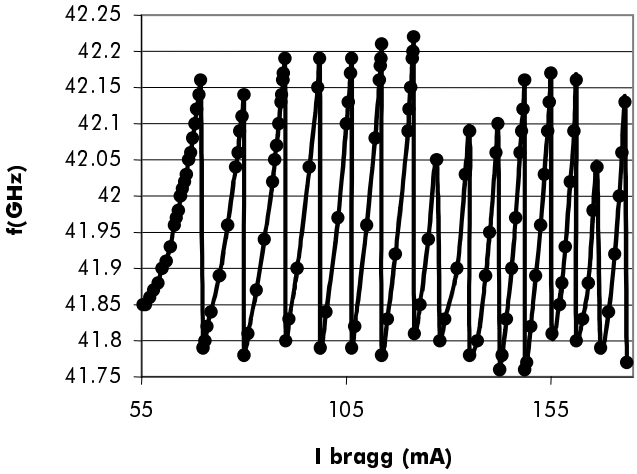


Figure 3 SP frequency as a function of the injection current into the Bragg section

3. Performances of the recovered clock

A 40Gbit/s incoming signal at 1540 nm is coupled via a lensed fiber into the described DBR laser. A maximum polarization sensitivity of 1 dB is estimated from measurements. The recovered clock is then analyzed in the time and RF domains. The RF spectrum of the output power in the locked state is also shown in figure 2(b). A shift of the SP peak to the bit rate of the incoming signal and a drastic decrease of the linewidth of the SP peak are observed from the figure, showing that the SP laser is locked to the incoming signal.

The recovered clock is analyzed by using a sampling oscilloscope. The extinction ratio and timing jitter measured are up to 7dB and around 1ps, respectively, with an injection power of 11dBm. The phase noise of the recovered clock is also studied. Figure 4 shows a typical example of the measured phase noise spectrum for the input clock and the recovered clock. One can observe that these two spectrums are identical for the analysis frequency from 0 to 100 kHz. After 100 kHz, the recovered clock has a higher phase noise than the input clock.

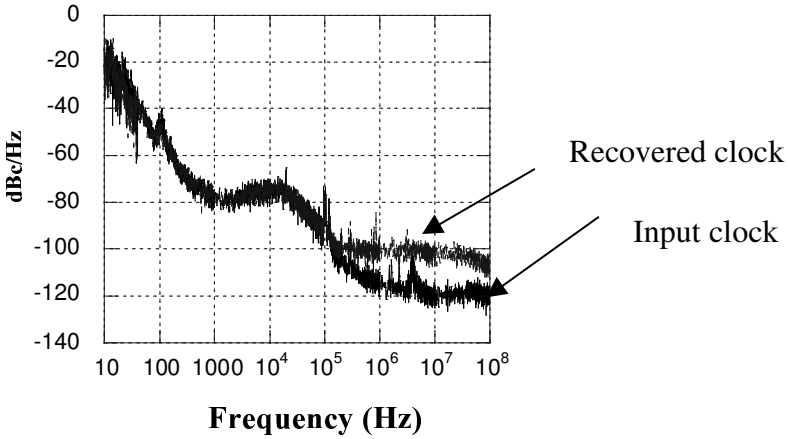
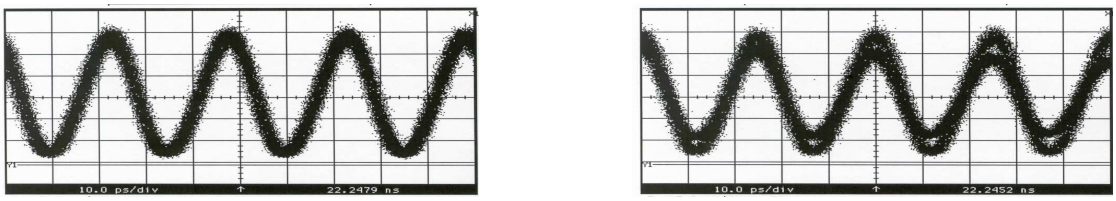


Figure 4 phase noise spectrum of the recovered clock

The ability of maintaining the clock for a series of zeros was investigated in detail. In such a study, the incoming data is programmed such that N marks are followed by N spaces. Figure 5 shows the recovered clock for an incoming sequence with (a) 48 and (b) 64 zeros. In the case of 48 zeros, the phase synchronization is perfectly maintained. For 64 zeros, a slight difference between "1" and "0" is observed, indicating the influence of patterning effects. However, the number of zeros that can be tolerated by the SP laser is much larger that needed for a pseudo-random binary sequence of a length of 2^{31}-1.



(a) (b)

Fig. 5. Recovered clock at 40Gbit/s for an incoming sequence with (a) 48 and (b) 64 zeros.

4. Conclusion

All-optical clock recovery over 40Gbit/s optical signals using polarization-insensitive distributed Bragg reflector lasers is demonstrated. Low time jitter (<1ps), good extinction ratio (>7dB) and the maintain of locking even for a series of 48 zeros are obtained. Experimental results of all-optical recovery in a complete all-optical regenerator will also be reported at the conference.

References

[1] M. Möhrle et al, " Multi-section DFB lasers for high-speed signal processing/regeneration", Paper TuU1, Proc. OFC'2002 , Anaheim (2002).

[2] S. Bauer et al., "Novel concept for tunable optical microwave source", Paper ThM5, Proc. OFC'2002 , Anaheim (2002).

[3] H. Yokoyama, et al, "All-optical subharmonic clock recovery and demultilexing", Proc. OFC'2000, paper ThP5-2, Baltimore (2000)

[4] S. Gurib, et al, "Realization of distributed Bragg reflector laser for polarization-independent wavelength-conversion application", paper CMF5, Proc. CLEO'1996, Anaheim (1996).

[5] K. Sato, "100 GHz optical pulse generation using Fabry-Perot laser under continuous wave operation", Electronics Letters, Vol. 37, n°12, pp. 763-764, 2001

Photonic Integrated Circuits using Crystal Optics (PICCO)

An overview

Thomas F Krauss[1,*], Rab Wilson[1], Roel Baets[2], Wim Bogaerts[2], Martin Kristensen[3], Peter I Borel[3], Lars H Frandsen[3], Morten Thorhauge[3], Bjarne Tromborg[3], Andrej Lavrinenko[3], Richard M De La Rue[4], Harold Chong[4], Luciano Socci[5], Michele Midrio[6], Stefano Boscolo[6] and Dominic Gallagher[7]

[1]University of St. Andrews, School of Physics and Astronomy, St. Andrews, UK.
[2]Ghent University - IMEC, Dept. of Information Technology (INTEC), Ghent, Belgium.
[3]Technical University of Denmark, Research Centre COM, Lyngby, Denmark.
[4]University of Glasgow, Dept. of Electronics & Electrical Engineering, Glasgow, UK.
[5]Pirelli Labs S.p.A, Advanced Photonics Research, Milan, Italy.
[6]University of Udine, Dept. of Electrical & Mechanical Engineering, Udine, Italy.
[7]Photon Design Europe Ltd. Oxford, UK.
* tfk@st-andrews.ac.uk

PICCO has demonstrated low loss, ultracompact photonic components based on wavelength-scale high contrast photonic microstructures and underpinned their design by sophisticated CAD tools. PICCO has also demonstrated device-fabrication via industrially viable deep UV lithography.

Introduction

Photonic crystals (PhCs) provide a fascinating platform for a new generation of integrated optical devices and components. Circuits of similar integration density as hitherto only known from electronic VLSI can be envisaged, finally bringing the dream of true photonic integration to fruition. What sets photonic crystals apart from conventional integrated optical circuits is their ability to interact with light on a wavelength scale, thus allowing the creation of devices, components and circuits that are several orders of magnitude smaller than currently possible. Apart from miniaturisation., a key property of photonic crystal components is their "designer dispersion", i.e. their ability to implement desired dispersion characteristics into the circuit. Functionalities include optical delay lines ("slow light"), optical pulse compression/dilation and wavelength splitters. In order to realise these functions, we need to understand the fundamental properties of photonic crystals and be able to fully master the technology of making them. Another key aspect is the understanding of the origin of propagation losses and their reduction to acceptable levels. While competitive values in terms of "loss per device" have now been demonstrated, the full potential of photonic crystal circuits will only be realised once many components can be cascaded together in complex circuits.

CAD tools

The ONYX-2 code [1], used for 3D-FDTD calculations, has been improved by implementing perfectly matched layers (PML) as absorbing boundaries, thereby effectively truncating the computational space in the program. The calculated 3D-FDTD spectra for PhC waveguide components are found to be in excellent agreement with experimentally observed spectra; the positions of dips and peaks in the spectra are typically predicted with an accuracy of 1-2% for SOI based components [2], and the actual measured propagation losses are also predicted correctly (fig. 2b).

Fabrication

E-beam lithography is the main lithographic workhorse of the consortium and is used extensively at Glasgow, also at COM and St. Andrews. It is a serial process, however, and thereby presents inherent limitations for high-volume mass-manufacture, so it is worthwhile to explore other routes to generating photonic crystal patterns. Classical photolithography, which is used for the current generation of planar lightwave circuits, lacks the resolution to fabricate these submicron structures with sufficient precision. Extending photolithography into the deep UV, however, where excimer lasers are used as light sources, changes the picture. With illumination wavelengths of 248 nm, moving on to 193 nm and eventually 157 nm, as well as projection optics with exceedingly high numerical apertures (nA), DUV lithography offers both the resolution and speed required for the high volume mass-manufacture of photonic circuits. Recent results obtained using 8" SOI wafers are very promising and highlight the viability of the process [3].

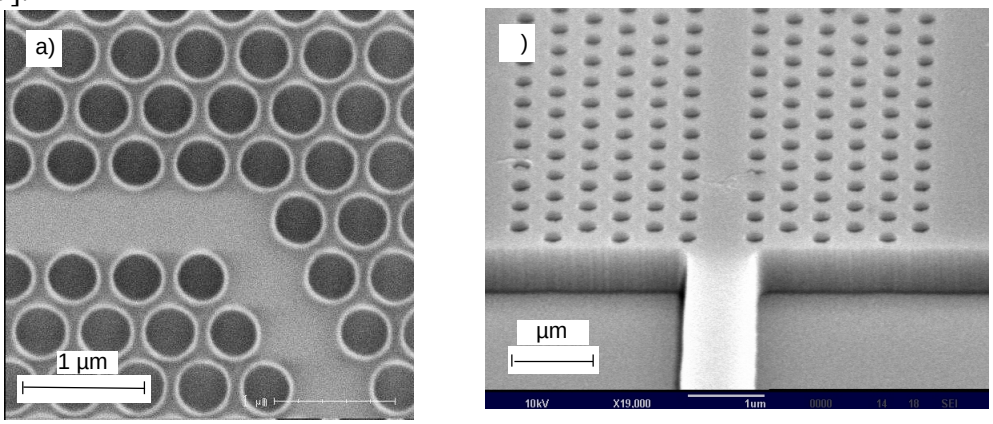
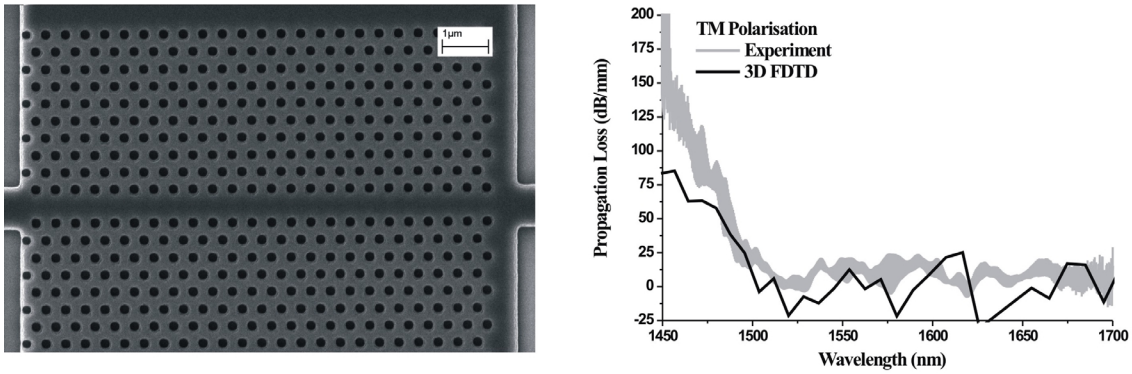


Fig. 1. SEM micrographs of photonic crystal waveguide patterns generated by DUV lithography. The period in both cases is 500 nm and the hole diameter is a) 380 nm and b) 230 nm.

Straight waveguides

Transmission properties of straight PhC waveguides have been investigated in the silicon-on-insulator (SOI) system. In the experiment, seven straight waveguides of type W1 (single line of missing holes) of lengths 10-150 m were fabricated using e-beam lithography and reactive ion etching [4]. The holes were arranged in a triangular lattice with a period of a=428 nm (fig. 2a). 3D-FDTD calculations of transmission spectra for four straight PhCWs of lengths 29-59Λ were also performed. The measured and calculated propagation losses for TM polarised light are displayed in Fig. 2(b). The losses are

extracted by calculating the slope of the measured transmission as function of waveguide length. Good agreement is seen between experiment and simulation. Especially noteworthy is the 200 nm bandwidth with propagation losses around 9±5dB/mm for the TM polarisation. It is noted that even lower propagation losses, less than 4dB/mm, have previously been observed in a narrower wavelength range [4].



(a) **(b)**

Fig. 2. (a) SEM micrograph of a straight PhC waveguide. (b) Measured and calculated propagation losses for TM polarised light in straight PhC W1 waveguides.

Y-junctions

While straight waveguides and bends have now been studied extensively, the very important problem of junctions that is essential for the operation of more complex circuits has only recently received attention [5-7].

Photonic crystals offer a real advantage in this case, as they make it possible, in principle, to construct 60¡ or even 90¡ bends at junctions, unlike in conventional integrated optics, where splitting angles are restricted to values around 2¡. Let us consider the problem in more detail. If we join three W1 waveguides together, the 60¡ bend (or 120¡ split) is the most natural configuration in a triangular lattice. As light enters the junction, it experiences an optical volume that is slightly larger than that of the constituent waveguides, so the mode expands laterally. This mode expansion is analogous to that in a multi-mode interference (MMI) coupler and leads to the excitation of higher-order modes at the output port. These higher order modes typically cannot propagate and most of the light that enters the junction is reflected. This issue can be addressed by placing a smaller hole at the centre of the junction. The optical volume is then reduced, the mode cannot expand and the excitation of higher order modes is suppressed. As a result, efficient transmission over a wide bandwidth is observed [6].
This effect has also been observed experimentally. We used the configuration shown in figure 3a) and placed two smaller holes of increasing size at the centre of the junction in order to achieve a graded transition. The results are very encouraging, with a good balance between the two ports and a total transmission around 80% being observed (fig. 3 b,c).

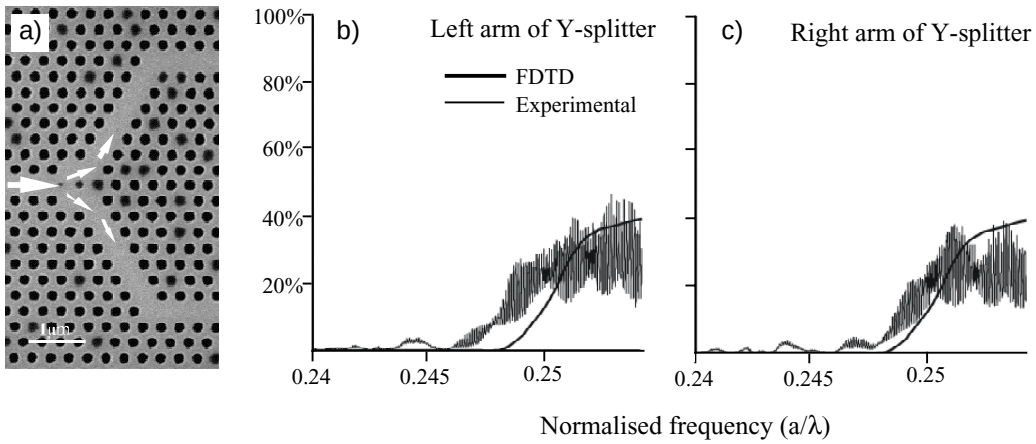


Fig. 3. SEM Micrograph and performance of a Y-junction with additional holes at the centre to avoid mode expansion. The vertical scale in b), c) represents transmission relative to a W1 waveguide. The oscillations in the experimental curves are due to Fabry-Perot resonances between the cleaved facets with superimposed resonances arising from reflections at the junction. The fact that the 2D FDTD agrees well with the 3D experiment indicates low out-of plane losses. The total transmission is between 70-80% over a relatively broad spectral range (30-40 nm @ 1300 nm). The bandwidth is limited by the bend rather than the junction.

Two of these Y-junctions mounted back-to back constitute a Mach-Zehnder interferometer, which has also been operated successfully (passive, no tuning) with 28% transmission observed relative to a W1 waveguide. The design of the interferometer is extremely compact, with overall dimensions of the order of 10 x 10 m^2 .

Cavities

One of the functions obtainable from photonic crystal structures is wavelength division multiplexing, due to the strongly wavelength selective nature of cavities within a photonic crystal environment. Such properties have been demonstrated, e.g., by S. Fan *et al*, [8] and S. Noda *et al*, [9]. Cavities formed by in-filling one or more holes in a 2D photonic crystal have already shown high quality factors [10-12]. We have fabricated, in an SOI guide layer, such a cavity immediately adjacent to a channel waveguide and used a smaller diameter hole between cavity and waveguide to increase coupling. The Q of the cavity can be controlled by changing the hole diameter (and mode volume) and by using hole trimming inside the cavity.

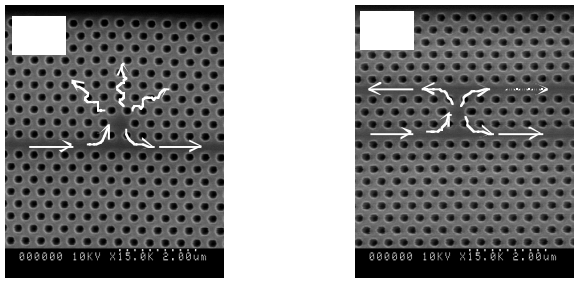


Fig 4. SEM micrographs of the single hole cavity with, (a) one channel waveguide giving drop function and (b) two channel waveguide providing add-drop function.

Cavities have also been fabricated for direct determination of the Q. Figure 3 (b) shows a single hole cavity with two channel waveguides where efficient adding or dropping of the resonant wavelength is expected from the decay rate of the resonance.

Circuits

While it is important to study individual devices, one of the ultimate aims of photonic crystal research is to realise more complex circuits. To this end, we have developed an analytical approach that allows us to engineer a complex circuit by borrowing simple concepts of propagation in transmission lines. Indeed, a photonic crystal waveguide may be seen as an equivalent transmission line that conveys equivalent currents and voltages among different loads . The loads may be formed by microcavities, junctions, bends, or even by an open waveguide that terminates into air, and they are all characterized by the fact that backreflections appear as soon as a guided field impinges on them. Once equivalent impedances are suitably defined for the photonic crystal waveguide and the loads, the behaviour of the circuit may be analytically described by looking at it as a connection of lumped elements, and use can be made of quantities that engineers have known for long time: the standing wave ratio, the partially standing waves the reflection coefficient, etc.

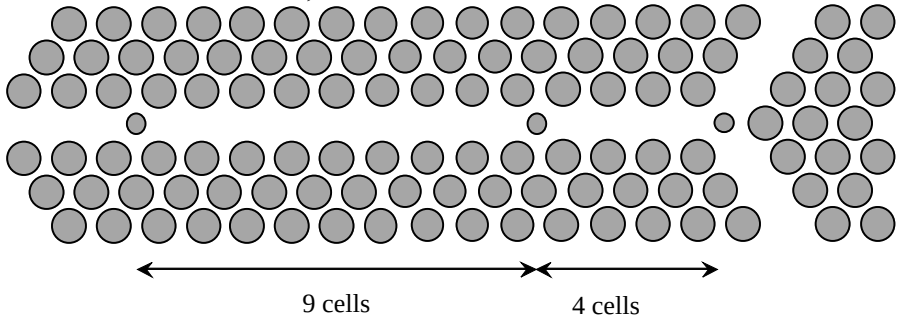


Fig 5. A Y-junction including tuning holes (double-stub tuner) to minimise reflections. A symetric Y-junction has a maximum splitting ratio of 44.4% into the two output branches, whereas the Y-junction with tuner shown here achieves, theoretically, up to 49.3 % [6].

An example highlighting the potential of the approach is shown in Fig.5, where we optimize the transmission through the junction by *matching* its impedance to that of the incoming photonic crystal waveguide. This is done by designing an *equivalent double-stub network*, which is realized by introducing suitable defects in the input arm of the junction. The underlying physics is the following. When we insert a defect in the guide, and the guided mode impinges on it, higher order modes are excited in the vicinity of the defect itself. If these higher order modes are below cut-off, they can not propagate. In other words, they have an imaginary wave impedance, which gives rise to an unbalance between electric and magnetic stored energies, i.e. they form an equivalent lumped reactive element

Discussion and Conclusion

Several examples of miniaturised photonic crystal circuit elements have now been demonstrated, such as low-loss waveguides, Y-junctions and cavity waveguides. We are also beginning to understand how to combine these elements into more complex circuits using impedance matching techniques, and how to fabricate photonic crystal circuits on a larger scale using DUV lithography. While this makes a clear argument in favour of the photonic crystal approach, miniaturisation alone may not be sufficient to

ensure their major impact in integrated optics. Take WDM components as an example; the photonic crystal approach will only succeed if miniaturisation can be achieved with comparable or better performance than already offered by existing devices. State-of-the-art arrayed waveguide gratings (AWGs), for example, offer 50 GHz channel spacing with a channel accuracy of 2.5GHz and a cross-talk in excess of 30dB. These are benchmarks that are presently well out of reach of photonic crystal circuits. While it is clearly worthwhile to achieve similar performance with photonic crystals, we also need to look for applications that come more natural or offer solutions that cannot otherwise be achieved.

Such an application would be an amplifier with integrated dispersion control, or a detector with tunable dispersion compensation at the input side. Alternatively, the effective light-matter interaction in a modulator could be increased via slow wave structures, i.e. photonic crystal waveguides that operate in a low group velocity regime. This should allow modulators to be realised with effective electro-optic coefficients that scale with the reduction in group velocity and can therefore be much shorter.

Overall, while much progress has been made, the real killer application has yet to be developed.

References

1. A.J. Ward and J.B. Pendry, Comp. Phys. Com. **128**, 590-621 (2000).
2. P.I. Borel, M. Thorhauge, L.H. Frandsen, J. Cheng, M. Kampanis, M. Kristensen, A. Lavrinenko, Y. Zhuang and H.M.H. Chong, accepted for CLEO-Europe 03.
3. Bogaerts, W, Wiaux, V, Taillaert, D, Beckx, S, Luyssaert, B, Bienstman, P and Baets, R., IEEE J. Select. Topic. Quantum Electron. **8**, 928 (2002).
4. Arentoft, J, Sondergaard, T, Kristensen, M, Boltasseva, A, Thorhauge, M and Frandsen, L. 2002, Electron. Lett. **38**, 27 (2002).
5. Lin, SY, Chow, E, Bur, J, Johnson SG and Joannopoulos, JD, Opt. Lett. **27**, 1400 (2002).
6. Boscolo, S, Midrio, M and Krauss, TF, Opt. Lett. **27**, 1001 (2002).
7. Wilson, R, Karle, T and Krauss, TF, submitted for publication.
8. Fan, S, Villeneuve, P, and Joanopoulos, JD, Phys. Rev. Lett, **80**, 960, (1998).
9. Noda, S, Chutinan, A, and Imada, M, Nature, **407**, 608, (2000).
10. Smith, CJM, Krauss, T, Benisty, H, Rattier M, Weisbuch, C, Oesterle, U, Houdre, R, J. Opt. Soc. Am. B, **17**, 12, 2043, (2000).
11. Painter, O, Vuckovic, J, and Scherer, A, J. Opt. Soc. Am. B, **16**, 2, 275, (1999).
12. Scherer, A, Painter, O, Vukovic, J, Loncar, M, Yoshie, T, IEEE Trans. Nano, **1**, 1, 4, (2002).

Nanoscale-domain Engineering of a $Sr_{0.61}Ba_{0.39}Nb_2O_6$ Crystal

Kazuya Terabe, Shinji Higuchi, Masaru Nakamura, Shunji Takekawa, Kenji Kitamura
National Institute for Materials Science, 1-1 Namiki, Tsukuba, Ibaraki 305-0044, Japan

Yasunori Furukawa
Oxide Corporation, Kobuchizawa 9633, Kitakoma, Yamanashi 408-0044, Japan
furukawa@opt-oxide.com

We investigated the ferroelectric domain structure formed in a $Sr_{0.61}Ba_{0.39}Nb_2O_6$ crystal. The crystal was grown by a newly developed double-crucible Stepanov method. A scanning force microscope (SFM) revealed that a multidomain structure of nanoscale island-like domains was formed in the crystal. Furthermore, tailored patterns of inverted-domain structure were fabricated using SFM.

Keywords: scanning force microscope, ferroelectric domain, domain engineering, SBN

Introduction

Ferroelectric single crystals have been used as materials for functional devices because they have various properties, such as electrooptic, nonlinear optic and piezoelectric properties and the photoreflective effect; strontium barium niobate ($Sr_{0.61}Ba_{0.39}Nb_2O_6$: SBN, hereafter) is one of ferroelectric crystals. Several functional devices, such as light modulation and holographic memory devices, have been produced thus far by exploiting the superior properties of SBN crystals. Recently, the development of functional devices utilizing the functions and characteristics obtained by patterning microscale domain structures in ferroelectric crystals such as the SBN and $LiNbO_3$ crystals has attracted attention. Thus far, second-harmonic generation (SHG) devices [1] and optical parametric oscillation devices [2] have been fabricated by exploiting quasi phase-matching (QPM) in the construction of a microscale periodically inverted-domain structure [3]. We anticipate the creation of functional devices that exploit the characteristics newly exhibited through the domain structure of ferroelectric crystals artificially structured at the nanoscale level in the future [4,5].

Recently, it has been found that SHG was emitted from an as-grown SBN crystal, in which the periodically inverted-domain structure was not formed artificially [6]. This is possible because a multidomain structure is naturally formed in the SBN crystal upon cooling through the Curie point (T_c), and these domains partially satisfy the QPM condition. On the basis of observations made using a transmission electron microscope, the formation of nanoscale 180° domains with the polarization that is parallel to the *c*-axis of the SBN crystal has been revealed [7]. However, the domain structure formed in the SBN crystal has not been investigated due to the difficulty in domain visualization using conventional optical microscopy.

We have investigated the imaging and engineering of the domain structure in the SBN crystal using a scanning force microscope (SFM). Imaging the etched SBN surface in both the topographic and piezoresponse [4,8-10] modes of the SFM revealed the nanoscale multidomain structure in the as-grown SBN crystal. Furthermore, inversion of the domains was achieved by applying an appropriate dc bias voltage using the conductive SFM tip [4,8,9,11]. Tailored-patterns of inverted-domain structure were fabricated

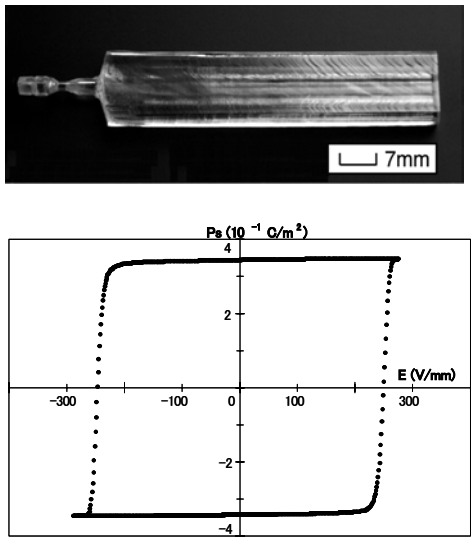


Fig.1: (a) Photograph of the SBN crystal grown by a newly developed double-crucible Stepanov method and (b) a ferroelectric hysteresis loop of the SBN crystal.

using the SFM. It was difficult to fabricate the nanoscale domain patterns by conventional electric field poling using lithographically defined electrodes [12].

Experimental method

A single crystal of $Sr_{0.61}Ba_{0.39}Nb_2O_6$ was grown by a newly developed double-crucible Stepanov method, in which fluctuation in Sr concentration is only one third of the value of the SBN crystal grown by a conventional Stepanov method [13]. A photograph of the SBN crystal is shown in Fig.1(a). The ferroelectric hysteresis loop of the SBN crystal was obtained by the conventional measurement using liquid electrodes of 4 mm diameter (saturated LiCl solution in water) at room temperature, as shown in Fig. 1(b). The hysteresis loop indicated that the polarization directions of the domains could be switched homogeneously by applying an appropriate electric field (the coercive field was approximately 250 V/mm). The as-grown crystal was annealed at 1350 °C for 24 h and then cooled to room temperature in the furnace. The crystal was cut perpendicular to the *c*-axis, and polished using alumina powder and colloidal silica solutions. Then, the crystal was etched in a HF aqueous solution at room temperature for 10 minutes. Imaging of the domain structure on the etched SBN surface was achieved using the SFM in two different modes. First, the etched surface was scanned in the topographic mode. The domain structure could be revealed in the topographic mode due to the different etching behaviors of the positive and negative polarized faces of domains. Second, the conductive SFM tip was used to perform domain imaging in the pizoresponse mode with an applied ac bias voltage of 10-14 V (peak-to-peak) at a frequency of 10 kHz. The piezoresponse mode is expected to be able to directly image the domain structures with nanoscale resolution. The piezoresponse and topographic visualizations of domain structures on the etched surface of the crystal were used as complementary methods to confirm the suitability of using the SFM approach for the SBN crystal.

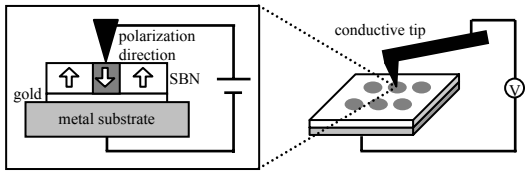


Fig.2 Domain engineering method by using SFM. Polarization directions of domains were locally switched by applying bias voltage using a conductive SFM cantilever.

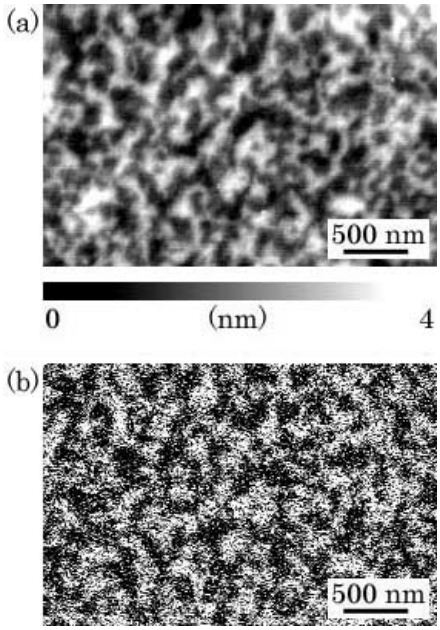


Fig.3 SFM images of the HF-etched SBN crystal (a) in the topographic mode and (b) in the piezoresponse mode. White and black areas in (a) and (b) represent the negatively and positively polarized faces of the domains, respectively.

The domain engineering of the SBN crystal was achieved by applying a dc bias voltage using the conductive SFM tip, as shown in Fig.2 The SBN samples for the domain engineering were prepared by the following procedure. Gold films were deposited on one side of the *c*-cut polished SBN crystals, after a poling treatment which was carried out so that the SBN crystal has a single 180°-domain structure (the polarization direction is parallel to the *c*-axis). The gold-coated surfaces were adhered to metal substrates using conductive paste. The crystals on the metal substrates were polished to 55~90 μm thickness. A certain bias voltage was applied between the conductive SFM tip and the metal substrates, where the tip was grounded.

Results and discussion

Fig.3(a) shows the topographic image of an etched SBN. The surface was etched preferentially with a depth of approximately 5 nm. The unetched area, white in the figure, looked like islands structure with the size of a few hundred nanometers. The same region was scanned in the piezoelectric-response mode. As shown in Fig.2 (b), island-like structures appeared with dark and bright contrast. The island-like structure imaged by the piezoelectric-response mode agreed with that of the topographic image, which suggests that the island-like structure corresponds to domain structure. It seems that the preferential etching in SBN is caused by etching rate anisotropy of 180°multi-domains, which was already observed in $LiNbO_3$ [14], $LiTaO_3$ [15] and $Pb_{1-x}Ba_xNb_2O_6$ [16] crystals. In order to determine the polarity of the etched regions, a SBN crystal which underwent a conventional poling treatment [17], in which negatively and positively polarized faces were formed artificially, was etched in the HF solution. The positively polarized face was determined to be preferentially etched. Thus, the white areas in Fig.3 (b) represent the negatively polarized faces of the domains.

We investigated the shapes of inverted domains in the SBN samples under different bias-applying condition. Fig.4 (a) shows the domains inverted by the application of voltage V = -80 V for treatment time of 40 s. The inverted domains were imaged in the piezoresponse mode (represented by the white area). The polarizations of these inverted domains are directed from the surface of the crystal to the bottom; namely, the surfaces of the domains are negatively polarized. As the bias voltage increased, the inverted domains grew. In addition, when the bias voltages were fixed, the inverted domains grew as the treatment time increased. The line-shape of inverted domain was also fabricated by scanning with the conductive SFM cantilever on the SBN crystal surface while applying the voltage, as shown in Fig.4 (b). These results indicate that inverted domains with arbitrary size and shape can be fabricated using SFM by controlling the bias voltage, treatment time, and scanning condition.

We fabricated tailored-domain-patterns in the SBN crystal by scanning with the conductive SFM cantilever on the SBN crystal surface while applying a certain bias voltage. Fig.5 shows a lattice pattern of inverted domains fabricated by scanning with the conductive cantilever. In this case, the lattice pattern was fabricated by scanning with the conductive cantilever at the rate of 1 μm/s, while applying voltage V = -30 V. The width of the lines of the

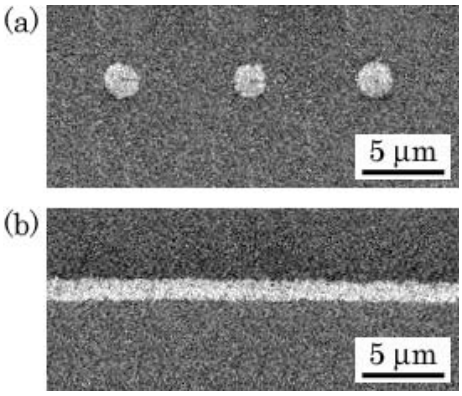


Fig.4. SFM piezoresponse images of (a) dotty inverted- domains fabricated by applying a bias voltage of V = -80 V for treatment time of 40 s, and (b) linear inverted-domains fabricated by applying a bias voltage of V = -80 V with scanning the cantilever at the rate of 0.5 mm/s

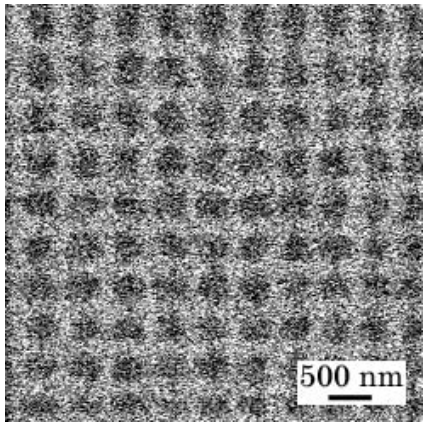


Fig.5 SFM piezoresponse image of a lattice pattern made of linear inverted-domains

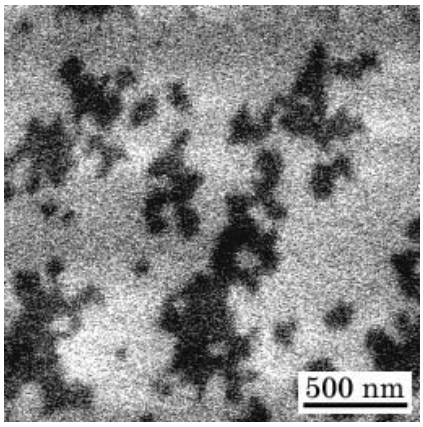


Fig.6 SFM piezoresponse image of back-switched domains in SBN crystal after the poling treatment

lattice pattern fabricated by the inverted domain was approximately 250 nm.

In addition to formation of the island-like domain structure upon cooling through the Curie point to room temperature, we founded formation of nanoscale domain structure by a back switching of the inverted- domain after a conventional poling treatment. The poling treatment was carried out so that the SBN crystal has a single 180°-domain structure. Fig.6 shows that the piezoresponse image of nanoscale domains formed by the back switching, where the black area represents back-switched domains. The size of back-switched domains was smaller than that of island-like domains naturally formed upon cooling to room temperature.

Conclusion

We have observed the domain structure of the SBN crystal using the topographic and piezoresponse modes of the SFM. The 180° nanoscale island-like domains were naturally formed upon cooling through the Curie point to room temperature. Furthermore, the domain engineering was achieved by applying the appropriate bias voltage by using the SFM. We were able to pattern domain structures on microscale to nanoscale levels by controlling the magnitude of the voltage applied to the SBN samples and treatment time while scanning a conductive SFM cantilever along the sample surfaces. We consider that the fabrication technologies of nanoscale domain patterns (nanoscale domain engineering) in ferroelectric single crystals, such as a SBN crystal, by using SFM may be effective for development of novel functional devices such as photonic crystals, optical MEMS and wavelength- conversion devices.

Reference

[1] K. Yamamoto, K. Mizuuchi, K. Takeshige, Y. Sasai and T. Taniuchi, *J. Appl. Phys.*, **70**, 1947 (1991).

[2] R. W. Wallace, *Appl. Phys. Lett.*, **17**, 497 (1970).

[3] J. A. Armstrong, N. Bloembergen, J. Duccing and P. S. Pershan, *Phys. Rev.*, **127**, 773 (1962).

[4] K. Terabe, S. Takekawa, M. Nakamura, K. Kitamura, S. Higuchi, Y. Gotoh and A. Gruverman, *Appl. Phys. Lett.*, **81**, 2044 (2002).

[5] K. Terabe, M. Nakamura, S. Takekawa, K. Kitamura, S. Higuchi, Y. Gotoh and Y. Cho, *Appl. Phys. Lett.*, **82** (2003) in press.

[6] S. Kawai, T. Ogawa, H. S. Lee, R. C. DeMattei and R. S. Feigelson, *Appl. Phys. Lett.*, **73**, 768 (1998).

[7] L. A. Bursill and P. J. Lin, *Philosophical Magazine B*, **54**, 157 (1986).

[8] A. Gruverman, O. Auciello and H. Tokumoto, *Appl. Phys. Lett.*, **69**, 3191 (1996).

[9] Y. G. Wang, W. Kleemann, T. Woike and R. Pankrath, *Phys. Rev. B*, **61**, 3333 (2000).

[10] A. Gruverman, O. Auciello, J. Hatano and H. Tokumoto, *Ferroelectrics*, **184**, 11 (1996).

[11] T. Hidaka, T. Maruyama, S. Saitoh, N. Mikoshiba, M. Shimizu, S. Shiosaki, L. A. Wills, R. Hiskes, S. A. Dicarolis and J. Amano, *Appl. Phys. Lett.*, **68**, 2358 (1996).

[12] M. Yamada, N. Nada, M. Saitoh and K. Watanabe, *Appl. Phys. Lett.*, **62**, 435 (1993).

[13] S. Takekawa, Y. Furukawa, M. Lee and K. Kitamura, *J. Cryst. Growth*, **229**, 238 (2001).

[14] Y. Y. Zhu, S. N. Zhu, Z. Y. Zhang, H. Shu, J. F. Hong, G. Z. Ge and N. B. Ming, *Appl. Phys. Lett.*, **66**, 408 (1995).

[15] K. Kitamura, Y. Furukawa, K. Niwa, V. Gopalan and T. E. Mitchell, *Appl. Phys. Lett.*, **73**, 3073 (1998).

[16] M. Lee, R. S. Feigelson and R. K. Route, *J. Cryst. Growth*, **193**, 347 (1998).

[17] J. E. Myers, R. C. Eckardt, M. M. Fejer, R. L. Byer, W. R. Bosenberg and J. W. Pierce, *J. Opt. Soc. Am. B*, **12**, 2102 (1995).

InP-Based High-Speed Photoreceivers for Optical Fibre Communications

Heinz-Gunter Bach
Fraunhofer Institut für Nachrichtentechnik, Heinrich-Hertz-Institut
Einsteinufer 37, D-10587 Berlin, Germany
bach@hhi.de

Monolithic photoreceivers for 40/43 Gbit/s fibre-based communication systems are reviewed. A versatile integration concept supports the fabrication of special high-power photodetectors as well as electrically post-amplified receivers. Future developments towards 80 Gbit/s data rates are discussed, based on fabricated 60 Gbit/s pinTWA photoreceivers.

Keywords: high-speed photoreceivers, InP, PIN, photodiodes, waveguides, HEMT, OEIC, pig-tailed modules

Introduction

Actually long-haul optical communication systems are upgraded for single channel bit rates of 40/43 Gbit/s, helping to exploit the transport capacities of the SMF of about 10 Tbit/s by joint progress in combining TDM and WDM techniques (e.g. 256 channels). The Internet traffic growth is boosting such developments, dominated by growth rates in Asia-Pacific of 126 % in 2002, followed by european Internet traffic growth of 115 % last year, just only 11% less than in Asia. For 2003, it is expected (RHK) that European traffic growth will outpace Asia-Pacific. High-bit rate photoreceivers are key components for optical network extensions on all system levels (transport, metro).
Within the framework of KomNet (BMBF) Heinrich-Hertz-Institut developed several kinds of 40/43 Gbit/s photoreceivers for industry partners. Depending on the system concept, i.e. the extend of optical pre-amplification and driving needs of high-speed demultiplexing electronics, high-power photodiodes of special structure (twin-type or balanced) and InP-based monolithically integrated photoreceivers (OEIC receiver), based on a flexible integration concept, using semi-insulating substrates and semi-insulating optical waveguide layer stacks, have been developed. In the first section, this integration concept will be explained in detail, which allows the monolithic integration of waveguides, MMI splitters, evanescently coupled pin photodiodes, HEMTs and (distributed) amplifiers. The latter besides the HEMTs comprise further passive components like coplanar transmission lines, capacitors and resistors, thus forming an MMIC technology in conjunction with optoelectronics (photoreceiver OEICs). In the second section, based on this integration concept, special high-power photodetectors of the twin-type and balanced type will be shown for 40 Gbit/s detection and in the third section, several types of pinTWA receiver OEICs up to 60 Gbit/s data rate handling capability will be presented. The paper finishes with an outlook towards concepts for receiver integration for 80 Gbit/s and higher.

I. The versatile photodetector and receiver OEIC integration concept

The concept of photodetectors, realized within a monolithic integration scheme, should provide superior single photodiode performance, e.g. with respect to ultrahigh bandwidth in the 70 GHz range [1] and high-power signal conversion [2], as well as flexible applications of several photodiodes in different, but in all cases optical waveguide-fed circuit configurations, e.g. twin-type [3, 4] or balanced type [5] detector configurations. The waveguide-fed evanescently coupled photodiode concept thus should exhibit advantages in all cases, where hybrid realisations suffer from critical stability using fibre networks, where stable operation is often paid by thermal stabilisation needs. Using generally semi-insulating optical

waveguides for signal feeding, a monolithically integrated taper at the waveguide facet has to be included, to lower the coupling losses to a standard butt-ended SMF and to increase the adjustment tolerances into the ±2 µm range. This detector integration is carried out within a one-step MOVPE growth of the semi-insulating optical waveguide layers and the active photodiode layer stack. The mask levels for structuring the optical feeding waveguides may be used as well to form e.g. MMI couplers or 3dB splitters, in case of e.g. the twin-type photodetectors [3, 4].
Within this, so far solely detector integration concept, we face now towards the next step of integrating electrical amplifiers, i.e. the InP-based photoreceiver comprises additionally a HEMT-based traveling wave amplifier [6, 7]. These OEICs were fabricated employing now a two-step MOVPE/MBE epitaxial approach for the WG-integrated PD/HEMT layer stacks, allowing an independent optimization of the single devices [8]. All devices are integrated on top of a semi-insulating waveguide layer stack being composed of three quaternary optical guiding layers embedded within InP and an upper thicker waveguide layer, see Fig. 1. The evanescently coupled photodiode is grown on top of this stack within a single MOVPE growth run, see the left part of Fig. 1.

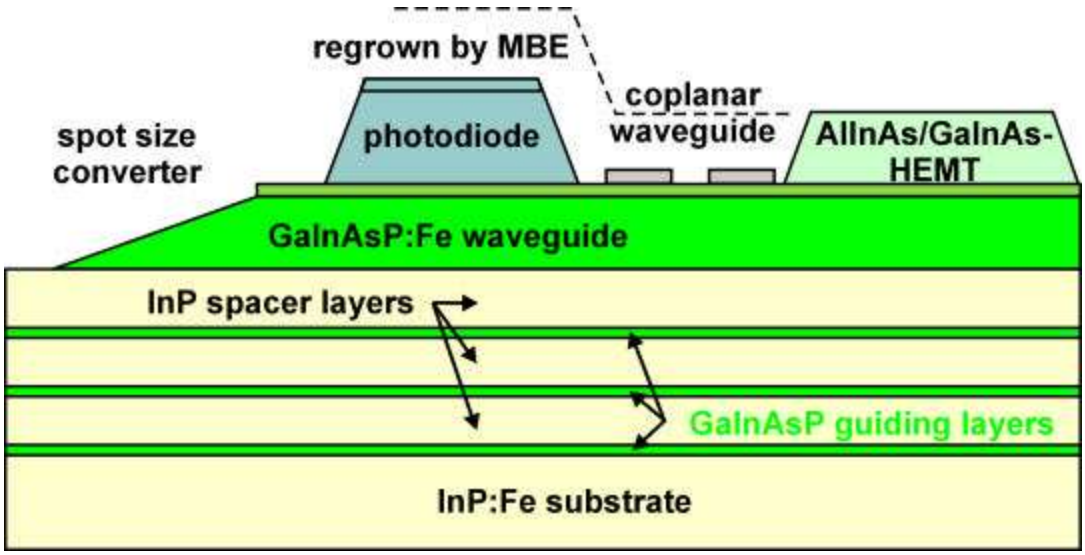


Fig. 1: Cross section of the versatile integration concept, showing the integration of a pinTWA photoreceiver with an evanescently coupled pin photodiode on top of a semi-insulating optical waveguide layer stack (one-step MOVPE growth) and an MBE re-grown HEMT-based traveling wave amplifier (second growth step).

After structuring the photodiode(s) by combined wet and dry chemical etching steps, MBE re-growth is applied for the AlInAs/GaInAs lattice-matched HEMT layer stack. All devices are well insulated from each other due to the good dielectric properties of the MOVPE grown Fe-doped layer stack with specific resistances higher than $5*10^7$ Ωcm.
The HEMT gate recess and the photodiode mesa are defined by dry chemical etching (RIE). The subsequent MMIC processing includes the formation of the NiCr resistors, MIM capacitors, and metallization for interconnections. MIM capacitors and metal film resistors are used as passive devices, applied for the amplifier as well as for the biasing network of the photodiode. Gold electroplating forms coplanar waveguide interconnections employing air bridges. The HEMTs are coupled to coplanar transmission lines by quasi-microstrip lines, which are formed by airbridges over a groundplane. A further BCB layer is used for passivation purposes of the mesa pin diodes.

The spot size converter is integrated by exploiting the additional diluted waveguide formed by the buried semi-insulating GaInAsP guiding layers beneath the more confining GaInAsP:Fe waveguide, which feeds the photodiode. The latter is vertically tapered with a ramp of less than 1 µm over a length of approx. 1 mm to provide a quasi-adiabatical conversion of the spot size. The spot size converter increases the fibre alignment tolerances by one order of magnitude and enables the use of a cleaved instead of a lensed fibre. For antireflection purposes, the optical input facet of the photoreceiver OEIC was covered by TiO_2/SiO_2. This integration sequence can be also used to fabricate kinds of waveguide-fed evanescently coupled detectors only, or to fabricate purely electrical HEMT-based amplifiers, simply by selecting subsets from the entity of all mask levels.

II. High-power photodetector receivers

Since single photodetectors, based on this integration concept, are now commercially available [9], this paper focuses on special applications of waveguide-integrated detectors like twin-type (section II. A) and balanced type detectors (section II. B), which take profit from the waveguide-fed integration scheme.

II. A Twin-type photodetectors

For compact integration of 40 Gbit/s optical frontends a distortion robust detector type is useful, which effectively suppresses all radiated or electromagnetically coupled interference signals from digital circuitry mounted within the same housing. Therefore it is desirable to provide directly from the detector two symmetrical electrical signals with opposite polarity to the inputs of the differential amplifier at the demultiplexer stage. This is achieved with a twin-type photodetector module featuring broadband differential operation at λ=1.55 µm. Our InP-based photonic integrated twin-photodetector comprises a vertically tapered spot size converter, a multimode interference (MMI) coupler for optical 3 dB power splitting and two waveguide-fed evanescently coupled high-speed pin photodiodes [3, 4], one with inverse polarity. The design of our differential detector was described earlier [3] and is schematically depicted in Fig. 2.

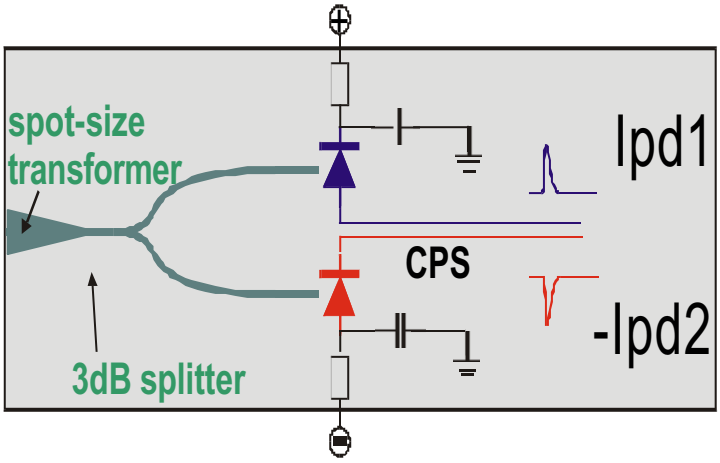


Fig. 2: Basic design of the twin-photodiode; the input light coupled from a butt-ended fibre into the integrated spot-size transformer is guided to an MMI 3dB splitter, which guides 50 % of the input light to each of both photodiodes, which exhibit opposite output polarities. These outputs are guided via coplanar stripes to the chip edge.

To realize a robust packaging the photodetector chip was mounted on a ceramic substrate, containing a 50 Ω termination, too, and connected via bonding wires to the coplanar stripes (CPS) leading to the two V-connector output ports [4]. In order to minimize optical reflection the input facet of the chip was TiO_2/SiO_2-coated and a low-reflective butt-fibre with optical return loss better than 27 dB was used. Fig. 3 shows a top view into the twin-photodetector module.

For differential operation of a subsequent electronic circuit (e.g. demux stage) it is necessary to receive equal absolute photocurrents from both photodiodes.

Therefore we firstly examined the ratio

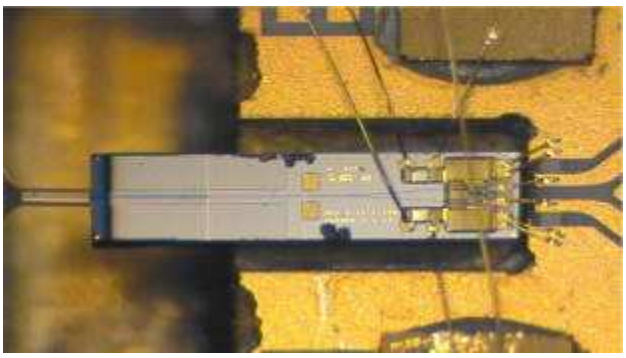


Fig. 3: Twin-photodetector OEIC after mounting, bonding and optical coupling with a butt-ended fibre.

I_{PD1}/I_{PD2} in dependence of the fibre-chip coupling. Using on-wafer probing techniques we varied the lateral position of the butt-fibre, monitoring both photocurrents. Due to the integrated spot-size transformer we obtained large alignment tolerances of more than ±2 µm @ 1 dB additional loss for both states of polarization, revealed by the sum of both photocurrents. The photocurrent ratios remain within 1 dB for all applicable offset positions indicating that values of less than 0.5 dB are achievable by minor lateral detuning during the fibre-chip coupling. To estimate the polarization dependence of the device we measured both photocurrents at different polarization angles of the incoming light. Both total photocurrent and photocurrent ratio exhibit little deviations of less than 0.5 dB promising balanced polarization insensible operation.

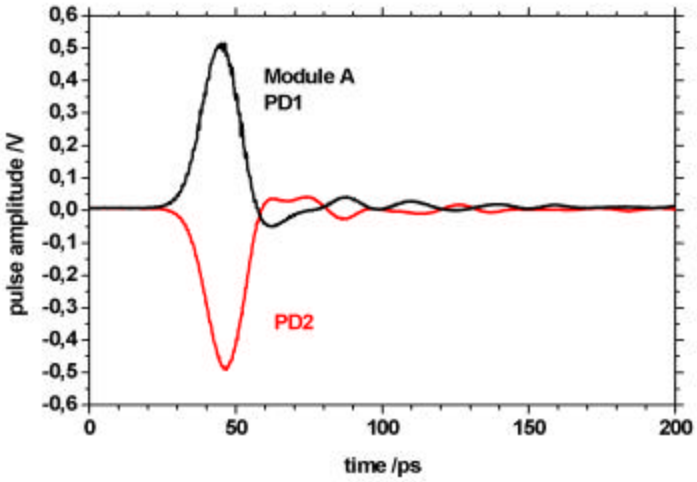


Fig. 4: Pulse measurements of the twin-photodetector module, showing symmetric differential amplitude of 1 V. The excitation was applied from a 3 ps laser pulse source.

Pulse response measurements of the twin-photodetector module were performed in the time domain using a picosecond laser source (FWHM: 3 ps, repetition rate: 16 MHz) and a 50 GHz sampling scope. We observed symmetric narrow pulses and negligible ringing. Fig. 4 shows the received pulses of both photodiodes with 500 mV peak voltages corresponding to a photocurrent of 10 mA, which is sufficiently high to drive directly the demultiplexer stage. At a reverse bias of 2 V the FWHM of 13.97 ps and 14.36 ps remained constant up to optical input energies of 0.94 pJ, demonstrating the high power capability of the photodiodes. Using a heterodyne setup to study the power transfer functions of the twin-photodetector module, a 3 dB cut-off frequency of 45 GHz was achieved, well suited for 40 Gbit/s NRZ and RZ operations. The total responsivity amounts to 0.31 A/W. Such modules operated successfully at 43 Gbit/s data rates in the Siemens AG KomNet test bed long haul transmission between Darmstadt and Mannheim (107 km), their dynamic range of photocurrents for fixed BER=10^{-9} is typically 40 % higher than using comparable single photodiodes.

II. B Balanced photodetectors

A balanced photodetector is a key element for direct detection in differential phase shift keying (DPSK) transmission formats, where a bipolar reception scheme is desired [10]. Furthermore it is a useful component in high-performance radio-frequency (RF) photonic systems for effective noise suppression resulting in an enhanced signal-to-noise-ratio. One important parameter of the balanced photodetector

required by these applications is the common-mode-rejection ratio (CMRR), which specifies the symmetry of the two photodiodes over the entire bandwidth, defined as (I_{PD1}-I_{PD2}/I_{PD1}+I_{PD2}). Monolithically waveguide-integrated balanced photodetectors provide excellent RF-matching of both photodiodes, broad bandwidth, high power capability and reduced packaging cost. In this section we report on the design, packaging and characterization of a fully packaged high-speed balanced photodetector module, suitable for operation in 40 Gbit/s transmission systems [5].

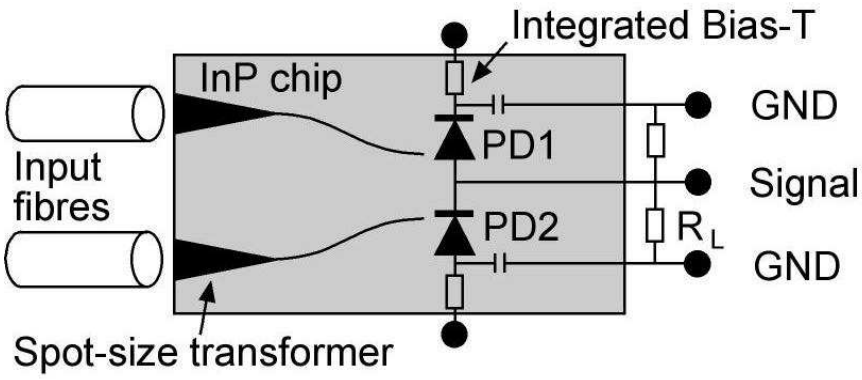


Fig. 5: Schematic view of the balanced photodetector.

Fig. 5 depicts the basic design of the integrated balanced photodetector based on InP, which contains two spot-size transformers, two waveguide S-bends and a pair of high speed pin-photodiodes (PD1 and PD2) with high power capability [2]. The evanescently coupled photodiodes with an active area of 5 µm*25 µm are located on top of the semi-insulating waveguide layer stack and are biased by means of integrated bias-circuits. The photodiodes are electrically connected in series; hence current subtraction is done directly on chip, essentially improving the RF performance at high frequencies. To achieve a robust packaging the chip was mounted on ceramic substrate and wire bonds realized all electrical connections. The RF output is provided via a short coplanar waveguide (CPW) transmission line on TMM 10i substrate leading to the output port. Using a standard two-way fibre array with 250 µm pitch the optical coupling was performed simultaneously for both inputs. By monitoring both photocurrents the fibre array was aligned. Once the position with maximum currents was reached, two glass blocks laterally fixed the array. In this way a responsivity of 0.24 A/W of each PD with a polarization dependent loss of less than 0.8 dB in a first prototype module was achieved. At least 0.5 A/W, known from chip-based measurements, should be possible by the use of a more suitable fibre array and a further improved fibre-to-chip coupling procedure. In order to expand the RC limitation with respect to two parallel-interconnected pin diodes a hybrid NiCr load resistor on an InP chip R_L was implemented between the detector chip and the CPW output transmission line. The finished module provides two fibre pigtails for the optical input, two pins for +2 and –2 Volt biasing, respectively, and one coaxial V-connector output port [5].

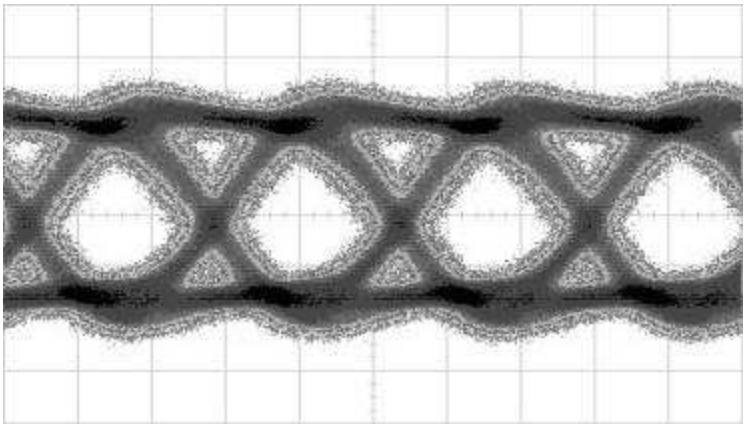


Fig. 6: Received NRZ eye pattern of one of the diodes of the balanced receiver module at 40 Gbit/s with PRBS 2^{31}-1 (10 mV/div, 10ps/div).

The module shows a 3 dB cut-off frequency of 34 GHz and pulse widths of 15 ps [5]. By integrating the load resistor on the detector chip, bandwidth could be further improved, as circuit simulation shows. The measurements demonstrate high symmetry between both photodiodes up to signal frequencies of 30 GHz due to our compact monolithic integration scheme. This results in a broadband common-mode-rejection ratio of more than 20 dB.

Utilizing a 40 Gbit/s optical transmitter we measured the NRZ modulation format eye pattern characteristics with PRBS 2^{31}-1 at an input power of 4.3 dBm in the unbalanced operation mode. The received eye diagram is clearly opened, as shown in Fig. 6 for one photodiode illuminated at 1.55 µm.

III. PinTWA photoreceiver OEICs

Amplified receivers, i.e. photodetectors, monolithically integrated with an electrical post amplifier are useful in those cases, where optical input power is limited, or high power is too expensive, or if more loop gain is needed. The electrical amplifier circuit in the 40 Gbit/s range may be of the transimpedance type [11] or of the distributed (traveling wave) type [6]. In our laboratory we prefer the traveling wave type amplifier (TWA), because this amplification scheme exhibits higher frequency performance in view of forthcoming single channel bit rates of 80 to 160 Gbit/s. PinTWA receiver OEICs, comprising a tapered optical input waveguide, an evanescent-coupled pin photodiode and several high-electron mobility FETs (HEMT), have been developed for 40/43 Gbit/s bit rates and NRZ or RZ modulation format according to industry specifications.

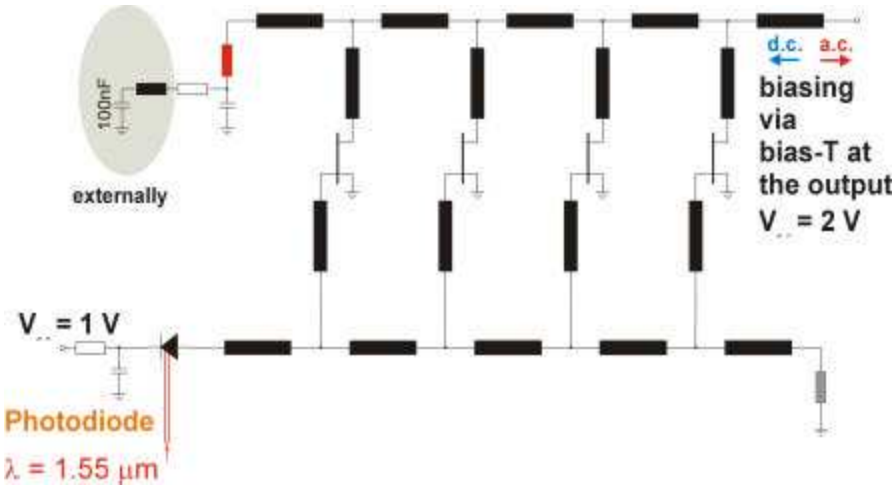


Fig. 7 Circuit scheme of a pinTWA photoreceiver OEIC comprising the waveguide-integrated pin photodiode and a HEMT-based traveling wave amplifier. Biasing is applied via an external bias-T back at the RF output.

Following the integration scheme in section I a pinTWA photoreceiver circuit according to Fig. 7 was implemented [11].

In a module optical coupling is done by fixing the butt fibre directly at the OEIC's tapered waveguide facet by UV curable resin. The optical return loss was better than 30 dB. This coupling type provides high robustness against vibration and thermal cycling under field operating conditions. The RF output of the OEIC was connected via bonding wires to a short coplanar waveguide on TMM 10i substrate, which leads to a 1.85 mm connector at the end. A return loss of better than 10 dB was measured over 40 GHz bandwidth. Fig. 8 shows the finished photoreceiver module with FC/PC connector.

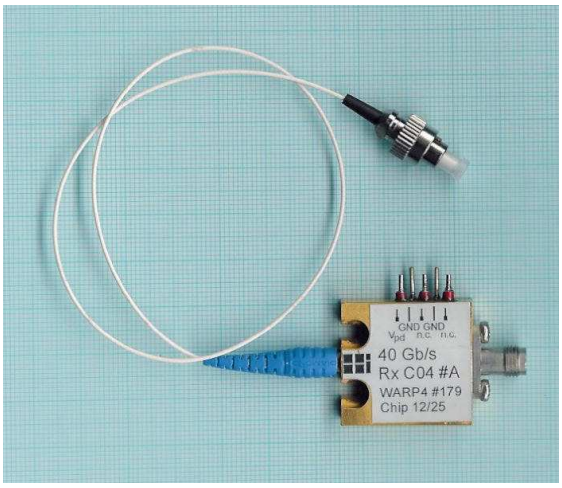


Fig. 8: 50 GHz single-chip pigtailed photoreceiver module with a pinTWA InP-receiver OEIC for λ=1.55 µm.

The TWA and the photodiode are supplied with a single bias voltage of 2 V. The total power consumption is as low as 90 mW. The characterization of the module was carried out by optical heterodyne measurement of the power transfer function, delivering a bandwidth of 50 GHz [12]. A further test of the broadband conversion capability was done within an ETDM experiment using a 40 Gbit/s bit stream (Lucent Technologies). Fig. 9 shows the measured

eye pattern at the photoreceiver module output. The eye is widely opened even for the 500 mV_{pp} Rx module output voltage scaling, demonstrating good demux driving capability.

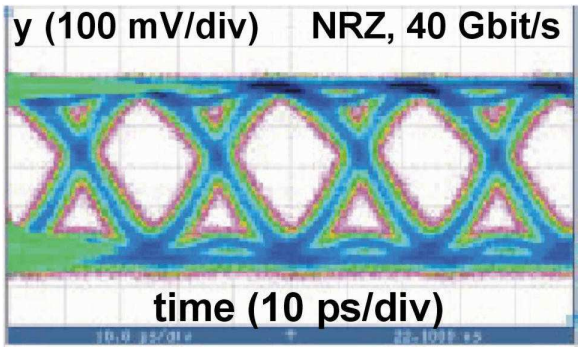


Fig. 9: Measured 40 Gbit/s eye pattern of the receiver module at an optical input power of +6.4 dBm.

The Rx module's bandwidth of 50 GHz is even well suited to support the 40 Gbit/s RZ modulation format.

So far an external bias-T was used, due to OEIC circuit simplicity. These bias-Ts are expensive and show transmission losses of about 1.5 dB in the range of 40 GHz, such loss values increase in cases of higher frequencies (60 GHz) and unfortunately partly compensate the gain of the build-in amplifier. The improved circuit scheme of a recent pinTWA photoreceiver is given in Fig. 10 [13].

The DC current is now fed into the terminal V_{dd}, which is blocked additionally at the ceramic board in the module with larger capacitors (100 nF) to GND, to provide flat low-frequency gain down to 30 kHz. Concerning the circuit scheme at the output, the TWA RF output is still DC-coupled to the subsequent electronics, but the amplifier's/HEMT source bias return path is DC-decoupled from the RF output GND employing an on-chip MIM capacitor of 100 pF in Fig. 10 [14]. Due to the applied negative bias at the source terminal the necessary reverse bias for the photodiode is generated automatically, thus the bias V_{pd} pad of the photodiode may remain at zero bias in most cases of low and moderate optical input power. Only for very high input power (> 5 dBm) it is advantageous with respect to the pulse width to increase the bias at this terminal slightly by +1 V. The supply voltages V_{dd} (+4.3 V) and V_{ss} (~ -2 V at the source terminal) can be fine adjusted to provide an arbitrary DC potential at the DC-coupled TWA output, in order to precisely fit the input specifications of the subsequent amplifier or DEMUX circuitry.

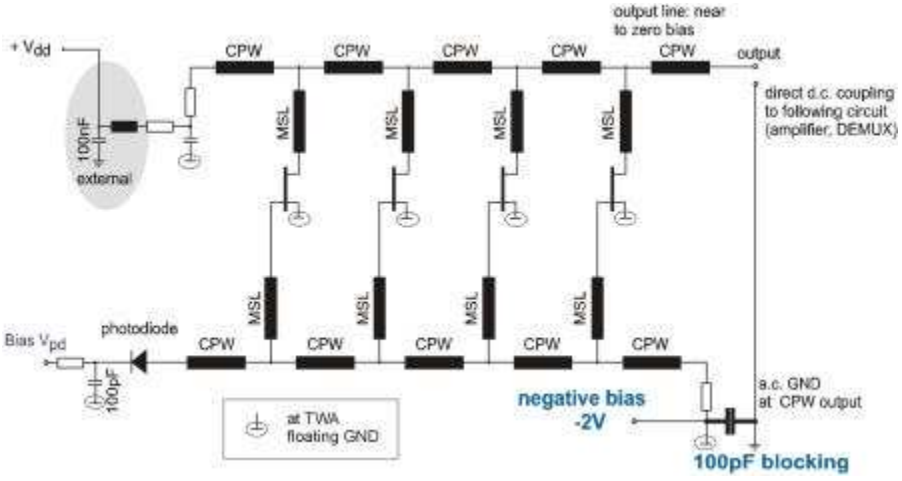


Fig. 10: Circuit scheme of the improved negative bias photoreceiver, where the bias-T is omitted; biasing is done by feeding the DC power into terminal V_{dd}. The AC output is still DC coupled to subsequent electronics (post/limiting amplifier or DEMUX).

By this OEIC modification the bias-T is omitted and the system costs of photoreceiver operation are considerably reduced. Additionally, the effective gain is increased by the amount of external losses of the bias-T, and the useable bandwidth and gain flatness are improved, too.

Packaging of this receiver OEIC was done within the same package familiy as shown in Fig. 8. The module bandwidth exceeded 50 GHz [13]. The measurement of the 40 Gbit/s NRZ modulation format eye pattern characteristics was done using a 40 Gbit/s optical transmitter SHF 4003A (SHF Communication Technologies) and a digital communication analyzer hp 83480A with SD32 50 GHz sampling head. The optical input power was -1.6 dBm. The received eye pattern is widely opened with output voltages of

110 mV_{pp}, see Fig. 11. The Q-factor amounts to 11.8, indicating that the potential of the photoreceiver extends to even higher bitrates, for which digital measurement equipment is not commercially available.

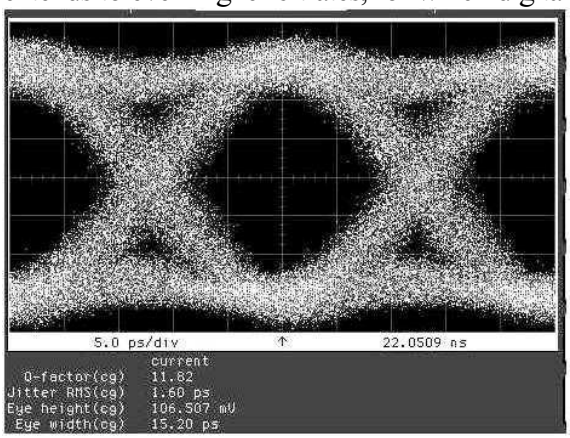


Fig. 11: Measured 40 Gbit/s NRZ eye pattern of the photoreceiver module at -1.6 dBm, PRBS: 2^{31}-1; the Q-factor exceeds 11.8.

To obtain reliable eye pattern information for this photoreceiver module at arbitrary higher bitrates, a procedure of calculating the minimum phase of the module (Hilbert's transform) and using this phase together with the measured amplitude by heterodyne technique [15] was applied, to synthesize eye patterns for the NRZ modulation format at 60 and 66 Gbit/s, both of which are shown in Fig. 12 a, b.

It can be seen, that the standard mask for STM64 (10 Gbit/s), which is assumed to be valid also at those higher bitrates, is unaffected up to bitrates of 60 Gbit/s and the eye pattern is still well opened at 66 Gbit/s for the NRZ modulation format.

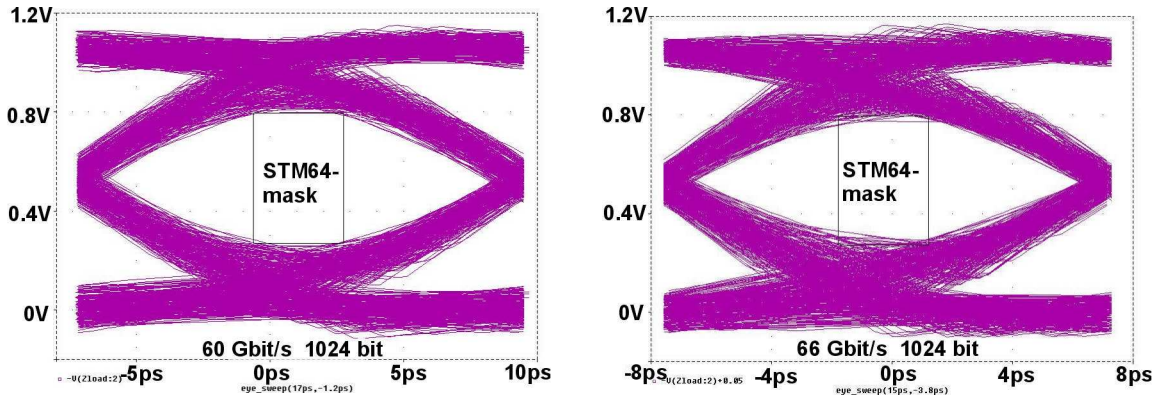


Fig. 12 a, b: Synthesized eye pattern at 60 Gbit/s and 66 Gbit/s with 1024 bits for NRZ modulation [15].

IV. Monolithic photoreceivers for 80/85 Gbit/s and higher

Photoreceiver OEICs for bit rates higher than 40/43 Gbit/s will be continueously developed at FhG-HHI based on further optimisation of evanescently coupled photodiodes und based on distributed amplifiers employing AlInAs/GaInAs/InP HEMT technology. Actually, gate lengths of about 0.2 µm are used, achieving f_T/f_{max} values of 110/240 GHz. Reducing the gate length into the 130 nm range, increased cut-off frequencies of f_T/f_{max} of 170/300 GHz are expected, which are sufficient for the 80/85 Gbit/s receivers. Both active components, evanescently coupled photodiode and distributed amplifier, have a very promising broadband frequency potential exceeding 100 GHz, thus the 80/85 Gbit/s photoreceivers shall be developed within the existing integration concept. Corresponding electrically multiplexing and demultiplexing circuits for 80/85 Gbit/s are now realizable applying SiGe or InP-based technology for digital circuits (HBT-based as well as HEMT-based [16]). For even higher bit rates (160 Gbit/s) the TWA concept will still be preserved [17], but now using further reduced HEMT gate lengths in the 80 nm range, for the photodiode the evanescent coupling will be complemented by a traveling wave design.

V. Conclusion

An universal integration scheme for photodetector and photoreceivers was presented. It is based on waveguide-integrated photodiodes and an underlying semi-insulating optical waveguide layer stack (GaInAsP:Fe), which allows, to fabricate arbitrary stable optical feeding networks also for specialized detectors, like twin-photodetectors and balanced receivers. The underlying waveguide stack is the basis for an MBE re-growth of a HEMT layer stack, if electronics have to be integrated, too. In this way photoreceiver OEICs comprising different circuit configurations of traveling wave amplifiers have been fabricated, which operate in the 40…60 Gbit/s data range. Several photodetector and receiver modules were successfully tested within field trials by the partners Siemens AG, Alcatel SEL AG and Lucent Technologies up to 43 Gbit/s (including FEC schemes).
The way to 80/85 Gbit/s monolithic photoreceivers was described, based on the photoreceiver integration with 60 Gbit/s data rate handling capability.
The integration scheme is also applicable for narrow-band photoreceivers with resonant enhanced responsivity, useful for clock recovery purposes or optic/mm-wave signal converters [18]. Respective devices for 80/85 GHz detection bands are under fabrication. Balanced receivers of the next generation may include an MMI coupler at the input of the two diodes, for on-chip optical signal mixing. Further advanced versions of those balanced receivers may integrate a bit delay within a waveguide Mach-Zehnder network for DPSK demodulation purposes.

VI. Acknowledgements

The author acknowledges contributions from his colleges A. Beling, W. Ebert, Th. Eckhardt, H. Ehlers, R. Gibis, G. Jacumeit, R. Kunkel, G.G. Mekonnen, W. Passenberg, W. Schlaak, D. Schmidt, A. Seeger, R. Steingrüber, M. Stollberg, and P. Wolfram of the receiver team at FhG Heinrich-Hertz-Institut, the assistance of students A. Becker, V. Eisner, J. Jayasooriya and S. Jatta for measurements as well as contributions of former colleagues C. Schramm, A. Umbach, G. Unterbörsch and R. Ziegler (now with u2t Innovative Optoelectronics Components AG, Berlin) and help of Th. Engel (now with Siemens AG, Berlin). Special thanks are due to our partners B. Schmauß at Lucent Technologies, Nürnberg and B. Wedding at Alcatel SEL AG, Stuttgart and E. Gottwald and C.-J. Weiske at Siemens AG, ICN, Munich for valuable suggestions and system characterizations in TDM- and ETDM based test beds. This work was financed under the KomNet and MultiTeraNet programmes of the german BMBF and by the Senate of Berlin.

VII. References

[1] G. Unterbörsch, A. Umbach, D. Trommer, G.G. Mekonnen, "70 GHz long-wavelength photodetector", *Proc. 23rd Europ. Conf. on Optical Communications (ECOC '97)*, (Edinburgh, U.K.), September 1997, Conf. Publication No. 448 IEE, vol. 2, pp. 25-28, 1997.

[2] G. Unterbörsch, D. Trommer, A. Umbach, R. Ludwig, and H.-G. Bach, "High-power performance of a high-speed photodetector", *24th European Conference on Optical Communication (ECOC'98)*, p. 67, Madrid, Spain, 20-24 Sept. 1998.

[3] A. Umbach, G. Unterbörsch, D. Trommer, C. Schramm, G. G. Mekonnen, C.-J. Weiske, "Integrated Differential Photoreceiver for 40 Gbit/s Systems" *Proc. Of the 12th Int. Conf. On InP and Rel. Mat. (IPRM'00)*, Williamsburg, VA, USA, 2000.

[4] A. Beling, D. Schmidt, H.-G. Bach, G. G. Mekonnen, R. Ziegler, V. Eisner, M. Stollberg, G. Jacumeit, E. Gottwald, C.-J. Weiske, A. Umbach, "High power 1550 nm twin-photodetector modules with 45 GHz

bandwidth based on InP“, *Proc. Optical Fiber Commun. (OFC 2002)* , March 17-22, 2002, Anaheim, CA, USA, paper WN4.

[5] A. Beling, H.-G. Bach, D. Schmidt, G. G.Mekonnen, M. Rohde, L. Molle, H. Ehlers, A. Umbach, "High-Speed Balanced Photodetector Module with 20dB Broadband Common-Mode Rejection Ratio," *Proc. Optical Fiber Commun. (OFC 2003)* , March 23-28, 2003, Atlanta, GA, USA, paper WF4.

[6] H.-G. Bach, A. Umbach, S. van Waasen, R.M. Bertenburg, G. Unterbörsch, “Ultrafast monolithically integrated InP-based photoreceiver: OEIC-design, fabrication, and system application”, *Special Issue of IEEE Journal of Selected Topics in Quantum Electronics on Integrated Optics (JSTQE)* Vol. 2, No. 2, pp. 418- 423, 1996.

[7] W. Schlaak, G.G. Mekonnen, H.-G. Bach, C. Bornholdt, C. Schramm, A. Umbach, R. Steingrüber, A. Seeger, G. Unterbörsch, W. Passenberg, and P. Wolfram, “40 Gbit/s Eyepattern of a Photoreceiver OEIC with Monolithically Integrated Spot Size Converter”, *Technical Digest, OFC 2001*, Mar 17-22, 2001, Anaheim, CA, USA, paper WQ4, pp. 1-3.

[8] G. G. Mekonnen, W. Schlaak, H.-G. Bach, R. Steingrüber, A. Seeger, Th. Engel, W. Passenberg, A. Umbach, C. Schramm, G. Unterbörsch, S. van Waasen: “37-GHz Bandwidth InP-Based Photoreceiver OEIC Suitable for Data Rates up to 50 Gb/s”, *IEEE Photon. Technol. Lett.,* vol. 11, No. 2, pp. 257-259, 1999.

[9] see www.u2t.de

[10] M. Rohde, C. Caspar, N. Heimes, M. Konitzer, E.-J. Bachus and N. Hanik, “Robustness of DPSK direct detection transmission format in standard fibre WDM systems”, *Electron. Lett.,* vol. 36, no. 17, pp. 1483-1484, Aug. 2000.

[11] M. Bitter, R. Bauknecht, W. Hunziker, and H. Melchior: “Monolithically Integrated 40-Gb/s InP/InGaAs PIN/HBT Optical Receiver Module”, *11th Int. Conf. on InP and Rel. Materials*, 16-20 May 1999, Davos, Switzerland, Proceedings: paper WeA1, pp. 381-384.

[12] H.-G. Bach, W. Schlaak, G.G. Mekonnen, R. Steingrüber, A. Seeger, W. Passenberg, W. Ebert, G. Jacumeit, Th. Eckhard, R. Ziegler, A. Beling, B. Schmauß, A. Munk, Th. Engel, A. Umbach: ”50 GHz Photoreceiver Modules for RZ and NRZ Modulation Format Comprising InP-OEICs”, *27th European Conf. On Optical Communication, ECOC2001,* September 30 – October 4, Amsterdam, The Netherlands, Proceedings, paper Th. M.2.5, pp. 560-561.

[13] H.-G. Bach, A. Beling, G.G. Mekonnen, W. Schlaak, and C. Bornholdt: “60 Gbit/s InP-Based Monolithic Photoreceiver”, *28th European Conf. On Optical Communication, ECOC2002*, September 8 – 12, Copenhagen, Denmark, Proceedings, Vol. 4, paper Th. 10.5.2.

[14] G. G. Mekonnen, H.-G. Bach, W. Schlaak, R. Steingrüber, A. Seeger, W. Passenberg, W. Ebert, G. Jacumeit, Th. Eckhardt, R. Ziegler, and A. Beling, “40 Gbit/s Photoreceiver with DC-Coupled Output and Operation without Bias-T”, *14th Intern. Conf. on InP and Related Materials (IPRM 2002),* May 12-16, 2002, Stockholm, Sweden, paper A8-1.

[15] H.-G. Bach, A. Beling, G. G. Mekonnen, and W. Schlaak, "Design and fabrication of 60-Gb/s InP-based monolithic photoreceiver OEICs and Modules", *IEEE J. Select. Topics Quantum Electron*., vol. 8, pp. 1445-1450, Nov./Dec. 2002.

[16] K. Murata, K. Sano, S. Sugitani, H. Sugahara, and T. Enoki, “100 Gbit/s multiplexing and demultiplexing IC operations in InP HEMT technology”, *Electronics Letters*, 21st Nov. 2002, Vol. 38, No. 24.

[17] M. Rodwell, D. Mensa, Q. Lee, B. Agarwal, R. Pullela, J. Guthrie, S. Jaganathan, T. Mathew, “High-Densitiy Mixed-Mode Microwave Integrated Circuits for Radar and Communication Systems”, Final Report MICRO, University of California (www.ucop.edu/research/micro/96_97/96_080.pdf) 1996.

[18] G. Unterbörsch, Th. Engel, D. Rohde, M. Rohde, D. Bimberg, G. Großkopf, „Hybrid and monolithic integrated optic/millimeter-wave converters for 60 GHz radio-over-fiber systems“, *Technical Digest, OFC’99 / IOOC*, Feb 21-26, 1999, San Diego, paper TuI8, pp. 117-119.

InGaAsP/InP Compact Monolithic SOA-Integrated Mach-Zehnder Interferometer All-Optical Switches by Single-Step Selective-Area MOVPE and their Switching Performance

Xueliang Song, Daisuke Miyashita, Zhenrui Zhang, Naoki Futakuchi, and Yoshiaki Nakano
Research Center for Advanced Science and Technology, the University of Tokyo, JST-CREST
4-6-1 Komaba, Meguro-ku, Tokyo, 153-8904, Japan
song@hotaka.t.u-tokyo.ac.jp

Abstract: Compact (3.5 x 1mm) monolithic Mach-Zehnder interferometer optical switch circuits were fabricated by single-step selective-area InGaAsP/ InP MOVPE and dry etching. Static switching performance, measured with current injection into an integrated SOA on the interferometer arm, includes 18π phase shift by 60mA. Preliminary dynamic all-optical switching experiments revealed carrier recovery time in the selective-area-grown SOA of about several hundred picoseconds.

Keywords: all-optical switch, selective area growth, monolithic integration, Mach-Zehnder interferometer

Introduction

SOA (semiconductor optical amplifier)-integrated Mach-Zehnder interferometer optical switches attracted much attention these years for there capability of processing ultra-fast optical data streams [1-4]. In particular, monolithically integrated all-optical switches are important for their compact size, stability, and low cost [2-4]. However, fabrication of such devices was not simple because they generally require bad yield etch-and-regrowth technique for active and passive components integration. On the other hand, the selective area growth (SAG) technique has also been known as another simpler technique for its requiring of only one step epitaxy, though its applicability has been limited. We previously reported fabrication and static switching measurement of shallow ridge waveguide type optical switches [3]. In this paper, we report fabrication of compact size high-mesa (deep ridge) waveguide type switches and their static switching performance with current injection as well as preliminary dynamic switching with optical control pulses.

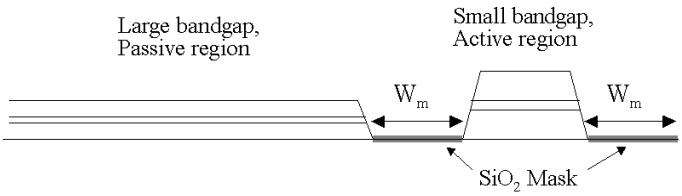


Fig.1. *Schematic view of Selective Area Growth.*

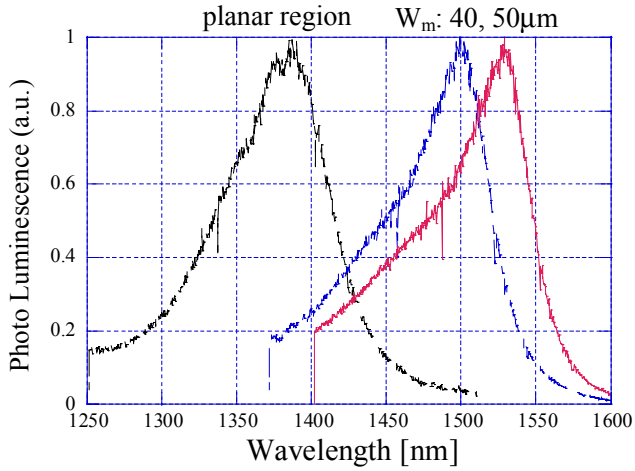


Fig.2. *Photoluminescence from planar (passive) region and SAG (active) regions (W_m=40, 50μm).*

SAG for monolithic integration

Depicted in Fig.1 is the schematic of the SAG technique. The SAG (active) region is sandwiched by SiO_2 mask film, resulting in faster grow speed than planar (passive) region due to more supply of grow source. Monolithic integration with SAG technique is enabled by large bandgap shift in SAG region. The first reason for this shift is the thicker wells of SAG region in MQW (multi-quantum well), resulting in lower quantum levels than in planar region. The second reason is the larger incorporation of

In source than Ga source, and thus shrinks the bandgap of SAG region furthermore. Fig.2 shows the PL (photoluminescence) of planar region and SAG region with SiO_2 mask width of 40μm and 50μm. The PL peak in planar region is 1380nm; in SAG region it shifts to longer wavelength, i.e. 1500nm for W_m=40μm and 1530nm for W_m=50μm. Up to 150nm PL peak shift enables the active components to be integrated in SAG region, while passive components work transparently in planar region. In the following sections, we describe fabrication and measurement of switches with 50μm width SAG region.

Design and Fabrication

To achieve compact size, we adopted high-mesa (deep-ridge) type waveguide for passive components for strong confinement of guided lightwave. With the strong confinement structure, the width of MMI (multi-mode interference) couplers can be narrow (and thus shorter MMI length) but still excites enough higher order modes for self-imaging, and bend radius can be small with little radiation loss. In our design, the width and length was each 12μm and 200μm for 3dB MMI couplers; bend radius was mostly 500μm, except for 800μm at the control input port (where larger bend radius does not effect the length of the total switch). The width of SOA and other parts of the passive waveguide was 2.5μm. The two control light input ports and central signal input port were spaced with even intervals of 250μm, for the future experiments with tapered fiber array where we could couple two control pulses together with a time delay for push-pull operation. The total length

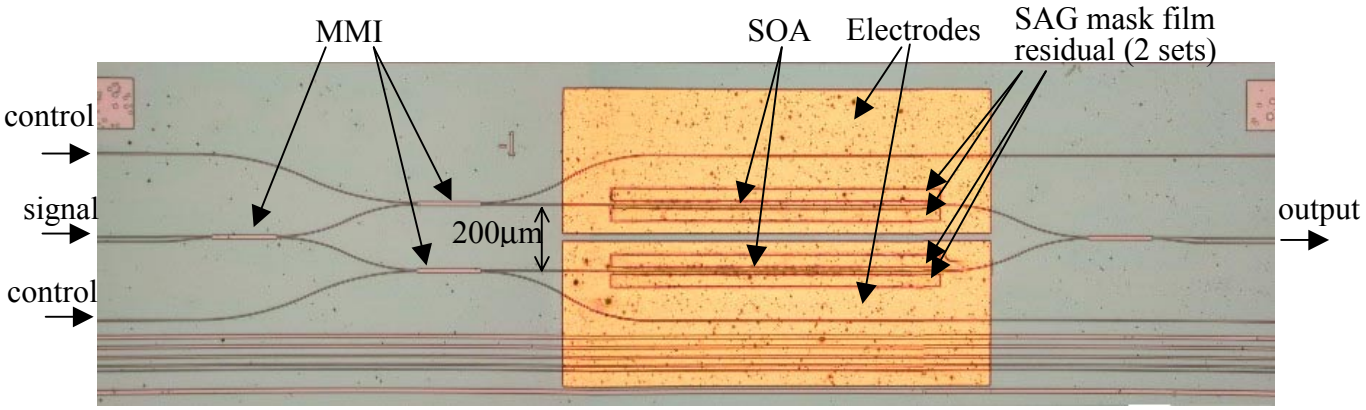
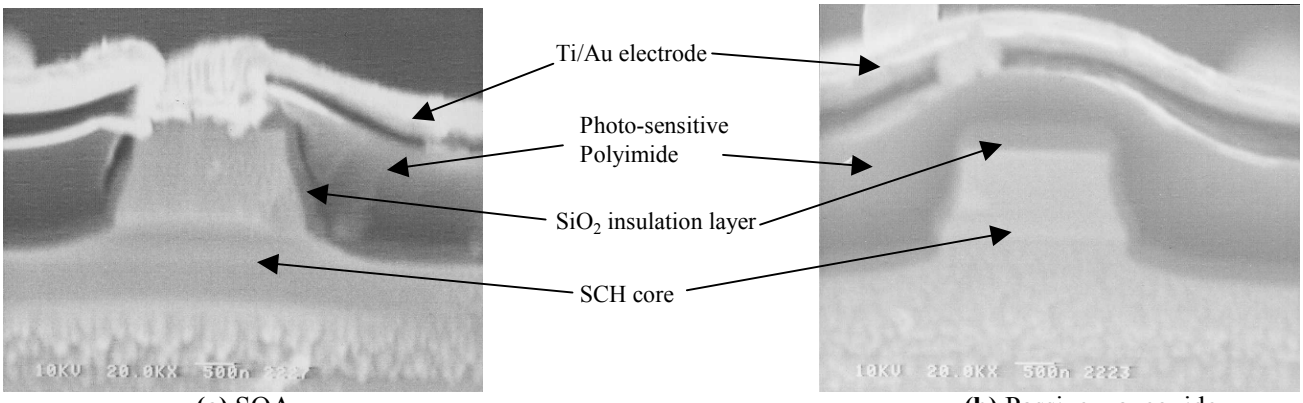


Fig.3. *Microscope photograph of fabricated switch. Four MMI couplers were fabricated in planar region and two SOA's in SAG region. The spacing between two SAG regions is 200μm.*



(a) SOA **(b)** Passive waveguide

Fig.4. SEM *Section view of SOA and passive waveguide. .*

of the switch was 3.5mm. Fig. 3 is the microscope photograph of the fabricated switch.

The waveguide mesa was formed with ECR (Electron Cyclotron Resonance) ion etching machine. SiNx film was used as etching mask and the switch pattern was defined with photolithography. Though the etching depth 1.6μm was the same for both SAG region (SOA) and planar region (passive waveguide), due to different upper InP clad thickness, etching went thoroughly through the SCH (separate confinement heterostructure) core layer with passive waveguide, while stopped above the core layer with SOA mesa, as can be seen in Fig.4.

The contact opening for SOA electrode was done with photosensitive polyimide. After the waveguide mesa forming, SiO_2 insulation film was sputtered and then photosensitive polyimide was spun over the substrate. With another photolithography, only the SOA part formed opening windows. Then the electrode contact was established after SiO_2 insulation layer wet etching, Ti/Au layer EB (electron beam) evaporation.

Measurement

First, we measured the static switching performance with changing current injection to SOA's. Fig.5 shows the experimental setup, where the signal light was coupled into the input port of the optical switch through a PC (polarization controller) to select TE or TM mode. A tapered fiber was used to couple the signal light into semiconductor waveguide. Current bias to the upper SOA I_1 was fixed to 80mA, while current I_2 to the lower one was changed from 0 to 160mA. The output signal was coupled into a BPF (band pass filter) through a tapered fiber to cut off ASE (amplified spontaneous emission) from SOA, and then lead to a power meter.

Depicted in Fig. 6 is the static switching result with both output ports, TE and TM modes. The input light wavelength was 1540nm. One can see that phase shift of 14π (18π) occurred with TE mode when changing I_2 from 0 to 60mA (160mA), while only less than 7π (11π) occurred with TM mode in that range. This is due to much less gain change in TM mode with current injection, and

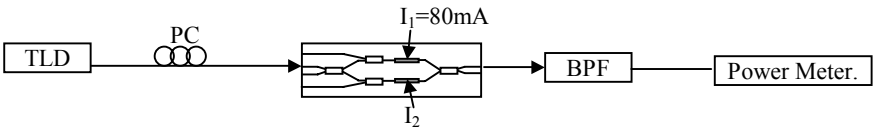


Fig.5. *Experimental setup for static switching by current injection. TLD: Tunable Laser Diode. PC: Polarization Controller. BPF: Band Pass Filter.*

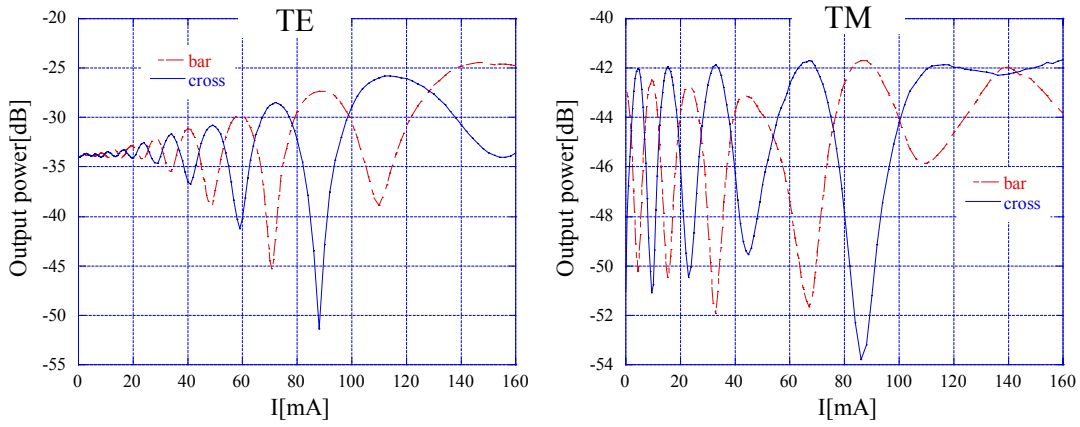


Fig.6. *Switching performance with current injection to one SOA. Input signal was 1540nm with this result. I_1 injected to upper SOA was fixed to 80mA, and I_2 to lower SOA was changed from 0 to 140mA. Phase shift of 14π occurred for TE mode when changing I_2 from 0 to 60mA, while only less than 7π phase shift occurred for TM mode in that current range.*

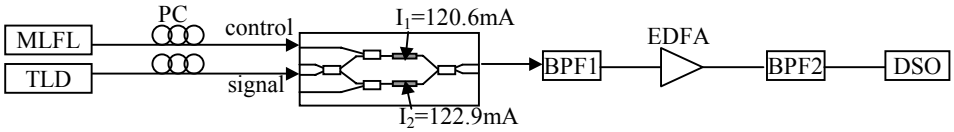


Fig.7. *Experimental setup for pulse response measurenent of all-optical switch. MLFL: mode-locked fiber laser. TLD: tunable laser diode. PC: polarization controller. BPF: band pass filter. EDFA: erbium-doped fiber amplifier. DSO: digital sampling oscilloscope.*

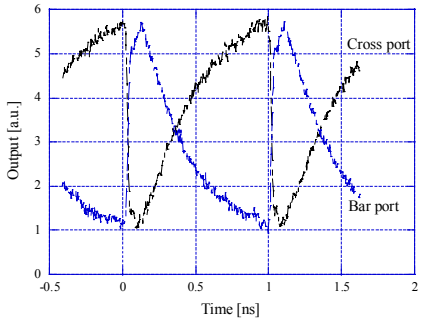


Fig.8. *Pulse response of the switch at output ports. The control pulse energy induced phase shift of π was estimated to be 0.36pJ considering coupling loss and internal loss of the switch.*

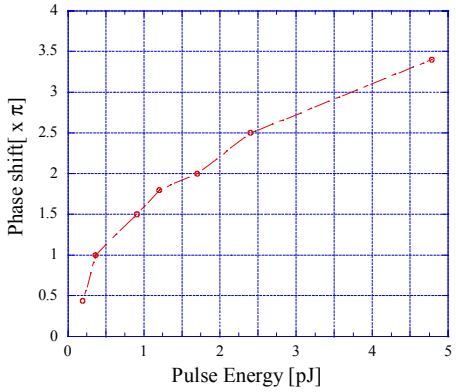


Fig.9. *Estimated control pulse energy coupled into SOA versus induced phase shift.*

thus less refractive index change according to Kramers - Krönig relation. In TE mode, over 20dB extinction ratio was obtained when I_2 injected to the lower SOA was balanced with I_1 to the upper SOA, at around 80mA.

Preliminary dynamic switching performance was also measured with CW (continuous wave) light for signal and pulse for control light. Depicted in Fig.7 is the experimental setup. MLFL (mode-locked fiber laser) was experimentally built with a loop consists of EDFA, LN (lithium niobate) modulator, BPF and other components, and the repetition rate was 1GHz. The control pulse wavelength was 1535nm, and CW signal light was 1550nm. At the output of the switch, the control pulse was filtered off by BPF1, and only signal light was amplified by the EDFA. After cutting ASE of EDFA with BPF2, the output signal was lead into DSO (digital sampling oscilloscope), which has a photodetector sensing head. The current bias of the two SOA's was 120.6mA and 122.9mA each. Fig.8 shows the waveform of cross and bar ports measured with DSO, which indicates phase shift of π occurred in the upper SOA with control pulse energy 0.36pJ. Since the control pulse was injected into only one SOA, the relaxation time was dominated by carrier recovery time, about several hundred picoseconds. Depicted in Fig.9 is the estimated control pulse energy versus its induced phase shift in the upper SOA. Up to 3.4π phase shift was induced when the pulse energy was near 5pJ.

As a conclusion, we have successfully fabricated compact Mach-Zehnder SOA integrated all-optical switch circuits with high-mesa waveguide in the passive region. Static switching with current injection and preliminary all-optical dynamic switching performance revealed 18π and 3.4π phase shift at maximum in each case.

This work was supported in part by the Monkasho Grant-in-Aid for Scientific Research #14205055. Photomasks used here were fabricated with the EB equipment of VDEC (VLSI Design and Education Center), the University of Tokyo.

References

[1] Y. Ueno et al., *Jpn. J. Appl. Phys.*, Part 2, vol. 39, pp. L806-L808, 2000.
[2] J. Leuthold et al., *J. Lightwave Technol.,* vol. 17, no. 6, pp. 1056-1066, June 1999.
[3] X. Song et al., in *Proc. ECIO'01*, Paderborn, 2001, WeA3.4, pp.102-105.
[4] T. Tekin, et al., in *Proc. ECIO'01*, Paderborn, 2001, Postdeadline Papers.

A Widely Tunable Optical Filter Using Ladder-Type Structure

S. Matsuo, Y. Yoshikuni, T. Segawa, Y. Ohiso, and H. Okamoto
NTT Photonics Laboratories, NTT Corporation
3-1 Morinosato Wakamiya, Atsugi, Kanagawa, Japan
mash@aecl.ntt.co.jp

A novel widely tunable optical filter using ladder-type structure is proposed. This device decreases the electrode area compared with a tunable filter using an AWG. The device was fabricated using the InGaAsP-InP material system, and exhibits the tuning range of 58 nm.
Keywords: tunable optical filter, arrayed waveguide, MMI coupler

Introduction

The wavelength division multiplexing (WDM) transport network has emerged as the best way to realize the flexible large-capacity network needed for future Internet traffic. For example, in Local Area Networks (LANs), there is a demand for transmitting a large capacity data in a few moments. When WDM technologies used, a large-capacity network using tunable optical filters can be constructed inexpensively because the network has flexible connections. In such networks, widely tunable optical filters are needed because coarse-WDM is usually used in the LANs, WANs, and SANs.

A tunable filter using an arrayed waveguide grating (AWG) has already been developed using the polymer waveguide [1,2]. That device has a tuning range of more than 30 nm. It has the electrodes for changing the refractive index on each waveguide in the array and the length of each electrode successively increases by the same length. This type of tunable filter could feasibly achieve a tunable range of more than 100 nm because the tuning range is determined by the electrode length on waveguide array and there is no theoritical limitation on the electrode length. However, the problem is that this device needs a large electrode area because the length of each electrode on the waveguide array increases successively.

In this letter, we propose a novel tunable filter using a ladder-type structure that uses multiple MMI couplers and a waveguide array. The electrodes are on the input and output waveguides and increasing the length of the electrodes is unnecessary. Thus, the electrode area is smaller than that of the previously reported device using the AWG. The device was fabricated using the InGaAsP-InP material system, and exhibits a wide tuning range of 58 nm.

Device structure and design

Figure 1 shows a schematic diagram of the proposed tunable filter using the ladder-type structure. The device consists of input and output waveguides, the waveguide array, and optical couplers. Each arrayed waveguide is connected to the input and output waveguides by optical couplers. The interference between the lights from output and arrayed waveguide occurs at every optical coupler of the output waveguide. When the length of the waveguides is increased one after another by ΔS as shown in Fig. 1 and the distances between the optical couplers in input and output waveguides, L_1 and L_2, are the same, the resonant wavelength in every optical coupler of the output waveguide is the same. Then the resonant wavelength of this filter, λ_0, is given by

$$\lambda_0 = \frac{n_{eff}\Delta S}{m} \qquad (1)$$

where n_{eff} is the effective refractive index of a waveguide and m is the diffraction order.

When the refractive index in the input waveguide is decreased, the optical path length difference between the optical path from the output and arrayed waveguides is decreased. Therefore, the resonant wavelength change, $\Delta\lambda$, is given by

$$\Delta\lambda = \frac{\Delta n_{eff} L_1}{m} \qquad (2)$$

where Δn_{eff} is the effective refractive index change in the input waveguide. On the other hand, when the refractive index is decreased in output waveguide, the optical path length difference is increased. Thus the resonant wavelength shifts for longer wavelength when the refractive index is increased. Note that the length of waveguide for refractive index change is no limitation as shown in eq. (1). Thus, this device has capability for wide range tuning.

The total tuning electrode length of the input waveguide in proposed device, $L_{propose}$, is given by

$$L_{propose} = (N-1)L_1 \qquad (3)$$

where N is number of arrayed waveguides. On the other hand, the total tuning electrode length of the device in Ref [2] to obtain the same tuning range with proposed device, L_{AWG}, is given by,

$$L_{AWG} = \frac{N(N-1)}{2} L_1 \quad . \qquad (4)$$

Thus, the total length of the tuning electrode is improved by

$$\frac{L_{propose}}{L_{AWG}} = \frac{(N-1)L_1}{N(N-1)L_1/2} = \frac{2}{N} \quad . \qquad (5)$$

It seems that the proposed device would have low power consumption and high yield.

Figure 2 shows the calculated input-output characteristics of the proposed device as a function of arrayed waveguide number. In this calculation, we assumed that the diffraction order, m, was 20. We use an MMI coupler as an optical coupler because it is suitable for use with the high-mesa waveguide structure. We assumed the splitting ratio of the MMI coupler was 0.15 in power. This value is the smallest value for a simple MMI structure [3]. As shown in this figure, the 3-dB bandwidth decreases from 7.0 to 3.6 nm with increasing arrayed waveguide number. The loss of the device, however, increased from 2.84 to 3.87 dB when the arrayed waveguide number was 20. Thus, we choose the arrayed waveguide number of 15. In this case, the loss was 2.84 dB and 3-dB bandwidth was 4.8 nm.

Figure 3 shows the calculated tuning characteristics of the proposed device. The solid line shows the frequency response without tuning and the dashed lines are frequency responses for refractive index change of -0.15 % for input and output waveguides, respectively. In this calculation, we assumed that L_1 and L_2 were 100 μm, the other parameters were the same as in Fig. 2. When –0.15 %-refractive index change occurred in the input waveguide, the resonant peak decreased for 25.4 nm. When –0.15 %-refractive index change occurred in the output waveguide, the resonant peak increased for 25.4 nm. Thus, the total resonant wavelength shifts were 50.8 nm.

Device Characteristics

Figure 4 is photograph of the fabricated tunable optical filter using the ladder-type structure. The device structure was grown by MOCVD on an n-doped InP substrate. It consists of a p^+-InGaAs contact layer, a 0.3-μm-thick p-InP cladding layer (doping concentration of 1 x 10^{18} cm^{-3}), a 1.2-μm-thick p^--InP cladding layer (doping concentration of 2 x 10^{17} cm^{-3}), a 0.3-μm-thick InGaAsP layer (1.3Q), and a 0.5-μm-thick n-InP buffer layer. The high-mesa waveguide structure was formed by Cl_2 ICP-RIE. Waveguide width and height were 1.6 and 4.0 μm, respectively. The MMI couplers, which had the power-splitting ratio of 15:85, were 5.2-μm wide and 56.0-μm long. The diameter of the arrayed waveguides was 400 μm. For current injection to change the refractive index, Ni/Zn/Au electrodes were deposited on the p^+-InGaAs contact layer. The device is 3.2 x 0.9 mm^2, including the bonding pads.

Figure 5 shows the optical frequency response of the tunable filter for TE polarization. The

light source was an ASE light from a fiber amplifier. The transmissivity was normalized by the loss of the reference waveguide. This device was designed for a diffraction order of 20 and arrayed waveguide number of 15. The resonant peak was observed at 1539.5 nm and a side-lobe was also observed. The loss compared with a reference waveguide was 7.5 dB, which is larger than calculated value due to the loss of MMI couplers. The contrast ratio was 12.5 dB and 3-dB bandwidth was 4.5 nm, which agrees with calculation in Fig. 2.

Figure 6 shows the tuning characteristics of the tunable filter. There was no injection current, and two-resonant wavelengths were observed at 1534.6 and 1609.0 nm. Thus, the FSR of this device was 74.4 nm. The injection current of the input waveguide was changed from 0 to 30 mA, while that of the output waveguide was kept constant at 0 mA. The refractive index in input waveguide decreased with increasing injection current. Thus, the resonant wavelength of the filter gradually decreased. The resonant wavelength shift was 29 nm at injection current of 30 mA. When the injection current of the output waveguide was changed from 0 to 30 mA, the resonant wavelength increased by 29 nm. Thus, the total tunable range is 58 nm. As described before, increasing the length of the current injection area could be the reason for the increased tunable range.

Conclusion

We have proposed and demonstrated a widely tunable optical ladder-type filter that uses the multiple MMI couplers and a waveguide array. The device shows loss, compared with a reference waveguide, of 7.5 dB. The contrast ratio is 12.5 dB and the 3-dB bandwidth is 4.5 nm. These values are consistent with the calculation results. The total tuning range is 58 nm.

Acknowledgement

We thank J. Yumoto and C. Amano for helpful discussions and T. Kodaira and K. Ishibashi for device fabrication and measurements.

References

[1] T. Watanabe, Y. Inoue, K. Kaneko, N. Ooba, and T. Kurihara, “Polymeric arrayed-waveguide grating multiplexer with wide tuning range,” *Electron. Lett.*, vol. 33, no. 18, pp. 1547-1548, 1997.

[2] S. Toyoda, N. Ooba, K. Kitoh, T. Kurihara, and T. Maruno, “Wide tuning range and low operating power AWG-based thermo-optic wavelength tunable filter using polymer waveguide,” *Electron. Lett.*, vol. 37, no. 18, pp. 1130-1132, 2001.

[3] M. Bachmann, P.A. Besse, and H. Melchior, “Overlapping-image multimode interference couplers with a reduces number of self-images for uniform and nonuniform power splitting,” *Appl. Optics*, vol. 34, no. 30, pp.6898-6910, 1995.

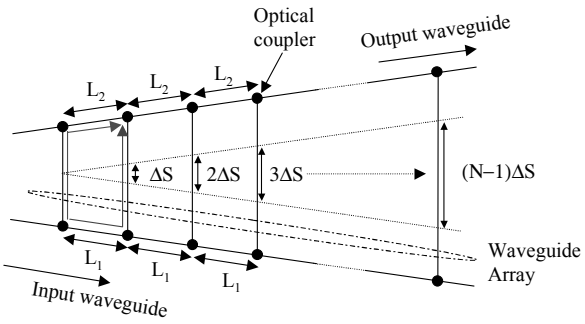


Fig. 1 Schematic diagram of the proposed device.

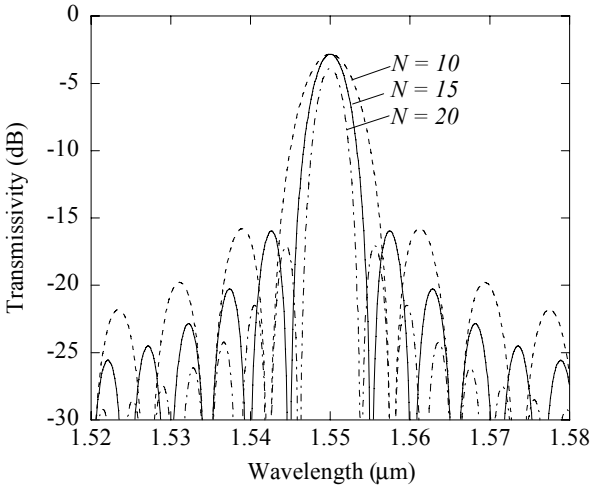


Fig. 2 Calculated input-output characteristics as a function of waveguide number.

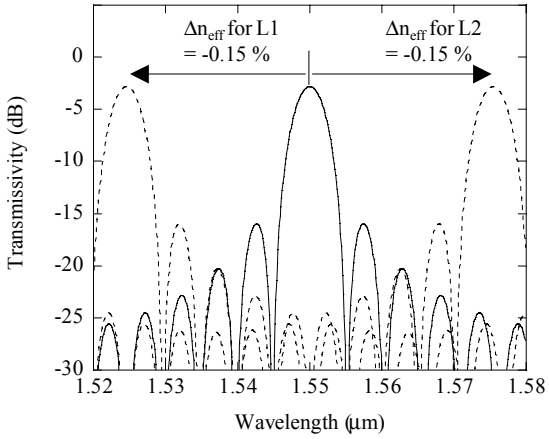


Fig. 3 Calculated tuning characteristics.

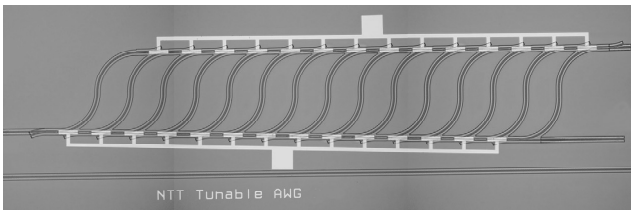


Fig. 4 Photograph of the device.

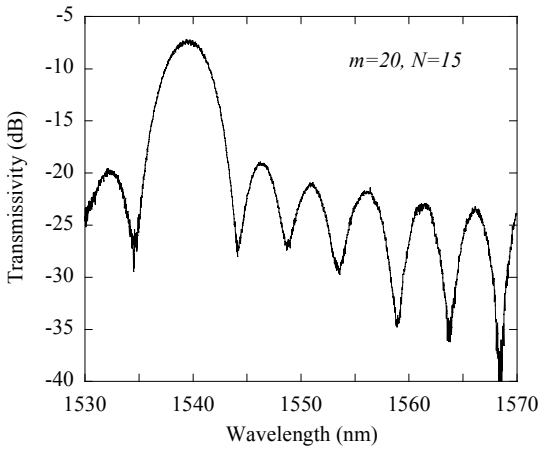


Fig. 5 Input-output characteristics of the device.

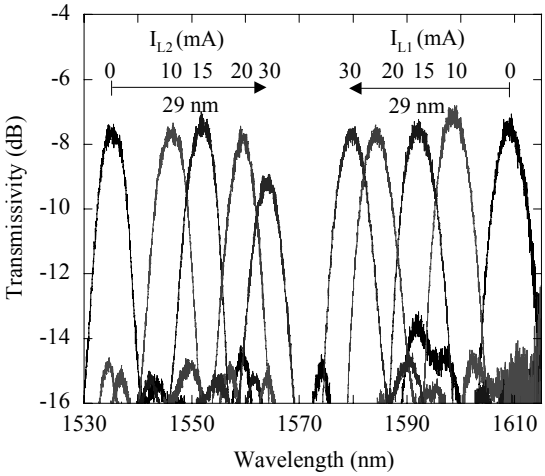


Fig 6. Tuning characteristics of the device.

Finite Element Analysis of Optical Notch Filters based on Photonic Crystals

A. Cucinotta, S. Selleri
Dipartimento di Ingegneria dell'Informazione. University of Parma
Parco Area delle Scienze 181/A, 43100 Parma, Italy
stefano.selleri@unipr.it

L. Vincetti, M. Zoboli
Dipartimento di Ingegneria dell'Informazione. University of Modena and Reggio Emilia
Via Vignolese 905B, 41100 Modena, Italy

A Photonic crystal based notch filter is analyzed by means of Finite Element Method. Simulation results show that the filter exhibits a notch with very narrow bandwidth and its position can be easily tuned with high accuracy over a wide range of wavelengths.

Keywords: Notch Filter, Photonic Crystals, Finite Element Method

Introduction

Photonic crystal (PCs) based devices are expected to meet the demand of the modern optical systems requiring compact devices able to carry out more and more complicated functionalities. It has already been shown low-loss and very compact splitters, sharp bend waveguides, switches, lasers and filters [1]-[4] can be obtained using PCs. In particular, several typology of optical filters can be obtained by exploiting the strong wavelength dependence of the PCs characteristics [1]-[3]. Add-drop filters have been proposed or by coupling two waveguides by means of a resonant cavity [1], [2], or by considering a PCs directional coupler [3]. In this work notch filters based on a PCs waveguide coupled with a resonant cavity are numerically analyzed by means of finite element method (FEM) approaches both in time and in frequency domain [3]. The two approaches present complementary properties. The first one allows a wide band analysis (hundreds of nm) with just one simulation, whereas the latter is very useful when the impact of the material dispersion effects can not be neglected and/or a limited range of frequency must be considered. The FEM is a very powerful method to analyze PCs based devices. It is able to describe with high accuracy any kind of geometrical shape and refractive index profile without heavy computational resources. These properties have been already successfully used to investigate the impact of the geometrical variations on the spectral properties [5]. The analysis reported in this work shows that compact optical filters can be obtained having bandwidth compatible with the channel spacing of the present wavelength division multiplexing (WDM) systems. This result can be achieved by working both on the coupling coefficient between the waveguide and the cavity and on the cavity quality factor Q. In addition, by changing the characteristics of the PCs cells between the waveguide and the resonant cavity, an accurate tuning of the spectral characteristics over a wide range is possible.

Numerical methods

The analysis of PCs based devices can be done by means of numerical approaches able to handle reflected and scattered waves. This is possible both in the time domain and in the frequency domain.
Consider a two-dimensional photonic crystal waveguide in the yz-plane, with no variation in the x direction, and anisotropic media described by relative permittivity and relative permeability diagonal tensors $\overline{\overline{\varepsilon}}_r$ and $\overline{\overline{\mu}}_r$ respectively. In this condition, the analysis of the electromagnetic field propagation can be performed simply by considering the x-component Φ_x of the electric

or of the magnetic field, in the case of TE or TM waves respectively.

Time Domain Approach
By assuming Φ_x of the form

$$\Phi_x(y,z,t) = \phi_x(y,z,t)\, e^{j\omega t}, \tag{1}$$

being ω the angular frequency and ϕ_x the complex amplitude, the wave equation reads:

$$\frac{q_x}{c^2}\frac{\partial^2\phi_x}{\partial t^2} + 2j\omega\frac{q_x}{c^2}\frac{\partial\phi_x}{\partial t} - \omega^2\frac{q_x}{c^2}\phi_x \; - \frac{\partial}{\partial y}\left(p_z\frac{\partial\phi_x}{\partial y}\right) - \frac{\partial}{\partial z}\left(p_y\frac{\partial\phi_x}{\partial z}\right) = 0, \tag{2}$$

with p_i and q_i, $i = x, y, z$, the elements of the tensors $\overline{\overline{p}}$ and $\overline{\overline{q}}$. In particular $\overline{\overline{p}} = \overline{\overline{\mu}}_r^{-1}$, $\overline{\overline{q}} = \overline{\overline{\varepsilon}}_r$ when $\phi_x = E_x$ for TE modes, $\overline{\overline{p}} = \overline{\overline{\varepsilon}}_r^{-1}$, $\overline{\overline{q}} = \overline{\overline{\mu}}_r$ when $\phi_x = H_x$ for TM modes. Choice (1) allows the propagation analysis of the amplitude ϕ_x rather than of the original field Φ_x which varies very quickly in time. Larger time step can thus be considered for the simulations, thus reducing the computational time required for a given time interval analysis. By applying the standard finite element technique to the spatial coordinates of (2) and to the time variable as well, it yields the following recursive algebraic formula:

$$[P]\{\phi_x\}_{n+1} = [Q]\{\phi_x\}_n - [P]^*\{\phi_x\}_{n-1}$$

with

$$[P] = \frac{[B]}{c^2\Delta t} + \frac{j\omega}{c^2}[B] + \frac{\Delta t}{2}([A] + [C] - \frac{\omega^2}{c^2}[B]), \quad [Q] = \frac{2}{\Delta t c^2}[B].$$

The elements of the $[A]$, $[B]$ and $[C]$ matrices are defined by the proper products of the shape functions and their derivatives [6]. It is important to highlight that the described approach does not neglect the second order derivatives in t. This allows the propagation analysis of very narrow time pulses. By Fourier transforming the temporal evolution of the field, spectral information over a wide band can be obtained with only one simulation. Notice that material dispersion effects should be considered through convolution integral. Nevertheless, as the considered devices are very short, they can be neglected without affecting substantially the result accuracy.

Frequency Approach
Starting from the curl-curl equation in the frequency domain and considering Φ_x and the medium as above, it yields:

$$\frac{\partial}{\partial y}\left(p_z\frac{\partial\Phi_x}{\partial y}\right) + \frac{\partial}{\partial z}\left(p_y\frac{\partial\Phi_x}{\partial z}\right) - \frac{\omega^2}{c^2}q_x\Phi_x = 0. \tag{3}$$

The application of the standard finite element technique to the spatial coordinates of (3) directly yields

$$\left([A] + [C] - \frac{\omega^2}{c^2}[B]\right)\{\Phi_x\} = [D]\{\psi_x\} \tag{4}$$

where $\{\psi_x\}$ is the known vector of the input field ψ_x; it is defined on a portion of the domain boundary Γ. Once chosen the input field ψ_x and the working frequency, the resolution of the standard algebraic equation (4) provides the field distribution on the whole domain. Perfectly Matched Anisotropic layers (PMA) have been used to enclose the domain in both approaches [7].

Results

The analyzed structure, consists on a square lattice of circular dielectric rods in air, with a $85.7\,nm$ radius, having a lattice constant of $600\,nm$. It is reported in figure 1. The coupling among the waveguide mode and those of the resonant cavity causes the filtering effect according to the coupling coefficient and to the Q factor [1]. Higher the Q factor, more selective is the spectral response. To increase Q, the number of the rods separating the cavity and the waveguide must increase [8]. Unfortunately, this also reduce the coupling; if the rod number is too high, the waveguide and the cavity are uncoupled. In the PCs under investigation, a trade-off is introduced by separating the cavity and the waveguide with two rods; it is shown in figure 1. The spectral response has been firstly calculated by means of the time domain approach to obtain information over a wide range of wavelength with only one simulation. The obtained curve is shown in figure 1. Very narrow notches are evident near $1.51\,\mu m$ and near $1.7\,\mu m$. For this kind of spectral response, a time domain approach is not the best tool. In the high Q value cavity, the decay rate of the electromagnetic energy stored in the cavity is very low and this forces very long time simulation in order to obtain the necessary frequency resolution. On the contrary, by means of the frequency approach the spectral characteristics near the notch can be evaluated with the user desired frequency resolution. The trasmittance spectrum near the notch at $1.51\,\mu m$ is reported in the inset of figure 1. It was obtained by means of the frequency approach. The full width at half maximum (FWHM) of this filter is less than $0.7\,nm$ and the center band transmittance is about $-27\,dB$.
The notch position can be tuned over a wide range of wavelengths by changing the characteristics of the crystal cell between the waveguide and the cavity. In figure 2(a) the transmittance spectra obtained by a change of the 5% in the refractive index of the rod near the cavity or of the rod near the waveguide or both are reported. This figure points out an important property of this filter; by changing the rod near the cavity, strong variations are obtained, whereas by changing that one near the waveguide a more accurate tuning is possible. In all cases the transmittance value at center band is almost unchanged. The same behaviour is observed by changing the rod radius. In figure 2(b), notch shift obtained by changing the radius of the rod near the cavity or the one near the waveguide is reported. The rod near the waveguide allows to control the notch position on a scale comparable with the channel spacing, while the rod near the cavity allows to control the notch position over a range of several nanometers.
In conclusion, it has been shown that highly selective notch filters accurately tunable within a range of several nanometers, can be obtained by means of a proper design of the PC structures.

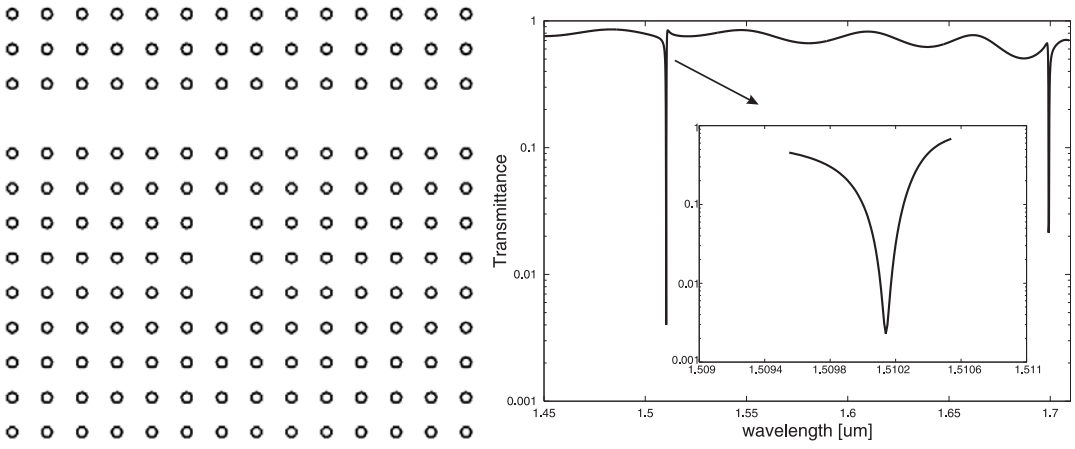


Fig. 1. Left:PC notch filter. Right: transmittance spectrum of the notch filter

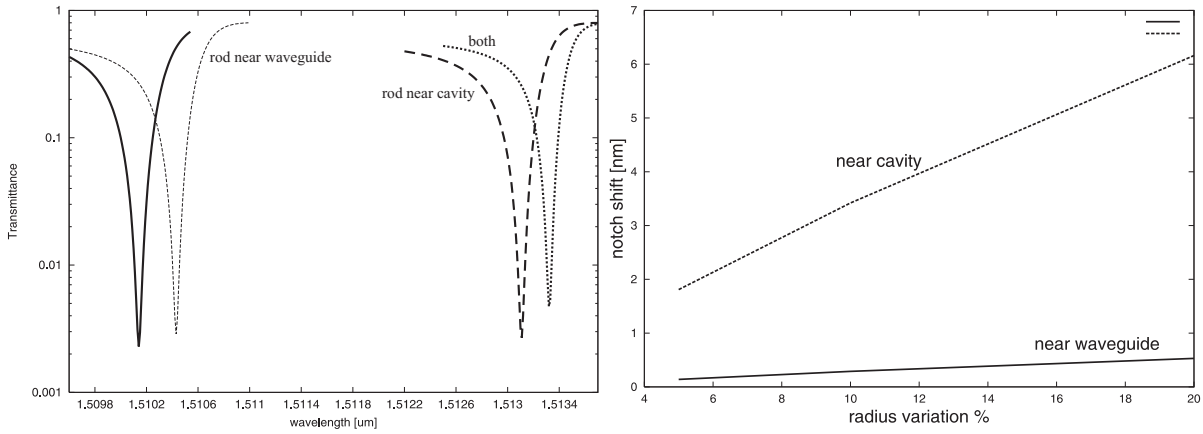


Fig. 2. Left: transmittance spectrum of the notch filter. Right: notch shift.

[1] S. Fan, P.R. Villeneuve, J. D. Joannopoulos, H. A. Haus, "Channel drop filters in photonic crystals", *Opt. Express*, **3**, 4-11, 1998.

[2] A. Sharkawy, S. Shi, D.W. Prather, "Multichannel Wavelength Division Multiplexing with Photonic Crystals", *Appl. Phys.*, **40**, 2247-2252, 2001.

[3] M. Koshiba, "Wavelength Division Multiplexing and Demultiplexing with Photonic Crystal Waveguide Couplers", *J. Lightwave Technol.*, **19**, 1970-1974, 2001.

[4] R. Stoffer, H.J.W.M. Hoekstra, R.M. De Ridder, E. van Groesen, F.P.H. van Beckum,"Numerical studies of 2D photonic crystals: waveguides, coupling between waveguides and filters", *Opt. Quantum Electron.*, **32**, 947-961, 2000.

[5] A. Cucinotta, S. Selleri, L. Vincetti, M. Zoboli, "Impact of the cell geometry on the spectral properties of photonic crystal structures", *Appl. Phys. B*, **73**, 595-600, 2001.

[6] V.F. Rodríguez-Esquerre and H.E. Hernandèz-Figueroa, "Novel Time-Domain Step-by-Step Scheme for Integrated Optical Application", *IEEE Photon. Technol. Lett.*, **13**, 311-313, 2001.

[7] S. Selleri, L. Vincetti and M. Zoboli, "Full-Vector Finite-Element Beam Propagation Method for Anisotropic Optical Device Analysis", *IEEE J. Quantum Electron.*, **36**, 1392-1401, 2000.

[8] P.R. Villeneuve, S. Fan, J.D. Joannopoulos, "Microcavities in Photonic Crystals: Mode Symmetry, Tunability and Coupling Effiency", *Phys. Rev. B*, **54**, 7837-7842, 1996.

Domain inversion in phase-velocity matched $LiNbO_3$ electro-optic modulators for large bandwidth and low driving voltage

M. Belmonte, V. Pruneri and M. Orio
Corning OTI, Viale Sarca 222, Milano Italy
e-mail: belmontem@corning.com

Abstract - An appropriate sign reversal of the electro-optic interaction is proposed in velocity matched modulators to significantly increase the bandwidth to driving voltage ratio (BW/V_π). The concept is applied to domain inverted $LiNbO_3$ and may lead to >30% increase for BW/V_π.

Keywords: Optoelectronic devices, modulators, guided-wave optics

Introduction

In electro-optic (EO) phase and intensity modulations there are two main limiting factors for the bandwidth (BW): phase-velocity mismatch between the optical waves and microwaves and frequency-dependent microwave loss [1]. The former is due to dispersion, i.e. different effective refractive indices (Δn_{eff}) at optical and microwave frequencies, and produces an increasing phase-shift between the optical wave and microwave along the modulator length, which eventually leads to a reversal of the sign of the EO interaction. This phase-shift, which increases with the microwave frequency, would limit the effective interaction length (i.e. the modulation efficiency): the higher the microwave frequency the lower the modulation efficiency, which is equivalent to say that the longer the modulator the lower the bandwidth. To overcome this limitation, phase velocity matching (i.e. $\Delta n_{eff} = 0$) can be achieved by an appropriate design of the transverse modulator geometry, for example through the use of buffer layers and thick electrodes. However even in the case of phase velocity matching (PVM) the BW would be limited by the frequency dependent microwave loss, which increases with microwave frequency, thus the higher the microwave frequency the lower the effective interaction length. On the other hand the driving voltage V_π, i.e. the voltage that produces a π phase shift of the optical wave, decreases for increasing modulator length, thus a trade-off exists between large BW and low V_π. Therefore one can assume the ratio BW/V_π as figure of merit for an EO phase or intensity modulator.

In this paper we present a simple method that allows to overcome the limitation due to frequency dependent microwave loss of conventional PVM modulators, which can lead to a significant improvement of the BW/V_π ratio.

Summary

The idea at the basis of our work is to provide a two-section modulator, such that the phase modulation of the optical wave in the second section, located near the end of the device, has opposite sign to that of the first section. Since the phase-shift is proportional to the product of the electro-optic coefficient (r) and the applied electric field (E_{app}), one could change the sign of either r or E_{app} in order to change the sign of the phase modulation contribution. The sign of r is related to tensorial properties and can be usually changed by reversing the crystal orientation (e.g. in $LiNbO_3$ through domain inversion [2]) or poling orientation (e.g. in poled polymers and poled glass). The sign of E_{app} can instead be changed by an appropriate electrode design, e.g. interdigitated electrodes.

It is worth noting that while interdigitated electrodes [3] and domain inversion [4] have already been proposed with the aim of compensating for the phase-velocity mismatch between

optical and micro waves, in our application these techniques are instead used in structures which are already PVM (or at least nearly PVM).

From now on we will refer to a $LiNbO_3$ based Mach Zehnder modulator which is domain inverted to change the sign of *r* along the direction of propagation of the optical and microwave signals (see fig.1). However it is clear that the idea can be applied to other materials, e.g. poled polymers or glasses, as well as to other modulator designs, e.g. interdigitated electrodes.

Due to the frequency dependence of the microwave loss, at high frequency the electric field becomes rapidly attenuated, so that only the first section is significant in inducing the optical phase shift. On the other hand, at low frequency the microwave attenuation is lower and almost the whole modulator length is effective in inducing the phase shift. The result of the discontinuity in *r* (in combination with phase velocity matching) is that the device operates in three successive zones along the modulator length: in the upstream zone, desirable phase modulation of the optical wave is induced for all frequencies in the bandwidth of the device; in the middle zone, desirable phase modulation is induced for frequencies in the upper part of the bandwidth, but phase modulation in the lower frequencies becomes excessive; while in the downstream zone, there is no significant phase modulation at higher frequencies but the excess modulation at lower frequencies is reduced by the fact that phase modulation has opposite sign with respect to the upstream and middle zones.

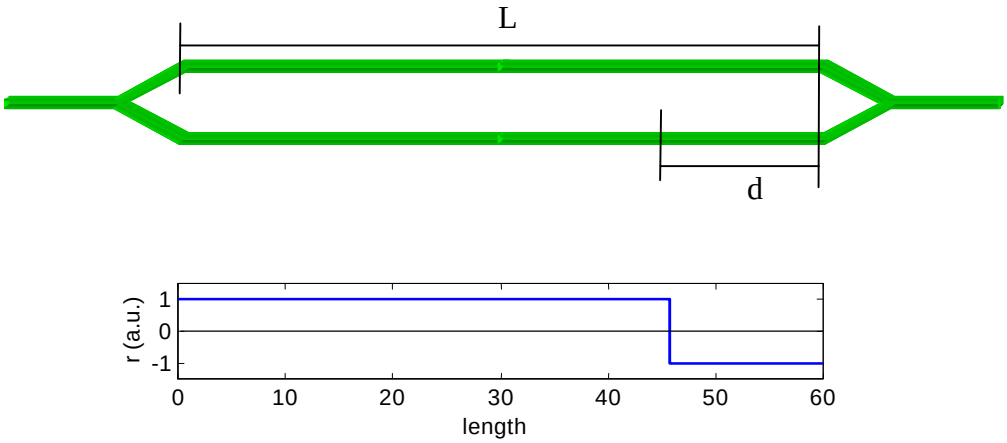


Fig. 1 Mach-Zehnder intensity modulator with double-domain inverted structure. L is the modulator length and *d* the last section with opposite domain orientation.

In the ideal case in which phase-velocity matching is exact throughout the device, the optimum distance from the downstream end of the device to the discontinuity (*d*) can be determined by solving the equation

$$\sqrt{2}/2 \cdot (L-2d) = 1/\alpha \cdot (1 - 2e^{-\alpha (L-d)} - e^{-\alpha L})$$

where L is the total optical length of the device and α is the microwave loss at the upper limit of the intended microwave bandwidth of the device (at which the optical output is 3dB below its maximum).

The EO response is in this way flattened even with large modulator lengths *L* . This allows to combine low values for V_π (basically stemming from large length *L*) with large bandwidth (arising from flattened response). Figs. 2 and 3 show a comparison between conventional (single domain) modulators and our proposal (double domain structure). For this comparison we have

assumed the same transversal modulator structure. This is justified by the fact that domain inversion does not change the linear properties of the material, so that the optimization of transversal structure for conventional (single domain) and our modulators (double-domain) is basically identical. In fig. 2, the green (dotted) and red (dotted-dashed) lines show the EO response of conventional modulators with lengths L = 25.6 mm and L = 32 mm respectively, and corresponding V_π = 5.3 V and V_π = 4.3 V . The blue (continuous) line shows the EO response of a modulator with our design: with a modulator length of 60 mm we reach the same bandwidth as the conventional modulator with the larger V_π obtaining on the other hand a lower V_π. Fig. 3 shows V_π as a function of the modulation frequency. It can be clearly seen that with our design we ensure a bandwidth of 30 GHz with a V_π of 4.35 V, while, on the one hand, a conventional modulator with the same bandwidth would require V_π = 5.3 V and a conventional modulator with the same V_π as ours achieves a bandwidth of only 20 GHz.

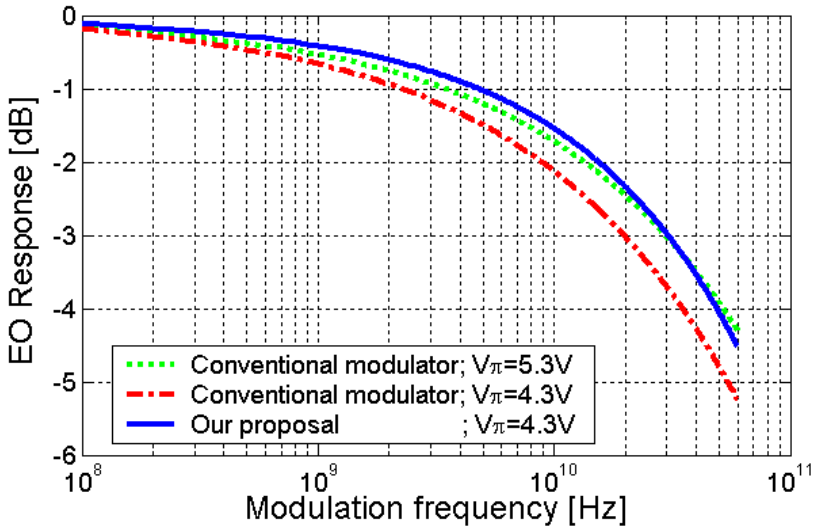


Fig. 2 Comparison between our proposal and conventional modulators in terms of EO response

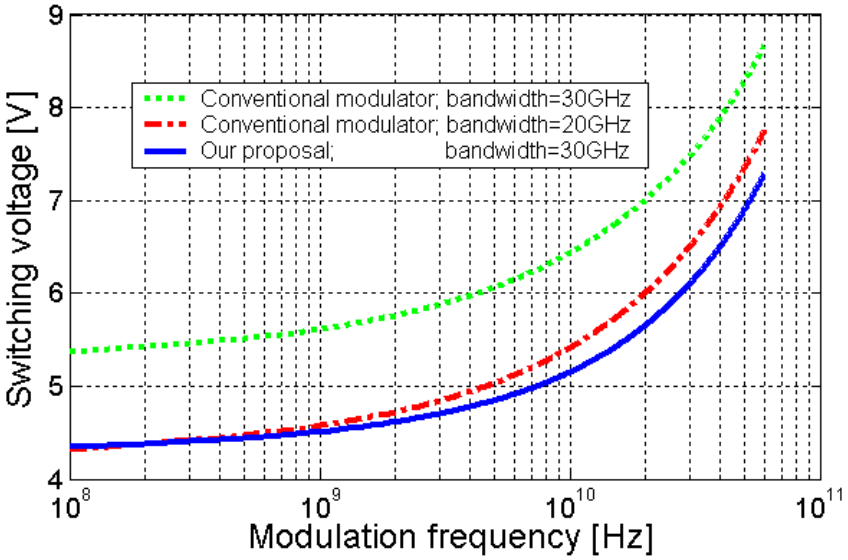


Fig. 3 Comparison between our proposal and conventional modulators in terms of V_p

Conclusions

We have presented a novel and simple method to increase the bandwidth to driving voltage ratio in phase-matched electro-otpic modulators. With respect to conventional modulators an improvement of up to 50% is expected and this could be crucial in applications, eg. at high bit rates (modulation frequencies) a decrease of driving voltage could be welcome to use cheaper electronic drivers. Experiments are underway to realise the proposed double domain inverted structure in a $LiNbO_3$ intensity modulator. However the concept can be applied to other materials (where the electro-optic coefficient can be modulated, e.g. semiconductors, poled polymers and glasses) and achieved by other means (e.g. intedigitated electrodes in a uniformly poled material).

References

[1] E.L. Wooten, K.M. Kissa, A. Yi-Yan, E.J. Murphy, D.A. Lafou, P.F. Hallmeier, D. Maack, D.V. Attanasio, D.J. Fritz, G.J. McBrien, and D.E. Bossi, "A review of lithium niobate modulators for fiber-optic communications systems", IEEE J. of Quantum Electronics, vol.6, p. 69 (2000).

[2] J. Webjörn, V. Pruneri, P.St.J. Russell, J.R.M. Barr and D.C. Hanna, "Quasi-phase-matched blue light generation in bulk lithium niobate, electrically poled via periodic liquid electrodes", Electronics Lett., vol. 30, p. 894 (1994).

[3] J.H. Schaffner and R.R. Hayes, "Velocity-matching in millimiter wave integrated optic modulators with periodic electrodes", J. of Lightwave Tech., vol. 12, p. 503 (1994).

[4] Y. Lu, M. Xiao, G. J. Salamo, "Wide-bandwidth high-frequency electro-optic modulator based on periodically-poled $LiNbO_3$ ", Appl. Phys. Lett., vol.78, p. 1035 (2001).

Laser oscillation in proton implanted Nd:YAG waveguides

M. Domenech[*a], E. Cantelar[a],G.V. Vázquez[b] and G. Lifante[a]
[a]Depto. Física de Materiales, C-IV. Universidad Autónoma de Madrid
28049 – Madrid (SPAIN)
[b]Centro de Investigaciones en Óptica, Loma del Bosque 115, Lomas del Campestre, Apartado Postal 1-948, 37000 León, GTO., (MÉXICO)
[*]e-mail address: manuela.domenech@uam.es

This work reports continuous laser oscillation at λ=1064.4 nm at room temperature in Nd:YAG waveguides fabricated by proton implantation technique. The resulting index profiles after the multi-implant, the spectroscopic characteristics of the Nd^{3+} ions in the waveguide, as well as the laser characteristics of the proton implanted Nd:YAG waveguide laser are reported.

Keywords: laser, waveguide, rare earths, ion implantation.

Introduction

Nd doped YAG is one of the most attractive dielectric materials for solid state lasers. The efficiency of laser operation is enhanced by using waveguide geometries, because the optical modes propagate well confined in the waveguide structure, avoiding thus diffraction effects. Several techniques have been proposed to fabricate optical waveguides in Nd:YAG, including epitaxially grown Nd:YAG layers on pure YAG substrates [1], or helium implantation on Nd doped YAG crystals [2], allowing high slope efficiency and low threshold laser operation at 1.06 μm. In fact, Nd:YAG was the first material that demonstrated the suitability of the ion implantation technique to fabricate waveguide lasers [3].

The ion implantation process produces at the end of the ion track an amorphization of the crystal, giving rise to a decrease of the refractive index in many dielectric materials [4]. This low-density region generates an optical barrier that confines the radiation, producing an optical waveguide. One of the problems faced when He^+ is used to produce optical waveguides is the short range of the implanted ions. Typically, a 2.8 MeV ion energy produces an optical barrier situated at around 6 μm beneath the surface. As higher energies is difficult to achieve in practice, a different approach becomes necessary. An alternative to fabricate wider waveguides using ion implantation technique is to use proton instead of He^+ ions, as for a given energy the ion range is much deeper in the case of lighter ions [5].

In this work the characterization of a Nd:YAG waveguide laser operating at 1.06 μm fabricated by proton implantation is reported. The characterization includes the waveguide index profile induced by the ion implantation, the main spectroscopic features of the Neodymium ions inside the waveguide, as well as the laser characteristics such as slope efficiency and threshold obtained using a Ti:Sapphire as the pump source.

Experimental Procedure

A planar waveguide was fabricated at room temperature on Nd:YAG by the technique of ion implantation using protons of energy around 1 MeV. In order to produce a broad barrier to avoid tunneling losses, a multi-implant was performed in the Nd:YAG substrate. Four different implants, with energies of 1.0, 1.05, 1.1 and 1.25 MeV, were performed on a single substrate, with a total dose of $6x10^{16}$ ions/cm^2.

To obtain the waveguide refractive index profile, the propagation constants of the modes were measured by the standard m-line method, using a rutile prism to couple the light into the waveguide coming from a polarized He-Ne laser (λ=633nm).

A CW Ti:sapphire laser, with a tuning range between 750-850 nm, was used as the excitation source. The pump beam was coupled into the waveguide with a x10 microscope objective by the end-fire coupling technique. The output light was collected through a x20 microscope objective and directed to the entrance slit of a monochromator (ARC SpectraPro 500-i) being detected by using an InGaAs photodiode.

A laser cavity was formed by butting mirrors to the polished end-faces of the waveguide. A >99.9 % reflectivity mirror at 1064 nm and transmission of 98% at 816 nm was placed in the front face, while on the other face a 97% at 1064 nm and >99.8% at 816 nm reflecting mirror was used. The pump power as well as the laser output power from the waveguide were measured by a silicon detector (Newport Model 1815-C and Spectra Physics Model 407A power meters).

Results and discussion

Figure 1 shows the calculated refractive index profile of the resulting waveguide after the multi-implant, using the experimental dark mode set measured at 633 nm. The profile exhibits an optical barrier height of approximately 0.98 % (decrease in refractive index relative to the substrate) located at a depth of 9.5 μm induced by the ion implantation process. Note that the profile in the figure is plotted as an index decrease in order to emphasize the concept of "optical well" and "optical barrier". It is also important to remark that the effective index in the surface region is slightly higher than that of the substrate by a 0.03%.

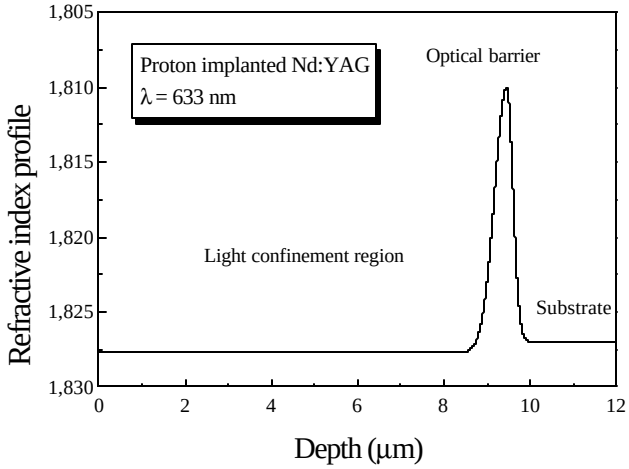


Figure 1: Refractive index profile corresponding to a proton implanted waveguide, measured at λ = 633 nm.

Before the laser experiments, the main spectroscopic characteristics of the Nd^{3+} ions in the waveguide were studied, using a Ti:sapphire as excitation source. After excitation to the $^2H_{9/2}$:$^4F_{3/5}$ manifold (λ= 816 nm) the neodymium ions relax non-radiatively to the $^4F_{3/2}$ level. From this level the relaxation is mainly radiative to the lower levels, giving rise to the apparition of three near-infrared emission bands at around 940, 1064 and 1340 nm corresponding to $^4F_{3/2} \rightarrow {}^4I_{9/2}$, $^4F_{3/2} \rightarrow {}^4I_{11/2}$, $^4F_{3/2} \rightarrow {}^4I_{15/2}$ transitions, respectively. The spontaneous spectrum associated to the radiative relaxation from the $^4F_{3/2}$ level, measured in the waveguide, which exhibits the highest emission

cross section, is presented in figure 2. The luminescence from the waveguide shown in this figure is coincident with that previously reported from bulk in Nd:YAG [5] having the same structure. Also, the lifetime measured in waveguide configuration is coincident to that measured in bulk crystal, around 240 μs.

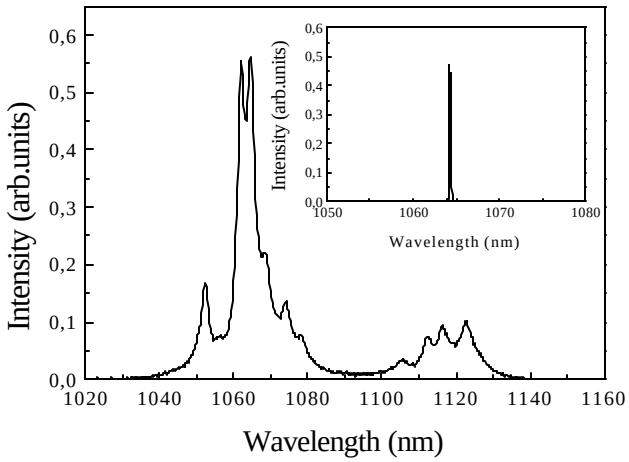


Figure 2: Spontaneous emission of the Nd3+ ions in waveguide configuration after pumping at 816 nm. The inset shows the laser output spectrum using 120 mW pump power.

It is well known that when neodymium is coupled to a resonant cavity it can operated as a four level scheme leading to laser action [6]. By fabricating a laser cavity with two mirrors attached directly to the proton implanted Nd:YAG waveguide, an intense infrared beam is observed. If stimulated emission occurs, the $^4F_{3/2} \rightarrow {}^4I_{11/2}$ transition dominates over all other de-excitation processes. The inset of figure 2 shows the recorded spectrum of the laser emission after pumping at 816 nm, where a narrow band centered at 1064.4 nm with a full width at half maximum (FWHM) of 3 nm, is observed. This laser emission corresponds in fact to the maximum gain transition of the Nd^{3+} ions in YAG crystals.

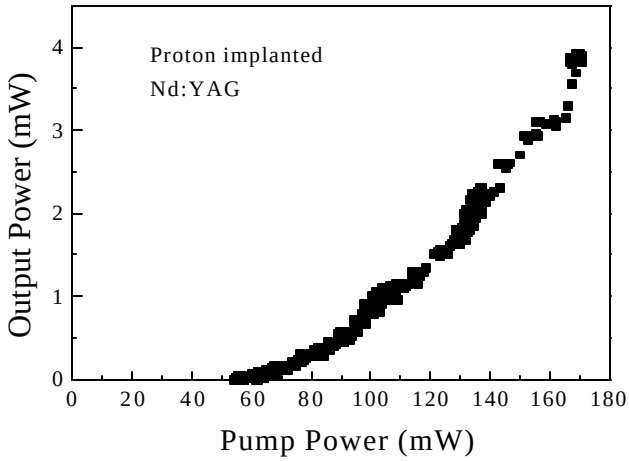


Figure 3: Output characteristics of the proton implanted waveguide Nd:YAG laser, showing a threshold of around 54 mW pumping at 816 nm.

The output characteristics of the proton implanted Nd:YAG waveguide operating in CW mode are given in figure 3, where the laser output power versus the pump power is presented. The pump power needed to reach laser oscillation gives a threshold of P_{th}= 54 mW, being the slope efficiency (the ratio of the output power to pump power above threshold) around 5%. The laser output showed a very high stability, even under continuous wave pump operation at room temperature, which clearly confirms the excellent mechanical, thermal and optical properties of the YAG matrix, besides the suitability of the ion implantation to construct miniaturized integrated devices.

Acknowledgements

Work partially supported by Ministerio de Ciencia y Tecnología (Spain) under project TIC2002-00147.

References

[1] I. Chartier, B. Ferrand, D. Pelenc, S.J. Field, D.C. Hanna, A.C. Large, D.P. Shepherd and A.C. Tropper, Optics Letters **11**, 810-812 (1992)
[2] S.J. Field, D.C. Hanna, D.P. Shepherd, A.C. Tropper, P.J. Chandler, P.D. Townsend and L. Zhang, IEEE J. of Quantum Electronics **27**, 428-432 (1991)
[3] P.J. Chandler, S.J. Field, D.C. Hanna, D.P. Shepherd, P.D. Townsend, A.C. Tropper and L. Zhang, Electron. Lett. **25**, 985-986 (1989)
[4] P.D. Townsend, Nuclear Instruments and Methods in Physics Research **B65**, 243-250 (1992)
[5] G. V. Vázquez, J. Rickards, H. Márquez, G. Lifante, E. Cantelar and M. Domenech, Optical Materials (submitted for publication)
[6] R.E. Di Paolo, E. Cantelar, P.L. Pernas, G. Lifante and F. Cussó, Applied Physics Letters **79**, 4088-4090 (2001)

CW, Broadly Tunable, Red, Green and Blue Light Generation in Aperiodically Poled Zn-Diffused $LiNbO_3:Er^{3+}/Yb^{3+}$ Channel Waveguides

E. Cantelar[(1)*], G. A. Torchia[(1)], J.A. Sanz-García[(1)], P.L. Pernas[(2)], F. Jaque[(1)], G. Lifante[(1)] and F. Cussó[(1)]

[(1)]Departamento de Física de Materiales, C-IV. Universidad Autónoma de Madrid
28049–Madrid (Spain)

[(2)] Departamento de Física Aplicada, C-XII. Universidad Autónoma de Madrid
28049–Madrid (Spain)

[*] e-mail address: eugenio.cantelar@uam.es

In this work, the CW broadly tunable simultaneous generation of the primary colors, red, green and blue in aperiodically poled Zn-diffused $LiNbO_3:Er^{3+}/Yb^{3+}$ channel waveguides is presented. The red and green emissions arise from energy transfer and up-conversion mechanisms between Yb^{3+} and Er^{3+} ions, while the blue light is produced by quasi-phase matching processes.

Keywords: second harmonic generation, non-linear waveguides, Zn-diffusion, up-conversion, rare earth, lithium niobate

Introduction

The modulation, periodic or aperiodic, of the non-linear coefficients offer the possibility of obtaining non-linear frequency conversion via quasi-phase matching (QPM) [1,2]. The large effective non-linear coefficient of lithium niobate ($LiNbO_3$) compares favourably with that of other ferroelectric crystals [1,3].

Several non-linear devices based on $LiNbO_3$, in which the periodic modulation is combined with the high power densities available in waveguiding structures have been reported [4]. Zn-diffusion from the vapor phase [5], represents an alternative waveguide fabrication technique to produce low-loss optical waveguides in $LiNbO_3$ in which the initial ferroelectric domain patterns of the substrate are preserved [6]. It has been also reported that the waveguides prepared by this technique exhibit a high optical damage resistance [7] highly useful to sustain stable operation, in continuous wave regime, in RGB integrated devices.

In this work, APPLN crystals have been grown adding erbium and ytterbium oxides to the initial melts by using the appropriate growth conditions [8]. A *y*-cut wafer has been used to fabricate Zn-diffused APPLN channel waveguides in which second harmonic generation in the blue spectral range has been explored. A high stability in the generation of blue light has been found, even under continuous wave operation at room temperature. Red and Green emissions can be also achieved using up-conversion processes between Er^{3+} and Yb^{3+} ions leading finally to CW simultaneous generation of Red, Green and Blue light.

Experimental Procedure, Results and Discussion

APPLN crystals were grown by the off-centered Czochralski method, along the *a*-axis, with automatic diameter control by crucible weighing system. The initial melts containing the congruent $LiNbO_3$ ([Li]/[Nb] = 0.945), were doped with erbium (0.5 mol %) and ytterbium (0.5 mol %) oxides with a purity grade of 99.99%. The growth conditions, pulling and rotation rates and seed crystal shift, were adjusted appropriately to favor the formation of modulated ferroelectric domain distributions [9].

A *y*-cut wafer from the APPLN crystals, in which the ferroelectric domain distribution was previously characterized, has been used to fabricate the channel waveguides by the Zn-diffusion

technique following a two-step process (exchange and diffusion) [5,10]. It was shown that this waveguide fabrication process does not alter the domain distribution in the crystal [6], being compatible with rare earth doped congruent lithium niobate [7,11].

When the light from a Ti:Sapphire laser (operating at 920 nm) was coupled into the channels by using the end-fire coupling technique a strong green emission is observed. However when the output is spatially separated by using a dispersive prism, four intense spots can be seen even by the naked eye, Figure 1. From right to left, blue, green, and red colors are clearly distinguished, besides an additional spot coming from the IR pump beam, which appears as "white" due to saturation effect of the imaging device.

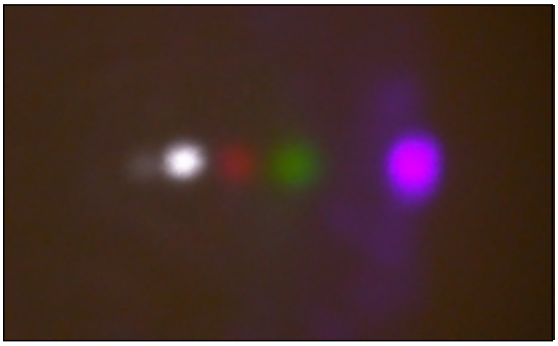


Figure 1.- Photograph of the output waveguide focused on a screen, after passing a dispersive prism, showing the three fundamental colors, besides the spot coming from the infrared pump at 920 nm.

In order to investigate the origin of the three fundamental colors produced in the channel waveguide by infrared pumping, the waveguide output was focused on the entrance slit of a monochromator, and the dispersed light was detected by using a photomultiplier tube. Figure 2(a) shows the emission spectrum from the waveguide in the visible range (450-700 nm). As it can be appreciated, the output light is the combination of two broad emissions bands in the red and in the green, and a narrow line in the blue.

The blue emission (right spot on Figure 1) is due to SHG in the non-linear channel waveguide. The experimental configuration used in the measurements, crystal axis and polarization of the incident and output beams, has been sketched in Figure 2(b). As it is indicated, only when the fundamental wave is coupled as extraordinary wave (TE propagating mode) an output narrow blue emission is detected. The blue light exhibits the same polarization as the incident ω-wave as well as the expected quadratic dependence for a second order process indicating that the frequency conversion process involves the d_{33} non-linear coefficient of $LiNbO_3$. The aperiodic ferroelectric domain distribution of the substrate provides a big set of reciprocal vectors for quasi-phase matching compensation (QPM) between the ω-wave and the 2ω-wave [11]. As a consequence, the SH signal exhibits a broadly tunable band at the expense of peak efficiency [12]. In Figure 2(b), the blue light obtained for a discrete set of fundamental wavelengths in the channel waveguide under study (4 μm width and 1 cm length) is presented. As it can be appreciated, the maximum efficiency in the frequency conversion is obtained for fundamental wavelengths around 970 nm (2ω-wave at around 485 nm).

The red and green emission bands, presented in Figure 2(a), are mainly due to the presence of energy transfer up-conversion mechanisms (ETU) involving the Er^{3+} and Yb^{3+} ions [12]. As it has been recently reported [13], the sensitization of $LiNbO_3$:Er^{3+} with Yb^{3+} ions opens an extra path for the population of the $^4F_{9/2}$ erbium level being the red emission enhanced, relative to the green one, nearly in an order of magnitude. The inset in Figure 2(a) shows the ratio between the red and green intensities measured in co-doped samples with fixed Er^{3+} concentration (0.5 mol %) and variable

Yb^{3+} concentration. As the green and red emissions are induced by ETU processes from Yb^{3+} ions, the broad and intense absorption bands of these ions (880-1040 nm) can be used to tune efficiently both erbium emissions ($^2H_{11/2}$:$^4S_{3/2} \rightarrow {}^4I_{15/2}$ and $^4F_{9/2} \rightarrow {}^4I_{15/2}$ transitions). The dependencies on pump power of both emissions, green and red, were found to be lower than the expected quadratic law. This fact could be related with the presence of saturation effects or due to the presence of the several population paths: the energy transfer processes from Yb^{3+} ions and the direct absorption of the blue light within the Er^{3+} ions ($^4I_{15/2} \rightarrow {}^4F_{5/2,\,3/2}$ absorption band).

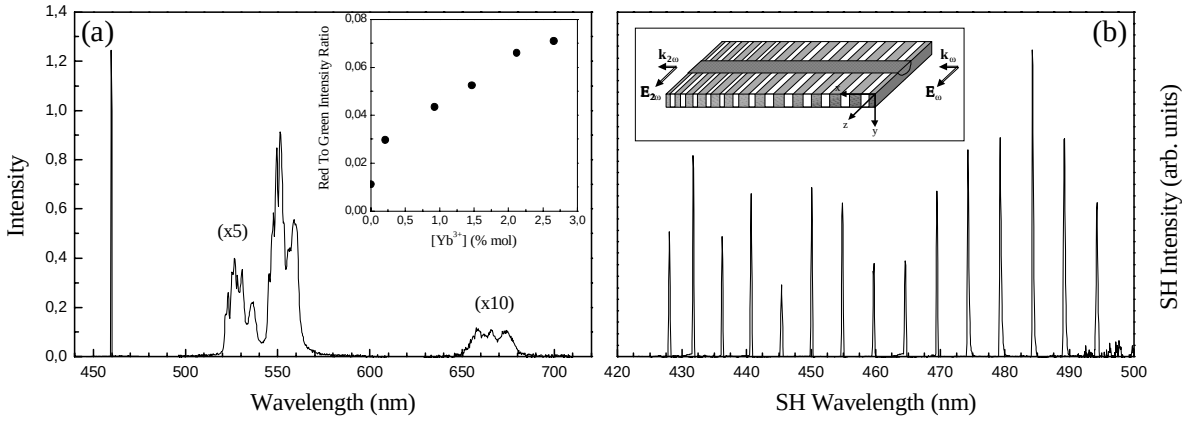


Figure 2.- (a) Emission spectrum measured in the channel waveguide after pumping at 920 nm. The inset shows the ration between the red and green intensities measured in the co-doped samples. (b) Blue SHG for a discrete set of fundamental wavelengths between 850 nm and 990 nm. The inset shows the experimental configuration used in the measurements.

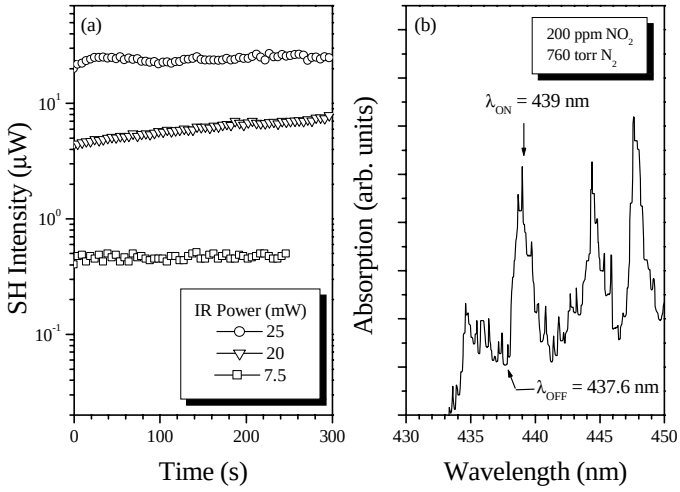


Figure 3.- (a) Evolution of the blue second harmonic, at 485 nm, measured in the Zn-diffused APPLN channel waveguide as function of time and pump power. (b) Absorption spectrum of NO_2 gas in N_2 atmosphere at a pressure of 760 torr.

It should be remarked that the channel waveguide sustains stable operation without intensity fluctuations induced by the presence of high power beams. Figure 3(a) shows the SH signal, measured at the maximum efficient peak (485 nm), as function of time for different pump powers.

The highest blue intensity propagated in the channel waveguide was found to be 20 μW corresponding to the maximum infrared pump power coupled into the waveguide, 25 mW. As it can be appreciated in the figure, the optical damage threshold is highly enough to sustain the stable SHG in the blue spectral range, even under CW conditions at room temperature.

The characteristics reported in this work, tuning range and temporal stability, are interesting features for the development of useful integrated optical sensors. In particular, the presence of some toxic gases can be detected by applying conventional absorption techniques. Such is the case of NO_2 whose absorption band, shown in figure 3(b), overlaps completely with the tuning range of figure 2(b). The concentration can be estimated by comparing the attenuation of the SH intensity by measuring at two different wavelength in the absorption spectrum, λ_{ON} and λ_{OFF} at 439 nm and 437.6 nm respectively (Differential Optical Absorption Spectroscopy [14]).

Conclusions

APPLN crystals have been grown by the off-centered Czochralski method by adding erbium and ytterbium oxides to the melt. The simultaneous, CW, RGB generation in Zn-diffused Er^{3+}/Yb^{3+} co-doped APPLN channel waveguides have been obtained. The red and green colors are produced by up-conversion processes between the Er^{3+} and Yb^{3+}ions while the blue one is generated by SHG involving the d_{33} non-linear coefficient of $LiNbO_3$. The optical damage threshold of the Zn-diffused APPLN channel waveguides was found to be highly enough to sustain the stable visible light generation, even in the continuous wave regime at room temperature.

Acknowledgements

Work partially supported by Ministerio de Ciencia y Tecnología under projects TIC2001-0226, TIC2002-00147 and HI2000-0041. G.A. Torchia is supported by a grant from Ministerio de Educación, Cultura y Deporte.

References

[1] M.M. Fejer, G.A. Magel, D.H. Jundt and R.L. Byer, IEEE J. Quantum Electron., **28**, 2631, 1992.
[2] M. Houé and P.D. Townsend, J. Phys. D, **28**, 1747, 1995.
[3] V. Pruneri, S. Butterworth and D.C. Hanna, Appl. Phys. Lett., **69**, 1029, 1996.
[4] D. Hofmann, G. Schreiber, C. Haase, H. Hermann, R. Ricken and W. Sohler, Proc. 9th Eur. Conf. Integr. Opt. (ECIO'99), Torino, Italy, 505, 1999.
[5] R. Nevado and G. Lifante, Appl. Phys. A, **72**, 725, 2001.
[6] R. Nevado, E. Cantelar, G. Lifante and F. Cussó, Jpn. J. Appl. Phys., **39**, L488, 2000.
[7] R.E. Di Paolo, E. Cantelar, R. Nevado, J.A. Sanz-García, M. Domenech, P.L. Pernas, G. Lifante and F. Cussó, Ferroelectrics, **273**, 229, 2002.
[8] J. Wallace, Laser Focus World, **35**, 15,1999.
[9] E.P. Kokanyan, V.G. Babajanyan and G.G. Demirkhanyan, J. Appl. Phys., **92**, 1544, 2002.
[10] P.L. Pernas, M.J. Hernández, E. Ruíz, E. Cantelar, R. Nevado, C. Morant, G. Lifante and F. Cussó, Appl. Surf. Sci., **161**,123, 2000.
[11] E. Cantelar, R. Nevado, G. Martín, J.A. Sanz-García, G. Lifante, F. Cussó, M.J. Hernández and P.L. Pernas, J. Lumin., **87-89**, 1096, 2000.
[12] E. Cantelar, J.A. Muñoz, J.A. Sanz-García and F. Cussó, J. Phys. : Condens. Matter **10**, 8893, 1998.
[13] E. Cantelar and F. Cussó, J. Lumin. (in press).
[14] F. Molero and F. Jaque, Opt. Mat. **13**, 167, 1999.

Modeling of holographic gratings in photorefractive graded-index planar waveguides

Vittorio M. N. Passaro, Daniele Marseglia
Optoelectronics Laboratory, Dipartimento di Elettrotecnica ed Elettronica
Politecnico di Bari, Via Edoardo Orabona 4 – 70125 Bari, Italy
passaro@poliba.it, maddanny@libero.it

In this paper an accurate modeling of both collinear and non collinear wave interaction in the formation of holographic gratings in photorefractive graded-index planar waveguides is presented. Results for lithium niobate waveguide technologies are given.

Keywords: holographic gratings, lithium niobate waveguides, photorefractive effect, modeling.

Introduction

Nowadays, a significant research interest is devoted to the holographic grating formation in photorefractive waveguides, whose deep knowledge should lead to design new types of integrated optical devices. In fact, light beams in optical planar waveguides are confined in one dimension to regions only a few micrometers in width and so the high optical intensities, which are thus readily obtained, make it relatively easy to observe effects of photorefractivity to be used in integrated photorefractivity-based devices [1]. In recent literature it is possible to find a lot of examples, such as linear filters providing for high-resolution spectral filtering [2], beam splitters and couplers [3] or dynamic interconnections for neural networks [4]. With the aim to design such devices with high accuracy, we have developed a numerical model of the holographic grating formation in graded-index planar waveguides, which is not yet available in literature.

Theoretical model

The model can analyze the holographic grating formation in arbitrary graded-index waveguides having a generic electro-optic crystal (r_{ij} tensor), both in case of collinear and non collinear, intermode and intramode wave interaction. This paper is based on the extension of the model presented in [5]. Fig. 1 shows the vector diagram of the non collinear interaction geometry, where ρ is the propagation direction, τ is the transverse direction, $\overline{K}_A$ and $\overline{K}_B$ are the incidence vectors of the interacting fields A and B, respectively, $\overline{K}_g$ is the induced grating vector and ϑ_C is the crossing angle. Furthermore, an arbitrary overlay can be also taken into account.

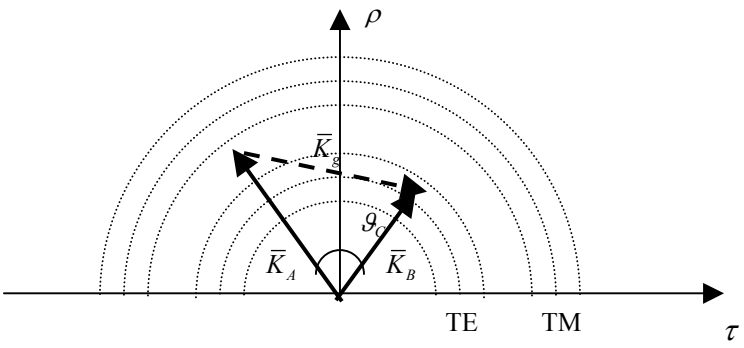


Fig. 1. Vector diagram for a non collinear interaction between two generic modes, A and B.

It is well known that the perturbations of the dielectric permittivity tensor ε_{ij}, caused by the photorefractive effect, are physically related to the photo-induced potential distribution, φ.
For a generic mode interaction (i.e. either intermode or intramode), we have derived from the continuity equation (see [6]) the equation of induced oscillations, considering only the photogalvanic current (neglecting the diffusion current) and admitting that the its spatially oscillating components depend only on the cut-axis (hereinafter named cut). In the absence of any applied electric field and assuming the cut-axis and the direction of propagation both coincident with the crystallographic axes, the equation of induced oscillations can be written in the very general formulation as follows:

$$\frac{d^2\varphi}{dcut^2} - K_g^2 \frac{\varepsilon_\rho^S}{\varepsilon_{cut}^S}\varphi = f(t)\frac{t_0}{\varepsilon_{cut}^S}\left(-jK_g\delta_\rho^{ph} + \frac{\partial\delta_{cut}^{ph}}{\partial cut}\right) \tag{1}$$

where K_g is the grating vector amplitude [7], i.e. $K_g = \left|\overline{K}_g\right|$, ε_{cut}^S and ε_ρ^S are the static (i.e. without any interaction) dielectric tensor components along the *cut*-axis and ρ-axis, respectively, and δ_{cut}^{ph} and δ_ρ^{ph} are the photogalvanic current components along the *cut*-axis and ρ-axis, respectively. The physical meaning of the characteristic time t_0 and function $f(t)$ can be better understood by discussing about φ. In fact, the photo-induced potential φ can be explicated as follows:

$$\varphi = \varphi(cut,\rho,t) = \varphi_0(cut,t_0)f(t)\exp(-j\left\langle\overline{K}_g\right\rangle_\rho) \tag{2}$$

where the function $\varphi_0 = \varphi_0(cut,t)$ represents the photo-induced potential for the initial recording section, when the conductivity currents are negligible, and its dependence on time and spatial coordinates have been simultaneously considered. $\left\langle\overline{K}_g\right\rangle_\rho$ is the $\overline{K}_g$ projection along ρ-axis.

Furthermore, by neglecting the photo-conductivity respect to the dark conductivity σ^d, $f(t)$ is an increasing exponential function (having the Maxwell relaxation time τ_m as a time constant) and t_0 is equal to τ_m [6]. We remember that $\tau_m = \varepsilon_{cut}^S / \sigma_{cut}^d$, where σ_{cut}^d is the dark conductivity component along *cut*-axis.

The photogalvanic current is strictly related to the photogalvanic tensor β, which depends on the structure considered. For a graded-index waveguide β changes along the *cut* axis, $\beta = \beta(cut)$. However, it is possible to define an effective photogalvanic tensor $\tilde{\beta}$, which can be evaluated by a quasi-empirical model [6]. We can evaluate the photogalvanic current vector as follows:

$$\delta^{ph} = \beta E^A E^{B*}\exp(-j\left\langle\overline{K}_g\right\rangle_\rho) \tag{3}$$

where E^A and E^B are the electric field vectors of two generic guided modes A and B, respectively. In this way, our model is applicable to both an intermode and intramode interaction, without any restriction over the incidence angle. Therefore, by using Eqns. (1), (2) and (3), we can write the equation of induced oscillations as

$$\frac{d^2\varphi_0}{dcut^2} - K_g^2 \frac{\varepsilon_\rho^S}{\varepsilon_{cut}^S}\varphi_0 = \frac{t_0}{\varepsilon_{cut}^S}\left(-jK_g\left\langle\beta E^A E^B\right\rangle_\rho + \frac{\partial}{\partial cut}\left\langle\beta E^A E^B\right\rangle_{cut}\right) \tag{4}$$

The numerical solution of Eqn. (4) allows to evaluate the perturbations of the dielectric tensor components $\Delta\varepsilon_{ij}$ (as a multidimensional array), or otherwise, of the permeability tensor

components by the linear electro-optic effect, as in [5], by which each information about the holographic grating properties can be derived.

Numerical results

In the numerical results, we have assumed z-propagation for X-cut, and x-propagation for Y-cut and Z-cut. As a first example, we have considered a Ti:$LiNbO_3$ Gaussian index profile waveguide ($\Delta n_{e\max} \cong 0.0005$, $\Delta n_{o\max} \cong 0.001$), at room temperature (T = 300 K), wavelength λ = 632.8 nm, without any overlay. In Fig. 2, the largest value of dielectric tensor perturbation is shown as a function of the crossing angle ϑ_C. The other components are found to be at least one order of magnitude lower with respect to the largest one. Of course, the photorefractive sensitivity is strongly related to this main component. From Fig. 2 we can see the comparison among various substrate cuts and non collinear mode interactions, i.e. TE_0-TM_0 in Y-cut ($\Delta\varepsilon_{23}$), TM_0-TM_0 in Y-cut ($\Delta\varepsilon_{23}$), TE_0-TM_0 in Z-cut ($\Delta\varepsilon_{33}$) and TE_0-TE_0 in Z-cut ($\Delta\varepsilon_{33}$).

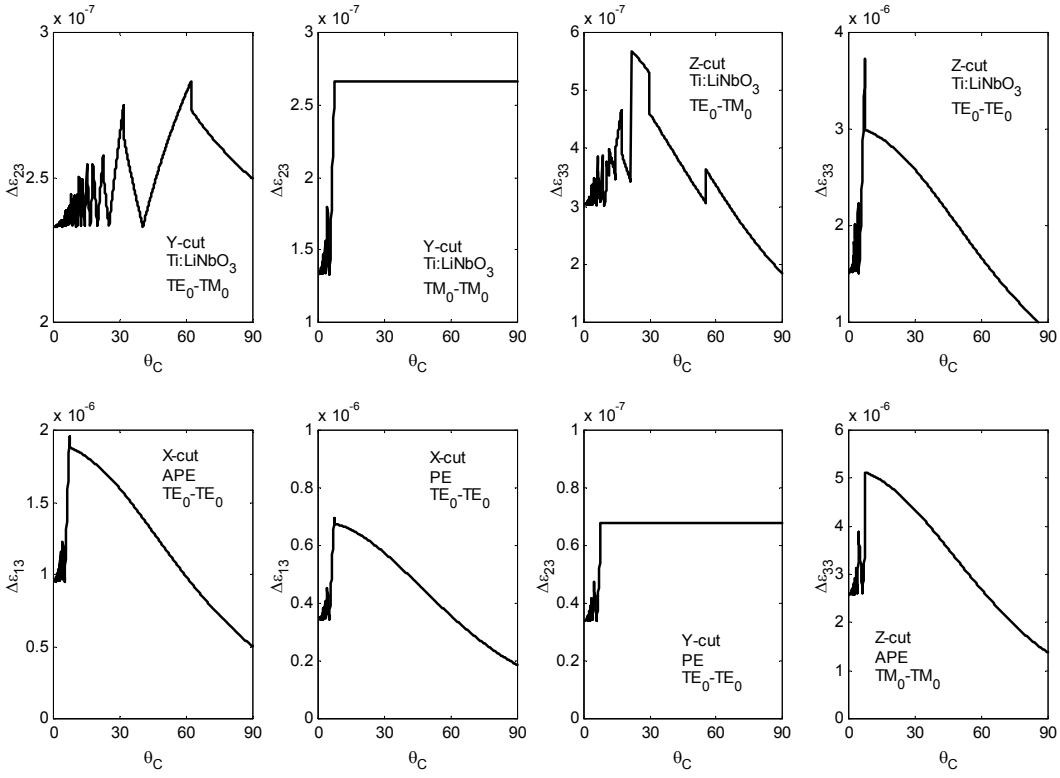


Fig. 2. Dielectric tensor main perturbation dependence on the crossing angle.

Similarly, at constant wavelength and temperature, we have considered a proton exchanged (PE) waveguide (step-index profile, $\Delta n_o = 0$ and $\Delta n_e = 0.01$, and strongly reduced electro-optic activity, r ≅ r/10 in the highly protonated layer) and an annealed PE (APE) waveguide (exponential profile; $\Delta n_{o\max} = 0.005$ and $\Delta n_{e\max} = 0$, and partially restored electro-optic activity, r ≅ r/2). In Fig. 2, the largest dielectric perturbations are sketched for the TE_0-TE_0 interaction in a X-cut $LiNbO_3$ waveguide, by assuming either an APE ($\Delta\varepsilon_{13}$) or a PE technology ($\Delta\varepsilon_{13}$), the TE_0-TE_0 interaction in an Y-cut PE:$LiNbO_3$ waveguide ($\Delta\varepsilon_{23}$), and TM_0-TM_0 interaction in an Z-cut APE:$LiNbO_3$ waveguide ($\Delta\varepsilon_{33}$). We can see from Fig. 2 that a similar angle can be recognized for all the

intramode interactions where the perturbation is maximum, about 7.5°, the value remaining constant only for Y-cut substrate. Moreover, we have carried out a number of simulations changing the fabrication technology and crystal cut, in case of collinear geometry. We have evaluated and compared the order of magnitude of all the induced dielectric tensor perturbations. Table I summarizes the results in a normalised form, where the components lower than 10^{-8} have been considered negligible (~ 0).

Table I. Comparison among different $LiNbO_3$ technologies (T = 300 K, λ = 632.8 nm).

Cut	*Technology*	*Interaction*	$\Delta\varepsilon_{11}$	$\Delta\varepsilon_{12}$	$\Delta\varepsilon_{13}$	$\Delta\varepsilon_{22}$	$\Delta\varepsilon_{23}$	$\Delta\varepsilon_{33}$
X	Ti-diffused	TE_0-TM_0	~ 0	10	100	~ 0	~ 0	~ 0
		TE_0-TE_0	~ 0	10	100	~ 0	~ 0	~ 0
		TM_0-TM_0	~ 0	10	100	~ 0	~ 0	~ 0
	APE	TE_0-TE_0	~ 0	10	100	~ 0	~ 0	~ 0
	PE	TE_0-TE_0	~ 0	1	10	~ 0	~ 0	~ 0
Y	Ti-diffused	TE_0-TM_0	1	~ 0	~ 0	1	10	~ 0
		TE_0-TE_0	1	~ 0	~ 0	1	10	~ 0
		TM_0-TM_0	1	~ 0	~ 0	1	10	~ 0
	APE	TE_0-TE_0	1	~ 0	~ 0	1	10	~ 0
	PE	TE_0-TE_0	~ 0	~ 0	~ 0	~ 0	1	~ 0
Z	Ti-diffused	TE_0-TM_0	1	~ 0	~ 0	1	~ 0	10
		TE_0-TE_0	10	~ 0	1	10	~ 0	100
		TM_0-TM_0	10	~ 0	1	10	~ 0	100
	APE	TM_0-TM_0	10	~ 0	1	10	~ 0	100
	PE	TM_0-TM_0	1	~ 0	~ 0	1	~ 0	10

From Table I, the best technological conditions for high efficiency guided-wave holographic devices can be easily found. Other calculations obtained by including an overlay (refractive index 1.5, 2 μm in depth) have shown similar results.

Conclusions

The numerical analysis of the dielectric tensor perturbations by photorefractive effect in graded-index planar waveguides has been presented. A powerful software tool has been developed to investigate any kind of guided mode interaction, i.e. collinear or not-collinear and either intermode or intramode interaction. Related results have been presented to select the best condition, i.e. the crossing angle, the crystal cut and the waveguide fabrication technology, in terms of the maximum sensitivity, to be used for design purposes.

[1] V. E. Wood, P. J. Cressman, R. L. Holman and C. M. Verber, *Photorefractive Materials and their Applications II* **62**, 45-100, Springer-Verlag, Berlin,1988.
[2] T. W. Mossberg, *Optics Letters* **26**, 414-416, 2001.
[3] K. Itoh, K. Ikewaza, W. Watanabe, Y. Furuya and Y. Masuda, *Opt. Express* **2**, 503-508, 1998.
[4] O. Matoba, K. Ikewaza, K. Itoh and Y. Ichioka, *Opt. Review* **2**, 438-443, 1995.
[5] V. M. N. Passaro and D. Marseglia, *Opt. Express* **10**, 1133-1138, 2002.
[6] G. Glazov et al., *J. Opt. Soc. Am. B* **7**, 2279-2288, 1990.

Characterization of Static and Photorefractive Scattering in Channel $LiNbO_3$ Waveguides Fabricated by Novel High Temperature Proton Exchange Technique

S.M. Kostritskii, Yu.N. Korkishko, V.A. Fedorov, A.N. Alkaev , V.S. Kritzak
Moscow Institute of Electronic Technology, Optolink Ltd, 103498, Zelenograd, Russia;
skostritskii@optolink.ru

P. Moretti, S. Tascu, and B. Jacquier
Laboratoire de Physico-Chimie des Materiaux Luminescents, Universite de Lyon 1, France

Insertion losses, mode profiles and photorefractive damage were measured in channel HTPE-$LiNbO_3$ waveguides. The guided modes scattering was mapped by scanning near-field optical microscopy. These measurements offer important information about loss mechanisms in our waveguides.

Keywords: Lithium niobate, waveguides, scanning near-field optical microscopy

Introduction

Optical channel waveguides in lithium niobate are a very useful technique for building a variety of integrated optical components. Proton exchange (PE) is now an established technique for fabricating integrated optical devices in $LiNbO_3$ and offers possibility of obtaining low-loss waveguiding material with a good electro-optical performance [1,2]. Annealing is an important step in the common fabrication sequence of PE waveguides. In fact, most of the published results have been obtained using heavily annealed PE (APE) waveguides**,** whose index profiles indicate that they are in the α-phase. However, it was recently reported [3,4], that APE process reduces the electro-optical coefficients and provides some marked level of propagation loss related mainly to the guided power leakage. The two primary sources of this leakage are the following: (1) static light scattering caused by residual distortion of a near-surface waveguide part, where several phase transitions occur during annealing [2]; and (2) time-dependent photorefractive damage [5]. To avoid these undesirable effects, we propose the new method of high temperature proton exchange (HTPE) [3], as there is no any phase transition when the α-phase waveguides are fabricated by HTPE and a concentration of photorefractive defects are smaller comparatively to the APE process.

In this paper, we report characterization of propagation loss sources related to guided modes scattering in the $LiNbO_3$ optical waveguides fabricated by HTPE technique.

Experimental

A series of straight channel guides, ranging from 3 to 7 μm in 0.2-μm steps were delineated in optical grade X-cut $LiNbO_3$ substrates, using standard photolithographic technique. The substrates were proton exchanged with the aid of the HTPE method at 370^0C for 3 – 6 hrs in stearic acid diluted by lithium stearate (0.7 - 0.85 wt.%). The mentioned above fabrication parameters were chosen by us in accordance with results obtained by X-ray diffraction, prism coupling modal spectroscopy and IR-reflection in test samples of a planar waveguide. This study of test samples gives possibility to determine roughly a range of fabrication parameters, where formation of a low-loss single mode channel waveguide, operating at a certain wavelength region, is expected. A target wavelength of our optimization procedure was 810 - 840 nm, as fabrication of an integrated optical phase modulator is developed. Final optimization of the fabrication parameters was made according to data of direct measurements of the modes shape and insertion losses in channel waveguides.

The modes shape was measured by coupling depolarized light from a superfluorescent diode (a center wavelength is 830 nm) into the waveguides with the aid of an isotropic single mode fiber. The output light of waveguides was imaged on CCD camera, operating in its linear region. To determine insertion losses and evaluate a propagation loss, we use a fiber-to-fiber coupling set-up.

Scanning near field optical microscopy (SNOM) has been also used to investigate the guided mode in the waveguides. In situ optical near field investigation of the waveguides has been performed by using a "Twin SNOM-OMICRON" system in collection mode. A three directional small micromechanical system has been added on the piezoelectric table of the microscope supporting the samples in order to end-fire couple light by mean of a PM optical fiber. Light from an He-Ne laser (632.8 nm) is endfire coupled into the waveguide by mean of a SM fiber while the evanescent field is probed at the waveguide surface through the small aperture of the optical fiber of the SNOM which position is controlled by shear force measurements. The guided mode intensity is therefore mapped with a sub-wavelength resolution (<100 nm).

Experimental results and discussion

The crucial influence of lithium stearate concentration on properties of channel waveguides has been established. In order to examine these properties, two techniques were employed. The first, a more qualitative analysis, involved tracking change in the region of single-mode operation range at 830 nm in terms of waveguide channel width. The range of waveguide widths supporting only extraordinary fundamental mode was recorded and monitored as function of both the lithium stearate concentration C_{LS} in ion-exchanging melt and proton-exchange time. Along these measurements, we studied the qualitative confinement of fundamental mode. According to this study, a smaller C_{LS} within used range provides better mode confinement in the waveguides of widths from 3.4 to 4.6 μm at appropriate choice of proton exchange time for each certain C_{LS} value. This width range corresponds to acceptable level of matching the fundamental modes of channel $LiNbO_3$ waveguide with both in-coupling and out-coupling fibers. Note, that the term "waveguide width" used here means the width of window (gap) in a Cr/SiO_2 mask used at proton exchange.

In order to quantify the waveguiding properties change, a second technique using fiber-to fiber coupling was employed. Here, the difference in light level between the input and output fibers was related to the corresponding insertion losses. It was established that a minimum of the insertion losses α_{min} for a given IOC is observed always in the mentioned above range of waveguide widths at some specific value of the proton exchange time. This specific time t_s and the minimum losses available α_{min} are dependent on C_{LS}. While dependence of t_s on C_{LS} is monotonous, i.e. a smaller C_{LS} is shorter t_s, α_{min} is smallest at intermediate values of C_{LS} from 0.75 to 0.78 wt % (Fig. 1).

As the use of C_{LS} values larger than 0.78 wt % decreases sharply a surface refractive index and, therefore, requires a relatively long exchange for $t_s \geq 4.5$ hrs, the observed growth of insertion losses can be related to the fact that the waveguides are becoming weakly confining and their mode size is more larger than the fiber mode. The insertion losses growth with C_{LS} decrease, within the C_{LS} range < 0.75 wt %, is more surprising, as waveguide mode confinement became better and no evident mismatch of fundamental mode with fiber mode was observed. However, a comparative study of channels with different lengths has shown a very high level of propagation loss (≥ 2 dB/cm) in waveguides fabricated with C_{LS} < 0.75 wt %.

The comparison of waveguides fabricated with different C_{LS} was performed by measurement of insertion losses at a fixed level of the low in-coupled powers (around 100 μW), as the pronounced time-dependent growth of insertion losses is observed with increase of in-coupled power, when it is larger than 200 μW. Such behavior is typical consequence of the photorefractive damage effect in channel $LiNbO_3$ waveguides [5].

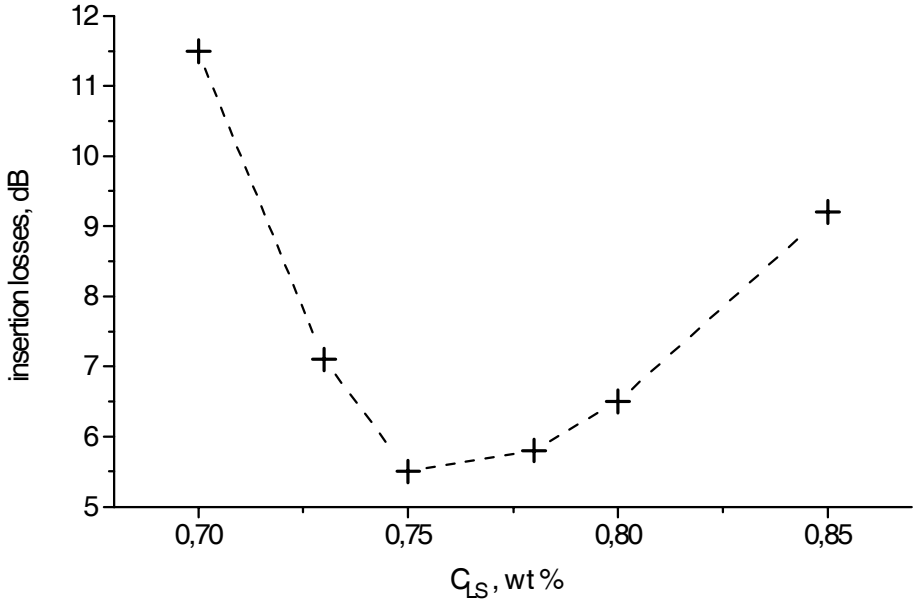


Fig. 1. Dependence of minimum insertion losses α_{min} on lithium stearate concentration C_{LS} in melt used for waveguides fabrication. These minimum values were found among the waveguides of different widths in the samples proton-exchanged for varied time at a given C_{LS}. Optimal values of the width and proton-exchange time t_s were changed with variation of C_{LS}.

The growth of propagation loss, when C_{LS} drops below 0.75 wt %, may be related to our IR-reflection data on appearance of phase-composition inhomogeneity,. For example, at very oblique incidence (incidence angle $\Theta = 70^0$) of IR radiation on waveguide surface, the OH-libration band (wavenumbers range is 960-980 cm^{-1}) specific for κ_1 phase [2] was observed only in waveguides fabricated with $C_{LS} < 0.75$ wt %. Such band was not observed into spectra measured at $\Theta = 20^0$, where depth of photometered area is much larger than at $\Theta = 70^0$. Thus, we can conclude existence in an upper part of α-phase waveguide of the shallow near-surface κ_1-phase layer, which is not detected by X-ray diffraction method. Actually, an extremely high level of propagation loss in the κ-phase and compositionally inhomogeneous wavegudes is well known fact [1,3].

To investigate mechanisms of this contribution and other marked sources of the loss, we used SNOM technique. By probing the evanescent field present in the air region above a waveguide, we can measure with near field spatial resolution the optical power distribution associated with the optical waveguide as well as the effective index of refraction of the structure [6]. It has been established, that guide light is scattered due to inhomogeneity at the proximity of the surface of the waveguide. These scatterings offer some information about loss mechanisms in our waveguides. Fig. 2 shows the measured intensity-distribution profile of guided mode and the topographical image of a straight channel waveguide within a scanned area 16×100 μm^2. The results show the strong topographical strip structure that is correlated to the SNOM image of the guided mode. There are some bright spots in a mode image of any waveguide studied. Random distribution allows to assume that these bright spots are observed due to scattering on composition inhomogeneities at the proximity of waveguide surface [7]. For example, a very strong intensity independent static contribution in mode scattering is observed in the multiphase waveguides, having most pronounced

IR-spectroscopy evidence of κ_1-phase shallow layer on a surface of the α-phase waveguides fabricated by HTPE technique at $C_{LS} \leq 0.7$ wt %, or standard APE technique. In monophase HTPE waveguides, containing mainly α phase, this contribution is much smaller, but exists always and correlates with variation of the propagation loss in the fiber-to-fiber coupling experiments. Thus, fabrication conditions allowing minimize the propagation loss in HTPE waveguides have been identified: $0.75 \leq C_{LS} \leq 0.78$ wt.%, and exchange time should be in a range from 3.5 to 4.1 hours.

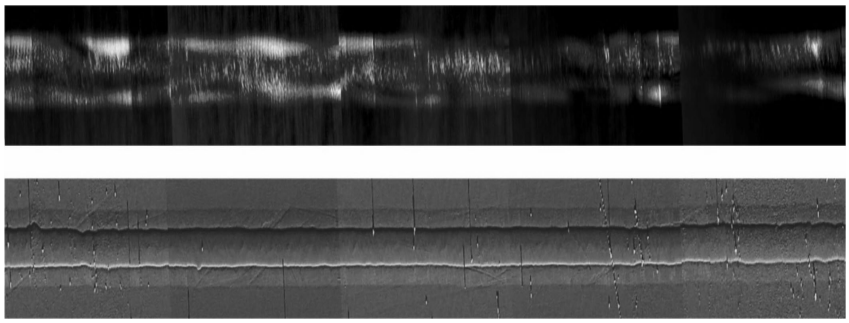


Fig. 2. SNOM data on intensity-distribution profile of guided modes (upper picture) and the topographical image (down picture) of a straight channel double-mode waveguide fabricated by HTPE technique. Guided light propagates from left to right side of upper picture.

The temporal evolution of SNOM images between successive scans of the same area of high-intensity mode allows us to determine the light-induced scattering related to photorefractive damage because of specific kinetics of photorefractive response [5] in the waveguide. This temporal evolution becomes detectable only with in-coupled powers higher than 40 μW. The threshold values of in-coupled power for light-induced changes observed by fiber-to-fiber coupling and SNOM experiments are significantly different, but there is clear correlation between these two threshold values at comparison of different waveguides. It was established, that this photorefractive damage is smaller than in APE waveguides and can be decreased for a desirable level by prefabrication treatment of a $LiNbO_3$ wafer and appropriate choice of in-coupled power.

Conclusion

By using SNOM, the very strong intensity-independent static contribution in mode scattering is found to be the specific feature of proton-exchanged $LiNbO_3$ waveguides. This contribution correlates clearly with additional losses observed with fiber-to-fiber coupling experiments and related to leakage of a guided mode into substrate. Time-dependent growth of light scattering is observed only at in-coupled powers above some threshold related to intensity dependence of photorefractive damage. Fabrication conditions allowing a significant reduction of such static and photorefractive scatterings in HTPE-$LiNbO_3$ channel waveguides have been identified.

[1] M.M. Howerton, W.K. Burns, P.R. Skeath, A.S. Greenblatt, *IEEE J. Quant. Electron.* **QE-27**, 593-600, 1991.
[2] Yu. N. Korkishko, V.A. Fedorov, S.M. Kostritskii, *J. Appl. Phys.* **84**, 2411-2419, 1998.
[3] Yu.N. Korkishko, V.A. Fedorov, E.A. Baranov, M.V. Proyaeva, T.V. Morozova, F. Caccavale, F. Segato, C. Sada, S.M. Kostritskii, *J. Opt. Soc. Am. A* **18**, 1186-1191, 2001.
[4] R. Narayan, *IEEE. J. of Selected Topics in Quantum Electron.* **3**, 796-807, 1997.
[5] E.E. Robertson, R.W. Eason, Y. Yokoo, P.J. Chandler, *Appl. Phys. Lett.* **70**, 2094-2096, 1997.
[6] A.L. Campillo, J.W.P. Hsu, C.A. White, C.D.W. Johes, *Appl. Phys. Lett.* **80**, 2239-2241, 2002.
[7] Y. Toda, M. Ohtsu, IEEE Photonics Techn. Lett. **7,** 84-86, 1995.

Broadband DBR Recorded Holographically into Cu-Doped Ti-Indiffused Channel Waveguide on Z-Cut $LiNbO_3$

S.M. Kostritskii, Yu.N. Korkishko, V.A. Fedorov
Moscow Institute of Electronic Technology, Optolink Ltd, 103498,Zelenograd, Russia;
skostritskii@optolink.ru

R.F. Tavlykaev and R.V. Ramaswamy
Photonics Research Lab, Department of Electrical and Computer Engineering,
University of Florida, Gainesville, FL 32611, USA

A broadband DBR has been recorded by use of a holographic technique into Z-cut Ti-indiffused channel $LiNbO_3$ waveguides, which were doped by proton-assisted copper exchange. In a first approach we obtain a reflectivity of 17 % and bandwidth (FWHM) of 1.2 nm for IR light with center wavelength 1534.3 nm.

Keywords: lithium niobate, Ti-indiffused waveguide, photorefractive grating, DBR filter

Introduction

Waveguide gratings in $LiNbO_3$ operating around 1550 nm have attracted much interest in integrated optics. Holographically written photorefractive gratings are shown already [1-3] to be one of the most effective and technologically simplest ways for realization of a narrow-band distributed Bragg reflector (DBR) filter integrated with a channel waveguide. On the other hand, broadband operation is much desired in a variety of applications, for example in high-speed guided-wave electro-optic modulators in $LiNbO_3$. A broadband filter requires a grating of high reflectivity and a short interaction length ($\leq$ 0.5 mm). Therefore, extremely strong index modulation ($\geq 5*10^{-4}$) within the photorefractive grating is necessary, which poses a difficult problem, since it requires a high doping level with transient ion impurities (Fe or Cu). Another problem is related to the fact, that all the recent photorefractive grating technologies [1-3] have been developed only for channel waveguides of Y(or X)-cut, Z-propagating geometry. Of course, such geometry cannot be employed in the electro-optic modulators based on $LiNbO_3$.

In this communication, we discuss a DBR recorded directly in Z-cut channel Ti:$LiNbO_3$ waveguides, those photorefractive sensitivity has been increased by a recently developed technique of proton-assisted copper exchange [4] that can achieve a doping level much higher than that available with the commonly used indiffusion and bulk doping techniques. Unique mechanism of photorefractive recording [5], having no equivalent in bulk materials, was used for fabrication of a holographic grating in Z-cut $LiNbO_3$ waveguides.

Experimental methods and samples fabrication.

An array of channel waveguides was fabricated by indiffusion of an array of Ti strips with width ranging from 2 to 10 μm in Z-cut $LiNbO_3$. The 100-nm-thick strips were indiffused for 18 h at temperature of 1000 ^oC. To increase the photorefractive sensitivity of these waveguides, two technological procedures were implemented. Firstly, $LiNbO_3$ samples were immersed in a melt of benzoic acid mixed with 0.75 mol% of $CuCO_3$ and 0.65% of Li_2CO_3. Processing was performed at 240^oC for 80 to 110 min and produced a Cu-doped surface layer. Li_2CO_3 was used to suppress strong proton exchange and avoid surface damage. Secondly, the samples were annealed in dry air at 370^oC for 28 to 40 hours. Such annealing significantly decreased the proton concentration and hence, restored the electro-optic effect in the near-surface layer, where Ti-indiffused channel

waveguides were located. At the same time, Cu spread into the substrate more efficiently due to the proton-assisted enhancement of Cu diffusion (1/e depth is expected to be about 5 μm). Moreover, oxidation of a significant proportion of Cu ions from (1+) to (2+) valence state took place [4]. As result, a significant photo-induced space-charge field was expected to build-up upon spatially inhomogeneous illumination of the copper-doped region [3].

Photorefractive gratings were written using a He-Cd laser (λ = 441.6 nm) in a holographic setup with writing times ranging from 0.5 to 2.5 hours at light intensities within the 0.1 – 0.3 mW/cm^2 range. Note, that the upper limit of light intensity used is caused by maximally available output power of our He-Cd laser. A spatial filter was used to produce a clean wavefront of He-Cd laser light. The beam was not collimated. A mirror placed immediately next to the sample at 90^0 splits a portion of the beam in two. These two writing beams of an equal intensity illuminate the whole sample with the waveguide layer on its top face. The light polarization is chosen to be in the plane of incidence. These beams intersect at an angle $2\Theta = 79.366^0$ in air. Assuming a planar wavefront, the grating period Λ is related to the angle Θ by $\Lambda = \lambda / (2 \sin \Theta)$. Our setup permits very precise adjustments to the grating period because the optics are placed on a single motorized rotation stage with an angle accuracy of 1/1000 of a degree and, therefore, the gratings are reproducible with average periods accurate to better than 0.1 nm.

The use of an uncollimated beam resulted in a more uniform exposure over an illuminated area of the sample, but could have yielded a chirped grating. To minimize the chirp and nonuniformity of light intensity across the small area of the sample, the beam diameter at the distance where the sample was positioned was chosen to be large enough (30 cm). As result, the grating chirp was reduced to 0.18 nm/cm; that is, a period shift of 0.18 nm along 1cm of the grating.

Transmission and reflection spectra of the fabricated gratings were measured using a tunable laser source HP 8168 (range from 1500 to 1570 nm) and an optical spectrum analyzer HP 70951A. Laser radiation is coupled into a channel by a PM single-mode fiber and radiation reflected by waveguide grating is outcopled from the channel with the aid of same fiber. By this way interaction of the TM_0 guided mode with waveguide gratings was studied. Fiber directional coupler is used to extract reflected radiation and send it to the optical spectral analyzer. IR radiation transmitted through a waveguide is collected by microscope objective and imaged on photodetector.

Experimental results and discussion.

Recently, the feasibility of efficient photorefractive gratings in Z-cut $LiNbO_3$ waveguides has been demonstrated using holographic recording in planar waveguides with extraordinarily polarized guided beams [4,5]. For this crystal orientation, photovoltaic currents perpendicular to the sample surface and the grating vector induce space-charge fields. We have carried out experimental verification of this mechanism, which has no equivalent in bulk materials [5], and used it, for the first time, for direct recording of a DBR in channel waveguides. It is important to note, that realization of this mechanism requires limitation of a grating fringe length in depth direction in order to reach a sufficient magnitude of space-charge field, e.g. in case of $LiNbO_3$ fringe depth should be ≤ 10 μm. To obtain necessary limitation of grating fringe depth in substrate with channel waveguides, we propose to use shallow surface doping of $LiNbO_3$ substrate with photorefractive impurities. Proton-assisted copper exchange gives unique possibility to make the heavy surface doping for gradually variable depth up to ten micrometers. Note, that an interference pattern fringe is not limited by waveguide depth, but it extends over whole thickness of a substrate. However, as a space-charge voltage is following to depth distribution of photovoltaic currents, which should copy roughly copper concentration profile, a marked photorefractive grating is formed within copper-doped surface layer only.

Measured reflection and transmission spectra indicate that the diffraction efficiency and reflectance of the fabricated gratings increase with longer copper exchange and subsequent annealing. Such dependence is in full accordance with the results of our previous study [4] on the effect of $Cu^{+/2+}$ and H^+ concentration profiles on the photorefractive sensitivity of $LiNbO_3$ waveguides doped by proton-assisted Cu exchange. It should then be expected that a further improvement of the grating efficiency can be achieved by increasing the Cu salt content in the melt used for Cu exchange and by extending the time of Cu exchange. Note, that the highest grating efficiency was achieved at the highest light intensity used for holographic recording. Thus, a significant enhancement of the grating efficiency may be expected if a more powerful laser is used for recording.

The data for waveguide gratings recorded in a strongest Cu-doped (doping time is 110 min) and longer annealed (for 40 hrs) sample are most promising. For example, the peak reflectivity of 17 ± 1 % (measured in TM polarization) has been observed for a 0.73-mm-long grating in a 8.5 μm wide single mode waveguide, it has maximum value at the wavelength λ_m = 1534.3 nm. There is good correspondence of this reflection peak wavelength to the Bragg wavelength in transmission spectrum. Decrease of grating length allows increase the FWHM filter bandwidth up to 2.7 nm, but grating reflectance drop for a very small value of 2 - 3 %. Of course, such value is out of any practical interest, but further optimization of doping and holographic recording technologies could improve significantly this parameter.

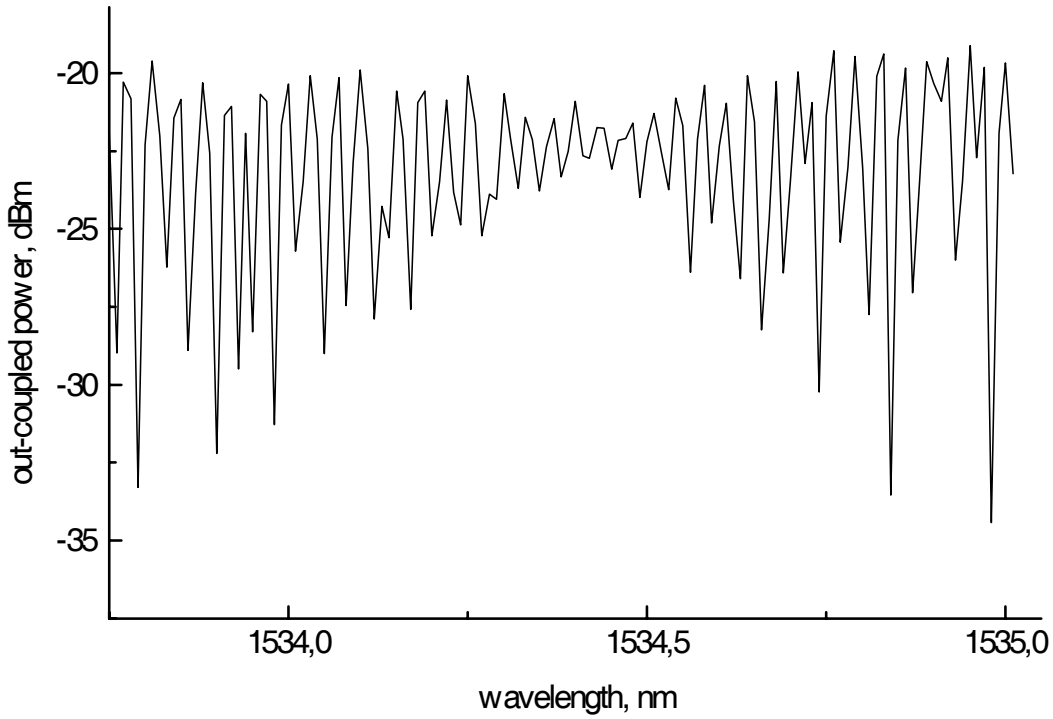


Fig. 1. Spectral dependence of backward out-coupled power for asymmetric Fabry-Perot interferometer formed by a waveguide grating and polished air-waveguide interface. The grating Bragg wavelength is 1534.3 nm. Grating was recorded by He-Cd laser radiation with intensity of 0.2 mW/cm^2 for 1 hour in the sample copper-exchanged for 100 min and annealed for 40 hrs. Before grating recording, there is no any spectral band with significant attenuation of Fabry-Perot fringes contrast and some increase of average power P_{av} (where $P_{av} = (P_{max} + P_{min})/2$). Wavelength step of tunable laser sources was 0.01 nm.

Main lot of our Integrated Optical Chips (IOC) were fabricated by polishing their ends at a sufficient slant angle (10°) to avoid Fresnel backward reflection from air-waveguide interfaces and, hence, to escape a parasitic Fabry-Perot interferometer (FPI). However, some test samples have perpendicular air-waveguide interfaces at the both optical-grade polished lateral edges. It was used, as application of such test samples for holographic recording allows evaluation of a grating efficiency, as an asymmetric FPI was created through photorefractive grating formation. The term "asymmetric" is used to refer to the case of two reflectors (air-waveguide interface and DBR) with vastly different reflection spectra.

In fact, grating formation induced the specific wavelength-selective change of both contrast and period of Fabry-Perot fringes in reflection spectra of a channel waveguide (Fig.1). The maximum change was observed at wavelength range of 1534.38 to 1534.42 nm, coinciding closely with Bragg wavelength of 1534.3 ± 0.04 nm for holographically recorded DBR. FWHM of differential reflectivity related to asymmetric FPI was wider than a FWHM of the peak in reflection spectrum of similar waveguide DBR recorded in a sample with slanted interfaces at lateral edges. For example, a 1.41-mm grating, having 0.62-nm-FWHM peak in the reflection spectrum, provides ~0.8-nm-FWHM band in response of asymmetric FPI. For shorter gratings the difference between these two FWHMs is smaller and it is not detectable for gratings with $L \leq 0.73$ mm. It is important to note, that evaluation of grating reflectivity, according to the common theory of asymmetric FPI, gives a value around 9.5 ± 0.5 % in the case shown here (Fig.1), while direct measurement of reflection spectrum of same waveguide grating in IOC with slanted ends gives the significantly smaller value of 5 ± 1 %. It was also found that grating reflectance increased monotonically with grating length for up to 3 mm and remained nearly the same after that. This anomaly may be related to the imperfections of the holographic recording processes, such as long-term instability [3], parasitic recording of noise gratings caused by light-induced scattering [6,7], etc.

Conclusion

Our first attempt at making a broadband DBR yielded a filter with a reflectivity of 17% and bandwidth (FWHM) of 1.2 nm centered at 1534.3 nm. Some gratings exhibited bandwidths as broad as 2.7 nm, however with lower reflectivity. Further improvement of DBR performance is expected, according to the previous studies [4,7] of holographic recording in the Cu-doped $LiNbO_3$ waveguides, to be possible by optimizing Cu content in molten benzoic acid, annealing time, and writing light intensity.

[1] J. Hukriede, I. Nee, D. Kip, E. Kratzig, *Opt. Lett.* **23**, 1405-1407, 1998.
[2] Ch. Becker, A. Greiner, Th. Oesselke, W. Sohler, H. Suche, *Opt. Lett.* **23**, 1194-1196, 1998.
[3] J. Hukriede, D. Kip, E. Kratzig, *J. Opt. A: Pure Appl. Opt.* **2**, 481-487, 2000.
[4] S.M. Kostritskii, Yu.N. Korkishko, V.A. Fedorov, A.N. Alkaev, *Proc. SPIE* **4358**, 88-97, 2001.
[5] D. Kip, F. Rickermann E. Krätzig, *Opt. Lett.* **20**, 1139-1141, 1995.
[6] J. Frejlich, P.M. Garcia, A.A. Freschi, *Proc. SPIE* **2778**, 941 –944, 1996.
[7] S.M. Kostritskii, P. Moretti, *In "IR Holography for Optical Communications: Techniques, Materials and Devices"*, P. Boffi, D. Piccinin and M.C. Ubaldi (Eds.), *Topics in Applied Physics*, vol. **86,** pp. 59-74 (Springer-Verlag, Berlin, 2002).

90°-turns with polarization-independent single-mode waveguide on silicon-on-insulator for telecommunication wavelengths

Eric Cassan, Laurent Vivien, and Suzanne Laval
Institut d'Electronique Fondamentale, UMR CNRS 8622, bât. 220, Université Paris-Sud, 91405 Orsay, France
eric.cassan@ief.u-psud.fr

Three-dimensional Finite Difference Time Domain simulation is used to study the optical properties of waveguide 90°-turns in single-mode silicon-on-insulator rib and strip waveguides at telecommunication wavelengths.

Keywords: Rib and strip waveguides, Silicon-On-Insulator, Single-mode waveguides, Polarization independence, 90°-turns

Introduction and purpose

Silicon-on-insulator (SOI) material is of interest for integrated microphotonics since it offers the potentiality of monolithic integration of optical and electronic functions on a single substrate. Moreover, silicon is transparent at telecommunication wavelengths, around 1.55 µm. The silicon film of SOI substrates can be used as a low-loss waveguide [1].The main advantages of the SOI arise from the strong light confinement in very small waveguides, due to the large refractive index difference between silicon and silicon oxide ($\Delta n \approx 2$), and from the possibility of using established silicon microelectronics technology. In addition to the low cost of silicon technology and the availability of large wafers, SOI allows to significantly miniaturize the optical devices. Within this photonic technology, laterally confined optical waveguides can be mainly obtained either by a partial etching of the silicon film (rib waveguides), or by a full etching of the silicon film down to the buried oxide (strip waveguides).

Wavelength Division Multiplexing (WDM) is one of the technologies that is rapidly evolving to increase transmission capacity and flexibility in broadband optical fiber telecommunication networks. An important point is that most of the devices for telecommunication applications require polarisation insensitivity at wavelengths ranging from 1.53 µm to 1.61 µm [2] for single-mode waveguides. The problem is that for most SOI waveguide dimensions, there is a strong birefringence effect between the quasi-TE and quasi-TM optical modes, that is basically quantified by the effective index mismatch Δn_{eff} between the two light polarizations.

In the case of SOI rib waveguides, polarization independence was demonstrated for height larger than several microns [3]. Such solutions obviously pose problems of compactness. Recently, we made an analysis of the influence of geometrical parameters on the polarization sensitivity properties for smaller single-mode silicon-on-insulator rib waveguides [4]. We showed that a proper design of the rib waveguide dimensions ensure polarization independence, with rib heights ranging from 2 µm to 0.5 µm. The SOI rib-waveguide dimensions (height, width and etching depth) leading simultaneously to single mode propagation and polarization independence were calculated for telecommunication wavelengths, from 1.53 µm to 1.61 µm. The minimum etching depth is obtained for a nearly constant value of the ratio of the rib width over the waveguide height, within the considered height range, and is close to the rib width.

In the case of SOI strip waveguides, polarization independence can be obtained with waveguides having a square section, which theoretically ensures a degeneracy between the quasi-TE and quasi-TM optical modes. Single-mode propagation at telecom wavelengths requires waveguides with square section below 0.35 µm × 0.35 µm. Whereas such small dimensions obviously constitute an advantage for the compactness of devices, they make light coupling from a single-mode optical

fiber into SOI microwaveguides more difficult than for rib waveguides. Even if solutions for efficient light coupling into such strip SOI waveguide have been recently pointed out [5], such guides potentially suffer from increased losses, if compared with rib guides, due to the larger sensitivity to sidewall roughness.

For these reasons, both rib and strip waveguides are considered in this work. The basic question that is addressed is the following: how is it possible, with SOI polarization-insensitive waveguides, to make light take a 90°-turn ?

SOI waveguide-based 90°-turns

Intrinsically, rib waveguides suffer from a lower confinement of light if compared with the strip geometry. For this reason, 90°-bends based on rib SOI waveguides generally require high radii to minimize losses, due to the light leakage into the SiO_2/partially-etched Si film/SiO_2 slab waveguide. It has recently been shown that fully-etched corner mirrors offer an interesting alternative solution, in terms of both compactness and losses [6]. Even if the rib waveguides considered in ref 6 were not polarization insensitive, these results have encouraged us to evaluate the properties of fully-etched mirrors for SOI single-mode polarization-insensitive waveguides.

Optical modes have been calculated with a three-dimensional full-vectorial mode solver [7], for both quasi-TE and quasi-TM polarizations. Field distributions determined by this solver are then used as input conditions in a three-dimensional FDTD calculation [8]. Power transmittance is calculated for a range of wavelengths by a discrete Fourier transform of the field components recorded during the whole temporal simulation.

Fig. 1 shows the field distribution in the rib waveguide for the quasi-TE and quasi-TM polarizations for a 1 µm-width rib waveguide at λ = 1.55 µm, which is typical of the obtained fields for all considered waveguide geometries. Despite effective indices of the polarizations differ from only 10^{-5} (n_{eff} = 3.38117 at λ = 1.55 µm), it is obvious from fig. 1 that the quasi-TE field slightly expands in the thinner silicon film region, whereas the quasi-TM mode appears to be better confined in the central part of the rib waveguide.

Fig. 2 shows the power transmittances obtained at λ = 1.55 µm for fully-etched corner mirrors based on polarization-insensitive rib waveguides, with heights ranging from 0.5 µm to 1.75 µm. Two tendencies can be drawn from fig. 2.

On the one hand, the larger the waveguide dimensions, the higher the power transmittance. Moreover, power transmittance variation with wavelength is weak. Fig. 3, which is a plot of the field obtained at half-height for the 1.75 µm-high rib waveguide for a quasi-TE polarization, confirms the weak level of losses depicted in fig. 2 for this waveguide height. 3D-FDTD simulations we have performed have proved that excessive losses obtained for small waveguides mainly originate from an excessive field compression in the corner region area. This effect does not occur in the case of slightly-etched rib waveguides, for which losses of corner mirrors below 0.1 dB can be obtained [6]. To our knowledge, this effect is reported for the first time. Small polarization-independent rib waveguides are approximately obtained by a reduction of all dimensions from larger waveguides. Small rib waveguides thus remain deeply-etched devices, i.e. they keep a strong lateral optical confinement. With the reduction of the height, corner mirrors based on polarization independent rib waveguides then tend to have properties similar to those of simple corner mirrors based on strip waveguides, which typically present power transmittances about 0.4 [9].

On the other hand, it is noticeable from fig. 2 that losses obtained for a quasi-TE or a quasi-TM polarization are close to each other, in spite of the different field extensions observed in fig. 1. This result is due to the fact that corner mirror device operation basically relies on total reflection, whatever the field is. Power transmittances obtained at λ = 1.55 µm for the 1.75 µm-high rib waveguide for the quasi-TE and quasi-TM polarizations are 0.945 and 0.942, respectively, which represents a loss difference between the two polarizations of only 0.014 dB

90°-turns for strip SOI waveguides have been studied in details [9]. Design of corner mirrors are possible, but efficient 90°-turns are obtained with mirrors having several slopes. Alternatively, it has been shown that 90°-bends with curvature radius of only few µm with strip waveguides have very low losses [10]. Following this latter approach, we have focused our study on the properties of 90°-bends based on SOI strip waveguides, using 3D-FDTD. To ensure independence to polarization, the considered waveguides have square sections.

Fig. 5 shows the power transmittances obtained for a 0.35 µm-square waveguide, for two curvature radii (R = 1 µm and R = 4 µm), and for the quasi-TE and quasi-TM polarizations. This waveguide dimension has been chosen because it is close to the largest one that ensures single-mode propagation at λ = 1.55 µm. We see from fig.5 that losses are weaker for the R = 4 µm-based than for the R = 1 µm-based 90°-bend, as waited. We also see from fig.5 that losses are weak in all cases, with the lowest level obtained for the quasi-TM polarization of the R=4 µm-based 90°-bend (T=98.2%), whereas T=97.35% for the quasi-TE polarization. The loss difference between the two polarizations is about 0.04 dB for the two considered 90°-bends. It is slightly more than those obtained with the largest polarization-independent rib waveguides (0.014 dB), which have yet lower power transmittance.

A comparison between 90°-turns based on the two kinds of SOI waveguides, i.e. rib and strip waveguides, will be presented in the full contribution, including a discussion of other important aspects for telecommunication purposes, as the magnitude of propagation losses and coupling efficiency from a single-mode fiber.

[1] A. Layadi, A. Vonsovici, R. Orobtchouk, D. Pascal, A. Koster, *Optics Communications* **146**, 31-33, 1998.

[2] P.D. Trinh, S. Yegnanarayanan, F. Coppinger and B. Jalali, *IEEE Photonics Technology Letters* **9**, 940-942, 1997.

[3] J. Schmidtchen, A. Splett, B. Schüppert, and K. Petermann, *Electronics Letters* **27**, 1486-1487, 1991.

[4] L. Vivien, S. Laval, B. Dumont, S. Lardenois, A. Koster, and E. Cassan, *Optics Communications*, **210**, 43-49, 2002.

[5] L. Vivien, S. Laval, E. Cassan, X Leroux, D. Pascal, *"2-D taper for low-loss coupling between polarization-insensitive microwaveguides and single-mode optical fibers"*, submitted to *Photonic Techn. Letters*.

[6] Eric Cassan, Suzanne Laval, Sébastien Lardenois, and Alain Koster, *"On-chip optical interconnects with compact and low-loss light distribution in silicon-on-insulator rib waveguides"* , submitted to *IEEE Journ. of Selected Topics in Quantum Electron*.

[7] http://www.photon.com: FIMMWAVE

[8] http://www.ise.ch: EMLAB

[9] C. Manolatou, S. G. Johnson, S. Fan, P. R. Villeneuve, H. A. Haus, and J. D. Joannopoulos, *Journal of Lightwave Techn*. **17**, vol. 9, pp. 1682-1692, 1999.

[10] R. L. Espinola, R. U. Ahmad, F. Pizzuto, M. J. Steel, and R. M. Osgood, *Optics Express* **8**, vol. 9, pp. 517-528, 2001.

Figure 1: Intensity map for 1.5 µm high rib waveguide
Height = 1.5 µm, Width = 1 µm and Etching depth = 0.8925 µm

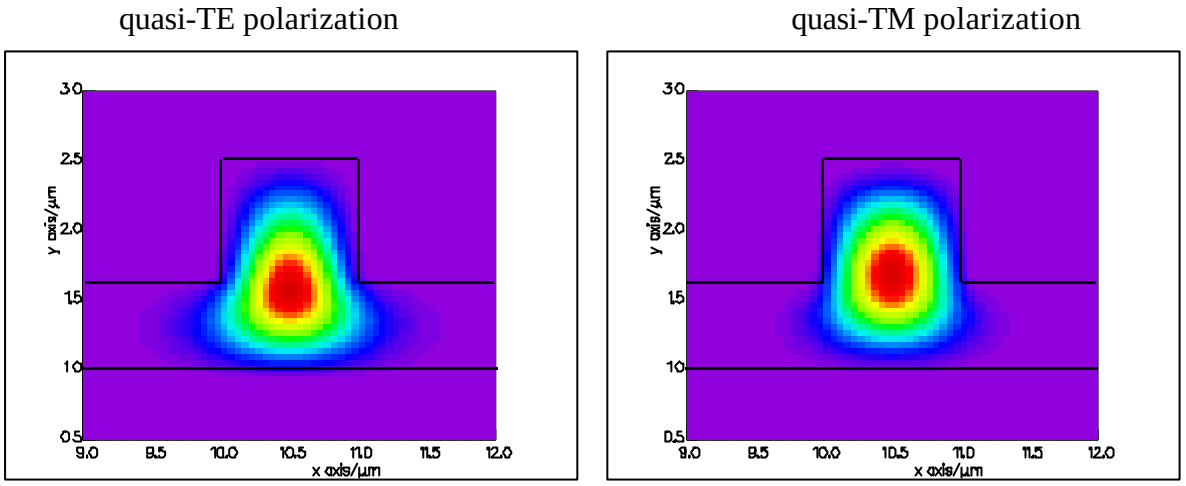


Figure 2: Power transmittances of corner mirrors based on polarization-independent rib waveguides

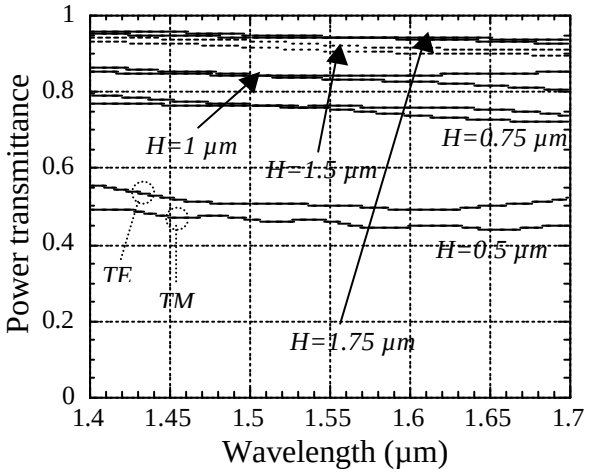


Figure 3: Field map obtained for the fully-etched mirror based on the 1.75 µm-high rib

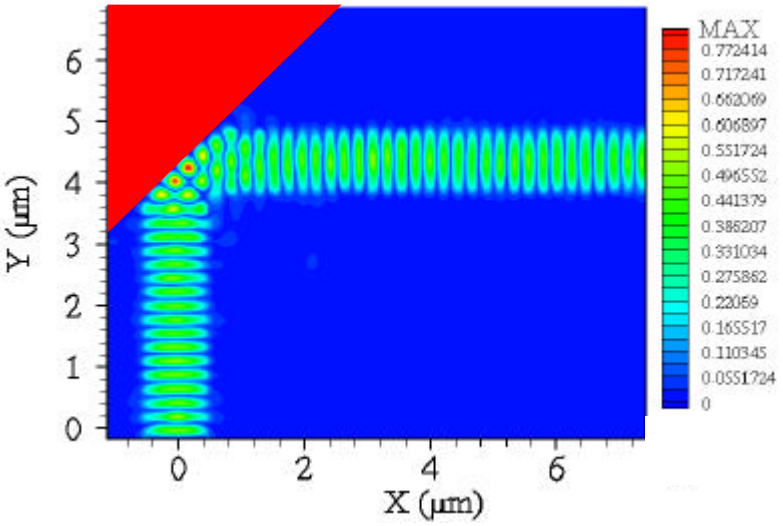


Figure 4: Power transmittance of rib waveguide-based corner mirrors at λ = 1.55 µm versus waveguide height

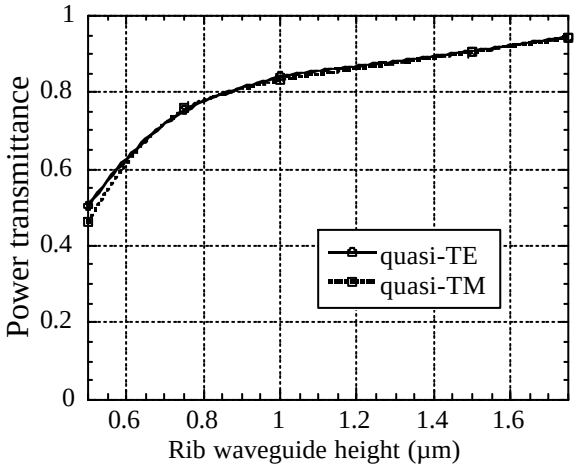
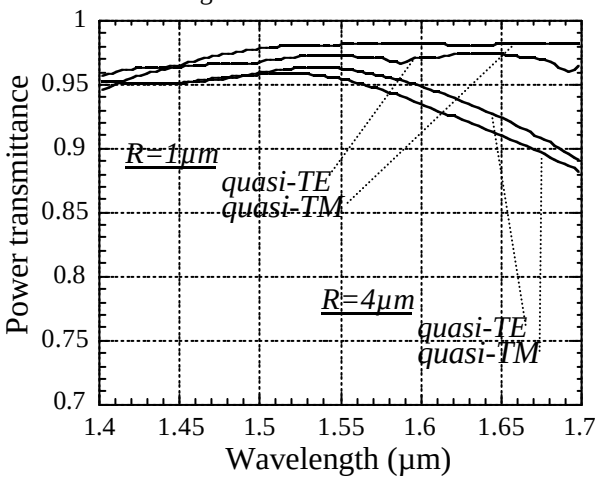


Figure 5: Power transmittances of SOI strip waveguide-based 90°-bends



Nonlinear Algorithms for the Quantum Mechanical Simulation of Electroabsorption

Marco Wiedenhaus, Andreas Ahland, Dirk Schulz and Edgar Voges
Lehrstuhl Hochfrequenztechnik, Universität Dortmund, Germany
wiedenhaus@hft.e-technik.uni-dortmund.de

An overview of nonlinear simulations of electroabsorption modulators and their physical and numerical requirements is given. The algorithm includes all important aspects, like excitonic and carrier-dependent effects, a self-consistent treatment and quantum mechanical behaviour.

Keywords: Electroabsorption modulator, excitons, density matrix, absorption, quantum-confined Stark effect

Introduction

Although electroabsorption modulators (EAM) become increasingly important, there is a huge gap between requirements and state of the art semiconductor technology and simulation. The high complexity of the nonlinear behaviour of modulators is still a challenge, which is not sufficiently accepted.
The presented algorithm is one of the most extensive tools to model EAMs and to analyze nonlinear behaviour. It includes the most important optoelectronic effects, which are essential for the modulator's performance, e.g. the quantum-confined Stark effect and the Franz-Keldysh effect, and also accounts for carrier-dependent effects. Therefore coupled descriptions of electrical and optical properties are needed. A drift-diffusion model and quantum corrections primarily characterize the electronical parameters, while a density matrix formalism, instead of $\vec{k}$-space solutions, determines the optical behaviour. Density matrices allow boundary conditions in real space and provide efficient calculations.
This procedure includes the excitonic effect, all important quantum mechanical effects, nonlinear carrier-dependent effects and enables self-consistent and time-dependent methods.

Solution in $\vec{k}$-space

If the bound states of the calculated structure are known, it is possible to gain a first estimation of the absorption [1]. The exciton equation in k-space is solved by expanding the exciton states in terms of subband states, which result from band structure calculations in the envelope function approximation (EFA) [2, 3] by solving the stationary Schrödinger equation using a kp-Hamiltonian. Discretisation generates an eigenvalue problem, which can be efficiently solved. Unfortunately, the calculation of the matrix elements makes this procedure time consuming. The exciton wave function, on the other hand, is used for solving the density matrix equation, which determines the complex dielectric function. This directly results in the refractive index and chirp parameter [1].

For an accurate description of the optical properties of EAMs Wannier-excitons must be included. Therefore, the following Schrödinger equation is solved to determine the exciton states Ψ_{ex}

$$\mathbf{H}_{ex}(z)\Psi_{ex} = E_{ex}\Psi_{ex}, \tag{1}$$

where $\mathbf{H}_{ex}(z)$ is the effective Hamiltonian including a Coulomb term. To Ψ_{ex} an expansion is applied, which is based on the eigenfunctions resulting from the single-particle Schrödinger equation. The numerical evaluation of this expansion is very time-consuming.

The density matrix for interband processes is used to calculate the optical properties. It determines the complex dielectric function and renders a tedious Kramers-Kronig transformation to calculate the refractive index change unnecessary. We expand the coherent electron-hole

wavefunction in terms of the exciton wavefunction. The emerging integrals in $\vec{k}$-space lead to tedious band structure calculations, which makes this method unsuitable for nonlinear computations. Therefore, an alternative algorithm is applied.

Density matrix in real space

The solution of the density matrix in real space yields a more accurate description of excitonic effects and provides the following advantages.
The Coulomb singularity can be resolved analytically by polynomial finite elements [4]. Bound, quasi-bound and free states are as well modelled as all electric field dependent effects like quantum confined Stark effect (QCSE), Franz-Keldysh effect (FKE) and Wannier-Stark effect (WSE) and mixtures of these. The density matrix formalism allows to calculate both real and imaginary part of the susceptibility. The finite coherence length can be used to terminate the calculation space efficiently by open boundary conditions like the perfectly matched layers (PML) [5].
The stationary equation for the coherent electron-hole amplitude Y

$$(\mathbf{H}_{eh} - \hbar\omega - \mathrm{j}\hbar\Gamma_{eh})\, Y = \mu\vec{E}\,, \tag{2}$$

with the Hamiltonian $\mathbf{H}_{eh}$ for parabolic bands, which is used for general quantum well structures and superlattices allowing spatially dependent effective masses for electrons and holes

$$\begin{aligned} \mathbf{H}_{eh} \;=\; & -\frac{\partial}{\partial z_e}\frac{\hbar^2}{2m_e}\frac{\partial}{\partial z_e} - \frac{\partial}{\partial z_h}\frac{\hbar^2}{2m_h}\frac{\partial}{\partial z_h} - \frac{\hbar^2}{2m_r}\frac{1}{r}\frac{\partial}{\partial r}\left(r\frac{\partial}{\partial r}\right) \\ & + E_c(z_e) - E_v(z_h) - \frac{e^2}{4\pi\epsilon\sqrt{r^2+(z_e-z_h)^2}}\,, \end{aligned} \tag{3}$$

the driving electric field $\vec{E}$, the optical dipole matrix element μ and a phenomenologic dephasing rate Γ to describe the reduction of Y by scattering processes, is solved by applying a nodal finite elements (FE) approach. m_e and m_h are the position dependent electron and hole effective masses in z direction, $m_r = 1/(m_{e||}^{-1}+m_{h||}^{-1})$ is the reduced mass in radial direction. The electron and hole band energies are labelled E_c and E_v, respectively.
The main advantage of this approach is that the Coulomb singularity is modelled exactly for polynomial base functions [4]. Due to this the approach presented is more accurate.
The optical polarization $\vec{P}$ and the optical susceptibility χ result from an integration over relative coordinates r and z

$$\vec{P}(Z) = \iint \mu Y(Z,z,r) r\,\mathrm{d}r\,\mathrm{d}z\,, \qquad \chi = \frac{P}{\epsilon_0 E}\,. \tag{4}$$

In typical waveguide modulators the induced optical field only slightly differs, thus a first order perturbation theory is appropriate to calculate a complex effective dielectric function

$$\epsilon_{\mathrm{eff}} = \frac{\int (1+\chi(Z))E^2(Z)\mathrm{d}z}{\int E^2(Z)\mathrm{d}z} \tag{5}$$

from the material susceptibility χ.

Semiconductor Equations

The single particle equations for electron-electron and hole-hole interactions are approximated by a semi-classical drift-diffusion model (DDM). Therefore, a system containing Poisson's

equation (6), the continuity equations (7) and (8) and carrier transport equations of the drift-diffusion model with an additional quantum correction (9) and (10) is solved in a decoupled manner to determine the electrical properties of the structure:

$$\nabla \cdot (\epsilon \nabla \Psi) = -e(p - n + N_D - N_A)\,, \tag{6}$$

$$\nabla \cdot \vec{J}_e - e\frac{\partial n}{\partial t} = eR\,, \qquad n = N_e F_{1/2}(\eta_e)\,, \tag{7}$$

$$\nabla \cdot \vec{J}_h + e\frac{\partial p}{\partial t} = -eR\,, \qquad p = N_h F_{1/2}(-\eta_h)\,, \tag{8}$$

$$\vec{J}_e = -en\,\mu_e \nabla \Phi_e\,, \tag{9}$$

$$\vec{J}_h = -ep\,\mu_h \nabla \Phi_h\,. \tag{10}$$

These equations contain the self-consistent potential Ψ, the carrier concentrations n (electrons) and p (holes) and the concentrations of completely ionized acceptors N_A and donors N_D. Further, the difference between recombination and generation rates R, the carrier current densities $\vec{J}_e$ and $\vec{J}_h$ for electrons (e) and holes (h), respectively, and the mobilities μ_e and μ_h are as well used as the quasi Fermi potentials Φ_e and Φ_h. N is the effective density of states, $F_{1/2}$ the Fermi integral of order 1/2 and carrier densities are calculated for Fermi distributions. To account for quantum mechanical effects the classical potential is corrected by the Bohm potential, which smoothes the carrier densities. The Poisson equation (6) is solved by the Gummel algorithm [6, 7].

Coupling of electronical and optical properties and nonlinear effects

To investigate nonlinear behaviour and saturation effects the optical properties have to be coupled to the semiconductor equations to account for carrier dependent phenomena. This can be realized by an additional generation rate, which is determined by the exciton equation.
The saturation terms in the source terms of the density matrix equation, neglected in Eq. (2), lead to an optical generation of carriers. This generation can be accounted for in the continuity equations (7) and (8) - a coupling of the electrical and the optical system can be realized this way. Consequently, an additive generation-recombination rate R_{opt} can be derived

$$R_{opt} = -E^2 \mathrm{Im}(\chi)\frac{\epsilon_0}{\hbar} \tag{11}$$

leading to a nonlinear calculation [8].
Saturation effects can be modelled due to the coupling of electrical and optical system by including R_{opt}. A small band gap and a small density of states cause a fully occupied band near the band edge, the so-called Burstein-Moss effect, which appears in terms of a modified Coulomb term. As a counterpart to the Burstein-Moss effect, a reduction of the band gap has to be regarded. Concerning high carrier concentrations, this follows from exchange terms in the interband density matrix equations.
For an accurate analysis of delay times and saturation phenomena transient models are implemented as explicit algorithms, Crank-Nicolson schemes and fully implicit algorithms.

Calculation

A laser-modulator structure (InGaAlAs/InP) is shown, where both regions contain the same active regions (Fig. 1). Fig. 2 shows the absorption spectra (averaged over the respective active region) for modulator mode and the contributions of the laser and modulator to it. The laser region has a huge damping impact on the light in modulator mode, as absorption in this region is very effective.

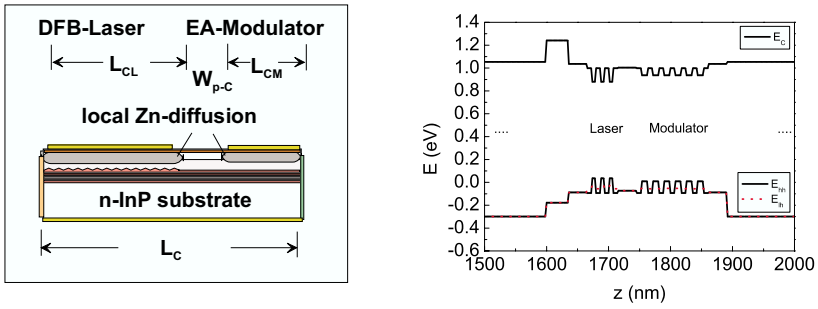


Fig. 1. Left: MESA-Structure of the Laser-Modulator Device; Right: Band Structure of the Active Region.

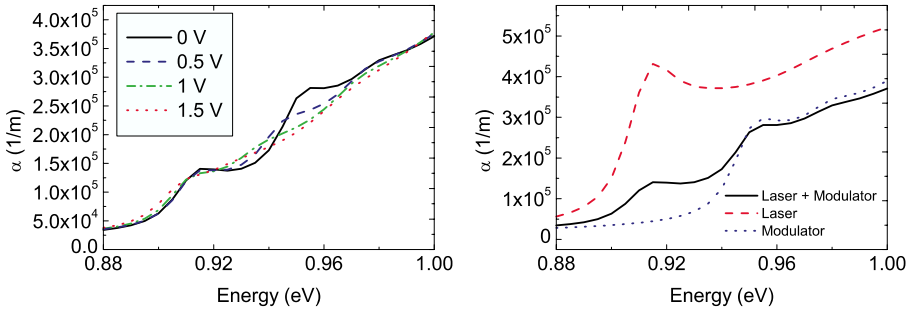


Fig. 2. Left: Absorption Spectra of the Device for Modulator Mode; Right: Contributions of Laser and Modulator to the Absorption

[1] A. Ahland, D. Schulz, and E. Voges, "Modelling and design of electroabsorption modulators on GaInAsP," *Int. J. Electron. Commun. (AEÜ)*, Vol. 52, No. 5, 322–328, 1998.

[2] G. Bastard and J.A. Brum, "Electronic states in semiconductor heterostructures," *IEEE J. Quantum Electron.*, Vol. 22, No. 9, 1625–1644, 1986.

[3] M. Altarelli, *Band structure, impurities and excitons in superlattices, in:* Proceedings of Les Houches Winterschool Semiconductor Superlattices and Heterojunctions, G. Allan, G. Bastard, N. Boccara, M. Lanno, M. Voos, Springer.

[4] A. Ahland, M. Wiedenhaus, D. Schulz, and E. Voges, "Calculation of exciton absorption in arbitrary layered semiconductor nanostructures with exact treatment of the Coulomb singularity," *IEEE J. Quantum Electron.*, Vol. 36, No. 7, 842–848, 2000.

[5] A. Ahland, D. Schulz, and E. Voges, "Accurate mesh truncation for Schrödinger equations by a perfectly matched layer absorber: Application to the calculation of optical spectra," *Phys. Rev. B*, Vol. 60, No. 8, r5109–5112, 1999.

[6] H. K. Gummel, "A self-consistent iterative scheme for one-dimensional steady state transistor calculations," *IEEE Trans. Electron Devices*, Vol. 11, No. 10, 455–465, 1964.

[7] D. L. Scharfetter and H. K. Gummel, "Large-signal analysis of a silicon read diode oscillator," *Solid State Electronics*, Vol. 16, No. 1, 64–77, 1969.

[8] M. Wiedenhaus, A. Ahland, D. Schulz, and E. Voges, "Dynamical simulation of quantum well structures," *IEEE J. Quantum Electr.*, Vol. 37, No. 5, 684–690, 2001.

Experimental and Theoretical Analysis of Polarization Insensitive Integrated-Waveguides Fabricated using Ion Implantation-Induced Disordering

H.S. Djie*, S.L. Ng, O. Gunawan, P. Dowd
[1]Photonics Research Group, School of Electrical and Electronic Engineering,
Nanyang Technological University, Singapore 639798
*hery@pmail.ntu.edu.sg

V. Aimez, J. Beauvais and J. Beerens
Centre de recherche sur les propriétés électroniques des matériaux avancés,
Département de Génie Électrique et Génie Informatique, Université de Sherbrooke, Sherbrooke,
Québec, Canada J1K 2R1

A theoretical model of the quantum well waveguide interdiffusion process has been developed to understand the polarization insensitive behavior through the strain build up at 1.55 μm-wavelength operation using the low energy ion implantation-induced disordering.

Keywords: waveguide, polarization, quantum well intermixing, ion implantation.

Introduction

Quantum well (QW) waveguide on lattice-matched InGaAs/InP laser structures have exhibited an inherent drawback: a strong polarization dependence on the incident light (transverse electric (TE) and transverse magnetic (TM)). This is due to the separation between the electron-light-hole (E-LH) and the electron-heavy-hole (E-HH) transition energies in an unstrained QW, resulting in a large discrepancy between TE and TM gain at any operating wavelength. As a result, this leads to polarization sensitive performance, which is disadvantageous, as the light polarization would not be preserved after travelling through a given distance. In recent years, Quantum well intermixing (QWI) based on the ion implantation–induced disordering (IID) technique has been used as a successful photonic integration technique [1]. The interdiffusion of QW and barrier material has been shown to modify the strain at the QW, and hence the HH and LH band splitting [1,2,3]. This indicates the possibility of using the IID technique to produce polarization-insensitive QW waveguide structures, which could interconnect the multiple photonic devices for photonic integration purposes, such as laser, modulator, amplifier etc in a single chip.

In this work, we report on the polarization insensitive performance of intermixed QW waveguides using a lattice-matched InGaAs/InGaAsP QW structure, and operating at a wavelength of about 1.55 μm. The fabrication method is based on the combination of using gray-mask lithography and a low-energy As and P ion-implantation process at 360 keV [4]. To understand the polarization-dependent behavior of the fabricated QW waveguide, a theoretical model based on interdiffusion of group III and V atoms through the strain build-up and the refractive index change has been developed.

Theoretical Model

In the $In_xGa_{1-x}As_yP_{1-y}$ QWs structure, In and Ga represent the group-III sublattices while As and P represent the two group-V sublattices. The extent of the interdiffusion can be characterized by the diffusion length parameter, $L_d = \sqrt{D\,t}$, where D is the diffusion coefficient and t is the diffusion time normally associated with annealing time. The diffusion length ratio of group-V to group-III can be defined as interdiffusion ratio $k = L_{dV}/L_{dIII}$, which $L_{d\,III}$ and $L_{d\,V}$ denote the diffusion length of group-III and -V respectively. Given additional knowledge of k, and the strain contribution is known, the more accurate band edge profile can be calculated. Assuming Fick's law and

concentration independent diffusion coefficients, the concentration profile of the QW can be derived in term of superposition of error functions. The group-III concentration in the active layer profile can be expressed as a superposition of the active layers:

$$x(z, L_{dIII}) = x_B + \sum_{n=1}^{N} \Delta x_n \left[1 - \frac{1}{2} erf\left(\frac{z + \frac{1}{2} L_{Zn}}{2L_{dIII}} \right) + \frac{1}{2} erf\left(\frac{z - \frac{1}{2} L_{Zn}}{2L_{dIII}} \right) \right] \quad (1)$$

where $x(z,L_{dIII})$ is the group-III concentration and x_B is the concentration at the outer barrier, Δx_n is the difference in the concentration of the subsequent layers, z is the direction along growth, L_{Zn} is the nth layer's width and n is the QW layer number. The group-V concentration can be formulated using the analogy of Eq (1). After interdiffusion process, the QW confinement profiles (V_r) calculation of C, HH, and LH is expressed as:

$$V_r(z) = Q_r \left[E_g(z) - E_{go} - S_{r\,biaxial}(x, y) \right] \pm S_{r\,uniaxial}(x, y) + z q_e E_{Field} \quad (2)$$

Q_r is the band offset splitting ratio, E_g is the energy bandgap, $S_{r\ biaxial}$ is the change in the bulk band gap due to the biaxial component of strain and the $S_{r\ uniaxial}$ is the potential corresponding to the HH and LH band edge splitting induced by the uniaxial component of strain. The positive sign represents the confined HH profile, the negative sign represents the confined LH profile, and for the confined electron profile, $S_{C\ uniaxial}$, is equal to zero. The presence of an applied external field is denoted as E_{Field}. All the parameters above are assumed to obey Vegard's law, so that they depend directly on the compositional profile across the QW. The sub-band states in the QW were calculated [5] by solving the Ben Daniel Duke's equation, through transformation of the differential equation into an eigen-value matrix equation, called the Finite Difference Eigen Value (FDEV) method.

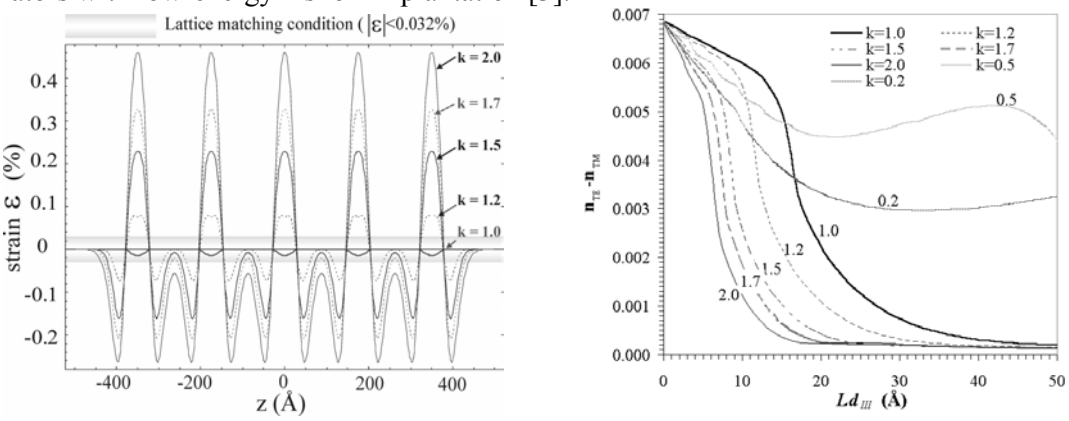
Based on the interdiffused composition profile of the QW layers, the refractive index profiles in the transparency region, where the transition occurs in the centre of Brillouin zone, can be calculated using Interband Transition Model [6]. Since the operating wavelength is apart from the bandgap of devices, the effective index of QWs structure in the transparency region is then approximated by the root mean square (RMS) extended model [7].

Experimental Works

The QW waveguide laser structure was designed for wavelength operation at around 1.55 μm, grown by metal-organic vapour phase epitaxy (MOVPE) on a (100)-orientated n+-type S-doped InP-substrates [5]. It consists of an undoped lattice-matched InGaAs/InGaAsP/InP QW material with five 5.5 nm wide $In_{0.53}Ga_{0.47}As$ wells, separated by six 12 nm InGaAsP barriers and utilised GRIN optical confinement layers. The as-grown sample gave a photoluminescence (PL) peak at 1.55 μm at room temperature. The waveguide sample was first coated with 450 nm and 900 nm thick SiO_2 layer, to minimize the damage due to 360 keV As and P ions. Next, a photolithography step was carried out to transfer the gray patterns on to the samples. A single step reactive ion etching (RIE) was then performed to transfer the graded photo-resist pattern into SiO_2 such that 10 different thickness of SiO_2, ranging from 0 nm to 450 nm (As) and 900 nm (P) were achieved across the wafer to perform different degrees of intermixing. The sample was then implanted at 200 ºC with As dose of $1x10^{14}cm^{-2}$, accelerated at 360keV with the ion angle tilted by 7º. The created point defects are subsequently diffused through the QW by a rapid thermal processor (RTP) at 590 ºC for 2 min. As-grown samples (without implantation) were included into each run to act as control samples. As a result, 10 degrees of intermixing can be obtained laterally across the wafer by introducing different concentration of impurities into materials. Each individual waveguide has dimensions of 400x500 μm^2 with a 50 μm wide active window, 500 μm cavity length and 20 μm wide isolation trenches. To conduct the photocurrent absorption measurement for observation of the polarization behaviour between TE and TM modes, the electrodes are defined on the top and bottom of waveguides after thinning down the sample to 180 μm.

Results and Discussion

It has been reported that the group-V interdiffusion ratio is faster than group-III (k>1) for InGaAs/InP QW amplifiers with high-energy P ion implantation [8] and electro-absorption (EA) modulators with low-energy As ion implantation [3].



(a) (b)

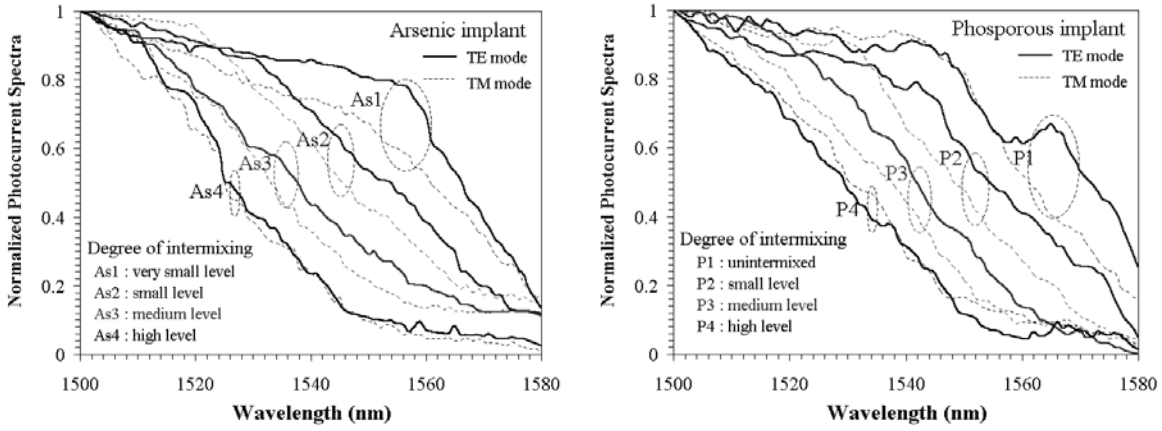
Figure 1 (a) The in-plane strain build-up of interdiffused QW waveguide with different interdiffusion ratios at L_{DIII}=10 Å (b) Refractive index change between TE and TM at 1.55 μm operation at different interdiffusion ratios and diffusion lengths

The in-plane strain profile in Figure 1 (a) shows interesting feature of the strain buildup with different diffusion length ratio, varied from *1.0<k<2.0* . Ld_{III} is taken 10Å for correspond the large strain build-up difference within the wells. The QWs structure is no longer lattice-matched (ε>0.032%) after interdiffusion at *k>1.0* and shows the presence of both compressive and tensile strains across the structure due atoms contents change, dominated by group V atoms. Both the compressive and tensile strain exhibit the tendency to increase as the interdiffusion ratio *k* increase and the tensile strain value at the center of well is higher than the compressive strain in the barrier close to interface for the same interdiffusion ratio. This presence of internal strain build-up not only shifts the band edge energies but also modifies the refractive index for different polarization mode.

Figure 1 (b) shows the refractive index difference of TE and TM modes at *0.2<k<2.0* on the different interdiffusion levels. At Ld_{III}=0, the uninterdiffused refractive index difference between TE and TM modes is 0.0069 or 0.2 %. The refractive index changes of TE and TM modes are strongly dependent on the interdiffusion ratio *k* and diffusion length. At *k<1.0*, the interdiffusion ratio assumes that group-III is faster than group-V and it shows the polarization degeneracy at higher interdiffusion degree but it then saturates at refractive index change greater than 0.003. While at *k>1.0*, the refractive index difference between TE and TM tends to zero at the sufficiently high interdiffusion level. This model implies polarization independent behavior of the waveguide can be achieved for a certain diffusion length of group III atoms. As *k* increases, it requires a shorter group III diffusion length to produce polarization insensitive behavior, due to higher strain build-up across the structure. Thus choosing the appropriate implantation level, and hence interdiffusion level, can lead to a merging of the TE and TM refractive index profiles, resulting in polarization-independent performance of the interdiffused QW waveguide.

Fabricated QW waveguides using ion implantation- induced disordering have been characterized at room temperature (RT) through photocurrent measurements, using the end-fire-coupling technique to couple the light from a tunable laser diode, operating between 1500 nm and 1580 nm. The polarization-resolved photocurrent absorption spectra for selected waveguides, which have undergone different degree of intermixing, are shown in Figure 2. The energy blue shifts, resulted from levels are 11 nm, 29 nm, 46 nm, 65 nm for As ions and 0 nm, 18 nm, 53 nm, 71 nm

for P ions. It can be observed that there is a quenching of the excitonic peak at higher diffusion lengths due to the more disordered QW structure, making the excitonic bond weaker. The photocurrent absorption curves have been blue-shifted as a function of SiO_2 thickness, and hence the degree of the quantum well intermixing. As the SiO_2 thickness decreases, the diffusion coefficients increases thus allowing higher point-defects created by ion implantation. For the waveguides formed using both As and P ion implantation, it can be seen that the measured bandgap energy with TE (solid lines) measurement is smaller than that of TM (dashed lines) measurement for each device. The separation of the TE and TM photocurrent absorption curves for a given waveguide decreases significantly as the degree of intermixing increases. Thus, the photocurrent curves at the highest levels of intermixing are virtually identical between TE and TM then lead to polarization independent behaviour of fabricated waveguides using low-energy ion-implantation process at 360 keV.



(a) (b)

Figure 2. Polarization-resolved TE-TM photocurrent absorption curves of intermixed QW waveguides with different degrees of intermixing for (a) As ions and (b) P ions

Conclusions

An interdiffusion model that includes strain build-up effect at different interdiffusion ratios of group-III and -V atoms has been developed to understand the polarization dependent behaviour of of InGaAs/InGaAsP/InP QW waveguide structures that have undergone different degrees of intermixing. Polarization insensitive waveguide operation has been demonstrated by proper choice of implantation mask thickness, linked to the amount of blueshift obtained and interdiffusion level. The blue shift amount of 65 nm and 71 nm for As and P ion respectively is sufficient to fabricate a transparent waveguide in polarization insensitive fashion.

[1] S. Charbonneau et.al, *J. Select. Quantum Electron.* **4**, 772-793, 1998.
[2] W.C.H. Choy et.al, *J. Quantum Electron.* **35**, 913-921, 1999.
[3] S.L. Ng et. al., *Jpn. J. Appl. Phys.* **41**, 1080-1084, 2002.
[4] S.L. Ng et. al, *Electron. Lett.* **38**, 241-242, 2002.
[5] H.S. Djie et. al, *IEE Optoelectron.*, **149**, 138-144, 2002.
[6] S. Adachi, *Physical Properties of III-V Semiconductor Compounds* (John Willey&Sons, New York, 1992).
[7] D.A. Trivedi and N.G. Anderson, *Guided Wave Optoelectronics* (Plenum Press, New York, 1995).
[8] H. Chen et al, *Appl. Phys. Lett.* **75**, 79-81, 1999.

Radiation to Guided Modes Power Transfer for the Characterization of Reverse-Proton-Exchanged Waveguides

M. Marangoni, R. Osellame, R. Ramponi,
INFM, Dipartimento di Fisica-Politecnico and IFN-CNR, Piazza L. da Vinci 32, 20133 Milan, Italy
phone +39-02-23996156; fax +39-02-23996126; e-mail marco.marangoni@.polimi.it

E. Giorgetti
IFAC, Istituto di Fisica Applicata "Nello Carrara"; Via Panciatichi 64, 50127 Firenze, Italy

The characterization of buried waveguides realized through reverse-proton-exchange in lithium niobate is achieved in a non-conventional way by measuring the coupling angles of radiation modes giving phase matching with second harmonic guided modes

Keywords: reverse-proton-exchanged waveguides, second harmonic generation.

Introduction

Buried waveguides are attracting an increasing interest in many fields of integrated optics since they allow a reduction of scattering losses with respect to conventional waveguides lying on the surface of the substrate, and, moreover, they present a nearly symmetrical refractive index-profile in the depth direction, which results in an improved matching between fibre and waveguide fields [1,2]. In the case of guiding structures realized for second order nonlinear interactions, they present a further advantage as to a better fields overlap between modes at different frequencies. By exploiting this feature in a second-harmonic generation process from a fundamental field at 1.55μm, a normalized conversion efficiency of 150% $W^{-1}cm^{-2}$ has been recently achieved in reverse-proton-exhanged (RPE) waveguides [3] realized in periodically-poled lithium niobate .

For RPE waveguides in lithium niobate and in lithium tantalate, no exhaustive modelling of the fabrication process has been reported so far in the literature. One of the main reasons is that, due to the buried refractive index profile, it is not possible to fully exploit standard characterization techniques based on prism coupling, such as m-lines spectroscopy for planar waveguides [4]. The field profile of the low order modes is in fact so confined below the substrate surface that the overlap with the field generated below the prism by total reflection is not sufficent for coupling. Only the effective indices of high order modes can thus be measured, and this fact limits the accuracy in the determination of the refractive index profile and hence in the modelling of the waveguides fabrication process.

This paper is addressed to the characterization of planar RPE waveguides and describes a new method which allows the determination of the effective refractive indices (n_{eff}) of the guided modes, even of the lower order ones. The method exploits a second harmonic generation process between fundamental (ω) ordinary radiation modes, coupled into the structure through a conventional prism, and second harmonic (2ω) extraordinary guided modes, which are the only guided modes supported by RPE waveguides [5]. When phase matching occurs, the effective index of the guided mode at 2ω equals that of the radiation mode at ω, so that the former can be easily determined from the coupling angle of the latter. Preliminary results obtained by applying such method to a multi-mode RPE waveguide realized in lithium niobate are presented and discussed.

Operation principle

The method exploits the second harmonic generation process schematically reported in Fig.1, where the fundamental (ω) field is given by prism-coupled radiation modes of a RPE waveguide while the second harmonic (2ω) field by guided modes. The key point of the operation principle is that phase-matching between ω radiation and 2ω guided modes can be satisfied in lithium niobate if the former present an ordinary polarization and the latter an extraordinary one. When such a birefringence phase matching occurs, the effective indices of the interacting modes are the same, i.e. $n_{eff}^{\omega} = n_{eff}^{2\omega}$, so that the n_{eff} of the 2ω guided modes can be determined from the coupling angle θ of the ω radiation modes. It is worth pointing out that a direct prism-coupling of the guided modes of RPE waveguides is very often not possible in the case of the lowest order modes, whose field does not superimpose the evanescent field tail generated by total reflection below the prism base. On the contrary, by use of radiation modes, which deeply extend inside the substrate, a sufficient fields overlap is achieved, even with the most confined modes.

The method thus exploits an interaction between two orthogonally polarized modes through the d_{31} nonlinear coefficient of lithium niobate. In order to achieve phase matching it is worth pointing out that, since ω and 2ω modes are respectively guided and radiation-like modes, the n_{eff} at ω is lower than the substrate ordinary index, i.e $n_{eff}^{\omega} < n_{o}^{\omega}$, while the n_{eff} at 2ω is higher than the substrate extraordinary index, i.e. $n_{eff}^{2\omega} > n_{e}^{2\omega}$. As a consequence, phase matching occurs only if $n_{e}^{2\omega} < n_{eff}^{2\omega} < n_{o}^{\omega}$. If the ω frequency corresponds to a wavelength $\lambda^{\omega} = 1.55\mu m$, one has $n_{e}^{2\omega} = 2.1788$ and $n_{o}^{\omega} = 2.2112$ [6]: therefore, every guided mode at 2ω can be phase-matched provided that the index change does not exceed ~0.033. The latter is a commonly satisfied condition for α-crystallographic phase waveguides [7]. The method thus proves suitable for the full characterization of most RPE waveguides, and, furthermore, it allows one to obtain directly the n_{eff} at a wavelength $\lambda^{2\omega} = 0.775\mu m$, which is particularly useful when the poling period of waveguides designed for nonlinear processes in the telecom bandwidth are to be designed [3].

Before going into the details of the experimental set-up and results, two further remarks emerge from the operation principle: i) the interaction length of the process is necessarily limited to the dimensions of the coupling region and the effective interaction area suffers from the poor overlap between ω and 2ω fields, thus resulting in a modest conversion efficiency. However, this interaction is not aimed to the best conversion efficiency but to characterization purposes, and, moreover, it involves a new interesting configuration where guided modes are pumped by radiation modes; ii) as in the Cerenkov second harmonic generation process [8], phase matching is very easy to achieve since radiation modes are characterized by a continuous range of effective indices;

Experimental set-up

The experimental set-up is sketched in Fig.1. The laser source is a parametric amplifier pumped by a 10Hz duplicated Nd:Yag laser providing pulses about 20ps long. The energy-per-pulse is kept below 10μJ before the coupling prism by means of additional filters. A beam-splitter (Bs), a diaphragm (D) previously aligned with the laser beam, and an InGaAs photo-detector (Pd1) are used to obtain the orthogonality between the beam and the prism, so to fix the zero angle for the following rotations. A cylindrical lens (L) having f=100mm provides a focusing in the plane of the waveguide, so to increase the energy density in the interaction region without affecting the mode-selectivity of the prism coupling technique. A silicon diode placed just at the end of the waveguide

is used to detect the second harmonic beam. Once the orthogonality condition is reached, the prism-waveguide ensemble is rotated until second harmonic is detected by Pd2. The phase-matching condition is finely tuned by varying the angle θ until maximum reading is obtained from Pd2. The n_{eff} of the 2ω guided mode, equal to the n_{eff} of the ω radiation one, is then readily calculated from θ.

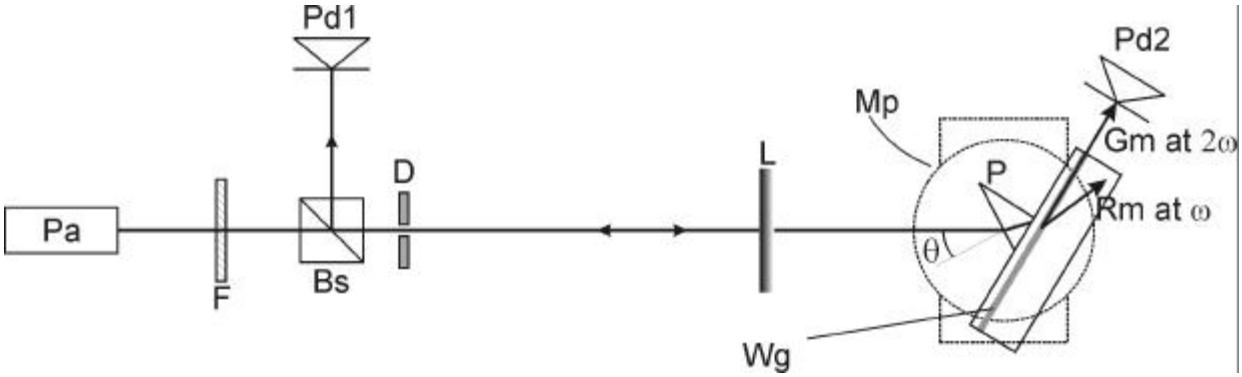


Fig.1 Experimental set-up: parametric amplifier (Pa), filters (F), beam-splitter (Bs), InGaAs detector (Pd1), diaphragm (D), cylindrical lens (L), prism (P), waveguide (Wg), silicon detector (Pd2), Gm (extraordinary guided mode), Rm (ordinary radiation mode).

Experimental results and discussion

The method was applied to the characterization of a Z-cut waveguide whose fabrication parameters were chosen in order to reach an α crystallographic phase for the guiding layer ($\Delta n<\sim 0.3$ at $\lambda=0.633\mu m$) and a number of modes at $\lambda^{2\omega} = 0.775\mu m$ sufficient to obtain an accurate determination of the refractive index profile (at least 4/5). The proton exchange process was performed at T=247°C for 12.5h in a benzoic acid melt diluted with 1% lithium benzoate, followed by an annealing of 11.3h at T=350°C. The reverse exchange was obtained by dipping the sample for 18h at 320°C in an eutectic melt composed by $NaNO_3$, $LiNO_3$ and KNO_3.

The coupling angle of 1.55μm TE-polarized ordinary radiation modes was varied until a second harmonic TM-polarized extraordinary guided mode was generated. In this way, four phase matching conditions were reached, each corresponding to a different second harmonic mode. The n_{eff} of the guided modes, as calculated from the coupling angles of the radiation modes, are reported in the first column of Table I.

Table I Effective refractive indices n_{eff} at 0.775μm as determined through the method proposed (1) and the conventional m-lines spectroscopy (2).

Mode	n_{eff} (1)	n_{eff} (2)
TM_0	2.1908	-
TM_1	2.1865	-
TM_2	2.1830	2.1830
TM_3	2.1807	2.1809

In order to verify the reliability of the method, the n_{eff} were also determined through an independent measurement. To this aim, a conventional m-lines spectroscopy technique was applied at 0.775μm by means of a Ti: sapphire laser, obtaining the n_{eff} reported in the second column of Table I. The agreement between the two sets of n_{eff} is really excellent, even if the comparison is not possible for TM_0 and TM_1 modes, that can not be directly coupled by prism due to the lack of a sufficient fields overlap. The method thus proves as the only mean to capture the n_{eff} of the lowest order modes, and particularly of the TM_0 mode, whose knowledge is of the uppermost importance for the design of poling periods of all-optical devices based on χ^2 processes in RPE waveguides. Further measurements are currently in progress on other waveguides realized with different fabrication parameters in order to achieve a comprehensive investigation of the reverse-proton-exchange process.

Conclusions

A new configuration for the second harmonic generation process, involving fundamental ordinary radiation modes and second harmonic extraordinary guided modes, has been proposed and demonstrated in RPE waveguides in lithium niobate, which are nowadays the most efficient guiding structures for all-optical nonlinear processes.. This method proved very effective for an accurate determination of the effective refractive indices of the guided modes, even of the lower order ones.

References

[1] G. Sorbello, S. Taccheo, M. Marano, M. Marangoni, R. Osellame, R. Ramponi, P. Laporta, *Opt. Mat.* **17**, 425-435, 2001.

[2] Y. N. Korkishko, V. A. Fedorov, T. M. Morozova, F. Caccavale, F. Gonella, F. Segato, *J. Opt. Soc. Am A*, **15**, 1838-1842, 1998.

[3] K. R. Parameswaran, R. K. Route, J. R. Kurz, V. Roussev, M. M. Fejer, M. Fujimura, *Opt. Lett.* **27**, 179-181, 2002.

[4] P. K. Tien, R. Ulrich, *J. Opt. Soc. Am.* **60**, 1325-1337, 1970.

[5] J. L. Jackel, C. E. Rice, J. J. Veselka, *Appl. Phys. Lett.* **41**, 607-608, 1982.

[6] G. J Edwards, M Lawrence, *Opt. Quantum Electron.* **16**, 373-374, 1984.

[7] Y. N. Korkishko, V. A. Fedorov, *J. Appl. Phys.* **82**, 1010-1017, 1997.

[8] H. Tamada, *IEEE J. Quantum. Electron.* **26**, 1821-1826, 1991.

Amplified Spontaneous Emission in Broad-band Confining Embedded Strips Produced By Electron-Beam Lithography in LiF Crystals and Films

Rosa Maria Montereali, Angelo Pace
ENEA, C.R. Frascati, Tecnologie Fisiche Avanzate, P.O.Box 65, 00044 Frascati, Roma, Italy
montereali@frascati.enea.it

Marco Montecchi, Enrico Nichelatti
ENEA, C.R. Casaccia, Tecnologie Fisiche Avanzate, Via Anguillarese 301, 00060 S. Maria di Galeria, Roma (Italy)

Antonio Grilli, Massimo Piccinini
INFN-LNF, Via E. Fermi 40, 00044 Frascati, Roma, Italy

Amplified spontaneous emission of aggregate colour centres, laser active in a broad wavelength interval in the visible, has been measured in confining embedded strips produced by electron-beam lithography in lithium fluoride crystals and films.

Keywords: amplified spontaneous emission, colour centres, Lithium Fluoride, photoluminescence

Introduction

Nowadays a renewed interest has been increasing for broad-band emitting materials. The area of growth and characterisation of thin films has seen a considerable expansion due to the need for a substantial shrink of scale and cost of optical devices. Colour centres (CCs), consisting in lattice vacancies trapping electrons or holes, are among the most investigated electronic defects in insulating materials [1], and in particular in ionic crystals [2]. Several of them are used for tuneable solid-state lasers due to the inhomogeneous broadening of their emission bands characterised by large oscillator strength and high quantum efficiencies [3].

Recently very promising results have been obtained in the generation [4], confinement [5] and amplification [6] at room temperature (RT) of visible light in active channel waveguides produced by electron beam lithography (EBL) at the surface of Lithium Fluoride (LiF) crystals. The limited penetration (from about 0.1 to 3.7 μm) of low energy (2-20 keV) electrons allows the formation of stable primary and aggregate CCs in an irradiated layer of controlled depth located at the surface of the crystalline materials. A local modification of the complex refractive index in this irradiated layer is induced by CCs embedded in it [7]. In particular, the efficient formation of F_3^+ and F_2 laser-active defects (two electrons bound to three and two close anion vacancies, respectively), characterised by broad photoemission bands in the green and in the red spectral ranges and almost overlapped absorption bands located at around 450 nm [8], is accompanied by a simultaneous local increase of the real part of the refractive index in the same wavelength interval where their emission are located [7,9]. So through a direct-writing process it is possible to create an active channel waveguide.

Research activities about CCs in alkali halide films [10] started more recently. The use of EBL techniques allows the definition of coloured embedded strips at the surface of LiF films grown on different types of substrates. This approach shows high potentialities for the development of novel active waveguide devices, like miniaturised broad-band optical amplifiers and waveguide tuneable lasers, due to the peculiar optical characteristics of the irradiated material, to the lower cost and simpler fabrication processes as well as to the easier integration with optical fibres and other passive and active optical components.

Generation [11], confinement[12] and amplification [13] of visible light in active coloured embedded strips produced by low energy electrons at the surface of LiF films grown by thermal evaporation on few types of substrates have been demonstrated. However much efforts are required to improve their design, preparation and performances. In this work some peculiarities of the LiF

films with respect to single crystals are discussed, with particular emphasis on the amplification properties of LiF confining active strips based on CCs.

Experimental results and discussion

Several coloured strips were produced by EBL on LiF single crystals and polycrystalline films, grown by thermal evaporation on glass substrates, with irradiation doses in the range $10^{-3} \div 10^{-2}$ C/cm^2 and 12 keV electrons, whose penetration depth in LiF is estimated around 1.5 μm [14].

Photoluminescence (PL) represents a simple and powerful tool to investigate CCs formation efficiency and their optical behaviour, particularly on samples characterized by restricted geometries, like channels, which preclude the use of conventional optical absorption measurements.

On coloured LiF strips, photoemission measurements are generally performed by exciting the samples with the 458 nm line of an argon laser impinging on the irradiated sample surface and collecting the PL signal, properly filtered, by a photomultiplier (S20 response) placed on the same side of the sample. In this frontal geometry, the unconfined PL laterally emitted by the coloured strip is measured along the direction normal to the sample surface. The same set-up, in a perpendicular geometry between pumping source and detector, has been used to determine the optical gain coefficients *g* by measuring the amplified spontaneous emission (ASE) signal [15]. In this perpendicular geometry, the guided PL that comes out of the strip end is collected.

Fig.1 shows the RT photoemission spectra, acquired in the frontal geometry, of 25 μm wide coloured strips, irradiated by 12 keV electrons with a dose of 6×10^{-3} C/cm^2 in the same experimental conditions, at the surface of a LiF single crystal and of a LiF film of thickness 1.8 μm grown on a glass substrate at a temperature of 250°C. They consist of two broad emission bands, peaking at around 540 nm and 680 nm, typical of F_3^+ and F_2 CCs [8]; their intensities are about four times higher in film than in bulk, although their spectral features are quite similar. The increase in the visible photoemission signal from coloured LiF films is attributed to larger concentrations of F_3^+ and F_2 active defects. As a matter of fact, it is accompanied by a higher intensity of their superimposed absorption bands, located at 450 nm, as it has been measured on the same samples of Fig.1, irradiated on large areas with a dose of 10^{-4} C/cm^2. Their absorption spectra are reported in Fig.2: in the case of LiF film, this main absorption is superimposed to the interference fringes due to the refractive index difference between the LiF film (<1.39) and glass substrate (~1.5).

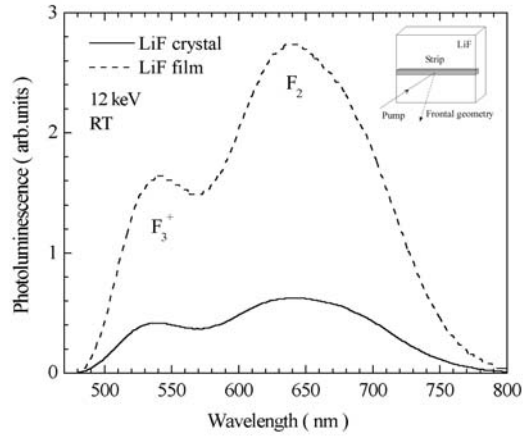


Fig.1. RT PL spectra of 25 μm wide strips coloured by 12 keV electrons in a LiF crystal (solid) and film (dashed) irradiated at RT in the same conditions. The frontal collecting scheme is reported in the inset.

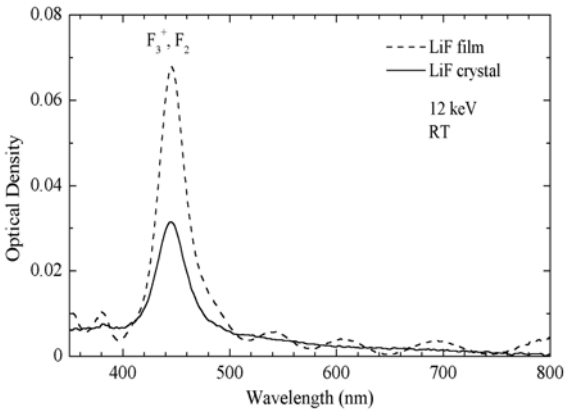


Fig.2. RT absorption spectra of a LiF crystal (solid) and the film of Fig.1 coloured by 12 keV electrons in the same conditions on a large area. They are roughly corrected for the absorption of the unirradiated part.

In terms of gain, ASE occurs when the spontaneous emission from a distribution of inverted systems is amplified by stimulated emission without the help of a resonant cavity. Sizeable optical gain coefficients, several cm^{-1}, have been measured at RT on the coloured strip induced by 12 keV electron beams on the LiF film thermally evaporated on glass substrates of Fig.1 [13] by means of the standard ASE technique [15]. At constant power density of the exciting beam, the photoemission spectra are collected in a perpendicular geometry between pumping source and detector as a function of the pumped length of the coloured strip, which is varied by moving a screen perpendicular to the exciting beam. Spontaneous luminescence was amplified (stimulated luminescence) as it passed through the excited volume to the edge of the sample. The excited medium can be treated as a simple one-dimensional optical amplifier. The optical gain has been determined by monitoring the ASE signal as function of the pumped length. The output signals, measured around the emission peaks of F_3^+ (540 nm) and F_2 (680 nm), show an exponential behaviour. The gain coefficients were computed in all the emission spectral range and amplification has been observed in the two intervals 510-590 nm and 620-710 nm, which are centred on the emission peaks of both the laser active defects.

On several strip waveguides, coloured by 12 keV electrons on LiF crystals at doses of $2.2x10^{-3}$, $3.3x10^{-3}$and $8.8x10^{-3}$ C/cm^2, emission spectra were acquired in the perpendicular geometry as a function of the pump power density in a quasi c.w. regime, keeping constant the length of the excited strip. Around the peak of the F_2 emission band, the signal supra-linearly grows by increasing the pump power [16]. Sizeable values of the gain coefficient, several cm^{-1}, have been obtained again. Their numerical values increase with increasing irradiation dose. The same supra-linear behaviour was observed in the wavelength range extending from 580 to 730 nm [17]. On these confining structures, a strong reduction of the F_3^+ emission band and a narrowing of the F_2 one are observed in the perpendicular geometry, as shown in Fig.3, where their ASE spectra are compared with the ASE spectrum of the coloured strip on LiF film in Fig.1. Both these effects are more pronounced for the coloured waveguides irradiated at higher doses. The typical F_3^+ and F_2 broad PL bands, due to the light isotropically emitted, are spectrally modified due to confinement effects at the interfaces with the lower refractive index surrounding media. The great differences they undergo upon waveguiding should be related to the wavelength-dependent behaviour of the complex refractive index of the irradiated layers [7,9].

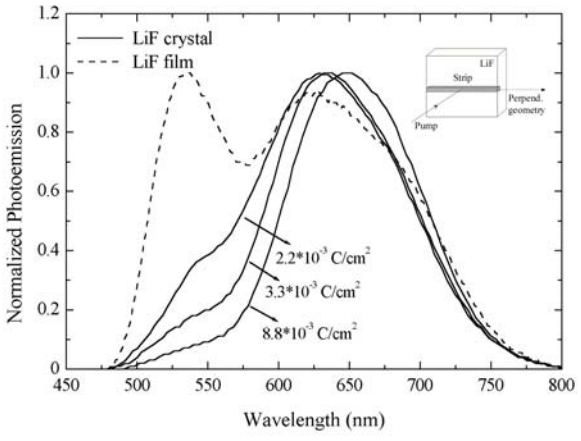


Fig.3. RT normalized ASE spectra of three strip waveguides coloured by 12 keV electrons at different doses in a LiF crystal (solid) and of the strip on film of Fig.1, measured for an excitation length of 2.5 mm at a power density of 0.2 W/cm^2. The perpendicular collecting scheme is reported in the inset.

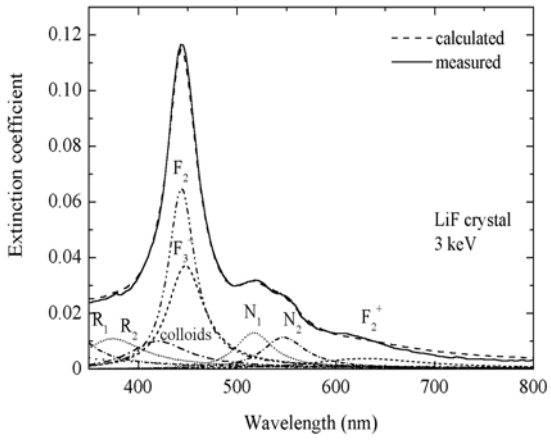


Fig.4. Extinction coefficient of a LiF crystal coloured by 3 keV electrons at RT on a large area. The measured curve is obtained through ellipsometry, the calculated one from spectrophotometry through a model [7], which allows computing the single contributions of different kinds on defects, is also plotted.

Higher defect densities imply the improvement of the confining properties of the waveguides; on the other hand, the presence of different aggregate CCs causes optical losses due to emitted light re-absorption. In the coloured LiF based amplifying strips under investigation, the net gain coefficient is independent from the position along the medium in the direction of amplification. It is expressed as the difference between the gain coefficient *g*, dependent on the luminescence process, and the losses α, due both to the optical quality of the active media as well as to other processes, like re-absorption. The absence of amplification in the green is probably due to parasitic centres, like the F_4 ones, which possess associated N_1 and N_2 absorption bands, peaked around 515 and 545 nm. Their presence is not distinguishable in the absorption spectra of Fig.2, but it is clearly appreciable in the extinction coefficient of the irradiated part of a LiF crystals heavily bombarded by low energy electrons with a dose of 10^{-1} C/cm^2 on a large area, shown in Fig.4. Its experimental values are in excellent agreement with the calculated ones.

Although the optical losses for light scattering, related to the quality of the hosting matrix, are higher in polycrystalline LiF films [12], they show less optical losses in the green spectral range than single crystals irradiated in similar conditions. This behaviour should be ascribed to the polycrystalline nature of LiF films, which increases the formation efficiency of visible active CCs, and also reduces the final densities of larger complex aggregate defects, like F_4. Further investigation could allow for a selective generation of the requested defects and therefore an improvement of light emission performance.

Acknowledgements

The authors thank Dr. G. Baldacchini (ENEA Frascati), Prof. E. Burattini (INFN-LNF), Prof. G.C. Righini and Dr. S. Pelli (CNR-IFAC, Florence) for valuable discussions.

[1] N. Itoh and M. Stoneham, *Materials Modification by Electronic Excitation* (N. Itoh and M. Stoneham, Cambridge University Press, 2000).
[2] W. B. Fowler, *Physics of Color Centers* (W. B. Fowler, New York and London, Academic Press, 1968).
[3] L. F. Mollenauer, *Tunable Lasers* (L. F. Mollenauer, Springer Verlag, Berlin, 1987).
[4] G. Baldacchini, M. Cremona, R. M. Montereali, L. C. Scavarda do Carmo, R. A. Nunes, S. Paciornik, F. Somma, V. Kalinov, *Opt. Commun.* **94,** 139-142, 1992.
[5] R. M. Montereali, A. Mancini, G. C. Righini and S. Pelli, *Opt. Commun.* **153**, 223-5, 1998.
[6] R. M. Montereali, M. Piccinini and E. Burattini, *Appl. Phys. Lett.* **78**(26), 4082-4, 2001.
[7] M. Montecchi, E. Nichelatti, A. Mancini and R. M. Montereali, *J. Appl. Phys.* **86**, 6, 3745-50, 1999.
[8] J. Nahum and D. A. Wiegand, *Phys. Rev.* **154**, 817-30, 1967.
[9] M. Montecchi, R. M. Montereali, E. Nichelatti, *Opt. Mater.* **17**, 347-50, 2001.
[10] R. M. Montereali, in *Handbook of Thin Film Materials*, Vol.3: Ferroelectric and Dielectric Thin Films (H. S. Nalwa, Academic Press, 2002) Ch.7, p.399-431.
[11] R. M. Montereali, G. Baldacchini and L. C. Scavarda do Carmo, *Thin Solid Films* **201**, 106-8, 1991.
[12] L. Fornarini, S. Martelli, A. Mancini, R. M. Montereali, S. Pelli, G. C. Righini, in Proc. 9th European Conference on Integrated Optics, ECIO'99, Turin, Italy, 1999, p.343-6.
[13] G. Baldacchini, A. Mancini, R. M. Montereali, S. Pelli, G. C. Righini, in Proc. 8th European Conference on Integrated Optics, ECIO'97, Stockolm, 1997, p.373-6.
[14] C. A. Andersen, *The Electron Microprobe* (T. D. McKinley, K. F. Heinrich, D. B. Wittry, New York, John Wiley, 1964).
[15] K. L. Shanklee, R. E. Nahory and R. F. Leheny, *J. Lum.* **7,** 284-309, 1973.
[16] O. Svelto, S. Taccheo, C. Svelto, *Opt. Commun.* **149,** 277-82,1998.
[17] R. M. Montereali and M. Piccinini, *Opt. Commun.* **209**, 201-8, 2002.

Optical and Structural Properties of Proton Exchanged $MgO:LiNbO_3$ waveguides

Yuri Korkishko, Vyacheslav Fedorov, Sergey Kostritskii, Evgeny Maslennikov, Marina Frolova, Alexander Alkaev

Moscow Institute of Electronic Technology (Technical University),
Moscow 124460, Zelenograd, Russia, *korkishk@chem.miee.ru*

We show that proton exchanged $MgO:LiNbO_3$ optical waveguides exhibit complex structural chemistry which is different from known for congruent material. It's shown that Annealing Proton Exchange process leads to strong degradation of surface region of waveguides, but Soft Proton Exchange preserves the crystal structure of $MgO:LiNbO_3$.

Keywords: proton exchange, magnesium doped lithium niobate, waveguide, crystal structure.

Introduction

Lithium niobate, $LiNbO_3$, is very important ferroelectric crystal with various acoustical, integrated optical and optoelectronic applications. Integrated optical devices require material improvements in optical homogeneity and optical damage resistance. It is known [1-3], that resistance to optical damage in $LiNbO_3$ is effectively improved if more than 4.5 mol.% MgO is added to the melt.

One of basic methods to make optical waveguides in $LiNbO_3$ crystals is proton exchange (PE) [4]. Despite the simplicity of the proton exchange technique, the PE $LiNbO_3$ waveguides exhibit very complex structural chemistry. Our works [5,6] have allowed us to identify seven different crystallographic phases, β_4, β_3, β_2, β_1, κ_2, κ_1 and α- $H_xLi_{1-x}NbO_3$, which can be realized in the PE $LiNbO_3$ waveguides. Annealing is an important parameter in the fabrication of PE waveguides. Actually, most of the published results were obtained using PE waveguides, whose index profiles indicate that they are in the α-phase. These waveguides can be fabricated by two step process, including proton exchange and subsequent annealing (APE waveguides [7]) or by one step process, so-called Soft Proton Exchange (SPE) [8,9]. In contrast to APE $LiNbO_3$, the SPE $LiNbO_3$ waveguides preserve nonlinear coefficients of bulk material [10].

Several fundamental issues in the fabrication of waveguides by proton exchange in $MgO:LiNbO_3$ have not been addressed to date. Previously published investigations of PE $MgO:LiNbO_3$ waveguides have been incomplete and restricted to particular fabrication process [11-15].

Up to date, there are no reports about crystallographic study on proton exchange layers in $Mg:LiNbO_3$. In the present paper we shall show that structural and optical properties of the different types of PE $MgO:LiNbO_3$ waveguides depend strongly on fabrication conditions.

Preparation of samples and their characterization

PE waveguides were fabricated in optical grade X-cut $MgO:LiNbO_3$ substrates, containing 5.5 mol.% of MgO, supplied by Crystal Technology, Inc.

As the source of PE we used benzoic acid whose acidity can be reduced by adding up to 5 wt.% of lithium benzoate. Postexchange annealing at 330°C was used to modify the parameters of the waveguides. HTPE process [9] has been performed in the mixture of stearic acid and lithium stearate. Soft Proton Exchange process has been realized by HTPE in melts with lithium stearate concentration higher than the threshold value. In this case uniform α-phase waveguides are formed.

In order to find modes effective indices, we measured excitation angles of dark m-lines of modes with one prism coupler setup at the 633 nm wavelength. The refractive index profiles throughout the guide depth were reconstructed by the IWKB technique [16]. The strains perpendicular to the substrate surface, ε''_{33}, were calculated from rocking curves on plane (220) obtained by double-crystal X-ray diffractometer DRON-3 (Cu $K\alpha_1$ radiation, Si (311) monochromator):

$$\varepsilon''_{33} = -\Delta\theta_{hkl} \cdot ctg\theta_{hkl} \quad (1)$$

where θ_{hkl} is the Bragg angle of the reflected surface plane for stress-free substrate.

Experimental results

Fig.1 shows the surface extraordinary index increase, Δn_e as a function of strain ε''_{33} for X-cut $MgO:LiNbO_3$ substrates. One can see that this structural phase diagram is absolutely different from such diagram, obtained for congruent material [6]. No doubt that some $MgO:H_xLi_{1-x}NbO_3$ phases exist, however, in contrast to structural phase diagram for congruent material [6], the possible phase transitions for PE $MgO:LiNbO_3$ are not so evident.

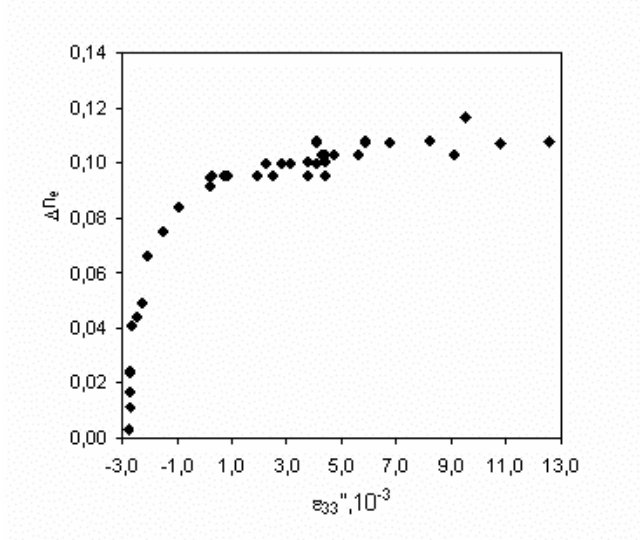


Fig.1. Dependence of the extraordinary index variation Δn_e measured at λ=633 nm versus the surface value of deformation ε''_{33} normal to surface plane.

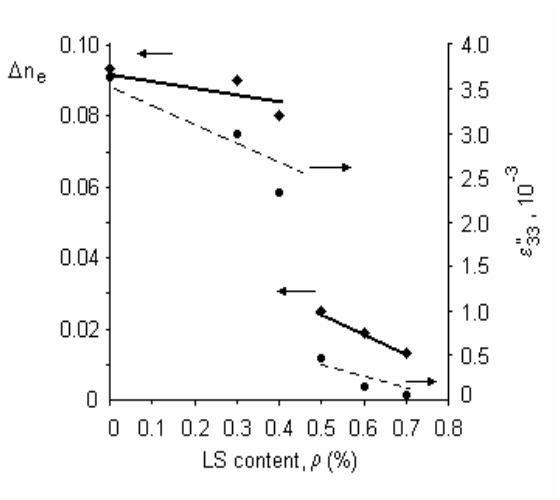


Fig.2 Refractive index change (rectangular dots, solid curve) and strains ε''_{33} (circular dots, dotted curve) as a function of melt composition in stearic acid + lithium stearate melts at 370°C.

Fig.2 shows the variation of the $MgO:H_xLi_{1-x}NbO_3$ surface value refractive index increment, Δn_e, and deformations ε''_{33} as a function of the LS content for HTPE at 370°C. The two regions can be clearly recognized. These regions correspond to, at least, two different phases. The Δn_e and ε''_{33} are found to be largely independent of melt composition for dilution up to threshold value, ρ_o (Fig.2). The α-phase $MgO:H_xLi_{1-x}NbO_3$ fabricated at $\rho>\rho_0$ is characterized by low index increment and deformations.

The rocking curves on plane (220) and refractive index profiles for X-cut PE $MgO:LiNbO_3$ samples obtained under different exchange and annealing conditions are presented in Fig. 3.

As exchanged waveguides, similar to PE waveguides in congruent $LiNbO_3$, are characterized by positive deformations ε''_{33}. Three peaks can be clear recognized at X-ray rocking curve (Fig.3a). Most probably, these three peaks correspond to three different phases in PE $MgO:LiNbO_3$. However, after some time of annealing, ε''_{33} becomes negative. It is possible to obtain waveguide with large index increment (Δn_e = 0.1) and with zero deformation ε''_{33} (Fig.3b). Future annealing leads to increasing of absolute value of negative deformation.

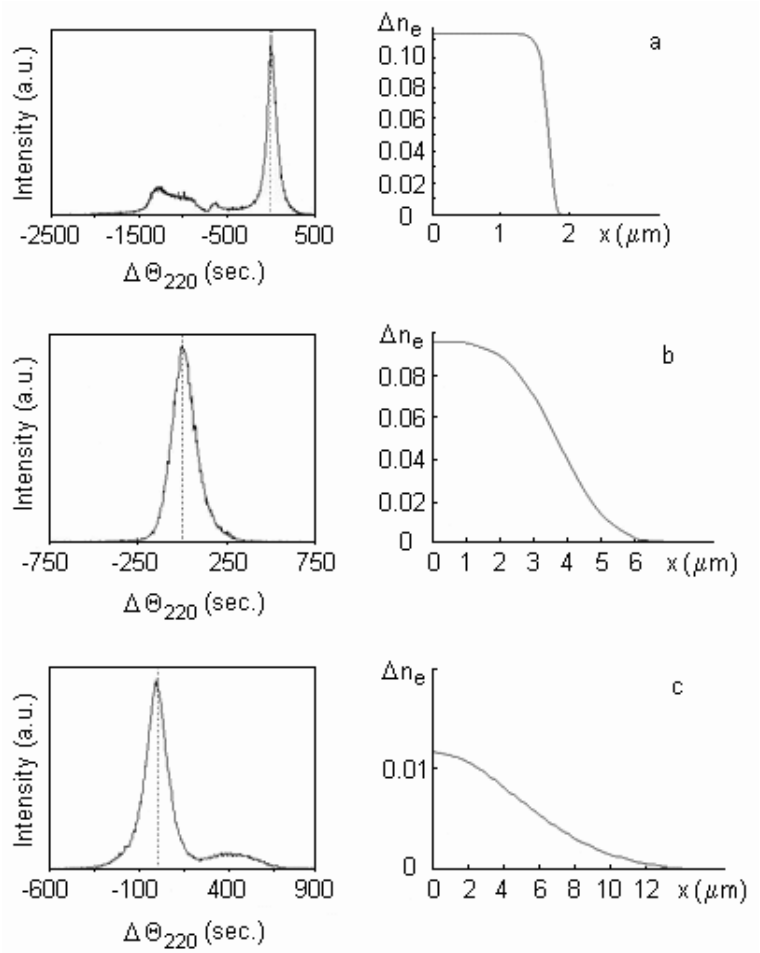


Fig.3. Evolution of X-ray rocking curves and refractive index profiles for PE MgO:$LiNbO_3$ sample, fabricated at benzoic acid melt at 220°C for 6 h with annealing at 330°C. a) as-exchanged sample; b) after 17.5 h of annealing; c) after 462 h of annealing.

It is very surprising that well annealed APE Mg:$LiNbO_3$ waveguides contain distorted layer with deformations $\varepsilon''_{33} \approx -3\cdot10^{-3}$. Rocking curves for APE samples with $\Delta n_e<0.1$ show broad additional peak (Fig.3c). Precise polishing shows that thickness of this layer is very close to thickness of initial as-exchanged layer.

It was obtained that this distorted layer is not been removed even after long reverse proton exchange process in $LiNO_3$-KNO_3-$NaNO_3$ melt. IR spectral measurements show that after RPE process at 330°C during 15 h, the intensity of -OH absorption at 3485 cm^{-1} becomes similar to one for initial MgO:$LiNbO_3$ crystal, however the rocking curve shows additional peak (Fig. 4) with even larger deformation than that for initial APE sample.

Therefore, one can conclude that APE process leads to structural damage of surface layer, that can be a reason of additional scattering of light in APE MgO:$LiNbO_3$ waveguides.

Fig.5 shows the X-ray rocking curve for HTPE MgO:$LiNbO_3$ sample fabricated at 370°C for 5 h at the melt with ρ=0.7%. One can see, that in contrast to α-phase MgO:$H_xLi_{1-x}NbO_3$ fabricated by APE technology (Fig.3c), the α-phase MgO:$H_xLi_{1-x}NbO_3$ prepared by HTPE technology characterized by absence of distorted surface layer. Therefore, the HTPE process preserves the crystal structure of α-phase MgO:$LiNbO_3$ waveguides. It is expected that such waveguides would show lower optical losses than APE waveguides.

Conclusion

The crystal structure and optical properties of PE MgO:$LiNbO_3$ structures are strongly depended on proton exchange and annealing conditions. Some crystal phases MgO:$H_xLi_{1-x}NbO_3$ can be generated on surface of MgO:$LiNbO_3$ single crystals depending on exchange and annealing conditions. It has been shown that traditional for congruent $LiNbO_3$ crystals APE technology leads to formation of distorted layer at the surface of MgO:$LiNbO_3$. It is expected that it would drastically increase the optical losses in APE MgO:$LiNbO_3$ waveguides. In contrast, the HTPE MgO:$LiNbO_3$ waveguides do not contain any distorted layer at the surface region. Therefore, such waveguides should show lower propagation losses.

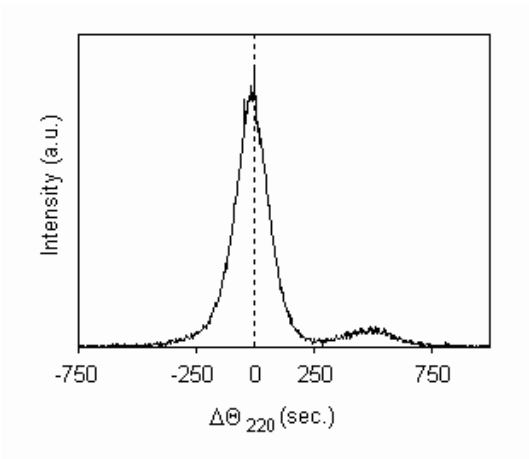


Fig.4 X-ray rocking curve for PE MgO:$LiNbO_3$ sample, fabricated at benzoic acid melt at 220°C for 6 h then annealed at 330°C for 552 h and treated at the melt $LiNO_3$-KNO_3-$NaNO_3$ at 320°C for 24 h.

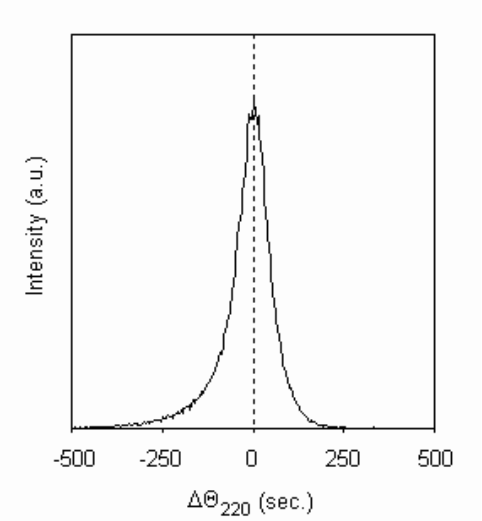


Fig. 5. X-ray rocking curve for HTPE MgO:$LiNbO_3$ sample fabricated at 370°C for 5 h at the melt with ρ=0.7%.

References

[1] D.E.Zelmon, D.L.Small, D.Jundt, *J.Opt.Soc.America B* **14**, 1663-1667, 1997.

[2] Gi-Guo Zhong, Jin Jian, Zhong-Kang Wu, *in Proc.11th Intern.Quantum Electronics Conf*., June 1980, IEEE Cat. No80, Ch.1561-0, p.631.

[3] V.Hinkov, *EMIS Datareviews series*, **No.28** (Ed.K.K.Wong), Ch.15.3, 396-397, 2002.

[4] J.L.Jackel, C.E.Rice, and J.J.Veselka, *Appl.Phys.Lett*. **41,** 607-608, 1982.

[5] Yu.N.Korkishko, V.A.Fedorov, Ion exchange in single crystals for integrated optics and optoelectronics (Cambridge International Science Publishing, Cambridge, UK, 516 p., 1999.

[6] Yu.N.Korkishko and V.A.Fedorov, *IEEE J. Sel. Topics Quantum Electron*., **2**, 187-196, 1996.

[7] P.G.Suchoski, T.K.Findakly, F.J.Leonberger, *Opt.Lett.* **13**, 1050-1052, 1988.

[8] Y.N. Korkishko, V.A. Fedorov, O.Y. Feoktistova, *IEEE J. Lightwave Technol.* **18**, 562-568 2000.

[9] P. Baldi, M.P. De Micheli, K. El Hadi, S. Nouh, A.C. Cino, P. Aschieri, D.B. Ostrowsky, *Opt. Eng*. **37**, 1193-1202, 1998.

[10] Yu.N.Korkishko, V.A.Fedorov, F.Laurell, *IEEE J. Selected Topics in Quantum Electron.* **6**, 132-142, 2000

[11 J.L.Jackel, *Electron.Lett.* **21**, 509-511, 1985.

[12] M.Digonnet, M.Fejer, R.Byer, *Opt.Lett.* **10**, 235-237, 1985.

[13] A.Loni, R.W.Keys, R.M. De La Rue, *J.Appl.Phys.* **67**, 3964-3967, 1990.

[14] G.Hagner, T.Bachmann, *Phys.stat.sol. (a),* **165**, 205-212, 1998.

[15] Z.Zhuo, T.G.Chong, Y.T.Chow, *Jpn.J.Appl.Phys.* **36**, 139-142, 1997.

[16] J.M.White, P.F.Heidrich, *Appl.Opt.* **15**. 151-155, 1976.

Electro-optic guided-wave router using nematic liquid crystals

Rita Asquini and Antonio d'Alessandro
Dept. Electronic Engineering & INFM, University of Rome "La Sapienza", Via Eudossiana 18, 00184 Rome-Italy.

Gaetano Assanto
N*OO*EL - Nonlinear Optics and Optoelectronics Lab., Dept. Electronic Engineering & INFM
University "Roma Tre", Via della Vasca Navale 84, 00146 Rome-Italy
assanto@ele.uniroma3.it

An original approach is illustrated and analyzed for the realization of an electro-optic waveguide router to be fabricated by standard liquid crystal technology. The proposed device enables complete switching with modulation voltages as small as 120 mV.

Keywords: guided-wave optics, liquid crystals, electro-optic devices, switching.

Introduction

In recent years a significantly large research activity has been undertaken aiming at the realization of passive integrated optics components for telecommunication networks and internet systems encompassing wavelength division multiplexing protocols [1]. While semiconductors, glass and lithium niobate are the most employed in this field, polymers and liquid crystals (LC) are promising solutions for a wide range of specific problems, and are actually used in thermo-optic and electro-optic elements [2]. Even more than polymers, liquid crystals are rather well known and offer such advantages as a mature technology, low cost, low driving voltages, low losses and wide spectral transparency from the visible to the near infrared [3-4].

In this Communication, we propose and investigate an optical routing/switching element consisting of a bi-modal liquid-crystal waveguide which can be electro-optically controlled and has two outstanding features: (i) its guiding properties depend and rely on the application of an external voltage; (ii) the structure can be driven to route an optical signal towards either of two outputs using a small voltage modulation. The device is based on a version of the well-known Y-junction, as described in [5]: from a two-mode guiding region, two identical mono-mode output branches depart with a small but finite angular separation. When both modes are injected at the input, the corresponding power will couple to one or another output channel depending on their relative phase, as sketched in Fig. 1. When employing an electro-optic dielectric, however, the relative phase and the corresponding interference between the two lowest-order eigenmodes in the bi-modal region can be controlled by varying the applied voltage: one of the two output channels can be preferentially excited as the resulting pattern will exhibit a maximum on the upper or lower portion of the transverse section (Fig. 1). A phase change of π will result, therefore, in complete switching or rerouting of the optical signal.

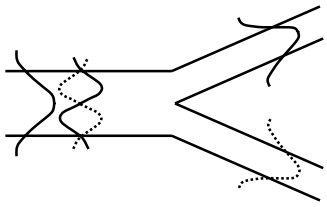


Fig. 1. Sketch of the field distribution due to two superimposed TM guided modes in a 1x2 optical switch encompassing an output Y-junction.

To this extent, we propose to employ electro-optic nematic liquid crystals, in the configuration represented in Fig. 2. A thin layer of nematic liquid crystal is sandwiched between fused quartz substrates with anchoring (Teflon, silica or Nylon) films to enforce a planar molecular orientation, i. e. one with LC molecules parallel to the interfaces. In such ordered form, a nematic LC is a

positive uniaxial (n_z>n_y with reference to Fig. 2). Transparent electrodes, e. g. indium tin oxide films, can be pre-deposited on the same plates to permit the application of an external voltage.

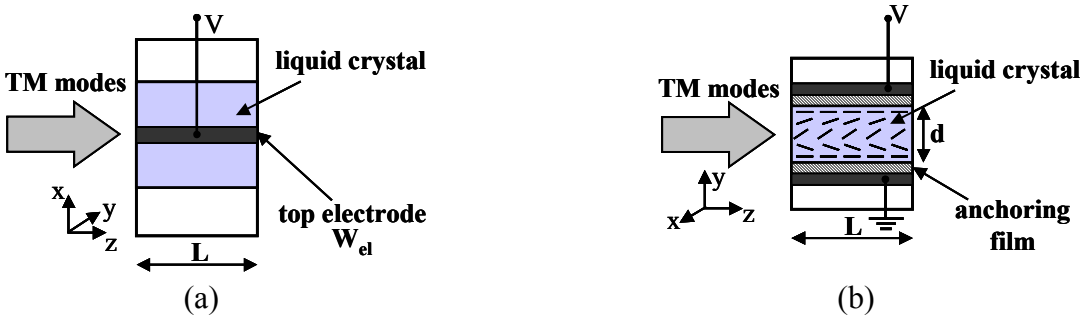


Fig. 2. Top (a) and side (b) views of the proposed nematic LC geometry .

With reference to the input portion of the proposed switching device (Fig. 1), the electrodes can be patterned in such a way (Fig. 2a) that a channel waveguide is formed in the LC medium only upon the application of a suitable voltage across the cell thickness d. The resulting electrostatic field, in fact, will induce dipoles and a torque on the elongated LC organic molecules, giving rise to their angular reorientation in the principal plane containing their axes and the dominant field component, i. e. the plane (y, z) in Fig. 2b. A voltage-controlled channel waveguide can then be obtained, with degree of confinement and cutoff depending on the external bias at each optical wavelength. In particular, the electrode width can be tailored to allow two-mode guidance in a given wavelength range of operation. Moreover, a slight change in voltage will perturb the phase velocity (i.e., the eigenvalue or effective index) of each of the two eigenmodes, leading to an overall relative phase shift between them upon propagation along z. For two modes interfering in z=L and producing an electric field profile with a maximum on one side of the 2-mode channel, a phase-change of π will switch the output to the other side.

Device design and voltage evaluation

In order to estimate the voltage required to obtain the correct tilt of the LC director $\boldsymbol{n} = (0, \sin\vartheta, \cos\vartheta)$ in our positive uniaxial and so define a bi-dimensional waveguide, we consider an applied electric field along y axis (Fig. 2b). ϑ is the angle between the director and the z axis. With no voltage applied to the cell, the director $\boldsymbol{n}$(y) is uniformly parallel to the z axis ($\vartheta = 0$), because of initial anchoring at top and bottom interfaces (Fig. 2b). A nonzero voltage can then force the elongated LC molecules to re-align and redistribute with their major axis closer to y in order to reduce the field-dipole interaction energy. While such reorientation will not be uniform across the thickness d of the cell due to the anchorage at the boundaries, an index gradient will be induced with a maximum value in y=d/2 ($\vartheta = \vartheta_m$), i. e., in the middle of the cell.

The director redistribution comes from elastic and electrostatic energy balance. The voltage needed to induce a particular angle ϑ_m in the middle of the LC cell can be derived by minimizing the total free energy [6-7]:

$$U = \int_0^d \left(U_{EL} + \Delta U_{EM}\right) dy \tag{1}$$

with U_{EL} the elastic energy density

$$U_{EL} = \frac{1}{2}\left(k_1 \cos^2\vartheta + k_3 \sin^2\vartheta\right)\left(\frac{d\vartheta}{dy}\right)^2 \tag{2}$$

and ΔU_{EM} the change of the electrostatic energy due to the reorientation of the molecular director:

$$\Delta U_{EM} = \frac{1}{2}\frac{D_y^2}{\left(\varepsilon_{\|}\sin^2\vartheta + \varepsilon_{\perp}\cos^2\vartheta\right)} - \frac{1}{2}\frac{D_y^2}{\varepsilon_{\perp}} \tag{3}$$

D_y being the y component of the displacement field vector, constant throughout the cell. k_1 and k_3 are splay and bend elastic constants of the considered LC, respectively, while $\varepsilon_{\|}$ and $\varepsilon_{\perp}$ are the dielectric constants parallel and perpendicular to **n**, respectively. The latters determine the anisotropy $\Delta\varepsilon = \varepsilon_{\|} - \varepsilon_{\perp}$. By minimizing the total free energy and imposing boundary conditions with **n** parallel to the quartz surfaces in y=0 and y=d,

$$\begin{aligned} \delta U &= 0 \\ \vartheta(0) &= \vartheta(d) = 0 \end{aligned} \tag{4}$$

we finally get the voltage able to induce the desired director angle ϑ_m:

$$V_{\vartheta_m} = V_{th}\frac{2}{\pi}\int_0^{\pi/2}\left(\frac{\sqrt{\left(1+\kappa\eta^2\sin^2\psi\right)\left(1+\gamma\eta^2\right)}}{\sqrt{\left(1-\eta^2\sin^2\psi\right)\left(1+\gamma\eta^2\sin^2\psi\right)}}\right)d\psi \tag{5}$$

with:

$$\eta = \sin\vartheta_m \quad , \qquad \gamma = \frac{\varepsilon_{\|}-\varepsilon_{\perp}}{\varepsilon_{\perp}} \quad , \qquad \kappa = \frac{k_3 - k_1}{k_1}$$

and

$$V_{th} = \pi\frac{\sqrt{k_1}}{\sqrt{\left(\varepsilon_{\|}-\varepsilon_{\perp}\right)\varepsilon_0}}$$

the threshold voltage (Freedericks value) to have a nonzero mid-layer tilt angle ϑ_m. The variable of integration in (5) accounts of the connection between ϑ_m and $\vartheta(y)$, i. e. sin $\vartheta(y)$ = sin $\vartheta_m \cdot$ sin ψ, and the integral (5) can be numerically evaluated to yield the voltage required for the desired refractive index n_{LC} and index increase to define a channel waveguide along z.
In our calculations we considered the case of a standard nematic LC, the mixture E7. For the latter material, $k_1=12\cdot10^{-12}$ N, $k_3=19.5\cdot10^{-12}$ N, $\varepsilon_{\|}=19.6$, $\varepsilon_{\perp}=5.1$, $V_{th}=0.96$ V, $\gamma=2.843$ and $\kappa=0.625$. From a standard analysis of dielectric waveguides with a graded index profile, for a thickness d=1 μm and width W_{el}=3 μm and operating at λ=1550 nm, a channel waveguide supporting the two lowest-order quasi-TM modes requires a maximum index increase Δn=0.0493 in y=d/2. The corresponding eigenvalues are $n_{eff0}=1.4860$ for TM_{00} and $n_{eff1}=1.4571$ for TM_{01}. This provides ϑ_m = 33° for $n_{LC} \cong 1.5493$ and, from (5), $V_{33°}=1.257$ V.

Since a change of ϑ_m from 33° to 40° yields $n_{LC} \cong 1.5701$ at $V_{40°}=1.376$ V and the new effective indices $n_{eff0}=1.5007$ and $n_{eff1}=1.4685$, for propagation over a device length L=233 μm such variation gives rise to a relative phase shift ΔΦ=π, i.e. what is required to switch output port.

The BPM (Beam Propagation Method) propagation in a 3D structure (3 μm along x, 1 μm along y and 233 μm along z) leads to single-mode light confinement along y and bimodal along x, as shown in Fig. 3. The three cases refer to ϑ_m=33° in (a), ϑ_m=40° in (b) and ϑ_m=0° in (c). It is apparent the peak shift in z=L from the left (Fig. 3a) to the right (Fig. 3b), corresponding to a

voltage variation of 119 mV only. The case of zero applied voltage (Fig.3c) shows the absence of lateral confinement along x: the input beam freely diffracts in the (x,z) plane.

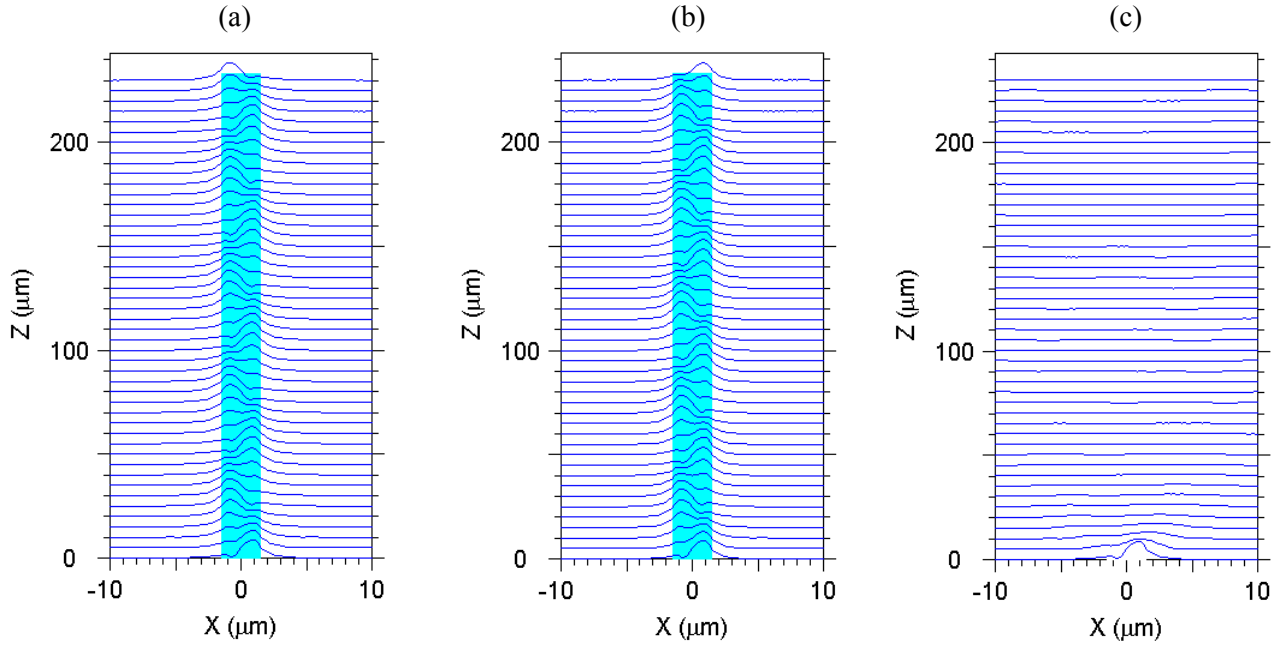


Fig. 3. Propagation of the electric field along z for a device length L = 233 μm and ϑm = 33° (a), ϑm = 40° (b) and ϑm = 0° (c). The shaded area in (a) and (b) indicates the LC area reoriented by the bias.

The output light intensity z = L is plotted in Fig. 4, to emphasize the lateral shift of the peak on either side of the waveguide output facet.

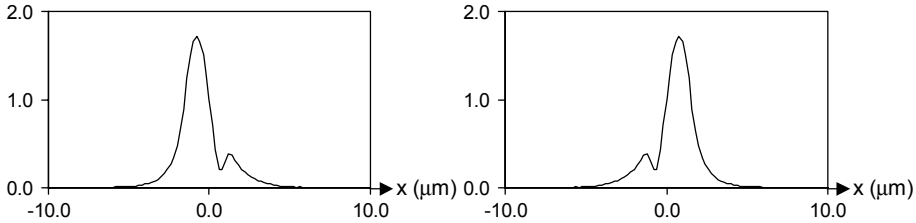


Fig. 4. Output intensity (arbitrary units) versus x for applied voltages differing by 119 mV.

Conclusions

A novel liquid crystal channel waveguide structure has been proposed and analyzed. In this electro-optically controlled device, an applied voltage lower than 1.5 V can provide lateral confinement of the signal, whereas its increase of about 119 mV can switch the light output between two different positions. The investigated geometry allows the realization of a versatile and fully electro-optic Y-junction switch, which can be optimized for operation at any wavelength of interest by acting on the bias.

[1] J. Bannister, J. Touch, A. Willner, and S. Suryaputra, *Opt. Networks* **1**, 17, 2000.
[2] See, for example, BeamBox Newsletter, publ. Akzo-Nobel, Arnhem,The Netherlands, **1**, 1, 1997.
[3] R. Asquini and A. d'Alessandro, *Proc. IEEE-LEOS 2000 Ann. Meet.* **1**, 119, 2000.
[4] R. Asquini and A. d'Alessandro, *Mol. Cryst. Liq. Cryst.* **375**, 243, 2002.
[5] H. Nishihara, M. Haruna, and T. Suhara, *Optical integrated circuits*, McGraw-Hill, 1985.
[6] P. Yeh and C. Gu, *Optics of Liquid Crystal Displays*, Wiley-New York, 1999.
[7] I. C. Khoo, *Liquid Crystals: Physical Properties and Nonlinear Optical Phenomena*, Wiley-New York, 1995.

Hybrid Sol-gel Integrated Optics on High Index Substrate for Heterogeneous Integration

Dong Lu, Oleg V. Mishechkin, Mahmoud Fallahi
Optical Sciences Centre, University of Arizona, Tucson, AZ 85721, USA
fallahi@optics.arizona.edu

Material synthesis, device design and fabrication of integrated optics using multi-layer hybrid sol-gel on high index substrate are presented. The results show the potential of hybrid sol-gel for heterogeneous integration with semiconductors.

Keywords: hybrid organic-inorganic sol-gel, guided-wave optics, integrated optics

Introduction

Heterogeneous integration is the enabling approach for the development of complex, low cost integrated optoelectronic components and subsystems. Hybrid organic-inorganic materials have great potential for integrated optics [1]. With the introduction of an organic chain containing C=C bond, the hybrid sol-gels show properties similar to glass and polymers [2,3]. These include photopatternability, low optical loss and long-time stability. In addition, their planarization and masking capabilities make them attractive for semiconductor processing and integration [4]. One major limitation for the integration of hybrid sol-gels with semiconductors is their low refractive index. Thick, crack-free, low index buffer layer is used to solve this problem. In this paper, the hybrid multi-layer sol-gel waveguide and integrated optics on high index semiconductor is reported. The material synthesis based on methacryloxypropyl trimethoxysilane (MAPTMS) as well as device fabrication are presented and characterized.

Waveguide structure design

Prior to fabrication, the design and optimisation of ridge and buried sol-gel waveguides on high index Si substrate is conducted by effective index as well as BPM using BPM-CAD software. We consider the materials with refractive indices of $n_{cladding}$ = 1.467 and n_{core} = 1.501. In order to eliminate any radiation into the substrate, the thickness of the lower cladding layer should be greater than 10 μm. The core size is chosen as 3 μm thick, and the top cladding is chosen as 6 μm thick (about 3 μm above the top of the core). The wavelength used for simulation is 1550 nm. The mode profile of the structure is shown in Fig. 1. Symmetric mode with good confinement is obtained.

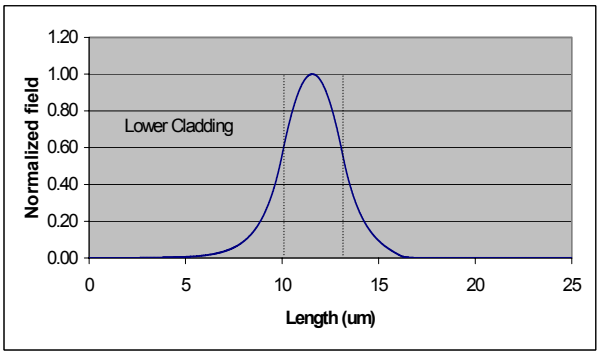


Fig. 1 Buried waveguide mode profile by simulation with BPM_CAD

The mode coupling between the waveguide and a single mode fiber is of great importance and can be evaluated from the overlap filed integral of Equation (1).

$$C = \frac{(\iint E_i^*(x,y) \times E_e(x,y)dxdy)^2}{(\iint E_i^*(x,y) \times E_i(x,y)dxdy) \times (\iint E_e^*(x,y) \times E_e(x,y)dxdy)} \quad (1)$$

With a Δn of 0.033 between the core and cladding material, the waveguide has a NA of ~ 0.31. Considering a conventional single mode fiber a coupling loss of about 2 dB is calculated for a simple butt-coupling technique.

Material synthesis and buried waveguide fabrication

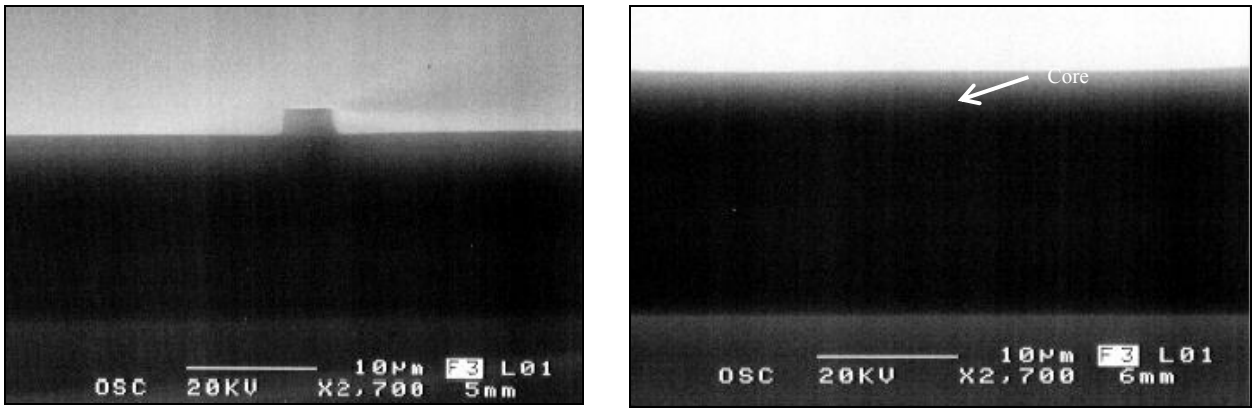
Two kinds of hybrid sol-gel materials based on MAPTMS with different refractive indices are synthesized for the core and the cladding layers. The Zirconium Propyloxide (ZPO) - MAPTMS is chosen for the core for its high refractive index. A molar ratio of 78 : 22 between MAPTMS and ZPO is chosen, which gives a refractive index of 1.501 at 1550 nm. 1.3 wt.% of IRGACURE 1800 (CIBA) is added as photoinitiator for UV-polymerization of the methacryloxy group. The lower and upper claddings are a mixture of MAPTMS and tetraethoxysilane (TEOS). The two precursors are hydrolysed separately with different concentrations of hydrochloric acid (0.01M for MAPTMS and 0.1 M for TEOS) prior to their mixing. The molar ratio between MAPTMS and TEOS is 65 : 35, which gives a refractive index of 1.467 at 1550 nm. After their mixing, a 2 wt.% of hydroxy methyl propiophenone (HMPP) is added in as a photoinitiator. The sols are aged for 24 hrs.

The sol for the cladding is spin-coated on silicon wafer at 1500 rpm for 30 seconds. After the spin, the film thickness can reach 9 μm. The thickness can also be adjusted by spin speed. The film is soft baked in an oven to help the surface relax. The hard bake is performed at 140 °C for 2 hours with 1 °C/min ramp. In order to reach a lower cladding thickness of over 10 μm a second spin at 2500 rpm is done after the wafer is cooled down. This spin not only increases the thickness but also helps control the thickness uniformity. The wafer is again baked. The lower-cladding thickness after the second spin is over 12 μm.

The MAPTMS-Zr for the core is spin-coated at 3000 rpm on the lower cladding in a saturated solvent vapour environment. The spin-speed and the solvent amount can be adjusted to obtain the desired thickness in the 1-5 μm range. The wafer is soft baked at 100 °C for 10 minutes. After the wafer cools down, the waveguides are defined by exposure through a quartz mask at 15 mW/cm^2 using an I-line contact mask aligner. The sample is developed in a strong solvent such as Acetone. Afterwards, the wafer is hard-baked in the vacuum oven for 6 hours to further densify the core.

The MAPTMS-TEOS upper cladding is spin-coated at 2500 rpm on the patterned wafer. After several minutes of soft bake and 20 minutes of flood UV exposure to control the planarity of the top surface, the film is vacuum oven dried for 2 hours at 100 °C. Fig. 2 shows the cross sections of the waveguides before and after deposition of the upper cladding layer. Crack-free, high quality interfaces have been achieved for the ridge and buried waveguides.

Besides the straight channel waveguide, several integrated optical components are also fabricated in the same way.



a). Two layer lower cladding and patterned core

b). Top cladding is put on to bury the core

Fig. 2: The SEM pictures of the multi-layer sol-gel waveguide before and after burying

Characterization and discussion

A tunable laser operating in the 1510 – 1580 nm range is used as the light source. The light is coupled into the waveguide with a lensed fibre. A microscope objective is used to image the near field of the output waveguides onto an IR camera. The output light is also coupled into a single mode fibre connecting to an optical spectrum analyser to measure the power and spectral response of the waveguiding devices. Fig. 3 shows the nearfield images of the modes for the ridge and buried waveguides for the structures shown in Fig. 2.



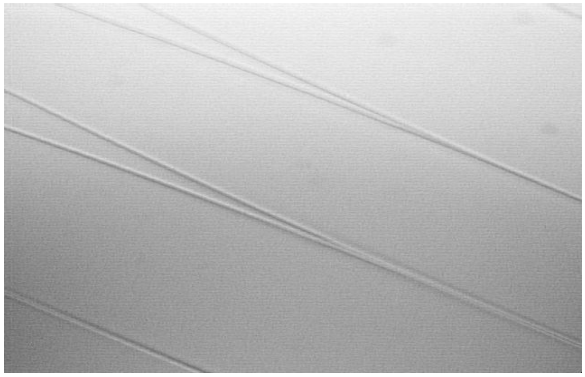
a). Output mode of a ridge waveguide

b) Output mode of a buried waveguide

Fig. 3: Near field mode of the multi-layer sol-gel waveguide

It can be seen that the ridge waveguide on the thick lower cladding can efficiently confine the mode within the core (Fig. 3a) with a small degree of asymmetry and some surface scattered light. On the other hand, the mode for the buried waveguide is very well confined and circular. This assures a low coupling loss between the waveguide and single mode optical fibers.

A y-splitter and a 4-output MMI splitter are also fabricated with the similar procedure. Figure 4 shows the top view micrograph of the buried y-splitter and its output modes. The scattered light between the modes is caused by slight scattering at the splitter region, and can be easily eliminated. Fig. 5 shows the top view micrograph of the MMI outputs and its modes. The detailed results will be reported.

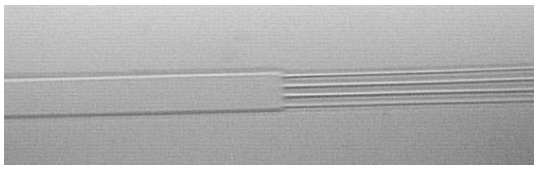


a). Y-splitters



b). Output modes

Fig. 4: Y-splitter with Multi-layer hybrid sol-gel



a). Output of a MMI



b). The modes for above MMI

Fig. 5: A MMI with Multi-layer hybrid sol-gel

Conclusion

The multi-layer waveguides by hybrid sol-gel technology are developed on high index semiconductor substrates with a simple material synthesis and fabrication method. The technology is promising for heterogeneous integration and can reduce optical loss and fabrication cost, opening the door for complex optoelectronic integrated circuits.

References:

[1] U. Schubert, N. Husing, A. Lorentz, *Chem. Mater.,* Vol. 7, p. 2010, 1995,.

[2] S. I. Najafi, T. Touam, R. Sara, M. Andrews, A. Fardad, *J. Lightwave Tech.* Vol. 16, p. 1640, Sept. 1998.

[3] A. Fardad, O. V. Mishechkin and M. Fallahi, *J. of Lightwave Tech.* Vol. 19, p. 84, Jan. 2001.

[4] M. Fallahi, R. Bedford and D. Lu, *JVST B*. , Nov/Dec, 2002.

Long-Period Waveguide Gratings

H. C. Tsoi, W. H. Wong, and E. Y. B. Pun

Department of Electronic Engineering, City University of Hong Kong, Tat Chee Avenue, Kowloon, Hong Kong

Phone:852-2788 8609, Fax: 852-2788 7791, E-Mail: eeeybpun@cityu.edu.hk

Abstract: Polymeric long period waveguide gratings (LPWGs) were fabricated and characterized. A maximum attenuation of –18dB and a minimum bandwidth of 6nm were measured, and the grating length is as short as 1 cm.

Keywords: waveguide gratings, long period gratings, polymeric waveguides.

Introduction

Long-period grating (LPG) devices are useful for both telecommunication and sensor arenas. Many LPG devices have been demonstrated in recent years, such as band-rejection filters [1], gain flattening elements for erbium-doped fiber amplifier (EDFA) [2], optical sensors [3], wavelength selective polarizing elements [4], sensing elements/demodulators [5], and codirectional coupler filters [6]. Up to now, most of the LPG devices have been realized in optical fiber. Long period waveguide grating (LPWG) is attractive because of its small size, low cost, simple process, and potential integration with other components on the same substrate.

Polymeric optical waveguides and Bragg grating filters based on a negative tone epoxy novolak resin (ENR) have been fabricated recently using electron-beam direct writing [7, 8]. In this work, we report the fabrication and characterization of ENR polymeric LPWG.. The temperature property of the polymeric LPWG is also investigated.

Experiments

The LPWG was fabricated using standard cleanroom processing steps: 1) UV photolithography to pattern the photoresist grating on Si wafer, 2) reactive ion etching (RIE) to transfer the grating pattern onto the surface of the Si wafer, 3) thermal oxidation to form the buffer SiO_2 layer, and 4) spin coating and UV photolithography to form the ENR polymeric waveguide. Fig.1 shows the schematic diagram of the fabrication process of the polymeric LPWG.

An amplitude mask was used to expose a grating pattern on Si substrate, and the periodicity varies from 370μm to 450μm. The substrate area was ~3cm x 1cm. The grating pattern was then transferred to the Si surface by RIE using a mixture of O_2 and SF_6 gases. The grating depth is ~150nm, and the grating length L_g is ~1.7cm which is shorter than the values

used for LPFGs. In general, the LPFG length is longer than 2.5cm [1,4]. After etching, the Si substrate surface was thermally oxidized, and ~1.5μm thick silicon dioxide (SiO_2) layer was used as the lower cladding layer. The refractive index of ENR polymer is ~1.575 at 1.55μm and is higher than that of SiO_2. The polymeric channel waveguide was formed on the grating embedded SiO_2/Si substrate by spin-coating and ultraviolet (UV) exposure. ENR polymer was spun at 4500 rpm for 180 s, and a pre-exposure bake of 3 min at 90°C was carried out. The polymer was exposed using a Karl Suss Mask Aligner having a highly pressurized mercury lamp with 350W power and 365nm exposure wavelength. The exposure time was 60 s. After exposure, a post-exposure bake time of 3 min at 90°C was carried out before development in propylenglygol-monomethylether-acetate (PGMEA) for 15s. The sample was then rinsed in fresh PGMEA again.

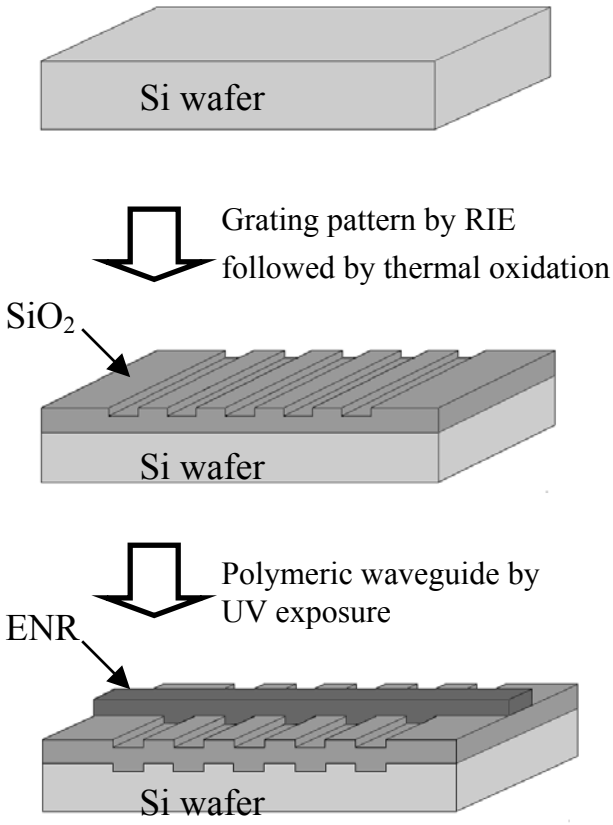


Fig. 1 Schematic diagram showing the fabrication process of polymeric LPWG

The width and height of the waveguide are 6μm and 2.2μm, respectively, and the grating pattern appears as bottom surface corrugations. The grating depth is controlled by the RIE etching time, and the designed amplitude mask determines the grating period.

Discussion and results

The transmission spectrum of the LPWG was obtained by coupling the output light from a broadband source, either an EDFA (1.5 μm wavelength band) or a superluminescent light emitting diode (SLED, either1.3 μm or1.4 μm wavelength band), into one of the cleaved ends of the device. The output light of the device was collected using a single mode fiber and analyzed using a HP8210A optical spectrum analyzer (OSA), and index matching fluid was used to minimize Fresnel reflections during the measurements. Fig. 2 shows the dependence of transmission peak wavelength on grating period. As expected, a linear relationship is obtained in accordance to the phase matching condition, and Δn_{eff}, defined as the effective index difference between the guided and radiation modes, corresponds to the slope of the

straight line. From Fig. 2, the slope is ~3.9×10^{-3}. In Fig. 3(a), a transmission peak of ~ –10dB at 1.3μm wavelength was observed, corresponding to > 90% attenuation, and in Fig. 3(b), a transmission peak of ~ –13dB at 1.5μm wavelength was observed, corresponding to an > 95% attenuation. The bandwidths are ~6nm in both cases. The sidelobes, -1dB and –3dB, that appear in the spectra in Fig 3(a) and Fig. 3(b), respectively, are similar to those reported in [4] and [6], indicating that there is some non-uniformity in the LPWG. As shown in Fig. 3(c), by optimizing the fabrication processes and the structure, a transmission peak of ~ –18dB at 1.4μm wavelength with negligible sidelobes was observed, corresponding to >98% attenuation. The grating length and depth in this case are ~1cm and ~400nm, respectively, and the bandwidth is ~13nm. Compared to LPFG the attenuation in LPWG is similar (> -10dB), the L_g is shorter (<2cm), and the 3dB bandwidth is narrower (<13nm). LPWG offers many advantages, because of its compact size and possible integration with other components on the same substrate.

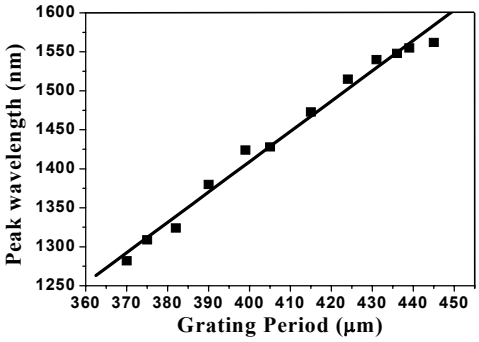


Fig. 2. Transmission peak wavelength as a function of grating periodicity

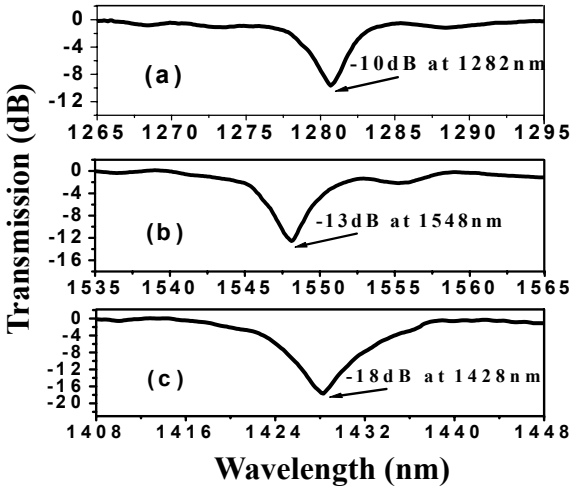


Fig. 3. Transmission characteristics of LPWG at (a) 1.3μm wavelength, (b) 1.5μm wavelength and (c) 1.4μm wavelength

The temperature characteristic of the LPWG was investigated, and the change in peak wavelength versus temperature $d\lambda/dT$ is found to be ~ –0.165nm/^{o}C. This value is similar to those measured in LPFGs, which exhibit temperature sensitivity in the range of 0.05-0.16nm/^{o}C [3,9]. The insertion loss of the LPWG device was also measured, and is in the range 9-10dB which is similar to that reported in [10]. This high value is due to the mode mismatch, the propagation loss, and the end-face scattering loss between the waveguide and the fiber. Polishing the two end faces can reduce further the insertion loss.

Conclusion

In conclusion, LPWG has been demonstrated in ENR polymeric waveguide using standard cleanroom fabrication processes. Experimental results show a linear relationship between the grating period and the transmission peak wavelength. The grating depth and period can be controlled easily in the fabrication steps. The LPWG exhibits high attenuation transmission (up to -18dB), narrow bandwidth (down to 6nm), and short grating length (less than 2cm). In addition, the temperature characteristic of the LPWG was also measured, and is similar to those reported for LPFGs. LPWG is attractive because of its small size, low cost, and potential integration with various optical components and functional devices on the same SiO_2/Si substrate.

Acknowledgment

This work was supported by Research Grants Council of the Hong Kong Special Administrate Region, China, under Grant Project CityU 1194/02E.

References:

[1] A. M. Vengsarkar, P. J. Lemaire, J. B. Judkins, V. Bhatia, T. Erdogab, and J. E. Sipe, *IEEE J. Lightwave Technol*., **QE-14**, 58-85, 1996.

[2] A. M. Vengsarkar, J. R. Pedrazzani, J. B. Judkins, P. J. Lemaire, N.S. Bergano, and C. R. Davidson, *Opt. Lett*., **21**, 336-338 , 1996.

[3] V. Bhatia, and A. M. Vengsarkar, "Optical fiber long-period grating sensors," *Opt. Lett*., **21**, 692-694, 1996.

[4] A. S. Kurkov, M. Douay, O. Duhem, B. Leleu, J. F. Heninot, J. F. Bayon, and L. Rivoallan, *Electron. Lett*., **33**, 616-617 , 1997.

[5] H. J. Patrick, G. M. Williams, A. D. Kersey, J.R. Pedrazzani, and A.M. Vengsarkar, *IEEE Photonics Tech. Lett*., **8**,1223-1225 , 1996.

[6] She-Won Ahn and Sang-Yung Shin, *Opt. Comm*., **197**, 289-293, 2001.

[7] W. H. Wong, J. Zhou, and E. Y. B. Pun, *Appl. Phys. Lett*., **78**, 2110-2113 , 2001.

[8] W. H. Wong, and E. Y. B. Pun, *Appl. Phys. Lett*., **79**, 3576-3578 , 2001.

[9] S. Savin, M. J. F. Digonnet, G. S. Kino, and H. J. Shaw, *Opt. Lett*., **25**, pp. 710-712, 2000.

[10] Wol-Yon Hwang, Min-Cheol Oh, Hyang-Mok Lee, Heuk Park, and Jang-Joo Kim, *IEEE Photonics Tech. Lett*., **9**, 761-763 , 1997.

Design and the fabrication of the small v-bend optical waveguide using an elliptic mirror

Takanori Suzuki, Yutaka Shibata, and Hiroyuki Tsuda
Department of Electronics and Electrical Engineering, Faculty of Science and Technology, Keio University
3-14-1 Hiyoshi, Kouhoku-ku, Yokohama, 223-8522 Japan
suzutaka@tsud.elec.keio.ac.jp

The small v-bend optical waveguide using an elliptic mirror using polyimide is designed and fabricated. Total loss, the wavelength and the polarization dependent loss were 10 dB, 0.7 dB and 0.1 dB, respectively.
Keywords: optical waveguide, small bend, elliptic mirror, polyimide, misalignment

Introduction

Small sized planar lightwave circuits [1] are necessary for large capacity communication systems. Generally, the curved waveguide is used to bend the light in the optical waveguide. The size of the curved waveguide is limited by the minimum radius of the curvature. We proposed the small v-bend optical waveguide using an elliptic mirror, as shown in Fig.1. The v-bend waveguide has a large tolerance on the mirror position misalignment. On the other hand, the total reflection mirror could not bend at a sharp angle and had high loss against mirror position misalignment. Furthermore, total reflection mirror had high wavelength dependent loss [2].

In this paper, the structure of the v-bend optical waveguide was optimized and it was fabricated with fluorinated polyimide [3]. The loss characteristics were also described. Other optical waveguide using the mirror, i.e. N:N optical coupler, was proposed.

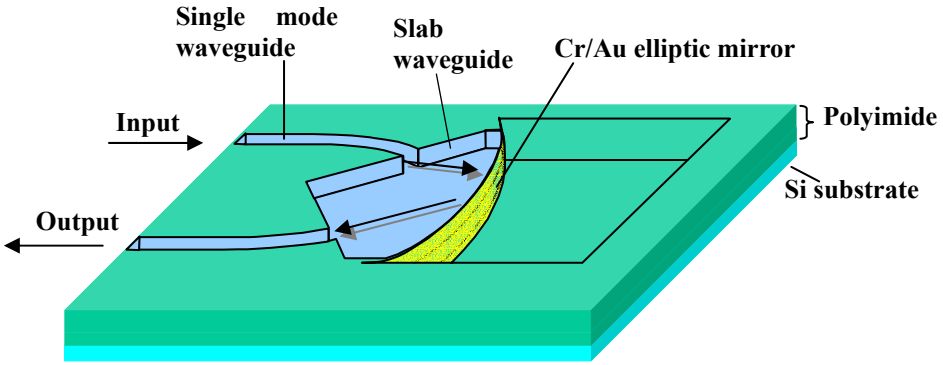


Fig.1 Schematic of small v-bend optical waveguide using an elliptic mirror

Optimized design of the v-bend optical waveguide

The light emitted from one focal point reflects in the elliptic surface and converges on the other focal point. We utilized this property for v-bend waveguide. The Gaussian beam approximation [4] was used for the light propagation in the slab waveguide. High coupling efficiency between the reflected beam and the output waveguide might provide low loss bending. Figure 2 shows the structure of the v-bend optical system. The spot size and the position of the waist of the reflected beam depend on those of the incident beam and the geometrical focal length of the lens f. When $\omega_1 = \omega_2$ and $d_0 = d_1$ are assumed, at the minimum scale Gaussian beam condition, we obtained

$$d_0 = d_1 = f = \frac{\pi \omega_1^2 n}{\lambda}. \quad (1)$$

where n is the effective index of slab waveguide, $d_0(d_1)$ is the distance from the incident (reflected) beam waist to the vertex of the elliptic mirror and $\omega_1(\omega_2)$ is the spot size of the incident (reflected)

beam. The shortest length of the v-bend (Xmin) and high coupling efficiency between reflected Gaussian beam and the output waveguide are obtained if w2 equals the fundamental mode field radius of the output waveguide which core width is 2a. For example, when 2a = 10 μm, λ = 1.55 μm and n =1.534 were assumed, Xmin was calculated to be only 1 mm for Rmin = 10 mm and L = 50 μm.

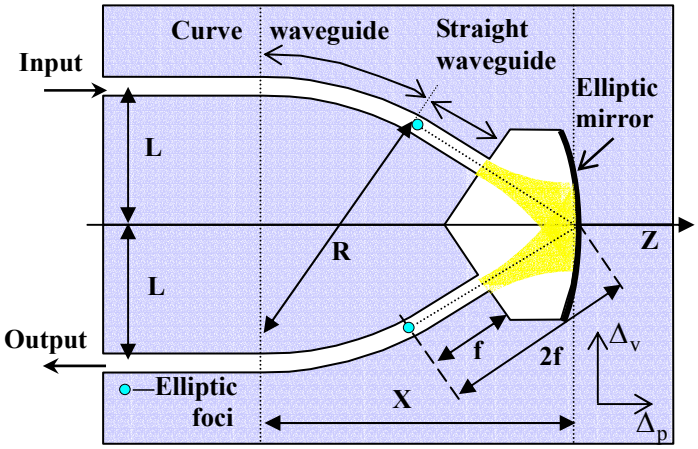


Fig.2 Structure of the optimized v-bend waveguide.

Mirror Loss

The v-bend optical waveguide was fabricated by photolithography and RIE (reactive ion etching). After etching of the waveguide, Cr/Au metal was deposited on the facet. We assumed that origins of the mirror loss could classify into 4 categories [5], (1) the mirror position misalignment, (2) the mirror facet tilt angle, (3) the mirror facet roughness and (4) the mirror absorption.

The excess loss due to the misalignment of the mirror with the parallel direction and the vertical direction against the optical axis (z-direction in Fig.2) were calculated. Figure 3 shows how the excess loss varies with the parallel direction misalignment Δ_p. The excess loss due to the parallel direction misalignment was less than 0.07 dB at $\Delta_p = \pm 2$ μm and that of the vertical direction misalignment Δ_v was 1×10^{-5} dB at $\Delta_v = \pm 2$ μm, it could be almost ignored.

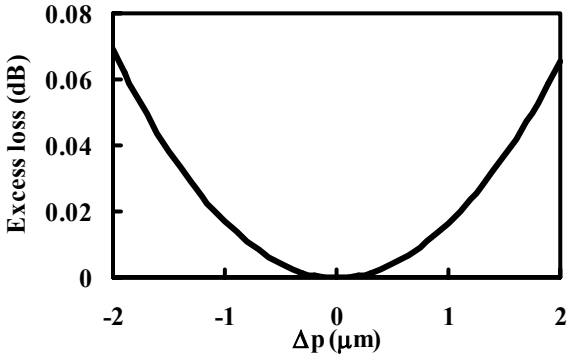


Fig. 3 Excess loss as a function of the parallel direction misalignment(Δp).

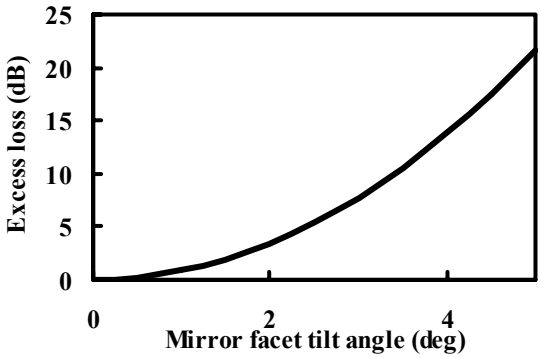


Fig. 4 Excess loss as a function of the mirror facet tilt angle against depth direction.

On the other hand, the excess loss significantly depends on the tilt angle of the mirror facet to the normal direction. Figure 4 shows the excess loss as a function of the mirror facet tilt angle. To keep the loss less than 1 dB, the mirror facet tilt angle has to be less than almost 1 (deg). Mirror roughness is often estimated with the RMS (root mean square) value. The RMS value of the mirror facet roughness etched by the RIE was less than few hundred nanometers. Therefore, it might be also ignored [6].

Fabrication and measurement of the polyimide v-bend waveguide

We have fabricated the v-bend waveguide with fluorinated polyimide which propagation loss is 0.6 dB/cm and 0.9 dB/cm for both TE and TM polarization at the wavelength of 1.55 μm. The minimum size of the v-bend structure was 0.5 mm × 2.22 mm, when the core width of the waveguide (2a), the refractive index difference and the separation length of the input/output waveguides (2L) were 10 μm, 0.46 % and 500 μm, respectively. The measurement setup consists of the tunable optical source, the polarization scrambler and the optical power meter. Figure 5 shows the total loss of the v-bend waveguide as a function of the wavelength. The average total loss was about 10.64 dB. The polarization and wavelength dependent loss were only 0.1 dB and 0.7 dB from 1.525 μm to 1.6 μm, respectively. It seems that the v-bend waveguide did not depend on the wavelength of the optical source.

Figure 6 is the SEM (scanning electron microscope) photograph of the mirror facet. There were the vertical stripes on the facet. As the spacing of these stripes was almost few hundred nanometers and the height of the stripes was less than one hundred nanometers, the scattering loss at the mirror facet might be almost neglected like the loss due to the mirror position misalignment. Since the mirror facet tilt angle was about 2 degree, the excess loss due to the mirror facet tilt was about 3.5 dB. The reflectivity of the Cr/Au mirror seems to be low due to the absorption of the Cr layer. This absorption is one of the reasons of the high total loss.

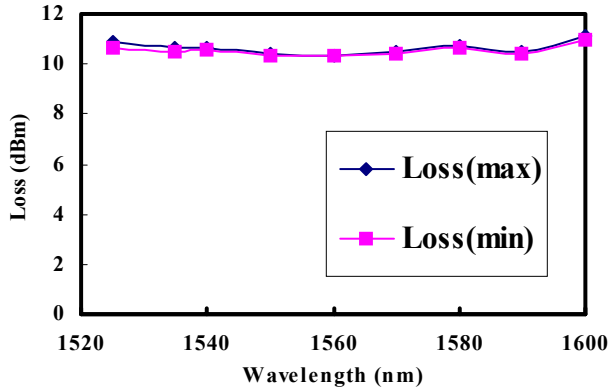


Fig. 5 Total loss of the v-bend waveguide as a function of the wavelength.

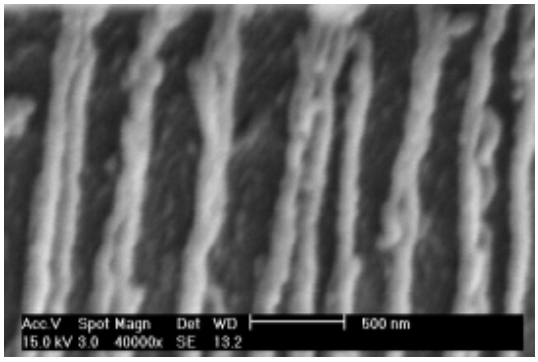


Fig. 6 SEM photograph of the mirror facet.

N:N optical coupler using a mirror

Figure 7 illustrates the N:N optical coupler using a mirror in slab waveguide. The proposed coupler consists of the input waveguides, output waveguide, slab waveguide and the waveguide mirror. The incident light from input waveguides to the slab waveguide will be reflected at the mirror and the light changes to the collimated light and this reflected light will be coupled into output waveguides. The advantages of the proposed coupler are that the length of the device can be almost half compared with that of the conventional one, both input and output fibers can be connected to the same side of the substrate, and the various shapes of mirrors can be designed to reduce aberration. The mirror shape that can collimate the reflected beam was optimized by using numerical calculation. Figure 8 shows the simulated coupling losses of the proposed 8:8 coupler and the conventional one as a function of the distance from the end of the central input waveguide to a mirror (S). The fluctuation was the difference between the maximum and the minimum coupling loss in dB unit. And the maximum loss was the difference between the maximum loss and $-10\times\log_{10}(1/8)$, which was the ideal loss when input signal was divided equally into every waveguide. Figure 9 shows the experimental results of the fabricated 1:4 optical coupler. This graph shows the coupling loss as a function of the wavelength. These results indicate that the loss at 1550nm was about 30dB. The loss dependence on the wavelength was about 2.7dB, the fluctuation

of the loss was about 2.9dB and the PDL was about 0.6dB. These values will be reduced by using more refined etching technique.

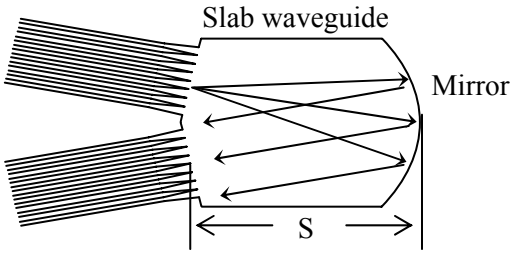


Fig. 7 Schematic of the proposed N:N coupler using a waveguide mirror.

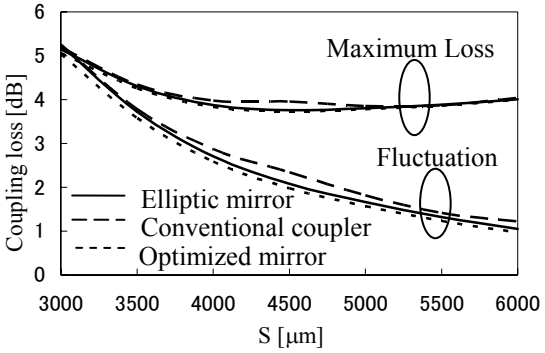


Fig. 8 Calculation results.

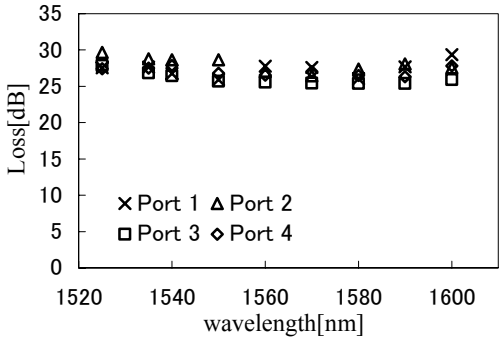


Fig. 9 Experimental results of 1:4 coupler.

Summary

We have designed the v-bend optical waveguide using an elliptic mirror, which can perform 180 degree light path bending and has a large tolerance on the mirror position misalignment. The minimum length of the v-bend waveguide became 1-2 mm in which conventional waveguide could not be fabricated. We have fabricated the polyimide v-bend optical waveguide. The total loss was about 10 dB, which mainly attributed to the mirror facet tilt and the absorption of the Cr/Au mirror. The wavelength and polarization dependent loss were only 0.7 dB and 0.1 dB, respectively. The N:N optical coupler using a mirror in slab waveguide was proposed. The performance of this coupler is almost the same compared with the conventional coupler.

Acknowledgement

This study was supported by Grant in Aid for the 21st century center of Excellence from the Ministry of Education, Culture, Sport, Science, and Technology in Japan, the Ministry of Public Management, Home affairs, Posts and Telecommunications, the support center for advanced telecommunications technology research and the international communications foundation.

References

[1] K. Okamoto, Fundamentals of Optical Waveguides, *Academic Press*, 2000.

[2] R. V. Roijen, G. L. A. V. D. Hofstad, M. Groten, J. M. M. V. D. Heyden, P. J. A. Thijs and B. H. Verbeek, *Appl. Opt*., vol.32, No.18, 3246-3248, 1993

[3] J. Kobayashi, T. Matsuura, Y. Hida, S. Sasaki and T. Maruno, *J. Lightwave. Technol.*, vol.16, No.6, 1024-1029, 1998

[4] A. Yariv, Optical Electronics, *Oxford University Press*, 2000

[5] A. L. Burness, P. H. Loosemore, S. N. Judge, I. D. Henning, S. E. Hicks, G. F. Doughty, M. Asghari and I. White, *Electron. Lett.*, vol.29, No.6, 520-521, 1993

[6] P. Buchmann and H. Kaufmann, *J. Lightwave. Technol.*, Vol.LT-3, No.4, 785-788, 1985

Anisotropy and dispersion of quadratic nonlinear properties of electrooptic azo-polymer thin films

P. Nagtegaele, E. Brasselet and J. Zyss
Laboratoire de Photonique Quantique et Moléculaire, Ecole Normale Supérieure de Cachan, 61 avenue du président Wilson, 94235 Cachan Cedex, France.
Zyss.Joseph@lpqm.ens-cachan.fr

Different components (iiz) of the $\chi^{(2)}(-\omega;\omega,0)$ and $\chi^{(2)}(-2\omega;\omega,\omega)$ nonlinear quadratic susceptibilities tensors of a nonlinear optical polymer are both measured independently using a Fabry-Pérot interferometric technique and the second harmonic Maker fringes method. Electro-optic dispersion is obtained from visible wavelengths up to 1.55µm while second harmonic generation measurements are performed at 1.32µm. These techniques agree with a wavelength independent $\chi^{(2)}_{zzz} / \chi^{(2)}_{xxz}$ ratio close to 5 for the copolymer Poly(methyl methacrylate)-Dispersed Red 1 (PMMA-DR1) and close to 3 for the guest-host PMMA-DR1 blend, thus designating the interaction of the chromophores with their environment as an important feature in electro-optic device design.

Keywords : nonlinear quadratic susceptibilities, Fabry-Pérot interferometric technique, electrooptic polymer

1. Introduction

Organic nonlinear optical (NLO) materials have emerged over the last decade as appealing candidates towards integrated optics technology in view of some of their specific advantages as compared to inorganic materials. The low-cost and relatively easy processability of NLO polymers exhibiting large nonlinearities have allowed the demonstration of very performing active integrated organic optical components with impressive figures of merit [1]. Accurate measurement of nonlinear quadratic susceptibilities $\chi^{(2)}(-\omega;\omega,0)$ and $\chi^{(2)}(-2\omega;\omega,\omega)$ which respectively pertain to electro-optic modulation and second harmonic generation is a prerequisite step towards subsequent design of devices for light modulation and all-optical signal processing [2].

Several methods have been developed for the determination of the electro-optic related tensor coefficient and related NLO susceptibility. First, reflection techniques have been developed for determining the electro-optic coefficient r_{33} of poled polymers based on a weak field cylindrical symmetry imposed r_{33} / r_{13} ratio set at a fixed value of 3 [3,4]. Uchiki and Kobayashi have proposed a Fabry-Pérot interferometric technique to measure the coefficient r_{13} by varying the light beam wavelength [5]. Moreover, an attenuated total reflection technique allows to evaluate both r_{13} and r_{33} coefficients independently [6]. However, this technique requires the knowledge of the metallic layers thickness with a high level of accuracy.

In this paper, we used two techniques to measure independently nonlinear quadratic susceptibilities of a PMMA-DR1 copolymer from the visible up to the 1.55µm telecom window. The r_{33} and r_{13} electro-optic coefficients are evaluated using a Fabry-Pérot interferometric technique that has been initially introduced by Meyrueix and coworkers [7,8]. The second order nonlinear coefficients d_{33} and d_{31} are then determined by second harmonic measurements following the Maker fringes envelope method. The $\chi^{(2)}_{zzz} / \chi^{(2)}_{xxz}$ ratio obtained with theses techniques is then compared to the theoretical values predicted by various models.

2. Experimental

The nonlinear co-polymer was synthesized at Ecole Nationale Supérieure de Chimie de Montpellier. The chromophore tethered to the backbone of the PMMA polymeric matrix is the azo-dye Disperse Red 1 from Aldrich. The experimental molar composition MMA/MMADR1 = 76/24. The same polymeric matrix and chromophore are used to prepare a 10% weight doped PMMA. Linear optical properties, namely refractive index and linear absorption of these materials were characterized using tranditional spectroscopic ellipsometry and spectrophotometry.

Electrooptic measurements are achieved with thin film Fabry-Pérot cavities while second-harmonic measurements are performed using a thin film spin coated on a glass substrate. Fabry-Pérot thin film processing starts with the semi-transparent aluminium bottom electrode deposition by sputtering on a glass substrate. Then, the active organic material, a concentrated solution of 10% weight nonlinear optical polymer in 1,1,2 trichloroethan, is filtered through a 0.2 µm Teflon filter and spun coated onto the bottom aluminium electrode. The film is then dried at 120°C for two hours. Finally, the upper semi-transparent aluminium electrode is sputtered. Electric wire bonding is ensured by gluing onto the two electrodes coated with a silver contact layer. Initially, the active polymer in the cavity is centrosymmetric which precludes quadratic nonlinear effects. Thermo-assisted electric field poling is subsequently used to induce noncentrosymmetry.

3. Electrooptic Measurements

Electro-optic measurements were obtained using the Fabry-Pérot under oblique incidence set-up. The poled Fabry-Pérot cavity is placed on a motorized rotating stage and a quasi-static field (30 V peak to peak at Ω = 1 kHz) supplied by an AC generator is applied onto the electrodes of the cavity. Angular transmission spectra, $T_S(\theta)$ and $T_P(\theta)$ at zero frequency, and $T_S^{EO}(\theta)$ and $T_P^{EO}(\theta)$ at Ω frequency, are simultaneously measured at a discrete set of wavelengths using different laser diodes operating respectively at 675, 785, 1064, 1330 and 1550 nm. Modulated spectra $T_S^{EO}(\theta)$ and $T_P^{EO}(\theta)$ are recorded with a lock-in amplifier. Experimental data at 1.55µm for S and P polarization are presented in Figs. 1 for the co-polymer (dotted curves).

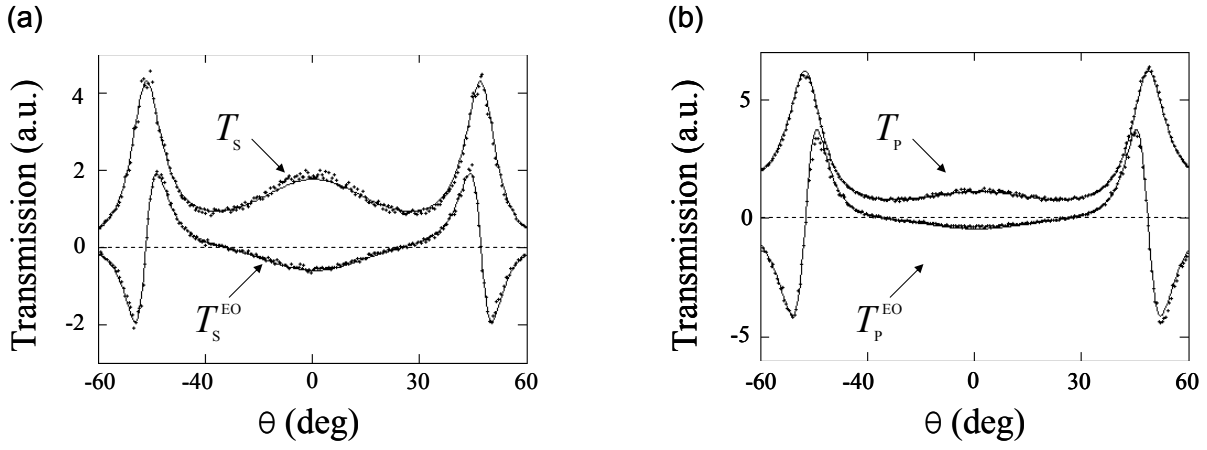


Figure 1 : Direct transmission ($T_{S,P}$) and modulated transmission ($T_{S,P}^{EO}$) at λ = 1.55µm. The polymer thickness is L=3.5 µm and the poling field Ep = 63 V/µm. (a) S-polarization; (b) P-polarization.

Electro-optic coefficients r_{13} and r_{33} are obtained from experimental data fits (solid lines) using standard matrix propagation method. First, the fits of $T_S(\theta)$ and $T_P(\theta)$ allow the determination of polymer thin film and aluminium electrodes thicknesses. Then, r_{13} (respectively r_{33}) is inferred from $T_S^{EO}(\theta)$ (respectively $T_P^{EO}(\theta)$ and the value of r_{13} deduced previously). Fig. 2 (a) and (b) summarize respectively the results for r_{13} (dots) and r_{33} (squares) at different wavelengths with the same sample.

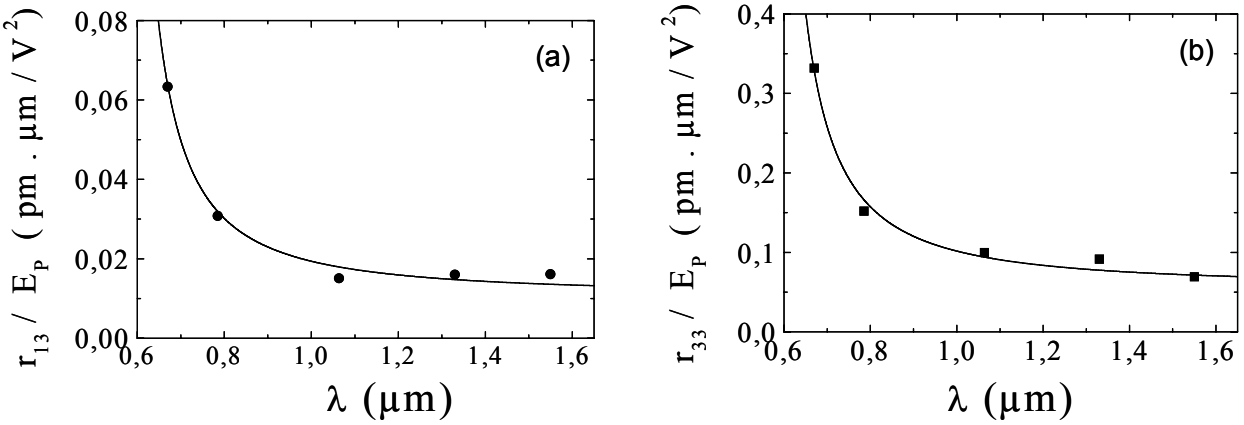


Figure 2 : Electro-optic dispersion normalized to the poling field Ep. (a) r13 coefficient; (b) r33 coefficient. (a) and (b) are fitted using a two level model with λ_0 = 532nm and λ_0 = 530nm respectively.

In first approximation, the dispersion of electro-optic coefficients, $r_{13}(\lambda)$ and $r_{33}(\lambda)$, is fitted by the two level model and rather good agreement is obtained. We found a ratio $r_{33}/r_{13} \approx 5$ which is almost constant over the investigated wavelength range. This ratio is greater than the theoretical value 3 predicted by the Langevin model in the limit of small field which points out that chromophores interact with their environment. The Van der Vorst – Picken model based on the Maier-Saupe theory, which takes into account the dipole interaction with their environment, gives much better results, even if the predicted r_{33}/r_{13} ratio is smaller than measured [9]. The wavelength independence confirms the intrinsic structural character of the underlying physical mechanism. As expected, a ratio $r_{33}/r_{13} \approx 3$ is obtained with DR1 dye-doped PMMA guest-host system, where the chromophores interaction with their environment is expected to be much weaker.

4. Second harmonic measurements

Second harmonic generation measurements are performed on a polymer thin film spun coated on a glass substrate. The sample is placed on a motorized rotating stage and is poled in situ by a 6 kV Corona needle set-up. A Q-switched nanosecond Nd3+YAG laser operating at 1.32µm was used. Envelope fringes corresponding to the second harmonic signal in function of the incidence angle, $I_{2\omega}(\theta)$, are detected using a photomultiplier linked to a boxcar integrator for different polarization configurations. Fig. 3a and 3b present the $I_{2\omega}^{polymer}(\theta)$ (dotted curves) and $I_{2\omega}^{quartz}(\theta)$ (solid curves) for a S and P polarized fundamental incident beam.

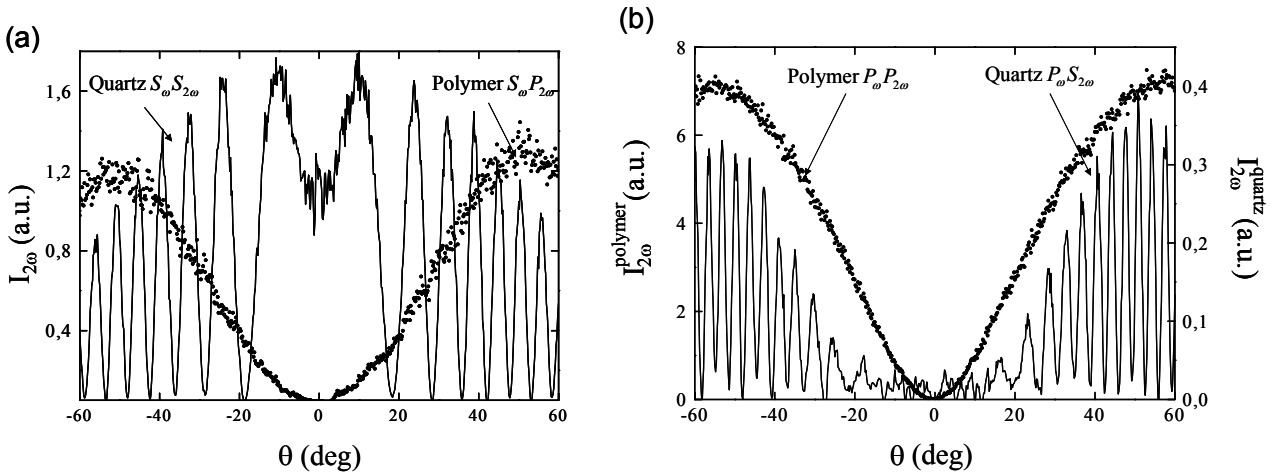


Figure 3 : Maker fringes for the polymer thin film and the quartz crystal. (a) S-polarized fundamental incident beam. (b) P-polarized fundamental incident beam

The thickness of the polymer being less than the coherence length, no fringing is observed in contrast with the thicker 2mm-quartz, for which many coherence lengths are seen throughout the angular variation. In these figures, notation $X_\omega Y_{2\omega}$ refers to X-polarized fundamental incident beam and detection of Y-polarized second harmonic field. The components of the nonlinear quadratic susceptibility tensor, $2d_{13} = \chi^{(2)}_{xxz}(-2\omega;\omega,\omega)$ and $2d_{33} = \chi^{(2)}_{zzz}(-2\omega;\omega,\omega)$, are evaluated comparing results obtained with polymer thin film with those obtained from 2mm-thick quartz crystal for which d_{11} = 0.5 pm/V at 1.32 µm. First, d_{13} is evaluated from a $P_\omega S_{2\omega}$ polymer configuration. Then, the $P_\omega P_{2\omega}$ configuration allows for the determination of d_{33}. We found a ratio $d_{33}/d_{13} \approx 5$, that confirms previous results obtained from electro-optic measurements.

Conclusion

In conclusion, Fabry-Pérot interferometric technique and second harmonic measurement were used to determinate independently the components of nonlinear quadratic susceptibilities tensors from the visible up to 1.55µm, allowing to determine the dispersion of the electro-optic coefficients was measured. A constant $\chi^{(2)}_{zzz} / \chi^{(2)}_{xxz}$ ratio over the investigated wavelength range is greater than the theoretical value 3 predicted by the weak field independent molecule Langevin model. This points out the interaction of the chromophores with their environment which is further confirmed by the second harmonic generation measurements.

[1] M. Lee, H.E. Katz, C. Erben, D.M. Gill, P. Gopalan, J.D. Heber and D.J. McGee, *Science*, **Vol. 298**, 2002.
[2] A. Donval, E. Toussaere, R.Hierle and J. Zyss, *J. Appl. Phys.*, **Vol. 87**, N° 7, 2000.
[3] C. C. Teng and H. T. Man, *Applied Physics Letter*, **Vol. 56**, pp.1734-1736, 1990.
[4] J. S. Schildkraut, *Applied Optics*, **Vol. 29**, N° 19, pp. 2839-2841, 1990.
[5] H. Uchiki and T. Kobayashi, *J. Appl. Phys.*, **Vol. 64**, N° 5, 1988.
[6] M. Dumont and Y. Lévy, *Nonlinear Optics of Organics and Semiconductors*, **Vol. 36**, 1989.
[7] R. Meyrueix, M. Dickens, O.Lemonnier, J.Lecomte and G. Tapolsky, *Optics Communications*, **Vol. 110**, 445-455, 1994.
[8] R. Meyrueix, J.Lecomte and G. Tapolsky, *Nonlinear Optics*, **Vol. 1**, pp. 201-211, 1991.
[9] C. P. J. M. van der Vorst and S. J. Picken, *J. Opt. Soc. Am. B*, **Vol. 7**, N°3, pp 320-325, 1990.

Numerical Study of a Wavelength Converter Based on Cascaded Interactions in a PPLN Waveguide

Luca Razzari, Carlo Liberale, Ilaria Cristiani, Riccardo Tediosi,
and Vittorio Degiorgio
Istituto Nazionale per la Fisica della Materia and Dipartimento di Elettronica,
Università di Pavia, via Ferrata 1, 27100 Pavia, Italy
razzari@ele.unipv.it

A wavelength conversion device based on $\chi^{(2)}$ cascaded interactions is presented. The conversion mechanism relies on the combination of amplification and nonlinear dephasing of the signal occurring during the cascaded process. The device performance is numerically evaluated in the pulsed regime.

Keywords: guided-wave optics, nonlinear phase, all-optical wavelength conversion

1. Introduction

All-optical switching devices are required for future photonic network systems. Possible candidates are devices using quasi-phase-matched (QPM) cascaded second-order interactions in lithium niobate waveguides, which can present ultrafast response, potentially low switching power, wide wavelength coverage, and integration compatibility.

The cascade involves second-harmonic generation (SHG) of a pump field *p* at frequency ω_p followed by difference-frequency generation (DFG) between the second harmonic of *p* and an additional input field *s* at frequency ω_s. The cascaded interaction permits the generation of a new field *c* at frequency $\omega_c = 2\omega_p - \omega_s$ and the amplification of *s*. [1-4] This effect can indeed give rise to large effective third-order nonlinearities with ultrafast response times and perfect transparency of the nonlinear medium.

In this article we present a numerical study of a new optical wavelength converter scheme based on cascaded interactions in a periodically poled lithium niobate (PPLN) waveguide. We discuss the performance of the device by considering a Mach-Zehnder interferometer configuration. The conversion mechanism is based on the signal amplification combined with a large nonlinear phase shift generated by the cascading process. The resulting performance indicates high conversion efficiency and wide band operation.

The nonlinear phase shift has been previously demonstrated only by considering one input beam, *p*, propagating in a $\chi^{(2)}$ material close to, but not exactly at, phase-matching [5]. Conversely, we show that a considerable nonlinear dephasing can be induced on the signal field *s* by a cascaded interaction that is phase-matched for SHG of the pump, but is appropriately mismatched for the DFG process between SH and signal.

Whereas the previous literature on the subject is limited to the case of stationary waves, to study the device performance we numerically solve the nonlinear time-dependent propagation equations. The efficiency of the optical converter is calculated as a function of the detuning of the DFG process and of the duration of the pump pulse.

2. Scheme of the device

Our model considers a PPLN waveguide having poling period Λ and length L. The pulse propagation and the conversion phenomena into the waveguide are described by a standard nonlinear system, valid under the slowly-varying-envelope-approximation, including second-order dispersion terms. The system of equations is solved by the split-

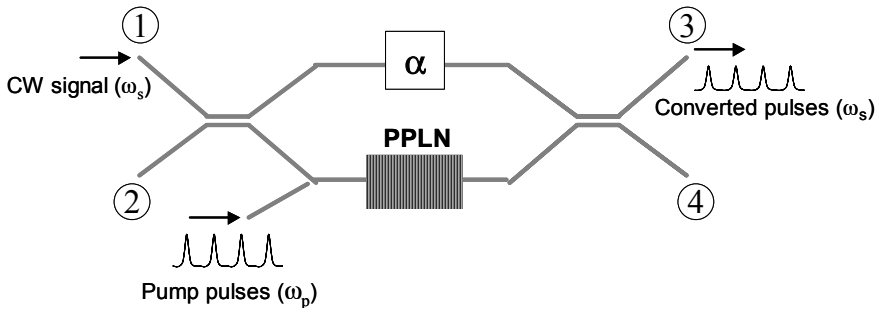


Fig. 1 Scheme of the proposed device.

step Fourier method. The simulation is performed by assuming a CW input signal with a power of 1 mW, and a pulsed pump with peak power of 1 W. The pump pulses are taken to be transform-limited hyperbolic-secant pulses with full-width-half-maximum duration T.

The waveguide is inserted in the Mach-Zehnder interferometer schematically shown in Fig.1. In presence of the pump, the signal travelling through the PPLN waveguide is amplified and phase-shifted. On both arms we consider a loss per unit length α. The port 1 to port 3 transfer function is the following

$$T_{1-3} = \left| \frac{1}{2} \left(e^{-\alpha L} - \left| \frac{s(L)}{s(0)} \right| e^{-i\phi_{NL}} \right) \right|^2 \tag{1}$$

where ϕ_{NL} is the nonlinear phase shift induced on s by the cascading process. The interferometer arms are balanced in such a way that, in absence of pump, the CW signal entering at port 1 appears only at port 4. In fact, when the pump is switched off the second term in the parenthesis equals $e^{-\alpha L}$, giving $T_{1-3} = 0$. It can be easily seen from equation 1 that, when the pump pulse is present, the interferometer can be unbalanced both by the signal gain and by the nonlinear phase. The signal appearing at port 3 is a temporal replica of the pump pulse train at the central frequency ω_s.

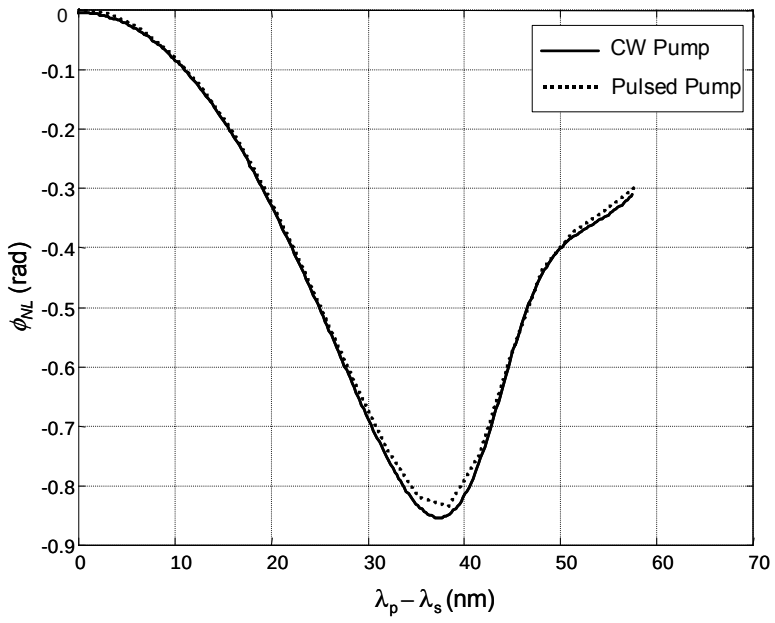


Fig. 2 Nonlinear phase shift of the signal due to a CW pump (solid line) or to a pulsed pump (dotted line)

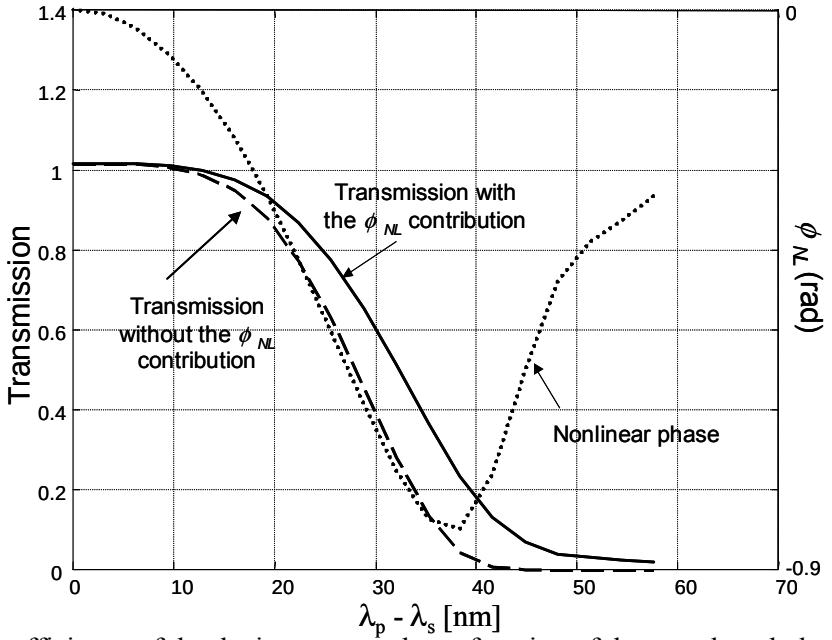


Fig. 3 Conversion efficiency of the device presented as a function of the wavelength detuning (solid line). The dashed line represents the conversion efficiency obtained without considering the nonlinear phase shift. The behaviour of ϕ_{NL} is reported in dotted line.

We have numerically derived the nonlinear phase shift ϕ_{NL} induced on the signal field by the cascaded interaction. We present in Fig. 2 the behavior of ϕ_{NL} as a function of the detuning between pump and signal, by assuming an input pump power of 1 W and a waveguide length of 6 cm. The phase shift attains the maximum value when the detuning is around 37 nm. The figure shows also that the result obtained by using 150-ps pump pulses is almost identical to that obtained with a CW pump. In the pulsed case we consider the phase shift induced by the peak power.

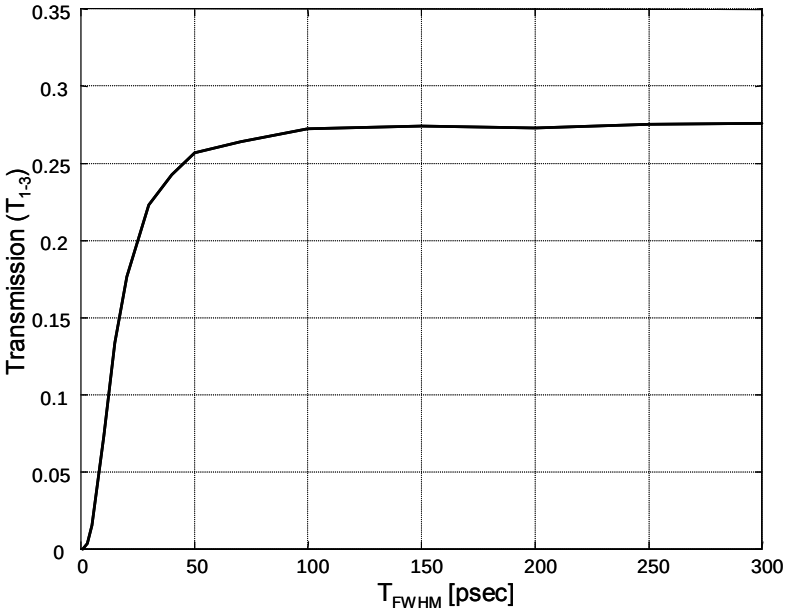


Fig. 4 T_{1-3} as a function of the pump pulse duration. The transmission is calculated at the wavelength at which the nonlinear phase shift is maximum

In figure 3 is reported T_{1-3} as a function of the wavelength detuning between the pump and the signal. For a 6 cm long PPLN waveguide the overall bandwidth is about 32 nm. The nonlinear phase shift contribution prevails when the detuning is larger and results in a widening of the conversion band.

Fig.4 shows the transmission T_{1-3} of the Mach-Zehnder interferometer, as a function of the pulse duration. The transmission drops considerably for short pulses: this fact has to be ascribed to the temporal walk-off due to the group-velocity mismatch between pump and second-harmonic field in the PPLN waveguide. Of course shorter pulses can be efficiently converted by decreasing the waveguide length.

To test the quality of the converted pulses obtained at the device output, we calculated the time dependent phase of the output pulses and their optical spectrum. Due the intrinsic characteristics of the cascading phenomenon and to the Mach-Zehnder transfer function, the output pulses have a different envelope shape and a shorter duration when compared to the sech input. At low values of the wavelength detuning between pump and signal, the conversion is mainly due to the signal amplification and the output pulses results transform limited. In the case of large detuning the nonlinear phase gives a larger contribution to the conversion phenomenon and the output pulses result slightly chirped.

3.Conclusions

As a conclusion, we have proposed a scheme for an all-optical wavelength converter exploiting the effects of amplification and nonlinear phase shift due to cascaded second-order interactions. By using waveguided interactions, the converter exhibits good efficiency and wide operation band with a limited input power. In order to limit the effects of temporal walk-off related to SH generation, an appropriate pulse duration and waveguide length have to be chosen.

References

[1] G.P. Banfi, P.K. Datta, V. Degiorgio, and D. Fortusini, "Wavelength shifting and amplification of optical pulses through cascaded second-order processes in periodically poled lithium niobate" *Appl. Phys. Lett.* **73**, 136-138, 1998 .

[2] I. Cristiani, G.P. Banfi, V. Degiorgio, L. Tartara "Wavelength shifting of optical pulses through cascaded second-order processes in a lithium-niobate channel waveguide" *Appl. Phys. Lett.*, **75,** 1198-1200, 1999.

[3] M.H. Chou, I. Brener, M.M. Fejer, E.E. Chaban, S.B. Christman, "1.55-μm-band wavelength conversion based on cascaded second-order nonlinearity in $LiNbO_3$ waveguides", *IEEE Photon. Technol. Lett.*, **11,** 653-655, 1999.

[4] G. Schreiber, H. Suche, Y. L. Lee, W. Grundkötter, V. Quiring, R. Ricken, and W. Sohler, "Efficient cascaded difference frequency generation at 2 GHz and 10 GHz repetition rate in a periodically poled Ti:$LiNbO_3$ waveguide" *Proc. ECIO* 209-212, 2001.

[5] G. I. Stegeman, D.J. Hagan, and L. Torner, "$\chi^{(2)}$ cascading phenomena and their applications to all-optical signal processing, mode-locking, pulse compression and solitons", *Opt. Quantum Electron.* **28** 1691-1740, 1996.

Epitaxial and polycrystalline ferroelectric $BaTiO_3$ thin films used for optical switching

A. Petraru, J. Schubert, M. Schmid and Ch. Buchal
Institut für Schichten und Grenzflächen (ISG1-IT), Forschungszentrum Jülich, D-52425 Jülich, Germany
a.petraru@fz-juelich.de

Keywords: Mach-Zehnder modulators, ferroelectrics, electro-optic

Introduction

$BaTiO_3$ is an attractive material for electro-optical devices in thin film technology due to its large electro-optic coefficients[1], its high transparency in the visible and near infrared range and its favorable growth characteristics.

The $BaTiO_3$ (BTO) films used in our experiments have been grown by pulsed laser deposition (PLD). By modifying the growth conditions (substrate temperature, oxygen pressure and energy per pulse) we have grown epitaxial c-axis and a-axis thin $BaTiO_3$ films and also polycrystalline films on MgO substrates.

Mach-Zehnder waveguide modulators have been patterned using optical lithography and ion beam etching. The waveguides are of the ridge type, 3 µm wide with a ridge step height of 70 nm on a 1 µm thick $BaTiO_3$ film. They allow to propagate a single optical mode both at 633 nm wavelength and 1550 nm wavelength. A lithographic lift-off process with subsequent deposition of a metal layer of 10 nm Cr and 90 nm Au was used to prepare the electrodes. The length of the electrodes is 3 mm and the distance between adjacent electrodes is 10 µm. The modulator input and output faces have been cleaved.

Epitaxial $BaTiO_3$ thin film optical switches

c-axis films

The c-axis oriented $BaTiO_3$ films on MgO were grown by PLD using a laser power of 1100 mJ/pulse, a substrate temperature of 800 ºC at an oxygen pressure of 10^{-3} mbar. More detailed growing conditions and structural characterization of the films can be found in Ref. [2]. The measured damping coefficient of the planar waveguide is typically about 3 dB/cm.

The optical axis of the $BaTiO_3$ films is perpendicular to the substrate plane in this case, and the applied electrical field is perpendicular to the optical axis, as it is shown in Fig.1.

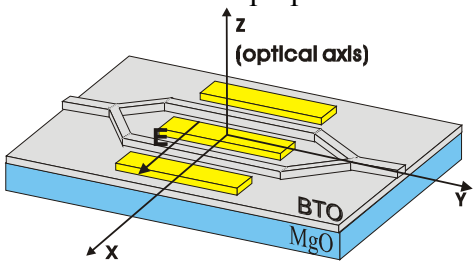


Figure 1. The geometry of the c-axis optical modulator and the orientation of the applied electrical field in respect with the crystallographic axes of the epitaxial $BaTiO_3$ film.

The TE polarized light given by a laser diode is end-fire coupled into the waveguide. The experiments were performed for two wavelengths: 633 nm and 1550 nm. The output of the waveguide is coupled to another single mode fiber, which leads to a silicon detector. Contact needles, supported by micromanipulators, are used to apply the voltage to the middle and to one outer electrode. The transmitted optical intensity is measured as a function of the applied voltage.

Figure 2 presents the result of the measurement for a c-axis modulator at 1550 nm wavelength, with an electrodes spacing of 10 μm.

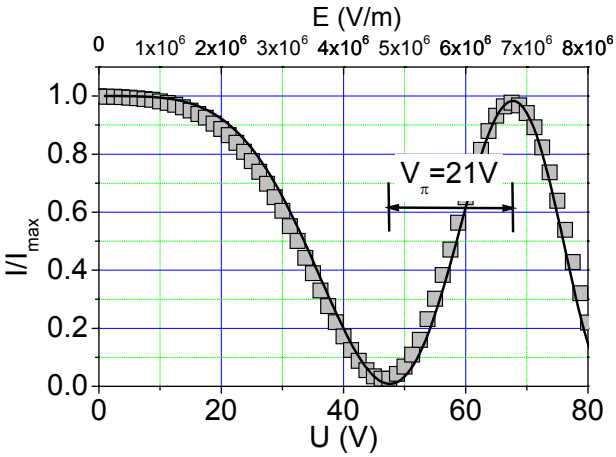


Figure 2. Intensity modulation of a c-axis film thin-film Mach-Zehnder modulator vs. applied voltage at 1550 nm. Dots are the measured data, the line is given by the theory.

The r_{51} Pockels coefficient is involved in this case for the electro-optical response of the modulator, as it is shown in Ref. [3]. The line graph represents the theoretical response of the device with r_{51} = 48 pm/V. The measured values for the ordinary and extraordinary refractive indices used for determining of the r_{51} coefficient are n_o = 2.252 and n_e = 2.247. The refractive indices are measured at 1550 nm wavelength with a prism-coupling set-up [4].

A V_π of 21 V is measured at an applied electric field of about 6 V/μm, as is shown in Fig. 2. An improvement of the device performances can be achieved by lowering the electrodes separation and increasing the length of the active region (electrodes). Thus, a V_π of 15 V at an applied electrical field of 4.5 V/μm has been achieved by reducing the electrodes separation from 10 μm to 5 μm, at the same operating wavelength.

a-axis films

a-axis $BaTiO_3$ films (c-axis in-plane) were formed using a reduced laser power of 300 mJ/pulse and a substrate temperature of 850 °C. The samples showed a slightly higher damping coefficient then for the c-axis films of 4 dB/cm.

The Mach-Zehnder modulators have been fabricated in the same way like for the c-axis films. Because of the different film orientation, the applied electrical film is parallel with the optical axis of the film. Thus, the r_{13} and r_{33} Pockels coefficients are involved now, the output intensity is given by [3]:

$$I_{out} = \left| \frac{1}{2} e^{i\frac{\pi l}{\lambda}\left[(n_e - n_o) - \frac{1}{2} n_c^3 r_c E_z\right]} + \frac{1}{2} e^{i\frac{\pi l}{\lambda}(n_e - n_o)} \right|^2, \qquad (1)$$

where l is the length of the electrodes, n_o, n_e are the ordinary and the extraordinary refractive indices of the film, E_z is the driving electrical field and $r_c = r_{33} - \left(\frac{n_o}{n_e}\right)^3 r_{13} \cong r_{33} - r_{13}$ is an effective electro-optic coefficient.

The experimental results are shown in Fig. 3.

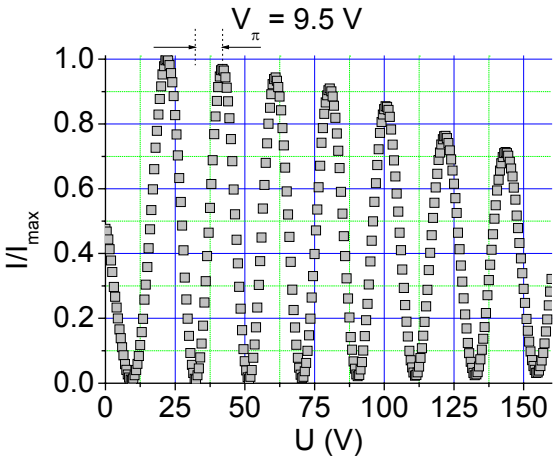


Figure 3. Intensity modulation of an a-axis film thin-film Mach-Zehnder modulator vs. applied voltage at 1550 nm. A half wave voltage V_π of 9.5 V can be observed.

An effective Pockels coefficient r_c of 56 pm/V has been estimated. The modulation depth is 99.1%, corresponding to a 20.5 dB extinction ratio.

Polycrystalline $BaTiO_3$ thin film optical switches

The integration of these devices on Si and on other substrates is desirable, but the very different thermal expansion coefficients of the isolating layer and of the $BaTiO_3$ film make this a difficult task. The replacement of the epitaxial $BaTiO_3$ layer by a polycrystalline layer simplifies a potential integration considerably, because the deposition temperature can be lowered and the optical separation layer to the substrate could be replaced by an amorphous SiO_2 layer. The polycrystalline films were grown on MgO substrates at relatively low temperature (400°C) by pulsed laser deposition at an oxygen pressure of $2x10^{-3}$ mbar. The polycrystalline films are still highly transparent with an estimated waveguide propagation loss of 4 dB/cm at 633 nm wavelength. Although polycrystalline, the BTO is still birefringent with n_o= 2.316 and n_e = 2.301.

The composition and the thickness of the sample were measured by Rutherford Backscattering Spectroscopy (RBS). The Ba: Ti ratio is 1: 1 within the resolution, in accordance with the initial target composition. In RBS/Channeling experiments, no channeling in the Ba signal could be detected, indicating that the $BaTiO_3$ films are not preferentially textured on the MgO substrate.

Grazing incidence X-Ray Diffraction (XRD) measurements were performed, confirming the films are polycrystalline. The lines are broadened, therefore it is difficult to distinguish between tetragonal and cubic phases of $BaTiO_3$. AFM measurements on a 1x1 μm^2 area gave an rms roughness of 0.9 nm, comparable with the epitaxial grown films. The in-plane and the out-of-plane refractive indices of the $BaTiO_3$ polycrystalline films with the thickness of around 1 μm have been measured using a prism coupling setup and the values measured at 633 nm wavelength are n_o =

2.316 ± 0.002 and n_e = 2.301 ± 0.002. The birefringence of the films is about 0.015 ± 0.002. The measured damping coefficient of the planar waveguide is 4 dB/cm.

Mach-Zehnder modulators have been fabricated using the same method like for the epitaxial films modulators, with identical geometrical characteristics.

The electro-optical response of the modulator for 633 nm (line) wavelength and 1550 nm (dots) wavelength is shown in Fig. 4.

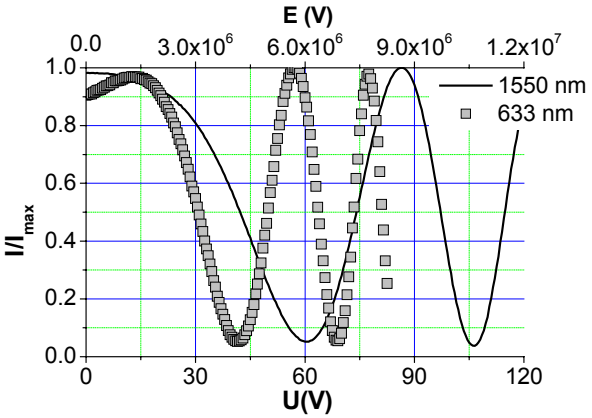


Figure 4. Response of the modulator while changing the applied voltage at 633 nm wavelength and 1550 nm wavelength. The voltage was applied to one arm of the modulator and the electrode spacing was 10 μm.

An effective electro-optic coefficient of r_{eff} = 24 pm/V at a bias of 6 V/μm has been estimated.

Identical optical modulators with smaller separation distance between the electrodes of 5 μm have been fabricated. Infrared measurements at 1550 nm wavelength show a V_π=17 V at 10 V/μm applied electrical field.

Conclusion

Epitaxial thin film $BaTiO_3$ Mach-Zehnder modulators with two different film orientation (c-axis and a-axis) have been demonstrated. For the c-axis film modulators, has been evaluated an r_{51} Pockels coefficient of 48 pm/V. In the case of the a-axis film modulators, an effective electro-optical coefficient r_c of 56 pm/V has been evaluated. Polycrystalline $BaTiO_3$ thin film modulators suitable for integration on Si have also been demonstrated, with an effective electro-optical coefficient of 24 pm/V.

Acknowledgements

This work was supported by the DFG (Graduiertenkolleg Azentrische Kristalle)

References

[1] M. Zgonik, P. Bernasconi, M. Duelli, R. Schlesser, and P. Günter, Phys. Rev. **B 50**, 5941 (1994)
[2] L. Beckers, J. Schubert, W. Zander, J. Ziesmann, A. Eckau, P. Leinenbach, Ch. Buchal, J. Appl. Phys. **83**, 3305 (1998)
[3] A. Petraru, J. Schubert, M. Schmid and Ch. Buchal, Appl. Phys. Lett. **81**, 1375 (2002)
[4] R. Ulrich and R. Torge, Appl. Phys. Lett. **12**, 2901 (1973)

The Segmented Waveguide sensor: principle and experiments

Joris van Lith, Paul.V. Lambeck, Hugo.J.W.M. Hoekstra, Rene. G. Heideman
Lightwave Devices Group, MESA^{+}-institute, University of Twente, P.O. Box 217,
7500 AE Enschede, the Netherlands
J.vanLith@el.Utwente.nl

A novel type of chemo-optical sensor has been designed, fabricated and characterized. The sensor is simple to fabricate and it shows a resolution of the chemically induced refractive index changes better than 5.10^{-7}

Keywords: Segmented waveguides, Sensing, guided-wave optics

Introduction

Integrated optical sensor systems have a large potential to be small, very sensitive and relatively cheap [1]. A novel type of sensor, in which chemically induced changes of refractive index are read out as index dependent losses, has been investigated. This sensor has low demands on the technology and on the quality of the light source, but still enables high resolution. Using standard peripheral equipment a resolution of 5.10^{-7} should be feasible. The sensor can be used as an on/off alarm sensor or for continuous measuring. In this paper first the principle will be treated, followed by presenting the design, the realization, the characterization and conclusions.

Device principle

In figure 1 a longitudinal cross-section of the sensing part is depicted: a ridge type wave-guiding channel consisting of two types of segments: segments with SiON as cladding and segments with a sensing material as cladding. The sensing material is a chemically active material whose refractive index depends on the concentration of a specific chemical compound. A guided mode is launched into the first segment of the waveguide. Due to the difference in field profiles of both types of segments not all guided mode power launched into this segment will be transferred to the guided mode of the adjacent segment. At the transition radiation will be generated. The amount of lost guided mode power of course depends on the difference in refractive index Δn between SiON and the sensing material and hence is a measure for the concentration of the measurand. At one transition the chemically induced loss of guided mode power is very small; however, with a few thousand transitions a quite sensitive sensor can be obtained.

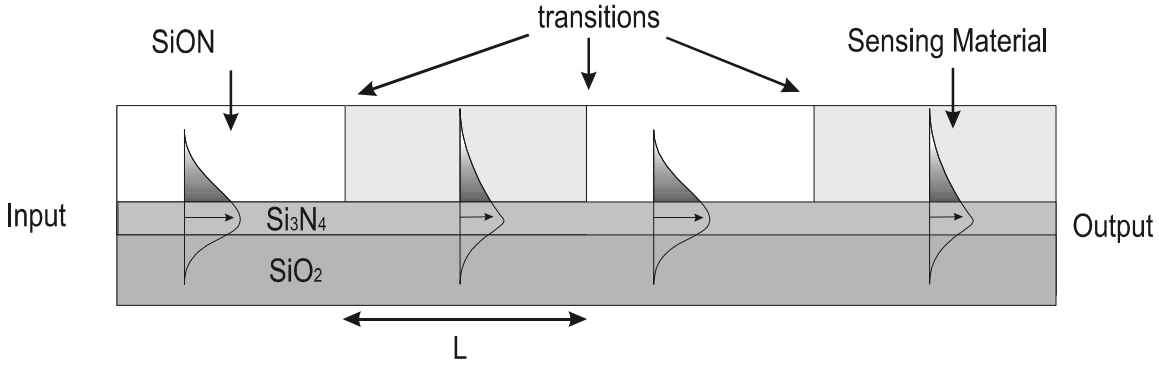


Figure 1. Longitudinal cross-section of the sensor

If there is no difference in refractive index between SiON and sensing material, then no radiation will be emitted: this state is called the working point. The index of the SiON cladding layer can be tailored to that of the sensing material [2], allowing e.g. to define the alarming point of an alarm sensor

Part of the power radiated out at one transition can be transferred to guided modes at the next transition. Depending on the phase difference, there can be constructive or deconstructive interference at the transition between the electrical fields of the original guided mode and the radiation coupling back into the guided mode. The distance L between two transitions mainly determines this phase difference and is thus an important design parameter. Note that the larger the segment length, L, the less radiation is coupled back into the guided mode. Although not required, for simplicity reasons we have chosen for a periodic structure. Note however that the principle works for any distribution in L and that the nature of the distribution itself is a design consideration.

Design

For the design of the Segmented Waveguide Sensor (SWS) it is important to have a simulation method that can handle radiation very well. Three methods have been used: a finite difference beam propagation method [3], a bi-directional eigenmode propagation method [3] and a spectral decomposition method [4,5] all methods being 2D-ones. Unfortunately there were none 3D simulation tools available that could handle the very thin Si_3N_4 core layers, applied in the sensors. The vast majority of the radiation is expected to be directed into the transversal direction, so using 2D methods is probably an acceptable approximation. Results of all methods agreed very well with each other. The spectral decomposition method is very useful for gaining extra insight because in this method the influence of the waveguide structure and the segmentation are expressed as independent factors within the power transfer function.

In the design the sensitivity S, is optimised. This sensitivity is defined as $S = \partial\eta / \partial\Delta n$ where η is the functional loss expressed in dB/mm. So the sensitivity is defined for 1 mm of sensor length and Simulation results show that the functional loss is in approximation a quadratic function of Δn around $\Delta n = 0$.

The two most important design parameters are the thickness of the core layer and the segment length L. The core layer has to be thick enough to guarantee confinement of the modal field in the a layer stack of acceptable thickness (about 5 μm). However it appeared that a thicker core layer results in a decrease in sensitivity while the optimum L will shift towards small values (<2 μm). Such small L values give problems with the fabrication. A core thickness has been chosen that copes optimally with both effects. At this core thickness the waveguide is single mode in the transverse direction and only guides TE light. The sensor has been designed for a 850 nm wavelength because at this wavelength there are cheap commercial light sources available.

Fabrication

The SiO_2 optical buffer layer was grown by thermal oxidation of the silicon wafer. Then the Si_3N_4 core layer was deposited using low-pressure chemical vapor deposition and the channel waveguides were wet-etched using BHF. After that an index matched SiON cladding was deposited using plasma enhanced chemical vapor deposition. The SiON cladding was etched using reactive ion etching. After the deposition of the core layer V-grooves were etched in the wafer for easy fiber-to-chip coupling [6]. In figure 2 a SEM picture of the sensor is shown. In the middle the Si_3N_4 channel waveguide can be seen. On top of the waveguide there are the blocks of the SiON cladding. On top of this structure the sensing layer can be spun, or the structure can be submerged into a liquid. In table 1 the relevant parameters of the fabricated SWS are listed.

Table 1. Parameters of the fabricated SWS

Layer	Thickness	Index (850 nm)
SiO_2	2.8 ± 0.1 μm	1.453 ± 0.001
Si_3N_4	58 ± 0.1 nm	1.996 ± 0.001
SiON	2.00 ± 0.02 μm	1.520 ± 0.001

	Property	Value
SiON	Under-etch	0.5 ± 0.1 μm
SiON	Transition angle	53 ± 5°
Si_3N_4	Channel width	6.9 ± 0.1 μm

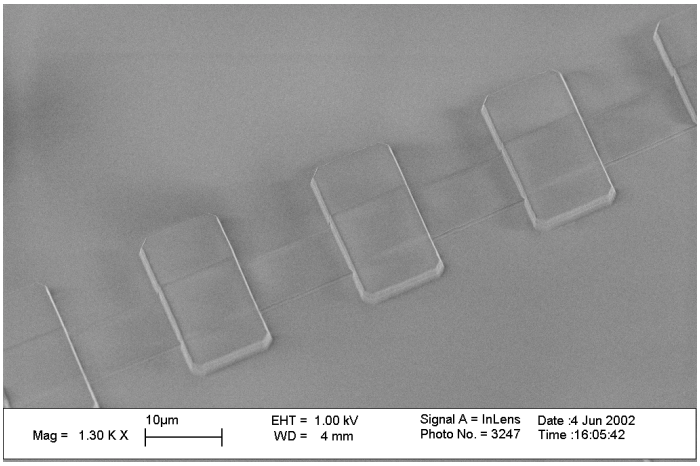


Figure 2. SEM photo of SWS

Characterization and analysis

To demonstrate the principle of the sensor and to check the validity of the calculations, the SWS has been characterized using liquids with a controlled refractive index. For this a cuvette has been clamped on top of the sensing region and varying benzyl-alcohol/alcohol mixtures were fed into the cuvette. The index of this mixture was measured with an Abbe refractometer (accuracy ± 5.10^{-4}, white light). A single mode input fiber is attached to the chip using a V-groove. A multimode fiber is used for the output. The output power was measured as a function of Δn. A typical experimental result is shown in figure 3. As can be seen η (Δn) is approximately a square function, which means that the sensitivity is approximately a linear function of Δn.

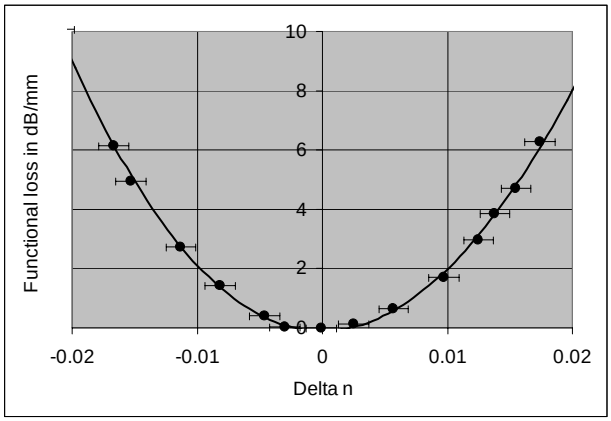


Figure 3. SWS characteristic for L = 9 μm, measurements (points) and simulations (line)

Because of the temperature dependent index and the unknown dispersion, the absolute refractive index of the mixture could not be determined exactly, therefore the whole characteristic has been shifted along the Δn- axis to put the minimum in functional loss at Δn = 0,while the transmitted power at minimum loss itself has been taken as the reference power. The uncertainty in absolute value of Δn is the main contribution to the error bars in figure 3 and 4. In figure 4 both the experimentally obtained and theoretically calculated η(L)- dependences are presented. for Δn = ± 0.01.

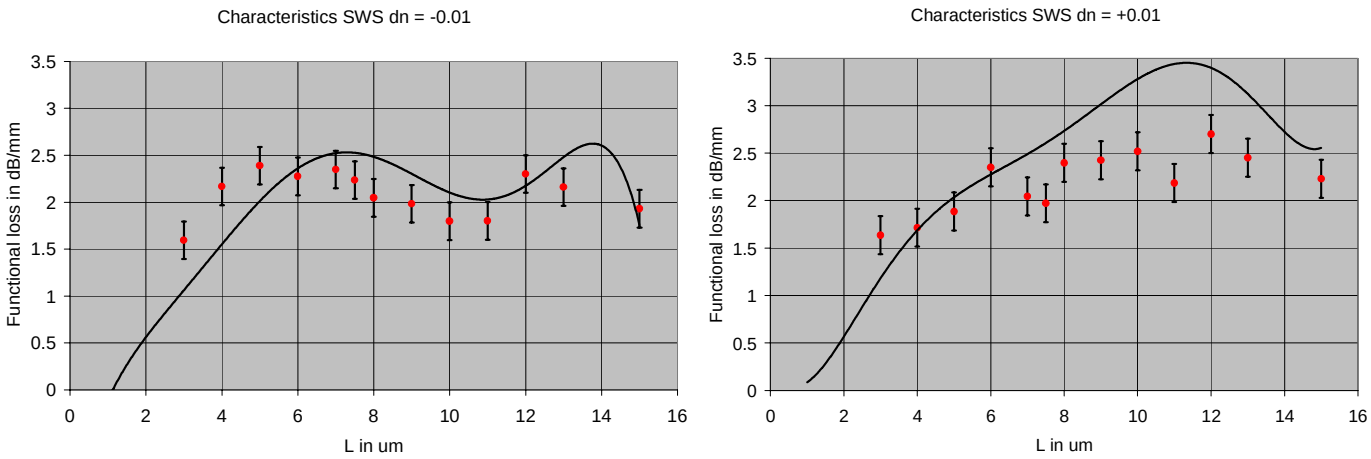


Figure 4. SWS characteristics for different L, measurements (points) and simulations (line)

As can be seen, the experimental points agree reasonably well with the theory. We suppose that their difference can be attributed to the fact that all the calculations were done in 2D and not in 3D. Further it can be seen that it is important that L > 5 μm; the highest sensitivities are obtained for these L-values. In this region the dependency of the sensitivity on L is small.

From these measurements the resolution can be derived. From figure 3, it can be concluded that the sensitivity (proportional to the slope of the characteristic) increases linearly with Δn. Hence the further away from Δn = 0, the larger the sensitivity. We define Δn_w as the refractive index difference at the concentration around which small concentration changes have to be measured. The sensitivity now increases linearly with Δn_w, but the non-functional loss increases with $(\Delta n_w)^2$. Therefore it is more efficient to make the SWS as long as possible and to choose Δn_w close to zero. The propagation losses eventually limit the size of the sensor. Channel losses of the individual segments have been measured to be less than 1 dB/cm. Besides the optical part, also the processing electronics influence the resolution. For the derivation of the resolution a commercially available optical detector with an accuracy of 0.01 dB and a noise level of –90 dBm was taken. Further constant temperature and constant light source power was assumed. After optimizing the segment length and the Δn_w, a theoretical resolution of $\Delta n = 5.10^{-7}$ is theoretically feasible. Adding a reference channel can reduce the influence of disturbances like fluctuations in power and polarization of the light source. We also expect that the resolution can be improved by smart processing schemes. There are also several other possibilities, not mentioned in this paper, for improving the optical part of the SWS.

Summary /Conclusions

The principle of a novel type of a refractive integrated optical chemical sensor, the segmented waveguide sensor, has been explained. This sensor combines a simple technology with a resolution in the refractive index of the chemo-optical transduction layer better than 5.10^{-7}. Experimental performance, measured on a sensor fabricated in SiON technology agrees reasonably well with the theoretical performance as has been calculated by applying several 2D simulation programs. Optimization of the sensing system is expected to enable improved performance.

[1] P.V. Lambeck, *ECIO 2001*, pp. 153-163, 2001

[2] K. Wörhoff, P.V. Lambeck, A. Driessen, *J.Lightwave Techn.*, Vol. 17, No. 8, 1401-1407, 1999.

[3] OlympIOs; *C2V software*, version 5.1.12

[4] S. Gaál, doctoral thesis, Lightwave Devices Group, University of Twente, dec. 2002.

[5] H.J.W.M. Hoekstra, S. Gaál, P.V. Lambeck, *ECIO 2003*, to be published.

[6] R.G. Heideman, P.V. Lambeck, *Sensors and Actuators B*, vol. 61, 100-127, 1999.

Reactive Ion Etching in Silica-on-silicon Planar Waveguide Technology

Haiyan Ou

COM centre, Technique University of Denmark (DTU),
2800, Kgs. Lyngby, Denmark
ho@com.dtu.dk

Reactive ion etching has a wide range of applications in optical waveguide fabrication and is the enabling technology for hybrid integration. The etching mechanism, etch rate, mask material, and selectivity over mask are discussed for core etching, deep glass etching and deep silicon etching.

Key words: reactive ion etching, silica-on-silicon waveguide, groove

Introduction

Since in 1969 Miller proposed the concept of integrated optical circuits (IOC)[1], it has evolved tremendously, especially during the past decade. Silicon was first used as the integration platform and it still has the prominent role until now, which can be ascribed to historical reasons. Long before the dawn of IOC, silicon-based microelectronics technology had been fully developed. Transferring the technology of silicon from microelectronics directly to photonics gives silicon-based IOC technology a substantial headstart. However, silicon is an indirect bandgap semiconductor, and it is very hard to realize efficient light emission and detection. Limited by this property, silicon was only confined to passive IOC, and indium phosphide (InP) was used as IOC platform for active and passive integration [2]. Compared to the silicon platform, InP is of direct bandgap, but it is expensive, and its high refractive index results in compatibility problems with standard fibres. Thus, both material platforms have advantages and drawbacks. Hybrid integration on a silicon platform takes advantage of both material platforms [3].

Different kinds of materials have been applied in silicon-based waveguide technology, such as germanium (Ge) doped glass [4], silicon oxynitride [5], and silicon nitride [6]. Reactive ion etching (RIE) is a key process to define the core geometry of the waveguides, and to etch deep structures across waveguides, which enables hybrid integration. In our cleanroom, Ge-doped glass waveguides on silicon substrate (silica-on-silicon) have been developed. In this paper, etching of glass and silicon using RIE is optimised with regards to the mechanism, mask material, selectivity over mask material, etch rate, sidewall roughness and sidewall angle.

Waveguide fabrication

Waveguide fabrication consists of five main steps: buffer layer growth, core layer deposition, photolithography, core layer etching and top-cladding layer deposition, in which eight processing steps are utilized as: 1) Wet oxidization of the silicon wafer to form a thick silica buffer layer; 2) Deposition of Ge-doped silica to form the core layer by plasma enhanced chemical vapour deposition (PECVD); 3) Spinning and baking of photoresist on wafer; 4) Exposure of photoresist, transferring the waveguide structures from the photolithography mask to the photoresist; 5) Development of photoresist; 6) Etching of the core pattern using RIE; 7) Stripping of photoresist; 8) Deposition of boron and phosphorus co-doped silica to form the top cladding layer by PECVD, with refractive index matched to that of the buffer layer.

During the development of silica-on-silicon planar waveguides, fabrication processing is optimised step by step to achieve best performance and cost ratio. For hybrid integration the

performance is further complicated by the coupling between various elements as these are required to obtain different functionalities. For example, polarization independence of an IOC is becoming more and more important in applications within high bite rate telecommunication. One way to insure polarization independence is by inserting a half-wave plate in the middle of a symmetrical component [7]. Etching of deep grooves across a waveguide and into the silicon substrate therefore becomes a crucial process, requiring an optimised RIE process. A schematic view, demonstrating a groove cutting through the waveguide and into the silicon is shown in Fig. 1.

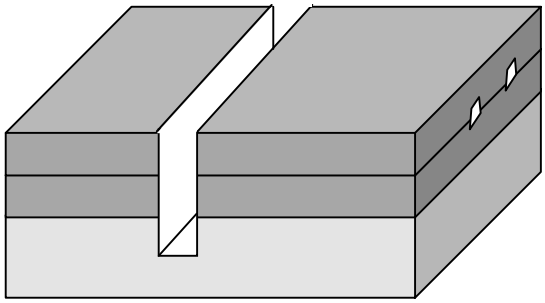


Fig. 1 A groove etched through the waveguide

In Summary, the application of RIE on silica-on-silicon planar waveguide consists of glass etching and silicon etching. Moreover, glass etching is used for two purposes: to define the geometrical structure of the core layer for the waveguide and to form deep grooves. The Silicon etching is performed to extend the groove deep into the substrate.

Mechanism of glass and silicon etching

The main parameters for the RIE process are the gas mixture, the applied RF power, and the chamber pressure. Other parameters such as the configuration of the etch chamber, the masking material on the wafer, and the design of the mask will also affect the etch process. In our cleanroom facilities a fluorine based gas mixture consisting of CF_4 and CHF_3 is used for the glass etching.

The etch process is dependent on the required functionality of the structure. Light is guided in the core layer, which requires that the sidewall and the top surface of the core are smooth, i.e. without roughness, particles and contamination. The core structures subsequently have to be covered by a PECVD glass layer. A slightly sloped sidewall is favourable with respect to step coverage. Photoresist was chosen as masking layer for this purpose because of the simplicity and the sloped and smooth sidewall. On the other hand, deep glass etching requires vertical sidewalls and a high etch rate. Poly-silicon is selected as the mask layer with regard to its high selectivity towards glass.

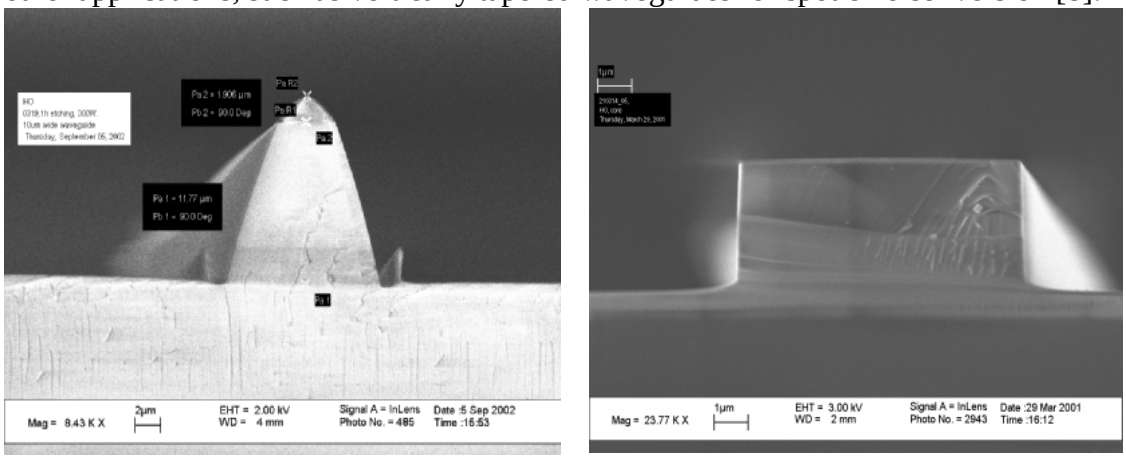
When deep etching of silicon into the substrate, the etched glass layer turns into the mask layer. Therefore, we use SF6 for silicon etching, which has a higher selectivity towards glass and exhibits a higher etch rate in silicon than the freon gasses.

Results and discussion

To arrive at optimised processing we need to categorize our results into three subsections, glass etching to define the geometrical structure of the core layer, deep glass etching to form a groove, etching into silicon to achieve a deep groove reaching into the substrate.

1) *Glass etching to define the geometrical structure of the core layer*

The etch process for the core layer, used to define the structure of the waveguide, has been fully optimised resulting in a record low propagation loss of 0.01 dB/cm. To our knowledge this is the lowest propagation loss ever reported. A big advantage of using photoresist as mask layer is that the sidewall angle of the core layer can be engineered by adjusting the thickness of the resist, as shown in Fig.2 (a) and (b). From the coupling point of view, a square core with vertical sidewall is desired to have a low coupling loss with standard fibres. However, a core layer with angled sidewall has other applications, such as vertically tapered waveguides for spot-size conversion [8].



(a) (b)

Fig. 2 Cross-section profile of angled (a) and vertical (b) glass etching by adjusting the thickness of the mask layer. Resist is still on top of the glass in (a). The etch rate is about 0.12 µm/min. and the selectivity over photoresist is about 5.

2) *Deep glass etching to form a groove*

Resist is excluded in the deep glass etching because fine structures are hard to obtain when thick resist is spun on to act as deep glass etch mask (limited by the aspect ratio of the photoresist). Poly-silicon was applied as the mask layer for the deep glass etching. Fig. 3 shows a SEM picture of a deep and vertical groove. The groove is about 15 µm deep, with smooth sidewall and flat bottom.

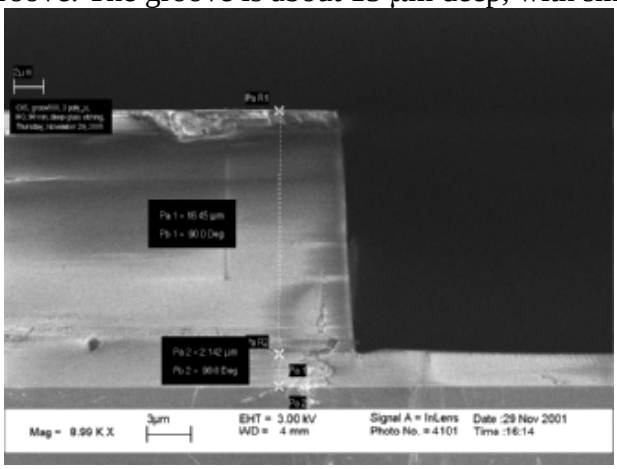


Fig. 3 Cross-section profile of a 15µm deep and vertical groove. The etch rate of glass is 0.24µm/min., and the selectivity of glass over poly-silicon is about 6. The mask layer is still on top of the glass.

3) *Silicon etch for the deep groove into the substrate*

When the groove was etched through the glass into the silicon substrate, glass becomes the mask layer. A SEM picture of a deep groove etched into the silicon substrate is shown in Fig. 4. The

etched thickness of the glass layer (cladding, core and buffer) is about 30 μm, and the etch is continued down into the silicon for another 80 μm. It can be seen that the silicon layer is under etched. By varying the oxygen concentration in the gas mixture, a passivation layer can be formed on the silicon sidewall. This will allow a vertical sidewall.

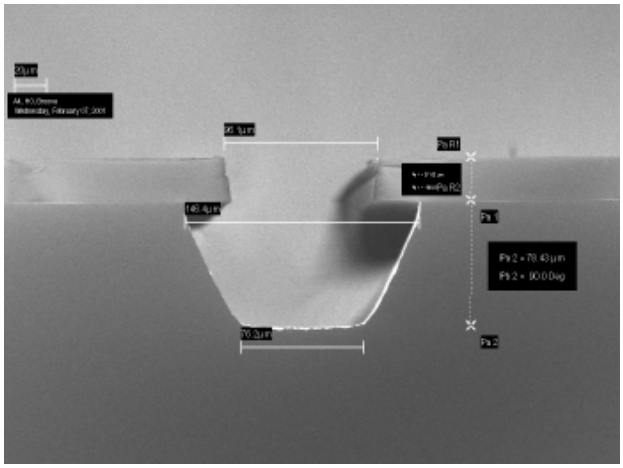


Fig. 4 Cross-section profile of deep silicon etching into the substrate. The etch rate of silicon is 1.12 μm/min, and the selectivity over glass is about 12.

Conclusion

The application of RIE in silica-on-silicon planar waveguide technology includes imprinting of a waveguide structure into the core layer and groove etching. Etching mechanism for core glass, thick glass and thick silicon in the formation of grooves is described. The core was etched with photoresist as mask, and record low propagation losses of 0.01 dB/cm have been obtained after optimisation. A poly-silicon mask was employed for the deep glass etch enabling a high etch rate and smooth vertical sidewalls. Deep silicon etching was shown to have a very high etch rate of 1.12 μm/min with the glass mask and optimisation with respect to the underetch is in progress.

Reference:

[1] S. E. Miller. *Bell Syst. Tech. Journal*, **48(7)**, 2059-2069, 1969.
[2] Smit, M.K. *Optical Fiber Communication Conference 2000*, **2**. 76, 2000.
[3] M. Kawachi, *Optical and Quantum Electron.*, **22**, 391-416,1990.
[4] S. Suzuki, M. Yanagisawa, Y. Hibino, and K. Oda, *J. Lightwave technol.* **12 (5)**, 790-796, 1994.
[5] M. Bohn, F. Horst, and B. J. Offrein, et al, *ECOC' 02*, paper **4.2.3**, 2002.
[6] W. E. Swendsen, H. T. Philipp, M. Svalgaard, et al, *ECOC' 02*, paper **4.2.4**, 2002.
[7] H. Takahashi, K. Oda, H. Toka and Y. Inoue, *J. Lightwave Technol.* **13**, 447-455, 1995.
[8] A. Sugita, A. Kaneko, and K. Okamoto, et al, *IEEE photonics Technol. Lett.*, **12**,1180-1182, 2000.

The multiple channel acoustooptic tunable filter with super narrow optical linewidth based on the set of multi-reflector beam expanders

Andrei Tsarev, Eugeny Kolosovsky
Institute of Semiconductor Physics SB RAS, Prospect Lavrenteva, 13, Novosibirsk, 630090, Russia
tsarev@thermo.isp.nsc.ru

The new architecture of multiple channel noncollinear acoustooptic tunable filter (AOTF) based on multi-reflector beam expanders is presented. It provides simultaneous multiple drop of individual wavelength at different fiber output by single SAW frequency operation.

Keywords: guided-wave optics, acoustooptics, tunable filters, DWDM

Introduction

Noncollinear acoustooptic tunable filters (AOTF) [1, 2] based on multi-reflector (MR) beam expanders [3, 4] overcomes some traditional restrictions of acoustooptics and have some advantages to it's competitive technologies since it will have the smaller size, thinner linewidth, better thermostability, etc. [5, 6] Here are presented additional advantages of MR-AOTF that provides simultaneous multiple drop of individual wavelength from the set of MR-beam expanders coupled with different fibers output [1, 2]. Device operates at single SAW frequency that totally eliminates “coherent crosstalk”, due to the interaction of the lightwave with several acoustic waves that is traditional for other types of AOTF. Independent wavelength drops provided by electrooptic/thermooptic individual tuning of refractive index in the beam expanders vicinity.

Principal description

The principal view of the device is shown on Fig.1. It contains monomode planar and strip waveguide structures, interdigital transducer (IDT) for excitation of SAW, and a set of individually tuning multi-reflector optical beam expanders (BE) [3, 4] that further evolves the fruitful idea of grating beam expanders. The work of multi-channel AOTF can be described as follows [1, 2, 5]. Let optical beam of multiple wavelengths within spectrum range $\Delta\lambda$ comes from the input Fiber "in" to the input strip waveguide. Then it passed through optical beam expander that contains an array of multiple partially reflected mirrors. It extends the optical beam and transforms it to the planar optical waveguide. The efficiency of transformation depends on device parameters and in optimal conditions can be as much as 90%. Than the expanded optical beam comes to the area of acoustooptic interaction and diffracts by SAW. Expanded optical beam contains a set of angular spectrum components but only one of them of the largest intensity satisfied the Bragg conditions and comes into interaction with SAW. This spectral component is chosen by SAW and changes the angle of propagation by the double Bragg angle and directes to the beam expander of the drop channels. These beam expanders works as a reciprocal optical elements. They can transform wide optical beam to the output "drop" fibers 1-4. However, it picks up (drops) only those optical beams that at every desired optical wavelength have the proper designed direction of propagation, depending of the parameters of the beam expander (angle and period of reflectors, as well as refractive index in the strip waveguide vicinity). By changing the SAW frequency due to the Bragg conditions one can change the direction of propagation of the diffracted

beam that enter the set of beam expanders and thus arrange wide tuning the optical wavelength that are individually dropped by beam expanders of the multi-channel AOTF [1, 2].

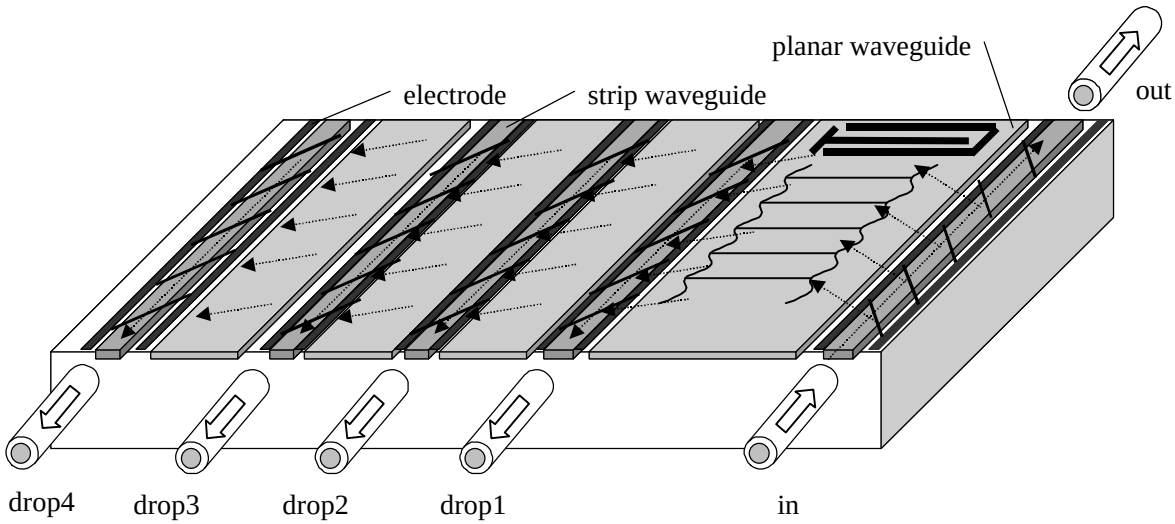


Fig.1. Principal view of the multiple channel acoustooptic tunable filters with multi-reflector beam expanders.

Results of simulations

The quantitative descriptions of the AOTF is very complicated thus the first reasonable quantitative estimates had be done by simple and evident approximation analyse [1, 2, 5] based only on the calculation of beam expander spectrum [5]. Now present more precise simulations of AOTF performances based on phenomenological descriptions of the properties of reflector array as a set of parameters R, T, and α (reflection and transmission coefficients and scattering losses, respectively).

For the simplicity the lateral distribution of optical filed of TM guided mode in the strip waveguide is described by Gaussian function with the half width w_0=3.25 μm that good adjusts the real optical filed distribution. The reflector spacing d=10 μm and waveguide effective refractive index Nm=2.31 are chosen from the condition of 15th order interference of the beam expander sub-beams at central optical wavelength 1.54 μm. Reflector apertures regarded infinitive that hardly simplifies the simulations as optical spectrum of beam expander can be descried as a sum of analytic functions [5]. Angular optical spectrum of the beam expander looks like the spectrum of Michelson echelon and is used to calculate the optical field at any point of optical waveguide by reverse Fourier transformation. The SAW aperture is rather large (several millimetres) that provides Bragg regime of acouistooptic interactions. Thus acoustooptic Bragg sell chose part of the beam expander spectrum that forms the wide optical beam with the aperture function generally described by apodisation of reflector coefficients. By known spectrum that leaves acoustooptic area we calculate optical field that enters the beam expanders of "drop" channels. The simulated signal from every drop channels is calculated taking into account multiple reflection and interference of reflected sub-beams from every reflector. The efficiency of transformation of wide optical beam into guided mode of strip waveguide is calculated by overlap integral of input optical field with that of guided mode of TM polarisation. The other (TE) polarisation is not take into account as the reflectors are arranged close to Brewster angle and influence of TE guided wave on device performances is negligible.

The response of the tunable filter at different drop channels and single operated SAW wavelengths are shown on Fig.2 for the case of 25 GHz ITU grid. It is well visible that by the change of refractive index in the vicinity of beam expanders one can individually tune the drop wavelength. The tuning range corresponds to 0.06% of the refractive index change per ITU wavelength channel. Device provides good extinction ratio (-29 dB) between neighbour channels and internal losses around -3.7 dB. To decrease optical losses one need to optimise the waveguide's width and reflector spacing of the beam expanders, but this extends the used proposition that reflected beams have a very small area of intersection that allow us use infinite aperture function of reflector beams.

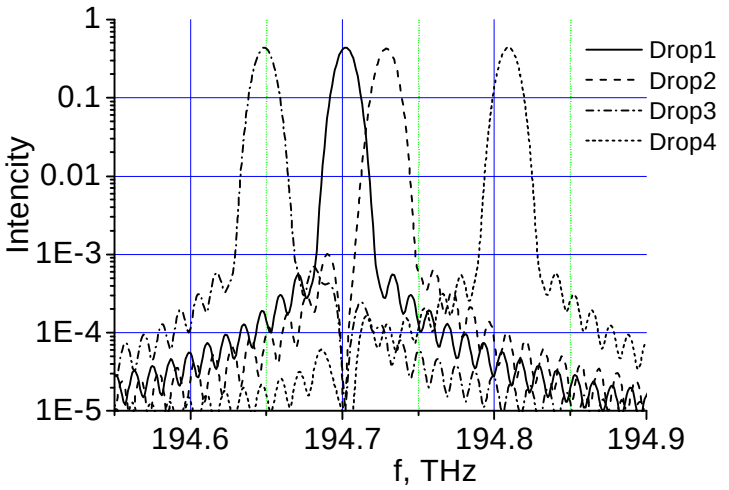


Fig.2. The response of AOTF at different drop channels wide tuned by the single SAW frequency (700 MHz). dNm/Nm=0.0000, 0.0006, -0.0012 and 0.0024 for drop channels 1-4, respectively. N=580, d=10 μm , total aperture is 0.58 cm.

Conclusions

Presented results of small-size multi-channel AOTF are very promising and may stimulate experimental investigation and development of the novel type of AOTF that can make the base of the future DWDM fiber optical networks with 25 GHz and 12.5 GHz wavelength ITU grid.

The work was done under the Grant 03-02-16264 from Russian Fund of Basic Research.

References

[1] A.V.Tsarev "Acoustooptic tunable filter", *Patent of the Russian Federation* **No 2182347** *Bulletin* **No 13**, 10.05.2002.
[2] A.V.Tsarev: Acousto-Optical Variable Filter, *PCT Publication Number* **WO 02/12953**, 2002.
[3] A.V.Tsarev. Optical beam expander, *Patent of the Russian Federation* **No 2183337**, *Bulletin* **No 16**, 10.06.2002.
[4] A.V.Tsarev, Beam-Expanding Device, *PCT Publication Number* **WO 02/06873**, 2002.
[5] A. Tsarev. *Applied Physics B*, **V. 73** , **No 5-6**, 495 – 498, 2001.
[6] A. Tsarev, *2002 IEEE/LEOS Meeting, 10-14 November 2002, Glasgow, Scotland, Conference Proceedings,* ThVI, pp. 823-824, 2002.

Erbium Incorporation and Optical Properties of Er^{3+} ions in APE Er:$LiNbO_3$ Waveguides

Pavel Čapek, Josef Schröfel,
Faculty of Electrical Engineering, Czech Technical University
Technická 2, 160 00 Praha 6, Czech Rep.
xcapekp@feld.cvut.cz

Anna Macková,
Nuclear Physics Institute of ASCR, Rez near Prague, 250 68, Czech Rep.

R. Groetzschel,
Institute of Ion Beam Physics and Material Analysis, Forschungzentrum Rossendorf, Dresden, Germany.

Volkmar Dierolf, Christian Sandmann,
Dept. of Physics, Lehigh University, Bethlehem, PA, USA

Pavla Nekvindová, Jarmila Špirková, Petr Macháč,
Institute of Chemical Technology, Technická 5, 166 28 Prague 6, Czech Rep.

We investigated the erbium incorporation in $LiNbO_3$ planar waveguides produced by annealed proton exchange using the RBS-channeling technique and site selective excitation-emission spectroscopy at low temperature. We found that, different from other methods of waveguide-production, the proton exchange has almost no influence on the incorporation and optical properties of the Er^{3+} ions.

Keywords: Er ions, proton exchange waveguides, site-selective spectroscopy, RBS-channeling

Introduction

Optical amplifiers and lasers based on rare earth dopants are important integrated optical devices with large application potential [1]. In recent years $LiNbO_3$ has emerged as one of the main host materials due to its very favorable electrooptical, acustoptical and non-linear properties. Moreover, several techniques have been established to create low loss optical waveguides. Among the rare earth ions Er^{3+} plays a prominent role due to its optical transition around 1.5 μm which makes it the active ion of choice for optical communication applications. Despite the well shielded character of the 4f electrons the optical transitions are influenced within a crystal by the presence of the other ions. Most notably the degeneracy of the states is removed leading in $LiNbO_3$ to a splitting in (2J+1)/2 Stark sublevels. Details of these splittings and the separation between states is determined by details of the local environment. It was found in several studies (e.g.: [2]) on bulk material that several different environments ("sites") are present in $LiNbO_3$, which are distinct by the way the required charge compensation is achieved.

An earlier systematic study [3] under application of external perturbations established an intuitive tool to connect spectral shifts in the optical transitions to changes in the nearest neighborhood and long range intrinsic electric fields and to distinguish between these two interaction types. These results make the Er^{3+} an ideal probe for the local environment and allow the study of interaction effects among dopants in $LiNbO_3$. While investigations on bulk material are abundant only few waveguide specific studies exist [4, 5, 6]. These are mainly limited to waveguides produced by Ti-diffusion and show that the Ti^{4+} ion strongly influence the local electric field experienced by the Er^{3+} while leaving the direct neighbor unchanged. The influence is manifested in the optical spectra by a significant inhomogeous broadening.

The proton exchange (PE) waveguides is another method for fabricating optical waveguides [7]. PE is based on a reaction of the lithium niobate wafer with a suitable acidic source

which results in a large increase of the extraordinary refractive index. The PE waveguides have high loss and degrade electro-optic properties. However, they can be substantially improved by the annealing of the waveguides. Properties of the resulting annealed proton exchange (APE) waveguides strongly depend on the exchange conditions as well as on any subsequent annealing conditions. One of the main advantages of APE waveguides is guiding only TM polarization or TE polarization for Z-cut $\langle 0001 \rangle$ or for X-cut $\langle 11\bar{2}0 \rangle$ of the $LiNbO_3$, respectively.

In this paper we extend our approach to APE waveguides and study how Er^{3+} ions are influenced in the this waveguide environment.

Sample preparation and experimental methods

The samples of $LiNbO_3$ used in this work were grown from the congruent melt to which our Er^{3+} dopant was added ($[Er^{3+}]$ = 500 ppm). The planar waveguides were fabricated by annealed proton exchange process at 213 ^oC for 3 hours. The waveguides were single mode for 1.5 μm and the proton profile reaches about 10 μm into the sample.

For comparision we used $LiNbO_3$ channel waveguides produced by Ti-diffusion (110 nm layer thickness, $T_{diff} = 1060^oC$, t = 10h) in the group of Prof. Sohler (University Paderborn, Germany). These waveguides were also designed to be single mode at 1.5 μm. The Er^{3+} doping levels in these samples were comparable to those of the bulk doped samples but the incorporation was achieved by indiffusion. For details see Ref. [8].

In order to study the lattice location of Er^{3+} we used the RBS (Rutherford Backscattering Spectrometry)-channeling technique which is based on the effect that channeling of energetic ion beam occurs when the beam is carefully aligned with a major symmetry direction of a single crystal. Channeled particles cannot get close enough to the atomic nuclei to undergo large angle Rutherford scattering - hence scattering from the substrate is drastically reduced by a factor of 100. Scattering kinematics separates the signal of the impurity Er^{3+} and host lattice of $LiNbO_3$. The angular yield curve is obtained by monitoring the yield of the impurity and the host lattice. From the angular yield curves (angular scans) of the axial channels in $LiNbO_3$ in 3 different directions (cuts) is possible to determine the Er^{3+} position in the measured cut and finally in the $LiNbO_3$ lattice [9]. In order to determine the lattice position of Er^{3+} in $LiNbO_3$ several relevant crystallographic directions have been selected to perform the angular scans. The angular scans along the X $\langle 11\bar{2}0 \rangle$, Y $\langle 01\bar{1}0 \rangle$, and Z $\langle 0001 \rangle$ axis were measured for the samples treated by APE X-cut, Y-cut and Z-cut. The RBS experiment was performed in the Forschungzentrum Rossendorf, Dresden (Germany) using a Van de Graaff accelerator. The beam of alpha particles 1.8 MeV was used.

Combined excitation-emission spectroscopy (CEES) is a very powerful tool to investigate subtle changes in the optical transitions to investigate the local energetical environment of erbium. It is described in detail in Ref. [5]. The CEES measurements were performed in the Lehigh University, Dept.Physics, PA, USA.

Experimental results and discussion

RBS. In the structure of $LiNbO_3$ four different lattice sites are available to be occupied by foreign ions: two substitutional octahedral sites (Li^+ and Nb^{5+}), an additional free octahedron and a tetrahedral vacancy sites. The scan along the $\langle 0001 \rangle$ axis is useful to disregard any position out from the z axis. The signal from Nb^{5+} ions is practically identical to that of Er^{3+} ions (see Fig. 1) and so it can be concluded that they are located in three possible positions along the z axis i.e. Nb^{5+} site, Li^+ site or structural octahedral site. For precise determination of Er^{3+} position inside the Li^+ octahedron we studied the scan along $\langle 01\bar{1}0 \rangle$ and $\langle 11\bar{2}0 \rangle$ axis (see Fig. 1). In the case of the octahedral position we should see the maximum in the scan along $\langle 11\bar{2}0 \rangle$ axis see [10], but we don't in our case. Finally, on the basis of computer simulations of

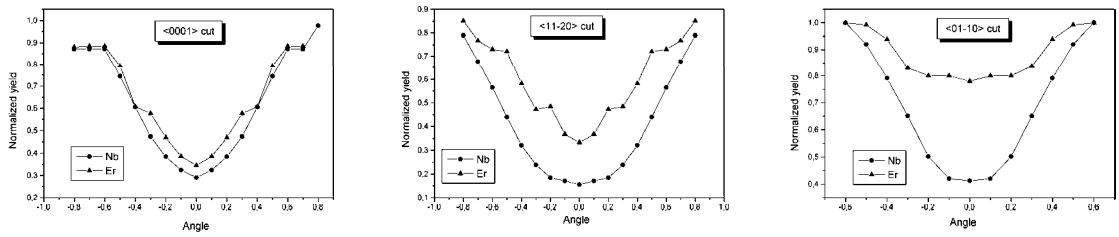


Fig. 1. $LiNbO_3$ angular scans along $\langle 0001 \rangle$, $\langle 01\bar{1}0 \rangle$ and $\langle 11\bar{2}0 \rangle$ axis.

the RBS data (Fig. 1) we can conclude that the Er^{3+} ion sites on the Li^+ site and is shifted in the direction along -z axis, similar as has been found for bulk material [10].

Excitation-Emission Spectroscopy. Inspecting the CEES data of the emission at around 550 nm obtained in the APE waveguides under excitation at around 450 nm and comparing it to bulk material and Ti:diffused waveguides reveals that the major sites are essentially unchanged. Subtle differences are found when individual emission spectra under identical excitation energies are compared for APE waveguide, the bulk and in the Ti-diffused waveguide. For instance, in the spectra shown in Fig. 2 three sites can be distinguished by decomposition. Earlier studies [2] showed that they all have the same primary charge compensation and are distinct in the secondary one. The sites, which are least perturbed (i.e. the secondary charge compensation is distant), exhibit in the depicted spectral range the emission peaks at the low energy side of the spectrum. Comparing first the APE waveguide and the bulk area we find a small tendency to the more perturbed sites, in which the secondary charge compensation or other perturbations are closer. Quite apparent is the absence of inhomogenous broadening (found in Ti-diffused waveguides) in the APE waveguides.

Although a quantitative interpretation of the difference between the perturbation induced by Ti and H require a more profound knowledge of the underlying defect configurations, a qualitative explanation is quite apparent. Both defects exchange for the Li^+ ion or occupy in congruent $LiNbO_3$ crystals the abundant Li-vacancies [11]. While H^+ requires on this site no charge compensation, the Ti^{4+} ion is quite "out of place" in terms of its charge and requires a complex compensation. This will result in changes in the electric field, which then are experienced by the Er^{3+} ion. These changes will increase as the Ti concentration increases and will hence lead to the observed inhomogenous linewidth. This phenomena is completely absent for H^+. The absence of any special new sites indicates that the H^+ ions - despite its charge neutrality - still seems to avoid the vicinity of the Er^{3+} ion. They only slightly perturb the more distant environment as indicated by the reduction of unperturbed sites.

The site-selectivity of the up-conversion excitation processes under 980 nm excitation have been investigated in bulk material and in Ti:$LiNbO_3$ waveguides. It was shown that two processes coexist in moderately Er^{3+} doped samples: (1) two-step excitation of a single Er^{3+} ion through two subsequent absorption processes and (2) up-conversion through a cross-relaxation process induced by energy transfer between two Er^{3+} ions within a cluster of ions. Choosing the emission energy appropriately the two processes and the involved defect sites can be distinguished. As expected from the barely changed site distribution, the up-conversion resembles the results obtained in bulk material. The most notable difference is a reduced overall up-conversion efficiency which can be explained by a reduction of the $^4I_{11/2}$ lifetime encountered in proton enriched samples due to the additional non-radiative decay channel into localized modes related with the hydrogen.

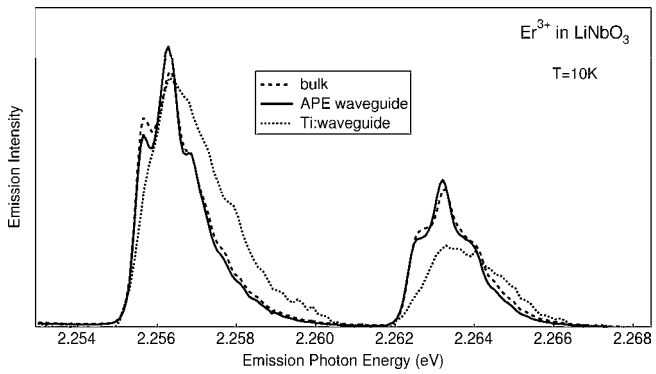


Fig. 2. Emission spectra (in the green spectral region) for two of the Stark-split transitions from the $^4S_{3/2}$ under excitation into the $^4F_{5/2}$ in the blue. Bulk doped Er^{3+}:$LiNbO_3$(dotted line), bulk doped Er^{3+}:$LiNbO_3$ with APE waveguide (solid), and Er^{3+}:$LiNbO_3$ Ti-diffusion waveguide (dashed).

Summary and conclusion

We investigated the incorporation and optical properties of Er^{3+} ions in lithium niobate waveguides produced by APE treatment. We found that the Er^{3+} ions occupy the Li^+ sites, just as in bulk $LiNbO_3$. No additional Er^{3+} sites appear, the distribution of sites is only slightly changed, showing a small reduction of the number of unperturbed defect sites, and in contrast to Ti-diffused waveguides, the spectral transitions exhibit no additional inhomogeous broadening.

In summary, it appears that the APE treatment leaves the environment of the Er ion almost unperturbed such that almost no waveguide specific properties could be observed.

[1] W. Sohler, H. Suche *Integrated Optical Circuits and Components: Design and Applications*, Marcel Dekker, New York, 127–159, 1999.

[2] V. Dierolf, M. Koerdt, *Phys. Rev. B* **61**(12), 8043–8052, 2000.

[3] V. Dierolf, A. Kutsenko, C. Sandmann, T. Tröster, G. Corradi, *J. of Lumin.* **87-89**, 989–992, 2000.

[4] B. Herreros, G. Lifante, F. Cusso, P. Townsend, P. Chandler, *J. of Lumin.* **72-74**, 198–200, 1997.

[5] V. Dierolf, A. Kutsenko, A. Ostendorf, W. von der Osten, W. Sohler, H. Suche, *Appl. Phys. B* **72**(7), 803–810, 2001.

[6] V. Dierolf, A. Kutsenko, A. Ostendorf, C. Sandmann, *Appl. Phys, B* **73**, 443–448, 2001.

[7] J. L. Jackel, C. E. Rice, J. J. Veselka, *Appl. Phys. Lett.* **41**(7), 607–608, 1982

[8] P. Becker, R. Brinkmann, M. Dinand, W. Sohler, H. Suche, *Appl. Phys. Lett.* **61**(11), 1257–1259, 1992.

[9] J. R. Tesmer, M. Nastasi, Contributing Editors J. Ch. Barbour, C. J. Maggiore, *Handbook of Modern Ion Beam Materials Analysis, Material Research Society*, Pittsburg, Pennsylvania, 1995

[10] L. Rebouta, P. J.´ M. Smulders, D. o. Boerma, F. Agulló-Lopez, M. F. da Silva, J. C. Soares, *Phys. Rev. B* **48**(6), 3600–3610, 1993.

[11] T. Gog, M. Griebenow, T. Harasimowicz, G. Materlik, *Ferroelectrics* **153 (1-4)**, 249–254, 1994.

Hybrid sol-gel silica channel waveguide Bragg grating fabrication using single-step UV patterning

P. J. Moreira[a], P. V. S. Marques[a,b], A. P. Leite[b]
[a]UOSE, INESC-PORTO, Rua do Campo Alegre 687, 4169-007 Porto, Portugal
[b]Departamento de Física, Faculdade de Ciências, Universidade do Porto,
Rua do Campo Alegre 687, 4169-007 Porto, Portugal
pmoreira@inescporto.pt

Abstract

A new method to fabricate Bragg gratings in hybrid sol-gel silica ridge waveguides, based on single-step 248 nm UV radiation patterning, is proposed and demonstrated. Heat treatment and UV exposure effects are analyzed.

Keywords: hybrid sol-gel, waveguide optics, Bragg grating

Introduction

The sol-gel process is recognised to be an alternative route for production of low cost silica-based integrated optic devices. Hybrid sol-gel technology, which provides organically modified glasses, offers an important additional advantage when the organic component is photopolymerizable. In this case, ridge waveguides can be easily defined without recourse to relatively complex and high cost reactive ion etching processing [1].

Optical waveguides with Bragg gratings are useful in many integrated optic devices, such as wavelength division multiplexers and laser cavities, and can be fabricated either by periodic modulation of the waveguide core refractive index or by surface corrugation of the waveguide. Several techniques have been used for this purpose [2], the most common ones being the interferometric and the phase mask techniques, and specific methods to print a waveguide grating in the context of hybrid sol-gel technology have already been reported [3-6]. All of them use a hybrid photosensitive material based on the methacryloxypropyltrimethoxysilane (MAPTMS) precursor. The interferometric technique with an argon laser was used to imprint a grating by direct refractive index change of a planar sol-gel layer [3]. For channel waveguide Bragg grating fabrication, two solutions have already been described: a Bragg grating was imprinted with UV radiation, by the phase mask technique, in a sol-gel ridge waveguide, using a 193nm excimer laser [4]; in [6], the grating was etched in the silicon oxide buffer layer and the sol-gel ridge waveguide was fabricated over this layer. However, both methods require two UV exposure steps and involve two masks and two UV sources.

The possibility to pattern channel waveguides using a 248nm UV excimer laser has already been reported by the authors [7]. Here, a new method for channel waveguide Bragg grating fabrication using a single exposure step with an excimer laser beam is proposed and demonstrated.

Channel waveguide fabrication

The basic hybrid sol-gel waveguide fabrication procedure comprises several steps: sol synthesis, film deposition, pre-baking, UV exposure and, eventually, post-baking.

Hydrolysis and polycondensation of MAPTMS mixed with zirconium(IV) propoxide (ZPO) which is stabilised with methacrylic acid (MA) was performed in 10:4:4 ratio. Pre-hydrolysis of MAPTMS (diluted in ethanol) with acidic water (0.1M HCl) was realised with a water/MAPTMS ratio of 0.75. Additional deionized water was added to the MAPTMS/(ZPO+MA) mixture to

achieve a water/MAPTMS ratio of 1.5. Soda-lime glass substrates were spin-coated (60s rotation time), and pre-baking at 100ºC for 30 min was employed to evaporate the solvent and avoid sticking of the film to the photolithographic mask during contact exposure. Channel waveguides were patterned by exposure through an amplitude NiCr on fused silica mask, using a 248nm pulsed excimer laser (240 mJ/cm^2, 10 Hz, typical exposure times 15 to 45s). Removal of the unexposed film by soaking the sample in ethanol, followed by pure water rinsing and drying, resulted in ridge waveguides. Post-baking (130ºC, 24h) was performed, in general. Fig.1a shows an example of a single mode ridge waveguide, and Fig.1b displays a channel waveguide with MAPTMS/tetramethoxysilane (TMOS) uppercladding.

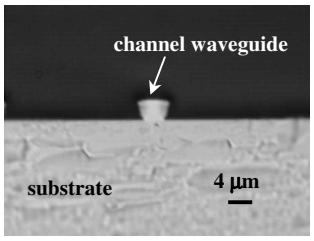


Fig. 1a - Cross-section of a single mode ridge channel waveguide.

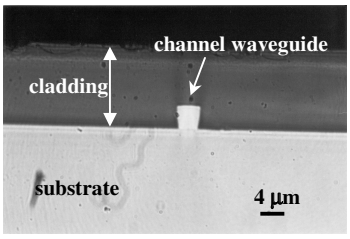


Fig. 1b - Cross section of a single mode buried channel waveguide.

The transmission absorption spectra of a wide (multimode) uncladded waveguide, before and after post-baking, are shown in Fig 2. An absorption band at 1190 nm (due to C-H bonds) and a 1420 nm band due to OH (most probably due to incomplete reaction of the inorganic network) can be easily seen, and important loss at 1550 nm is clear. No significant change in those absorption bands results from the heat treatment, and no improvement at 1550 nm could be verified, while absorption at 1620 nm (due to C=C bonds) decreases with post-baking.

Different UV exposure doses change the strength of the 1620 nm absorption band, and this will cause a refractive index variation with exposure, useful for Bragg grating inscription. The effect of the UV dose can be seen in Fig. 3, where a ridge channel waveguide fabricated using a low dose (240 mJ/cm^2, 10 Hz, 15 s) was subsequently re-exposed after development. Similarly to the post-baking effect, the 1620 nm band was also affected by the second UV irradiation.

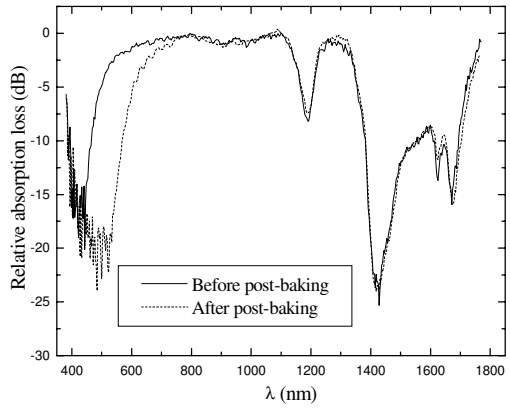


Fig. 2 - Spectral attenuation of multimode channel waveguide, before and after post-baking.

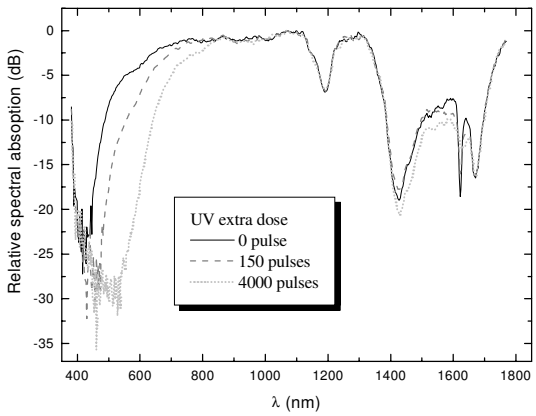


Fig. 3 - Spectral attenuation of multimode channel waveguide using different UV exposure doses.

A multimode ridge waveguide was subsequently exposed to UV laser radiation through a phase mask (period 726nm and length 8 mm) resulting in the grating transmittance shown in Fig. 4. The efficiency attained was low (44%), as the waveguide core refractive index saturated quite easily in the already exposed material.

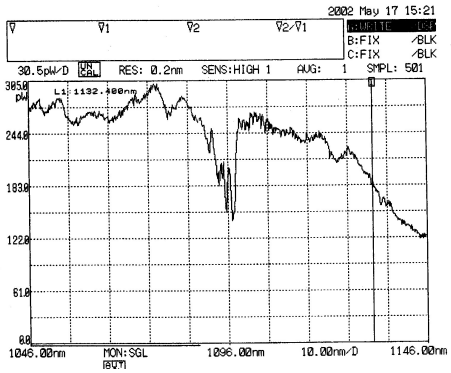
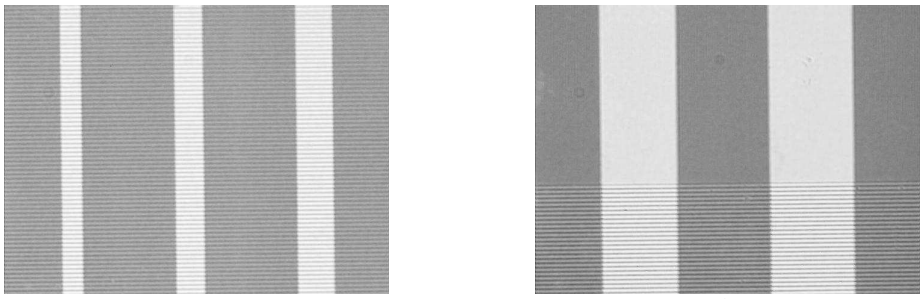


Fig. 4 – Transmission of dual exposure Bragg grating in multimode channel waveguide.

Single-step waveguide grating fabrication

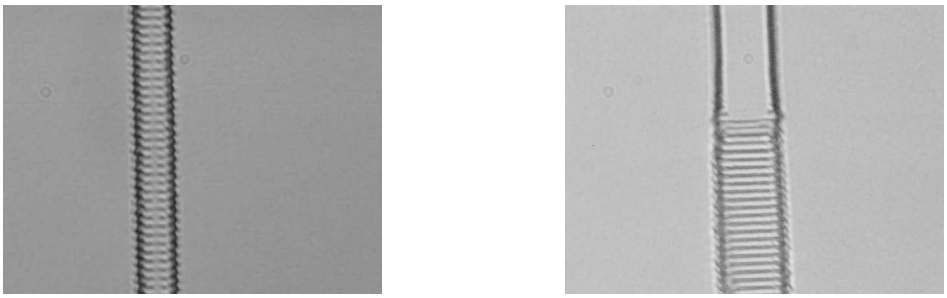
A method was devised and implemented to simultaneously produce a single-mode ridge waveguide with an inscribed Bragg grating, using a single photolithographic mask. Starting from a grating phase mask, a NiCr thin film was then deposited on it and standard lithography was used to define windows representing the channel waveguides, perpendicularly aligned with the phase mask grooves, Fig. 5.



(a) (b)

Fig. 5 – (a) Channel openings on phase mask grating zone; (b) boundary between zones with and without grating phase mask.

A hybrid sol-gel core layer was deposited on soda-lime glass substrates, following the procedure summarized above. Exposure through that mask (during 25s) resulted in ridge channel waveguides incorporating gratings, Fig 6. Some roughness of the sidewalls can be observed, in synchronism with the grating lines.



(a) (b)

Fig. 6- Top view of: (a) Bragg grating in a 5 μm wide ridge waveguide; (b) Bragg grating boundary on a 10 μm wide ridge waveguide.

A sample with waveguides of varying width and a length of 20 mm was characterized in terms of optical transmission spectrum. Fig 7 shows the case of a 10 μm wide ridge waveguide, where propagation of more than one guided mode causes several oscillations in the response. This method, where grating and channel waveguide are simultaneously defined, resulted in more efficient gratings, and the fabrication process is much simpler since there is only one UV exposure step. In addition, the grating/waveguide alignment is facilitated, since it is already defined in the mask.

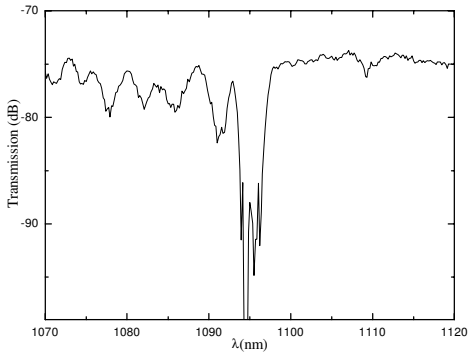


Fig. 7 – Transmission spectrum of a Bragg grating in a ridge channel waveguide (10×3.5 μm² core).

Samples with an improved uppercladding (TMOS/DMDMOS) have also been fabricated and their performance will be reported.

Conclusion

A single-step method to fabricate hybrid sol-gel channel waveguides incorporating a Bragg grating was successfully demonstrated, using a combined amplitude/phase mask illuminated by 248 nm excimer laser radiation, and the MAPTMS basic material.

***A*cknowledgment:** P. J. Moreira thanks the Portuguese Research Council (FCT) for financial support through a PhD research fellowship.

References

[1] M.P. Andrews and S.I. Najafi, *Sol-Gel and Polymer Photonic Devices*, SPIE CR68, 1997.
[2] Andreas Othonos, *Rev. Sci. Instrum.,* **68 (12)**, 4309-4340, 1997.
[3] Yves Moreau et al., *Opt. Eng.*, **37(4)**, 1130-1135, 1998.
[4] M. A. Fardad, T. Touam et al., *Electron. Lett.*, **33(12)**, 1069-1070, 1997.
[5] S. Iraj Najafi et al., *J. Lightwave Technol.,* **16(9)**, 1640-1646, 1998.
[6] M. A. Fardad, M. Fallahi, *Opt. Commun.*, **163**, 33-37, 1999.
[7] P. J. Moreira, P. V. S. Marques, A. P. Leite, *Proceedings ICO 19, Firenze*, 131-132, 2002.

Features of photorefractive gratings recorded with two – color scheme in doubly doped surface layer of a lithium niobate crystal

Vladymir Shandarov, Pavel Karpushin, Arkady Mandel, and Stanislav Shandarov
State University of Control Systems and Radioelectronics
40 Lenin Ave., Tomsk 634050, Russia
shan@svch.rk.tusur.ru

The features of the photorefractive grating recording and storage in lithium niobate crystal with surface doping by iron and copper in conditions of additional incoherent short – wavelength illumination are experimentally investigated and discussed.

Keywords: lithium niobate, photorefractive grating, incoherent illumination

Introduction

Nonvolatile photorefractive gratings both in bulk and waveguide samples of some electrooptic crystals like lithium niobate ($LiNbO_3$) or strontium – barium niobate (SBN) are promising elements for different applications in photonics. For example, similar reflection gratings may be well suited for integrated waveguide lasers as distributed Bragg mirrors, or as narrow – band selective elements for dense division multiplexing. The one of general requirements to such gratings is their stability against the decay caused by the finite conductivity of the materials as in darkness as in conditions of their illumination with light of operating wavelength. To overcome this problem, the methods of thermal [1] and electrical fixing [2] of photorefractive gratings in both, $LiNbO_3$ and SBN, have been suggested and developed. Besides, the nonvolatile storage of holographic gratings using two – color scheme of their recording, e.g. the preliminary illumination of crystal samples with short – wavelength irradiation and recording light with longer wavelength, has been recently demonstrated for $LiNbO_3$ doped by two different impurities, like iron (Fe) and manganese (Mn) [3]. To form nonvolatile holograms, these impurities should exhibit different photoexcitation energies for electrons of which excitation and redistribution in space results in the holographic pattern recording. Besides Fe and Mn, another interesting couple of similar dopants, which significantly and in different ways influence the photorefractive properties of $LiNbO_3$, is Fe and copper (Cu). It has been revealed that they result in significantly different values of the light absorption coefficients of $LiNbO_3$ at the same wavelength in the blue – green range of the visible [4]. Additionally, in some earlier experiments we observed the considerable decreasing of the dark conductivity for Fe – doped $LiNbO_3$ owing to its additional doping by Cu. Even the very low Cu concentration (as less than 0,1 % by weight) resulted in the dark conductivity decreasing of $LiNbO_3$:Fe similar an order of magnitude [5]. The possible origin of these effects is the different positions of Cu and Fe donor centers within the band gap of a $LiNbO_3$ crystal.

In this research we investigate an influence of an incoherent green illumination to the recording and decay characteristics of photorefractive gratings which are formed in two – beam coupling configuration by the external coherent light beams in a $LiNbO_3$ wafer with surface doping by combination both of Fe and Cu.

Experimental setup

The schematic of experimental setup is shown in Fig. 1. In experiments we use the coherent irradiation of a He – Ne laser (λ=0.63 μm) with a total power 10 – 15 mW to record the photorefractive gratings, and incoherent green irradiation of a light – emitting diode (LED) as the gating light, which makes possible a participation of deep donors in the photorefractive process. The incidence plane of external recording red beams coincides with YZ plane of a $LiNbO_3$ crystal with light polarization along its Z axis. The intersection angle of red beams is about 5 degrees. The

crystal dimensions are 12× 1.5× 8 mm^3 along X, Y, Z axes, respectively. The green light is focused by a spherical lens with a focal length of 10 cm and directed to the XZ plane of the crystal near to its normal. The intensity of incoherent illumination at the crystal surface is near to 30 mW/cm^2. We investigate two different conditions of the photorefractive grating recording and decay. In the one case we use the preliminary illumination of a $LiNbO_3$ sample with green light and following recording stage with only red beams. In another case we inspect the recording of such gratings using simultaneously as red beams as green illumination. The process of the grating decay is studied either with permanent or periodic readout of these gratings using a weak probing red beam.

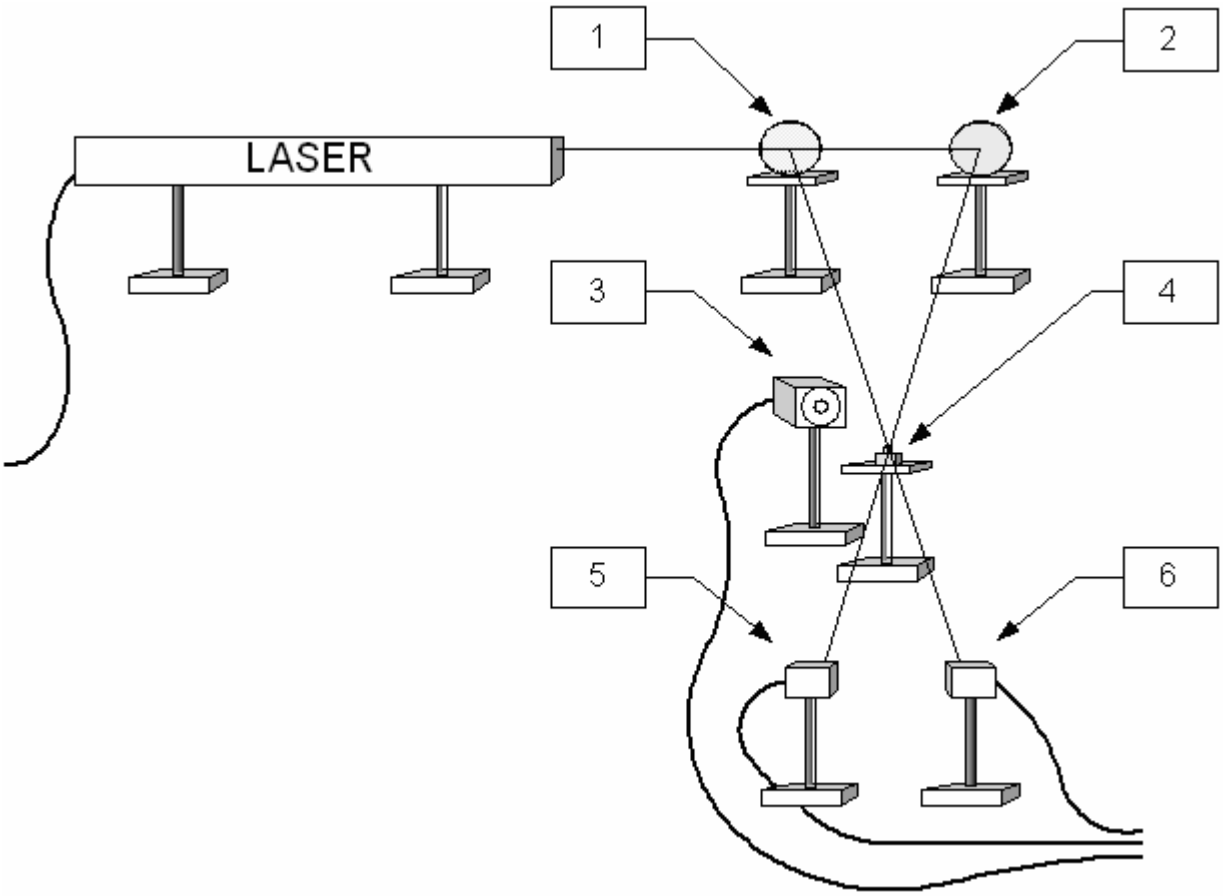


Fig. 1. Experimental setup. 1, beam splitter; 2, mirror; 3, LED; 4, $LiNbO_3$ sample; 5 and 6, photodiodes.

Doubly – doped $LiNbO_3$ sample

The crystal sample investigated is a Y cut $LiNbO_3$ wafer with its XZ surface doped by Fe and by a combination of Fe and Cu in the part of the whole surface. The thermal diffusion of Fe is performed at a diffusion temperature of 950°C and for Cu it makes 900°C. The diffusion time is 10 hours for Fe and 6 hours for Cu. The initial thickness of metal films formed by vacuum evaporation is ~40.0 nm. It should be noted that Fe diffusion results in the increasing of both, as extraordinary as ordinary refractive indices of $LiNbO_3$, e.g. it forms in $LiNbO_3$ a planar optical waveguide. We use this property to estimate the thickness of Fe – doped crystal layer and an average concentration of Fe within it. We also can estimate the Cu distribution within the crystal by comparison of the effective refractive indices of TE modes within waveguide areas with only Fe doping and with

doping by Fe and Cu. In the sample discussed the thicknesses of boundary layers doped with Fe and Cu are estimated as ~6 and ~30 μm, respectively. The waveguide supports up to 8 TE modes along the X direction at λ=633 nm. Parameters of refractive index profiles are reconstructed from the measured TE mode indices through a numerical solution procedure for the corresponding wave equation using a Runge – Kutta method. We find that the perturbation of the initial Fe – caused refractive index profile of the waveguide due to the Cu diffusion is insignificant (slight decreasing of the extraordinary refractive index is observed with respect to the Fe – doped region).

Experimental results

As the clear evidence of the strong Cu influence to the photorefractive characteristics of $LiNbO_3$ we previously test the decay of photorefractive gratings formed by the same guided modes within waveguide parts with only Fe doping and with Fe and Cu content. The significant difference in the dark conductivity of a crystal for these parts is illustrated by Fig. 2 with time dependences of the diffraction efficiency for the gratings formed within the waveguide by TE_1 modes. The photoconductivity of the material does not contribute in this experiment as the periodic readout of the decaying grating by weak light beam is used. The diffraction efficiency of the waveguide gratings in both parts is practically the same for the same power of recording light beams.

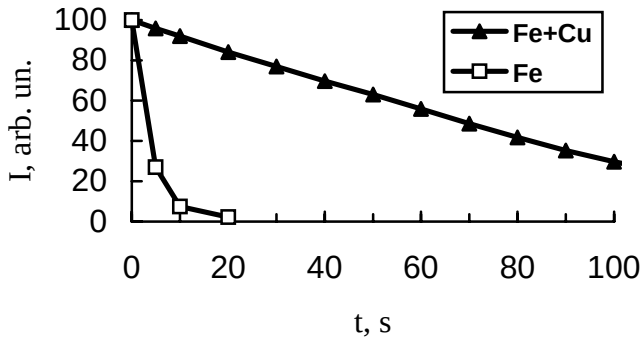


Fig. 2. The relative intensity of readout beam during decay of photorefractive gratings formed by TE1 modes within Fe- and Fe:Cu – doped areas of the waveguide.

In the experiments with recording of photorefractive gratings by external light beams in surface – doped $LiNbO_3$ we also find the significant distinctions of this process for areas with single and double doping. For example, we practically do not observe the grating formation in the area with only Fe doping. At the same experimental conditions the diffraction efficiency of photorefractive gratings formed in the doubly – doped area may achieve values of up to 10%. In part it may be explained by the distinction of the depths of Fe- and Fe:Cu – doped crystal layers. The same undoped crystal also shows very low photorefractive sensitivity for the red light.

The grating recording in the doubly – doped area by red beams with its preliminary illumination by incoherent green light for 5 – 15 minutes shows the slight distinctions between diffraction efficiencies of these gratings with respect to similar formed without such incoherent illumination. Incoherent gating light may increase this diffraction efficiency for the same recording time and light intensity. The time decay of such gratings shows slower decreasing of the grating amplitude for the case of previous incoherent illumination. It is illustrated by the results in Fig. 3 for time evolution of the diffraction efficiency of photorefractive gratings formed with previous crystal illumination with green light for 5 minutes and without it. In this experiment we use the permanent readout of gratings by red beam with its power near 0.1 mW.

The regime of simultaneous incoherent illumination of a crystal and recording of photorefractive grating by coherent red light demonstrates the significant influence of the illumination characteristics to diffraction efficiency of the grating formed. As we observe, the diffraction efficiency, e.g. the grating amplitude in some conditions may be considerably increased even at green light intensity near to 1 mW/cm^2.

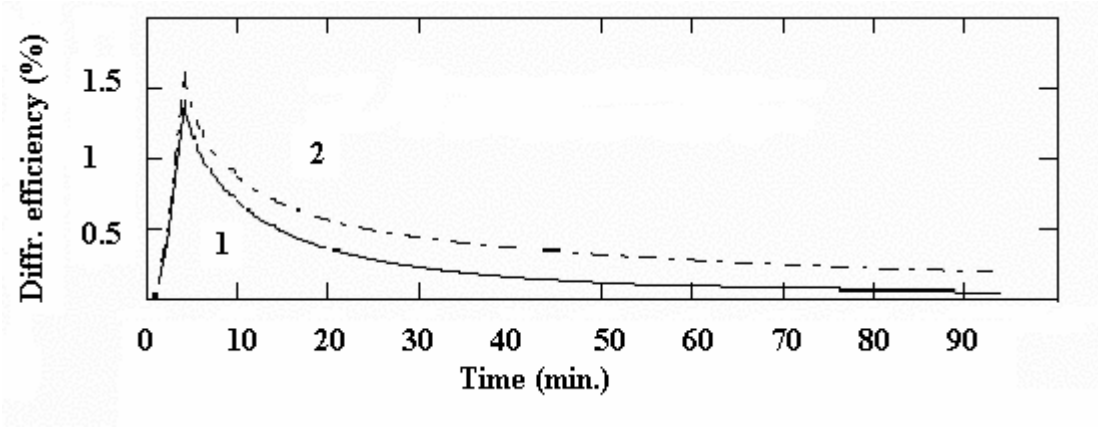


Fig. 3. Time evolution of the diffraction efficiency of photorefractive gratings while their recording and decay. Gratings are formed: 1, by only red beams; 2, with previous incoherent illumination.

These results may be useful for design of photonics elements as with stable grating elements as with stable channel waveguide structures formed in planar waveguides by spatial optical solitons. All the experimental results and the features of the photorefractive grating recording and decay in the two – color scheme will be discussed in more details in the report.

This research is supported by INTAS (grant INTAS 01 – 0481).

[1] J.J.Amodey, and D.L.Staebler, *Appl. Phys. Lett.*, **18**, 540 (1971).
[2] Jian Ma, Tallis Chang, John Hong, Ratnakar Neurgaonkar, George Barbastathis and Demetri Psaltis, *Optics Letters*. Vol. 22, No. 14, 1116 – 1118, 1997.
[3] K.Buse, A.Adibi, and D.Psaltis, *Nature*, **393**, 665 – 668 (1998).
[4] I.Pracka, A.L.Bajor, S.M.Kaczmarek, M.Swirkowicz, B.Kaczmarek, J.Kisielewski, and T.Lukasiewicz, Cryst. Res. Technol., 34, 627 – 634 (1999).
[5] V.M.Shandarov, In: Proc. of the Topical Meeting on Photorefractive Materials, Effects, and Devices - PRM'95 (Colorado, USA, Aspen Lodge at Estes Park, 1995), pp. 528 - 531.

Interpretation of high poling effects with short lifetimes

Carl J. Marckmann
NKT Research & Innovation A/S, Diplomvej, DTU Bygning 373, DK-2800 Kgs. Lyngby, Denmark
cjm@com.dtu.dk

Rune Shim, Yitao Ren, and Martin Kristensen
COM, DTU Bygning 345v, DK-2800 Kgs. Lyngby, Denmark
rune@com.dtu.dk, yr@com.dtu.dk, and mk@com.dtu.dk

This paper gives a possible interpretation of the high valued, short lived, linear electro-optic coefficients obtained by some groups. The effect may partly be explained by cracks in the waveguide/fiber system reducing the effective electrode-distance.

Keywords: Amorphous materials, electro-optic devices, electro-optic Kerr effect, electro-optic measurements, Pockels effect, poling

Introduction

Induction of a linear electro-optic effect in silica glass was first obtained in 1991 by Myers *et al* [1] through thermal poling. This discovery opened a door to glass based switches, modulators and tunable filters etc. Unfortunately, the thermal poling induced effect is still too small or decays too fast [2] to be used for industrial purposes.

Sample preparation

The two samples described in this article consist of a buffer layer made by thermal oxidation of Sb doped Si ($\sim 3.3\mu m$), an etched core ($\sim 2.0\mu m$ high and $\sim 4.0\mu m$ wide) and either a hard top-cladding, SiO_2 (sample 3_5_1), or a soft top-cladding, $B, P : SiO_2$ (sample 17_1). The core and the top-cladding layers were deposited using Plasma Enhanced Chemical Vapour Deposition. The total height of the glass-layers is $9.5\mu m$ for sample 17_1 and $14.5\mu m$ for sample 3_5_1. The core was doped with germanium in order to make it sensitive to UV light [3] and with nitrogen in order to stabilize the poling due to increased charge trapping density [4] and to be able to make smaller components due to the higher refractive index-step. A Bragg grating was UV-written in the samples using the phase-mask method [5]. Annealing the samples at $375°C$ for 1.5h ensured that changes measured in the Bragg wavelength in the poling experiments are due to nonlinearities and not annealing effects. Finally, a top-electrode was made covering the region with Bragg gratings and the Si-wafer was used as back-electrode.

Measurements

Two different types of measurements were performed on the samples. Interferometric measurements [6] were performed to find the induced linear electro-optic coefficient, r, and the Bragg gratings were used to probe the third-order nonlinearities, $\chi^{(3)}$, and the built-in internal electric field, E_{int}.

Bragg gratings as probes

The setup for Bragg gratings used as probes is illustrated in Fig. 1. Light from a tunable laser is sent through a polarization controller, then through the sample and into an optical spectrum analyzer. Transmission spectra were recorded with different voltages applied across the samples. Since silica glass is a centrosymmetric material, the change in refractive index Δn as function of electric field E can be written as

$$\Delta n(E) = \frac{3\chi^{(3)}}{2n} E^2 \ , \tag{1}$$

where n is the refractive index and $\chi^{(3)}$ is the third-order nonlinearity. Terms of higher order than E^2 have been neglected. In the charge separation model [7], mobile charges in the glass move towards the electrodes during poling. These charges will predominantly be trapped at the interfaces between core and cladding layers, giving a sheet of charge on each side of the core layer with different polarity, yielding an internal field E_{int} across the core layer. If an external field is applied, the total field across the sample becomes $E = E_{int} + E_{ext}$. Substituting into equation 1 yields [10]

$$E_{int} = \frac{B}{2C} \ , \quad \chi^{(2)}_{eff} = \frac{nB}{A} \quad \text{and} \quad \chi^{(3)} = \frac{2nC}{3A} \ , \tag{2}$$

where A, B and C are coefficients of the parabola $\lambda_{Bragg}(E) = A + BE_{ext} + CE^2_{ext}$ representing the change in Bragg wavelength as function of the externally applied electric field. [1])

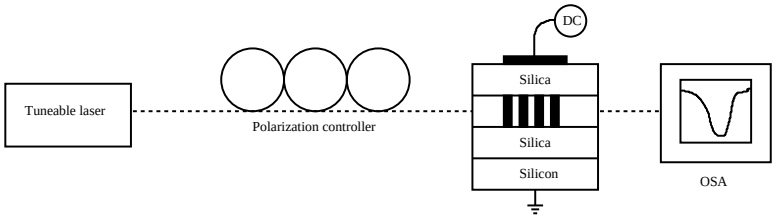


Fig. 1. The setup using Bragg gratings as probes.

Discussion

From Fig. 2 it is clear that cracks are present in the sample with hard top-cladding, sample 3_5_1, but not in the sample with soft top-cladding, sample 17_1 as in Fig. 3. The breakdown voltage for glass and air is 850 [8] and 3 [9] $V/\mu m$, respectively. As the electric fields used in the Bragg grating measurements and used for the thermal poling are stronger than 16 $V/\mu m$ the air-holes/cracks will act as short circuits. Thus, the effective electrode distance in a sample with cracks is much less than the physical electrode separation.

Sample 3_5_1 is poled at temperatures as low as room temperature. This is seen in Fig. 4, where the Bragg wavelength is measured in two different sweeps before thermal poling: Firstly, the voltage is swept from 0 to -1.5kV and secondly from -1.5kV to 0.5kV. The step-length in both curves is 0.25kV. The curves are not identical since a field of approximately $(21.4 \pm 3.3) V/\mu m$ [2]) has been built into the sample during the first sweep from 0 to -1.5kV.

Thermal poling of sample 3_5_1 at $357°C$ for 20 minutes at -2.5kV yields a linear electro-optic coefficient between 0.02 and $0.05 pm/V$ measured right after poling using the interferometric setup. One day after poling, r has decreased with between 60% and 80% of the initially induced value and one week after poling, r was measured to zero within the measurement error. The built-in field is thus quasi stable with a lifetime longer than the sweeping time used in the Bragg gratings measurements.

Room temperature poling is not observed in sample 17_1 as seen in Fig. 5. The two curves are identical within the experimental error and no internal field has been built in during the sweep from 0 to -2.5kV.

---

[1]) $r = \frac{2\chi^{(2)}_{eff}}{n^4}$.

[2]) Under the assumption that there are no cracks i.e. that the effective distance between the electrodes is $14.5 \mu m$.

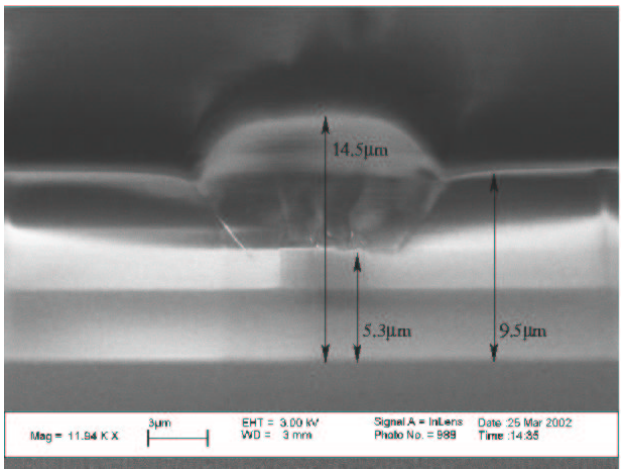


Fig. 2. SEM picture of sample 3_5_1. Cracks are clearly visible.

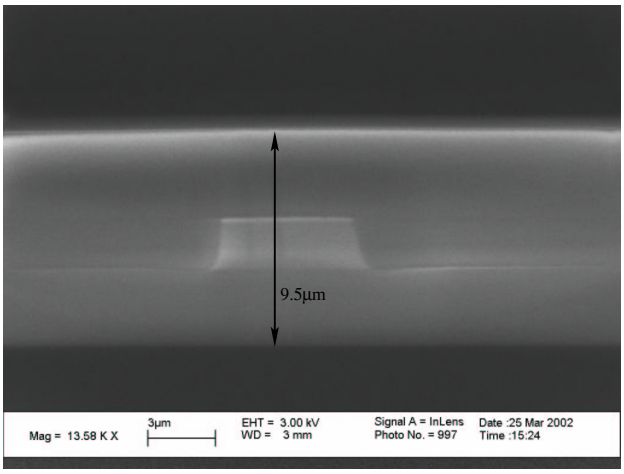


Fig. 3. SEM picture of a $6\mu m$ wide sample similar to sample 17_1. No cracks are observed.

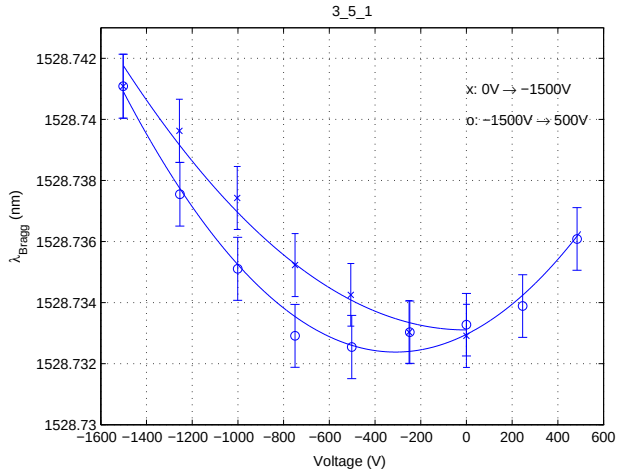


Fig. 4. Sample 3_5_1, TE polarization, measured from 0 to -1.5kV and from -1.5 to 0.5kV using the Bragg grating as probe before thermal poling.

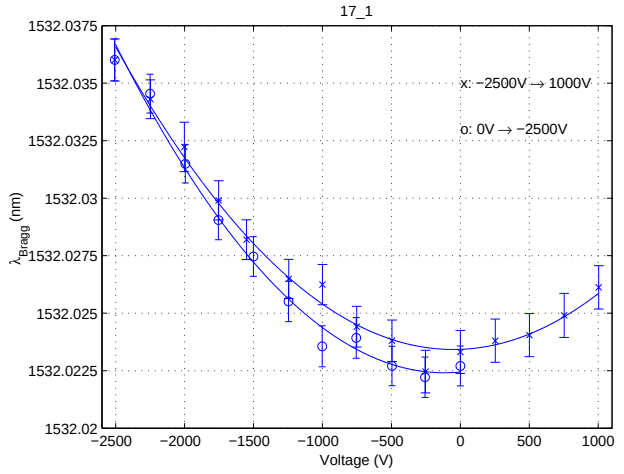


Fig. 5. Sample 17_1, TE polarization, measured from 0 to -2.5kV and from -2.5 to 1.0kV using the Bragg grating as probe before thermal poling.

From the SEM pictures it is not possible to determine the length of the cracks in sample 3_5_1 and therefore the $\chi^{(3)}$ and induced internal electric field E_{int} values are calculated for four different effective electrode distances and the values for sample 17_1 are given for comparison in Table 1. The measurements were performed using the Bragg grating method. The effective electrode distance of $8.0\mu m$ has been included in Table 1 since it yields the same $\chi^{(3)}$ value as the one obtained in a previous measurement [10] on a sample with the same core glass as sample 3_5_1 but without cracks in the top-cladding.

The instability of the poling induced internal field can also be a result of the cracks, since charges trapped at the interfaces can escape through the cracks. The lifetime of the poling at $357°C$ might very well exceed the lifetime of the room temperature poling since the charges can be trapped temporarily at the ends of the cracks.

	3_5_1($14.5\mu m$)	3_5_1($9.5\mu m$)	3_5_1($8.0\mu m$)	3_5_1($5.3\mu m$)	17_1
$\chi^{(3)}(10^{-22}\frac{m^2}{V^2})$	6.46 ± 0.17	2.77 ± 0.07	1.97 ± 0.05	0.86 ± 0.02	1.87 ± 0.09
$E_{int}(\frac{V}{\mu m})$	44.0 ± 1.7	67.2 ± 2.6	79.8 ± 3.1	120.4 ± 4.6	9.8 ± 3.9

Table1. The measured values of $\chi^{(3)}$ and E_{int} for samples 3_5_1 (different effective electrode distances) and 17_1.

Conclusion

In this paper we have observed cracks in the hard top-cladding of a sample. Apparently, the measured $\chi^{(3)} = (6.46 \pm 0.17) \cdot 10^{-22}\frac{m^2}{V^2}$ value of this sample was very high compared to a similar sample [10] without cracks in the top-cladding. The poling-induced r value had a very short lifetime, in the order of days. This decay time is comparable to the fast decaying r component seen by others [2]. Both the apparently large $\chi^{(3)}$ and the fast-decaying r can be explained by the cracks in the top-cladding since these reduce the effective electrode distance by acting as short-circuits. The apparently large $\chi^{(3)}$ is caused by the wrong electrode distance used in the calculation of the electric field E. The fast-decaying r value can be explained by trapped charges escaping through the cracks. This also explains the room temperature poling as charges can be trapped temporarily at the ends of the cracks when high voltage is applied during measurements. Under the assumption of cracks all the way from the electrodes to the core in [2], the naive corrected r value is reduced from 0.4 to $0.15pm/V$.

[1] R. A. Myers, N. Mukherjee and S. R. J. Brueck, "Large second-order nonlinearity in poled fused silica", *Opt. Lett.*, vol. 16, no. 22, pp. 1732-1734, 1991.

[2] M. Janos, W. Xu, D. Wong, H. Inglis, and S. Fleming, "Growth and Decay of the Electrooptic Effect in Thermally Poled B/Ge Codoped Fiber", *Jour. of Lightwave Tech.*, vol. 17, no. 6, pp. 1037-1041, 1999

[3] K. O. Hill, Y. Fujii, D. C. Johnson and B. S. Kawasaki, "Photosensitivity in optical fiber waveguides: Application to reflection filter fabrication", *Appl. Phys. Lett.*, vol. 32, no. 10, pp. 647-649, 1978.

[4] D. Frohman-Bentchkowsky and M. Lenzlinger, "Charge Transport and Storage in Metal-Nitride-Oxide-Silicon (MNOS) Structures", *J. Appl. Phys.*, vol. 40, no. 8, pp. 3307-3319, 1969.

[5] K. O. Hill, B. Malo, F. Bilodeau, D. C. Johnson and J. Albert, "Bragg gratings fabricated in monomode photosensitive optical fiber by UV exposure through a phase mask", *Appl. Phys. Lett.*, vol 62, no. 10, pp. 1035-1037, 1993.

[6] Y. Ren, C. J. Marckmann, J. Arentoft, and M. Kristensen, "Thermally poled channel waveguides with polarization independent electro-optic effect", *IEEE Photon. Technol. Lett.*, vol. 14, no. 5, pp. 639-641, May 2002.

[7] P. G. Kazansky and P. St. J. Russel, "Thermally poled glass: Frozen-in electric field or oriented dipoles?", *Opt. Commun.*, vol. 110, pp. 611-614, 1994.

[8] F. Haberl, J. Hochreiter, J. Zehetner, and A. J. Schmidt, "Electrical breakdown in ge-doped silica glass fibres", *Int. Jour. of optoelectron.*, vol. 5, no. 4, pp. 363-366, 1990.

[9] D. K. Cheng, "Fundamentals of engineering electromagnetics", *Addison-Wesley*, pp. 108, 1993.

[10] C. J. Marckmann, Y. Ren, G. Genty, and M. Kristensen, "Strength and symmetry of the third-order nonlinearity during poling of glass waveguides", *IEEE Photon. Technol. Lett.*, vol. 14, no. 9, pp. 1294-1296, 2002.

Planar optical waveguides fabricated by sol-gel derived inorganic silicate glass

Charles K.F. Ho*, Dexter C.L. Gwee, Rajni, Kantisara Pita, Ngo Quoc Nam, Kam Chan Hin
Photonics Research Group, Department of Electrical and Electronics Engineering,
Nanyang Technological University, Singapore 639798
pvd702663@ntu.edu.sg*

Optical waveguide slabs are synthesized using germano-silicate glass by the sol-gel process. A systematic study of the design of the low-loss material is presented. A propagation loss of <0.5 db/cm at 1550 nm has been achieved.

Keywords: Germano-silicate, sol-gel, optical waveguides.

Introduction

It is well known that the sol-gel method allows the synthesis of homogeneous materials at low temperatures and offers control of chemical purity and ease of multi-dopants mixing. In a sol-gel process, the formation of amorphous materials is by chemical means at low temperature as opposed to a physical route where an abundance of energy is consumed in the process. For example, in process like CVD, substrates have to be kept at an elevated temperature typically above 500°C and FHD where flame temperature is above 1000°C. In addition, plasma and vacuum equipment for these other methods often incur huge overhead and maintenance costs. Among the different systems which can be obtained by the sol-gel route, the binary $GeO_2 – SiO_2$ material has been recognised as being excellent for obtaining lightwave waveguides in films with controllable refractive index [1],[2]. As well, the photosensitivity of $GeO_2 – SiO_2$ based materials [3],[4] gives another good reason for further study. Silicate-based glasses provide a material for waveguides with optimum compatibility with single-mode fibre and very high stability.

In this work, a systematic study for the design of Germano-silicate planar waveguide is carried out resulting in a low-loss waveguide. Optimisation of chemistry process, with annealing temperature and deposition parameters were achieved.

Experimental Procedure

Figure 1 schematizes the sequence of the different synthesis steps. A detailed outline of the preparation of the germano-silicate sol has been documented elsewhere [5]. In this experiment, high purity alkoxide precursors were used (99.999% TEOS by Aldrich and 99.99% Germanium isopropoxide by Chemat Technology Inc.). Once the sol has been aged to a spinnable state, it was deposited onto a 10-micron-thick SiO_2 on a silicon substrate by a syringe. Then, a thin layer of xerogel film (~200 nm) was formed by spin-coating at 1500 rpm for 30 s followed by a thermal treatment of 900°C in a rapid thermal processor for 10 s under oxygen atmosphere. In order to build a waveguiding structure, a high-index, core layer typically requires a thickness of, at least, several microns. Hence, an iterative thin film deposition routine was carried out until the desired thickness was achieved. One distinct advantage of such method is that residual organic solvents and OH/H_2O content can be driven off before each thin layer is deposited, making the removal of such detrimental matter much easier than other waveguide fabrication technique. Lastly, the densified multi-layer germania doped silicate was consolidated in electric furnace at 1100°C in air for one hour. By subjecting the sample to an extended and elevated thermal treatment, the purpose of this consolidation step is to equilibrate the optical properties of each successively coated layer.

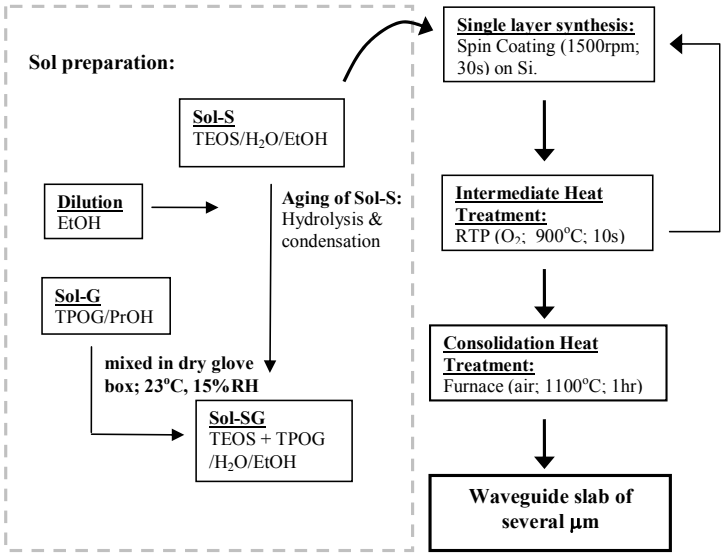


Figure 1: Schematic diagram of the process flow.

Results and discussion

Before proceeding to the multi-layer thick film, single layer films were studied extensively to ensure a material of optical quality with minimal loss of light due to absorption and scattering. As proposed in [5], 20 mol% Ge doped silicate yields the highest index for this material system while reducing the likelihood of nano-dimension Ge clusters or crystals. And at a processing temperature of greater than 800°C, porosity and OH content are both minimized as suggested by a refractive index of close to 1.47 at 1550 nm. The FTIR spectra in Figure 2 show the signature absorption of OH related bonds for the sample annealed at 500°C but absent in 900°C samples. Furthermore, from the same figure, the absence of Ge-O-Ge linkages (2 peaks between 860 – 980 cm^{-1} [6]) can be viewed as the onset of Ge-O clustering or phase separation. In the inset of Figure 2, one can note that the Ge-O-Ge presence in the 20 mol% Ge annealed at 900°C is substantially less than that of the 30 mol% Ge sample. Secondly, the Ge-O-Si absorbance as seen as shoulders indicated by an arrow in Figure 2. The presence of such linkages (960 – 1020 cm^{-1} [6]) suggests the homogeneous incorporation of the GeO_2 into the SiO_2 host network.

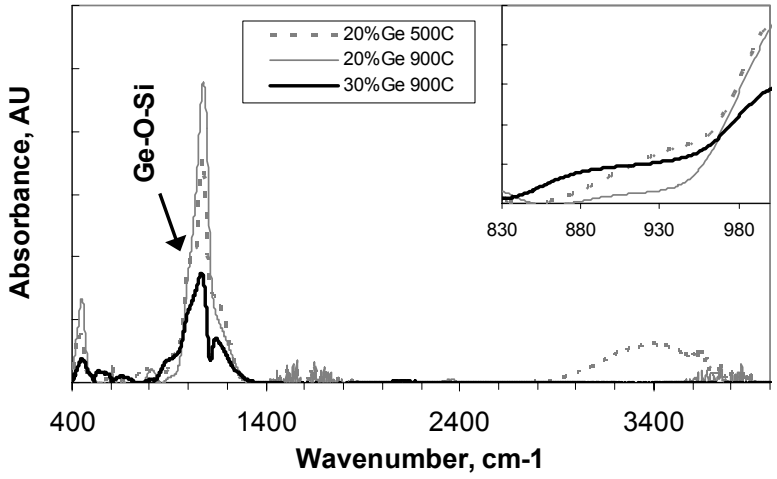


Figure 2: FTIR spectra for 20 mol% and 30 mol% Ge doped single-layer films

Micro-Raman and XRD have been used to confirm the amorphous state of the thin films. No crystallinity was observed. The TEM micrograph as shown in Figure 3, shows that no Ge-concentrated clusters larger than 20 nm are visible. Inherent to the sol-gel spin-coating technique is that surface roughness is less than 1 nm even for the multi-layer as measured by AFM. Such surface smoothness contributes to a low-loss waveguide.

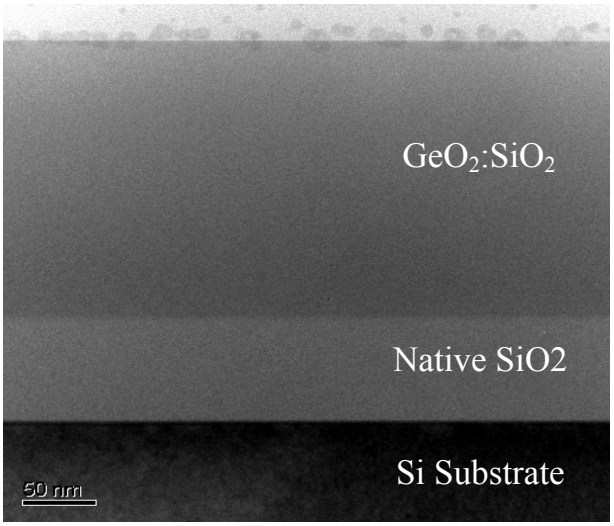


Figure 3: TEM Micrograph of a 20 mol% Ge single-layer sample annealed 1 hour under 1100°C in air.

Once the necessary parameters for single layers have been determined, the multilayer film was fabricated. It was then characterized by a prism-coupler equipment (Metricon 2010) with an He-Ne laser at 632.8 nm and a semiconductor diode laser at 1550 nm. The result for a sample is summarized in Table 1. The uncertainties accompanying the optical values are standard deviations of a number of readings carried out at different locations of the sample. From the fact that indices for TM waves and TE waves closely match each other, one can infer that birefringence is insignificant.

Table 1: Derived optical properties of the multi-layer and single-layer films

	21-layer		1-layer			
	632.8 nm	1550 nm	RTA900°C		RTA900°C/FA1100°C	
Thickness (μm)	4.97 ± 0.05	4.97 ± 0.06	0.269		0.240	
Number of modes	4	2	--		--	
Refractive index (TE)	1.4830 ± 0.0002	1.4687 ± 0.0002	632.8 nm	1550 nm	632.8 nm	1550 nm
			1.4816	1.4663	1.4836	1.4685
Refractive index (TM)	1.4835 ± 0.0005	1.4694 ± 0.0005	--		--	
Attenuation coefficient (dB/cm)	1.27 ± 0.2	0.3 ± 0.2	632.8 nm	1550 nm	632.8 nm	1550 nm
			0.36	0.06	0.36	0.06

Following the same analysis as [7] to account for the loss in our GeO_2-SiO_2 system, assuming an invisible separation of Ge-O clusters of 20 nm occupying a volume fraction of 10%, the Rayleigh-Mie scattering losses are ~ 0.51 and 0.01 dB/cm at 632.8 and 1550 nm respectively. From these figures, one can see that a significant portion of the loss is due to other foreign particles introduced to the system during the process. Our waveguides can therefore be improved through better precaution to prevent other particles falling to the sample especially during spin-coating.

For a comparison, the optical properties of single layers deposited on an Si substrate were derived from reflectance measurements. One sample was subjected to 1 cycle of rapid thermal annealing (RTA) at 900°C whereas another was subjected to 21 cycles of RTA followed by furnace annealing (FA) at 1100°C. The Lorentz oscillator model (LOM), as before [5], was used to model the reflectance data taken from a Filmetrics F20. The results are also tabulated in Table 1. An expected reduction in thickness corresponds to an increase in refractive index between the two single-layer samples. The average thickness of the consolidated single-layer sample of 0.240 μm seems to concur with the average 1-layer thickness of 0.237 μm for the multi-layer sample. The attenuation coefficients (α) were estimated by using $\alpha = 4\pi k/\lambda$ (λ refers to wavelength of probing photons), from the extinction coefficient (k) from the LOM. These values are found to be less than the measured values which make physical sense as the single-layer film should be more homogeneous and defect free than the multi-layered film. We should stress that these derived α values are only as good as the LOM can model the real material. However, these values do suggest that the LOM parameters found represent a reasonable optical model for our analysis.

Conclusion

A birefringence-free optical waveguide fabricated using germania doped silicate materials by the sol-gel process has been demonstrated. With a propagation loss of less than 0.5 dB/cm, our planar waveguide is suitable for realizing high performance polarization-independent optical devices. The optical properties of the multi-layer slab correspond very well with the single layer properties illustrating the effectiveness of the consolidation step to eliminate differences of the optical properties between layers of the multi-layer stack formed by the iterative deposition and annealing process.

Acknowledgements

The authors are indebted to Dr. S.R. Natarajan, Dr. Zhou Jun and Dr. Zhang Qin Yuan for their invaluable technical advice. We would also like acknowledge the financial support of the ONFIG program provided by A*STAR in Singapore.

[1] D.G. Chen, B.G. Potter, J.H. Simmons, *J. Non-Cryst. Solids*, **178**, 135, 1994.

[2] R. R. A. Syms, V. M Schneider, W. Huang and M. M. Ahmad, *Electron. Lett.,* **33**, 1216-1217, 1997.

[3] K. D. Simmons, G. I. Stegeman, B. G. Potter Jr. and J. H. Simmons, J. Non-Cryst. Solids, 179 (1994) 254-259.

[4] D.L. Williams, B. J. Ainslie, J. R. Armitage, R. Kashyap, R. Campbell, *Electronics Letters*, **29**, 45-47, 1993.

[5] Charles K.F. Ho, K. Pita, N.Q. Ngo, Q.Y. Zhang, C.H. Kam, *submitted to J. Non-Crystalline Solids.*

[6] S. P. Mukherjee and S. K. Sharma, *J. Am. Ceram. Soc.,* **69**, 806-810, 1988.

[7] R.M. Almeida, P.J. Morais and H.C. Vasconcelos, *Sol-gel optics IV*, **SPIE 3136**, 296-303, 1997.

Analysis of the Resonant Wavelength Router

Andrea Melloni
**DEI, Politecnico di Milano, via Ponzio 34/5, Milano 20133, Italy*
melloni, martinelli@elet.polimi.it

Paolo Monguzzi and Mario Martinelli*
CoreCom, via G. Colombo 81, Milano 20133, Italy
monguzzi@corecom.it

The Wavelength Resonant Router (λ-ReR) is an optical integrated crossbar matrix based on ring resonators. The λ-ReR is similar but more flexible than an AWG. Both the spectral characteristic and the impact on WDM systems are investigated.

Keywords: integrated optics, ring resonator, optical filter, router, Bit Error Rate

Introduction

In the last years ring resonators attracted the attention of many researchers, mainly thanks to the selective frequency response, the small dimensions and because they can be exploited as the main building block of an add-drop, a de-multiplexer or even a crossbar matrix. In this contribution the integrated optic crossbar matrix based on ring resonators, named *Resonant Router (*ReR) and shown in Fig. 1, is described and its application as wavelength router (λ-ReR) is investigated. The nodes characteristics are described and the routing performance in terms of *Q*, extinction ratio and BER are discussed. An effective method for the estimation of the impact on BER is also presented. Preliminary experimental results on a single node realized with one ring conclude the contribution.

The wavelength resonant Router (λ-ReR)

The ReR can be exploited either as a Cross Connect or as a λ-Router, depending on the FSR of each node respect to the channel spacing of the WDM system. The characteristics of the ReR in the Cross Connect configuration have been already investigated in Ref. [3] and here we focus on the λ-Router function. As shown in Fig. 1 this device consists in a crossbar matrix with *N* inputs and *N* outputs each one carrying *N* wavelengths, forming a grid of *N*×*N* straight waveguides with *N*×*N* nodes. In each node one or more rings connect the two crossing waveguides. A single ring is often sufficient but the transfer function of each node can be improved by cascading two or more rings per node, as shown in Fig. 1a) and 1b).

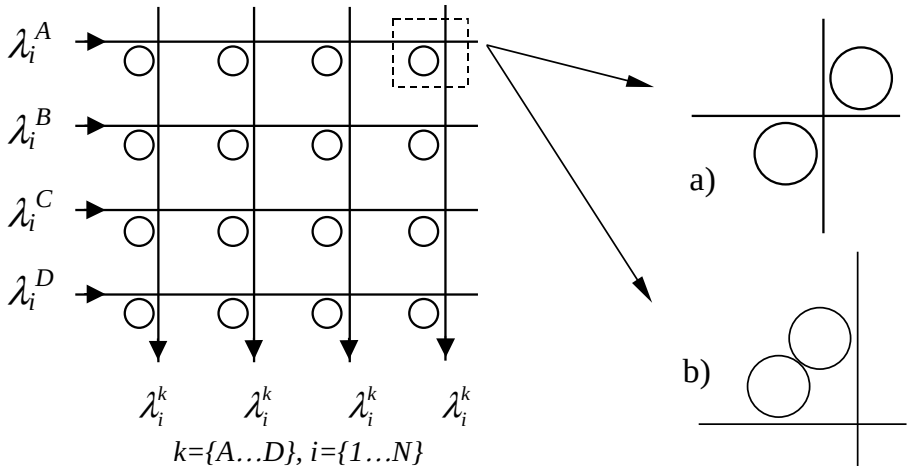


Fig. 1 – Structure of a 4×4 λ-ReR. Node with a) two rings in parallel and b) with two rings in series.

The FSR of each node must be at least equal to the channel spacing multiplied by the number of channels. Each node redirects the input channel at wavelength λ_i to the output vertical waveguide if

λ_i is the resonating wavelength of the node itself. Instead, if λ_i do not resonate, the signal propagates unaffected toward the next node. The ReR can be fully reconfigurable by tuning the resonant frequency of the rings, for example, with small thermo-controllers placed over the rings. An important feature of the ReR is that only one resonating node is encountered in the input/output optical path, reducing at maximum the filtering impairments and the insertion losses.

As an example, let's consider a λ-Router with a FSR=400 GHz and dimension *N*=8. The ReR is suitable for a 8-channels WDM system with channel spacing of 50 GHz but it can be used also in systems with a smaller number of channels. The input/output transfer function shown in Fig. 2 refers to a ReR with two rings per node. The nulls in the transmission transfer function are present only if at that wavelength a resonant ring is encountered on the input/output path. The in-band spectral behaviour depends mainly on the characteristics of the single node that must be accurately designed to avoid group delay distortions, losses, intersymbolic interference (ISI), cross talk, and dispersion impairments [2]. The ISI affects the shape of the pulses and is due to the filtering properties of the resonant nodes. The out-of-band behaviour, instead, depends also on the input/output path.

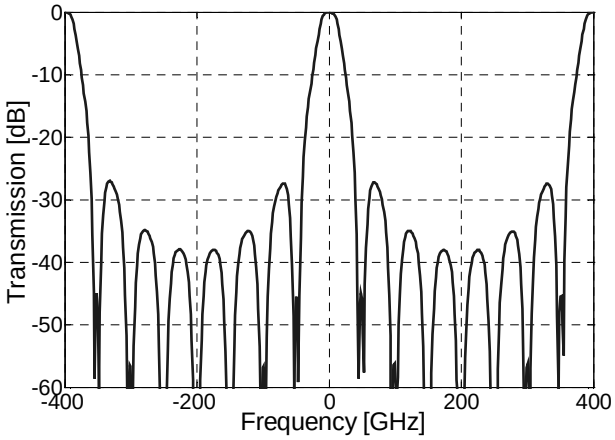


Fig. 2–Typical transfer function of a λ-ReR with N=8, FSR=400 GHz and two rings per node.

BER Estimation Method

Because of the presence of ISI and cross talk, the Q-factor and the Bit Error Rate (BER) of a system that includes a ReR cannot be calculated from the eye diagram as usual. The method used to estimate the ReR impact on the BER is shown in Fig. 3. An Additive White Gaussian Noise (AWGN) is added to the input sequence *s*. Then, passing through the matrix, the noisy sequence is filtered by the resonant node with transfer function H_{21} and by all the others non resonant nodes H_{11}. This operation introduces losses, distortion and an additive intersymbolic interference term *i*. Moreover, if *N* is the matrix dimension, *N-1* cross talk contributions *x* are added to the filtered sequence. The cross talk signals are considered incoherent with the considered channel, so their powers are added to the power of the reference sequence to obtain the output sequence. Finally, the receiver discriminates the bits 1 and 0 by mean of an optimum threshold *t* that minimizes the BER.

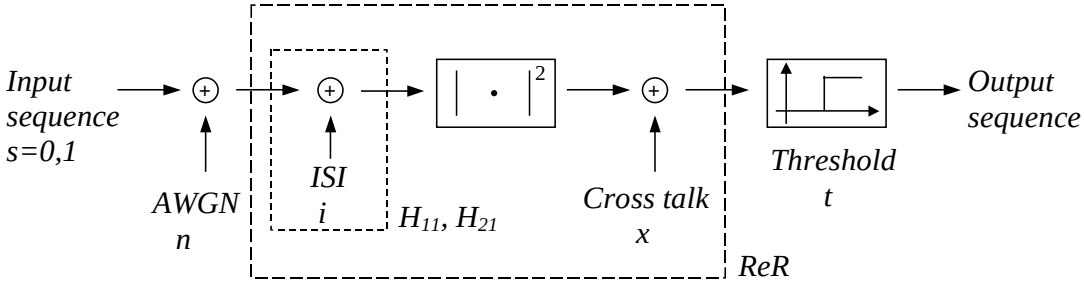


Fig. 3 – Model used to estimate the ReR impact on the BER.

The BER is estimated assuming that when the transmitted bit is 0, an error is obtained when $|s+n|^2+x>t$, that is when $n > \sqrt{t-x} - s$. The BER conditioned to the transmission of the bit 0 is

$$P(\varepsilon \mid 0) = BER0 = \sum_i \sum_x \frac{1}{2} erfc\left(\frac{\sqrt{t-x}-s}{\sigma_n \sqrt{2}}\right) P(i) P(x), \qquad (1)$$

where σ_n is the standard deviation of the noise in the output sequence, and *P(i), P(x)* are the distribution of ISI and cross talk respectively. In the same way, the error probability conditioned to the transmission of bit 1 is found as

$$P(\varepsilon\,|\,1) = BER1 = \sum_i \sum_x \frac{1}{2} erfc\left(\frac{1+s-\sqrt{t-x}}{\sigma_n\sqrt{2}}\right) P(i)P(x). \qquad (2)$$

The final Bit Error Rate is then the average between *BER1* and *BER0* and the *Q*- factor can be derived from the calculated BER:

$$BER = \frac{BER0 + BER1}{2} = \frac{1}{2} erfc\left(\frac{Q}{\sqrt{2}}\right). \qquad (3)$$

λ-ReR System Performance

In this section we analyse the impact of a λ-ReR with FSR=400 GHz on a 10 Gbit/s NRZ system. Three cases have been considered: 4 channels spaced by 100 GHz (*N=4*); 8 channels spaced 50 GHz (*N=8*) and 16 channels spaced 25 GHz (*N=16*). An unfiltered slightly noisy input sequence formed by supergaussian pulses (*m=2*) is used.

The design of the nodes consists in the determination of their bandwidth as a function of the bit rate, the modulation format and number of the WDM channels, the maximum achievable FSR being imposed by the available technology. In Fig. 4a) and b) the Extinction Ratio and the *Q*-Factor versus the bandwidth *B* at –3 dB for a single-ring based λ-ReR is shown. The same analysis was performed for λ-ReR with two rings in series and in parallel per node but we have found that the single-ring structure is sufficient to handle the three considered systems. Two or three rings are required only by systems with a higher spectral efficiency.

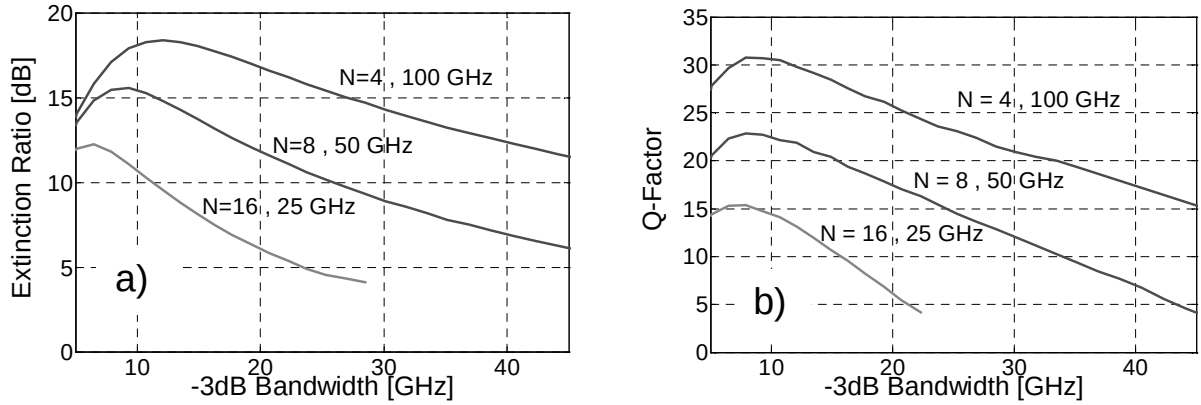


Fig. 4 – Extinction Ratio (a) and Q-Factor (b) versus the node bandwidth of the λ-ReR *used in three different 10 Gbit/s WDM systems. Each node consists in a single ring.*

The signal routed by the λ-ReR is affected by ISI and, in the worst operating conditions, by *N-1* cross talk signals. Nodes with a large bandwidth ensure a negligible pulse distortion and ISI but present a poor out-band extinction ratio and hence a high cross talk level. The reduction of the cross talk is achieved by increasing the node selectivity but this increases pulse distortion and hence ISI. The trade off between the two impairments leads to the optimum node bandwidth clearly evident from the graph shown in Fig. 4a) and 4b): in the considered cases we found that a bandwidth between 8 and 9 GHz is a good compromise that optimize the performance of the λ-ReR.

Below 9 GHz the λ-ReR is limited by ISI and above by cross talk. In general, with the optimal *B* the performance of the device are strictly dependent on the spectral efficiency of the system that is on the ratio between the bit rate (or the required bandwidth *B*) and the channel spacing. Moreover, it results that, to a first order and for a given channel spacing, the optimum bandwidth and the achievable system Q-factor do not depend on the matrix dimensions or the number of channels *N*.

The calculated output eye diagrams obtained from a λ-ReR with *B*=9 GHz for *N*=4 (100 GHz spaced) and *N*=16 (25 GHz spaced) are shown in Fig. 5. Comparing Fig. 5a) and b) it appears that the pulse shape is almost the same because the distortion depends only on the node bandwidth. Instead, the cross talk level is much higher in the 16-channels WDM system (Fig. 5b), affected by 15 contributions, respect to the *N*=4 case that is affected by only 3 contributions. Note that the sequence shown in Fig. 5b) can be considered error-free even if its extinction ratio is only 12 dB.

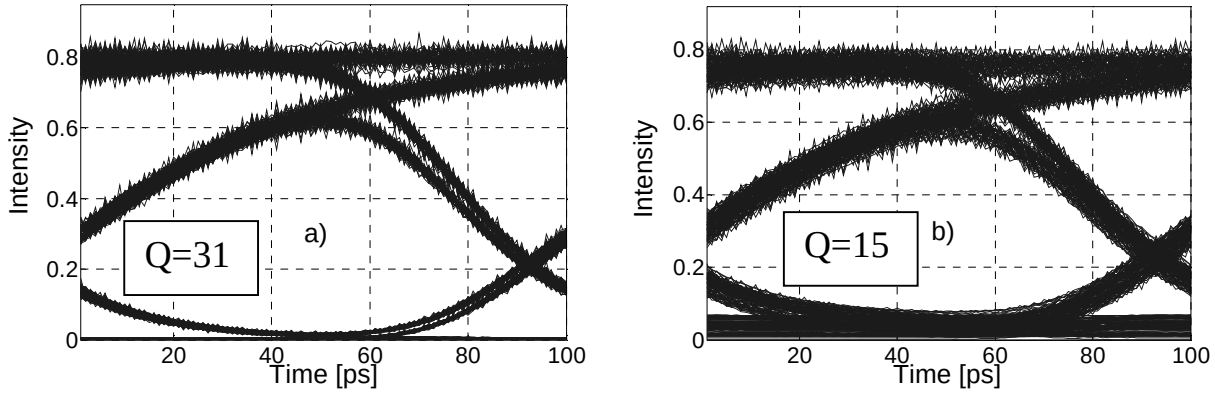


Fig. 5 –Eye Diagrams of the 10 Gbit/s output sequence from a 4×4, 100 GHz and 16×16, 25 GHz spaced λ-ReR. Each node consists in a single resonant ring with FSR=400 GHz.

To check the feasibility of a ReR, several switching nodes based on single and double ring resonator have been realized by using SiON technology with an index contrast Δn≈6% (LioniX BV [4]). This index contrast allows a bend radius of about 300 μm, providing a FSR of 100 GHz. A FSR=400 GHz should be achievable with a slightly higher Δn (8%). By using different coupling coefficients we have obtained bandwidth from 3.75 to 12.5 GHz and out-band extinction ratios from 25 to 14 dB. Two examples of the measured transfer function 'fiber-to-fiber' are reported in Fig. 6. According to the results of our simulations, these spectral characteristics are sufficient for the implementation of a 4×4 λ-ReR with channel spacing of 25 GHz.

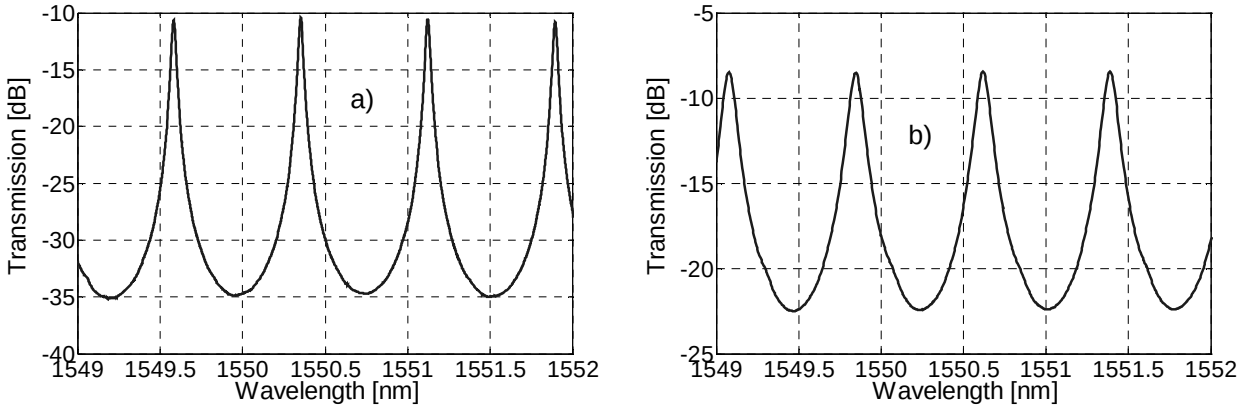


Fig. 6 – Measured transfer function of two single-ring resonators with a) bandwidth of 3.75 GHz and extinction ratio of 25 dB b) bandwidth of 12.5 GHz and extinction ratio of 14 dB.

References

[1] S.T. Chu, B.E. Little, W. Pan and Y. Kokubun, "Microring resonator arrays for VLSI photonics", *IEEE Photonic Technology Letters*, Vol. **12,** No. **3,** 323-325, (2000).

[2] A. Melloni and M. Martinelli, "Synthesis of direct-coupled resonators band pass filters for WDM systems", *IEEE Journal of Lightwave Technology*, Vol. **20**, No. **2**, 296-303, (2002).

[3] A. Melloni, P. Monguzzi, R. Costa and M. Martinelli, "Switching Characteristics of the Resonant-Ring Based Router", *2nd Workshop on Fibres and Optical Passive Components*, June 2002

[4] LioniX BV. www.lionixbv.nl

Discrete solitons in liquid crystals waveguide arrays

Kasia A. Brzdąkiewicz and Mirek A. Karpierz
Warsaw University of Technology, Faculty of Physics, Koszykowa 75, 00-662 Warsaw - Poland

Gaetano Assanto
N*OO*EL - Nonlinear Optics and Optoelectronics Lab., Dept. Electronic Engineering & INFM
University "Roma Tre", Via della Vasca Navale 84, 00146 Rome-Italy
assanto@ele.uniroma3.it

Discrete diffraction and discrete optical solitons are investigated in a voltage controlled channel waveguide array in nematic liquid crystals. A large nonresonant nonlinearity, proper waveguide design and voltage tunability of the coupling strength provide a unique and versatile test-bed for the addressed phenomena.

Keywords: guided-wave optics, liquid crystals, electro-optic devices, switching, optical solitons

In the past decade, families of optical spatial solitons have been investigated theoretically and demonstrated experimentally in media characterized by various kinds of nonlinearity, including cubic Kerr, photorefractive and parametric nonlinear responses. Theoretical analyses and experiments were performed in various configurations and dimensionalities, i. e., in planar waveguides and in bulk, demonstrating that it is possible to obtain stable spatial solitons both in one and two transverse dimensions, respectively.[1]
More recently, linear and nonlinear effects in discrete systems such as photonic structures with a periodic modulation of the refractive index (or waveguide arrays) have become the subject of intensive investigations. This interest is also motivated by the potentials of discrete solitons. [2,3] Similarly to continuous systems, in fact, stable spatial solitons can be generated in discrete waveguide arrays when self focusing is strong enough to balance (discrete) diffraction. The properties of discrete optical solitons have been described by Christodoulides at el. [3] and studied theoretically in a host of nonlinear materials. They have been experimentally observed in AlGaAs, in silica, in photorefractive SBN-crystals and also in Lithium Niobate. [4] It has been shown that discrete optical solitons are very promising in novel generations of all-optical switching circuits and optical networks. [2,5]
Using a different nonlinear mechanism, it has been demonstrated that spatial solitons can be efficiently generated in nematic liquid crystals (LC) and propagate for distances of a few millimeters (i. e., much larger than the Rayleigh range). In such media, soliton formation occurs due to the large non-resonant, saturable and non-local nonlinearity arising from molecular reorientation.[6] Their large birefringence with their giant nonlinear response makes nematic liquid crystals a very promising medium for nonlinear optics applications and solitons.[7] In fact, it has been shown that, at variance with other nonlinear responses, the reorientational nonlinearity in nematic liquid crystals allows generation of spatial solitons in both waveguide and bulk geometries, requiring only a few mW of light power. [6-7] Finally, nematic LC are highly anisotropic and exhibit large electro-optic and magneto-optic responses: this implies that their optical properties can be tuned/controlled by applying an external electric or/and magnetic field.
Combining the specific properties of discrete (linear and nonlinear) systems and the unique nonlinear response of nematic liquid crystals, we propose hereby the realization of liquid crystalline waveguide arrays. In this Communication we introduce the concept of a periodic photonic structure with refractive index changes controlled by an electric field. We show that such a voltage-tunable

geometry, in conjunction with a reorientational nonlinearity, offers a wealth of possibilities for the study of discrete optical phenomena.

A sketch of the proposed device is presented in Fig. 1. A glass cell (formed by two parallel slides) is filled with the nematic LC of appropriate thickness, making a planar waveguide (in the x coordinate). The anchoring conditions at both top and bottom surfaces determine the planar alignment of the molecules, i.e. with their longer axes parallel to the surfaces and the direction of light propagation. To introduce a refractive index modulation and obtain a voltage-adjustable nonlinear response, a set of periodically-spaced electrodes is deposited on the top surface to apply a reorientational bias across the cell.

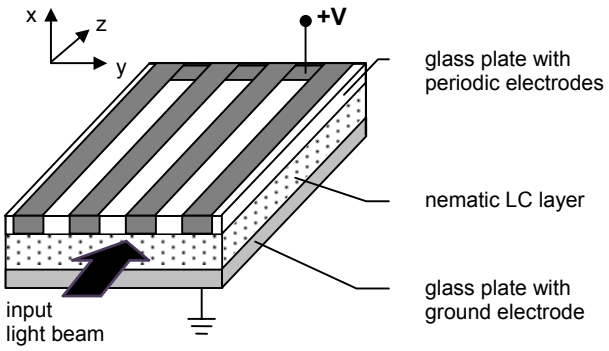


Figure 1. Sketch of the LC waveguide array.

The application of an appropriate voltage allows to reorient the LC molecules (which tend to be parallel to the direction of the electric field), increasing the refractive index and thereby defining channel waveguides through lateral confinement along y. An example of refractive index distribution is shown in Fig 2a.

We investigated the propagation of a light beam in the nematic LC layer with the Beam Propagation Method, using TM polarized Gaussian beams as the input. The refractive index changes were calculated from the Euler-Lagrange equation describing the LC molecular reorientation due to the bias and the electric field of the electromagnetic (optical) wave. Typical results of our numerical simulations, as presented in this summary, were obtained for the characteristic constants of the nematic 6CHBT, which exhibits refractive indices n_o=1.52 and n_e=1.69 at 1064nm.

In the proposed geometry, it is possible to obtain discrete diffraction via the coupling between adjacent and parallel 2D waveguides. Moreover, the magnitude of the discrete diffraction can be easily modified in our LC array not only by varying physical or geometrical parameters, but also by controlling the applied voltage. This bears important consequences on both the linear and the nonlinear properties of this discrete system, and the efficiency of nonlinear processes can be ameliorated in properly designed devices.

First, let us consider the requirements for 2D guidance in the linear (low light excitation) regime. In this case the electric bias plays a crucial role in the reorientation process. Figure 2b shows how the coupling strength between channels and the character of the resulting discrete diffraction change with applied voltage. As one can intuitively expect, by increasing the bias it is possible to induce a higher and higher refractive index change within each channel, progressively reducing the directional power transfer between them. On the other hand, however, excessive voltages tend to saturate and flatten the index profile, thereby weakening the transverse definition of the channels. It should be underlined, in fact, that the reorientation has a nonlocal (and for high voltages saturating) character, and substantial electric fields increase the refractive index not only under but also between the electrodes.

As shown for two cases in Fig. 2, we calculated and optimized LC thickness, electrode spacing and electrode width in order to obtain properly coupled and well defined channel arrays with suitable values of the applied voltage across the cell.

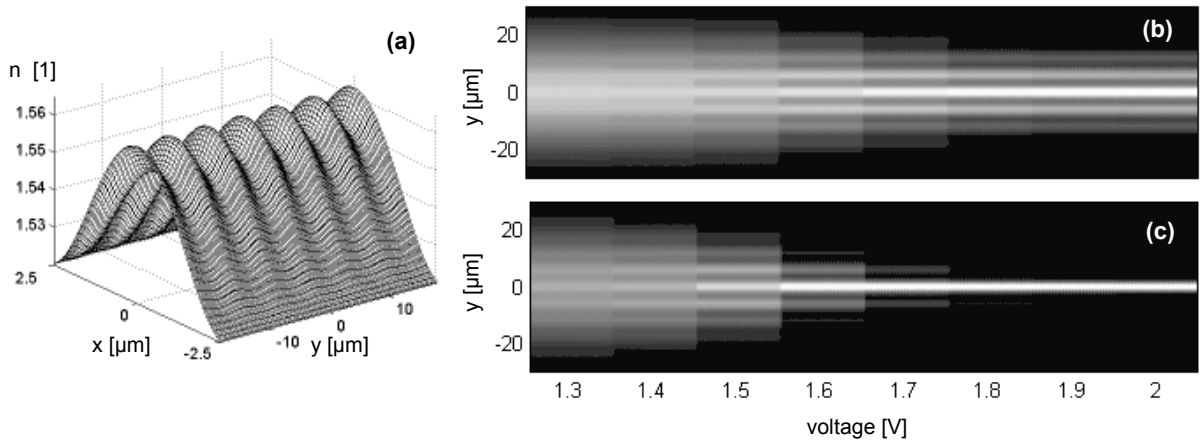


Figure 2. (a) Refractive index modulation obtained for an LC thickness of 5µm, electrode width and spacing are 3µm and V=1.65V. (b)-(c) Linear coupling between channels and its dependence on applied voltage for LC thicknesses of 5µm and 2.5µm, respectively. The graphed field is evaluated after propagation over 1mm.

In particular, by reducing the LC thickness we obtained better defined guides, in the sense that the difference between the refractive indices within each channel and in the gaps between the finger electrodes could be maximized (see two cases in Fig 2b-c). The spatial intensity distribution of the light is shown versus applied bias after 1mm of linear propagation and corresponding to a Gaussian input of waist w_o=2µm. In both cases, the top electrodes have a width of 3µm, while the LC thickness goes from 5 to 2.5µm. In the latter case the injected light remains confined in a single channel for voltages higher than 1.7V, i. e., when the channels are effectively de-coupled: even in the linear regime the beam is trapped into a single waveguide and discrete diffraction cannot be observed.

In the investigated structure, when transverse coupling is present but the intensity of the input beam is large enough, the nonlinear response can balance discrete diffraction, thereby resulting in discrete solitons. Moreover, due to the inherent 2D light confinement, the threshold power required for spatial soliton formation can be lower than in slab or "continuous" waveguides. Going from the linear to the nonlinear regime as the input intensity is increased, the refractive index of the excited waveguide(s) is modified by the reorientational nonlinearity. Under particular conditions, then, high power beams can propagate and maintain a stable transverse profile. The optical field is localized in a limited transverse portion of the array or, at high enough excitation levels, in a single channel. It is important here that, in the case of a reorientational nonlinearity, saturation and nonlocality contribute to and affect the overall phenomenology.

The plots in Fig. 3 (a thru c) present the evolution of the light beam from discrete diffraction (a) to discrete soliton (b-c) as the input power was increased from 0.3 to 1.1 mW (for a bias voltage of 1.65V). The graphs (d) thru (f) show the corresponding refractive index distributions at the output (L=1.5mm).

Fig. 3(a) is an example of discrete linear diffraction, and the input excitation spreads among 9 adjacent channels. When the power is increased, diffraction is reduced and a spatial discrete optical soliton is generated, either "wide" because the overall energy is carried by a few channels (Fig. 3b) or "narrow", when all the light is essentially confined in the input guide (Fig. 3c).

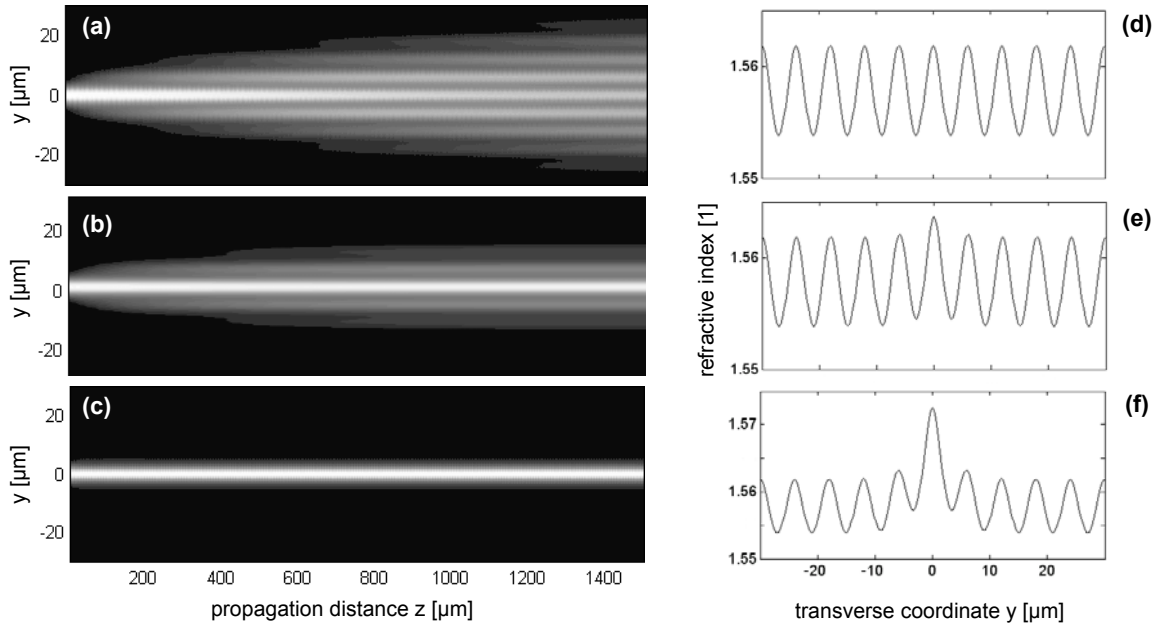


Figure 3. a) Discrete diffraction for a w_0=2μm Gaussian beam launched into one of the guides; b)-c) Generation of discrete spatial solitons as the input light power was increased from 0.3mW (b) to 1.1mW (c); e)-d) Refractive index distributions in the middle of the LC layer (i.e. in x=0μm with reference to Fig. 2c) corresponding to cases a) thru c), respectively.

To study the role of the input conditions, we varied the input profile of the beam (its waist) and its direction of propagation with respect to the channel axis in the array. When a wide beam was employed (e.g. w_0=8μm), the stronger linear coupling was such that a higher excitation of 15mW was required to obtain single waveguide trapping (a "narrow" soliton).

In conclusion, we have proposed a novel linear /nonlinear array of 2D waveguides obtainable and controllable through the reorientational response of nematic liquid crystals. The combination of discrete diffraction and a large nonlinearity in such system allows to predict discrete solitons at mW power levels. The flexibility offered by voltage-controlled transverse coupling between provides an ideal test-bed for a thorough investigation of discrete diffraction and soliton phenomena.

1. S. Trillo and W. Torruelllas, *Spatial Solitons,* Wiley, New York (2002)
2. F. Lederer, S. Darmanyan, and A. Kobyakov, in *Spatial Solitons*, eds. S. Trillo and W. Torruelllas, Wiley, New York (2002)
3. D. N. Christodoulides and R. I. Joseph, Opt. Lett. **13**, 794 (1988)
4. A. B. Aceves *et al*., Phys. Rev. E **53**, 1172 (1996); R. Morandotti, *et al*.,, Phys. Rev. Lett. **86**, 3296 (2001); R. Morandotti, *et al*., Phys. Rev. Lett. **83**, 2726 (1999); U. Peschel, *et al*.,, Appl. Phys. Lett. **75**, 1348 (1999); H. S. Eisenberg, *et al*., Phys. Rev. Lett. **87**, 3902 (2001); N. K. Efremidis, *et al*., Phys. Rev. E **66**, 046602 (2002)
5. E. D. Eugenieva, *et al*., Opt. Lett. **26**, 1978 (2001); D. N. Christodoulides *et al*., Phys. Rev. Lett. **87**, 233901 (2001)
6. M. Peccianti, *et al*., Appl. Phys. Lett. **77**, 7 (2000); M. Karpierz, Phys. Rev. E **66**, 036603 (2002)
7. M. Peccianti and G. Assanto, Phys. Rev. E **65**, 035603 (2002)

Bloch wave engineering for high Q's small V's optical microcavities

Philippe Lalanne, Jean-Paul Hugonin
Laboratoire Charles Fabry de l'Institut d'Optique, Centre National de la Recherche Scientifique, 91 403 Orsay Cedex, France
Philippe.lalanne@ iota.u-psud.fr

Keyword: guided-wave optics, microcavity, radiation losses, Bloch modes

Introduction

Many important devices use periodic microstructures of alternating layers of dielectric materials to enhance reflection. Usually the refractive index contrast of dielectric layers is low, typically 1% in a distributed Bragg reflector, and a large number of small reflections over a long propagation distance are needed to warrant high reflectivity [1]. Alternatively, periodic microstructures deeply etched into a semiconductor waveguide offer high refractive-index contrasts and much shorter interaction lengths. Examples include photonic wires or air-bridge microcavities [2,3] and very compact Bragg reflectors [4,5,6]. Responding to the quest for miniaturization in optoelectronics, these new mirrors implemented in short cavities additionally offer interesting perspectives: large free spectral ranges, small modal volumes as is required for controlling the spontaneous emission of atoms in microcavities [7], and low threshold lasers. However, for strong corrugations, the Bragg mirror cannot be considered as a perturbation of the uncorrugated waveguide and out-of-plane scattering losses (radiation) in the claddings are inevitable. Apparently strong corrugations required for short interaction lengths and small radiation losses required for high performance seems to be two conflicting objectives.

Two routes are known to achieved high Q's and small V's in optics. The first one refers to the complete 3D photonic crystal approach (the cage for light [8]). Another exploits a judicious refractive index engineering of the core and cladding layers [9]. Both approaches provide theoretically lossless operation, but requires a complex 3D refractive-index engineering. *We proposed another approach which can be fully implemented in planar systems.* As shown by numerical computations in [10] and by experimental results in [11], tapered mirrors that incorporate a series of etches whose feature dimensions vary progressively can provide short interaction lengths and low radiation losses.

The radiation-loss problem

To illustrate our purpose, let us consider the one-dimensional photonic-bandgap air-bridge cavity shown in Fig.1. The periodicity constant Λ is 450 nm and the hole diameter w is 250 nm. Hereafter, we assume that the semiconductor bridge ($n = 3.48$) is 340-nm-thick, 500-nm-wide. Similar microcavities have been studied previously [3], and Q's of ≈ 300 for $V \approx 0.03\ \mu m^3$ have been observed at $\lambda = 1.5\ \mu m$. In the wavelength range of interest, the waveguide supports a single TE-like mode (electric field primarily horizontal at the center of the waveguide) with a double mirror symmetry. For $\lambda = 1.56\ \mu m$, the calculated losses L of

the semi-infinite mirrors illuminated by the fundamental mode of the bridge are 4.5%. Thus one expects that a short microcavity formed by the association of these two mirrors has a Q factor $Q_{FP} = m\pi(R)^{1/2}/L$. For a cavity order m= 3 (as it is the case for a single hole defect cavity), one expects that $Q_{FP} \approx 200$.

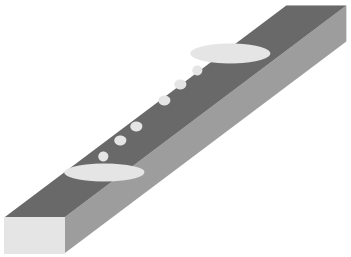


Figure 1. Microcavity discussed in this work. The cavity is formed by two-periodic holes arrays separated by a small defect, typically a single hole defect.

Engineered mirrors and cavities

As shown hereafter, this low Q value can be increased by several orders of magnitude while keeping constant the mode volume V of the cavity. Let us first explain the raison for this low Q value. In [10], the authors propose an approximate model that interpretates the origin of the loss at the interface between the waveguide and the mirror as an impedance mismatch between the incident guided mode and some electromagnetic quantity directly to the fundamental Bloch wave associated to the mirror (we will refer this quantity to as a half-Bloch mode). The losses vary as the square of the integral overlap η between the half-Bloch mode and the incident guided mode [10]. An immediate consequence is that if one desires to reduce the radiation losses to increase the cavity Q, one must engineer the periodic mirrors to taper the incident guided mode into the fundamental Bloch mode of the mirrors. As suggested in [10], a possible solution consists in designing tapered mirrors formed by a series of "segments" whose feature dimensions vary progressively. An illustration of an engineered mirror is shown in Fig. 2, where two "segments" are inserted between the waveguide and the periodic mirror.

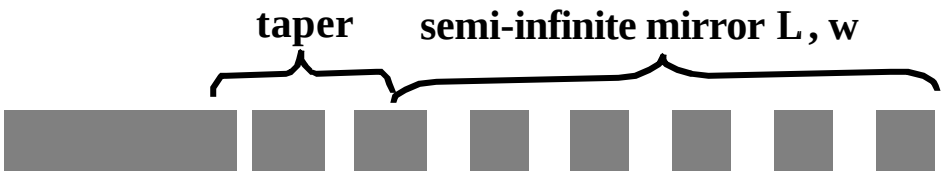


Figure 2. Exemple of tapered mirror obtained by varying the two first hole dimension and spacing of the periodic mirror.

Microcavities with high Q's and small V's

As will be shown at the conference, two different approaches can be used to design microcavities with high Q's and small V's.

The first approach is simple in its principle. It consists in designing mirrors with small radiation losses. At the conference, we will show that the design mainly consists an engineering of the fundamental Bloch mode, and that the main degree of freedom to be used for the design is the length Λ of the segments.

The second approach is more counterintuitive. It can be shown [12] that the performance of microcavities formed by a defect surrounded by two short Bragg mirrors is not ultimately driven by the modal mirror reflectivity and transmission, i.e. by the mirror losses. In other words, cavities formed with quite lossy mirrors can exhibit unexpected high Q factors. As shown in [12], this anomalous Q's of microcavities can be explained by a radiation recycling mechanism, a pure electromagnetism effect on transient fields at subwavelength scale in the cavity defect. Once appropriately engineered, the recycling boosts the Q's and peak transmissions by several orders of magnitude.

The two approaches can cooperate in practice. To illustrate our purpose, we performed calculations for symmetric cavities with slightly different hole geometries. Only two degrees of freedom, namely the location and the diameter of the two inner holes, were varied for optimizing the intrinsic Q factor. Due to the great computational loads, the configuration space was not thoroughly explored, but many cavity geometries with Q's much larger than that achieved with the periodic mirror were obtained. The three-dimensional computation is performed with the frequency-domain Fourier modal method described in [13]. One of the best performance is achieved for a geometry which corresponds to a 30-nm reduction of the hole diameter and to a 65-nm outer displacement of the center hole locations. Circles in Fig. 3 represent the calculated Q's of the engineered cavity for $\lambda = 1.56$ µm and for the third cavity order ($m = 3.15$) as a function of the number N of holes.

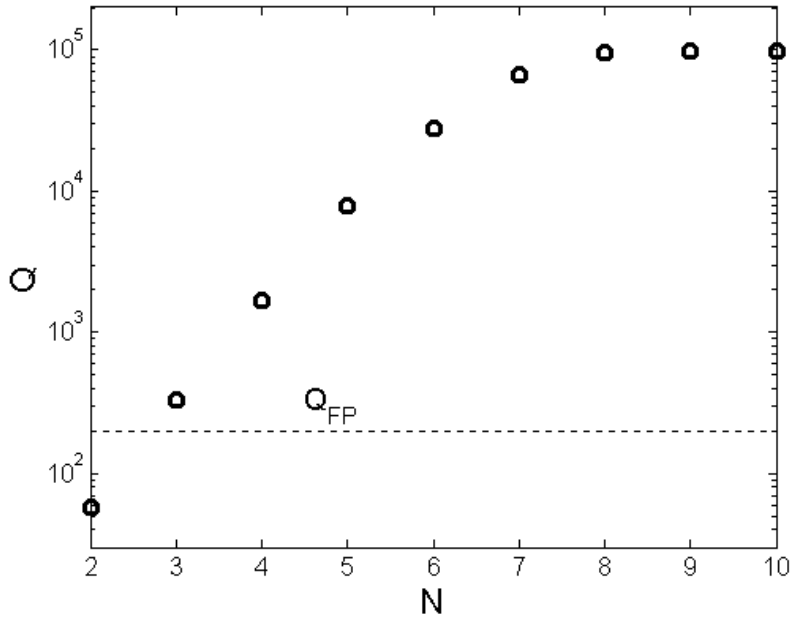


Figure 3. Calculated Q of the engineered cavity as a function of the number of holes. The horizontal dashed line represents the Q factor in the absence of recycling for the cavity formed with the semi-infinite periodic mirrors.

The Q's of the engineered cavity are several order of magnitude higher than the predicted value $Q_{FP} \approx 200$ (horizontal dashed line in the Figure) for the cavity with fully periodic mirrors. This increase has two causes. First, the engineered mirror losses are smaller than those of the periodic mirror increasing the cavity Q from 200 to 750, and secondly, the

radiation recycling is responsible for an other increase by more than a factor one hundred. Finally let us note that, since the modal volume of the engineered cavity is only 6% larger than that of the cavity with fully periodic mirrors, the engineering results in an enhancement of the Purcell factor (Q/V) by a factor 500.

Mirel Palamaru and **Eric Silberstein** were previously involved in this research as master and PhD students. The authors thanks their colleagues **D. Peyrade, A. Talneau, and Y. Chen** from the Laboratoire de Photonique et de Nanostructures at Marcoussis for fruitful discussions and experimental works on the fabrication and characterization of microcavities note reported here in this abstract.

[1] L.A. Coldren and S.W. Corzine, Diode lasers and photonic integrated circuits, First ed. (Wiley, New York, 1995).
[2] J.P. Zhang, DY. Chu, S.L. Wu, W.G. Bi, R.C. Tiberio, R.M. Joseph, A. Taflove, C.W. Tu, S.T. Ho, IEEE Photon. Technol. Lett. **8**, 491 (1996).
[3] J.S. Foresi, P.R. Villeneuve, J. Ferrera, E.R. Thoen, G. Steinmeyer, S. Fan, J.D. Joannopoulos, L.C. Kimerling, H.I. Smith and E.P. Ippen, Nature **390**, 143 (1997).
[4] T.F. Krauss and R. M. De La Rue, Appl. Phys. Lett. **68**, 1613 (1996).
[5] T. Baba, M. Hamasaki, N. Watanabe, P. Kaewplung, A. Matsutani, T. Mukaihara, F. Koyama and K. Iga, Jpn. J. Appl. Phys. **35**, 1390 (1996).
[6] T.F. Krauss, O. Painter, A. Scherer, J.S. Roberts, R. M. De La Rue, Opt. Eng. **37**, 1143 (1998).
[7] *Spontaneous emission and laser oscillation in microcavities*, edited by H. Yokoyama and K. Ujihara, Boca raton, FL: CRC Press, 1995.
[8] D. Normile, Science **286**, 1500 (1999).
[9] J. Ctyroky, J. Opt. Soc. Am. A **18**, 435 (2001). See also, M. R. Watts, S.G. Johnson, H.A. Haus and J.D. Joannopoulos, Opt. Lett. **27**, 1785 (2002).
[10] M. Palamaru and Ph. Lalanne, Appl. Phys. Lett. **78**, 1466 (2001).
[11] D. Peyrade, E. Silberstein, P. Lalanne, A. Talneau, Y. Chen, Appl. Phys. Lett. **81**, 829 (2002).
[12] Philippe Lalanne, Jean-Paul Hugonin, « Radiation recycling in microcavities », submitted for publication.
[13] E. Silberstein, Ph. Lalanne, J.P. Hugonin and Q. Cao, J. Opt. Soc. Am. A. **18**, 2865 (2001).

Time Domain Numerical Model for linear and nonlinear Grating-Assisted Codirectional Coupler

Mariangela Gioannini, Ivo Montrosset
Dept. of Electronic Engineering, Politecnico di Torino, C.so Duca degli Abruzzi, 24, Torino, Italy.
ivo.montrosset@polito.it

A time domain model is presented for the dynamic analysis of linear and nonlinear devices based on coupled modes propagating with different group velocities. As a test, the numerical algorithm is applied to the analysis of a linear grating assisted co-directional coupler and the limitation of the method are investigated.

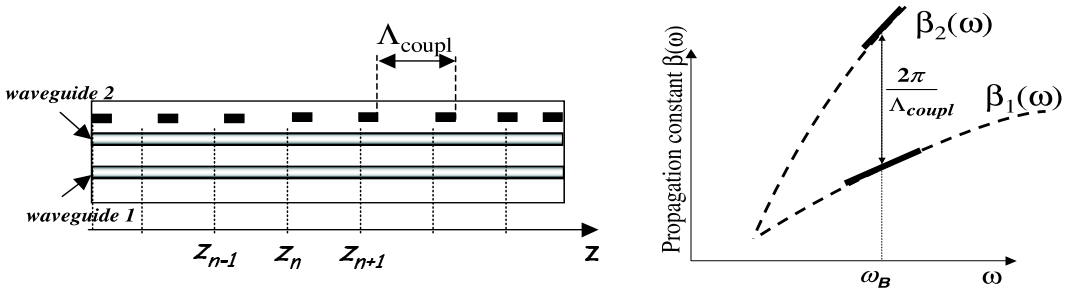
Keywords: linear and nonlinear co-directional coupling, GACC filter, TDTW model, simulation

Introduction

Narrow band filters, tunable over a wide wavelength range and integrated with other photonic devices, are important elements for WDM multi/demultiplexing systems. Apart from the distributed Bragg reflectors based on contra-directional coupling, linear and nonlinear filters having a Grating Assisted Codirectional Coupler (GACC) [1] have also been used in many laser and integrated optic structures [2]-[5]. Fig. 1(a) show the typical GACC structure with the two waveguides coupled through a long period grating with pitch Λ_{coupl}. As shown in Fig. 1(b) the modes of the two waveguides, coupled through the perturbation created by the grating, propagate co-directionally with different propagation constants, $\beta_1(\omega)$ and $\beta_2(\omega)$. The different dispersion of the two propagation constants gives different group velocities, v_{g1} and v_{g2}, and the group velocity difference determines the GACC filter bandwidth and tuning capability [6]. Several papers have been published in the literature on the spectral domain analysis and design of these filters [5]-[7], but, to our knowledge, there is not any model that analyze dynamically the propagation of two coupled modes having different group velocities. Furthermore this kind of simulation is essential whenever waveguide nonlinear effects have to be included [5]. The purpose of this paper is to present an extension of the Time Domain Travelling Wave (TDTW) model [8] applied to this case. The TDTW equations and the numerical algorithm for their solution presented in the literature concern indeed only with the case of two coupled modes travelling with the same group velocity, v_g, as for example in DFB and DBR lasers [8],[9]. For these devices the TDTW equations are numerically solved using a space-time discretization grid, defined to satisfy the condition $\Delta z = v_g \Delta t$, where Δz and Δt are respectively the space and time discretization steps. This condition allows the field samples to propagate according to the differential equation characteristic lines, keeping null the numerical error accumulated during the propagation [9]. We have observed that the the standard TDTW approach [8],[9] can not take into account the case of modes with different group velocities and this leads, for example, to significant errors in the simulated GACC filter bandwidth and tunability. A proper numerical method and the conditions to solve correctly the TDTW system of coupled mode equations with different group velocities is thus presented. The numerical errors that result moving away from these proper working conditions are also evaluated.

Model and numerical algorithm

The GACC TDTW equations can be obtained from the spectral domain equations that result from coupled mode theory [1]. To define the notations we report the final equations for



(a) (b)

Fig. 1. (a) GACC structure with the spatial discretization grid and (b) scheme of the dispersion of the propagation constants.

the slow varying forward components, $\mathcal{A}_1^+(z,t)$ and $\mathcal{A}_2^+(z,t)$, of the electric field.

$$\begin{cases} \dfrac{\partial \mathcal{A}_1^+(z,t)}{\partial z} + \dfrac{1}{v_{g1}} \dfrac{\partial \mathcal{A}_1^+(z,t)}{\partial t} = -j\,\widetilde{\delta}_1\,\mathcal{A}_1^+(z,t) + j\,k\,\mathcal{A}_2^+(z,t) \\ \dfrac{\partial \mathcal{A}_2^+(z,t)}{\partial z} + \dfrac{1}{v_{g2}} \dfrac{\partial \mathcal{A}_2^+(z,t)}{\partial t} = -j\,\widetilde{\delta}_2\,\mathcal{A}_2^+(z,t) + jk\,\mathcal{A}_1^+(z,t) \end{cases} \tag{1}$$

These slow varying components have been obtained for each waveguide, i, extracting from the time domain electric field an arbitrary reference pulsation, ω_0, and a reference propagation constant $\beta_{i0} = \omega_0/c \cdot n_{eff\,i0}$, with c the light velocity and $n_{eff\,i0}$ the effective refractive index of waveguide i. In equation (1) k is the mode coupling coefficient and $\widetilde{\delta}_1$ and $\widetilde{\delta}_2$ are in general complex detuning terms that take into account the detuning of the reference pulsation ω_0 from the Bragg condition, the waveguide loss, gain and nonlinear effects. Analogous equations can be also obtained for the backward components. For the numerical solution the coupler structure has been divided in slices $\Delta z = v_{g_{num}}\,\Delta t$ (Fig. 1a), having chosen $v_{g_{num}} = \max\{v_{g\,1}, v_{g\,2}\}$ for convergency reasons [10]. In the following we will assume that $v_{g\,1}$ is the maximum group velocity. The system of equations (1) has then been solved with a split step algorithm. For each spatial node z_n, we have calculated the field propagation from time instant t_m to t_{m+1} in two steps. In the first step we have solved the temporal propagation equation, obtaining, as shown in equations (2) and (3), the field samples $\overline{\mathcal{A}}_{1\,n,m+1}^+$ and $\overline{\mathcal{A}}_{2\,n,m+1}^+$

$$\frac{\partial \mathcal{A}_1^+(z,t)}{\partial z} + \frac{1}{v_{g\,1}} \frac{\partial \mathcal{A}_1^+(z,t)}{\partial t} = 0 \implies \overline{\mathcal{A}}_{1\,n,m+1}^+ = \mathcal{A}_{1\,n-1,m}^+ \tag{2}$$

$$\frac{\partial \mathcal{A}_2^+(z,t)}{\partial z} + \frac{1}{v_{g\,2}} \frac{\partial \mathcal{A}_2^+(z,t)}{\partial t} = 0 \implies$$

$$\overline{\mathcal{A}}_{2\,n,m+1}^+ = \mathcal{A}_{2\,n,m}^+ - \frac{v_{g\,2}\Delta t}{2\,\Delta z}[\mathcal{A}_{2\,n+1,m}^+ - \mathcal{A}_{2\,n-1,m}^+] + \frac{1}{2}\left(\frac{v_{g\,2}\,\Delta t}{\Delta z}\right)^2[\mathcal{A}_{2\,n+1,m}^+ - 2\mathcal{A}_{2\,n,m}^+ + \mathcal{A}_{2\,n-1,m}^+] \tag{3}$$

Since $\Delta z = v_{g_1}\,\Delta t$, equation (2) is solved exactly [9] whereas equation (3) have been solved numerically using a second order Lax-Wendroff scheme [10]. In the second step we have then included the coupling and the complex detuning, $\widetilde{\delta}_1$ and $\widetilde{\delta}_2$, solving the following equations:

$$\frac{\mathrm{d}\,\mathcal{A}_1^+}{\mathrm{d}\,z} = -j\,\widetilde{\delta}_1\,\mathcal{A}_1^+(z) + jk\,\mathcal{A}_2^+(z) \quad \text{and} \quad \frac{\mathrm{d}\,\mathcal{A}_2^+}{\mathrm{d}\,z} = -j\,\widetilde{\delta}_2\,\mathcal{A}_2^+(z) + jk\,\mathcal{A}_1^+(z) \tag{4}$$

The transfer matrix for the solution of (4) can be easily obtained from the calculation of eigenvalues and eigenvectors of (4). Thus we obtain:

$$\begin{pmatrix} \mathcal{A}^+_{1\,n,m+1} \\ \\ \mathcal{A}^+_{2\,n,m+1} \end{pmatrix} = \begin{pmatrix} T_{11}(\Delta z) & T_{12}(\Delta z) \\ \\ T_{21}(\Delta z_2) & T_{22}(\Delta z_2) \end{pmatrix} \begin{pmatrix} \overline{\mathcal{A}}^+_{1\,n,m+1} \\ \\ \overline{\mathcal{A}}^+_{2\,n,m+1} \end{pmatrix} \tag{5}$$

We have observed that evaluating the matrix elements T_{11}, T_{12} in $\Delta z = v_{g\,1}\,\Delta t$ and T_{21}, T_{22} in $\Delta z_2 = v_{g\,2}\,\Delta t$, the solution obtained is less affected by numerical errors respect to the solution calculated evaluating all the elements in the same $\Delta z = v_{g\,1}\,\Delta t$, as done in a standard split-step TDTW approach [9].

Numerical results

To demonstrate the accuracy and efficiency of the proposed time-domain method, we analyze a 540 μm long GACC, with a grating coupling coefficient of 29 cm^{-1} and group refractive index $n_{g1} = 3.524$ and $n_{g2} = 3.867$. We show in Fig.2a and 2b the power distribution of the CW fields $\mathcal{A}^+_1(z,t)$ and $\mathcal{A}^+_2(z,t)$ when the GACC Bragg pulsation is equal to the reference pulsation ω_0. The boundary conditions are $\mathcal{A}^+_1(0,t) = 1$ and $\mathcal{A}^+_2(0,t) = 0$. Fig. 2a shows that, evaluating all the transmission matrix elements in the same $\Delta z = v_{g\,1}\,\Delta t$ the solution is not correct because the upper waveguide receives too much power from the lower one and the total power is not conserved. On the contrary, as demonstrated in Fig. 2b, the total power maintains constant along z, if the transfer matrix is calculated as indicated in (5). To test the method also in a

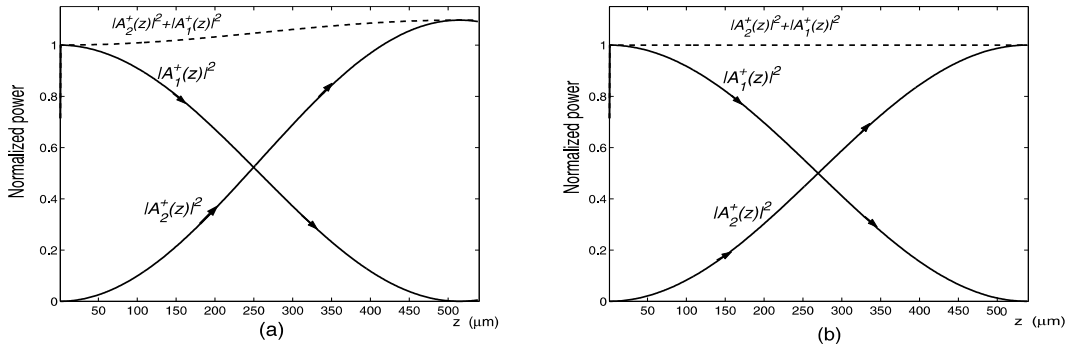


Fig. 2. Normalized power distribution, along the GACC, of the CW forward fields at the Bragg wavelength. Simulation evaluating (a) all the transfer matrix elements in $\Delta z = v_{g1}\Delta t$ and (b) as indicated in equation (5).

wide wavelength range, we compare in Fig. 3a-b the GACC transmission spectrum, obtained with our TDTW analysis, with the exact result obtained with a spectral domain analysis. Fig. 3a shows that in case of zero detuning, $\Delta\lambda$, between the numerical procedure extracted reference wavelength (λ_0=1570 nm) and the GACC Bragg wavelength, λ_B, the two solutions practically overlap. However the error becomes significant when we move away from $\lambda_B = \lambda_0$, as shown in Fig. 3b for $\Delta\lambda = 20$ nm. This leads to errors in the simulated GACC Bragg wavelength and maximum transmission coefficient. We have observed that these numerical errors are mainly due to the dispersion and distortion introduced by the Lax-Wendroff scheme [10] and can be partially compensated at λ_B since they can be analytically evaluated [10] for each wavelength component of the fields. Fig. 3c-d report, as an example, the errors on GACC Bragg wavelength and peak transmissivity versus the detuning $\Delta\lambda$ when the numerical algorithm is applied without and with the application of a simple error correction scheme at λ_B.

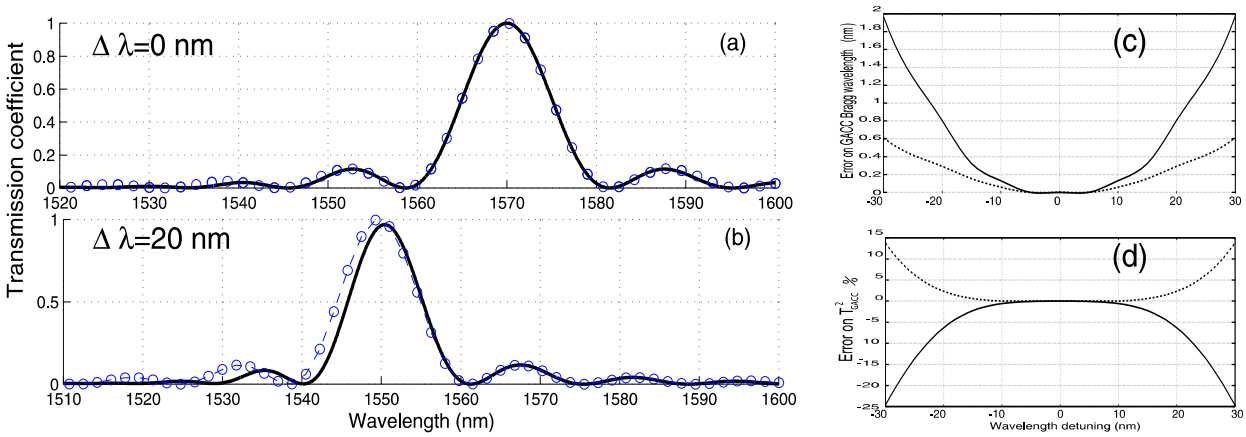


Fig. 3. GACC transmission coefficient versus wavelength for the cases we choose (a) zero and (b) 20 nm detuning of the extracted λ_0=1570 nm from the Bragg wavelength. Solid line: TDTW solution, Circle: exact reference solution. (c) Error in the GACC Bragg wavelength and (d) maximum transmissivity versus wavelength detuning without (solid line) and with (dash line) error correction.

Conclusion

We have presented a numerical method for the solution of the TDTW equations of two co-directionally coupled modes travelling at different group velocities. As a reference case to validate the proposed algorithm, we have considered a GACC filter. It has been shown that with a proper choice of the reference pulsation the numerical error is practically null over a wide wavelength range. Furthermore, for non zero detuning in the device selected reference pulsation, it can be partially compensated around ±10 nm with a simple error correction procedure. The model proposed can find interesting applications in the time-domain analysis of photonic integrated devices that include a GACC such as active and nonlinear filters, lasers and whenever the nonlinearity does not allow a straightforward application of the spectral domain approach.

[1] D.Marcuse, *IEEE J. Lightwave Technol.*, **LT-5**, 268–273, 1987.

[2] R.C. Alferness et alii, *Appl. Phys. Lett.*, **APL-60**, 3209–3211, 1992.

[3] M. Oberg et alii, *IEEE Photon. Tech. Lett.*,**PTL-5**, 735–738, 1993.

[4] S. Illek et alii *Electron. Lett.*, **EL-27**, 920–924, 1989.

[5] B.E. Little et alii, *IEEE J. Lightwave Tech.*, **LT-11**, 1990–1997, 1993.

[6] G.Griffel et alii, *IEEE J. Quantum Electron.*, **QE-27**, 1115–1118, 1991.

[7] Z.M. Chuang et alii, *IEEE J. Quantum Electron.*,**QE-29**, 1071–1080, 1993.

[8] J. Carroll et alii, *Distributed feedback semiconductor lasers*, Ed. The institution of Electrical Engineers, London, 1998.

[9] B.S. Lim et alii, *IEEE J. Quantum Electron.*,**QE-36**, 787–794, 2000.

[10] J.C. Strikwerda, *Finite difference schemes and partial differential equations*, Wandroff and Brook/Cole Advanced Books and Software, Pacific Grove, California, 1989.

Detailed analysis of spatiotemporal stability of the ultra-short optical pulses propagating in non-linear step-index optical waveguide

Elena A.Romanova, Leonid A.Melnikov
Saratov State University, Astrakhanskaya 87, 410026 Saratov, Russia
romanova@optics.sgu.ru

Propagation of the ultra-short optical pulse through a boundary of linear and non-linear segments of planar dielectric waveguide with step-like distribution of the refractive index is simulated numerically. Impact of self-steepening and normal dispersion effects as well as role of retarded non-linear response of the waveguide material are analysed separately in detail. Solution of the paraxial wave equation with non-linear susceptibility is shown to be stable in space in time provided that the quasi-static approximation is used.

Keywords: optical waveguides, ultra-short pulses, Kerr-like non-linearity, spatiotemporal dynamics

Recent experiments with propagation of femtosecond optical pulses in fused silica has demonstrated a complicated dynamics of both spatial and temporal pulse distribution that reveal itself in splitting of the pulse and filamentation of the gaussian beam [1]. These effects are mainly due to the high peak intensities of the beam focused on a bulk silica with a relatively small Kerr-constant $n_2 \approx 10^{-16} cm^2/W$. In optical waveguides, self-action of ultra-short pulses was considered before predominantly as a temporal self-action but the self-focusing effect was assumed to be negligibly small [2]. However the above mentioned experiments with fused silica as well as design of new glasses with greater non-linearity [3] show that there is a need to consider both the spatial and temporal effects of high-intensity pulse propagation through dielectric waveguiding structures.

In our previous works, we studied spatial transient process of fundamental mode propagation through a boundary between linear and non-linear segments of step-index waveguide [4]. Behind a region of spatial transient process in the non-linear segment, a steady-state field distribution was obtained as a numerical solution of paraxial wave equation with non-linear susceptibility (so-called "non-linear mode"). This effect depends on geometry of the guiding structure and can be used to manage parameters of the propagating radiation. However these CW results can be generalised onto the pulsed power propagation provided that the pulse duration is much greater than period of optical oscillations and non-linear response of the waveguide material.

In this work, we simulate numerically propagation of femtosecond optical pulse in planar step-index waveguide with the Kerr-like non-linearity embedded and analyse spatiotemporal dynamics of slowly varying envelope $A(x,z,t)$ of the total filed $E(x,z,t) = A(x,z,t)\exp(i\omega t - i\beta z)$ in the quasi-static approximation and with account of self-steepening effect and finite non-linear response as well as second-order dispersion of the waveguide material.

Numerical modeling is based on solution of the (2+1) paraxial wave equation written in a moving-frame coordinate system ($z = z,\ t = t_0 - z/u$) :

$$2i\beta\frac{\partial A}{\partial z}+\frac{\partial^2 A}{\partial x^2}+\varepsilon_1\frac{\partial^2 A}{\partial t^2}+(k^2n^2(x)-\beta^2)A+2i\varepsilon_2\frac{\partial(|A|^2\ A)}{\partial t}+\varepsilon_3\left(|A|^2\ A-\tau_R\frac{\partial|A|^2}{\partial t}A\right)=0 \qquad (1)$$

where $\varepsilon_1 = k_2 k/\tau^2(0)$, $\varepsilon_2 = n_2 k/(c\tau(0))$, $\varepsilon_3 = n_2 k^2$, k_2 is dispersion coefficient, n_2 is the Kerr constant, k is the mean wave number, c is the light velocity in vacuum, β is longitudinal propagation constant of the TE_0 mode, τ_R is the retarded non-linear response, $\tau(0)$ is initial pulse duration (time coordinate t and τ_R are normalised to $\tau(0)$). The waveguide is assumed to have step-index distribution of the refractive index: $n(x) = n_{co}$ ($|x| \le d$), n_{cl} ($|x| > d$), where d denotes half-width of the waveguide core (in our simulations we used $n_{co} = \mathbf{1.491}$, $\mathbf{n_{cl} = 1.487}$, $\mathbf{d = 3\mu m}$). The alternative-direction implicit method was used to solve the six-point finite-difference equations obtained from Eq.(1) with improved interface conditions [5]. Non-linear part of the dielectric permittivity was

inserted into the finite-difference scheme in such a way that the value of *A(x,z,t)* obtained on a previous layer was used as a zero approximation for the next layer. In order to avoid the boundary reflection problem, complex scaling of coordinates was applied near the grid edges [6] beginning from $x=X_b=15d$. Initial field distribution $A(x,0,t) = A_0\psi(x)\exp(-t^2/2)$ with transverse profile $\psi(x)$ of linear TE_0 mode (Fig.1,a) was launched numerically into a non-linear waveguide segment where a spatial transient process was observed (Fig.1,b).

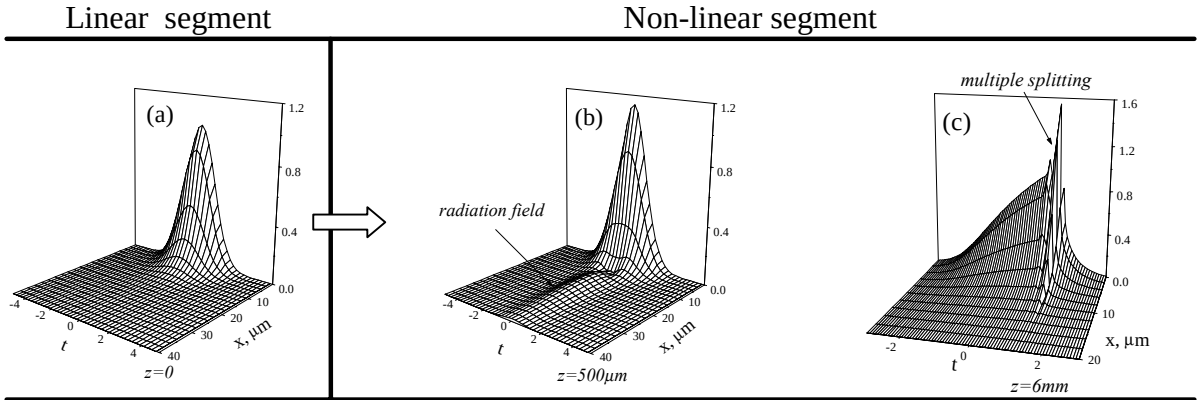


Fig.1 Spatiotemporal distribution of the pulse intensity

In the quasi-static approximation ($\varepsilon_1=0$, $\varepsilon_2=0$, $\tau_R=0$), we assume that only self-focusing and temporal self-action determine non-linear dynamics of the total field so that its spatial and temporal distribution depends on input power and doesn't depend on the initial pulse duration (Fig.2). Similarly to CW propagation [4], total losses resulting from the leakage of radiation field outside the guiding region grow with input power (in our simulations we used the output parameter $\mathrm{T}(X,z) = \int_{-X}^{X} dxdt \mid A(x,z,t\mid^2 / \int_{-X}^{X} dxdt \mid A(x,0,t)\mid^2)$.

Behind the region of spatial transient process, stable spartiotemporal field distribution is observed with increased power flow propagating inside the core ($T(d,z)>1$). Pulse duration on the waveguide axis $\tau_a(z)$ is less than its initial value ($\tau_a(z)/\tau(0)<1$) and increases with transverse coordinate tending to $\tau(0)$ in the cladding. The beam width also is minimal at the pulse peak. In general, the stable field distribution is consistent with "non-linear mode" or "spatial soliton" representation.

Self-steepening effect and retarded non-linear response are the factors which destroy stability of the solution so that constant leakage of the power outside the guiding region is observed along the propagation distance (Fig.3).

The self-steepening effect results from intensity dependence of the group velocity and manifests itself through a shift of the pulse peak and optical shock in the trailing edge of the pulse (Fig.4). This variation of the temporal (longitudinal) pulse distribution influences the transverse profile and cancels balance between self-focusing and diffraction so that stable distribution is no longer obtained.

The retarded non-linear response similarly shifts the pulse peak to the trailing edge however don't disturb symmetry of the frontal and trailing parts. With $\tau_R=0.1$ that is typical for femtosecond pulse propagation at $1.53\mu m$ in fused silica, this effect is much less than the self-steepening one.

In the far-field, mutual action of the self-steepening and retarded non-linear response results in the pulse splitting (Fig1,c). For increasing input power or decreasing pulse duration, the splitting moves to the near field.

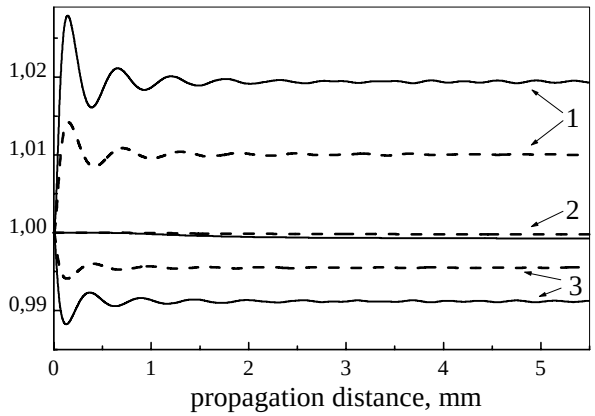


Fig.2 Quasi-static approximation: 1 - *T(d,z);* 2 - *T(X$_b$,z)*; 3- $\tau_a(z)/\tau(0)$; solid curves – $n_2I=0.002$; dashed curves - $n_2I=0.001$.

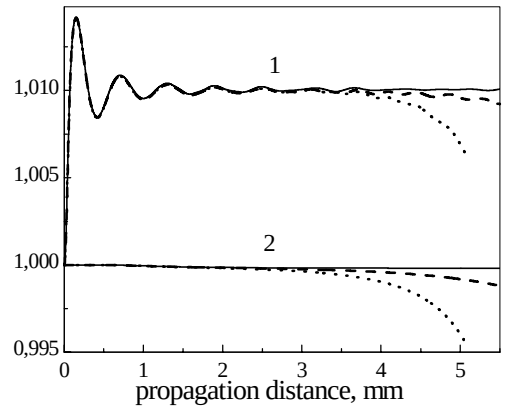


Fig.3 Self-steepening effect: 1 – *T(d,z);* 2 – *T(X$_b$,z)*; $n_2I=0.001$; dashed curves- $\tau(0)=30fs$, dotted ciurves - $\tau(0)=20fs$.

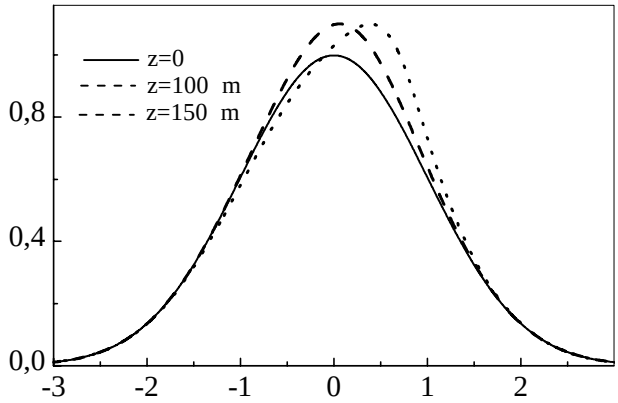


Fig.4 Displacement of the pulse peak due to the self-steepening effect. $n_2I=0.001$, $\tau(0)=20fs$

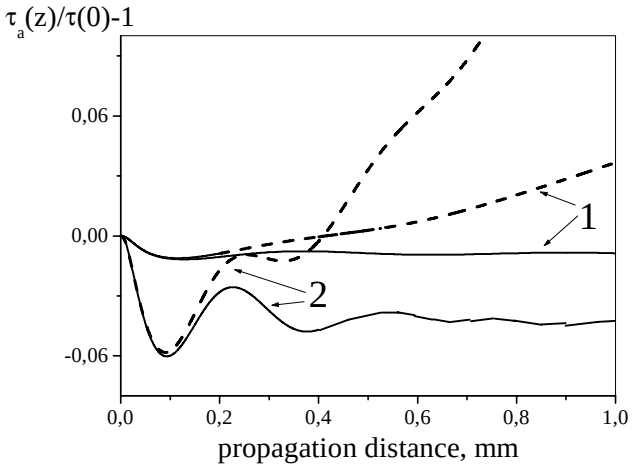


Fig.5 Relative variation of the pulse duration with account of normal dispersion (dashed curves) and in quasi-static approximation (solid curves):
1 - $n_2I=0.002$, $\tau(0)=30$ fs, $k_2 = -0.001$ fs^2/μm;
2 - $n_2I=0.01$, $\tau(0)=10$ fs, $k_2 = -0.036$ fs^2/μm.

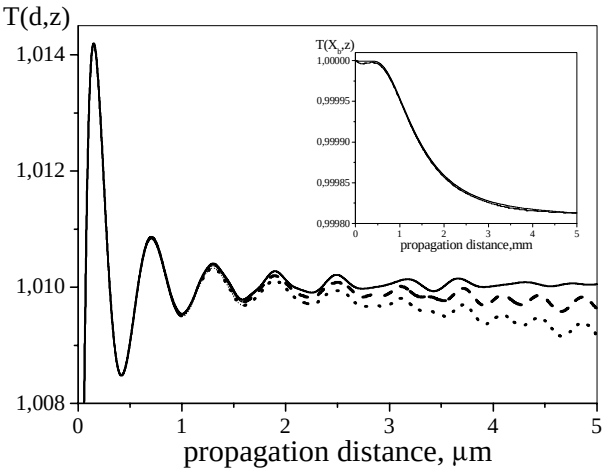


Fig.6 Effect of normal dispersion: dashed curves - $\tau(0)=30fs$, dotted curves - $\tau(0)=10$ fs; $n_2I=0.002$, $k_2 = -0.036$ fs^2/μm.

Normal group velocity dispersion ($k_2<0$) plays an important part in propagation of ultra-short pulses. In idealized model based on non-linear Schrodinger equation, the self-phase modulation and the second-order dispersion are accounted for. As a result of balance between non-linear and dispersion effects, this model gives a stable solution (soliton) for space-time field distribution [2]. If diffraction term is taken into consideration, the normal group velocity dispersion prevents catastrophic collapse of high-power beam in a uniform Kerr medium via multi-splitting of the pulse, however the self-focusing and splitting events are spatially separated [1]**.** In the step-index waveguide, character of spatiotemporal dynamics of the total field depends also on magnitudes of the dispersion and diffraction lengths: $l_{ds}=\tau^2(0)k/(k_2\beta)$ and $l_{df}=\beta d^2/2$. If $l_{ds}>> l_{df}$ that is typical for picosecond pulse propagation in optical waveguide, the pulse broadening is small over the region of spatial transient process initiated by the self-focusing effect (Fig.5,curves 1). In this case, the self-focusing and the dispersion broadening are separated in space and can be treated independently. If a femtosecond pulse is taken into consideration, the characteristic lengths can be of the same order, $l_{ds}\sim l_{df}$, so that significant variations of the pulse duration along the propagation distance are observed (Fig.5,curves 2). These variations of the pulse duration change in turn the spatial distribution of the field leading to constant leakage of the power outside guiding region along the propagation distance (Fig.6). Contrary to the self-steepening effect, the frontal and trailing parts of the pulse keep symmetric. Comparison of the parameter $T(X_b,z)$ (Fig.3 and Fig.6) shows that the radiation field excited as a result of dispersion effect is more paraxial than the radiation field leaking from the guiding region due to the self-steepening effect.

In summary, simulations of the modal field transformation behind the boundary of linear and non-linear segments of planar waveguide has demonstrated that the self-steepening effect, retarded non-linear response of the waveguide material and normal material dispersion create instability in the high-power ultra-short pulse spatiotemporal dynamics. This results in constant leakage of the power outside the guiding region. The self-steepening effect leads also to multiple pulse splitting in the far-field.

This results can be generalized on any irregular guiding structures of integrated circuits where spatial and temporal transformation of high-intensity pulsed power takes place.

The work was supported in part by Award No.REC – 006 of the U.S.Civilian Research & Development Foundation for the Independent States of the Former Soviet Union (CRDF).

[1] A.A.Zozulya, S.D.Diddams, A.G.Van Engen, T.S.Clement, *Phys.Rev.Lett.*,**82**(7),1430-1433, 1999.
[2] S.A.Akhmanov, V.A.Vysloukh, A.S.Chirkin, Optics of Femtosecond Laser Pulses, American Institute of Physics. NY,1992.
[3] S.Smolorz, I.Kang, F.Wise, B.G.Atiken, N.F.Borrelli, *Journ.of Non-Crystalline Solids*, **256&257**, 310-317, 1999.
[4] E.A.Romanova, L.A.Melnikov, E.V.Bekker, *Microwave and Opt. Technol. Lett*.,**30(**3),212-216, 2001.
[5] Y-P. Chiou, Y-C. Chiang and H-C. Chang, *Journ. of Lightwave Technol*.,**18**(2),243-249, 2000.
[6] C.W. McCurdy and C.K. Stroud, *Computer Phys. Commun.*, **63**, 323-328,1991.

Transition Loss in Bent Waveguides and Fibres

Jim Katsifolis
Dept. of Electronic Engineering, La Trobe University, Bundoora, Victoria 3083, Australia
j.katsifolis@ee.latrobe.edu.au

Shane Huntington
School of Chemistry, University of Melbourne, Parkville, Victoria 3010, Australia

Adrian Ankiewicz, John Love
Research School of Physical Sciences, Australian National University, ACT 0200, Australia.

Laurie Cahill
Dept. of Electronic Engineering, La Trobe University, Bundoora, Victoria 3083, Australia

We determine the origin of transition loss in bent waveguides and fibres. We show that transition loss can be suppressed, even in very tight bends provided that, in the geometrical transition from the straight to the bent waveguide or fibre, the local curvature is increased sufficiently slowly along the bend. Experimental results demonstrate this effect and are shown to be consistent with numerical simulations.

Keywords: bend loss, transition loss, beat length

Introduction

When a straight single-mode fibre or waveguide enters a bend, it is well known that power is radiated from the fundamental mode into the cladding as it propagates along the bend. The total radiated power along the bend can be expressed in terms of a superposition of two physically different effects, namely pure bend loss and transition loss. Pure bend loss is associated with the radiation of fundamental mode power from each position along the bend and is independent of the transition from the straight to the bent waveguide [1]. Conversely, transition loss is normally associated with the abrupt change in curvature between the straight and bent waveguides and its contribution to overall bend loss occurs over a relatively short distance along the bend.

Pure bend loss has been investigated in detail by many authors and can be quantified using a number of different analytical techniques. As a result, approximate analytical expressions are available for pure bend loss from e.g. step-profile slab waveguides [2] and fibres [1].

Transition loss arises from the mismatch between the fundamental mode fields of the straight and bent waveguides or fibres. For a bent waveguide, the effect of curvature is to introduce a small offset in the fundamental mode that displaces its field slightly outwards relative to the centre of the bend in the plane of the bend. As a result of this shift, not all of the incident mode power of the straight waveguide is transmitted into the fundamental mode on the bend. The power that is lost excites the non-guided field and thus forms part of the radiation field of the bent fibre.

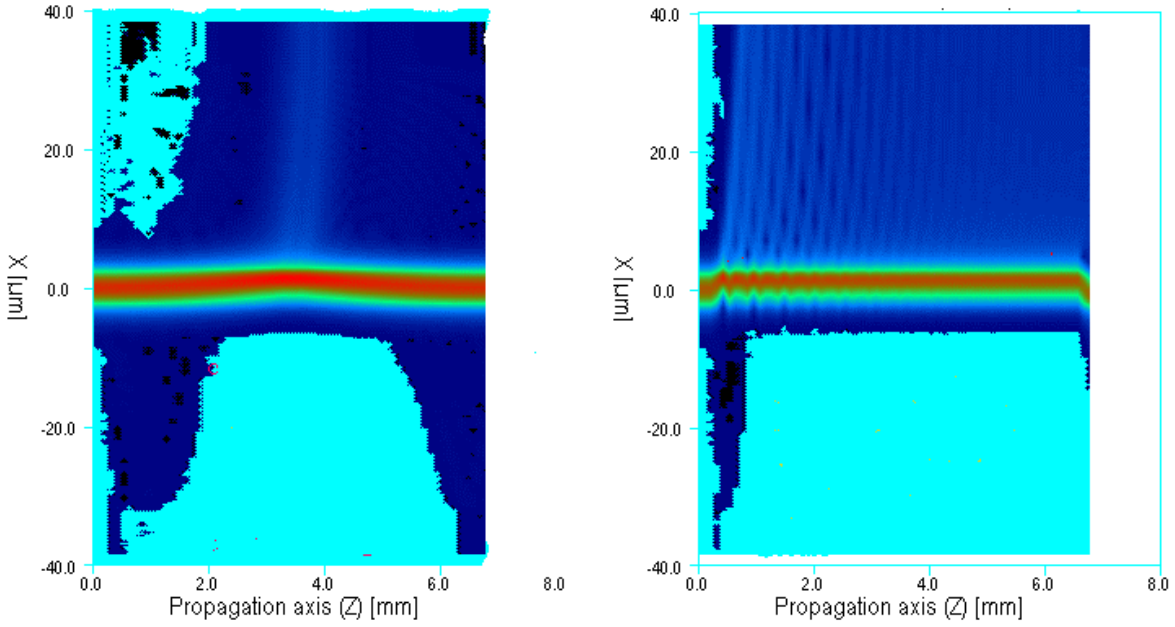
Although the radiation loss from the fundamental mode is continuous along the bend, the superposition of the transition loss can lead to the generation of discrete beam radiation within the bend region. This effect was first reported by Gambling et al [3] using a coiled fibre stripped of its coating and immersed in a cladding-index matching liquid. It was subsequently investigated by others during an early study of loss from curved single mode fibres [4][5]. Their analyses suggested that; (i) the beam phenomenon was due to a beating effect between the fundamental mode and a dominant higher-order leaky mode that is quasi-guided by the bend, and (ii) the coupling between the fundamental and leaky modes was caused by the constant-radius bend.

In this paper we show that, although the beams are due indeed to a beating effect as previously observed, the effect is actually induced by the relatively rapid increase in curvature from the beginning of the bend, rather than by the constant-radius bend itself. We also show that it is possible to suppress excitation of the leaky mode and therefore the discrete beams, even in a tight bend, by introducing a transition region leading into the bend with a sufficiently slow increase in curvature.

Numerical Simulation

Bend loss in fibres and waveguides occurs predominantly in the plane of the bend. Accordingly it is adequate for the present investigation to model bend loss from a single-mode bent waveguide and thereby simplify the complexity of the numerical simulation. The 2-dimensional bent step-profile waveguide is then replaced by a straight graded 1-dimensional waveguide using a standard conformal transformation. The effect of this transformation is to tilt the refractive index profile. Thus, by varying the tilt of the profile either abruptly or continuously along the waveguide, the effect of a jump or continuous increase in curvature on propagation can be quantified. The numerical quantification of bend loss and the radiation field along the bends was simulated using Olympios BPM software. In each case the fundamental mode field of the straight waveguide was launched at the beginning of the bend.

Results showed the presence of discrete beam radiation occurred along bends where there was an abrupt or relatively fast change in curvature. Where the change of radius of curvature was minimized, the discrete beam radiation was also minimized or effectively suppressed. These results are plotted in Figure 1 for a bend radius of 2.1mm.



(a) (b)

Figure 1: Simulation results for slab waveguides. In (a), the waveguide is bent into a parabolic curve with a low rate of curvature change everywhere along its length, and no discrete beam radiation is present. In (b) the parabolic curve has a more rapid change in curvature at the beginning of the bend, and discrete beam radiation is now present.

The simulation results in Figure 1(a) show that even for a tight parabolic bend there are no discrete beams generated, since there is only a low rate of change in the radius of curvature. Only continuous radiation due to pure bend loss is present. In the case where there is a more abrupt change in curvature radius, as in Figure 1(b), the higher-order leaky mode is excited at this transition point, and the resultant beating between this mode and the fundamental along the bend generates the set of discrete beams.

Experimental Investigation

Several single-mode fibres were bent into different radii and, after removal of the coating, were immersed in an oil medium with a slightly higher refractive index than the cladding in order to view any discrete radiation. In each experiment only the fundamental mode of the fibre was excited.

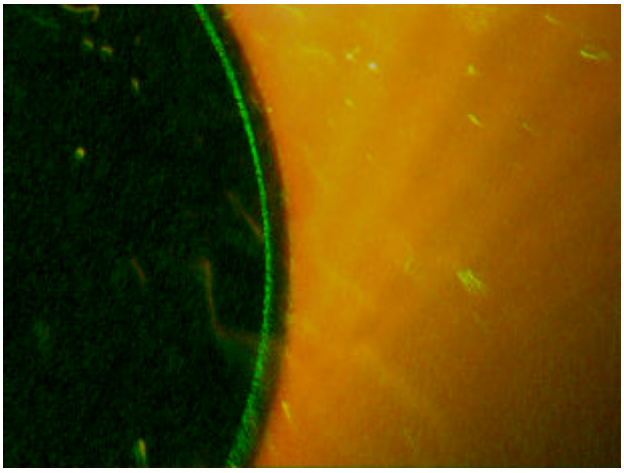


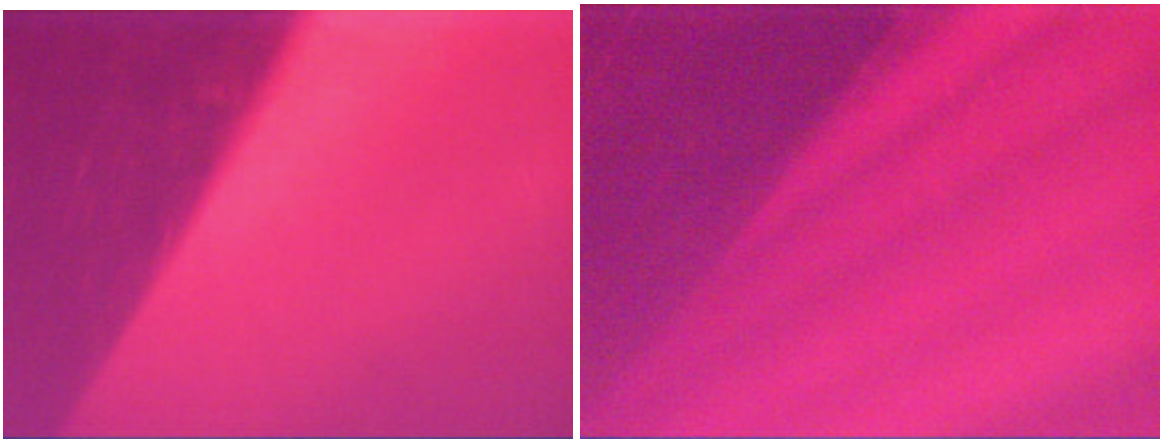
Figure 2. Discrete beam radiation from a single-mode fibre bent into a semi-circular arc of 1.5mm radius.

Figure 2 shows the discrete beam radiation from a single-mode fibre bent in a semi-circular arc with uniform radius of 1.5mm. The measured beat length between the beams is approximately 180 microns and is consistent with the numerical simulation, allowing for the difference between modal effective indices between the fibre and slab geometries. The discrete beams can be accounted for by the fairly abrupt change of curvature between the straight part of the fibre and the circular bend. The abruptness couples power from the fundamental mode into the leaky second mode and the two modes beat together to generate the discrete beams.

This phenomenon is illustrated better in Figure 3, where a near single-mode fibre is bent into a 180º parabolic-shape bend with a low rate of curvature change at any point along its length. Using a fibre with a higher V-value allows discrete beam radiation to be observed at larger bend radii for the same excitation wavelength. Only the fundamental mode is excited in the straight part of the fibre.

In Figure 3(a), no discrete beams are present and only the expected continuous radiation due to pure bend loss from the fundamental mode is present. In Figure 3(b), the lead-in fibre is straightened slightly so that a small transition region with more abrupt change in curvature is introduced close to the beginning of the parabola. In this case, discrete beam radiation is again clearly evident.

A more detailed and quantified analysis of transition loss will be presented at the conference, including a criterion for minimising transition loss.



(a) (b)

Figure 3 A fibre bent into a 180º parabolic bend shape. In (a), no discrete beam radiation is present due to the low rate of change in curvature along the fibre. In (b) the lead in fibre is straightened slightly to give a more abrupt change in curvature and discrete beam radiation is now present.

Conclusions

The origin of discrete beams observed in the radiation field of bent single-mode waveguides and fibres has been shown to be due to the coupling of power from the fundamental mode to the first leaky along the bend. Such coupling only occurs when the bend curvature changes rapidly along the bend and can be virtually suppressed by introducing a sufficiently slow change in curvature.

This prescription allows, in particular, for the design of transition-loss free waveguide bends with a smooth variation in curvature, and provides an alternative to the standard practice of inserting an offset between the straight and bent waveguide cores in the case of an abrupt change in curvature.

Acknowledgements

This research was supported by the Australian Photonics Cooperative Research Centre.

References

[1] A. W. Snyder and J.D. Love, ”Optical Waveguide Theory”, Chapman and Hall, 1983, Chapter 23.

[2] D. Marcuse, “Light Transmission Optics”, Bell Laboratories Series, Section 9.6, 398–406, 1972.

[3] W.A Gambling, D. N. Payne and H. Matsumura, “Radiation from curved single-mode fibres”, Electronics Letters, Vol. 12, No. 21, 567 – 569, 1976.

[4] R. A. Sammut, “Discrete radiation from curved single-mode fibres”, Electronics Letters, Vol.13, No.14, 418-419, 1977.

[5] C. G. Someda, “Radiation of discrete beams from curved single-mode fibres”, Electronics Letters, Vol. 13, No.14, 712-713, 1977.

Effective and Flexible Analysis for Propagation in Time Varying Waveguides

A Al-Jarro, P Sewell, TM Benson, A Nerukh
Electromagnetics Research Group, School of Electrical and Electronic Engineering, The University of Nottingham, University Park, Nottingham, NG7 2RD, UK.
eexaa@nottingham.ac.uk

The equivalence between the propagation of dispersive modal fields in two and three dimensional waveguides, and plane waves in a one dimensional plasma is presented. A computationally efficient time domain integral equation is discussed for this important practical case and its stability is improved by means of both a semi-implicit formulation and the use of rectangular meshing.

Keywords: time domain analysis, numerical algorithm, dimensionality reduction.

Introduction

Recently, significant interest has been focused upon the interaction of electromagnetic signals and time varying media, [1,2]. The motivation for studying such phenomena include, wavelength shifting and terahertz wave generation applications, as well as gaining insight into the behaviour of high speed switches and lasers. In contrast to the early research in this area, which concentrated upon plane waves, the leading edge of this work is now considering the effects of time varying materials upon optical fields transversely confined by waveguide geometries.

Computational methods that can account for time varying and inhomogeneneous media, include the finite difference time domain method, FDTD, the transmission line method, TLM as well as time domain integral equation techniques. A particular advantage of the latter approach is that it can often identify the general properties of a particular class of problems rather than just solving specific instances, [3]. Unfortunately in all cases, the move from 1D plane wave problems to 2D, let alone 3D waveguide configurations severely increases the computational overhead incurred. However, for initial design purposes, it is recognised that it is not strictly necessary to model the complete 2D or 3D nature of the structure, rather it is sufficient to consider just the fundamental modal fields which indicate the presence of the waveguide confinement by possessing frequency dependent propagation constants and modal impedances. Exclusively concentrating upon the fundamental modes is justifiable given that the temporal changes in the waveguide parameters are usually small in practice so that excitation of higher order transverse modes is of secondary importance to the overall behaviour observed. The significant advantage gained by this approach is a reduction in the dimensionality of the problem that needs to be simulated.

Theory

If the transverse mode shape is frequency independent, which is a reasonable engineering approximation for semiconductor slab waveguides confined by large refractive index steps such as occur in SOI structures, then it is straightforward to demonstrate that the dispersive effects exhibited by a waveguide mode whose cutoff frequency is ω_c, are the same as those observed for plane waves in a 1D plasma defined by the following relationship between electric field and electric flux density, $D(t) = \varepsilon_o \varepsilon_1 E(t') + \int^{t} dt' \ (t-t')\omega_c^2 E(t')$ where ε_1 is the relative permittivity of the material filling the guide. The electric field in a 1D structure satisfies Volterra integral equation, [3],

$$E(t,z) = E_o(t,z) - \frac{1}{2\varepsilon_o \varepsilon_b}\frac{d}{dt}\int_0^t dt' \int_0^a dz' \ \delta\left(t - t' - \frac{|z-z'|}{v_b}\right)\left[P(t',z') - \varepsilon_o(\varepsilon_b - 1)E(t',z')\right] \qquad (1)$$

where ε_b is a background relative permittivity, P is the polarisation of the media, E_o is the excitation field and t and z are the time and space coordinates. It is a significant advantage of the approach, compared to FDTD for example, that the domain of the spatial integration only encompasses the discontinuity, i.e. the region whose properties differ from the background medium, here taken as 0<z<a. Similarly, there is no need to terminate the calculation window with artificial absorbers as the kernel of the integral equation intrinsically contains the correct asymptotic behaviour at infinity. To perform the simulation of the modal fields in a 2D waveguide as introduced above, E is now interpreted as the modal amplitude and the equivalent 1D material modelling the modal dispersion is defined by the polarisation function,

$$P(t,z) = \varepsilon_o(\varepsilon_1 - 1)E(t,z) + \varepsilon_o\omega_c^2 \int_o^t dt'(t-t')E(t',z) \qquad (2)$$

In previous simulations of 1D plasmas using Volterra equations, [4], the field was discretised in space-time using a square mesh with respect to the speed of light in the background material, i.e. $\Delta z = v_b \Delta t$. Furthermore, the integration over t' in (1) was performed using a semi-open integration scheme and the derivative with respect to t evaluated using a backward difference. Given that using $\Delta z = v_b \Delta t$ is tantamount to operating at precisely the Courant condition, these features give rise to a slightly explicit scheme which causes problems for stability and accuracy. To overcome these problems, a very simple Crank-Nicolson approach is adopted; a central difference formula is used for the derivative with respect to t, coupled with $E(t - dt/2) = \alpha E(t) + (1-\alpha)E(t - dt)$. Using $\alpha = 0.5$ ensures maximal accuracy and theoretical stability, but in practice α is set slightly larger than 0.5 to compensate for rounding error induced instability. As shall be shown below, this revised implementation of the algorithm, reported here for the first time, significantly enhances its utility.

A second novel and complimentary change to the algorithm is to relax the need for a square mesh in space-time, which effectively allows Δt to be lower than that of the Courant condition. Evaluating the numerical quadratures along lines of constant $z \pm vt$ which are required in (1), involves interpolation for non-square meshes, although this is straightforward to implement in practice. Here we specifically demonstrate the stability and accuracy improvements that can be obtained by using a rectangular mesh with $\Delta t = \Delta z/(2v_b)$.

Results

First, the equivalence between modal propagation in waveguide and 1D propagation in a plasma as well as the efficacy of our improved algorithm shall be shown. In figure 1, an incident pulse, with a Gaussian distribution in both time and space, strikes a section of waveguide sandwiched between 2 free space regions and frequency dependent reflection and transmission occurs. The problem parameters used here and below have been chosen to clearly demonstrate the approach and are therefore not necessarily realistically achievable.

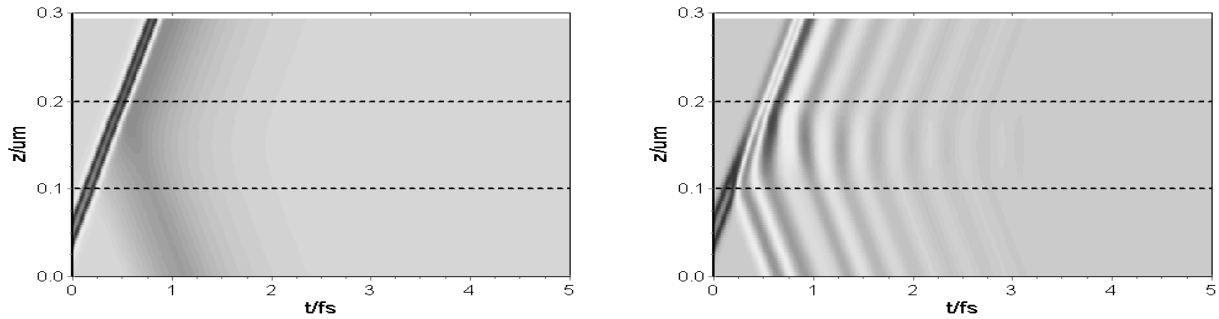


Figure 1: The modal amplitude excited by a Gaussian pulse striking a section of waveguide, 0.1μm<z<0.2 μm with (a) f_c=500THz and (b) f_c=2500THz. Here, $\varepsilon_1 = \varepsilon_b = 1$, $\Delta t = \Delta z/v_b$=0.01fs and α=0.6.

To precisely quantify the accuracy of the numerical implementation, figure 2 compares the transmission coefficient obtained by Fourier transforming the time dependent field just before and after the waveguide with the exact theoretical result.

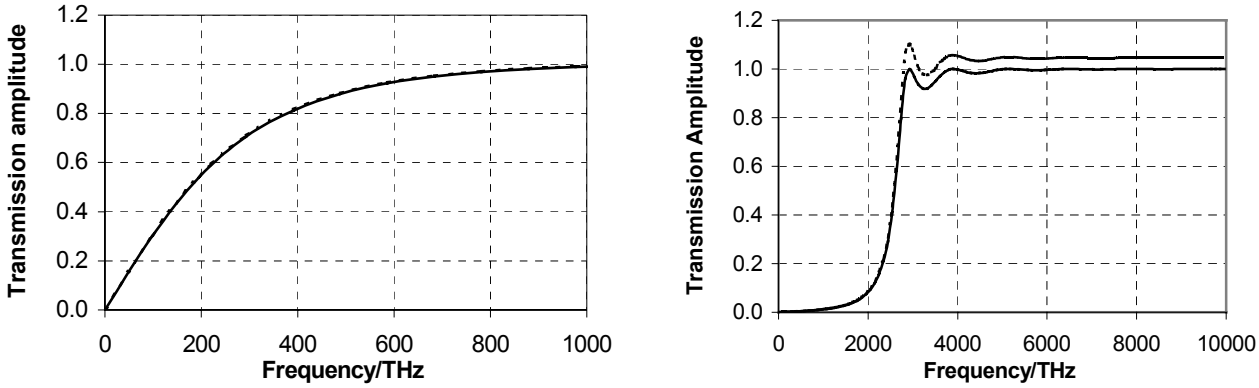
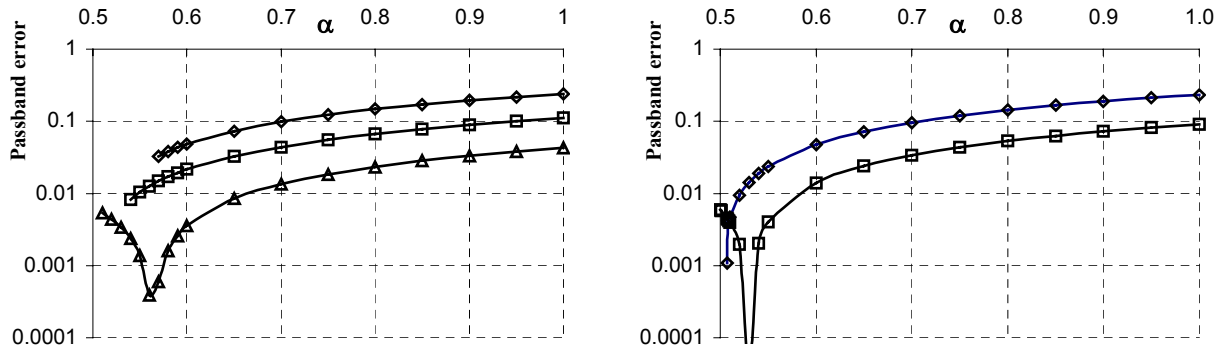


Figure 2: The numerical (dotted) and theoretical (solid) transmission coefficient obtained for the examples of figure 1

Although the agreement is excellent for the case of relatively weak dispersion, for the case of more severe dispersion there is both an overshoot at the cutoff frequency as well as a "steady state" pass band amplitude error. This is attributable to the use of a stability factor of α=0.6 and a fairly large time step. To illustrate this, the pass band error is plotted in figure 3(a) against α for different Δt.



(a) (b)

Figure 3: The effect of α and Δt on the errors for a Square (a) and Rectangular (b) mesh for the example of figure 1b: (a) diamonds ($\Delta t=\Delta z/v_b$ =0.01fs), squares ($\Delta t=\Delta z/v_b$=0.005fs) and triangles ($\Delta t=\Delta z/v_b$=0.0025fs); (b) diamonds ($\Delta t=\Delta z/v_b/2$=0.005fs) and squares ($\Delta t=\Delta z/v_b/2$=0.0025fs).

It is clear that this measure of error is significantly reduced as both α approaches 0.5 and by using a smaller time step. However, it is also observed that each of the curves starts at a value α which is greater than 0.5, as below this value instability occurs. Therefore it is not possible to obtain the accuracy that would appear asymptotically available for a given value of Δt. As using smaller Δt implies using smaller Δz in a square mesh, improving the accuracy this way incurs an undesirable increase in numerical effort. This is precisely the reason for considering rectangular meshing as it moves the algorithm away from the accuracy-stability knife-edge associated with the Courant condition. Figure 3(b) shows the same measure of error obtained from a mesh with $\Delta t=\Delta z/(2v_b)$.

As a further visual illustration of the wavguide-plasma equivalence we consider the case of a rib waveguide resonator. A section of waveguide is sandwiched between two sections of waveguide having a higher cutoff frequency, and this combination is surrounded by free space. Modelling each waveguide as an appropriate 1D plasma (without consideration of the mismatch in modal profiles)

is in essence a time domain effective index model, the frequency domain a of which has achieved widespread acceptance as a fast initial design tool. Figure 4 shows the fields excited by a Gaussian pulse incident from free space and the frequency dependent confinement and resonances are plainly seen.

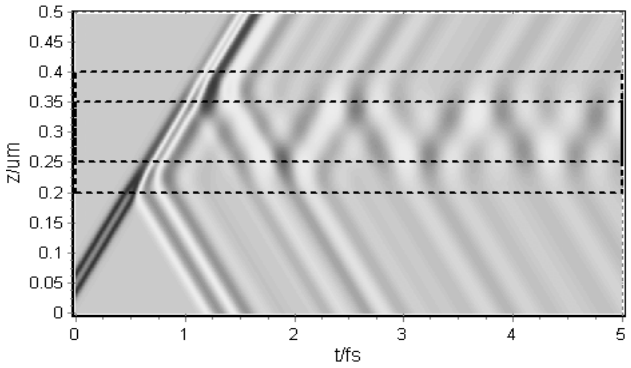
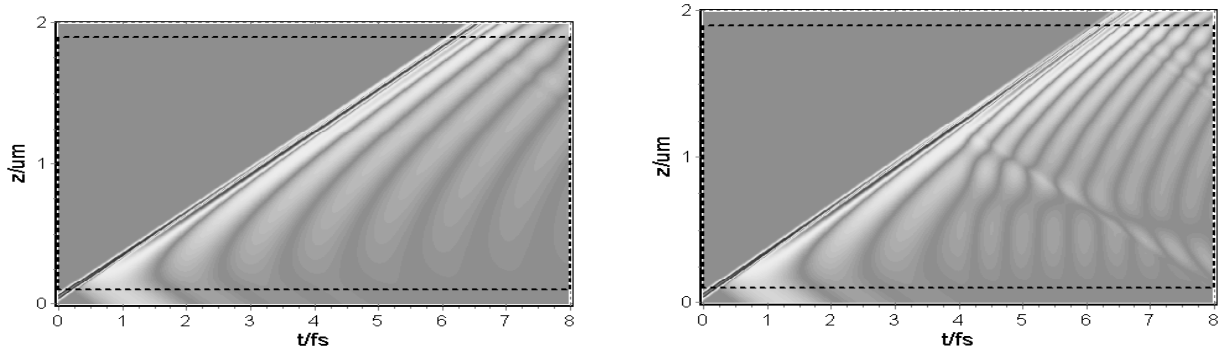


Figure 4: The modal amplitude excited by a Gaussian pulse striking a cascade of three waveguides with f_c=2500THz for 0.2μm<z<0.25μm and 0.35μm<z<0.40μm and f_c=1000THz for 0.25μm<z<0.35. $\Delta t=dz/v_b$=0.005μm, α=0.6 and $\varepsilon_l=\varepsilon_b$=1.

Finally, attention is focused on the case of a time jump in the waveguide parameters. Figure 5 shows the effect of switching the cutoff frequency of the waveguide region as the field passes through it, the reflection at the instant of switching, t=4fs, being clearly visible.



(a) (b)

Figure 5: The modal amplitude excited by a Gaussian pulse striking a section of waveguide, 0.1μm<z<1.9 μm with f_c=500 THz, $\varepsilon_l=\varepsilon_b$=1, $\Delta t=\Delta z/v_b$=0.01fs and α=0.6. In (b) f_c is switched to 2500THz at t=4fs.

Conclusion

In this paper we have presented and demonstrated two practical improvements for time domain simulations. Firstly, that simulations of 2D and 3D waveguide structures can be efficiently performed using a time domain effective index approach, which promises fast initial design tools. Secondly, for Volterra integral equation formulations, both the use of stabilised algorithms and non-square meshes have been quantifiably shown to substantially improve the accuracy that can be obtained. Finally, qualitative examples of dealing with more complex geometries as well as time variant cases have been presented to illustrate the flexibility of the approach.

References

[1] J.W.D. Chi, L. Chao, M.K.Rao, *IEEE J. Quantum Electronics*, vol. 37, No 10, 1329-1336, 2001
[2] Y. Jeong, B. Lee, *IEEE J. of Quantum Electronics*, vol. 37, No 10, 1292-1300, 2001.
[3] A.G Nerukh, I.V. Scherbatko, M. Marciniak, *National Institute of Telecommunications Publishing House*, Warsaw, 2001.
[4] K.M.Yemelyanov, F.V. Fedotov, A.G. Nerukh, *Transparent Optical Networks conf*. 226 –229, 2001.

Proposal of an All-Optical Flip-Flop Using a Cross-Coupled MMI Bistable Laser Diode

Mitsuru Takenaka and Yoshiaki Nakano
Research Center for Advanced Science and Technology, University of Tokyo, JST-CREST
7-3-1 Hongo, Bunkyo-ku, Tokyo, 113-8656, Japan
takenaka@hotaka.t.u-tokyo.ac.jp

We propose a novel bistable laser diode (BLD) with active multi-mode interference (MMI) cavity. Using FD-BPM, we predict that the MMI-BLD shows bistable switching between two cross-coupled modes, which can be utilized as an all-optical flip-flop or an optical memory.

Keywords: bistable laser diode, MMI coupler, two-mode bistability, all-optical flip-flop, FD-BPM

Introduction

Bistable laser diodes (BLDs) are expected to be important elements of future optical communications such as packet buffering, bit-length conversion, retiming, reshaping, demultiplexing, and wavelength conversion. However, conventional absorptive BLDs [1] have the difficulty of optical reset. To overcome this problem, two-mode intensity bistability [2], which originate from cross gain saturation between the two lasing modes, have been investigated. Although this type of bistability has been demonstrated by cross-coupled bistable laser diodes (XCBLDs) [3], they had a bit complicated waveguide structures.

In this paper, we propose a novel two-mode BLD including an active multi-mode interference (MMI) cavity (Fig.1). An all-optical flip-flop will be realized by the MMI-BLD whose simple structure is matched to the conventional LD fabrication technique. Moreover, it gets the benefits of the MMI's features, i.e, compactness, high design tolerances, a large optical bandwidth and polarization insensitivity. We design a 2 × 2 MMI which couples light signal from an input port totally into a cross output port. Two-mode bistability between two cross-coupled modes will occur in this configuration due to cross gain saturation. The static characteristics of the MMI-BLD are investigated using a finite difference beam propagation method (FD-BPM).

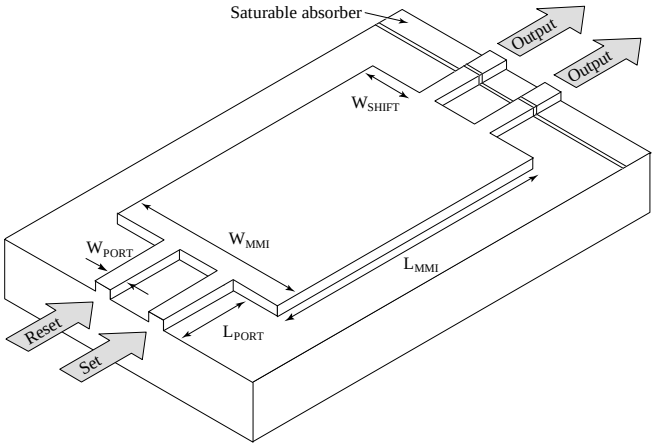


Fig. 1 Schematic view of MMI-BLD.

Simulation Method

The modeling of an MMI coupler requires special attention because several modes inside the coupler interfere with each other. Moreoever, the behavior of an active MMI coupler has been not well know yet. Therefore, we chose FD-BPM [4] which can treat complex distributions of photon, refractive index, and gain inside the cavity. However, the BPM models only take forward propagating lights into account, thus reflections inside the cavity are neglected. In this paper, we analyse uni-directionally forward and backward propagating lights, respectively, and only reflections from the cleaved facets of LDs [5] are considered.

In describing light propagation through the waveguides, the wave equation for a TE mode derived from Maxwell's equations is solved. The scalar Helmholtz equation for a TE-polarized light propagating a planar waveguide in the direction of *z* axis becomes:

$$\frac{\partial^2 E}{\partial z^2}+\frac{\partial^2 E}{\partial x^2}+k_0^2 n^2 E=0 \tag{1}$$

where $E(x, z)$ is the space-dependent electric field, $n(x, z)$ the space-dependent refractive index, k_0 the wave vector in vacuum and a temporal dependence of $\exp(j\omega t)$ is assumed. This equation can be reduced to the paraxial wave equation:

$$E(x,z)=\phi(x,z)\exp(-j\beta_0 z) \tag{2}$$

$$2j\beta_0\frac{\partial\phi}{\partial z}=\frac{\partial^2\phi}{\partial x^2}+(k_0^2 n^2-\beta_0^2)\phi \tag{3}$$

where β_0 is a reference propagation constant. Equation (3) is obtained by a slowly varying envelope approximation. It is solved using finite differences in the transverse (x) direction and a Cranck-Nicolson scheme for the longitudinal (z) coordinate. In order to avoid nonphysical reflections from the computational window edges, Hadley's transparent boundary condition [6] is implemented.

We also take photon-carrier interactions into account. To evaluate the carrier density $N(x, z)$, the steady-state carrier rate equation is expressed as:

$$\frac{J}{ed}=R(N)+\Gamma v_g g_1 S_1+\Gamma v_g g_2 S_2 \tag{4}$$

where J is the current density, e the electron charge, d the thickness of the active layer, R the recombination rate, Γ the confinement factor, v_g the group velocity, g the material gain and S the photon density (the subscripts 1 and 2 refer to the two cross-coupled modes in the MMI cavity respectively).

Using a detailed model including Auger recombination [7], the recombination rate is written as:

$$R(N)=c_1 N+c_2 N^2+c_3 N^3 \tag{5}$$

where c_1, c_2, and c_3 are recombination constants.

For the unsaturated material gain g_0, a linear dependence on carrier density is assumed:

$$g_0(N)=a(N-N_0) \tag{6}$$

where a is gain constants, N_0 the carrier density at transparency.

As two-mode bistability originates in cross gain saturation, it is necessary that this effect is included in bistability analysis. The saturated gains for the cross-coupled modes are related to the unsaturated gain g_0 through the photon densities of the two modes as follows:

$$g_1(N)=\frac{g_0}{1+\varepsilon_{11}S_1+\varepsilon_{12}S_2},\ g_2(N)=\frac{g_0}{1+\varepsilon_{22}S_2+\varepsilon_{21}S_1} \tag{7}$$

where ε_{11}, ε_{22} and ε_{12}, ε_{21} are the self-saturation and the cross-saturation coefficients, respectively.

To take into account the refractive index dependence on carrier density, a linearly dependent equation is assumed:

$$n=n_0+\frac{dn}{dN}N \tag{8}$$

where n_0 is the refractive index without carrier injection, and dn/dN is refractive index shift coefficient, which is taken to be negative. We only consider the refractive index change of the waveguide's core, whereas the refractive index of the clad is assumed to be fixed.

Bistability Analysis

An InGaAsP multiple quantum well (MQW) structure whose band gap energy is around 1.55 μm is studied. We assume that the self-saturation coefficient is 8.0×10^{-17} cm^3 and the cross-saturation coefficient is 1.6×10^{-16} cm^3. The other parameters are shown in [8].

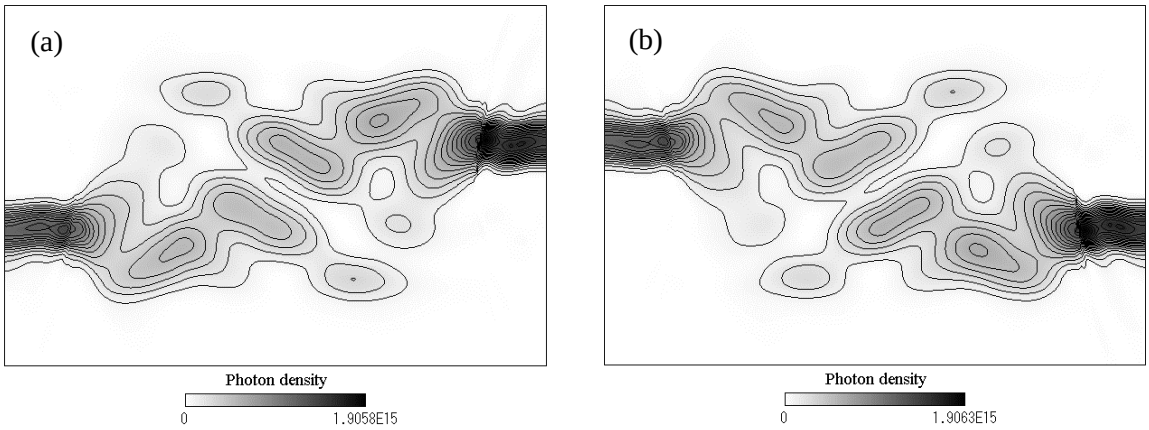


Fig. 2 Photon density [cm^{-3}] distributions of the MMI-BLD at (a) mode-1 and (b) mode-2.

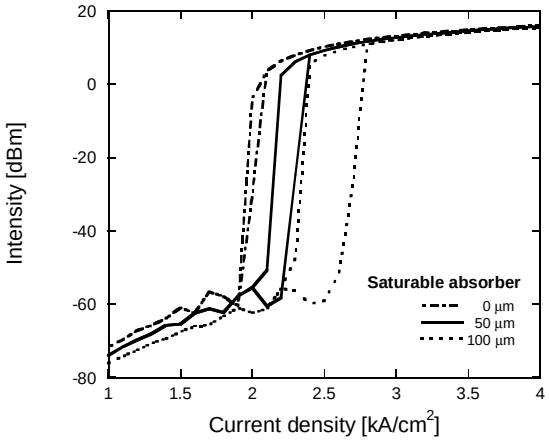


Fig. 3 L-I characteristics of the MMI-BLD with saturable absorber, 0, 50, and 100 μm.

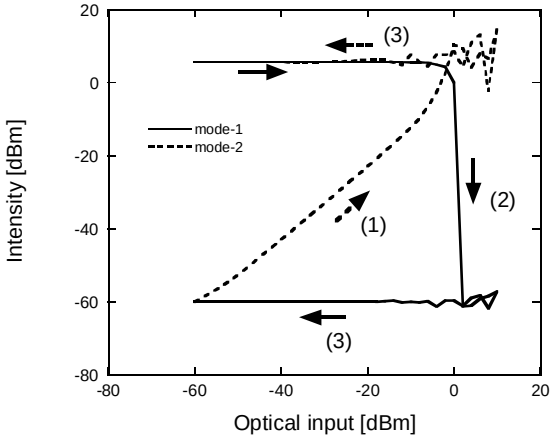


Fig. 4 Bistable switching characteristics of the MMI-BLD.

The 2 × 2 MMI coupler section should be designed in such a way that the input light totally couples into the cross output port. In the case of ridge waveguides whose refractive indices of core and clad are 3.255 and 3.24, respectively, the cross-coupled MMI coupler assumes the following physical dimensions: W_{MMI} = 12 μm, L_{MMI} = 540 μm, and W_{SHIFT} = 2.7 μm. The port width W_{PORT} and length L_{PORT} are 2 μm and 100 μm, respectively. In this design, the MMI-BLD has two cross-coupled lasing modes as shown in Fig. 2.

The saturable absorbers are equipped at the end of the output ports. Figure 3 shows L-I characteristics with the lengths of the saturable absorber (biased at 0.1 kA/cm^2) being 0, 50, and 100 μm, respectively. By increasing the saturable absorber length, the lasing threshold and the width of the hysteresis loop increase due to nonlinear absorption. The injection current of the gain region should be within the hysteresis loop in order to make use of the two-mode bistability. We adopt 50 μm as the saturable absorber length and 2.1 kA/cm^2 as the bias current density of the gain region.

External light injection of a set-signal saturates the absorption to mode-1, causing mode-1 to start lasing (ON state). At the same time cross gain saturation and the absorption to mode-2 by the saturable absorber suppress mode-2. In a similar manner, light injection of a reset-signal at the ON state suppresses mode-1 through cross gain saturation, therefore stopping laser oscillation in mode-1. Simultaneously, the absorption of mode-2's saturable absorber is decreased by the light injection to mode-2, resulting in lasing of mode-2 (OFF state). Even when the light injection is terminated, cross gain saturation and recovered absorption of the mode-1's absorber prevent mode-1 from

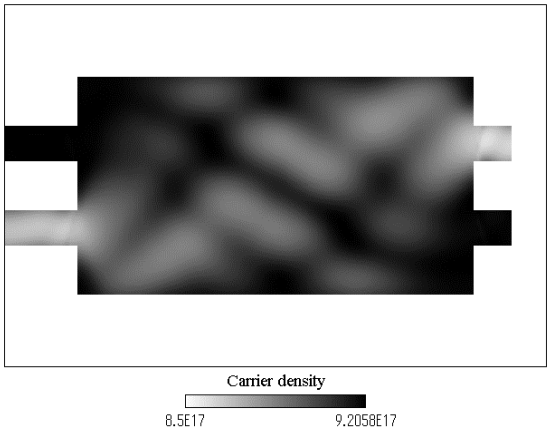


Fig. 5 Carrier density [cm^{-3}] distribution of the MMI-BLD lasing at mode-1.

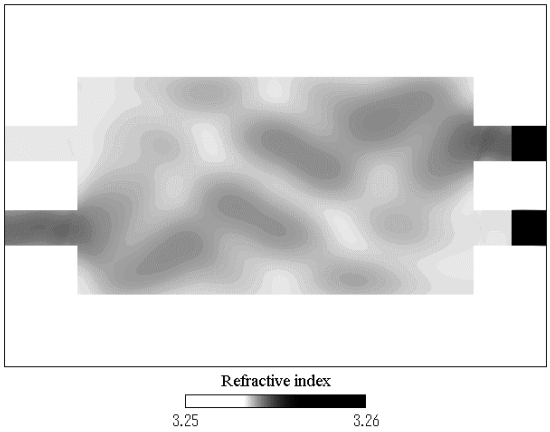


Fig. 6 Refractive index distribution of the MMI-BLD lasing at mode-1.

lasing again. Figure 4 shows this bistable switching characteristics. The MMI-BLD is set to the ON state by set-pulse at the beginning of the calculation. Increasing the optical injection to mode-2 (1) suddenly results in extinction of mode-1 (2) at around 0 dBm, thus switching MMI-BLD into the OFF state. When the optical injection is eliminated, the OFF state is maintained (3). As shown in Fig. 4, the two-mode bistability overcomes the optical reset problem of the absorptive BLDs, and the all-optical flip-flop operation will be realized using the MMI-BLD.

Figure 5 and 6 show the distributions of carrier density and refractive index in the case of the ON state, respectively. Because there were strong stimulated emission at the large optical intensity regions, the carrier distribution becomes uneven, i.e., spatial hole-burning occurs. Inside the MMI coupler, the range of the carrier density is 8.8×10^{17} to 9.2×10^{17} cm^{-3}. This difference of carrier density leads to the uneven distribution of refractive index, 3.2535 to 3.254 inside the MMI coupler. The range of refractive index is small enough for the tolerance of the MMI coupler, so the spatial hole-burning does not make some unstable operation, and the laser radiations of the mode-1 and mode-2 exist stably.

Conclusion

We have proposed and investigated a novel BLD with an active 2×2 MMI coupler. The static characteristics of the MMI-BLD have been simulated by using FD-BPM which takes into account the photon-carrier interaction through the carrier rate equation. We have predicted that the MMI-BLD shows bistable switching between the two cross-coupled modes by 0 dBm external light injection, which can be used as an all-optical flip-flop or an optical memory.

[1] G. J. Lasher, *Solid-State Electronics*, vol. 7, pp. 707-716, 1964.
[2] C. L. Tang, A. Schremer, and T. Fujita, *Appl. Phys. Lett.*, vol. 51, pp. 1392-1394, 1987.
[3] B. B. Jian, *Electron. Lett.*, vol. 32, no. 20, pp. 1923-1925, 1996.
[4] Y. Chung, and N. Dagli, *IEEE J. Quantum Electronics*, vol. 26, pp. 1335-1339, 1990.
[5] H. K. Bissessur, F. Koyama, and K. Iga, *IEEE J. Select. Topics in Quantum Electronics*, vol. 3, pp. 344-352, 1997.
[6] G. R. Hadley, *IEEE J. Quantum Electronics*, vol. 28, pp. 363-370, 1992.
[7] R. Olshansky, C. B. Su, J. Manning, and W. Powazinik, *IEEE J. Quantum Electronics*, vol. QE-20, pp. 838-854, 1984.
[8] M. Takenaka, and Y. Nakano, *COIN+PS2002*, PS.TuB5, pp. 78-80, Cheju Island, July, 2002.

The Spectral Decomposition Method: a Transparent Theory for Losses in Segmented Waveguides

Hugo J.W.M. Hoekstra, Joris van Lith, Szabolcs B. Gaal and Paul V. Lambeck
Lightwave Devices Group, MESA$^+$ Research Institute, Faculty EWI, University of Twente,
Po box 217, 7500 AE Enschede, The Netherlands. h.j.w.m.hoekstra@tn.utwente.nl

An approximate theory, giving insight into the effects of device parameters on loss in segmented waveguides, is presented. Computational results on low and high loss structures, and structures showing anomalous length dependence of the loss are discussed.

Keywords: guided wave optics, segmented waveguides, gratings, theory.

Introduction

Segmented waveguides (SWs) have raised a lot of interest due to their potential as devices for quasi-phase matching in second harmonic generation (SHG)[1], for tuning the size of the modal field [2] and for sensing [3,4]. In the latter use is made of the dependence of the loss on the index of the segments. Optimization of SWs for any of these or other purposes involves many parameters, related to both the basic structure of the waveguide (WG) and its segmentation, i.e., the distribution of transitions along the propagation direction. In order to be able to get insight into the effects of these device parameters we have developed the spectral decomposition method (SDM). This 2D method, which is correct only in the limit of low losses, leads to analytical expressions for the relative loss in terms of the segmentation and the parameters describing the basic structure.

The rest of the paper is organized as follows: below the main features of the SDM are introduced. This is followed by a section in which results are shown, discussed and compared with that of the finite difference beam propagation method (BPM) [5] and the mode expansion method (MEM)[6]. The paper ends with conclusions.

Theory

Below analytical expressions will be given for modal losses in a 2D SW for an arbitrary segmentation. The polarization is assumed to be TE, TM polarization can be treated along the same lines. A time-dependence $\exp(iwt)$ is assumed but suppressed. The wave equation to be solved is given by (see also figure 1):

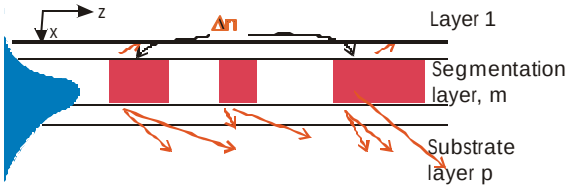


Figure 1. *Schematic picture of the considered waveguide, with segmentation in one of the layers.*

$$\{\partial_{xx} + \partial_{zz} + k_0^2 e(x,z)\}E_y = 0. \qquad (1)$$

Here $k_0 (\equiv 2p/l)$ is the wavenumber and $e(x,z)(\equiv n^2(x,z))$ is the relative permittivity. In the below it is assumed that we may write

$$e(x,z) = e_b(x) + h(x)g(z)\Delta e\,, \qquad (2)$$

where e_b describes the so-called basic structure, assumed to be mono-modal, Δe describes the change in permittivity, which is here assumed to occur in one layer, layer m, for which $h(x)=1$; $h(x)=0$ in the other layers. The segmentation is described by $g(z)$, which may be of any form. It is assumed that the segmentation occurs for, say $z \geq 0$, and that for $z < 0$ the incoming field is that of the fundamental mode, corresponding to the basic structure, given by:

$$E_0 = e_0(x)\exp(-ib_0 z)\,, \qquad (3)$$

with propagation constant $b_0 \equiv k_0 N_0$, where N_0 is the modal index. It is assumed that the fundamental mode propagates undepleted along z. The total field is written as

$$E_y = E_0 + E_r, \tag{4}$$

where E_r is the field excited by the perturbation. Below we will concentrate on solving the radiative part of it. Substituting (4) into (1) leads to:

$$\{\partial_{xx} + \partial_{zz} + k_0^2 e_b\} E_r = A(E_0 + E_r) \approx AE_0;\ A \equiv -g(z)h(x)k_0^2 \Delta e\ . \tag{5}$$

Here we used the modal field equation for E_0, and for the second equality that the effect of modulation is weak. In the SDM (5) is solved by taking the Fourier transform of (5) with respect to z, and solving the resulting equation for each value of the spatial frequency, k_z, corresponding to radiation modes.

A lengthy but rather straightforward derivation [3] leads to the following expression for the power, radiated into the substrate and the cladding, P_p and P_1, respectively:

$$P_p + P_1 = \int_{-K}^{K} |\, G_0 H_p \,|^2\, dk_z + \int_{-K_1}^{K_1} |\, G_0 H_1 \,|^2\, dk_z \equiv \int_{-K}^{K} H\, |\, G_0 \,|^2\, dk_z\ , \tag{6}$$

with $K_1 \equiv k_0 n_1$, $K \equiv k_0 n_p$ and $H \equiv |\, H_1 \,|^2 + |\, H_p \,|^2$. The relative loss, h, is given by:

$$h = (P_p + P_1)/P_0, \tag{7}$$

with P_0 the power of the incoming fundamental mode. The characteristic functions, $H_{1/p}$, introduced in (6) are given by:

$$|\, H_p \,|^2 \equiv |\, a_p \,|\, |\, t_{mp}(T_1 + S_1)/\{2D(k_z^2 - b_0^2)\} \,|^2\ /(2k_0 Z_0) \tag{8}$$

and

$$|\, H_1 \,|^2 \equiv |\, a_1 \,|\, |\, t_{m1}(T_2 + S_2)/\{2D(k_z^2 - b_0^2)\} \,|^2\ /(2k_0 Z_0), \tag{9}$$

with $H_{1/p} = 0$ if $|\, k_z \,| > k_0 n_{1/p}$. In the above the following notations have been used:

$a_l \equiv \sqrt{k_z^2 - k_0^2 n_l^2}$, $l = 1, p, m$; $D \equiv \exp(a_m d_m) - r_{m1} r_{mp} \exp(-a_m d_m)$; $Z_0 \equiv \sqrt{m_0 / e_0}$;

$T_1 \equiv \partial_x e_{0,m}(0)(1 + r_{m1})/a_m - e_{0,m}(0)(1 - r_{m1})$; $T_2 \equiv \partial_x e_{0,m}(d_m)(1 + r_{mp})/a_m + e_{0,m}(d_m)(1 - r_{mp})$;

$S_1 = \{\exp(a_m d_m) - r_{m1} \exp(-a_m d_m)\} e_{0,m}(d_m) - \{\exp(a_m d_m) + r_{m1} \exp(-a_m d_m)\} \partial_x e_{0,m}(d_m)/a_m$

$S_2 = -\{\exp(a_m d_m) - r_{mp} \exp(-a_m d_m)\} e_{0,m}(0) - \{\exp(a_m d_m) + r_{mp} \exp(-a_m d_m)\} \partial_x e_{0,m}(0)/a_m$.

d_m is the thickness of segmentation layer m, reflection and transmission coefficients are denoted by r and t, respectively and should be evaluated for k_z. The field of the incoming zero-order mode in layer m is denoted by $e_{0,m}(x)$, and we have used a local coordinate system for layer m ($x = 0 - d_m$). The function G_0 corresponds to the Fourier transform of $g(z)$ as follows:

$$G_0(k_z) \equiv k_0^2 \Delta e \int_0^{\infty} g(z) \exp\{i(k_z - b_0)z\} dz / \sqrt{2p} \tag{10}$$

Results and discussion

To illustrate the above we consider a three-layer structure, with refractive indices of 1, 1.8 and 1.457. The wavelength is chosen to be $l = 1mm$. The central layer is segmented, and its thicknesses are chosen to be either $d_2 = 500nm$ or $d_2 = 591nm$, corresponding to modal indices of $N_0 = 1.6795$ and $N_0 = 1.7034$, respectively. The thickness $d_2 = 591nm$ corresponds to a special situation (see below) for which the first order mode is just below cut-off, i.e., $|\, D \,| \sim 0$ at $k_z \sim\!< k_0 n_3$.

The characteristic functions H as a function of $n_{eff}\ (\equiv k_z / k_0)$ are given, for both considered thicknesses, in figure 2. As follows from the above H is an even function of n_{eff}. For the relatively simple (three-layer) structure the functions H are also simple showing only a few maxima and minima. Choosing $n_p \geq n_1$, the large values at $|n_{eff}| <\sim n_p$ (note here p=3) are typical, and are

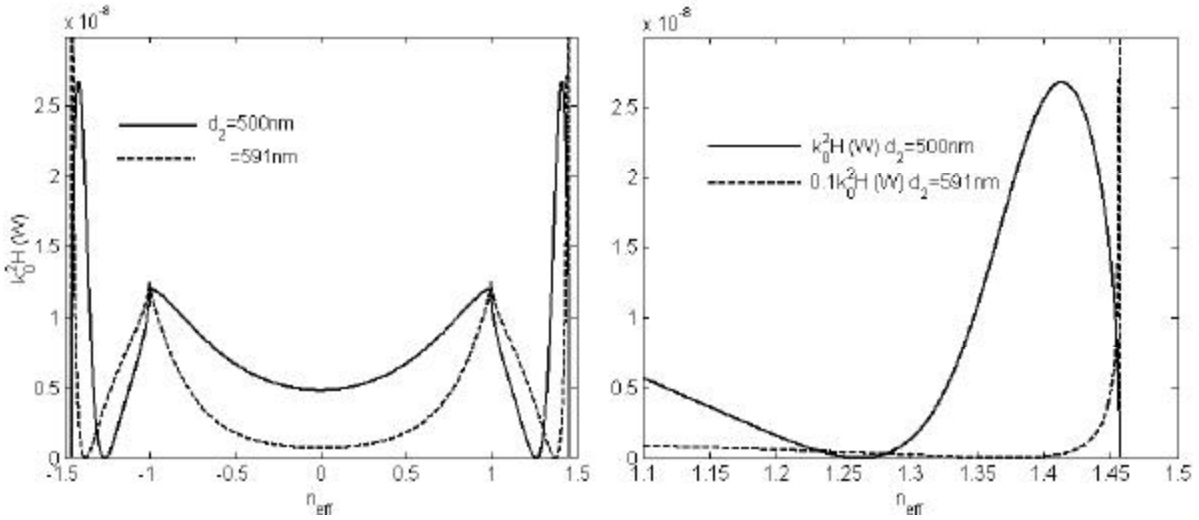


Figure 2. Characteristic functions H, for the two considered thicknesses and a modal power of $P_0 = 1W/m$ (left hand side). The right hand side shows a detail.

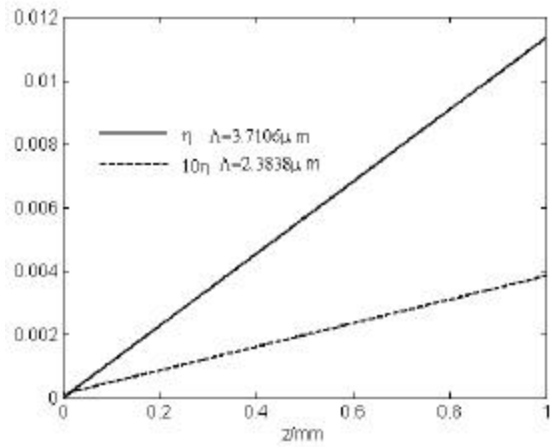


Figure 3. *Relative loss as a function of z for two different grating periods (see text, $\Delta e = 0.01$).*

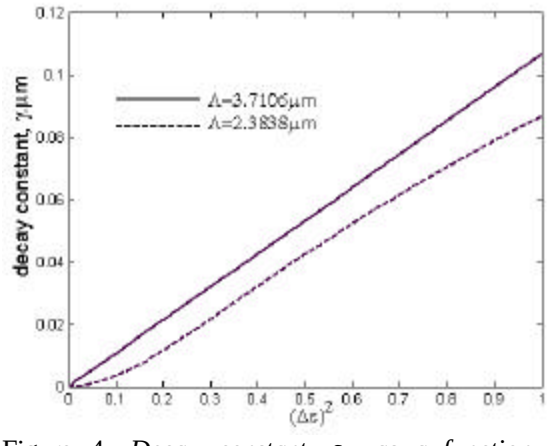


Figure 4. *Decay constant, g, as a function of $(\Delta e)^2$ for two different grating periods (see text).*

related to the term $(k_z^2 - b_0^2)^2$ occurring in the denominator of (8). At $|n_{eff}| = n_p$ usually $H = 0$, as there $a_p = 0$, unless there is a resonance (i.e., $D = 0$) exactly at that position. Then it can be shown [3] that $H \propto 1/\sqrt{K^2 - k_z^2}$. This explains the strong enhancement of H at $|n_{eff}| <\sim n_3$ in figure 2, for $d_2 = 591nm$, for which the resonance (i.e. $|D| \sim 0$), occurs just below cut-off.

In this paper we consider gratings with segments of equal lengths (duty cycle 0.5; period Λ). From (10) it can be shown that then $|G_0^2|$ consists of a central peak at $n_{eff} = N_0$ and peaks at

$n_{eff} = N_0 + (2m+1)\,l/\Lambda$, where m is an integer. The weight of the latter peaks is proportional to $1/(2m+1)^2$. All peaks narrow if the length of the grating is increased.

The above features in H can be utilized to design low-loss or, as desired for SW sensors, high-loss SWs. Examples thereof are given in figure 3, showing the relative loss, h, as a function of z according to the SDM for the cases of indicated grating periods, both calculations used $\Delta e = 0.01$. The considered grating periods correspond to a first-order ($m = -1$) peak of $|G_0^2|$ coinciding with the peak in H at $n_{eff} = 1.41$ and with the zero of H at $n_{eff} = 1.26$, leading, as expected, to high and low loss SWs, respectively.

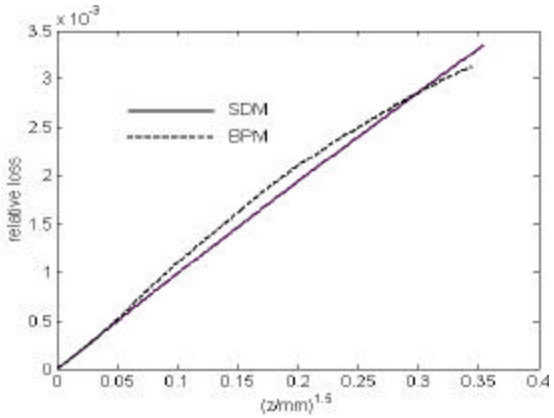


Figure 5. *Anomalous length dependence in the SW, with* $d_2 = 591nm$ *and* $\Delta e = 0.0036$.

If the index contrast increases the large difference between the losses for the two grating periods remains until $\Delta e \approx 0.3$. This can be seen from the MEM calculations given in figure 4, showing the decay constant g, defined by $P_0(z) = P_0(0)\exp(-gz)$.

If there is a resonance at cut-off and if also the 1st order peak of $|G_0^2|$ is also positioned exactly with $n_{eff} = n_p$ it can be shown with the SDM [3] that $h \propto z^{1.5}$. Hereby the relatively small effect of the other peaks in $|G_0^2|$ has been neglected. The above behaviour is similar to the anomalous length dependence of Cerenkov SHG [7,8]. Figure 5 shows the approximate $h \propto z^{1.5}$ dependence, according to both SDM and BPM, for the case that $d_2 = 591nm$ and a grating period of $\Lambda = 4.0577\,mm$, corresponding to a 1st order peak in $|G_0^2|$ at $n_{eff} = n_3$. This remarkable result is slightly counterintuitive, but well understandable in the light of the above: on increasing the length of a grating the k_z-region of the excited radiation modes (i.e., peaks of $|G_0^2|$) always narrows; if the excitation to these modes (i.e., H) in the considered region is peaked the relative loss will increase faster than linearly with the length.

Conclusions

An approximate theory, leading to analytical expressions for the loss in SWs has been presented. The theory opens the way to study the effect of device parameters on all kind of phenomena that may play a role in SWs

Acknowledgments

The presented work was supported by STW, project number TOE.5071

[1] J. Webjorn, F. Laurell, G. Arvidsson, *J. Lightw. Technol.* **7**, 1597-1600, 1989.
[2] Z. Weisman, A. Hardy, *J. Lightw. Technol.* **11**, 1831-1838, 1993.
[3] S.B. Gaal, thesis, Twente, 2002. H.J.W.M.Hoekstra, S.B. Gaal, P.V. Lambeck, to be published.
[4] J. van Lith, P.V. Lambeck, H.J.W.M. Hoekstra, R.G. Heideman, submitted to ECIO '03.
[5] H.J.W.M. Hoekstra, *Opt. Quant. Electron.* **29**, 157-171, 1997.
[6] OlympIOs; *C2V software*, version 5.1.12
[7] J. Ctyroky, L. Kotacka, *Opt. Quant. Electron.* **32**, 799-818, 2000.
[8] H.J.W.M. Hoekstra, J. Ctyroky, L. Kotacka, *J. Lightw. Technol.* January 2003.

Nonlinear Integrated Optics with Periodically Poled Waveguides in $LiNbO_3$

W. Grundkötter, D. Hofmann, M. C. Hübner, Y. L. Lee, J. H. Lee, Y. H. Min, V. Quiring, R. Ricken, G. Schreiber, H. Suche, and W. Sohler
Angewandte Physik, Universität Paderborn, D-33098 Paderborn, Germany.
sohler@physik.uni-paderborn.de

The recent development of nonlinear integrated optics with waveguides in periodically poled $LiNbO_3$ (PPLN) is reviewed. Besides a whole family of near- and mid-infrared quasi-phase matched parametric frequency converters of excellent efficiency also devices for ultrafast all-optical signal processing are presented.

Keywords: nonlinear integrated optics, $LiNbO_3$, PPLN, SHG, SFG, DFG, OPA, OPF, OPO

Introduction

The advent of the electric field poling method to fabricate periodically poled, ferroelectric, nonlinear optical materials resulted in a renaissance of nonlinear optics. Since then quasi-phase matching has been used for efficient wavelength conversion in devices like frequency doublers, difference frequency generators (DFG) and optical parametric oscillators (OPO). Periodically poled Lithium Niobate (PPLN) proved to be not only one of the best materials for nonlinear bulk optics, but also the most attractive and suitable substrate material for nonlinear integrated optics. It is commercially available as high quality mono crystalline wafer of a diameter of up to 5" and has large nonlinear coefficients. Moreover, the electric field assisted poling technique is compatible with the two most important waveguide fabrication methods – (annealed) proton exchange and Ti-indiffusion. The development of nonlinear integrated optical devices did not only result in a considerable inprovement of device efficiency and stability in comparison with bulk frequency converters; also all-optical ultrafast functions like time-domain multiplexing, polarisation conversion, switching and sampling could be demonstrated with significantly reduced power levels (see e.g. [1]).

It is the aim of this tutorial to review the recent development of nonlinear integrated optics with waveguides in PPLN. The relevant microfabrication technologies are described as well as the poling technique to generate ferroelectric microdomain structures in $LiNbO_3$ (LN) of different crystalline orientation. Advanced microscopic and spectroscopic methods are used for the characterization of these structures.

It is of particular interest to fabricate microdomain structures also in Erbium-doped optical waveguides. This possibility allows to combine integrated optical amplifiers and lasers with quasi-phase matched nonlinear devices in the same structure. Self-frequency doubling lasers and amplifying difference frequency generators are corresponding examples.

Very long (up to 90 mm) waveguides have been developed in PPLN for the visible, near- (NIR, 1 $\mu m < \lambda < 2\ \mu m$) and mid- (MIR, $2\ \mu m < \lambda < 5\ \mu m$) infrared spectral ranges. They enabled the development of efficient second harmonic generators (SHG), sum- (SFG) and difference frequency generators (DFG), optical parametric amplifiers (OPA) as well as singly and low-threshold doubly resonant optical parametric oscillators (OPO) for different spectral ranges. Corresponding examples will be presented. The combination of harmonic generation and simultaneous difference-frequency generation led to the development of cascaded-difference frequency generators (cDFG) with more than 100 % efficiency and simultaneous parametric amplification. Moreover, spontaneous parametric fluorescence is used for the generation of entangled photon pairs, whereas stimulated optical parametric fluoresence (OPF) might become a useful source for widely tunable radiation.

Waveguide Fabrication and Characterisation

The two most popular techniques to fabricate waveguides in LN are the annealed proton exchange (APE) and the Ti-indiffusion. Both are used to get waveguides in PPLN. Usually APE-waveguides are fabricated in a (Z-cut) PPLN substrate, i.e. after the periodic domain inversion. They allow the propagation of an extraordinary wave (a TM-mode in Z-cut LN) only, as the APE increases the extraordinary, but lowers the ordinary index of refraction. APE-waveguides have a strong and broad absorption band around 2.7 µm wavelength, due to OH-vibrations. Therefore, they are mainly used for applications in the NIR and visible spectral ranges.

To fabricate Ti:PPLN waveguides, photolithographically defined Ti-stripes on the surface of a single domain Z-cut LN wafer are indiffused at high temperatures (e.g. 8.5 hrs @ 1060 °C). Afterwards, substrate and waveguide are poled together. Modes of both polarisations can be guided in Ti:PPLN channels (see also Fig. 1). They have very low losses (down to ~0.03 dB/cm) without the strong OH-absorption and can therefore be used in the MIR as well. However, their susceptibility to photorefractive effects is higher than that of APE-waveguides. Besides planar and channel guides also directional couplers and waveguide arrays have been developed as Ti:PPLN structures.

Ti:PPLN waveguides can also be fabricated in an Er-doped substrate to take advantage of the internal optical gain by optically pumped Er-ions. This effect cannot be exploited in APE-guides as the proton exchange reduces the lifetime of the upper laser level drastically (see e.g. [2]).

By preferential etching of the surface the microdomain structure can be made visible (see Fig. 1). It can also be investigated by scanning SH-microscopy and spectroscopy of the Er-states in the domain walls.

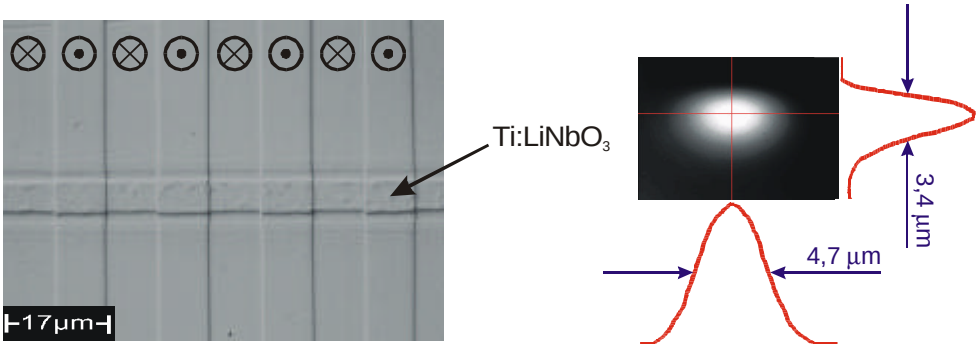


Fig. 1. left: Microphotograph of a selectively etched surface of a periodically poled sample with channel waveguides; the orientation of the optical axis of the different microdomains is indicated; right: TM polarized near field intensity distribution of a waveguide mode at about 1530nm wavelength.

Second Harmonic Generation (SHG)

Second Harmonic Generation (SHG) has been demonstrated in APE-PPLN as well as in Ti:PPLN waveguides with efficiencies exceeding 1%/mW. Its most important application is the generation of blue radiation using semiconductor lasers as fundamental source. The SHG-characteristic, i.e. SH-power as function of the fundamental wavelength, can also be used to assess the homogeneity of a nonlinear optical waveguide. By comparing the experimental response with the simulated one an effective interaction length can be derived which approaches the physical waveguide length in samples of best homogeneity of ferroelectric domain structure and effective

index of refraction. Fig. 2 presents as example the SHG-characteristic of a nearly ideal, 55 mm long Ti:PPLN channel guide.

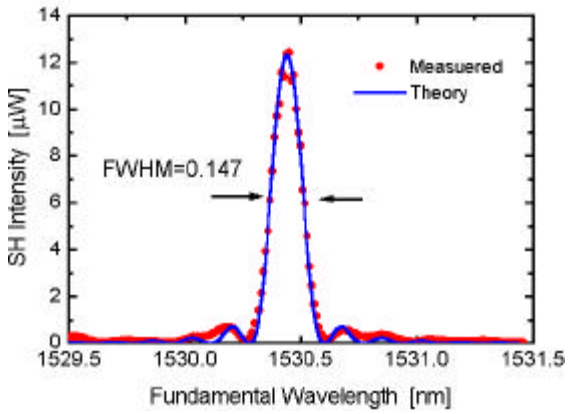


Fig. 2. SHG power vs. fundamental wavelength measured in a 55 mm long Ti:PPLN channel guide.

Self-Frequency Doubling Laser [3]

The combination of quasi phase-matched frequency conversion in amplifying or even laser active waveguides allows to develop a variety of new integrated optical devices. As an example a self-frequency doubling laser is described taking advantage of intracavity SHG in a periodically poled, Er-doped Ti:$LiNbO_3$ channel guide.

The experimental setup is schematically shown in Fig. 3.

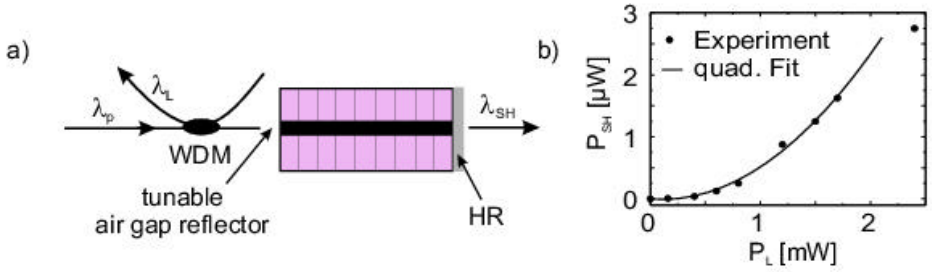


Fig. 3. a) Schematical setup for the investigation of intracavity self-frequency doubling in a periodically poled Ti:Er:$LiNbO_3$ laser. b) Measured second harmonic power as function of the laser output power at λ_L = 1531 nm.

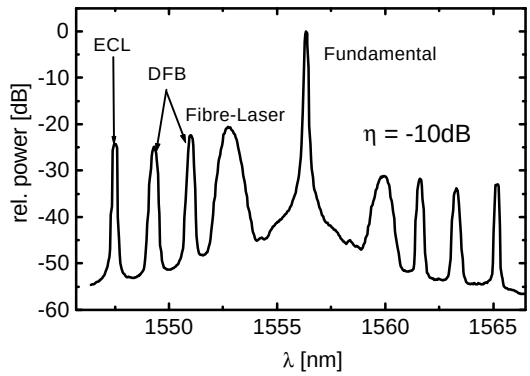
A fiber-optic wavelength division multiplexer (WDM) is used to couple up to 135 mW of pump radiation of a high power semiconductor laser diode at 1480 nm center wavelength into the Ti:Er:$LiNbO_3$ waveguide resonator. The input mirror is a tunable, low finesse Farby-Perot etalon, formed by the end face of the optical fiber and the polished, uncoated front face of the waveguide. The fiber is mounted on a piezo-driven translator allowing to adjust the thickness of the air gap and in this way the effective (wavelength dependent) reflectivity of the etalon between 5 % and 30 % ("tunable air gap reflector"). Due to its wavelength dependence the preferred laser wavelength can be selected among emission at λ_L = 1531 nm, 1546 nm, 1575 nm and 1602 nm. The output mirror is a dielectric multilayer (12 layers) high reflector (HR) vacuum-deposited on the polished rear waveguide end face with a broadband reflectivity of > 95 % in the wavelength range 1480 nm < λ < 1800 nm. Around 765 nm wavelength the mirror transmission was high, exceeding 80 %.

To get quasi-phase-matched SHG in the periodically poled (Λ = 17 µm) waveguide at room temperature the laser emission wavelength has to be adjusted to λ_L = 1531 nm. In this configuration the laser threshold is at 87 mW coupled pump power. Due to waveguide losses the slope efficiency is poor allowing only up to 2.4 mW of output power. Simultaneously, frequency doubled radiation at λ_{SH} = 765.5 nm is generated and emitted in both, forward and backward directions. Up to 2.7 ìW of SH-power was measured in forward direction with a quadratic dependence on the fundamental laser power (see Fig. 3). By using a narrow bandwidth fiber Bragg grating of high reflectivity instead of the "air gap reflector" up to 20 µW of SH-power has been observed. Nevertheless, there is still a large potential for a further improvement of this type of integrated self-frequency doubling laser.

(Cascaded) Difference Frequency Generation (cDFG) [4]

In cDFG a strong fundamental wave at λ_f is used to generate via SHG a pump wave at $\lambda_p = \lambda_f /2$. Simultaneously, this pump wave interacts with a signal wave at λ_s to generate an idler wave at λ_i with $\lambda_i^{-1} = 2\lambda_f^{-1} - \lambda_s^{-1}$. cDFG in PLLN waveguides proved to be very attractive for several applications in optical communications such as wavelength conversion, dispersion compensation, all-optical switching, but also for spectroscopy in the mid infrared (MIR) spectral range.

As an example, Fig. 4 presents simultaneous multi-wavelength conversion of the emission of two DFB lasers, of an extended cavity semiconductor laser (ECL) and of an actively mode-locked fibre laser (5 ps pulses at 10 GHz repetion rate) at ITU-wavelengths. The amplified fundamental and the signal radiation(s) were multiplexed using an arrayed waveguide grating (AWG) of 200 GHz channel spacing with about 3dB insertion loss. 175 mW of fundamental power and 10 mW of signal power were fed to the input pigtail of the Ti:PPLN-wavelength converter operated at 188.5°C. The TM-polarization was adjusted using polarization controllers. A conversion efficiency of –10dB was achieved. By switching individual signal channels on and off no measurable change of the efficiency was observed. There was also no difference in conversion efficiency for cw- and pulsed channels. The conversion bandwidth is about 55 nm (FWHM).



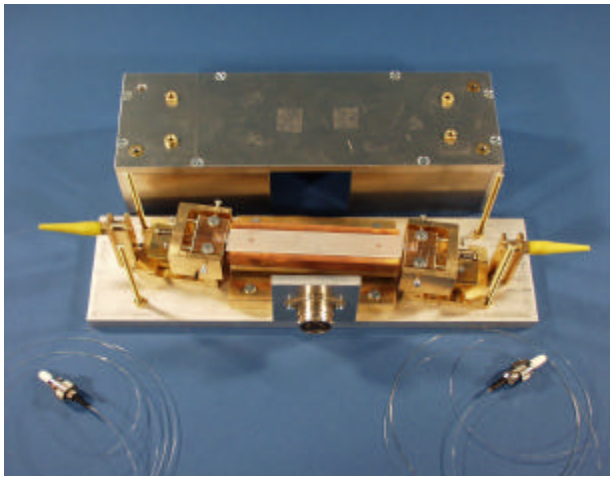


Fig. 4. (left) Output spectrum of the Ti:PPLN-wavelength converter for multi-channel conversion; (right) Packaged and fiber-pigtailed device, allowing high temperature operation.

The excellent performance of this device enabled a transmission experiment using wavelength-converted data from a 4×10Gbit/s OTDM-transmitter as signal at 1561.1 nm wavelength. This experiment was done within the IST-ATLAS project in cooperation with Pirelli Labs., Milano. No BER-penalty between the back-to-back measurements of the converted and unconverted data was observed. After 500 km the penalty at BER=10^{-13} remained below 1dB for both, the converted and unconverted channel.

Optical Parametric Amplification (OPA) [5]

Cascaded difference frequency generation (cDFG) is always accompanied by optical parametric amplification (OPA) of the signal. Theory predicts that in PPLN waveguides a small signal gain larger than 30 dB can be achieved, high quality waveguides of sufficient length, negligible photo-refractive effects and sufficient pump power assumed. Such parametric amplifiers would be attractive devices of quantum limited noise figures for future all-optical transparent communication networks. It is remarkable that the center wavelength of their gain characteristics with a spectral width of 50-70 nm can be adjusted by the period of the microdomain structure alone. As an example Fig. 5 presents the calculated small signal gain in 80 mm and 160 mm long Ti:PPLN waveguides as function of the wavelength.

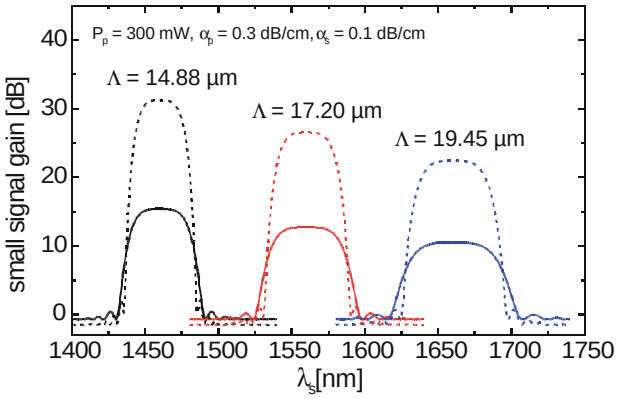


Fig. 5. Calculated small signal gain as function of the wavelength for three different periodicities of the microdomain structure; solid and dashed lines indicate the results for 80 mm and 160 mm long waveguides.

Experimentally, a cw-gain of up to 4 dB was observed in a 8.3 cm long s tructure with 765 mW coupled pump power (λ = 1558 nm). To reduce photorefractive effects the device was operated at 195 °C . If operated in a pulsed mode with 5 ps pulses at 10 GHz repetition rate a gain of 11.5 dB

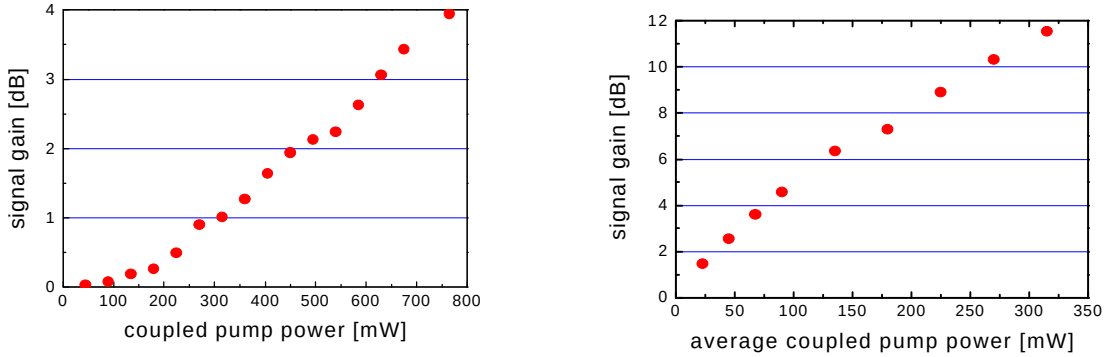


Fig. 6. Measured parametric gain as function of the coupled pump power at ë = 1558.5 nm for (left) cw and (right) pulsed pumping (5 ps; 10 GHz repetition rate). ë$_s$ = 1552.4 nm.

was achieved at 325 mW average power (see Fig. 6). The measured gain is still considerably smaller than the predicted one; the causes of this behavior are currently explored.

Cascaded Sum and Difference Frequency Generation (cSFG/DFG) [6]

Among various wavelength conversion schemes proposed, all-optical wavelength conversion based on cascaded sum and difference frequency generation (cSFG/DFG) in a Ti:PPLN channel waveguide is especially promising. It offers a broad tuning range, low spontaneous emission noise, and ultrafast operation speed.

The principle of operation is shown in Fig. 7. Transform limited gaussian signal pulses (λ_s) of 5 ps width are superimposed with two cw pump waves (λ_{p1}, λ_{p2}) by a 10/90 coupler and launched together into the 5.5 cm long channel guide of 16.6 µm microdomain periodicity by fiber butt-coupling. The pulsed signal and the pump (λ_{p1}) generate sum frequency pulses (λ_{sf}) perfectly phase matched. At the same time, a second pump (λ_{p2}) interacts with the sum frequency wave (λ_{sf}) to generate idler pulses (λ_i) by DFG. This process is slightly phase mismatched, but the conversion efficiency is only slightly reduced in comparison to a phase matched interaction. The idler wavelength can be tuned by the wavelength of the second pump.

Fig. 7 shows the optical spectra for two different wavelengths of the second pump, measured with 0.1 nm resolution. The power levels of both pump waves were controlled to be equal (~275 mW); the coupled power of the signal was 1.6 mW. The conversion efficiency from the (transmitted) signal to the generated idler was measured to be –4.7 dB. When the wavelength of the second pump (λ_{p2}) was varied from 1533 nm to 1568 nm, the idler wavelength was tuned from 1524 nm to 1559 nm almost linearly. In this wavelength range, no significant change of the conversion efficiency was found. The theoretical calculation predicts a very wide tuning range of more than 100 nm. There is a broadening of the idler pulses due to group velocity mismatch (3 ps/cm) of about 28 %.

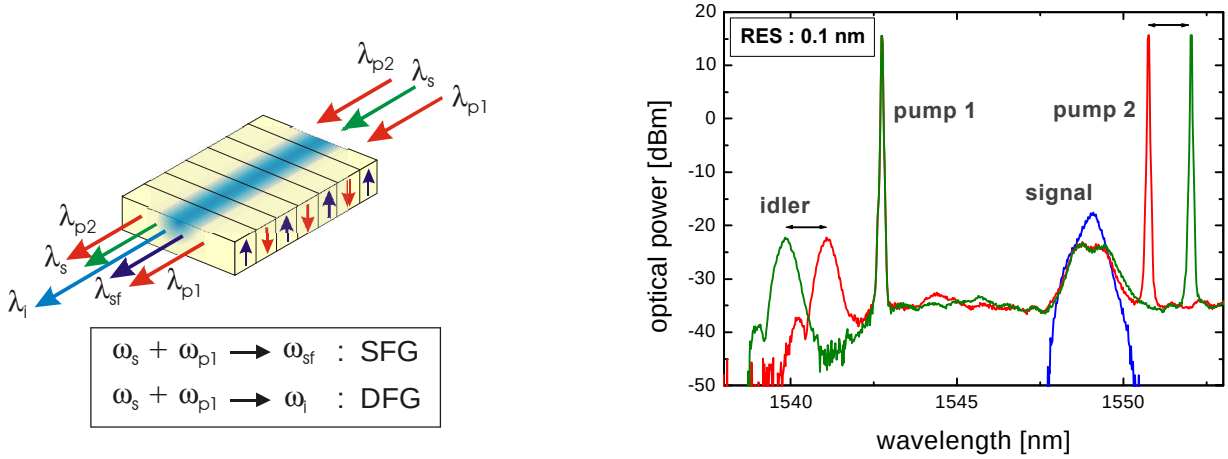


Fig. 7. (left) Schematic diagram of cSFG/DFG in a Ti:PPLN channel waveguide and (right) optical spectra of signal and idler showing the tuning of the idler by changing the wavelength of pump 2.

Optical Parametric Fluorescence (OPF) [7]

Optical Parametric Fluorescence (OPF) results from the spontaneous decay of pump photons into signal- and idler-photons by the influence of the zero-point fluctuations of the electromagnetic vacuum field. This process, which is described by energy- and wave-vectors conservation, can be stimulated and exploited to generate widely tunable radiation without the need of resonant structures. The spectral bandwidth of the emission strongly depends on parameters like pump wavelength, pump power and interaction length. Nonlinear waveguides are very attractive devices to generate in particular stimulated OPF because of the high intensity of the guided pump wave and the very long interaction lengths possible.

Fig. 8 shows as an example the tuning characteristics of the signal and idler waves generated in an 18 µm wide waveguide of 31.36 µm domain periodicity. The coupled (cw) pump power was approximately 300 mW. The MIR-OPF was continuously tunable from 2760 to 3000 nm (signal) and from 3360 to 3450 nm (idler). A gap remained near degeneracy due to the limited tuning range of the pump source. Moreover, selected spectral characteristics are given as insets; they all have one pronounced sidelobe, probably due to waveguide inhomogeneities. A calculated phase matching curve shows excellent accordance with the measured results. In waveguides of larger domain periodicity the tuning characteristics shifts as a whole to the left reducing the gap near degeneracy. The same happens, if broader waveguides or higher temperatures are used. The OPF-power grows exponentially at higher pump power levels.

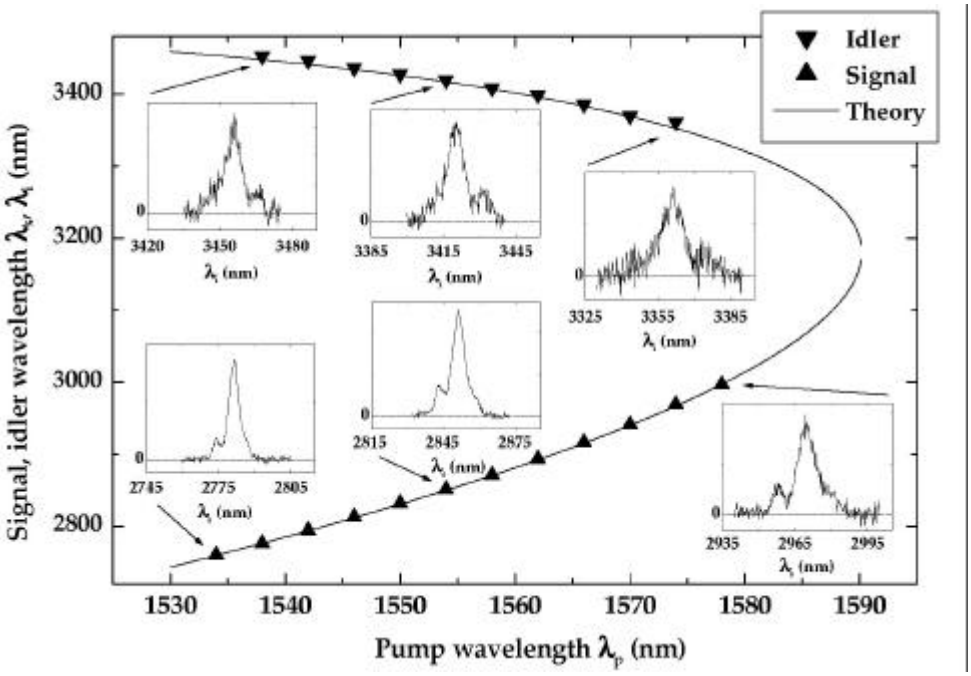


Fig. 8. Measured ( ) and calculated (--) tuning characteristics of OPF from an 18 µm wide waveguide with a domain period of 31.36 µm as signal and idler wavelengths versus the pump wavelength in cw-operation. Selected spectral characteristics of the fluorescence are shown in the insets.

Optical Parametric Oscillation (OPO)

Integrated optical parametric oscillators (IOPOs) are attractive devices to generate tunable coherent radiation in a broad tuning range. A schematic diagram is given in Fig. 9. Contrary to their bulk counterparts IOPOs promise a low oscillation threshold, low waveguide losses provided. Based on Ti:PPLN waveguides singly as well as doubly resonant IOPOs have been developed for

the near- and mid-infrared spectral ranges with unprecedented properties. In the following three examples are presented.

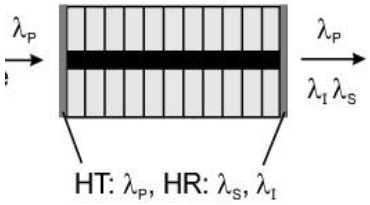


Fig. 9. Schematic diagram of a doubly resonant integrated optical parametric oscillator.

NIR Doubly Resonant Optical Parametric Oscillator (NIR-DR-IOPO) [8]

Using a periodic microdomain pattern with a period of ~17 μm over the total waveguide length of 80 mm a cw doubly resonant optical parametric oscillator was developed for the NIR spectral range. Typical waveguide losses are 0.1 B/cm. The endfaces of the samples are coated with dielectric mirrors of high transmission for the pump (~ 780 nm, T > 90 %) and of high reflectivity for signal and idler around 1550 nm wavelength (R > 95 %). Oscillation starts near degeneracy at a coupled pump power of 4.2 mW only. Fig. 10 shows on the left the measured output power of signal and idler $P_s + P_i$ as function of the coupled pump power $P_{p,c}$. The slope efficiency is ~ 3 %. Tuning of the IOPO is determined by the wavelength range of mirror reflectivity exceeding 87 %; it covers the wavelength range from ~1400 nm to ~ 1750 nm (Fig. 10 (right)).

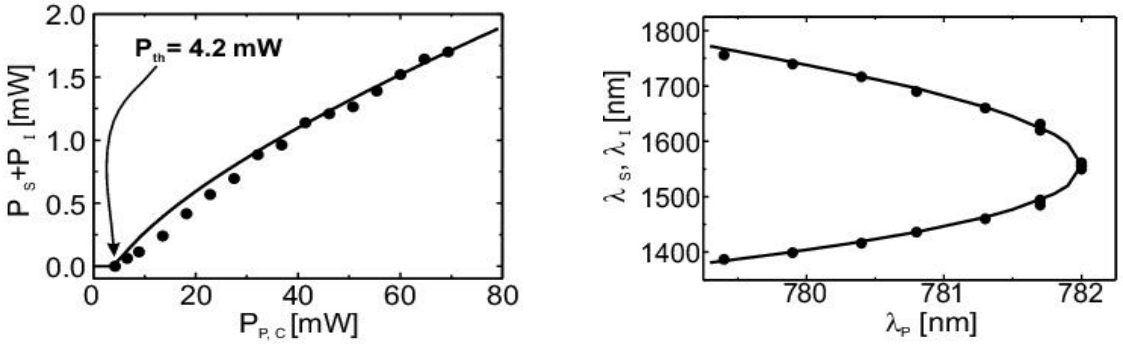


Fig. 10. Power characteristics (left) and tuning characteristics (right) of a doubly resonant NIR-IOPO.

MIR Doubly Resonant Optical Parametric Oscillator (MIR-DR-IOPO) [9]

The IOPO consists of a 90 mm long Ti:PPLN waveguide (80 mm periodically poled with a periodicity of ~31 μm) in a 0.5 mm thick and 12 mm wide Z-cut, X-propagation $LiNbO_3$ substrate with external dielectric mirrors in contact with the waveguide end faces. The periodically poled waveguide of excellent homogeneity has very low losses down to 0.03 $dBcm^{-1}$ in the MIR. To achieve doubly resonant optical parametric oscillation the dielectric mirrors are optimized for high signal (λ_s) and idler (λ_i) reflectivity (> 95 %) in the 2800 to 3400 nm spectral range and high pump transmission (80..92 %) between 1500 and 1580 nm wavelength. The IOPO is pumped by a tunable, single-frequency external cavity semiconductor laser (1500 nm $< \lambda_p <$ 1580 nm) in combination with a high power (up to 27 dBm) fiber amplifier. Optical parametric oscillation starts at 14 mW (external) pump power. With rising pump power level also signal and idler power increases up to 6.5 mW at 300 mW pump power. At even higher levels the MIR-output saturates at about 7.8 mW. The measured threshold and output characteristic agrees well with modelling results.

The tuning behaviour of signal and idler radiation of three IOPOs of different waveguide width has been investigated using a grating monochromator and a Fabry-Perot interferometer (Fig. 11). The maximum continuous tuning range from 2804 to 3379 nm is achieved with the IOPO of 17.5 μm waveguide width and Λ = 31.6 μm domain periodicity by pump wavelength tuning from 1532 to 1570 nm. The overall tuning range is 2765 to 3476 nm determined by the spectral width of the high reflectivity band of the dielectric mirrors. The fine tuning behaviour is determined by the double resonance for signal and idler. As an example, a relative signal frequency is plotted on the right of Fig. 8 as function of the pump frequency detuned from λ_{p0} = 1540 nm. The signal frequency does not follow the exact phase-matching curve (straight line), but obeys a sawtooth-characteristics with a spectral width of about 180 GHz.

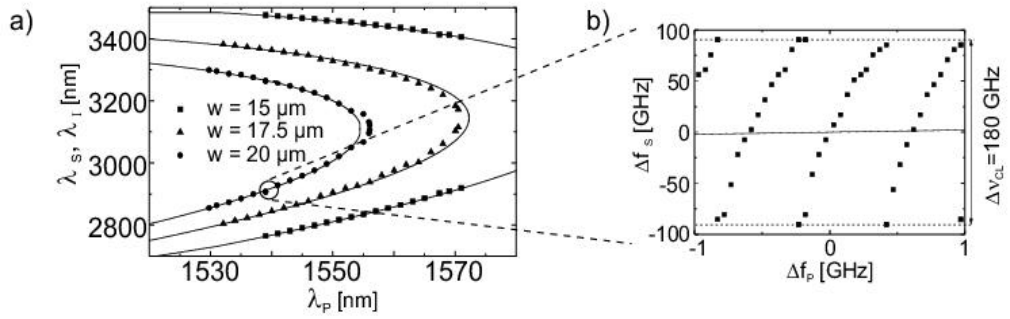


Fig. 11. Tuning characteristics as signal and idler wavelength versus the pump wavelength of three doubly resonant MIR-IOPOs of different waveguide width. Fine tuning characteristics at ë$_p$ = 1540 nm on the right.

MIR Singly Resonant Optical Parametric Oscillator (MIR-SR-IOPO) [10]

Singly resonant integrated optical parametric oscillators (SR-IOPO) are attractive candidates for efficient frequency conversion, nearly continuously tunable in a broad wavelength range without a sawtooth-characteristics as for a doubly-resonant device. Our SR-IOPO consists of a 90 mm long channel guide of 17.5 μm width in a Z-cut, X-propagation $LiNbO_3$ substrate. The waveguide losses are as low as 0.06 dB/cm measured at λ = 3391 nm. Using the electric field poling technique the substrate has been periodically poled over a length of 80 mm with a domain periodicity of 31.3 μm. Dielectric mirrors on a sapphire substrate (R > 95 % for 3200 < λ < 3800 nm, R < 5 % for 2650 < λ < 2980 nm) are in contact with the waveguide end face to form the resonator. A tunable narrow linewidth extended cavity semiconductor laser, amplified by a high power EDFA (33 dBm), is used as pump source to operate and to investigate the SR-IOPO. As an example, Fig. 12 (left) presents the power characteristic of the device in cw operation as signal plus idler power in forward direction versus the external pump power (λ_p = 1560 nm). The oscillation threshold is 275 mW in good agreement with the theoretical prediction, if a 60 % coupling efficiency is assumed. At 1.25 W pump power the mid-infrared emission (λ_s = 2883 nm, λ_i = 3364 nm) grows up to ~ 300 mW; this result corresponds to an overall slope efficiency of 30 %. Due to the SR-configuration of the oscillator the signal power always exceeds the idler power considerably. The SR-IOPO output can be tuned within the range 2720 nm < λ_s, λ_i < 3500 nm by changing the pump wavelength λ_p from 1530 nm to 1580 nm (see Fig. 12, right).

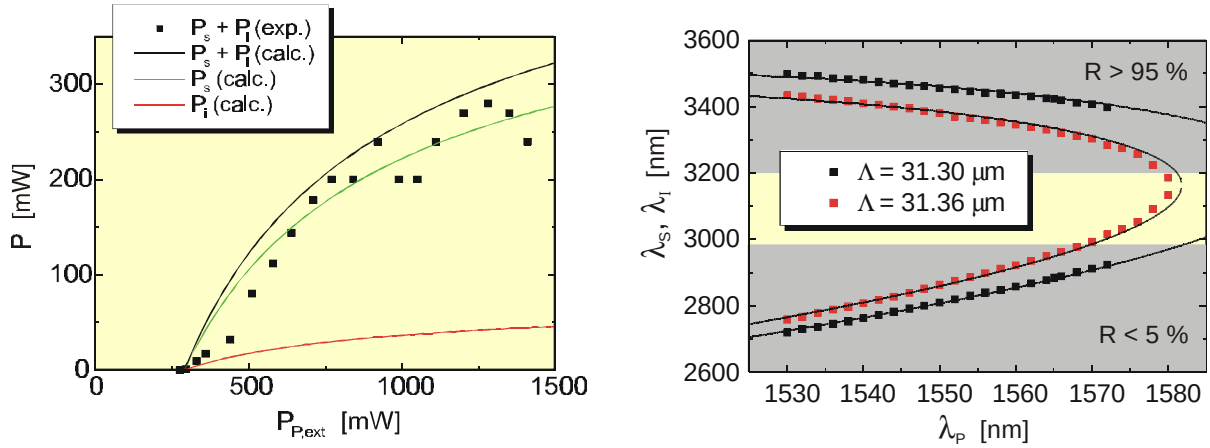


Fig. 12. Measured and calculated power characteristics of a SR-IOPO with 17.5 µm wide channel guide of domain period of 31.36 µm (left) and tuning characteristic of two SR-IOPOs of different domain periodicity as signal and idler wavelengths versus the pump wavelength in cw-operation.

Conclusions

The field of nonlinear integrated optics with waveguides in PPLN has been reviewed. A variety of all-optical frequency converters and signal processing devices with excellent properties has been presented. All these devices are based on single channel, straight waveguides in PPLN. It is a great challenge to develop devices with more complex nonlinear waveguide structures like waveguide arrays, engineered ferroelectric microdomains and even photonic bandgap structures in PPLN without and with doping by laser-active ions such as Erbium. They will allow to realise a whole bunch of new all-optical functions.

References

[1] J. Kurz et al., *Proc. Contemporary Photonics Technology (CPT 2003),* 93-94, 2003

[2] G. Schreiber et al*., Proc. SPIE,* vol.4277, 144 (2001)

[3] G. Schreiber et al., *Technical Digest Novel Lasers and Devices – Basic Aspects 1999,* paper LWA9, p. 147 (1999)

[4] H. Suche et al., *Proc. European Conf. on Opt. Commun. (ECOC`01), Amsterdam, Oct. 2001,* vol 6, post deadline papers, p. 42

[5] Y. H. Min et al., *unpublished*

[6] Y. H. Min et al., *CLEO/Europe 2003, Munich, accepted*

[7] M. C. Hübner et al., *Nonlinear Guided Waves (NLGW`02), Stresa/Italy, Sept. 2002,* post deadline paper

[8] G. Schreiber, *Ph.D. thesis, University of Paderborn, 2001*

[9] D. Hofmann et al., *Proc. Europ. Conf. Integrated Optics (ECIO`99),* post deadline paper, p. 21 (1999)

[10] D. Hofmann et al., *Conf. Digest 2000 Conf. on Lasers and Electro-Optics Europe (CLEO`00), Nice/France, Sept. 2000,* paper CDM4

Efficient Waveguide Bend Design in Photonic Crystals

Rumen Iliew, Christoph Etrich, Ulf Peschel, and Falk Lederer,
Institut für Festkörpertheorie und Theoretische Optik,
Friedrich-Schiller-Universität Jena, Max-Wien-Platz 1, 07743 Jena, Germany
Rumen.Iliew@uni-jena.de

By interpreting line defects in photonic crystals as strongly coupled point defects we predict basic properties of the waveguide modes from the properties of the point defects and compare the results with rigorous calculations.

Keywords: guided-wave optics, photonic crystals, periodic structures, waveguide modes

The realization of efficient sharp and compact waveguide bends is still a challenging task in microoptics. With the introduction of photonic crystals (PCs) major interest has also focused on the issue of efficient waveguide bends embedded in PCs. There are various proposals for bend design in order to minimize losses. Examples are smoothening the sharp bends [1], introducing cavities or intermediate straight sections [2] or placing smaller holes around the bend [3]. To inhibit the modal mismatch at a Y splitter [4] an additional hole has been added at the bend. On the other hand, it has been shown that a coupled-defect waveguide (CDW) composed of a chain of point defects in a PC can also have a very high transmission for a certain wavelength range at sharps bends [5] when the single defect is single moded. In that case it can be shown that for the single point defect in a square or hexagonal lattice this mode is invariant under all symmetry operations of the C_{4v} or the C_{6v} point group of the underlying crystal, respectively.

The aim of this contribution is to put forward an efficient tool for bend optimization. In our approach we start from the localized modes of a single point defect (e. g. a removed rod or a filled air hole) in a photonic crystal lattice at frequencies within the bandgap. Grouping such defects separated by a few lattice constants into a chain leads to the well-known CDW whereby it is assumed that the modal field of the single defect is not changed significantly and hence the properties of the modes in the arising miniband are determined by the properties of the single defect. This is validated by the good agreement of coupled-mode description and rigorous treatment.

Here we apply this approach to strongly coupled defects where the spacing is one lattice constant and arrive at a W1 line defect waveguide. The complete electromagnetic fields of the waveguide in Fourier domain are again written by means of a superposition of the modal fields of the single point defect located at the individual defect sites l and modified with a complex amplitude a_{kl}:

$$\mathbf{E}(\mathbf{r},\omega)=\sum_{k,l} a_{kl}(\omega)\,\mathbf{e}_k(\mathbf{r}-\mathbf{R}_l),\quad \mathbf{H}(\mathbf{r},\omega)=\operatorname{sgn}(\omega)\sum_{k,l} a_{kl}(\omega)\,\mathbf{h}_k(\mathbf{r}-\mathbf{R}_l) \tag{1}$$

Here $\mathbf{e}_k$ and $\mathbf{h}_k$ denote the orthogonal electric and magnetic field of the k-th mode of the single defect, respectively and $\mathbf{R}_l$ is the l-th defect site. For a wave-like excitation $a_{kl}=a_{k,0}\exp(ilKa)$ (K…Bloch wave vector, a…lattice pitch) for the case where we have a twofold degenerate point defect mode we get two decoupled minibands as solutions for the defect chain. This fact we identify as one cause of reduced bend transmission due to coupling to the respectively other mode at the bend.

When instead we have only one point defect mode, that necessarily then bears the full symmetry of the underlying lattice there occurs only one miniband with the following dispersion relation

obtained from coupled mode analysis (CMA) for only nearest neighbor interaction describing the relation between the excitation frequency ω and the Bloch vector K:

$$\omega(K) = \frac{1 + 2\beta\cos(Ka)}{1 + \frac{1}{2}\gamma_0 + (2\beta + \gamma_1)\cos(Ka)} \tag{2}$$

with $\beta, \gamma_0, \gamma_1$ being overlap integrals of the electric field of the single point defect with the spatial distribution of the dielectric constant for the line defect. For describing bends sections of line defect waveguides must be put together at different angles and additional terms in the equations for the coefficients occur [5] modifying the transmission characteristics.

Plane-wave calculations [6] of the line defect reveal that for square or hexagonal lattices inside the occuring miniband the field structure is still mainly given by the superposition of the field of the single defects shifted by the defect distance. This is also confirmed by the good agreement of the dispersion relation of the miniband obtained from rigorous planewave calculations and from equation (2) as shown in Figure 1 for a sample structure composed of a two-dimensional hexagonal array of dielectric (semiconductor) cylinders in air with removed cylinders as defects and for TM polarization of the electromagnetic field.

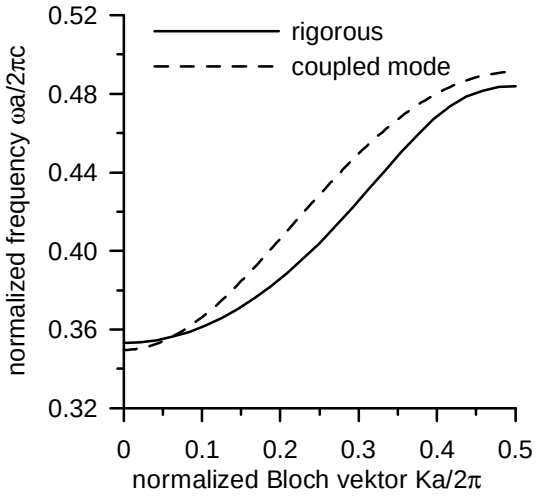


Figure 1. Comparison of the dispersion relations obtained from rigorous (planewave) and coupled mode calculations for a line defect in the TM example structure.

We will utilize this knowledge for designing efficient waveguide bends by following the idea that a point defect mode with the full symmetry of the point group will have the same coupling strength into all equivalent lattice directions. For instance, for point defects arranged in ΓK direction in a hexagonal lattice this would mean there are six equivalent directions for coupling to a second point defect. Exploitation of this idea leads us to a geometry of hexagonally arranged dielectric rods with a double bend where we expect a high transmissivity within a reasonable wavelength range. The result of a two-dimensional finite-difference time-domain (FDTD) calculation of this double bend for a continuous wave excitation at the left end is shown in Figure 2.

In Figure 3 we show the result of the respective FDTD transmissivity calculation for the interesting wavelength range confirming the expected high efficiency of the bend. If we have instead a doubly degenerate point defect mode with a twofold symmetry both of the point defect modes have two different coupling constants to the modes of neighboring defects, depending

whether it is a straight line or a bend. Additionally, it will couple to both modes of the next defect resulting in mode mixing and hence to reduced transmission into the original mode of the waveguide.

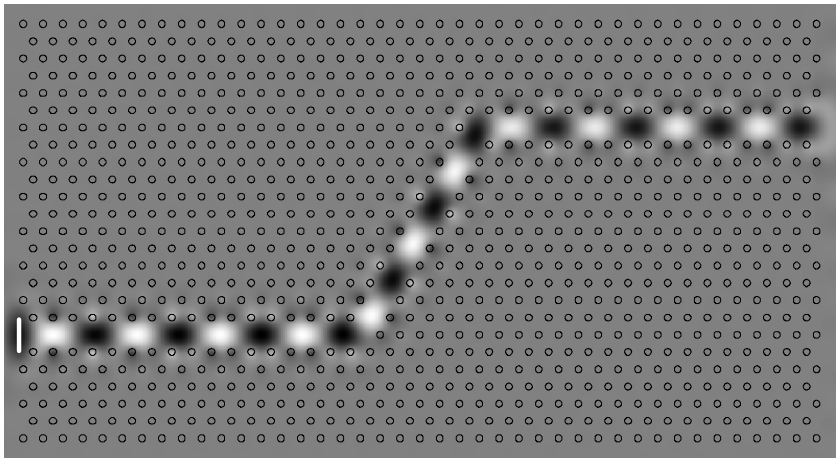


Figure 2. Image plot of the *z* component of the electric field of a W1 waveguide double bend realized in a 2D photonic crystal for TM polarization. The excitation is shown as a white line in the left part.

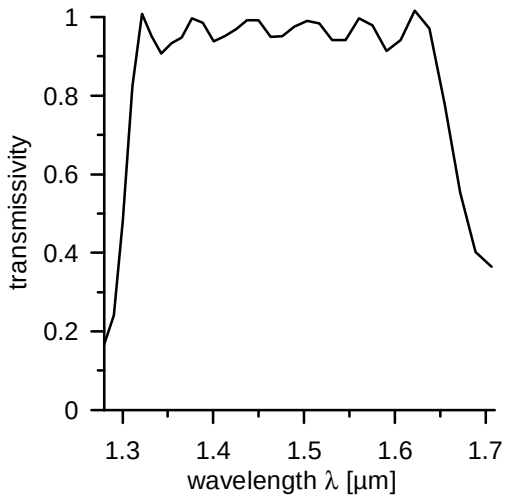


Figure 3. Transmissivity (intensity transmission) obtained for the structure in Fig. 2 from 2D FDTD calculations.

In our paper we will predict the bending performance of W1 line defect waveguides in PCs from the behavior of the single defect for different geometries and compare with FDTD calculations. We will explore the reliability of quantitative predictions based on a CDW description for different geometries.

References

[1] J. Moosburger, M. Kamp, A. Forchel, S. Olivier, H. Benisty, C. Weisbuch, U. Oesterle, "Enhanced transmission through photonic-crystal-based bent waveguides by bend engineering," *Appl. Phys. Lett.* **79**, 3579-3581, 2001.

[2] S. Olivier, H. Benisty, C. Weisbuch, C. J. M. Smith, T. F. Krauss, R. Houdré, and U. Oesterle, "Improved 60° Bend Transmission of Submicron-Width Waveguides Defined in Two-Dimensional Photonic Crystals," *J. Lightwave Technol.* **20**, 1198-1203, 2002.

[3] A. Talneau, Ph. Lalanne, M. Agio, and C. M. Soukoulis, "Low-reflection photonic-crystal taper for efficient coupling between guide sections of arbitrary widths," *Opt. Lett.* **27**, 1522-1524, 2002.

[4] S. Boscolo, M. Midrio and T. F. Krauss, "Y junctions in photonic crystal channel waveguides: high transmission and impedance matching," *Opt. Lett.* **27**, 1001-1003, 2002.

[5] U. Peschel, A. L. Reynolds, B. Arredondo, F. Lederer, P. J. Roberts, T. F. Krauss, and P. J. I. de Maagt, "Transmission and Reflection Analysis of Functional Coupled Cavity Components," *IEEE J. Quantum Electron.* **38**, 830-836, 2002.

[6] S. G. Johnson and J. D. Joannopoulos, "Block-iterative frequency-domain methods for Maxwell's equations in a planewave basis," *Opt. Express* **8**, 173-190, 2001.

Sidewall Roughness in Photonic Crystal Slabs: A Comparison of High-Contrast Membranes and Low-Contrast III-V Epitaxial Structures

Wim Bogaerts, Peter Bienstman, Roel Baets
Ghent University – IMEC, Dept. of Information Technology (INTEC)
Sint-Pietersnieuwstraat 41, B-9000 Gent, Belgium
wim.bogaerts@intec.rug.ac.be

We have simulated sidewall roughness in photonic crystal slabs. Structures with a low vertical index contrast (like III-V waveguides) are shown to be more prone to scattering at sidewall roughness than membranes or SOI-like structures.

Keywords: photonic crystals, scattering, roughness, silicon-on-insulator

Introduction

Today's photonic crystal slab waveguides are limited in their performance by propagation losses. A large fraction of these losses can be attributed to out-of-plane scattering. While in-plane scattering in photonic crystal slabs is prevented by the photonic bandgap effect, in the vertical direction the light is only bound by a vertical index contrast. Most photonic crystal structures consist of a lattice of holes etched into a slab waveguide structure. These holes break the vertical confinement, allowing the light to radiate to the top or bottom cladding. Evidently, the amount of scattering is highly dependent on the refractive index profile of the layer structure in which the photonic crystals are fabricated. One can use a conventional III-V grown layer structure in the GaAs or InP material system. These structures have a low index contrast between the guiding core and the cladding. Alternatively, photonic crystals can be made in a layer structure with a high index contrast, like silicon-on-insulator (SOI) or semiconductor membranes. Both systems have their merits, but exhibit a drastically different behaviour with respect to out-of-plane scattering losses.

Out-of-plane scattering accounts for a large fraction of the losses in photonic crystals. Current state-of-the-art single-mode photonic crystal waveguides have losses of 6dB/mm in SOI [1], and 11dB/mm in III-V materials [2]. These losses are orders of magnitude larger than those of classical waveguides. To reduce these losses, good management of out-of-plane scattering is needed.

Intrinsic Out-of-Plane Scattering

Out-of-plane scattering in photonic crystal slabs has a number of different causes. Even in perfect photonic crystal slabs light is not necessarily confined vertically, and can leak away gradually as it propagates through the structure. This is true for modes located above the light line in the dispersion diagram. These modes extend into the top and bottom cladding and have a radiation component. As is discussed in [3] and [4], these losses increase strongly with the index contrast between core and cladding. Therefore, III-V semiconductors with a low index contrast are a good material system to keep these losses low. On the other hand, when the photonic crystal waveguide modes are located below the light line, they propagate without loss as long as the periodicity is not disturbed. However, it is only possible to construct such a photonic crystal when it has a cladding with a low refractive index and therefore a light line with a steep slope. This implies a high vertical refractive index contrast, as found in SOI or semiconductor membranes.

To reduce intrinsic losses one can either use a low refractive index contrast, so the intrinsic losses are kept low (but not zero) or use a high refractive index contrast, designing a waveguide with a guided Bloch mode. However, in the latter case, careful engineering is needed for defects, as these might cause large scattering losses [3].

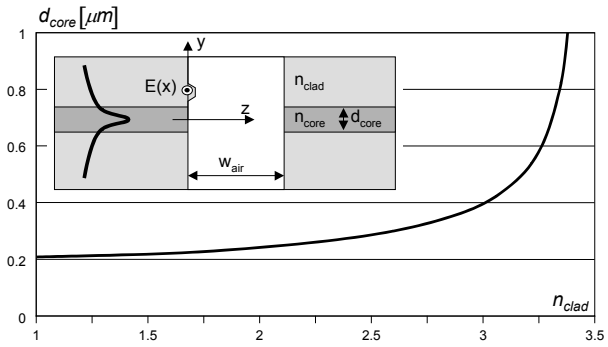


Figure 1: 3-layer slab waveguide with air slot. To guarantee single-mode behaviour, the thickness of the slab core is dependent on the refractive index of the cladding.

Out-of-Plane Scattering at Sidewall Roughness

Although one can design photonic crystal waveguides that are intrinsically lossless, this will never be the case for fabricated structures. The most common fabrication technique for photonic crystals consists of high-resolution lithography combined with dry etching. Although the quality of this technology is improving steadily, a certain amount of roughness due to the etching process is unavoidable. These irregularities, mostly located on the sidewalls of the holes, can scatter light and give rise to losses. Again, we expect the vertical index profile to play a role.

To model the out-of-plane scattering caused by sidewall roughness, we used a 2-D approximation of a photonic crystal slab: 1-D air slots etched into a slab waveguide (Figure 1). We then modelled the scattering roughness by a dipole excited by the incident electromagnetic field, i.e. the mode of the slab waveguide. Because the scatterer radiates in all directions, a fraction of the light will be recaptured by the slab waveguide core. This fraction is of course dependent on the index profile of the slab waveguide and the position of the roughness on the sidewall. We calculated a measure for the losses by averaging over position y of the irregularity on the sidewall:

$$L_{tot} \sim \int_y P(y)L(y)dy\,, \tag{1}$$

with $P(y)$ the power radiated by the dipole and $L(y)$ the fraction not recovered by the slab waveguide core. We calculated this using CAMFR [5][6], a vectorial eigenmode expansion tool with PML absorbing boundary conditions. Along the propagation axis, the structure is cut into sections with a constant index profile, in which the electromagnetic field is expanded into the local eigenmodes. Radiation modes are supported through PML absorbing boundary conditions. At the interface between sections, mode matching is used to decompose the field into the eigenmodes of the new section. This way, a scattering matrix describing the entire structure is obtained.

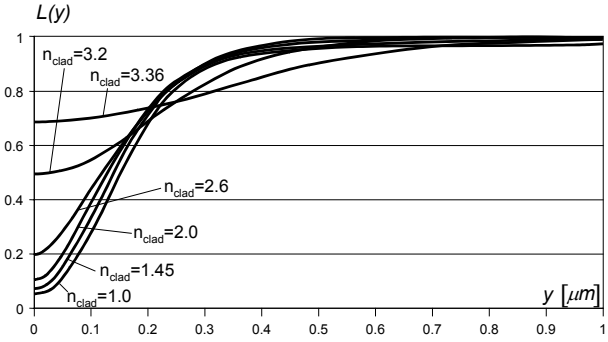


Figure 2: Fraction of light radiated by a dipole in position y that is not recaptured by the waveguide core.

To compare structures with a different refractive index contrast, we defined a slab structure with a constant *v*-number of 2.79. Because the *v*-number depends on the cladding index and core thickness, the core will be thicker for lower cladding index. The core thickness is plotted in Figure 1 as a function of cladding index. For the slab core a refractive index of 3.45 was chosen. The air slots in the slab waveguide are considered to be etched through completely and have a width of 280nm.

Using CAMFR, we then calculated the excitation of the dipole, as well as the fraction of light that can be recovered. This was done in a rigorous way, taking into account the effects of the surroundings on the radiation pattern of the dipole. Because in a photonic crystal, backward and forward propagating light is coupled, we consider the radiated light coupled into the forward and backward propagating mode as *not* lost. Figure 2 plots the lost fraction $L(y)$ of the light as a function position y of the dipole for different values of the cladding index. We see that for low cladding indices (i.e. high vertical index contrast) much light is recovered when the dipole is near the cladding. This can be explained by the fact that a narrow waveguide with high index contrast automatically has a large numerical aperture and can capture much light.

The integrand of equation (1) also contains the power of the radiating dipole. This power depends on two factors: The field strength in position y and the geometry of the roughness on the material-air interface. In a first-order approximation, the incident field strength can be derived from the slab waveguide guided mode. The excitation of the dipole by this incident field is determined by the geometry of the sidewall roughness, as well as by the refractive index contrast along the material-air interface. We can write the radiated power of the dipole $P(y)$ as

$$P(y) = \eta(y)^2 . \frac{E^2(y)}{2.Z_{rad}(y)}, \tag{2}$$

with $E(y)$ the field in position y, $\eta(y)$ describing the effect of the roughness and $Z_{rad}(y)$ the radiative impedance of the environment in position y. The first and last term are easily calculated using CAMFR. To study the effect of the geometry $\eta(y)$ we simulated the scattering of a plane wave incident on an irregularity on a smooth interface between a homogeneous material and air. We did this for different material refractive indices and found that $\eta(y)$ behaves very much like

$$\eta^2 = \gamma . (\Delta\varepsilon_h)^2, \tag{3}$$

with $\Delta\varepsilon_h$ the difference in dielectric constant (i.e. the square of the refractive index) at the interface. If we use this result in our slab waveguide configuration we see that $\eta(y)$ is indeed dependent on the position y, as the index contrast along the interface changes from core to cladding.

Taking into account these results, we can now calculate the integrand in equation (1). $P(y).L(y)$ is

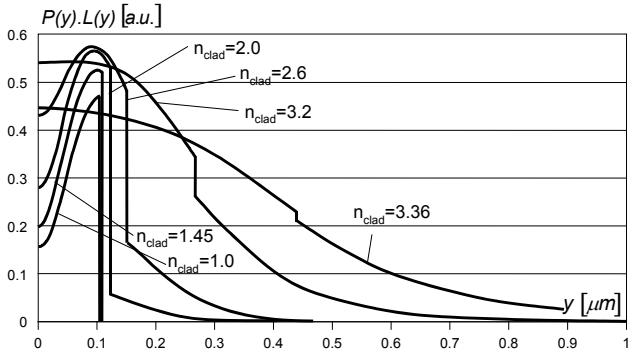


Figure 3: Power lost by radiation caused by an irregularity as a function of position y for different values of the cladding refractive index.

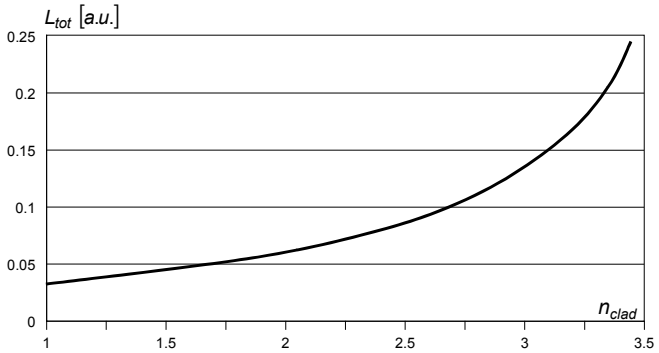


Figure 4: A measure for the average power lost due to sidewall roughness as a function of the refractive index of the slab waveguide cladding.

plotted in Figure 3 for different values of the cladding index. The discontinuity in the curves is caused by the discontinuity in $\eta(y)$ at the core-cladding interface. We see that the amount of scattering is significantly lower for structures with a high refractive index contrast.

Figure 4 plots the measure for scattered light as described in equation (1). We see that for low refractive index contrast, like in III-V, losses due to scattering are considerably higher than in the case of SOI or membranes, and this for a similar amount of sidewall roughness.

Conclusion

Out-of-plane scattering is the major loss mechanism in photonic crystals, and scattering at sidewall roughness can contribute to these losses. Although there are two beneficial regimes for intrinsic losses, i.e. the very high and the very low index contrast, only the high vertical index contrast promises to alleviate these losses for the same level of manufacturing technology.

This advantage with respect to out-of-plane scattering losses might provide an explanation as why photonic crystal waveguides in SOI seriously outperform their III-V competitors [1][2]. Also, these results again show the importance of high-quality fabrication technology. Especially when photonic crystal-based structures are to be commercialised, reproducible mass-fabrication techniques are required.

Acknowledgements

Part of this work was carried out in the context of the European IST-PICCO project. Part of this work was carried out in the context of the Belgian IAP PHOTON network.

Wim Bogaerts thanks the Flemish Institute for the Industrial Advancement of Scientific and Technological Research (IWT) for a specialisation grant.

Peter Bienstman acknowledges the Flemish Fund for Scientific Research (FWO-Vlaanderen) for a postdoctoral fellowship.

References

[1] M. Notomi, A. Shinya, et al., *IEEE J. Quant. Electron.* 38(7), p.736, 2002
[2] Talneau, L. Le Gouezigou, N. Bouadma, *Opt. Lett.* 26(16), p. 1259, 2001
[3] W. Bogaerts, P. Bienstman, D. Taillaert, R. Baets, D. De Zutter, *IEEE Phot. Technol. Lett.* (13), p.565 (2001)
[4] H. Bénisty, D. Labilloy, C. Weisbuch, et al., *Appl. Phys. Lett.* (76), p. 532 (2000)
[5] P. Bienstman and R. Baets, *Opt. Quant. Electron.* 33(4-5), p. 327 (2001)
[6] CAMFR website: http://camfr.sourceforge.net

Photonic crystal waveguides in highly dispersive materials

D. Michaelis, U. Peschel*, C. Waechter, A. Braeuer, and F.Lederer*
Fraunhofer Institute for Applied Optics and Precision Engineering Jena, Micro Optics Department,
Winzerlaer Str. 10, 07745 Jena, Germany
dirk.michaelis@iof.fraunhofer.de

*Friedrich-Schiller-University Jena, Institute for Solid State Theory and Optics,
07743 Jena, Max-Wien-Platz 1, Germany

We derive a reciprocity theorem for photonic crystal waveguides (PCWs) which can be used for analytical descriptions of perturbed PCWs. Especially we analytically investigate polaritons in PCWs and transmission-reflection problems between PCWs and conventional waveguides.

Keywords: photonic crystals, waveguides, polaritons, transmission – reflection analysis

Introduction

Due to their potential applications photonic crystals (PCs) are intensively studied in the last decade. In particular photonic crystal waveguides (PCWs) are of great interest because they allow for an efficient transport of optical signals in highly integrated all-optical circuits. However, there is still a strong need in both numerical modelling as well as fundamental understanding of the field dynamics in these sub-wavelength structures. The frequencies and modes of straight, ideal PCWs are usually calculated by means of plane-wave expansion methods or band structure calculations. However, the field distribution in perturbed, bended or mutually interacting PCWs has still to be determined by solving the complete set of Maxwell's equation via a Finite Difference Time Domain (FDTD) simulations. The latter one is extremely time- and memory consuming and do often not provide for a deeper insight into the physics of the investigated structures. Therefore some simpler modelling or even analytical descriptions of the field dynamics in perturbed PCWs are desirable.

Here we derive a reciprocity theorem and a orthogonality relation for PCW modes starting from Maxwell's equations. Using the reciprocity theorem a set of strongly coupled discrete equations for the field amplitudes in the PC unit cells is deduced. This equations can be used for the modelling or even analytical description of PCWs with arbitrary perturbations. As an example, the theory is applied to the investigation of the influence of polaritons on the band structure of a PCW. Furthermore, the new orthogonality relation is used to derive the coupling coefficients between different PCWs or between a PCW and a conventional waveguide.

Orthogonality relation and coupling coefficients

Starting from Maxwell's equation and using the symmetries of Bloch modes of a PCW in *z*-direction (electric field: $\vec{E}_q = \vec{e}_q(x,y,z)\exp(iqz)$, magnetic field: $\vec{H}_q = \vec{h}_q(x,y,z)\exp(iqz)$, Bloch vector: q) a orthogonality relations for the eigenmodes can be derived

$$\int_{-\infty}^{+\infty} dx \int_{-\infty}^{+\infty} dy \left[\vec{e}_{q_2} \times \vec{h}_{q_1}^{*} + \vec{e}_{q_1}^{*} \times \vec{h}_{q_2}\right]_z = \delta_{q_1 q_2}\, s(q_1), \tag{1}$$

which generalize the well known formulas for conventional waveguides of integrated optics [1]. δ is the Kronecker symbol and *s* denotes the energy flux in the respective mode. This orthogonality relation is different to the common, well known orthogonality relation of PCs where a integration over the whole volume of the PC has to be carried out $\iiint_{PC} dx\,dy\,dz\, \vec{H}_{q_1}^{*} H_{q_2} \sim \delta_{q_1 q_2}$. Because the new orthogonality relation only needs an integration over a plane it can be used for the description of coupling between different waveguides where a mode decomposition in the coupling plane has

to be carried out. Because of the lack of space we concentrate here on approximation formulas for one of the most important case of coupling problems, where both the left and the right waveguide have only one bound mode of a given symmetry. Additionally, for an efficient coupling the transverse shape of both modes has to be similar. Therefore, only a small amount of radiation and evanescent modes is excited. In this case the field structures can be approximated by the left and right bound mode respectively and the following simple approximation formulas yields for the reflectivity:

$$R = -\frac{\iint\limits_{\text{coupling plane}} d\vec{A}\left[\vec{E}^{(t)}_{\text{left}} \times \vec{H}^{(t)}_{\text{right}} - \vec{E}^{(t)}_{\text{right}} \times \vec{H}^{t}_{\text{left}}\right]}{\iint\limits_{\text{coupling plane}} d\vec{A}\left[\vec{E}^{(t)^*}_{\text{left}} \times \vec{H}^{(t)}_{\text{right}} + \vec{E}^{(t)}_{\text{right}} \times \vec{H}^{(t)^*}_{\text{left}}\right]} \tag{2}$$

Similar equations can be derived for the transmission. They can be considered as generalizations of the well known coupling formulas in integrated optics deduced by Marcuse [2]. By means of these formulas approximations for the transmission – reflection – analysis can be obtained very simply. The physics of the coupling can be easily discussed by means of symmetries, phase relations and overlaps of the eigenmodes. Here we only demonstrate the validity of such approximations by means of an example shown in fig. 1. Light couples from a potentially displaced, conventional monomode waveguide to a monomode PCW. In fig. 1c the transmission, obtained by above approximations, is compared to Finite-Difference Time-Domain simulations and shows a good agreement even for a rather large displacement.

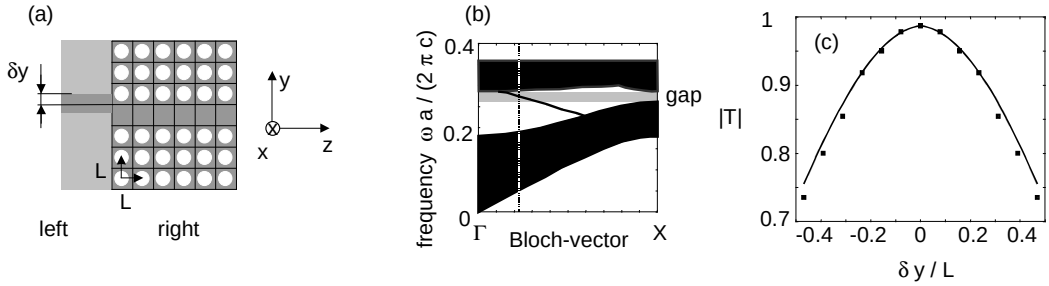


Fig. 1: Coupling of light from a conventional waveguide ($\varepsilon_{\text{guide}}$ = 12, $\varepsilon_{\text{layer}}$ = 9, width / L = 0.4) to a PCW (subtsrate: ε = 12, holes: ε = 1 radius / L = 0.4), (a) scheme of system under consideration, (b) band structure of the PCW, (d) Transmission of the light from the conventional waveguide to the PCW for q = 0.11, solid line: approximation formulas, points: FDTD – simulations.

Photonic crystal waveguides as strongly coupled discrete systems

Using eq. (1) for a mode decomposition $\vec{E} = \sum_q a_q(z)\,\vec{e}_q(\vec{r}) + b_q(z)\,\vec{e}_q^{\,*}(\vec{r})$ $\vec{H} = \sum_q a_q(z)\,\vec{h}_q(\vec{r}) - b_q(z)\,\vec{h}_q^{\,*}(\vec{r})$ of a field in a PCW in the presence of an arbitrary perturbation $\vec{P}_{\text{pert}}$ a set of strongly coupled discrete equations for the amplitudes of the forward $a(z)$ and backward $b(z)$ propagating eigenmodes can be derived from Maxwell's equations:

$$\begin{aligned} &a_q[(k+1)L]\exp[-iq(k+1)L] - a_q[kL]\exp[-iqkL] \\ &= \frac{i\omega}{s(q)} \int_{-\infty}^{\infty} dx \int_{-\infty}^{\infty} dy \int_{kL}^{(k+1)L} dz\; \vec{e}_q^{\,*}\,\vec{P}_{\text{pert}}\,\exp(-iqz) \end{aligned} \tag{3}$$

$$b_q[(k+1)L]\exp[iq(k+1)L]-b_q[k\,L]\exp[iqk\,L]$$
$$=-\frac{i\omega}{s(q)}\int_{-\infty}^{\infty}dx\int_{-\infty}^{\infty}dy\int_{k\,L}^{(k+1)L}dz\;\vec{e}_q\;\vec{P}_{\text{pert}}\;\exp(iqz)$$

,

where we have assumed the kth unit cell to extend between $kL \le z = (k+1)L$. Here the mutual coupling between distant unit cells is of great importance and no nearest neighbour approximation holds. The above discrete set of equation can be used to describe a variety of problems with linear and/or nonlinear perturbations. In particular the most significant frequency dependence is incorporated into the Bloch vector $q(\omega)$.

Polaritons in photonic crystal waveguides

Here we apply eq. (3) to one of the simplest examples, namely a spatially constant but dispersive perturbation $\vec{P}_{\text{pert}} = \varepsilon_0\,\Delta\varepsilon(\omega)\left[a_q(z)\,\vec{e}_q(\vec{r})+b_q(z)\,\vec{e}_q(\vec{r})^*\right]$. Band structure calculations usually do not take into account the dispersion of the dielectric function of the PC materials. This dispersion can be regarded as a perturbation of the nondispersive PC. Therefore eqs. (3) represent an ideal tool to include the dispersion. Here we analytically discuss the influences of a two level systems $\Delta\varepsilon(\omega)=\dfrac{f\;(\omega_0-\omega)}{(\omega_0-\omega)^2+\gamma^2}$ (ω_0 : resonsance frequency, γ: line width, f ~ oscillator strength) on the band structure of a PCW of fig. 2a. A homogenously doped PC with quantum dots represents an example for such a configuration. Applying a slowly varying envelope approximation eq. (3) results in a matrix equation for the amplitudes of the modes in the kth unit cell (a_{k} , b_{k}) and $(k+1)^{\text{th}}$ unit cell ($a_{\text{k+1}}$, $b_{\text{k+1}}$):

$$\begin{pmatrix}a_{k+1}\\ b_{k+1}\end{pmatrix}=\hat{M}\begin{pmatrix}a_k\\ b_k\end{pmatrix}$$
$$\hat{M}=\frac{1}{1+\kappa^2-|c|^2}\begin{pmatrix}\left[(1+i\kappa)^2+|c|^2\right]\exp(iqL) & 2c\exp(iqL)\\ 2c^*\exp(-iqL) & \left[(1-i\kappa)^2+|c|^2\right]\exp(-iqL)\end{pmatrix}, \qquad (4)$$

where the coefficients read as $\kappa=\Delta\varepsilon(\omega)\kappa'(\omega)$ and $c=\Delta\varepsilon(\omega)c$ with $\kappa'=\dfrac{\omega\varepsilon_0}{2\,s(q)}\int_{-\infty}^{\infty}dx\int_{-\infty}^{\infty}dy\int_0^L dz\;\;|\vec{e}|^2$ and $c'=\dfrac{i\omega\varepsilon_0}{2\,s(q)}\int_{-\infty}^{\infty}dx\int_{-\infty}^{\infty}dy\int_0^L dz\;\;\vec{e}^{*2}\exp(-2iqz)$. κ' and c' do not depend on the perturbation. They are exclusively determined by the band structure of the unperturbed PCW and represent the quantities which describe the sensitivity for a deformation of the band due to perturbations. Fig. 2b shows these parameters for the PCW of fig. 2a. The eigenvalues analysis of the matrix $\hat{M}$ gives the new eigenmodes of the perturbed PCW. A field in the perturbed waveguide can be written as:

$$\begin{pmatrix}A_k\\ B_k\end{pmatrix}=\alpha_+\lambda_+^k\begin{pmatrix}1\\ e_+\end{pmatrix}+\alpha_-\lambda_-^k\begin{pmatrix}1\\ e_-\end{pmatrix}, \qquad (5)$$

where the eigenvalues read as $\lambda_\pm=\pm\sqrt{[\text{Re}(\eta)]^2-1}+\text{Re}(\eta)$ with $\eta=\dfrac{(1+i\kappa)^2+|c|^2}{1+\kappa^2-|c|^2}\exp(iqL)$

.

$\alpha_{\pm}$ are the amplitudes of the new forward and backward propagating mode. For $\mathrm{Re}(\eta) \le 1$ the eigenvalues are complex $\lambda_{\pm} = \mathrm{Re}(\eta) \pm i\sqrt{1-[\mathrm{Re}(\eta)]^2}$. Their amounts are equal to unity. Therefore they can be written as $\lambda_{\pm} = \exp(iqL)$, where the new Bloch vector reads as $q = \arctan\left(\sqrt{1-\mathrm{Re}(\eta)}/\eta\right)/L$. In this case the mode dynamics is given by a simple phase evolution, i.e. eq. (5) describes the mode propagation in the perturbed PCW. For $|\mathrm{Re}(\eta)| > 1$ the eigenvalues become purely real. Thus the former propagating modes pass over to evanescent modes. A closer look at eq. (5) reveals the physical meaning of the parameters κ and c. Depending on the sign, κ shifts the band towards larger or smaller Bloch vectors, whereas c leads to a band shrinkage. For a strong enough of Δε of the two level system the PCW band structure is not only deformed, there could be even a splitting of the original band and a new gap is created (evanescent modes appear). The sensitivity of the PCW – band for a creation of a new gap depends strongly on the corresponding frequency. A new gap is created for $|\mathrm{Re}[\eta(\Delta\varepsilon_{crit})]| = 1$ which defines the critical value of perturbation $\Delta\varepsilon_{crit}$ for band splitting (see fig. 2c). Close to the Γ – point the band is very sensitive for a negative $\Delta\varepsilon$, whereas for increasing frequencies the sensitivity becomes larger for positive $\Delta\varepsilon$ - values. In our case for a normalized resonance frequency of 0.32 (see fig. 2d) close to the Γ – point the gap emerges for negative $\Delta\varepsilon$, i.e. above the resonance frequency. The situation reverses for larger resonance frequencies, i.e. the gap appears below the resonance. This is in contrast to the common dispersion relations of polaritons in bulk media. The backward bended branch in fig. 2d occurs in the resonance of the two level system. In this frequency range strong absorption is present. Thus no ideal band can be defined in this region.

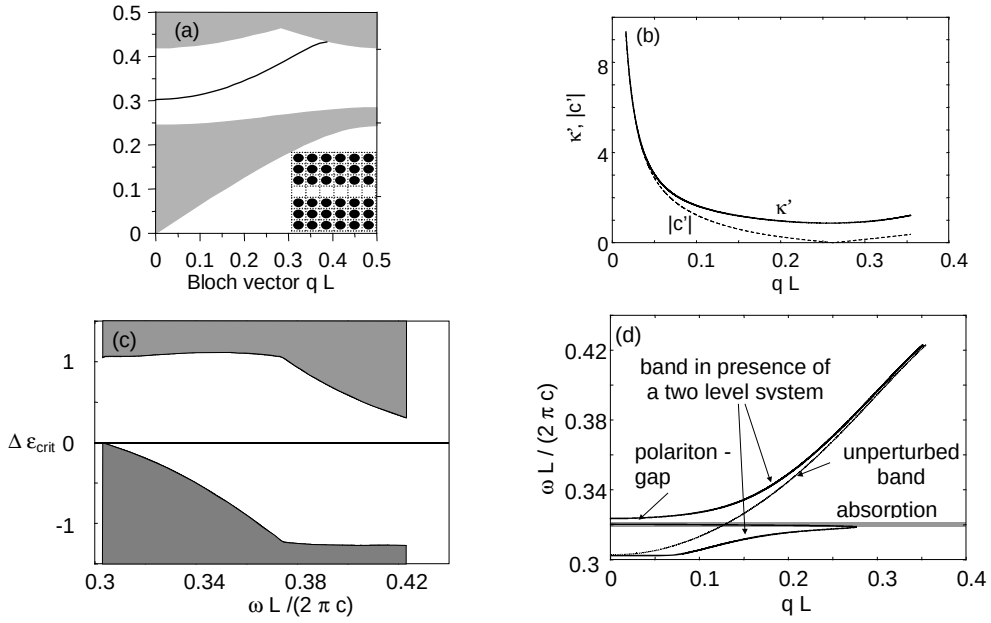


Fig. 2: Polaritons in a PCW (rods: ε = 12, radius / L = 0.2), (a) band structure (b) coefficients for the perturbation theory describing perturbation induced band deformations (c) critical perturbation for band splitting (shaded regions: band splitting - evanescent modes) ,(d) unperturbed and perturbed band structure due to the existence of polaritons

[1] R. März, 'Integrated Optics, desing and modeling', Artech House, Boston London (1994).

[2] D. Marcuse, 'Theory of Dielectric Optical Waveguides', Academic Press, New York, (1974).

Grating assisted rectangular integrated optical microresonators

Manfred Hammer*, Didit Yudistira
MESA$^+$ Research Institute, University of Twente, The Netherlands

A wide, multimode segment of a dielectric optical waveguide, enclosed by Bragg reflectors and evanescently coupled to adjacent port waveguides, can constitute the cavity in an integrated optical microresonator. We outline a design strategy for these devices and give results of numerical simulations by means of mode expansion techniques, that exemplify the specific spectral response of the standing wave resonators.

Keywords: integrated optics, numerical modeling, optical microresonators, rectangular microcavities.

Introduction

Optical microresonators are at present discussed as basic elements for large scale integrated optics [1, 2], typically for applications in optical wavelength division multiplexing. The focus is on compact cylindrical disk- or ring shaped structures, designed for material systems with high refractive index contrast, where the technological implementation or the application itself usually requires a facility for post fabrication adjustment. If the tuning is to be realized by electrooptical means, a major obstacle may be encountered in the form of the strong anisotropy of some of the most promising electrooptic materials [3, 2]. The birefringence must be suspected to lead to a pronounced modulation, if not to leakage, of the circulating optical waves, i.e. to a lossy cavity.

These problems can be avoided in standing wave resonators, where the light propagation is restricted basically to one axis. Integrated optical microresonators with square or rectangular cavities have attracted attention only quite recently [4, 5, 6, 7]. In their conventional form, also these concepts have a severe technological disadvantage: An extremely high refractive index contrast is required for the total reflection effect at the facets of the waveguide segments [8] that serve as cavities; with the presently available materials a realization seems to be difficult.

A way out is found by replacing the waveguide facets by Bragg reflectors. This leads to a concept for a standing wave resonator in the form of a Fabry-Perot cavity with lateral, evanescent coupling. Fig. 1 sketches the structure and introduces the relevant parameters. While a parameterized time-domain coupled mode theory model is given in Ref. [4], so far apparently neither rigorous nor approximate simulations of these devices exist. This is what we would like to provide with this paper.

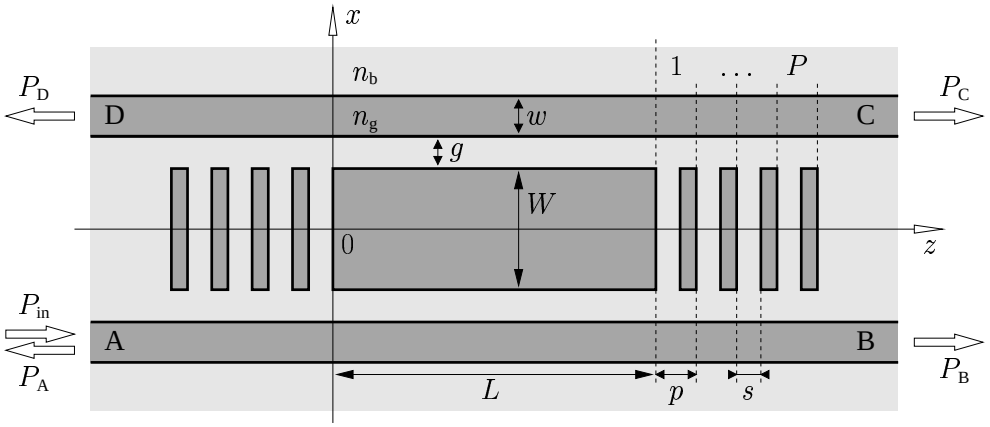


Fig. 1. Grating assisted rectangular resonator: Two parallel waveguide cores of width w are coupled by a cavity of width W and length L, separated by gaps g. Gratings with P periods of length p with a spacing s enclose the cavity. The guiding regions with refractive index n_g are embedded in a background medium with index n_b. Capital letters A to D denote the input and output ports.

* Manfred Hammer, Department of Applied Mathematics, University of Twente, P.O. Box 217, 7500 AE Enschede, The Netherlands. Phone: ++31(0)53/489-3448, Fax: ++31(0)53/489-4833, E-mail: m.hammer@math.utwente.nl

Design strategy

Assuming that the hypothetical device will be realized on the basis of rectangular Si_3N_4 cores (refractive index 1.98) surrounded by a SiO_2 background medium, we fix a common channel thickness of $0.223\,\mu$m. Then the values given in Table 1 correspond to the effective index projection of the realistic 3D structure, at a design wavelength of $\lambda_0 = 1.55\,\mu$m. For simplicity, all considerations are restricted to this 2D model and to TE polarization.

As a starting point of the resonator design we choose the width w of the port waveguides, such that these are single mode in a suitable wavelength region around λ_0; the values of Table 1 lead to an effective mode index $n_{\text{eff}} = 1.540$ at λ_0.

Reasoning along the coupled mode model of Ref. [6], only few (one or two) guided modes of the cavity segment are likely to be relevant for specific standing wave resonances. These modes are to be excited in the cavity; hence, to satisfy the phase matching condition, we adjust W such that the cavity waveguide supports a guided mode that is degenerate with the port fields. In the present case, W should be among the discrete values $(1.0 + j\,1.791)\,\mu$m, for integer j.

As a second condition, pronounced resonances require a reflectivity close to unity for the relevant modes at the ends of the cavity [6]. In contrast to an ordinary high contrast waveguide facet, where two cavity modes are necessary [8], with the present gratings a single cavity mode is sufficient. The corresponding Bragg reflectors can be constructed on the basis of a model of tilted plane wave incidence on a multilayer stack with equivalent refractive index composition. We consider an incidence angle θ that corresponds to the angle of the relevant mode in the cavity, defined by $\cos\theta = n_{\text{eff}}/n_{\text{g}}$. Optimization of the layer stack for the present mode angle of 15.69° at λ_0 leads to the grating parameters p and s as given in Table 1.

To select a suitable cavity width W, we computed single mode reflectivities for Bragg gratings according to the specification of Table 1 and Fig. 1, for $P = 5$ and $W = (1.0 + j\,1.791)\,\mu$m, in each case for incidence of the j-th order mode. Levels of 0.17, 0.21, 0.23, 0.24, 0.25, 0.26 were observed for $j = 1, 2, \ldots, 5$, with the last value already close to the limiting level of 0.28, the reflectivity of a plane wave, incident under an angle of 15.69° on a laterally unbounded equivalent multilayer stack. Obviously the reflectivity is the higher, the larger the fraction of the mode profile is that actually encounters the corrugation of the Bragg reflector. Therefore a width W corresponding to a higher order mode is preferred, (such that the phase matching condition is still sufficient to distinguish the cavity modes, the propagation constants of which become closer for large W). We set W to the value for order $j = 5$ for the present simulations. Fig. 2 shows that in this way indeed a suitable Bragg grating can be designed, with a spectral response that resembles the curve expected from the plane wave model surprisingly well.

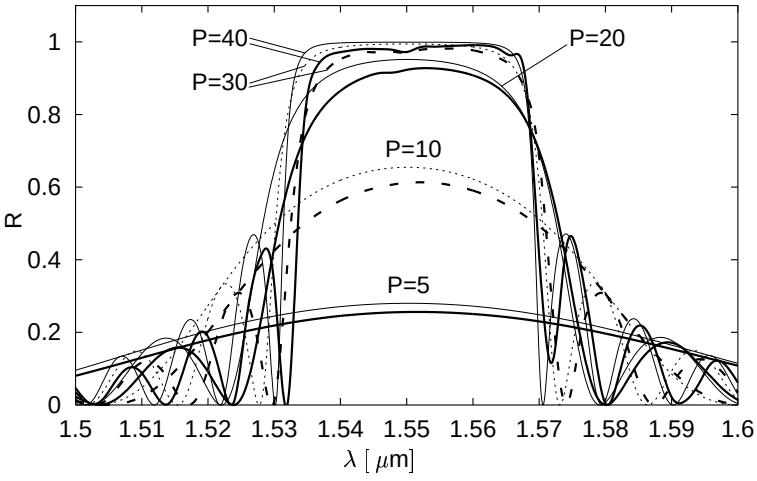


Fig. 2. Reflectivity R of Bragg-reflectors according to the specification of Table 1, versus the vacuum wavelength, for different numbers of grating periods P. The guided 5th order mode is launched in the wide cavity waveguide segment; the thick lines show the relative power levels that are reflected into that specific mode. The thin curves indicate the plane wave reflectivity of an equivalent multilayer stack for wave incidence under the respective mode angle (15.69° at $\lambda = 1.55\,\mu$m).

Given the complex valued amplitude reflection coefficient $r\ \exp \mathrm{i}\varphi$ of the Bragg gratings, a resonance at λ_0 requires the total phase gain along one propagation cycle through the cavity to match an integer multiple of π. This amounts to a condition $L = (m\pi + \varphi)\lambda_0/(2\pi n_{\text{eff}})$ for the cavity length [6], with integer m. Neglecting the wavelength dependence of n_{eff} and assuming a long cavity $m\pi \gg \varphi$, one obtains $\Delta\lambda = \lambda_0/m = \lambda_0^2/(2Ln_{\text{eff}})$ for the spectral distance of two neighboring resonances. L, or m, respectively, is to be selected such that there is a chance for pronounced resonances in the window of high Bragg reflectivity around the design wavelength (m is about 119 and 159 in Fig. 3).

The gap width g is to be determined such that on the one hand there is a sufficient power transfer between the port waveguide and the cavity along the long unfolded light path in case of a resonance, while on the other hand the level of direct, unidirectional coupling (as in a conventional three-guide directional coupler, without a pronounced wavelength dependence) remains negligible. This parameter is selected finally on the basis of numerical experiments.

Numerical results

The design procedure leads to simulation parameters as listed in Table 1. The devices were simulated by means of the mode expansion techniques as described in Refs. [9, 5]; Fig. 3 shows the spectral response obtained in this way. We verified the results using an only recently released commercial simulation tool [10], based on bidirectional eigenmode propagation.

Table 1. Geometrical and material parameters for the simulations of Fig. 3. Including two Bragg reflectors and the cavity, the overall lengths of the devices are 182 μm and 203 μm.

n_{g}	n_{b}	$w/\,\mu$m	$g/\,\mu$m	$W/\,\mu$m	$L/\,\mu$m	$p/\,\mu$m	$s/\,\mu$m	P	$\lambda/\,\mu$m
1.60	1.45	1.000	1.600	9.955	59.860, 79.985	1.538	0.281	40	$\in [1.5, 1.6]$

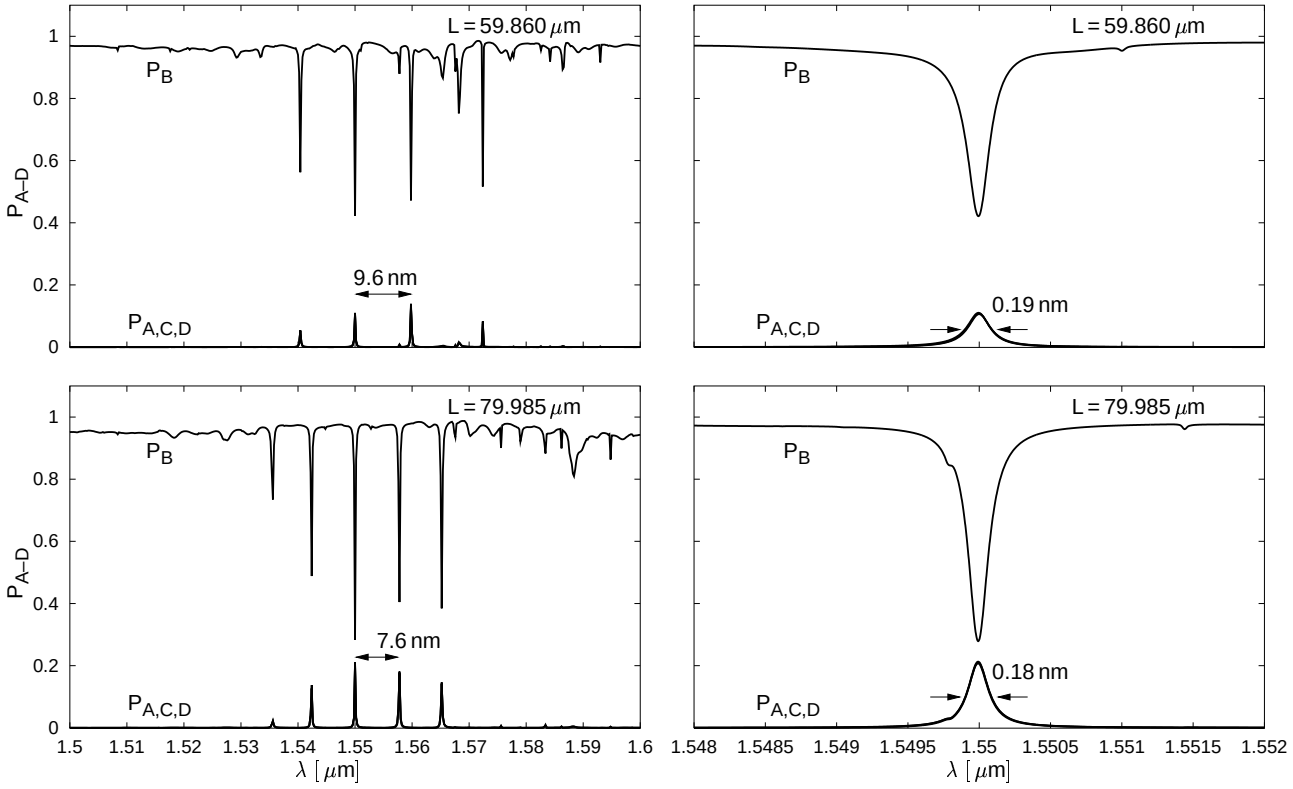


Fig. 3. Spectral responses of resonators according to Fig. 1, with the parameters of Table 1, for cavity lengths $L = 59.860\,\mu$m (top) and $L = 79.985\,\mu$m (bottom). P_{A} to P_{D} are the relative power fractions that are reflected or transmitted into ports A to D. The curves related to P_{A}, P_{C}, and P_{D} are almost completely superimposed.

The resonators are excited in port A by the right traveling guided mode of the lower core. For most wavelengths, the major part of the input power is directly transmitted to port B. Resonant states appear as a drop in P_{B} and a simultaneous increase of the reflected and dropped power fractions P_{A}, P_{C}, and P_{D}. As expected, the resonances are restricted to the range of high reflectivity of the Bragg gratings (cf. Fig. 2). The finesse for the two resonators is 51 (top) and 42 (bottom), here defined as the ratio between the free spectral range and the width at half maximum.

While at resonance the present device distributes the input among all four ports, a filter that properly drops the power into a single output channel can be realized with two cascaded single cavity resonators at a specific distance [4, 5]. The total length of the add-drop filter could be about $500\ \mu$m.

Remarks and conclusion

Based on quite simple design guidelines and moderate numerical means, the former results clearly demonstrate the working principle of the grating assisted rectangular microresonators, at least in terms of numerical simulations. We find the shape of resonances as predicted for high contrast standing wave resonators with finite waveguide segments as cavities, but in the present case with realistic material parameters, at the cost of an increased, but still acceptable length of the devices. Light propagation is oriented along a single axis; hence combination of this concept with an anisotropic electrooptic material for purposes of tuning poses no principal problems.

The design leaves plenty of room for further optimization. Apart from the theoretical limit of equal quarter transmission to all four ports at resonance, this concerns in particular the Bragg reflectors: Modifying the grating with the aim of a narrow, properly positioned bandgap should allow to restrict the spectral response to a single resonance. Alternatively, this could be achieved by means of two slightly different Bragg gratings at both ends of the cavity, adjusted such that their regions of high reflectivity overlap in only a narrow wavelength region. In principle, this should lead to devices with infinite free spectral range and finesse.

The authors would like to thank E. van Groesen, H. J. W. M. Hoekstra, and R. Stoffer for many fruitful discussions on the subject. Financial support by the European Commission (project IST-2000-28018, 'NAIS') and by the Royal Netherlands Academy of Arts and Sciences (KNAW, project 99–WI–44) is gratefully acknowledged.

[1] B. E. Little, S. T. Chu, W. Pan, and Y. Kokubun. Microring resonator arrays for VLSI photonics. *IEEE Photonics Technology Letters*, 12(3):323–325, 2000.

[2] Next-generation active integrated optic subsystems. Information society technologies programme of the European Commission, project IST-2000-28018, http://www.mesaplus.utwente.nl/nais/

[3] S. Follonier, M. Fierz, I. Biaggio, U. Meier, Ch. Bosshard, and P. Günter. Structural, optical, and electrical properties of the organic molecular crystal 4–N,N–dimethylamino–4'–n–methyl stilbazolium tosylate. *Journal of the Optical Society of America B*, 19:1990–1998, 2002.

[4] C. Manolatou, M. J. Khan, S. Fan, P. R. Villeneuve, H. A. Haus, and J. D. Joannopoulos. Coupling of modes analysis of resonant channel add-drop filters. *IEEE J. of Quant. Electr.*, 35(9):1322–1331, 1999.

[5] M. Lohmeyer. Mode expansion modeling of rectangular integrated optical microresonators. *Optical and Quantum Electronics*, 34(5):541–557, 2002.

[6] M. Hammer. Resonant coupling of dielectric optical waveguides via rectangular microcavities: The coupled guided mode perspective. *Optics communications*, 214(1–6):155–170, 2002.

[7] S. Kriswandhi. Simulation of a rectangular optical microresonator using bidirectional eigenmode propagation, 2002. C2V app. note A2002005, http://www.c2v.nl/software/support/appnotes/A2002005.pdf

[8] M. Hammer and E. van Groesen. Total multimode reflection at facets of planar high contrast optical waveguides. *Journal of Lightwave Technology*, 20(8):1549–1555, 2002.

[9] M. Lohmeyer and R. Stoffer. Integrated optical cross strip polarizer concept. *Optical and Quantum Electronics*, 33(4/5):413–431, 2001.

[10] OlympIOs Integrated Optics Software. C2V, P.O. Box 318, 7500 AH Enschede, The Netherlands; http://www.c2v.nl/software/

Photonic Functional Devices Based on a Silica Planar Lightwave Circuit

Koichi Takiguchi
NTT Photonics Laboratories, NTT Corporation
3-1 Morinosato Wakamiya, Atsugi, Kanagawa 243-0198, Japan
taki@aecl.ntt.co.jp

I review our recent progress on photonic functional devices based on a silica planar lightwave circuit. First, I describe lattice-form optical devices for chromatic dispersion slope compensation, and the dynamic equalization of chromatic and polarization-mode dispersion and gain non-uniformity, in high-speed wavelength division multiplexing transmissions. Then, I describe optical signal processing devices for communications that contain label recognition and optical code division multiple access circuits for next-generation optical networks.

Keywords: integrated-optic devices, dynamic compensators, optical signal processing

1. Introduction

Silica planar lightwave circuit (PLC) based devices are widely used in wavelength division multiplexing (WDM) systems because of their superior properties [1]. Optical communication systems are advancing steadily [2]. The bit rate per wavelength is being increased to 40 Gbit/s or more in point-to-point WDM transmissions, and optical networks are progressing toward ring, cross-connect, and packed-switched systems. These advanced optical systems require highly functional optical devices in order to exceed the electrical speed limit. If we are to realize high-speed WDM links, we must develop compensators to deal with the undesirable characteristics of optical fibers, namely, chromatic and polarization-mode dispersion and gain non-uniformity. Lattice-form filters, which comprise cascades of alternating symmetrical and asymmetrical Mach-Zehnder interferometers (MZIs), are suitable for realizing these compensators, because they can achieve various characteristics adaptively and flexibly. After a brief description of PLC fabrication, properties, and development, I report recent advances in these lattice-form filters. In the latter half of this review, I describe optical signal processing devices for next-generation networks, mainly focusing on a label recognition device based on optical digital-to-analogue (D/A) conversion and an optical code division multiple access (CDMA) circuit for the two-dimensional coding of time and wavelength. I shall conclude by commenting on the future development of PLC based functional devices.

2. PLC technology

PLC based circuits are fabricated on a silica on silicon substrate by a combination of flame hydrolysis deposition and reactive ion etching [1]. The typical waveguide bending radius is around 2 to 25 mm, and large-scale integrated circuit chips can be as large as several centimeters square. This fabrication process can provide a uniform refractive index and core geometry, and the propagation loss throughout a large wafer is low (about 0.01 dB/cm). The cross-sectional configuration and the basic properties of the waveguide are summarized in Fig. 1 and Table 1, respectively. We utilize the thermo-optic (TO) effect for precise phase adjustment with an accuracy of better than 0.01π. Hybrid integration with a PLC and active components including lasers, modulators, amplifiers, and detectors is also being vigorously developed [3]. As shown in Fig. 2, PLCs are steadily progressing toward highly functional devices based on the development of basic fabrication, design, and measurement technologies. Arrayed-waveguide gratings (AWGs) utilizing

multi-beam interference are widely used in WDM networks, and their characteristics, including crosstalk, channel number and spacing, are being improved. Lattice- and transversal-form filters are adequate for constructing compensators to deal with undesirable fiber characteristics.

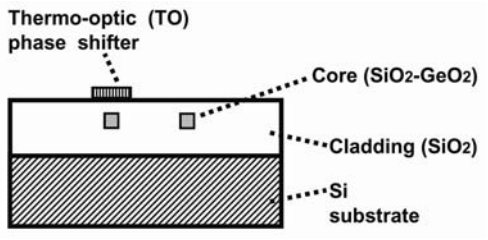


Fig. 1 Cross-section of PLC

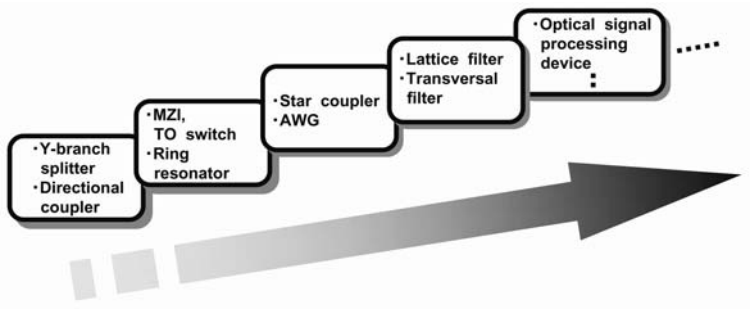


Fig. 2 Progress on PLC devices

Table 1 Properties of PLC

	Low-Δ	Medium-Δ	High-Δ	Super high-Δ
Index difference (%)	0.3	0.45	0.75	1.5 ~ 2.0
Core size (μm)	8 x 8	7 x 7	6 x 6	4.5 x 4.5 ~ 3 x 3
Loss (dB/cm)	< 0.01	0.02	0.04	0.07
Coupling loss (dB/point) *	< 0.1	0.1	0.4	2.0 (~ 0.7 ***)
Bending radius (mm) **	25	15	5	2

* Connection with standard single-mode fiber
** Bending radius where bending loss in a 90-degree arc is 0.1 dB
*** When PLC spot-size converter is used

3. Compensators for undesirable fiber characteristics

3-1. Lattice-form optical filters

Figure 3 shows the basic configuration of a lattice-form optical filter, which comprises a cascade of alternating n+1 symmetrical and n asymmetrical MZIs (n: natural number) [4]. The symmetrical and asymmetrical MZIs function as tunable couplers and delay applying parts, respectively. Such filters are attractive because they can realize several kinds of dynamic compensator for chromatic and polarization-mode dispersion, and gain non-uniformity. Since they confine lights in the MZIs without radiation, their properties are superior to those of transversal-form devices [5] in that their losses and loss variations are intrinsically smaller. The transfer functions of the lattice filters are given by a Fourier series with terms identical to the symmetrical MZIs,

$$T(z)=\sum_{i=1}^{n+1} a_i z^{-i} \tag{1}$$

where z denotes $\exp(j2\pi n_{eff}\Delta Lf/c_0)$ and a_i is the complex expansion coefficient of the series (j: imaginary unit, n_{eff}: effective refractive index of the waveguide, ΔL: length difference between two arms of the asymmetrical MZI, f: frequency, c_0: light speed in a vacuum). By changing a_i, we can

obtain arbitrary and flexible filter characteristics whose performance limits are determined by the number n.

The problem with the lattice filters lies in the difficulty of tuning the MZI phase parameters [6]. Recently, we proposed a novel method for tuning the phases in lattice filters accurately to obtain desired characteristics without the need for monitor couplers, thus reducing both device size and loss [7]. As shown in Fig. 4, our method utilizes an incoherent light and a coherent wavelength tunable laser, respectively, to derive phase information selectively for each symmetrical and asymmetrical MZI. TO phase shifters are then driven using the obtained results.

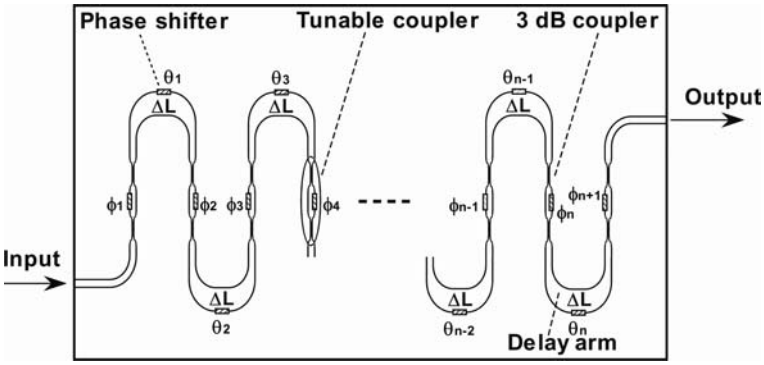


Fig.3 Basic configuration of lattice-form filter

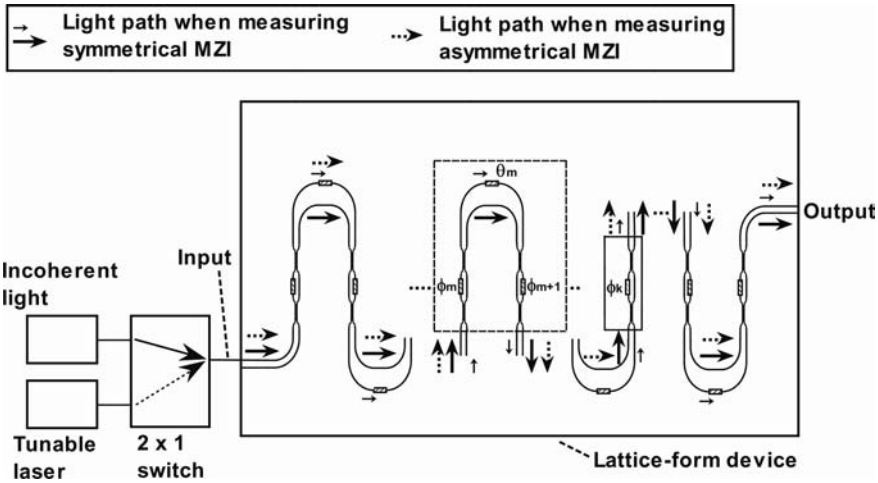
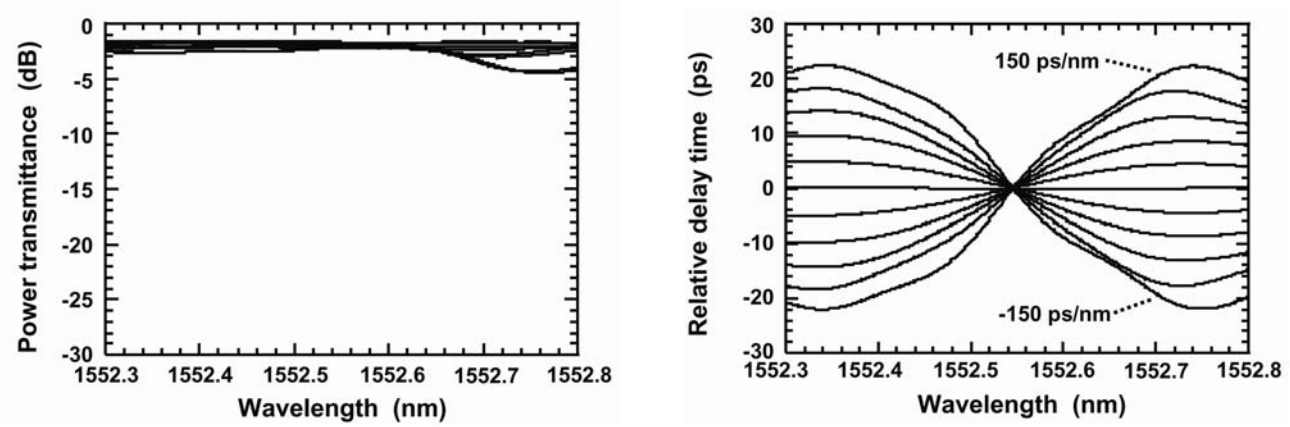


Fig. 4 Experimental setup for measuring relationship between phase and intensity

3-2. Chromatic dispersion compensators

Variable chromatic dispersion compensators are becoming increasingly important in high-speed optical transmission systems with bit rates of 40 Gbit/s or more, where it is essential to compensate adaptively for the various dispersions of installed fibers and the dispersion change caused by changes in the environmental temperature or path differences in optical networks. The allowable dispersion limit is inversely proportional to the square of the bit rate. We realized the first variable dispersion compensator with a lattice configuration [6], and have recently improved its characteristics by adopting the adjustment method shown in Fig. 4 [7]. Figure 5 (a) and (b), respectively, show the measured power transmittance and the relative delay time versus the

wavelength of the compensator (TE mode), whose size, relative index difference (Δ), ΔL, and numbers of symmetrical and asymmetrical MZIs are 33 x 75 mm^2, 0.75 %, 2.067 mm, and seven and six, respectively. The minimum fiber-to-fiber loss was 1.7 dB and the loss deviation was less than 2 dB over the entire band. The dispersion could be varied from –150 to 150 ps/nm every 30 ps/nm over 40 GHz, which can be used for 40 Gbit/s based non return to zero (NRZ) signals. We have also realized a low-loss compensator module with polarization insensitive properties, and confirmed its operation over the entire C-band [8].



(a) Power transmittance (b) Relative delay time

Fig. 5 Measured characteristics of variable chromatic dispersion compensator

The fiber dispersion slope, which generates a different dispersion in each wavelength channel, is also one of the factors that degrade the quality of high-speed WDM transmission systems. However, it has been difficult to compensate stably for the dispersion slope of dispersion shifted fiber (DSF) and non-zero dispersion shifted fiber (NZ-DSF), which are indispensable if we are to achieve large capacity transmissions. We used the lattice configuration

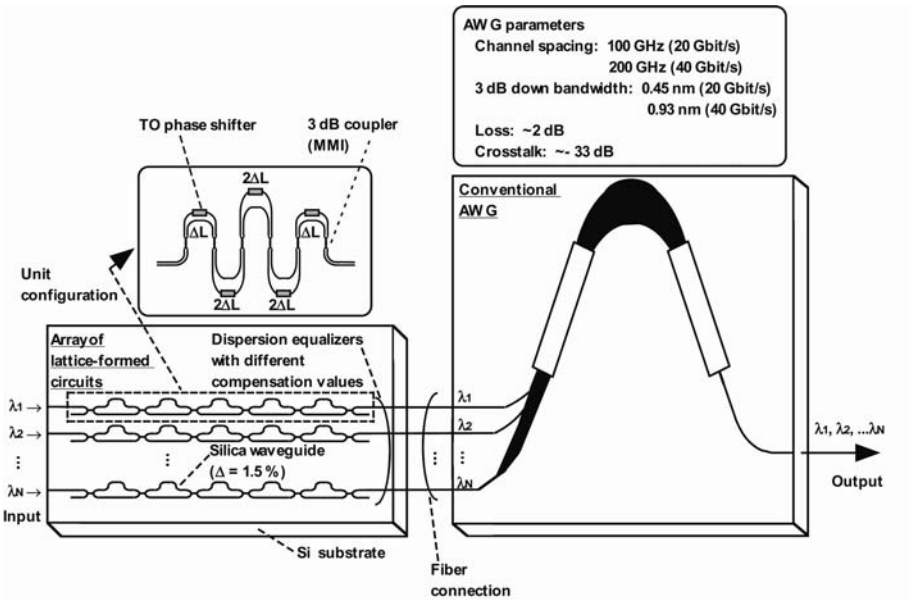
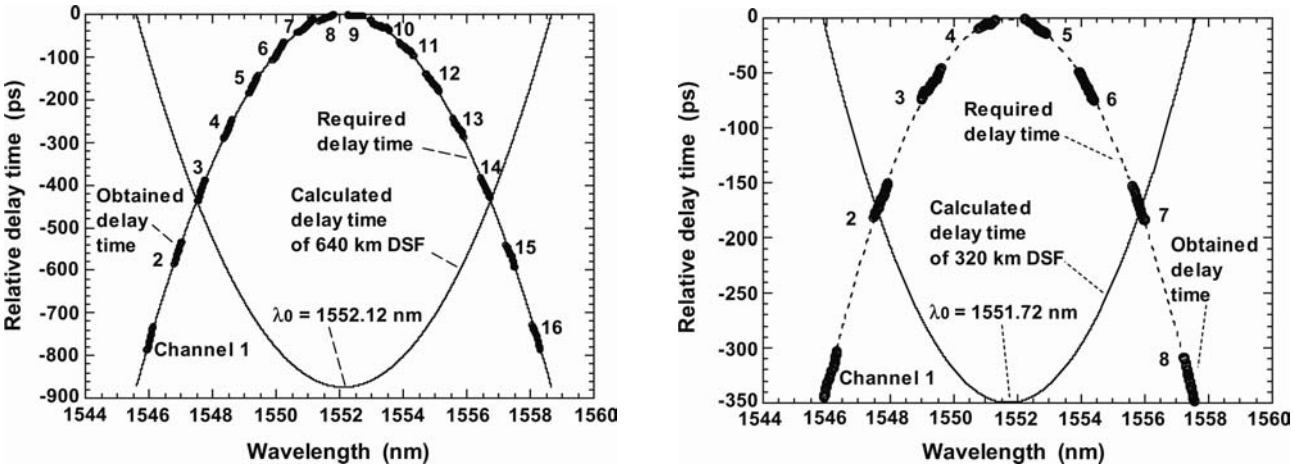


Fig. 6 Configuration and parameters of dispersion slope compensator

to realize slope compensators for N x 20 and 40 Gbit/s transmissions, whose configuration and parameters are shown in Fig. 6 [9], [10]. An array of lattice compensators was integrated on one silica waveguide wafer with a Δ of 1.5 % in order to integrate all the equalizers monolithically. The pre-dispersion compensated wavelength components on the International Telecommunication Union (ITU) grids are combined by a conventional multiplexing AWG and transmitted into the fibers. Each compensator is composed of five asymmetrical MZIs cascaded in series, and each has a different compensation value. Figure 7 (a) and (b), respectively, show the relative delay time obtained with the compensators for 16 x 20 Gbit/s, 640 km and 8 x 40 Gbit/s, 320 km DSFs, respectively. The fiber-to-fiber losses were about 7 dB. We trimmed the waveguide phase shifts using local heating and quenching with a high electrical power to decrease the electrical offset power, and reduced the total power of a few tens of watts by over 80 %. We were able to construct two other configurations flexibly, namely, two AWGs interleaved with a compensator array or a compensator array installed behind a demultiplexing AWG, for in-line or post-dispersion compensation, respectively. In addition, we have been investigating a slope compensator within a single signal bandwidth for ultra high-speed time division multiplexing (TDM) transmissions of more than 100 Gbit/s [11].



(a) 16 x 20 Gbit/s compensator (b) 8 x 40 Gbit/s compensator

Fig. 7 Measured relative delay time of dispersion slope compensators

3-3. Polarization-mode dispersion compensator

Polarization-mode dispersion (PMD) is becoming a serious problem, especially in North America and Europe, where even 10 Gbit/s based transmission is impossible in some installed fibers because their PMD coefficient is a few ps/km$^{0.5}$. The differential group delay and polarization state of the two orthogonal polarization modes vary greatly and randomly with time depending on changes in environmental perturbation. This makes adaptive compensation essential for PMD compensators. Figure 8 shows the configuration and parameters of our PMD compensator [12]. The polarization beam splitters have symmetrical MZI configurations with stress-applying amorphous silicon films. The compensator splits an incoming signal into TE and TM modes at polarization beam splitter (PBS) 1, and converts the polarization of the TM components to TE at half waveplate 1. Phase shifters 1 and 2 change the relative phase between the original TE and TM modes, and tunable couplers 1 and 2 couple the two modes. The two combinations of the phase shifter and tunable coupler balance each other complimentarily, and function as an endless

polarization controller with PBS1 providing the reset operation. The two modes are then introduced into a polarization dependent delay line for compensation and combined again. This compensator is inherently transparent in terms of signal speed. The on-chip loss was 8.2 dB. We evaluated the compensator with a 43 Gbit/s, NRZ signal, and the measured power penalty versus PMD is shown in Fig. 9. The PMD providing a 1 dB power penalty could be enlarged by 5.5 to 12.0 ps by using the PMD compensator.

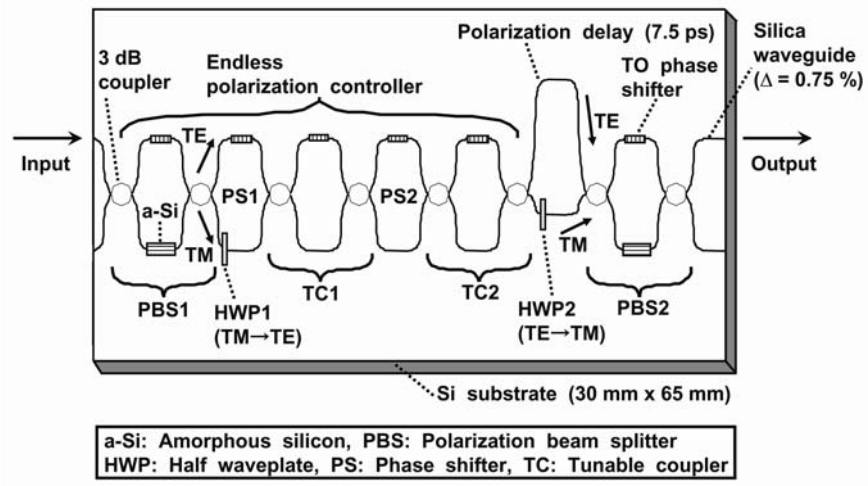


Fig. 8 Configuration and parameters of PMD compensator

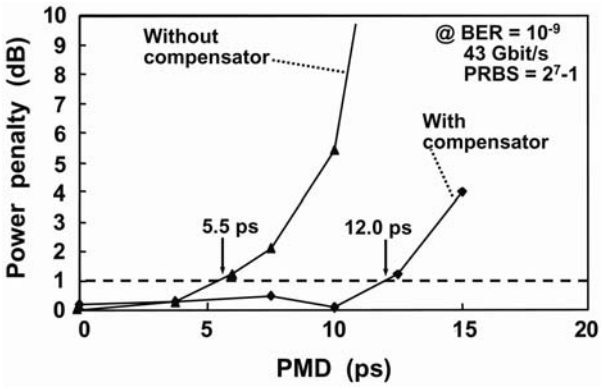


Fig. 9 Measured power penalty versus PMD

3-4. Dynamic gain equalizer

A dynamic gain equalizer is needed to flatten the various gain profiles of optical fiber amplifiers, whose gain spectra may change due to environmental fluctuations or the add/drop of WDM signals. We have developed a dynamic gain equalizer whose configuration is shown in Fig. 10 [13]. The polarization properties were eliminated by the polarization diversity technique. The fiber-to-fiber loss including the diversity device was 9.0 dB. The equalizer comprises ten asymmetrical MZIs with one tunable coupler on either side whose free spectral ranges (FSRs) increase in 8 nm steps from 8 to 80 nm. One output port in each asymmetrical MZI is connected to one input port in the next-stage MZI in series. Although the device in Fig. 10 is not completely lattice-form and its loss properties are somewhat inferior to the configuration in Fig. 3, it is easier to adjust and thus obtain the desired characteristics. Figure 11 shows raw and equalized spectra

for the amplified spontaneous emission (ASE) of an erbium-doped tellurite fiber amplifier (EDTFA). The ASE spectrum is flattened over a 68 nm wavelength range with a 0.9 dB ripple, and we were able to attain a wideband gain equalizer that covers both the C- and L-bands.

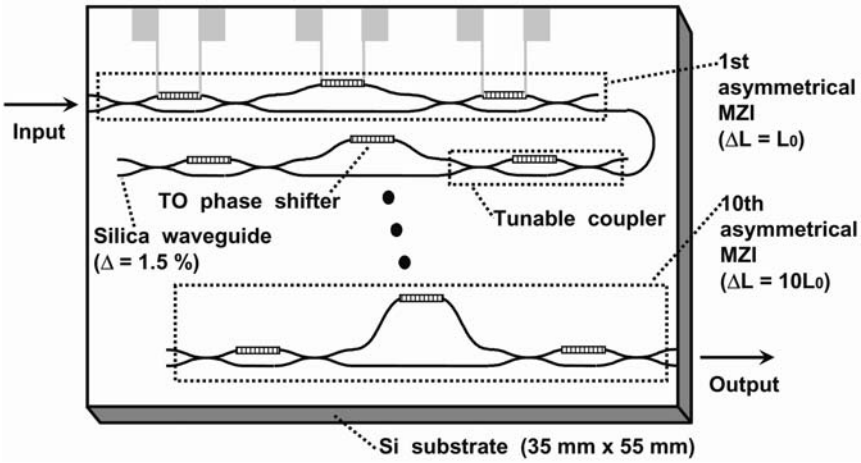


Fig. 10 Configuration of dynamic gain equalizer

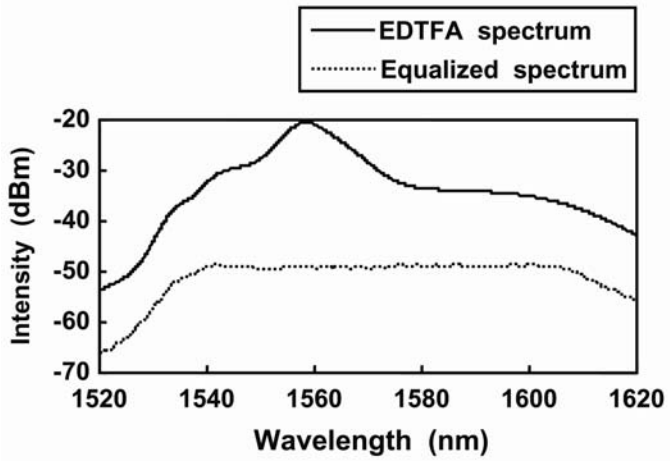


Fig. 11 Raw and equalized spectra of EDTFA ASE

4. Optical signal processing devices for communications

4-1. Label recognition device

Optical label recognition may become one of the key technologies for future photonic routing networks, where each router has to provide an ultra-high throughput exceeding the electrical speed limit. Figure 12 shows a PLC device for recognizing a 10 Gbit/s, four bit pulse pattern based on an optical digital-to-analogue (D/A) conversion technique and its operational principle [14]. The pulse train is split into four replicas that are delayed by an integer multiple of the pulse interval and are weighted by different factors corresponding to each delay time. Then one time slot of the multiplexed output pulses is extracted by gating. Thus the label is recognized by this D/A conversion in the optical region. The total fiber-to-fiber loss was 9.9 dB including a weighting loss of 6.6 dB. Figure 13 shows the measured D/A output versus the pulse patterns. We used 10 Gbit/s,

return to zero (RZ) pulse sequences with a wavelength of 1550 nm for the measurement. The solid curve is theoretical. With the current measurement system, the D/A output has a minimum detection limit due to noise, but the experimental and theoretical data agreed well.

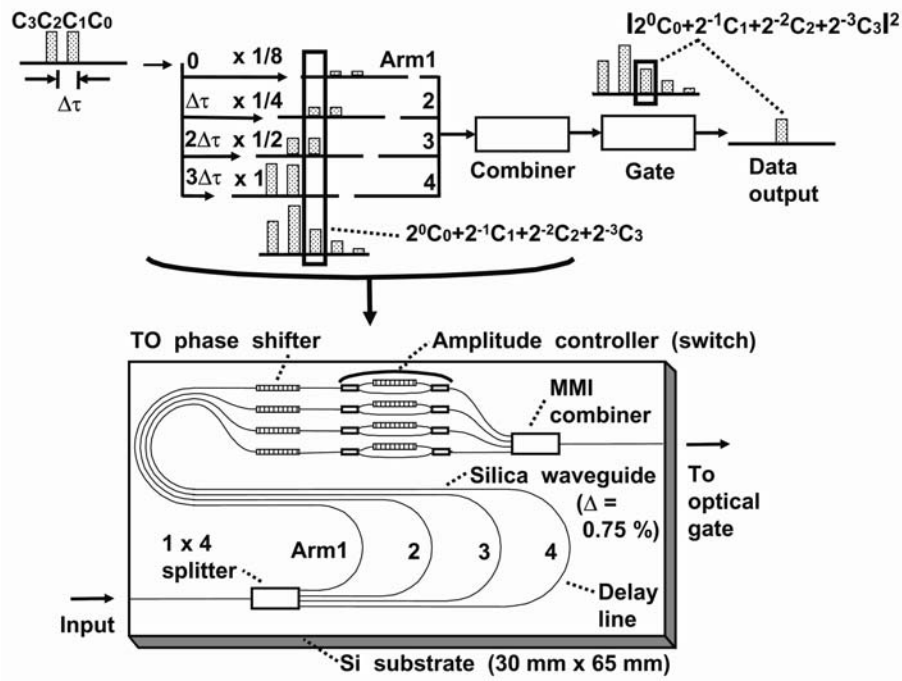


Fig. 12 Configuration and operational principle of optical label recognition device

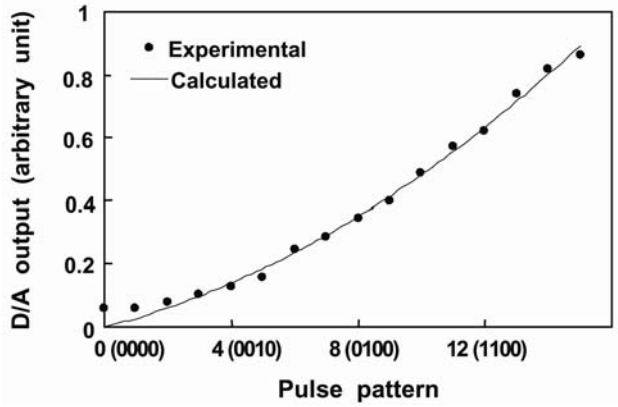


Fig. 13 Measured D/A output versus the pulse patterns

4-2. Optical CDMA device

Optical CDMA (OCDMA) is a multiple access scheme that discriminates channels with differently assigned codes. It is attractive because it can offer asynchronous multiple access and is capable of realizing 1:1 or 1:N access and routing operations in a common channel without optical switches, in addition to allowing flexible bandwidth assignment. We have proposed a novel optical encoder/decoder, shown in Fig. 14, for time-spreading/wavelength-hopping (two-dimensional) OCDMA, that can provide more flexible codes and greater capacity than two schemes utilizing only

time or wavelength coding [15]. We monolithically integrated an AWG and an array of sixteen delay lines. The fiber-to-fiber loss was 9.0 dB. The AWG demultiplexes optical signals with a wide bandwidth into sixteen wavelength components. Each wavelength component is followed by a delay line with an alternate cascade of five symmetrical and four asymmetrical MZIs in series. The symmetrical MZIs with TO heaters operate as switches, and we doubled the arm length differences of the asymmetrical MZIs in order. We can obtain delays of 0 to 15 ΔL, where ΔL was set at 0.542 mm for 10 Gbit/s operation. A millisecond order switching time is sufficient for OCDMA code assignment. This delay line configuration requires the fewest MZIs, and consequently reduces the device size. Each wavelength component experiences a different delay based on the code assignment and is again multiplexed into the output waveguide by the same AWG. We fabricated three devices, two for encoders and one for a decoder, and measured auto- and cross-correlations, namely, recovered and unrecovered properties, respectively, in sixteen one-coincidence code combinations. We encoded the two RZ pulses with a wide bandwidth over a data signal time slot at the two encoders where different code sequences were assigned. The encoded

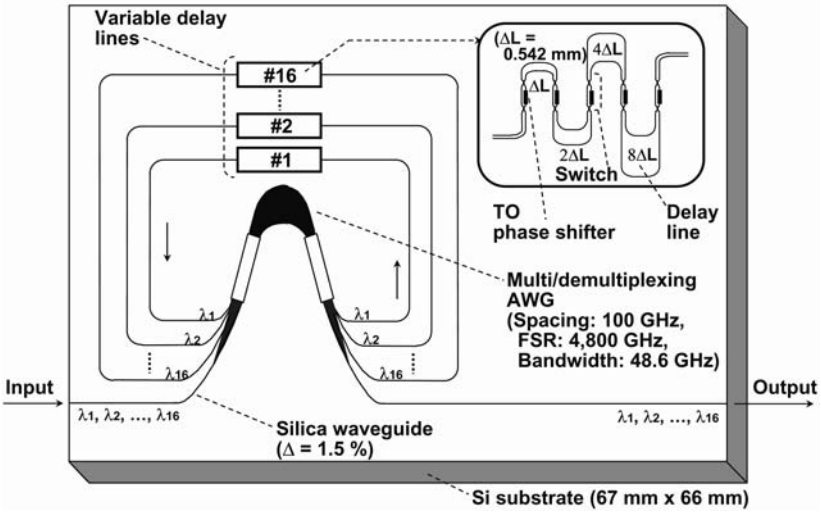


Fig. 14 Encoder/decoder for time-spreading/wavelength-hopping OCDMA

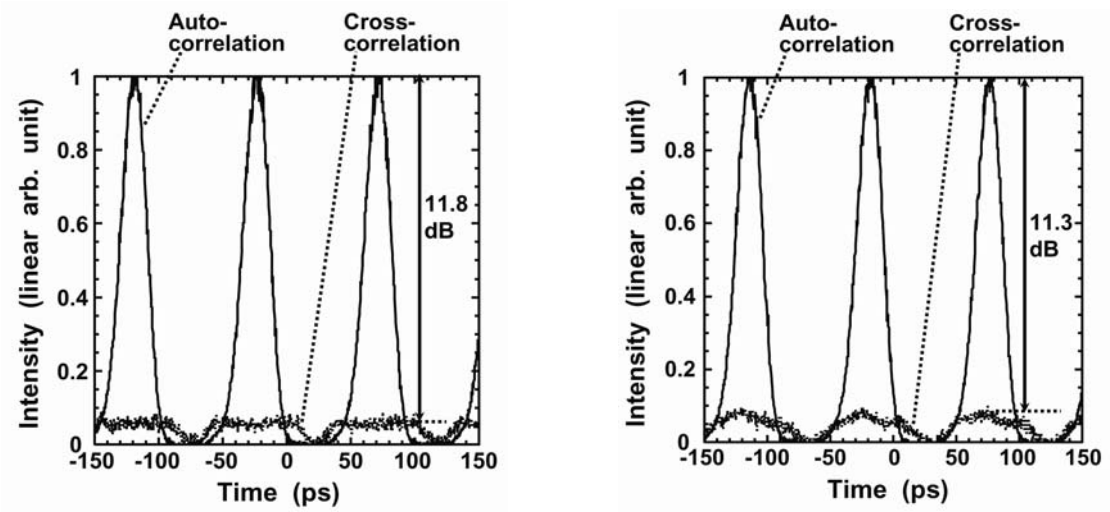


Fig. 15 Measured auto- and cross-correlations

pulses are recovered only when they have a conjugate code sequence that matches that in the decoder, and under this condition the total delay at each wavelength becomes the same through the encoding and decoding procedure. With twelve code combinations, we were able to obtain extinction ratios of more than 10 dB between auto- and cross-correlations, two of which are shown in Fig. 15. The device has other uses including label generation and recognition in photonic routing networks.

5. Summary

I described our recent advances in photonic functional devices based on PLC technology with reference to optical systems requirements. My main focus was on chromatic dispersion and PMD compensators, a gain equalizer, and optical signal processing devices for communications, namely, an optical label recognition device and an encoder/decoder for two-dimensional optical CDMA. I believe that these devices will play important roles in the coming advanced optical networks. Low-loss and stable PLC technologies continue to be used to develop highly functional optical devices, by themselves or in combination with high-speed active devices.

Acknowledgments

The author thanks Dr. T. Maruno and all other members of our laboratories for their continuous encouragement and suggestions, and Dr. K. Okamoto of NTT Electronics Corporation for valuable discussions.

References

[1] T. Miya, *IEEE J. Select. Topics Quantum Electron.*, **6**, 38-45, 2000.
[2] P. Green, *IEEE Commun. Mag.*, **39**, 54-61, 2001.
[3] K. Kato, Y. Tohmori, *IEEE J. Select. Topics Quantum Electron.*, **6**, 4-13, 2000.
[4] K. Jinguji, M. Kawachi, *J. Lightwave Technol.*, **13**, 73-82, 1995.
[5] K. Sasayama, M. Okuno, K. Habara, *J. Lightwave Technol.*, **9**, 1225-1230, 1991.
[6] K. Takiguchi, K. Jinguji, Y. Ohmori, *Electron. Lett.*, **31**, 1240-1241, 1995.
[7] K. Takiguchi, S. Suzuki, T. Shibata, *submitted to Electron. Lett.*
[8] S. Suzuki, K. Takiguchi, T. Shibata, *to be presented at OFC '03*, Atlanta, USA, 2003.
[9] K. Takiguchi, K. Okamoto, T. Goh, *Electron. Lett.*, **37**, 701-703, 2001.
[10] K. Takiguchi, K. Okamoto, T. Goh, *Electron. Lett.*, **37**, 1469-1470, 2001.
[11] K. Takiguchi, S. Kawanishi, H. Takara, A. Himeno, K. Hattori, *J. Lightwave Technol.*, **16**, 1647-1656, 1998.
[12] T. Saida, K. Takiguchi, S. Kuwahara, Y. Kisaka, Y. Miyamoto, Y. Hashizume, T. Shibata, K. Okamoto, *Photon. Technol. Lett.*, **14**, 507-509, 2002.
[13] K. Suzuki, T. Kitoh, S. Suzuki, Y. Inoue, Y. Hibino, T. Shibata, A. Mori, M. Shimizu, *Electron. Lett.*, **38**, 1030-1031, 2002.
[14] T. Saida, K. Okamoto, K. Uchiyama, K. Takiguchi, T. Shibata, A. Sugita, *Electron. Lett.*, **37**, 1237-1238, 2001.
[15] K. Takiguchi, T. Shibata, M. Itoh, *Electron. Lett.*, **38**, 469-470, 2002.

Design of compact spectral slicers based on vertically coupled microring resonators

F.S. Tan, D.H. Geuzebroek, A. Driessen
Lightwave Devices Group, MESA$^+$ Research Institute, University of Twente
P.O. Box 217, 7500 AE Enschede, The Netherlands
t.f.susanto@el.utwente.nl

Spectral slicers for WDM access networks have been designed. The ultra-compact device consists of microring resonators with slightly increasing radius to generate a series of WDM channels. The spectral efficiency of the individual channels can be substantially improved by using a cascade of two identical ringresonators as higher order filter without introducing additional channel crosstalk.

Keywords: spectral slicers, WDM system, vertically coupled microring resonators, spectral efficiency, broadband source, crosstalk

Introduction

Conventional Wavelength Division Multiplexing (WDM) systems utilize narrowband coherent laser diodes as light source. These laser diodes are normally fabricated to be tunable over a wide range of wavelengths. With an increasing number of WDM channels, the number of laser diodes is also increasing and consequently the costs. Especially in the access network the use of spectral slicers is an attracting low-cost alternative as they utilize a single broadband source for creating the desired WDM channels. By using spectral slicers, however, the spectral efficiency and the shape of the optical filter response becomes an issue, as the power budget in these low-cost systems without optical amplifiers is critical. In order to realize spectral slicers, several devices such as Arrayed Waveguide Gratings (AWG) and Waveguide Grating Routers (WGR) [1] have been demonstrated. The drawback of these devices, however, is the relatively large space needed. Microring resonators, on the other hand, offer the possibility to realize ultra-compact devices with a chip area well below 1 mm^2. Moreover, the spectral efficiency of the individual WDM channels can be improved by cascading several microring resonators as a higher order filter with a nearly box-car shape.

In the following a feasibility study of spectral slicers based on microring resonators is carried out in detail. In addition, a discussion is given of the influence of cascading of microring resonators for a single WDM channel to the spectral efficiency.

Vertically coupled Microring Resonators

In order to realize the spectral slicers vertically coupled microring resonators are proposed, see ref. [2]. The cross section of the single device is given in Fig. 1. The straight waveguides are embedded in Plasma Enhanced Chemical Vapor Deposition (PECVD) SiO_2 and function as input and output channels. For an optimal technological realization a relatively thin straight waveguide core should be used to minimize overgrowing effects of the PECVD SiO_2 separation layer (g) due to the straight waveguides underneath. By using high refractive index material such as Low Pressure Chemical Vapor Deposition (LPCVD) Si_3N_4 (n = 1.98), the core thickness of the single mode straight waveguide with a width of 2 μm can be reduced to 140 nm. The ring resonator, also realized in Si_3N_4, has been designed such that the ring is single mode and has only a small phase mismatch with respect to the in- and output waveguides. During fabrication, Chemical Mechanical Polishing (CMP) is applied twice to remove the surface roughness of the intermediate PECVD SiO_2 layers. Fig. 2 shows a typical response of a single MR with 25 μm radius.

Fig. 3 shows the typical propagation loss of a MR as a function of wavelength determined by two ways, first the propagation loss is calculated back for each peak from the spectral responses and

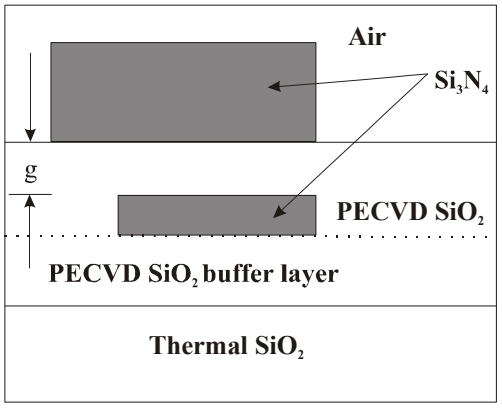


Fig. 1: Schematic cross-section of a vertically coupled waveguide-microring resonator

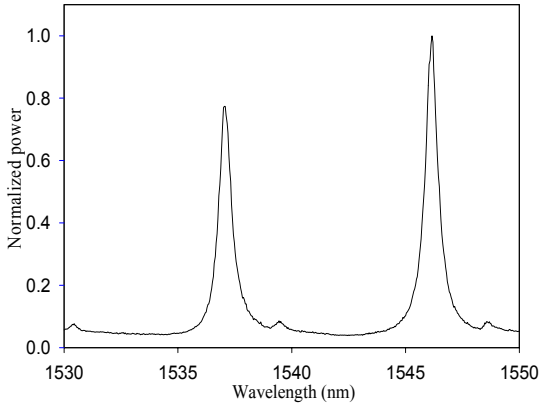


Fig. 2:Spectral response of the drop port of a MR with radius 25 μm

second the propagation loss has been calculated by using quantitative image analysis [3]. The propagation loss increase for longer wavelengths is mainly due to the increasing bending loss of the MR. The ring resonator with the vertically coupled configuration show a relatively low off-resonance on-chip insertion loss, less than 0.1 dB [3].

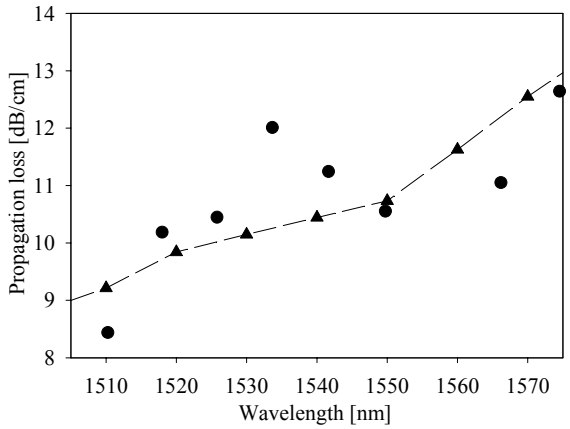


Fig. 3: Propagation loss in a single MR; triangles: scattering and material losses in Fig 4 plus calculated bending loss of the MR; dots: calculated back from the spectral responses

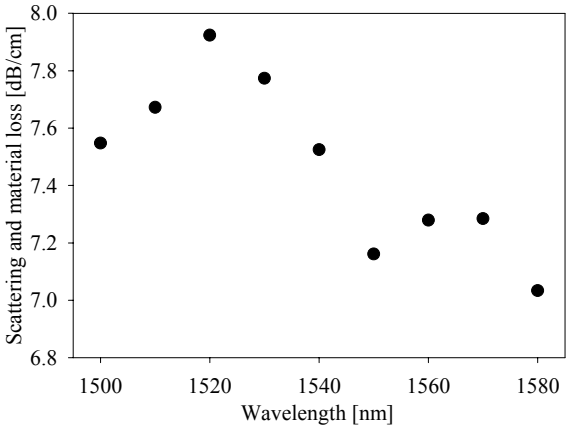


Fig. 4: Scattering and materials losses of waveguide channels with 1μm width and air cladding obtained by measuring the scattered light

The scattering and material loss of the in- and output waveguides is given in Fig. 4. The enhanced loss around 1520 nm is mainly due to the N-H overtone vibration, typically for as deposited PECVD SiON [6], [7]. In principle, by annealing the sample at a temperature of 1150 ^{o}C the maximum loss can be reduced to about 0.6 dB/cm [7].

Design of Spectral slicers devices

The spectral slicers are designed to be a part of a WDM transceivers for the access network as proposed in [8], [9]. Fig. 5 shows schematically its working principle. The broadband infrared source is fed to the input port of the spectral slicer made of a number of microring resonators with slightly different ring radius for selecting the desired part of the source spectrum. The radius of the

individual ringresonators (around 25 μm) is critical as an increase of 12.5 nm is sufficient to select an adjacent channel with 100 GHz channel spacing. In order to have a certain central wavelength based on the ITU grid, tuning can also be applied as demonstrated in [10].

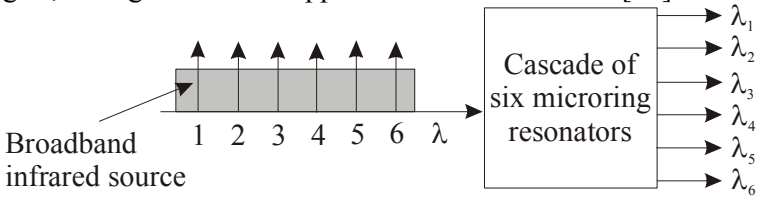


Fig. 5: Working principle of the microring resonators as spectral slicers with a broadband infrared source

For tuning purposes, a cladding layer such as polymers should be put on top of the microring resonators to allow efficient local heating by electrodes on top of the ring.

In the application of spectral slicers the spectral efficiency, which is the selected part of the power spectrum compared to the power spectrum in the same wavelength range of the source is becoming critical. Cascadation of at least two microring resonators in a single WDM channel can substantially improve the spectral efficiency. Fig. 6 shows schematically the layout of the spectral slicers with single ring resonator (S1 with radius 25 μm and S2 with radius 25.0125 μm) and cascade of two identical ring resonators (D1 and D2). Fig. 7 shows the simulation results of drop responses for a single and a cascade of two ring resonators with different ring radius.

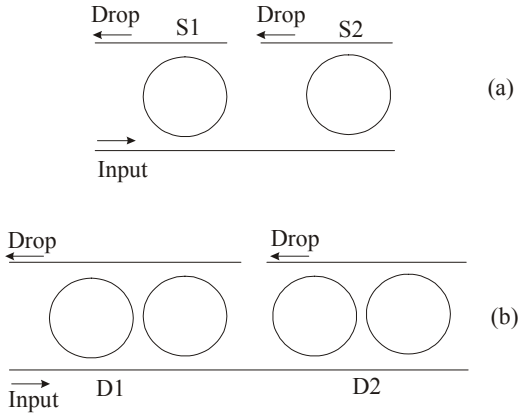


Fig. 6: lay-out of a two-channel spectral slicer based on microresonators: *S1: single ring resonator with radius 25 μm; S2: single ring resonator with radius 25.0125 μm; D1 and D2: set of ring resonators when S1 and S2 are cascaded by two identical ring resonators*

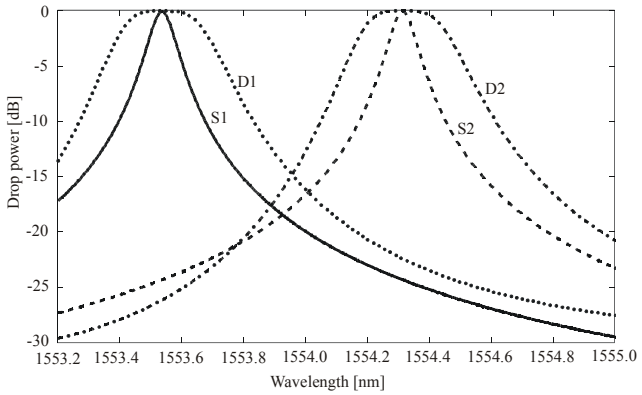


Fig. 7: Drop port responses of a microring resonator based two channel spectral slicer; S1 and S2 curves obtained with single ring resonator ; D1 and D2 obtained with the double ring resonators, see also Fig. 6

Table 1 shows the parameters obtained from simulations for a two channel spectral slicer based on single or double ring resonators for each WDM channel. The crosstalk level of the single ring resonator response is –25 dB while for double ring resonator is –27 dB. In order to maintain the crosstalk level at –25 dB, the spectral efficiency of the selected WDM channel is relatively low for the single microring resonator due to the Lorentzian shape of the response. Cascading of at least two microring resonators in a single device results in a box-like shape response [10], [11]. By increasing the coupling factor of the double ring resonators with respect to the single ring resonator,

the response of the double ring resonators can be broadened without deterioration of the crosstalk level. In this way, the spectral efficiency of the WDM channel can be improved by 240%.

	Radius (μm)	Coupling factor	Propagation loss (dB/cm)	Crosstalk (dB)	Spectral efficiency
Single ring	25 and 25.0125	0.017	2	-25	0.18
Double ring	25 and 25.0125	0.04	2	-27	0.43

Table 1: Summary of the parameters of a microring resonator based spectral slicer obtained by simulations

Considering a realistic launch power of 1 mW/ channel an estimated output power of the spectral slicer per channels is –7.4 dBm for single ring and –3.7 dBm for double rings. If the receiver sensitivity is –26 dBm then the power budget is 18.6 dB for a single ring and 22.3 dB for a double ring spectral slicer.

Conclusion

A feasibility study of microring resonators as spectral slicers has been carried out in detail. Cascading ring resonators in a single WDM channel can substantially improve the spectral efficiency. The shift of the resonant wavelengths can be obtained by changing the ring radius of the microring resonators. In order to fit the central wavelengths to the ITU grid, probably thermal tuning should be applied.

Acknowledgment

This work has been carried out within the EC funded IST project NAIS, Next-generation Active Integrated optics Subsystems, IST-2000-28018.

[1] D.K. Jung, S.K. Shin, C.H. Lee, Y.C. Chung, *Photon. Technol. Lett.* **10**, 1334-1336, 1998
[2] D.J.W. Kunder, E. Krioukov, F.S. Tan, T. van der Veen, H.F. Bulthuis, G. Sengo, C. Otto, H.J.W.M. Hoekstra, A Driessen, *Applied Physics B*. **73**, 603-608, 2001
[3] F.S Tan, D.J.W. Klunder, G. Sengo, H. Kelderman, A. Hollink, H.J.W.M. Hoekstra, A. Driessen, *submitted to JNOPM*
[4] F.S Tan, D.J.W. Klunder, H.F. Bulthuis, G. Sengo, H.J.W.M. Hoekstra, A. Driessen, *Proc. ECIO*, 489-492, 2001
[5] D.J.W. Klunder, F.S Tan, E. Krioukov, T. van der Veen, H.F. Bulthuis, G. Sengo, C. Otto, H.J.W.M. Hoekstra, A. Driessen, *Proc. ECIO*, 485-488, 2001
[6] K. Wörhoff, Paul V. Lambeck and Alfred Driessen, *J. Lightwave Technol.* **17**, 1401-1407, 1999
[7] M.G. Hussein, K. Wörhoff, C.G.H. Roeloffzen, L.T.H. Hilderink, R.M. de Ridder and A. Driessen, *Proc. LEOS Benelux Chapter*, 265-268, 2001
[8] Next-generation Active Integrated optics Subsystems (NAIS), project EC-IST-2000-28018, www.mesaplus.utwente.nl/nais
[9] A. Driessen, D.H. Geuzebroek, D.J.W. Klunder and F.S. Tan, *Proc. LEOS Benelux Chapter*, 25-28, 2001
[10] D.H. Geuzebroek, E.J. Klein, H. Kelderman, F.S. Tan, D.J.W. Klunder, A. Driessen, *Proc. ECOC*, Paper 4.2.5, 2002
[11] Y. Yanagase, S. Suzuki, Y. Kokubun, S.T. Chu, *J. Lightwave Technol.***1** , 1-5, 2002.

Multimode arrayed waveguide grating-based demultiplexers for short-distance communication

S. Musa, A. Borreman, A. A. M. Kok, M. B. J. Diemeer, and A. Driessen
Lightwave Devices Group, MESA+ Research Institute,
University of Twente, P.O. Box 217,
7500 AE Enschede, The Netherlands, e-mail: s.musa@el.utwente.nl

Abstract: A multimode fiber-matched arrayed waveguide grating demultiplexer is presented based on multimode waveguides in the array section. The device, which can be used in short-distance communication, has been realized using low-cost polymer planar waveguide technology.

Keywords: AWG, multimode waveguide, polymeric waveguides, SU-8.

I. Introduction

Multimode fiber and multimode planar waveguide technologies provide robust and very cost-effective solutions in broadband local area networks (LAN's). This major advantage, however, is hindered by the drawback that the bandwidth of the multimode fiber is limited by modal dispersion in contrast to that of the single mode fiber. Of the many schemes proposed to increase the transmission capacity of the multimode fiber-based LAN's, wavelength division (de-)multiplexer (WDM) is the most promising [1].

Multimode fiber-matched WDM represents a serious challenge because of the competition between modal and spectral dispersion. The fabrication of these devices also poses a formidable difficulty, especially due to the need of very low-cost production technologies. A number of multimode fiber-matched WDM has been developed using conventional diffraction gratings [2] or dielectric filters in different design configurations [1].

In this paper we present a novel design of multimode fiber-matched array waveguide grating (AWG) demultiplexer. The design, which utilizes, for the first time, multimode waveguides as array channels has many advantages over other demultiplexers as it can be easily fabricated in a single mask process using low-cost polymer waveguide technology.

After explaining the device principle the design will be given. The fabrication and characterization results will be presented and discussed in section IV. In the last section conclusions will be given.

II. Principle of operation

In Fig. 1a a schematic layout of an array waveguide grating demultiplexer is given. It consists of input and output waveguides connected to a dispersive array of waveguides through two slab couplers. The array is designed in such away that there is a constant length difference between successive waveguides given by

$$\Delta L = \frac{m\lambda_c}{N_{eff,c}} \tag{1}$$

where m is the order of the grating, λ_c is the central wavelength of the demultiplexer, and $N_{eff,c}$ the effective refractive index of the mode in the array channels at λ_c. For the time being we assume that the array channels are single mode. Light propagating at λ_c through the array will arrive with a common phase front at the end of the array and consequently focus on the image plane. When the wavelength is

shifted to $\lambda_c+\Delta\lambda$ there will be a linear increase in the phase across the array and the wavefront will be tilted. From Fig. 1b the tilt angle can be inferred to be (see also Refs. [3,4])

$$\theta = \left(\frac{\lambda_c + \Delta\lambda}{N_{eff}} - \frac{\lambda_c}{N_{eff,c}} \right) \frac{m}{d_a} \tag{2}$$

where d_a is the pitch of the array at its aperture. By placing waveguides at the image plane different wavelengths can be selected.

When the array channels are multimode there will be various modes propagating with different speeds in these waveguides. Each of these modes will construct a common wavefront at the end of the array, which is tilted with respect to that of fundamental mode and thus focuses on a different position in the image plane. The maximum tilt angle between the wavefront of the fundamental modes and that of the highest order modes in the array can be obtained from Eq. (2) to be:

$$\Delta\theta_{md} = \left(\frac{\lambda_c}{N_{eff,jmax}} - \frac{\lambda_c}{N_{eff,0}} \right) \frac{m}{d_a} \tag{3}$$

where $N_{eff,0}$ and $N_{eff,jmax}$ are the effective refractive indices of the fundamental and highest order mode, respectively. For a realistic design of multimode demultiplexer $\Delta\theta_{md} << \theta$. This can be obtained by using low dispersion gratings, i.e. small m-values, and large spectral channel separation $\Delta\lambda$.

III. Design

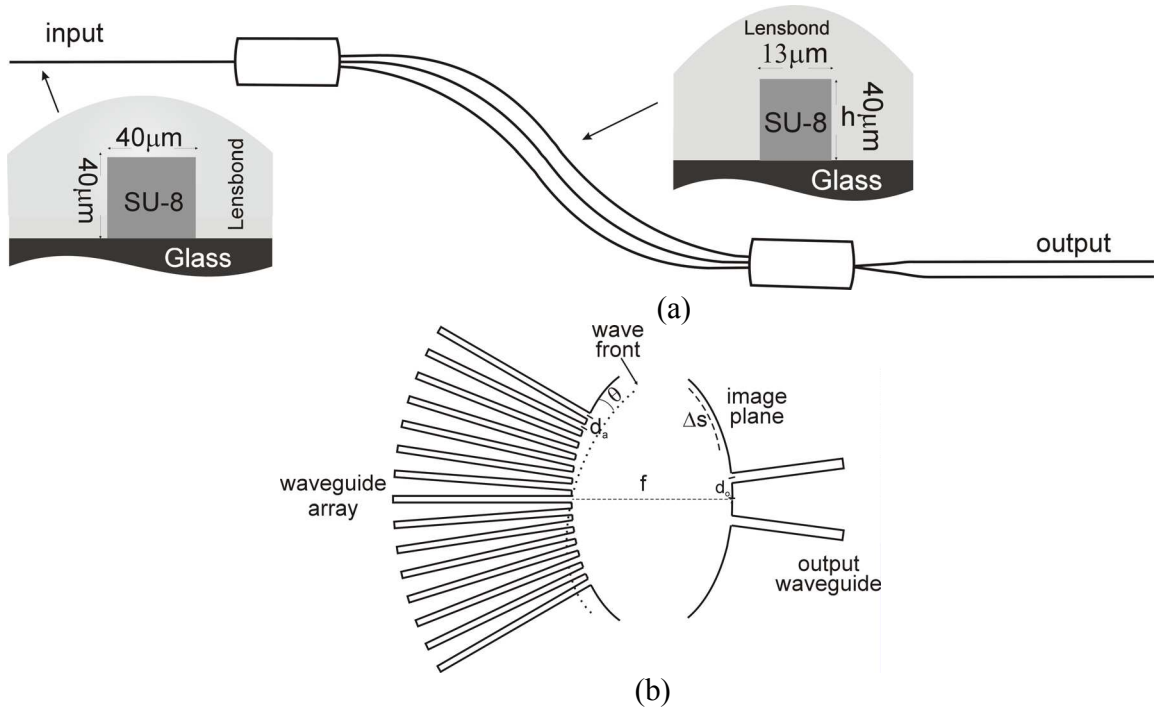


Fig. 1: (a) Layout of a broadband 1 x 2 AWG with the chosen layer structure. The inserts show the cross section of the waveguide structures.(b) schematic illustration of the output star.

We have designed a 1 x 2 multimode fiber-matched broadband AWG-demultiplexer using highly multimode rectangular waveguides as array channels. In Fig. 1a the basic layout and the waveguide

structures of the 1 x 2 demultiplexer are given. The input and the output waveguides are multimode with cross sections of 40 x 40 μm^2 and NA = 0.2. This cross section dimensions and numerical aperture facilitate good coupling to standard multimode fiber with Ø = 50 μm. The array design is based on the anti-symmetrical arrangement [3] for it can be used for demultiplexers with very low dispersion. For the array channels we have used multimode waveguides with cross sections of 13 x 40 μm^2.

In our design we have chosen a channel separation of 100 nm at λ_c = 790 nm. The distance between the two output waveguides is 55 μm and the slab focal length 6.52 mm. The array consists of 16 channels and is operating at a grating order of m = 3. The pitch of the array at the aperture is set to 19 μm.

IV. Fabrication and characterization

The device was fabricated in polymer waveguide technology using the photo-delineation method. The waveguide structure consists of SU-8 photo-resist having a refractive index of 1.58 at λ = 800 nm as a core layer deposited on 1 mm-thick borosilicate substrate with refractive index of 1.47 at λ = 800 nm. For the upper cladding an epoxy called Lensbond mixed with 9-vinylcarbazole (98%) was used. The refractive index of the epoxy is 1.565. Details of the fabrication process can be found in [4,5].

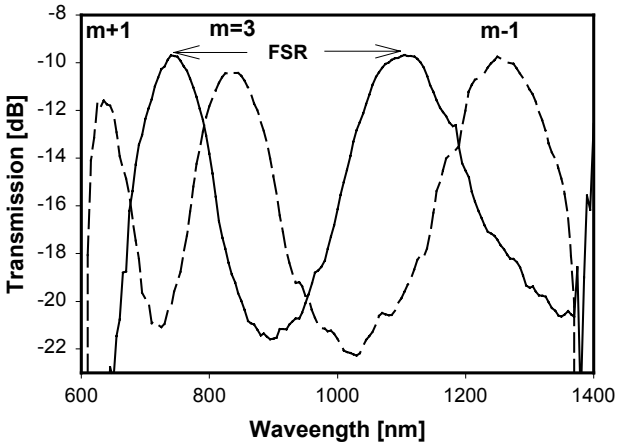


Fig. 2: Transmission spectrum of 1 x 2 AWG-demultiplexer with highly multimode array channels. The transmission is determined with respect to a straight multimode channel waveguide with the same length as the AWG. The two lines (solid and dashed) are the responses obtained at the two output ports.

Optical characterizations of the devices were done using the end-fire coupling method. In the setup a 50/125 μm graded-index multimode fiber was used to couple light in and out of the device. The spectral response of the device was measured using a halogen lamp as a light source and a spectrometer.

Fig. 2 shows the spectral response of the 1 x 2 demultiplexer operating at a central wavelength λ_c = 790 nm. The measured channel spacing, $\Delta\lambda$ = 100 nm and the free spectral range, $\Delta\lambda_{FSR}$ = 395 and 197.5 nm at the longer and shorter wavelength side, respectively, are in good agreement with the designed values. In the figure the response due to orders next to the deign order (m = 3) are also shown. The obtained excess losses are ~ 9.5 dB and the channel cross-talk is about – 9 dB. The largest

contribution to the excess loss is probably originated at the slab to array interface. In the ideal case the slab-to-array losses is calculated to be ~ 2.85 dB for a designed gap width of 6 μm between the array channels. The extra measured excess losses are due to irregularities in the gap widths and to the fact that the designed array aperture is smaller than what is required for capturing all the light from the input waveguide. The designed array aperture, θ_a = 0.085 radians, is much smaller than what is predicted using the numerical aperture of the multimode input waveguide, being 0.25 radians. We have also observed that there is significant amount of power lost to the neighboring orders. As can be seen from Fig. 3, the power coupled into the adjacent orders is obviously much higher than what is expected from the design, being only 0.002 dB. This unexpected coupling to undesired orders of the grating might also be due to coupling between the array waveguides caused by irregularity in the widths of the gaps between the channels. The cross-talk is mainly influenced by modal dispersion, the width of the output waveguide, and/or fabrication irregularities. The measured line width is much broader than what is expected from modal dispersion. This increased broadening of the line width could be caused by irregularity in the opening of the gaps between the waveguides at the array apertures and especially by spectral broadening induced by the large width of the in- and output waveguides.

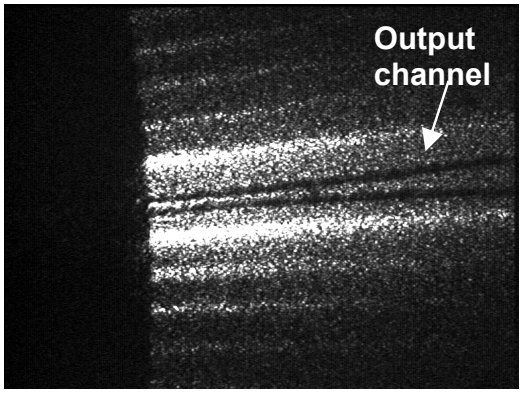


Fig. 3: Optical microscope picture of the curved image plane as schematically given in the right part of Fig. 1 (b) showing the different grating orders of an AWG-demultiplexer with multimode array channels. The two dark lines are the output waveguides.

The polarization dependence of the demultiplexer was measured by launching TE and TM polarized light into the device. The results show that there is no spectral dependence on the polarization and the polarization dependence loss of the device is negligible within the experimental error.

V. Conclusions

Multimode fiber-matched AWG-demultiplexer, employing multimode waveguides as array channels, has been demonstrated. The device was fabricated in low cost polymer waveguide technology. The measured excess loss is 9.5 dB and the cross talk is – 9 dB. The device performance can substantially be improved by further optimizing the design and the fabrication process.

References:

[1] B. E. Lemoff, L. B. Aronson, and L. A. Buckman, *Hewlett-Packard Journal*, pp. 42-52, December, 1997.

[2] T. Suhara, J. Viljanen, and M. Leppihalme, *Appl. Opt.*, **vol. 21, no. 12**, pp. 2195 –2198, 1982.

[3] R. Adar, C. H. Henry, C. Dragone, R. C. Kistler, and M. A. Milbrodt, *J. Lightwave Technol.,* **11(2)**, pp. 212-219, 1993.

[4] S. Musa, Ph.D. thesis University of Twente, 2003.

[5] A. Borreman, S. Musa, A. A. M. Kok, M. B. J. Diemeer, A. Driessen**,** *Proceedings of the 7th IEEE/LEOS Benelux chapter symposium,* pp. 83-86, Amsterdam, The Netherlands, 2002.

Planar Lightwave Circuits for Polarisation Mode Dispersion and Residual Chromatic Dispersion Compensation at 40 Gbit/s

Rudolf Wessel, André Heid
Alcatel SEL AG, Research & Innovation, Lorenzstr. 10, 70435 Stuttgart, Germany
Rudolf.Wessel@alcatel.de

Fred Buchali, Henning Bülow, Jörg Gehler
Alcatel SEL AG, Research & Innovation, Holderaeckerstr. 35, 70499 Stuttgart, Germany

Lattice Filter type planar lightwave circuits on silica on silicon have been developed for the use in PMD and Residual chromatic dispersion compensation schemes at 40 Gbit/s. A five stage MZI-filter allowed to cover a dispersion range of 145 ps/nm and the compensation of several channels within a wavelength band of 14 nm. PMD mitigation of higher order has been demonstrated using a lattice filter with integrated Polarisation Beam Splitter.

Keywords: planar lightwave circuits, polarisation mode dispersion, residual chromatic dispersion compensation

Introduction

Temporal variations of residual chromatic dispersion (RCD) and polarisation mode dispersion (PMD) in future ultra high bit rate optical transmission systems are demanding an adaptive receiver design which ensures the required quality of service. Optical filters in planar lightwave circuits (PLC) are well suited within these receivers as they are potentially cheap and can be integrated together with demultiplexers and power monitors.

Tuneable chromatic dispersion compensation with lattice filter type PLCs can exploit the periodical transfer function allowing the compensation of several WDM channels simultaneously. Such RCD compensators in silica on silicon have been demonstrated at a low bit rate of 2.5 Gbit/s [1]. Recently, dispersion compensation of +/- 120 ps/nm at 40 Gbit/s has been shown with 13 Mach-Zehnder interferometers (MZIs) in SiON [2]. We propose here a shorter lattice filter in silica on silicon which has the advantage of a low polarisation dependence and of the possibility for a smooth continuous adaptation.

A first order PMD compensator for 40 GBit/s in silica on silicon has been published before [3]. In literature it is well known that higher order PMD compensation is superior to PMD compensation of first order. We propose here a so called “higher order canceller” design which suppresses the undesired polarisation component in a second stage [4]. This higher order canceller comes together with an easier design to reduce the complexity and the loss of the compensator.

Design and Fabrication

Both designs have been optimised aiming maximum efficiency while minimising the device complexity. The RCD compensator is composed of 5 MZI stages as shown in Fig. 1. Opposite to the filters reported so far [1,2], an alternative filter approach was proposed, which is based on uneven delays τ and 2τ in the MZI arms [5]. The delay time τ of 5.4 ps was maximised irrespective of resulting free spectral range (FSR). Simulations predict a continuous change of chromatic dispersion by parallel tuning of the two optical phase shifters of the second and fourth symmetrical MZI (called tuneable couplers). Wavelength tuning and compensation of fabrication induced imbalances can be controlled by the three phase shifters of the asymmetric MZIs. The wavelength can be monitored with the tap couplers feeding light out of the two tuneable couplers.

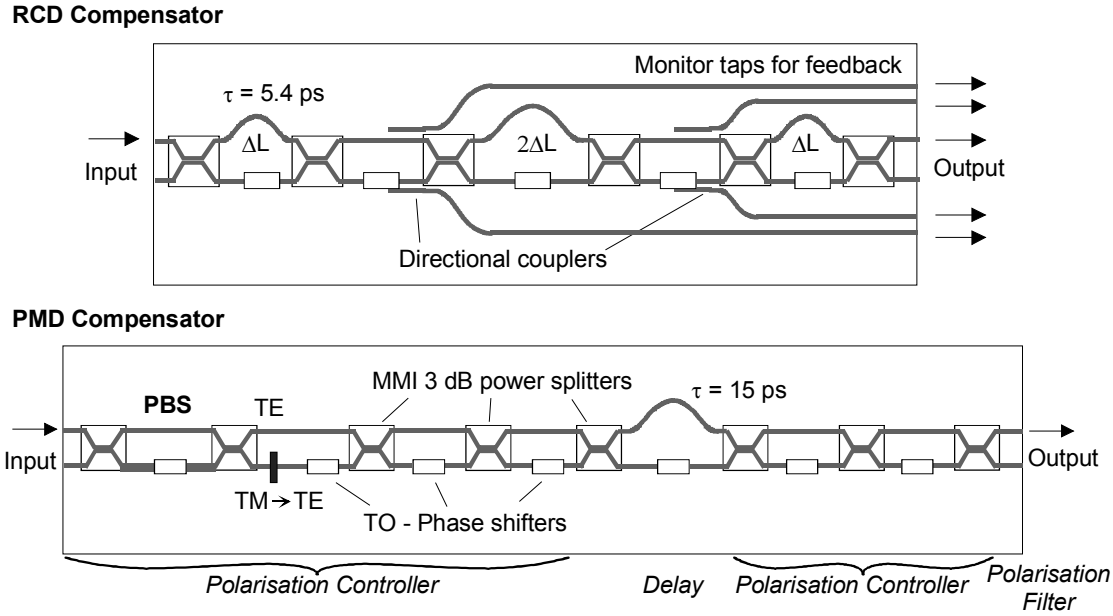


Fig. 1: Design of Residual Chromatic Dispersion Compensator and PMD compensator

For PMD compensation it is mandatory to integrate polarisation beam splitters (PBS) and TE-TM mode converters [3]. Together with the subsequent MZI chain a polarisation controller is built up. We simplified the design of [3] according to [6] from a 4 stage to a 3 stage lattice filter allowing endless polarisation control as well. The main difference to [3] is that instead of another mode converter and a polarisation beam combiner after the delay section here another MZI chain is used. This second lattice filter serves as a second polarisation controller which works together with a quasi natural polarisation filter due to the fact that only one polarisation component is coupled out. In this way an undesired polarisation component can be suppressed in the second stage and the performance is superior to a first order PMD compensator [4]. Moreover, this design allows to reduce the number of lossy TE-TM mode converters. The polarised output may be of advantage if polarisation dependent receivers are applied especially for nonlinear receiver designs for optical 3 R regeneration.

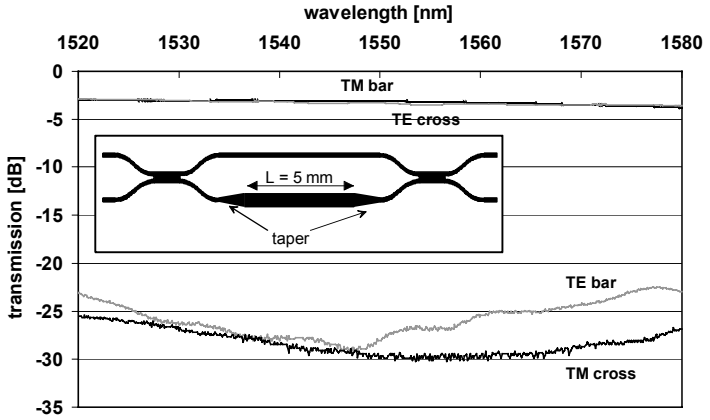


Fig. 2: Transmission of integrated polarisation beam splitter; inset: configuration

The compensators have been realised as silica on silicon planar lightwave circuits with 1% refractive index contrast. Linear arrangements of the MZIs have been chosen leading to chip sizes of 58.6 mm x 4.5 mm and 67 mm x 4.5 mm of the RCD and PMD compensator, respectively. Multi-mode interference (MMI) couplers used for 3 dB power splitting exhibit small polarisation dependence and insensitivity versus variations of technology parameters. The tap output coupler of the monitor output ports have been realised with directional couplers with a coupling efficiency of about 5%. Chromium electrodes have been deposited to build thermo-optical phase shifters. Commercially available lambda half plate with a thickness of 14.5 μm has been inserted in

the PMD compensator chip for TE-TM mode conversion. The integrated PBS has been realised similar to [7] employing the stress induced birefringence of a broadened waveguide in an MZI. In Fig. 2 the design of the PBS and the measured performance is shown. With a waveguide width broadening of 9 μm and a length of the broadened waveguide of 5 mm a polarisation extinction ratio better than 20 dB in a broad wavelength range of 50 nm has been obtained. The fibre to fibre insertion loss of the RCD and the PMD compensator chips was measured to be 3.5 dB and 6.2 dB, respectively, where the loss of the PMD compensator was slightly higher than expected.

System Experiments

The RCD compensator was tested in a system experiment consisting of a 40 Gbit/s NRZ ETDM transmitter, a CD-emulator made of 8 fibre spools with a dispersion step of 30 ps/nm and a 40 Gbit/s ETDM receiver with eye opening monitoring. An automatic adaptation routine to control the phase shifters of all five stages of the dispersion compensator has been implemented using the eye opening as a monitor signal. The time constant of several seconds for the adaptation process was mainly determined by the dither step and the software algorithm. The bit error ratio (BER) with and without CD-adaptation is shown in Fig. 3. Since the 40 Gbit/s NRZ-modulator was not chirp-compensated the minimum BER of the optical link was at about -40 ps/nm. The dispersion tolerance for a given BER is more than doubled for the compensated signal. The polarisation induced penalty of the RCD compensator was less than 0.5 dB. It is noticeable from Fig. 3 that the sensitivity with compensator is about 1 dB lower than without compensation. This is explained by vestigal side band filtering and pulse shaping of the filter leading to an unsymmetrical signal spectrum with a lower receiver sensitivity.

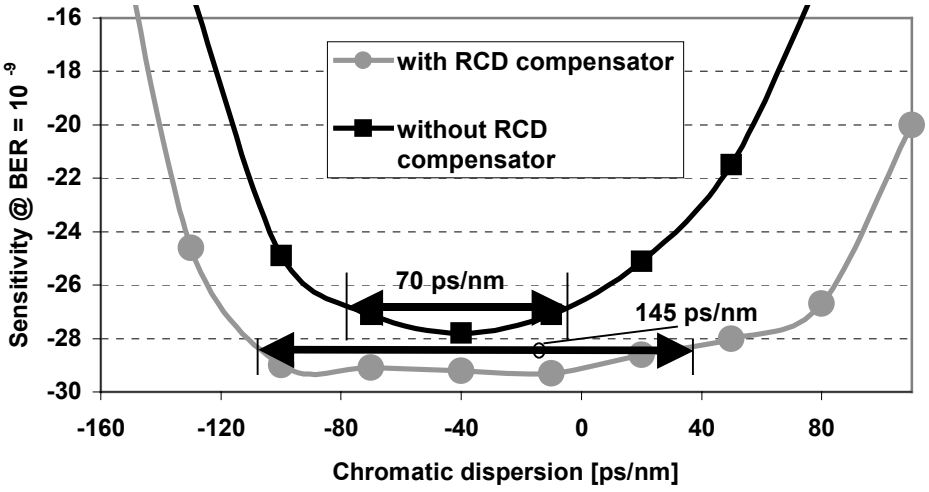


Fig. 3: Receiver Sensitivity at a Bit Error Ratio of 10^{-9} with respect to the chromatic dispersion with and without RCD compensation

To confirm the periodicity of the device we changed the signal wavelength according to the compensator free spectral range (FSR) of 178 GHz after running the adaptation process for one channel. With the same phase shifter parameters a variation of the receiver sensitivity of less than 0.8 dB have been measured for 10 neighbouring channels. So the RCD compensator can be used for at least 10 WDM channels simultaneously.

The PMD compensator has been characterised in an 40 Gbit/s NRZ experimental set up with an 12 stage high order statistical PMD emulator with a mean differential group delay (DGD) of 8.9 ps. Additional to the eye monitor as a feedback here the 10 GHz spectral line of the detected signal was employed which is necessary for the start up routine if the BER is high. The integrated optical PMD

compensator is compared with fibre optical compensators composed of fibre squeezers and birefringent fibre. One has been built up as a 1 stage compensator (1 polarisation controller and 1 PM fibre with a DGD of 14 ps) and the second one was a 2 stage compensator (2 polarisation controllers with 2 PM fibres with a DGD of 10 ps each). Fig. 4 shows the result of the comparison between the different compensators. The penalty has been measured for a BER of 10^{-9}. Due to limited measurement time the experiment gives only the cumulative probability for low penalty values. Simulations for 1 stage and 2 stage compensators have shown that the gain of the compensator is clearly enlarged for higher penalties and lower probabilities at e.g. 10^{-5}.

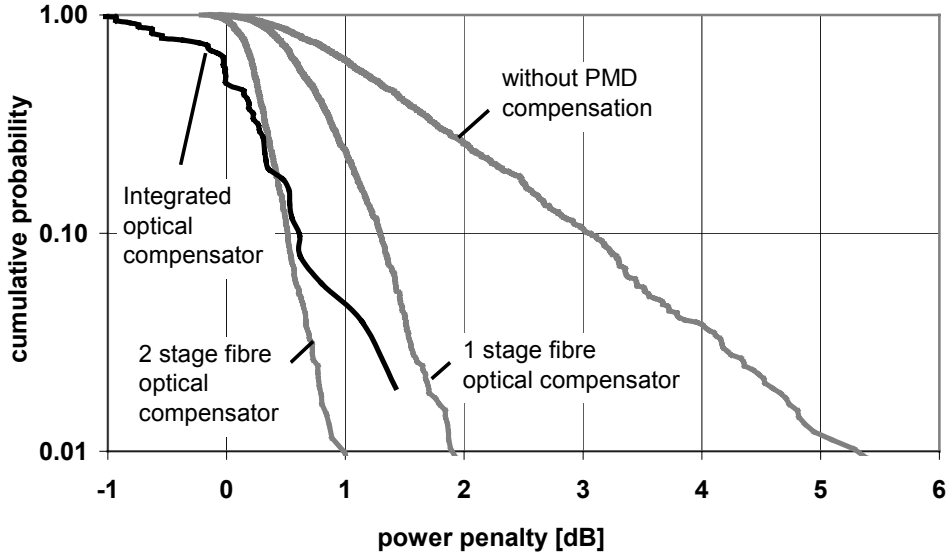


Fig. 4: Cumulative probability at a BER of 10^{-9} of the receiver penalty for 1 and 2 stage fibre optical PMD compensators and the integrated optical compensator at statistical PMD of higher order with a mean DGD of 8.9 ps.

It can be seen from Fig. 4 that the performance of the integrated optical PMD compensator is better than the 1 stage fibre optical compensator but not as good as the 2 stage compensator. This confirms simulations which have been carried out before [4]. The irregularities observed in the measured curve of the integrated optical PMD compensator will be reduced by improving the feedback algorithm which was implemented for the fibre optical compensators.

Conclusions

Compensators for RCD and PMD at 40 Gbit/s have been developed in silica on silicon PLCs. The RCD compensator is composed of a 5 stage lattice filter allowing a smooth and continuous adaptation of the filter within a dispersion range of 145 ps/nm. Dispersion compensation has been demonstrated for 10 neighbouring WDM channels with a distance of the filter FSR. This FSR should be adapted to the ITU grid in a redesign. A new design for a higher order PMD canceller has been proposed and set up with a lattice filter integrating only one PBS and one mode converter. The performance of the compensator was shown to be superior to a first order PMD compensator.

[1] K. Takiguchi, K. Okamoto, K. Moriwaki, *IEEE J.Lightwave Techn.* **14**, 2003-2011, 1996.
[2] M. Bohn et al., *Proc. ECOC 2002* , paper 4.2.3, 2002.
[3] T. Saida et al., *IEEE Photon. Techn. Letters.* **14**, 507-509, 2002.
[4] J. Poirrier et al., *Proc. OFC 2002* , paper WI4, 2002.
[5] M. Sharma, H. Ibe, and T. Ozeki., *IEEE Journal of Lightwave Techn.,* **12**, 1759-1765, 1994.
[6] L. Möller, *IEEE Photon. Techn. Letters,* **13**, 585-588, 2001.
[7] Y. Hahizume et al., *Electronic Letters,* **37**, 1517-1518, 2001.

Experimental investigation on ring resonator based filters in SiON technology

Andrea Melloni
DEI, Politecnico di Milano, via Ponzio 34/5, Milano 20133, Italy
melloni@elet.polimi.it

Raffaella Costa, Paolo Monguzzi, Francesco Morichetti, Giuseppe Cusmai and Mario Martinelli
CoreCom, via G. Colombo 81, Milano 20133, Italy
costa,monguzzi,morichetti,cusmai,martinelli@corecom.it

The characteristics of ring resonators as building block of selective filters are discussed. The results of an experimental research of various ring-based filters realised in SiON technology with Δn=6% are presented.

Keywords: guided-wave optics, ring resonators, optical filters

Introduction

Promising candidates for filtering, packing, separating and managing large numbers of channels in a Dense Wavelength Division Multiplexing DWDM systems are the circuits based on ring resonators. Rings with Free Spectral Range FSR ranging from few GHz [1] up to some THz [2] have been demonstrated in various technologies, both passive and active. However, there are several constraints in using ring resonators: losses, tolerances sensitivity, technological issues, tunability, transfer function and so on. In this contribution we analyse the characteristics of a single ring, try to find the limits of various known ring based circuits and present the results of an experimental investigation on rings realised with SiON technology with an index contrast Δn=6% [3, 4].

The Ring Resonator

The transfer function of a single ring resonator coupled to an input and an output waveguide is identical to that one of a Fabry-Perot cavity. The FSR depends on the ring group optical length $n_g L_r$ (FSR=$c/n_g L_r$), the resonant frequencies f_{0M} depend on the ring phase optical length $n_{eff} L_r$ ($f_{0M}=cM/n_{eff}L_r$) and the bandwidth B is related to the coupling coefficients κ with the input/output waveguides ($B \approx \kappa FSR/\pi\sqrt{1-\kappa}$). An important and characteristic parameter of the ring is the Q-factor or finesse, defined as Q=FSR/B. Before discussing the properties of ring-based filters and experimental results, we briefly investigate the characteristics of the single ring.

Technology: One of the main difficulty on ring design is the choice of the waveguide index contrast Δn: the higher is Δn, the lower is the minimum bending radius supported by the waveguide and the higher is the selectivity and the maximum achievable FSR. In literature, rings with diameter of few microns have been reported [2] but with waveguides dimensions and directional coupler gaps of few hundreds of nanometer. Besides technological problems in controlling such small dimensions, very high index contrast waveguides are often critical in terms of scattering losses and fiber-to-waveguide coupling losses, and require additional technological steps to reduce them to acceptable values. A good compromise between losses (scattering, radiation and coupling), minimum bending radius and resolution of common actual technologies is found for a Δn in the range 0.1 to 0.2 [5]. For glass or polymer technology (n≈1.5) this means an index contrast Δn between 5% and 10%.

Losses: The attenuation of high index contrast waveguides is usually much larger then losses of classical low contrast waveguides (0.1 dB/cm or less). If, on one side, this is not a problem because the ring dimension is of the order of the millimetre or less, the losses can be strongly enhanced by resonance. To better understand their impact, let's consider the two simple cases shown in the inset of Figs.1a) and b). Fig. 1a shows the insertion loss at the drop port of a single ring filter for different values of Q versus the roundtrip ring attenuation. If more rings are cascaded, the insertion losses are even higher. Even if, to a first order, the shape of the transfer function is not compromised, the

higher is the desired selectivity the smaller must be the roundtrip attenuation (including the couplers losses). A filter with Q=100 would require waveguide losses hard to obtain with present technologies. The second considered example is the phase shifter often employed for dispersion compensation. The intensity transfer function should be flat but at resonance the losses are enhanced and the attenuation can become unacceptable. The considered coupling coefficients are κ={0.77; 0.45; 0.27; 0.06; 0.03}, corresponding to Q={2;5;10;50;100}.

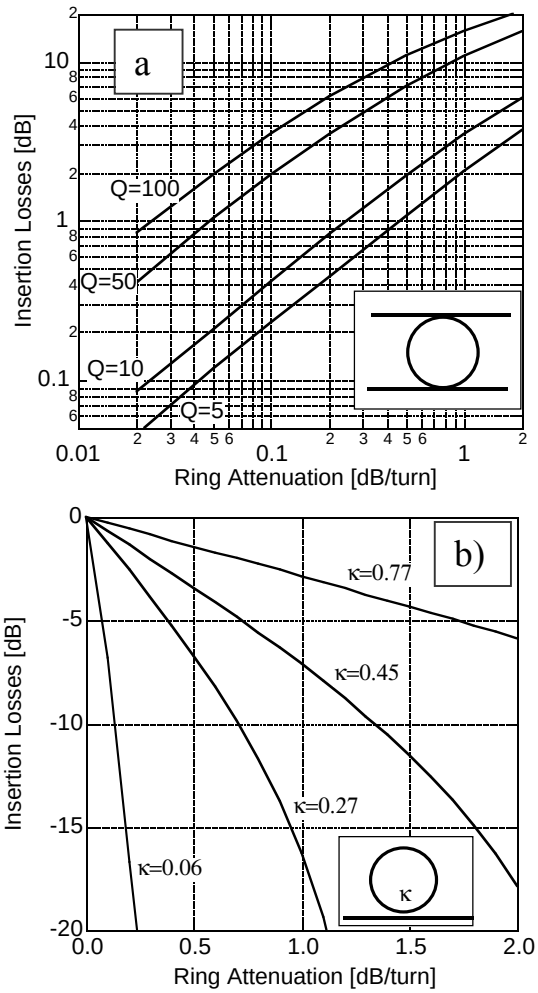


Fig. 1- Insertion losses of a single ring a) *bandpass filter and b) allpass filter, versus the roundtrip attenuation.*

<u>*Tolerances sensitivity*</u>: A realistic analysis on the impact of the fabrication tolerances is very complex and would require considerations on waveguide structure, materials employed and process flow, besides the circuit itself. However, some general considerations on the sensitivity of the frequency response on uncertainty of the circuit parameters can be drawn. In general the sensitivity to the coupling coefficients is rather low and a variation of ±10% can be accepted. The most influenced is the cross talk (the through port in resonance and the drop port out of resonance) but both the rejected and the transmission bands remain practically unaffected. Highly selective filters are more critical because the coupling coefficients are very small and the absolute tolerance is tighter.

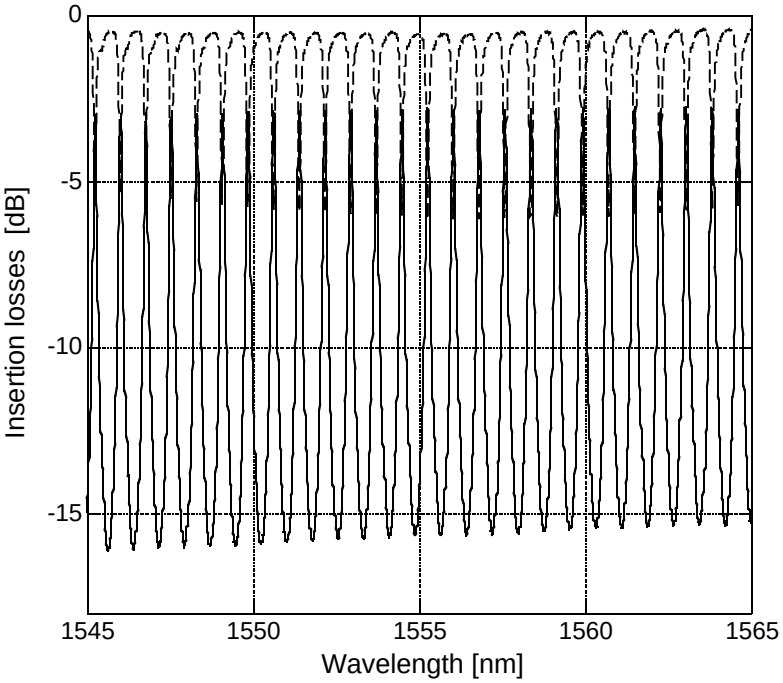
The ring length has the greatest sensitivity. A variation of the ring optical length equal to one wavelength shifts its frequency response by one FSR, as for every other filter. The maximum allowed variation is related to Q. If a frequency shift equal to a fraction x of the bandwidth is accepted, the optical ring length must be controlled within λ/xQ. Hence, from this point of view, the ring is similar to Mach-Zehnder and AWG .

<u>*Tunability*</u>: The thermal control of the ring optical length is an interesting way to tune and adjust the filters transfer function. The frequency shift Δf induced by a temperature variation ΔT is given by $\Delta f = \Delta T K f_{0M}/n_{eff}$, where K is the thermooptic coefficient. For SiON waveguides with Δn=6% we have measured $K=1.0 \cdot 10^{-5}$ °C^{-1}, a value higher then that one of SiO_2, and the frequency shift is therefore equal to 1.33 GHz °C^{-1}. As an example, in order to tune a ring over a full FSR, the heating ΔT must be 75 °C for 100 GHz and 300 °C for 400 GHz, which seems the limit for this kind of control. Note that a small tuning of the center frequency is always possible, even for very high FSR and Q, being Δf independent on both.

Experimental Results

According to the considerations expressed in the previous section, the ring resonator seems to be a promising candidate for DWDM systems with channel spacing in the range 10 to 100 GHz. The major potentiality is the periodicity of the transfer function, its selectivity and the small dimensions whereas the ratio FSR/B should be kept small to reduce losses, tolerance sensitivity and avoid critical technologies. Curvature radii of few hundreds microns are thus required, and a good choice is a waveguide with an index contrast $\Delta n \approx 6\%$. Among the existing passive technologies, SiON is

nowadays the most promising material to realise such an index contrast [3] (active technologies are even more interesting but more complex).
A large number of ring based filters have been designed and tested (the realization was carried out at LioniX BV, [4]). The realized SiON waveguides have a rib-shaped core 1.8μm high and 2.5μm wide. The choice of a rib-shaped core has many advantages respect to the buried. First of all the form birefringence can compensate the material birefringence, in order to have polarization independent devices. Scattering losses due to surface roughness are lower and the coupling with optical fibers is more efficient. Moreover, the directional couplers may have wider gaps respect to the buried case and hence are less critical from the technological point of view. In the considered case, the gaps are 1.2μm wide and can be realized and controlled with common technologies. The measured attenuation of the straight waveguides at 1550nm is equal to 2.5dB/cm without annealing and 0.35dB/cm after annealing.
In Fig. 2 the spectral response of a single resonant ring with a nominal FSR=100GHz over 25 FSRs from 1545nm to 1565nm is shown. Both the drop and through port response are shown. The ring has a constant bending radius of 303μm with two classical straight directional couplers. In this wavelength range the average FSR is 96.13 GHz with a variance of only 0.10GHz, corresponding to the measurement system accuracy. This excellent uniformity is a fundamental property and SiON ring based filters can work on almost the whole S, C or L band.
The experimental response is in excellent agreement with theoretical simulations and shows a bandwidth B=13.3GHz at -3dB and an extinction ratio of 13.5dB, corresponding to κ=0.36. At the resonances, the fiber-to-fiber insertion loss is equal to 4.4dB for the drop port and 2.1dB for the through port. These include the filter losses, the fiber-to-waveguide coupling losses, estimated around 0.8dB/facet in the experimental set-up used, and 0.5dB for the input and output waveguides. At the through port the insertion losses are very small and correspond to the input/output waveguide losses and coupling because there is not resonance enhancement. The insertion loss of the ring is 2.3dB, the lowest value never reported in literature for ring resonators. A careful analysis indicates that the ring looses 0.75dB per turn, as confirmed by Fig.1. We estimate that the couplers contribute with 0.2dB each, the material absorption contributes with 0.07dB and that radiation and scattering losses contribute with 0.045 dB/rad. Waveguides have been butt-coupled with a small core fiber through an index matching oil. The coupling losses are mainly due to a mode mismatch between fiber and waveguide and they can be reduced down to 0.3 dB with a suitable mode adapter.



F*ig. 2- Experimental spectral response of a single ring filter with FSR=96.13 GHz.*

In Fig. 3a the photograph of a double ring filter is shown. The nominal FSR is 50 GHz and the bandwidth at -1dB is 8GHz. The coupling coefficients κ_i={0.66;0.24;0.66} shape a Butterworth response and are realised with classical straight directional couplers. The overall dimensions of the filter are 1.4x2.3 mm^2, the constant

curvature bending radius being 570µm. The fiber-to-fiber experimental spectral response measured at the drop port is shown in Fig. 3b) for both the TE and TM polarizations. The extinction ratio of 15 dB is very close to the expected one and the polarization dependence is very weak. The uniformity over a range of 4nm, corresponding to 22 channels of a 25 GHz spaced DWDM system, is excellent. The measured FSR is 47.6GHz, indicating a ratio n_g/n_{eff}=1.0504 and in the wavelength range between 1540nm and 1580nm, corresponding to 105 FSRs, no appreciable variations of the FSR are observed. Fig. 3b) refers to a chip without annealing.

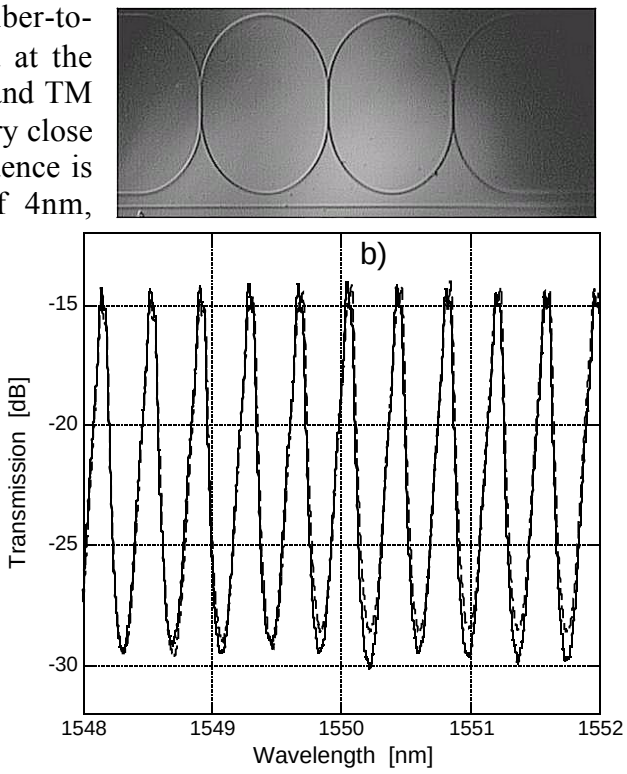


Fig. 3- a) Photograph and b) fiber-to-fiber spectral response of a double ring filter. FSR=47.6 GHz.

The filter shown in Fig. 4a) is a balanced Mach-Zehnder with a ring coupled to one arm. This solution is particularly interesting because the coupling coefficient of the ring is always very high and therefore the ring losses do not affect the total transfer function (see Fig.1b). Fig. 4b shows a nice fiber-to-fiber spectral behaviour of the through port while the drop port is visible distorted. The asymmetry comes from the ring coupler that is slightly lossy and produces a phase shift between the two output ports of the coupler itself.

In conclusion, the measured performance are encouraging in terms of bandwidth, out-of-band rejection, operating wavelength range and polarization independence. We firmly believe that ring-based passive filters are promising candidates for the management of the closely spaced channels in DWDM systems.

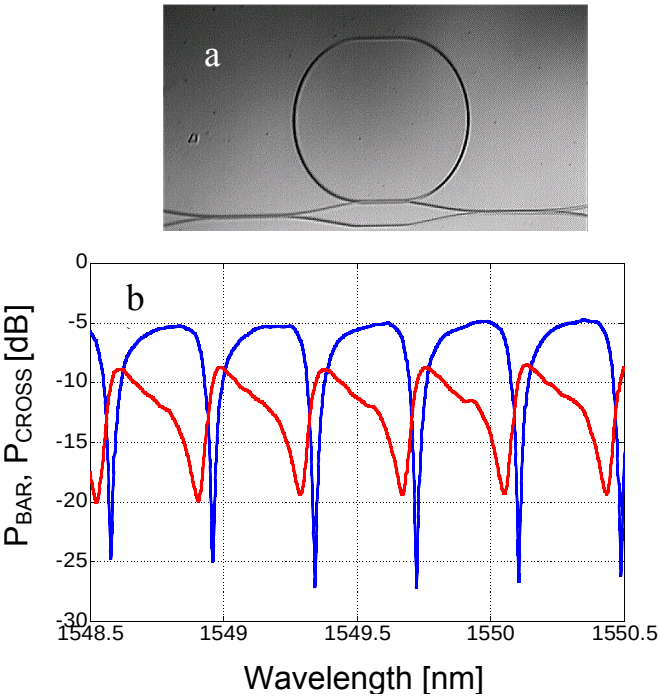


Fig. 4- a) Photograph and b) fiber-to-fiber spectral response of a loaded MZ filter. FSR=47.6 GHz

References

[1] C. K. Madsen, J. H. Zhao, "Optical Filters Design and Analysis", J. Wiley and Sons, 1999.

[2] D. Rafizadeh, et al., "Waveguide-coupled AlGaAs/GaAs microcavity ring and disk resonators with high finesse and 21.6-nm free spectral range", Optics Letters, Vol. 22, pp. 1244-1226, 1997.

[3] G.N. De Brabander, J.T. Boyd. G. Beheim, "Integrated optical ring resonator with micromechanical diaphragm for pressure sensing", IEEE Photon. Technol. Lett., Vol. 6, No. 5, pp. 671-673, 1994.

[4] LioniX BV. www.lionixbv.nl

[5] L.C. Kimerling, "Silicon microphotonics", OSA Technical Digest *IPR 2002*, Paper IFB1.

[6] A. Melloni and M. Martinelli, "Synthesis of direct-coupled resonators band pass filters for WDM systems*", IEEE Journal of Lightwave Technology*, Vol. **20**, No. **2**, 296-303, (2002).

Ultrafast All-Optical Signal Processing in Engineered Quadratic Nonlinear Waveguides

F. Lederer, T. Pertsch
Institut für Festkörpertheorie und Theoretische Optik, Friedrich-Schiller-Universität Jena, Max-Wien-Platz 1, 07743 Jena, Germany

R. Schiek, R. Iwanov, G. I. Stegeman

School of Optics and Center for Research and Education in Optics and Lasers, University of Central Florida,4000 Central Florida Boulevard, Orlando, U.S.A.

A. Barthelemy, V. Couderc, P. Pioger
Faculte des Sciences, Institut de Recherches en Communications Optiques et Microondes, 123 Avenue A. Thomas,87060 Limoges, France

C. De Angelis
Dipartimento di Electtronica per l'Automazione, Istituto Naz. per la Fisica della Materia, Università di Brescia,via Branze 38, 25123 Brescia, Italy

Y. Min, and W. Sohler
Angewandte Physik, Universität Paderborn, 33095 Paderborn, Germany

The potential of a $\chi^{(2)}$ photonics, implemented in periodically poled Lithium Niobate (PPLN) waveguides with an engineerable quadratic nonlinearity, for ultrafast all-optical signal routing and switching will be evaluated. High bit rate signal regeneration and routing, based on spatial soliton formation in film waveguides, as well as transparent switching, based on parametric amplification in waveguide arrays, will be demonstrated.

Keywords: quadratic nonlinearity, signal processing, waveguide arrays, spatial solitons

Introduction

In order to meet the requirements of future communication networks high bitrate data transmission in optical fiber lines has to be ultimately complemented by ultrafast all-optical signal regeneration, processing and routing, which requires the usage of nonlinear effects.
One option is to use active semiconductor devices with electrically injected free carriers. They are fast and need very low control powers but suffer from the known drawbacks of semiconductor optical amplifiers as limited processing speed, noise, and reduced compatibility with the fiber geometry. Nonresonant nonlinear effects as the cubic or the quadratic interaction are weaker but quasi-instantaneous. The degenerate interaction based on the cubic nonlinearity needs too large control powers and provides only with a phase modulation that needs to be transformed into an amplitude modulation by phase sensitive devices.
On the contrary parametric processes in quadratic nonlinear waveguides provide phase modulation and gain the latter being essential for transparent operation. Moreover, the strength of interaction can be locally controlled by varying the poling characteristic. Light confinement in PPLN film waveguides allows spatial soliton formation with unprecedented low peak powers. We will show that this dichromatic self-trapping of light can be used for effective ultrafast signal routing and regeneration. Moreover, evanescently coupled PPLN channel waveguides

form a waveguide array, which exhibits a peculiar refraction and diffraction behavior. We will show that this unusual behavior in conjunction with parametric effects in these waveguides offer novel interesting options for signal routing and switching.

Routing and regeneration of signals in PPLN film waveguides

Recently it has been shown at Université de Limoges that self-trapped beams (or spatial solitons) can form in a 58 mm long Ti:PPLN waveguide, fabricated at the University of Paderborn, at unprecedented low intensities of about 50 MW/cm^2 even if the launched FF beam is as short as 4 ps. The fact that the huge linear temporal walk off can be arrested has important consequences for high bit rate processing in using these solitons.
Self-trapping can be used to clean up pulses from low-intensity pedestals and to compress them. Only the fraction of the input pulse with a power higher than the threshold for spatial soliton formation will be trapped and subsequently pass through the aperture (see Fig.1). The low power parts of the pulse, both in time and space, undergo diffraction and are thus mainly blocked at the output. The device can be understood as a saturable absorber with an ultrafast response similar to a Kerr lens. The width of the aperture placed at the output as a spatial filter was about 88% of the soliton width. The input beam width was 56 µm FWHM.

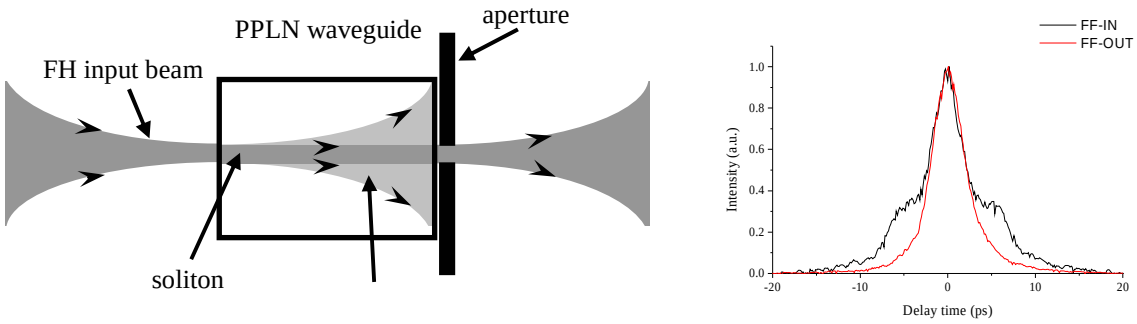


Fig.1 Pulse shape regeneration in a PPLN waveguide with aperture. Input pulse length was 4.3 ps.

Collision-induced soliton formation can be used for high bit rate pulse switching. Both FF beams are forced to interact before a quadratic soliton was formed, i.e., near the input face or a few millimetres inside the waveguide. Two FF beams (control and signal) are launched with

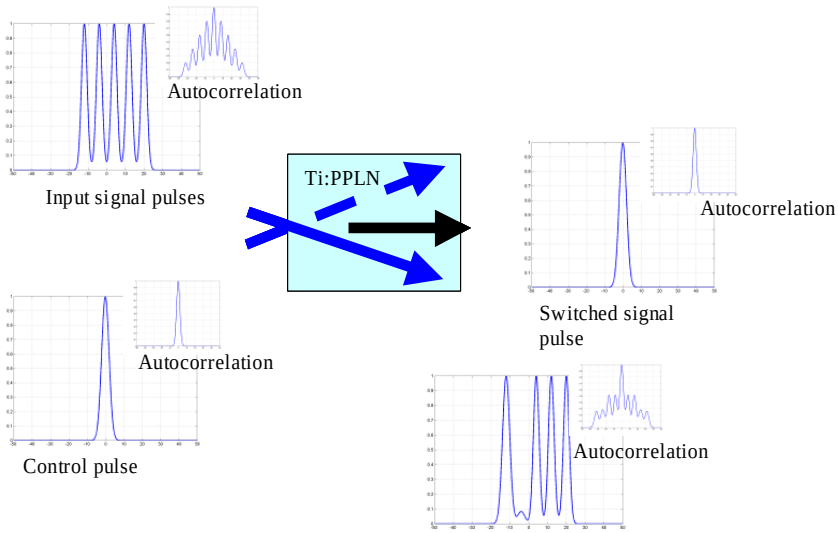


Fig.2 125 Gbit/s pulse routing by collision-induced soliton formation. input angle = 0.4°

different directions into the waveguide ($\Delta\theta$=0.4° within the crystal). Each beam carried a power sufficiently high to give rise to self-trapping. For zero phase difference a single soliton is formed upon collision, which propagates on-axis. Thus by applying a control pulse routing of a single bit in a high bit rate data stream can be achieved (see Fig.2). At present, the processing speed is limited by the laser pulse length and amounts to 125Gbit/s. The switching efficiency is as high as 90% and the contrast ratio for the switched output is about 20dB.

Parametric switching in waveguide arrays

Although the soliton scheme discussed above provides with exciting new opportunities for ultrafast processing it still lacks from the high signal power required. On the contrary schemes that are based on parametric interaction require only a weak (mW) signal to interact with a stronger local control. Moreover, the parametric gain makes the device transparent and thus cascadable. Evidently this scheme can also be implemented in film waveguides. Here we are concerned with this type of switching in evanescently coupled PPLN channel waveguides. Recently is has been shown that these waveguide arrays exhibit peculiar diffraction properties as zero and negative diffraction for certain input angles of the light beam [2]. It turns out that this behavior in conjunction with the particular phase and amplitude dynamics of a nondegenerate quadratic interaction offers exciting incoherent switching opportunities [3].

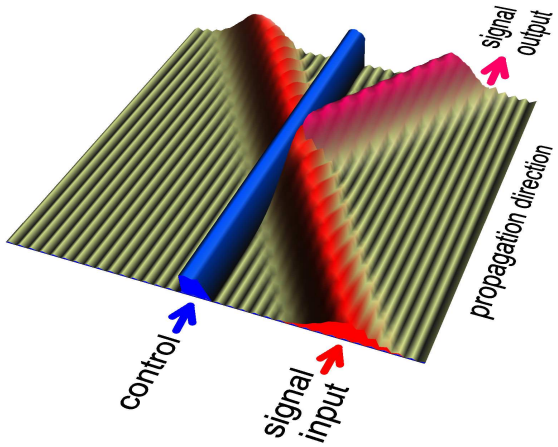


Fig.3 Parametric routing in a PPLN waveguide array

Figure 3 shows how a highly confined SH beam interacts with a diffractionless propagating signal train to route the signal to a definite output port. Experiments performed at CREOL Orlando have confirmed that transparent switching of a few mW signal can be achieved with a 10 ps control pulse of 10 W peak power.

The authors appreciate funding of the European Community in the framework of the IST programme for the ROSA project.

[1] P. Pioger, V. Couderc, Laurent Lefort, A. Barthélémy, F. Baronio, C.De Angelis, Y. Min, V.Quiring, W. Sohler; 'Spatial trapping of short pulse in Ti:PPLN waveguides', Opt. Lett. 27 (2002)2182.
[2] T. Pertsch, T. Zentgraf, U. Peschel, A. Bräuer, and F. Lederer, 'Anomalous Refraction and Diffraction in Discrete Optical Systems', Phys. Rev. Lett. 88 (2002) 093901.
[3] T. Pertsch, U. Peschel, and F. Lederer, 'All-optical switching in quadratically nonlinear waveguide arrays', Opt. Lett. 28(2003)102.

Second harmonic generation in He+-implanted oxoborates and PPLN waveguides

A. Boudrioua, B. Vincent and R. Kremer
Laboratoire Matériaux Optiques, Photonique et Systèmes (MOPS) - CLOES
Université de Metz et Supélec, CNRS - FRE 2304, 2, rue E. Belin , 57070 Metz , France
Tel : (33).03.87.37.85.47 Fax : (33).03.87.37.85.59
E-mail: boudriou@ese-metz.fr
P. Moretti
Laboratoire de Physico-chimie des Matériaux Luminescents
Unité Mixte de Recherche (UMR), Centre National de la Recherche Scientifique
(CNRS) n° 5620, Université Claude Bernard, Lyon I, France

Abstract: Second harmonic generation has been investigated in He+-implanted waveguides in the new non linear crystals, GdCOB and YCOB, and periodically poled lithium niobate (PPLN), as well.

Keywords: frequency conversion, periodically poled lithium niobate, oxoborates, waveguides.

1. Introduction

Light ion beam implantation has been used to form optical waveguides in numerous non linear crystals pure or doped [1]. This versatile technique is now reaching its maturity and it is subject to valuable application phases. Besides, it has been shown that this method does not, virtually, affect the linear and the non linear optical properties of the guiding region [2].

Any technique employing the process of frequency conversion must solve a major problem: the realization of phase matching between the pump and the harmonic beams. On one hand, to obtain phase matching, one can use natural birefringence existing in the uniaxial or biaxial crystals to compensate for the difference of refractive indices dispersion. On the other hand, one can reach quasi phase matching between the harmonic and the fundamental signals by a periodic variation of the material polarization. In this case, the highest nonlinear coefficient (d_{33}) of the crystal become accessible. The mechanisms of frequency conversion in this configuration are well controlled, particularly, in crystals such as periodically poled $LiNbO_3$ (PPLN) [3].

In this paper, we report, the investigation of second harmonic generation in He+-implanted waveguides in two crystals of the oxoborate family, GdCOB and YCOB, and in PPLN crystals. We attempt to combine together the benefits of the implantation technique with those of the new nonlinear crystals and the use QPM method in order to obtain high conversion efficiencies and to enlarge the generated harmonic wavelength range.

2. SHG in He+-implanted waveguides in oxoborate crystals

Oxoborates crystals have been grown by using Czochralski method as described in reference [4]. Since 1996, the group of G. Aka studied and tested all the possibilities of second harmonic generation (SHG) in bulk oxoborates, $Ca_4GdO(BO_3)_3$ (GdCOB) and $Ca_4YO(BO_3)_3$ (YCOB), crystals [4]. Both phase matching in the plans ZX and YX were investigated. For instance, they showed that the conversion efficiency may reach 50% by using a pulsed YAG pump laser at 1.06 μm [4].

The growth of high optical quality crystals of GdCOB and YCOB been now well established and their non linear performances are well demonstrated, the objective of this program consists of using these crystals in waveguiding configuration in order to increase their capabilities of producing efficient laser beams in the visible and the UV ranges. For instance, we recently demonstrated SHG in GdCOB

planar waveguides fabricated by He+-implantation [5]. This technique appears to be the only one that can be used with this type of non linear crystals.

The samples were cut and optically polished in order to fulfil type I phase matching in the plans ZX and YX respectively. The fabrication conditions of the planar waveguides are reported in reference [5]. Implantation parameters are indicated in table 1. We employed triple consecutive implantations in order to reduce optical losses caused by leakage through the created optical barrier. To design a channel waveguide, we used multiple implantations by varying the beam energy from 0.3 to 1.7 MeV at a dose of $1x10^{15}$ ions/cm^2 through a micrometric split in order to produce two optical 'walls' (barriers) that permit the lateral confinement of the propagating light - see figure 1. The distance between these "walls" gives the waveguide width.

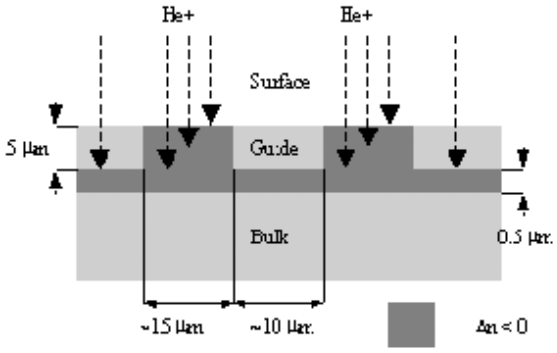


Fig.1 : Fabrication of channel waveguides by He+ implantation.

Tab.1 : Features of planar waveguide in GdCOB and YCOB crystals.

Sample	E (MeV)	Dose (ions/cm^2)	Δn (%)		Losses (632 nm)
			Guide	Barrier	
GdCOB	2.0	0.66 x 10^{16}	-0.02	-1.2	2 dB.cm^{-1}
	1.9	0.40 x 10^{16}	+0.02	-1.2	
	1.8	0.33 x 10^{16}	0.0	-1.2	
YCOB	2.0	1.0 x 10^{16}	-0.01	-1.2	1.8 dB.cm^{-1}
	1.9	0.6 x 10^{16}	+0.01	-1.1	
	1.8	0.6 x 10^{16}	0.0	-1.7	

The linear optical parameters of the obtained planar waveguides were determined by using the well known prism-coupling technique [6]. Refractive index profiles of GdCOB and YCOB waveguides respectively, obtained by utilizing iWKB method [7] showed a step-like guides with a very weak index variations in the guiding core and a substantial decrease in the optical barrier - see table 1. For the optical loss measurements, we used a CCD camera to collect the scattered light from the surface of the guide when a guided mode is propagating. Losses were found to be less than 2 dB.cm^{-1} at λ = 632 nm (tab.1). Note that, in these measurements, we did not apply any heating treatment to our samples.

As an example, we present here the study of SHG within GdCOB channel waveguide performed in the sample which fulfills phase matching in the plan ZX. The SHG experiments were carried out with a TE-polarized cw Ti: sapphire laser. Figure 2 shows the measured SH intensity at the output of the GdCOB channel waveguide as a function of the input fundamental wavelength. The maximum of SH signal is observed at 810.9 nm. The experimental data were fitted by using the standard sinc function giving the shape of the second harmonic signal versus the pump wavelength. The interaction length is found to be about of 4 mm which is in a good agreement with the sample length used. Besides, the theoretical analysis shows that this second harmonic process corresponds to a TM_{OO}^{ω} to $TE_{01}^{2\omega}$ conversion. Figure 3 displays the variation of the generated harmonic power $P^{2\omega}$ versus the fundamental power P^{ω}. The experimental data were fitted by a linear function with a slope of 1.9 which is very close to the theoretical value of 2.

Finally, for a pump power of 200 mW, the conversion efficiency was estimated to be about of 2 W^{-1}.cm^{-2}. This value is 20 % higher than that obtained with planar waveguides. Results of all SHG processes within He+-implanted GdCOB and YCOB will be presented and discussed. We are also focusing on the investigation of the heating treatment to improve the efficiency conversion.

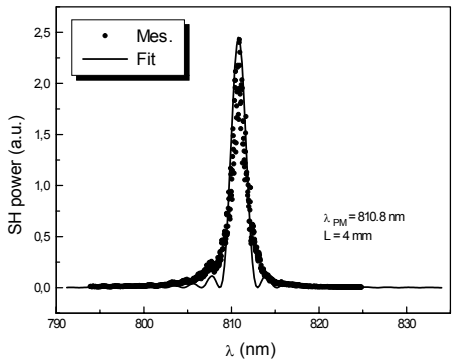


Fig.2 : SH intensity vs the fundamental wavelength.

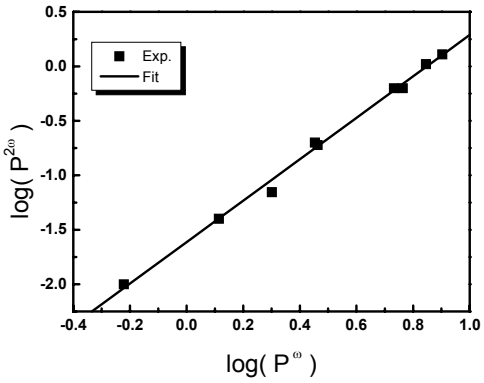


Fig.3 : SH intensity vs the fundamental power.

3. SHG in He+-implanted PPLN planar waveguides

According to this program, we carried out two studies: the first one states on the investigation of the feasibility of waveguides by He+-implantation in PPLN crystals. For that we used a PPLN sample with a grating period of 10 μm. The second study deals with the investigation of waveguides in 4.8 μm-period PPLN samples. This period is suitable for frequency doubling of IR diode laser emitting at 960 nm in order to generate first order QPM blue laser.

To carry out the periodically polarized (PP) $LiNbO_3$ structures, we used LiCl saturated solution as liquid electrodes with a 10 μm-period photoresist grating of 1.3 μm thickness deposited on Z^+-face of the sample. The poling was achieved by applying several voltage pulses of 10.5 kV and 100 ms on a 0.5 mm-thick Z-cut $LiNbO_3$ wafer. It should be noted that Z^+ face was beforehand identified by pyroelectric effect. To control the periodically polarized structures, we used chemical etching. The etching speed depends on the face of the crystal. It is faster on the faces Z^- and Y^- than on Z+ and Y+ (face X, does not have any difference due to symmetry). Under these conditions, a chemical etching carried out on a PPLN crystal causes periodic deteriorations of the surface (see figure 4).

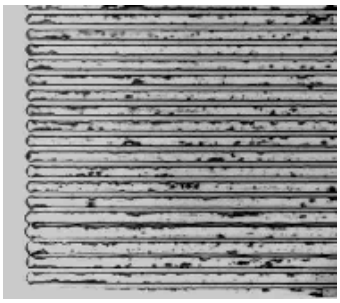


Fig.4 : 10-μm PPLN structure revealed by chemical etching.

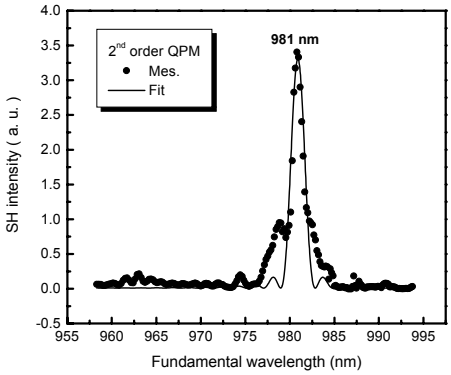


Fig.5 : 2nd order QPM SH intensity vs fundamental Wavelength PPLN : He+ planar waveguide.

Tab.1 : Theoretical QPM wavelengths of PPLN:He+ planar waveguides.

QPM order	Bulk PPLN measured λ_{QPM} (nm)	SHG in PPLN : He+ waveguide			
		Theory			Experiment
		Interaction	λ_{QPM} (nm)	I_{OVL} ($m^{-1/2}$)	λ_{QPM} (nm)
2nd	969	$TM_0^{\omega} \rightarrow TM_0^{2\omega}$	978	1373	981
3rd	800	$TM_0^{\omega} \rightarrow TM_0^{2\omega}$	866	1430	869
4th	794.8	$TM_0^{\omega} \rightarrow TM_0^{2\omega}$	800	1474	804

As in the first study, we used triple-implantation of He+ (with energies of 1.5, 1.6 and 1.7 MeV at a dose of 0.5×10^{16} ions.cm^{-2}, respectively). Subsequently, the sample was annealed at 200 °C during 1 hour. The linear optical properties of our waveguides were characterized at different wavelengths ranging from 514 nm to 980 nm by using the same prism-coupling technique. The reconstructed index profiles of our He+-implanted PPLN waveguides (by iWKB method) indicate a slight refractive index variation at the surface and a maximum variation of 3×10^{-2} at the barrier position. Eventually, the optical losses measured were less than 2 dB.cm^{-1}.

Figure 5 shows the SHG signal related to the fundamental wavelength of a tunable Ti-sapphire laser. The experimental data were fitted by the sinc function giving, therefore, an interaction length about of 1 mm. This result indicates that our PPLN is not homogenous throughout the sample. Moreover the asymmetric experimental curve is due to the inhomogeneity of the waveguide. The second harmonic generation was found to be a TM_0^{ω} to $TM_0^{2\omega}$ second order QPM conversion process at 981 nm. This wavelength is in a good agreement with the theoretical value. Moreover, we measured the conversion efficiency of our waveguides relatively to that of the bulk PPLN. We found that it was 40% higher than in a bulk interaction. Finally, table 1 reports the results of experiments and computations of SHG process within our PPLN: He+ waveguides. The calculation concerns 2nd, 3th and 4th QPM orders as well. The small discrepancy between the experiments and the theory is very likely due to the model used in our computation procedure.

4. Conclusion

Waveguides have been fabricated and studied in GdCOB, YCOB and PPLN crystals by using He+ implantation in the MeV range. Frequency doubling generating blue laser beams in GdCOB and YCOB channel waveguides have been demonstrated. SHG in He+-implanted planar PPLN waveguide have been also investigated by using 2nd, 3rd and 4th QPM orders. These results emphasize that the non linear grating remains in the guiding region after the implantation. We are pursuing our work to investigate SHG in He+-implanted waveguides in 4.8 μm-period PPLN samples.

References

[1] P. D. Townsend, P. J. Chandler and L. Zhang, (Cambridge University Press), 1994.
[2] A. Boudrioua, F. Laurell, P. Moretti and J. C. Loulergue, J. Opt. Soc. Am. **B**, **18(12)**, 1832-1840,
[3] L. E. Myers, R. C. Eckardt, M. Fejer, R. L. Byer, W. R. Bosenberg and J. W. Pierce, J. Opt. Soc. Am. B, **(12)**,11, 2102-2116, 1995.
[4] F. Mougel, PhD thesis, University of Paris VI (France), 1999.
[5] A. Boudrioua, J. C. Loulergue, P. Moretti, B. Jacquier, G. Aka and D. Vivien, Optics. Letters **24(18)**, 1299- 1301, 1999.
[6] R. Ulrich and R. Torge, Appl. Opt. **12(12)**, 2901-2909, 1973.
[7] K. S. Chiang, J. Lightwave Tech. **LT-3**, 385-391, 1985.

Recovery of Second Order Optical Nonlinearity in H:$LiNbO_3$ Waveguides by Reverse Proton Exchange

Vyacheslav Fedorov, Yuri Korkishko, Alexander Alkaev, Evgeny Maslennikov
Moscow Institute of Electronic Technology, Department of Materials and Technology of Solid-State Electronics, 124498 Moscow, Zelenograd, Russia, Fax: 7095 5369934, fedorov@chem.miee.ru

Fredrik Laurell
Laser Physics and Quantum Optics, Department of Physics, Royal Institute of Technology, Roslagsvägen 30b, S-106 91 Stockholm, Sweden, Tel.: 46 (8) 5537 8153; Fax: 46 (8) 5537 8216, fl@laserphysics.kth.se

Reverse proton exchange has been used to restore the second-order nonlinear susceptibility in H:$LiNbO_3$ waveguides to almost the original value of the virgin crystal both in high-concentrated direct exchanged and in annealed low-concentrated $H_xLi_{1-x}NbO_3$ phases.

Keywords: lithium niobate, proton exchange, Second Harmonic Generation, nonlinear properties

Introduction

Proton exchange (PE) in lithium niobate ($LiNbO_3$) is an attractive technique for application of waveguiding photonic devices [1]. Second-harmonic generation (SHG) in PE $LiNbO_3$ waveguides either using the quasi-phase matching (QPM) technique or through Cherenkov generation has been successfully demonstrated and permitted a way of realizing a compact blue-green light sources. Seven crystallographic phases, the α, κ_1, κ_2, β_1, β_2, β_3 and β_4 $H_xLi_{1-x}NbO_3$ phases, have been identified in PE layers depending on exchange and annealing conditions [2-4], and the correlation between the crystal structure, the ordinary and extraordinary refractive indices [2-3] and hydrogen concentration [4] in all these phases has been experimentally determined. A detailed correlation between the nonlinear properties, the processing conditions, the refractive index changes and the optical losses of as-exchanged and annealed proton-exchanged (PE) waveguides in different $H_xLi_{1-x}NbO_3$ phases was also investigated by using reflected SHG measurements from the polished waveguide end face [5]. It was found that for the direct PE samples, where the β_4, β_3 and β_1 phases are generated at the surface, the nonlinearity in the guide is strongly reduced by more than 85 % of its bulk value, while for waveguides prepared in the β_2 phase the nonlinear coefficient is about 55% of the bulk one. There were a lot of reports that nonlinearity is restored by post-exchange annealing when low-concentrated κ_2, κ_1 and α $H_xLi_{1-x}NbO_3$ phases are generated. However, it was observed [5-6] that the restoring and even apparently increasing of nonlinearity in annealed waveguides is accompanied by a high scattering and a strong degradation of the quality of the reflected beam in the region of initial waveguide. The recently proposed high-temperature proton exchange [7] and soft proton-exchange techniques [6] have been shown to produce high-quality waveguides with essentially undegraded nonlinearity.

The reverse proton exchange (RPE) is the only known method for complete recovery of composition and bulk properties on the surface of waveguides [8] and for fabrication of surface guiding layers on ordinary refractive index as well as buried guiding layers on extraordinary index in annealed PE (APE) $LiNbO_3$, as well as in $LiTaO_3$ crystals [9-10]. In this method a sample with an ordinary first produced PE layer is then immersed in a melt, very rich in lithium. During RPE the outer (surface) part of the PE layer recovers its original lithium content [8] and as a consequence it also recovers the substrate values of the refractive indices [8-10]. Reverse Proton Exchange is interesting for two reasons. First, it allows realising buried extraordinary waveguides which present several advantages: better fiber-waveguide coupling because of the more symmetrical shape of the

waveguide modes, higher conversion efficiency in non-linear processes due to a better overlap between the interacting modes and lower losses due to a reduction of the influence of surface imperfections. Second, ordinary waveguides are created at the surface using the PE region as an index barrier. Such a two-layer system is very attractive for SHG and other nonlinear optical devices, achieving phase matching by ordinary-extraordinary mode coupling or periodic poling of domains. First measurements of nonlinear susceptibility in RPE $LiNbO_3$ waveguides have been reported by Rams et al. [11]. Recently, efficient frequency doubling in buried RPE $LiNbO_3$ waveguides has been predicted [12] and has been demonstrated (150 %/W cm^2 for 1550 nm) [13]. Also, the recovery of electro-optic activity in RPE layers appeared even better then in annealed PE guide [14].

In this paper we report the detailed study of nonlinear optical properties of reverse PE waveguides realised by RPE process in different $H_xLi_{1-x}NbO_3$ phases fabricated on Z-cut $LiNbO_3$ substrates.

Preparation of samples and their characterization

Proton exchanged waveguides were fabricated in optical grade virgin Z-cut $LiNbO_3$ substrates by using as proton sources melts and solutions of different acidity. Annealed PE (APE) $LiNbO_3$ waveguides were fabricated by annealing in air at temperatures from 320 to 400°C. The conditions for fabricating the different $H_xLi_{1-x}NbO_3$ phases were early reported [2]. The reverse proton exchange was performed in eutectic melt $LiNO_3$ (37.5 mol.%)-KNO_3 (44.5 mol.%)-$NaNO_3$ (18.0 mol.%) (melting point of this eutectic mixture is 120°C) at temperature ranged from 300°C to 350 °C .

The obtained planar waveguides were characterized optically by using one-prism coupler setup at the 633 nm for measuring the effective indices of dark *m*-lines and for reconstructing the extraordinary and ordinary refractive indices profiles using an inverse WKB method. To estimate the extraordinary index profiles in the RPE $LiNbO_3$ waveguides we used the procedure described in paper [9].

For reflection SHG characterization of the waveguides we used the experimental setup earlier proposed [15] and used for previous investigations of SHG response in PE $LiNbO_3$ waveguides [5].

Results and discussion

Using the SHG characterization technique described above, we have analyzed the change of nonlinear properties of PE guides during reverse proton exchange in different $H_xLi_{1-x}NbO_3$ phases.

Reverse proton exchange in the β_4, β_3 and β_2 phases

The β_4, β_3 and β_2 $H_xLi_{1-x}NbO_3$ phases are formed during the direct PE process in $LiNbO_3$ [2-4]. These phases are characterized by the presence of interstitial protons, which quickly exchange with lithium ions at the first stage of RPE [8]. As a result, the β_1-$H_xLi_{1-x}NbO_3$ waveguides on the extraordinary index are formed after few minutes of RPE at 300°C. These guides are still at the surface, therefore it turns out that it is impossible to create buried waveguides when either the β_2 , β_3 or the β_4 phase are presented in the exchanged layer.

Reverse proton exchange in the β_1 phase

For the PE waveguide prepared in the β_1 phase it was observed that the reflected SH signal practically disappears in the exchanged region [5-6]. Fig. 1a shows the measured ordinary and imaginable extraordinary index profiles of the waveguide after the reverse exchange process, performed at 350 °C for different times. At first stage of RPE the β_1-$H_xLi_{1-x}NbO_3$ phase still present in the buried region and there was no reflected SHG signal in this region while on the surface of reverse exchanged guide, the intensity of reflected SHG signal is practically the same as in the bulk (Fig.1b). The SIMS measurements [8] as well as the value of surface ordinary refractive index [9] (Fig.1a) showed that pure lithium niobate was realized at the surface of RPE guides. All these results suggest a recovery of the non-linear optical properties in RPE waveguides prepared in the β_1 phase.

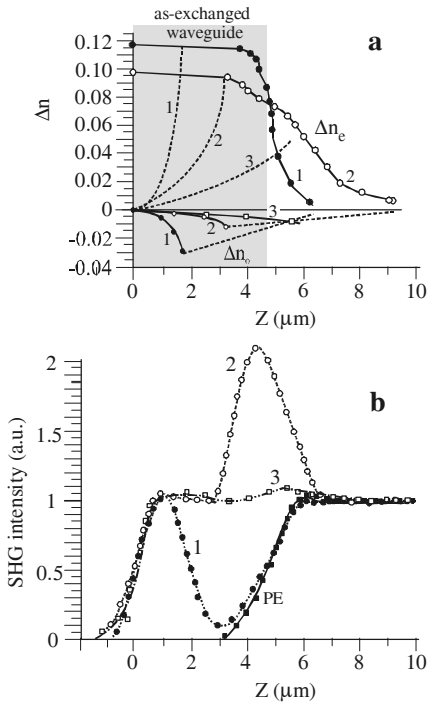


Fig.1. (a) Refractive indices profiles and (b) reflected SH signal distributions for sample R1: initial (β_1 phase) and reverse exchanged for 24 h (1), 75 h (2) and 200 h (3) at 300°C.

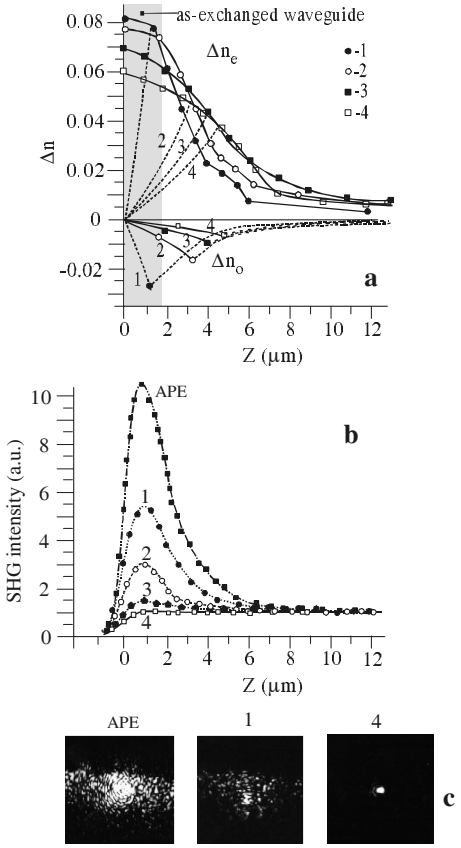


Fig.2. (a) Refractive indices profiles, (b) reflected SH signal distributions and (c) photographs of the reflected SH beam for sample R2 in the point I : initial (κ_2^{LT} phase) and reverse exchanged for 24 h (1), 50 h (2), 75 h (3) and 100 h (4) at 300°C.

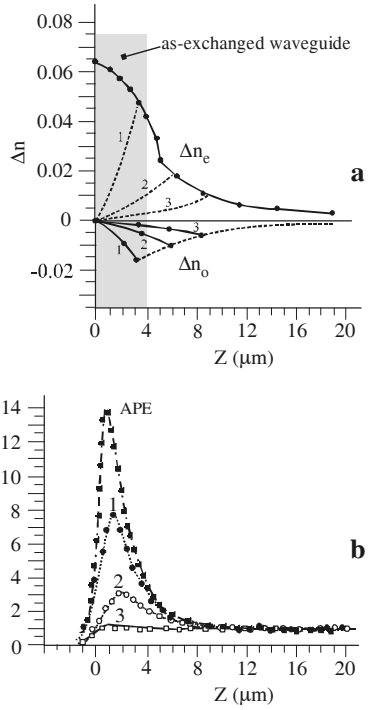


Fig.3. (a) Refractive indices profiles and (b) reflected SH signal distributions for sample R3: initial (κ_1^{LT} phase) and reverse exchanged for 50 h (1), 100 h (2), and 100 h (3) at 300°C.

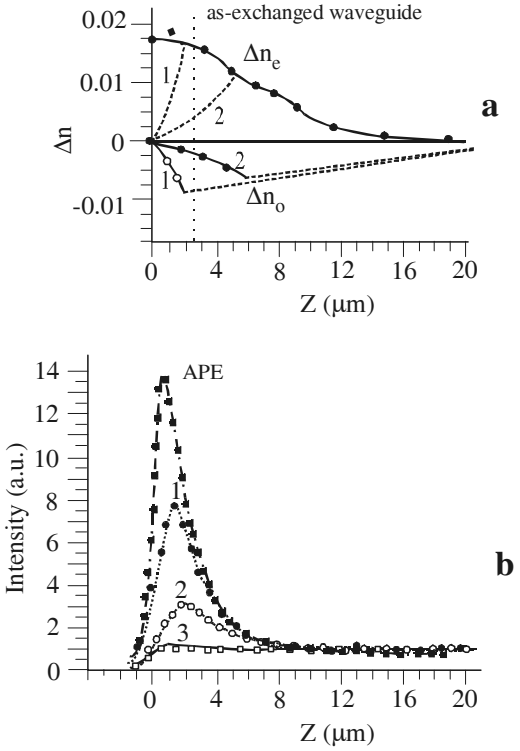


Fig.4. (a) Refractive indices profiles, (b) reflected SH signal distributions for sample R4: initial (α phase) and reverse exchanged for 24 h (1) and 100 h (2) at 300°C.

However, a longer RPE, due to simultaneously ongoing annealing process leads to formation of the κ_2-phase at the embedded part of the waveguide. For that region the measured intensity of the reflected SH signal is higher then that for bulk $LiNbO_3$ (Fig.1b (curve 3)). However, this apparent increase of nonlinearity is accompanied by a strong degradation of the quality of the reflected beams. Therefore, the result obtained shows, that behaviour of SH reflected beam does not depend ever κ_2 phase placed at surface [5-6], as in APE waveguides, or in the buried region.

Reverse proton exchange in APE $LiNbO_3$ waveguides

Reverse proton exchange for APE waveguides (REAPE process [10]) with κ_1, κ_2 and α-phase at the surface is an effective method to produce buried waveguides with graded refractive index profiles. We found that RPE process completely recovers the nonlinear properties of APE waveguides. Figs.2-4 show the measured ordinary and the estimated extraordinary index profiles (a), reflected SH signal distributions (b), as well as a picture of reflected beam (c) for the samples R2-R4, respectively, for reverse exchanged at 300 ^oC for different times. One can see, that an increase of the RPE time leads to a complete recovery of quality of reflected beam (Fig.2c (4)). At first stage of RPE, when the depth of RPE process is smaller than a thickness of initial PE waveguide, a large scattering of reflected SHG signal is observed for the embedded region while at the surface of reverse exchanged guide, the intensity and the quality of reflected SHG signal is practically the same as for the bulk $LiNbO_3$ (Fig.2b). With an increase of the reverse exchange time, when the RPE region becomes deeper than the depth of initial step-like PE waveguide (Figs.2a-4a), the samples displayed constant reflected SH signal over the entire unexchanged side with intensities equal to that from bulk $LiNbO_3$ (Fig.2b-4b) and there is no difference in reflected beam quality between the waveguide and the bulk regions (Fig.2c). All these results suggest the recovery of non-linear optical properties in REAPE waveguides.

Finally, the second-order nonlinearity has been measured in reverse proton exchanged $LiNbO_3$ waveguides in different $H_xLi_{1-x}NbO_3$ phases. We show that reverse exchange restores the nonlinear susceptibility to almost the original value of the virgin crystal both in the high-concentrated direct exchanged phases with initial strongly reduced nonlinearity and in the annealed low-concentrated phases manifested initially apparent increasing of SH signal due to high scattering of SH radiation.

1. Yu.N.Korkishko and V.A.Fedorov, *Ion exchange in single crystals for integrated optics and optoelectronics* (Cambridge International Science Publ., Cambridge, 1999), 516 p.
2. Yu.N.Korkishko, V.A.Fedorov, *J. Sel. Topics Quantum Electron.* **2,** 187-196, 1996.
3. Yu.N.Korkishko, V.A.Fedorov, S.M.Kostritskii, *J.Appl.Phys.* **84**, 2411-2419, 1998.
4. Yu.N. Korkishko, V.A.Fedorov, *J.Appl.Phys.* **82,** 171-183, 1997.
5. Yu.N.Korkishko, V.A.Fedorov, F.Laurell, *J. Sel. Topics Quantum Electron.* **6**, 132-142, 2000.
6. K.El Hadi, M.Sundheimer, P.Aschieri, P.Baldi, M.P.De Micheli, D.B.Ostrowsky, F.Laurell, *J.Opt.Soc.Am.B* **14**, 3197-3203, 1997.
7. Yu.N.Korkishko, V.A.Fedorov, O.Y.Feoktistova, *J. Lightwave Technol.***18**, 562-568, 2000.
8. Yu.N.Korkishko, V.A.Fedorov, T.M.Morozova, F.Caccavale, F.Gonella, F.Segato, *J.Opt.Soc.Am.A* **15,** 1838-1842, 1998.
9. Yu.N.Korkishko, V.A.Fedorov, M.P.De Micheli, P.Baldi, K.El Hadi, A.Leycuras, *Appl. Opt.* **35,** 7056-7060, 1996.
10. Yu.N.Korkishko, V.A.Fedorov, S.V.Katin, A.V.Kondrat'ev, *Proc.SPIE*, **2401**, 149-163, 1995.
11. J.Rams, J.Olivares, J.M.Cabrera, *Electron.Lett.* **33**, 322-323, 1997.
12. A.Di Lallo, C.Conti, A.Cino, G.Assanto, *IEEE Photon Technol. Lett.* **13**, 323-325, 2001.
13. K.Parameswaran, R.Route, J.Kurz, R.Roussev, M.Fejer, *Opt.Lett.* **27**, 179-181, 2002.
14. G.de la Paliza, A.García-Cabanes, J.M.Cabrera, *Phys.stat.solidi (a)* **193**, R7-R9, 2002.
15. H.Åhlfeldt, *J.Appl.Phys.* **76**, 3255-3260, 1994.

Tunable double micro-ring (DMR) filters for widely tunable lasers

Payam Rabiei
Department of Electrical Engineering, University of Southern California, Los Angeles, CA 90089, USA
rabiei@usc.edu
William H. Steier
Department of Electrical Engineering, University of Southern California, Los Angeles, CA 90089, USA

Abstract: Widely tunable double micro-ring filters by thermo-optic effect are demonstrated. The tuning range is more than 40nm. The required electrical power to achieve 40 nm using thermo-optic effect is less than 20 mW. A widely tunable laser using this filter and EDFA gain is demonstrated. The side mode suppression ratio is greater than 30dB and the tuning range is 40nm.

Keyword: Tunable laser, Micro-resonator, Electro-optic polymer, Thermo-optic effect

Introduction

Widely tunable filter and lasers are highly required for the wavelength division multiplexing (WDM) systems. Previously widely tunable lasers were demonstrated using vernier effect and Bragg gratings [1][2]. These structure use semiconductor Bragg gratings and tune by injecting current to the Bragg section of the device. Sampled grating DBR is used to achieve periodic reflections. Widely tunable lasers are demonstrated using this technology.
Recently Bin Liu et.al [3] introduced the idea of using micro-resonator (MR) instead of Bragg gratings to fabricate widely tunable lasers. There are many advantages to DMR devices. First the frequency response of MR is periodic and the transmission is equal for all the wavelengths. However the SG frequency response is not constant and the peak reflection decreases far from the Bragg condition. This limits the enhancement factor practically to 10 for SG-DBR structure [3]. However in a MR structure provided that Q is high enough the enhancement factor can be very large.
Also for the tuning mechanism previously carrier injection was demonstrated. However carrier injection changes the absorption and changes the threshold of the laser. Using electro-optic effect not only the absorption remains the same but also it is possible to change the lasing wavelength very rapidly. However since the change in the refractive index is very small only DMR structure with very high M can be used to achieve a widely tunable laser using electro-optic effect. The DMR device has narrow linewidth due to the long cavity formed by MR [4]. Since electro-optic effect is used it might be possible to make ultra-fast tunable devices, which might open the door to optical frequency shift keying (OFSK) or OCDMA systems.
Polymers can be used to make micro-resonator with very high Q [5]. Also electro-optic polymers with very large electro-optic coefficient can be used to make micro-resonators [5]. In this paper we have demonstrated for the first time the tunable DMR. For tuning thermo-optic effect is used. However electro-optic effect can also be used. Finally using an EDFA gain medium we have demonstrated a widely tunable laser.

Thermo-optic device fabrication

The fabrication of the device is very similar to previous structures we have fabricated [5]. The cross section and top view of the device is shown in Fig 1. The fabrication of thermo-optic devices starts with spin coating a lower cladding of UV15 epoxy. The lower cladding is chosen to be 15μm. This layer is a thermal isolator between the thin film heater and the bottom substrate. Two micro-resonators with 240μm and 246μm radius are fabricated. The FSR of MR is approximately 120GHz. The tuning enhancement factor is 40. The distance between the waveguide and the MR is chosen so that 10% coupling is achieved. Based on this design one would get discrete tuning with 120GHz spacing. Notice that one can easily modify these dimensions to achieve ITU standards.

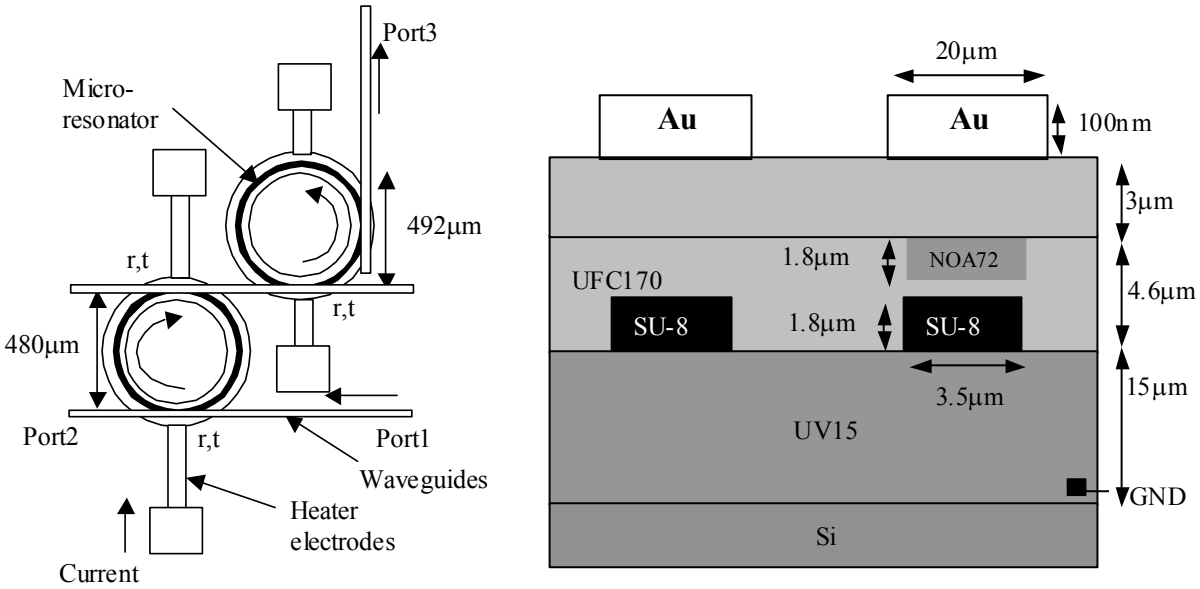


Fig. 1: (a) The structure of the device. The micro-resonators, Waveguides and electrodes geometry. (b) The cross section of the device. The SU-8 is the MR and the NOA72 is the waveguide

Device characterization

To characterize the device first we use a tunable laser to obtain the loss of cavity and the coupling to the device. The light is coupled through port 1 and is collected in port 2 while the laser wavelength is changed. Using the transmission in the through port (port2) it is possible to calculate the loss of the cavity and the coupling to the cavity. Based on this measurement at 1550 nm the r is measured to be 0.966. Hence the coupling of "power" to cavity is 6%. The round trip power loss of the cavity is 30%. This corresponds to a waveguide loss of 10dB/cm. SU-8 has a material loss of 4dB/cm in this wavelength. The rest of the loss is probably due to the scattering.

Next we use a wideband source to characterize the device tuning performance. A Newport EDFA (FPA-35) is used as the spontaneous emission source and gain region. The EDFA has a small signal gain of 40dB. A polrizer and a polarization controller are used to ensure single mode operation. For the testing of the device the light is butt coupled through small core fibers to the port 1 of the device and the output of port 2 is coupled to a second small core fiber and is sent to optical spectrum analyzer (OSA). Fig 2 shows the filtered spontaneous emission and the EDFA spectrum. Also it is clear how the filter response changes by changing the temperature. By passing current through the electrodes of the

device the temperature of one of the ring changes. This change in temperature causes a change in refractive index. The change in refractive index is $1.11X10^{-4}$/°C. It is interesting to see that only 5°C is enough to move the peak transmission wavelength 20nm while the resonance wavelength of the single MR is only moved 0.5nm. This is of course due to tuning enhancement factor of 40. As it is can be seen from the figure there is a very small difference in transmission between the maximum and the adjacent mode. The total insertion loss of DMR device is 20dB. The coupling loss from the fiber to the input and output waveguides is negligible using small core fibers.

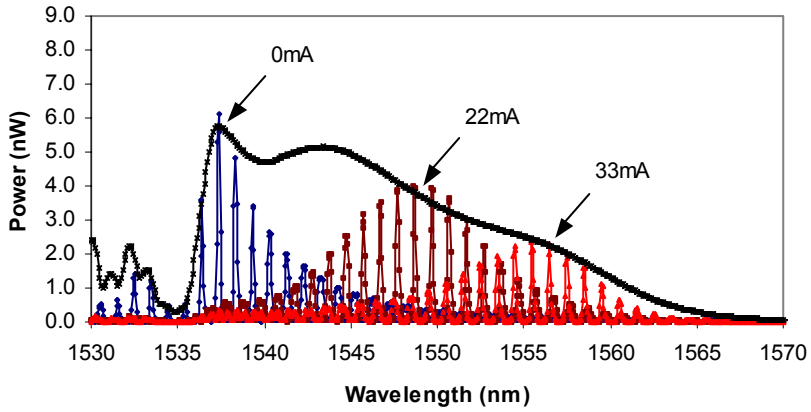


Fig. 2: The filtered spontaneous emission of the device for different values of the current to the electrode heater and the EDFA spontaneous emission spectrum

Next the output of the device is fed back to the input of the EDFA. Fig. 3-a shows the spectrum of the device output at port 3. The device lases with side mode suppression better than 30dB. It is noticeable that the gain of EDFA is very large (40dB) and lasing is obtained easily. Also due to the large EDFA gain good side mode suppression is obtained.
Finally Fig. 3-b shows the tuning characteristic of the laser. The lasing wavelength can be tuned by heating. However it does not lase at some region in the tuning range. This is due to the shape of the gain of EDFA. As it is clear from the tuning curve lasing is not achieved in the 1544 to 1550 and 1530

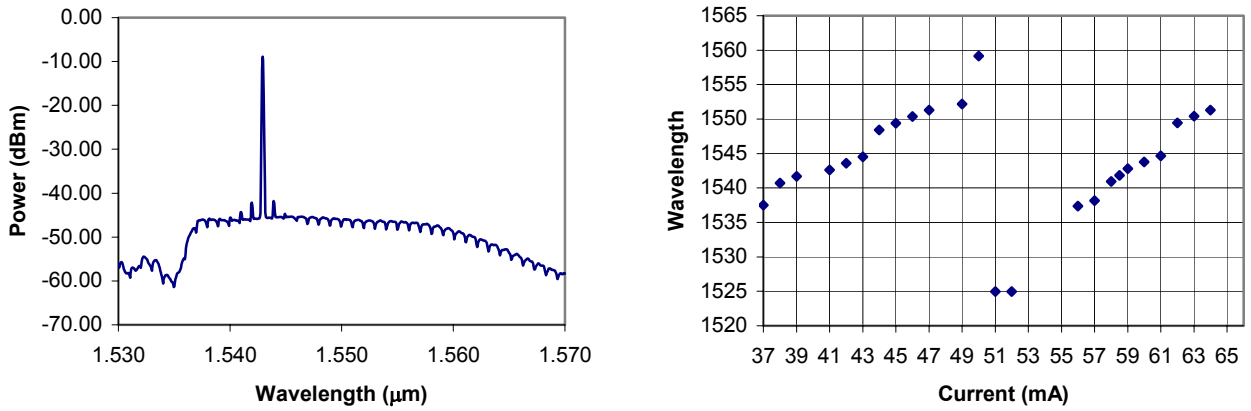


Fig. 3: (a)The lasing spectrum of the DMR thermo optic device. (b) The tuning characteristic of the DMR device as a function of the current in the electrodes

to 1536 region. Using semiconductor optical amplifier (SOA) one can probably obtain lasing in the whole range since there is less features in the gain shape of SOA.
The switching time for the wavelength is also measured. The device would require 1msec to increase the temperature and 2msec to decrease the temperature. So a few msec is required for the output light to stablize.
Notice that by heating only one of the electrodes one will obtain a discrete tuning. This is possibly ideal for some WDM networks which one only requires lasing on the ITU wavelengths. However one can achieve a continuous tuning by changing the refractive index of both micro-resonators.

Conclusion

We have demonstrated for the first time control of laser wavelength using two micro-ring structure. The lasing wavelength can be tuned over 35 nm and possibly larger provided enough gain bandwidth. The tuning can be either discrete or continuous. It is fairly easy to achieve tuning with 50GHz or 100GHz spacing. (ITU standard). The cost for making these kind of devices is very low compared to Bragg structures and semiconductors. The tuning speed for the thermo-optic version is in msec range and for the electro-optic can be very fast. The measured output power for the device is 1mW. The side mode suppression ratio of better than 30dB is demonstrated.
To achieve a practical device one probably need to obtain better coupling control between the waveguides and ring structure to minimize the device loss. Also one should integrate these devices with SOA to achieve a compact cheap tunable laser. Further research is also required to achieve higher Q for the resonators using lower loss materials

References

[1] V. Jayaraman, Z. M. Chuang, and L. A. Coldren, "Theory, design, and performance of extended tuning range semiconductor lasers with sampled gratings," *IEEE J. Quantum Electron.*, 29, 1824–1834 (1993)
[2] L. Zhang and J. C. Cartledge, "Fast wavelength switching of three-section DBR lasers," IEEE J. Quantum Electron., 31, 75–81, (1995)
[3] Bin Liu; Shakouri, A.; Bowers, J.E., "Wide tunable double ring resonator coupled lasers", IEEE Photonics Technology Letters , 14, 600-602, (2002)
[4] Bin Liu, Ali Shakouri and John E. Bowers, "Passive microring-resonator-coupled lasers", Applied Physics Letters, 79, 3561-3563, (2001)
[5] P.Rabiei, W.H. Steier, C. Zhang, L. Dalton, "Polymer micro-ring filters and modulators", IEEE J. Lightwave Technology", No.11, Nov (2002)

Wavelength Tuning and Switching of a Thermo-Optic Microring Resonator

D.H.Geuzebroek, E.J. Klein, H. Kelderman, A Driessen
Lightwave Devices Group, University Twente
POBox 217, 7500 AE Enschede, The Netherlands
d.h.geuzebroek@el.utwente.nl

The wavelength tuning of a compact microring resonator with a chromium heater is described. A tuning of 12 pm/°C is measured with extremely low driving power. This property together with the small footprint makes applications feasible in filter or switching arrays.

Keywords: Microring Resonator, Thermal Tuning, WDM filter, Switching

Introduction

Currently a shift in the deployment of integrated optical techniques towards the metro and access network can be observed. In these short-haul networks the reduction of both cost and space is an important issue. Large scale integrated optics is able to satisfy this challenge, since low-cost high density integration of functional elements in mass-produced devices is feasible. For these integrated applications tunable wavelength filters and switches are desired. In the following the thermal behavior of an integrated optic microring resonator is described. Both the static tuning as needed in a wavelength filter and the dynamic behavior as a switch will be described.

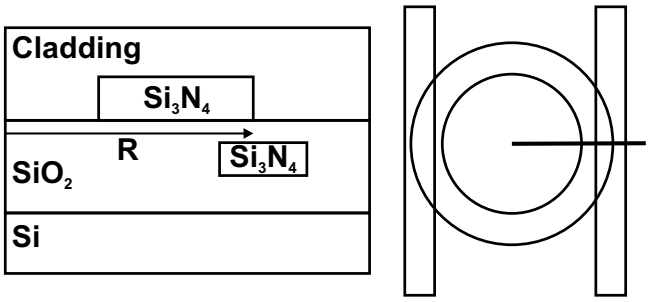


Fig. 1. Crossection and top view of a microring resonator

Microring Resonator

Micro-ring resonators (MR) can be deployed as WDM filters, switches, and modulators [1, 2]. Their small dimensions are advantageous for densely integrated and cost-limited applications. The functional behavior of a single MR is explained in [3]. The highly selective properties of the Lorentzian filter shape of the MR make it a good candidate for WDM filter applications. The properties of the MR can be exploited even more when multiple resonators are combined to perform specific functions. By cascading MRs, for example, a more desirable box-shaped filter response can be created [4]. A wavelength selective switch based on microrings is described in [5].
A schematic picture and a cross section of a single MR is shown in Fig 1. The MRs described in this work are fabricated of Si_3N_4 waveguide channels embedded in SiO_2, vertically coupled to the Si_3N_4 ring with radius R. With this technology high Finesse MRs with air cladding have been demonstrated [3, 6]. For thermal tuneability and switching a cladding layer as depicted in Fig. 1 is favorable since it allows optical isolation from an efficient local heating structure on top of

the resonator. The thermo-optical MRs have a PECVD SiO2 cladding. Improved performance is expected by applying a material that has a high temperature dependent refractive index, e.g. a polymer.

Thermal Tuning

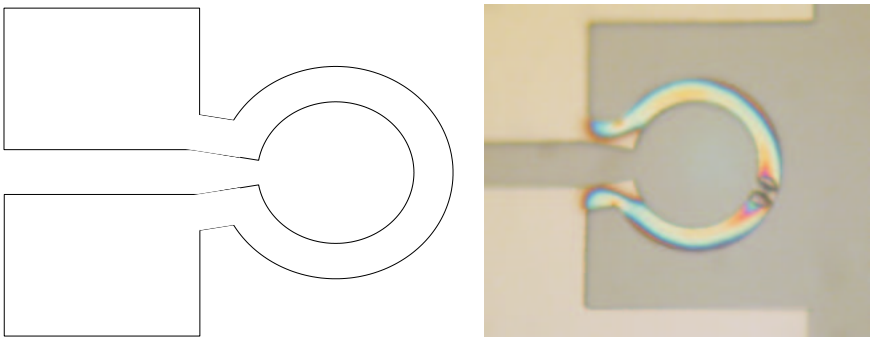
By locally applying a change in temperature, the effective index of the MR changes as a consequence also the resonance wavelength. The condition for resonance is:

$$\frac{2\pi}{\lambda} \cdot R \cdot N_{eff,ring} = m \tag{1}$$

Where λ is the wavelength, R the radius of the ring and $N_{eff,ring}$ the effective index of the mode propagating through the ring. Consequently one obtains for the shift in resonance wavelength ($\delta\lambda_c$) as a function of the change in effective refractive index due to tuning ΔN_{eff}:

$$\frac{\lambda \cdot \Delta N_{eff}}{N_{eff,ring}} \approx \delta\lambda_c \tag{2}$$

Simulations on a MR as described above with a radius of 25 μm and a ring thickness of 300 nm based on a thermal coefficient of $1.1 \cdot 10^5$ resulted in a ΔN_{eff} of $1.12 \cdot 10^{-3}$ for a temperature increase of 100 °C. This corresponds to a change in the center wavelength of approximately 11 pm/°C.



(a) (b)

Fig. 2. (a) Schematic view of the Ω-heater and (b) Chromium heater structure after destructive test

Heater Design

An optimized heater structure is used to generate efficiently the only locally desired change in temperature. The chromiun based thin film heater is shaped in a so-called Ω-shape see Fig. 2(a) for a schematic drawing. The Ω-shape proved to be the most favorable shape in terms of power consumption and heat distribution as is described in [7]. The picture of a Ω-heater after a destructive test is shown in 2(b). It shows that the heated power is distributed evenly across the heater. The heater has deliberately been broken by an excessive heater current at a point where most of the heat is dissipated, in this case at a random position in the Ω-shaped structure. The Ω-heaters are characterized by heating the heater externally and measuring the resistance changes, see Fig. 3. During normal operation an approximate heater temperature can easily be obtained by measuring the its resistance.

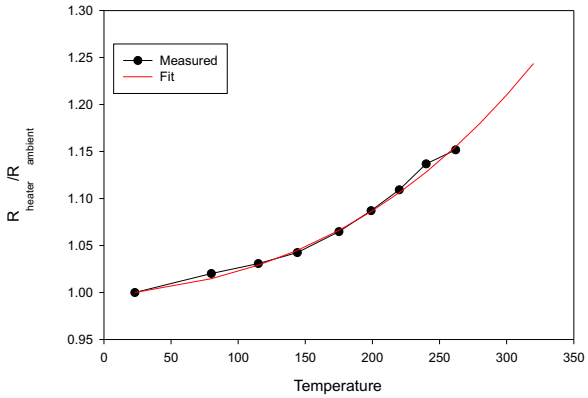
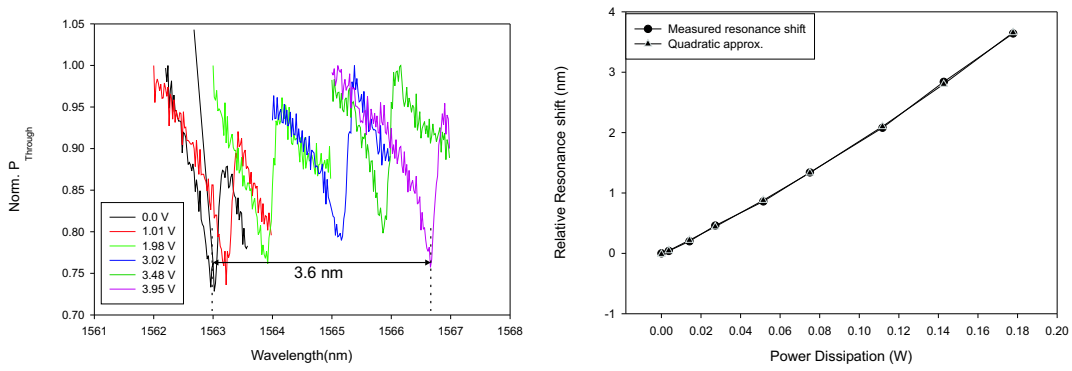


Fig. 3. Reference graph for determining the temperature of the compact Ω-heater

Measurements on Thermal Tuning

Measurements were performed on a MR with a PECVD SiO_2 cladding and chromium heaters. The results are shown in Fig. 4, which gives the resonant dips at the through-port as a function of heater voltage as well as the relative shift in resonance wavelength as a function of the dissipated power. As can be seen a shift of 3.6 nm could be reached at a heater power of around 180 mW. There is a slight nonlinearity in the relative resonance shift as a function of the heater power. This can be explained by the fact that the silicon wafer at the highest heater powers does not act any more as an ideal heat-sink with consequently a temperature rise of the complete wafer. When a linear dependency is assumed a relative resonance shift of 20 pm/mW can be found. The heater temperature at the highest shift (3.6 nm, 180 mW) can be found using Fig. 3 to be 315 °C ± 20°C. This gives a tunability of the ring of 12 pm/°C ± 1 pm. This is in accordance with the above calculated value.



(a) (b)

Fig. 4. (a) Normalized ring responses at the through-port for different heater voltages; (b) Shift of the resonance wavelength as a function of heater power

Switching

For application of thermo-optic MR as a switch as described in [5] the switching speed is an important issue. The limiting factor is the speed of the distribution of the heat generated in the heater. The previous section showed that small powers already allow a large tuning range for the resonance wavelength. This looks promising for switching applications, since for this application only small shifts are needed. To switch a microresonator from ON to OFF state,

only a small shift sufficient to cover the flank of a resonant peak is needed. Simulations on the thermal behavior of a MR show a switching frequency of 2 KHz. Also measurements have been done to find the maximum switching frequency by measuring the response of the MR when the heater current is modulated by a square wave. In Fig. 5 the detected differential voltage of a photodiode at the through port is shown as a function of the wavelength of the source. This figure shows the expected maximum in modulation depth around the resonance wavelength, where the ring response has the highest derivative. The maximum switching speed is estimated by observing at which point the amplitude of the received signal drops when increasing the frequency. For the device mentioned above a maximum switching frequency of around 2 kHz is obtained with a power dissipation of around 10 mW.

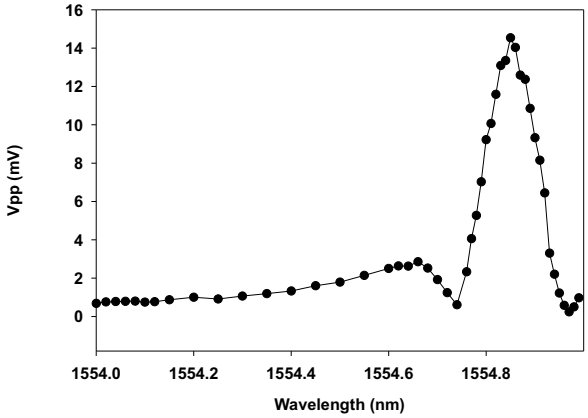


Fig. 5. Differential response of a MR to a modulated heater current as a function of wavelength

Conclusion

A thermally tunable microring resonator has been measured. A shift of the resonance wavelength as large as half of the free spectral range were possible with low power dissipations. Furthermore the fast switching capability is experimentally demonstrated.

Acknowledgement

The work presented was done within the frame work of the IST project NAIS.

References

[1] A. Driessen et Al. Analysis of a microring resonator based ultra-compact transceiver for the access network. *Proc. Symposium IEEE/LEOS Benelux*, pages 25–28, 2001.

[2] P. Rabiei. Integrated WDM polymer modulator. *Proc. OFC*, pages 31–33, 2002.

[3] D.J.W. Klunder. Vertically and laterally waveguide-coupled cylindrical microresonators in si3n4 on sio2 technology. *Applied Physics B*, 73:603–608, 2001.

[4] C.K. Madsen J.H.Zhao. *Optical Filter Design and Analysis*. Wiley, 1999.

[5] D.H. Geuzebroek. Thermal wavelength-selective switch based on micro-ring resonators. *Proc. ECOC*, page 4.2.5, 2002.

[6] F.S. Tan. High finesse vertically coupled waveguide microring resonators based on Si3N4-SiO2 technology. *Proc. WFOPC Glasgow*, pages 228–232, 2002.

[7] E.J. Klein. Wavelength selective switching using thermally tunable microring resonators. Master's thesis, University Twente, 2002.

Optimizing geometry of ring microresonators with respect to bending losses

Milan Hubálek, Jiří Čtyroký, Ladislav Prkna
Institute of Radio Engineering and Electronics AS CR, Chaberská 57, 182 51 Praha 8, Czech Rep.
hubalek@ure.cas.cz

Dependence of key parameters of low-contrast ring microresonators on cross-section dimensions is studied by numerical simulations. We found that bending losses very critically depend on these dimensions. Very high finesse resonators can be designed for optimum choice of waveguide cross-sections.

Keywords: guided-wave optics, microresonators, integrated optical circuit (IOC), radiating loss, scattering loss

Introduction

Guided-wave structures based on ring microresonators can be potentially used not only to significantly minimize optical integrated circuits (IOCs) but also to add functionality to the optical chip while preserving desirable technological uniformity of its fabrication. Although the operational principles are well known for more than thirty years [1], their real applications in IOCs appeared only recently as a result of significant technological progress in integrated-optical technology [2]. Consecutively, a few research groups have started detailed and intensive exploration of devices based on ring microresonators [3], [4]. In this contribution, the influence of cross-section dimensions of a low-contrast polymer rib waveguide on the radiation losses of the ring resonator is studied using the full vectorial numerical method [7].

The application of microresonators was impeded for so long because of losses due to surface roughness scattering at the waveguide edges. These losses increase very rapidly with the increased refractive index contrast between the waveguide core and the surrounding medium. On the other hand, this high contrast is needed for keeping up the radiation losses due to curvature at a tolerable level. Contrary to the scattering losses, radiation losses increase with the decreasing contrast of the refractive indices. It is thus apparent that in order to fabricate good structures, very high-quality technology for high-contrast waveguides (e.g., semiconductor/air, see [5]) is required.

High-contrast structures have also some disadvantages, however. If we ignore the high cost of the technological equipment like MOCVD or even MBE required for their fabrication, still other problems remain such as low coupling efficiency between the high-index waveguide and a standard optical fiber. In the next section we show that it is possible to drastically reduce the radiation losses even in low-contrast structures by proper modification of the cross-section geometry of the ring waveguide.

Optimizing the waveguide cross-section geometry

In the "classical" approach to the fabrication of microresonators (MR), a rib waveguide is etched down in a semiconductor [5]. The typical cross-section geometry of the resultant structure is shown in Fig. 1a.

In case that the radius of curvature of the MR need not to be smaller then about 25 μm, it is possible to make the MR from the low-contrast materials (e.g. polymers). Radiation losses can be kept at a reasonably low level by optimization the cross-section geometry. Its modified shape is depicted in Fig. 1b. The way to reduce the radiation loss leads via redistributing the optical field in the core of the MR waveguide. To this aim, the structure is supplemented with the cover on the inner and the top boundaries of the core (see the picture). Owing to this

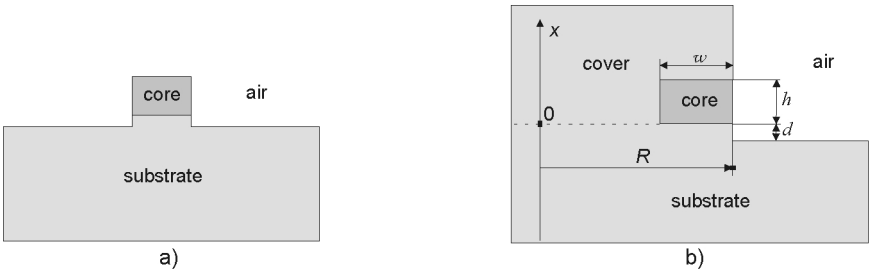


Fig. 1. The cross-section geometry of the rib of ring MR. a) the "classical" approach, b) the modified structure.

modification, the optical field power is shifted towards the inner boundary of the ring. Thus, only a smaller portion of the optical power at the outer boundary contributes to the radiating part of a mode that leaks out of the waveguide. At the outer boundary, the maximum refractive index contrast of the structure is preserved. Power leakage into the substrate can be further reduced by etching the substrate close to the outer boundary. The maximum etching depth is limited by affecting the coupling between the resonator and input/output ports (vertical coupling after [6] is assumed).

The described geometry has some potential for reducing scattering losses as well. Because of overlay from cover material, the total area of the surface with high refractive index contrast is remarkably reduced. Additionally, the redistribution of the field within the core also reduces the optical power propagating close to the remaining high-contrast interface. Thus, the proposed modification of the cross-section of the structure is expected to suppress even the scattering losses. Note that for polymer structures, the scattering losses are usually lower than for structures based on semiconductors or silicon nitride due to lower refractive index contrast [2].

Numerical results

We made a series of calculations with the aim of optimizing the structure with respect to radiation losses. The calculations are performed for the free-space wavelength of the optical wave of $1.55\,\mu$m in the centre of the standard optical communication band. The refractive indices of the considered polymer materials are 1.5965 for the core and 1.4468 for both the substrate and the cover, at this wavelength. The radius of curvature of the ring resonator was fixed to $50\,\mu$m. The fully vectorial 2D bend mode solver based on the finite-difference technique from the commercial software package OlympIOs by the C2V company [7] was used for the numerical analysis.

Since the future complex devices are expected to be composed of many MRs with various radii, the loss values are shown in dB per round trip (l_r) rather than in dB per unit length in the figures. The relation between the round-trip loss and the resonator finesse is given by a simple expression

$$F = 20\pi/(l_r \ln 10). \tag{1}$$

First we calculated the loss and the field distribution of the fundamental mode for the standard structure without any optimization. The rib width was chosen to be $w = 1.4\,\mu$m, the height $h = 1\,\mu$m, with no etching into the substrate, $d = 0\,\mu$m. The calculated loss per round trip was $l_r = 15.8\,$dB. Then we calculated the dependencies of the radiation loss on the width w, height h and the etching depth d of the resonator cross-section. The results are presented in the following graphs.

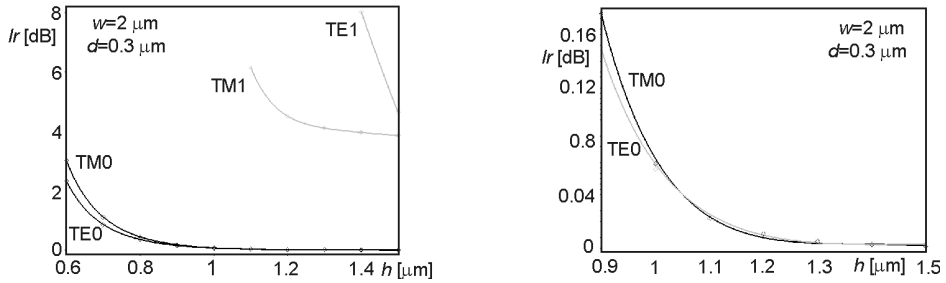


Fig. 2. The dependence of round-trip radiation losses on the heigth of the waveguide core.

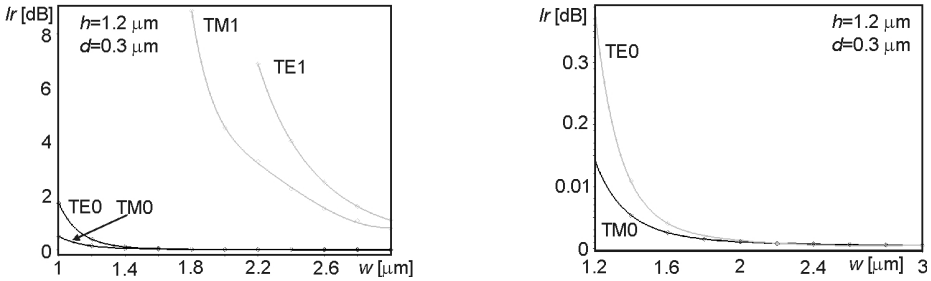


Fig. 3. The dependence of round-trip radiation losses on the width of the core.

Figs. 2 and 3 show the dependencies of radiation losses on the cross-section dimensions h and w, respectively. Very rapid decrease of radiation loss with increased dimensions of the core is evident. The maximum size of the core is generally limited by the onset of the higher-order mode. However, as it can be seen from Figs. 2 and 3, radiation losses of these modes are significantly higher, which means that these modes would not play an important role even if they are exited.

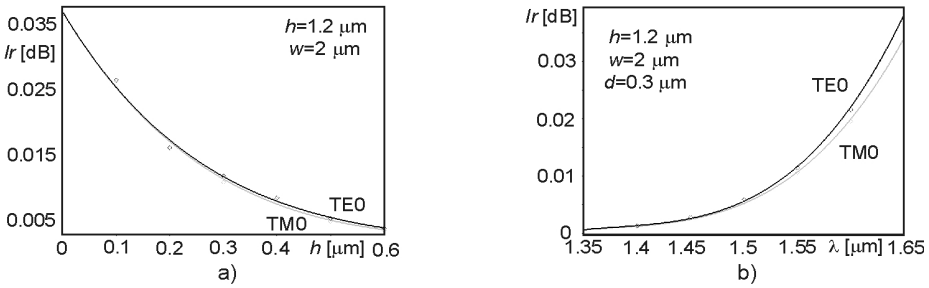


Fig. 4. a) The dependence of round-trip radiation losses on the substrate etching depth at the outer boundary of the core. b) The dependence of round-trip radiation losses on the free-space wavelength.

The dependence of the losses on the depth of the etching into the substrate d can be seen in Fig. 4a). The dimensions of the core are chosen in correspondence to the previous graphs; the "most suitable" values are selected. This graph shows that etching of substrate suppresses the radiation losses remarkably. As we have already mentioned, the only limitation for the depth of this etching is given by the vertical structure of the devices; the vertically coupled input/output waveguides should not be affected by this intervention. For a particular fabrication process it seems to be possible to optimize this depth also with respect to the scattering losses (the area with high-index contrast grows with this etching).

Finally, we calculated the wavelength dependence of the radiation losses for the "optimized" structure. The result is depicted in Fig. 4b). Material dispersion is neglected in this computation. As expected, radiation loss strongly increases with wavelength.

Note that the optimization of the structure leads to a significant reduction of the radiation loss; the "optimized" structure with $w = 2\,\mu$m, $h = 1.2\,\mu$m and $d = 0.3\,\mu$m exhibits 1500--times lower round-trip loss than the original one. In the following figures we show the field distributions of the TM_0 modes of these structures. Notably better confinement and significant suppression of the field radiating into the substrate for the optimized structure is clearly seen.

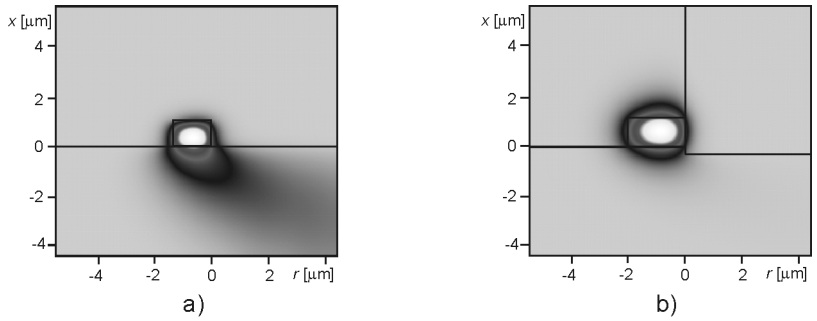


Fig. 5. Distribution of dominant component of the magnetic field vector of TM_0 mode for a) original, and b) modified structure.

Conclusion

We have shown by numerical study that low-loss microresonators can be created even in lowindex- contrast structures like organic polymers, if their cross-section is suitably optimized. The strong dependence of the radiation losses on the cross-section dimensions has been reported. Very small radiation losses of the low-contrast MR with the radius of curvature 50 μm have been demonstrated by numerical simulations. The possibility of simultaneous reduction of scattering losses has also been briefly discussed.

This work was done in the framework of the EC 5FP project IST-2000-28018 "NAIS".

[1] E. A. J. Marcatili, *Bends in Optical Dielectric Guides. The Bell System Technical Journal.* Vol. 48, 2103–2132, 1969.

[2] B. E. Little, J. S. Foresi, G. Steinmeyer, E. R. Thoen, S. T. Chu, H. A. Haus, E. P. Ippen, L. C. Kimerling, and W. Greene, *Ultra-Compact Si-SiO_2 Microring Resonator Optical Channel Dropping Filters. IEEE Photonics Technology Letters*, Vol. 10, No. 4, 549–551, 1998.

[3] Massachusetts Institute of Technology. http://web.mit.edu/cmse/www/Haus98.pdf

[4] NAIS - Next generation Active Integrated optic Sub-systems. Project IST 2000-28018, http://www.mesaplus.utwente.nl/nais/

[5] J. V. Hryniewicz, P. P. Absil, B. E. Little, R. A. Wilson, and P.-T. Ho, *Higher Order Filter Response in Coupled Microring Resonators. IEEE Photonics Technology Letters*, Vol. 12, No. 3, 320–322, 2000.

[6] S. T. Chu, B. E. Little, W. Pan, T. Kaneko, S. Sato, and Y. Kokubun, *An Eight-Channel Add-Drop Filter Using Vertically Coupled Microring Resonators over a Cross Grid. IEEE Photonics Technology Letters*, Vol. 11, No. 6, 691–693, 1999.

[7] OlympIOs C2V software package. Concept to Volume, The Netherlands.

Hybrid and passive mode-locking of quantum dot lasers at ~10GHz.

M. G. Thompson, C. Marinelli, K.T. Tan, K. A. Williams, R. V. Penty and I. H.White
Engineering Department, University of Cambridge, Trumpington St, CB2 1PZ, United Kingdom
mgt32@cam.ac.uk

I. N. Kaiander, R. L. Sellin and D. Bimberg
Institut für Festkörperphysik, Technische Universität Berlin, Hardenberg Str., 10623 Berlin, Germany

D.-J. Kang and M. G. Blamire
Interdisciplinary Research Centre in Nanotechnology , 11 JJ Thompson Ave., CB3 0FF, United Kingdom

F. Visinka, S. Jochum and S. Hansmann
Opto Speed Deutschland GmbH, Am Kavalleriesand 3, D-64295 Darmstadt, Germany

We demonstrate for the first time a hybrid mode-locked quantum dot laser and show improved performance over passive mode-locking. Hybrid and passive mode-locking at ~10GHz is achieved for the first time in quantum dot lasers.

Keywords: quantum dot laser, mode locking, passive, hybrid

Introduction

Picosecond and sub-picosecond optical pulse sources based on laser diodes (LDs) are desirable for applications such as high-speed data transmission, clock signal generation and electro-optic sampling. Monolithic multisection mode-locked LDs can provide compact, mechanically stable and low-jitter sources of ultrashort optical pulses at repetition rates higher than the laser modulation bandwidth [1,2].

Quantum dot lasers grown on GaAs substrate are of great interest for mode-locking applications, due to the possibility of integration with other electronic components and their potential for achieving enhanced performance by virtue of a very low threshold current density [3], high characteristics temperature [4], high temperature stability of the emission wavelength [5], high differential gain [6] and low wavelength chirp [7].

Previous studies have characterised the properties of quantum dot layers as saturable absorbers and have reported passive Q-switching and passive mode-locking of quantum dot lasers with a repetition rate ≤7.6GHz [8-11]. Our study focuses on monolithic hybrid mode-locking of quantum dot lasers, as this can significantly reduce timing jitter with respect to passive mode-locking [12] and additionally provide the repetition rate tunability required in time multiplexing applications. We compare the performance of hybrid and passive mode-locked quantum dot lasers operating at a repetition rate of ~10GHz.

Device structure and characterisation

The devices under test are grown on GaAs:Si substrates using metalorganic chemical vapor deposition (MOCVD) [13]. The laser active region comprises of a triple stack of self-organised $In_{0.5}Ga_{0.5}As$ quantum dots embedded in a 300nm thick undoped GaAs waveguiding layer. The top and bottom cladding layers consist of a 1µm thick $Al_{0.65}Ga_{0.35}As$:C and $Al_{0.65}Ga_{0.35}As$:Te layers, respectively. The epitaxial structures are dry etched using a titanium etch mask to form 3.9mm long, 30µm wide ridge waveguide structure. Electrical isolation is achieved using SiO_2 and TiPtAu deposited on both sides to form the contacts. Focussed ion beam (FIB) etching is subsequently used to split the contact of fully fabricated devices and create a monolithic two-section laser incorporating gain and absorber regions.

To reduce thermal effects all the experimental characterisations are performed at a controlled temperature of 20°C using pulsed current injection. Drive electrical signals with a duration of 50µs

and a repetition rate of 1KHz (corresponding to a 5% duty cycle) are used throughout this study. Prior to FIB etching, the devices typically exhibit a threshold current density in the 85-90A/cm^2 range and an emission wavelength centred around 1106nm originating from the quantum dots ground state recombination.

Using a stream of gallium ions accelerated by a 30kV potential, a 330pA beam current and a 1.42nJ/µm^2 ion dose, we FIB-etch a 35x5µm trench parallel to the laser facets. The contact is split in two sections: a 3570µm long gain region and a 330µm long absorber region. The trench is 1.6µm, deep stopping prior to the confinement layer and providing a 52kΩ electric isolation between the two sections. Post-etch characterisations indicate a threshold current density of 98A/cm^2 with bias applied only to the 3.57mm-long gain section.

Experimental results.

Three types of characterisations are performed under passive and hybrid mode-locking conditions: measurements of pulse traces in time domain, measurement of wavelength and RF optical power spectra. In order to achieve passive mode-locking the gain and absorber sections of the quantum dot laser are independently but synchronously pulsed using 50µs long electrical signals at a repetition rate of 1kHz. For hybrid mode-locking a gated RF signal is generated in synchronous with the 50µs pulses and superimposed to the absorber pulsed bias using a bias tee. The lasing emission is collected from the laser facet using a single mode cleaved fibre.

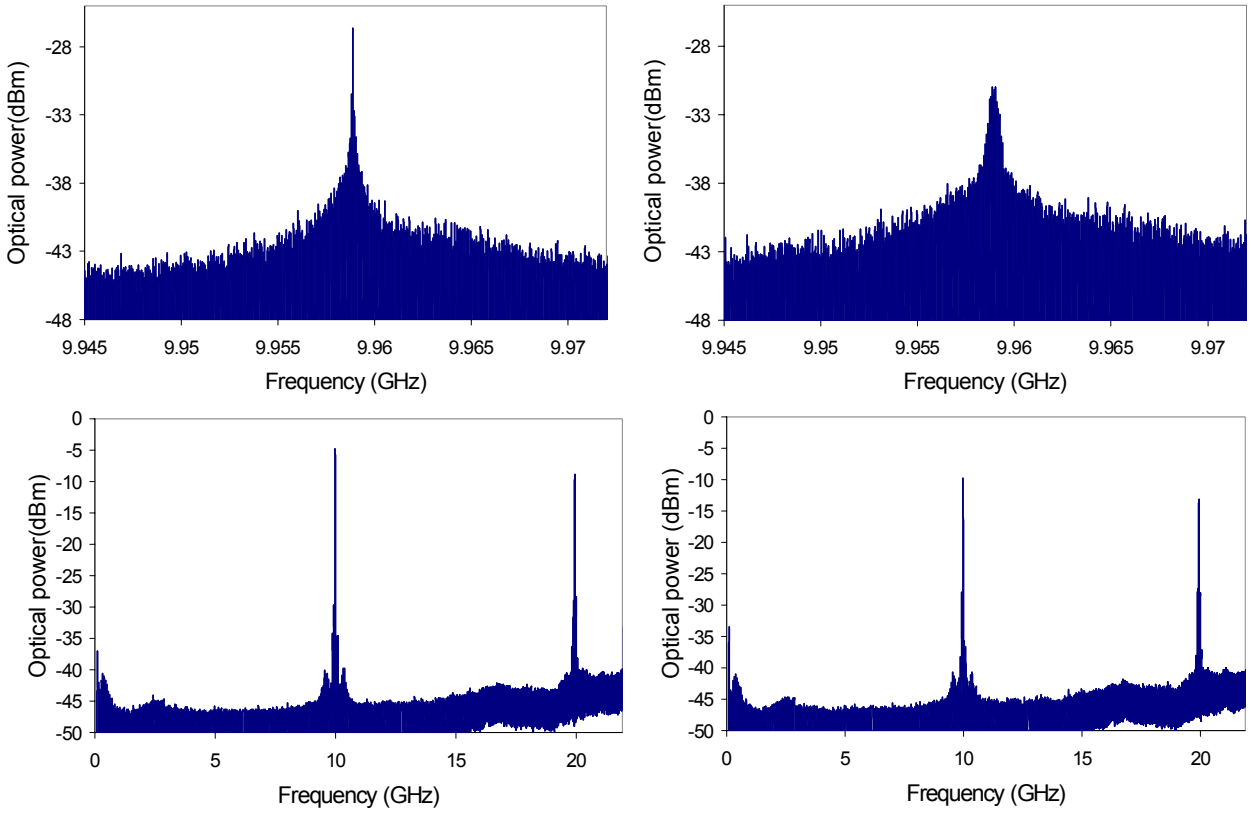


Figure 1. Optical RF spectra of hybrid (left) and passive (right) mode-locked quantum dot laser. The resolution bandwidth is 10kHz and 10okHz for the top and bottom spectra, respectively.

We first optimize the passive mode-locking conditions. The gain section of the laser is driven at a fixed current of 120mA (15mA above threshold). Due to the length of the absorber, a forward bias is applied to this section to controllably reduce losses and obtain sufficient round trip gain to allow lasing to occur. To optimise the passive mode-locking conditions the voltage across the absorber

section is varied and the optical RF power at 10GHz is monitored. An optimum 3dB operating range of 0.2V, centred at 1.06V is found. Under these conditions the estimated peak power for the mode-locked optical pulses is ~4mW.

Hybrid mode-locking is achieved by superimposing a ~10GHz RF modulation on the optimised absorber bias. Using a 16dBm RF driving signal we fine-tune the RF frequency to obtain optimum hybrid mode-locking. Figure 1 shows a comparison of optimized hybrid and passive mode-locking. The upper optical RF spectra of figure 1 demonstrate a significant performance enhancement upon hybrid mode-locking. Compared to passive mode-locking, the phase noise at a 5MHz offset is improved by 11.7dB, whereas the FWHM of the optical RF spectrum is reduced from 720kHz to 97kHz This sharpening of the optical RF spectrum indicates a reduction in the intrinsic device jitter, due to the fact that under hybrid mode-locking the cavity modes are locked to the frequency of the external RF source. The high power observed in the 20GHz harmonic (lower spectra of figure 1) is further evidence of strong mode-locking with narrow pulses in both hybrid and passive mode-locking. It is also likely that there will be higher harmonics, beyond the 22GHz bandwidth of our RF spectrum analyser.

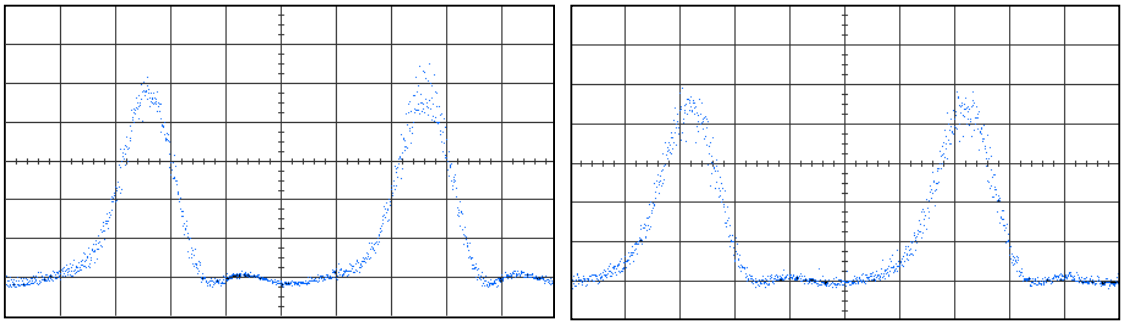


Figure 2. Time domain pulse traces of hybrid (left) and passive (right) mode-locked quantum dot laser. The oscilloscope horizontal axis is 20ps/div and the pulse repetition rate is 10.04GHz

Figure 2 compares the averaged time domain pulse traces for hybrid and passive mode-locking. The measured pulse width is ~21ps. This value is strongly affected by the timing jitter in our experimental set-up (5.5ps) and the time response of the 30GHz oscilloscope (14.66ps, assuming a Gaussian pulse shape). One can therefore estimate the de-convolved pulse width to be not greater than 14ps. Figure 2 also suggests a sharpening of the pulse trace upon hybrid mode-locking.

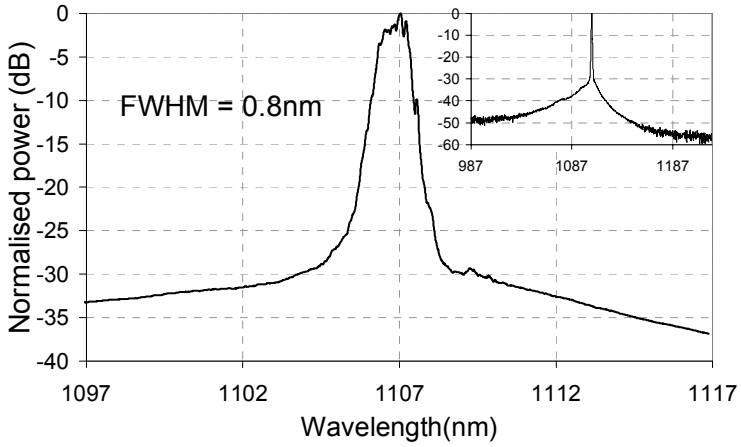


Figure 3. Wavelength spectra of a mode-locked quantum dot laser.

The measured wavelength spectrum indicates that the pulse width could be significantly less than 14ps. This wavelength spectrum in figure 3 is measured with a 0.07nm resolution and shows a FWHM of 0.8nm. In the Fourier limit such spectral width corresponds to a time-domain pulse width of 2.2ps. Since it has been reported that quantum dot lasers exhibit low wavelength chirp [7], we expect the time-bandwidth product for our devices to be much closer to the Fourier limit than indicated by our time-domain characterisation. The wavelength spectra for hybrid and passive mode-locking show no significant difference. Additionally, the inset in figure 3 shows no evidence of stimulated emission from the excited quantum dot states.

Conclusions

We demonstrate the first monolithic hybrid mode-locked quantum dot laser and show a significant enhancement in the quality of the optical RF spectrum with respect to passive mode-locking. A 11.7dB improvement in phase noise at a 5MHz offset and a 620kHz reduction in the FWHM of the optical RF spectrum is reported. Hybrid and passive mode-locking at 10GHz using quantum dot lasers is also demonstrated for the first time. Our results therefore confirmed the great potential of mode-locked quantum dot laser in optical communication and ultra-fast photonic application.

[1] P. Vasil'ev, *Ultrafast Diode Lasers*, Artech House, Boston-London, 1996

[2] B. Zhu, I.H. White, R.V. Penty, A.Wonfor, E. Lach, and H.D Summers, *IEEE J.Quantum Electron* **QE-33**,1216-1220, 1997

[3] G. Park, O. B. Shchekin, D. L. Huffaker, D. G. Beppe, *IEEE Phot. Technol. Lett* **13**, 230-232, 2000

[4] K. Klopf, J.P. Reithmaier, and A. Forchel, *IEEE Phot. Technol. Lett* **13**, 764-766, 2001

[5] J.D. Thompson, H.D. summers, P.M. Smowtown, E. Hermann, P. Blood and M. Hopkins, *Appl. Phys. Lett.* **90**, 4859-4861, 2001

[6] S. Gosh ..S.Pradhan, nad P. Battcharraya, *Appl. Phys. Lett.* **81**, 3055-3057, 2002

[7] Saito, H.; Nishi, K.; Kamei,A.; Sugou,S., *IEEE Phot. Technol. Lett* **12,** 1298-1300,2000

[8] X. Huang, A. Stintz, L. Hua, L.F. Lester, J. Cheng, and K.J. Malloy, *Proc. CLEO '01*, 359-361, 2001

[9] D.R. Matthews, H.D. Summers, and P. M. Smowtown, M. Hopkins, *Proc. 18th Semic. Laser Conf. '02*, p. 75-76, 2002

[10] A.Garnache, S. Hoogland, A. C. Trooper, J.M. Gerard, V. Thierry-Mieg, J.S. Roberts, *Proc. 14th IPRMC '02*, 311-314, 2002

[11] X. Huang, A. Stintz, L. Hua, L.F. Lester, J. Cheng, and K.J. Malloy, *Appl. Phys. Lett.* **78**, 2825-2827, 2001

[12] D. J. Derickson, P. A. Morton, and J. E. Bowers, R. L. Thornton, *Appl. Phys. Lett.* **59**, 3372-3374, 1991

[13] R.L. Sellin, I. Kaiander, D. Ouyang, T. Kettler, U. W. Pohl, and D. Bimberg, N. D. Zakharov and P.Werner, *Appl. Phys. Lett.* **82**, 841-843, 200

A Compact Two-dimensional Grating Coupler used as a Polarization Splitter

Dirk Taillaert, Roel Baets
Ghent University - IMEC, Department INTEC, Gent , Belgium
dirk.taillaert@intec.rug.ac.be

Harold Chong, Richard M. De La Rue
Glasgow University, Department of Electronics and Electrical Engineering, Glasgow, UK

Peter I. Borel, Lars H. Frandsen
Technical University of Denmark, Research Center COM, Lyngby, Denmark

A novel polarization splitter based on a 2-D grating coupler in a SOI waveguide is demonstrated. The device couples orthogonal modes from a single-mode fiber into identical modes of two ridge waveguides. The extinction ratio is better than 18dB in the wavelength range 1530nm-1560nm and the coupling efficiency is 20%.

Keywords: grating coupler, polarization, integrated optics, silicon-on-insulator

Introduction

Photonic crystal waveguides and photonic wires show great potential for high-density integrated circuits. Ultra-compact waveguides in silicon-on-insulator (SOI) with relatively low losses have been demonstrated [1][2]. However, the strong polarization dependence of these waveguides is a major disadvantage and limits the potential use in optical fiber communication networks. Also it is difficult to achieve a high coupling efficiency to fiber because of the huge mismatch in spotsize between these waveguides and a fiber.

Grating couplers can be used to couple light into submicrometer thin SOI waveguides [3]. It has also been demonstrated that a grating-coupler can be used to butt-couple light between a vertical single-mode fiber and these waveguides [4].

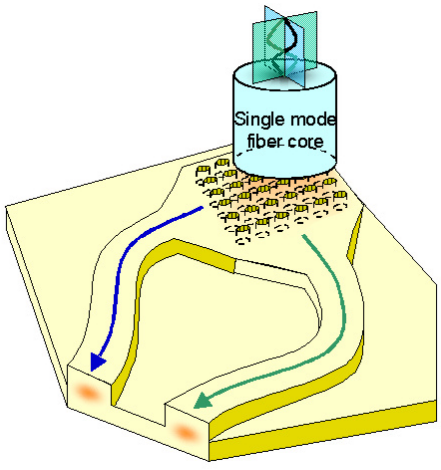


Figure 1. Schematic drawing (not to scale) of the coupler - splitter

In this paper we demonstrate a coupler based on a 2-D grating etched in a SOI waveguide. The device couples orthogonal modes from a single-mode optical fiber into identical modes of two planar ridge waveguides. It may be used in a polarization diversity configuration to implement a polarization insensitive photonic integrated circuit based on photonic crystal waveguides.

Concept

Consider a grating coupler consisting of a 2-D grating etched in a single ridge waveguide. In general the coupling efficiency from fiber to waveguide is polarization dependent. For the waveguides and gratings we use, the coupling efficiency for TE is much larger than the coupling efficiency for TM. The coupling from fiber to waveguide 1 will be maximum if the input is linearly polarized in the y direction.

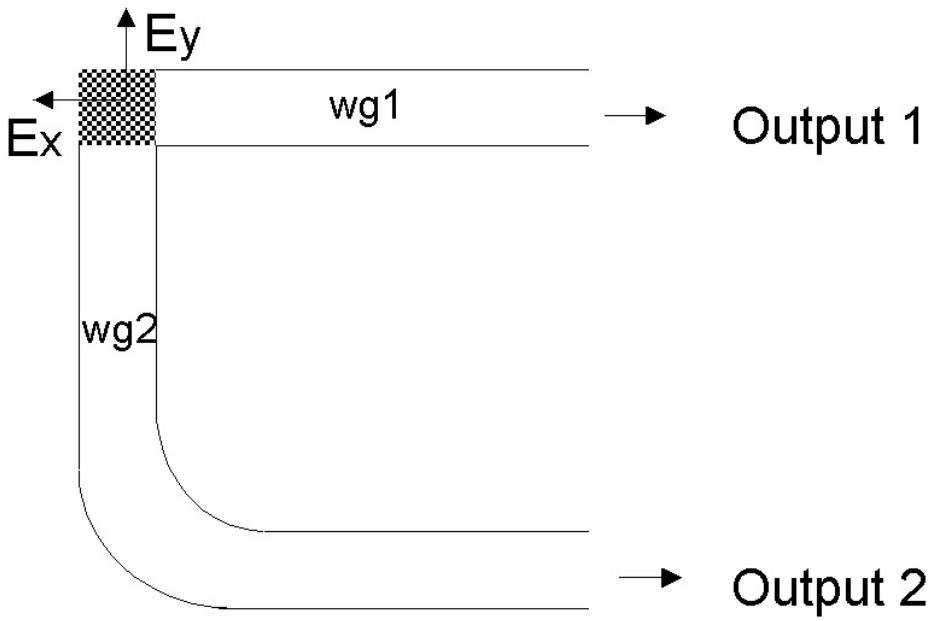


Figure 2. Top view of the splitter structure

The structure of fig. 2 consists of 2 ridge waveguides that are orthogonal. The 2-D grating is etched into the crossing of the waveguides and is invariant for a 90 degree rotation. The linear polarization with electric field Ey will couple to waveguide 1 and the other polarization with electric field Ex to waveguide 2. In general, eliptically polarized light from a single mode fiber will couple both to waveguide 1 and 2. The coupling ratio will depend on the state of polarization, but the coupling to wg1 and wg2 together will be independent of it. The 90 degree bend in waveguide 2 is only used for practical reasons (to have the 2 outputs at the same cleaved facet). We have described the working principle as input coupler, but the device can also be used as output coupler.

There is a very important difference between conventional polarization splitters described in literature [5] and our splitter. In a conventional splitter, the input light is splitted in a TE and TM waveguide mode. In our device, the light from a fiber is splitted in two TE waveguide modes. Because in the two waveguides the same polarization (TE) is used, the device can be usefull to make polarization insensitive photonic integrated circuits, using waveguides which are very strongly polarization sensitive.

Experimental results

The structures were fabricated on SOI wafers with a top silicon film thickness of 220nm and a buried SiO_2 layer thickness of 1µm. Gratings and waveguides were defined using electron beam lithography and reactive ion etching. A top view is shown in figure 3. The grating is a square array of holes, the etch depth is 90nm and the lattice period 580nm. The hole diameter is 300nm. The ridge waveguides are 10µm wide. A 90 degree bend is inserted in one of the waveguides to be able to detect both ouputs at one cleaved facet.

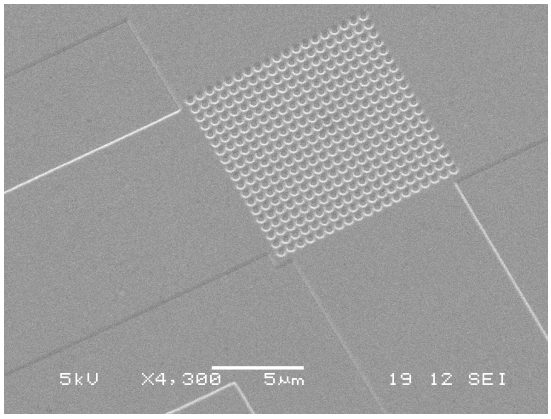


Figure 3. SEM top view

We used the structures from fig. 2 to measure the extinction ratio and check the polarization of the light in the waveguides. A vertical fiber couples light from a tunable laser into the waveguides via the grating. We detect the output power of waveguides 1 and 2 at the cleaved facet using a 40x objective and a power detector. After the initial alignment, the position of the fiber is fixed and only the polarization and wavelength are changed during the further measurements. The polarization of the input light is changed using a Lefevre type polarization controller to maximize output 1 or ouput 2. Then the extinction ratio between the 2 outputs is measured for both cases. The extinction ratio is shown in fig. 4a for different wavelengths. The extinction ratio is better than 18dB in the wavelength range 1530-1560nm. The difference between the 2 cases is caused by radiation losses in the 90 degree bend in waveguide 2. We have also verified the polarization of the light in the waveguides. The ouput power versus wavelength for the case when output 1 is maximised is shown in fig. 4b. The fringes in these curves are caused by a cavity between the grating and a cleaved facet.

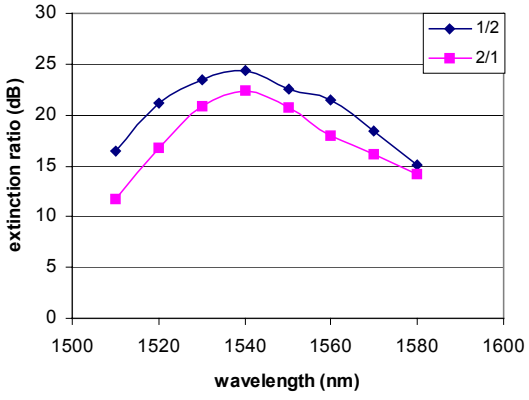
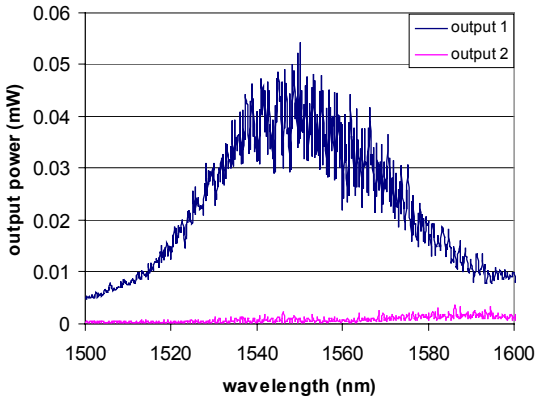


Figure 4a. Extinction ratio measurement



4b. Output power versus wavelength

It is not straightforward to determine the coupling efficiency from the power detected at the cleaved facet because of the facet reflectivity and the high numerical aperture of the waveguides. Therefore we estimate the coupling efficiency from a transmission measurement from fiber to waveguide to fiber on a structure consisting of a waveguide with a grating coupler at both ends. In this measurement, the fibers are tilted slightly to shift the wavelength out of the second order grating reflection peak and thus avoid cavity effects between the two gratings. The fiber to fiber transmission is 4% for TE-polarization, so the coupling efficiency is 20% if we take into account that the coupling from fiber to waveguide is the same as from waveguide to fiber.

Summary

We have demonstrated a polarization splitter based on a 2-D grating etched in a SOI waveguide. The device couples light from a single-mode optical fiber into two identical planar ridge waveguides. The extinction ratio is better than 18 dB in the wavelength range 1530-1560nm and the coupling efficiency is approximately 20%. The device is very compact and couples light only to TE-modes of the planar waveguides. Therefore, it may be used in a polarization diversity configuration to implement a polarization insensitive photonic integrated circuit based on photonic crystal waveguides.

Acknowledgements

This work was supported in part by the European Union in the context of the IST project PICCO and by the Belgian government in the context of the IAP PHOTON project.

References

[1] M. Notomi, A. Shinya, K. Yamada, J. Takahashi, C. Takahashi, I. Yokohama, *IEEE J. Quantum Electron.,* vol. 38, 736-742, 2002

[2] K.L. Lee, D.R. Lim, L.C. Kimerling, J. Shin, F. Cerrina, *Opt. Lett.*, vol. 26, 1888-1890, 2001

[3] R.M. Emmons, D.G. Hall, *IEEE J. Quantum Electron.*, vol. 28., 164-175, 1992

[4] D. Taillaert, W. Bogaerts, P. Bienstman, T.F. Krauss, P. Van Daele, I. Moerman, S. Verstuyft, K. De Mesel, R. Baets , *IEEE J. Quantum Electron.*, vol. 38, 949-955, 2002

[5] J. Van der Tol, J.W. Pedersen, E.G. Metaal, J. Van Gaalen, Y.S. Oei, F.H. Groen, *IEEE Photonics Tech. Lett.*, vol.9, 209-211, 1997

Planar Photonic Crystal Microcavities for Add/Drop Filter Functionality

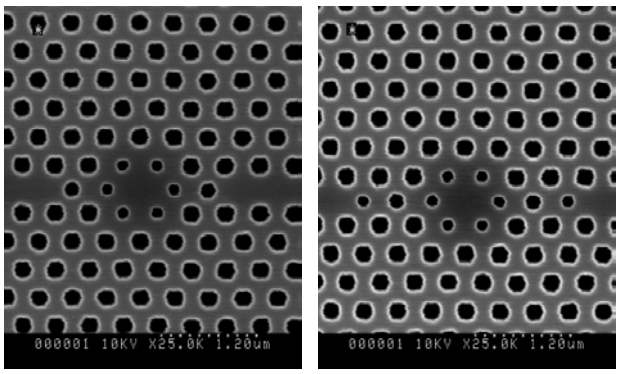
H. Chong and R. M De La Rue
Department of Electronics and Electrical Engineering, University of Glasgow, Rankine Building, Oakfield Avenue, Glasgow G12 8LT, SCOTLAND
h.chong@elec.gla.ac.uk

Abstract
We have fabricated and measured hexagonally shaped microcavities within triangular symmetry 2D photonic crystal regions of silicon-on-insulator (SOI) planar waveguides, using reduced diameter in-filling holes. Device structures based on such microcavities have been realised using direct input and output coupling through channel waveguides with size-graded holes in the channels at both the input and output of the microcavity. A measured Q-value of ~ 800 has been obtained in a structure with a transmission resonance wavelength of 1542.6 nm.

Keywords*:* Photonic crystal, cavity, WDM, Add/Drop Filters, silicon-on-insulator (SOI).

Introduction

Photonic crystal microcavities have been studied widely for their ability to confine light selectively at different operating wavelengths. This property is clearly highly desirable in the application areas of wavelength division multiplexing and channel add/drop filtering. Photonic crystal cavities with high Q-values have been reported by several authors [1,2,3,6,7] and various techniques have been used to couple light into the cavities [3,4]. We have fabricated and measured microcavities with partially in-filled holes of different diameter [6] that exhibit selective control of the cavity mode excitation and resonance frequency. The cavities are excited by direct coupling of light via a channel waveguide with size-graded holes [8]. The photonic crystal microcavities were fabricated in SOI material and a Q-value of greater than 800 has been measured.



(a) *(b)*

Figure 1. (a) Hexagonal cavity in-filled 185 nm diameter holes with single size-graded holes and (b) Hexagonal cavity in-filled 185 nm diameter holes with two size-graded holes.

The microcavity uses a hexagonal lattice period of 420 nm and hole diameter of 280 nm. The smaller in-filling holes have diameters of 185 nm, as shown in Fig.1. The small change in the modal volume produced by the in-filling holes in the cavity is used to tune the resonance frequency [6]. Size-graded holes of 240 nm and 185 nm in the input and output channel waveguide confine the light at resonance and enhance the Q-factor and transmission of the

cavity by reducing unwanted reflection due to mismatch and through minimisation of vertical leakage [8,9]. The SOI waveguide structure has a silicon core thickness of 340 nm, with a lower cladding of 3 μm. Reactive ion etching was used for pattern transfer and the gas used for the silicon layer was $SiCl_4$.

The microcavities were measured with TE-polarised light in the S- to L-band wavelength range of 1480 nm to 1580 nm. Light is coupled into and out the waveguide using the end-fire approach and detected using a germanium-diode detector. Figure 2 shows measured TE transmission spectra for (i) a hexagonal cavity with in-filling holes of 185 nm diameter and one input/output reduced-size hole and (ii) an in-filled hexagonal cavity with 185 nm holes and two input/output reduced-size and graded holes. The measured Q-value for the cavity with a single reduce size input/output hole is about 150, at $\lambda \sim 1545.9$ nm. The measure Q-value for the cavity with 2 graded-size input/output holes is about 800 at $\lambda \sim 1542.6$ nm. The sharp transmission peak of the cavity with $Q \sim 800$ demonstrates the enhanced confinement effect produced by increasing the number of size-graded holes.

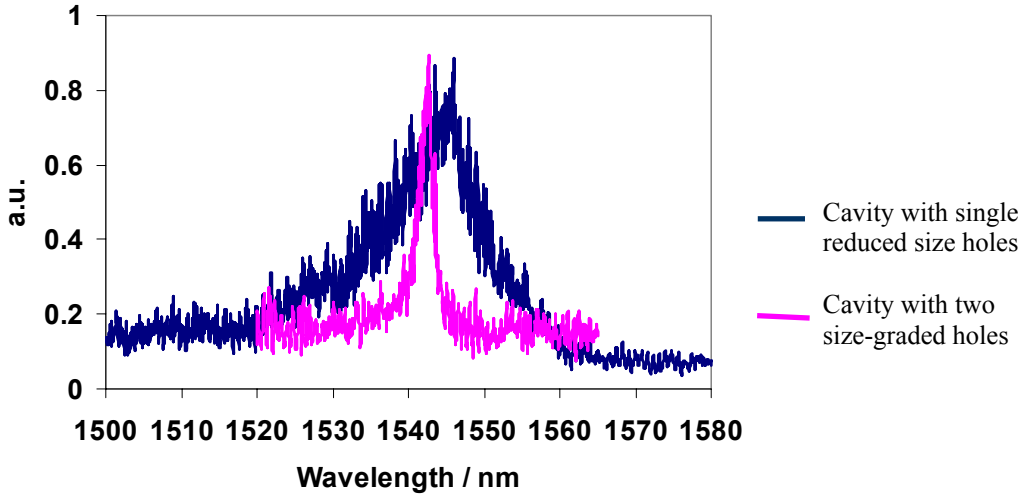


Figure 2. Transmission measurement for (i) a hexagonal cavity in-filled with 185 nm diameter holes and single reduced-size coupling holes, giving $Q \sim 150$ and (ii) a cavity in-filled with 185 nm diameter holes and two size-graded coupling holes, giving $Q \sim 800$.

Such confinement has also been observed by Noda et al. [3] in a microcavity of seven smaller holes together with a larger three rows wide channel waveguide and four periods of photonic crystal as a confinement barrier for the microcavity. However, this three rows wide channel waveguide can exhibit mini stop-band behaviour and is substantially multi-moded [5]. The slight shift in the resonance wavelength between the two configurations is small, but indicates the expected impact on the resonance of using more coupling holes.

Conclusions

The partially in-filled, directly-coupled cavity gives the ability to tune the resonance frequency by varying the interior hole diameter. A usefully large cavity Q-value of ~ 800 at $\lambda \sim 1542.6$ nm has been achieved and the resonance frequency has been shown to depend on the number of size-graded holes used in the input and output waveguide channels.

Acknowledgement
This research was supported through the PICCO project under the European Community IST programme.

References

[1] C. J. M. Smith, R. M. De La Rue, M. Rattier, S. Olivier, H. Benisty, C. Weisbuch, T. F. Krauss, R. Houdre, U. Oesterle, *Applied Physics Letters*, **Vol. 78**, No. 11, 1487-1489, 2001

[2] S. Fan, H. Haus, P. Villeneuve, J. Joanopoulos, *Optics Express*, **Vol. 13**, Iss. 1, 1998.

[3] S. Noda, A. Chutinan, M. Imada, *Nature*, **Vol. 407**, 608-610, 2000.

[4] S. Y. Lin, E. Chow, S. G. Johnson, J. D. Joanopolous, *Optics Letters.* **Vol. 26**, No. 23, 1903-1905, 2001.

[5] C. J. M. Smith, H. Benisty, S. Olivier, M. Rattier, C. Weisbuch, T. F. Krauss, R. M. De La Rue, R. Houdre, U. Oesterle, *Applied Physics Letters*, **Vol. 77**, No. 18, 2813-2815, 2000.

[6] H. G. Park, J. K. Hwang, J. Huh, H. Y. Ryu, Y. H. Lee, J. S. Kim, *Applied Physics Letters,* **Vol. 79**, No. 19, 3032-3034, 2001.

[7] O. Painter, J. Vuckovic, A. Scherer, *J. Opt. Soc. Am. B*, **Vol. 16**, No. 2, 1999.

[8] M. Palamaru, Ph. Lalanne, *Applied Physics Letters,* **Vol. 78**, No. 11, 1466-1468, 2001.

[9] J. S. Foresi, P. R. Villeneuve, J. Ferrera, F. R. Thoen, G. Steinmeyer, S. Fan, J. D. Joanopolous, L. C. Kimerling, H. I. Smith, E. P. Ippen, *Nature*, **Vol. 390**, 143-145, 1997.